COASTAL BIOGEOMORPHOLOGY

EDITED BY: Zhan Hu, Zeng Zhou, Simon Marius Mudd, Iris Möller and Zheng Gong

PUBLISHED IN: Frontiers in Marine Science

frontiers Research Topics

Frontiers eBook Copyright Statement

The copyright in the text of individual articles in this eBook is the property of their respective authors or their respective institutions or funders. The copyright in graphics and images within each article may be subject to copyright of other parties. In both cases this is subject to a license granted to Frontiers.

The compilation of articles constituting this eBook is the property of Frontiers.

Each article within this eBook, and the eBook itself, are published under the most recent version of the Creative Commons CC-BY licence. The version current at the date of publication of this eBook is CC-BY 4.0. If the CC-BY licence is updated, the licence granted by Frontiers is automatically updated to the new version.

When exercising any right under the CC-BY licence, Frontiers must be attributed as the original publisher of the article or eBook, as applicable.

Authors have the responsibility of ensuring that any graphics or other materials which are the property of others may be included in the CC-BY licence, but this should be checked before relying on the CC-BY licence to reproduce those materials. Any copyright notices relating to those materials must be complied with.

Copyright and source acknowledgement notices may not be removed and must be displayed in any copy, derivative work or partial copy which includes the elements in question.

All copyright, and all rights therein, are protected by national and international copyright laws. The above represents a summary only. For further information please read Frontiers' Conditions for Website Use and Copyright Statement, and the applicable CC-BY licence.

ISSN 1664-8714
ISBN 978-2-88976-942-1
DOI 10.3389/978-2-88976-942-1

About Frontiers

Frontiers is more than just an open-access publisher of scholarly articles: it is a pioneering approach to the world of academia, radically improving the way scholarly research is managed. The grand vision of Frontiers is a world where all people have an equal opportunity to seek, share and generate knowledge. Frontiers provides immediate and permanent online open access to all its publications, but this alone is not enough to realize our grand goals.

Frontiers Journal Series

The Frontiers Journal Series is a multi-tier and interdisciplinary set of open-access, online journals, promising a paradigm shift from the current review, selection and dissemination processes in academic publishing. All Frontiers journals are driven by researchers for researchers; therefore, they constitute a service to the scholarly community. At the same time, the Frontiers Journal Series operates on a revolutionary invention, the tiered publishing system, initially addressing specific communities of scholars, and gradually climbing up to broader public understanding, thus serving the interests of the lay society, too.

Dedication to Quality

Each Frontiers article is a landmark of the highest quality, thanks to genuinely collaborative interactions between authors and review editors, who include some of the world's best academicians. Research must be certified by peers before entering a stream of knowledge that may eventually reach the public - and shape society; therefore, Frontiers only applies the most rigorous and unbiased reviews.
Frontiers revolutionizes research publishing by freely delivering the most outstanding research, evaluated with no bias from both the academic and social point of view. By applying the most advanced information technologies, Frontiers is catapulting scholarly publishing into a new generation.

What are Frontiers Research Topics?

Frontiers Research Topics are very popular trademarks of the Frontiers Journals Series: they are collections of at least ten articles, all centered on a particular subject. With their unique mix of varied contributions from Original Research to Review Articles, Frontiers Research Topics unify the most influential researchers, the latest key findings and historical advances in a hot research area! Find out more on how to host your own Frontiers Research Topic or contribute to one as an author by contacting the Frontiers Editorial Office: frontiersin.org/about/contact

COASTAL BIOGEOMORPHOLOGY

Topic Editors:
Zhan Hu, Sun Yat-sen University, Zhuhai Campus, China
Zeng Zhou, Hohai University, China
Simon Marius Mudd, University of Edinburgh, United Kingdom
Iris Möller, Trinity College Dublin, Ireland
Zheng Gong, Hohai University, China

Citation: Hu, Z., Zhou, Z., Mudd, S. M., Möller, I., Gong, Z., eds. (2022). Coastal Biogeomorphology. Lausanne: Frontiers Media SA.
doi: 10.3389/978-2-88976-942-1

Table of Contents

05 ***Editorial: Coastal biogeomorphology***
Zhan Hu, Zeng Zhou, Yujie Chen, Simon Marius Mudd, Iris Möller and Zheng Gong

08 ***Processes Influencing Autocompaction Modulate Coastal Wetland Surface Elevation Adjustment With Sea-Level Rise***
Kerrylee Rogers and Neil Saintilan

26 ***Estimating Waves and Currents at the Saltmarsh Edge Using Acoustic Doppler Velocimeter Data***
Bing Liu, Yining Chen, Tinglu Cai, Yan Li and Li Sun

41 ***Sediment Bulk Density Effects on Benthic Macrofauna Burrowing and Bioturbation Behavior***
Lauren E. Wiesebron, Natalie Steiner, Claudia Morys, Tom Ysebaert and Tjeerd J. Bouma

57 ***Mechanisms of Pond Expansion in a Rapidly Submerging Marsh***
Joshua Himmelstein, Orencio Duran Vinent, Stijn Temmerman and Matthew L. Kirwan

72 ***Key Bioturbator Species Within Benthic Communities Determine Sediment Resuspension Thresholds***
Jaco C. de Smit, Muriel Z. M. Brückner, Katherine I. Mesdag, Maarten G. Kleinhans and Tjeerd J. Bouma

83 ***ADV-Based Investigation on Bed Level Changes Over a Meso-Macro Tidal Beach***
Wenhong Pang, Xiaoyan Zhou, Zhijun Dai, Shushi Li, Hu Huang and Yaping Lei

104 ***Effects of Waves and Sediment Disturbance on Seed Bank Persistence at Tidal Flats***
Zhenchang Zhu, Tjeerd J. Bouma, Qin Zhu, Yanpeng Cai and Zhifeng Yang

115 ***Salt Marsh and Tidal Flat Area Distributions Along Three Estuaries***
Maarten G. Kleinhans, Harke Douma, Elisabeth A. Addink, Laura Coumou, Tessa Deggeller, Robert Jentink, Edwin Paree and Jelmer Cleveringa

133 ***Experimental Tree Mortality Does Not Induce Marsh Transgression in a Chesapeake Bay Low-Lying Coastal Forest***
David C. Walters, Joel A. Carr, Alyssa Hockaday, Joshua A. Jones, Eliza McFarland, Katya E. Kovalenko, Matthew L. Kirwan, Donald R. Cahoon and Glenn R. Guntenspergen

145 ***Facilitating Salt Marsh Restoration: The Importance of Event-Based Bed Level Dynamics and Seasonal Trends in Bed Level Change***
Pim W. J. M. Willemsen, Erik M. Horstman, Tjeerd J. Bouma, Martin J. Baptist, Marinka E. B. van Puijenbroek and Bas W. Borsje

163 ***Green Nourishment: An Innovative Nature-Based Solution for Coastal Erosion***
Wen L. Chen, Peter Muller, Robert C. Grabowski and Nicholas Dodd

180 ***How Turbidity Mediates the Combined Effects of Nutrient Enrichment and Herbivory on Seagrass Ecosystems***
Xinyan Wang, Junhong Bai, Jiaguo Yan, Baoshan Cui and Dongdong Shao

191 ***Short-Term Sedimentation Dynamics of Temperate Mangroves in Western Port Bay, Victoria***
Sabrina Sayers and Ruth Reef

204 ***Oyster Reef Surfaces in the Central Wadden Sea: Intra-Reef Classification and Comprehensive Statistical Description***
Jan Hitzegrad, Leon Brohmann, Kai Pfennings, Tom K. Hoffmann, Anne K. Eilrich, Maike Paul, Mario Welzel, Torsten Schlurmann, Jochen Aberle, Achim Wehrmann and Nils Goseberg

226 ***Coastal Wetland Surface Elevation Change Is Dynamically Related to Accommodation Space and Influenced by Sedimentation and Sea-Level Rise Over Decadal Timescales***
Kerrylee Rogers, Atun Zawadzki, Laura A. Mogensen and Neil Saintilan

246 ***Linkage Between Mangrove Seedling Colonization, Sediment Traits, and Nitrogen Input***
Ziying He, Lingwei Yen, Hongjie Huang, Zihao Wang, Lili Zhao, Zhonghan Chen, Shing Yip Lee and Yisheng Peng

256 ***A Minimalist Model of Salt-Marsh Vegetation Dynamics Driven by Species Competition and Dispersal***
Alvise Finotello, Andrea D'Alpaos, Marco Marani and Enrico Bertuzzo

279 ***An Eco-Morphodynamic Modelling Approach to Estuarine Hydrodynamics & Wetlands in Response to Sea-Level Rise***
Kristian Kumbier, Kerrylee Rogers, Michael G. Hughes, Kirti K. Lal, Laura A. Mogensen and Colin D. Woodroffe

299 ***Wave Attenuation Over Mangroves in the Nanliu Delta, China***
Xiaoyan Zhou, Zhijun Dai, Wenhong Pang, Jie Wang and Chuqi Long

frontiers | Frontiers in Marine Science

TYPE Editorial
PUBLISHED 02 August 2022
DOI 10.3389/fmars.2022.988804

Check for updates

OPEN ACCESS

EDITED AND REVIEWED BY
Charitha Bandula Pattiaratchi,
University of Western Australia,
Australia

*CORRESPONDENCE
Yujie Chen
chenyj363@mail.sysu.edu.cn

SPECIALTY SECTION
This article was submitted to Coastal Ocean Processes, a section of the journal Frontiers in Marine Science

RECEIVED 07 July 2022
ACCEPTED 11 July 2022
PUBLISHED 02 August 2022

CITATION
Hu Z, Zhou Z, Chen Y, Mudd SM, Möller I and Gong Z (2022) Editorial: Coastal biogeomorphology. *Front. Mar. Sci.* 9:988804. doi: 10.3389/fmars.2022.988804

COPYRIGHT
© 2022 Hu, Zhou, Chen, Mudd, Möller and Gong. This is an open-access article distributed under the terms of the Creative Commons Attribution License (CC BY). The use, distribution or reproduction in other forums is permitted, provided the original author(s) and the copyright owner(s) are credited and that the original publication in this journal is cited, in accordance with accepted academic practice. No use, distribution or reproduction is permitted which does not comply with these terms.

Editorial: Coastal biogeomorphology

Zhan Hu[1,2,3], Zeng Zhou[4], Yujie Chen[1,2,3]*, Simon Marius Mudd[5], Iris Möller[6,7] and Zheng Gong[4]

[1]School of Marine Science, Sun Yat-Sen University, and Southern Marine Science and Engineering Guangdong Laboratory (Zhuhai), Zhuhai, China, [2]Guangdong Provincial Key Laboratory of Marine Resources and Coastal Engineering, Guangzhou, China, [3]Pearl River Estuary Marine Ecosystem Research Station, Ministry of Education, Zhuhai, China, [4]State Key Laboratory of Hydrology-Water Resources and Hydraulic Engineering, Hohai University, Nanjing, China, [5]School of GeoSciences, University of Edinburgh, Edinburgh, United Kingdom, [6]Department of Geography, Trinity College Dublin, Dublin, Ireland, [7]Department of Geography, University of Cambridge, Cambridge, United Kingdom

KEYWORDS

coastal wetlands, sea level rise (SLR), hydrodynamic process, bioturbation, biogeomormorphology, intertidal zone, bio-physical interaction

Editorial on the Research Topic
Coastal biogeomorphology

Biogeomorphic feedbacks are the two-way interactions between ecological and geomorphological processes, such as the effects of organisms on earth surface processes and landforms, and vice versa (Naylor et al., 2002). Approximately 84% of the continents' surface is covered by vegetation that is sufficiently dense to affect geomorphologic processes (Corenblit et al., 2011). In extreme environments with low vegetation coverage (e.g., drylands and Antarctica), the effect of biological crusts and bioturbation can still significantly affect geomorphic processes (Cannone et al., 2008; Viles, 2020). Knox (1972) presents one of the first studies on biogeomorphic feedbacks. As a precursor to subsequent works on the interplay between landform and biota changes, Knox reveals the non-linearities in the interactions between climate, vegetation and fluvial morphology processes. Since 2000, the field of biogeomorphological research has been thriving with a rapid increase in the number of related references and citations (Viles, 2020).

In coastal environments, various ecosystems such as intertidal mudflats, salt marshes, mangroves, sea grass beds and coral reefs are typical biogeomorphic systems, where landscape development is closely linked to the interaction between biota and abiotic conditions at multiple spatiotemporal scales (Mudd, 2011; Gong et al., 2021). It is increasingly recognized that biogeomorphic processes in these coastal ecosystems determine their key services and resilience (Kirwan and Mudd, 2012; Zhou et al., 2016). For instance, saltmarsh and mangrove wetlands can provide important services as coastal protection by attenuating wave energy and preventing sediment erosion (Spencer and Möller, 2013; Möller et al., 2014; Yao et al., 2018; Hu et al., 2022). These processes are clear examples of biostabilisation, which enhances accretion and makes coasts more resilient to storm impacts and Sea Level Rise (SLR). Biostabilization thus promotes the persistence of

these coastal ecosystems. In turn, bioturbation of the sediment by macrozoobenthic organisms' activities is an example of a biogeomorphic process that releases sediment into the coastal system, which has an important impact at both local and landscape scales (Cozzoli et al., 2020, Cozzoli et al., 2021).

Although the general concept of two-way bio-physical interactions is known to the research community, our understanding of the key biogeomorphic mechanisms and the related thresholds for ecosystem survival is still lacking. Thus, more research effort is needed to improve our capacity for a better, scientifically-informed, management of the coast. This is especially important in the context of coastlines' natural dynamism and their response to human interference and global climate change. These factors are driving changes to sea level, wave climates and sedimentary regimes that are unprecedented over Holocene timescales (De Dominicis et al., 2020; Hu et al., 2021). Appropriate coastal management must rely on advancements in theory and methodology, as well as, crucially the application of biogeomorphological research in coastal contexts (Viles, 2020). The 19 papers in this Research Topic address important coastal biogeomorphic processes, and can be grouped as: 1) coastal wetlands under SLR, 2) coastal protection services, 3) key traits and dynamics of coastal ecosystems, and 4) innovative research methodologies and their application.

The first group of articles in this Research Topic investigates the resilience of coastal wetlands under SLR. From a modelling perspective, Kumbier et al., shows that SLR may influence tidal range by changing wetland extents and intertidal wetland geomorphology through sedimentation. Thus, in channelized estuaries, interconnections between hydrodynamics and intertidal wetlands needs to be accounted for when estimating wetland response to SLR. Rogers et al. focus on relationships between SLR, sedimentation and coastal wetland dynamics, using short-term (< 10s years) data of surface elevation observation and long-term (> 10s years) data of ^{210}Pb chronology of shoreline change. It provides a rare comprehensive dataset of coastal wetland sedimentation and elevation adjustment in the southern hemisphere, and an interesting record of diverse marsh and mangrove response to SLR. As a complimentary study, Rogers and Saintilan assess the processes influencing surface morphodynamics including variation in substrate characteristics, autocompaction and vertical accretion. Walters et al. report a 5-year long field experiment to reveal the ability of marsh to retreat to adjacent uplands. Himmelstein et al. investigate the characteristics and mechanism of pond growth in coastal marshes under SLR. Importantly, they provide an empirical power-law equation to predict the pond growth and the critical time window for interventions to prevent the irreversible pond expansion or merging.

The second group of articles investigates the coastal protection service provided by wetlands. Zhou et al. document variations in wave attenuation by mangroves of different ages, providing a rare *in-situ* dataset and useful information on wetlands' wave attenuation capacity needed for nature-based coastal protection scheme. Besides wave attenuation, the promotion of sedimentation is another important ecosystem service of mangroves. Sayers and Reef report that while large scale (1 km^2) patterns of sedimentation are temporally consistent, small scale patterns (< 100 m^2) consist of large temporal variations, where local mangrove density and wave height seem to have no direct impact. Based on an XBeach model, Chen et al. illustrate that the combination of sand nourishment and seagrass meadow restoration (i.e., so-called 'green nourishment'), can be an effective nature-based coastal protection measure for sandy coasts.

The third group of contributions aims to reveal the key traits and dynamics of coastal ecosystems, which are closely related to their resilience and function. Hitzegrad et al. report topographical roughness parameters of *Magallana gigas* oyster reef surfaces in the central Wadden Sea. The obtained information can assist the quantification of the interaction between hydrodynamics and reef structures. Based on a mesocosm experiment, He et al. reveal that root morphological features of mangrove seedlings are significantly affected by substrate (sediment characteristics) but not by nitrogen input, providing implications for restoration. Contrastingly, Wang et al. report that nitrogen input together with herbivory may both influence the health of seagrass ecosystems, but their relative importance is mediated by turbidity. Zhu et al. investigate the impact of wave and related sediment dynamics on saltmarsh seed banks and imply that climate change may threaten saltmarsh persistence by wearing away its seed banks. Smit et al. find that when considering the reduction in critical bed shear stress (τ_{cr}) for sediment resuspension by a group of macrobenthic species, the specie that has the largest individual effect in reducing τ_{cr} plays a dominated role in determining τ_{cr} variation, rather than that with the highest metabolic rate. Continuing with the subject of bioturbation, Wiesebron et al. reveal that benthic macrofauna change their behavior under different sediment bulk densities (a measure of sediment compaction and water content): lower bulk density conditions lead to more active macrofaunal movement and sediment reworking. This subtle but important variation may have long-term impacts on tidal flat biogeomorphology.

The last group of articles develops either predictive modelling or new data processing techniques that can be used to quantify or predict ecogeomorphic evolution of coastal wetlands. Finotello et al. build a new marsh vegetation dynamics model based on the fundamental niche of each halophytic species, enabling the quantification of dispersal and interspecific competitions. Kleinhans et al. present a novel automated image classification method that allows objective mapping of saltmarsh and tidal flat area dynamcis at an unprecedented resolution. This method offers a practical tool for estuary-scale ecosystem management and

comparison between estuaries. Willemsen et al. applied recently-developed Optical (Hu et al., 2015) and Acoustic Surface Elevation Dynamics sensors (O-SED and A-SED) to continuously monitor bed level dynamics around the edge of natural and semi-natural salt marshes. The obtained data highlights possibilities of developing favorable conditions for marsh restorations. Liu et al. and Pang et al. address the technical challenges of using ADV (Acoustic Doppler Velocimeter) to separate wave and tidal current forcing and detect bed level change in coastal biogeomorphic systems.

Overall, the 19 articles in this Research Topic represent important datasets, interesting dynamics as well as novel methodology in coastal biogeomorphology. This Research Topic as a whole advances our current understanding and research capacity towards better management of the dynamic coastal biogeomorphic systems, and we hope that it inspires further discussion and exploration.

Author contributions

All authors listed have made a substantial, direct, and intellectual contribution to the work and approved it for publication.

Acknowledgments

We thank the authors of the papers included in this Research Topic for their excellent contributions. The authors thank the fundings from National Natural Science Foundation of China (No. 42176202), Innovation Group Project of South- ern Marine Science and Engineering Guangdong Laboratory (Zhuhai; No. 311021004), and 111 Project (B21018).

Conflict of interest

The authors declare that the research was conducted in the absence of any commercial or financial relationships that could be construed as a potential conflict of interest.

Publisher's note

All claims expressed in this article are solely those of the authors and do not necessarily represent those of their affiliated organizations, or those of the publisher, the editors and the reviewers. Any product that may be evaluated in this article, or claim that may be made by its manufacturer, is not guaranteed or endorsed by the publisher.

References

Cannone, N., Wagner, D., Hubberten, H. W., and Guglielmin, M. (2008). Biotic and abiotic factors influencing soil properties across a latitudinal gradient in Victoria land, Antarctica. *Geoderma* 144, 50–65. doi: 10.1016/j.geoderma.2007.10.008

Corenblit, D., Baas, A. C. W., Bornette, G., Darrozes, J., Delmotte, S., Francis, R. A., et al. (2011). Feedbacks between geomorphology and biota controlling earth surface processes and landforms: A review of foundation concepts and current understandings. *Earth-Sci. Rev.* 106, 307–331. doi: 10.1016/j.earscirev.2011.03.002

Cozzoli, F., Gomes da Conceição, T., Van Dalen, J., Fang, X., Gjoni, V., Herman, P. M. J., et al. (2020). Biological and physical drivers of bio-mediated sediment resuspension: A flume study on cerastoderma edule. *Estuarine Coast. Shelf. Sci.* 241, 106824. doi: 10.1016/j.ecss.2020.106824

Cozzoli, F., Shokri, M., Gomes da Conceição, T., Herman, P. M. J., Hu, Z., Soissons, L. M., et al. (2021). Modelling spatial and temporal patterns in bioturbator effects on sediment resuspension: a biophysical metabolic approach. *Sci. Total. Environ.* 792, 148215. doi: 10.1016/j.scitotenv.2021.148215

De Dominicis, M. D., Wolf, J., Jevrejeva, S., Zheng, P., and Hu, Z. (2020). Future interactions between Sea level rise, tides, and storm surges in the world's largest urban area. *Geophys. Res. Lett.* 47, e2020GL087002. doi: 10.1029/2020GL087002

Gong, Z., Chen, X., Zhou, Z., Ge, R., Chen, X., Yu, X., et al. (2021). The roles of biological factors in coastal sediment transport: a review. *Chin. Sci. Bull.* 66 (1), 53–62. doi: 10.1360/TB-2020-0291

Hu, Z., Borsje, B. W., van Belzen, J., Willemsen, P. W. J. M., Wang, H., Peng, Y., et al. (2021). Mechanistic modeling of marsh seedling establishment provides a positive outlook for coastal wetland restoration under global climate change. *Geophys. Res. Lett.* 48, e2021GL095596. doi: 10.1029/2021GL095596

Hu, Z., Lenting, W., van der Wal, D., and Bouma, T. J. (2015). Continuous monitoring bed-level dynamics on an intertidal flat: Introducing novel, stand-alone high-resolution SED-sensors. *Geomorphology* 245, 223–230. doi: 10.1016/j.geomorph.2015.05.027

Hu, Z., Lian, S., Zitman, T., Wang, H., He, Z., Wei, H., et al. (2022). Wave breaking induced by opposing currents in submerged vegetation canopies. *Water Resour. Res.* 58, e2021WR031121. doi: 10.1029/2021WR031121

Kirwan, M. L., and Mudd, S. M. (2012). Response of salt-marsh carbon accumulation to climate change. *Nature* 489, 550–553. doi: 10.1038/nature11440

Knox, J. C. (1972). Valley alluviation in southwestern Wisconsin. *Ann. Assoc. Am. Geograph.* 62, 401–410. doi: 10.1111/j.1467-8306.1972.tb00872.x

Möller, I., Kudella, M., Rupprecht, F., Spencer, T., Paul, M., van Wesenbeeck, B. K., et al. (2014). Wave attenuation over coastal salt marshes under storm surge conditions. *Nat. Geosci.* 7, 727–731. doi: 10.1038/ngeo2251

Mudd, S. M. (2011). The life and death of salt marshes in response to anthropogenic disturbance of sediment supply. *Geology* 39, 511–512. doi: 10.1130/focus052011.1

Naylor, L. A., Viles, H. A., and Carter, N. E. A. (2002). Biogeomorphology revisited: looking towards the future. *Geomorphology* 47, 3–14. doi: 10.1016/S0169-555X(02)00137-X

Spencer, T., and Möller, I. (2013)Mangrove systems. in: Sherman, D.J. (Ed.), coastal geomorphology. In: *Treatise on geomorphology* (San Diego: Academic Press). Available at: http://www.sciencedirect.com/science/article/pii/B9780123747396002906 (Accessed September 29, 2016).

Viles, H. (2020). Biogeomorphology: Past, present and future. *Geomorphology* 366, 106809. doi: 10.1016/j.geomorph.2019.06.022

Yao, P., Chen, H., Huang, B., Tan, C., Hu, Z., Ren, L., et al. (2018). Applying a new force-velocity synchronizing algorithm to derive drag coefficients of rigid vegetation in oscillatory flows. *Water* 10, 906. doi: 10.3390/w10070906

Zhou, Z., Ye, Q., and Coco, G. (2016). A one-dimensional biomorphodynamic model of tidal flats: Sediment sorting, marsh distribution, and carbon accumulation under sea level rise. *Adv. Water Resour.* 93, 288–302. doi: 10.1016/j.advwatres.2015.10.011

frontiers in Marine Science

ORIGINAL RESEARCH
published: 21 July 2021
doi: 10.3389/fmars.2021.694039

Processes Influencing Autocompaction Modulate Coastal Wetland Surface Elevation Adjustment With Sea-Level Rise

Kerrylee Rogers[1] and Neil Saintilan[2]*

[1] School of Earth, Atmospheric and Life Sciences, University of Wollongong, Wollongong, NSW, Australia, [2] Department of Earth and Environmental Science, Macquarie University, Sydney, NSW, Australia

The fate of coastal wetlands and their ecosystem services is dependent upon maintaining substrate elevations within a tidal frame that is influenced by sea-level rise. Development and application of morphodynamic models has been limited as few empirical studies have measured the contribution of key processes to surface elevation change, including mineral and organic matter addition, autocompaction of accumulating sediments and deep subsidence. Accordingly, many models presume that substrates are in equilibrium with relative sea-level rise (RSLR) and the composition of substrates are relatively homogenous. A 20-year record of surface elevation change and vertical accretion from a large tidal embayment in Australia coupled with analyses of inundation frequency and the character of sediments that have accumulated above mean sea level was analyzed to investigate processes influencing surface elevation adjustment. This study confirms the varying contribution of addition, decomposition and compression of organic material, and mineral sediment consolidation. Autocompaction of substrates was proportional to the overburden of accumulating sediments. These processes operate concurrently and are influenced by sediment supply and deposition. Vertical accretion was linearly related to accommodation space. Surface elevation change was related to vertical accretion and substrate organic matter, indicated by carbon storage above mean sea level. Surface elevation change also conformed to models that initially increase and then decrease as accommodation space diminishes. Rates of surface elevation change were largely found to be in equilibrium with sea-level rise measured at the nearest tide gauge, which was estimated at 3.5 mm y^{-1} over the period of measurements. As creation of new accommodation space with sea-level rise is contrary to the longer-term history of relative sea-level stability in Australia since the mid-Holocene, striking stratigraphic variation arises with deeper sediments dominated by mineral sands and surficial sediments increasingly fine grained and having higher carbon storage. As the sediment character of substrates was found to influence rates of surface elevation gain, we caution against the unqualified use of models derived from the northern hemisphere where substrates have continuously adjusted to sea-level rise and sediment character is likely to be more homogenous.

Keywords: accommodation space, sedimentation, vertical accretion, subsidence, consolidation, surface elevation tables, marker horizons

OPEN ACCESS

Edited by:
Simon Marius Mudd, University of Edinburgh, United Kingdom

Reviewed by:
Begoña Pérez-Gómez, Ports of the State, Spain
Inmaculada Rodríguez-Santalla, Rey Juan Carlos University, Spain

****Correspondence:***
Kerrylee Rogers
kerrylee@uow.edu.au

Specialty section:
This article was submitted to Coastal Ocean Processes, a section of the journal Frontiers in Marine Science

Received: *12 April 2021*
Accepted: *16 June 2021*
Published: *21 July 2021*

Citation:
Rogers K and Saintilan N (2021) Processes Influencing Autocompaction Modulate Coastal Wetland Surface Elevation Adjustment With Sea-Level Rise. Front. Mar. Sci. 8:694039. doi: 10.3389/fmars.2021.694039

INTRODUCTION

The influence of accelerating sea-level rise (SLR) (Church et al., 2013) on tidal dynamics has directed attention to the fate of saline coastal wetlands and the ecosystem services they provide (Reed, 1990; Morris et al., 2002; Krauss et al., 2014). The response of coastal wetlands to SLR is dependent upon feedbacks between hydrodynamics, sedimentation, plant productivity, sediment diagenesis, and organic matter decomposition (Pethick, 1981; Allen, 2000; Morris et al., 2002; Alongi, 2008). These feedbacks influence wetland substrate elevations and are important when considering the fate of coastal wetlands exposed to rising sea level. As such, there has been increasing focus on measuring and parameterizing processes contributing to elevation adjustment (see reviews by Fagherazzi et al., 2012; Wiberg et al., 2020). Allen (2000) conceptualized a relatively simple one dimensional model describing substrate elevation adjustment relative to a moving tidal frame that is influenced by SLR (ΔE). In this model, the change in tidal position of a wetland surface is attributed to the addition of mineral sediment (ΔS_{min}) and organic material (ΔS_{org}), and the degree of change due to autocompaction (ΔP). Critically, this adjustment is relative to the additional vertical space created by SLR for sediment accumulation (ΔM). The term "accommodation space" is used to describe the vertical space for mineral and sediment accumulation. In the context of this model, the variable ΔM incorporates available accommodation space created by both eustatic, tectonic and isostatic processes influencing relative SLR, whilst ΔP describes the additional accommodation space created by autocompaction.

$$\Delta E = \Delta S_{min} + \Delta S_{org} - \Delta P - \Delta M \quad (1)$$

Resolving spatial and temporal patterns in surface elevation change is crucial for developing and validating morphodynamic models of the response of coastal wetlands to a shifting tidal frame as sea level rises, and some efforts have been directed toward this task. Early empirical studies found that accretion was proportional to tidal position and proposed that this was due to negative feedbacks between these factors; the ensuing outcome of negative feedbacks was proposed to be an asymptote in substrate elevations as they age (Kestner, 1975; Pethick, 1981). Subsequent empirical models described sedimentation in the context of inundation depth and distances to sediment sources, such as creeks and channels, with functions taking an exponential (Temmerman et al., 2003) or linear form (Krone, 1987; French, 1993). Physical models built upon Exner's equation of conservation of mass applied advection diffusion equations (Rinaldo et al., 1999) that could be modified to account for distances to sediment sources. As empirical data of processes contributing to surface elevation change became available, models have evolved and increased in complexity. The empirically developed model of Morris et al. (2002) ascribed surface elevation change to both organic matter addition and mineral sediment addition that was proportional to depth below mean high tide and organic matter addition was parameterized as a function of the standing density of plant biomass or above ground productivity. The productivity function was expressed as a second order polynomial that describes the relationship between productivity of *Spartina alterniflora* and depth below mean high tide, and coefficients describe the tolerance of vegetation to inundation and the inundation depth of peak productivity. Application of a modified form of Exner's equation by Marani et al. (2013) quantified sediment deposition on the basis of settling velocity, bulk density and sediment porosity, and was governed by hydrodynamic transport regulated by tidal flooding. It also allowed for the rate of organic matter production to be modulated by compaction and decomposition processes, and incorporated the varying tolerance of different species to inundation and associated feedbacks with organic matter addition to substrates. The Organic-Inorganic Marsh Accretion and Stratigraphy-Numerical (OIMAS-N) model (Mudd et al., 2009) takes a one-dimensional form and simulates the evolution of a sediment column with SLR. It specifically incorporates organic matter addition, decay of three carbon pools (refractory, fast labile, and slow labile), inorganic sedimentation, and compaction. The model is parameterized so that organic matter declines linearly away from the surface and is proportional to above-ground biomass (as per Morris et al., 2002) and inorganic sedimentation is linearly related to and inundation. Compaction is a function of void space and the compressibility of substrate material of varying fabric (i.e., mineral or organic) and size (i.e., sand and silt). The Wetland Accretion Rate Model of Ecosystem Resilience (WARMER) model (Swanson et al., 2014; Thorne et al., 2018) has a similar structure and incorporates mineral sediment accretion, organic matter addition and decomposition and compaction. Mineral sediment is parameterized to increase linearly with increasing inundation depth, organic matter addition follows Morris et al. (2002), organic matter decomposition declines exponentially from the surface, and compaction varies with sediment porosity (as per Callaway et al., 1996).

Currently there is general agreement that net vertical accretion, arising from mineral sedimentation and erosion, is a function of accommodation space. This is commonly and expressed in models on the basis of elevation or depth below mean high tide and related to energy pathways that transport sediment for deposition or erosion (Fagherazzi et al., 2012). Model functions variably take a linear form (for example Krone, 1987; French, 1993) or exponential form (for example Temmerman et al., 2003). Organic matter accretion may also be expressed as a function of accommodation space, either linearly (D'Alpaos et al., 2007), or as a second-order polynomial with peak productivity delimited by the vertical distribution of vegetation (Morris et al., 2002). However, there is less agreement on attribution of the post-depositional behavior of mineral and organic matter in substrates (Wiberg et al., 2020; Zhang et al., 2020).

Empirical data and associated models are commonly derived from wetlands of the mid-Atlantic coasts of the United States and Europe, southern coasts of the North Sea, and Pacific coasts of the United States, where wetlands have been adjusting to relative sea-level rise (RSLR) for millennia (Fagherazzi et al., 2012; Wiberg et al., 2020). These locations, often termed intermediate-field locations due to their proximity to extensive

areas of land-based ice, have been undergoing vertical land movement due to glacio-isostatic adjustment (Murray-Wallace and Woodroffe, 2014; Khan et al., 2015). This adjustment has contributed to ongoing RSLR throughout the Holocene, despite relatively stable eustatic sea levels over the past ∼7,000 years. Holocene sea level records at intermediate-field locations contrast far-field locations, predominantly in the southern hemisphere, where sea level records generally exhibit a mid-Holocene highstand (the timing and magnitude is spatially variable) before falling to present levels over the past few millennia. Rogers et al. (2019) proposed that movement of the tidal frame relative to land surfaces at intermediate-field locations over the past few millennia promotes preservation of organic matter and creation of new accommodation space. Conversely, sea-level stability, or a fall following a highstand, promotes decomposition of organic matter and accommodation space becomes increasingly limited (Rogers et al., 2019). This hypothesis was confirmed in global-scale analyses of carbon content within saltmarsh sediments, which found carbon content is generally lower at far-field locations than intermediate-field locations, and carbon is generally concentrated near the active rooting zone of saltmarsh vegetation at far field locations. The predominance of models derived from intermediate-field empirical data may be problematic when applied to the southern hemisphere as they commonly presume substrates are relatively homogenous with little variation in stratigraphy, or that elevations gain corresponds to RSLR. Empirical data from a range of settings, particularly in the southern hemisphere where there are considerable data gaps, are needed to fully elucidate controls on coastal wetland evolution under SLR.

This paper seeks to address some of these data gaps by analyzing a 20-year observational record of surface elevation change, vertical accretion and by deduction, autocompaction of wetland surfaces from a tidal embayment in southern Australia. Westernport Bay, located east of Melbourne, has a complex intertidal vegetation composition that includes zones dominated by mangroves, saltbush, herbaceous saltmarsh and rushes. Differentiation of processes contributing to autocompaction, namely addition/decomposition of organic matter, compression of organic matter and consolidation of mineral sediments was facilitated by analyses of substrate composition. The overall aim of this study was to conceptualize processes contributing to surface elevation adjustment with SLR. The specific objectives were to:

i) identify processes influencing surface morphodynamics that account for variation in substrate characteristics, autocompaction and vertical accretion;
ii) validate existing modeling approaches by applying functions of varying structure (i.e., linear, exponential, peak models) to develop relationships between vertical accretion, surface elevation change, autocompaction, and indicators of tidal position (i.e., elevation and inundation frequency); and
iii) verify whether surface elevation change is in equilibrium with the shifting tidal frame.

MATERIALS AND METHODS

Study Site and Design

Westernport Bay (38°21′S, 145°13′E) is a large coastal embayment (∼680 km^2). It drains a catchment area of 3,433 km^2 and is located east of Melbourne Victoria, Australia (**Figure 1**). The region is relatively tectonically and isostatically stable and vertical land movement of tide gauges is negligible (White et al., 2014; Khan et al., 2015). Post-glacial sea level is reported to have increased to a highstand of 1–1.5 m above present levels approximately 6,900 cal. yr BP before falling to present levels after 2,000 cal. yr BP (Lewis et al., 2013; Dougherty et al., 2019). The region is also prone to periodic drought associated with negative phases of the Southern Oscillation, and an increase in the frequency of positive phases of the Southern Annular Mode and the Indian Ocean Dipole (Dey et al., 2019). The influence of drought on rainfall has been associated with changes in substrate elevations of coastal wetlands around Westernport Bay (Rogers et al., 2005b).

Westernport Bay has two entrances to Bass Strait; the constriction of the eastern entrance near San Remo causes tides to propagate relatively freely through the Western entrance, clockwise around French Island until they converge with anticlockwise tidal movement. The tidal regime is semi diurnal with a tidal range of up to 3.1 m. Significant tidal amplification occurs along the upper North Arm of Westernport Bay (Water Technology, 2014). Despite its size, the embayment is relatively shallow and tides comprise approximately 30% of the total volume at high tide (Lee in Boon et al., 2011). Westernport Bay includes extensive intertidal flats (∼270 km^2) that supports mangrove and saltmarsh communities along its low energy intertidal shorelines, estimated to cover approximately 12.3 and 10.9 km^2, respectively (Boon et al., 2011). These wetlands comprise a lower elevation mangrove zone that supports the cold tolerant mangrove, *Avicennia marina*, which is near its most latitudinal limit at this location. The upper intertidal zone also supports a dense thicket of saltmarsh shrubs of the genus *Tecticornia* and a landward zone of herbs, grasses and sedges that are regarded to be highly diverse (Boon et al., 2011).

Rogers et al. (2005b) presented results from a network of surface elevation tables (SET) and marker horizons (MH) established in 2000. These SETs were established to provide quantitative information on the dynamics of mangrove and saltmarsh vegetation and changes in rates of sedimentation and surface elevation. This network comprised 24 SET-MH stations in a nested design whereby six SETs were co-located at French Island, Kooweerup, Quail Island, and Rhyll (**Figure 1**). At each location, SETs were positioned in groups of three within structurally similar vegetation; three were located in the mangrove zone, lower in the tidal frame, and three were located in herbaceous saltmarsh zones higher in the tidal frame. Some saltmarsh SET locations have become increasingly dominated by *Tecticornia* over the 20 year analysis period, particularly at Kooweerup (*pers. obs.*). This paper provides an updated analysis from this network.

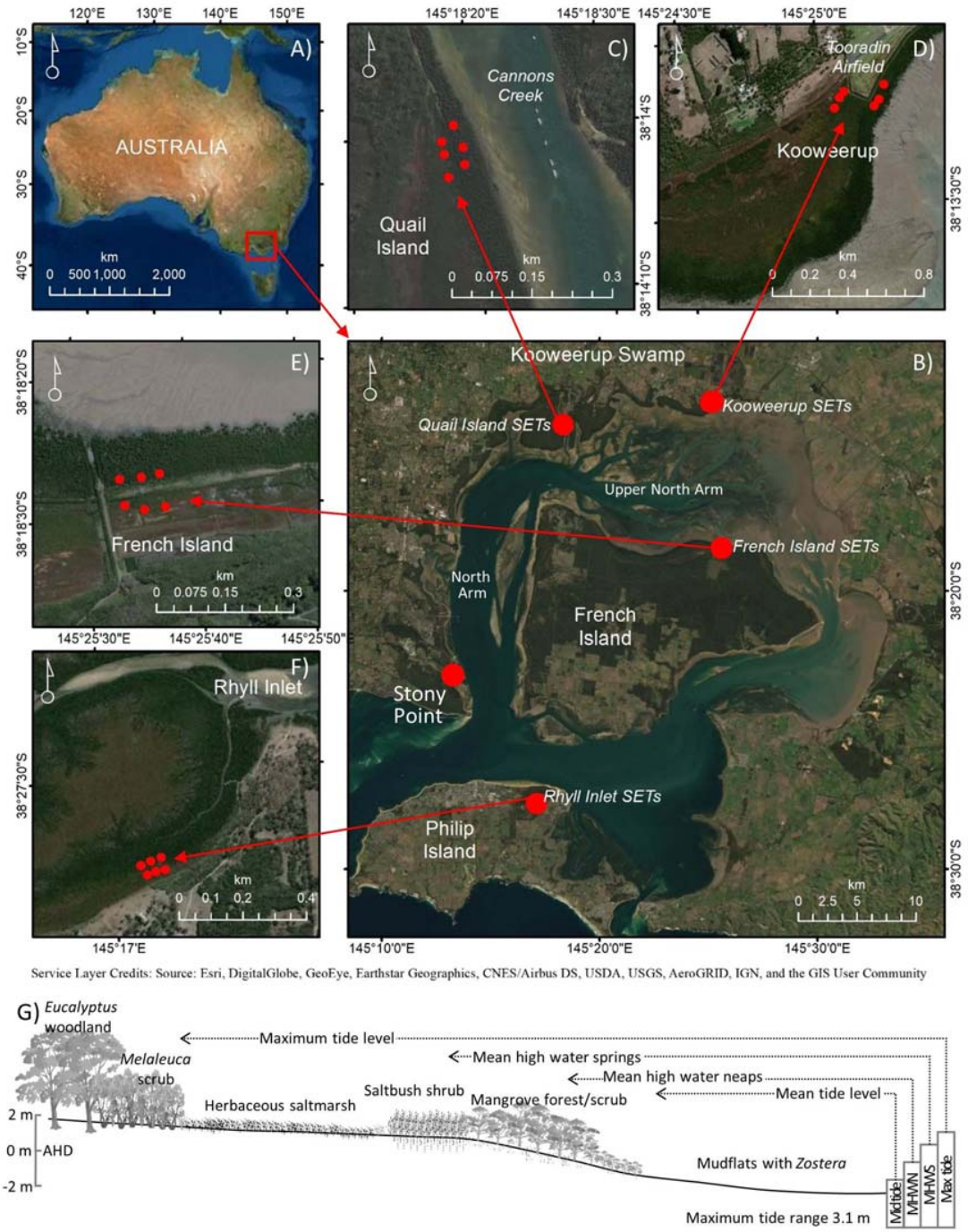


FIGURE 1 | Location of **(A)** Westernport Bay, Australia, and the **(B)** focal sites in this study at **(C)** Quail Island, **(D)** Kooweerup, **(E)** French Island, **(F)** Rhyll, and **(G)** distribution of vegetation communities with respect to the tidal frame [adapted from Bird (1986)].

Inundation Frequencies and Water Levels

Analyses of variation in water levels associated with tidal inundation at co-located mangrove and saltmarsh SETs at each study site were undertaken using hobo water level loggers. The vertical and horizontal position of each SET and hobo water level logger was determined using RTK-GPS during field campaigns. All vertical positions are henceforth reported according to the Australian height datum (AHD). The frequency of inundation was determined for each logger on the basis of whether the logger was inundated for each 15 min logging increment over the logging period; logging periods exceeded 6 months at each study

site and included highest high spring tides. The nearest tide gauge is managed by the local port authority and is located at Stony Point (Station no. 586268). This gauge underwent repositioning in 2017, and to control for inaccuracies that may arise from moving the tide gauge, processed data was only used for the period of August 1981 to July 2017. Processed data was converted to AHD. Maximum daily water level from each logger (logged at 15-min intervals) and the Stony Point tide gauge (logged at 6-min intervals) was compared to identify tidal modification at study sites. The maximum, minimum and mean recorded water level recorded at the tide gauge at Stony Point over the period of water-level logging was also determined. This facilitated the development of a relationship between elevation and inundation frequency. To do so, the elevations above the maximum water level were presumed to be rarely inundated; elevations below the minimum water level were presumed to be inundated 100% of the time, whilst the mean water level was presumed to represent the elevation with an inundation frequency of 50%. Inundation frequencies were plotted against elevation and the best model was used to determine a relationship between elevation and inundation frequencies. This model was used to determine inundation frequency of each SET-MH monitoring station and core locations.

Processed minimum, mean and maximum monthly water-level data for the Stony Point tide gauge was also accessed for the full record length. Conversion of this data to be relative to AHD meant the position of SETs and the tidal frame were determined using the same datum. This processed tide gauge data underwent additional processing to remove any months where data gaps were greater than 10% of the gauging frequency each month. Linear regressions were used to identify the rate of change in minimum, mean, and maximum monthly water levels for the full record length. As intertidal vegetation is typically positioned above mean sea level, mean and maximum linear regressions were subsequently used to indicate change in intertidal vegetation tidal position.

Sediment Characterization

Sediment cores of approximately 1.5 m length were collected in 2017. Cores were collected adjacent to mangrove and saltmarsh SET monitoring stations at each study site. Cores were extracted in aluminum tube of 75 mm diameter. The degree of sediment compaction that occurred during core collection was determined and cores were capped to ensure they remained continuous and intact. Cores were placed in cold storage at 4°C until sample preparation was undertaken. The position of each core at the time of extraction was determined using an RTK-GPS. Sediment cores were split longitudinally and half of the core was subsampled at intervals of 2 cm for the upper 10 cm of sediment, every 5 cm to 1 m depth and every 10 cm below 1 m depth for further analysis. The remaining core was placed in storage. Grain size of each sample was determined (μm) using a Malvern Mastersizer 2000 laser diffractometer. To determine dry bulk density (g cm^{-3}), samples were oven dried to constant weight at 60°C. Dry sample weight was determined and bulk density (BD) was estimated as the ratio of dry sample mass to wet sample volume. Each sample was then homogenized by grinding to a fine powder using a Retsch three-dimensional vibrator mill (Type-MM-2: Haan, Germany). Samples were analyzed for percentage carbon (%C) using dry combustion techniques by the Environmental Analysis Laboratory at Southern Cross University.

Sediment profiles were developed that characterized grainsize, bulk density and carbon content for each core. Core depths were calibrated to AHD to facilitate comparisons on the basis of elevation. Depth constrained cluster analysis was undertaken for grainsize fraction, bulk density and carbon content in R using the Rioja package. The depth of clusters, with respect to AHD were used to identify consistent patterns between study sites. Total carbon content in the upper 30 cm was quantified to indicate near surface carbon content of each core. Total carbon content was also quantified for sediments positioned between 0 m AHD (approximating MSL) and the wetland surface to represent carbon storage across the vertical distribution of intertidal vegetation. ANOVAs were undertaken on both estimates of carbon in the upper 30 cm and above MSL to identify statistical differences between cores extracted from mangrove and saltmarsh. C content above MSL was standardized for the volume of sediment above MSL; this characterized the C content per meter of substrate (i.e., g cm^{-2} m^{-1}). Linear regression analyses were undertaken to establish relationships between C content either in the upper 30 cm, C content above MSL (i.e., above 0 m AHD), standardized C content, and elevation and inundation frequency.

Surface Elevation Morphodynamics

SET-MH techniques were used to characterize surface elevation morphodynamics and SETs were established in Westernport Bay in 2000 (Rogers et al., 2005b). The SET acts as a stable benchmark against which measurements in substrate elevation change can be determined (Cahoon et al., 2002). Each SET monitoring station includes a platform that protects substrates from compression and compaction during installation and whilst taking measurements. At each SET monitoring station, a vertical benchmark pole was inserted to the point of refusal and extends to substrate depths of up to 6 m. The original SET design was used in this study and is composed of a horizontal arm that is positioned on the vertical benchmark pole; this horizontal arm is positioned in the same location using a spirit level. A plate at the end of the horizontal arm accommodates pins that are lowered to the wetland surface, and the height of each pin above the horizontal plate is measured. At each SET monitoring station, measurements of nine pins are taken in four arm directions; this generated 36 measurements of substrate elevation at each monitoring station. Repeated measurements of the height of pins above the horizontal plate were taken in four arm directions at each station. This provided time-series data of relative surface elevation change for each pin. This large dataset was subsequently reduced to determine the mean relative surface elevation change for each SET monitoring station at each measurement time. Measurements of SET elevation using an RTK-GPS allowed measurements of surface elevation change to be calibrated to AHD and for distances to the wetland edge and

main channel at Rhyll to be calculated. Due to the multi-decadal period of measurements, some benchmark poles had undergone corrosion or were damaged by debris. In some cases, damage became substantial enough that the benchmark was no longer regarded to be stable. This was evident for one mangrove SET at Quail Island and one saltmarsh SET at Kooweerup. Deficits in funding limited the capacity to undertake annual measurements. Measurements were taken initially in October 2000 and repeated measurements were taken in November 2001, November 2003, December 2009, May 2015, April 2016, May 2017, December 2018, and November 2019.

Feldspar marker horizons were established in three replicate plots of 50 cm × 50 cm at the margins of each SET monitoring station platform when baseline measurements were undertaken in 2000. When subsequent SET measurements were taken, mini cores were extracted from each MH plot and the vertical increase in sediment that had accumulated above the MH was determined. This provided time-series data of vertical accretion at each plot; this data was subsequently reduced to indicate vertical accretion at each monitoring station over time. The MH is prone to loss due to dispersal associated with bioturbation and tides (Cahoon and Turner, 1989). Over the study period, the ability to detect MH diminished and results were reported only when the MH could be detected; this was particularly apparent for mangrove MH.

Statistical Analyses of Surface Elevation Morphodynamics

Linear regression analyses of surface elevation change and vertical accretion were undertaken to determine mean rates of surface elevation change and vertical accretion for each SET-MH monitoring station. Analyses of coefficient of determination (r^2) and rates of change were undertaken to determine confidence in linear regression analyses of rates of vertical accretion and surface elevation change. Results of surface elevation change at one SET monitoring station in the mangrove at Quail Island was excluded from subsequent analyses due to damage.

Subsequent analyses were undertaken to identify processes influencing rates of surface elevation change (i.e., $\Delta S_{min} + \Delta S_{org} - \triangle P$). Linear regression analyses were undertaken to determine the relationship between rates of surface elevation gain, vertical accretion and available accommodation space; the elevation of SET-MH monitoring stations and modeled inundation frequency was used to indicate accommodation space. These relationships were assessed on the basis of coefficient of determination and Akaike information criterion with correction for small sample sizes (AICc). An exponential model that relates accretion to elevation, and distances to sediment sources (i.e., wetland edge and main channel) was also applied to measurements of vertical accretion using elevation and also substituting inundation for elevation (Temmerman et al., 2003). This model describes sedimentation rates on the basis of depth below mean high tide (H), distance to nearest creek edge (Dc), and marsh edge (De), and parameters (k, l, m, n), and has the form indicated in equation 2. Parameters were solved on the basis of 1,000 iterations until convergence was achieved at a significance level of 0.05.

$$Sedimentation\ rate = ke^{lH} \cdot e^{mD_c} \cdot e^{nD_e} \quad (2)$$

For measurements of surface elevation change, we also investigated whether peaks associated with organic matter production were evident in rates of surface elevation change. As surface elevation change describes the combined influence of surface accretion and processes operating within the substrate, it was not appropriate to fit a second order polynomial, as per Morris et al. (2002). Rather, best-fit Gaussian and Lorentzian peak models were applied to the relationship between surface elevation change, and elevation and inundation; care was taken to recognize zonation by generating a peak for mangrove and saltmarsh surface elevation change.

A two-way paired *t*-test was undertaken to determine whether rates of surface elevation change differed from rates of vertical accretion at each SET-MH monitoring station. The deficit between rates of vertical accretion (i.e., ΔS_{min}) and surface elevation change, which incorporates the combined influence of sediment consolidation, organic matter addition/decomposition and compression (i.e., $\Delta S_{org} - \triangle P$) was determined; for simplicity this was termed autocompaction. Autocompaction error was determined by propagating errors in rates of surface elevation change and vertical accretion. Linear regression analyses were undertaken to establish relationships between rates of surface elevation change, vertical accretion, autocompaction and substrate organic matter, using carbon storage above MSL to indicate volume of organic matter. A mixed model linear regression analysis was undertaken to determine the relationship between surface elevation change, vertical accretion and substrate carbon storage above MSL, with the hypothesis confirmed on the basis of coefficient of determination and *p*-value.

Equilibrium Analysis: Changing Tidal Position

Maintenance of tidal position (i.e., $\Delta E = 0$) indicates that the wetland substrate is adjusting in equilibrium with increasing accommodation space created by RSLR and autocompaction (i.e., $\Delta S_{min} + \Delta S_{org} - -\Delta P - -\Delta M$). Analyses of maximum, mean and minimum monthly water levels confirmed that rates of change to boundaries defining intertidal vegetation accommodation space were not consistent; that is, the rate of rise of mean water level was higher than the rate of rise of maximum water level between 1981 and 2017 (see **Figure 2F**). A more sophisticated approach for measuring changes to the tidal frame was required prior to assessing changes to tidal position. Changes to the tidal frame relevant to intertidal vegetation (i.e., from mean water level to maximum water level) was defined at each time step. The relative increase in substrate elevation was then defined as the difference between the substrate surface elevation and mean water level at each time step. By deduction, change in tidal position (i.e., ΔE) was determined as the difference between the rate of change in the tidal frame and relative substrate elevation at each time step. All measurements

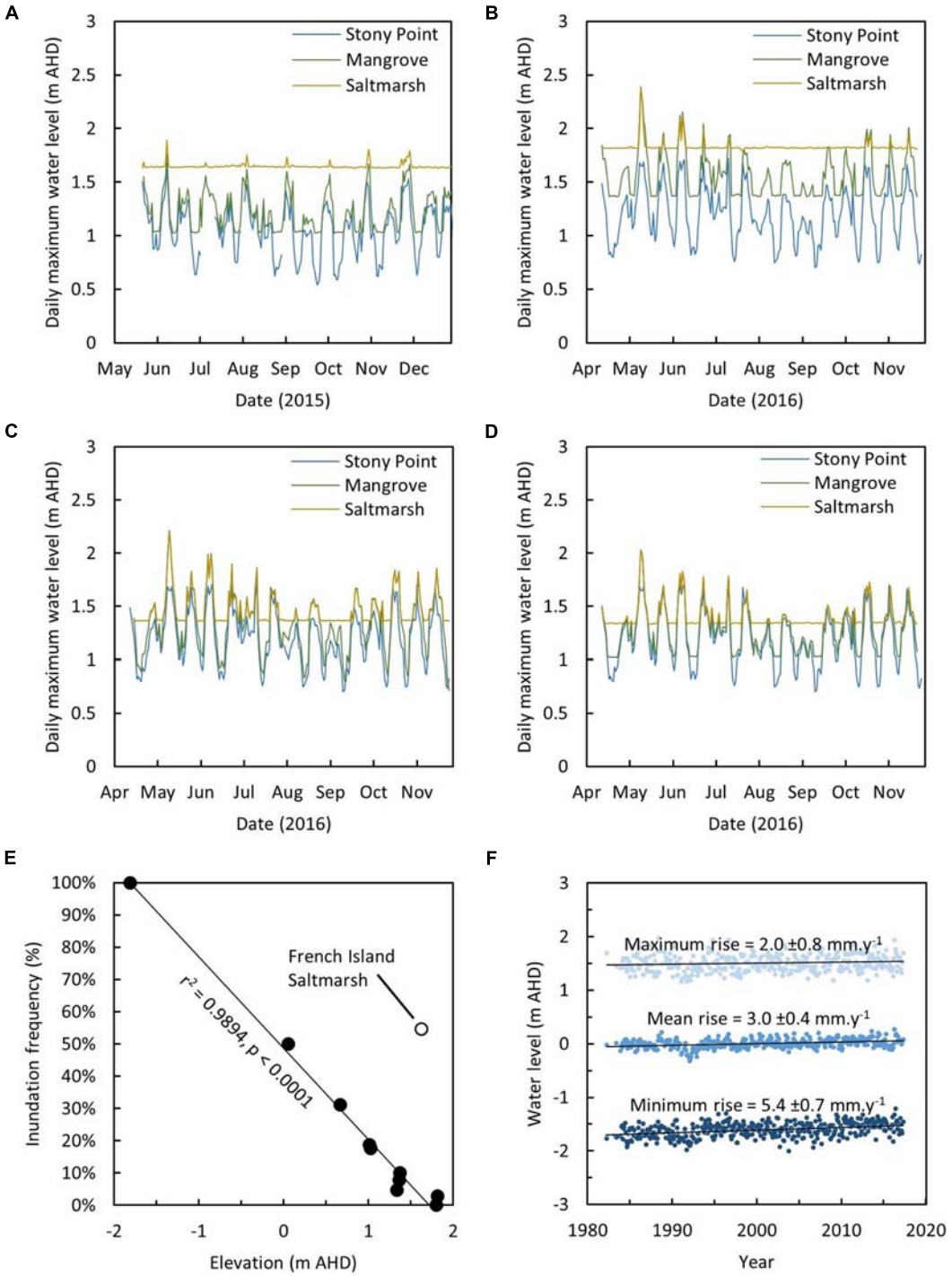


FIGURE 2 | Daily maximum water levels recorded in the mangrove and saltmarsh at **(A)** French Island, **(B)** Kooweerup, **(C)** Quail Island, and **(D)** Rhyll, **(E)** relationship between inundation frequency and elevation (m AHD) and **(F)** increase in maximum, mean, and minimum monthly water levels at the Stony Point tide gauge.

were made relative to AHD. Accordingly, values near zero were presumed to indicate maintenance of tidal positions, positive values indicate an increase in tidal position and negative values indicate decreasing tidal position. To account for any errors in SET measurements and subsequent analyses, a buffer of ±2 mm y^{-1} was applied to all values, particularly when determining values near zero Values exceeding 2 mm y^{-1} were regarded to be increasing their position in the tidal frame and values lower than −2 mm y^{-1} were regarded to be decreasing their position in the tidal frame.

Variation in tidal position (i.e., ΔE) should be interpreted in the context of available accommodation space or substrate elevation, particularly as mineral vertical accretion and organic matter accumulation (i.e., $\Delta S_{min} + \Delta S_{org}$) are likely to vary on the basis of accommodation space. Hence, rates of change in tidal position were compared to substrate elevation at the time of last SET measurement. This also provided the capacity to determine the elevation at which substrate elevation gain corresponded to the rate of increase in accommodation space, or the equilibrium elevation. The mean elevation of all values where tidal position was maintained (i.e., $\Delta E = 0 \pm 2$ mm y^{-1}) were used to approximate the equilibrium elevation range across Westernport Bay.

The longer-term resilience of locations where tidal positions were diminishing were estimated by projecting observed surface elevation change, mean water level and maximum water level trajectories. Resilience was presumed to be exhausted when substrate elevations were less than mean water level, as this elevation delimits the lower boundary of mangrove vegetation and inundation frequencies at lower elevations are presumed to be beyond the physiological tolerance of mangroves. This analysis does not incorporate anticipated projections in SLR or loss of tidal position due to erosion rates beyond that already incorporated in rates of surface elevation change.

RESULTS

Inundation Frequencies and Increasing Water Levels

Inundation frequency was variable between study site logging locations, but was generally higher in the mangrove where substrate elevations are lower than in the saltmarsh (**Supplementary Figure 1**). The saltmarsh SETs at French Island were the only exception where inundation frequency was estimated at approximately 55%. This high inundation frequency was attributed to ponding of water within areas that were previously used as a salt works and that has since been abandoned. The maximum tidal height at Stony Point was less than the maximum inundation height recorded at each study site (**Figures 2A–D**), and the timing of maximum water level at all study sites coincided with the tidal peak recorded at Stony Point. The deviation between tidal height at study sites and the Stony Point tide gauge increased as the tidal height increased, indicating significant amplification of tides as they propagate around French Island and along the Upper North Arm. This was most prominent in the mangrove at Kooweerup where tides on 10 May 2016 were amplified to an elevation of 2.388 m AHD and was markedly greater than the maximum tide gauge height of 1.652 m AHD on the same day. The observed pattern of amplification of tides was consistent with analyses of spatial variation in the mean high water springs tidal plane throughout Westernport Bay (Water Technology, 2014).

Inundation frequency was anomalously high in the saltmarsh at French Island, whilst tidal peaks were attenuated. Analyses focused on areas where salt ponds had been abandoned, and earthworks associated with salt generation remain evident in aerial photography, and likely influence both drainage of the saltmarsh and tidal incursion into the saltmarsh. A linear relationship was established between surface elevation and inundation frequency when inundation patterns in the saltmarsh at French Island were excluded ($r^2 = 0.9894$, AICc = −31.8384, $p < 0.0001$, **Figure 2E**). The relationship remains significant when the saltmarsh at French Island was included in the analysis ($r^2 = 0.7358$, AICc = −1.2417, $p < 0.0001$).

Mean water level at Stony Point tide gauge increased at a rate of 3.0 ± 0.4 mm y^{-1} over the ∼40 years of tide gauge records and increased at a higher rate than the monthly maximum water level (2.0 ± 0.8 mm y^{-1}). This implies a decrease in the vertical space between mean water level and maximum water level over the tide gauge period (**Figure 2F**); crucially, this is the component of accommodation space occupied by intertidal vegetation. However, since 2000 when SET-MH were established, monthly maximum water level (3.5 ± 2.3 mm y^{-1}) increased at approximately the same rate as monthly mean water level (3.5 ± 1.2 mm y^{-1}).

Sediment Characterization

For most cores, sediments increasingly comprised sand fractions at lower elevations beyond approximately 0.8 m AHD (**Supplementary Figures 2–5**). The inverse pattern was evident in the saltmarsh core at Rhyll where the grainsize was finer at depths of 0.4–1.0 m AHD and then increased at depths below approximately 0.4 m AHD. Above 0.8 m AHD, sediments were typically finer grained, and sediments from the saltmarsh at Rhyll exhibited a tendency toward finer grain sizes with increasing elevation in the core. Bulk density reflected this pattern of increasing grain size as elevation decreased with sediments typically becoming less bulky toward the surface. Carbon content was generally higher in the topmost-cluster where grainsize was typically smaller, and diminished to negligible volumes at depths corresponding to mean sea level (i.e., approximately 0 m AHD). Anomalous carbon peaks were evident in some cores, and these sediment depths clustered separately.

Overall, C stock increased with elevation within the core, decreased with inundation frequency and was generally higher in the saltmarsh; however, the density of C was greater in the mangrove and increased with inundation frequency. No statistical difference was found in total C content in cores extracted from mangrove and saltmarsh for C in the upper 30 cm ($p = 0.3528$) where living root material dominates. There was also no statistical difference in C to MSL ($p = 0.6001$), and this is likely due to the greater sediment volume above mean sea level in the saltmarsh than the mangrove. As inundation frequency was disproportionately high despite the high elevation of the saltmarsh at French Island, subsequent analyses of relationships between C content and elevation and inundation excluded data from the saltmarsh at French Island. C content in the upper 30 cm ($r^2 = 0.1309$, $p = 0.3784$) and above MSL ($r^2 = 0.1779$, $p = 0.2980$) were positively related to elevation. Standardized C content was negatively related to elevation ($r^2 = 0.2870$, $p = 0.1703$), confirming a greater concentration of C within mangrove dominated sediments (**Figure 3A**). The inverse pattern was evident for relationships with inundation frequency. C

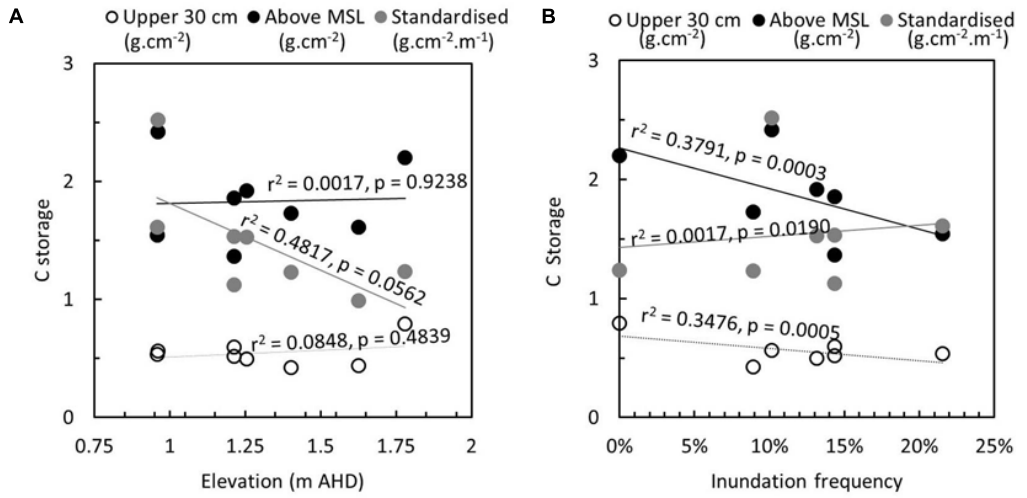


FIGURE 3 | Relationship between carbon storage, estimated in the upper 30 cm (g cm^{-2}), above mean sea level (estimated at 0 m AHD, g cm^{-2}), and standardized over depth (g $cm^{-2}m^{-1}$) and **(A)** elevation of the core (m AHD) and **(B)** inundation frequency, estimated from model presented in **Figure 2E**.

content in the upper 30 cm (r^2 = 0.3476, p = 0.0005) and above MSL (r^2 = 0.3791, p = 0.0003) was negatively related to inundation frequency. Standardized C content was positively correlated to inundation frequency (r^2 = 0.0017, p = 0.0190), although the relationship was weak when French Island study sites were excluded (**Figure 3B**).

Surface Elevation Morphodynamics

Vertical accretion trends were reasonably well-modeled using linear regression analyses over time, with analyses indicating that 96% of SETs had r^2-values exceeding 0.5 (**Supplementary Table 1**); however there was considerable loss of feldspar marker horizons at mangrove SETs due to bioturbation. Similarly, surface elevation change was modeled with reasonable confidence using linear regression analyses and 75% of SETs exhibited $r^2 > 0.5$. Where the coefficient of determination was less than 0.5, surface elevation change was negligible (<1 mm y^{-1}) (**Supplementary Table 1** and **Supplementary Figure 6**). Based on patterns of vertical accretion or surface elevation over time (**Supplementary Figures 7–10**), low r^2-values and insignificant p-values were regarded to be indicative of little vertical accretion or surface elevation change and were therefore included in subsequent analyses. Rates of change for the saltmarsh at French Island were excluded from analyses involving inundation as pooling of water within abandoned ponds was regarded to be unrepresentative of other saltmarsh locations in Westernport Bay.

Temporal variation in vertical accretion was particularly evident in the mangrove zone and this was likely related to bioturbation of MH and the shorter duration over which they were detectable. Irrespectively, vertical accretion was linearly related to elevation (**Figure 4A**, r^2 = 0.2821, p = 0.0076) and inundation (**Figure 4B**, r^2 = 0.2736, p = 0.0150). This relationship was improved with an exponential model (as per Temmerman et al., 2003) that accounted for distances to sediment sources for both elevation (**Figure 4C**, r^2 = 0.3429, p = 0.0026) and inundation (**Figure 4D**, r^2 = 0.3297, p = 0.0065). The strength of these relationships was not maintained in linear regression analyses relating rates of surface elevation change to elevation (**Figure 5A**, r^2 = 0.0098, p = 0.6530) or inundation (**Figure 5B**, r^2 = 0.0021, p = 0.5317). Lorentzian peak models provided the best fit when mangrove surface elevation change was related to elevation (r^2 = 0.3022, AICc = 45.67) or inundation (r^2 = 0.3022, AICc = 45.67), whilst Gaussian peak models provided the best fit when saltmarsh surface elevation change was related to elevation (r^2 = 0.6070, AICc = 38.33) or inundation (r^2 = 0.2414, AICc = 34.66). When both peak models were merged to provide a bimodal distribution the fit markedly improved upon linear models for elevation (**Figure 5C**, r^2 = 0.4558, p = 0.0004) or inundation (**Figure 5D**, r^2 = 0.3364, p = 0.0073).

Paired t-test confirmed rates of surface elevation change were statistically different to rates of vertical accretion (**Figure 6A**, r^2 = 0.0076, p = 0.6927). Differences between vertical accretion and surface elevation change were attributed to autocompaction operating on both mineral and organic material. Vertical accretion was related autocompaction (**Figure 6B**, r^2 = 0.8632, $p < 0.0001$). However, this did not translate to a similar correlation with surface elevation change (**Figure 6C**, r^2 = 0.0802, p = 0.1905). Processes modulating the relationship between vertical accretion and accommodation space were influential, but were not related to accommodation space. Mixed model linear regression analysis, which excluded anomalous values at French Island saltmarsh, confirmed the contribution of vertical accretion and substrate organic matter (indicated by carbon storage above MSL) to surface elevation change (**Figure 6D**, r^2 = 0.9343, p = 0.0280).

Equilibrium Analysis: Changing Tidal Position

Most SET locations exhibited a surface elevation gain that ensured that tidal position was maintained under observed

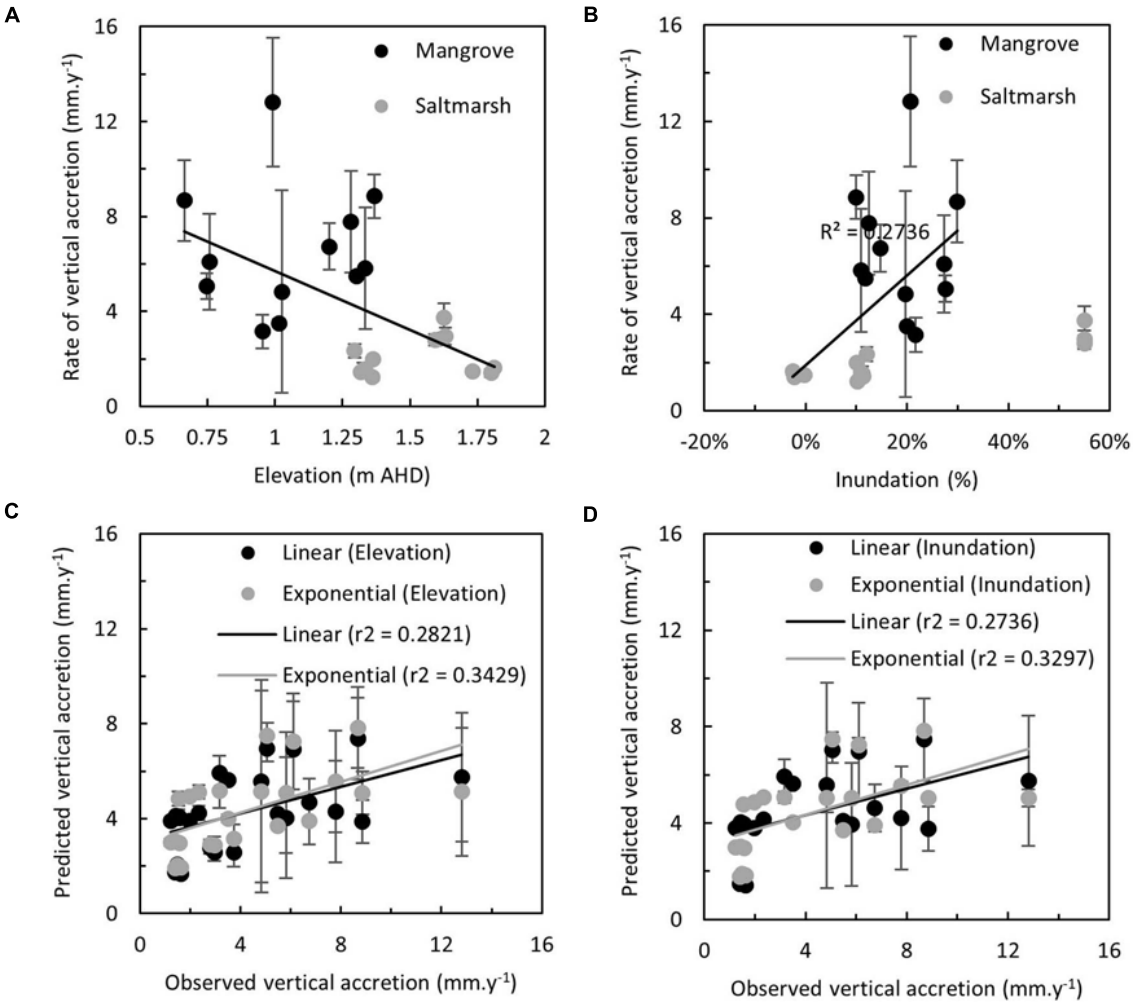


FIGURE 4 | Relationship between the observed rate of vertical accretion in mangrove and saltmarsh at study sites and **(A)** elevation (m AHD), and **(B)** modeled inundation (percentage, derived from **Figure 2E**). Relationship between observed and predicted rate of vertical accretion (mm y^{-1}) derived from linear and exponential models of rates of vertical accretion proportional to **(C)** elevation (m AHD) and **(D)** modeled inundation (%, derived from **Figure 2E**).

rates of RSLR; few locations exhibited a marked decline in tidal position or an increase tidal position (**Figure 7A**). The equilibrium elevation at which changes to the tidal frame corresponded to an increase in substrate elevation was centered around 1.2 ± 0.3 m. This value is remarkably close to estimated mean high water springs tidal plane, reported to be at an elevation of 1.15 m (Water Technology, 2014), and the height at which mangroves give way to saltmarsh vegetation and both vegetation types may occur (Water Technology, 2014). A mangrove SET at Kooweerup exhibited a decline in tidal position that is of little concern given its elevated position in the tidal frame (corresponds to saltmarsh tidal positions). A mangrove and a saltmarsh SET at Quail Island also exhibited a decline in tidal position; these SETs are positioned at the lower end of the vertical distribution for mangrove and saltmarsh, respectively. Given the declining tidal position of the mangrove SET at Quail Island, and the increasing tidal position of the other mangrove SET at Quail Island, it is probable that the location adjacent to the creek draining Kooweerup Swamp (i.e., Cannons Creek) provides considerable hydrodynamic energy that is highly variable, even at the scale of distances between SET monitoring stations. The declining saltmarsh SET remains positioned relatively high in the tidal frame. However, should it continue to loose elevation and the tidal frame shifts according to current rates, this location may transition to being mangrove dominated. Projections indicate that this is not likely to occur until approximately the year 2190 under current rates of change (**Figure 7B**).

DISCUSSION

Processes Influencing Morphodynamics

This study confirmed that wetland surfaces positioned lower in the tidal frame were inundated more frequently, which provided additional opportunities for sediments to be removed from suspension and deposited on wetland surfaces. The role

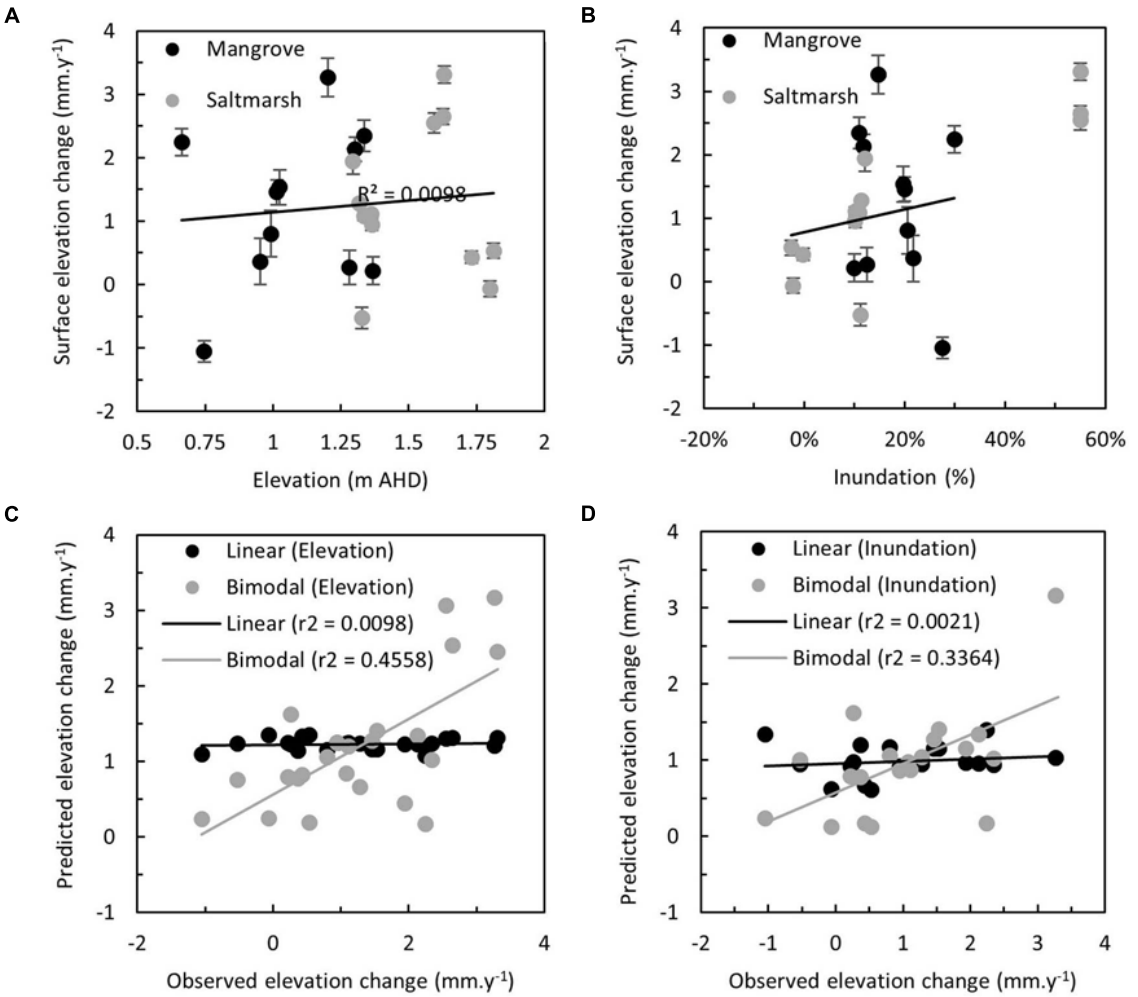


FIGURE 5 | Relationship between the observed rate of surface elevation change (mm y^{-1}) in mangrove and saltmarsh at study sites and **(A)** elevation (m AHD), and **(B)** modeled inundation (percentage, derived from **Figure 2E**). Relationship between observed and predicted rate of surface elevation change (mm y^{-1}) derived from linear and exponential models of rates of vertical accretion proportional to **(C)** elevation (m AHD) and **(D)** modeled inundation (%, derived from **Figure 2E**).

of tidal inundation in facilitating vertical accretion within the vegetated intertidal zone has been established for mangroves and saltmarshes (Pethick, 1981; Rogers et al., 2005a; Kirwan and Megonigal, 2013). However, this observed pattern did not translate into a similar degree of surface elevation gain as processes influencing substrate organic matter and mineral sediment volume caused significant autocompaction and modulated the degree of elevation gain. More specifically, no relationship was found between surface elevation gain, substrate elevation or inundation frequency. This deviation was attributed to processes that alter the substrate volume and contribute to autocompaction. These processes, including decomposition/addition of organic material, consolidation of mineral sediments and compression of organic material, do not operate linearly with inundation.

Higher carbon storage toward surfaces in most cores implies that there is some degree of organic matter turnover near substrate surfaces with living vegetation contributing new organic material to substrates as decomposition occurs. The outcome of this is net accumulation of organic material at wetland surfaces. Depletion of carbon away from the rooting zone of *in situ* vegetation was particularly evident in saltmarsh cores (except Kooweerup saltmarsh), where rooting zones are generally shallower and deeper organic material is likely to have had considerably more time for decomposition. This decomposition of older organic material is consistent with global-scale analyses that relate depleted carbon storage in saltmarshes of the southern hemisphere to relatively stable sea levels since the mid-Holocene (Rogers et al., 2019). The compensatory role of organic matter addition was further validated by relatively high rates of surface elevation change in the mangrove zone at Rhyll being associated with high substrate carbon storage and relatively low rates of autocompaction, despite modest vertical accretion.

The degree of autocompaction that occurred was positively related to the degree of vertical accretion on wetland surfaces, indicating that either recently deposited sediments underwent

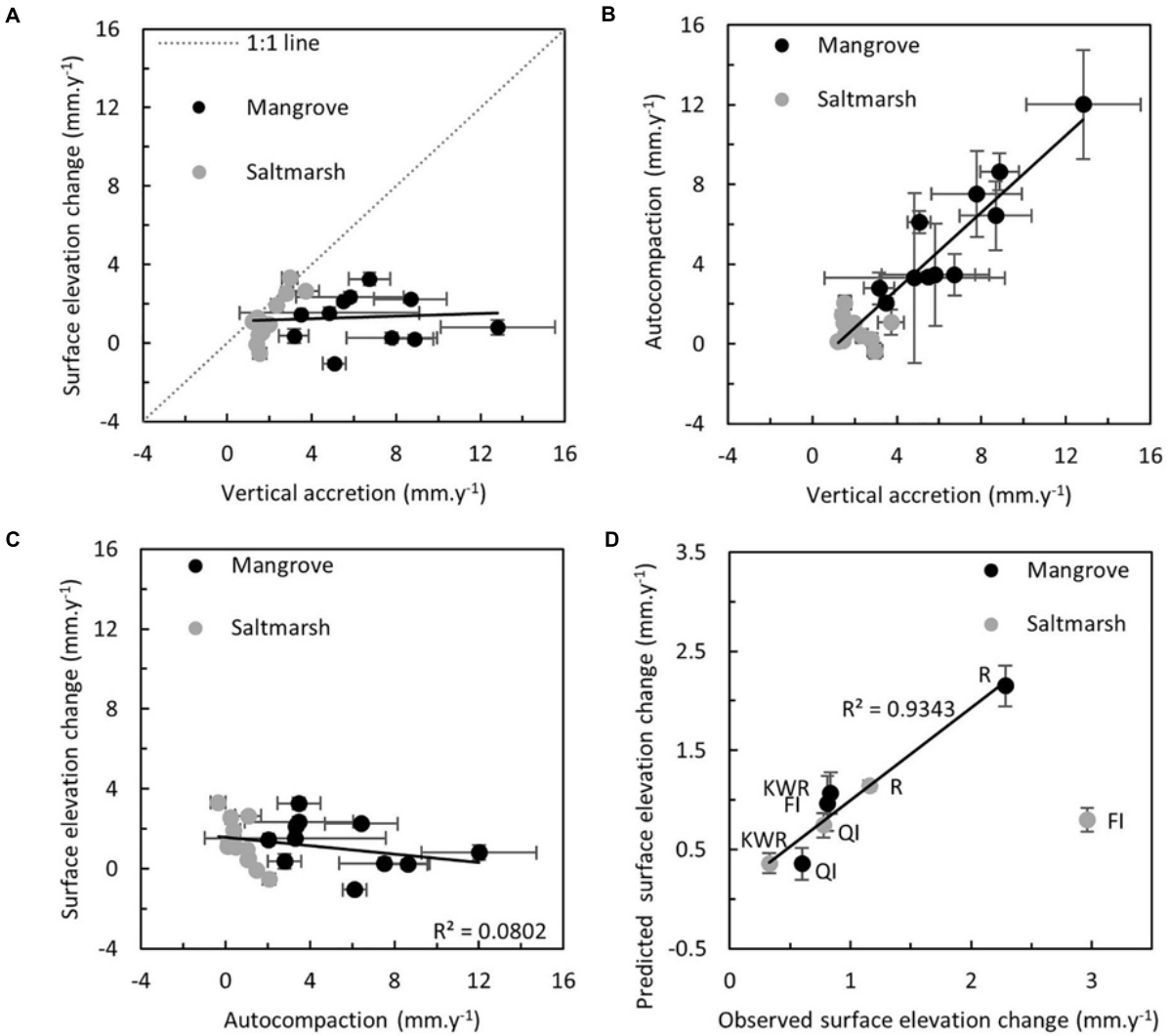


FIGURE 6 | (A) Relationship between rate of surface elevation change (mm y^{-1}) and rate of vertical accretion (mm y^{-1}). **(B)** Relationship between rate of autocompaction (mm y^{-1}) and rate of vertical accretion (mm y^{-1}). **(C)** Relationship between rate of surface elevation change (mm y^{-1}) and rate of autocompaction (mm y^{-1}). **(D)** Relationship between observed and predicted rate of surface elevation change (mm y^{-1}) derived from mixed linear regression model of rates of surface elevation change proportional to rates of vertical accretion (mm y^{-1}) and carbon storage above MSL (g cm^{-2}).

significant consolidation and/or the overburden of accumulating material contributed to deeper consolidation and compression of organic matter. As autocompaction is measured on the basis of changes occurring below marker horizons, processes of autocompaction are operating on mineral sediments below marker horizons and that accumulated prior to the commencement of this study. Autocompaction is regarded to be asymptotic and there is a limit to the reduction in substrate volume that can be achieved (Allen, 2000). Additionally, larger grain sizes are more resistant to consolidation (Bandini and Sathiskumar, 2009). The general trend of increasing grain size with depth below 0.8 m AHD implies consolidation largely operates on sediments above 0.8 m. The predominance of silt and clay grain sizes near wetland surfaces provides further support that consolidation is likely to dominate surface sediments. Paradoxically and unlike other locations, the saltmarsh at Rhyll exhibited both low rates of autocompaction and vertical accretion. This was attributed to the predominance of sand fractions at the surface that are resistant to consolidation. Low rates of surface elevation change, high rates of autocompaction and high substrate carbon content in the saltmarsh at Kooweerup imply that compression of organic material may be the primary process contributing to autocompaction at this location. Despite this autocompaction, substantial substrate carbon and low bulk density was quantified in the upper 40 cm of sediments, indicating that vertical growth of the saltmarsh was more recently associated with organic matter addition. Due to the relatively high position of the saltmarsh at this location and low inundation frequency, compression of this thickness of organic material is critical for maintaining substrates within the

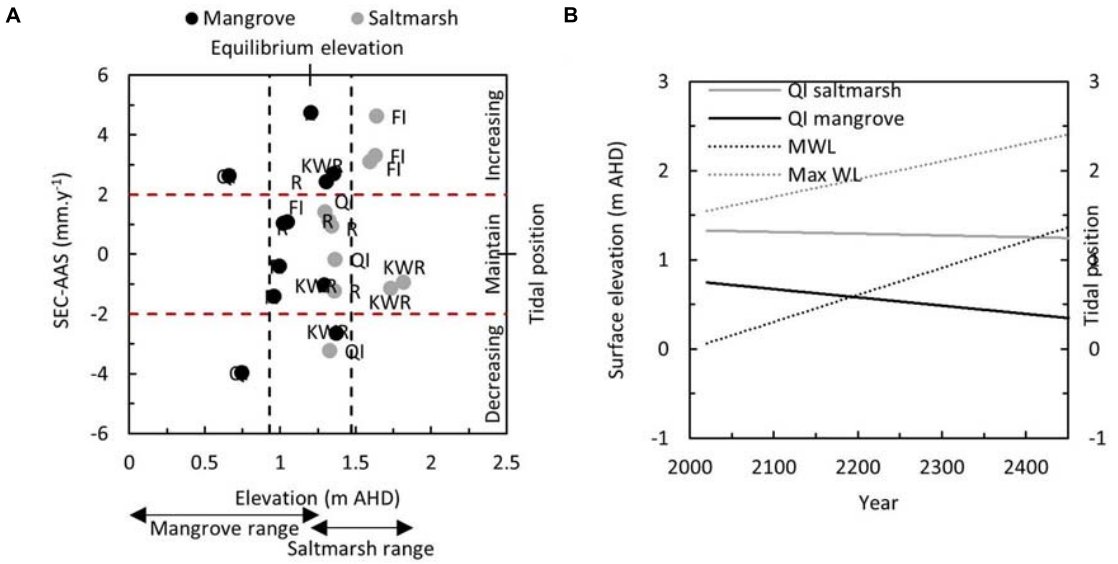


FIGURE 7 | (A) Relationship between changing tidal position (mm y^{-1}) [estimated using Eq. 1 and defined as the deficit between the rate of surface elevation change (mm y^{-1})] and rate of increase in accommodation space associated with RSLR (mm y^{-1}), and substrate elevation at the time of last measurement in 2019. Where rates of surface elevation change match rates of increase in available accommodation space (±2 mm y^{-1}), rates of surface elevation change are presumed to be at or near equilibrium with change to available accommodation space. The mean elevation of these location were used to define the equilibrium elevation range of 1.2 ± 0.3 m. **(B)** Projected decline in tidal position of SETs at Quail Island with trajectory of declining tidal position based on continuing rates of decline in tidal position and increase in water level trajectories, indicated by mean and maximum water levels. This projection indicates that it is some time before substrates at Quail Island are below mean water level, and the time is modulated by their starting elevation within the tidal frame.

vertical range of accommodation space, else accommodation space will become exhausted and terrestrialization of vegetation cover may occur.

The varying contribution of addition, decomposition and compression of organic material, and mineral sediment consolidation to autocompaction limits the capacity to develop relationships between trajectories of surface elevation change and accommodation space. This problem was predicted by Allen (2000) who recognized the difficulty in realistically modeling autocompaction of Holocene coastal deposits due to the diversity and complexity of process involved and the environmental context. However, this is contrary to the structure of many existing empirical and physical models. Many models either presume processes causing autocompaction operate solely on organic material through decomposition (For example, Zhang et al., 2020), are implicitly incorporated in models of net surface elevation change (Morris et al., 2002; Rogers et al., 2012), or apply a constant rate of autocompaction irrespective of tidal position (For example, Marani et al., 2013). There are exceptions: the WARMER (Swanson et al., 2014) model includes parameters of mineral sediment accretion, organic matter addition and decomposition, and compaction; and OIMAS-N (Mudd et al., 2009) includes parameters of mineral and organic matter addition, decay of carbon pools and compaction. This study confirms that sandy substrates tend to undergo less autocompaction than substrates where surface sediments are largely fine grained. The upward fining of sediments within substrates (with the exception of Rhyll saltmarsh) indicates that grain size of accreting material and associated resistance to consolidation is positively related to available accommodation space. Given the elevation at which sandy and carbon-depleted sediments have typically accumulated in wetland substrates (i.e., <0.8 m AHD, though some peaks in carbon are preserved at lower elevations, particularly in mangrove-dominated locations), it is probable that the high-energy conditions required for sand deposition occurred some time ago. If this is the case, most of the autocompaction that could have occurred on these sediments is nearing completion.

Conceptualizing Processes of Autocompaction

The physical, biological and chemical processes contributing to autocompaction operate across different timescales (Allen, 2000). However as these processes are asymptotic, we propose that the bulk of autocompaction at Westernport Bay occurs in sediments either above approximately 0.8 m AHD or corresponding to the active rooting zone of mangrove vegetation. Autocompaction is also dependent upon the proportion of organic material in substrates, sediment characteristics and prior rates of surface elevation gain. We identify four critical factors that influence the degree of autocompaction: rooting depths of vegetation, sediment characteristics, rates of surface elevation gain, and vegetation distribution changes.

i) Rooting depths of vegetation: Whilst mangrove species diversity is low at Westernport Bay, saltmarsh species diversity is extraordinarily high with discernible zones dominated by saltbush, highly diverse herbaceous

saltmarsh, and landward rushes. The varying rooting depth of this vegetation influences whether addition of organic material to substrates exceeds processes of decomposition. In this study, mangrove cores typically exhibited deeper zones of higher carbon storage near the surface, whilst the surficial zones of higher carbon storage at saltmarsh locations were typically shallower (i.e., with the exception of the saltmarsh at Kooweerup). Despite herbaceous saltmarshes generally having shallower, carbon-rich surficial zones, their overall deeper sediment columns above MSL (i.e., 0 m AHD) resulted in carbon storage above MSL being relatively consistent across the intertidal gradient. However, it is feasible to characterize the variation in rooting depths associated with optimal tidal positions to generate multi-peak models of organic matter addition, as was coarsely undertaken in this study by merging peak models to relate surface elevation change to elevation and inundation.

ii) Sediment characteristics: Supply of high volumes of fine-grained sediments generates a larger volume of substrate that is prone to processes of sediment consolidation. This was particularly evident in mangrove cores as they generally exhibited high accretion rates and greater silt to sand ratios in surficial sediments. The exception was Quail Island mangrove locations where sands dominated most of the substrate. The dominance of sands at wetlands surfaces attests to higher energy conditions and the possibility of erosion. The supply and subsequent deposition of sediments are hydro-dynamically governed and improvements on hydrodynamic models such that they account for sediment characteristics and their contribution to processes of autocompaction could be considered.

iii) Rates of surface elevation gain: Surface elevation gain, achieved through either organic matter and/or mineral sediment addition exceeding the rate of autocompaction, creates conditions favorable for increasing tidal position of wetland surfaces. When this occurs rapidly, either rooting zones of vegetation are transposed vertically, or lateral vegetation transitions occur (e.g., replacement of mangrove by saltmarsh) with a corresponding change in the depth of the active root zone. In both situations, the overall outcome is an increase in the depth of surficial carbon-rich zones until the deeper zones associated with prior root zones undergoes decomposition. High rates of vertical accretion may transition substrate elevations rapidly from lower positions in the tidal frame to optimal positions for organic matter addition (as per Morris et al., 2002), although the inverse may also occur. Whilst deeper active rooting zones will be increasingly abandoned and exposed to processes of decomposition, insufficient time may have passed for processes of decomposition and compression of organic material and consolidation of mineral sediments to significantly influence autocompaction. Increases in the height of the tidal frame with RSLR has been related to greater carbon storage (McKee et al., 2007; Toscano et al., 2018), and is likely facilitated by increasing exposure to anaerobic conditions (Rogers et al., 2019). It is feasible that this process may have resulted in instances of increasing tidal positions at "equilibrium elevations" as occurred for mangrove locations at Rhyll and Kooweerup, and for saltmarsh locations at French Island.

iv) Vegetation distribution changes: Changes in tidal position of vegetation may occur when surface elevation gain does not correspond to changes to the tidal frame with RSLR. As mangroves at Westernport Bay are positioned at lower tidal positions and have relatively deep rooting zones, and herbaceous saltmarsh positioned at higher tidal positions has shallower rooting zones, vegetation encroachment upon herbaceous saltmarsh may promote rapid addition of organic material to substrates. When this occurs, surficial carbon stocks may markedly increase and offset processes of autocompaction occurring deeper in the substrate. There is substantial evidence in southeastern Australia and elsewhere (Doughty et al., 2016; Kelleway et al., 2016) of increasing surficial carbon storage as mangroves have encroached upon saltmarsh over the past few decades. In Westernport Bay, this process is further promoted as the intermediary saltbush zone dominated by *Tecticornia arbuscula* grows to heights of approximately 2 m (*pers. obs.*), and are likely to have deeper rooting zones than herbaceous saltmarsh. This subsidy may be critical for achieving the high rates of surface elevation change in mangrove locations at Rhyll where relatively recent encroachment of mangrove along the nearby tidal creek and across formerly saltmarsh-dominated surfaces has been documented (Rogers et al., 2005b; Whitt et al., 2020).

Validation of Model Structure

Processes of net vertical accretion are typically related to accommodation space and our analyses confirmed this; minor improvements in vertical accretion model fit were achieved when distances to sediment sources were incorporated according to an exponential function, as per Temmerman et al. (2003). Whether accretion behaves linearly or exponentially is of little consequence when accommodation space becomes limited at high tidal positions (i.e., in saltmarsh) as modeled values converge, as demonstrated by Mogensen and Rogers (2018). Nevertheless, it is particularly important at lower tidal positions where differences between values derived from linear or exponential models can be significant. Unfortunately, preservation of marker horizons in mangrove zones at Westernport Bay was poor due to bioturbation and this markedly reduced confidence and increased variability in vertical accretion data. Hence, our ability to discern optimal model functions for vertical accretion was limited. Complementary analyses of sedimentation derived from measurements of ^{210}Pb activity in sediments and using a time for space substitution indicate that peak models (Gaussian or Lorentzian) improved predictive ability (Rogers et al. in prep). More specifically, peak models can account for lower rates of sedimentation when accommodation space and hydrodynamic energy is high, accelerating sedimentation as accommodation space infills, and decelerating sedimentation as accommodation space becomes limited.

The linear relationship between vertical accretion and autocompaction indicates that autocompaction may also behave according to an inundation depth/frequency-constrained model; models may be either peak or linear in behavior. Disaggregating processes contributing to autocompaction that operate on organic and mineral material in substrates requires further investigation of intertidal variation in the behavior of these processes. Stratigraphic controls on compression were related to accommodation space with sandy, compression-resistant sediments dominating when accommodation space was high, and conforms closest to the OIMAS-N model structure of Mudd et al. (2009). Due to the greater complexity of vegetation at Westernport Bay, more information is needed to describe the vertical distribution of vegetation within the tidal frame, rooting depths of *in situ* vegetation, and time-depth dependence of decomposition. Application of merged peak models to describe surface elevation change within mangrove and saltmarsh zones indicate that quantifying the range and peak productivity of vegetation may correlate with the full range of processes operating on organic matter that modulates surface elevation change. Irrespective of these data gaps, our data indicates that processes influencing surface elevation change are largely depth constrained, and their behavior is more likely to conform with peak model structures rather than linear. There remains considerable scope to calibrate this data against OIMAS-N model to characterize changing tidal position and substrate carbon storage.

Equilibrium Analysis

Given the relatively recent change in trajectory of sea level across the southern hemisphere, it was feasible that equilibration of processes to recent SLR may be lagging. Additionally, there remains some concern that short-term datasets, such as those derived from SET-MH approaches, may not have sufficient temporal range to characterize surface elevation trajectories with confidence (Breithaupt et al., 2018; Wiberg et al., 2020). There was a surprising degree of confidence in elevation trajectories over the 20-year analysis period. We found that relatively few locations exhibited surface elevation trajectories beyond that required to maintain tidal positions (i.e., 0 ± 2 mm y^{-1}). This implies that presumptions of equilibrium may not be misplaced, particularly when models are parameterized using high confidence data that is not influenced by perturbations operating over shorter timescales. Mean trajectories of elevation change and vertical accretion in this study were generally within the error range of rates reported in the earlier study of Rogers et al. (2005b); with the exception of rates of surface elevation change at French Island, and surface elevation change in the mangroves at Quail Island. We recommend analyses of confidence in trajectories before model application, as undertaken in this study and others (Jankowski et al., 2017).

Some locations that exhibited an increase in tidal position were associated with relatively recent transition of mangrove into saltmarsh (i.e., Rhyll mangrove locations were saltmarsh prior to the commencement of this study). Organic matter addition to substrates achieved by vegetation encroachment plays a critical role in increasing substrate surface elevations. Hydrological alterations in the saltmarsh at French Island appeared to provide a productivity subsidy and improve sediment-trapping efficiency, resulting in an increase in tidal position beyond that expected for its elevation. Increasing hydrodynamic energy along the creek draining Kooweerup Swamp and adjacent to Quail Island (i.e., Cannons Creek) may be influencing lateral movement of sediment on the eastern shores of Quail Island and contributing to declines in tidal positions at this location (**Figure 1**). The dominance of larger grain sizes in sediments and relatively low rates of vertical accretion at Quail Island indicate that hydrodynamic energy is generally too high for finer grain sediment deposition within the mangrove zone. Hydrodynamic modeling will be critical for conceptualizing the restructuring of shorelines of Quail Island and other locations where hydrodynamic energy is changing.

The analysis of equilibrium elevation undertaken in this study intriguingly indicated an equilibrium elevation corresponding to both the height of mean high tide and the approximate elevation that the mangrove niche transitions into the saltmarsh niche. The reported equilibrium elevation of 1.2 m is approximately 0.3 m below the upper boundary of accommodation space and where only ∼15% of total accommodation space remains for sediment accumulation. Saltmarsh is evidently a climax intertidal community in this region, and mangroves are a pioneering community. However, it would be misplaced to describe mangroves as "land-builders," as proposed by Bird (1971, 1986) following work in Westernport Bay. This is because mineral sediment supply to create an intertidal surface at an elevation suitable for mangroves is a critical precursor for their establishment. This was confirmed in this study by the predominance of sandy substrates with little organic material at elevations at or below MSL. Accordingly, the most critical component of "land-building" is related to sediment supply, driven by hydrodynamic energy, and occurs prior to mangrove establishment. Commentary from Spenceley (1987) implied that there was not enough evidence to confirm that sedimentation would not have occurred in the absence of mangroves and proposed that sediment characteristics, prevailing energy conditions and faunal activity may be more critical for erosion and deposition than the presence of pneumatophores at Westernport Bay. Spenceley (1987) lamented the absence of more data and research into the role of mangrove roots in promoting mineral sediment deposition, and unfortunately, little has changed in subsequent years.

Projected acceleration in SLR (Oppenheimer et al., 2019) is proposed to deepen equilibrium elevations (Fagherazzi et al., 2012) and should this occur mangroves forests will increasingly dominate the intertidal zone of Westernport Bay by encroaching upon adjacent saltmarsh. Mangrove forests may eventually give way to un-vegetated mudflat and subtidal elevations should SLR acceleration exceed the capacity for maintaining equilibrium elevations. There is substantial evidence that this is already occurring with mangrove encroachment of saltmarsh well-documented in Westernport Bay (Rogers et al., 2005b; Whitt et al., 2020). Management efforts to maintain the areal distribution of saltmarsh and limit mangrove encroachment should recognize the subsidizing effect mangroves provide by

adding considerably more organic material to substrates than herbaceous saltmarsh vegetation. Actions that limit expansion, such as controlling propagule dispersal and removing seedlings, may be detrimental and promote the development of ponds and open water within saltmarshes (Coleman et al., 2021).

CONCLUSION

This study established that a range of processes influence autocompaction; these processes vary spatially, are proportional to vertical accretion, and can feasibly be modeled with reference to accommodation space or depth below high water. Surface elevation change was related to vertical accretion and substrate organic matter, as indicated by carbon storage above mean sea level. Additionally, surface elevations do not adjust linearly with accommodation space and peak model structures will likely improve model performance. More research is required to improve characterization of model structures; however, it may be reasonable to presume equilibration with current rates of SLR providing models are parameterized with highly accurate data.

We propose that the outcomes of this study can only be achieved by analyzing processes of surface elevation change at locations with a longer history of stable or falling sea level, as occurred in much of the southern hemisphere over the mid- to late-Holocene. Relatively stable sea levels over the past 7,000 years provided favorable conditions for estuarine infill and this has been demonstrated in numerous studies (Woodroffe et al., 1993, 2000; Hashimoto et al., 2006; Kennedy et al., 2021). Since the mid-Holocene, processes influencing autocompaction operating on older/deeper sediments have had more time to reach completion and this is evident by depleted carbon stocks in saltmarsh sediments below 0.8 m AHD. This provides local-scale confirmation of the global-scale pattern of lower saltmarsh carbon stocks along coastlines where sea level was relatively stable throughout the mid- to late-Holocene (Rogers et al., 2019).

Recent increases in sea level are contrary to antecedent conditions and new accommodation space is now being created for mineral and organic material accumulation. Striking stratigraphic variation is generated as new accommodation space infills with mineral and organic material above older strata that have undergone processes of autocompaction and are increasingly dominated by mineral sediments. The sediment character of these new strata subsequently influences the degree of surface elevation occurring today. This stratigraphy contrasts locations where wetlands are exposed to a longer history of rising sea levels and creation of new accommodation space, as conditions influencing vertical accretion and processes of autocompaction are more likely to equilibrate, and the homogeneity of substrates will be higher. Considerably more research is required in the southern hemisphere to characterize spatial variation in processes influencing surface elevation change to improve and validate model structures and confidently parameterize models. We caution the use of models derived from the northern hemisphere, particularly those that presume constant rates of autocompaction or linear behavior of surface elevation change.

DATA AVAILABILITY STATEMENT

The raw data supporting the conclusions of this article will be made available by the authors, without undue reservation, to any qualified researcher.

AUTHOR CONTRIBUTIONS

KR and NS undertook data collection, analysis, and writing. This has been a collaborative research project since its inception. Both authors contributed to the article and approved the submitted version.

FUNDING

The Victorian Government provided financial support to establish this research in 2000 and subsequent funding in 2017 to maintain research continuity and deliver knowledge that assists with management of coastal wetlands of Westernport Bay. KR received an Australian Research Council Future Fellowship (FT130100532) that provided financial support for measurements and sediment analyses from 2014 to 2018.

ACKNOWLEDGMENTS

We acknowledge the custodians of the Western Port area, the Bunurong (Boonerwrung) people of the Kulin Nation. We recognize the contribution of field and laboratory assistants in undertaking this work; over 20 years of analysis there are too many to mention but we remember every field trip fondly. Special thanks given to Lawrance Ferns who has supported this research and the Victorian Government who has provided financial support with the initial establishment and recent measurements.

SUPPLEMENTARY MATERIAL

The Supplementary Material for this article can be found online at: https://www.frontiersin.org/articles/10.3389/fmars.2021.694039/full#supplementary-material

REFERENCES

Allen, J. R. L. (2000). Morphodynamics of holocene salt marshes: a review sketch from the Atlantic and Southern North sea coasts of Europe. *Quat. Sci. Rev.* 19, 1155–1231. doi: 10.1016/s0277-3791(99)00034-7

Alongi, D. M. (2008). Mangrove forests: resilience, protection from tsunamis, and responses to global climate change. *Estuar. Coast. Shelf Sci.* 76, 1–13. doi: 10.1016/j.ecss.2007.08.024

Bandini, P., and Sathiskumar, S. (2009). Effects of silt content and void ratio on the saturated hydraulic conductivity and compressibility of sand-silt mixtures.

J. Geotech. Geoenviron. Eng. 135, 1976–1980. doi: 10.1061/(asce)gt.1943-5606.0000177

Bird, E. C. F. (1971). Mangroves as land builders. *Vic. Nat.* 88, 189–197.

Bird, E. C. F. (1986). Mangroves and intertidal morphology in Westernport Bay, Victoria, Australia. *Mar. Geol.* 69, 251–271. doi: 10.1016/0025-3227(86)90042-3

Boon, P. I., Allen, T., Brook, J., Carr, G., Frood, D., Harty, C., et al. (2011). "Mangroves and coastal saltmarsh of Victoria: distribution, condition, threats and management," (Melbourne, VIC: Institute for Sustainability and Innovation, Victoria University).

Breithaupt, J. L., Smoak, J. M., Byrne, R. H., Waters, M. N., Moyer, R. P., and Sanders, C. J. (2018). Avoiding timescale bias in assessments of coastal wetland vertical change. *Limnol. Oceanogr.* 63, S447–S495.

Cahoon, D. R., Lynch, J. C., Hensel, P., Boumans, R., Perez, B. C., Segura, B., et al. (2002). High-precision measurements of wetland sediment elevation: i. recent improvements to the sedimentation-erosion table. *J. Sediment. Res.* 72, 730–733. doi: 10.1306/020702720730

Cahoon, D. R., and Turner, R. E. (1989). Accretion and canal impacts in a rapidly subsiding wetland II. Feldspar marker horizon technique. *Estuaries* 12, 260–268. doi: 10.2307/1351905

Callaway, J., Nyman, J., and Delaune, R. D. (1996). Sediment accretion in coastal wetlands: a review and a simulation model of processes. *Curr. Top. Wetl. Biogeochem.* 2, 2–23.

Church, J. A., Clark, P. U., Cazenave, A., Gregory, J. M., Jevrejeva, S., Levermann, A., et al. (2013). "Sea level change," in *Climate Change 2013: The Physical Science Basis. Contribution of Working Group I to the Fifth Assessment Report of the Intergovernmental Panel on Climate Change*, eds T. F. Stocker, D. Qin, G.-K. Plattner, M. Tignor, S. K. Allen, J. Boschung, et al. (Cambridge: Cambridge University Press).

Coleman, D. J., Rogers, K., Corbett, D. R., Owers, C. J., and Kirwan, M. L. (2021). The geomorphic impact of mangrove encroachment in an Australian salt marsh. *Estuar. Coast. Shelf Sci.* 251:107238. doi: 10.1016/j.ecss.2021.107238

D'Alpaos, A., Lanzoni, S., Marani, M., and Rinaldo, A. (2007). Landscape evolution in tidal embayments: modeling the interplay of erosion, sedimentation, and vegetation dynamics. *J. Geophys. Res.* 112, 1–17. doi: 10.1007/978-1-4615-0575-4_1

Dey, R., Lewis, S. C., Arblaster, J. M., and Abram, N. J. (2019). A review of past and projected changes in Australia's rainfall. *Wiley Interdiscip. Rev. Clim. Change* 10:e577.

Dougherty, A. J., Thomas, Z. A., Fogwill, C., Hogg, A., Palmer, J., Rainsley, E., et al. (2019). Redating the earliest evidence of the mid-holocene relative sea-level highstand in Australia and implications for global sea-level rise. *Plos one* 14:e0218430. doi: 10.1371/journal.pone.0218430

Doughty, C. L., Langley, J. A., Walker, W. S., Feller, I. C., Schaub, R., and Chapman, S. K. (2016). Mangrove range expansion rapidly increases coastal wetland carbon storage. *Estuar. Coasts* 39, 385–396. doi: 10.1007/s12237-015-9993-8

Fagherazzi, S., Kirwan, M. L., Mudd, S. M., Guntenspergen, G. R., Temmerman, S., D'alpaos, A., et al. (2012). Numerical models of salt marsh evolution: ecological, geomorphic, and climatic factors. *Rev. Geophys.* 50:RG1002.

French, J. R. (1993). Numerical simulation of vertical marsh growth and adjustment to accelerated sea-level rise, North Norfolk, U.K. *Earth Surf. Process. Landf.* 18, 63–81. doi: 10.1002/esp.3290180105

Hashimoto, T. R., Saintilan, N., and Haberle, S. G. (2006). Mid-holocene development of mangrove communities featuring rhizophoraceae and geomorphic change in the richmond river estuary, New South Wales, Australia. *Geogr. Res.* 44, 63–76. doi: 10.1111/j.1745-5871.2006.00360.x

Jankowski, K. L., Törnqvist, T. E., and Fernandes, A. M. (2017). Vulnerability of Louisiana's coastal wetlands to present-day rates of relative sea-level rise. *Nat. Commun.* 8:14792.

Kelleway, J. J., Saintilan, N., Macreadie, P. I., Skilbeck, C. G., Zawadzki, A., and Ralph, P. J. (2016). Seventy years of continuous encroachment substantially increases 'blue carbon'capacity as mangroves replace intertidal salt marshes. *Glob. Change Biol.* 22, 1097–1109. doi: 10.1111/gcb.13158

Kennedy, D., Wong, V., and Jacobsen, G. J. (2021). Holocene infill of the Anglesea Estuary, Victoria: a keep-up estuary in a geologically constrained environment. *Aust. J. Earth Sci.* doi: 10.1080/08120099.2021.1879266 [Epub ahead of print].

Kestner, F. J. (1975). The loose-boundary regime of the wash. *Geogr. J.* 141, 388–414. doi: 10.2307/1796474

Khan, N. S., Ashe, E., Shaw, T. A., Vacchi, M., Walker, J., Peltier, W. R., et al. (2015). Holocene relative sea-level changes from near-, intermediate-, and far-field locations. *Curr. Clim. Change Rep.* 1, 247–262. doi: 10.1007/s40641-015-0029-z

Kirwan, M. L., and Megonigal, J. P. (2013). Tidal wetland stability in the face of human impacts and sea-level rise. *Nature* 504, 53–60. doi: 10.1038/nature12856

Krauss, K. W., Mckee, K. L., Lovelock, C. E., Cahoon, D. R., Saintilan, N., Reef, R., et al. (2014). How mangrove forests adjust to rising sea level. *New Phytol.* 202, 19–34. doi: 10.1111/nph.12605

Krone, R. B. (1987). "A method for simulating historic marsh elevations," in *Coastal Sediments '87*, ed. N. C. Krause (New Orleans, LA: American Society of Civil Engineers).

Lewis, S. E., Sloss, C. R., Murray-Wallace, C. V., Woodroffe, C. D., and Smithers, S. G. (2013). Post-glacial sea-level changes around the Australian margin: a review. *Quat. Sci. Rev.* 74, 115–138. doi: 10.1016/j.quascirev.2012.09.006

Marani, M., Da Lio, C., and D'alpaos, A. (2013). Vegetation engineers marsh morphology through multiple competing stable states. *Proc. Natl. Acad. Sci. U.S.A.* 110, 3259–3263. doi: 10.1073/pnas.1218327110

McKee, K. L., Cahoon, D. R., and Feller, I. C. (2007). Caribbean mangroves adjust to rising sea level through biotic controls on change in soil elevation. *Glob. Ecol. Biogeogr.* 16, 545–556. doi: 10.1111/j.1466-8238.2007.00317.x

Mogensen, L., and Rogers, K. (2018). Validation and comparison of a model of the effect of sea-level rise on coastal wetlands. *Sci. Rep.* 8:1369.

Morris, J. T., Sundareshwar, P. V., Nietch, C. T., Kjerfve, B., and Cahoon, D. R. (2002). Responses of coastal wetlands to rising sea-levels. *Ecology* 83, 2869–2877. doi: 10.1890/0012-9658(2002)083[2869:rocwtr]2.0.co;2

Mudd, S. M., Howell, S. M., and Morris, J. T. (2009). Impact of dynamic feedbacks between sedimentation, sea-level rise, and biomass production on near-surface marsh stratigraphy and carbon accumulation. *Estuar. Coast. Shelf Sci.* 82, 377–389. doi: 10.1016/j.ecss.2009.01.028

Murray-Wallace, C. V., and Woodroffe, C. D. (2014). *Quaternary Sea-Level Changes: A Global Perspective*. Cambridge: Cambridge University Press.

Oppenheimer, M., Glavovic, B., Hinkel, J., Van De Wal, R., Magnan, A. K., Abd-Elgawad, A., et al. (2019). "Chapter 4: sea level rise and implications for low lying islands, coasts and communities," in *IPCC Special Report on the Ocean and Cryosphere in a Changing Climate*, eds H.-O. Pörtner, D. C. Roberts, V. Masson-Delmotte, P. Zhai, M. Tignor, E. Poloczanska, et al. (Geneva: Intergovenmental Panel on Climate Change).

Pethick, J. S. (1981). Long-term accretion rates on tidal salt marshes. *J. Sediment. Res.* 51, 571–577.

Reed, D. J. (1990). The impact of sea-level rise on coastal salt marshes. *Prog. Phys. Geogr.* 14, 465–481. doi: 10.1177/030913339001400403

Rinaldo, A., Fagherazzi, S., Lanzoni, S., Marani, M., and Dietrich, W. E. (1999). Tidal networks: 2. watershed delineation and comparative network morphology. *Water Res. Res.* 35, 3905–3917. doi: 10.1029/1999wr900237

Rogers, K., Kelleway, J. J., Saintilan, N., Megonigal, J. P., Adams, J. B., Holmquist, J. R., et al. (2019). Wetland carbon storage controlled by millennialscale variation in relative sea-level rise. *Nature* 567, 91–95. doi: 10.1038/s41586-019-0951-7

Rogers, K., Saintilan, N., and Cahoon, D. (2005a). Surface elevation dynamics in a regenerating mangrove forest at Homebush Bay, Australia. *Wetl. Ecol. Manag.* 13, 587–598. doi: 10.1007/s11273-004-0003-3

Rogers, K., Saintilan, N., and Copeland, C. (2012). Modelling wetland surface elevation and its application to forecasting the effects of sea-level rise on estuarine wetlands. *Ecol. Model.* 244, 148–157. doi: 10.1016/j.ecolmodel.2012.06.014

Rogers, K., Saintilan, N., and Heijnis, H. (2005b). Mangrove encroachment of salt marsh in Western Port Bay, Victoria: the role of sedimentation, subsidence and sea level rise. *Estuaries* 28, 551–559. doi: 10.1007/bf02696066

Spenceley, A. P. (1987). Mangroves and intertidal morphology in Westernport Bay, Victoria, Australia — Comment. *Mar. Geol.* 77, 327–330. doi: 10.1016/0025-3227(87)90121-6

Swanson, K. M., Drexler, J. Z., Schoellhamer, D. H., Thorne, K. M., Casazza, M. L., Overton, C. T., et al. (2014). Wetland accretion rate model of ecosystem resilience (WARMER) and its application to habitat sustainability for endangered species in the San Francisco estuary. *Estuar. Coasts* 37, 476–492. doi: 10.1007/s12237-013-9694-0

Temmerman, S., Govers, G., Wartel, S., and Meire, P. (2003). Spatial and temporal factors controlling short-term sedimentation in a salt and freshwater tidal

marsh, scheldt estuary, Belgium, SW Netherlands. *Earth Surf. Process. Landf.* 28, 739–755. doi: 10.1002/esp.495

Thorne, K., Macdonald, G., Guntenspergen, G., Ambrose, R., Buffington, K., Dugger, B., et al. (2018). US Pacific coastal wetland resilience and vulnerability to sea-level rise. *Sci. Adv.* 4:eaao3270. doi: 10.1126/sciadv.aao3270

Toscano, M. A., Gonzalez, J. L., and Whelan, K. R. T. (2018). Calibrated density profiles of Caribbean mangrove peat sequences from computed tomography for assessment of peat preservation, compaction, and impacts on sea-level reconstructions. *Quat. Res.* 89:201. doi: 10.1017/qua.2017.101

Water Technology (2014). *Western Port Local Coastal Hazard Assessment. Inundation Hazards Report 04 (R04)*. Melbourne, VIC: Melbourne Water Technology.

White, N. J., Haigh, I. D., Church, J. A., Koen, T., Watson, C. S., Pritchard, T. R., et al. (2014). Australian sea levels—trends, regional variability and influencing factors. *Earth Sci. Rev.* 136, 155–174. doi: 10.1016/j.earscirev.2014.05.011

Whitt, A. A., Coleman, R., Lovelock, C. E., Gillies, C., Ierodiaconou, D., Liyanapathirana, M., et al. (2020). March of the mangroves: drivers of encroachment into southern temperate saltmarsh. *Estuar. Coast. Shelf Sci.* 240:106776. doi: 10.1016/j.ecss.2020.106776

Wiberg, P. L., Fagherazzi, S., and Kirwan, M. L. (2020). Improving predictions of salt marsh evolution through better integration of data and models. *Ann. Rev. Mar. Sci.* 12, 389–413. doi: 10.1146/annurev-marine-010419-010610

Woodroffe, C. D., Mulrennan, M. E., and Chappell, J. (1993). Estuarine infill and coastal progradation, Southern van Diemen Gulf, Northern Australia. *Sediment. Geol.* 83, 257–275. doi: 10.1016/0037-0738(93)90016-x

Woodroffe, C. W., Buman, M., Kawase, K., and Umitsu, M. (2000). Estuarine infill and formation of Deltaic Plains, Shoalhaven River. *Wetlands* 18, 72–84. doi: 10.31646/wa.232

Zhang, Y., Rowland, J. C., Xu, C., Wolfram, P. J., Svyatsky, D., Moulton, J. D., et al. (2020). Understanding the eco-geomorphologic feedback of coastal marsh under sea level rise: vegetation dynamic representations, processes interaction, and parametric sensitivity. *J. Geophys. Res. Earth Surf.* 125:e2020JF005729.

Conflict of Interest: The authors declare that the research was conducted in the absence of any commercial or financial relationships that could be construed as a potential conflict of interest.

Copyright © 2021 Rogers and Saintilan. This is an open-access article distributed under the terms of the Creative Commons Attribution License (CC BY). The use, distribution or reproduction in other forums is permitted, provided the original author(s) and the copyright owner(s) are credited and that the original publication in this journal is cited, in accordance with accepted academic practice. No use, distribution or reproduction is permitted which does not comply with these terms.

frontiers in Marine Science

ORIGINAL RESEARCH
published: 22 July 2021
doi: 10.3389/fmars.2021.708116

Estimating Waves and Currents at the Saltmarsh Edge Using Acoustic Doppler Velocimeter Data

Bing Liu[1], Yining Chen[1], Tinglu Cai[1], Yan Li[2] and Li Sun[1]*

[1] Second Institute of Oceanography, Ministry of Natural Resources, Hangzhou, China, [2] Dongshan Swire Marine Station, Xiamen University, Xiamen, China

Waves, currents, and related sediment transport are important factors driving the development of saltmarshes. Separating the effects of waves and currents accurately from simple field observations is a technical challenge in shallow water environments with limited inundation such as saltmarshes. In this paper, the estimation method of both wave and current information was studied mainly through the data obtained by a solely used field ADV (Acoustic Doppler Velocimeter, Vector). Phase and pressure inversion wave methods were both used to estimate wave parameters, which were then compared to synchronous observation by wave loggers at the front of a saltmarsh. Our results show that ADV is able to achieve simultaneous observations of tidal currents and waves independently. The pressure inversion wave method ($r^2 \sim 0.996$) is more effective than the phase method ($r^2 \sim 0.876$) in estimating wave energy when comparing with wave logger results. However, the former is more restricted by submergence depth and duration in field, while the latter provides cut-off frequencies for the pressure inversion wave method. Both methods can be combined to best estimate wave parameters from field ADV data. Further, hydrodynamic observation on a *Scirpus mariqueter* patch at the front of a saltmarsh was used as an application to indicate the importance of obtaining both wave and current information from field data. The patch was found to mainly reduce the advection of tidal currents, but it slightly increases wave energy. Therefore, it is necessary to consider the different effects of plants on tidal currents and waves simultaneously in field observations. This study confirms that ADV and associated analysis can detect waves and currents at reliable accuracy at the marsh edge, which is vital in assessing the long-term resilience of marshes to sea level rise and increased storm severity.

Keywords: coastal saltmarsh, wave, current, acoustic Doppler velocimeter, hydrodynamic

OPEN ACCESS

Edited by:
Zeng Zhou,
Hohai University, China

Reviewed by:
Cai Ladd,
University of Glasgow,
United Kingdom
Charlie Emma Louise Thompson,
University of Southampton,
United Kingdom

***Correspondence:**
Yining Chen
yiningchen@sio.org.cn

Specialty section:
This article was submitted to Coastal Ocean Processes, a section of the journal Frontiers in Marine Science

Received: *11 May 2021*
Accepted: *30 June 2021*
Published: *22 July 2021*

Citation:
Liu B, Chen Y, Cai T, Li Y and Sun L (2021) Estimating Waves and Currents at the Saltmarsh Edge Using Acoustic Doppler Velocimeter Data. Front. Mar. Sci. 8:708116. doi: 10.3389/fmars.2021.708116

INTRODUCTION

Coastal saltmarshes refer to coastal zones that border saline water bodies, which are vegetated by halophytes (salt-tolerant grasses or low shrubs) and regularly submerged and emerged under the motion of tides (Davidson-Arnott et al., 2002; Mitsch and Gosselink, 2007). Coastal saltmarshes serve as a transition zone between terrestrial and marine ecosystems, and provide many critical

ecosystem functions (Teal and Howes, 2002; Barbier et al., 2011; Deegan et al., 2012; Duarte et al., 2013; Temmerman et al., 2013). Coastal saltmarshes play a significant buffering effect on waves and tidal currents. Recent studies have revealed that saltmarshes reduce wave energy even during storms (Fagherazzi, 2014; Möller et al., 2014; Narayan et al., 2017; Paquier et al., 2017; Cao et al., 2020). Saltmarsh plants also reduce the flow velocity and dissipate turbulent energy by additional bed friction and through eddy viscosity (Neumeier and Amos, 2006; Nepf, 2012; Chen et al., 2016; Mossa et al., 2017).

The action of tidal currents and waves are the main hydrodynamic driving force working on saltmarshes (Schwimmer, 2001; Carniello et al., 2009). It is therefore essential to measure wave and current properties accurately at the marsh edge. Field acoustic Doppler velocimeter (ADV) has been developed into a high-frequency mode (up to 32 Hz) recently and they are widely used to measure tidal flat hydrodynamics (MacVean and Lacy, 2014; Chen et al., 2016, 2018; Lu et al., 2016). Besides its convenient deployment in shallow water environments, this instrument records three dimensional flow data with high sampling rate, allowing an observation on turbulence. Although field ADV data were traditionally analyzed to obtain flow and turbulent energy information, attempts was also made to extract wave information from ADV records. Gordon and Lohrmann (2002) demonstrated that field ADVs in shallow waters can observe wave spectra and wave heights. However, low sampling frequency resulted in a certain deviation in the high frequency band of the wave spectrum ($>$0.3 Hz). On this basis, the high-frequency field ADV was developed and used to observe hydrodynamics in a variety of field sites. The data were used to calculate the wave height, period, orbital velocity, and turbulent Reynolds stress in the wavy environment (MacVean and Lacy, 2014; Lu et al., 2016; Bian et al., 2018).

Previous studies have found that saltmarsh vegetation can reduce water flow and dissipate wave energy (Knutson et al., 1982; Neumeier and Ciavola, 2004). Marsh vegetation reduces the near bed flow speed (Neumeier and Ciavola, 2004), an order of magnitude more than adjacent mudflats (Bouma et al., 2005b). It is generally believed that saltmarsh vegetation attenuates waves effectively (Möller et al., 1999, 2014; Bouma et al., 2010). Wave dissipation over the submerged vegetation canopy depends on water depth and incident wave energy, and a hydrodynamic threshold may exist, beyond which the marsh will lose its wave dissipation effect (Yang et al., 2012; Mariotti and Fagherazzi, 2013). In the case of low stem density, the resistance will locally enhance turbulence, even leading to increased shear stress and potential bed erosion (Nepf, 1999; Bouma et al., 2009). In order to control the hydrodynamic conditions, researchers often utilize mimic plants or live plants to simulate the hydrodynamic processes during wave-current interactions (Gaylord et al., 2003; Paul et al., 2012; Hu et al., 2014; Möller et al., 2014; Maza et al., 2015; Lara et al., 2016), however, related factors such as natural seasonal changes of plants and the environmental settings are rarely taken into account (Maza et al., 2015). Traditional field observations mostly consider the hydrodynamics of saltmarshes solely dominated by either tidal currents (Wang et al., 1993; Leonard and Luther, 1995; Christiansen et al., 2000; Bouma et al., 2005b; Temmerman et al., 2005, 2012) or waves (Wayne, 1976; Möller et al., 1999; Möller and Spencer, 2002; Möller, 2006; Fagherazzi and Wiberg, 2009; Jadhav and Chen, 2012). Recently, due to the importance of vegetation patches in establishing new saltmarshes, interactions between vegetation patches- currents-waves at the pioneer zones of saltmarshes have been reported through flume observations (Bouma et al., 2013; Rupprecht et al., 2017; Maza et al., 2019). However, direction evidence from field is still hardly reported to further support laboratory results, particularly, those including both currents and waves. Even small differences in wave and current velocity determine whether marshes expand or erode (e.g., Bouma et al., 2013), therefore measuring wave-current dynamics accurately across a range of field conditions is important.

On-site observations of wave-current association have been conducted in shallow water environments such as tidal flats (Callaghan et al., 2010; Shi et al., 2012; Karimpour et al., 2016), which usually involved complicated co-deployment of multiple instruments, combining flow meters (e.g., EMF, PC-ADP, ADP-XR, field ADV) and wave loggers (e.g., Druck PTX1830, ABE 26plus, Ocean Sensor Systems) to detect wave and current separately. However, considering the minimal disturbance on vegetated flats and the limitation of access to multiple instruments, it is still in need to use solely instrument to obtain both current and wave information in shallow waters with limited inundation, such as saltmarshes. ADVs were mainly designed to monitor high-frequency three dimensional velocity components, however, attempts to extract wave signals have proved that ADVs are also able to capture wave information (Gordon and Lohrmann, 2002; Wiberg and Sherwood, 2008; Lu et al., 2016). Among those studies, the wave estimations were mainly tested in environments with relatively long submergence where pressure sensors of ADV could also record long data length. It is still unclear whether application of ADV signals can describe both flow and wave in shallow water environments, such as saltmarshes and mangroves with short submergent periods. In addition, it is practical to extend the usage of field ADV so that both flow and wave information can be obtained when wave loggers are absent.

The objective of this study is twofold. Firstly, we propose a field data processing protocol for obtaining both waves and currents using a simple and conventional hydrodynamic instrument, field ADV (Vector, manufactured by Nortek), which was deployed on the front of a saltmarsh. We adopted both phase method (Stapleton and Huntely, 1995; Bricker and Monismith, 2007; MacVean and Lacy, 2014) and pressure inversion wave method (Tucker and Pitt, 2001) to process the ADV high-frequency flow velocity and pressure data, respectively. Phase method was introduced for wave-turbulence decomposition using power spectra while pressure inversion wave method extracted wave parameters by the pressure variation based on linear wave theory. In parallel, the measured wave parameters by pressure based wave loggers (RBRsolo D| wave) were used to verify the accuracy of the ADV results, and further test the feasibility of the

ADV estimation method. Secondly, we also analyzed the mediation effects of vegetation patch on tidal currents and waves at the saltmarsh edge by comparing hydrodynamics above the adjacent. This part was used as an application of field ADV, to indicate the necessity of separating waves and currents from field data, in order to support the logistic of this study.

PHYSICAL SETTINGS OF THE STUDY AREA

Hangzhou Bay, located in the northeast of Zhejiang Province, China (**Figure 1**), is a typical funnel-shaped, macrotidal estuary with multiple sources of water and sediment (Liu et al., 2012; Wang et al., 2015). The water depth of Hangzhou Bay is shallow, with an average depth of about 10 m. The width of the estuary is about 98.5 km and is gradually reduced to about 20 km, with a total area of about 4800 km^2 (Xie et al., 2017). Hangzhou Bay has a large tidal range (3∼6 m), resulting in strong tidal currents with a maximum measured velocity of 3.0 m s^{-1} in the main channel. The north is the main passage of flooding tides, while the south bank is the primary region for sediment deposition (Su and Wang, 1989; Xie et al., 2013, 2017). The semi-diurnal tide is the main driving force in Hangzhou Bay, with M_2 as the main component. Waves in Hangzhou Bay are mainly driven by wind, with annual average wind speed of 2.3-7.3 m s^{-1} and an average annual wave height of 0.2-0.5 m (Editorial Committee for Chinese Harbors and Embayment (ECCHE), 1992; Xie et al., 2013). The wind direction of Hangzhou Bay is mainly characterized by monsoon, with northerly wind in winter and southerly wind in summer, and spring and autumn are transitional periods (Editorial Committee for Chinese Harbors and Embayment (ECCHE), 1992).

Andong shoal is a large-scale shoal developed near the turbidity maximum zone on the south bank of Hangzhou Bay, which is the main region of saltmarsh wetlands in Hangzhou Bay (Li and Xie, 1993a,b; Huang et al., 2020). Since 2008, the south bank of Hangzhou Bay has undergone a large-scale reclamation along the shore, and as a consequence, saltmarshes nearly completely disappeared. New saltmarshes have developed in front of the seawall and rapidly expanded towards the sea. The width of the saltmarsh currently reaches 3 km, close to its width before reclamation (Huang et al., 2020). The Andong Shoal is mainly dominated by tidal currents due to its large tidal range (∼6 m) and waves are mild in the upper part of the tidal flat where is occupied by plants. Since 2017, two new large T-shaped dams had been built in Andong Shoal to promote sediment deposition. These dams provide access to the front edge of the saltmarsh, where wave action is relatively severe. Patches of *Scirpus mariqueter*, a native species, are sporadically distributed on the front of this saltmarsh (Huang et al., 2020). *Scirpus mariqueter* is a perennial rhizomatous, corm-forming grass, which is mainly distributed in the saltmarshes along the Yangtze River Estuary and Hangzhou Bay (Ysebaert et al., 2011). We chose a patch of *Scirpus mariqueter* on the front as showed by the study area map (**Figure 1c**) for field deployment.

METHODS

Due to a large tidal range in this region, the saltmarsh is flooded for 2-3 h daily only during middle to spring tides. To carry out this research, two stations were set up (121°10′25.44″E, 30°23′3.56″N) from June 19 to 22, 2020 (spring to middle tides) at the locations shown in **Figure 1b**, namely Station A and Station B. Station A is located on the bare mudflat seaward of the vegetation patch, at a distance of 3.9 m from Station B in the patch center. The elevation of Station A is about 6 cm lower than that of Station B. The *Scirpus mariqueter* patch under investigation was nearly round with a diameter approximately 7 m. Plant density of the *Scirpus mariqueter* patch was 960 shoots m^{-2}, the aboveground dry biomass was 0.2 kg m^{-2}, and the average stem height was approximately 45-55 cm. Although this region is dominated by semi-diurnal tides, the patch and the sensors were submerged for approximately 2 h daily during each high tide (only 4 tidal cycles in 4 days observation).

Description of General Instrument Deployment

Synchronous observation were conducted at the two stations, and the instruments contained ADVs (Vector, by Nortek), wave loggers (pressure based, RBRsolo D| wave) and water level gauges (pressure based, OBS3A, Campbell Scientific). Wave loggers were only launched on June 21 and 22 due to limited availability, and water level gauges were used to record the water level during the rest survey. Water level gauges were installed 10 cm above the bed at stations A and B to collect single-point water level data every 10 s. Mean water level was calculated in 5-min windows. Limited by the position of the pressure sensor, the effective dataset length of ADV pressure was usually shorter than the flow velocity data, and only part of the data in the tidal cycle could be collected because of the limited inundation period. Hence, the ADV water level data are inefficient to cover a tidal cycle in this study and additional instrument is need for compensation, including wave loggers and water level gauges.

Acoustic Doppler velocimeter uses the acoustic Doppler principle to measure velocity components of X, Y, and Z corresponding to the east, north, and upward directions, respectively. The ADVs used in this study were both set to sample downward. The flow velocity sensor was placed 22 cm above the bed and the measurement volume was 10 cm above the bed. The speed measurement range of the instrument was set between 0 and 0.3 m s^{-1} with measurement accuracy of 0.5% of the measured value. The sampling was in a continuous mode at a frequency of 16 Hz. The pressure sensor of ADV was 40 cm away from the mudflat surface, at a same sampling frequency of 16 Hz. ADV can simultaneously collect the high frequency variation information of flow velocity and pressure data. The former can describe the flow velocity variation, and the latter can retrieve the wave parameters, to synchronously observe tidal currents and waves. However, due to the submergent duration difference, the latter records shorter data length than the former.

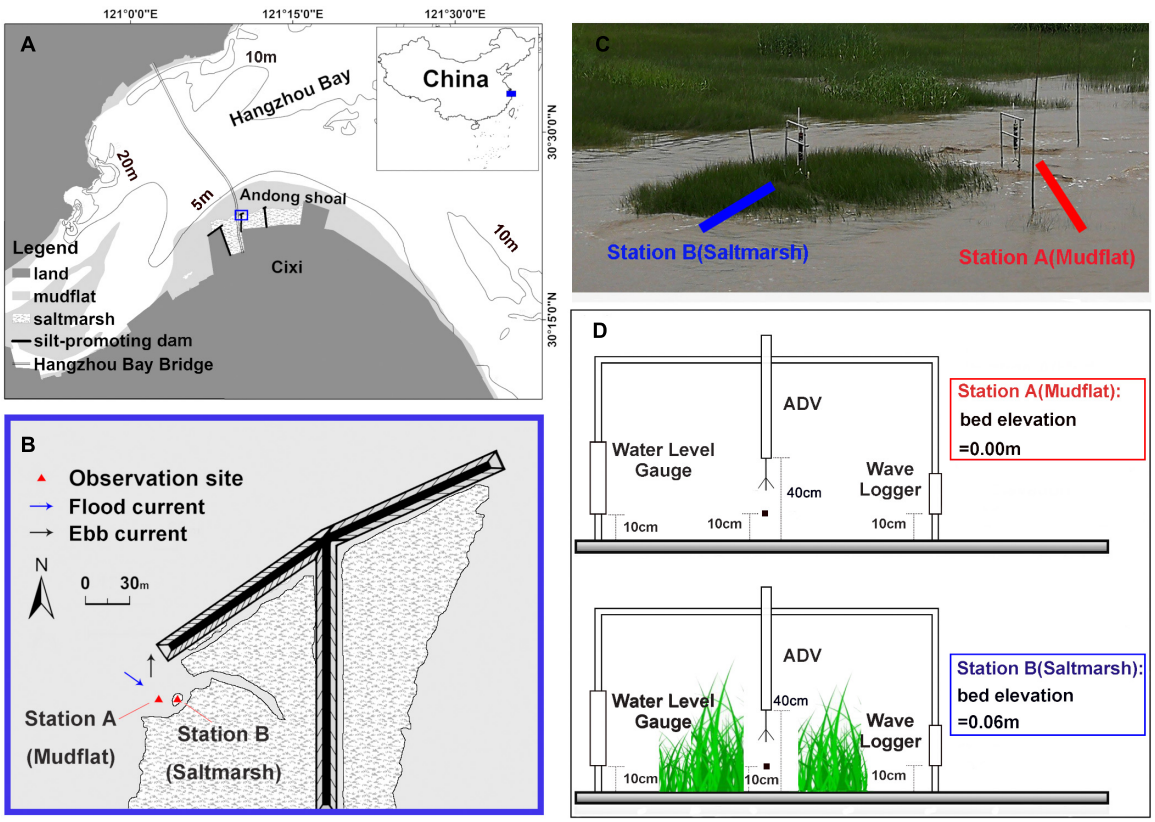


FIGURE 1 | Study area and observation sites: **(A)** map of Hangzhou Bay area, the study area (in the blue box) is located on the top of a T-shaped dam; **(B)** the deployment locations of the observation sites, Station A (mudflat) and Station B (saltmarsh). The blue arrow represents the direction of flooding, and the black arrow represents the direction of ebbing; **(C)** a field picture of the deployment of the observatory; **(D)** the position of the deployed instruments: the pressure sensor of ADV is located at 40 cm above the bed whilst the velocity sampling volume of ADV is 10 cm above the bed; water level gauge and wave logger are both 10 cm above the bed; the elevation of the bottom bed of Station B is 6 cm higher than that of Station A.

Wave loggers (RBRsolo D| wave) used in this study are single-channel self-contained marine instruments with advantages of small size, light weight, and flexibility in use. In this study, wave loggers were fixed at 10 cm above the bed at two stations, to conduct intermittent sampling every 5 min for 128 s at a frequency of 16 Hz. The method of operation during wave sampling is to collect a burst of pressure data and hence depth data and to relate this to the sea surface to obtain a view of the waves. The supporting Ruskin software could perform wave data analyses and acquire basic wave parameter information such as wave height, wave period, and wave energy. Ruskin software generates a time sequence of the surface of the sea. This can be undertaken in three major steps (Gibbons et al., 2005):

(a) The time sequence is transformed to its frequency components using Fourier analysis, the pressure correction range is 0.05∼0.33 Hz (Lancaster et al., 2021).
(b) Each frequency component is multiplied by the inverse of the attenuation suffered by that particular frequency due to the depth of the logger.
(c) The augmented frequency information is transformed back to a time sequence using the inverse Fourier transform.

Phase Method

All ADV data during submergence was extracted and divided into 5-minute intervals for further processing. Before calculating the velocity change, the phase-space threshold method (Goring and Nikora, 2002) was taken to suppress noise. The phase-space threshold method required to construct an ellipsoid in three-dimensional phase space, and data outside the ellipsoid was defined as spikes and needed to be replaced by interpolation. High-frequency velocity data usually contain low-frequency advection flows, and relatively high-frequency waves and turbulence, which can be distinguished by the velocity power spectral density diagram. The low-frequency advection could be obtained by filtering the velocity data measured by ADV through low-pass filtering, and the cut-off frequency was fixed to 0.067 Hz as most of power spectra results from our observations show a transition at this point (**Figure 2**). Waves and turbulence overlapped on the frequency scale, which could not be processed by simple filtering. Waves could be separated, and the main frequencies of wave motion in the study area distinguished according to the velocity power spectrum using the phase method (Bricker and Monismith, 2007; MacVean and Lacy, 2014) to process the velocity power spectrum density diagram. The

cut-off frequencies of high-frequency varied with the spectral shapes as shown in **Figure 2A**, that is, the frequency at which the high-frequency turbulence in the spectrum begins to overlap with the -5/3 power law and thus it is case specified. Kolmogorov theory argues that in the inertial sub-region of the energy spectrum, the turbulent energy dissipation process conforms to the -5/3 law (Kolmogorov, 1941a,b,c). Therefore, the power spectrum within the wave motion range could be interpolated in logarithmic coordinates according to the power spectrum within the frequency range of the turbulence motion to obtain the power spectrum of the turbulence motion (**Figure 2B**). The time series of velocity data was converted into frequency spectrum by Fourier Transform, keeping the phase consistent, and then the inverse Fourier transform was performed on the Fourier term to obtain the flow velocity signal after removing the wave motion. Using the original velocity power spectral density (**Figure 2A**) minus the velocity power spectral density processed by the phase method (**Figure 2B**), the wave signal could be separated and the wave-current separation completed. After above processing, parameters such as the TKE (Turbulent Kinetic Energy) density and wave energy could be calculated.

Turbulent Kinetic Energy is a measure of the intensity of turbulent motion in a shear fluid (Dade et al., 2001). The total TKE density, combination of current TKE density and wave TKE density, is estimated using the following equation (Soulsby, 1983; Soulsby and Humphrey, 1990):

$$TKE_{density\ tot} = 0.5\rho\left(\overline{U'^2} + \overline{V'^2} + \overline{W'^2}\right) \quad (1)$$

ρ is seawater density at 1028 kg m^{-3}, U'(east),V'(north), and W'(upward) are components of fluctuating velocity obtained by ADV. After the wave signal was removed from original data, the TKE density of current is calculated using the following formula:

$$TKE_{density\ cur} = 0.5\rho\left(\overline{U1'^2} + \overline{V1'^2} + \overline{W1'^2}\right) \quad (2)$$

$U1'$, $V1'$, and $W1'$ are components of fluctuating velocity after wave filtering. Based on above calculations, the TKE density of wave is then calculated by the total TKE density minus the TKE density of current.

Wave energy (each 5-min window) is calculated by power spectral density integration:

$$E_{wave} = \left(\int_{f_l}^{f_h} S_{orginal} - \int_{f_l}^{f_h} S_{phase}\right)\rho g T^2 \quad (3)$$

Where, $S_{orginal}$ is the original velocity power spectral density, S_{phase} is the power spectral density of the velocity after the phase method is processed, f_l is the low-frequency cut-off frequency, f_h is the high-frequency cut-off frequency, ρ is the seawater density, g is the gravity acceleration, and T is the effective time for calculating wave energy by power spectrum.

Pressure Inversion Wave Method

In addition to the phase method, ADV pressure data could also be used to retrieve wave parameters. The original ADV pressure data was converted into water level fluctuations, and then corrected by eliminating false spikes, frequency shifts, damaged bursts by setting thresholds, low-frequency tidal components could be removed from each burst by detrending the water level fluctuations using a polynomial fit (Callaghan et al., 2010; Christianen et al., 2013). The method of retrieving wave parameters from water depth was based on linear wave theory (Tucker and Pitt, 2001). It is noted that the pressure correction ranges should be consistent with the cut-off frequencies of the phase method during the same interval. The effective wave height and wave energy are defined as functions of spectral moments, which can be given by the following nth spectral moment:

$$m_n = \int_0^\infty f^n S(f)\,\mathrm{d}f \quad (4)$$

Where f is the wave frequency, $S(f)$ is the spectral density, and the effective wave height and wave energy are defined as:

$$H_s = 4\sqrt{m_0} \quad (5)$$

$$E_{wave} = \rho g m_0 \quad (6)$$

Where m_0 is the zero moment (variance) of the spectrum, ρ is the density of sea water, and g is the acceleration of gravity (9.8 m s^{-2}).

The inversion of the high-frequency pressure data of ADV could allow wave parameters such as wave height, period, energy to be obtained.

Estimating Wave Direction

PUV method uses ADV pressure data P and ADV velocity data U (east) and V (north) to estimate wave direction. The direction Dir calculation formula is as follows (Gordon and Lohrmann, 2002):

$$Dir = atan2(C_{pu}, C_{pv}) \quad (7)$$

Where atan2 is a 4-quadrant arctangent, and C_{pu} and C_{pv} are the real parts of the pressure-velocity cross-spectra for the two velocity components U and V.

Similarity Evaluation of Wave Energy Calculated by Two Methods

The wave energy of each interval (5 min) were calculated by both phase method and pressure inversion method. The accuracy of the results was verified by wave logger measurements. The comparison process was based on the correlation analysis method and unary linear regression was chosen in a SPSS software package. Unary linear regression was used for consistency evaluation qualitatively. The slope and intercept of the equation reflected the difference between the two data sets. In addition to R-squared and P-values, if the slope of equation is close to 1 and the intercept is close to 0 (implies very limited systematic shift between two variables), the difference between the two sets was considered insignificant.

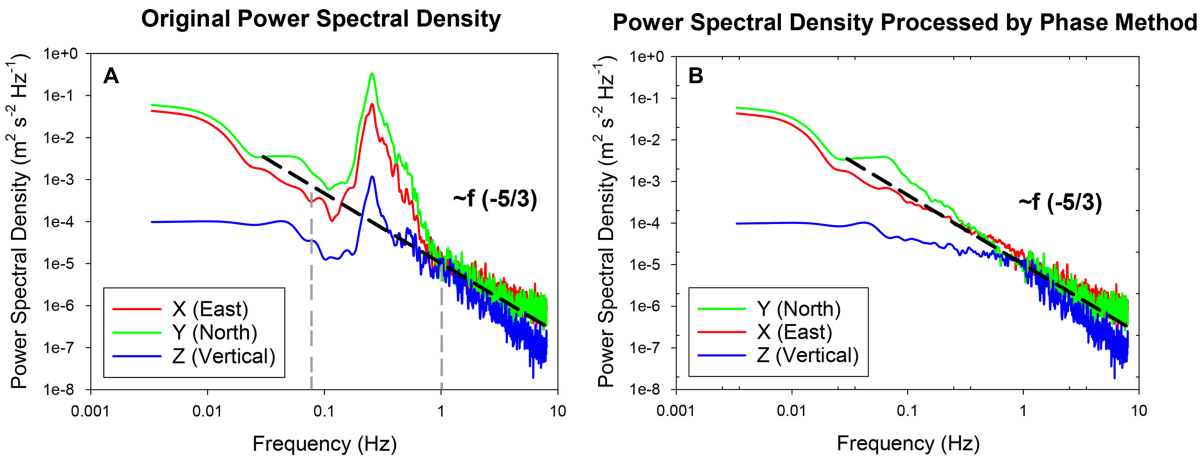


FIGURE 2 | Acoustic doppler velocimeter high frequency velocity data analysis: **(A)** original velocity power spectral density diagram (as an example); **(B)** the velocity power spectral density diagram processed by phase method after wave removal (X, Y, Z are the east, north, and upward velocity components measured by ADV, respectively, and the dotted line indicates that the turbulent energy dissipation process conformed to the -5/3 power of the Kolmogorov theory in inertial sub-regions).

Moreover, the dimensionless consistency index (Callaghan et al., 2010) was used to evaluate the accuracy of the calculation results with wave logger data:

$$I = 1 - \sum (x - y)^2 \Big[\sum \left(|x - \bar{y}| + |y - \bar{y}| \right)^2 \Big]^{-1} \quad (8)$$

Here $0 \leq I \leq 1$, $I = 0$ means no agreement, $I = 1$ indicates complete agreement (Willmott, 1981). Wherein, the measured value and the calculated value are represented by x and y respectively.

RESULTS

Analysis of Wave-Current Separation Results

Using the phase method and pressure inversion method, we acquired wave parameter information at the two stations. The reliability of these results could be verified by comparing them with the observation results of the wave loggers. Since wave loggers had a limited deployment (June 21 and June 22), only the results of 2 days were available for analysis. There was a considerable difference in wave energy between June 21 and June 22, which was related to the wind strength of the 2 days. Referring to Beaufort scale, June 21 was dominated by fresh breeze with average wind speed $\sim$ 9.4 m s^{-1}; June 22 was dominated by moderate breeze with average wind speed $\sim$ 6.7 m s^{-1}. Overall, the comparison on the wave energy data calculated by phase method and pressure inversion wave method from ADV records (**Figure 3**) shows a good agreement for those two methods, although a deviation is also noted on the day of mild winds.

Calculation result of the phase method showed a significant correlation with the measurement result of the wave loggers (**Figure 4**, P-value <0.001). The slope changes in data sets suggest that estimates by the phase method on June 21 are consistent to those values from wave loggers (**Figures 4A,C**) while the estimates under the calm conditions on June 22nd are less consistent (**Figures 4B,D**).

The estimation by inversion wave method using ADV pressure data could also be used to calculate wave energy and verified through the wave parameters measured by wave loggers. Compared with the phase method, the calculation results of the pressure inversion wave method had a good consistency, despite differences in wind condition (**Figures 4E-H**). The off-set was also noticed and this was mainly caused by system pressure correction (including air pressure correction) for different pressure sensors. However, ADV pressure data inversion wave methods were usually restricted by water depth conditions, and long-time series wave data could not be obtained in limited flooded areas such as saltmarshes. For solely used ADV deployment, the ADV pressure data that was available for pressure inversion analyses only covered about 78% of the observation period in our study, while the phase method based on ADV velocity data could cover the entire effective observation period. Although the pressure inversion wave method provides more consistent wave results with wave logger records, the calculation of the phase method at low water level can be compensated for the depth limitation of the pressure inversion wave method. More importantly, the phase method provides cut-off frequencies for the pressure inversion wave method to improve its accuracy. Consequently, the combination of phase method and pressure inversion wave method is found capable of separating current and wave information using single ADV measurement.

Wave parameters such as wave height and period could also be calculated with the ADV pressure inversion wave method. As shown in **Table 1**, waves in the study area are dominated by capillary (wave period $<$ 1 s) and gravity waves (1 s $\leq$wave period $<$ 30 s), and the effective wave height and energy reaches the maximum on June 21, which is consistent with the strong wind on that day (approximately 9.4 m s^{-1}). The wave direction varies mainly between north and east direction

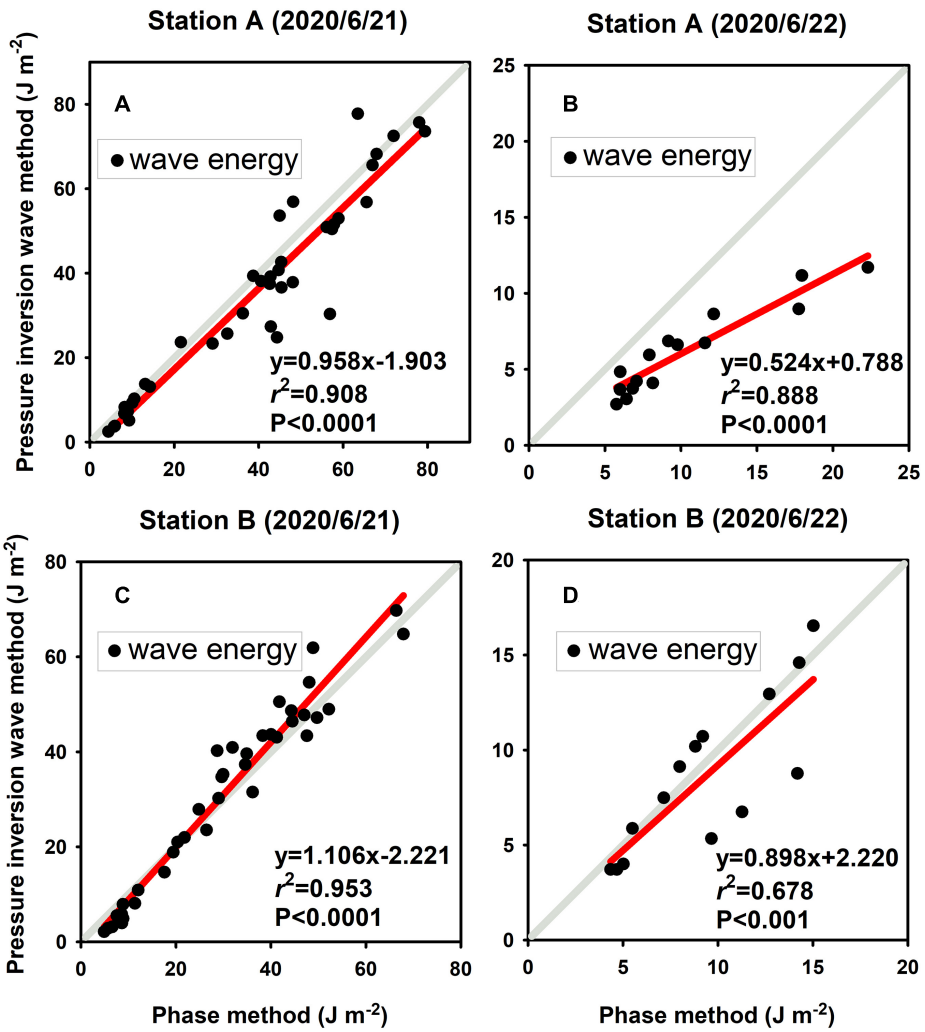


FIGURE 3 | (A–D) Results of correlation analysis of wave energy calculated by phase method and pressure inversion wave method.

as revealed by **Table 1**, although the wind direction is mainly east. It appears that flood and ebb phases have some influences on wave direction.

Hydrodynamic Characteristics of the Saltmarsh Front: Mudflat and Patch Center

Figure 5A reveals the water level variations at Station A (mudflat), including records of four tidal cycles. On average, the duration of the flooding phase was slightly longer than that of the ebbing phase. The tides in the study area were semi-diurnal with diurnal inequality, causing only half tidal cycles were able to submerge both velocity sensor and pressure sensor of the ADV. Thus, only four tidal cycle data were collected.

The flood of the mudflat station generally followed a southeast direction and then receded toward a near-northward direction (**Figure 5B**). The velocity variation was mainly controlled by the bottom, and the impact of the wind was greatly weakened due to the sheltering of the dam, with a maximum flow speed of approximately 0.15 m s^{-1}. When the water level was low (Tide 4), the bottom bed friction was considerable, leading to the maximum speed of only 0.04 m s^{-1}. To define the attenuation of waves and currents under different conditions, the phase method was used to calculate the variation of the TKE density of currents and the TKE density of waves (**Figure 5C**). In general, the TKE density of waves was more than one order of magnitude higher than that of currents, indicating the importance of wave action. When the wind speed was high (Tide 2 and Tide 3), the TKE density of both currents and waves was higher, while the TKE density of currents and the TKE density of waves were lower in the two tidal cycles with a minimum wind speed (Tide 1) and minimum water level (Tide 4). However, during the ebbing phase of T3, a switch in dominance between the wave and current occurred (**Figure 5C**). The reason is likely to be associated with the very shallow water layer under relatively strong wave action

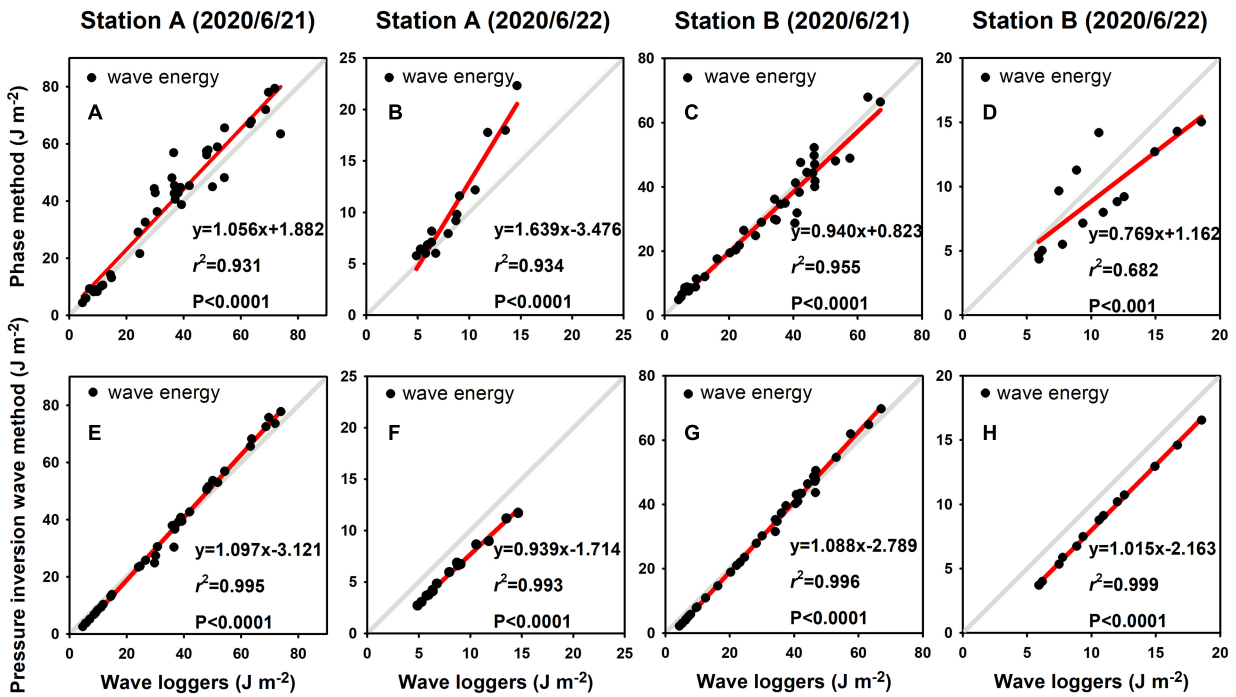


FIGURE 4 | Correlation analysis of wave energy measured by wave loggers and calculated by ADV data: **(A–D)** the comparison between wave loggers results and calculated results from phase method; **(E–H)** the comparison between wave loggers results and calculated results from pressure inversion wave method. Station A is mudflat site and Station B is patch center site; the observation took place on June 21 and June 22.

TABLE 1 | Wind conditions and wave characteristics of stations A (mudflat) and B (vegetation) from 19th June to 22nd June, 2020.

Date	**2020/6/19**		**2020/6/20**		**2020/6/21**		**2020/6/22**	
Wind (m s^{-1})	**3.5 (undirected)**		**5.6 (east)**		**9.4 (east)**		**6.7 (east)**	
Station	**A**	**B**	**A**	**B**	**A**	**B**	**A**	**B**
Effective wave height (m)	0.06 ± 0.01	0.07 ± 0.01	0.06 ± 0.01	0.06 ± 0.01	0.16 ± 0.07	0.15 ± 0.06	0.08 ± 0.02	0.08 ± 0.02
Effective period (s)	0.78 ± 0.29	0.80 ± 0.30	0.68 ± 0.15	0.62 ± 0.19	2.38 ± 0.83	2.12 ± 0.82	1.04 ± 0.25	1.16 ± 0.31
Wave direction (flood/ebb) (°)	57 ± 90/ 86 ± 15	13 ± 15/ 56 ± 43	22 ± 174/ 105 ± 42	9 ± 39/ 93 ± 49	31 ± 73/ 91 ± 22	357 ± 30/ 44 ± 27	12 ± 33/ 56 ± 24	7 ± 23/ 27 ± 27
Wave energy 1 (J m^{-2})	5.8 ± 2.7	6.6 ± 3.1	4.8 ± 1.3	5.0 ± 1.7	35.6 ± 22.6	30.5 ± 19.5	6.2 ± 2.8	8.6 ± 3.9
Wave energy 2 (J m^{-2})	\	\	\	\	35.2 ± 20.5	30.6 ± 17.9	8.4 ± 2.9	10.6 ± 3.9

Wave direction is defined as 0 to the north °, rotate 90 clockwise ° to the east. Wave energy 1 is calculated by ADV data, wave energy 2 is calculated by wave logger data.

in which surface wave can better affect the bottom water volume measured.

The variations of water level, flow velocity, and TKE density at Station B (vegetation patch center) show some differences from those at Station A (**Figure 6**). The flow direction of the tidal current in the vegetation patch (**Figure 6B**) was similar to that on the mudflat, and the flow velocity was restricted by the vegetation and the friction of the bottom bed, which generated a maximum flow speed of 0.03 m s^{-1}. When the mean water level was the lowest (Tide 4), the maximum flow speed was only 0.01 m s^{-1}, less than that of the mudflat station, which was affected by the dense plant canopy. The TKE density variation

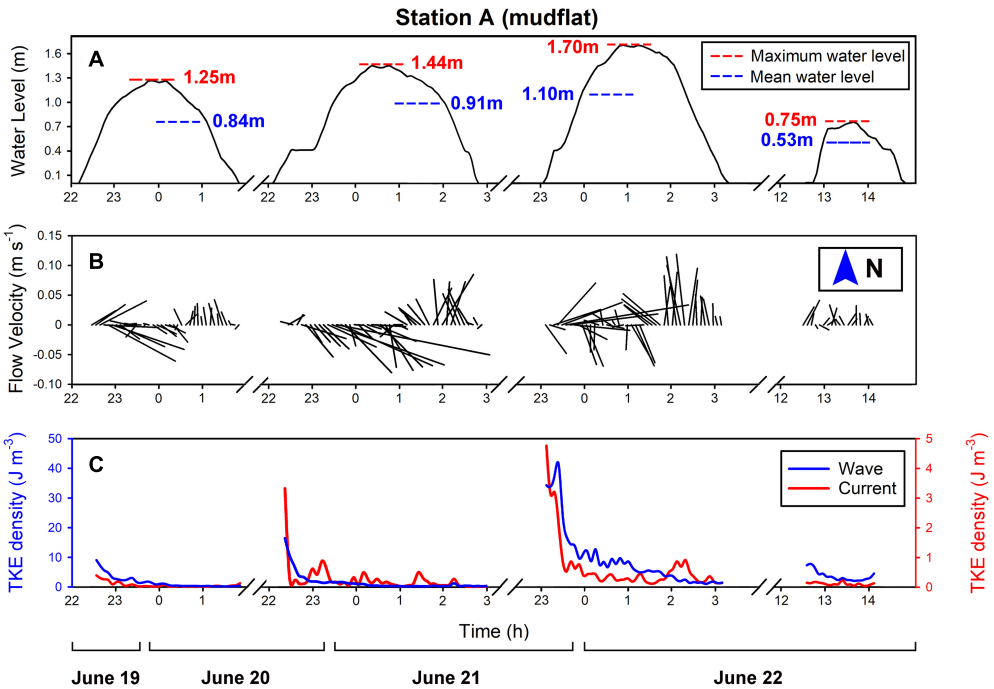


FIGURE 5 | Four tidal cycles were recorded at Station A (mudflat) from June 19 to 22: **(A)** water level variations in each tidal cycle, the maximum water level and the average water level are given separately; **(B)** flow velocity variations of each tidal cycle (the length of the flow vector segment represents the flow magnitude); **(C)** the TKE density variations of waves and currents in each tide cycle.

trend of currents and waves (**Figure 6C**) of the patch center station is similar to the mudflat observation, except for the period with the relatively strong wind speed (Tide 2). This difference indicates that relatively high wind speed could cause variation of currents and waves in mudflat but had no obvious effect on vegetation patch. During the period of maximum wind speed (Tide 3), the TKE density of currents and the TKE density of waves were also the largest, and the value of them was smaller at other periods.

The TKE density also showed tidal asymmetry in the bare mudflat, which was much greater during the flooding phase than the ebbing phase. This pattern is similar to other observations with the existence of vegetation (e.g., Chen et al., 2018), indicating a great effect of vegetation in damping turbulent energy. In terms of waves, the measured wave parameters show that the average wave height of the waves at mudflat station was 0.042∼0.143 m with an average of 0.075 m and an average period of 0.975 s. The average wave height at patch center was 0.074 m, and the average period was 0.908 s. Different from the trend of evident attenuation of tidal currents, the wave heights of the two stations were found close. However, an increase of wave energy within the patch center was observed for most of the tidal cycles, expect June 21 of strong winds when wave height in patch center was slightly lower than the mudflat (**Table 1**). On average, a magnitude of 9% of wave energy increase was found within the vegetation patch center.

DISCUSSION

Estimation Methods of Wave-Current Separation and Their Limitations

Phase method verification results show the difference between June 21 and June 22 in **Figure 3**. This difference may be related to the wind conditions. Whereas, during the period of relatively strong wave energy (**Figures 3A,C**), there was a very good consistency between two datasets as implied by equation slope close to 1. While the wave effect was relatively weak on June 22 (**Figures 3B,D**), the ADV estimates deviated greater from the wave logger values, as the wave energy signals might be contaminated by small overlap between wave, turbulence and vegetation generated disturbance (such as swing leaves). Over a spectrum scale. This comparison indicates that the phase method is more effective in calculating wave energy in the overall trend and the conditions with greater wave energy. The comparison indicates that the calculation result of pressure inversion wave method is better than that of phase method. This is because the wave inversion through pressure data was consistent with the working principle of the wave loggers pressure sensor except for the pressure correction ranges.

Our results find that the phase method and the pressure inversion wave method all have good verification results with wave loggers. However, the former had a greater deviation during weak wave actions, while the latter restricted by low water level conditions and required the cut-off frequencies from the former. In addition to correlation analyses and the qualitative analysis of

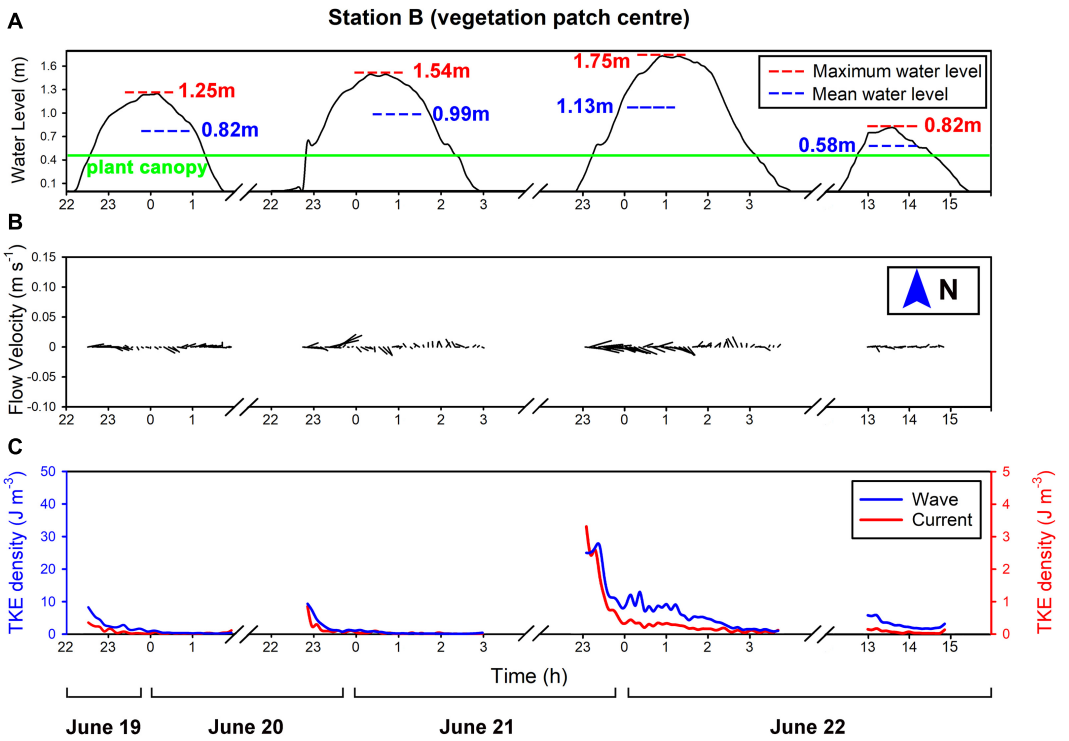


FIGURE 6 | Four tidal cycles were observed and recorded at Station B (vegetation patch center) from June 19 to 22: **(A)** water level variations of each tidal cycle (the maximum water level and the average water level are given separately); **(B)** the flow velocity variations of each tidal cycle (the length of the flow vector segment represents the velocity magnitude); **(C)** the TKE density variations of the currents and waves in each tide cycle.

TABLE 2 | The consistency index statistics of the calculation results of the phase method and the pressure inversion method compared with the measurement results of the wave loggers (1 = strong agreement, 0 = no agreement).

Station	A(mudflat)	A(mudflat)	B(vegetation)	B(vegetation)
Date	**June 21**	**June 22**	**June 21**	**June 22**
I (Phase method)	0.97	0.84	0.98	0.88
I (Pressure inversion)	0.99	0.87	0.99	0.94

the differences between datasets, the accuracy of the wave energy estimated by the two wave-current separation methods should be evaluated and discussed. We use the consistency evaluation method to further evaluate the similarity between wave energy dataset estimated from ADVs and wave loggers.

The consistency evaluation results are shown in **Table 2**. This table indicates that the wave energy data obtained by phase method and pressure inversion wave method both have a good similarity with the measured results of wave loggers, although the pressure inversion wave method is slightly more accurate than the phase method. In addition, a relatively large difference is observed on 22nd June, and this is because the deviation between phase method and pressure inversion wave method of ADV data under calm wave conditions is greater than severe conditions (**Figure 3**).

There are some differences between the wave energy magnitudes calculated by the phase method and the actual measured value, illustrated by **Table 2**. This may be related to the selection of the high-frequency cut-off frequency. Some attempts were done to determine which method was more suitable combined with previous studies. Chen et al. (2002) note that the high-frequency cut-off frequency was dependent on the depth of the instrument in the water when observing the breaking wave zone on the flat:

$$f_{max} = \frac{1}{2}\sqrt{g/(\pi h_p)} \tag{9}$$

h_p is the depth of the instrument; Wiberg and Sherwood (2008) deemed that the selection of the high-frequency cut-off frequency was related to the water depth of the measuring point, that is:

$$f_{max} = \frac{1}{2}\sqrt{g/(\pi d)} \tag{10}$$

d is the water depth; when observing the muddy tidal flat with ADV, MacVean and Lacy (2014) set the high-frequency cut-off frequency as a fixed value, that is, $f_{max} = 0.5Hz$. All three groups considered it reasonable to choose the same cut-off frequency in the same region. Assuming that the above three formulas are

TABLE 3 | Attenuation comparisons of flow speed and total TKE density from bare mudflat to *Scirpus* saltmarsh.

Source	Vegetation width (m)/Distance of measurement sites (m)*	Attenuation of flow speed	Attenuation of total TKE density
Yang, 1998	10-20	16-66%	\
Yang et al., 2008	8.5	30%	\
Chen et al., 2018	4	7%	48%
This study	3.9	75%	24%

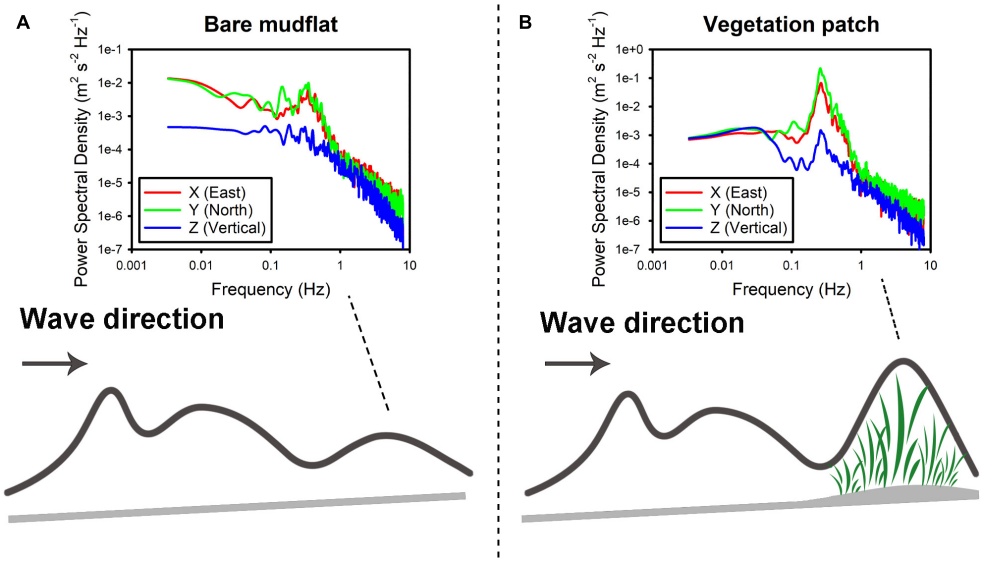


FIGURE 7 | Wave strengthening occurs under the combined action of elevation and vegetation: **(A)** wave motion in the bare mudflat; **(B)** wave enhancement when the vegetation patch appears.

applied to our research area, the three high-frequency cut-off frequencies should be 0.82 Hz, 0.78 Hz, and 0.5 Hz, respectively, which lead to 270%, 231%, and 16% deviation rate, respectively (the deviation rate is defined as the degree of deviation between the calculated wave energy and the actual wave energy).These results are higher than our 6% deviation rate in this paper. Hence, it is reasonable to choose different cut-off frequencies according to different spectral shapes from phase method, even in the same study area.

The wave energy data obtained by the pressure inversion wave method show a good similarity with the measured results of the wave loggers as revealed by **Table 2**. Therefore, when ADV pressure sensor is fully submerged, it can completely replace the wave loggers to do current and wave observation simultaneously. Meanwhile, the phase method not only provides the cut-off frequencies for processing pressure inversion, but also is used as the supplement for low water stages. It is also noticed, during the observation interval of 5 min, the effective observation times of the wave loggers and ADV pressure sensor are 128 s and 300 s, respectively. This may be the main reason for the slight difference between the wave energy measured by the wave loggers and the wave energy retrieved by the ADV pressure data. However, our data were collected within a relatively short term in relatively tranquil conditions, more tests in various environments should be conducted to further validate the estimation methods proposed by our study.

The Role of Vegetation Patch in Mediating Currents and Waves

The average flow speed in the bare mudflat was 0.04 m s^{-1}, while the average speed of the vegetation patch was only 0.01 m s^{-1}, revealing a sharp damping in flow magnitude. The total TKE density of bare mudflat and vegetation patch center were reduced by a magnitude of 24%, comparing the data of two stations of same submergence periods. Although vegetation may locally enhance turbulence (Nepf, 2012), turbulence is generally weakened by the present of plants in compared with bare mudflats (e.g., Leonard and Luther, 1995; Chen et al., 2016). The TKE density of current of vegetation patch station was greatly suppressed compared with the bare mudflat, by a magnitude of 50%, while the TKE density of waves showed a less decrease from the bare mudflat to the patch center (21%). Moreover, for this tidal flat, the TKE density of wave was always higher than the TKE density of current, reflecting the importance of waves in the saltmarsh pioneer zone. Overall, comparing Station A (mudflat) and Station B (vegetation patch center) reveals that when the waves and currents cross the bare mudflat-vegetation

junction and entered the vegetation patch, the friction dominated by the vegetation caused the flow speed and turbulence energy to attenuate, reducing them by about 75% and 24%, respectively. However, wave energy shows an increase by 9%, indicating an enhanced wave action in the patch center. Those patterns indicate that vegetation patch is better at dissipating high-frequency energy than non-vegetated areas, but the slightly enhancing wave energy. It is fundamental to separate the influence of vegetation patches on currents and waves.

Previous studies have found that when water flows into saltmarshes from bare mudflats, turbulent kinetic energy is lost by a magnitude of 77∼91% due to the blockage, friction, and diversion of plant stems and leaves, and the flow velocity is greatly reduced by a magnitude of 16∼69% (Leonard and Luther, 1995; Shi et al., 2000; Leonard and Croft, 2006; Neumeier and Amos, 2006; Tempest et al., 2015; Chen et al., 2016), while the flow direction can also be changed slightly (Chen et al., 2016). Some comparisons on attenuation of flow speed and turbulent kinetic energy by the same vegetation species are shown in **Table 3**. Chen et al. (2018) studied a *Scirpus* patch in the upper marsh and found that main function of patch was to reduce TKE density rather than flow speed. In this study, a small *Scirpus* patch in the pioneer zone was found to reduce 24% of total turbulent energy and 75% of flow speed. It appears that the attenuation effect of flow velocity by patches is more considerable in the pioneer zone in compared with TKE density reduction. This difference can be explained by relatively high water levels in the pioneer zone which caused longer canopy submergence and consequently reduced the turbulence suppression.

It is generally understood that the resistance of plant canopy can extract the mean flow energy and convert it into turbulent kinetic energy (Raupach and Shaw, 1982). In fact, only formal resistance is converted into turbulent kinetic energy, and viscous resistance is immediately dissipated to heat (Tanino and Nepf, 2008). For the submerged flexible canopy, the resistance is mainly viscosity (Nikora and Nikora, 2007). In this study, *Scirpus mariqueter*, which is dominated by viscous resistance, provided more thermal energy conversion, which may be the main reason for the decrease of TKE density in vegetation.

It is also generally recognized that the propagation of waves in saltmarshes undergoes attenuation (Bouma et al., 2005a; Yang et al., 2012; Jadhav et al., 2013; Anderson and Smith, 2014; Maza et al., 2015). Hydrodynamic conditions such as submergence height, wave height and period, as well as plant characteristics, play an important role in the wave energy damping capacity of saltmarshes (Garzon et al., 2019). Early studies have revealed that wave dissipation over heterogeneous saltmarshes was much greater than the mudflats in the two saltmarshes-mudflat transition regions (Möller and Spencer, 2002). The wave dissipation through the saltmarsh was at least twice that of the mudflat, and the attenuation amplitude varied between each cross-section (Cooper, 2005). In the case of emergent vegetation, the wave attenuation per wavelength was 50∼200% greater than that of near-emergent, and the wave attenuation increases with the increase of stem density (Augustin et al., 2009). In this study, more than 87% of the dry biomass of *Scirpus mariqueter* is concentrated within 30 cm of the bottom, so the density of the upper stem is low. The ability to attenuate waves by vegetation patch is reduced as it is close to near-emergent condition. In addition, *Scirpus mariqueter* was found to be highly flexible based on laboratory tests [plastic folder cut into strips/cross linked polyolefin (XLPO) tubing] and this property also decreased its ability of damping waves (Bouma et al., 2005a; Anderson and Smith, 2014).

In our study, the presence of a single *Scirpus mariqueter* patch is found no obvious changes in wave height and wave period, but a slight increase (9%) in wave energy, which is inconsistent with the commonly understood effects of saltmarsh vegetation in reducing waves. *Scirpus mariqueter* is similar in structure to seagrasses rather than common saltmarsh plants (e.g., *S. alterniflora, P. communis*) because of its low plant height and high flexibility. It has been observed flexible *Laminaria* macroalgae can "drift with the waves" and effectively eliminate resistance, so no significant drop in wave energy was observed (Koehl, 1986; Elwany et al., 1995). Field observations of the saltmarsh (dominated by waves) in the Yangtze Estuary even revealed a significant increase in wave height and wave energy at low water period within *Scirpus mariqueter* canopy of 5 m width (Ysebaert et al., 2011). That enhanced wave impact was explained by 2 cm elevation change, which lead to the step effect and resulted in an increase in wave height (Ysebaert et al., 2011). The similar mechanism can be also used to explain our observation: the patch center is 6 cm higher than that of the mudflat site, due to the sediment trap by vegetation, and the step effect set-off the damping effect by vegetation. Moreover, the high density of vegetation canopy may act like an impermeable step, blocking the incoming flow to achieve the purpose of elevation, which forces the step effect to further strengthened (Bradley and Houser, 2009).

At a smaller scale, another explanation of this phenomenon has been proposed by previous studies (Järvelä, 2005; Lowe et al., 2005; Finnigan et al., 2009; Okamoto and Nezu, 2009; Dijkstra and Uittenborgaard, 2010). For high-density submerged canopies, the resistance discontinuity at the top will produce a shear layer containing canopy-scale vortices. The wave motion in flexible blades caused by canopy-scale vortices is called monami (Nepf, 2012). Monami is a mechanism generated to overcome the buoyancy and rigidity of the blades and then move forward along the blades, which works in the form of canopy-scale vortex (Nepf, 2012). When the combined action of waves and tidal currents is introduced into a saltmarsh, the dense canopies of *Scirpus mariqueter* are gradually submerged by the water, and the instantaneous resistance generated by the canopy-scale vortexes force the leaves to bend and move along the depressed canopy interface. At this time, in order to protect the vegetation from being "damaged," the canopy will inevitably use its own toughness to hinder monami (Nepf, 2012). This kind of counteraction of monami may cause an accumulation of wave energy in a short period, resulting in an increase in wave height to set-off the reduced wave height. This phenomenon of wave strengthening is represented in a schematic form in **Figure 7**.

In summary, *Scirpus mariqueter* patches in the front of the saltmarsh is good at reducing currents, including flow speed and TKE density, but they have limited effects on wave energy

damping, due to the bed elevation changes, their high flexibility and long submergence.

CONCLUSION

In this contribution, we proposed a data processing method of wave-current separation in a saltmarsh front using a field ADV. Moreover, the effects of a *Scirpus mariqueter* patch and adjacent bare mudflat on hydrodynamics were investigated, as an application of this method. Several important points were evident from this study, including:

(1) The wave-current separation of ADV deployed in shallow water environments can be achieved using both phase method and pressure inversion wave method. The two methods can be complementary to each other for simultaneous observation of waves and currents.
(2) For field ADV measurements, the pressure inversion wave method is overall more effective than the phase method, according to the comparison with wave logger results. However, the former is limited by submergence depth (>0.4 m) in the shallow water environments, and it relies on the latter to provide cut-off frequencies for processing pressure inversion. A combination of those two methods will provide a better way to separate currents and waves observed by ADV.
(3) Observations on *Scirpus mariqueter* patch and above its adjacent confirm that the ADV is able to monitor waves and currents independently. *Scirpus mariqueter* patch is better at reducing flow velocity (75%) and total TKE density (24%) than adjacent bare mudflat, but it increases wave energy by a magnitude of 9% in compared with bare mudflat. This finding could be further applied into the practice of coastal protection designs.
(4) Two possible mechanisms can be used to explain the wave enhancement by the *Scirpus mariqueter* patch in the front of the saltmarsh. At a bedform scale, the step effect related to the elevation variations and dense canopy set-off the damping effect by elevation. At a vegetation scale, the counteraction of monami cause an accumulation of wave energy in a short period, resulting in an increase in wave height to set-off the reduced wave height.

DATA AVAILABILITY STATEMENT

The raw data supporting the conclusions of this article will be made available by the authors, without undue reservation.

AUTHOR CONTRIBUTIONS

YC and YL contributed to conception and design of the study. YC, TC, and BL conducted the field observation. BL performed the data analysis and wrote the draft of the manuscript under the supervision of YC and YL. TC and LS wrote sections of the manuscript. All authors contributed to the manuscript revision, read, and approved the submitted version.

FUNDING

This work was funded by the National Natural Science Foundation of China (Grant No. 41776096), the Key Project of Zhejiang Provincial Natural Science Foundation of China (Grant No. LZ21D060001), and the Scientific Research Fund of the Second Institute of Oceanography, MNR (Grant No. JG1524).

ACKNOWLEDGMENTS

We would like to Mr. Silong Huang and Mr. Minmin Ding (GDOC and SIO) for their support in fieldwork. Thanks extend to the Tidal Flats Management Office of Hangzhou Bay, for the site access. Two reviewers are thanked for their valuable and constructive comments in improving the overall quality of this work.

REFERENCES

Anderson, M. E., and Smith, J. M. (2014). Wave attenuation by flexible, idealized salt marsh vegetation. *Coastal Eng.* 83, 82–92. doi: 10.1016/j.coastaleng.2013.10.004

Augustin, L. N., Irish, J. L., and Lynett, P. (2009). Laboratory and numerical studies of wave damping by emergent and near-emergent wetland vegetation. *Coastal Eng.* 56, 332–340. doi: 10.1016/j.coastaleng.2008.09.004

Barbier, E. B., Hacker, S. D., Kennedy, C., Koch, E. W., Stier, A. C., and Silliman, B. R. (2011). The value of estuarine and coastal ecosystem services. *Ecol. Monogr.* 81, 169–193. doi: 10.1890/10-1510.1

Bian, C., Liu, Z., Huang, Y., Zhao, L., and Jiang, W. (2018). On estimating turbulent Reynolds stress in wavy aquatic environment. *J. Geophys. Res. Oceans* 123, 3060–3071. doi: 10.1002/2017JC013230

Bouma, T. J., De Vries, M. B., Low, E., Peralta, G., Tánczos, I. V., van de Koppel, J., et al. (2005a). Trade-offs related to ecosystem engineering: a case study on stiffness of emerging macrophytes. *Ecology* 86, 2187–2199. doi: 10.1890/04-1588

Bouma, T. J., Friedrichs, M., Van Wesenbeeck, B. K., Temmerman, S., Graf, G., and Herman, P. M. J. (2009). Density-dependent linkage of scale-dependent feedbacks: a flume study on the intertidal macrophyte Spartina anglica. *Oikos* 118, 260–268. doi: 10.1111/j.1600-0706.2008.16892.x

Bouma, T. J., Temmerman, S., Van Duren, L. A., Martini, E., Vandenbruwaene, W., Callaghan, D. P., et al. (2013). Organism traits determine the strength of scale-dependent bio-geomorphic feedbacks: a flume study on three intertidal plant species. *Geomorphology* 180, 57–65. doi: 10.1016/j.geomorph.2012.09.005

Bouma, T. J., Vries, M. D., and Herman, P. M. (2010). Comparing ecosystem engineering efficiency of two plant species with contrasting growth strategies. *Ecology* 91, 2696–2704. doi: 10.1890/09-0690.1

Bouma, T. J., Vries, M. D., Low, E., Kusters, L., Herman, P. M. J., Tanczos, I. C., et al. (2005b). Flow hydrodynamics on a mudflat and in salt marsh vegetation: identifying general relationships for habitat characterisations. *Hydrobiologia* 540, 259–274. doi: 10.1007/s10750-004-7149-0

Bradley, K., and Houser, C. (2009). Relative velocity of seagrass blades: Implications for wave attenuation in low-energy environments. *J. Geophys. Res.* 114:F01004. doi: 10.1029/2007JF000951

Bricker, J. D., and Monismith, S. G. (2007). Spectral wave–turbulence decomposition. *J. Atmospheric Oceanic Technol.* 24, 1479–1487. doi: 10.1175/JTECH2066.1

Callaghan, D. P., Bouma, T. J., Klaassen, P., Van der Wal, D., Stive, M. J. F., and Herman, P. M. J. (2010). Hydrodynamic forcing on salt-marsh development: distinguishing the relative importance of waves and tidal flows. *Estuarine Coastal Shelf Sci.* 89, 73–88. doi: 10.1016/j.ecss.2010.05.013

Cao, H., Zhu, Z., James, R., Herman, P. M. J., Zhang, L., Yuan, L., et al. (2020). Wave effects on seedling establishment of three pioneer marsh species: survival, morphology and biomechanics. *Ann. Bot.* 125, 345–352. doi: 10.1093/aob/mcz136

Carniello, L., Defina, A., and D'Alpaos, L. (2009). Morphological evolution of the Venice lagoon: evidence from the past and trend for the future. *J. Geophys. Res.* 114:F04002. doi: 10.1029/2008JF001157

Chen, Y., Cai, T., Chang, Y., Huang, S., and Xia, T. (2018). "Comparison of flow and energy reduction by representative intertidal plants, southeast china," in *Proceeding of The 28th International Ocean and Polar Engineering Conference. International Society of Offshore and Polar Engineers*.

Chen, Y., Li, Y., Cai, T., Thompson, C., and Li, Y. (2016). A comparison of biohydrodynamic interaction within mangrove and saltmarsh boundaries. *Earth Surface Proc. Land.* 41, 1967–1979. doi: 10.1002/esp.3964

Chen, Z., Li, Z., Li, Z., and Cao, J. (2002). Propagation of the complex cracks in rocks without water pressure. *Acta Sci. Natur. Univers. Sunyat.* 41, 86–90.

Christianen, M. J., van Belzen, J., Herman, P. M., van Katwijk, M. M., Lamers, L. P., van Leent, P. J., et al. (2013). Low-canopy seagrass beds still provide important coastal protection services. *PLoS One* 8:e62413. doi: 10.1371/journal.pone.0062413

Christiansen, T., Wiberg, P. L., and Milligan, T. G. (2000). Flow and sediment transport on a tidal salt marsh surface. *Estuarine Coastal Shelf Sci.* 50, 315–331. doi: 10.1006/ecss.2000.0548

Cooper, N. J. (2005). Wave dissipation across intertidal surfaces in the Wash tidal inlet, eastern England. *J. Coastal Res.* 211, 28–40. doi: 10.2112/01002.1

Dade, W. B., Hogg, A. J., and Boudreau, B. P. (2001). *Physics of Flow Above the Sediment-Water Interface*. New York: Oxford University Press, 4–43.

Davidson-Arnott, R. G., Van Proosdij, D., Ollerhead, J., and Schostak, L. (2002). Hydrodynamics and sedimentation in salt marshes: examples from a macrotidal marsh, Bay of Fundy. *Geomorphology* 48, 209–231. doi: 10.1016/s0169-555x(02)00182-4

Deegan, L. A., Johnson, D. S., Warren, R. S., Peterson, B. J., Fleeger, J. W., Fagherazzi, S., et al. (2012). Coastal eutrophication as a driver of salt marsh loss. *Nature* 490, 388–392. doi: 10.1038/nature11533

Dijkstra, J. T., and Uittenborgaard, R. E. (2010). Modeling the interaction between flow and highly flexible aquatic vegetation. *Water Resour. Res.* 46, 1–14. doi: 10.1029/2010wr009246

Duarte, C. M., Losada, I. J., Hendriks, I. E., Mazarrasa, I., and Marbà, N. (2013). The role of coastal plant communities for climate change mitigation and adaptation. *Nat. Clim. Change* 3, 961–968. doi: 10.1038/nclimate1970

Editorial Committee for Chinese Harbors and Embayment (ECCHE) (1992). *Chinese Harbors and Embayment (Part V)*. Beijing: China Ocean Press.

Elwany, M. H. S., O'Reilly, W. C., Guza, R. T., and Flick, R. E. (1995). Effects of Southern California kelp beds on waves. *J. Waterway Port Coastal Ocean Eng.* 121, 143–150. doi: 10.1061/(asce)0733-950x1995121:2(143)

Fagherazzi, S. (2014). Coastal processes: storm-proofing with marshes. *Nat. Geosci.* 7, 701–702. doi: 10.1038/ngeo2262

Fagherazzi, S., and Wiberg, P. L. (2009). Importance of wind conditions, fetch, and water levels on wave-generated shear stresses in shallow intertidal basins. *J. Geophys. Res.* 114:F03022. doi: 10.1029/2008jf001139

Finnigan, J. J., Shaw, R. H., and Patton, E. (2009). Turbulence structure above a vegetation canopy. *J. Fluid Mech.* 637, 387–424. doi: 10.1017/s0022112009990589

Garzon, J. L., Maza, M., Ferreira, C. M., Lara, J. L., and Losada, I. J. (2019). Wave attenuation by Spartina saltmarshes in the Chesapeake Bay under storm surge conditions. *J. Geophys. Res. Oceans* 124, 5220–5243. doi: 10.1029/2018JC014865

Gaylord, B., Denny, M. W., and Koehl, M. A. R. (2003). Modulation of wave forces on kelp canopies by alongshore currents. *Limnol. Oceanogr.* 48, 860–871. doi: 10.4319/lo.2003.48.2.0860

Gibbons, D. T., Jones, G., Siegel, E., Hay, A., and Johnson, F. (2005). *Performance of a New Submersible Tide-Wave Recorder*. OCEANS: MTS/IEEE, 1057–1060.

Gordon, L., and Lohrmann, A. (2002). *Near-shore Doppler Current Meter Wave Spectra. Proc. Fourth Int. Symp. on Ocean Wave Measurement and Analysis, WAVES2001*. (San Francisco, CA: ASCE), 33–43. doi: 10.1061/40604(273)4

Goring, D. G., and Nikora, V. I. (2002). Despiking acoustic doppler velocimeter data. *J. Hydraulic Eng.* 128, 117–126. doi: 10.1061/(ASCE)0733-94292002128:1(117)

Hu, Z., Suzuki, T., Zitman, T., Uittewaal, W., and Stive, M. (2014). Laboratory study on wave dissipation by vegetation in combined current–wave flow. *Coastal Eng.* 88, 131–142. doi: 10.1016/j.coastaleng.2014.02.009

Huang, S., Chen, Y., and Li, Y. (2020). Spatial dynamic patterns of saltmarsh vegetation in southern Hangzhou Bay: exotic and native species. *Water Sci. Eng.* 13, 34–44. doi: 10.1016/j.wse.2020.03.003

Jadhav, R., and Chen, Q. (2012). Field investigation of wave dissipation over salt marsh vegetation during tropical cyclone. *Coastal Eng. Proc.* 1:41. doi: 10.9753/icce.v33.waves.41

Jadhav, R. S., Chen, Q., and Smith, J. M. (2013). Spectral distribution of wave energy dissipation by salt marsh vegetation. *Coastal Engineering* 77, 99–107. doi: 10.1016/j.coastaleng.2013.02.013

Järvelä, J. (2005). Effect of submerged flexible vegetation on flow structure and resistance. *J. Hydrol.* 307:241. doi: 10.1016/j.jhydrol.2004.10.013

Karimpour, A., Chen, Q., and Twilley, R. R. (2016). A field study of how wind waves and currents may contribute to the deterioration of saltmarsh fringe. *Estuaries Coasts* 39, 935–950. doi: 10.1007/s12237-015-0047-z

Knutson, P. L., Brochu, R. A., Seelig, W. N., and Inskeep, M. (1982). Wave damping in Spartina alterniflora marshes. *Wetlands* 2, 87–104.

Koehl, M. A. R. (1986). "Seaweeds in moving water: form and mechanical function,", in *On the Economy of Plant Form and Function*, ed. T. J. Givnich (New York: Cambridge Univ. Press), 603–634.

Kolmogorov, A. N. (1941a). The local structure of turbulence in incompressible viscous fluid for very large Reynolds numbers. *CR Acad. Sci. URSS* 30, 301–305.

Kolmogorov, A. N. (1941b). On degeneration (decay) of isotropic turbulence in an incompressible viscous liquid. *Dokl. Akad. Nauk SSSR* 31, 538–540.

Kolmogorov, A. N. (1941c). Dissipation of energy in locally isotropic turbulence. *CR Dokl. Acad. Sci. USSR* 32, 16–18.

Lancaster, O., Cossu, R., Boulay, S., Hunter, S., and Baldock, T. E. (2021). Comparative wave measurements at a wave energy site with a recently developed low-cost wave buoy (spotter), ADCP, and pressure loggers. *J. Atmosph. Oceanic Technol.* 38, 1019–1033. doi: 10.1175/JTECH-D-20-0168.1

Lara, J. L., Maza, M., Ondiviela, B., Trinogga, J., Losada, I. J., Bouma, T. J., et al. (2016). Large-scale 3-D experiments of wave and current interaction with real vegetation. Part 1: Guidelines for physical modeling. *Coastal Engineering* 107, 70–83. doi: 10.1016/j.coastaleng.2015.09.012

Leonard, L. A., and Croft, A. L. (2006). The effect of standing biomass on flow velocity and turbulence in Spartina alterniflora canopies. *Estuarine Coastal Shelf Sci.* 69, 325–336. doi: 10.1016/j.ecss.2006.05.004

Leonard, L. A., and Luther, M. E. (1995). Flow hydrodynamics in tidal marsh canopies. *Limnol. Oceanogr.* 40, 1474–1484. doi: 10.4319/lo.1995.40.8.1474

Li, Y., and Xie, Q. (1993a). Geomorphological evolution law of Andong shoal in Hangzhou bay. *J. Mar. Sci* 11, 27–35.

Li, Y., and Xie, Q. (1993b). Sedimentary zoning and sedimentary rate of Andong shoal. *J. Mar. Sci.* 11, 23–25.

Liu, S., Liu, Y., Yang, G., Qiao, S., Li, C., Zhu, Z., et al. (2012). Distribution of major and trace elements in surface sediments of Hangzhou Bay in China. *Acta Oceanol. Sinica* 31, 89–100. doi: 10.1007/s13131-012-0223-y

Lowe, R. J., Koseff, J. R., and Monismith, S. G. (2005). Oscillatory flow through submerged canopies: 1. velocity structure. *J. Geophys. Res.* 110:C10016. doi: 10.1029/2004jc002788

Lu, J., Fan, D., Tu, J., Zhang, Y., and Zhang, Y. (2016). Application of ADV in the tidal flat to observe wave processes and calculate their characteristic parameters. *Mari. Sci. Bull.* 35, 523–531. doi: 10.11840/j.issn.1001-6392.2016.05.006

MacVean, L. J., and Lacy, J. R. (2014). Interactions between waves, sediment, and turbulence on a shallow estuarine mudflat. *J. Geophys. Re. Oceans* 119, 1534–1553. doi: 10.1002/2013JC009477

Mariotti, G., and Fagherazzi, S. (2013). Critical width of tidal flats triggers marsh collapse in the absence of sea-level rise. *Proc. Natl. Acad. Sci. U.S.A.* 110, 5353–5356. doi: 10.1073/pnas.1219600110

Maza, M., Lara, J. L., and Losada, I. J. (2019). Solitary wave attenuation by vegetation patches. *Adv. Water Resour.* 98, 159–172.

Maza, M., Lara, J. L., Losada, I. J., Ondiviela, B., Trinogga, J., and Bouma, T. J. (2015). Large-scale 3-D experiments of wave and current interaction with real

vegetation. part 2: experimental analysis. *Coastal Eng.* 106, 73–86. doi: 10.1016/j.coastaleng.2015.09.010

Mitsch, W. J., and Gosselink, J. G. (2007). *Wetlands*. 4th Edn (New Jersey, USA: John Wiley and Sons, Hoboken), 582.

Möller, I. (2006). Quantifying saltmarsh vegetation and its effect on wave height dissipation: results from a UK East coast saltmarsh. *Estuarine Coastal Shelf Sci.* 69, 337–351. doi: 10.1016/j.ecss.2006.05.003

Möller, I., Kudella, M., Rupprecht, F., Spencer, T., Paul, M., Van Wesenbeeck, B. K., et al. (2014). Wave attenuation over coastal salt marshes under storm surge conditions. *Nat. Geosci.* 7, 727–731. doi: 10.1038/ngeo2251

Möller, I., and Spencer, T. (2002). Wave dissipation over macro-tidal saltmarshes: Effects of marsh edge typology and vegetation change. *J. Coastal Res.* 36, 506–521. doi: 10.2112/1551-5036-36.sp1.506

Möller, I., Spencer, T., French, J. R., Leggett, D. J., and Dixon, M. (1999). Wave transformation over salt marshes: a field and numerical modelling study from North Norfolk, England. *Estuarine Coastal Shelf Sci.* 49, 411–426. doi: 10.1006/ecss.1999.0509

Mossa, M., Meftah, M. B., De Serio, F., and Nepf, H. M. (2017). How vegetation in flows modifies the turbulent mixing and spreading of jets. *Sci. Rep.* 7, 1–14. doi: 10.1038/s41598-017-05881-1

Narayan, S., Beck, M. W., Wilson, P., Thomas, C. J., Guerrero, A., Shepard, C. C., et al. (2017). The value of coastal wetlands for flood damage reduction in the northeastern USA. *Sci. Rep.* 7, 1–12. doi: 10.1038/s41598-017-09269-z

Nepf, H. M. (1999). Drag, turbulence, and diffusion in flow through emergent vegetation. *Water Resour. Res.* 35, 479–489. doi: 10.1029/1998wr900069

Nepf, H. M. (2012). Flow and transport in regions with aquatic vegetation. *Ann. Rev. Fluid Mech.* 44, 123–142. doi: 10.1146/annurev-fluid-120710-101048

Neumeier, U., and Ciavola, P. (2004). Flow resistance and associated sedimentary processes in a Spartina maritima salt-marsh. *J. Coastal Res.* 20, 435–447. doi: 10.2307/4299301

Neumeier, U. R. S., and Amos, C. L. (2006). The influence of vegetation on turbulence and flow velocities in European salt-marshes. *Sedimentology* 53, 259–277. doi: 10.1111/sed.2006.53.issue-2

Nikora, N. F., and Nikora, V. I. (2007). *A Viscous Drag Concept for Flow Resistance in Vegetated Channels*. Spain: IAHR World Congress.

Okamoto, T. A., and Nezu, I. (2009). Turbulence structure and "Monami" phenomena in flexible vegetated open-channel flows. *J. Hydraulic Res.* 47, 798–810. doi: 10.3826/jhr.2009.3536

Paquier, A. E., Haddad, J., Lawler, S., and Ferreira, C. M. (2017). Quantification of the attenuation of storm surge components by a coastal wetland of the US Mid Atlantic. *Estuaries Coasts* 40, 930–946. doi: 10.1007/s12237-016-0190-1

Paul, M., Bouma, T. J., and Amos, C. L. (2012). Wave attenuation by submerged vegetation: combining the effect of organism traits and tidal current. *Mari. Ecol. Prog. Series* 444, 31–41. doi: 10.3354/meps09489

Raupach, M. R., and Shaw, R. H. (1982). Averaging procedures for flow within vegetation canopies. *Boundary Layer Meteorol.* 22, 79–90. doi: 10.1007/bf00128057

Rupprecht, F., Möller, I., Paul, M., Kudella, M., Spencer, T., Van Wesenbeeck, B. K., et al. (2017). Vegetation-wave interactions in salt marshes under storm surge conditions. *Ecol. Eng.* 100, 301–315.

Schwimmer, R. A. (2001). Rates and processes of marsh shoreline erosion in Rehoboth Bay, Delaware, USA. *J. Coastal Res.* 17, 672–683. doi: 10.2307/4300218

Shi, B., Yang, S., and Wang, Y. (2012). Relating accretion and erosion at an exposed tidal wetland to the bottom shear stress of combined current–wave action. *Geomorphology* 138, 380–389. doi: 10.1016/j.geomorph.2011.10.004

Shi, Z., Hamilton, L. J., and Wolanski, E. (2000). Near-bed currents and suspended sediment transport in saltmarsh canopies. *J. Coastal Res.* 16, 909–914. doi: 10.2307/4300101

Soulsby, R. L. (1983). The bottom boundary layer of shelf seas. *Oceanogr. Series* 35, 189–266. doi: 10.1016/S0422-9894(08)70503-8

Soulsby, R. L., and Humphrey, J. D. (1990). *Field Observations of Wave-Current Interaction at the Sea Bed. Water Wave Kinematics*. Dordrecht: Springer, 413–428.

Stapleton, K. R., and Huntely, D. A. (1995). Seabed stress determinations using the inertial dissipation method and the turbulent kinetic energy method. *Earth Surface Proc. Land.* 20, 807–815. doi: 10.1002/esp.3290200906

Su, J., and Wang, K. (1989). Changjiang river plume and suspended sediment transport in Hangzhou Bay. *Continental Shelf Res.* 9, 93–111. doi: 10.1016/0278-4343(89)90085-X

Tanino, Y., and Nepf, H. M. (2008). Laboratory investigation of mean drag in a random array of rigid, emergent cylinders. *J. Hydraulic Eng.* 134, 34–41. doi: 10.1061/(ASCE)0733-94292008134:1(34)

Teal, J. M., and Howes, B. L. (2002). *Salt Marsh Values: Retrospection From the End of the Century. In Concepts and Controversies in Tidal Marsh Ecology*. Dordrecht: Springer, 9–19.

Temmerman, S., Bouma, T. J., Govers, G., and Lauwaet, D. (2005). Flow paths of water and sediment in a tidal marsh: relations with marsh developmental stage and tidal inundation height. *Estuaries* 28, 338–352. doi: 10.1007/bf02693917

Temmerman, S., Meire, P., Bouma, T. J., Herman, P. M. J., Ysebaert, T., and De Vriend, H. J. (2013). Ecosystem-based coastal defence in the face of global change. *Nature* 504, 79–83. doi: 10.1038/nature12859

Temmerman, S., Moonen, P., Schoelynck, J., Govers, G., and Bouma, T. J. (2012). Impact of vegetation die-off on spatial flow patterns over a tidal marsh. *Geophys. Res. Lett.* 39:L03406. doi: 10.1029/2011GL050502

Tempest, J. A., Moller, I., and Spencer, T. (2015). A review of plant-flow interactions on salt marshes: the importance of vegetation structure and plant mechanical characteristics. *Wiley Interdisciplinary Rev. Water* 2, 669–681. doi: 10.1002/wat2.1103

Tucker, M. J., and Pitt, E. G. (2001). *Waves in Ocean Engineering*, Vol. 5. Amsterdam: Elsevier, 521.

Wang, F., Lu, T., and Sikora, W. B. (1993). Intertidal marsh suspended sediment transport processes, terrebonne Bay, louisiana, USA. *J. Coastal Res.* 9, 209–220. doi: 10.2307/4298078

Wang, J., Yao, P., Bianchi, T. S., Li, D., Zhao, B., Cui, X., et al. (2015). The effect of particle density on the sources, distribution, and degradation of sedimentary organic carbon in the Changjiang Estuary and adjacent shelf. *Chem. Geol.* 402, 52–67. doi: 10.1016/j.chemgeo.2015.02.040

Wayne, C. J. (1976). The effects of sea and marsh grass on wave energy. *Coastal Res. Notes* 4, 6–8.

Wiberg, P. L., and Sherwood, C. R. (2008). Calculating wave-generated bottom orbital velocities from surface-wave parameters. *Comput. Geosci.* 34, 1243–1262. doi: 10.1016/j.cageo.2008.02.010

Willmott, C. J. (1981). On the validation of models. *Phys. Geogr.* 2, 184–194. doi: 10.1080/02723646.1981.10642213

Xie, D., Gao, S., Wang, Z., and Pan, C. (2013). Numerical modeling of tidal currents, sediment transport and morphological evolution in Hangzhou Bay. China. *Int. J. Sediment Res.* 28, 316–328. doi: 10.1016/S1001-6279(13)60042-6

Xie, D., Pan, C., Wu, X., Gao, S., and Wang, Z. B. (2017). Local human activities overwhelm decreased sediment supply from the Changjiang River: Continued rapid accumulation in the Hangzhou Bay-Qiantang Estuary system. *Mari. Geol.* 392, 66–77. doi: 10.1016/j.margeo.2017.08.013

Yang, S. (1998). The role of scirpus marsh in attenuation of hydrodynamics and retention of fine sediment in the yangtze estuary. *Estuarine Coastal Shelf Sci.* 47, 227–233. doi: 10.1006/ecss.1998.0348

Yang, S., Li, H., Ysebaert, T., Bouma, T. J., Zhang, W. X., Wang, Y. Y., et al. (2008). Spatial and temporal variations in sediment grain size in tidal wetlands, Yangtze Delta: on the role of physical and biotic controls. *Estuarine Coastal Shelf Sci.* 77, 657–671. doi: 10.1016/j.ecss.2007.10.024

Yang, S., Shi, B., Bouma, T. J., Ysebaert, T., and Luo, X. (2012). Wave attenuation at a salt marsh margin: a case study of an exposed coast on the Yangtze Estuary. *Estuaries Coasts* 35, 169–182. doi: 10.1007/s12237-011-9424-4

Ysebaert, T., Yang, S., Zhang, L., He, Q., Bouma, T. J., and Herman, P. M. J. (2011). Wave attenuation by two contrasting ecosystem engineering salt marsh macrophytes in the intertidal pioneer zone. *Wetlands* 31, 1043–1054. doi: 10.1007/s13157-011-0240-1

Conflict of Interest: The authors declare that the research was conducted in the absence of any commercial or financial relationships that could be construed as a potential conflict of interest.

Copyright © 2021 Liu, Chen, Cai, Li and Sun. This is an open-access article distributed under the terms of the Creative Commons Attribution License (CC BY). The use, distribution or reproduction in other forums is permitted, provided the original author(s) and the copyright owner(s) are credited and that the original publication in this journal is cited, in accordance with accepted academic practice. No use, distribution or reproduction is permitted which does not comply with these terms.

frontiers in Marine Science

ORIGINAL RESEARCH
published: 26 July 2021
doi: 10.3389/fmars.2021.707785

Sediment Bulk Density Effects on Benthic Macrofauna Burrowing and Bioturbation Behavior

Lauren E. Wiesebron[1], Natalie Steiner[1], Claudia Morys[1], Tom Ysebaert[1,2] and Tjeerd J. Bouma[1,3,4]*

[1] Department of Estuarine and Delta Systems (EDS), Royal Netherlands Institute for Sea Research, Utrecht University, Utrecht, Netherlands, [2] Wageningen Marine Research, Wageningen University & Research, Wageningen, Netherlands, [3] Building With Nature Group, University of Applied Sciences, Vlissingen, Netherlands, [4] Faculty of Geosciences, Utrecht University, Utrecht, Netherlands

Benthic macrofauna are a key component of intertidal ecosystems. Their mobility and behavior determine processes like nutrient cycling and the biogeomorphic development of intertidal flats. Many physical drivers of benthic macrofauna behavior, such as sediment grain size, have been well-studied. However, little is known about how sediment bulk density (a measure of sediment compaction and water content) affects this behavior. We investigated the effect of bulk density on the burrowing rate, burrowing depth, bioturbation activity, and oxygen consumption of bivalves (*Limecola balthica*, *Scrobicularia plana*, and *Cerastoderma edule*) and polychaetes (*Hediste diversicolor* and *Arenicola marina*) during a 29-day mesocosm experiment. We compared four sediment treatments consisting of two sediments of differing grain size classes (sandy and muddy) with two bulk densities (compact and soft). Overall, bulk density had a strong effect on benthic macrofauna behavior. Benthic macrofauna burrowed faster and bioturbation more intensely in soft sediments with low bulk density, regardless of grain size. In addition, *L. balthica* burrowed deeper in low bulk density sediment. Finally, we found that larger bivalves (both *C. edule* and *S. plana*) burrowed slower in compact sediment than smaller ones. This study shows that benthic macrofauna change their behavior in subtle but important ways under different sediment bulk densities which could affect animal-sediment interactions and tidal flat biogeomorphology. We conclude that lower bulk density conditions lead to more active macrofaunal movement and sediment reworking.

Keywords: grain size, bulk density, benthic macrofauna, intertidal mudflat, burrowing behavior, bioturbation, animal-sediment interactions

OPEN ACCESS

Edited by:
Zeng Zhou,
Hohai University, China

Reviewed by:
Peng Yao,
Hohai University, China
Helena Granja,
University of Minho, Portugal

****Correspondence:***
Lauren E. Wiesebron
lauren.wiesebron@nioz.nl

Specialty section:
This article was submitted to Coastal Ocean Processes, a section of the journal Frontiers in Marine Science

Received: *10 May 2021*
Accepted: *28 June 2021*
Published: *26 July 2021*

Citation:
Wiesebron LE, Steiner N, Morys C, Ysebaert T and Bouma TJ (2021) Sediment Bulk Density Effects on Benthic Macrofauna Burrowing and Bioturbation Behavior. Front. Mar. Sci. 8:707785. doi: 10.3389/fmars.2021.707785

INTRODUCTION

Estuarine intertidal systems are among the most productive ecosystems globally and are responsible for important ecosystem services such as providing coastal protection, carbon sequestration, food production, recreation areas, as well as habitat and nursery grounds for fish and birds (Meynecke et al., 2008; Koch et al., 2009; Barbier et al., 2011; Seitz et al., 2014). At the margins of the land and sea, many factors, both biotic and abiotic, drive the development of these ecosystems (Gray and Elliott, 2009). Benthic macrofauna are a key component of intertidal systems: not only are these animals important prey for birds and fish (Piersma et al., 1993; Zwarts and Wanink, 1993; Bocher et al., 2014), as ecosystem engineers

they modify their sedimentary environment (Bouma et al., 2009). Benthic macrofauna–sediment interactions vary considerably in space and time. They depend on species distribution and behavior as well as local environmental conditions such as sediment composition. The strength of these interactions, in turn, underpins the supply of ecosystem services delivered by intertidal ecosystems. Some sediment characteristics, such as grain size and mud content, have been highly investigated for correlation with species occurrence (Thrush et al., 2003; Pratt et al., 2014) and effects on benthic macrofauna behavior (Dorgan, 2015; McCartain et al., 2017). One sediment characteristic that does not have a well-known effect on benthic macrofauna and their behavior is sediment bulk density, an indicator of both sediment compaction and water content (Grabowski et al., 2011), which is the focus of this paper.

By being inversely related to sediment porosity, or the amount of water retained in a waterlogged sediment, bulk density influences the sediment oxygen content, chemistry, and organic matter (Gray and Elliott, 2009; Dowd et al., 2014). Thus sediment bulk density (dry sediment weight per sediment wet volume) is an important characteristic of intertidal geomorphology and describes a measure of sediment compaction which is missing from grain size gradients. The range of bulk density values vary on a regional and local scale. Bulk density tends to increase with grain size (Ysebaert et al., 2005) and sediment strength (Lucking et al., 2017), while it tends to decrease with silt content, erodibility, and organic matter content (Grabowski et al., 2011; Stringer et al., 2016; Joensuu et al., 2018). More compact sandy sediments typically have a bulk density of around 1–2 g cm^{-3} and softer muddier sediments typically have a bulk density of around 0.2–1.5 g cm^{-3} (Andersen et al., 2005; Grabowski et al., 2011; Stringer et al., 2016). However, sediments with similar grain size composition can have a range of bulk densities due to different water contents (e.g., Widdows et al., 2007; Soares and Sobral, 2009). At very low bulk densities, the sediment is viscous and more akin to a fluid (Grabowski et al., 2011). These conditions are found in many systems worldwide, in particular mangroves (Stringer et al., 2016) and intertidal mud flats (Walles et al., 2017). Furthermore, sediment bulk density tends to increase with erosion and decrease with sediment deposition (Dyer et al., 2000). Besides long-term erosion and sedimentation trends, intertidal flats experience short-term bed-level variation which differs between sites of contrasting wave exposure (Hu et al., 2017). These bed-level trends may contribute to the variation of sediment bulk density over several temporal and spatial scales in estuarine areas. Though bulk density is an important biogeomorphological characteristic of intertidal sediments, we still do not understand how significant this characteristic is for determining benthic macrofauna organism-sediment interactions.

Macrofauna's mixing of sediment, or bioturbation, typically affects parameters like sediment permeability, grain size, and erodibility (Volkenborn et al., 2009; Kristensen et al., 2013; Harris et al., 2016), and also drives many biogeochemical processes of tidal flats (Kristensen, 1988; Gray and Elliott, 2009). Sediment mixing by benthic macrofauna increases sediment permeability, which plays a vital role in nutrient cycling by driving the circulation of oxygen and nutrients below the sediment surface (Aller, 1994; Thrush et al., 2006). Though benthic macrofauna can move laterally by crawling through the sediment [e.g., *H. diversicolor* (Aberson et al., 2011) and *C. edule* (Richardson et al., 1993)] animals usually avoid crawling at the sediment surface since it exposes them to predation (Ens et al., 1997). In this study we focus on vertical sediment mixing which is produced mainly by burrowing and deposit feeding (Kristensen et al., 2012). The mode of mixing is important for determining what kind of ecosystem services the organisms provide. Local mixing, or biodiffusion (Boudreau, 1986a), such as by *C. edule*, can discourage the build-up of fine mud (Montserrat et al., 2008) and oxygenate the top sediment layers (Mermillod-Blondin et al., 2004). Non-local mixing, where surface particles are transported from depth to the surface and vice versa (Boudreau, 1986b), such as by the polychaete *H. diversicolor*, transports particles faster and deeper in the sediment, which creates new habitat for deeper living organisms (Gray and Elliott, 2009), thus increasing biodiversity (Sturdivant and Shimizu, 2017). Moreover, non-local mixing also facilitates biogeochemical processes such as denitrification and permanent burial of pollutants (Mermillod-Blondin et al., 2004).

While macrofauna drive tidal flat biogeomorphology and biogeochemistry through their movement behavior, they also change their behavior under different sediment conditions. Many studies have shown that sediment properties determine macrofauna behavior, for example, *Macomona liliana* decreases its siphon movement in cohesive muddy sediment compared to sandier sediment (McCartain et al., 2017), which could have consequences for sediment permeability and oxygen flow. While the effects of some sediment characteristics, like sediment grain size, on behavior have been well-studied, bulk density effects have not. Studying how macrofauna change their behavior under different bulk densities will help better understand how sediment conditions affect the ecosystem functioning of benthic macrofauna and thus the biogeochemistry and biogeomorphology of tidal flats.

The objective of this study was to investigate how five dominant and functionally different bivalve and polychaete species modify their burrowing and bioturbation behavior under different bulk densities. We hypothesized (1) that both bivalves and polychaetes would have lower mobility (slower burrowing speed, shallower burrowing depth, less active bioturbation) in more compact sediments, (2) that bulk density would have a similar effect on benthic macrofauna behavior in both sandy and muddy sediment, and (3) that larger bivalves would be slower and less active in higher bulk density sediments than the smaller and younger ones, due to greater biomass hampering their mobility. To test our hypotheses, we performed a mesocosm experiment where we subjected three bivalve species (*Limecola balthica*, *Scrobicularia plana*, and *C. edule*) and two polychaete species (*Hediste diversicolor* and *Arenicola marina*) to four sediment treatments of varying bulk density and mud content. We measured the following indicators of movement behavior: burrowing speed, burrowing depth, bioturbation activity and respiration rates. We selected the species based on their dominant prevalence in the Scheldt intertidal (Cozzoli et al., 2013) as well as

TABLE 1 | Overview of all 'species-types' and their traits per experimental block, including two size classes for *C. edule* and *S. plana*, plus a control treatment.

Species	Feeding trait	Mobility	Sediment reworking	Sediment preference	Size class (mm)	Animal number per pot
Cerastoderma edule	Suspension feeder[1]	Slow movement through sediment[1]	Surficial biodiffusor[6]	Sandy (median grain size 125 um)[9]	small: 8–13; large: 14–25	2
Limecola balthica	Surface deposit feeder[1]/ Suspension feeder[3]	Limited movement[1]	Surficial biodiffusor[6]/ Conveyor[5]	Mixed sandy/muddy (median grain size 100 um)[10]	10–14	5
Scrobicularia plana	Surface deposit feeder[1]/ Suspension feeder[4]	Limited movement[1]	Surficial biodiffusor[6]/ Conveyor[7]	Muddy (median grain size 75 um)[10]	small: 28–34; large: 38–43	1
Hediste diversicolor	Omnivore[1]	Free movement via burrow system[1]	Gallery biodiffuser[6]	Very muddy (median grain size 25 um)[10]	40–100	3
Arenicola marina	Sub-surface deposit feeder[2]	Limited movement via burrow system[2]	Up/downward conveyor[8]	Sandy (median grain size 175)[8]	25- 55	5
Controls						0

The main ecological traits for all species used in the experiment are listed. Species traits from literature: feeding and mobility trait (Olafsson, 1986[3]; Riisgård and Banta, 1998[2]; Orvain, 2005[4]; Van Colen et al., 2012[1]), sediment reworking (Queirós et al., 2013[6]; Morys et al., 2017[5], this study[7], Gerino et al., 2003[8]), sediment preference (Ysebaert et al., 2002[9]; Van Colen et al., 2014[10]).

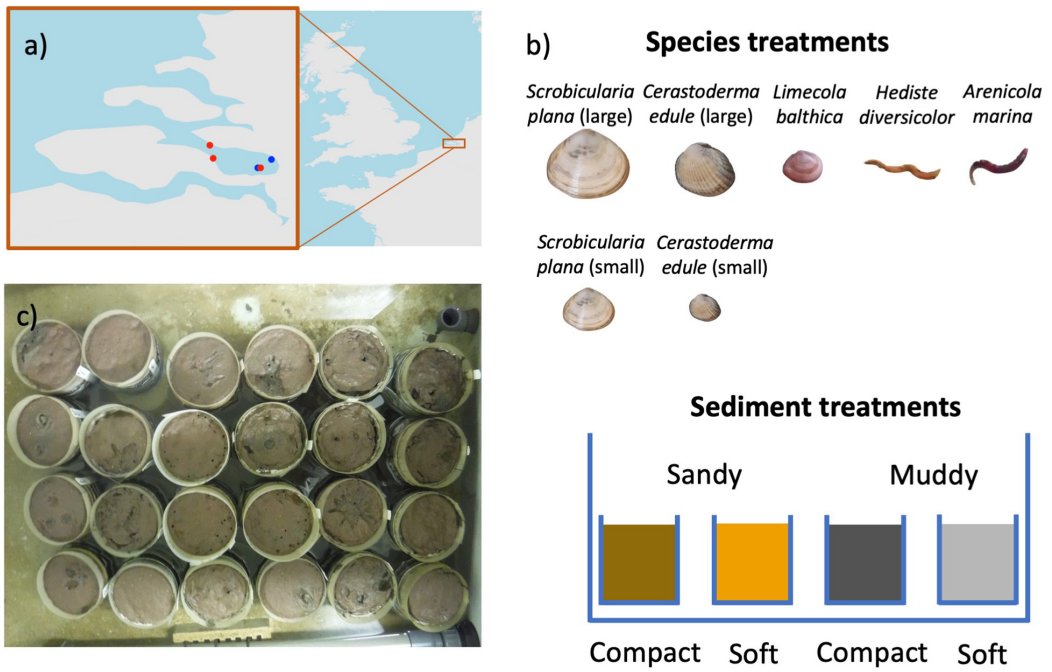


FIGURE 1 | Map of our study area in the Scheldt **(a)** with points of sediment collection (blue) and macrofauna collection (red). Experimental design **(b)** with (upper panel) seven species treatments, four of which were *C. edule* and *S. plana* size classes, and (lower panel) four sediment treatments. We had six replicates for each sediment – species combinations. A picture of the sediment cores in a tidal tank halfway through the experiment is shown in **(c)** with visible surface rugosity from bioturbation and animal movement.

their functional differences. In particular, the five species covered the different bioturbation types (**Table 1**).

MATERIALS AND METHODS

Experimental Design

We designed a mesocosm experiment in which three bivalve species (*Limecola balthica*, *Scrobicularia plana*, and *Cerastoderma edule*) and two polychaete species (*Hediste diversicolor* and *Arenicola marina*) were subjected to two crossed bulk density (dry sediment weight per sediment wet volume) and sediment grain size treatments (**Figure 1b**). Our four treatments were: compact-sandy (CS), soft-sandy (SS), compact-muddy (CM), and soft-muddy (SM) (see **Table 2** for sediment characteristics). We used two sediment grain sizes to cover a larger part of the range of bulk densities observed in the Scheldt intertidal, as well as to test the interaction between sediment bulk density and grain size on animal behavior. We prepared the treatments from two sediments collected from intertidal flats in the Eastern Scheldt

estuary (**Figure 1a**). The sandier sediment was collected at the Oesterdam (51.466700 and 4.221389) and the muddier sediment was collected from Prosperhaven (51.490305 and 4.259167) nearby. Both were collected several months before the start of the experiment and were stored in outdoor closed bins. The sandier sediment was drained and passed through a large (5 mm) sieve before use. The sticky consistency of the muddy sediment did not allow it to be passed through a sieve, therefore we removed the larger fragments, such as shells, by hand. We incorporated seawater (amount equaling 7% of the sediment weight for compact high bulk density treatments and 15% for soft low bulk density treatments) into the sifted sediments with a standing industrial mixer the day before we added the animals (see **Table 2** for resulting sediment characteristics). The sediment was mixed in batches of 5 kg for at least 5 min to ensure the mixture was homogenous. The sediment was placed in pots made from a sawed-off PVC pipe (height 12 cm, diameter 11.5 cm). Each PVC pipe was capped off on the bottom with a removable plastic cap and lined with a plastic bag to prevent water loss. We encircled the brims of the pots with mesh (1 mm mesh size) that extended 2 cm above the high tide height to keep the animals contained to their unit. The pots were filled to 0.5 cm below the brim and placed in the mesocosm tanks.

The experiment was conducted in ten tidal tanks in a climate-controlled room where the water was kept at 18°C, the same temperature as the Eastern Scheldt in July 2018 when the experiment was carried out. Each tidal tank was composed of two 1.2 m by 0.8 m tanks stacked on top of each other (see **Figure 1c** for example). Unfiltered water from the Eastern Scheldt estuary was pumped from the bottom tank up to the top tank to simulate tidal conditions. High tide conditions (5 cm water above experimental units) lasted 6 h and occurred twice a day. We changed the water once a week, and in addition to the nutrients contained in the raw Eastern Scheldt water, we fed the animals with an algal concentrate (Shellfish Diet from Reed Mariculture) 5 mL per tank twice per week.

We had eight experimental blocks composed of two polychaete species, three bivalve species with two size classes for *S. plana* and *C. edule*, and controls without animals (**Table 1**). We collected the animals at three sites in the Eastern Scheldt: *A. marina* were collected at the Oesterdam (51.46670 and 4.22139), *C. edule* and *L. balthica* were collected at Dortsman (51.543678 and 4.055841), and *S. plana* and *H. diversicolor* were collected in Yerseke (51.489245 and 4.057288), 3 days to 24 h before the start of the experiment and stored in a tidal tank in the mesocosm (**Figure 1a**). Each block was replicated six times for each sediment treatment. Thus, we had 24 units for each species/size block, resulting in a total experiment of $8 \times 24 = 192$ units (see details in **Table 1**).

All the animals used occurred naturally in the two sediments we used for the experiment (see Cozzoli et al., 2013 for biomass probability distribution in the Scheldt depending on grain size for *C. edule*, *L. balthica*, *H. diversicolor*, and *A. marina*; see probability distribution for *S. plana* depending on grain size in Van Colen et al. (2014). *A. marina* was the only species placed in unnatural conditions (muddy sediment) not found in the field. Not unexpectedly, *A. marina* had low survival in the muddy sediment treatment, especially the compact-muddy treatment. There was some low mortality for *H. diversicolor* (see Results section "Survival Rate and Growth") but this was not linked to any sediment treatment. We recorded no mortality in the bivalves.

The units were divided randomly into the ten tidal tanks (24 per tank) to minimize a tank effect. We used realistic but low animal densities to avoid competition for space and food resources. The realistic densities also allowed us to obtain realistic behavioral responses from the animals. Thus, the number of animals per core varied between species, which means that responses and animal abundances were colinear. The number of animals per pot were one *S. plana*, two *C. edule*, five *L. balthica*, five *A. marina*, and three *H. diversicolor*. We only compared the magnitude of the species effect between size class treatments (i.e., small and large *C. edule* and *S. plana*). Though the abundances varied per species, the biomass per pot was roughly similar.

Sediment Characterization

We prepared 24 extra cores to take bulk density and sediment penetration resistance measurements to determine whether the sediment treatments changed over the course of the experiment. The cores were placed in a separate tidal tank in the same climate room as the experiment. We used a universal testing machine (Instron, Baltimore, MD, United States) to measure sediment penetration resistance, or the amount of pressure necessary to compress the sediment. The universal testing machine measures the load as a crosshead penetrates the sediment and extends to the bottom of the sediment core at a constant speed (Bokuniewicz et al., 1975). To measure bulk density (dry sediment weight per sediment wet volume), we determined the water content of a fixed volume of sediment which was collected using a cut-off syringe and weighed before and after freeze-drying for 48 h. We took penetration resistance and bulk density measurements of the different sediment treatments after 12 h, 1 week, 2 weeks, and at the end of the experiment. The four sets of cores were only used for each set of measurements once because the sampling for bulk density destroys the core.

While the penetration resistance changed over time, there was no overlap in penetration resistance profiles between the four treatments by the end of the experiment (**Figure 2**). The bulk densities of the four treatments remained significantly distinct from each other over the course of the experiment, $F(3,80) = 649$, $p < 0.001$, and *post hoc* Tukey test $p < 0.008$ for all treatment comparisons. In addition, the inclusion of the measurement date in the linear model evaluating treatment effects on sediment bulk density did not improve the model fit, $F(1,79) = 0.001$, $p = 0.97$, indicating that the sediment bulk densities did not change between the beginning and end of the experiment.

Process Measurements: Burrowing Rates

Burrowing rates of bivalves were monitored by counting the animals still present at the sediment surface shortly after the start of the experiment and then every 12 h until they were all buried, after 2 days. This method worked well for

TABLE 2 | Median values for sediment characteristics (median grain size, grain size composition, water content, bulk density, penetration force as measured by a universal testing machine (Instron, Baltimore, MD, United States) for the four sediment treatments.

Sediment characteristic	Compact-sandy	Soft-sandy	Compact-muddy	Soft-muddy
Median grain size (μm)	108	106	44	43
Coarse sand (0.5–1 mm) (%)	2.23	3.49	0.26	0.21
Medium sand (0.25–0.5 mm) (%)	17.35	17.31	2.22	2.79
Fine sand (0.125–0.25 mm) (%)	25.88	24.4	10.78	11.07
Very fine sand (0.062–0.125 mm) (%)	16.66	15.74	24.09	22.85
Silt (0.004–0.062 mm) (%)	38.02	39.18	62.94	63.36
Water content (%)	17.87	21.94	47.39	53.14
Bulk density (g cm^{-3})	1.32	1.25	0.67	0.59
Penetration force (N)	25053	1058	799	264

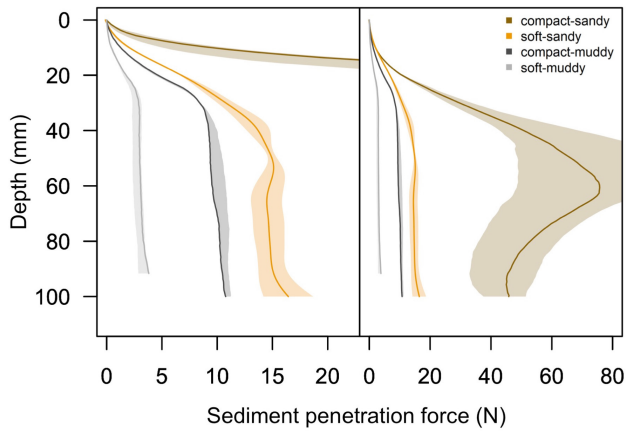


FIGURE 2 | Mean sediment penetration force profiles and 95% confidence intervals as measured by the universal testing machine for the four sediment treatments, with 95% confidence intervals encompassing the beginning and end of the experiment. We present a panel with a reduced x-axis scale on the left to show the details of the soft-sandy, compact-muddy, and soft-muddy sediment teatments, and we present a panel with a full x-axis scale on the right to show the extent of the compact-sandy sediment profile. Note that the penetration force of the compact-sandy treatment is an order of magnitude greater than the other three treatments and that in the right plot the profile for the compact-sandy sediment is scaled to 1/5 of the original sediment penetration force to fit into the plotting area.

the bivalves, but not for the fast burrowing polychaetes as they burrowed almost immediately. Hence, we performed an additional short experiment to investigate how bulk density impacted the burrowing ability of polychaetes. We prepared four sediment treatments with different bulk densities from the sandy sediment by adding in seawater at 2, 10, 15, and 25% of the sediment weight and homogenizing with the standing cement mixer. The four sediment treatments had average bulk densities of: 1.35, 1.31, 1.26, and 1.22 g cm^{-3}. We then added the sediment to empty pots in the same way as we did for the cores in the mesocosm. We placed six *A. marina* or six *H. diversicolor* on the sediment surface and recorded how many animals were still visible at thirty second intervals. We repeated the experiment twice for each species/sediment combination.

Process Measurements: Metabolic Activity

We performed oxygen incubation experiments to test whether different sediment characteristics affected macrofaunal metabolic activity. The incubation experiments were run 24 days after the experiment had begun so that the animals had acclimated to the different sediment conditions. We performed the oxygen consumption experiments with three replicates each for: the controls, *H. diversicolor*, *L. balthica*, both size classes of *S. plana*, and the large *C. edule*. We could not perform the oxygen consumption experiments on all species blocks because of equipment limitations. The experiment consisted of a water bath containing capped PVC tubes filled with Eastern Scheldt water. We placed each core into the larger PVC tube. The cores descended into the tube slowly and the surfaces of the sediment were not disturbed. We oxygenated the water to raise the oxygen content until it was near saturation and sealed the cores with a custom cap. The cap included a stirrer to homogenize the entire water column's oxygen content. We then measured the amount of oxygen in the water over time using a FireSting sensor (see Braeckman et al., 2014 for oxygen incubation method). The experiments ran for at least 5 h and we did not allow the oxygen level to descend below 60%. There was a possibility that differences in respiration rates between cores could have been due to animal death, however, all the bivalves used in the oxygen incubation experiments were alive at the end of the 29 days. *H. diversicolor* experienced low mortality, but without a sediment treatment effect.

Process Measurements: Sediment Mixing

To better understand how the sediment treatments would affect animal bioturbation activity and the resulting sediment mixing, we added luminophores (Environmental Tracing Systems, United Kingdom) to the sediment cores, which are inert natural sediment particles dyed with luminescent paint used to track bioturbation (Gerino et al., 2003; Solan et al., 2004). Luminophores are widely used as a non-toxic tracer to study sediment mixing by benthic animals as small amounts do not affect the animal behavior and do not harm the animals (Maire et al., 2008). We made frozen sediment disks following our

standard procedure for mixing the sediment treatments but replaced ten percent of the sifted sediment with luminophores. We added one 0.5 cm thick disk to the top of all cores after the animal had burrowed in to avoid recording the initial burrowing movement as bioturbation activity. Some of the large *S. plana* never burrowed and so we added the luminophores on top of them.

After 29 days, we processed the experiment. We sliced the cores once lengthwise to obtain a vertical profile of luminophore incorporation into the sediment. These profiles show the total amount of mixing that was done by the animal over the course of the experiment, thus representing the time-integrated outcome. As we were not using the luminophores to model bioturbation intensity, a single lengthwise slice was sufficient for our purposes of investigating the sediment treatment effect on bioturbation activity and mixing mode. In addition, the lengthwise slicing allowed us to recover the animals intact for subsequent physiological measurements. As a consequence of the vertical slicing, we may in some cases have underestimated bioturbation activity if a burrow did not traverse our slice. However, we compensated for possible underestimation by averaging the profiles over six cores for each species-sediment combination. This allowed us to obtain a general estimate of the bioturbation patterns.

To count the luminophores as a function of depth we photographed the two halves of the core under a blacklight using a digital mirror-reflex camera (Canon EOS 1100d) attached to a tripod. The pictures (2848 × 4247 pixels) were analyzed using a custom ImageJ (Fiji) script. In this process, the red layer of an RGB filter was used to highlight the magenta colored luminophores. The brightness value (125–255) was used to select luminophores from other pixels. We estimated bioturbation activity by counting the luminophore pixels in the pictures of the halved cores by 0.5 cm layer, or "bin." The bins had an area of 10.5 × 0.5 cm, which corresponded to 1722 × 82 pixels. Because one luminophore pixel does not necessarily correspond to a single luminophore grain, we use "luminophore pixels" instead of "luminophore count" as the unit for luminophore quantity throughout the text. The edges of the cores (0.5 cm from the sides and the bottom 1.5 cm) were excluded to avoid skewing our estimates because the plastic lining caused luminophores to accumulate at the sides and bottom of the cores. We used an pixel count value averaged between the two halves of the cores for each bin to get a more robust measure of the luminophore distribution through the sediment. We smoothed the average profiles by species and sediment treatment using local polynomials [R package *KernSmooth* (Wand, 2019)] to better show general patterns in mixing.

When examining the luminophore profiles we looked for subsurface peaks to differentiate between local (biodiffusion) and non-local (advective transport) mixing. Local mixing causes the number of luminophores to decrease exponentially with depth, whereas non-local mixing causes a peak in luminophores at depth. We determined whether there was non-local mixing by examining the depth of maximum values of luminophore pixel counts over a moving depth window. We were interested in how mixing activity might differ close to the surface and at depth, so we isolated the peaks in the diffusion layer (0–4 or 0–6 cm depending on species/sediment treatment) and in the lower part of the core. We compared the depth and intensity of peaks between species and sediment treatments.

Process Measurements: Burying Depth and Survival

To measure animal burrowing depth for the bivalves, we recorded the lowest point of the bivalve's position. For the polychaetes, we separated the cores containing polychaetes into 0 to 2 cm, 2 to 5 cm, and 5 to 12 cm layers and sieved each layer and recorded which contained animals. We considered all unrecovered animals as dead.

Statistical Analysis

We wished to determine the effect of sediment bulk density on the behavioral response of our species. Because we wished to know whether the response to bulk density would be different depending on grain size, we evaluated models with only main effects of the sediment treatment (Response ∼ Species + grain size + bulk density) and models that included an interaction between sediment grain size and bulk density (Response ∼ Species + grain size × bulk density). Because we wanted to compare the direction of the response between species, we also tested for an interaction between the species and sediment treatments (Response ∼ Species × grain size × bulk density). We selected the best models based on Akaike Information Criterion (AIC). We mainly used ANOVAs and logistic regression to evaluate the animal behavioral responses to sediment bulk density. See **Supplementary Table 2** for a summary of the logistic regression model and **Supplementary Table 3** for a summary of the best ANOVA models.

The model fit for all linear regressions and ANOVAs were evaluated using residual plots and QQ-plots. The logarithm of the dependent variable (i.e., depth and luminophore pixel count) was used when appropriate. For all models, the species treatments included separate categories for the two bivalve size classes. After performing ANOVAs, we used *post hoc* Tukey tests to compare relevant sediment treatment effects, as well as differences in responses between size classes for *C. edule* and *S. plana*.

We modeled the initial burrowing time of the bivalves using logistic regression. The response variable was the presence of animals at the surface in each unit at each time step. Our model was of the form of: Response ∼ Species + grain size + bulk density + hour, with interactions tested as detailed above. We used Wald tests to compare sediment treatment effects and investigate the effect of bivalve size on burrowing speed. We also used logistic regression to examine whether sediment treatment had an effect on polychaete survival and burrowing time.

The oxygen data were analyzed in R [R package *turbo* (K. Soetaert and Provoost, 2017)]. We corrected for the respiration of the microbial community by subtracting the mean control value for each sediment treatment from the values for cores containing animals. We evaluated whether oxygen consumption significantly varied among species, bulk density, and grain size using a three-way ANOVA.

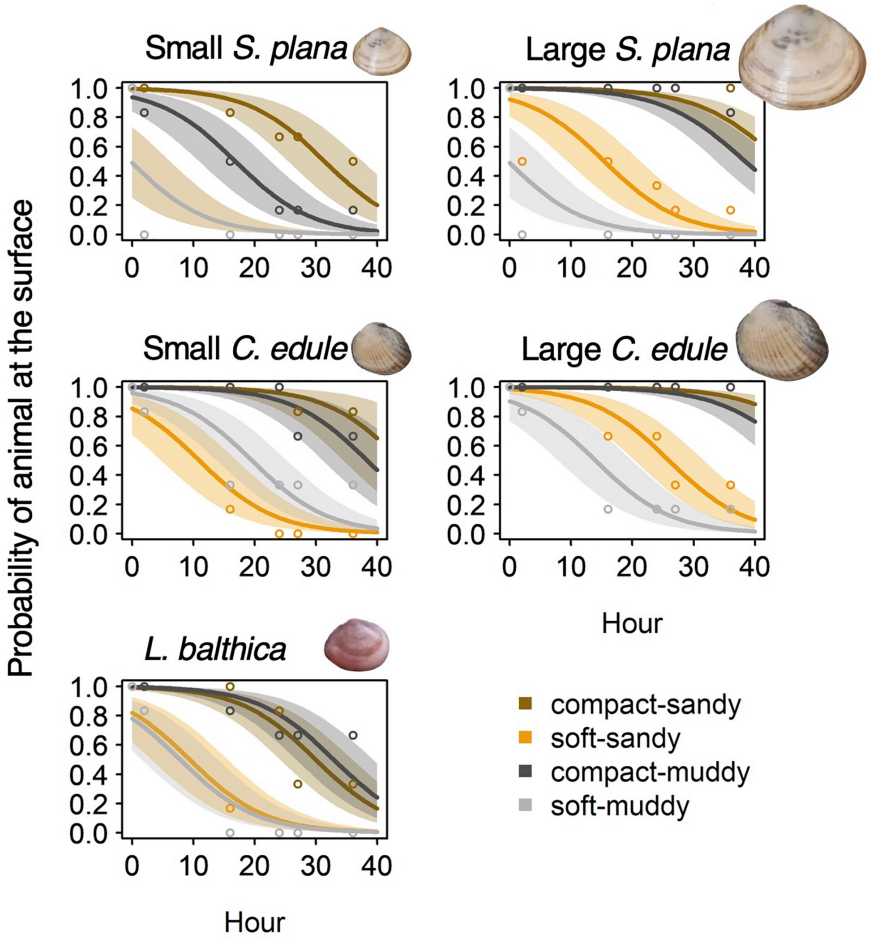


FIGURE 3 | Logistic regression models of bivalve burrowing showing the probability of a bivalve's presence at the sediment surface over the first 40 h of the experiment. The results are shown by species and sediment treatment, with best fit line and 95% confidence intervals. Mean observed values per time-step are depicted by open circles.

We performed a three-way ANOVA to test whether there were differences in burial depth among bivalve species and sediment bulk density, and grain size. To satisfy the condition of normality, we excluded zeros (non-buried *S. plana*). To compare polychaete depth strata, we performed a multinomial logistic regression using functions from R package *nnet* (W. Venables and Ripley, 2002).

Luminophore dispersal was calculated as an indicator for bioturbation intensity by summing the number of luminophore pixels counted in each 0.5 cm depth bin for each luminophore profile. The values of the luminophore dispersal increased when more luminophores were transported into the sediment. The final dispersal values were corrected for the average dispersal values of the controls. This correction allowed us to account for the greater permeability of the sandy sediments. We performed a three-way ANOVA to evaluate whether there were differences in luminophore dispersal among species, sediment bulk density, and grain size.

We also compared the depth and luminophore pixel counts of non-local mixing peaks for species that showed non-local mixing in the luminophore profiles: *L. balthica,* and *H. diversicolor*, and both size classes of *S. plana*. The peaks at depth for *L. balthica* were not as prominent in the profiles as for the other two species, however, there is evidence from literature that *L. balthica* induces non-local mixing (Morys et al., 2017). We evaluated whether there were differences in the depth and the value of the peak luminophore pixel counts between 4.5 and 10.5 cm among species and sediment treatments using a three-way ANOVA.

RESULTS

Survival Rate and Growth

Survival was very high for the bivalves (99 ± 7%). We recovered the polychaetes at a lower rate (71 ± 33% of *H. diversicolor* and 20 ± 31% for *A. marina*), but it's unclear to what extent this was due to mortality or due to the polychaetes escaping the cores. If we assume that the treatment effect was due to mortality, then *A. marina* survived at a higher rate in the soft sediments vs. the

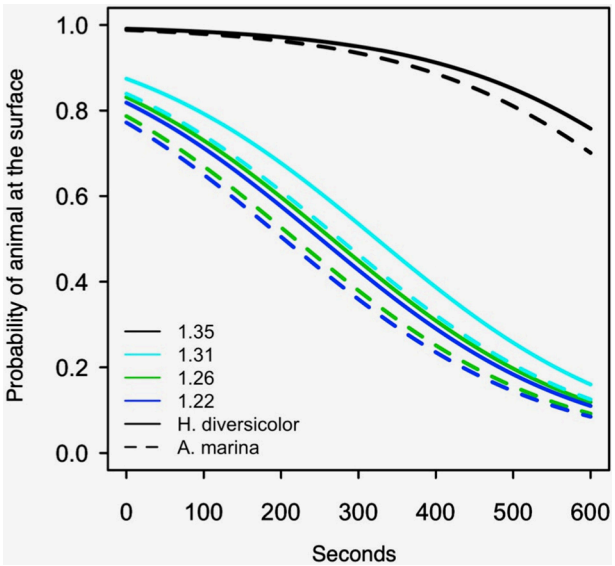


FIGURE 4 | Logistic regression models of polychaete burrowing, showing the probability of the polychaetes presence at the sediment surface for the first 600 s. The dotted lines are *A. marina* models and the solid lines are *H. diversicolor*. Results are shown for the sandy sediment with a bulk density (g cm^{-3}) of 1.35, 1.31, 1.26, and 1.22. The experiment was not performed with muddy sediment (see Methods section "Process Measurements: Burrowing Rates").

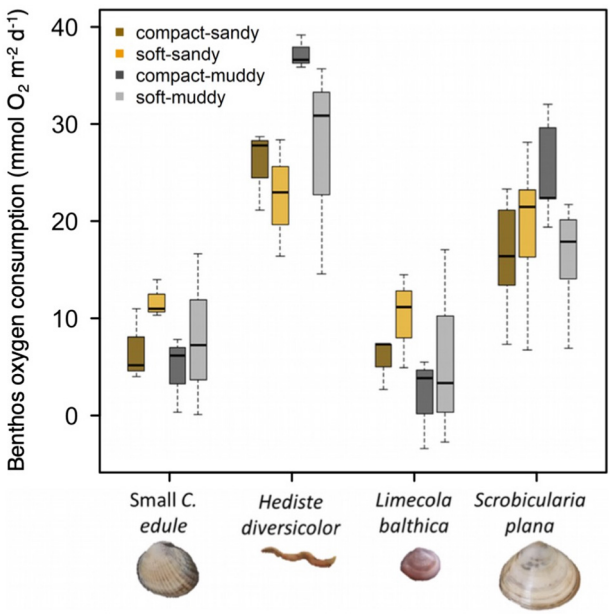


FIGURE 5 | Oxygen consumption rate for species by sediment treatment represented by boxplots where the box (25–75% of the data) contains a black line (median) and has whiskers extending to the minimum and maximum data values. Large *C. edule* and *A. marina* were not included in the experiment due to equipment limitations. We pooled the results for the large and small *S. plana* because they were so similar. Since the microbial respiration was different in the sandy vs. muddy sediment, we corrected the values of animal respiration obtained from the sediment cores by subtracting the mean respiration value of controls which represent the microbial respiration. 13.3 mmol O_2 m^{-2} d^{-1} were subtracted from sandy treatments, 20.7 mmol O_2 m^{-2} d^{-1} were subtracted from muddy sediments. There were no significant sediment treatment effects.

compact sediments (30 ± 39% vs. 10 ± 13% survival), Wald's X^2 (1) = 7, p = 0.008. There was no sediment treatment effect on *H. diversicolor* survival.

Burrowing Rates of Bivalves

The burrowing rate was significantly slower for the compact, high bulk density treatments than for the soft, low bulk density treatments, Wald's X^2 (1) $p < 0.001$ (**Figure 3** and **Supplementary Table 2**). Burrowing was around 200 times slower in the compact-sandy treatment and 80 times slower in the compact-muddy treatment than the corresponding soft treatments.

The small *S. plana* had significantly faster burrowing rates than the larger *S. plana*, Wald's X^2 (1) = 11.7, p = 0.001, but the effect was sediment dependent. The small *S. plana* burrowed 2 times faster than the large ones in the soft-sandy treatment and they burrowed 5 times faster than the large ones in the muddy-compact treatment, Wald's X^2 (1) = 9.9, p = 0.002. The small *C. edule* burrowed 0.7 times faster than the large *C. edule* in the soft-sandy treatment, Wald's X^2 (1) = 5.7, p = 0.017. Size had no effect on burrowing rate in the soft-muddy treatment (fastest burrowing rate overall) and compact-sandy treatment (slowest burrowing rate overall) for both species. And while all the small *S. plana* successfully burrowed, 60% of the large *S. plana* in the compact-sandy treatment and 30% of the large *S. plana* in the compact-muddy treatment failed to burrow at all.

Burrowing Rates of Polychaetes

The effect of bulk density on the burrowing of polychaetes followed a similar pattern to the bivalves, though at a different scale (i.e., note difference in the x-axis in **Figure 3** - hours vs. **Figure 4** - seconds). The polychaete burrowing rate significantly increased with the softness of the treatments (**Figure 4**), Wald's X^2 (4) = 357.6, $p < 0.001$. The biggest difference in burrowing rates was between the two sediment treatments with the highest bulk densities: burrowing rate was 150 times slower in the 1.35 g cm^{-3} treatment compared to the 1.31 g cm^{-3} treatment, Wald's X^2 (1) = 18.4, $p < 0.001$, suggesting that there might be an absolute threshold that prevents burrowing. Burrowing rates did not significantly differ between 1.26 and 1.22 g cm^{-3} treatments, Wald's X^2 (1) = 0.31, p = 0.58. *H. diversicolor* burrowed four times slower than *A. marina*, Wald's X^2 (1) = 5.7, p = 0.017.

Oxygen Consumption as an Indicator of Metabolic Activity

Overall, oxygen consumption significantly differed between species, F (3, 53) = 32.480, $p < 0.001$, but not sediment treatments (**Figure 5**). The mean oxygen consumption in the control muddy sediments was 1.6 times greater than the oxygen consumption in

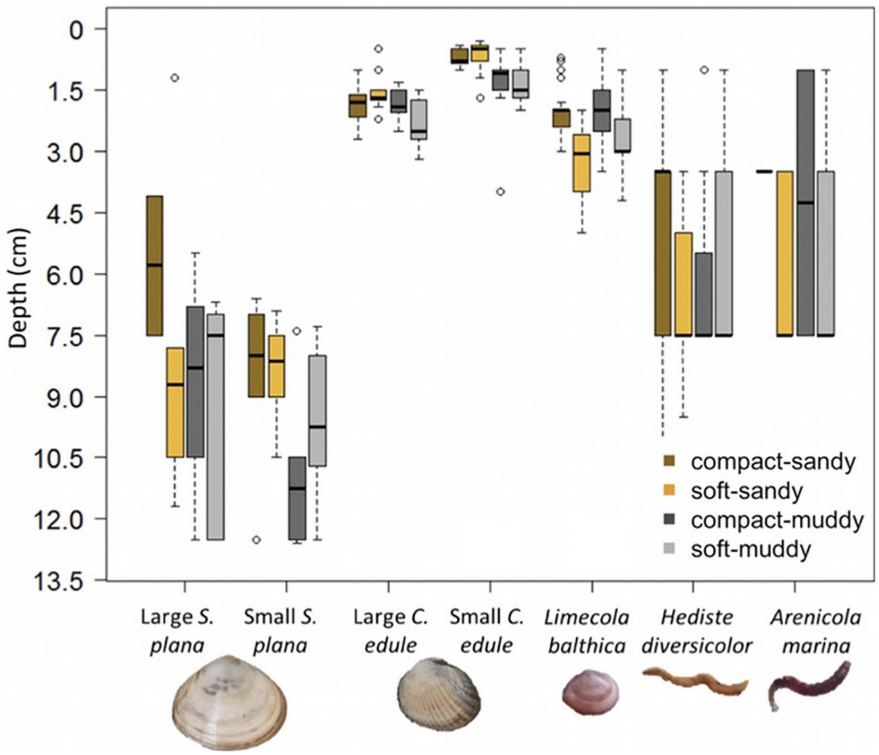


FIGURE 6 | Boxplots of burrowing depth by species and sediment treatment, where the box (25–75% of the data) contains a black line (median) and has whiskers extending to the minimum and maximum data values, with outliers as open circles. Bivalve burrowing depth was measured precisely (lowest point animal). Polychaete burrowing depth was measured by strata (0–2 cm, 2–5 cm, and 5–12 cm) and extrapolated to the mean value of each stratum. For some *H. diversicolor*, a burrow point was visible and was used instead of the strata. Note that the bottom of the pots was at 12.5 cm which is close to many of the *S. plana* positions. The sediment treatments only had a significant effect on the burrowing depth of *L. balthica* and the small *C. edule*.

the control sandy sediments. That is, the average muddy sediment oxygen consumption was 20.7 + 2.6 SE mmol O_2 m^{-2} d^{-1} vs. an average oxygen consumption of 13.3 + 2.3 mmol O_2 m^{-2} d^{-1} for sandy sediment, which might be explained by the greater amount of organic material available for microbial consumption in muddy sediment. There was no significant difference between the oxygen consumption of the large and small *S. plana*.

All the animals tended to be most active in the sediments that were closest to their natural habitat (see **Table 1** for sediment preferences). *C. edule* and *L. balthica* tended to have the greatest oxygen consumption in the soft-sandy sediments whereas the *H. diversicolor* and *S. plana* tended to have the greatest oxygen consumption in the compact-muddy sediment (**Figure 5**). While the sediment treatment effect on the species' oxygen consumption was not significant, the higher oxygen consumption in these sediments could indicate greater activity.

Macrofauna Burrowing Depth

Bivalve burrowing depth was significantly different between sediment bulk densities, grain size, and species, with interactions between the sediment characteristics and species (**Figure 6** and **Supplementary Tables 1**, **3**). A *post hoc* Tukey test showed that the sediment treatments affected the burrowing depth of two out of the five bivalve species: the *L. balthica* and small *C. edule*. The *L. balthica* burrowed deeper in the soft sediments and the small C. edule burrowed deeper in the muddy sediments (**Figure 6**). The lack of a visible treatment effect on depth for *S. plana* could be due to the short length (12 cm) of the cores. Many of the *S. plana* were found near the bottom of the cores and perhaps would have burrowed deeper had they been given more space. While there was a statistically significant difference in the burrowing depth for the two size classes of *C. edule*, this was not the case for *S. plana* (Tukey *post hoc* $p = 0.0001$ and 0.16, respectively). The best multinomial model of polychaete depth distribution included sediment treatment. Including species did not improve the model, X^2 (2) = 2.76, $p = 0.25$. There is small evidence that polychaetes burrowed deeper in compact muddy treatment than the soft muddy treatment ($p = 0.057$).

Sediment Mixing as Measured by Luminophores

Overall, the benthic macrofauna induced significantly greater luminophore dispersal in the soft sediments than in the compact sediments [**Figure 7**; F (1,154) = 32.7, $p < 0.001$]. The greatest luminophore dispersal occurred in the soft-muddy sediment (average = 4.02×10^5 luminophore pixels $\pm$ 0.78×10^5 luminophore pixels). The luminophore dispersal was greater in soft-sandy sediment (average 3.68×10^5 luminophore

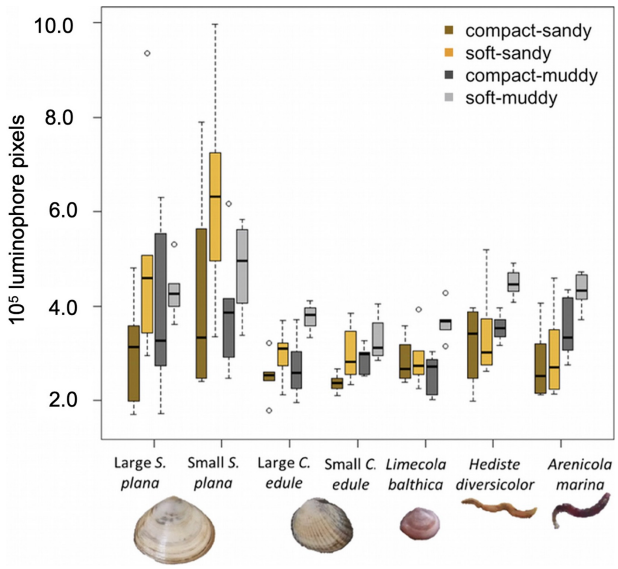


FIGURE 7 | Boxplots showing luminophore dispersal, i.e., the integral of luminophore profiles over depth (see **Figure 8** for average profiles), by species and sediment treatment, where the box (25–75% of the data) contains a black line (median) and has whiskers extending to the minimum and maximum data values, with outliers as open circles. All species transported more luminophores in soft vs. compact sediment and polychaetes also transported more luminophores in muddy vs. sandy sediment. The area has been corrected for the average control values (compact-sandy: –0.31 × 10^5 luminophore pixels, soft-sandy: –0.44 × 10^5 luminophore pixels, compact-muddy: +0.23 × 10^5 luminophore pixels, soft-muddy: +0.39 × 10^5 luminophore pixels).

pixels ± 1.75 × 10^5 luminophore pixels) than in the compact sandy-sediment (average 2.97 × 10^5 luminophore pixels ± 1.10 × 10^5 luminophore pixels).

Species induced different amounts of sediment mixing, F (6,154) = 9.4, $p < 0.001$ (**Figure 7**). Both size classes of the *S. plana* and the polychaetes mixed greater amounts of luminophores into the sediment than the *L. balthica* and *C. edule* (**Figure 7**). There was no significant difference between the luminophore dispersal of either *C. edule* or *S. plana* size classes, though the small *S. plana* tended to induce greater sediment mixing than large *S. plana* (**Figures 7**, **8**).

We further compared the bioturbation mode of the macrofauna by examining the shapes of the luminophore profiles, especially by looking at the presence and depth of non-local mixing (**Figures 8**, **9**). *C. edule* performed local mixing in the top three centimeters, with the greatest activity occurring in the low bulk density sediment which is visible by the greater quantity of luminophores mixed into the low bulk density sediments than the high bulk density sediments at the same depth (**Figure 8**). The luminophore profiles for *S. plana, L. balthica,* and *H. diversicolor*, showed non-local mixing peaks at depth (**Figures 8**, **9** white depth interval). The *L. balthica* and *H. diversicolor* peaks seemed most prominent in the soft sediments, and the *S. plana* appeared to produce greater peaks in the soft-sandy sediment (**Figure 8**).

For the species that showed the clearest non-local mixing (*S. plana* and *H. diversicolor*), the maximum luminophore pixel counts at depth were greater in soft sediment than in compact sediment, F (1, 64) = 8.7, $p = 0.004$ (**Supplementary Table 3**). Across all species that exhibited non-local mixing, the peaks were greatest in the soft-sandy sediment (average = 0.57 × 10^5 luminophore pixels ± 0.31 × 10^5 luminophore pixels).

For all species, greater mixing occurred in the soft treatments vs. the compact treatments. The polychaetes transported more luminophore in the muddy treatments than the sandy ones. Of all the species, *S. plana* mixed the greatest amount of luminophores into the sediment and was the only species that tended to transport more luminophores in the soft-sandy treatment than the soft-muddy treatment. *H. diversicolor* and *S. plana* had greater non-local mixing peak values at depth in the soft treatments than the compact treatments.

DISCUSSION

The aim of our study was to investigate how bulk density affects benthic macrofauna behavior, as a step toward understanding how biogeomorphological and biogeochemical processes on intertidal flats might change under different bulk density conditions. We found clear effects of bulk density on benthic macrofauna burrowing behavior and bioturbation activity, which are summarized in **Figure 10**. In line with our first hypothesis that the mobility of the benthic macrofauna would be lower in compact (i.e., high bulk density) vs. soft (i.e., low bulk density) sediment, we found that in compact (vs. soft) sediment all animals burrowed slower, all animals transported fewer luminophores, and *L. balthica* burrowed shallower. Our second hypothesis was that bulk density would have similar effects on the behavior of benthic macrofauna in both sandy and muddy sediment. We did not detect any significant interactions between sediment grain size and sediment bulk density, indicating that animal responses had similar directions in both muddy and sandy sediments. We also did not detect a sediment treatment effect on respiration rate, however, the animals tended to have the greatest respiration in the sediment that were closer to their natural habitat. In line with our third hypothesis that larger bivalves would be more sensitive to differences in bulk density than smaller bivalves of the same species, we found that smaller *C. edule* and *S. plana* burrowed significantly faster than the larger ones in the compact muddy treatment (*S. plana*) and soft sandy treatment (*C. edule*). In addition, the small *S. plana* tended to transport more luminophores than the larger ones, but this appeared to be independent of sediment treatment.

Importance of Sediment Grain Size vs. Bulk Density Effects on Burrowing

We found it surprising that the burrowing rates of bivalves were significantly faster in the soft treatments compared to the compact treatments, rather than being largely driven by sediment grain size. Indeed, we expected the burrowing rates to be driven by penetration resistance and the muddy treatments

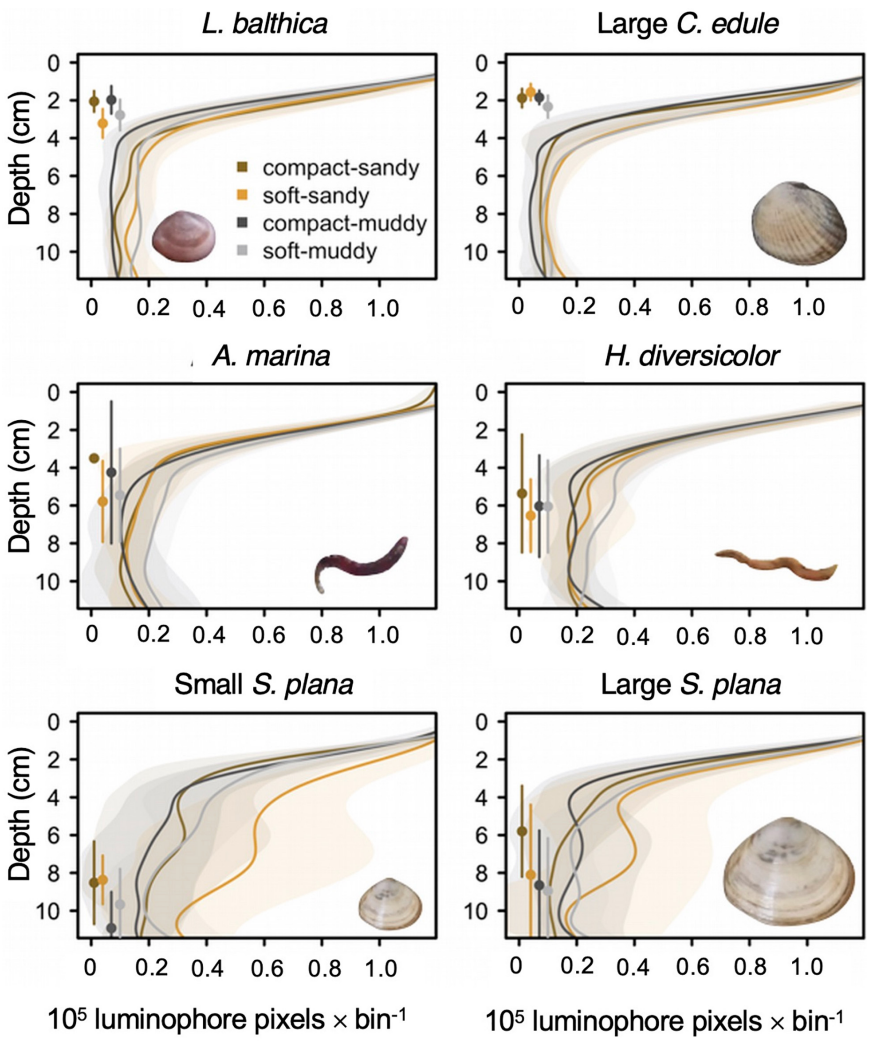


FIGURE 8 | Smoothed average luminophore profiles for *L. balthica*, *C. edule*, *H. diversicolor*, *A. marina*, and *S. plana* with standard deviation intervals, showing the incorporation of the luminophores into the sediment. We only show the profiles for the large *C. edule* because the two size classes produced very similar ones. The luminophores were counted in 0.5 cm bins. Luminophores are added to the sediment surface and permeate through the sediment. Local mixing causes the number of luminophores to decrease exponentially with depth whereas non-local mixing results in an increase of luminophores below the sediment surface. Depths where non-local mixing are dominant typically become visible as (small) bumps in the curve where the luminophore value reaches a local maximum. For example, the *S. plana* displays non-local mixing at 6–8 cm depth in the soft-sandy sediment. The points to the left of the profiles represent average depth for the species by sediment treatment (as in **Figure 6**), with standard deviations (vertical lines).

had much lower penetration resistance than the sandy treatments (**Figure 2** and **Table 2**). The observed burrowing patterns might be explained through the difference in sediment cohesiveness between the sandy and muddy treatments. Cohesiveness is largely governed by clay content (Joensuu et al., 2018). At high water contents, muddy sediment becomes akin to a viscous liquid and easy to entrain, whereas at low water contents, muddy sediments have much greater cohesion and a higher erosion threshold (Grabowski et al., 2011). In our study, although the compact-muddy sediment was more penetrable and had a lower absolute bulk density than the soft-sandy sediment (see **Table 2**), it was noticeably more cohesive and stickier than any of the other sediment treatments. The biomechanics of burrowing are different depending on the sediment type (Crane and Merz, 2017): in cohesive mud, animals burrow through crack propagation, whereas in coarse sand they may burrow through local fluidization or excavation (Dorgan, 2015). The cohesiveness of the compact-muddy sediment could have presented an obstacle to the bivalves' burrowing of similar magnitude to the high penetration resistance of the compact-sandy sediment, and probably affected the biomechanics of the burrowing animals.

Though we found that within our experiment behavioral differences between the treatments were mainly driven by sediment bulk density rather than grain size, in nature the sediment grain size provides important constraints for species

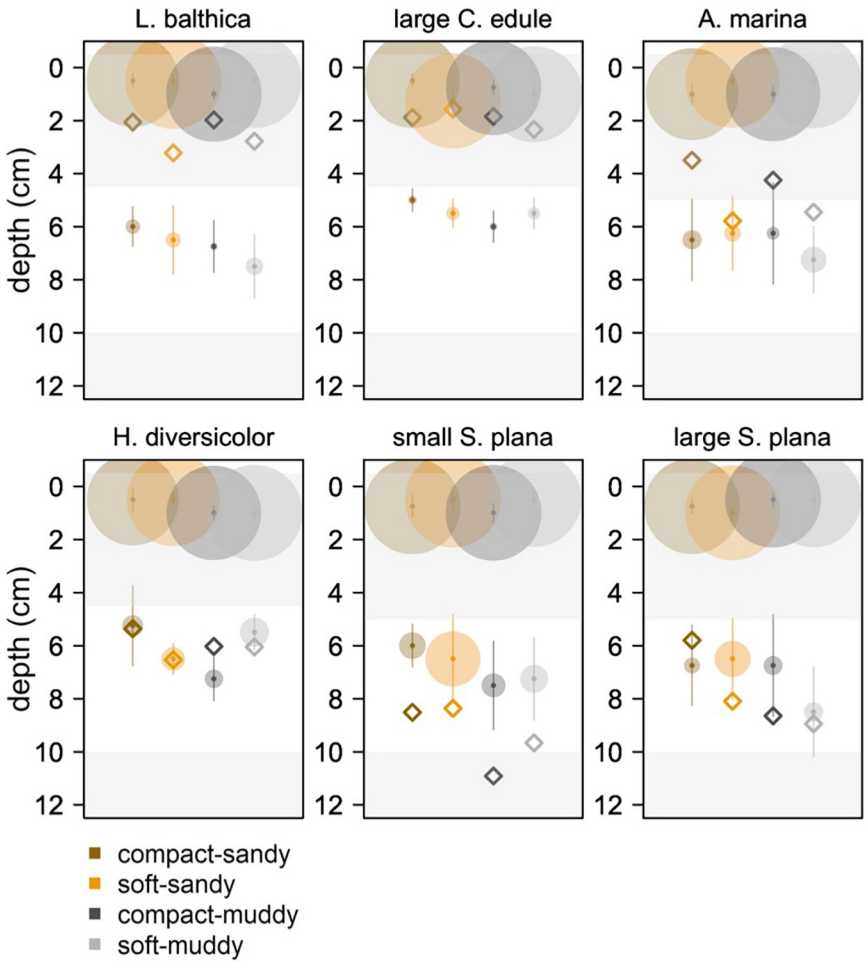


FIGURE 9 | Median locations (with standard deviation in vertical lines) of peak luminophore pixel counts (center of the circle circle) for the 0–4 cm diffusion layer interval and for the non-local mixing interval, represented by a white layer in the plot. We wanted to show peaks in luminophores in the top diffusion layer and at depth. The white depth interval excludes the diffusion layer (0–4.5 cm for *L. balthica*, *C. edule*, and *H. diversicolor*, 0–5 cm for *S. plana* and *A. marina*) and the bottom of the core (10–12 cm) where excess luminophores pooled. The limit of the diffusion layer was determined as the depth of first inflection point in the luminophore profile curves of the previous figure, rounded to the closest 0.5 cm. The 10 cm lower limit was a conservative estimate to exclude edge effects. The size of the circle is scaled to the median luminophore pixel count at the peak luminophore pixel location. The diamonds indicate the mean depth of the species/sediment block.

habitat. Many studies have described species assemblages to vary along a sediment grain size gradient (e.g., Ysebaert et al., 2002; Thrush et al., 2003; Compton et al., 2013; Pratt et al., 2014). However, most of these studies are correlative and the mechanics that underpin the habitat-animal associations prove to be elusive (Snelgrove and Butman, 1994). Other factors, like hydrodynamics, may be equally important. For example, the sandy areas in the Western Scheldt have a high degree of hydrodynamic stress and have impoverished benthos communities compared with the species-rich sandy areas in the Eastern Scheldt which have low hydrodynamic stress (Cozzoli et al., 2013). Bulk-density effects are generally not included in these kind of field studies. Our study highlights that including bulk density measurements may add an extra level of understanding to benthic macrofauna distribution and especially macrofauna activity in terms of sediment mixing.

High burrowing ability is essential for bivalves to survive in unstable sediments (Alexander et al., 1993; Takeuchi et al., 2015). All animals in our study burrowed faster in the soft sediments, and the small *C. edule* and *S. plana* burrowed faster than the larger adult ones in certain treatments. However, soft sediment is more easily eroded than compact sediment (Grabowski et al., 2011). In most bivalve species, like *C. edule* and *L. balthica*, juveniles live closer to the surface than adults and may hence be more easily dislodged by erosion during storms (Tallqvist, 2001; St-Onge and Miron, 2007). Yet, smaller and younger bivalves may compensate for their shallower living depth during erosion events by being able to burrow faster than adults in high bulk density conditions. It would be interesting to further investigate whether there is a tradeoff between sediment compaction effects on the erodibility and burrowing rate, and how this might impact the overwintering survival of juvenile versus adult bivalves.

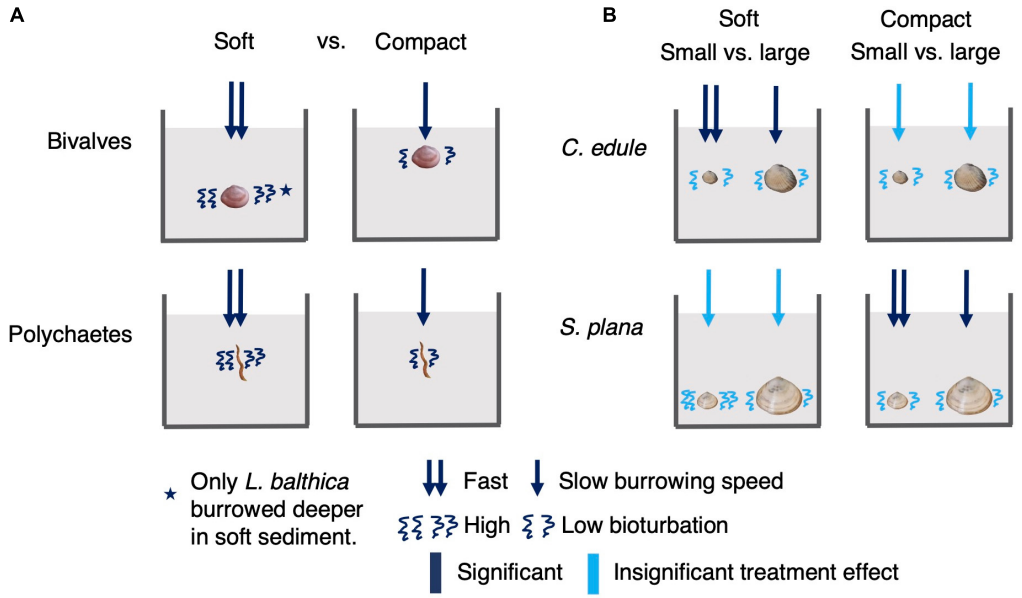


FIGURE 10 | Summary of sediment bulk density treatment main effects on burrowing speed, depth, and bioturbation amount. Because there were no significant interactions between sediment bulk density and grain size, we show a single figure to summarize bulk density effects under the different sediment grain sizes. We did not present respiration effects as there were no significant sediment bulk density effects on respiration. The left panel **(A)** shows bulk density treatment main effects on bivalves and polychaetes. The effect pertains to all bivalves or polychaetes unless indicated with a star. The right panel **(B)** shows comparisons between *C. edule* and *S. plana* size class responses under soft and compact sediments.

Sediment Bulk Density Effects on Benthic Macrofauna Survival and Predation

Extreme bulk density sediments may present difficult living conditions for benthic macrofauna and affect their survival due to physiological constraints. At very low bulk densities, sediments might become so soft that animals have to expend a great amount of energy to keep their position in the sediment or unclog their feeding apparatus of small mud particles (Lohrer et al., 2006; Mestdagh et al., 2018). High bulk densities would present different challenges. For example, our high bulk density treatments most likely inhibited *A. marina*'s ability to ventilate their burrows which is energetically costly in low sediment permeability (Meysman et al., 2005), thus greatly reducing their survival.

Other ecological mechanisms, like predation risk and growth efficiency, might be affected by sediment bulk density as well. At shallower depths, the feeding area of deposit-feeding bivalves is increased as the siphon can be extended onto a larger surface area (Zwarts et al., 1994), whereas bivalves respond to predator presence by burrowing deeper (Griffiths and Richardson, 2006; Flynn and Smee, 2010). In high bulk density sediment, *L. balthica* may have increased energy expenditure during burrowing or feeding, which would reduce *L. balthica* growth efficiency. In addition, *L. balthica* would also stay closer to the surface in high bulk density sediment, thereby increasing its vulnerability to predation. Similarly, when *H. diversicolor* feeds at the surface, it is vulnerable to predation and its escape depends on speed (Ens et al., 1997). Considering that *H. diversicolor* burrowed significantly faster in softer low bulk density sediments, we can conclude that *H. diversicolor* and other surface deposit feeding polychaetes might also be more vulnerable to predators in high bulk density sediments because of decreased possibility of escape. Thus benthic animals may have lower survival in high bulk density conditions due to increased risk of predation.

Implications for Animal-Sediment Interactions and Ecosystem-Scale Impacts

Benthic macrofauna change their behavior under different bulk densities which can have consequences for the biogeomorphology and biogeochemistry of tidal flats. Under higher bulk densities, a reduction in the depth at which infauna burrow, which we observed in particular for *L. balthica* (**Figure 6**), may lead to a shallower apparent redox potential discontinuity (Gerwing et al., 2017), which could decrease the depth of the biologically active zone depth (Sturdivant and Shimizu, 2017). Furthermore, a decrease in bioturbation and especially non-local mixing activity in high bulk density sediment, which we observed for important gallery diffusor *H. diversicolor* (**Figure 8**), could lead to reduced sediment permeability and oxygen penetration of the sediment (Aller and Aller, 1998; Michaud et al., 2006) as well as a build-up of a mud layer due to decreased resuspension or incorporation of mud into the sediment matrix (Montserrat et al., 2008; McCartain et al., 2017). In addition, a reduction in non-local mixing of *H. diversicolor* would decrease microbial processing of organic material which would reduce nutrient release into the porewater

(Mermillod-Blondin et al., 2004). Changes in bivalve behavior may also affect tidal flat biogeochemistry, for example, reduced siphon movement and pumping rate due to more compact high bulk density sediment would increase the time between bouts of oxygenation of the sediment which might lead to short-term anoxic conditions and decreased denitrification (Volkenborn et al., 2012). Thus higher sediment bulk densities may have negative consequences for the ecosystem function of benthic macrofauna. Indeed, a reduction in their burrowing depth and bioturbation activity could lead to a shallower and less well-oxygenated surface sediment layer which would impact microorganisms and eventually nutrient cycling. Low bulk density sediments may have the opposite effect and stimulate nutrient cycling due to increased bioturbation.

Because sediment bulk density tends to increase with sediment erosion and decrease with sediment deposition (Dyer et al., 2000), we speculate that the macrofauna in an eroding tidal flat are typically less mobile than macrofauna in a depositing tidal flat of a similar sediment grain size. Animal-sediment interactions between bioturbation and bulk density are likely to create positive feedback loops for tidal flat biogeomorphology. Bioturbation destabilizes sediment (Widdows et al., 2000) which decreases sediment bulk density and, as we found in our study, a soft sediment encourages animal movement. These interactions could create a positive feedback loop between low sediment bulk density conditions and elevated benthic macrofauna movement. The opposite feedback loop would occur under high bulk density sediment where sediment conditions discourage animal movement which in turn may lead to further sediment compaction. However, non-cohesive soft sediments are generally more vulnerable to erosion than compact sediments (Grabowski et al., 2011), and greater animal activity may cause these sediments to be even more easily eroded. Further investigation on animal-sediment interactions, particularly on whether animal activity under different bulk densities affects tidal flat biogeochemistry and generates positive biogeomorphology feedback loops, would be necessary to tease out the importance of sediment bulk densities for tidal flat functioning and evolution.

DATA AVAILABILITY STATEMENT

The raw data supporting the conclusions of this article will be made available by the authors, without undue reservation.

AUTHOR CONTRIBUTIONS

LW, TB, TY, and CM contributed to the study's conception. LW and NS contributed to the study's data acquisition and data analysis. LW wrote the first draft. All authors contributed to revising the manuscript and approved the final manuscript.

FUNDING

This study was funded by the Buitendijkse project of Rijkswaterstaat (Netherlands Ministry of Infrastructure and Water Management) and supported by the Netherlands Organisation for Scientific Research (NWO) via the project "EMERGO – Ecomorphological functioning and management of tidal flats" (850.13.020, 850.13.022, and 850.13.023).

ACKNOWLEDGMENTS

We would like to thank Werna Werna for help in carrying out the experiment. We would also like to thank Jeroen van Dalen, Lennart van Ijzerloo, Daniel Blok, Anton Tramper, and Justin Tiano for technical assistance.

SUPPLEMENTARY MATERIAL

The Supplementary Material for this article can be found online at: https://www.frontiersin.org/articles/10.3389/fmars.2021.707785/full#supplementary-material

REFERENCES

Aberson, M. J. R., Bolam, S. G., and Hughes, R. G. (2011). The dispersal and colonisation behaviour of the marine polychaete Nereis diversicolor (O. F. Müller) in south-east England. *Hydrobiologia* 672, 3–14. doi: 10.1007/s10750-011-0752-y

Alexander, R. R., Stanton, R. J., and Dodd, J. R. (1993). Influence of sediment grain size on the burrowing of bivalves: correlation with distribution and stratigraphic persistence of selected neogene clams. *PALAIOS* 8:289. doi: 10.2307/3515151

Aller, R. C. (1994). Bioturbation and remineralization of sedimentary organic matter: effects of redox oscillation. *Chem. Geol.* 114, 331–345. doi: 10.1016/0009-2541(94)90062-0

Aller, R. C., and Aller, J. Y. (1998). The effect of biogenic irrigation intensity and solute exchange on diagenetic reaction rates in marine sediments. *J. Mar. Res.* 56, 905–936. doi: 10.1357/002224098321667413

Andersen, T. J., Lund-Hansen, L. C., Pejrup, M., Jensen, K. T., and Mouritsen, K. N. (2005). Biologically induced differences in erodibility and aggregation of subtidal and intertidal sediments: a possible cause for seasonal changes in sediment deposition. *J. Mar. Syst.* 55, 123–138. doi: 10.1016/j.jmarsys.2004.09.004

Barbier, E. B., Hacker, S. D., Kennedy, C., Koch, E. W., Stier, A. C., and Silliman, B. R. (2011). The value of estuarine and coastal ecosystem services. *Ecol. Monogr.* 81, 169–193. doi: 10.1890/10-1510.1

Bocher, P., Robin, F., Kojadinovic, J., Delaporte, P., Rousseau, P., Dupuy, C., et al. (2014). Trophic resource partitioning within a shorebird community feeding on intertidal mudflat habitats. *J. Sea Res.* 92, 115–124. doi: 10.1016/j.seares.2014.02.011

Bokuniewicz, H. J., Gordon, R. B., and Rhoads, D. C. (1975). Mechanical properties of the sediment—water interface. *Ma. Geol.* 18, 263–278. doi: 10.1016/0025-3227(75)90016-X

Boudreau, B. P. (1986a). Mathematics of tracer mixing in sediments; I, Spatially-dependent, diffusive mixing. *Am. J. Sci.* 286, 161–198. doi: 10.2475/ajs.286.3.161

Boudreau, B. P. (1986b). Mathematics of tracer mixing in sediments; II, Nonlocal mixing and biological conveyor-belt phenomena. *Am. J. Sci.* 286, 199–238. doi: 10.2475/ajs.286.3.199

Bouma, T. J., Olenin, S., Reise, K., and Ysebaert, T. (2009). Ecosystem engineering and biodiversity in coastal sediments: posing hypotheses. *Helgol. Mar. Res.* 63, 95–106. doi: 10.1007/s10152-009-0146-y

Braeckman, U., Foshtomi, M. Y., Van Gansbeke, D., Meysman, F., Soetaert, K., Vincx, M., et al. (2014). Variable importance of macrofaunal functional biodiversity for biogeochemical cycling in temperate coastal sediments. *Ecosystems* 17, 720–737. doi: 10.1007/s10021-014-9755-7

Compton, T. J., Holthuijsen, S., Koolhaas, A., Dekinga, A., Ten Horn, J., Smith, J., et al. (2013). Distinctly variable mudscapes: Distribution gradients of intertidal macrofauna across the Dutch Wadden Sea. *J. Sea Res.* 82, 103–116. doi: 10.1016/j.seares.2013.02.002

Cozzoli, F., Bouma, T., Ysebaert, T., and Herman, P. M. J. (2013). Application of non-linear quantile regression to macrozoobenthic species distribution modelling: comparing two contrasting basins. *Mar. Ecol. Prog. Ser.* 475, 119–133. doi: 10.3354/meps10112

Crane, R. L., and Merz, R. A. (2017). Mechanical properties of sediment determine burrowing success and influence distribution of two lugworm species. *J. Exper. Biol.* 220, 3248–3259. doi: 10.1242/jeb.156760

Dorgan, K. M. (2015). The biomechanics of burrowing and boring. *J. Exper. Biol.* 218, 176–183. doi: 10.1242/jeb.086983

Dowd, M., Grant, J., and Lu, L. (2014). Predictive modeling of marine benthic macrofauna and its use to inform spatial monitoring design. *Ecol. Appl.* 24, 862–876. doi: 10.1890/12-2081.1

Dyer, K. R., Christie, M. C., and Wright, E. W. (2000). The classification of intertidal mudflats. *Continental Shelf Res.* 20, 1039–1060. doi: 10.1016/s0278-4343(00)00011-x

Ens, B. J., Bunskoeke, A. E. J., and Hoekstra, R. (1997). Prey choice and search speed: why simple optimality fails to explain the prey choice of oystercatchers Haematopus ostralegus feeding on Nereis diversicolor and Macoma balthica. *Oceanogr. Literature Rev.* 9:1018.

Flynn, A. M., and Smee, D. L. (2010). Behavioral plasticity of the soft-shell clam, Mya arenaria (L.), in the presence of predators increases survival in the field. *J. Exper. Mar. Biol. Ecol.* 383, 32–38. doi: 10.1016/j.jembe.2009.10.017

Gerino, M., Stora, G., François-Carcaillet, F., and Gilbert, F. (2003). Macor-invertebrate functional groups in freshwater and marine sediments: a common mechanistic classification. *Vie et Milieu* 53, 221–231.

Gerwing, T. G., Allen Gerwing, A. M., Macdonald, T., Cox, K., Juanes, F., and Dudas, S. E. (2017). Intertidal soft-sediment community does not respond to disturbance as postulated by the intermediate disturbance hypothesis. *J. Sea Res.* 129, 22–28. doi: 10.1016/j.seares.2017.09.001

Grabowski, R. C., Droppo, I. G., and Wharton, G. (2011). Erodibility of cohesive sediment: The importance of sediment properties. *Earth-Sci. Rev.* 105, 101–120. doi: 10.1016/j.earscirev.2011.01.008

Gray, J. S., and Elliott, M. (2009). *Ecology of Marine Sediments: From Science to Management*. Oxford, UK: OUP Oxford.

Griffiths, C. L., and Richardson, C. (2006). Chemically induced predator avoidance behaviour in the burrowing bivalve Macoma balthica. *J. Exper. Mar. Biol. Ecol.* 331, 91–98. doi: 10.1016/j.jembe.2005.10.002

Harris, R. J., Pilditch, C. A., Greenfield, B. L., Moon, V., and Kröncke, I. (2016). The influence of benthic macrofauna on the erodibility of intertidal sediments with varying mud content in Three New Zealand Estuaries. *Estuaries Coasts* 39, 815–828. doi: 10.1007/s12237-015-0036-2

Hu, Z., Yao, P., van der Wal, D., and Bouma, T. J. (2017). Patterns and drivers of daily bed-level dynamics on two tidal flats with contrasting wave exposure. *Sci. Rep.* 7:7088. doi: 10.1038/s41598-017-07515-y

Joensuu, M., Pilditch, C. A., Harris, R., Hietanen, S., Pettersson, H., and Norkko, A. (2018). Sediment properties, biota, and local habitat structure explain variation in the erodibility of coastal sediments: Variation in the erodibility of coastal sediments. *Limnol. Oceanogr.* 63, 173–186. doi: 10.1002/lno.10622

Koch, E. W., Barbier, E. B., Silliman, B. R., Reed, D. J., Perillo, G. M., Hacker, S. D., et al. (2009). Non-linearity in ecosystem services: temporal and spatial variability in coastal protection. *Front. Ecol. Environ.* 7, 29–37. doi: 10.1890/080126

Kristensen, E. (1988). "Benthic fauna and biogeochemical processes in marine sediments: microbial activities and fluxes," in *Nitrogen cycling in coastal marine environments*, eds T. H. Blackburn and J. Sorensen (London: John Wiley and Sons), 275–299.

Kristensen, E., Neto, J. M., Lundkvist, M., Frederiksen, L., Pardal, M. Â, Valdemarsen, T., et al. (2013). Influence of benthic macroinvertebrates on the erodability of estuarine cohesive sediments: Density- and biomass-specific responses. *Estuarine Coastal Shelf Sci.* 134, 80–87. doi: 10.1016/j.ecss.2013.09.020

Kristensen, E., Penha-Lopes, G., Delefosse, M., Valdemarsen, T., Quintana, C., and Banta, G. (2012). What is bioturbation? The need for a precise definition for fauna in aquatic sciences. *Mar. Ecol. Prog. Ser.* 446, 285–302. doi: 10.3354/meps09506

Lohrer, A., Hewitt, J., and Thrush, S. (2006). Assessing far-field effects of terrigenous sediment loading in the coastal marine environment. *Mar. Ecol. Prog. Ser.* 315, 13–18. doi: 10.3354/meps315013

Lucking, G., Stark, N., Lippmann, T., and Smyth, S. (2017). Variability of in situ sediment strength and pore pressure behavior of tidal estuary surface sediments. *Geo-Mar. Lett.* 37, 441–456. doi: 10.1007/s00367-017-0494-6

Maire, O., Lecroart, P., Meysman, F., Rosenberg, R., Duchêne, J., and Grémare, A. (2008). Quantification of sediment reworking rates in bioturbation research: a review. *Aquat. Biol.* 2, 219–238. doi: 10.3354/ab00053

McCartain, L. D., Townsend, M., Thrush, S. F., Wethey, D. S., Woodin, S. A., Volkenborn, N., et al. (2017). The effects of thin mud deposits on the behaviour of a deposit-feeding tellinid bivalve: implications for ecosystem functioning. *Mar. Freshwater Behav. Physiol.* 50, 239–255. doi: 10.1080/10236244.2017.1364123

Mermillod-Blondin, F., Rosenberg, R., François-Carcaillet, F., Norling, K., and Mauclaire, L. (2004). Influence of bioturbation by three benthic infaunal species on microbial communities and biogeochemical processes in marine sediment. *Aquat. Microb. Ecol.* 36, 271–284. doi: 10.3354/ame036271

Mestdagh, S., Bagaço, L., Braeckman, U., Ysebaert, T., De Smet, B., Moens, T., et al. (2018). Functional trait responses to sediment deposition reduce macrofauna-mediated ecosystem functioning in an estuarine mudflat. *Biogeosciences* 15, 2587–2599. doi: 10.5194/bg-15-2587-2018

Meynecke, J.-O., Lee, S. Y., and Duke, N. C. (2008). Linking spatial metrics and fish catch reveals the importance of coastal wetland connectivity to inshore fisheries in Queensland, Australia. *Biol. Conserv.* 141, 981–996. doi: 10.1016/j.biocon.2008.01.018

Meysman, F., Galaktionov, O., and Middelburg, J. (2005). Irrigation patterns in permeable sediments induced by burrow ventilation: a case study of Arenicola marina. *Mar. Ecol. Prog. Ser.* 303, 195–212. doi: 10.3354/meps303195

Michaud, E., Desrosiers, G., Mermillod-Blondin, F., Sundby, B., and Stora, G. (2006). The functional group approach to bioturbation: II. The effects of the Macoma balthica community on fluxes of nutrients and dissolved organic carbon across the sediment–water interface. *J. Exper. Mar. Biol. Ecol.* 337, 178–189. doi: 10.1016/j.jembe.2006.06.025

Montserrat, F., Van Colen, C., Degraer, S., Ysebaert, T., and Herman, P. (2008). Benthic community-mediated sediment dynamics. *Mar. Ecol. Prog. Ser.* 372, 43–59. doi: 10.3354/meps07769

Morys, C., Powilleit, M., and Forster, S. (2017). Bioturbation in relation to the depth distribution of macrozoobenthos in the southwestern Baltic Sea. *Mar. Ecol. Prog. Ser.* 579, 19–36. doi: 10.3354/meps12236

Olafsson, E. B. (1986). Density dependence in suspension-feeding and deposit-feeding populations of the bivalve Macoma balthica: A field experiment. *J. Anim. Ecol.* 55:517. doi: 10.2307/4735

Orvain, F. (2005). A model of sediment transport under the influence of surface bioturbation: generalisation to the facultative suspension-feeder Scrobicularia plana. *Mar. Ecol. Prog. Ser.* 286, 43–56. doi: 10.3354/meps286043

Piersma, T., de Goeij, P., and Tulp, I. (1993). An evaluation of intertidal feeding habitats from a shorebird perspective: Towards relevant comparisons between temperate and tropical mudflats. *Netherlands J. Sea Res.* 31, 503–512. doi: 10.1016/0077-7579(93)90062-W

Pratt, D. R., Lohrer, A. M., Pilditch, C. A., and Thrush, S. F. (2014). Changes in ecosystem function across sedimentary gradients in estuaries. *Ecosystems* 17, 182–194. doi: 10.1007/s10021-013-9716-6

Queirós, A. M., Birchenough, S. N., Bremner, J., Godbold, J. A., Parker, R. E., Romero-Ramirez, A., et al. (2013). A bioturbation classification of E uropean marine infaunal invertebrates. *Ecol. Evol.* 3, 3958–3985. doi: 10.1002/ece3.769

Richardson, C., Ibarrola, I., and Ingham, R. (1993). Emergence pattern and spatial distribution of the common cockle Cerastoderma edule. *Mar. Ecol. Prog. Ser.* 99, 71–81. doi: 10.3354/meps099071

Riisgård, H. U., and Banta, G. T. (1998). Irrigation and deposit feeding by the lugworm Arenicola marina, characteristics and secondary effects on the environment: a review of current knowledge. *Life Environ.* 48, 243–257.

Seitz, R. D., Wennhage, H., Bergström, U., Lipcius, R. N., and Ysebaert, T. (2014). Ecological value of coastal habitats for commercially and ecologically important species. *ICES J. Mar. Sci.* 71, 648–665. doi: 10.1093/icesjms/fst152

Snelgrove, P. V. R., and Butman, C. A. (1994). Animal-sediment relationships revisited: Cause versus effect. *Oceanogr. Mar. Biol. Ann. Rev.* 32, 111–177.

Soares, C., and Sobral, P. (2009). Bioturbation and erodibility of sediments from the tagus estuary. *J. Coastal Res.* 56, 1429–1433.

Soetaert, K., and Provoost, P. (2017). *Turbo: functions for fitting bioturbation to tracer data*. **COm.

Solan, M., Wigham, B. D., Hudson, I. R., Kennedy, R., Coulon, C. H., Norling, K., et al. (2004). In situ quantification of bioturbation using time lapse fluorescent sediment profile imaging (f SPI), luminophore tracers and model simulation. *Mar. Ecol. Prog. Ser.* 271, 1–12. doi: 10.3354/meps271001

St-Onge, P., and Miron, G. (2007). Effects of current speed, shell length and type of sediment on the erosion and transport of juvenile softshell clams (Mya arenaria). *J. Exper. Mar. Biol. Ecol.* 349, 12–26. doi: 10.1016/j.jembe.2007.03.020

Stringer, C. E., Trettin, C. C., and Zarnoch, S. J. (2016). Soil properties of mangroves in contrasting geomorphic settings within the Zambezi River Delta, Mozambique. *Wetlands Ecol. Manage.* 24, 139–152. doi: 10.1007/s11273-015-9478-3

Sturdivant, S. K., and Shimizu, M. S. (2017). In situ organism-sediment interactions: Bioturbation and biogeochemistry in a highly depositional estuary. *PLoS One* 12:e0187800. doi: 10.1371/journal.pone.0187800

Takeuchi, S., Yamada, F., Shirozu, H., Ohashi, S., and Tamaki, A. (2015). Burrowing ability as a key trait in the establishment of infaunal bivalve populations following competitive release on an extensive intertidal sandflat. *J. Exp. Mar. Biol. Ecol.* 466, 9–23. doi: 10.1016/j.jembe.2015.01.011

Tallqvist, M. (2001). Burrowing behaviour of the Baltic clam Macoma balthica: effects of sediment type, hypoxia and predator presence. *Mar. Ecol. Prog. Ser.* 212, 183–191. doi: 10.3354/meps212183

Thrush, S., Hewitt, J., Norkko, A., Nicholls, P., Funnell, G., and Ellis, J. (2003). Habitat change in estuaries: predicting broad-scale responses of intertidal macrofauna to sediment mud content. *Mar. Ecol. Prog. Ser.* 263, 101–112. doi: 10.3354/meps263101

Thrush, S. F., Hewitt, J. E., Gibbs, M., Lundquist, C., and Norkko, A. (2006). Functional role of large organisms in intertidal communities: community effects and ecosystem function. *Ecosystems* 9, 1029–1040. doi: 10.1007/s10021-005-0068-8

Van Colen, C., Rossi, F., Montserrat, F., Andersson, M. G. I., Gribsholt, B., Herman, P. M. J., et al. (2012). Organism-sediment interactions govern post-hypoxia recovery of ecosystem functioning. *PLoS One* 7:e49795. doi: 10.1371/journal.pone.0049795

Van Colen, C., Verbelen, D., Devos, K., Agten, L., Van Tomme, J., Vincx, M., et al. (2014). Sediment-benthos relationships as a tool to assist in conservation practices in a coastal lagoon subjected to sediment change. *Biodiv. Conserv.* 23, 877–889. doi: 10.1007/s10531-014-0638-1

Venables, W., and Ripley, B. (2002). *Modern Applied Statistics with S*, Fourth Edn. New York: Springer.

Volkenborn, N., Meile, C., Polerecky, L., Pilditch, C. A., Norkko, A., Norkko, J., et al. (2012). Intermittent bioirrigation and oxygen dynamics in permeable sediments: An experimental and modeling study of three tellinid bivalves. *J. Mar. Res.* 70, 794–823. doi: 10.1357/002224012806770955

Volkenborn, N., Robertson, D. M., and Reise, K. (2009). Sediment destabilizing and stabilizing bio-engineers on tidal flats: cascading effects of experimental exclusion. *Helgol. Mar. Res.* 63, 27–35. doi: 10.1007/s10152-008-0140-9

Walles, B., Brummelhuis, E., and Ysebaert, T. (2017). *Development of the benthic macrofauna community after tidal restoration at Rammegors: Progress report 1*. Yerseke: Wageningen Marine Research.

Wand, M. (2019). *KernSmooth: Functions for Kernel Smoothing Supporting Wand & Jones (1995)*. Available Online at: https://CRAN.R-project.org/package=KernSmooth.

Widdows, J., Brown, S., Brinsley, M. D., Salkeld, P. N., and Elliott, M. (2000). Temporal changes in intertidal sediment erodability: influence of biological and climatic factors. *Continental Shelf Res.* 20, 1275–1289. doi: 10.1016/S0278-4343(00)00023-6

Widdows, J., Friend, P. L., Bale, A. J., Brinsley, M. D., Pope, N. D., and Thompson, C. E. L. (2007). Inter-comparison between five devices for determining erodability of intertidal sediments. *Continental Shelf Res.* 27, 1174–1189. doi: 10.1016/j.csr.2005.10.006

Ysebaert, T., Fettweis, M., Meire, P., and Sas, M. (2005). Benthic variability in intertidal soft-sediments in the mesohaline part of the Schelde estuary. *Hydrobiologia* 540, 197–216. doi: 10.1007/s10750-004-7144-5

Ysebaert, T., Meire, P., Herman, P., and Verbeek, H. (2002). Macrobenthic species response surfaces along estuarine gradients: prediction by logistic regression. *Mar. Ecol. Prog. Ser.* 225, 79–95. doi: 10.3354/meps225079

Zwarts, L., Blomert, A.-M., Spaak, P., and de Vries, B. (1994). Feeding radius, burying depth and siphon size of Macoma balthica and Scrobicularia plana. *J. Exper. Mar. Biol. Ecol.* 183, 193–212. doi: 10.1016/0022-0981(94)90087-6

Zwarts, L., and Wanink, J. H. (1993). How the food supply harvestable by waders in the Wadden Sea depends on the variation in energy density, body weight, biomass, burying depth and behaviour of tidal-flat invertebrates. *Netherlands J. Sea Res.* 31, 441–476. doi: 10.1016/0077-7579(93)90059-2

Conflict of Interest: The authors declare that the research was conducted in the absence of any commercial or financial relationships that could be construed as a potential conflict of interest.

Publisher's Note: All claims expressed in this article are solely those of the authors and do not necessarily represent those of their affiliated organizations, or those of the publisher, the editors and the reviewers. Any product that may be evaluated in this article, or claim that may be made by its manufacturer, is not guaranteed or endorsed by the publisher.

Copyright © 2021 Wiesebron, Steiner, Morys, Ysebaert and Bouma. This is an open-access article distributed under the terms of the Creative Commons Attribution License (CC BY). The use, distribution or reproduction in other forums is permitted, provided the original author(s) and the copyright owner(s) are credited and that the original publication in this journal is cited, in accordance with accepted academic practice. No use, distribution or reproduction is permitted which does not comply with these terms.

frontiers in Marine Science

ORIGINAL RESEARCH
published: 29 September 2021
doi: 10.3389/fmars.2021.704768

Mechanisms of Pond Expansion in a Rapidly Submerging Marsh

Joshua Himmelstein[1,2], Orencio Duran Vinent[1,3]*, Stijn Temmerman[4] and Matthew L. Kirwan[1]*

[1] Virginia Institute of Marine Science, College of William and Mary, Williamsburg, VA, United States, [2] Institute of Marine Sciences, The University of North Carolina at Chapel Hill, Morehead City, NC, United States, [3] Department of Ocean Engineering, Texas A&M University, College Station, TX, United States, [4] Ecosystem Management Research Group, Department of Biology, University of Antwerp, Antwerp, Belgium

The development and expansion of ponds within otherwise vegetated coastal marshes is a primary driver of marsh loss throughout the world. Previous studies propose that large ponds expand through a wind wave-driven positive feedback, where pond edge erosion rates increase with pond size, whereas biochemical processes control the formation and expansion of smaller ponds. However, it remains unclear which mechanisms dominate at a given scale, and thus how, and how fast, ponds increase their size. Here, we use historical photographs and field measurements in a rapidly submerging microtidal marsh to quantify pond development and identify the processes involved. We find that as small ponds emerge on the marsh platform, they quickly coalesce and merge, increasing the number of larger ponds. Pond expansion rates are maximized for intermediate size ponds and decrease for larger ponds, where the contribution of wave-driven erosion is negligible. Vegetation biomass, soil shear strength, and porewater biogeochemical indices of marsh health are higher in marshes adjacent to stable ponds than in those adjacent to unstable ponds, suggesting that pond growth rates are negatively related to the health of the surrounding marsh. We find that the model of Vinent et al. (2021) correctly predicts measured pond growth rates and size distribution, which suggest the different mechanisms driving pond growth are a result of marsh drowning due to sea level rise (SLR) and can be estimated by simplified physical models. Finally, we show that all relevant processes increasing pond size can be summarized by an empirical power-law equation for pond growth which predicts the temporal change of the maximum pond size as a lower bound for the total pond area in the system. This gives a timescale for the growth of ponds by merging and thus the critical time window for interventions to prevent the irreversible pond expansion associated with large scale pond merging.

Keywords: microtidal, saltmarsh, merging, biogeochemical, geomorphology, pond, pool, hydrology

OPEN ACCESS

Edited by:
Zeng Zhou,
Hohai University, China

Reviewed by:
Giulio Mariotti,
Louisiana State University, United States
Mark Schuerch,
University of Lincoln, United Kingdom

****Correspondence:***
Joshua Himmelstein
jhimmel@email.unc.edu
Orencio Duran Vinent
oduranvinent@tamu.edu

Specialty section:
This article was submitted to Coastal Ocean Processes, a section of the journal Frontiers in Marine Science

Received: *03 May 2021*
Accepted: *09 August 2021*
Published: *29 September 2021*

Citation:
Himmelstein J, Vinent OD, Temmerman S and Kirwan ML (2021) Mechanisms of Pond Expansion in a Rapidly Submerging Marsh. Front. Mar. Sci. 8:704768. doi: 10.3389/fmars.2021.704768

INTRODUCTION

Marshes buffer coasts from storms, sequester carbon, improve water quality, and provide rich habitats for fish and wildlife (Shriver et al., 2004; Barbier et al., 2011; Möller et al., 2014; Nahlik and Fennessy, 2016; Zhu et al., 2020). Sea level rise (SLR) and reduced sediment supply threaten the sustainability of marshes (Reed et al., 1999; Kirwan and Megonigal, 2013; Weston, 2014).

While marshes have some ability to survive SLR by migrating into adjacent uplands and accreting soil vertically (Pethick, 1992; Temmerman et al., 2003; Kirwan et al., 2016; Fagherazzi et al., 2019), in many regions of the world they are eroding laterally, accreting less than the local rate of SLR, and converting to open water through the development of unvegetated ponds in the marsh interior (Stevenson et al., 1985; Day et al., 2000; Carniello et al., 2009).

Ponding is a primary driver of marsh loss in submerging marshes, and as such is considered an important indicator of marsh health (Kearney et al., 1988; Nyman et al., 1994; Mariotti and Fagherazzi, 2013; Mariotti, 2016; Schepers et al., 2017; Wang et al., 2021). While salt marsh vegetation enhances sediment deposition through flow baffling and resists soil erosion through root material (Allen, 1990; Pethick, 1992; Mudd et al., 2010; Vandenbruwaene et al., 2011), loss of vegetation can lead to sediment export and irreversible marsh collapse (DeLaune et al., 1994; van Huissteden and van de Plassche, 1998; Day et al., 2011; Temmerman et al., 2012) such that vegetated marshes and unvegetated ponds may be viewed as alternative stable states (Wang and Temmerman, 2013; Belzen et al., 2017; Schepers et al., 2020a). Indeed, marshes with large proportions of unvegetated area tend to export more sediment than those with large proportions of vegetated area (Ganju et al., 2013; Ganju et al., 2020), suggesting a positive feedback where pond development leads to sediment export, and potentially runaway marsh loss.

Ponds form through a variety of mechanisms, though the process usually begins in the interior marsh with a local loss or dieback of vegetation (DeLaune et al., 1994; Hartig et al., 2002). Physical mechanisms include disturbance events such as herbivory, bioturbation, ice scour, and wrack deposition (Pethick, 1974; Wilson et al., 2014). Ponds may also initiate through vegetation mortality associated with waterlogging stress affecting soil biogeochemistry and implying toxicity to vegetation, whereby root zone degradation leads to erosion and subsidence of otherwise cohesive marsh soils (Kearney et al., 1988; Nyman et al., 1993; Johnston et al., 2003; Spivak et al., 2017). These processes depend on the hydrologic properties of a marsh, especially its hydroperiod, elevation relative to tidal datums, and connectivity to channels. For example, ponds typically form and are most prevalent in the marsh interior, far from the tidal channels that deliver sediment and drain waterlogged soils (Redfield, 1972; Kearney et al., 1988; Schepers et al., 2017; Vinent et al., 2021). These processes are expected to accelerate with SLR, especially in marshes with limited sediment supply and low tidal range (Millette et al., 2010; Wilson et al., 2009; Schepers et al., 2017; Vinent et al., 2021; Wang et al., 2021).

Ponds tend to grow until they intersect tidal channels which may promote vegetation recovery under favorable sediment balances (Wilson et al., 2014; Mariotti, 2016), or else accelerate pond erosion (Schepers et al., 2020a; Wang et al., 2021). For large ponds, wave-driven erosion depends on ponds exceeding a critical width necessary for the development of wind waves, thought to be in the range 200–1,000 m (which corresponds to areas in the range $3 \times 10^{4-8} \times 10^5$ m^2, assuming circular ponds) in US Atlantic and Gulf Coast marshes (Mariotti and Fagherazzi, 2013; Ortiz et al., 2017). However, the processes by which ponds smaller than this critical width expand remain poorly understood. Peat collapse, rotational slumping, and current-induced sediment transport have been identified as potential contributors (Kearney et al., 1988; Day et al., 2011; Spivak et al., 2017; Schepers et al., 2020a). A recent model (Mariotti et al., 2020) simulates pond formation, expansion and merging in Barnstable, MA, with a particular focus on processes driving marsh edge erosion. In contrast, the model of Vinent et al. (2021) simulates pond dynamics simply as a result of marsh drowning due to SLR. The multiplicity of model assumptions and parameters can benefit from calibration and validation through empirical information.

Here we define and measure different rates of pond growth to show that both the rates and mechanisms of pond expansion depend on pond size and that the expansion of small ponds is driven largely by the coalescence of individual ponds and the health of surrounding marsh. By comparing our results with predictions of Vinent et al. (2021)'s model, we show that measured rates of pond formation, biochemical expansion and the initial stages of merging are consistent with marsh drowning due to SLR.

MATERIALS AND METHODS

Study Area

We studied the distribution of ponds in a portion of the Blackwater National Wildlife Refuge, near the headwaters of the Blackwater River, a tributary of the Chesapeake Bay (Maryland, United States) (**Figure 1**). This area is part of the mid-Atlantic SLR hotspot (Sallenger et al., 2012), with rates of relative SLR that are more than twice the global average (Ezer et al., 2013). Twentieth century relative SLR rates (3.83 mm yr^{-1} at Cambridge, MD; NOAA Station 8571892) generally exceed local accretion rates of 1.7–3.6 mm yr^{-1} (Stevenson et al., 1985). Marshes in the study area are microtidal, low in elevation, sediment deficient, and heavily ponded (Stevenson et al., 1985; Ganju et al., 2013).

Approximately half of the marshes in the Blackwater National Wildlife refuge have been lost to ponding since 1938 (Scott et al., 2009; Schepers et al., 2017). Marsh ponding increases with distance from the river mouth at Fishing Bay (**Figure 1**), following gradients in elevation, sediment supply, and tidal range (Schepers et al., 2017). The upper reaches of the Blackwater River, where this study is focused, are characterized by strong sediment export especially during northwesterly winds, when winds are oriented parallel to the long-axis of Lake Blackwater and other large ponds, resulting in wave erosion and sediment resuspension (Ganju et al., 2013). Tidal range decreases from ∼1.0 m at Fishing Bay to <0.2 m at Lake Blackwater (Wang and Elliott, 1978; Schepers et al., 2020a). Marshes consist of mesohaline vegetation, with *Schoenoplectus americanus* and *Spartina alterniflora* occupying the lowest elevation marshes, *Distichlis spicata* and *Spartina patens* occupying intermediate elevations, and *Spartina cynusuroides* and *Phragmites australis* occupying the highest elevations (Kirwan and Guntenspergen, 2012). Marsh elevations decrease with distance from Fishing Bay (Schepers et al., 2020b), and more than 80% of marshes near

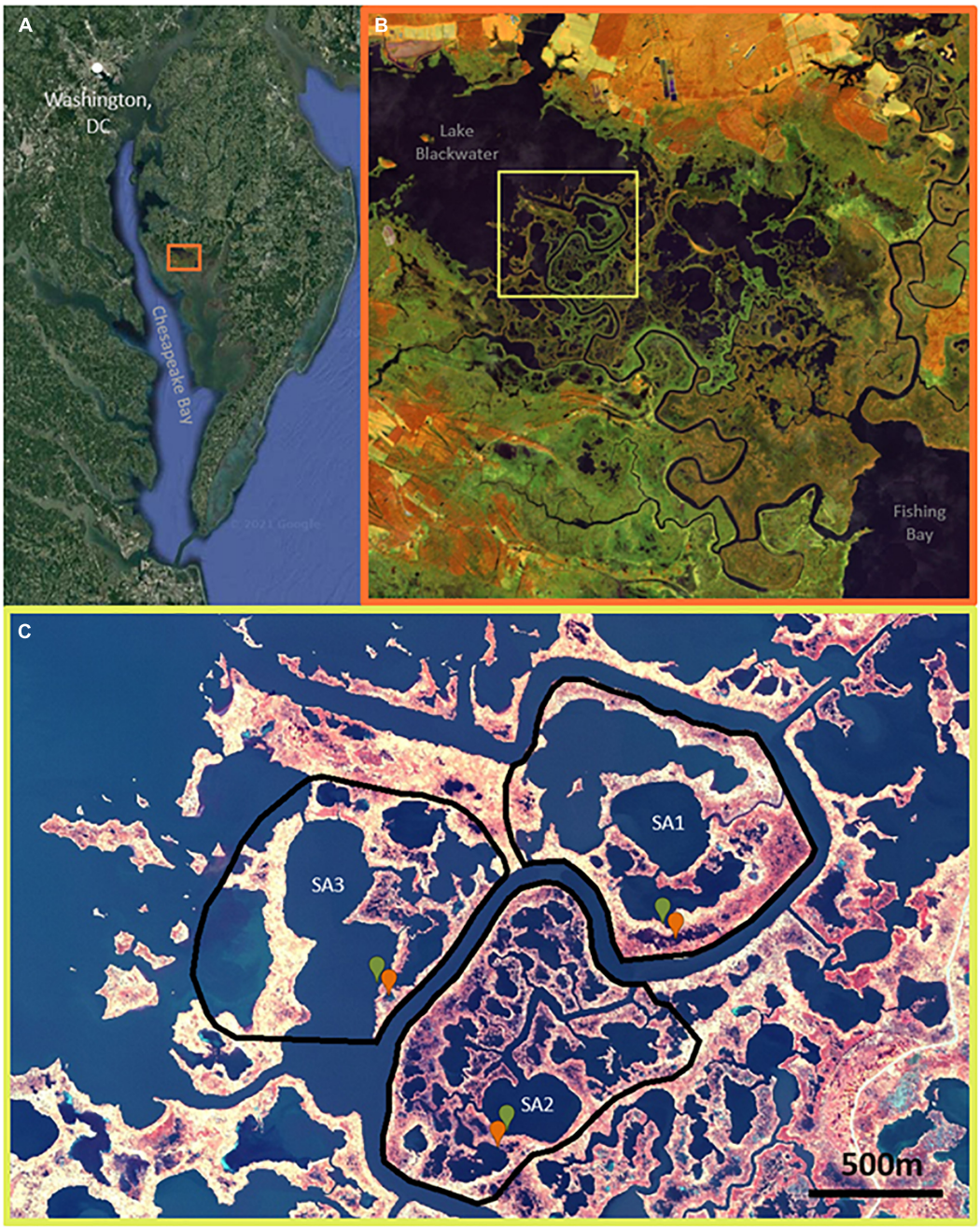


FIGURE 1 | (A) Location of Blackwater Wildlife Refuge (38.4220° N, 76.0624° W) outlined by orange square on the Eastern edge of Chesapeake Bay. **(B)** Overview of the 28,000-acre refuge, evidencing vegetation die-off and marsh loss following a gradient from low die-off near southeastern Fishing Bay to high die-off near Lake Blackwater at the northwest reaches of Blackwater River; false-color (NIR, SWIR, R) Sentinel-2 imagery 2020-11. **(C)** The three study areas used for remote sensing analyses with the field-sampled ponds (green is stable, red is unstable) indicated within; false-color (NIR, G, B) NAIP 2018-11-04.

the headwaters of the Blackwater River have elevations that are lower than the optimum elevation for *S. americanus* root growth and organic matter accretion (Kirwan and Guntenspergen, 2012, 2015). Extensive, permanent marsh loss has been observed through the past century, with vegetation loss increasing with distance from Fishing Bay toward our study areas (Stevenson et al., 1985; Schepers et al., 2017).

Historical Pond Growth

We examined patterns of historical pond growth in the upper Blackwater River marshes using historical photographs from 1938, 1960, 1981, and 2010 (**Table 1**). Imagery was resampled to the coarsest image resolution (1.55 m per pixel edge) to avoid resolution bias, and georeferenced to a common datum (Maryland State Plane—Lambert Conformal Conic NAD 1983).

TABLE 1 | Aerial photography summary, native resolutions were resampled before analysis to 1.55 m as described in text.

Image year	Image type	Native resolution (m)	Source	Digitization
1938	Black and white	0.86	Scott et al., 2009	Manual
1960	Black and white	1.55	U.S. Air Force	Manual
1981	Color infrared	1.55	USGS EarthExplorer	Manual
2010	Visible + NIR	0.3	Blackwater NWR	Classification

Three study areas (~10^6 m^2 each) were chosen adjacent to the upper reaches of the Blackwater River, where ponding is most extensive (**Figure 1**).

We delineated individual polygons to track pond growth through time and to explore differences between study areas. Each study area includes a large, central pond connected to the Blackwater River in the 1938 imagery. We recorded water patches ≥50 m^2 as individual ponds through extraction of existing digitized polygons (Schepers et al., 2017) and manual digitization and rectification in ArcGIS. Due to the small astronomical tidal range at this reach of Blackwater River (~0.25 m), and evidenced by water presence across all available imagery, depressions are consistently submerged and as such are defined as ponds. These ponds were considered to be merged with one another when connection widths were at least 25% that of the smaller pond's intermediate axis. Maximum likelihood classification of 2010 ponds in the study area had a 97% accuracy based on ground verification points in the most recently analyzed imagery (Schepers et al., 2017). All polygons were visually inspected for consistency with ponds in the historic imagery and amended when erroneous. The number of ponds, areal extent, and growth patterns (merging of multiple ponds vs. expansion of individual ponds) were recorded separately in each study area and at each timestep for use in the expansion and merging calculations described below. Each pond polygon was assigned a unique identifier, while ponds composed of previously individual ponds contained past identities appended to their own unique identifier.

We consider three possibilities for pond formation and growth (**Figure 2**): new ponds, when a pond appears where none existed before; single pond growth, when individual ponds overlap in consecutive images; and merged ponds, when an individual pond overlaps several ponds from a previous image.

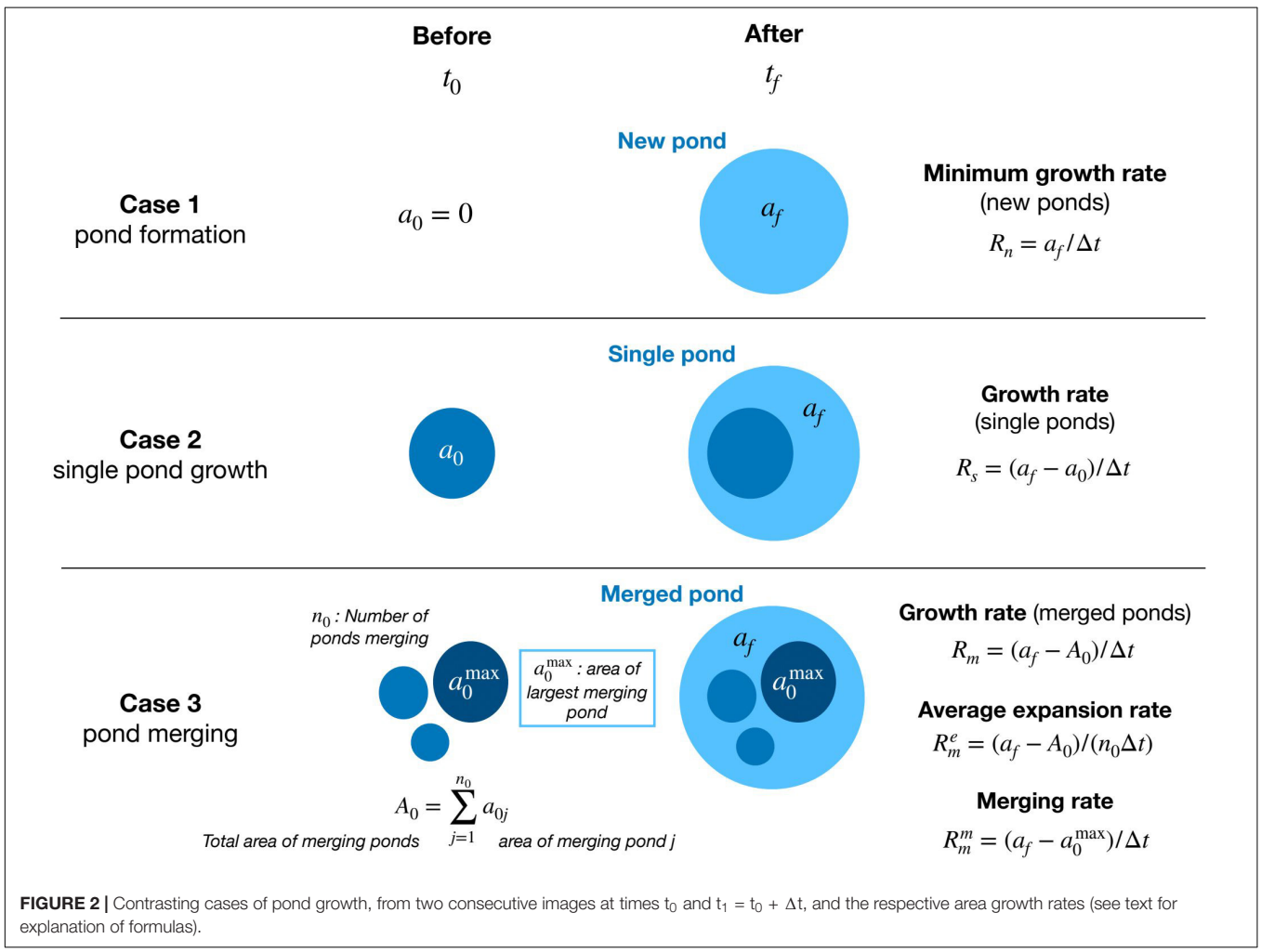


FIGURE 2 | Contrasting cases of pond growth, from two consecutive images at times t_0 and $t_1 = t_0 + \Delta t$, and the respective area growth rates (see text for explanation of formulas).

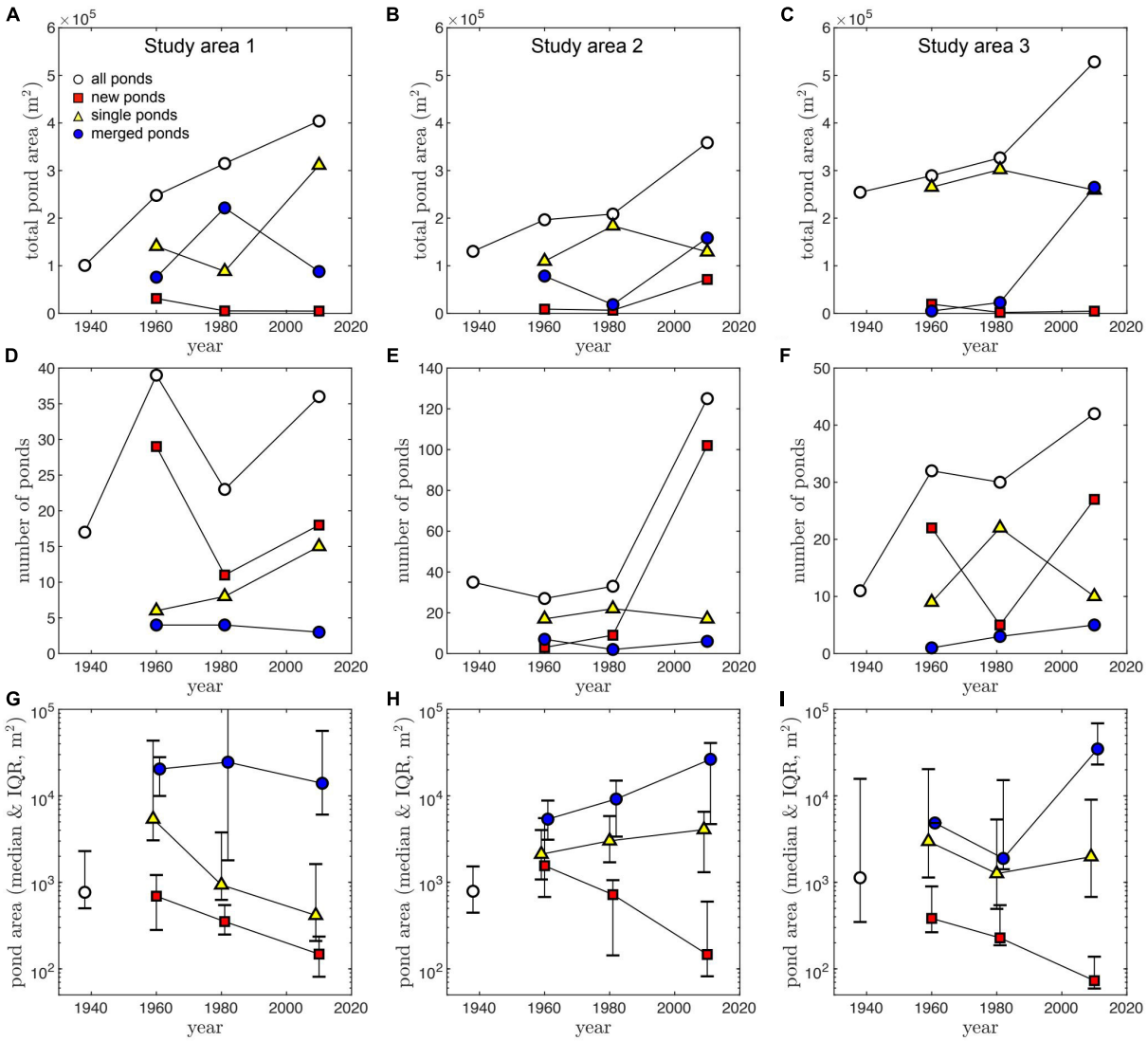


FIGURE 3 | Total pond area **(A–C)**, number of ponds greater than 50 m^2 **(D–F)**, and individual pond area **(G–I)**, as function of time and pond type, for the three study areas (columns). Due to the skewed distribution of individual pond areas, data points represent the median value, and error bars represent the Interquartile range (IQR), defined as the difference between the 75th and the 25th percentiles.

Single Ponds

The areal growth rate of single ponds is defined as

$$R_s = \left(a_f - a_0\right)/\Delta t \tag{1}$$

where a_0 and a_f are the initial and final pond areas and $\Delta t = t_f - t_0$ is the time between consecutive images. For single ponds, we also define a lateral (linear) growth rate (G) assuming circular shape, as:

$$G = \left(\sqrt{a_f/\pi} - \sqrt{a_0/\pi}\right)/\Delta t \tag{2}$$

which yields a first order estimate of the erosion rate at the pond's edge.

New Ponds

In the case of new ponds, we lack information regarding the exact time of pond formation because, by definition, the initial area is 0. Therefore, we can only estimate a lower bound for the rate of pond growth:

$$R_n = a_f/\Delta t \tag{3}$$

Merged Ponds

Similarly, for merged ponds the initial pond area is not unique (composed of several ponds) and the individual pond growth rate is not well-defined. Nevertheless, we can still define three relevant growth rates: a total growth rate of the merged pond (R_m), an average expansion rate (R_m^e) characterizing each pond's expansion during merging, and a merging rate (R_m^m)

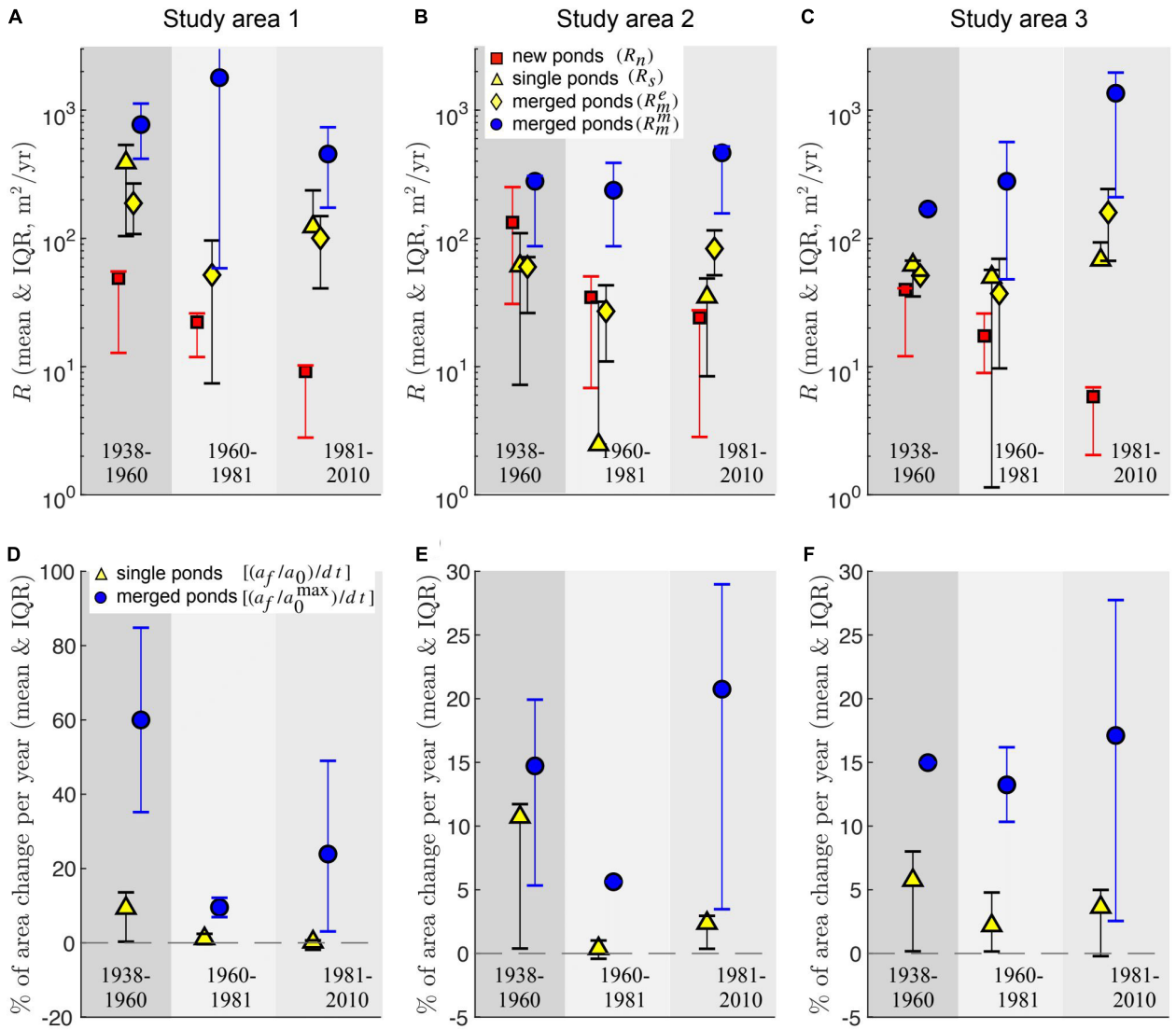


FIGURE 4 | Different area growth rates quantifying pond change **(A–C)** and relative change in pond area per year **(D–F)** area for the three time intervals and study areas. Symbols are error bars represents the mean and Interquartile range (IQR), respectively. IQR is defined as the difference between the 75th and the 25th percentiles. The relative change in pond area is defined as the ratio (a_f/a_0) between final and initial pond area divided by the time interval Δt. For merged ponds the initial pond area corresponds to the largest merging pond. The relative change in pond area is undefined for new ponds.

characterizing the net growth of the largest pond as merging takes place (**Figure 2**).

The growth rate (R_m) of the merged pond is defined as:

$$R_m = \left(a_f - A_0\right)/\Delta t \tag{4}$$

where a_f is the area of the merged pond and A_0 is the total area of the n_0 initial merging ponds (**Figure 2**). This rate represents the total change in water area during merging.

The average expansion rate (R_m^e) is defined by dividing the total growth rate by the number n_0 of merging ponds (**Figure 2**):

$$R_m^e = R_m/n_0 \tag{5}$$

and represents the growth rate of the average merged pond with initial area A_0/n_0 and final area a_f/n_0.

Finally, we define the merging rate (R_m^m) of the largest merging pond as:

$$R_m^m = \left(a_f - a_0^{max}\right)/\Delta t \tag{6}$$

where a_0^{max} is the area of the largest merging pond and a_f is the area of the final merged pond (**Figure 2**). By construction, the merging rate includes all relevant processes increasing the area of the largest pond during the time interval between consecutive images. This includes individual pond expansion and the formation and merging of new ponds.

As expected, if only one initial pond is present, $n_0 = 1$ and $A_0 = a_0^{max}$, and all rates for merged ponds are equal and

equivalent to the single pond case. On the contrary, when the number of ponds merging is large, the expansion rate R_m^e becomes negligible while the merging rate increases following the jump in pond size after merging.

Furthermore, to account for the potential effect of pond size on the growth rate, we also consider the relative change in pond area per unit time defined as the ratio (a_f/a_0) between final and initial pond area divided by the time interval $\triangle t$. For merged ponds the initial pond area corresponds to that of the largest merging pond a_0^{max}. The relative change in pond area is undefined for new ponds as $a_0 = 0$.

These different rates help distinguish patterns of pond growth through space and time, and quantify the relative contributions of new pond formation, growth of individual ponds, and pond merging as drivers of changes in pond size.

Contribution of Wind-Driven Wave Erosion to Edge Retreat

We used the formulation in Mariotti and Fagherazzi (2013) to estimate wave power density from linear wave theory and quantify the contribution of wave-driven erosion to edge retreat for the different pond sizes tracked here. We set the erodibility coefficient to 0.1 $m^2\ yr^{-1}\ W^{-1}$ to reproduce the range of erosion rates measured at Lake Blackwater using an average wind velocity of 6 m s^{-1} and water depths of 0.3 and 0.5 m, which are typical of the large ponds in our study areas (Schepers et al., 2020b). In the calculation of the wave power, we approximate the pond fetch by the diameter of a circle with the same measured pond area.

Characteristics of Stable and Unstable Ponds

To explore potential biological drivers of pond growth observed in the imagery, we measured several indicators of marsh health adjacent to a set of stable and unstable ponds. Within each of the three study areas we selected one stable pond (defined as annual areal growth rate $< 1\%$; 0.54, 0.22, and 0.17 for SA 1, 2, 3, respectively) and one unstable pond (annual areal growth rate $> 1\%$; 1.78, 1.79, and 6.39 for SA 1, 2, 3, respectively). At each of these six total ponds, we measured soil shear strength, above-ground biomass, and porewater chemistry in the surrounding marsh in August 2017. Three replicate measurements were made 1 m inland from the marsh-pond edge and compared to three replicate measurements from a reference marsh located 10 m inland from the marsh-pond edge, resulting in a total of 36 measurements of each indicator of marsh health.

Soil shear strength was measured using a Humboldt H-4227 Shear Vane to infer a relative measure for the erodibility of marsh soils surrounding ponds (Jafari et al., 2019). We measured shear strength at four depths below the soil surface (10, 25, 35, and 55 cm) to capture a profile of soil strength above and below the vegetation rooting depth (approximately 30 cm in the study area) (Schepers, 2017). Plant productivity was measured as end of season live aboveground biomass (Squiers and Good, 1974) using destructive harvest techniques in characteristic 0.25 m × 0.25 m plots.

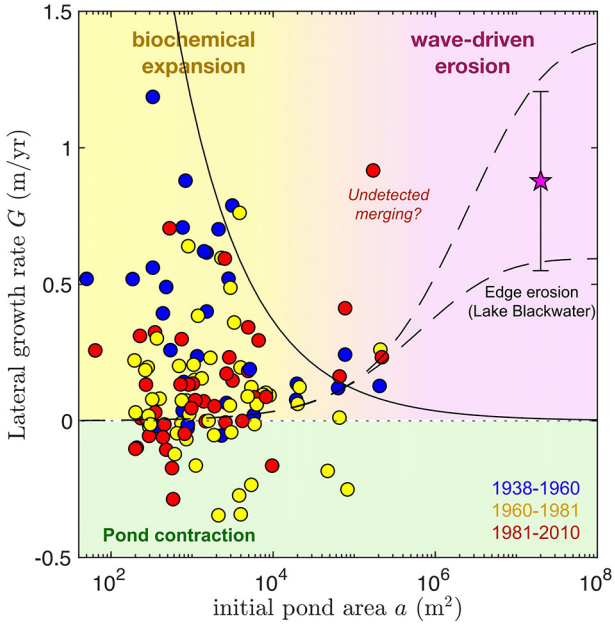


FIGURE 5 | Lateral growth rate **G** of single (non-merging) ponds as function of initial pond area **a** (circles) for the time intervals analyzed. The mean and standard deviation of the erosion rate of one edge of Lake Blackwater, along its longest axis, is also shown for comparison (star). Dashed lines correspond to a semi-empirical equation for wave-driven marsh edge erosion (Mariotti and Fagherazzi, 2013) evaluated at two characteristic pond depths, 0.3 m (lower) and 0.5 m (higher). The solid line shows the scaling of lateral growth rates corresponding to a constant area growth rate R =150 $m^2\ yr^{-1}$ (see **Figure 6**), assuming circular ponds: $G = R/(2\sqrt{\pi a})$. We suggest isolated pond growth is controlled by biochemical mechanisms below ~10^5 m^2, and by wave-driven erosion above it. Negative growth rates denoting pond contraction are highlighted in green. Given the large time spans between measurements, the central outlier could correspond to an undetected merged pond (see **Figure 6**).

Porewater was collected from the marsh soil at a depth of 15 cm using a syringe attached to a bottom-perforated metal rod then passed through a 45-micron filter to remove organic particulates. Porewater samples were analyzed in the lab to determine the concentration of Hydrogen sulfide (H_2S) and Ammonium (NH_4+), which are potential indicators of anaerobic soils, inhibited nitrogen uptake for plants, and reduced plant growth (Mendelssohn and McKee, 1988; Burdick and Mendelssohn, 1990; van Huissteden and van de Plassche, 1998; Spivak et al., 2017). We determined concentrations of H_2S and NH_4^+ via spectrophotometry using the Lachat QuikChem FIA (Method adapted from Cline, 1969).

RESULTS

Historical Pond Growth

Total ponded area continuously increased with time in each study area at an average rate of $(3.5 \pm 2.2) \times 10^3$ $m^2\ yr^{-1}$ (mean and standard deviation). It increased the most in Study Area 1, where pond area approximately quadrupled from 100,732 m^2 in

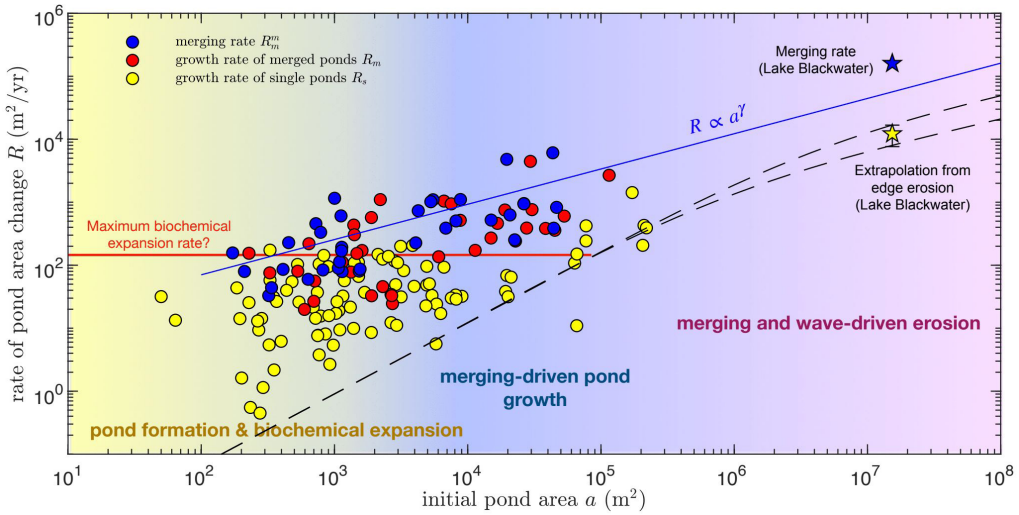


FIGURE 6 | Pond area growth rate R as function of initial pond area a, for single (yellow circles) and merging ponds (blue and red circles). The initial pond area for the growth rate of merged ponds is defined by the combined area of all merging ponds, whereas it corresponds to the size of the largest merging pond for merging rates. Dashed lines correspond to predictions of wave-driven marsh edge erosion rates G (see **Figure 5**) extrapolated to area rates assuming circular ponds: $R = G\left(2\sqrt{\pi a}\right)$. Stars represent two measures of the area growth rate of Lake Blackwater, the rate of area change itself (defined as the area difference divided by the time period and denoted as a merging rate because it involves merging with neighboring ponds) and an extrapolation from the measured edge erosion rate G (**Figure 5**), assuming a circular lake of area a: $R = G\left(2\sqrt{\pi a}\right)$. Pond growth seems to be dominated by biochemical expansion, with a minor contribution from merging, at relatively small pond areas, and by pond merging for intermediate and large pond areas. Wave-driven erosion seems to play a minor role in pond growth even at the scale of Lake Blackwater. Merging growth rates (blue circles) can be fitted by a power-law relation (solid blue line). Single pond growth has a maximum rate of about 150 m^2 yr^{-1} that changes little with pond area (solid red line).

1938 to 402,588 m^2 in 2010. During the same time, ponded area almost tripled in Study Area 2 (from 133,709 to 354,430 m^2) and more than doubled in Study Area 3 (from 254,817 to 528,370 m^2) (**Figures 3A–C**). By 2010, most ponds that existed in 1938 had visually merged to form larger ones, except for the large central pond already present in each study area.

At each timestep where new as well as existing ponds could be classified (1960, 1981, and 2010), the majority tended to be new (i.e., did not exist in the previous image). These numerous ponds, however, represent only a small fraction of the total ponded area (**Figures 3A–C**). The continuous formation of new ponds explains the increase in the total number of ponds from 1938 to 2010 in each study area (**Figures 3D–F**). Two exceptions are observed between 1960 and 1981 in Study Areas 1 and 3 where the number of ponds decreased, likely due to frequent pond merging. Study Area 2 began with a high number of ponds ($n = 36$) in 1938, but we detected relatively few new ponds occurring during the first two time-steps (notice y-axis differences in **Figures 3D–F**).

In general, smaller ponds are more common than large ponds; the median area of all ponds (n = 450) is 720 m^2, and only 40 ponds were $>10^4$ m^2. In all study areas, the largest ponds tend to be merged ponds, particularly after 1960, while new ponds are consistently the smallest ones (**Figures 3G–I**). These trends seem to increase in magnitude with time, with new ponds getting smaller and the scale separation between the area of merged ponds and single or new ponds increasing up to a maximum in 2010 (**Figures 3G–I**).

Merging pond rates (R_m^m, Eq. 6) are consistently higher than the growth rates of both new and existing single ponds, and also higher than the average expansion rates of merged ponds (R_m^e, Eq. 5) (**Figures 4A–C**). Furthermore, average expansion rates (R_m^e) are generally similar to the growth rates of single ponds (R_s), justifying our interpretation of R_m^e as a measure of pond expansion distinct from pond merging, characterized by the merging rate R_m^m (**Figures 4A–C**). Interestingly, in the Study Area 2, the scale separation between the size of new and existing single ponds (**Figure 3H**) is not reflected in their growth rate, as new ponds tend to grow at similar rates as single ponds (**Figure 4B**).

The dominant contribution of merging to the increase of pond size is also apparent when comparing the relative change in pond area per unit time between pond merging and single pond expansion (**Figures 4D–F**). Merging increases the area of the largest merging pond by more than 10% per year for almost every time interval in all study areas, and by about 20% per year during the last 30 years of data (1981–2010). In contrast, single ponds expand in average by less than 5% per year, except during the first period (1938–1960).

Mechanisms of Pond Growth

Lateral growth rates—a first order estimate of edge retreat, G—exhibit no clear trend with pond size in ponds that grow singularly between timesteps (**Figure 5**). Peak values are, however, observed for small-to-intermediate sized ponds (around 10^3 m^2), reaching up to 0.8–1.2 m yr^{-1} and decreasing for larger ponds. This decrease is consistent with a constant area growth rate $R =$ 150 m^2 yr^{-1} (see **Figure 6**), assuming circular ponds: $G = R/\left(2\sqrt{\pi a}\right)$. Maximum lateral growth rates are similar to those of Lake Blackwater (0.6–1.2 m yr^{-1}), a

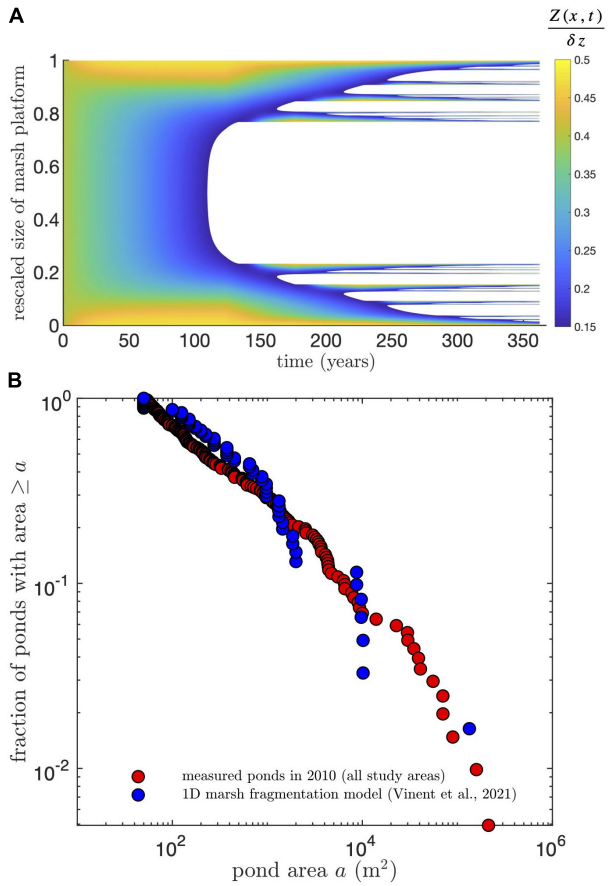


FIGURE 7 | Predictions from a simplified one-dimensional marsh drowning model (Vinent et al., 2021) applied to the conditions in our study areas. **(A)** Spatiotemporal diagram of predicted marsh fragmentation starting with a uniform marsh platform with tidal channels or mud flats at both sides. Marsh elevation Z is rescaled by tidal range dz. White areas indicate open water. **(B)** Comparison of simulated and measured exceedance probability of pond areas. Since the model is 1D, the simulated pond area is calculated by multiplying the simulated pond length by a constant pond width obtained from the condition that the smallest simulated pond has an area of 50 m^2 (the smallest area resolved in the measurements). Measured ponds correspond to ponds in all study areas in 2010.

much larger (1.8×10^7 m^2) open water area adjacent to our study area (**Figure 1**). Lateral growth rates seem to be larger during the 1938–1960 time period. Despite the dominance of pond expansion for all analyzed timesteps, pond contraction was relatively common across measured pond areas (10^2 m^2–10^5 m^2) particularly after 1960.

Lateral growth rates are in general much larger than those predicted by a semi-empirical formulation of wave-driven marsh edge erosion (**Figure 5**, dashed lines), which nevertheless captures the relatively small expansion rates of the largest measured ponds. When considering the dependence of areal growth rates on the initial pond area for both single and merged ponds, three scale-dependent regimes for pond growth in our study areas emerge (**Figure 6**). For pond areas smaller than about 10^3 m^2, pond growth seems to be dominated by what we define as biogeochemical processes. Measurements suggest that biogeochemical driven growth has a maximum area growth rate of about 150 m^2 yr^{-1} which changes little with pond size (**Figure 6**, red line). Second, for pond areas above 10^3 m^2, pond merging is by far the most important mechanism for pond growth, as suggested by both the total growth rate of merged ponds (R_m) and the merging rate (R_m^m) of the largest merging pond (**Figure 6**). Often both measures of pond growth rate due to merging are similar because one of the merging ponds is much larger than the others. Finally, for ponds with areas similar to or $>10^5$ m^2 the contribution of wave-driven erosion becomes relevant. However, we find that even at the scale of Lake Blackwater merging patterns seem to contribute heavily to growth. Indeed, the measured area growth rate of Lake Blackwater (calculated as the difference in measured lake area divided by the time interval between 1981 and 2010) is about 10 times larger than the rate [$R = G\left(2\sqrt{\pi a}\right)$ where a is the Lake Blackwater area in 1981] estimated from the measured wave-driven edge erosion ($G = 0.9$ m yr^{-1}, **Figure 5**) assuming a circular shape. Notice that the area growth rate of Lake Blackwater is a merging rate following our definition, as the growing lake is continuously merging with nearby ponds. The causes for these size-dependent growth rates are proposed in several prior studies and are further explored in the discussion.

We quantified the dependence of the pond merging rate (R_m^m) on the size of the largest merging pond by fitting a power law function of the type (**Figure 6**, blue line):

$$R_m^m(a) = \frac{da}{dt} = R_0(a/a_0)^\gamma \tag{7}$$

with fitting parameters $R_0 = 70 \pm 35$ m^2 yr^{-1} and $\gamma = 0.56 \pm 0.09$ and where for convenience we introduce the area scale $a_0 = 100$ m^2. This equation can then be used to estimate the time evolution of the size of the largest pond in the system (see Eq. 8 below). This provides a lower bound for the growth of total pond area, which is always larger than any single pond area.

Comparison With a 1D Marsh Fragmentation Model and Other Pond Data

We compared our measurements of pond growth rates and pond size distribution to the predictions of a simplified one-dimensional model of cross-platform sediment transport and SLR-driven marsh drowning (Vinent et al., 2021). We ran the model for the parameters characterizing our study area: tidal range 0.35 m, average suspended sediment concentration 40 g m^{-3} (Ganju et al., 2017) and rate of relative SLR 3.8 mm yr^{-1} and kept the other model parameters unchanged (see details in Vinent et al., 2021). Starting with a marsh platform with uniform elevation and tidal channels or mud flats at both sides (**Figure 7A**), the model predicts the formation of a large central pond after about 100 years and the subsequent runaway fragmentation of the marsh platform until complete drowning in about 150 years (**Figure 7A**).

This model reproduces both the frequency distribution of pond sizes measured in 2010 (**Figure 7B**) and pond growth

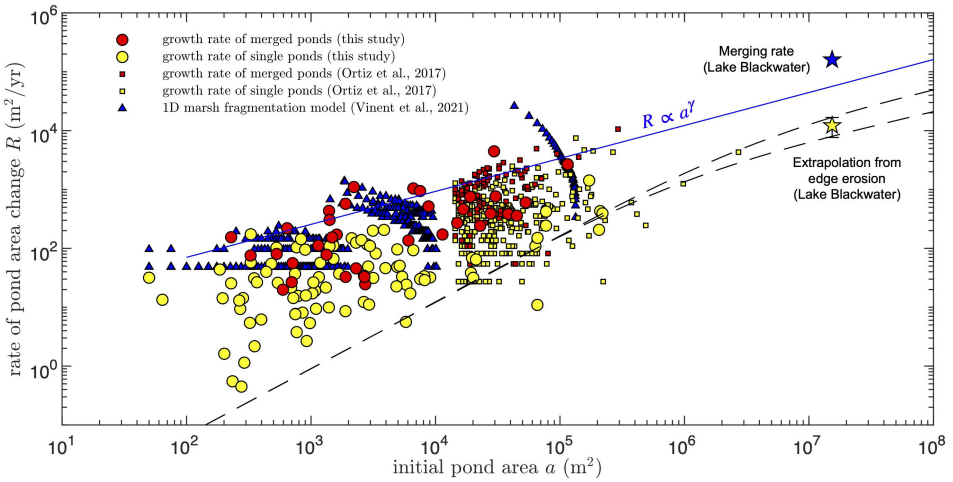


FIGURE 8 | Comparison of measured and simulated pond area growth rates as function of the initial pond size. For the growth rate of merged ponds, the initial area is defined as the combined area of all merging ponds. For the one-dimensional model, the simulated pond area is calculated by multiplying the simulated pond length by a constant pond width obtained from the condition that the smallest simulated pond has an area of 50 m^2 (the smallest area resolved in the measurements). Data reported by Ortiz et al. (2017) in the Mississippi delta was selected by the condition that the final pond area is no larger than four times the initial area, to conserve a meaningful correlation between both. Star symbols and dashed and solid lines as in **Figure 6**.

rates (**Figure 8**). Given the model is 1D, the simulated pond area is calculated by multiplying the simulated pond length by a constant pond width obtained from the condition that the smallest simulated pond has an area of 50 m^2 (the smallest area resolved in the remote sensing measurements). Since the size distribution follows a power law (**Figure 7B**, Vinent et al., 2021), this multiplicative factor does not affect the shape of the distribution. Interestingly, the simulated growth rates change little with pond size for small ponds, while they decay relatively fast for large ponds (**Figure 8**) due to the stabilization of pond growth once it connects to the channel network (a condition implemented in the model based on pond depth, see Vinent et al., 2021 for details).

To compare our results to observations in other microtidal saltmarshes, the growth rates of merged and single ponds reported by Ortiz et al. (2017) in the Mississippi delta (filtered by the condition that the final pond area is no larger than four times the initial area, to conserve a correlation between both) were included directly in **Figure 8**. The two datasets follow similar trends and in particular the merging rates from both are consistent with our empirical power-law growth relation (**Figure 8**).

Temporal Evolution of Total Pond (Water) Area

We can constrain the future expansion of total pond area in our study areas using the power-law relation for the merging rate (Eq. 7). Integrating Eq. 7 and assuming an initial pond area $a(0) = 5 \times 10^3$ m^2, which corresponds to the largest of the small merging ponds found in our study area in 1938, we find:

$$a(t) = a_0\left[(a(0)/a_0)^{1-\gamma} + (1-\gamma)\, t/\tau\right]^{1/(1-\gamma)} \qquad (8)$$

where $\tau = a_0/R_0 = 1.43$ yr is a characteristic time scale. This equation reproduces the temporal evolution of the largest merging pond (**Figure 9**) and predicts that our study areas, all of similar size $\sim 10^6$ m^2, will become a single large pond in about 150 years from the start of our measurements (1938). This is about 80 years sooner than an estimation based on the average growth rate of the total pond area (**Figure 9**, dashed line).

The predicted change in total pond area from the marsh fragmentation model introduced in the previous section (Vinent et al., 2021) closely follows the measured increase from 1938 to 2010 and predicts that 80% of marshes in our study areas will disappear after 150 years (from 1938, see **Figure 9**), which agrees in general with the prediction from the merging rate equation (Eq. 8). Note that to properly compare model predictions to the measurements, we substituted the size of the central pond in with one that was characteristic of central ponds in our study areas ($\sim 10^5$ m^2). We then rescaled the size of the marsh platform to 10^6 m^2, an adjustment that does not change the physical interpretation of the results due to the model's scale invariance (see Vinent et al., 2021).

The runaway ponding predicted by the 1D model of our study areas is not captured by the model of Mariotti et al. (2020). Using published results for a marsh complex that most resembles ours, with tidal range 0.7 m, rate of RSLR 4 mm yr^{-1} and SSC 5 g m^{-3} (**Figure 9**), Mariotti et al. (2020) predict a saturation of marsh loss area (either by ponds or tidal flats, as tidally connected ponds are defined in that study) at about 6×10^5 m^2 after more than 300 years.

Characteristics of Stable and Unstable Ponds

Analyzing data from our field campaign, we found that in-situ indicators of marsh health were greater near stable ponds

than near unstable ponds. Average live aboveground biomass was higher adjacent to stable ponds (841 ± 98 g m^{-2}) than unstable ponds (607 ± 110 g m^{-2}), both immediately adjacent to the ponds and at interior reference marshes 10 m from the edge (**Figure 10A**). Soil shear strength decreased with increasing depth within the rooting zone regardless of pond type and location (Himmelstein, 2018). Average soil strength at a depth of 10 cm was higher at the edge of stable ponds (2.70 ± 0.60 kPa) than unstable ponds (1.40 ± 0.50 kPa), with similar trends found in the interior reference marshes (**Figure 10B**). Hydrogen sulfide concentrations were twice as high in marsh soil porewater adjacent to unstable ponds than concentrations adjacent to stable ponds ($\mu_{unstable}$ = 6.4 ± 0.8 mM, μ_{stable} = 3.2 ± 0.5 mM) (**Figure 10C**). Similarly, porewater ammonium was higher in soils adjacent to unstable ponds than soils adjacent to stable ponds ($\mu_{unstable}$ = 161 ± 29 μM, μ_{stable} = 97 ± 38 μM; **Figure 10D**). Hydrogen sulfide and ammonium porewater in the interior marsh near unstable ponds followed the same trend; respectively $\mu_{unstable}$ = 6.7 ± 0.5 mM vs. μ_{stable} = 2.1 ± 0.8 mM and $\mu_{unstable}$ = 150.4 ± 37.8 μM vs. μ_{stable} = 76.9 ± 29.7 μM.

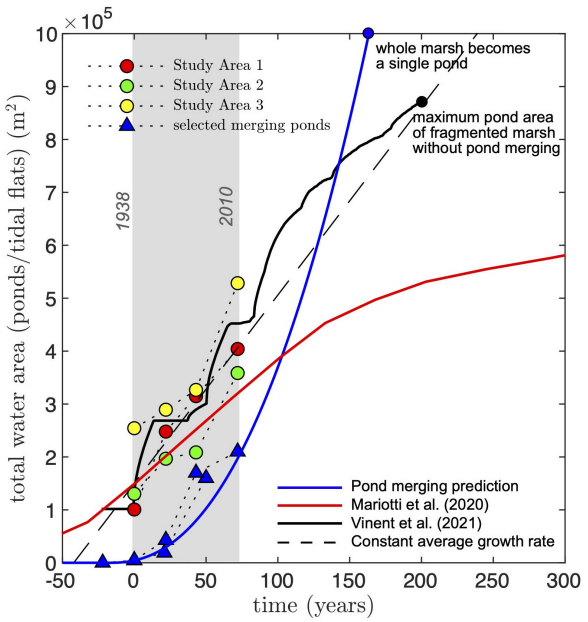


FIGURE 9 | Comparison of measured and predicted time evolution of total water area (ponds). Circles represent total pond area measured in our study areas. Triangles are selected merging ponds tracked through time (we selected the largest merging pond during different merging stages). Merging ponds are shifted in time such that they have a similar size [a(0) ≈ 5 × 10^3 m^2] at the reference time (t = 0, representing the initial year 1938). All predicted curves are shifted in time such that water area (total pond area) at t = 0 is 1.5 × 10^5 m^2. The dashed line represents a constant growth rate equal to the average growth rate of all study areas (3.5 × 10^3 m^2 yr^{-1}). The blue line is the prediction for the largest pond area at a given time using the merging rate approximation (Eq. 8). By definition, Eq. 7 represents a lower bound for the total pond area. The black solid line is the prediction using the model of Vinent et al. (2021; **Figure 7A**). To compare the model prediction to the measurements, we replaced the size of the central pond in the simulations by the one already present in some of the study areas (~10^5 m^2) and then rescaled the size of the marsh platform to 10^6 m^2. The red line is the prediction by the model of Mariotti et al. (2020) for similar marsh conditions (see text for details). To convert from water area fraction to actual water area, we multiplied by the area of their simulated domain (1.44 × 10^6 m^2).

DISCUSSION

Patterns of Pond Growth as a Result of Marsh Drowning Due to Sea Level Rise

The formation, expansion, and potential recovery of tidal marsh ponds is proposed to depend on interacting processes, both within our study region and more generally (Kearney et al., 1988; Wilson et al., 2009; Mariotti, 2016; Ortiz et al., 2017; Spivak et al., 2017). Pond formation often begins with vegetation stress associated with poor drainage and waterlogged soils (Johnston et al., 2003; Spivak et al., 2017), as evidenced by ponds that originate at drainage divides far from channels (Schepers et al., 2017; Vinent et al., 2021). Once formed, initially small ponds tend to expand through a combination of poorly understood processes, until they intersect tidal channels (Mariotti, 2016; Mariotti et al., 2020). After intersecting channels, ponds either expand (Schepers et al., 2020a) or contract (Wilson et al., 2014) depending on the elevation of the pond bottom and the sediment balance between the channel and pond (Mariotti, 2016; Schepers et al., 2020a).

In the stable ponds studied here, channelized connections to the Blackwater River likely exchange metabolites and nutrients despite only partial water exchange (Spivak et al., 2017). For microtidally influenced marshes elsewhere, tidal channel connections have been found to export unconsolidated material from the bottom of ponds, potentially counteracting the expected vegetation growth benefits afforded by frequent water exchange (Stevenson et al., 1985; Wilson et al., 2010). Schepers et al. (2017), showed that as tidal channel connections in Blackwater widened, pond bottom depth increased. If net basal sediment export deepens ponds and increases pond edge slope, processes like soil creep or bank slumping might in turn widen ponds (Stevenson et al., 1985). To determine the impact of connectivity in a specific marsh complex, biogeochemical health indicators as well as accretion/erosion rates should be monitored before and after pond connection—a sampling process requiring return field campaigns. Such efforts will help chronicle the emergence of large open-water bodies like Lake Blackwater.

Despite the complexity of the processes leading to pond formation and expansion, as reflected by recent numerical models (Mariotti et al., 2020) and summarized above, our results suggest two surprisingly simple conclusions. First, the complex growth of pond size, initiated with the formation of new ponds and then furthered by biochemical expansion and subsequent pond merging, can be approximated by a power-law equation for the temporal evolution of the size of the largest pond (Eqs. 7 and 8). This represents a lower bound for the total water area as total pond size is equal to or larger than the size of the largest pond, and can be used for simple predictions of future changes in marsh area.

The consistency of the Vinent et al. (2021) model with our measurements suggests that pond formation, biochemical

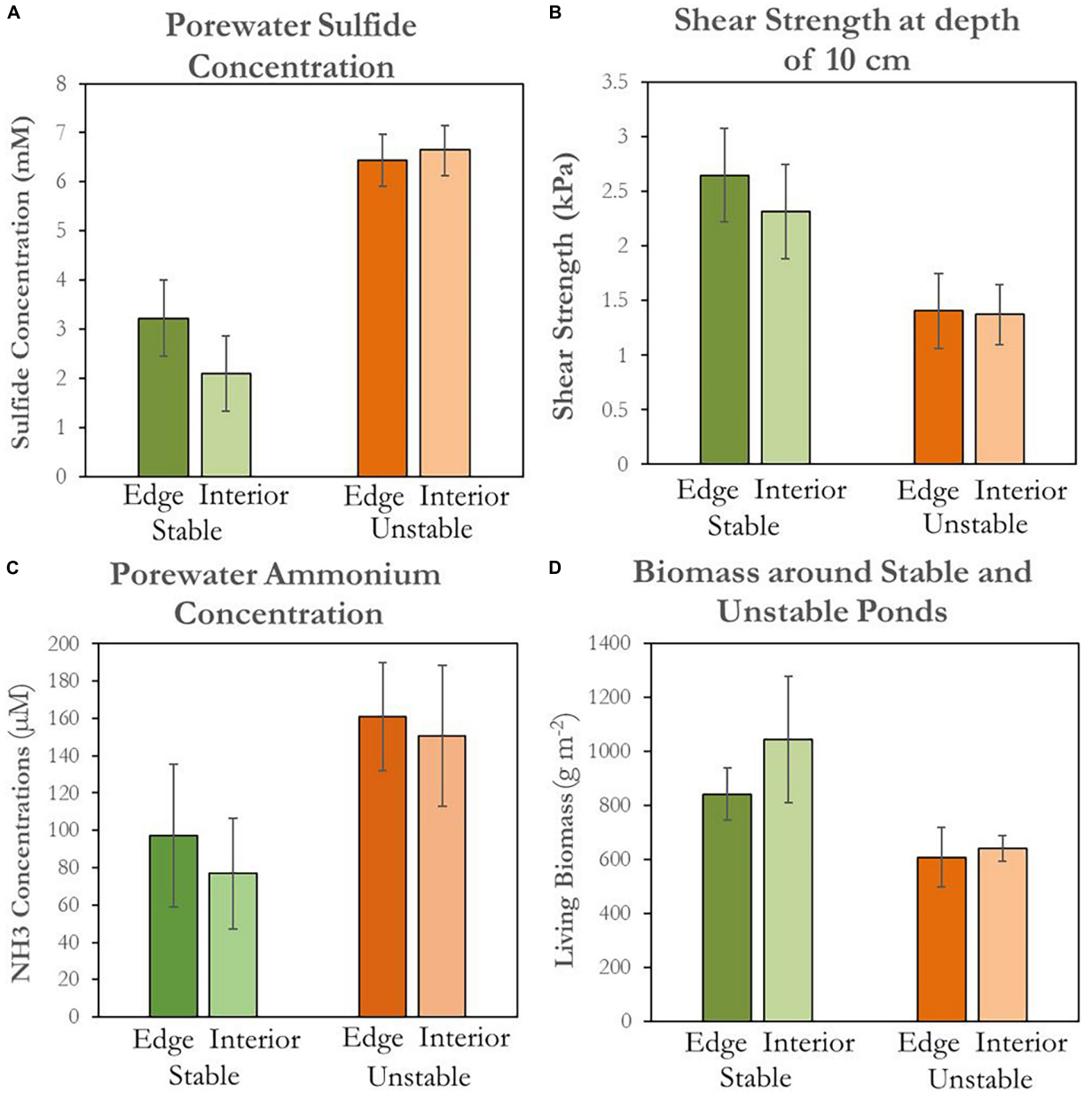


FIGURE 10 | Soil porewater chemistry surrounding stable and unstable ponds. Each bar represents the average of all measurements (n = 9) collected at a certain pond type and location. Error bars represent ± standard error. Green bars represent conditions around stable ponds and orange bars represents conditions around unstable ponds. Darker shades represent conditions at 1m from the pond edge and lighter shades represent conditions 10 m away in the marsh. **(A)** Concentrations for sulfide in millimolar. **(B)** Shear vane soil shear strength in rooting zone (10 cm soil depth) measured in kPa. **(C)** Concentrations for ammonium in micromolar. **(D)** Living biomass in g m^{-2}.

expansion, and initial merging can be explained as manifestations of a marsh drowning due to SLR. Both model simulations (**Figure 7A**) and our data show that ponds tend to initiate in the marsh interior in our study area and expand toward channels (also reported in Schepers, 2017), potentially due to more waterlogged soil conditions. The interior marsh experiences infrequent tidal flushing and low sediment supply (Vinent et al., 2021) both of which promote plant die-off (DeLaune et al., 1994). Qualitatively similar spatial patterns of ponds are found in other marsh areas such as in the Mississippi delta (Louisiana) (Morton et al., 2003), and Venice lagoon (Italy) and Scheldt estuary (Netherlands) (Wang et al., 2021), where ponds are preferentially found in marsh interiors while vegetation prevails closer to channels.

Marsh drowning in response to SLR could also explain the small expansion rates of isolated ponds in the remotely sensed, mesotidal Barnstable, MA, where ponds with 1 to ∼10 m diameter expanded at an average of 1.5 cm yr^{-1} (Mariotti et al.,

2020; **Figure 3**). Ponds of this size were inscrutable through the resampled resolutions used in this study thus direct comparisons are limited. Still, these rates, measured in a relatively stable marsh, are an order of magnitude lower than observed in the microtidal Blackwater marshes, where runaway marsh expansion is already occurring. This may, in part, be related to the lower tidal range found in the BNWR relative to Barnstable, MA.

Biogeochemical Feedbacks

A manifestation of marsh drowning due to SLR is the biogeochemical conditions that correspond with the early stages of pond growth. For example, high levels of hydrogen sulfide and salinity as well as low dissolved oxygen in stagnant pond water can inhibit vegetation growth, and decomposition of the existing substrate may deepen and enlarge ponds (Nyman et al., 1994; Spivak et al., 2017). This process is partially facilitated through the anaerobic decomposition of plant matter by sulfate reducing bacteria (van Huissteden and van de Plassche, 1998). Relatively high expansion rates (up to 1 m yr^{-1}) in ponds far too small to erode from waves are consistent with a biogeochemical explanation for early stages of pond growth (**Figure 5**). We find that marsh adjacent to rapidly expanding ponds has consistently lower vegetation biomass, lower soil strength, and higher porewater sulfide and ammonium concentrations than marsh adjacent to stable ponds (**Figure 10**). This finding indicates that biogeochemical processes are the expected drivers of unstable pond expansion. High sulfide and ammonium concentrations—byproducts of anaerobic decomposition—increase stress on vegetation growth. This results in reduced above-ground vegetation biomass, which implies reduced below-ground root biomass and therefore lower contribution of roots to substrate cohesion and in-situ organic accretion. Elevated concentrations of hydrogen sulfide and ammonium are also associated with plant stress and reduced nitrogen uptake, which may trigger vegetation die-off and peat collapse, hence resulting in new pond formation (van Huissteden and van de Plassche, 1998; Swarzenski et al., 2008; Lamers et al., 2013).

Biogeochemical mechanisms for the expansion of small ponds could also explain the observed trend of decreasing pond growth rate with increasing pond size for intermediate sized ponds (**Figure 5**). In this phase of pond growth, we hypothesize that larger ponds are more likely to intersect the channel network, which could in turn improve soil water drainage and hence relieve the biogeochemical stressors shown to be important at our study site (**Figure 10**). An alternative explanation is that as a pond grows as a result of marsh drowning, it gets closer to the channel network and thus sediment sources, which increases inorganic accretion. This in turn slows the relative drowning rate and thus the lateral expansion rate of that pond, as observed in a previous model (Vinent et al., 2021). When considering areal growth rates rather than lateral growth rates for single ponds, a constant maximum growth rate exists around 150 m^2 yr^{-1}. This is observed in single ponds of all sizes with widths below the threshold for the onset of wave-driven erosion (**Figure 6**, yellow markers). A constant maximum area growth rate (R) would lead to an upper bound for the lateral growth rate (G) decreasing with pond area (a) as $G = R/\left(2\sqrt{\pi a}\right)$ (solid line in **Figure 5**).

Potential Interventions to Slow Down Pond Growth

In the marshes of Blackwater, the capacity for revegetation and total pond recovery is low. Instead, efforts like "thin-layering" of dredged sediment have been and should continue being employed to preserve existing vegetated platforms through by raising elevations relative to sea-level and allowing the oxygenation of subsequently formed root networks. Our results suggest these efforts are optimal during the pond formation/single pond expansion phase before large-scale pond merging takes place. Once large, merged ponds connect to the channel network, sediment export and subsequent pond deepening makes their recovery costly and difficult (Schepers et al., 2020a). The pond merging equation we propose (Eq. 8) provides a useful timescale for the merging process which could help in establishing the critical time window, and related pond sizes, for interventions intended to slow down pond expansion.

CONCLUSION

Our observations from a rapidly submerging marsh in the Chesapeake Bay, United States suggest that the mechanisms and rates of pond expansion change with pond size. Historical photographs indicate that linear growth rates are maximized for intermediate size ponds (10^3–10^4 m^2), where wave driven erosion is negligible. Field measurements suggest that pond stability is related to the health of the surrounding marsh, implying a biogeochemical driver for early stages of pond expansion. We find that the formation and progressive merging of ponds, rather than the isolated expansion of existing ponds, dominates the growth of small-intermediate size ponds. These processes are summarized in an empirical power-law equation for pond growth that predicts the maximum pond size at a given time and thus constitutes a lower bound for total pond area in a given system. Comparison with the model of Vinent et al. (2021) suggests the mechanisms of pond growth, including initial merging, are a result of marsh drowning due to SLR. Our findings help establish the time and length scale for optimal interventions designed to slow down pond growth in the system, with a particular focus in preventing or reducing large-scale pond merging.

DATA AVAILABILITY STATEMENT

The original contributions presented in the study are included in the article/**Supplementary Material**, further inquiries can be directed to the corresponding author/s.

AUTHOR CONTRIBUTIONS

JH, OV, and MK jointly conceived this research. JH executed the data (remote and field) collection, processing, and analysis. OV formulated the rate of change equations. JH and OV produced the figures. ST contributed extensive edits to the manuscript. MK connected researchers, guided the project, and secured funding. All authors jointly wrote and edited the manuscript.

FUNDING

This work was supported by grants from the National Science Foundation (award #1832221, 1426981, and 1654374) and its Research Experiences for Undergraduates Program (#1659656). ST acknowledges support from the Research Foundation Flanders (FWO Grant Nos. G060018N and G031620N). OV acknowledges the support of the Texas A&M Engineering Experiment Station (TEES).

ACKNOWLEDGMENTS

We acknowledge Lennert Schepers who provided data to kick-start the project. We appreciate assistance from Ellen Herbert, Iris Anderson, Ken Czapla, and David Walters and appreciate helpful manuscript reviews from Giulio Mariotti and Mark Schuerch. This article is dedicated to the late David Nicks, our lab-mate and friend. This is contribution no. 4047 from the Virginia Institute of Marine Science, College of William & Mary.

SUPPLEMENTARY MATERIAL

The Supplementary Material for this article can be found online at: https://www.frontiersin.org/articles/10.3389/fmars.2021.704768/full#supplementary-material

REFERENCES

Allen, J. R. L. (1990). Salt-marsh growth and stratification: a numerical model with special reference to the severn estuary, Southwest Britain. *Mar. Geol.* 95, 77–96. doi: 10.1016/0025-3227(90)90042-I

Barbier, E. B., Hacker, S. D., Kennedy, C., Koch, E. W., Stier, A. C., and Silliman, B. R. (2011). The value of estuarine and coastal ecosystem services. *Ecol. Monogr.* 81, 169–193. doi: 10.1890/10-1510.1

Belzen, J. V., van de Koppel, J., Kirwan, M. L., van der Wal, D., Herman, P. M. J., Dakos, V., et al. (2017). Vegetation recovery in tidal marshes reveals critical slowing down under increased inundation. *Nat. Commun.* 8:15811. doi: 10.1038/ncomms15811

Burdick, D. M., and Mendelssohn, I. A. (1990). Relationship between anatomical and metabolic responses to soil waterlogging in the Coastal grass *Spartina Patens*. *J. Exp. Bot.* 41, 223–228. doi: 10.1093/jxb/41.2.223

Carniello, L., Defina, A., and D'Alpaos, L. (2009). Morphological evolution of the venice lagoon: evidence from the past and trend for the future. *J. Geophys. Res.* 114:F04002. doi: 10.1029/2008JF001157

Cline, J. D. (1969). Spectrophotometric determination of hydrogen sulfide in natural waters1. *Limnol. Oceanogr.* 14, 454–458. doi: 10.4319/lo.1969.14.3.0454

Day, J. W., Britsch, L. D., Hawes, S. R., Shaffer, G. P., Reed, D. J., and Cahoon, D. (2000). Pattern and process of land loss in the Mississippi delta: a spatial and temporal analysis of Wetland habitat change. *Estuaries* 23, 425–438. doi: 10.2307/1353136

Day, J. W., Paul Kemp, G., Reed, D. J., Cahoon, D. R., Boumans, R. M., Suhayda, J. M., et al. (2011). Vegetation death and rapid loss of surface elevation in two contrasting mississippi delta salt marshes: the role of sedimentation, autocompaction and sea-level rise. *Ecol. Eng.* 37, 229–240. doi: 10.1016/j.ecoleng.2010.11.021

DeLaune, R. D., Nyman, J. A., and Patrick, W. H. Jr. (1994). Peat collapse, ponding and wetland loss in a rapidly submerging coastal marsh. *J. Coast. Res.* 10, 1021–1030.

Ezer, T., Atkinson, L. P., Corlett, W. B., and Blanco, J. L. (2013). Gulf stream's induced sea level rise and variability along the U.S. Mid-Atlantic coast: gulf stream induces coastal sea level rise. *J. Geophys. Res.* 118, 685–697. doi: 10.1002/jgrc.20091

Fagherazzi, S., Anisfeld, S. C., Blum, L. K., Long, E. V., Feagin, R. A., Fernandes, A., et al. (2019). Sea level rise and the dynamics of the marsh-upland boundary. *Front. Environ. Sci.* 7:25. doi: 10.3389/fenvs.2019.00025

Ganju, N. K., Defne, Z., and Fagherazzi, S. (2020). Are elevation and open-water conversion of salt marshes connected? *Geophys. Res. Lett.* 47:e2019GL086703. doi: 10.1029/2019GL086703

Ganju, N. K., Defne, Z., Kirwan, M. L., Fagherazzi, S., D'Alpaos, A., and Carniello, L. (2017). Spatially integrative metrics reveal hidden vulnerability of microtidal salt marshes. *Nat. Commun.* 8:14156. doi: 10.1038/ncomms14156

Ganju, N. K., Nidzieko, N. J., and Kirwan, M. L. (2013). Inferring tidal wetland stability from channel sediment fluxes: observations and a conceptual model: inferring stability from sediment fluxes. *J. Geophys. Res.* 118, 2045–2058. doi: 10.1002/jgrf.20143

Hartig, E. K., Gornitz, V., Kolker, A., Mushacke, F., and Fallon, D. (2002). Anthropogenic and climate-change impacts on salt marshes of Jamaica Bay, New York City. *Wetlands* 22, 71–89.

Himmelstein, J. (2018). *The Mechanisms of Pond Expansion in the Marshes of Blackwater National Wildlife Refuge, Maryland*. William and Mary Honors Theses. Williamsburg, VA: William & Mary.

Jafari, N. H., Harris, B. D., Cadigan, J. A., Day, J. W., Sasser, C. E., Paul Kemp, G., et al. (2019). Wetland shear strength with emphasis on the impact of nutrients, sediments, and sea level rise. *Estuar. Coast. Shelf Sci.* 229:106394. doi: 10.1016/j.ecss.2019.106394

Johnston, M. E., Cavatorta, J. R., Hopkinson, C. S., and Valentine, V. (2003). Importance of metabolism in the development of salt marsh ponds. *Biol. Bull.* 205, 248–249. doi: 10.2307/1543278

Kearney, M. S., Grace, R. E., and Stevenson, J. C. (1988). Marsh loss in nanticoke estuary, Chesapeake Bay. *Geogr. Rev.* 78:205. doi: 10.2307/214178

Kirwan, M. L., and Guntenspergen, G. R. (2012). Feedbacks between inundation, root production, and shoot growth in a rapidly submerging brackish marsh: marsh root growth under sea level rise. *J. Ecol.* 100, 764–770. doi: 10.1111/j.1365-2745.2012.01957.x

Kirwan, M. L., and Guntenspergen, G. R. (2015). Response of plant productivity to experimental flooding in a stable and a submerging marsh. *Ecosystems* 18, 903–913. doi: 10.1007/s10021-015-9870-0

Kirwan, M. L., and Megonigal, J. P. (2013). Tidal wetland stability in the face of human impacts and sea-level rise. *Nature* 504, 53–60. doi: 10.1038/nature12856

Kirwan, M. L., Walters, D. C., Reay, W. G., and Carr, J. A. (2016). Sea level driven marsh expansion in a coupled model of marsh erosion and migration: sea level driven marsh expansion. *Geophys. Res. Lett.* 43, 4366–4373. doi: 10.1002/2016GL068507

Lamers, L. P. M., Govers, L. L. I, Janssen, C. J. M., Geurts, J. J. M., Van der Welle, M. E. W., Van Katwijk, M. M., et al. (2013). Sulfide as a soil phytotoxin—a review. *Front. Plant Sci.* 4:268. doi: 10.3389/fpls.2013.00268

Mariotti, G. (2016). Revisiting salt marsh resilience to sea level rise: are ponds responsible for permanent land loss? Salt marsh ponds. *J. Geophys. Res.* 121, 1391–1407. doi: 10.1002/2016JF003900

Mariotti, G., and Fagherazzi, S. (2013). Critical width of tidal flats triggers marsh collapse in the absence of sea-level rise. *Proc. Natl. Acad. Sci.* 110, 5353–5356. doi: 10.1073/pnas.1219600110

Mariotti, G., Spivak, A. C., Luk, S. Y., Ceccherini, G., Tyrrell, M., and Eagle Gonneea, M. (2020). Modeling the spatial dynamics of marsh ponds in New England salt marshes. *Geomorphology* 365:107262. doi: 10.1016/j.geomorph.2020.107262

Mendelssohn, I. A., and McKee, K. L. (1988). *Spartina alterniflora* die-back in louisiana: time-course investigation of soil waterlogging effects. *J. Ecol.* 76:509. doi: 10.2307/2260609

Millette, T. L., Argow, B. A., Marcano, E., Hayward, C., Hopkinson, C. S., and Valentine, V. (2010). Salt marsh geomorphological analyses *via* integration of multitemporal multispectral remote sensing with LIDAR and GIS. *J. Coast. Res.* 265, 809–816. doi: 10.2112/JCOASTRES-D-09-00101.1

Möller, I., Kudella, M., Rupprecht, F., Spencer, T., Paul, M., van Wesenbeeck, B. K., et al. (2014). Wave attenuation over coastal salt marshes under storm surge conditions. *Nat. Geosci.* 7, 727–731. doi: 10.1038/ngeo2251

Morton, R. A., Tiling, G., and Ferina, N. F. (2003). Causes of hot-spot Wetland loss in the Mississippi delta plain. *Environ. Geosci.* 10, 71–80. doi: 10.1306/eg100202007

Mudd, S. M., D'Alpaos, A., and Morris, J. T. (2010). How does vegetation affect sedimentation on tidal marshes? Investigating particle capture and hydrodynamic controls on biologically mediated sedimentation. *J. Geophys. Res.* 115:F03029. doi: 10.1029/2009JF001566

Nahlik, A. M., and Fennessy, M. S. (2016). Carbon storage in US wetlands. *Nat. Commun.* 7:13835. doi: 10.1038/ncomms13835

Nyman, J. A., Carloss, M., Delaune, R. D., and Patrick, W. H. (1994). Erosion rather than plant dieback as the mechanism of marsh loss in an estuarine marsh. *Earth Surf. Process. Landf.* 19, 69–84. doi: 10.1002/esp.3290190106

Nyman, J. A., DeLaune, R. D., Roberts, H. H., and Patrick, W. H. (1993). Relationship between vegetation and soil formation in a rapidly submerging coastal marsh. *Mar. Ecol. Prog. Ser.* 96, 269–279. doi: 10.3354/meps096269

Ortiz, A. C., Roy, S., and Edmonds, D. A. (2017). Land loss by pond expansion on the Mississippi river delta plain: pond expansion on mississippi marshes. *Geophys. Res. Lett.* 44, 3635–3642. doi: 10.1002/2017GL073079

Pethick, J. S. (1974). The distribution of salt pans on tidal salt marshes. *J. Biogeogr.* 1:57. doi: 10.2307/3038068

Pethick, J. S. (1992). "Saltmarsh geomorphology," in *Saltmarshes: Morphodynamics, Conservation and Engineering Significance*, eds J. R. L. Allen and K. Pye (Cambridge: Cambridge University Press), 41–62.

Redfield, A. C. (1972). Development of a New England salt marsh. *Ecol. Monogr.* 42, 201–237. doi: 10.2307/1942263

Reed, D. J., Spencer, T., Murray, A. L., French, J. R., and Leonard, L. (1999). Marsh surface sediment deposition and the role of tidal creeks: implications for created and managed coastal marshes. *J. Coast. Conserv.* 5, 81–90. doi: 10.1007/BF02802742

Sallenger, A. H., Doran, K. S., and Howd, P. A. (2012). Hotspot of accelerated sea-level rise on the Atlantic Coast of North America. *Nat. Clim. Chang.* 2, 884–888. doi: 10.1038/nclimate1597

Schepers, L. (2017). *Spatial Patterns and Bio-Geomorphological Effects of Vegetation Loss in a Submerging Coastal Marsh*. Belgium: Antwerpen University.

Schepers, L., Brennand, P., Kirwan, M. L., Guntenspergen, G. R., and Temmerman, S. (2020a). Coastal marsh degradation into ponds induces irreversible elevation loss relative to sea level in a microtidal system. *Geophys. Res. Lett.* 47:e2020GL089121. doi: 10.1029/2020GL089121

Schepers, L., Kirwan, M., Guntenspergen, G., and Temmerman, S. (2017). Spatio-temporal development of vegetation die-off in a submerging coastal marsh. *Limnol. Oceanogr.* 62, 137–150. doi: 10.1002/lno.10381

Schepers, L., Van Braeckel, A., Bouma, T. J., and Temmerman, S. (2020b). How progressive vegetation die-off in a tidal marsh would affect flow and sedimentation patterns: a field demonstration. *Limnol. Oceanogr.* 65, 401–412. doi: 10.1002/lno.11308

Scott, M., McDermott, L., Silva, E., and Watson, E. (2009). *Project report: Digital Spatial Data Capture of Marsh Extent in Blackwater National Wildlife Refuge, 1938 and 2006*. Eastern Shore Regional GIS Cooperative, Salisbury University.

Shriver, G., Hodgman, T. P., Gibbs, J. P., and Vickery, P. D. (2004). Landscape context influences salt marsh bird diversity and area requirements in New England. *Biol. Conserv.* 119, 545–553. doi: 10.1016/j.biocon.2004.01.016

Spivak, A. C., Gosselin, K., Howard, E., Mariotti, G., Forbrich, I., Stanley, R., et al. (2017). Shallow ponds are heterogeneous habitats within a temperate salt marsh ecosystem: shallow ponds are heterogeneous habitats. *J. Geophys. Res.* 122, 1371–1384. doi: 10.1002/2017JG003780

Squiers, E. R., and Good, R. E. (1974). Seasonal changes in the productivity, caloric content, and chemical composition of a population of salt-marsh cord-grass (*Spartina alterniflora*). *Chesapeake Sci.* 15:63. doi: 10.2307/1351263

Stevenson, J. C., Kearney, M. S., and Pendleton, E. C. (1985). Sedimentation and erosion in a Chesapeake Bay brackish marsh system. *Mar. Geol.* 67, 213–235. doi: 10.1016/0025-3227(85)90093-3

Swarzenski, C. M., Doyle, T. W., Fry, B., and Hargis, T. G. (2008). Biogeochemical response of organic-rich freshwater marshes in the Louisiana delta plain to chronic river water influx. *Biogeochemistry* 90, 49–63. doi: 10.1007/s10533-008-9230-7

Temmerman, S., Govers, G., Meire, P., and Wartel, S. (2003). Modelling long-term tidal marsh growth under changing tidal conditions and suspended sediment concentrations, Scheldt Estuary, Belgium. *Mar. Geol.* 193, 151–169. doi: 10.1016/S0025-3227(02)00642-4

Temmerman, S., Moonen, P., Schoelynck, J., Govers, G., and Bouma, T. J. (2012). Impact of vegetation die-off on spatial flow patterns over a tidal marsh: tidal marsh die-off and flow patterns. *Geophys. Res. Lett.* 39:L03406. doi: 10.1029/2011GL050502

Vandenbruwaene, W., Temmerman, S., Bouma, T. J., Klaassen, P. C., de Vries, M. B., Callaghan, D. P., et al. (2011). Flow interaction with dynamic vegetation patches: implications for biogeomorphic evolution of a tidal landscape: flow interaction with dynamic patches. *J. Geophys. Res. Earth Surf.* 116:F01008. doi: 10.1029/2010JF001788

van Huissteden, J., and van de Plassche, O. (1998). Sulphate reduction as a geomorphological agent in tidal marshes ('Great Marshes' at Barnstable, Cape Cod, USA). *Earth Surf. Process. Landf.* 23, 223–236.

Vinent, O. D., Herbert, E. R., Coleman, D. J., Himmelstein, J. D., and Kirwan, M. L. (2021). Onset of runaway fragmentation of salt marshes. *One Earth* 4, 506–516. doi: 10.1016/j.oneear.2021.02.013

Wang, C., Schepers, L., Kirwan, M. L., Belluco, E., D'Alpaos, A., Wang, Q., et al. (2021). Different coastal marsh sites reflect similar topographic conditions under which bare patches and vegetation recovery occur. *Earth Surf. Dyn.* 9, 71–88. doi: 10.5194/esurf-9-71-2021

Wang, C., and Temmerman, S. (2013). Does biogeomorphic feedback lead to abrupt shifts between alternative landscape states?: An empirical study on intertidal flats and marshes: shifts between intertidal flat and marsh. *J. Geophys. Res. Earth Surf.* 118, 229–240. doi: 10.1029/2012JF002474

Wang, D.-P., and Elliott, A. J. (1978). Non-tidal variability in the Chesapeake Bay and Potomac River: evidence for non-local forcing. *J. Phys. Oceanogr.* 8, 225–232. doi: 10.1175/1520-0485(1978)008<0225:NTVITC>2.0.CO;2

Weston, N. B. (2014). Declining sediments and rising seas: an unfortunate convergence for tidal wetlands. *Estuaries Coast.* 37, 1–23. doi: 10.1007/s12237-013-9654-8

Wilson, C. A., Hughes, Z. J., FitzGerald, D. M., Hopkinson, C. S., Valentine, V., and Kolker, A. S. (2014). Saltmarsh pool and tidal creek morphodynamics: dynamic equilibrium of northern latitude saltmarshes? *Geomorphology* 213, 99–115. doi: 10.1016/j.geomorph.2014.01.002

Wilson, K. R., Kelley, J. T., Croitoru, A., Dionne, M., Belknap, D. F., and Steneck, R. (2009). Stratigraphic and ecophysical characterizations of salt pools: dynamic landforms of the Webhannet salt marsh, Wells, ME, USA. *Estuaries Coast.* 32, 855–870. doi: 10.1007/s12237-009-9203-7

Wilson, K. R., Kelley, J. T., Tanner, B. R., and Belknap, D. F. (2010). Probing the origins and stratigraphic signature of salt pools from north-temperate marshes in Maine, U.S.A. *J. Coast. Res.* 26, 1007–1026. doi: 10.2112/JCOASTRES-D-10-00007.1

Zhu, Z., Vuik, V., Visser, P. J., Soens, T., van Wesenbeeck, B., van de Koppel, J., et al. (2020). Historic storms and the hidden value of coastal wetlands for nature-based flood defence. *Nat. Sustain.* 3, 853–862. doi: 10.1038/s41893-020-0556-z

Conflict of Interest: The authors declare that the research was conducted in the absence of any commercial or financial relationships that could be construed as a potential conflict of interest.

Publisher's Note: All claims expressed in this article are solely those of the authors and do not necessarily represent those of their affiliated organizations, or those of the publisher, the editors and the reviewers. Any product that may be evaluated in this article, or claim that may be made by its manufacturer, is not guaranteed or endorsed by the publisher.

Copyright © 2021 Himmelstein, Vinent, Temmerman and Kirwan. This is an open-access article distributed under the terms of the Creative Commons Attribution License (CC BY). The use, distribution or reproduction in other forums is permitted, provided the original author(s) and the copyright owner(s) are credited and that the original publication in this journal is cited, in accordance with accepted academic practice. No use, distribution or reproduction is permitted which does not comply with these terms.

frontiers in Marine Science

ORIGINAL RESEARCH
published: 04 October 2021
doi: 10.3389/fmars.2021.726238

Key Bioturbator Species Within Benthic Communities Determine Sediment Resuspension Thresholds

Jaco C. de Smit[1,2], Muriel Z. M. Brückner[2†], Katherine I. Mesdag[2], Maarten G. Kleinhans[2] and Tjeerd J. Bouma[1,2]*

[1] Department of Estuarine and Delta Systems, NIOZ Royal Netherlands Institute for Sea Research, Yerseke, Netherlands,
[2] Department of Physical Geography, Faculty of Geosciences, Utrecht University, Utrecht, Netherlands

OPEN ACCESS

Edited by:
Simon Marius Mudd, University of Edinburgh, United Kingdom

Reviewed by:
Charlie Emma Louise Thompson, University of Southampton, United Kingdom
Yining Chen, Second Institute of Oceanography, Ministry of Natural Resources, China

***Correspondence:**
Jaco C. de Smit
jaco.de.smit@nioz.nl

†Present address:
Muriel Z. M. Brückner
College of Life and Environmental Sciences, University of Exeter, Exeter, United Kingdom

Specialty section:
This article was submitted to Coastal Ocean Processes, a section of the journal Frontiers in Marine Science

Received: *16 June 2021*
Accepted: *27 August 2021*
Published: *04 October 2021*

Citation:
de Smit JC, Brückner MZM, Mesdag KI, Kleinhans MG and Bouma TJ (2021) Key Bioturbator Species Within Benthic Communities Determine Sediment Resuspension Thresholds. Front. Mar. Sci. 8:726238. doi: 10.3389/fmars.2021.726238

Abundant research has shown that macrobenthic species are able to increase sediment erodibility through bioturbation. So far, however, this has been at the level of individual species. Consequently, we lack understanding on how such species effects act on the level of bioturbator communities. We assessed the isolated and combined effects of three behaviorally contrasting macrobenthic species, i.e., *Corophium volutator*, *Hediste diversicolor,* and *Limecola balthica*, at varying densities on the critical bed shear stress for sediment resuspension (τ_{cr}). Overall, the effect of a single species on sediment erodibility could be described by a power function, indicating a relatively large effect of small bioturbator densities which diminishes toward higher individual density. In contrast to previous studies, our results could not be generalized between species using total metabolic rate, indicating that metabolic rate may be only suitable to integrate bioturbation effects within and between closely related species; highly contrasting species require consideration of species-specific bioturbation strategies. Experiments at the benthic community level revealed that the ability of a benthic community to reduce τ_{cr} is mainly determined by the species that has the largest individual effect in reducing τ_{cr}, as opposed to the species that is dominant in terms of metabolic rate. Hence, to predict and accurately model the net effect of bioturbator communities on the evolution of tidal flats and estuaries, identification of the key bioturbating species with largest effects on τ_{cr} and their spatial distribution is imperative. Metabolic laws may be used to describe their actual activity.

Keywords: bioturbation, sediment resuspension, benthic communities, tidal flat, flume experiment

INTRODUCTION

Muddy tidal flats are living landscapes, shaped not only by feedbacks between hydrodynamics, sediment transport, and morphology but also by the presence and behavior of benthic organisms that live within or on top of the sediment (Widdows et al., 2000; Widdows and Brinsley, 2002; Brückner et al., 2021). Erosion occurs when the forces that stabilize the sediment, expressed as the critical bed shear stress (τ_{cr}), are exceeded by the shear stress induced by flow or waves. Microphytobenthos can protect the mud from erosion through the creation of biofilms that

increase τ_{cr}. Macrobenthic species generally decrease τ_{cr}, as they disrupt muddy sediments and biofilms through their motility and feeding behavior (Herman et al., 2001; Le Hir et al., 2007), albeit that some species are able to stabilize sediment under specific conditions (e.g., Meadows and Tait, 1989). Consequently, the overall erodibility of tidal flat sediments is determined by complex interactions within and between benthic communities, causing significant spatiotemporal variations in sediment stability (Widdows et al., 2000; Le Hir et al., 2007; Montserrat et al., 2008). The influence of bioturbation on sediment erodibility is strongest in cohesive sediments, as bioturbation reduces the sediment stabilizing properties of the mud fraction (Li et al., 2017; Cozzoli et al., 2020). The destabilizing effect of macrobenthic species is particularly important on intertidal flats, as they mediate sediment export from tidal flats toward the estuary and can induce a redistribution of fines at the landscape level (Pearson and Rosenberg, 1978; Nilsson and Rosenberg, 2000; Orvain et al., 2012; Brückner et al., 2020, 2021).

Distinct benthic species communities can be observed along the salinity and tidal gradients of dynamic estuaries as a result of hydrodynamic stresses, salinity, and sediment properties of the bed (Ysebaert and Herman, 2002; Thrush et al., 2003, 2005; Ysebaert et al., 2003; Cozzoli et al., 2013, 2014). Moreover, species interactions and species-specific life-cycles and behavior influence species occurrence and community structure (Wilson and Parker, 1996). This includes the capacity of single organisms to modify their environment through, for instance, bioturbation, which creates new habitat for co-existing species additionally affecting species distributions (Crooks, 2002; Brückner et al., 2021). Given the diversity of macrobenthic species and their behavior, generalization of bioturbation effects across species is challenging (Nowell and Jumars, 1984; Le Hir et al., 2007). This knowledge gap hampers our understanding of the morphological evolution of intertidal flats and our capability to parameterize biogeomorphic models that represent species communities.

Biogeomorphological modeling is becoming increasingly important given that tidal flats are globally decreasing (Murray et al., 2019) and threatened by drowning under climate change (Leuven et al., 2019). Recently, total metabolic rate has been proposed as a method to scale the effects of bioturbation on sediment erodibility and to integrate this across species (Cozzoli et al., 2018). Many studies have confirmed the destabilizing potential of individual macrobenthic species (see, e.g., Le Hir et al., 2007 for a review; Cozzoli et al., 2019 for species distinction). However, the effect of multiple co-existing macrobenthic species has so far been neglected in experimental studies. It is possible that sediment erodibility varies under various compositions of the macrobenthic communities. However, current understanding of how co-occurring species facilitate or impede the activity of co-existing neighbors and consequently determine total resuspension rates remains limited. Hence, we aim to quantitatively compare the effect of single species against the combined effects of multiple species on the erodibility of muddy sediments defined in terms of critical bed shear stress (τ_{cr}).

To gain insight in how to upscale macrobenthos effects on sediment resuspension from an individual species to a community, we measured the effect of bioturbation on the critical bed shear stress of mud for three behaviorally highly contrasting macrobenthic species, both at the single species level and in mixed communities. To be able to assess many combinations, we used a newly developed mobile Oscillatory-Channel Resuspension flume (OsCaR). We selected three key species that are abundant on the tidal flats along the brackish-marine part of the Western Scheldt estuary (Netherlands) and represent distinct macrobenthic activities, including biofilm grazing, pellet formation, and burrow construction (Queirós et al., 2013): *Corophium volutator*, *Hediste diversicolor*, and *Limecola balthica*. We assessed whether total metabolic rate is an applicable measure to generalize bioturbation effects across behaviorally contrasting benthic communities, or whether sediment erodibility is dominated by one single species or by non-linear effects due to interactions between species.

MATERIALS AND METHODS

Experimental Design and Sediment Preparation

Sediment was collected from Groot Buitenschoor, a muddy tidal flat near the Antwerp harbor, Belgium (51°21′50″ N; 4°14′48″ E, **Figure 1**). The sediment had a median grain size (D_{50}) of 45 μm and an average mud content of 62% (measured with a Malvern laser diffractor), which is representative for the habitat of the selected species, and higher than typically used in erodibility studies (**Table 1**). There were only small, soft-tissue benthic invertebrates present in the sediment. Hence, in order to maintain the natural water content, the sediment was not sieved but instead frozen for a period of at least 48 h for defaunation and then thawed and mixed thoroughly. Any remaining larger items in the sediment, such as plant or shell fragments, were removed manually. The defaunated sediment was carefully placed in sediment cores (l × w × d = 22.5 cm × 15 cm × 5 cm) and left to consolidate, while covered with a thin layer of seawater to prevent desiccation, for at least 24 h before introducing the macrobenthic organisms.

Three key species were identified that commonly co-occur on the muddy intertidal flats of temperate estuaries in high numbers, but which are strongly contrasting in motility and feeding behavior:

- *Hediste diversicolor* is an intermediate to deep burrowing polychaete, which builds a complex network of galleries up to a depth of 15 cm, though most individuals can be found in the top 8 cm of the bed during summer (Davey, 1994). Typical densities of *H. diversicolor* range between 100 and 3,000 individuals per m^2 (Ysebaert and Herman, 2002). This species can be a biostabilizer in low densities under calm hydrodynamic conditions, as the building of galleries compacts the adjacent sediment and the secretion of mucus further fixates the sediment (Meadows and Tait, 1989). Under higher hydrodynamic stresses, however, i.e., shear stresses near τ_{cr} of the sediment, the created galleries and added surface roughness of *H. diversicolor* result

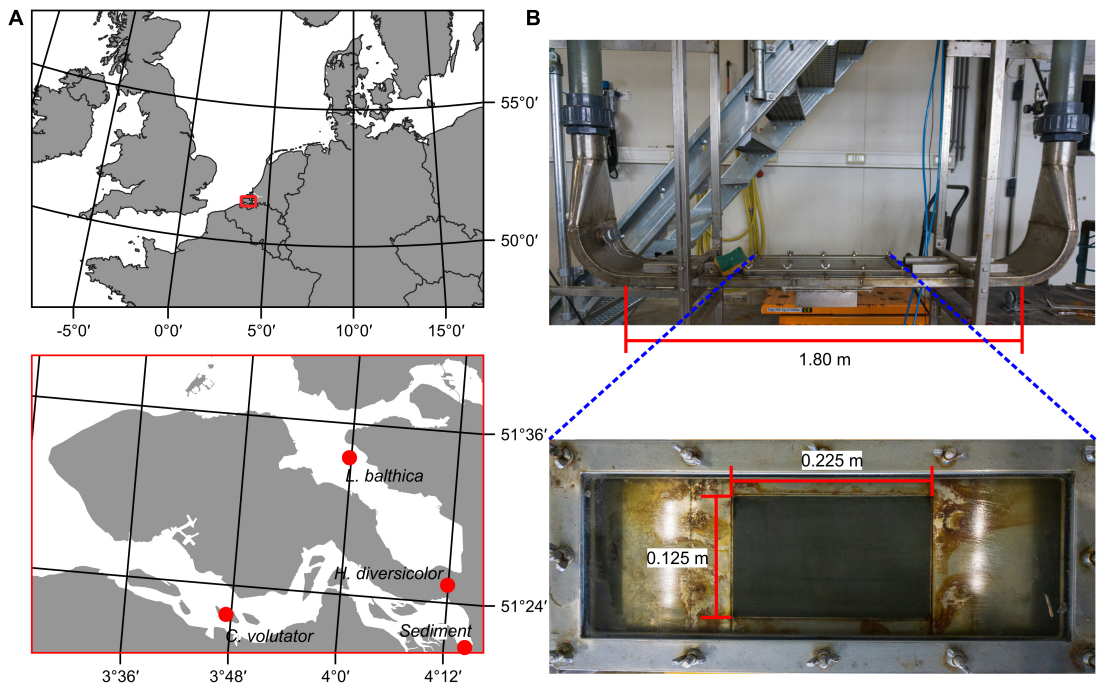


FIGURE 1 | (A) Sampling locations of selected species and sediment in the Scheldt estuary, Netherlands. **(B)** The OsCaR flume. A piston in one of the vertical tubes drives an oscillatory flow over the sediment core, which is pushed into the flume channel from below.

TABLE 1 | Experimental setting and sediment composition of experimental studies on sediment erodibility by species selected in this study.

References	Experimental setting	Median grain size D_{50} (mud%)	τ_{cr} or u_{cr} measured
Cozzoli et al., 2018	Lab, flume	100 μm (12% mud)	No
Cozzoli et al., 2019	Lab, flume	120 μm (12% mud)	No
Cozzoli et al., 2020	Lab, flume	305 μm (0% mud); 291 μm (4% mud); 257 μm (10% mud); 153 μm (28% mud)	No
de Deckere et al., 2000	Lab, flume	120 μm (mud% unknown)	Yes (u_{cr})
Fernandes et al., 2006	Lab, flume	Median grain size unknown (95% mud)	No
Li et al., 2017	Lab, flume	274 μm (0% mud); 101 μm (32% mud)	Yes (u_{cr})
Meadows and Tait, 1989	Lab, shear vane	No information given	No
Montserrat et al., 2008	Field, shear vane	Median grain size unknown (36–55% mud)	No
Widdows et al., 2000	Lab and field, flume	Median grain size unknown (0–42% mud)	No
Widdows et al., 2009	Lab, flume	Median grain size unknown (85% mud)	No
Willows et al., 1998	Lab, flume	22–84 μm (77–91% mud)	No

TABLE 2 | Number of individuals and total metabolic rate for the density and species community treatments.

	C. volutator (ind m^{-2})	*L. balthica* (ind m^{-2})	*H. diversicolor* (ind m^{-2})	Mean body length (mm)/ADFDM (mg)	I_{tot} (mW m^{-2})
C. volutator—low	2,400	–	–	5/0.25	7.20
C. volutator—high	9,000	–	–	5/0.25	27.00
L. balthica—low	–	450	–	20/30	76.05
L. balthica—high	–	1,500	–	20/30	253.50
H. diversicolor—low	–	–	210	40/20	14.70
H. diversicolor—medium	–	–	510	40/20	35.70
H. diversicolor—high	–	–	810	40/20	56.70
C. volutator and *L. balthica*	2,400	450	–	–	83.25
L. balthica and *H. diversicolor*	–	450	210	–	90.75
C. volutator and *H. diversicolor*	2,400	–	210	–	21.90
C. volutator and *L. balthica* and *H. diversicolor*	2,400	450	210	–	97.95

in an increase of the erodibility of intertidal sediments (Fernandes et al., 2006).

- *Limecola balthica* (also commonly called *Macoma balthica*) is an intermediate burrowing bivalve, which feeds by scraping the surface sediment with its siphons and deposits pseudofaeces, thereby increasing sediment erodibility (Willows et al., 1998; Van Prooijen et al., 2011). It typically occurs in densities ranging from 100 to 2,000 individuals per m^2 (Ysebaert and Herman, 2002). In this study, juveniles (0.02 m mean shell length) were used in order to keep the total biomass and total metabolic rate in the same order of magnitude as *H. diversicolor*.
- *Corophium volutator* is an intermediate burrowing amphipod which can occur in very high densities of up to 100,000 individuals per m^2 but typically occurs in densities ranging from 1,000 to 15,000 in m^{-2} (Flach, 1992; Ysebaert and Herman, 2002). It creates U-shaped burrows of approximately 5 cm depth. As a filter-feeder during high tide, *C. volutator* pumps large amounts of water through its burrows, enhancing sediment resuspension (De Backer et al., 2011). During low tide, it can also act as a deposit feeder, in which case it scrapes detritus of the sediment surface using its two antennae (Meadows and Reid, 1966).

In the flume experiments, we tested various densities for each species (**Table 2**) based on reported characteristic low and high individual densities (Ysebaert and Herman, 2002). Species community experiments were conducted using a low individual density only, as combining multiple species with high individual density yields unrealistically high total individual densities and total metabolic rates compared to those reported in literature.

The macrobenthic organisms were collected between June and August 2019 from various locations in the Eastern and Western Scheldt, The Netherlands (**Figure 1**). After being introduced to the sediment cores, they were acclimatized in a tidal mesocosm for 2 days (cf. Cozzoli et al., 2019) under natural conditions (18°C water temperature, 30 ppt salinity, 16–8 h light–dark cycle, and a semidiurnal tide with 50% inundation frequency). In order to retain all macrobenthic organisms, the sediment cores were covered with a 0.2-mm mesh size net. The 2-day acclimatization period was chosen based on results of a pilot experiment that had shown negligible differences in sediment erodibility between 2, 3, and 4 days of acclimatization. Hence, longer acclimatization periods were avoided as the absence of waves and currents in the tidal mesocosm can cause the uninterrupted accumulation of loose bioturbated sediment at the sediment surface, potentially leading to an unrealistically low erosion threshold. Prior to the erodibility measurements, pictures were taken of the sediment cores with benthos in order to compare bioturbation patterns visually. Quantifiable observations of bioturbation patterns created by benthic organisms were conducted using ImageJ 1.53a.

Calculation of Total Metabolic Rate

To quantify the effect of both density and species on sediment erodibility, and to directly compare the different benthic communities, the total benthic metabolic rate (I_{tot}, mW m^{-2}) was calculated as the product of individual metabolic rate (I_{ind}) and species density of each experiment. The metabolic rate is a measure for all benthic activity. This makes it a suitable single predictor to characterize benthic activity across different species and especially species communities, while accounting for various types of bioturbation activities such as increasing bed roughness or altering bulk sediment properties. I_{ind} was determined from the mean individual ash-free dry weight using the empirical model of Brey (2010), which also accounts for age in case of juvenile *L. balthica*. The ash-free dry mass (AFDM) of *L. balthica*, *H. diversicolor,* and *C. volutator* (**Table 2**) was estimated from the mean body length using empirical relations from Eklöf et al. (2017); Galasso et al. (2018), and Boates and Smith (1979), respectively:

$$AFDM_{L.\ balthica} = 0.001l^{3.48} \quad (1)$$

$$AFDM_{H.\ diversicolor} = 1.48l^{1.92} \quad (2)$$

$$AFDM_{C.\ volutator} = 0.003l^{3} \quad (3)$$

Where *AFDM* is the ash-free dry mass in mg, and l is the body length in mm.

Flume Description and Experimental Procedure

Sediment erodibility measurements were conducted in the Oscillatory-Channel Resuspension flume [OsCaR, **Figure 1** (de Smit et al., 2021)]. The OsCaR flume is an oscillatory (U-tube) flow channel, which imposes the near-bed hydrodynamic conditions under natural waves and can be used to measure the critical bed shear stress (τ_{cr}) of the sediment (cf. Jonsson and Carlsen, 1976). The flume consists of two vertical PVC tubes of which one contains a piston driving the oscillatory flow through the flow channel (l × w × h = 1.5 m × 0.21 m × 0.03 m). The sediment core (l × w = 0.225 m × 0.15 m) is pushed from below into an open measurement section (l × w = 0.2 m × 0.125 m) in the center of the flow channel. The placement of the core can be adjusted precisely, creating a smooth transition between the stainless-steel flume bottom and the sediment core. Subsequently, the flume is gradually filled with saline water (30 ppt salinity, 18°C). Oscillatory flow velocity was gradually increased from 10 cm s^{-1} in small increments in the order of 5 cm s^{-1} up to the point of sediment resuspension, which depending on species and density was between 22 and 69 cm s^{-1}. A pressure sensor (Drück 1800 series) placed in the open-ended tube measures the water level at 25 Hz. Given that the cross-sectional area of the flume is equal between the tubes and flow channel, the first derivative of the water level signal (m) is used to determine the flow velocity over the sediment core (m s^{-1}). The suspended sediment concentration was measured with a turbidity sensor at 25 Hz (Turner Cyclops 7). This sensor was placed sideways through a small hole located 0.2 m away from the edge of the sediment core in order not to disrupt the oscillatory flow over the sediment core.

We specifically chose to measure τ_{cr}, as it is applicable in quantitative modeling approaches used to upscale the

biogeomorphological interactions investigated here. τ_{cr} of the sediment was measured rather than that of the fluff layer, as the thickness of the latter is generally in the order of mm, while erosion on tidal flats during storms can be in the order of centimeters (de Vet et al., 2020). This is distinctly different from annular flume measurements (cf. Willows et al., 1998; Amos et al., 2010; Cozzoli et al., 2018, 2019), where equilibrium suspended sediment concentrations at a given shear stress are measured. As an indication, τ_{cr} is proportional to the bed shear stress step at which the largest increase in equilibrium sediment concentration is observed (Cozzoli et al., 2020). In order to quantify τ_{cr} of the sediment, rather than that of flocs, it is important to distinguish between resuspension of loose bed material and the cohesive sediments underneath. The erosion threshold was primarily defined based on a critical sediment resuspension rate. Secondarily, it was identified visually as the moment when resuspension of the cohesive sediment was observed (c.f. van Rijn, 2020), in order to ensure that turbidity observations were not skewed by edge scouring at the flow channel–sediment core transition. We specifically defined a critical sediment resuspension rate rather than a suspended sediment concentration, as the latter is influenced by the presence and amount of loose sediment and the active pumping, by e.g., *C. volutator*. The sediment resuspension rate was determined from the first derivative of the turbidity signal. Based on tests comparing visual observations of τ_{cr} against the corresponding turbidity signal for a variety of sediments ranging from sand to 70% mud concentration, a sediment resuspension rate of 0.06 g m^{-2} s^{-1} was defined as the threshold for the onset of sediment transport (de Smit et al., 2021). The erosion of loose bed material and erosion of cohesive sediments are well distinguishable in the resuspension rate signal, as loose flocculated material yields a much lower turbidity than well-dispersed resuspended sediments. Therefore, τ_{cr} as measured in this study corresponds to the onset of type 1b or type 2 erosion (Amos et al., 1992, 2010). Once sediment resuspension was observed, the velocity setting was kept constant for at least 1 minute to include a sufficient number of waves for determining the peak orbital velocity.

The critical peak orbital velocity (u_{cr}, m s^{-1}) was calculated as the mean of all velocity peaks during the 1-minute time frame that sediment resuspension was observed. The critical bed shear stress (τ_{cr}, N m^{-2}) was calculated from the critical peak orbital velocity as (Van Rijn, 1993):

$$\tau_{cr} = \frac{1}{2}\rho f_w {u_{cr}}^2 \quad (4)$$

Where ρ is the water density (1,025 kg m^{-3} for 30 ppt salinity water at 18°C) and f_w is a friction factor (-) to account for the properties of the wave boundary layer. Normally, f_w is calculated from the bed roughness. However, given that the sediment core only makes up a small part of the flume channel, the wave boundary layer inside the OsCaR flume is formed by the metal flume bottom rather than the sediment core. As a result, the bed roughness is not appropriate for calculating f_w. Therefore, f_w was back calculated from erodibility measurements using a non-cohesive sediment with a known τ_{cr} of 0.2 N m^{-2} following the Shields curve. u_{cr} of this sediment was 0.15 m s^{-1}, yielding an f_w of 0.017 following Equation 4. Assuming that f_w is proportional to the orbital excursion to the power of −0.52 (Soulsby, 1997), this yielded the following flume specific friction factor (de Smit et al., 2021):

$$f_w = 0.0076{A_{max}}^{-0.52} \quad (5)$$

where A_{max} is the orbital excursion (m). Equation 5 translates to a bed roughness of the sediment of 1.35 mm. If this roughness is significantly exceeded due to the presence of bioturbation patterns on the sediment core, f_w may be higher. However, by assuming a constant bed roughness instead, such bioturbation effects are included directly as a species property rather than indirectly *via* the bed roughness (Cozzoli et al., 2019).

Statistical Analyses

Erodibility measurements were replicated five times except for low-density *H. diversicolor*, which was replicated three times due to practical reasons. Five control measurements using defaunated sediment were conducted for each set of species experiments to account for potential changes in sediment properties between the sets of flume runs, which could have an effect on τ_{cr}. However, there was no significant change in τ_{cr} of control runs between the sets (p = 0.23), hence we did not account for this is in any subsequent analyses and considered all control measurements as a single group. Data were tested for normality using Shapiro–Wilks tests, and homogeneity of variance was tested using Bartlett tests. If these assumptions were met, ANOVAs and Tukey-HSD *post hoc* tests were used. These assumptions were, however, not met for the erodibility measurements, due to the stochastic nature of the onset of erosion. Therefore, statistical comparisons on erodibility were done using Kruskal–Wallis tests and Wilcoxon rank sum tests.

RESULTS

Emerging Visual Differences in Bioturbation Patterns

Clear visual differences in bioturbation patterns emerged at the sediment surface prior to the erodibility measurements (**Figure 2**). In the single species experiments, *L. balthica* immediately burrowed into the sediment and remained immobile during the acclimatization period, leaving clear holes on the sediment surface as there was no flow or wave action in the tidal mesocosm. In contrast, the mobile species *C. volutator* and *H. diversicolor* continuously bioturbated the sediment during the acclimatization period, leaving a large number of small holes and gullies at the sediment surface. In addition, *C. volutator* promoted the formation of a thin layer of fine loosened mud on top of the sediment as a result of their filter-feeding behavior.

In the community experiments, the traces on the sediment surface of *C. volutator* and *L. balthica* did not differ visually from the single species experiments. However, the number of holes by *H. diversicolor* was lower when combined with *L. balthica* (**Figure 3**, $p < 0.01$). In the communities where *C. volutator* was added, the number of holes was similarly reduced (**Figure 3**, $p < 0.01$), but the total length of the gullies at the sediment

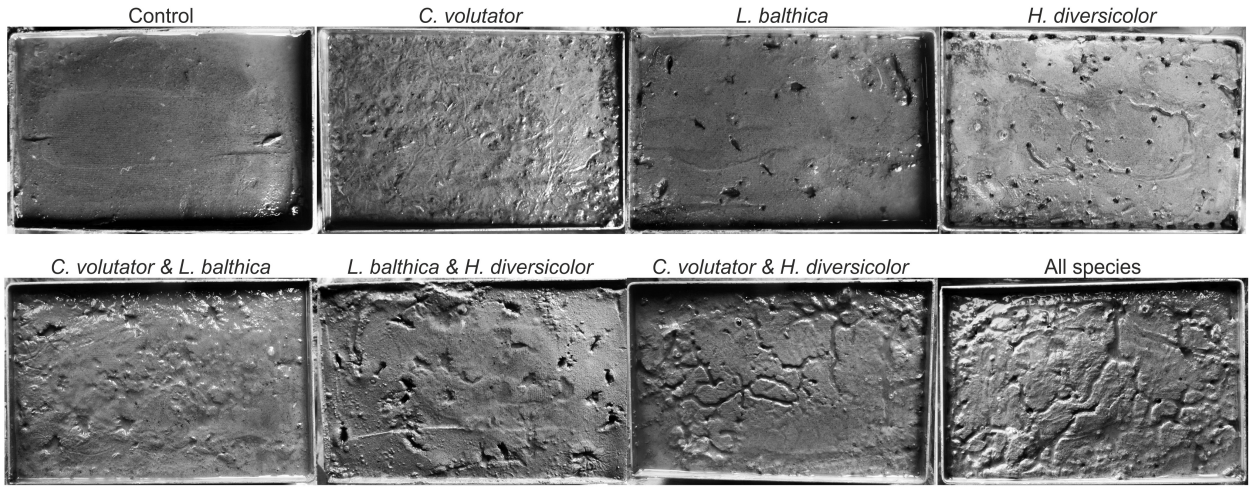


FIGURE 2 | Disturbance patterns on the sediment cores prior to the erodibility measurements.

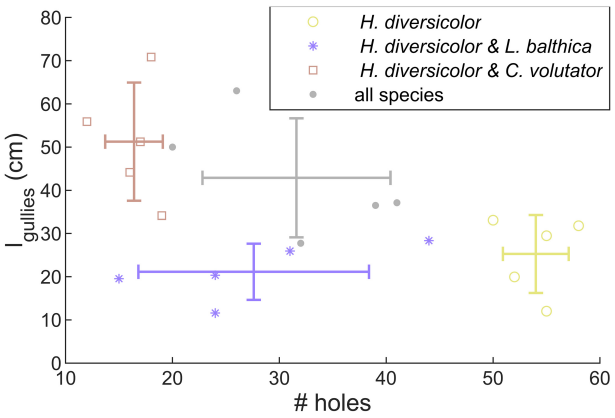


FIGURE 3 | Number of holes and total length of gullies created by *H. diversicolor* depend on the presence of other species. Lines show means ± SE.

surface created by *H. diversicolor* was higher (**Figure 3**, $p = 0.01$). Combining all species yielded an intermediate effect on the number of holes and gully length of *H. diversicolor* (**Figure 3**). This indicates that the composition of the benthic community influences the bioturbating behavior of *H. diversicolor*.

Single Species Experiments; Effects of Species and Individual Density on τ_{cr}

When macrobenthos were introduced to the sediment, the erosion threshold decreased by a factor of two to three (**Figure 4**). This reduction in τ_{cr} depended strongly on the specific species ($p < 0.01$) and on the individual density ($p < 0.01$), albeit that a higher individual density generally caused a much smaller reduction in τ_{cr} compared to adding a species to defaunated sediment. Interestingly, while having the lowest total metabolic rate of all tested species, *C. volutator* caused the largest reduction in τ_{cr}, followed by *L. balthica* and *H. diversicolor,* respectively (**Figure 4**). The effect of individual density on τ_{cr} reduction was largest for *H. diversicolor*, followed by *C. volutator* and *L. balthica,* respectively (**Figure 4**). Overall, the observed reduction in τ_{cr} could be explained by a power function:

$$\tau_{cr} = \tau_{cr,def} - aI_{tot}{}^{b} \quad (6)$$

where $\tau_{cr,def}$ is the erodibility of the defaunated sediment, and a and b are species-specific coefficients. a is related to the potential of a species to reduce τ_{cr}. A higher a value indicates a higher potential of the species to reduce τ_{cr} at low individual density. b is related to the effect of individual density on τ_{cr} reduction. A higher b value indicates a larger dependence of τ_{cr} reduction on individual density. Given the significant variation in a and b between the tested species, total metabolic rate could not be used to integrate bioturbation effects on τ_{cr} across these highly contrasting species.

Species Community Experiments

Overall, the results from the benthic community experiments indicate that the erodibility of natural sediments is dominated by the species that has the largest individual effect on sediment erodibility, here primarily *C. volutator* or *L. balthica* when combined with *H. diversicolor* only (**Figure 5** and **Table 3**), rather than the species that is dominant in terms of total metabolic rate. That is, the addition of *C. volutator* to a single species or a benthic community caused a significant reduction in τ_{cr} compared to benthic communities where *C. volutator* was absent (**Figure 5**, $p < 0.01$). As a result, τ_{cr} of the sediments with a benthic community containing *C. volutator* was similar to the values of τ_{cr} induced by low densities of *C. volutator* in the single species scenarios, showing that the addition of *H. diversicolor*, *L. balthica,* or both to *C. volutator* did not cause a significant change in τ_{cr} (**Figure 5** and **Table 3**, $p = 0.22$, 0.69, and 1, respectively). Even though the bioturbation activity of *H. diversicolor* was visually observed to increase once *C. volutator* was added to the sediment

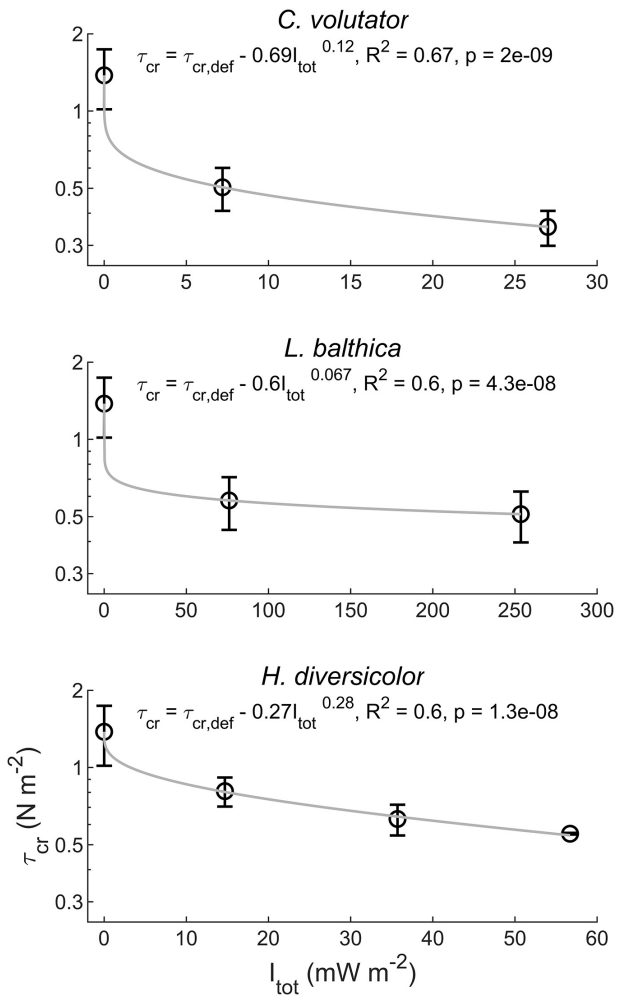


FIGURE 4 | Reduction of τ_{cr} depending on the total metabolic rate (I_{tot}) for the single species treatments.

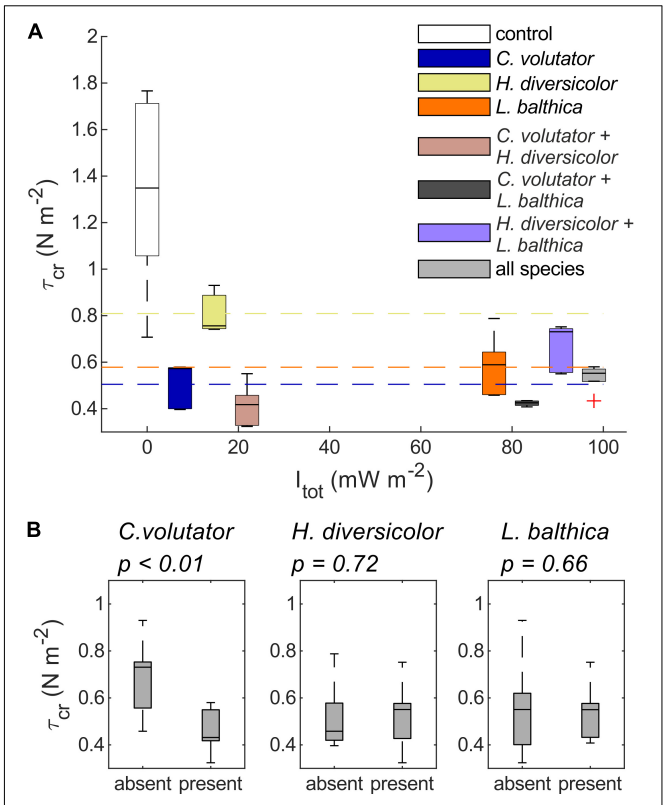


FIGURE 5 | (A) boxplots of τ_{cr} of low-density single species treatments and τ_{cr} of combined species treatments against I_{tot}. Dashed horizontal lines indicate the mean τ_{cr} for the single species treatments. **(B)** Boxplots of τ_{cr} measurements grouped based on the absence or presence of each species.

(**Figures 2**, **3**), this did not have measurable effects on sediment erodibility. These findings indicate that the addition of an extra species to a benthic communities does not necessarily induce a significant further reduction of τ_{cr}.

DISCUSSION

This study shows that the presence of bioturbating benthic species leads to a strong reduction in the critical bed shear stress (τ_{cr}) of muddy sediments, depending mainly on the species present and to a lesser extent on individual density and community structure. In general, measured τ_{cr} of the experiments with bioturbators is high compared to previously reported values. This can be attributed to the high mud concentration used in this study (**Table 1**), given that measured τ_{cr} of the defaunated sediment corresponds well with theory (Wu et al., 2018). Also, the variability in τ_{cr} of the control sediments was higher than that of the sediments with bioturbators. This may be caused by the increased likelihood of bed failure and subsequent mass erosion at higher bed shear stresses. While the direct effects of bioturbation may be smaller for less compacted sediments with lower τ_{cr}, the results presented here clearly show that in benthic communities the sediment erodibility is determined by the key bioturbating species, i.e., the species that individually causes the largest reduction in τ_{cr}, as opposed to the species which is dominant in terms of total metabolic rate.

Effects of Individual Bioturbation on Sediment Erodibility: Species Behavior and Individual Density

The net erodibility of the sediment under bioturbation is mainly the result of species behavior rather than individual density. Behavior characterizes how a species moves within or on top of the sediment and includes *(i)* their activity in modifying the sediment surface by creating tracks and burrows and *(ii)* the mobility of the organisms either locally or across larger areas. We found that the effect of increasing individual density of *Corophium volutator* and *Limecola balthica* minimally affected τ_{cr} after an initial reduction by the smallest number of individuals. Instead, we found a larger variation in sediment erodibility between species. This observation suggests that the species-specific behavior of these species controls the sediment

TABLE 3 | Wilcoxon rank sum test results from individual comparisons between low-density individual species and species combinations.

	L. balthica	*H. diversicolor*	C. v and H. d	*C. v* and *L. b*	*H. d* and *L. b*	All
C. volutator	0.22	**0.04**	0.22	0.69		1
L. balthica		0.14		**0.01**	0.55	0.42
H. diversicolor			**0.04**		0.14	**0.04**
C. volutator + *H. diversicolor*				0.42	**0.02**	**0.03**
C. volutator + *L. balthica*					**0.01**	**0.03**
H. diversicolor + *L. balthica*						0.22

Bold numbers indicate statistically significant differences.

properties. *C. volutator* is both a highly active and mobile species that diligently mobilizes the sediment surface through its feeding behavior (De Backer et al., 2011). Consequently, the effect of *C. volutator* on τ_{cr} is high even under low individual densities, as they are able to fully rework the sediment surface (de Deckere et al., 2000), albeit that future measurements of τ_{cr} at very low individual densities are needed for further validation of Equation 6.

Although *L. balthica* also actively modifies the sediment surface, it is largely immobile (Queirós et al., 2013), which limits the reworked sediment area by an individual to its direct surroundings. As a result, increasing individual densities rework an increasing area of surface sediment until individual feeding areas become overlapping (Van Prooijen et al., 2011). Although this affects the availability of erodible sediments at a given bed shear stress (Willows et al., 1998), we did not observe a significant effect of *L. balthica* individual density on τ_{cr}. A similar trend was observed by Li et al. (2017) and Cozzoli et al. (2020) for *Cerastoderma edule*, a bivalve similar to *L. balthica*, suggesting that τ_{cr} may be determined by local sediment destabilization, while sediment availability is determined by an average sediment stability over the inhabited area.

Hediste diversicolor showed a larger effect of individual density on τ_{cr} than the other tested species. While being highly mobile, *H. diversicolor* only passively reworks the sediment by burrowing (Queirós et al., 2013) and creating holes and gullies at the sediment surface. Therefore, increased sediment erodibility due to *H. diversicolor* bioturbation activity is likely a result of added bed roughness, rather than active destabilization of the sediment surface (Widdows et al., 2009). However, even for *H. diversicolor*, the additional decrease in τ_{cr} with increasing individual density was much smaller than the initial reduction in τ_{cr} upon adding the smallest number of individuals.

Present results therefore indicate that the effect of benthic macrofauna on sediment erodibility (τ_{cr}) is mainly affected by the presence or absence of a species, rather than by their abundance. Previous studies also reported either no or little influence of individual density on sediment erodibility at environmentally relevant individual densities (see, e.g., de Deckere et al., 2000 for *C. volutator*; Widdows et al., 2009 for *H. diversicolor*; Van Prooijen et al., 2011 for *L. balthica*). Our results modify the current postulate that metabolic rate scales with morphological modification proposed in Cozzoli et al. (2018). While metabolic rate may be useful for generalizing single species effects on sediment availability, it appears to be insufficient for generalizing bioturbation effects as an alteration to τ_{cr} across highly contrasting species. This is consistent with Cozzoli et al. (2019), who observed that total metabolic rate is sufficient for describing maximum suspended sediment concentrations at high bed shear stress, but found a significant species effect on the bed shear stress at which sediment resuspension rate peaked. The latter is proportional to the critical bed shear stress (Cozzoli et al., 2020).

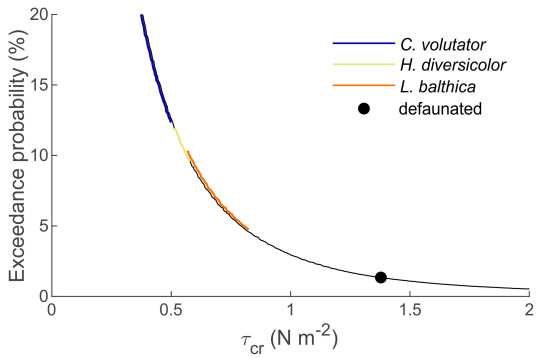


FIGURE 6 | Exceedance probability of a given wave-induced τ_{cr} for a typical tidal flat in the Western Scheldt estuary. Colored lines (shifted horizontally for visualization purposes) correspond to the τ_{cr} range of the indicated species. As exceedance probability increases exponentially with reducing τ_{cr} by, e.g., bioturbation, tidal flat morphodynamics are dominated by key benthic species causing the largest τ_{cr} reduction, as these have a disproportionate effect on τ_{cr} exceedance probability.

Effect of Benthic Communities on τ_{cr}

It has been both hypothesized and shown experimentally that benthic communities may have either cumulative or averaging effects on bioturbation activity when compared to the effects of each species individually, with the outcome depending on community structure and species interactions (Meadows and Tait, 1989; Cozzoli et al., 2019). It is therefore surprising that previous studies that directly measured the effect of bioturbation on sediment erosion in an experimental setting have so far been limited to single species (**Table 1**). We show for the first time how the community structure of bioturbating benthic macrofauna alters the net erodibility of muddy sediments on

intertidal flats compared to single species effects. When several organisms are present, the key bioturbator with the strongest effects on sediment erodibility determines the net erodibility of mud on tidal flats as opposed to species that are dominant in total metabolic rate. This key bioturbator modifies the sediment matrix and thereby seems to overwrite the lower bioturbation effect of the co-existing organisms. As a result, specific key species with a high potential to reduce τ_{cr} of muddy sediments, even if present in small numbers, may dominate the morphological evolution of estuaries instead of high densities of less efficient bioturbators (Brückner et al., 2021). This implies that a functional group approach may be more appropriate to describe the biogeomorphological effect of a benthic community rather than using total metabolic rate only.

Implications for Estuarine Biogeomorphological Processes and Modeling

Our findings have important implications for the morphological evolution of tidal flat-channel systems and the establishment of salt marshes. As sediment dynamics on tidal flats increase exponentially with increasing sediment erodibility, certain key species may have a disproportionate effect on the morphodynamics of tidal systems (**Figure 6**). Potentially enhanced sediment transport rates from the tidal flats toward the deeper channels of the estuary will affect local mud content of the bed and mud availability in other reaches of the estuary (Widdows and Brinsley, 2002; Townend et al., 2011; Brückner et al., 2021). The resulting changes in bed composition and elevation potentially affect the establishment and erosion of salt marshes through local bed level changes at the marsh edges (Hughes, 1999; Bouma et al., 2016; Brückner et al., 2020). In comparison with direct interactions between macrobenthic activity and saltmarshes, such as seed(ling) harvesting (Emmerson, 2000; Zhu et al., 2016a) that inhibits saltmarsh establishment or seed burial promoting saltmarsh germination (Zhu et al., 2016b), these indirect effects can play a significant role on the success of vegetation colonization (Volkenborn et al., 2007). Hence, the presence of key bioturbators on tidal flats may have important ramifications for the establishment and development of salt marshes.

To quantify the impact of benthic infauna on the sediment stability at the scale of tidal flats or even entire estuaries, there has been a growing interest in implementing bioturbation effects in morphodynamic models (e.g., Borsje et al., 2008; Van Prooijen et al., 2011; Brückner et al., 2021). Generally, this is implemented as an alteration to the critical bed shear stress and a calibration factor describing the erosion rate at a given bed shear stress. Calculated erosion rates are highly sensitive to τ_{cr} (Van Prooijen and Winterwerp, 2010; Van Prooijen et al., 2011). Hence, upscaling bioturbation effects to the ecosystem scale using models requires parameterization of bioturbation effects on τ_{cr}. Here we show that there are species-specific relations between total metabolic rate and τ_{cr}, which can be quantified, and that within benthic communities, τ_{cr} can be approximated as the minimum τ_{cr} imposed by the key species present.

DATA AVAILABILITY STATEMENT

The datasets presented in this study can be found in online repositories. The names of the repository/repositories and accession number(s) can be found below (when published): 4TU repository, doi: 10.4121/14790936.

AUTHOR CONTRIBUTIONS

JS, MB, MK, and TB: conceptualization. JS, MB, KM, and TB: experimental design. JS, MB, and KM: data curation and data analysis. JS and MB: manuscript writing. JS, MB, MK, KM, and TB: manuscript review and editing. All authors contributed to the article and approved the submitted version.

FUNDING

KM was supported by the Utrecht University - NIOZ student work experience program.

ACKNOWLEDGMENTS

We would like to thank Tom Ysebaert and Natalie Steiner for their inputs during the conceptualization of the research. We would also like to thank Lennart van IJzerloo and Chiu Cheng for their contributions with the fieldwork.

SUPPLEMENTARY MATERIAL

The Supplementary Material for this article can be found online at: https://www.frontiersin.org/articles/10.3389/fmars.2021.726238/full#supplementary-material

REFERENCES

Amos, C. L., Grant, J., Daborn, G. R., and Black, K. (1992). Sea Carousel-A benthic, annular flume. *Estuar. Coast. Shelf Sci.* 34, 557–577. doi: 10.1016/S0272-7714(05)80062-9

Amos, C. L., Umgiesser, G., Ferrarin, C., Thompson, C. E. L., Whitehouse, R. J. S., Sutherland, T. F., et al. (2010). The erosion rates of cohesive sediments in Venice lagoon, Italy. *Cont. Shelf Res.* 30, 859–870. doi: 10.1016/j.csr.2009.12.001

Boates, J. S., and Smith, P. C. (1979). Length-weight relationships, energy content and the effects of predation on Corophium volutator (pallas) (crustacea: amphipoda). *Proc. Nov. Scotian Inst. Sci.* 29, 489–499.

Borsje, B. W., de Vries, M. B., Hulscher, S. J. M. H., and de Boer, G. J. (2008). Modeling large-scale cohesive sediment transport affected by small-scale biological activity. *Estuar. Coast. Shelf Sci.* 78, 468–480. doi: 10.1016/j.ecss.2008.01.009

Bouma, T. J., van Belzen, J., and Balke, T. (2016). Short-term mudflat dynamics drive long-term cyclic salt marsh dynamics. *Limnol. Oceanogr.* 61, 2261–2275. doi: 10.1002/lno.10374

Brey, T. (2010). An empirical model for estimating aquatic invertebrate respiration. *Methods Ecol. Evol.* 1, 92–101. doi: 10.1111/j.2041-210x.2009.00008.x

Brückner, M. Z. M., Braat, L., Schwarz, C., and Kleinhans, M. G. (2020). What Came First, Mud or Biostabilizers? Elucidating Interacting Effects in a Coupled Model of Mud, Saltmarsh, Microphytobenthos, and Estuarine Morphology. *Water Resour. Res.* 56:2019wr026945. doi: 10.1029/2019wr026945

Brückner, M. Z. M., Schwarz, C., Coco, G., Baar, A., Boechat Albernaz, M., and Kleinhans, M. G. (2021). Benthic species as mud patrol - modelled effects of bioturbators and biofilms on large-scale estuarine mud and morphology. *Earth Surf. Process. Landforms* 2021, 1–17. doi: 10.1002/esp.5080

Cozzoli, F., Bouma, T. J., Ottolander, P., Lluch, M. S., Ysebaert, T., and Herman, P. M. J. (2018). The combined influence of body size and density on cohesive sediment resuspension by bioturbators. *Sci. Rep.* 8, 1–12. doi: 10.1038/s41598-018-22190-3

Cozzoli, F., Bouma, T. J., Ysebaert, T., and Herman, P. M. J. (2013). Application of non-linear quantile regression to macrozoobenthic species distribution modelling: Comparing two contrasting basins. *Mar. Ecol. Prog. Ser.* 475, 119–133. doi: 10.3354/meps10112

Cozzoli, F., Eelkema, M., Bouma, T. J., Ysebaert, T., Escaravage, V., and Herman, P. M. J. (2014). A mixed modeling approach to predict the effect of environmental modification on species distributions. *PLoS One* 9:15–17. doi: 10.1371/journal.pone.0089131

Cozzoli, F., Gjoni, V., and Pasqua, M. Del (2019). A process based model of cohesive sediment resuspension under bioturbators' influence. *Sci. Total Environ.* 670, 18–30. doi: 10.1016/j.scitotenv.2019.03.085

Cozzoli, F., Gomes da Conceição, T., and Van Dalen, J. (2020). Biological and physical drivers of bio-mediated sediment resuspension: A flume study on Cerastoderma edule. *Estuar. Coast. Shelf Sci.* 241:106824. doi: 10.1016/j.ecss.2020.106824

Crooks, J. A. (2002). Characterizing ecosystem-level consequences of biological invasions: The role of ecosystem engineers. *Oikos* 97, 153–166. doi: 10.1034/j.1600-0706.2002.970201.x

Davey, J. T. (1994). The architecture of the burrow of Nereis diversicolor and its quantification in relation to sediment-water exchange. *J. Exp. Mar. Bio. Ecol.* 179, 115–129. doi: 10.1016/0022-0981(94)90020-5

De Backer, A., Van Coillie, F., Montserrat, F., Provoost, P., Van Colen, C., Vincx, M., et al. (2011). Bioturbation effects of Corophium volutator: Importance of density and behavioural activity. *Estuar. Coast. Shelf Sci.* 91, 306–313. doi: 10.1016/j.ecss.2010.10.031

de Deckere, E. M. G. T., van de Koppel, J., and Heip, C. H. R. (2000). The influence of Corophium volutator abundance on resuspension. *Hydrobiologia* 426, 37–42. doi: 10.1023/A:1003978714382

de Smit, J. C., Kleinhans, M. G., Gerkema, T., and Bouma, T. J., (2021). Quantifying natural sediment erodibility using a mobile oscillatory flow channel. *Estuar. Coast. Shelf Sci.* 107574. doi: 10.1016/j.ecss.2021.107574

de Vet, P. L. M., van Prooijen, B. C., Colosimo, I., Steiner, N., Ysebaert, T., Herman, P. M. J., et al. (2020). Variations in storm-induced bed level dynamics across intertidal flats. *Sci. Rep.* 10, 1–15. doi: 10.1038/s41598-020-69444-7

Eklöf, J., Austin, Å, Bergström, U., Donadi, S., Eriksson, B. D. H. K., Hansen, J., et al. (2017). Size matters: Relationships between body size and body mass of common coastal, aquatic invertebrates in the Baltic Sea. *PeerJ* 2017, 1–14. doi: 10.7717/peerj.2906

Emmerson, M. (2000). Remedial habitat creation: Does Nereis diversicolor play a confounding role in the colonisation and establishment of the pioneering saltmarsh plant, Spartina anglica? *Helgol. Mar. Res.* 54, 110–116. doi: 10.1007/s101520050009

Fernandes, S., Sobral, P., and Costa, M. H. (2006). Nereis diversicolor effect on the stability of cohesive intertidal sediments. *Aquat. Ecol.* 40, 567–579. doi: 10.1007/s10452-005-8000-z

Flach, E. C. (1992). The influence of four macrozoobenthic species on the abundance of the amphipod Corophium volutator on tidal flats of the Wadden Sea. *Netherlands J. Sea Res.* 29, 379–394. doi: 10.1016/0077-7579(92)90077-R

Galasso, H. L., Richard, M., Lefebvre, S., Aliaume, C., and Callier, M. D. (2018). Body size and temperature effects on standard metabolic rate for determining metabolic scope for activity of the polychaete Hediste (Nereis) diversicolor. *PeerJ* 6:e5675. doi: 10.7717/peerj.5675

Herman, P. M. J., Middelburg, J. J., and Heip, C. H. R. (2001). Benthic community structure and sediment processes on an intertidal flat: Results from the ECOFLAT project. *Cont. Shelf Res.* 21, 2055–2071. doi: 10.1016/S0278-4343(01)00042-5

Hughes, R. G. (1999). Saltmarsh erosion and management of saltmarsh restoration; the effects of infaunal invertebrates. *Aquat. Conserv. Mar. Freshw. Ecosyst.* 9, 83–95. doi: 10.1002/(sici)1099-0755(199901/02)9:1<83::aid-aqc323>3.0.co;2-9

Jonsson, I. G., and Carlsen, N. A. (1976). Experimental and theoretical investigations in an oscillatory turbulent boundary layer. *J. Hydraul. Res.* 14, 45–60. doi: 10.1080/00221687609499687

Le Hir, P., Monbet, Y., and Orvain, F. (2007). Sediment erodability in sediment transport modelling: Can we account for biota effects? *Cont. Shelf Res.* 27, 1116–1142. doi: 10.1016/j.csr.2005.11.016

Leuven, J. R. F. W., Pierik, H. J., van der Vegt, M., Bouma, T. J., and Kleinhans, M. G. (2019). Sea-level-rise-induced threats depend on the size of tide-influenced estuaries worldwide. *Nat. Clim. Chang.* 9, 986–992. doi: 10.1038/s41558-019-0608-4

Li, B., Cozzoli, F., Soissons, L. M., Bouma, T. J., and Chen, L. (2017). Effects of bioturbation on the erodibility of cohesive versus non-cohesive sediments along a current-velocity gradient: A case study on cockles. *J. Exp. Mar. Bio. Ecol.* 496, 84–90. doi: 10.1016/j.jembe.2017.08.002

Meadows, P. S., and Reid, A. (1966). The behaviour of Corophium Volutator (Crustacea: Amphipoda). *J. Zool.* 150, 387–399. doi: 10.1111/j.1469-7998.1966.tb03013.x

Meadows, P. S., and Tait, J. (1989). Modification of sediment permeability and shear strength by two burrowing invertebrates. *Mar. Biol.* 101, 75–82. doi: 10.1007/BF00393480

Montserrat, F., Van Colen, C., Degraer, S., Ysebaert, T., and Herman, P. M. J. (2008). Benthic community-mediated sediment dynamics. *Mar. Ecol. Prog. Ser.* 372, 43–59. doi: 10.3354/meps07769

Murray, N. J., Phinn, S. R., and DeWitt, M. (2019). The global distribution and trajectory of tidal flats. *Nature* 565, 222–225. doi: 10.1038/s41586-018-0805-8

Nilsson, H. C., and Rosenberg, R. (2000). Succession in marine benthic habitats and fauna. *Mar. Ecol.* 197, 139–149. doi: 10.3354/meps197139

Nowell, A. R. M., and Jumars, P. A. (1984). Flow environments of aquatic benthos. *Annu. Rev. Ecol. Syst. Vol.* 15, 303–328. doi: 10.1146/annurev.es.15.110184.001511

Orvain, F., Le Hir, P., Sauriau, P. G., and Lefebvre, S. (2012). Modelling the effects of macrofauna on sediment transport and bed elevation: Application over a cross-shore mudflat profile and model validation. *Estuar. Coast. Shelf Sci.* 108, 64–75. doi: 10.1016/j.ecss.2011.12.036

Pearson, T. H., and Rosenberg, R. (1978). Macrobenthic succession in relation to organic enrichment and pollution of the marine environment. *Ocean. Mar. Bio. Ann. Rev.* 16, 229–331.

Queirós, A. M., Birchenough, S. N. R., and Bremner, J. (2013). A bioturbation classification of European marine infaunal invertebrates. *Ecol. Evol.* 3, 3958–3985. doi: 10.1002/ece3.769

Soulsby, R. (1997). *Dynamics of Marine Sands: A Manual for Practical Applications*. London: Thomas Telford Ltd.

Thrush, S. F., Hewitt, J. E., Herman, P. M. J., and Ysebaert, T. (2005). Multi-scale analysis of species-environment relationships. *Mar. Ecol. Prog. Ser.* 302, 13–26. doi: 10.3354/meps302013

Thrush, S. F., Hewitt, J. E., Norkko, A., Nicholls, P. E., Funnell, G. A., and Ellis, J. I. (2003). Habitat change in estuaries: predicting broad- scale responses of intertidal macrofauna to sediment mud content. *Mar. Ecol. Prog. Ser.* 263, 101–112. doi: 10.3354/meps263101

Townend, I., Fletcher, C., Knappen, M., and Rossington, K. (2011). A review of salt marsh dynamics. *Water Environ. J.* 25, 477–488. doi: 10.1111/j.1747-6593.2010.00243.x

Van Prooijen, B. C., and Winterwerp, J. C. (2010). A stochastic formulation for erosion of cohesive sediments. *J. Geophys. Res. Ocean.* 115, 1–15. doi: 10.1029/2008JC005189

Van Prooijen, B. C., Montserrat, F., and Herman, P. M. J. (2011). A process-based model for erosion of Macoma balthica-affected mud beds. *Cont. Shelf Res.* 31, 527–538. doi: 10.1016/j.csr.2010.12.008

Van Rijn, L. C. (1993). *Principles of sediment transport in rivers, estuaries and coastal seas, Aqua publications*. Blokzijl: Aqua publications.

van Rijn, L. C. (2020). Erodibility of Mud–Sand Bed Mixtures. *J. Hydraul. Eng.* 146:04019050. doi: 10.1061/(asce)hy.1943-7900.0001677

Volkenborn, N., Hedtkamp, S. I. C., van Beusekom, J. E. E., and Reise, K. (2007). Effects of bioturbation and bioirrigation by lugworms (Arenicola marina) on physical and chemical sediment properties and implications for intertidal habitat succession. *Estuar. Coast. Shelf Sci.* 74, 331–343. doi: 10.1016/j.ecss.2007.05.001

Widdows, J., and Brinsley, M. (2002). Impact of biotic and abiotic processes on sediment dynamics and the consequences to the structure and functioning of the intertidal zone. *J. Sea Res.* 48, 143–156. doi: 10.1016/S1385-1101(02)00148-X

Widdows, J., Brinsley, M. D., and Pope, N. D. (2009). Effect of Nereis diversicolor density on the erodability of estuarine sediment. *Mar. Ecol. Prog. Ser.* 378, 135–143. doi: 10.3354/meps07864

Widdows, J., Brinsley, M., Salkeld, P., and Lucas, C. (2000). Influence of biota on spatial and temporal variation in sediment erodability and material flux on a tidal flat (Westerschelde, The Netherlands). *Mar. Ecol. Prog. Ser.* 194, 23–37. doi: 10.3354/meps194023

Willows, R. I., Widdows, J., and Wood, R. G. (1998). Influence of an infaunal bivalve on the erosion of an intertidal cohesive sediment: A flume and modeling study. *Limnol. Oceanogr.* 43, 1332–1343. doi: 10.4319/lo.1998.43.6.1332

Wilson, W. H., and Parker, K. (1996). The life history of the amphipod, Corophium volutator: The effects of temperature and shorebird predation. *J. Exp. Mar. Bio. Ecol.* 196, 239–250. doi: 10.1016/0022-0981(95)00133-6

Wu, W., Perera, C., Smith, J., and Sanchez, A. (2018). Critical shear stress for erosion of sand and mud mixtures. *J. Hydraul. Res.* 56, 96–110. doi: 10.1080/00221686.2017.1300195

Ysebaert, T., and Herman, P. M. J. (2002). Spatial and temporal variation in benthic macrofauna and relationships with environmental variables in an estuarine, intertidal soft-sediment environment. *Mar. Ecol. Prog. Ser.* 244, 105–124. doi: 10.3354/meps244105

Ysebaert, T., Herman, P. M. J., Meire, P., Craeymeersch, J., Verbeek, H., and Heip, C. H. R. (2003). Large-scale spatial patterns in estuaries: Estuarine macrobenthic communities in the Schelde estuary, NW Europe. *Estuar. Coast. Shelf Sci.* 57, 335–355. doi: 10.1016/S0272-7714(02)00359-1

Zhu, Z., Cozzoli, F., Chu, N., Salvador, M., Ysebaert, T., Zhang, L., et al. (2016b). Interactive effects between physical forces and ecosystem engineers on seed burial: A case study using Spartina anglica. *Oikos* 125, 98–106. doi: 10.1111/oik.02340

Zhu, Z., Van Belzen, J., Hong, T., Kunihiro, T., Ysebaert, T., Herman, P. M. J., et al. (2016a). Sprouting as a gardening strategy to obtain superior supplementary food: Evidence from a seed-caching marine worm. *Ecology* 97, 3278–3284. doi: 10.1002/ecy.1613

Conflict of Interest: The authors declare that the research was conducted in the absence of any commercial or financial relationships that could be construed as a potential conflict of interest.

Publisher's Note: All claims expressed in this article are solely those of the authors and do not necessarily represent those of their affiliated organizations, or those of the publisher, the editors and the reviewers. Any product that may be evaluated in this article, or claim that may be made by its manufacturer, is not guaranteed or endorsed by the publisher.

Copyright © 2021 de Smit, Brückner, Mesdag, Kleinhans and Bouma. This is an open-access article distributed under the terms of the Creative Commons Attribution License (CC BY). The use, distribution or reproduction in other forums is permitted, provided the original author(s) and the copyright owner(s) are credited and that the original publication in this journal is cited, in accordance with accepted academic practice. No use, distribution or reproduction is permitted which does not comply with these terms.

frontiers in Marine Science

ORIGINAL RESEARCH
published: 13 October 2021
doi: 10.3389/fmars.2021.733923

ADV-Based Investigation on Bed Level Changes Over a Meso-Macro Tidal Beach

Wenhong Pang[1], Xiaoyan Zhou[1], Zhijun Dai[1], Shushi Li[2], Hu Huang[3] and Yaping Lei[4,5]**

[1] State Key Laboratory of Estuarine and Coastal Research, East China Normal University, Shanghai, China, [2] College of Resources and Environment, Beibu Gulf University, Qinzhou, China, [3] Key Laboratory of Coastal Science and Engineering, Beibu Gulf University, Qinzhou, China, [4] School of Marine Sciences, Sun Yat-sen University, Zhuhai, China, [5] Southern Marine Science and Engineering Guangdong Laboratory (Zhuhai), Zhuhai, China

Beach intra-tidal bed level changes are of significance to coastal protection amid global climate changes. However, due to the limitation of instruments and the disturbance induced by wave motions superimposed on water levels, it was difficult to detect the high-frequency oscillation of the submerged beach bed level. In this study, an observation, lasting for 12 days and covering the middle tide to the following spring tide, was conducted on a meso-macro tidal beach, Yintan Beach, to simultaneously detect the characteristics and influence mechanism of bed level changes at intra-tidal and tidal cycle scales. The collected data included water depth, suspended sediment concentration (SSC), waves, high-frequency three-dimensional (3-D) velocity, and the distance of the seabed to the acoustic Doppler velocimeter (ADV) probe, which were measured by an optical backscatter sensor, two Tide & Wave Recorder-2050s, and an ADV, respectively. The results showed that the tidal cycle-averaged bed level decreased by 58.8 mm, increased by 12.6 mm, and increased by 28.9 mm during neap, middle, and spring tides in succession, respectively, compared with the preceding tidal regimes. The net erosion mainly resulted from large incident wave heights and the consequent strong offshore-directed sediment transport induced by undertows. Moreover, the variations in the bed level were more prominent during a neap to middle tides than during middle to spring tides, which were jointly caused by the wave-breaking probability regulated by water depth and the relative residence times of shoaling wave, breaker, and surf zones that were determined by relative tidal range. In terms of the intra-tidal bed level, it displayed an intra-tidal tendency of increase during floods and decrease during ebb tides, i.e., the intra-tidal bed level changes were controlled by water depth, which modulated the effects of waves on sediment resuspension and vertical sediment exchange. To be specific, waves and SSC were responsible for the intra-tidal bed level changes under low-energy wave conditions, while mean current and bedform exerted important influences on the variations of the intra-tidal bed level under moderate wave conditions, which broke the foregoing interrelation between bed level, waves, and SSC. This study, therefore, emphasizes the usage of ADV measurement to investigate bed level changes in sandy coasts.

Keywords: bed level change, intra-tidal variation, wave conditions, meso-macro tidal beach, ADV measurement

OPEN ACCESS

Edited by:
Zeng Zhou,
Hohai University, China

Reviewed by:
Shiqiang Yan,
City University of London, United Kingdom
Zhiguo He,
Zhejiang University, China
Zhenghong Tang,
University of Nebraska-Lincoln, United States

***Correspondence:**
Zhijun Dai
zjdai@sklec.ecnu.edu.cn
Yaping Lei
eeslyp@mail.sysu.edu.cn

Specialty section:
This article was submitted to Coastal Ocean Processes, a section of the journal Frontiers in Marine Science

Received: *30 June 2021*
Accepted: *01 September 2021*
Published: *13 October 2021*

Citation:
Pang W, Zhou X, Dai Z, Li S, Huang H and Lei Y (2021) ADV-Based Investigation on Bed Level Changes Over a Meso-Macro Tidal Beach. Front. Mar. Sci. 8:733923. doi: 10.3389/fmars.2021.733923

INTRODUCTION

The beach is a highly dynamic and active morphological system that connects the land and the ocean and is affected by the combined actions of intense coastal forces including waves, tides, and currents, which constitute over 30% of the world's ice-free coastlines (Luijendijk et al., 2018; Vousdoukas et al., 2020). At the same time, the beach serves as a natural barrier, a soft defense compared with human-made hard structures, to protect the coastal hinterland against flooding and extreme storm surges using wave energy dissipation (Rijn, 2009, 2010; Slobbe et al., 2013; Stive et al., 2013). Hence, more and more concerns have been revealed on the mechanism of beach bed level changes since the twentieth century in the context of the higher frequency and greater intensity of extreme hydrological events (Vellinga, 1982; Rijn, 2011; Li et al., 2014; Masselink and Heteren, 2014; Hu et al., 2015) coupled with global sea-level rise (Nerem et al., 2018; Zhang et al., 2020), especially for low-lying coastal and island countries (Nicholls and Cazenave, 2010; Stive et al., 2013; Pucino et al., 2021).

So far, the major researches on bed level changes concerning meso-macro tidal and macro-tidal beaches (mean spring tidal range >3 m) were reported from the northern coasts of Australia, northwestern coasts of Netherlands, France, and Belgium, northern coasts of New Zealand, and almost all the coasts of England excluding its northern coasts (Kroon and Masselink, 2002; Austin and Masselink, 2006; Sedrati and Anthony, 2007; Masselink et al., 2008; Poate et al., 2014; Biausque and Senechal, 2019). For meso-macro tidal and macro-tidal beaches, which are mainly featured with gentle beach slopes and dissipative beach states, the bed level changes were suppressed and were at the level of <5 cm for most of the cases over one tidal cycle, even after going through a storm surge event (Aagaard et al., 1998b; Anthony et al., 2004; Masselink et al., 2007; Puleo et al., 2014). Meanwhile, there tend to be no conspicuous patterns in the amplitudes of bed level changes for different tidal regimes (i.e., neap to spring tides), as larger bed level change amplitudes could occur during either spring or neap tides erratically (Brand et al., 2020). Specifically, the subdued bed level changes in response to large tide ranges were associated with larger morphological relaxation times caused by the small residence time of wave-related swash and surf zone processes on account of the larger horizontal tidal translation for meso-macro tidal beaches (Kroon and Masselink, 2002; Anthony et al., 2004; Reichmüth and Anthony, 2007). On the other hand, it was suggested that the limited net bed level changes of meso-macro tidal beaches over one tidal cycle resulted from the compensation of onshore sediment transport-induced accretion, which was derived from swash zone processes during low tides, for the strong offshore sediment transport-induced erosion under surf zone conditions (Aagaard et al., 2005). In contrast, it was reported that the significant bed level changes occurring over micro-tidal beaches were owing to the strong offshore-directed undertows resulting from the sudden release of incident wave energy on steep slopes (Coco et al., 2004; Agredano et al., 2019). Hence, to find out the main factor dominating the mechanism of bed level changes, a comprehensive analysis of intra-tidal bed level changes throughout different tidal cycles and incident wave conditions over a meso-macro tidal beach is needed.

It is generally acknowledged that two different patterns of beach bed level change exist under low-energy waves and stormy conditions (Aagaard et al., 1998a, 2006; Houser and Greenwood, 2007). Under low-energy wave conditions, when bar-trough systems prevailed, the beach face shoreward of the bar crest tended to accrete due to mean onshore flows across the bar surface at relatively shallow water depths (Masselink et al., 2008; Capo et al., 2009). It was suggested that the mechanism of bed level accretion was associated with three-dimensional (3-D) cell circulation (Aagaard et al., 1998a, 2006), during which the onshore sediments transported by incident waves were not returned straightly seaward by weak offshore mean flows, but through alongshore feeders and rip channels, which eventually contribute to the infill of runnels landward of the bar crest and the weld of the bar to the beach face (Kroon and Masselink, 2002; Houser et al., 2006; Falqués et al., 2008). Under energetic wave conditions or stormy conditions, larger asymmetric incident waves broke at deeper locations once the breaker indices were approached, which lead to a wider and highly dissipative surf zone with high-energy water motions (Gallagher et al., 1998; Vidal-Ruiz and de Alegría-Arzaburu, 2020). As a result, the bed level at upper or whole beaches featured by the bar-trough system was strongly eroded, which was related to vertical undertow circulation (Quartel et al., 2008; Ribeiro et al., 2012; Brand et al., 2019). Specifically, a great amount of eroded sediments stirred up by incident waves and enhanced infra-gravity waves were transported offshore to the lower beach or the subtidal zone by a strong offshore-directed undertow (Beach and Sternberg, 1991; Russell, 1993; Aagaard et al., 2006, 2012, 2013), which led to a relatively plane cross profile. Since mean currents contributed inversely to the bed level changes under different wave conditions, further explorations need to be conducted to evaluate the role of mean currents on vertical sediment exchange and intra-tidal bed level changes.

For the studies about bed level changes concerning different geomorphic units over a meso-macro tidal beach, a portion of them focused on the measurement and prediction of intertidal bar evolution under different wave conditions (Vousdoukas et al., 2011; Ge et al., 2017; López-Dóriga and Ferreira, 2017; Brand et al., 2020), as the intertidal bar is a common feature of meso-macro tidal beaches, which are commonly short of other secondary morphological features such as beach cusps, low-tide terraces, skew bars, and rip morphology (Wright et al., 1987; Short, 1991; Masselink et al., 2007). Additionally, in recent years, more and more studies have attempted to distinguish the respective features of bed level changes within different wave zones (i.e., shoaling wave zone, surf zone, and swash zone). Specifically, net bed levels tended to increase persistently as a result of onshore-directed sediment transport by incident shoaling waves within the shoaling wave zone, where incident wave components dominate the net sediment transport direction (Russell et al., 1995; Tinker et al., 2009). At the surf zone, where wave break-induced turbulent eddies and undertows prevail, beach face erosion occurred persistently due to significant offshore-directed sediment transport induced

by strong offshore-directed mean currents coupled with large amounts of suspended sediments resulting from turbulence-enhanced bed shear stresses (Saulter et al., 2003; Masselink, 2004; Ruessink et al., 2016). Hence, the surf zone is the most dynamics-sensitive zone when it comes to bed level changes at the beach profile (Aagaard et al., 2002; Mariño-Tapia et al., 2007). Furthermore, in the swash zone, which is featured by cycled asymmetric uprush and backwash processes (Pritchard and Hogg, 2005), the net bed level changes were vitally determined by incident wave strength, during which the bed level gradually increased due to the uprush-dominated onshore-directed pre-suspended sediment transport during relatively low-energy wave conditions, while the beach face was eroded as backwashes became more efficient transporters of local sediments under energetic waves or stormy conditions (Masselink et al., 2005; Ruessink et al., 2016). Hence, a study analyzing the features of intra-tidal bed level changes within the surf zone under different wave conditions is also necessary.

Although much attention has been paid to beach bed level changes, only a few researchers accurately obtained the intra-tidal variations of bed levels as their data on bed levels were commonly obtained during low tides (beach face was exposed in the air) or the way that the bed levels were measured using inserted rods would, to some extent, affect the accuracy of the bed level (Arnaud et al., 2011; Ge et al., 2017; Agredano et al., 2019; van Bemmelen et al., 2020). Hence, in this study, we carried out an observation to measure the intra-tidal variations of bed levels using an alternative way, i.e., acoustic Doppler velocimeter (ADV) measurement, within the surf zone from shoaling wave conditions to surf conditions on a meso-macro tidal beach, Yintan Beach, with the aims (1) to detect the characteristics of bed level changes at intra-tidal and tidal cycle scales, respectively and (2) to analyze the influence mechanism of intra-tidal bed level changes under different wave conditions.

METHODOLOGY

Field Sites Setting

Comprehensive field observation was conducted at Yintan Beach (**Figures 1A–C**), Beihai City, China, from May 28 to June 9, 2016. The beach is defined as a meso-macro tidal beach with a mean spring tidal range of 3.6 m, and it experiences diurnal tidal conditions during middle and spring tides, whereas semidiurnal tides operate during neap tides (Huang et al., 2011). According to Huang et al. (2011), the mean values of the flood and ebb tidal currents in the spring tide within Lianzhou Bay are 0.13 and 0.31 m/s, respectively. The mean wave height in the nearshore of Yintan Beach is ∼0.5 m and varies significantly in different seasons (Zhou et al., 2015). In addition, the wave direction is northward during winter and southwest during summer under the impacts of the southwest monsoon. Especially, strong southwest wind waves attack the beach periodically for consecutive days each month during summer, according to the local inhabitants.

Bar-trough systems develop in both the intertidal and subtidal zones of Yintan Beach (Ge et al., 2017). An obvious and straight sandbar exists in the middle tide zone during the observation with an angle of 28° between the sandbar and latitude direction. The sediments here mainly consist of unconsolidated quartz sands, and the median grain size varies from 0.125 to 0.233 mm (Ma et al., 2019) across the intertidal zone, which leads to a whole averaged slope of 8‰ over the intertidal zone of Yintan Beach (Pang et al., 2019). Meanwhile, the beach face would suffer from tropical cyclones (typhoons) from May to November each year, which lead to the significant morphological changes of the intertidal beach (Ji, 2007; Ge et al., 2017).

Instrument Setup

The field measurement was conducted at the middle part (surf zone) and subtidal area of Yintan Beach synchronously (**Figures 1C,D**), which lasted from middle tide to neap tide, and finally, to spring tide (**Figure 2A**). During the observation, for the instrument site at the middle part of Yintan Beach (Site A, **Figures 1D,E**), an aluminum frame was equipped with an ADV (6-MHz vector current meter, Nortek AS, Rud, Norway) to record the distance from the seabed to the ADV probe (DSP) (at an accuracy of ±1 mm, Andersen et al., 2006; Zhu et al., 2019) and the high-resolution 3-D flow velocity (u, v, and w), an optical backscatter sensor (OBS-3A) (D&A Instrument Company, Port Townsend, Washington, USA) was used to measure the water depth (h) and turbidity (transferred to suspended sediment concentration, SSC), and a Tide & Wave Recorder-2050 (TWR-2050) (Company, RBR Ltd., Ottawa, Canada) was used to obtain wave heights. For the instrument site at the subtidal area (Site B, **Figures 1D,F**) which was ∼180 m seaward from Site A, another TWR-2050 was fixed within an aluminum quadripod to measure the wave heights.

To be specific, at Site A, two vertical rods of the aluminum frame were inserted into the ground for ∼1.2 m. Hence, it was assumed that the aluminum frame equipped with the ADV was stable and that the measurement of the bed level was hardly influenced by gravity-induced sink over the short-term 12-day observation. The ADV was fixed onto two horizontal rods with the sensors facing downward and the measurement volume located 7 cm above the seabed at the beginning of the observation (**Figure 1E**). Meanwhile, the ADV recorded 19,200 measurements at a frequency of 64 Hz every 10 min for the first three tidal cycles (**Table 1**). In the remaining tidal cycles, the ADV was sampling at 2 Hz for consecutive 1,024 s per 30 min. At the same time, the distance between the seabed and the DSP was recorded at the start and end of the real-time measurement. For the convenient analysis of bed level changes and velocity throughout the time series, the velocity data from the ADV for the first three tidal cycles were resampled at 2 Hz. It is worth noting that the way the bed level was obtained using ADV measurement in our study was acoustic and non-intrusive, which would hardly affect the natural characteristics of the bed level changes. Thus, it was deduced that using ADV measurement on bed levels is a better way than the classical methods (e.g., inserted rod method) with better accuracy.

In addition, at Site A, the OBS-3A was attached to a vertical pod and it obtained h and SSC at intervals of 1 min, with its turbidity probe being 7 cm above the seabed as well (**Table 1**). Moreover, the TWR-2050 at Site A was attached to the other

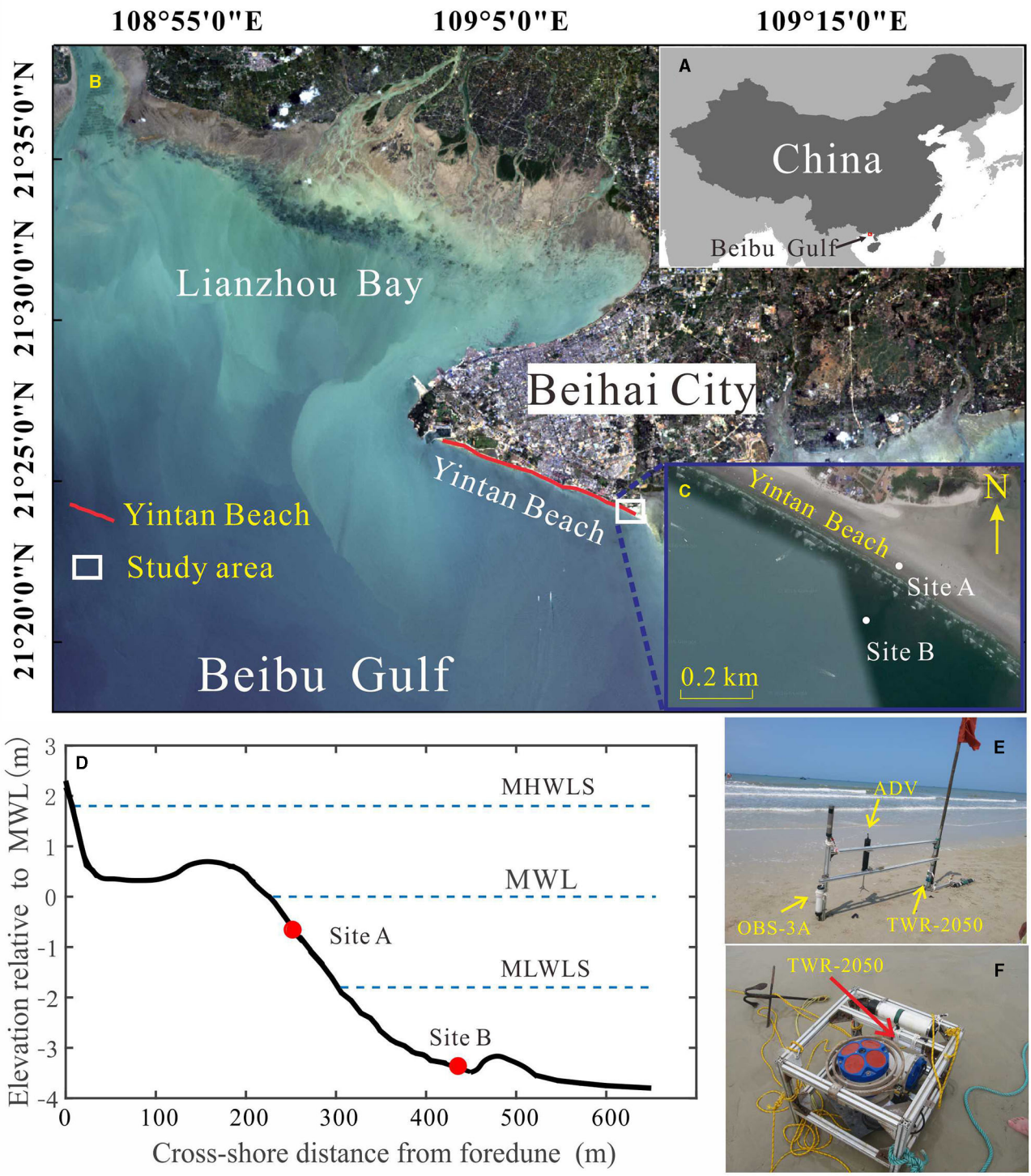


FIGURE 1 | Study area and instrument deployment. **(A)** The location of Beibu Gulf; **(B)** the location of Yintan Beach and **(C)** the study area of Yintan Beach with the location of instrument sites. **(D)** Beach profile of the instrument sites at the beginning of the field observation and the cross-shore location of Site A and Site B (x = 0 indicated the foot of foredune), with the three horizontal, dashed lines representing the mean high water level of spring tides (MHWLS), mean water level (MWL), and mean low water level of spring tides (MLWLS), respectively; **(E)** instrument deployment upon the aluminum frame at Site A and **(F)** the deployment of Tide & Wave Recorder-2050 (TWR-2050) upon the aluminum quadripod at Site B.

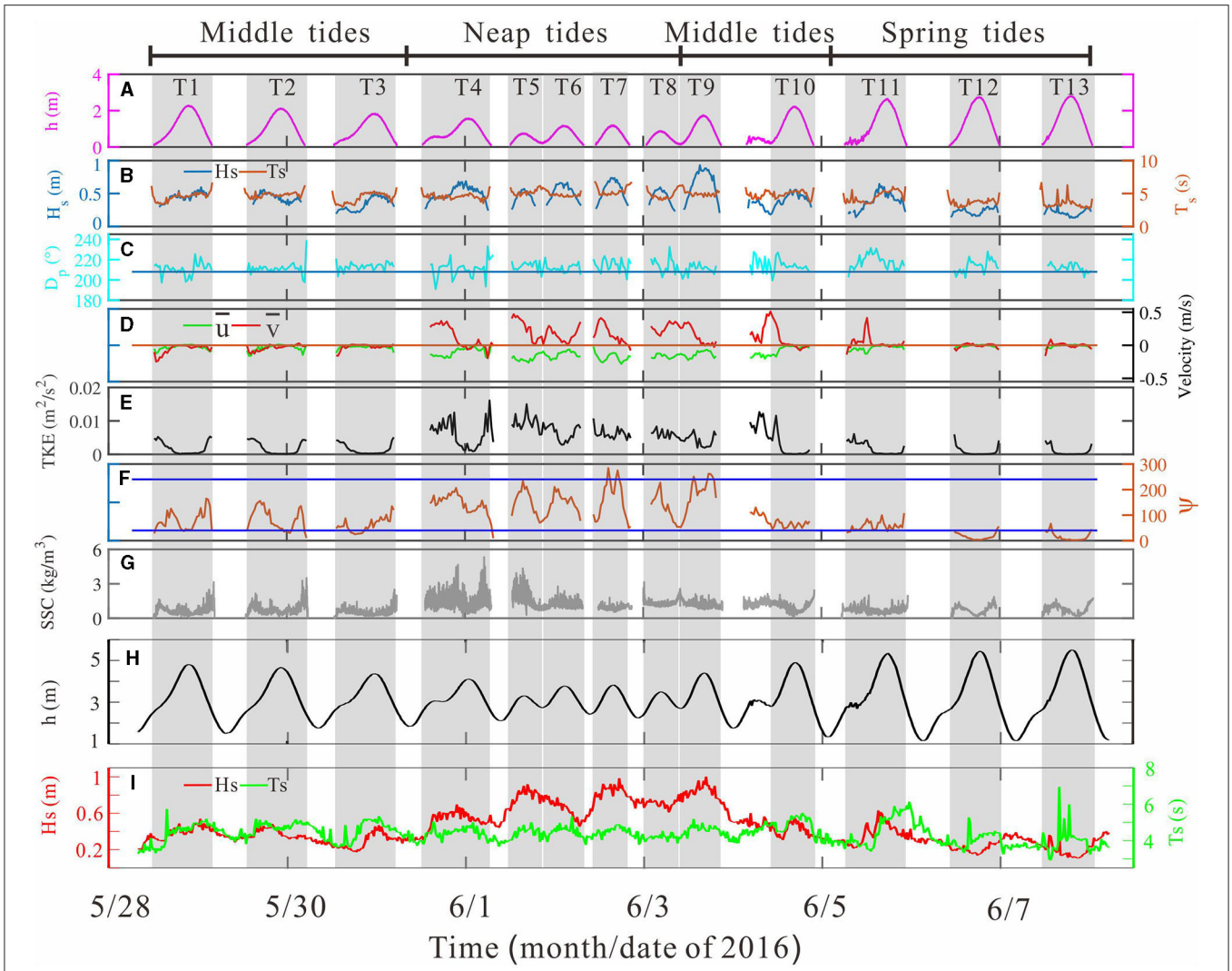


FIGURE 2 | Time series of **(A)** water depth, h; **(B)** significant wave height, Hs (blue line), and significant wave period, Ts (red line); **(C)** peak wave direction, Dp, and horizontal line indicated the normal direction (208°); **(D)** mean cross-shore velocity, $\overline{u}$ (green line), and alongshore velocity, $\overline{v}$ (red line); **(E)** turbulent kinetic energy, TKE; **(F)** mobility number, ψ (orange line), and two blue lines indicated $\psi = 240$ and 40, respectively; **(G)** suspended sediment concentration, SSC at Site A. Time series of **(H)** water depth, h; **(I)** significant wave height, Hs (red line) and significant wave period, Ts (green line) at Site B.

TABLE 1 | Overview of instrument setup and related obtained elements during the observation.

Instrument site	Instrument	Related obtained element	Sample rate/Burst (interval)	Measurement location above seabed (cm)
Site A	ADV	Distance of seabed to ADV probe (DSP), mean current, wave direction, Turbulent kinetic energy (TKE)	64 Hz/10 min (for the first three tidal cycles) 2 Hz/30 min (for the remaining tidal cycles)	7 7
	TWR-2050	Wave height (H), wave period (T)	4 Hz/20 min	10
	OBS-3A	Suspended sediment concentration (SSC), water depth (h)	10 Hz/1 min	7
Site B	TWR-2050	Wave height (H), Wave PERIOD (T)	4 Hz/20 min	40

vertical pod, with its pressure sensor placed 0.1 m above the seabed, and was logged at 4 Hz to record the pressure over a consecutive period of 512 s every 20 min (**Table 1**). Afterward, the recorded pressure was converted to wave height and wave period by linear wave theory (Gibbons et al., 2005). In addition, at Site B, the TWR-2050 was sampling with the same measurement

parameters as that of the TWR-2050 at Site A, and its probe was ∼0.4 m above the seabed (**Table 1**).

Data Processing

Estimate of Turbulent Kinetic Energy

Turbulent kinetic energy was used to describe the strength of the water turbulent velocity fluctuation and has a potential effect on the sediment suspension in the nearshore area (Alsina and Cáceres, 2011; Yoon and Cox, 2012; Christensen et al., 2019). Turbulent kinetic energy (TKE) was calculated following Svendsen (1987):

$$\mathrm{TKE} = \frac{1}{2}\left(u'^2 + v'^2 + w'^2\right) \tag{1}$$

where u, v, and w refer to the x, y, and z components of velocity, respectively, and $'$ indicates the turbulent oscillation component. Moreover, the turbulent fluctuations were obtained by separating the turbulent velocity (u'), off mean velocity ($\overline{u}$), and velocity due to waves (u_w), since the measured high-frequency velocity (u (t)) can be written as:

$$\mathrm{u(t)} = \overline{u} + u_w(t) + u'(t) \tag{2}$$

where $\overline{u}$ was the mean cross-shore velocity and the overbar of $\overline{u}$ indicated the time average, u_w was obtained by bandpass filtering (with a cut-off frequency of 0.5 and 0.005 Hz) the detrended and mean-subtracted u time series, wherein initially, the data quality was checked, the outliers were replaced, and the high-frequency noise was removed.

Calculation of Mean Daily Relative Tide Range and Horizontal Tidal Translation Rate

The mean daily relative tide range (MDRTR), modified from the relative tide range (RTR), which was a dimensionless parameter to reflect the relative importance of the shoaling wave, surf zone, and swash processes (Masselink and Short, 1993) over the sandy beach, was calculated by the ratio of the daily tide range (TR_D) to the mean breaker wave height (H_b) over a tidal cycle:

$$\mathrm{MDRTR} = TR_D/H_b \tag{3}$$

where H_b was estimated following Komar and Gaughan (1972):

$$H_b = 0.39g^{0.2}(T_sH_0^2)^{0.4} \tag{4}$$

where g was gravity acceleration, T_s was significant wave period, and H_0 was the deep-water wave height. In the study, H_0 was replaced with the significant wave height (H_s) from the instrument site at the subtidal area (Site B).

The horizontal tidal translation rate [V_{tide}(t)], which determined the duration of the wave zone processes and influenced the relaxation time of beach morphological changes, was calculated using the following equation modified from Anthony et al. (2004):

$$V_{tide}(t) = \frac{\frac{(h(t+dt)-h(t-dt))}{(2^*dt)}}{\tan\beta} \tag{5}$$

where $h\left(t+dt\right)$ and $h(t-dt)$ were the water depth at (t + dt) s and (t – dt) s. tan β was the local beach slope, which was ∼2.2% during the observation.

Bed Shear Stress Induced by Wave and Current

Bed shear stress is a characteristic index for the seabed hydrodynamic condition, which is related to the near-bed sediment mobilization (Grant and Madsen, 1979). In the study, the bed shear stress due to current (τ_c) was estimated following the vertical TKE method (e.g., Kim et al., 2000; Hu et al., 2020), given by

$$\tau_\mathrm{c} = \mathrm{c}{*}\rho w'^2 \tag{6}$$

where ρ = 1,025 kg/m^3 was the density of the seawater, w' was the vertical turbulent velocity referring to the current contribution, and $c = 0.9$ was the constant of proportionality under diverse conditions.

The bed shear stress due to waves (τ_w) was obtained by Soulsby (1997):

$$\tau_\mathrm{w} = \frac{1}{2}\rho \mathrm{f_w U_w^2} \tag{7}$$

where f_w was the wave friction factor and U_w was the maximum instantaneous horizontal wave-induced orbital velocity, which was calculated by

$$\mathrm{U_w^2} = \mathrm{u_w^2} + \mathrm{v_w^2} \tag{8}$$

where u_w and v_w were the maximum cross-shore and alongshore wave orbital velocity, respectively. Moreover, f_w was estimated by

$$\mathrm{f_w} = \exp\left[5.213(\frac{\mathrm{k_s}}{\mathrm{A}})^{0.194} - 5.977\right] \tag{9}$$

where k_s was the bed roughness height given by $2.5D_{50}$ (D_{50} = 0.125 mm was the median grain size) and A was the bottom orbital semi-excursion, which was estimated by

$$\mathrm{A} = \frac{\mathrm{U_m T}}{2\pi} \tag{10}$$

where U_m was the maximum wave orbital velocity over the incident wave cycle, which was determined by wave height, h, and wave period and was roughly equal to U_w of Equation (8). T was the individual wave period defined as the interval of two adjacent points by zero-down crossing.

Thus, the bed shear stress under combined wave and current (τ_{cw}) was calculated following Grant and Madsen (1979):

$$\tau_\mathrm{cw} = \sqrt{(\tau_\mathrm{w} + \tau_\mathrm{c}|\cos\varphi_\mathrm{cw}|)^2 + (\tau_\mathrm{c}\sin\varphi_\mathrm{cw})^2} \tag{11}$$

where φ_{cw} was the angle between the wave and the current. The current direction (φ_c) was obtained by cross-shore and alongshore mean velocity (u_m and v_m):

$$\varphi_\mathrm{c} = \arctan(\frac{\mathrm{u_m}}{\mathrm{v_m}}) \tag{12}$$

The wave direction (φ_w) was derived from the maximum number of direction counts of each measurement burst, where the instantaneous wave direction was acquired by instantaneous cross-shore and alongshore wave orbital velocity (u_w and v_w) in the form similar to Equation (12).

Calculation of Sediment Mobility Number

The sediment mobility number (ψ), which was defined as the ratio of the driving force to the resisting force on the sands over the seabed, was usually used to reflect the dynamics of the bottom boundary layer and the bedform morphology (Dingler and Inman, 1976; Nielsen, 1981). The mobility number was defined as

$$\psi = \frac{U_m^2}{(s-1)gD_{50}} \tag{13}$$

where $s = 2.65$ was the specific density of the sand, and U_m and D_{50} were the maximum wave orbital velocity and median grain size, respectively.

Normalization of Data Time Series

To detect the relationship between the intra-tidal variations of SSC, bed shear stress (τ), h, and bed level (reflected by the distance of the seabed to the DSP), the data on these parameters were normalized against relative tidal phases, $\frac{t}{T}$, and then phase-averaged. The obtained normalized data ($y(k)$) were expressed as follows:

$$y(k) = \frac{x(k) - \min(x(k))}{\max(x(k)) - \min(x(k))} \tag{14}$$

where $x(k)$ were the original measured data, $k = 1, 2, 3, \ldots n$ was the burst sequence of within tidal cycle, and $\max(x(k))$ and $\min(x(k))$ were the maximum and minimum values, respectively, of the original data of each tidal cycle.

Then, the normalized data mentioned above were divided into 20 ensembles, and the ensembles at the same normalized time ($\frac{t}{T}$) were averaged to obtain the relative data set of DSP, SSC, τ_w, and τ_c.

RESULTS

Hydrodynamics and Suspended Sediment Concentration Variations

The measured data went through 13 tidal cycles (marked as T1 to T13, respectively, where one tidal cycle was defined from low tide to the following low tide, **Figure 2A**), during which the highest h of each tide cycle ranged between 0.75 and 2.81 m throughout the observation. Additionally, h ranged between 1.12 and 5.55 m at Site B (**Figure 2H**). Accordingly, T1–T3 and T9–T10 were subjected to middle tide regimes, and T4–T8 was under neap tide regimes, while T11–T13 were encountered with spring tide regimes (**Figure 2A**).

At Site A, the Hs varied between 0.16 and 0.6 m during the first three tidal cycles (T1 to T3), and it did not show a positive relationship with h. The Hs increased abruptly over the following six tidal cycles due to the breakout of local wind. The maximum h reached 0.94 m at the high water level of T9. Then, the Hs began to decrease, and the minimum h of 0.12 m occurred at a high tide of T13. It was noted that the averaged tidal-cycle Hs ranged between 0.21 and 0.65 m during the observation (**Table 2**). At Site B, Hs ranged from 0.10 to 1.01 m and showed a similar variation trend compared with Site A during the observation (**Figures 2B,I**). Thus, we considered that the beach experienced two kinds of wave conditions (Masselink et al., 2006, 2007), i.e., moderate wave conditions (T4 to T9, tidal cycle-averaged Hs approximately >0.5 m) and low-energy wave conditions (T1 to T3 and T10 to T13, tidal cycle-averaged Hs <0.5 m). Accordingly, both the significant wave period (Ts) fluctuated between 2.7 and 6.8 s at Sites A and B. However, the Ts seemed to display no significant variation trend at Site A, while it showed a positive correlation with the h at Site B (**Figures 2B,I**). During the observation, the incident wave direction ranged between 182 and 240°, and the average of 212° (**Figure 2C**) indicated that Yintan Beach was dominated by southwest waves, which advanced obliquely with the alongshore sandbar (208°, relative to the north direction).

TABLE 2 | Tidal cycle-averaged significant wave height (Hs), cross-shore velocity ($\overline{u}$), turbulent kinetic energy (TKE), and near-bed suspended sediment concentration (SSC) of the observation at Site A.

Tidal cycle	Mean Hs (m)	Mean $\overline{u}$ (m/s)	Mean TKE (kg/ms^2)	SSC (kg/m^3)
T1	0.45	−0.03	1.93	0.67
T2	0.43	−0.04	1.91	0.75
T3	0.33	−0.03	1.50	0.56
T4	0.51	−0.10	6.13	1.52
T5	0.49	−0.19	9.49	1.65
T6	0.52	−0.14	6.28	1.20
T7	0.55	−0.18	6.34	0.93
T8	0.48	−0.16	6.02	1.34
T9	0.65	−0.14	4.26	1.20
T10	0.38	−0.09	4.38	1.01
T11	0.39	−0.04	1.85	0.69
T12	0.23	−0.01	0.89	0.73
T13	0.21	−0.01	0.93	0.78

The mean cross-shore velocity ($\overline{u}$) and alongshore velocity ($\overline{v}$) were weak and showed similar variation trends during the initial three tidal cycles (T1 to T3) and the last two tidal cycles (T12 and T13), during which the corresponding maximum values were negative and no more than 0.25 m/s (oriented northwest and offshore for $\overline{v}$ and $\overline{u}$, respectively). However, from T4 to T11, both $\overline{u}$ and $\overline{v}$ increased obviously and tended to maintain large levels at low h, with the peaks up to −0.29 and 0.50 m/s, respectively. At Site A, the averaged tidal-cycle $\overline{u}$ ranged between −0.01 and −0.19 m/s during the observation.

The TKEs were relatively small in T1–T3 and T11–T13, and they ranged between 4×10^{-5} and 0.006 m^2/s^2 at Site A (**Figure 2E**). Meanwhile, higher TKEs occurred at a relatively low h. During T4 and T10, the TKEs tended to be generated constantly in the water column, corresponding to large Hs and

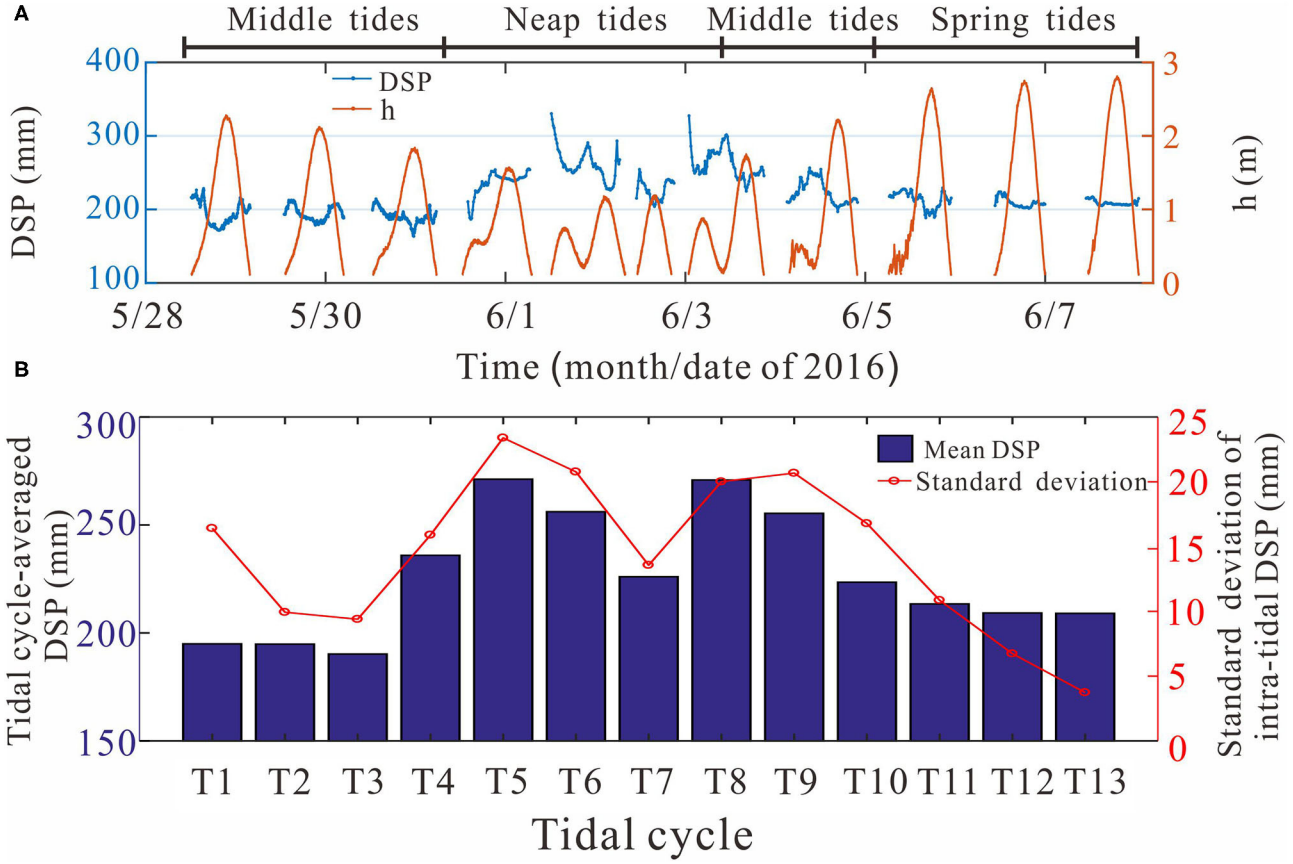


FIGURE 3 | Time series of **(A)** distance of seabed to acoustic Doppler velocimeter (ADV) probe (DSP, blue line) against h (red line); **(B)** tidal cycle-averaged distance of the seabed to the ADV probe (DSP, blue bars) and the SD of the intra-tidal distance of the seabed to the ADV probe of each tidal cycle (red circles and lines).

neap tides, during which the peak TKE (close to 0.016 m^2/s^2) occurred at the end of the ebb tide of T4 and the high tide of T5.

The ψ mainly varied between 40 and 240 for T1, T2, T3, T10, and T11 (ψ ranged from 3 to 203), while it was primarily lower than 40 for T12 and T13 (0–63) at Site A (**Figure 2F**). During the rest of the tidal cycles, almost all the ψ were larger than 40 and the ψ were even >240 during T7 and T9, where large Hs and relatively low tidal ranges coincided. The variations of ψ indicate that three kinds of seabed morphology existed during the observation, including vortex ripple, post-vortex ripple, and plane seabed.

The near-bed SSCs showed two kinds of variations in magnitude during the observation; for instance, SSCs mainly ranged between 0.4 and 5.3 kg/m^3 during T4 to T10 and varied from 0 to 3.4 kg/m^3 for the rest of the tides. It is noteworthy that fewer sediments were suspended into the water column during high tide, while more large SSCs occur at low h (0.4–0.8 m) for the beach face that commonly suffered from relatively strong surf zone processes within such h ranges. In summary, larger sediments were suspended into the water column by larger Hs as larger SSCs (SSC = 0.93–1.65 kg/m^3) occurred under moderate wave conditions (Hs = 0.48–0.65 m).

Bed Level Changes Under Different Tidal Cycles

The bed level changes could be well-reflected by the distances between the seabed and the DSP, which were recorded by the ADV at the beginning and the end of each burst. As shown in **Figure 3A**, the distances between the seabed and the DSP (note that a larger DSP indicated a lower bed level and vice versa) ranged between 163.4 mm at the high tide of T3 and 330.3 mm at the start of the flood tide of T4. By comparing the tidal cycle-averaged DSP, the temporal variations of bed level changes could be identified. As shown in **Table 3**, the variations of the adjacent tidal cycle-averaged DSPs ranged between −45.7 and +30.1 mm throughout the 13 tidal cycles. Reflected by the SD of intra-tidal bed level changes over each tidal cycle (**Table 3**), the largest amplitude (SD = 23.39) of tidal-cycle bed level changes occurred over T5, which was under the combination of neap tide and moderate wave conditions, while the smallest amplitude (SD = 3.73) of tidal-cycle bed level changes occurred over T13, which was subjected to spring tide coupled with low energy wave conditions.

The variations of tidal-cycle bed levels showed distinctive characteristics in different tidal regimes and wave conditions

TABLE 3 | The comparison of tidal cycle-averaged DSPs between different tidal cycles (negative value indicated erosion and positive value indicated accretion for beach bed level), and the standard deviation of intra-tidal bed level changes of each tidal cycle.

Tidal cycle	Compared to former tidal cycle (mm)	Compared to T1 (mm)	Standard deviation (mm)
T1	–	–	16.41
T2	0.1	0.1	9.93
T3	4.6	4.7	9.39
T4	−45.7	−41.0	15.89
T5	−35.3	−76.3	23.39
T6	15.1	−61.2	20.77
T7	30.1	−31.1	13.56
T8	−44.8	−75.9	20.01
T9	15.4	−60.4	20.67
T10	31.9	−28.5	16.78
T11	10.0	−18.5	10.85
T12	4.2	−14.3	6.73
T13	0.2	−14.1	3.73

TABLE 4 | The statistics of distances of seabed to ADV probe over tidal cycles (averaged DSPs), standard deviations of intra-tidal bed level changes, and averaged significant wave heights (averaged Hs) classified by tidal regimes and wave conditions.

Tidal regime/wave condition	Tidal cycle	Averaged DSP (m)	Averaged standard deviations of intra-tidal bed level changes (m)	Averaged Hs (m)
Middle tides	T1-T3	193.3	11.91	0.40
Neap tides	T4-T8	252.1	18.72	0.50
Middle tides	T9-T10	239.5	18.72	0.52
Spring tides	T11-T13	210.6	7.11	0.28
Low energy wave condition	T1-T3	193.3	11.91	0.40
Moderate wave condition	T4-T9	250.0	19.05	0.53
Low energy wave condition	T10-T13	214.5	9.53	0.30

(**Table 4**). During T4 and T8, which were subjected to neap tide regimes, the tidal cycle-averaged DSP was 252.1 mm, which meant that the bed level decreased by 58.8 mm compared with the preceding middle tides. During T9–T10, which were in middle tide regimes, the tidal cycle-averaged DSP was 239.5 mm, which indicated that the bed level increased by 12.6 mm compared with the preceding neap tides. Finally, during T11–T13, which were subjected to spring tide regimes, the tidal cycle-averaged DSP was 210.6 mm, which indicated that the bed level further increased by 28.9 mm compared with the preceding middle tides. Noticeably, the tidal cycle-averaged DSP of T13 was 14.4 mm smaller than that of T1, which indicated that the beach face was eroded as a whole throughout the entire field observation. Moreover, larger amplitudes ($SD = 18.72$) of tidal-cycle bed level changes occurred under both neap and middle tides, while the smaller amplitudes ($SD = 7.11$) of tidal-cycle bed level changes occurred under spring tides by comparing the SDs of their tidal-cycle bed level changes.

According to the wave conditions, the variations of the tidal cycle-averaged DSPs were mainly classified as three stages (**Table 4**), and the three stages correspond to T1–T3 (middle tides, mean Hs = 0.4 m, low-energy wave conditions), T4–T9 (neap tides to middle tides, mean Hs = 0.53 m, moderate wave conditions), and T10–T13 (middle tides to spring tides, mean Hs = 0.3 m, low-energy wave conditions), with the mean DSP equal to 193.3, 250, and 214.5 mm, respectively. The time series of the DSPs indicated that the bed levels experienced an overall erosion (−56.7 mm) during T4–T9 (moderate wave conditions) relative to T1–T3 (low-energy wave conditions), followed by a gradual deposition (+35.5 mm) during T10–T13 (low-energy wave conditions) until the end of the observation. Hence, it was suggested that the beach face tended to gain accretion under low-energy wave conditions and erode under moderate wave conditions. Meanwhile, the averaged SD of the tidal-cycle bed level changes over T4–T9, which were subjected to moderate wave conditions and neap to middle tides, was 19.05. In contrast, the averaged SDs over T1–T3 (middle tides) and over T10–T13 (middle to spring tides) were 11.91 and 9.53, respectively, which were merely 0.63 and 0.5 times as large as that over T4–T9 (**Table 4**). Hence, the comparison of the SDs of bed level changes indicated that bed level changes during relatively smaller tidal ranges (neap tides) were more pronounced and were sensitive to breaking wave and surf zone processes, while the variations of bed level changes under larger tidal ranges (spring tides) were limited (**Figure 3B**).

Comparison of Bed Level Variations Between Flood and Ebb Tides

Figure 4 shows the detailed time series of DSP during the flood and ebb processes of the observed 13 tidal cycles, respectively. For almost all the flood tides, the variations of DSP displayed a significant negative linear correlation (R ranged from −0.73 to −0.99) with h, despite of the increasing trends occurring during the low h, except T4 (**Figure 4D**). The negative linear correlation between DSP and h still existed during the ebb tides for all the tidal cycles (**Figures 4N–Z**). However, the correlation between DSP and h was slightly poorer in terms of the correlation coefficients, which varied between −0.54 and −0.91. The significant negative correlation between DSP and h during both flood and ebb tides indicated the intra-tidal tendency of bed level changes as the bed level increased during the flood and then decreased as ebb tide proceeded.

By statistics, the bed level showed a net increase during flood tides for all the tidal cycles except T4, where bed level changes were equal to −31.2 mm (**Figure 5**). Additionally, the larger net bed level changes occurred at T5 and T8–T10, accompanied by their values over 50 mm. In contrast, the bed level always showed a net reduction during the ebb tide for all the tidal cycles when the seabed was submerged. The maximum net bed level change during ebb tides was −41.1 mm, which occurred

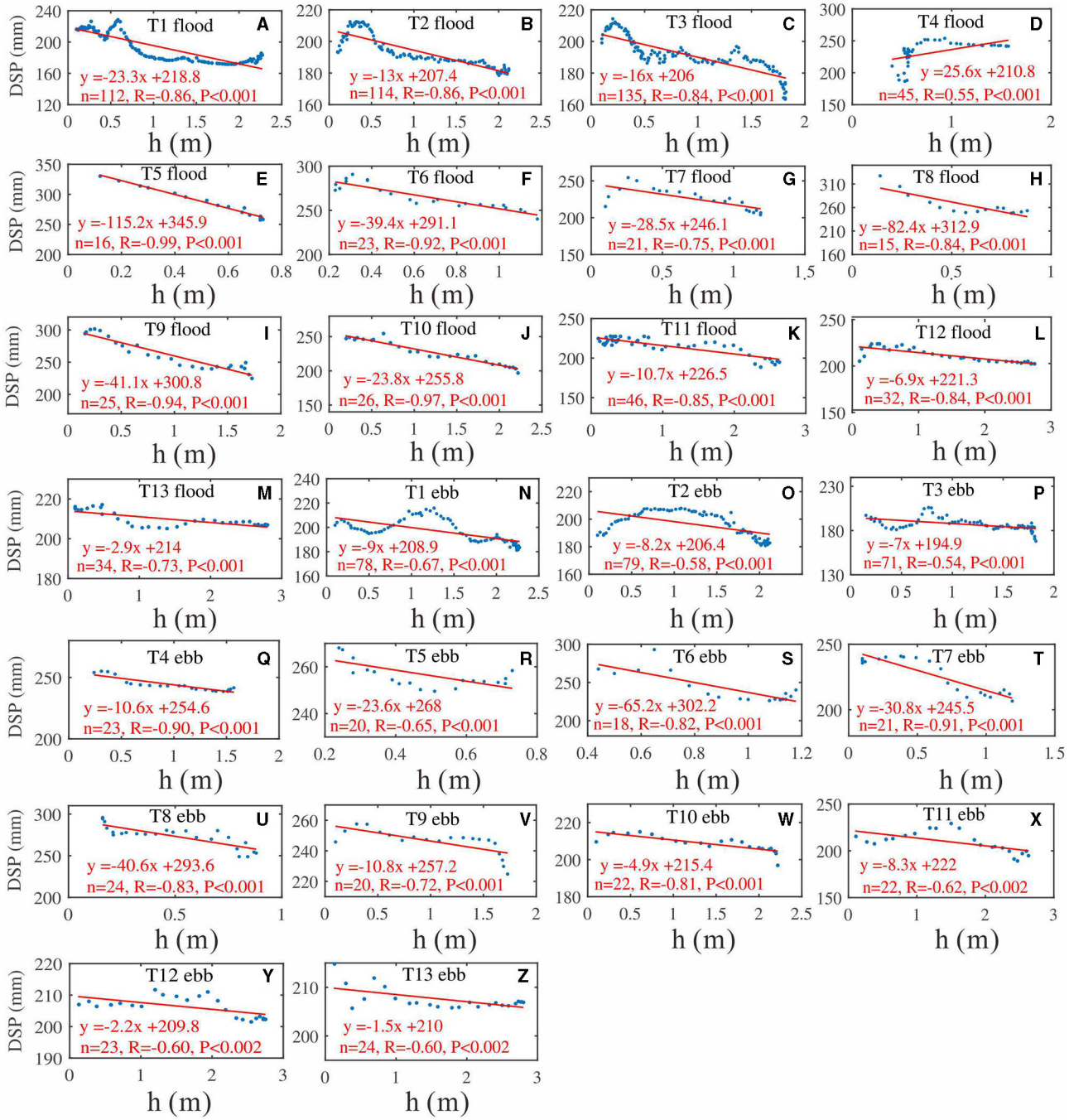


FIGURE 4 | DSP against water depth during the flood processes of **(A)** T1, **(B)** T2, **(C)** T3, **(D)** T4, **(E)** T5, **(F)** T6, **(G)** T7, **(H)** T8, **(I)** T9, **(J)** T10, **(K)** T11, **(L)** T12, **(M)** and T13 and during the ebb processes of **(N)** T1, **(O)** T2, **(P)** T3, **(Q)** T4, **(R)** T5, **(S)** T6, **(T)** 7, **(U)** T8, **(V)** T9, **(W)** T10, **(X)** T11, **(Y)** T12, and **(Z)** T13.

at T8. All the other net bed level changes during the ebb tides were smaller than −30 mm. On the other hand, the larger amplitude of bed level variations occurred more during flood tides (mean SD of bed level variations = 15.26 mm) than ebb tides (mean SD of bed level variations = 8.68 mm) since the larger SDs of DSP were obtained during flood tides for almost all the tidal cycles except T6. However, the relative magnitude of the net bed level changes between flood and ebb tides did not decide the net bed level changes over an entire tidal cycle, as not all the submerged bed level data were included, but qualitatively indicated the intra-tidal tendency of bed level changes.

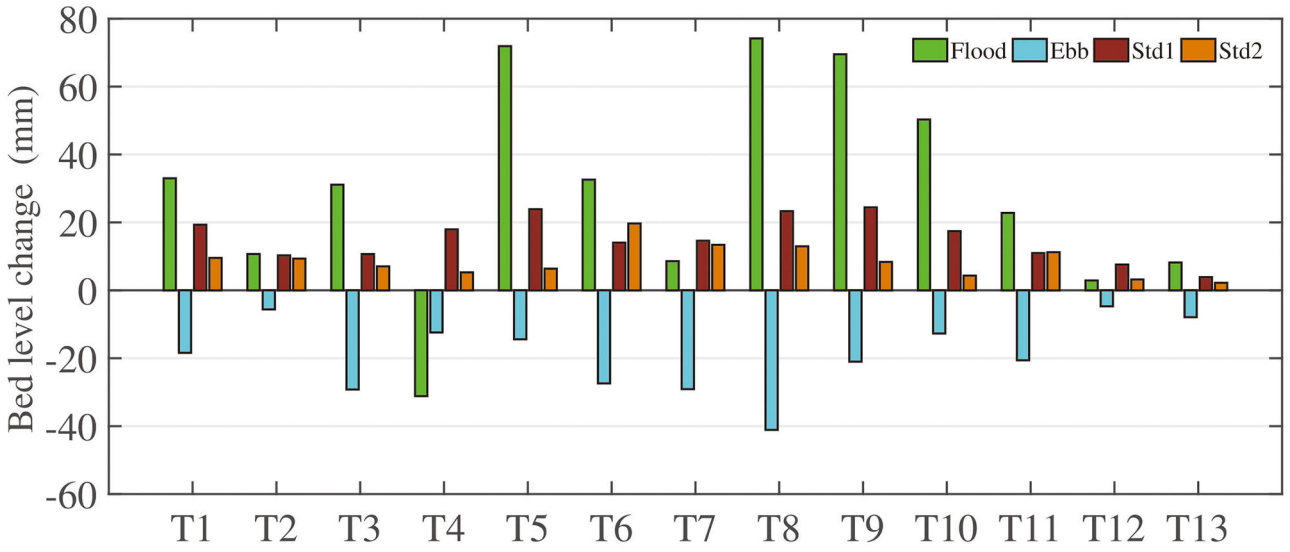


FIGURE 5 | Net bed level changes of the flood tide (green bar) and ebb tide (light blue bar) of each tidal cycle, and the SD of bed level changes during the flood tide (Std1, brown bar) and ebb tide (Std2, orange bar) of each tidal cycle. Note that not all the submerged bed level data were included.

DISCUSSIONS

The Factors Affecting Bed Level Changes Under Different Tidal Ranges

Distinct characteristics of bed level changes under different tidal ranges existed widely in the coastal area, which resulted from the coupling tides, wave processes, and beach slope, etc. In this study, it has been found that the bed level changes during neap tides were more pronounced than those under spring tides (**Figure 3**). To further detect the responsive features of bed level changes under tides and waves, we compared the bed level changes for a successive 30 min (burst time of ADV) against different Hs (**Figure 6A**) based on the recorded DSP series (**Figure 3A**). In general, the mean magnitude of the bed level changes at the interval of 0.4 m of h was not significant (<2 mm), and the maximum variation amplitude ($SD = 10.28$) occurred at a relatively low h (at an h of 0.4–0.8 m). At the same time, the minimum variation amplitude ($SD = 3.45$) of bed level changes occurred at an h of 1.2–1.6 m which were beyond the high water level of the neap tides. In addition, the secondary minimum variation amplitude ($SD = 4.01$) of the bed level changes existed at an h of 2.4–2.8 m, which was the highest water depth during the observation and took place only with the arrival of spring tides. The responsive characteristics of the beach bed level changes under different Hs might be consistent with the aforementioned results that bed level changes during a neap to middle tides were more pronounced than those under middle to spring tides, which was associated with the tide-related horizontal tidal translation rate (V_{tide}), h, tidal range, wave processes, etc.

The horizontal tidal translation rate, a variable obtained by h and local beach slope, decided the residence times of the different wave processes (shoaling, breaking, and surf processes in this study), which would influence the duration of the wave reworking on the beach seabed and the relaxation time of the bed level changes (Masselink and Anthony, 2001). For spring tides (T11–T13), all the maximum averaged V_{tide} exceeded 0.6 cm/s and reached 1 cm/s, which were significantly larger than those (smaller than 0.6 cm/s) under neap tides (T5–T8) (**Figure 6B**). The larger tidal range during spring tides induced a large V_{tide} during fast flooding and ebbing tides, which led to the rapid shifting of the three kinds of wave processes and enhancing the beach morphological relaxation at the measurement location. As a result, the bed level changes were subdued and limited during the middle tide level of spring tide (1.2–1.6 m of h, **Figure 6B**) where V_{tide} was largest, which was consistent with the results depicted in **Figure 6A** and demonstrated that the bed level changes under spring tides were limited.

Tide-modulated water depth (h) conducted a limitation on the incident wave heights (identified by the red line, $y = 1.09x + 0.18$) through energy dissipation and wave breaking, etc., by which the tide exerted influence on the beach bed level changes (i.e., Kroon and Masselink, 2002). As shown in **Figure 6C**, for relatively low h, especially h < 0.8 m, the maximum wave height (H_{max}) has a high possibility to reach the extremity where the wave breaker occurred. At the same time, the wave height was positively correlated with the h where the wave break occurred (**Figure 6C**), which was consistent with the relationship between Hs and h during neap tides (T4–T8, **Figures 2A,B**). In contrast, at an h >2.2 m, which showed up only at spring tides, the H_{max} was far from the extremity under non-storm conditions, which meant that, during normal wave conditions, the beach was seldom subjected to breaking wave conditions during spring tides for a fixed location. Hence, at neap tides whose tide-modulated h and tidal ranges were both smaller (largest h was 1.2 m during neap tides in the measurement location) than middle and spring tides, pronounced bed level changes would

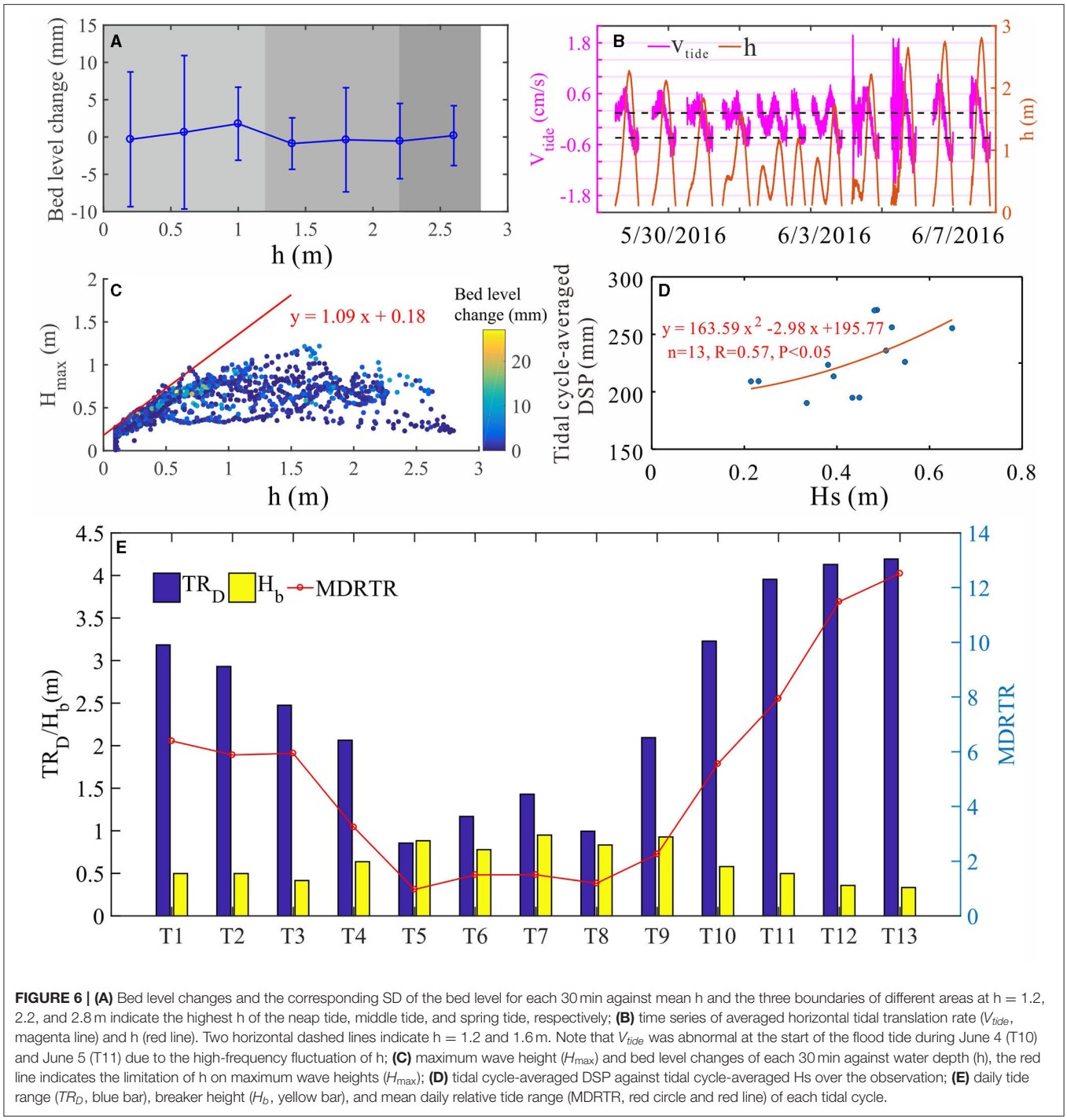


FIGURE 6 | (A) Bed level changes and the corresponding SD of the bed level for each 30 min against mean h and the three boundaries of different areas at h = 1.2, 2.2, and 2.8 m indicate the highest h of the neap tide, middle tide, and spring tide, respectively; **(B)** time series of averaged horizontal tidal translation rate (V_{tide}, magenta line) and h (red line). Two horizontal dashed lines indicate h = 1.2 and 1.6 m. Note that V_{tide} was abnormal at the start of the flood tide during June 4 (T10) and June 5 (T11) due to the high-frequency fluctuation of h; **(C)** maximum wave height (H_{max}) and bed level changes of each 30 min against water depth (h), the red line indicates the limitation of h on maximum wave heights (H_{max}); **(D)** tidal cycle-averaged DSP against tidal cycle-averaged Hs over the observation; **(E)** daily tide range (TR_D, blue bar), breaker height (H_b, yellow bar), and mean daily relative tide range (MDRTR, red circle and red line) of each tidal cycle.

take place due to the prolonged wave reworking associated with breaking wave and surf zone processes. Therefore, both the occurrences of the maximum and secondary minimum variation amplitudes of bed level changes in **Figure 6A** could be reasonably explained.

Wave height played an important role in the bed level changes at the surf zone, which was directly demonstrated by the larger DSP under moderate wave conditions (T4–T9, **Table 4**). According to the relationship between averaged tidal-cycle Hs and DSP, the larger the Hs was, the larger the mean DSP was over a tidal cycle (**Figure 6D**). Hence, it was indicated that incident wave height was a decisive factor for the variation tendency of the beach face. Larger Hs would lead to the tendency of the beach face to erode at the surf zone since more SSCs produced by larger Hs were transported seaward by large offshore-directed mean currents (**Table 2**).

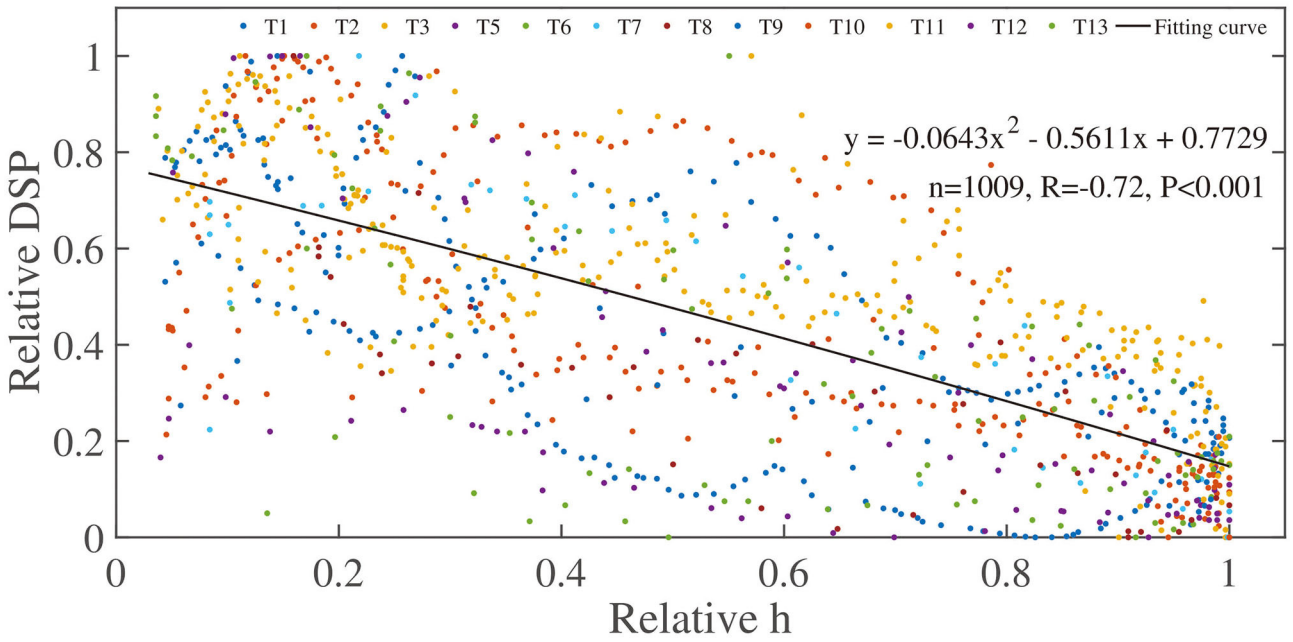


FIGURE 7 | The distribution of the relative DSP against the relative h from all tidal cycles, except T4 where wave climate was enhanced abruptly.

The relative tide range (modified as mean daily relative tide range, i.e., MDRTR in this study) was frequently used to characterize the relative importance of the swash, surf zone, and shoaling wave processes on the beach profiles, which synthesized the influence of tide range (modified as daily tide range, TR_D) and breaker height (H_b) on bed level changes (Masselink and Short, 1993; Qi et al., 2010). During the observation, the calculated TR_D decreased continually from 3.19 m at T1 to its minimum, 0.86 m, at T5, and then fluctuated over neap tides (0.85 m at T5 to 1.43 m at T7), followed by a gradual increase with a maximum of 4.19 m at T13 (**Figure 6E**). However, the variations of the mean H_b displayed an opposite tendency relative to TR_D and H_b, ranging between 0.34 and 0.95 m. As a result, the synthetic MDRTR varied between 0.97 and 12.52, with a similar variation trend relative to TR_D (**Figure 6E**). During the neap tides (T5–T8) in the observation, the maximum MDRTR was merely 1.51, which is significantly lower than 3, while the MDRTRs were primarily between 3 and 7 during middle tide (T1–T4 and T9–T10) except T9 (MDRTR = 2.26), and that varied between 7 and 13 (7.94–12.52) under spring tides (T11–T13). Thus, it was deduced that, during the neap tides where MDRTR <2, the entire beach profile was dominated by surf wave conditions (Masselink and Short, 1993), and the bed level changes were pronounced due to the wave breaking-induced high SSCs and strong undertows (Longuet-Higgins and Stewart, 1964; Rafati et al., 2021). However, the bed level changes would be limited and subdued during spring tides where 7< MDRTR <13, for the breaking wave and surf zone processes operated for <50% of the time near the mean sea level where the instruments were located and the bed level changes were mainly subjected to shoaling wave processes and gentle wave reworking.

Factors on Intra-Tidal Bed Level Variation

The intra-tidal variations of bed levels resulted from a combination of complex hydrodynamics (tide-modulated h, waves, mean current, and turbulent motions) and suspended sediment concentration in the water column. Illustrated by the time series of the DSP during flood and ebb tides, the significant negative correlations between the DSP and h during both flood and ebb tide processes for each tidal cycle except T4, where the incident waves were enhanced abruptly (**Figure 4**), indicating an intra-tidal tendency of increase during flood tides and decrease during ebb tides in the bed level variations. Hence, it was implied that tide-modulated h might affect the variations of bed levels. As expected, the relative DSPs were highly correlated ($R = -0.72$, $p < 0.001$, **Figure 7**) with relative h in terms of all the tidal cycles not including T4, where the sediment suspension mechanism and sediment transport pattern have been changed, induced by suddenly enhanced wave climates (Grasso and Ruessink, 2011), which is consistent with the results depicted in **Figure 5** that overall net accretion and erosion occurred during flood and ebb tides, respectively. The periodic behavior of the overall net accretion followed by the overall net erosion in the bed level, which was controlled by tide-modulated h, could be easily understood since h regulated the temporal variations of bed shear stress, wave motions, currents, TKEs, and SSCs in the near bottom.

To be specific, the wave-induced bed shear stress (τ_w) tended to be bimodal and exceeded critical shear stress (τ_{cr}) for the majority of the time, except at T12 and T13 (**Figure 8A**), while the current-induced bed shear stress was smaller than the τ_{cr} for most of the time excluding the moments where h was in extremely low values and the beach was subjected to moderate wave conditions

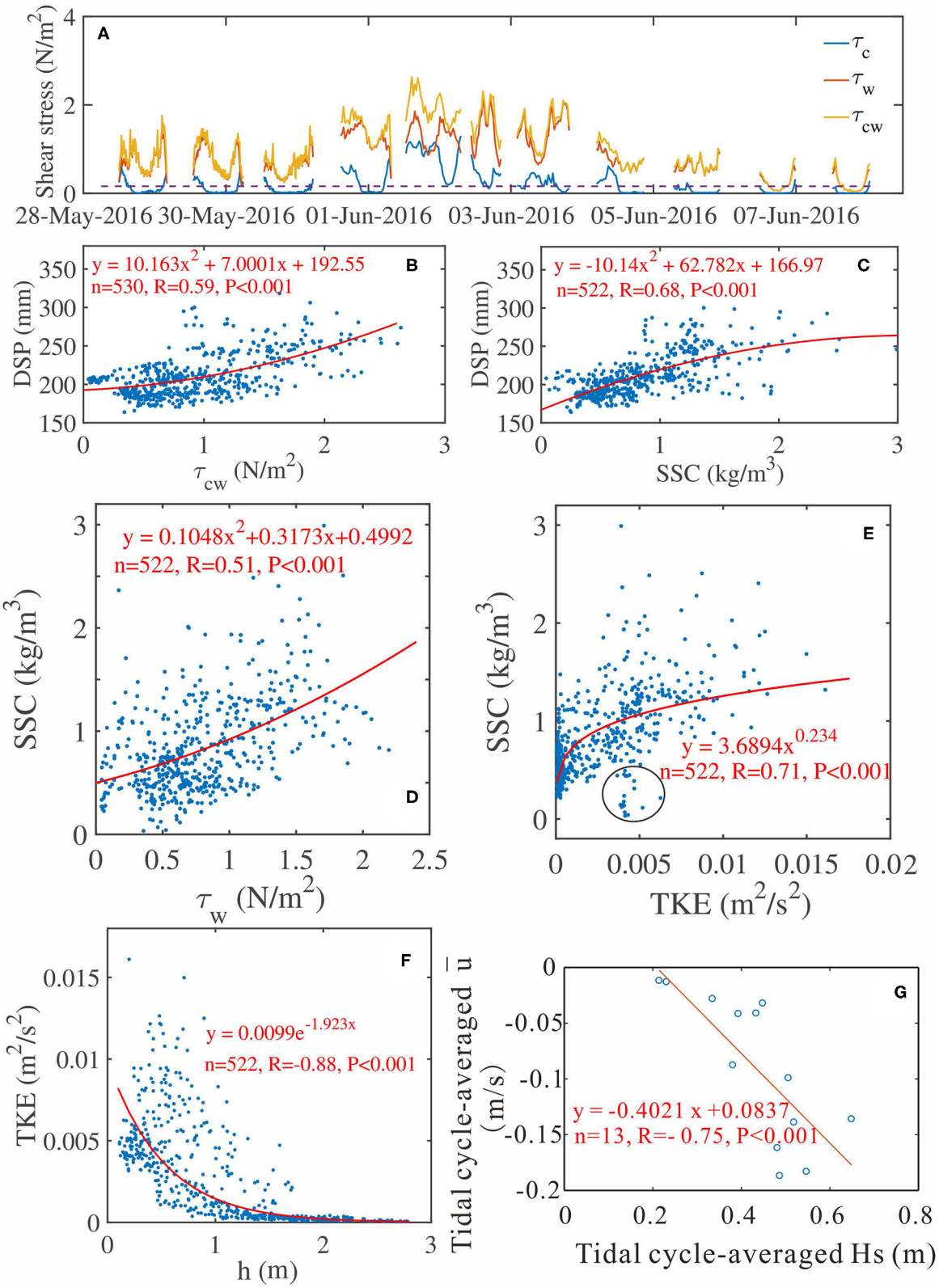


FIGURE 8 | (A) Variations of bed shear stress induced by combined wave and current (τ_{cw}, yellow line), induced by wave (τ_w, red line), and induced by current (τ_c, blue line), respectively. The horizontal dashed line indicated the critical bed shear stress (0.16 N/m^2); **(B)** DSP against bed shear stress induced by wave (τ_w) from all

(Continued)

FIGURE 8 | tidal cycles; **(C)** DSP against suspended sediment concentration (SSC) from all tidal cycles. **(D)** Relationship between suspended sediment concentration (SSC) and bed shear stress induced by wave (τ_w) for all tidal cycles; **(E)** relationship between SSC and TKE for all tidal cycles. The data points within the black circle indicated surface-generated TKE did not reach the seabed and stirred up the sediments into the measurement elevation at extremely low h; **(F)** relationship between TKE and h; **(G)** tidal cycle-averaged cross-shore velocity ($\overline{u}$) against tidal cycle-averaged Hs throughout the observation.

(T4–T9, **Figure 8A**). Under this circumstance, the mean current might not be the main factor affecting the bed level changes and τ_w could be used to stand for the strength of the near-bottom boundary layer. Moreover, the DSPs were positively correlated with τ_w ($R = 0.59$, $p < 0.001$, **Figure 8B**), which meant that wave height was a major dynamic factor driving the occurrence of bed level changes. Thus, the larger τ_w near the seabed indicated a larger DSP (i.e., lower bed level) and overall erosion of bed level, since the waves acted as a stirring mechanism, separated the sediments from the seabed, and then suspended it into the water column (Dally and Dean, 1984; Winterwerp and van Kesteren, 2004; Pang et al., 2020).

However, the bed level changes were not only affected by hydrodynamics but also by the suspended sediment concentration near the seabed, for the net bed level changes were determined by the balance between the sediment erosion flux induced by bed shear stress and the sediment deposition flux associated with the amount of settling suspended sediments (Winterwerp and van Kesteren, 2004; Shi et al., 2017). In this study, large SSCs tended to occur at a relatively low h (0.4–0.8 m) and maintained a high level during moderate wave conditions (**Figure 2G** and **Table 2**), which was in accordance with the variations of DSPs (**Figure 3A**). Hence, SSC was considered to be a better indicator for the variations of bed levels than waves, for the variation pattern of the SSC was similar to that of DSP (**Figures 2G**, **3A**), which was demonstrated by the better correlation between them ($R = 0.68$, $p < 0.001$, **Figure 8C**). Hence, as the SSC gradually increased, more sediments were suspended into the water column along with the seabed erosion, which led to a larger DSP on account of the effect of a lag deposition, associated with turbulent vortices releasing processes (Guillen and Palanques, 1996; Vincent and Hanes, 2002).

Though τ_w was the primary force driving sediment grain movement and explained parts of suspended sediment concentrations within the water ($R = 0.51$, $p < 0.001$, **Figure 8D**), a poor correlation between SSC and τ_w might occur under moderate wave conditions (**Figure 11C**) where the mean current was strong (maximum $\overline{u}$ and $\overline{v}$ increased up to −0.29 and 0.5 m/s, respectively) and bedforms might have transformed (ψ was over 240 for parts of time, which indicated a plane seabed, Dingler and Inman, 1976). The TKE originating from the wave breaking or friction between the flow and the seabed ejected and pumped sand-laden vortices into higher elevations (Aagaard and Jensen, 2013). Hence, TKE was a direct factor determining the level of SSCs, being the most important dynamic factor affecting the bed level change, and this was illustrated by the high correlation coefficient ($R = 0.71$, $p < 0.001$) between TKE and SSC, except some moments that surface-generated TKE did not approach the seabed and stirred up the sediments into the measurement elevation at an extremely low h (black circle, **Figure 8E**). In addition, the distribution of TKE was highly modulated by h, regardless of wave conditions (**Figure 8F**), it provided further evidence to support the deduction that tide-generated h was a controller on the variations of the bed level associated with **Figure 7**.

Patterns of Intra-Tidal Bed Level Variation Under Different Wave Conditions

Though the bed level showed an overall increasing trend during flood tides and a decreasing trend during ebb tides for both low-energy and moderate wave conditions (**Figures 4**, **9A,B**), the influence mechanisms on intra-tidal bed level variation were different. During low-energy wave conditions, where the wave height was seldom broken and reached the limitation for short time (**Figure 10A**), the relative DSP displayed an overall decreasing trend during flood tides and an increasing trend during ebb tides, along with two maximum values during the flood and ebb tides over the normalized tidal cycle (T1–T3 and T10–T13 were normalized and averaged against relative tidal phases to reflect the variation pattern of the intra-tidal bed level), with the largest relative DSP at 0.15 t/T of the tidal cycle, while the relative DSP maintained a low level at high tide (0.5< t/T <0.7). At the same time, the variation pattern of the relative SSC and τ_w behaved similarly to the relative DSP (**Figures 9A,C,E**), which indicated that waves and the related SSC were responsible for the intra-tidal variation of the bed level under low-energy wave conditions. Under this circumstance where both u and the horizontal advection process were weak, the similar variation pattern between the relative DSP and SSC might be explained by a lag deposition of suspended sediments, which indicated that, as SSC increased with decreasing water depth, more sediments were stirred up into water from the seabed and a larger DSP and seabed erosion, and vice versa (Guillen and Palanques, 1996; Vincent and Hanes, 2002). Hence, the intra-tidal variation trend of bed levels was explained.

Moreover, extra sediments transported by offshore-directed mean currents from the emersed beach led to the net beach face accretion under low-energy wave conditions, which emphasized the importance of sediment sources for bed level changes. Specifically, at t/T = 0.15, where both relative SSC and τ_w were at maximum level, the lowest bed level (largest relative DSP) resulted from the balance between the bed shear stress (erosion flux) and large settling SSCs (deposition flux) since the measurement location was close to the breakpoint where the relative wave height (γ) was approximate to 0.78 (t/T = 0.15, **Figure 10C**) and strong wave-induced bed shear stress occurred as ascribed to the breaker of highly skewed and asymmetric waves (Elgar et al., 2001). On the other hand, though the variation of relative τ_c showed two maximums at the start and end of the tidal cycle, mean currents would not play an important role in bed

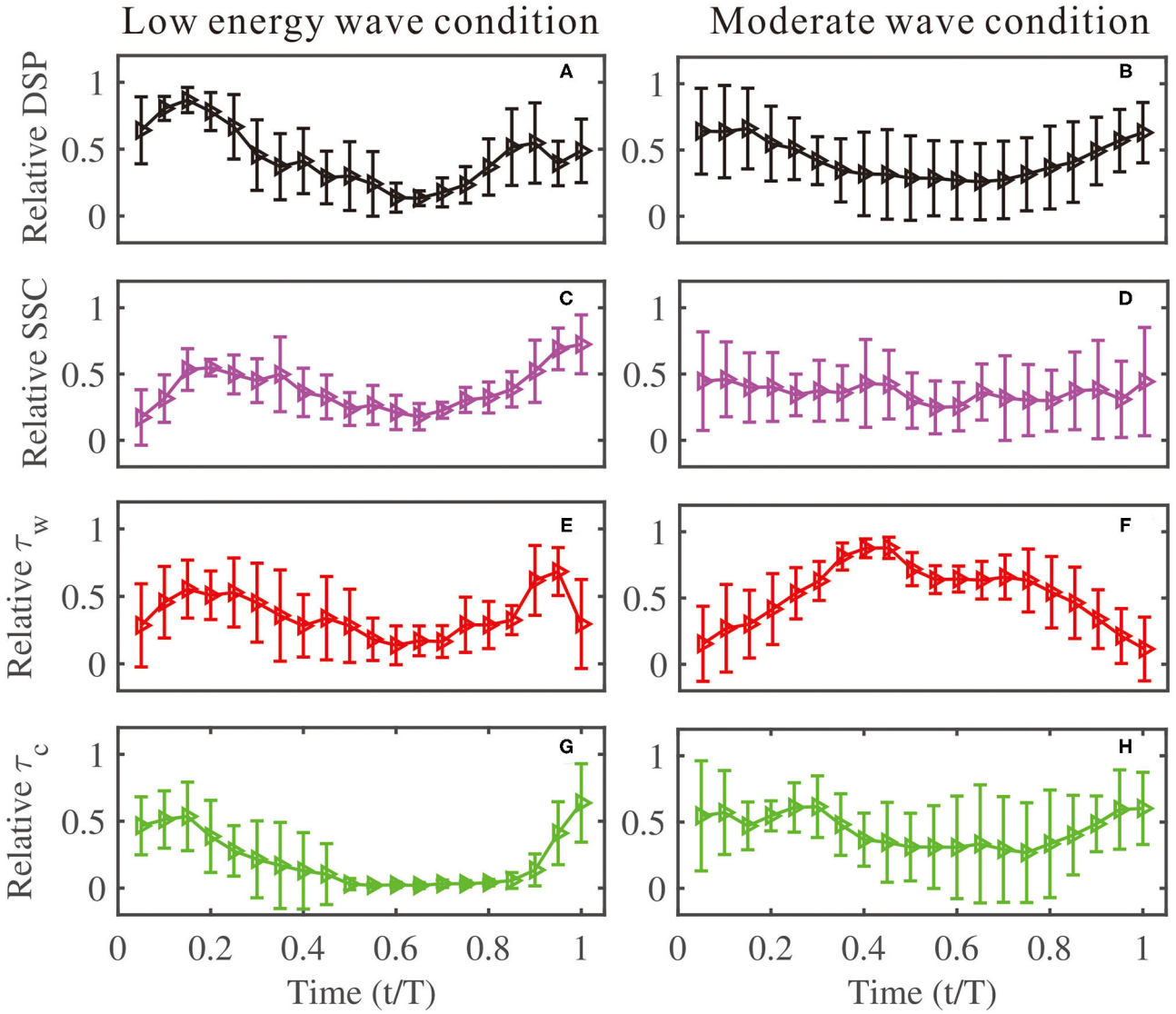


FIGURE 9 | Normalized time series of the DSP (relative DSP, black lines), SSC (relative SSC, magenta lines), bed shear stress induced by wave (relative τ_w, red lines), and bed shear stress induced by current (relative τ_c, green lines) against normalized tidal cycle (t/T) under **(A,C,E,G)** low-energy and **(B,D,F,H)** moderate wave conditions, respectively. The vertical segments indicated ± one SD.

level changes under low-energy wave conditions because the τ_c was lower than the critical bed shear stress (0.16 N/m^2) for most of the time.

Under moderate wave conditions, where wind waves were fully developed and limited by h (R = 0.9, **Figure 10B**), the relative DSP likewise showed a gradually declining trend followed by a gradually increasing trend all along the tidal cycle (T4–T9 were normalized and averaged against relative tidal phases to reflect the variation pattern of the intra-tidal bed level). Meanwhile, the relative SSC showed a similar but inconspicuous variation trend referring to the relative DSP with the correlation coefficient R = 0.54 (**Figure 11A**), which implied that SSC maintained a good indicator on bed level changes despite wave conditions. In contrast, two maximums occurred along the relative τ_w at a time of t/T approximately equal to 0.4 and 0.75, which was also ascribed to wave breaking (γ = 0.78 at t/T = 0.4 and 0.75, **Figure 10D**). Hence, it was implied that wave height was not an indicator for bed level changes in terms of all the wave conditions, based on the inconsistent correlation (R = −0.50, **Figure 11B**) between them under moderate wave conditions, though waves acted as a stirring mechanism for sediment motions.

In fact, under moderate wave conditions (T4–T9), the ψ, which originated from the modulation of h on waves, was greater than that under low-energy wave conditions most of the time and even exceeded 240 at T7 and T9. Thus, the dominant way

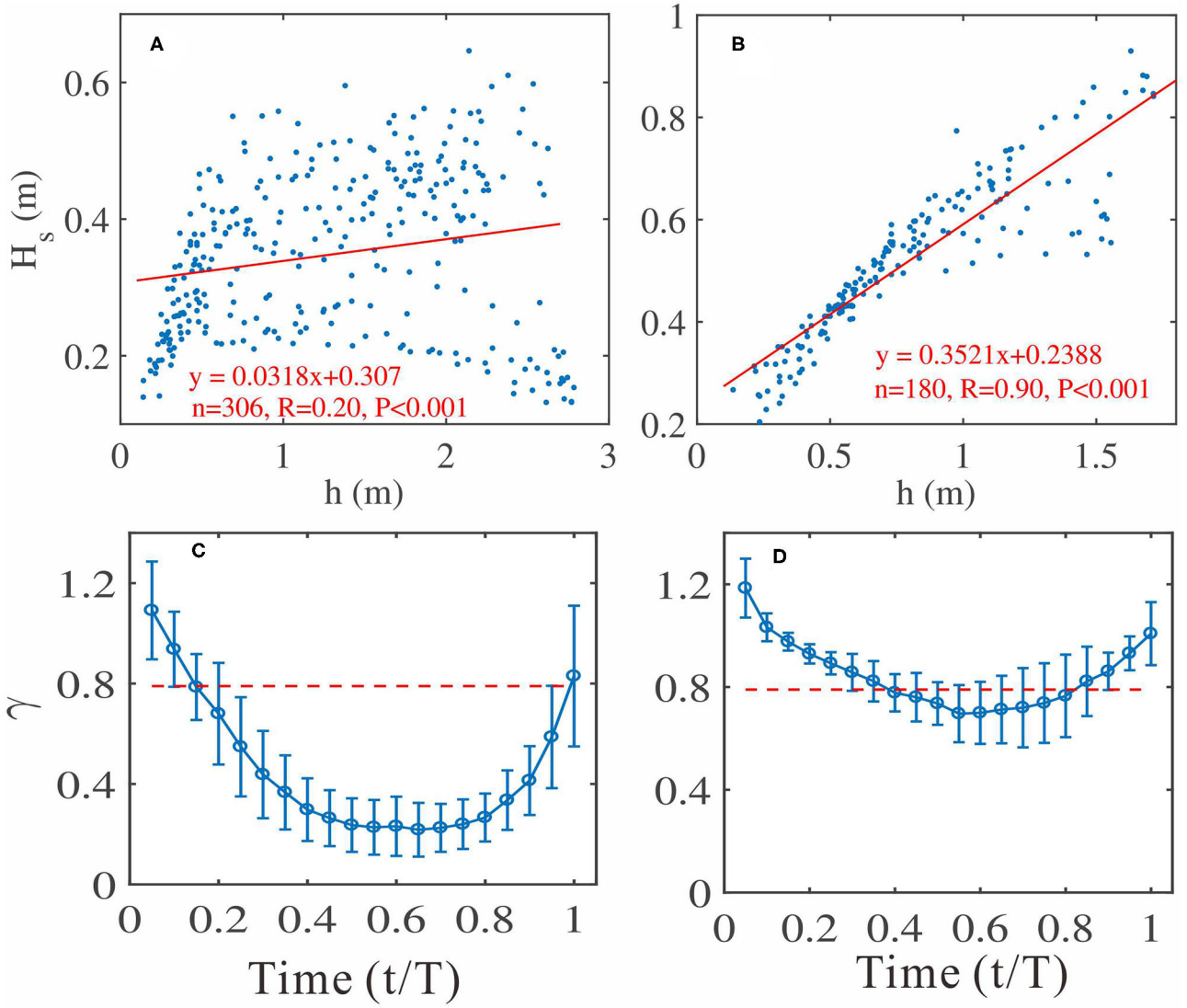


FIGURE 10 | H_s against h under **(A)** low-energy and **(B)** moderate wave conditions. Averaged relative wave height (γ) against normalized tidal cycle (t/T) under **(C)** low-energy wave conditions and **(D)** moderate wave conditions.

of vertical sediment exchange between the seabed and higher elevation turned to the diffusion process from the advection process, which was due to the bedform transformation from a steep ripple (vortex ripple) to a less steep ripple (post-vortex ripple) or a plane seabed under strong wave-induced currents, characterized by high reference concentrations in the vicinity of the seabed and limited suspended sediments at higher elevations (Dingler and Inman, 1976; Chalmoukis et al., 2020). At this moment, the lag deposition effect of the suspended sediments and the intensity of vertical sediment exchange was weakened compared with a low-energy steeper ripple environment (Lee and Hanes, 1996; Osborne and Vincent, 1996), which broke the foregoing interrelation between waves, measured SSCs, and bed level (**Figure 11**) and caused different variation patterns among them (**Figures 9B,D,F**). During these processes, the bed shear stress induced by mean current (τ_c) exceeded the critical bed shear stress most of the time (**Figure 8A**), and the current was capable of altering the bedform and dominating the way of the vertical sediment exchange (Chalmoukis et al., 2020). Hence, the influences of mean currents and bedforms on bed level changes were enhanced and highlighted under energetic wave conditions.

However, though the sediment deposition flux induced by the lag deposition effect of suspended sediments was weak during moderate wave conditions, the wave-breaking processes induced strong offshore-directed mean currents (undertow, **Figure 2D**), which added a great number of extra sediments from the emersed beach to the measurement site, leading to the gradual accretion of the bed level (i.e., a declining trend of the relative DSP). Throughout the course of the ebb tide, the lack of extra sediments from the emersed beach due to the decline in water level would

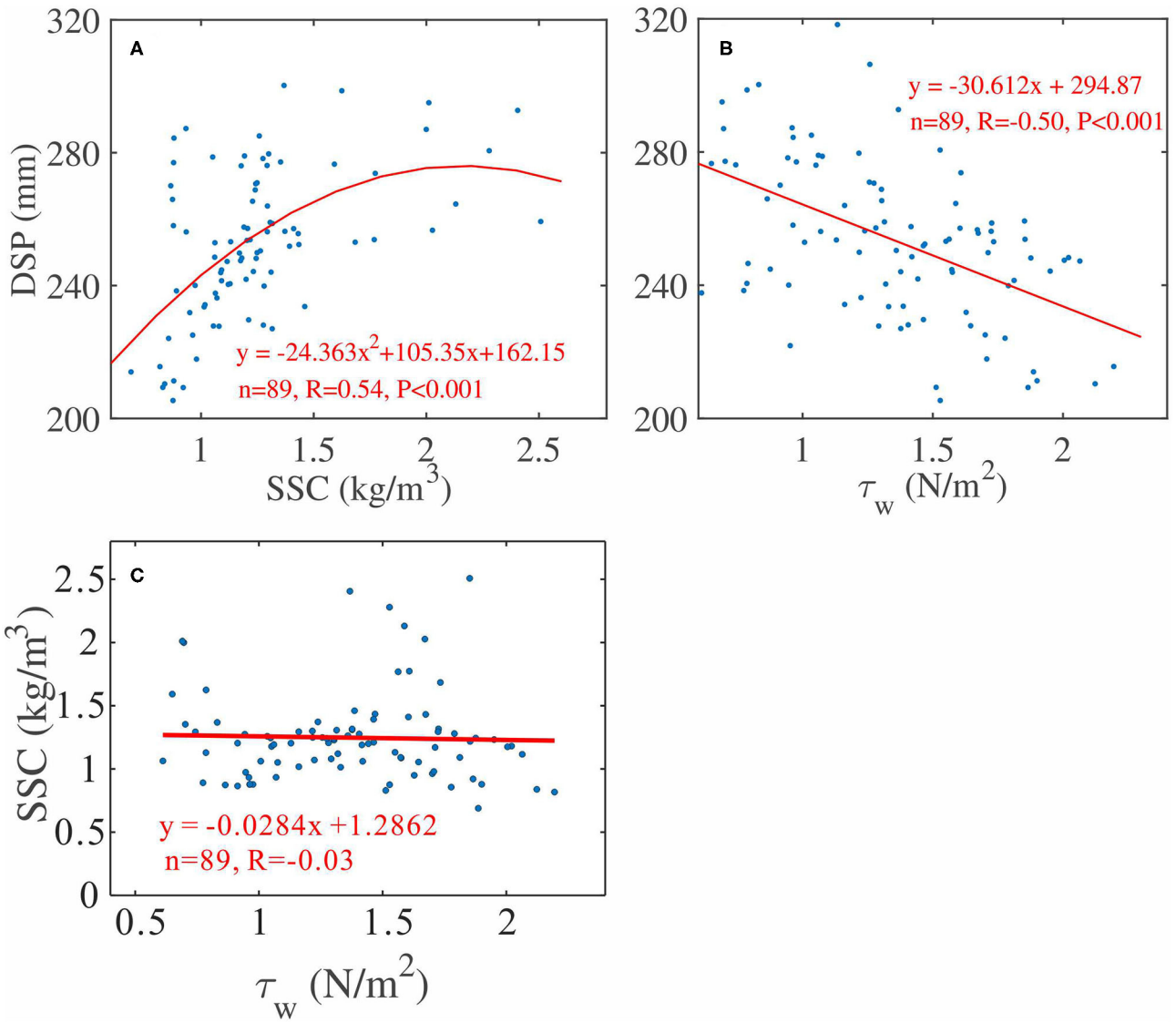


FIGURE 11 | (A) DSP against SSC; **(B)** DSP against bed shear stress induced by wave (τ_w); **(C)** SSC against bed shear stress induced by wave (τ_w) under moderate wave conditions.

make the strong offshore-directed mean currents (undertows) the main erosive force for the beach face. As a result, the gradual erosion of the bed level (gradual increasing trend of relative DSP) occurred during ebb tides, though weakened τ_w might bring little deposition flux to the beach face. In summary, h controlled the intra-tidal bed level changes by modulating the effects of waves on sediment resuspension (SSC variation) and vertical sediment exchange (mobility number) under different wave conditions. In addition, the net erosion of bed level over the entire tidal cycle occurred under energetic wave conditions, which mainly resulted from the coupling between larger incident wave-induced strong offshore-directed mean currents (**Figure 8G**) and large SSCs (Aagaard et al., 2012), associated with the lack of extra sediments from the emersed beach during ebb tides.

CONCLUSIONS

An observation, lasting for 12 days and covering the middle tide to and the following spring tide, was conducted over a meso-macro tidal beach, Yintan Beach, which is north of Beibu Gulf, China. The purposes of the study were to detect the characteristics of bed level changes with ADV measurement at intra-tidal and tidal cycle scales, respectively, and to explore the patterns and influence mechanisms of bed level changes under different wave conditions.

1) The variations of the intra-tidal bed level were more prominent during a neap to middle tides (overall erosion of 56.7 mm) than during middle to spring tides (overall

accretion of 35.5 mm), which was jointly caused by the wave-breaking probability regulated by h and the relative residence times of the shoaling wave zone, breaker zone, and surf zone that were determined by relative tidal range. The net erosion over the entire tidal cycle mainly resulted from large incident wave heights and the consequent strong offshore-directed sediment transport by mean currents (undertows).

2) The bed level displayed an intra-tidal tendency of increase during flood tides and decrease during ebb tides throughout the course of the tidal cycle. Generally, the variations of the intra-tidal bed level were controlled by h, which modulated the effects of waves on sediment resuspension (SSC variation) and vertical sediment exchange (mobility number) under low-energy and moderate wave conditions.
3) Under low-energy wave conditions, waves and the related SSCs were responsible for the intra-tidal variation of the bed level, and the lowest intra-tidal bed level occurring at 0.15 t/T was ascribed to wave breaking. Under moderate wave conditions, the interrelation between intra-tidal bed level, SSCs, and wave height was broken due to the transformation of vertical sediment exchange from the advection process to the diffusion process, during which the influence of the mean current and bedform on bed level changes was highlighted.

DATA AVAILABILITY STATEMENT

The original contributions presented in the study are included in the article/supplementary material, further inquiries can be directed to the corresponding author/s.

AUTHOR CONTRIBUTIONS

Every author has seen and contributed to the final draft. HH, YL, and ZD conceived of this research. WP, XZ, ZD, and SL conducted the field observations. WP performed the main data analysis. WP, XZ, and ZD wrote this paper. XZ, ZD, HH, and YL contributed to the discussion. All authors discussed the results and commented on the manuscript.

FUNDING

This study was supported by the National Natural Science Foundation of China (NSFC) (41930537 and 41866001) and the Key Projects of Science and Technology of Guangxi Province (AB21076016).

ACKNOWLEDGMENTS

The authors thank Jinghua Gu, Zhenpeng Ge, Jie Wang, and Binbin Ma for their assistance in the field.

REFERENCES

Aagaard, T., Black, K. P., and Greenwood, B. (2002). Cross-shore suspended sediment transport in the surf zone: a field-based parameterization. *Mar. Geol.* 185, 283–302. doi: 10.1016/S0025-3227(02)00193-7

Aagaard, T., Greenwood, B., and Hughes, M. (2013). Sediment transport on dissipative, intermediate and reflective beaches. *Earth Sci. Rev.* 124, 32–50. doi: 10.1016/j.earscirev.2013.05.002

Aagaard, T., Hughes, M., and Andersen, M. S. (2006). Hydrodynamics and sediment fluxes across an onshore migrating intertidal bar. *J. Coast. Res.* 22, 247–259. doi: 10.2112/04-0214.1

Aagaard, T., Hughes, M., Baldock, T., Greenwood, B., Kroon, A., and Power, H. (2012). Sediment transport processes and morphodynamics on a reflective beach under storm and non-storm conditions. *Mar. Geol.* 326–328. doi: 10.1016/j.margeo.2012.09.004

Aagaard, T., and Jensen, S. G. (2013). Sediment concentration and vertical mixing under breaking waves. *Mar. Geol.* 336, 146–159. doi: 10.1016/j.margeo.2012.11.015

Aagaard, T., Kroon, A., Andersen, S., Sørensen, R. M., Quartel, S., and Vinther, N. (2005). Intertidal beach change during storm conditions; Egmond, the Netherlands. *Mar. Geol.* 218, 65–80. doi: 10.1016/j.margeo.2005.04.001

Aagaard, T., Nielsen, J., Davidson-Arnott, R. G. D., Greenwood, B., and Nielsen, N. (1998b). Coastal morphodynamics at Skallingen, SW Denmark: high energy conditions. *Dan. J. Geogr.* 98, 20–30. doi: 10.1080/00167223.1998.10649407

Aagaard, T., Nielsen, J., and Greenwood, B. (1998a). Suspended sediment transport and nearshore bar formation on a shallow intermediate-state beach. *Mar. Geol.* 148, 203–225. doi: 10.1016/S0025-3227(98)00012-7

Agredano, R., Cienfuegos, R., Catalán, P., Mignot, E., Bonneton, P., Bonneton, N., et al. (2019). Morphological changes in a cuspate sandy beach under persistent high-energy swells: Reaca Beach (Chile). *Mar. Geol.* 417:105988. doi: 10.1016/j.margeo.2019.105988

Alsina, J. M., and Cáceres, I. (2011). Sediment suspension events in the inner surf and swash zone. Measurements in large-scale and high-energy wave conditions. *Coast. Eng.* 58, 657–670. doi: 10.1016/j.coastaleng.2011.03.002

Andersen, T. J., Pejrup, M., and Nielsen, A. A. (2006). Long-term and high-resolution measurements of bed level changes in a temperate, microtidal coastal lagoon. *Mar. Geol.* 226, 115–125. doi: 10.1016/j.margeo.2005.09.016

Anthony, E. J., Levoy, F., and Monfort, O. (2004). Morphodynamics of intertidal bars on a megatidal beach, Merlimont, Northern France. *Mar. Geol.* 208, 73–100. doi: 10.1016/j.margeo.2004.04.022

Arnaud, G., Mory, M., Abadie, S., and Morichon, D. (2011). "Measurements of bed level oscillation cycles in the surf zone of a sandy beach," in *OCEANS, IEEE – Spain* (Santander:IEEE), 1–8. doi: 10.1109/Oceans-Spain.2011.6003636

Austin, M. J., and Masselink, G. (2006). Observations of morphological change and sediment transport on a steep gravel beach. *Mar. Geol.* 229, 59–77. doi: 10.1016/j.margeo.2006.02.003

Beach, R. A., and Sternberg, R. W. (1991). "Infragravity driven suspended sediment transport in the swash, inner and outer-surf zone," in *Proc. Coastal Sediments'91. ASCE* (New York, NY), 114–128.

Biausque, M., and Senechal, N. (2019). Seasonal morphological response of an open sandy beach to winter wave conditions: the example of Biscarrosse beach, SW France. *Geomorphology* 332, 157–169. doi: 10.1016/j.geomorph.2019.02.009

Brand, E., Montreuil, A. L., Houthuys, R., and Chen, M. (2020). Relating hydrodynamic forcing and topographic response for tide-dominated sandy beaches. *J. Mar. Sci. Eng.* 8:151. doi: 10.3390/jmse8030151

Brand, E., Sloover, L. D., Wulf, A. D., Montreuil, A. L., and Chen, M. (2019). Cross-shore suspended sediment transport in relation to topographic changes in the intertidal zone of a macro-tidal beach (Mariakerke, Belgium). *J. Mar. Sci. Eng.* 7:172. doi: 10.3390/jmse7060172

Capo, S., Parisot, J. P., Bujan, B., and Senechal, S. B. (2009). Short time morphodynamics response of the Truc Vert Beach to storm conditions. *J. Coast. Res.* 56, 1741–1745. doi: 10.2307/25738088

Chalmoukis, I. A., Dimas, A. A., and Grigoriadis, D. (2020). Large-eddy simulation of turbulent oscillatory flow over three dimensional transient vortex ripple geometries in quasiquilibrium. *J. Geophys. Res. Earth Surf.* 125:e2019JF005451. doi: 10.1029/2019JF005451

Christensen, D. F., Brinkkemper, J., Ruessink, G., and Aagaard, T. (2019). Field observations of turbulence in the intertidal and shallow subtidal zones. *Continent. Shelf Res.* 170, 21–32. doi: 10.1016/j.csr.2018.10.002

Coco, G., Burnet, T. K., and Werner, B. T. (2004). The role of tides in beach cusp development. *J. Geophys. Res. Oceans* 109:C04011. doi: 10.1029/2003JC002154

Dally, W. R., and Dean, R. G. (1984). Suspended sediment transport and beach profile evolution. *J. Waterway Port Coast. Ocean Eng.* 110, 15–33. doi: 10.1061/(ASCE)0733-950X(1984)110:1(15)

Dingler, J. R., and Inman, D. L. (1976). Wave-formed ripples in nearshore sands. *Coast. Eng. Proc.* 1: 122. doi: 10.9753/icce.v15.122

Elgar, S., Gallagher, E. L., and Guza, R. T. (2001). Nearshore sandbar migration. *J. Geophys. Res. Atmos.* 106, 11623–11628. doi: 10.1029/2000JC000389

Falqués, A., Dodd, N., Garnier, R., Ribas, F., and Sancho, F. (2008). Rhythmic surf zone bars and morphodynamic self-organization. *Coast. Eng.* 55, 622–641. doi: 10.1016/j.coastaleng.2007.11.012

Gallagher, E. L., Elgar, S., and Guza, R. T. (1998). Observations of sand bar evolution on a natural beach. *J. Geophys. Res. Oceans* 103, 3203–3215. doi: 10.1029/97JC02765

Ge, Z. P., Dai, Z. J., Pang, W. H., Li, S. S., Wei, W., Mei, X. F., et al. (2017). LIDAR-based detection of the post-typhoon recovery of a meso-macro-tidal beach in the Beibu Gulf, China. *Mar. Geol.* 391, 127–143. doi: 10.1016/j.margeo.2017.08.008

Gibbons, D. T., Jones, G., Siegel, E., Hay, A., and Johnson, F. (2005). "Performance of a new submersible Tide-Wave recorder, Oceans," In *Proceedings of MTS/IEEE. Vol. 2* (New York, NY: IEEE), 1057–1060.

Grant, W. D., and Madsen, O. S. (1979). Combined wave and current interaction with a rough bottom. *J. Geophys. Res. Oceans Atmos.* 84, 1797–1808. doi: 10.1029/JC084iC04p01797

Grasso, F., and Ruessink, B. G. (2011). Vertical structure of turbulence dissipation rate in the shallow-water surf zone. *J. Coast. Res.* 64, 90–94.

Guillen, J., and Palanques, A. (1996). Short- and medium-term grain size changes in deltaic beaches (Ebro Delta, NW Mediterranean). *Sediment. Geol.* 101, 55–67. doi: 10.1016/0037-0738(95)00021-6

Houser,; C., and Greenwood, B. (2007). Onshore migration of a swash bar during a storm. *J. Coast. Res.* 23, 1–14. doi: 10.2112/03-0135.1

Houser,; C., Greenwood, B., and Aagaard, T. (2006). Divergent response of an intertidal swash bar. *Earth Surf. Proc. Landforms* 31, 1775–1791. doi: 10.1002/esp.1365

Hu, B. P., Xie, J., Li, W., He, Z., and Wu, W. (2020). A rans numerical study of experimental swash flows and its bed shear stress estimation. *Appl. Ocean Res.* 100, 102145. doi: 10.1016/j.apor.2020.102145

Hu, Z., Wang, Z. B., Zitman, T. J., Stive, M. J. F., and Bouma, T. J. (2015). Predicting long-term and short-term tidal flat morphodynamics using a dynamic equilibrium theory. *J. Geophys. Res. Earth Surf.* 120, 1803–1823. doi: 10.1002/2015JF003486

Huang, H., Dai, Z. J., Shi, W. Y., and Sheng, K. (2011). Deposition characteristics of beach profile in strong-tidal environment ? A case study of Yintan, Guangxi during spring. *J. Trop. Oceanogr.* 30, 71–76. doi: 10.3969/j.issn.1009-5470.2011.04.011

Ji, Y. X. (2007). *Study on Storm Surges Disasters of the Guangxi Coastal Areas in Beibu Gulf and Its Preventive Counter Measurements*. Nanning: Guangxi University.

Kim, S. C., Friedrichs, C. T., Maa, J. P. Y., and Wright, L. D. (2000). Estimating bottom stress in tidal boundary layer from Acoustic Doppler Velocimeter data. *J. Hydraul. Eng. ASCE* 126, 399–406. doi: 10.1061/(ASCE)0733-9429(2000)126:6(399)

Komar, P. D., and Gaughan, M. K. (1972). "Airy wave theory and breaker height prediction," in *Proceedings of the 13th International Conference on Coastal Engineering ASCE* (Vancouver, BC), 405–418. doi: 10.1061/9780872620490.023

Kroon, A., and Masselink, G. (2002). Morphodynamics of intertidal bar morphology on a macrotidal beach under low-energy wave conditions, North Lincolnshire, England. *Mar. Geol.* 190, 591–608. doi: 10.1016/S0025-3227(02)00475-9

Lee, T. H., and Hanes, D. M. (1996). Comparison of field observations of the vertical distribution of suspended sand and its prediction by models. *J. Geophys. Res.* 101, 3561–3572. doi: 10.1029/95JC03283

Li, F., van Gelder, P. H. A. J.M., Ranasinghe, R., Callaghan, D. P., and Jongejan, R. B. (2014). Probabilistic modelling of extreme storms along the Dutch coast. *Coast. Eng.* 86, 1–13. doi: 10.1016/j.coastaleng.2013.12.009

Longuet-Higgins, M. S., and Stewart, R. W. (1964). Radiation stresses in water waves; a physical discussion, with applications. *Deep Sea Res. Oceanogr. Abstr.* 11, 529–562. doi: 10.1016/0011-7471(64)90001-4

López-Dóriga, U., and Ferreira, O. (2017). Longshore and cross-shore morphological variability of a Berm–Bar system under low to moderate wave energy. *J. Coast. Res.* 335, 1161–1171. doi: 10.2112/JCOASTRES-D-16-00050.1

Luijendijk, A., Hagenaars, G., Ranasinghe, R., Baart, F., Donchyts, G., and Aarninkhof, S. (2018). The state of the world's beaches. *Sci. Rep.* 8:6641. doi: 10.1038/s41598-018-24630-6

Ma, B. B., Dai, Z. J., Pang, W. H., Ge, Z. P., Li, S. S., Mei, X. F., et al. (2019). Dramatic typhoon-induced variability in the grain size characteristics of sediments at a meso-macrotidal beach. *Continent. Shelf Res.* 191:104006. doi: 10.1016/j.csr.2019.104006

Mariño-Tapia, I. J., Russell, P. E., O'Hare, T. J., Davidson, M. A., and Huntley, D. A. (2007). Cross-shore sediment transport on natural beaches and its relation to sandbar migration patterns: 1. Field observations and derivation of a transport parameterization. *J. Geophys. Res. Oceans* 112, 1–15. doi: 10.1029/2005JC002893

Masselink, G. (2004). Formation and evolution of multiple intertidal bars on macrotidal beaches: application of a morphodynamic model. *Coast. Eng.* 51, 713–730. doi: 10.1016/j.coastaleng.2004.07.005

Masselink, G., and Anthony, E. J. (2001). Location and height of intertidal bars on macrotidal ridge and runnel beaches. *Earth Surf. Proc. Landforms* 26, 759–774. doi: 10.1002/esp.220

Masselink, G., Auger, N., Russell, P., and O'Hare, T. (2007). Short-term morphological change and sediment dynamics in the intertidal zone of a macrotidal beach. *Sedimentology* 54, 39–53. doi: 10.1111/j.1365-3091.2006.00825.x

Masselink, G., Austin, M., Tinker, J., O'Hare, T., and Russell, P. (2008). Cross-shore sediment transport and morphological response on a macrotidal beach with intertidal bar morphology, Truc Vert, France. *Mar. Geol.* 251, 141–155. doi: 10.1016/j.margeo.2008.01.010

Masselink, G., Evans, D., Hughes, M. G., and Russell, P. (2005). Suspended sediment transport in the swash zone of a dissipative beach. *Mar. Geol.* 216, 169–189. doi: 10.1016/j.margeo.2005.02.017

Masselink, G., and Heteren, S. (2014). Response of wave-dominated and mixed-energy barriers to storms. *Mar. Geol.* 352, 321–347. doi: 10.1016/j.margeo.2013.11.004

Masselink, G., Kroon, A., and Davidson-Arnott, R. G. D. (2006). Morphodynamics of intertidal bars in wave-dominated coastal settings — a review. *Geomorphology* 73, 33–49. doi: 10.1016/j.geomorph.2005.06.007

Masselink, G., and Short, A. D. (1993). The effect of tide range on beach morphodynamics and morphology: a conceptual beach model. *J. Coast. Res.* 9, 785–800.

Nerem, R. S., Beckley, B. D., Fasullo, J. T., Hamlington, B. D., and Mitchum, G. T. (2018). Climate-change–driven accelerated sea-level rise detected in the altimeter era. *Proc. Natl. Acad. Sci. U.S.A.* 115:201717312. doi: 10.1073/pnas.1717312115

Nicholls, R. J., and Cazenave, A. (2010). Sea-level rise and its impact on coastal zones. *Science* 328, 1517–1520. doi: 10.1126/science.1185782

Nielsen, P. (1981). Dynamics and geometry of wave-generated ripples. *J. Geophys. Res.* 86, 6467–6472. doi: 10.1029/JC086iC07p06467

Osborne, P. D., and Vincent, C. E. (1996). Vertical and horizontal structure in suspended sand concentrations and wave-induced fluxes over bedforms. *Mar. Geol.* 131, 195–208. doi: 10.1016/0025-3227(95)00002-X

Pang, W. H., Dai, Z. J., Ge, Z. P., Li, S. S., Mei, X. F., Gu, J. H., et al. (2019). Near-bed cross-shore suspended sediment transport over a meso-macro tidal beach under varied wave conditions. *Estuar. Coast. Shelf Sci.* 217, 69–80. doi: 10.1016/j.ecss.2018.11.007

Pang, W. H., Dai, Z. J., Ma, B. B., Wang, J., and Li, S. S. (2020). Linkage between turbulent kinetic energy, waves and suspended sediment concentrations in the nearshore zone. *Mar. Geol.* 425:106190. doi: 10.1016/j.margeo.2020.106190

Poate, T., Masselink, G., Russell, P., and Austin, M. (2014). Morphodynamic variability of high-energy macrotidal beaches, Cornwall, UK. *Mar. Geol.* 350, 97–111. doi: 10.1016/j.margeo.2014.02.004

Pritchard, D., and Hogg, A. J. (2005). On the transport of suspended sediment by a swash event on a plane beach. *Coast. Eng.* 52, 1–23. doi: 10.1016/j.coastaleng.2004.08.002

Pucino, N., Kennedy, D. M., Carvalho, R. C., Allan, B., and Ierodiaconou, D. (2021). Citizen science for monitoring seasonal-scale beach erosion and behaviour with aerial drones. *Sci. Rep.* 11:3935. doi: 10.1038/s41598-021-83477-6

Puleo, J. A., Lanckriet, T., and Blenkinsopp, C. (2014). Bed level fluctuations in the inner surf and swash zone of a dissipative beach. *Mar. Geol.* 349, 99–112. doi: 10.1016/j.margeo.2014.01.006

Qi, H., Cai, F., Lei, G., Cao, H., and Shi, F. (2010). The response of three main beach types to tropical storms in South China. *Mar. Geol.* 275, 244–254. doi: 10.1016/j.margeo.2010.06.005

Quartel, S., Kroon, A., and Ruessink, B. G. (2008). Seasonal accretion and erosion patterns of a microtidal sandy beach. *Mar. Geol.* 250, 19–33. doi: 10.1016/j.margeo.2007.11.003

Rafati, Y., Hsu, T. J., Elgar, S., Raubenheimer, B., and Dongeren, A. V. (2021). Modeling the hydrodynamics and morphodynamics of sandbar migration events. *Coast. Eng.* 166:103885. doi: 10.1016/j.coastaleng.2021.103885

Reichmüth, B., and Anthony, E. J. (2007). Tidal influence on the intertidal bar morphology of two contrasting macrotidal beaches. *Geomorphology* 90, 101–114. doi: 10.1016/j.geomorph.2007.01.015

Ribeiro, M., Ferreira, F., Rodrigues, A., Oliveira, A., and Pinto, J. P. (2012). "Seasonal morphological variation at the So Torpes beach: decoupling longshore and crossshore sediment transport components," in *VII Simpósio sobre a Margem Ibérica Atlantica* (Lisbon).

Rijn, L. (2009). Prediction of dune erosion due to storms. *Coast. Eng.* 56, 441–457. doi: 10.1016/j.coastaleng.2008.10.006

Rijn, L. C. (2010). *Coastal Erosion Control Based on the Concept of Sediment Cells*. EU-Project CONSCIENCE. Delft: Deltares.

Rijn, L. V. (2011). Coastal erosion and control. *Ocean Coast. Manag.* 54, 867–887. doi: 10.1016/j.ocecoaman.2011.05.004

Ruessink, B. G., Blenkinsopp, C., Brinkkemper, J. A., Castelle, B., Dubarbier, B., Grasso, F., et al. (2016). Sandbar and beach-face evolution on a prototype coarse sandy barrier. *Coast. Eng.* 113, 19–32. doi: 10.1016/j.coastaleng.2015.11.005

Russell, P. E. (1993). Mechanisms for beach erosion during storms. *Continent. Shelf Res.* 13, 1243–1265. doi: 10.1016/0278-4343(93)90051-X

Russell, P. E., Foote, Y., and Huntley, D. A. (1995). "An energetics approach to sand transport on beaches," in *Proc. Coastal Dynamics' 95, ASCE* (New York, NY), 829–840.

Saulter, A. N., Russell, P. E., Gallagher, E. L., and Miles, J. R. (2003). Observations of bed level change in a saturated surf zone. *J. Geophys. Res. Oceans* 108:3112. doi: 10.1029/2000JC000684

Sedrati, M., and Anthony, E. J. (2007). Storm-generated morphological change and longshore sand transport in the intertidal zone of a multi-barred macrotidal beach. *Mar. Geol.* 244, 209–229. doi: 10.1016/j.margeo.2007.07.002

Shi, B. W., Yang, S. L., Wang, Y. P., Li, G. C., Li, M. L., Li, P., et al. (2017). Role of wind in erosion-accretion cycles on an estuarine mudflat. *J. Geophys. Res. Oceans* 122, 193–206. doi: 10.1002/2016JC011902

Short, A. D. (1991). Macro-meso tidal beach morphodynamics - an overview. *J. Coast. Res.* 7, 417–436.

Slobbe, E. V., Vriend, H., Aarninkhof, S., Lulofs, K., and Dircke, P. (2013). Building with nature: in search of resilient storm surge protection strategies. *Nat. Hazards* 66, 947–966. doi: 10.1007/s11069-012-0342-y

Soulsby, R. (1997). *Dynamics of Marine Sands: a Manual for Practical Applications*. London: Thomas Telford.

Stive, M. J. F., Schipper, M. A. D., Luijendijk, A. P., Aaninkhof, S. G. J., and Ranasinghe, R. (2013). A new alternative to saving our beaches from sea-level rise: the Sand Engine. *J. Coast. Res.* 29, 1001–1008. doi: 10.2112/JCOASTRES-D-13-00070.1

Svendsen, I. A. (1987). Analysis of surf zone turbulence. *J. Geophys. Res.* 92, 5115–5124. doi: 10.1029/JC092iC05p05115

Tinker, J., O'Hare, T., Masselink, G., Butt, T., and Russell, P. (2009). A cross-shore suspended sediment transport shape function parameterisation for natural beaches. *Continent. Shelf Res.* 29, 1948–1960. doi: 10.1016/j.csr.2009.03.011

van Bemmelen, C. W. T., de Schipper, M. A., Darnall, J., and Aarninkhof, S. G. J. (2020). Beach scarp dynamics at nourished beaches. *Coast. Eng.* 160:103725. doi: 10.1016/j.coastaleng.2020.103725

Vellinga, P. (1982). Beach and dune erosion during storm surges. *Coast. Eng.* 6, 361–387. doi: 10.1016/0378-3839(82)90007-2

Vidal-Ruiz, J. A., and de Alegría-Arzaburu, A. R. (2020). Modes of onshore sandbar migration at a single-barred and swell-dominated beach. *Mar. Geol.* 426:106222. doi: 10.1016/j.margeo.2020.106222

Vincent, C. E., and Hanes, D. M. (2002). The accumulation and decay of nearbed suspended sand concentration due to waves and wave groups. *Continent. Shelf Res.* 22, 1987–2000. doi: 10.1016/S0278-4343(02)00051-1

Vousdoukas, M. I., Almeida, L. P., and Ferreira, Ó. (2011). "Modelling storminduced beach morphological change in a meso-tidal, reflective beach using XBeach," in *Proceedings 11th International Coastal Symposium,* ed K. Furmańczyk (Szczecin: Journal of Coastal Research), 1916–1920.

Vousdoukas, M. I., Ranasinghe, R., Mentaschi, L., Plomaritis, T. A., Athanasiou, P., Luijendijk, A., et al. (2020). Sandy coastlines under threat of erosion. *Nat. Clim. Change* 10, 260–263. doi: 10.1038/s41558-020-0697-0

Winterwerp, J. C., and van Kesteren, W. G. M. (2004). *Introduction to the Physics of Cohesive Sediment in the Marine Environment*. Amsterdam: Elsevier. doi: 10.1016/S0070-4571(04)80004-9

Wright, L. D., Short, A. D., Iii, J. D. B., Hayden, B., Kimball, S., and List, J. H. (1987). The morphodynamic effects of incident wave groupiness and tide range on an energetic beach. *Mar. Geol.* 74, 1–20. doi: 10.1016/0025-3227(87)90002-8

Yoon, H. D., and Cox, D. T. (2012). Cross-shore variation of intermittent sediment suspension and turbulence induced by depth-limited wave breaking. *Continent. Shelf Res.* 47, 93–106. doi: 10.1016/j.csr.2012.07.001

Zhang, X., Leonardi, N., Donatelli, C., and Fagherazzi, S. (2020). Divergence of sediment fluxes triggered by sea-level rise will reshape coastal bays. *Geophys. Res. Lett.* 47:e2020GL087862. doi: 10.1029/2020GL087862

Zhou, G., Huang, J., Tao, Y., Luo, Q., and Zhang, G. (2015). Temporal-spatial distribution of wave energy: a case study of Beibu Gulf, China. *Renew. Energy* 74, 344–356. doi: 10.1016/j.renene.2014.08.014

Zhu, Q., Prooijen, B. V., Maan, D. C., Wang, Z. B., Yao, P., Daggers, T., et al. (2019). The heterogeneity of mudflat erodibility. *Geomorphology* 345:106834. doi: 10.1016/j.geomorph.2019.106834

Conflict of Interest: The authors declare that they have no known competing financial interests or personal relationships that could have appeared to influence the work reported in this paper.

Publisher's Note: All claims expressed in this article are solely those of the authors and do not necessarily represent those of their affiliated organizations, or those of the publisher, the editors and the reviewers. Any product that may be evaluated in this article, or claim that may be made by its manufacturer, is not guaranteed or endorsed by the publisher.

Copyright © 2021 Pang, Zhou, Dai, Li, Huang and Lei. This is an open-access article distributed under the terms of the Creative Commons Attribution License (CC BY). The use, distribution or reproduction in other forums is permitted, provided the original author(s) and the copyright owner(s) are credited and that the original publication in this journal is cited, in accordance with accepted academic practice. No use, distribution or reproduction is permitted which does not comply with these terms.

frontiers in Marine Science

ORIGINAL RESEARCH
published: 20 October 2021
doi: 10.3389/fmars.2021.728065

Effects of Waves and Sediment Disturbance on Seed Bank Persistence at Tidal Flats

*Zhenchang Zhu[1,2], Tjeerd J. Bouma[3,4], Qin Zhu[1,2], Yanpeng Cai[1,2] and Zhifeng Yang[1,2]**

[1] Guangdong Provincial Key Laboratory of Water Quality Improvement and Ecological Restoration for Watersheds, Institute of Environmental and Ecological Engineering, Guangdong University of Technology, Guangzhou, China, [2] Southern Marine Science and Engineering Guangdong Laboratory, Guangzhou, China, [3] Department of Estuarine and Delta Systems, Royal Netherlands Institute for Sea Research, Utrecht University, Yerseke, Netherlands, [4] Department of Physical Geography, Faculty of Geosciences, Utrecht University, Utrecht, Netherlands

Coastal wetlands such as salt marshes have been increasingly valued for their capacity to buffer global climate change effects, yet their long-term persistence is threatened by environmental changes. Whereas, previous studies largely focused on lateral erosion risk induced by stressors like sea level rise, it remains poorly understood of the response of lateral expansion to changing environments. Seedling establishment is a key process governing lateral marsh expansion as seen in many coastal regions such as Europe and East Asia. Here, we evaluate mechanistically the response of seed bank dynamics to changing physical disturbance at tidal flats, using the globally common coastal foundation plant, cordgrass as a model. We conducted a large-scale field study in an estuary in Northwest Europe, where seed bank dynamics of cordgrass in the tidal flats was determined and linked to *in situ* hydrodynamics and sediment dynamics. The results revealed that wave disturbance reduced the persistence of seeds on the surface, whereas amplified sediment disturbance lowered the persistence of both surface and buried seeds. Overall, this indicates that increasing storminess and associated sediment variability under climate change threatens seed bank persistence in tidal flats, and hence need urgently be incorporated into models for long-term bio-geomorphological development of vegetated coastal ecosystems. The knowledge gained here provides a basis for more accurate predictions on how climatically driven environmental changes may alter the fitness, resilience and persistence of coastal foundation plants, with significant implications for nature-based solutions with coastal vegetation to mitigate climate change effects.

Keywords: waves, sediment disturbance, tidal flats, seed bank, persistence

OPEN ACCESS

Edited by:
Zheng Gong,
Hohai University, China

Reviewed by:
Peng Yao,
Hohai University, China
Yining Chen,
Second Institute of Oceanography, Ministry of Natural Resources, China

****Correspondence:***
Zhifeng Yang
zfyang@gdut.edu.cn

Specialty section:
This article was submitted to Coastal Ocean Processes, a section of the journal Frontiers in Marine Science

Received: *20 June 2021*
Accepted: *01 October 2021*
Published: *20 October 2021*

Citation:
Zhu Z, Bouma TJ, Zhu Q, Cai Y and Yang Z (2021) Effects of Waves and Sediment Disturbance on Seed Bank Persistence at Tidal Flats. Front. Mar. Sci. 8:728065. doi: 10.3389/fmars.2021.728065

INTRODUCTION

Vegetated wetlands (e.g., salt marshes, seagrasses, and mangroves) are among the most ecological and socio-economically valuable systems on the globe (Costanza et al., 1997). Over the last decades, there has been increasing recognition of the coastal defenses value of vegetation due to their efficacy in wave attenuation and sediment stabilization (Gedan et al., 2011; Temmerman et al., 2013; Moller et al., 2014; Zhu et al., 2020b). This initiated a paradigm shift to a more ecosystem-based

flood protection using vegetated foreshores in the face of climate change (Cheong et al., 2013; Temmerman et al., 2013). Given a rising sea level and increasing storminess as predicted for many parts of the world (Donat et al., 2011; Young et al., 2011) and the vulnerability of coastal wetlands to environmental variations like sea level rise (Kirwan and Temmerman, 2009; Kirwan and Megonigal, 2013) and waves (Callaghan et al., 2010; Marani et al., 2011), it raises uncertainties in the stability and long-term persistence of coastal wetlands.

Seedling establishment is a crucial process of vegetation recovery seen in many meso- and macrotidal marsh ecosystems around the world such as in Europe and East Asia (Gray et al., 1991; Temmerman et al., 2007; Strong and Ayres, 2013; Liu et al., 2017). Unfortunately, seedling recruitment often forms a bottleneck, as waves and associated sediment dynamics often impose difficulties for seedling survival (e.g., Bouma et al., 2009; Friess et al., 2012; Balke et al., 2013) and seed persistence (Groenendijk, 1986; Marion and Orth, 2012; Zhu et al., 2014). Although, the minimal period that seed banks need to persist can be short, to cover the period between when seeds become available (fall) and seedlings start to emerge (spring), seed persistence (i.e., seed retention and preservation of viability) during this short period is vital. Seed bank formation in the coastal sediment matrix can be facilitated by sediment mixing induced by hydrodynamics coupled with ecosystem engineering of benthic fauna (Delefosse and Kristensen, 2012; Blackburn and Orth, 2013; Zhu et al., 2016a). However, seed dislodgment due to sediment erosion serves as a major source for seed loss of coastal foundation species at tidal flats (Groenendijk, 1986; Marion and Orth, 2012; Zhu et al., 2014), in which wave action plays a critical role in remobilizing the initially deposited seeds (Chang et al., 2008; Koch et al., 2010; Zhu et al., 2020a). A flume study on marsh plant seeds showed that wave-generated orbital water movement is necessary to dislodge and move seeds from the bottom to the water column where they can be exported by current velocity, whereas even high currents have a very limited ability to export waterlogged seeds in the absence of waves (Chang et al., 2008). A recent field study found that seed removal from tidal flat surface increased with wave-induced bed shear stress (Zhu et al., 2020a). When seeds germinate, they can be more easily lifted off by currents because of enhanced buoyancy. A recent flume study of *Spartina* seeds shows that seed removal from the surface increased non-linearly with germination stage and current velocity (Zhao et al., 2021).

Although, climate-change intensified hydrodynamic disturbance and associated sediment disturbance at tidal flats (e.g., the removal of sediment particles) may be expected to reduce seed bank persistence of coastal foundation plants, with far-reaching consequences for long-term ecosystem stability and functions, this is lacking from current biogeomorphic models. One of the keystone coastal plant engineers is cordgrass (*Spartina* spp.), which globally defines and stabilizes the shoreline of many temperate marshes (Strong and Ayres, 2009, 2013; Bortolus et al., 2019). Seed colonization plays a vital role in its natural (re-) establishment and range expansion, as well as the fast spread in many areas where the species has been willingly or accidentally been introduced (Gray et al., 1991; Ayres et al., 2008; Xiao et al., 2009). Seedling establishment of cordgrass occurs mainly in the pioneer zone and adjacent bare mudflats at suitable elevations at the presence of an annually built soil seed bank (Wolters and Bakker, 2002; Xiao et al., 2009). Given the role of cordgrass in enhancing coastal defense as powerful ecosystem engineers and its worldwide distribution, it is highly relevant to study the potential effects of climate-induced shifts in physical disturbance on the fate of its (annual) seed bank.

In this article, we investigate the persistence of cordgrass seed bank at tidal flats under variable hydro-morphodynamic conditions. Since hydrodynamics induced seed dislodgment serves as a major source of seed loss from the local seed bank at tidal flats (Groenendijk, 1986; Marion and Orth, 2012; Zhu et al., 2014), we here focused on the physical presence of seeds in the sediment matrix. Other components of seed persistence that are not directly affected by hydrodynamics, such

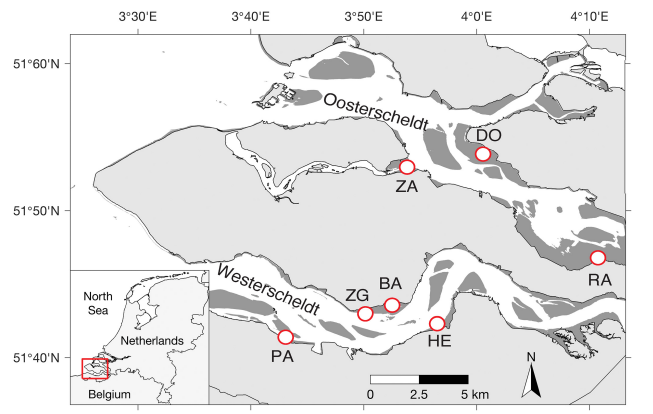


FIGURE 1 | Geographic locations of selected study sites. Site Paulinapolder (PA), Zuidgros (ZG), Baarland (BA), and Hellegateplder (HE) are in the Westerschelde, whereas Dortsman (DO), Rattekaai (RA), and Zandkreek (ZA) in the Oosterschelde (**Table 1**).

TABLE 1 | Study locations and their characteristics.

Location		Abbreviation	Elevation (cm NAP)	Grain size (D50, μm)	Current velocity (m/s)
Oosterschelde	Dortsman	DO	90	159.8	0.23*
	Rattekaai	RA	92	98.1	0.18*
	Zandkreek	ZA	85	96.3	0.17*
Westerschelde	Zuidgors	ZG_{LOW}	89	45.4	0.15**
	Zuidgors	ZG_{HIGH}	175	72.0	0.15**
	Baarland	BA	175	23.6	0.18**
	Hellegat	HE	102	109.6	0.13**
	Paulina	PA	82	76.0	0.09**

**Current velocity is the maximum current velocity at spring tide (Suykerbuyk et al., 2016). Data derived from SCAROOST 2D model from Rijkswaterstaat, Dutch Ministry of Infrastructure and Environment. The model uses the systems bathymetry (2010 data) and is validated by field measurements.*

***Current velocity is mean current speed measured on the tidal flat (Callaghan et al., 2010).*

as seed viability and seed germination, are beyond the scope of this study. Specifically, we examine whether increased physical disturbances decline seed bank persistence of cordgrass at tidal flats. Previous studies showed that the mobility of seeds on tidal flats was primarily determined by wave motion (Chang et al., 2008; Zhu et al., 2020a), and the retention of buried seeds at tidal flats increased with seed burial depth (Marion and Orth, 2012; Zhu et al., 2014). Hence, we hypothesize that stronger waves and greater sediment dynamics erode more seeds from the seed bank at tidal flats. To test these hypotheses, we conducted a large-scale field study in the Scheldt estuary in NW Europe, where seed bank persistence of cordgrass at tidal flats was determined and linked to local wave conditions and sediment dynamics. We aim to drive essential quantitative relationships to enable biogeomorphic modelers to include the potential effects of altered physical disturbance by environmental changes on the resilience and persistence of coastal foundation plants.

MATERIALS AND METHODS

Study Site

The Scheldt estuary is a macrotidal estuary situated near the border between Netherlands and Belgium (**Figure 1**). The mean tidal range increases from 3.8 m near the mouth of the estuary to > 5.0 m upstream of the border (Baeyens et al., 1998). It was originally composed of two aligned and interconnected water bodies called Westerschelde and Oosterschelde. Due to land reclamation, the Oosterschelde was progressively separated from the Westerschelde. The pioneer salt marsh vegetation consists mainly of the perennial common cordgrass (*Spartina*

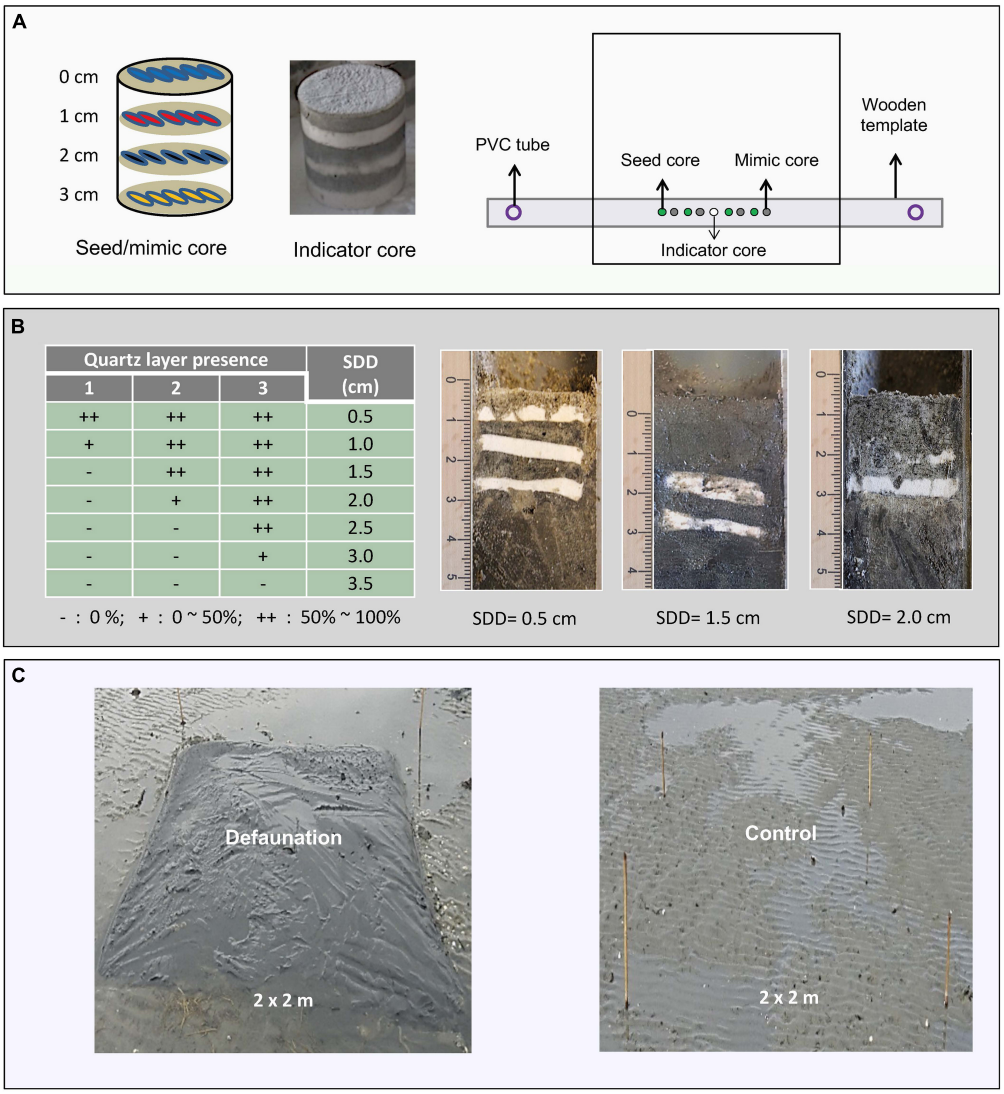


FIGURE 2 | (A) Seed bank core, indicator core, and their deployment in the plots. **(B)** Scoring rules and examples of sediment disturbance depth (SDD). **(C)** Defaunated and control plots.

anglica), which was introduced to the Scheldt estuary in the 1920s (Groenendijk, 1986; van der Wal et al., 2008). The study area comprises seven salt marshes with different wave exposure due to their position relative to the prevailing southwesterly winds (Callaghan et al., 2010; Suykerbuyk et al., 2016). Site Paulinapolder (PA), Zuidgros (ZG), Baarland (BA) and Hellegateplder (HE) are in the Westerschelde, whereas Dortsman (DO), Rattekaai (RA) and Zandkreek (ZA) in the Oosterschelde (**Table 1** and **Figure 1**). All the experiments and measurements were conducted in adjacent tidal flats in front of a salt marsh. The elevation of the experimental area was ca. 90 cm above NAP (i.e., Dutch ordinance level, which is close to local mean sea level) for most field sites, while a higher elevation (175 cm NAP) was adopted in two Westerschelde sites ZG & BA, where salt marshes extend less deep. At ZG, we included an additional location with a lower elevation (ca. 90 cm NAP) for direct comparison between the higher and lower elevations (ZG_{HIGH} and ZG_{LOW}). The mean velocity at tidal flats of the four Westerschelde site is less than 0.2 m/s (Callaghan et al., 2010), whereas the maximum velocity at tidal flats of the three Oosterschelde sites is around 0.2 m/s (Suykerbuyk et al., 2016; **Table 1**). A recent flume study on seed transport of cordgrass seeds shows that current velocity of <0.2 m/s has limited ability to lift-off ungerminated seeds (Zhao et al., 2021).

Manipulative Seed Bank Experiment

To examine the relationship between seed bank persistence and physical disturbance, we conducted a manipulative seed

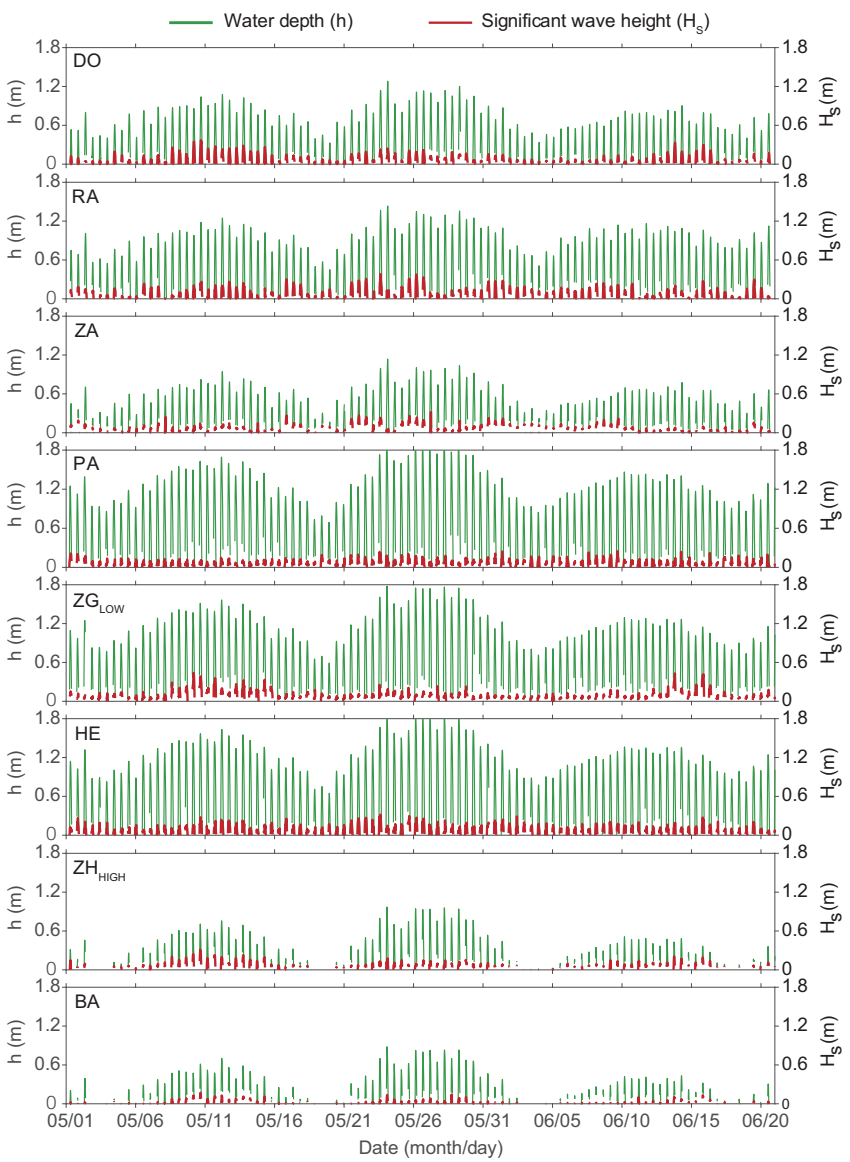


FIGURE 3 | Time-series water depth (*h*, m) and significant wave heights (H_s, *m*) at all locations during the experiment. The mean and maximum value of significant wave heights and wave periods are summarized in **Table 2**.

TABLE 2 | Significant wave heights (*Hs*), wave periods (*Ts*), wave-induced bed shear stress (τ_{wave}, time-averaged), and sediment disturbance depth (SDD) at each study location during the experiment.

Location	*Hs* (m)		*Ts* (s)		τ_{wave} (Pa)	SDD (cm)	
	Mean	Max	Mean	Max	Time-averaged	Defaunated	Control
DO	0.08	0.37	3.43	18.42	0.038	2.50	1.25
RA	0.10	0.38	4.10	14.93	0.042	3.25	1.25
ZA	0.06	0.32	2.97	18.56	0.036	1.25	1.00
ZG_{LOW}	0.10	0.44	3.13	19.09	0.045	2.00	1.25
ZG_{HIGH}	0.08	0.31	3.98	19.47	0.036	2.00	0.50
HE	0.09	0.32	7.06	19.88	0.011	1.00	0.50
BA	0.03	0.17	9.71	19.86	0.028	2.50	0.50
PA	0.07	0.25	4.00	19.86	0.035	1.75	3.50

bank experiment in all the selected locations. The manipulative seed bank was built by placing pre-prepared layered seed bank cores into the sediment. Seed mimics were also used to detect if any biogenic seed loss (e.g., predation and decomposition) occurred. For each core, five seeds/mimics were placed at the surface and the depth of 1–3 cm (**Figure 2A**). Layered indicator cores (Marion and Orth, 2012) were employed to estimate sediment disturbance depth (SDD) by placing tracer particles at known depths. Such particles were intended to wash away when momentarily resuspended by wave disturbance, leaving a record of scouring depth (Marion and Orth, 2012). In our experiment, Quartz Flour (manufactured silt, white, d50 = 100 μm) served as tracer particles, which were deployed at 0.5 cm intervals alternating with ambient sediments to make layered cores consisting of 3 tracer layers and 4 sediment layers (**Figure 2B**).

Layered seed/mimic cores were created in 200 ml top-truncated syringes (3.6 cm diameter) with homogenized ambient sediment and color-stained seeds/mimics, using the same methods and mimics (plastic chips of four colors) as described by Zhu et al. (2014). This material was proven to be highly effective in mimicking cordgrass seeds (Zhu et al., 2014). The sowed seeds were first sterilized by freezing them in a −20°C freezer for 2 weeks to prevent seed loss due to germination (Zhu et al., 2016b). Layered indicator cores for sediment disturbance were produced in the same syringes as the seed bank cores. Each layer was made by filling in homogenized tracer particles/ambient sediment to a thickness of 0.5 cm and then sent to the −20°C freezer. While still frozen, a new layer was added to minimize mixing. When all the layers were ready, these cores were taken out of the syringes and preserved in the freezer until use.

In each location, four permanent 2 × 2 m plots, ca. 3 m apart, were established and marked by PVC stakes (**Figure 2A**). Half of these plots were defaunated to detect the importance

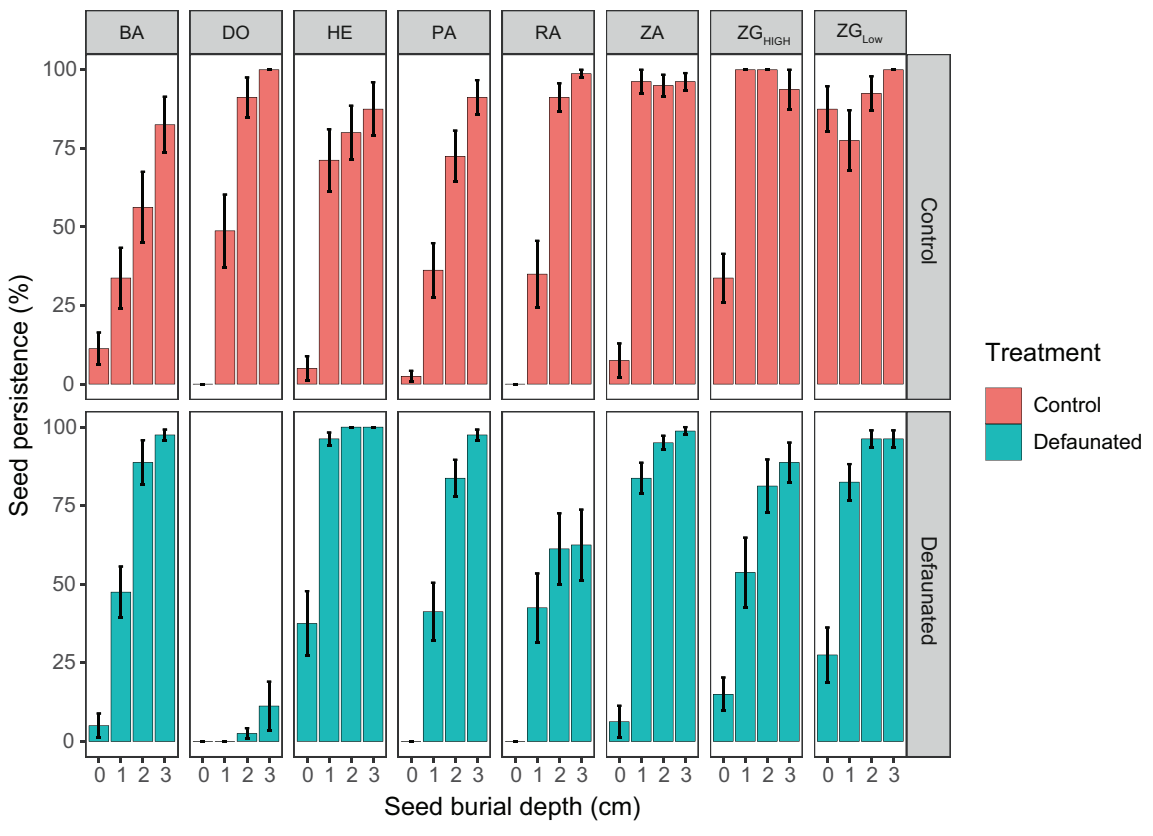


FIGURE 4 | The persistence of the manipulated seed bank at each study location, which was shown for the decaudated treatment (green bars) and the control (red bars), separately.

and the effects of the benthic animals on seed bank persistence (**Figure 2C**). The defaunation was implemented in January 2013 by covering the plots with a thick rubber sheets that were buried to a depth of 30 cm along the plot edges (Van Colen et al., 2008). Removing the aboveground rubber materials, the defaunated plots were opened after 12 weeks, which was sufficient long to kill the benthic animals by hypoxia (Van Colen et al., 2008). Seed bank cores and indicator cores were established 4 weeks later when the sediment surface in defaunated plots was leveled by natural physical process. This defaunation method has been proven to greatly lower the abundance of benthic animals; recovery takes at least one summer (Beukema et al., 1999; Van Colen et al., 2008).

In each defaunation/control plot, 4 seed cores, 4 mimic cores, and 1 indicator core were deployed. These cores were located in a line through a wooden template with 9 round holes (40 mm diameter), 15 cm apart. The indicator core was situated in the middle, while the seed cores and mimic cores were alternating each other on both sides at intervals of 15 cm (**Figure 2A**). All the cores were transported to the field in a foam box with dry ice to keep them frozen, and then placed with their surface level with the surrounding sediment in the method as described in Zhu et al. (2014). Both endpoints of the template possessed a hole that fitted a fixed PVC tube inserted into the soil, to allow accurate re-relocation upon retrieval.

After 8 weeks, all these cores were relocated using the same template and recovered to a depth of 100 mm, through PVC pipes which are larger in diameter (5 cm) than the original cores, to ascertain the whole core is re-sampled even if there is a slight imprecision in relocation. The recovered seed/mimic cores (Depth = 100 mm) were transported to the lab, sieved through a 1 mm sieve to retrieve deployed seeds and mimics, which were classified per layer according to their colors. Many seeds (but no mimics) turned black when retrieved because of the anaerobic condition within the sediment. To identify the stained color of those seeds, they were bathed in fresh water for at least 24 h until their original stain re-appeared (Zhu et al., 2014).The number of recovered seeds or mimics of each color was counted and recorded. Seed persistence (%) was then calculated as the recovered/total deployed.

Upon arrival in the lab, the retrieved indicator cores were stored in a −20°C freezer until processing. While still frozen, they were longitudinally cross-sectioned using a band saw. The frozen smear left by the band saw was removed using a razor. SDD was estimated through a scoring system that examines the presence of Quartz Flour layers in the profile of the half core (scoring rules and examples given in **Figure 2B**). In total, 30 out of 32 indicator cores were scored, whereas two cores retrieved from one control plot at ZG_{LOW} and one defaunation plot at PA failed due to the damage during processing.

This was implemented in a relative storm-free period (May–July, 2013) to exclude the impacts of severe storms, and to obtain a range of wave conditions including both small and large waves. During this period, the wind speed was usually less than 10 m/s and winds were mostly from Southwest or Southeast (**Supplementary Figure 1**). The wave forcing and tidal level of each location was measured using pressure sensors (OSSI-010-003C; Ocean Sensor Systems, Inc.) deployed in the experiment zone. The pressure sensors were placed 5 cm above the tidal flat surface. The measuring interval and period were 15 and 7 min, respectively. The wave analysis was based on pressure fluctuations, as measured with a frequency

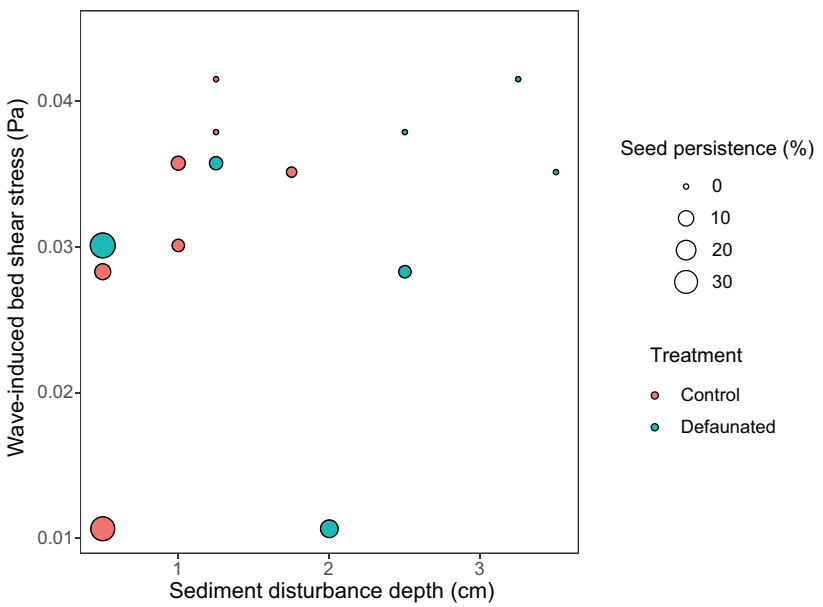


FIGURE 5 | The combined data from the decaudated treatment (green circles) and the control (red circles) showed that, the persistence of seeds on the surface (presented as the size of the circle) decreased with increased wave disturbance and sediment disturbance. Such relationship could be described by the function: z = 0.63 − 0.10 x −8.46 y, where x is sediment disturbance depth (cm), and y is wave-induced bed shear stress (Pa).

of 5 Hz. The recorded pressure readings were converted to water level fluctuations, which were then corrected by removing erroneous spikes, shifts, corrupted bursts, and low frequency tidal components (c.f. Callaghan et al., 2010; Christianen et al., 2013). From the detrended data, water depth (h) was determined meanwhile wave parameters, e.g., significant wave height (H_s) and wave period (Ts) were calculated based on the linear wave theory (Tucker and Pitt, 2001).

Based on water depth and wave parameters, we calculated the time-averaged bed shear stress induced by waves (τ_{wave}) with the same method (**Supplementary Methods**) as described in previous studies (Callaghan et al., 2010; Zhu et al., 2019, 2020a). τ_{wave} is a relevant proxy for the hydrodynamic energy in relation with sediment motion (Callaghan et al., 2010) and seed removal from tidal flat surface (Zhu et al., 2020a). The elevation in the experimental zone was monthly monitored during Mar and July, using a 3D Laser scanner (RIEGL VZ-400), as described in our previous study at the same locations (Zhu et al., 2020a).

Statistics

We first conducted Pairwise Wilcoxon Rank Sum Tests to detect the difference of seed bank persistence between seeds and seed mimics. Since the results showed no significant difference (p = 0.33) between them, these data were pooled together in further analysis. Due to the non-normally distributed data, GLMs (Generalized linear models) were employed to examine the effects of study location, seed burial depth and treatment (defaunated or not) on seed persistence. We specified "binomial" family to the model, given a negative binomial distribution of the data. When necessary, we refitted the model using "quasi-binomial" to account for the over-dispersion. We then calculated the averaged seed persistence for the control and defaunated plots at each location, respectively, and linked it to wave disturbance (τ_{wave}) and SDD at that location via linear models. Prior to the analysis, the data of seed persistence was square root transformed to satisfy the requirement of data normality. All the statistical analysis was done in R[1], applying a significance level of $\alpha = 0.05$.

TABLE 3 | ANOVA table for the linear models examining the response of seed persistence to sediment disturbance depth (SDD), wave disturbance (τ_{wave}), and treatment (defaunated/control).

Response variable	Source	Df	Sum Sq	Mean Sq	*F* value	Pr (>F)
Seed persistence of surface seeds (All locations)	SDD	1	0.280	0.280	3.932	0.083
	τ_{wave}	1	0.004	0.004	0.061	0.810
	Treatment	1	0.062	0.062	0.866	0.379
	SDD:τ_{wave}	1	0.001	0.001	0.010	0.921
	SDD:Treatment	1	0.000	0.000	0.000	0.991
	τ_{wave}:Treatment	1	0.051	0.051	0.713	0.423
	SDD:τ_{wave}:Treatment	1	0.151	0.151	2.116	0.184
Seed persistence of surface seeds (ZG_{LOW} excluded)	SDD	1	0.242	0.242	28.174	<0.01**
	τ_{wave}	1	0.191	0.191	22.199	<0.01**
	Treatment	1	0.063	0.063	7.368	0.035*
	SDD:τ_{wave}	1	0.011	0.011	1.276	0.302
	SDD:Treatment	1	0.005	0.005	0.615	0.463
	τ_{wave}:Treatment	1	0.000	0.000	0.001	0.971
	SDD:τ_{wave}:Treatment	1	0.011	0.011	1.260	0.304
Seed persistence of buried seeds	Treatment	1	0.203	0.203	5.477	0.029*
	SDD	1	0.268	0.268	7.207	0.014*
	τ_{wave}	1	0.001	0.001	0.036	0.852
	Treatment:SDD	1	0.022	0.022	0.583	0.453
	τ_{wave}:Treatment	1	0.018	0.018	0.476	0.498
	SDD:τ_{wave}	1	0.000	0.000	0.005	0.947
	SDD:τ_{wave}:Treatment	1	0.002	0.002	0.053	0.821

*Significance level: *0.05, **0.01.*

RESULTS

Overview of Physical Conditions at All Study Locations

The selected locations exhibited variable water depth and wave conditions during the experiment (**Figure 3** and **Table 2**). The maximum value of water depth h ranged between 0.9 m (Site BA) and 1.9 m (Site PA). The mean significant wave height Hs, covered a range of 0.03–0.10 m, the range of maximum Hs was between 0.17 and 0.44 m. The range of mean wave period Ts was 2.97 – 9.71 s, and the maximum value range was 47.28 to 410.90 s.

Sediment disturbance depth differed between locations as well as between defauated and control plots (**Table 2**). SDD ranged from 1.00 cm to 3.25 cm for the control plots, whereas it was 0.50 – 3.50 cm for the defaunated plots. The defaunation plots had greater SDD ($p < 0.001$), suggesting that at the local scale benthic animals may affect seed bank persistence by influencing sediment erodibility to hydrodynamics.

Relationship Between Physical Disturbance and Seed Bank Persistence

Seed persistence at tidal flats was dependent on their vertical positions, and varied between control and defaunated plots, as well as between locations that differed in the strength of wave disturbance and sediment disturbance (**Figure 4**).

For the seeds on the surface, their persistence declined with the growth of wave-induced bed shear stress (τ_{wave}) and SDD (**Figure 5**). Such relationship could be described by the function: $z = 0.63 - 0.10\ x\ -8.46\ y$, where x is SDD (cm), and y is wave-induced bed shear stress (Pa). This relationship was not significant when including data from all locations, whereas it became highly significant if the only continuously fast accreting location ZG_{LOW} (ca. 1.2 mm/d, **Supplementary Figure 2**) was removed from the analysis (**Table 3**). The fast accretion most likely resulted from the dumping of dredged sediment near this location (Sistermans and Nieuwenhuis, 2019), which might offer the surface seeds a window of opportunity to get sufficiently buried to escape wave disturbance.

When seeds were buried, their persistence decreased significantly with growing SDD, whereas there was no significant effect from wave disturbance (**Figure 6A** and **Table 3**). Further analysis revealed that seed persistence was enhanced non-linearly with increasing seed burial depth and the response curve was

[1]http://www.R-project.org

affected by SDD (**Figure 6B**). Greater SDD led to lower seed persistence and vice versa.

Additional Pairwise Wilcoxon Rank Sum Tests showed that there was no significant difference of surface seed persistence between the defaunated and control plots ($p = 0.09$). In contrast, seed persistence of the buried seeds in the defaunated plots was significantly lower ($p < 0.001$) than that in the control plots, where SDD was generally higher (**Figure 6A**).

DISCUSSION

Whereas, previous studies and modeling work largely focused on lateral marsh erosion risk induced by stressors like sea level rise, much less is known on the response of lateral marsh expansion to changing environments. Physical disturbance (e.g., waves and sediment mixing) on seedling establishment has been suggested as a main bottleneck for seed-based lateral expansion of coastal marsh vegetation (Lovelock et al., 2010; Friess et al., 2012; Balke et al., 2013). Using cordgrass as an example, this study clearly showed that wave disturbance affected the persistence of seeds on the surface, whereas sediment disturbance decreased the persistence of both surface and buried seeds. Overall, our findings indicate that (i) climate change likely reduce seed bank persistence in coastal wetlands via intensifying wave forcing and associated sediment disturbance and (ii) this process hence needs to be incorporated in biogeomorphic models predicting the future of coastal wetlands.

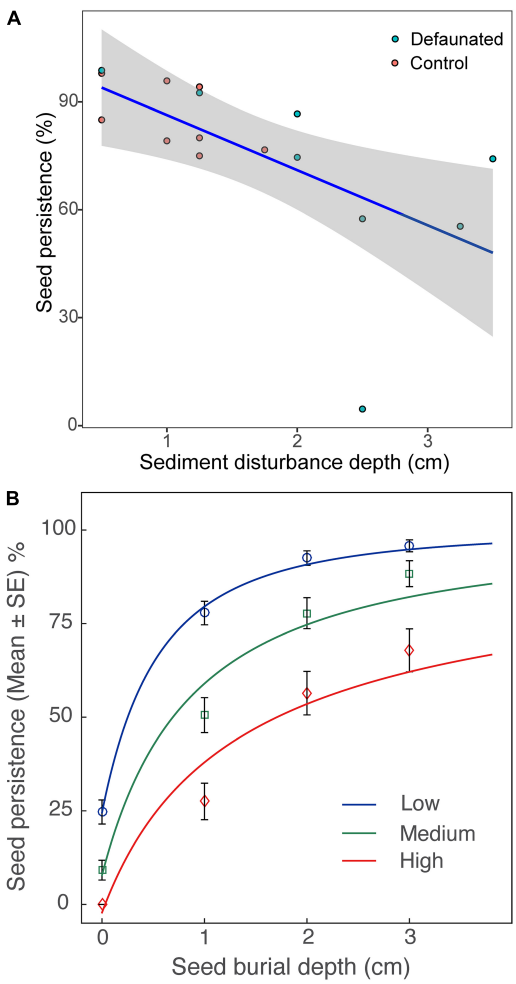


FIGURE 6 | (A) The persistence of the buried seeds decreased with increased sediment disturbance depth (curve fit: y = 1.01 – 0.15x). **(B)** Effects of sediment disturbance depth (SDD, three levels: low, medium and high) on the persistence of seeds from different burial depths; Low: SDD < = 1 cm, Medium: 1 < SDD < = 2 cm, and High: SDD > 2 cm; the response curves were fit with function: y = 1 – (x + a)^b (Zhu et al., 2014).

Seed burial can non-linearly enhance seed persistence. However, the buried seeds would still be turned over by sediment disturbance. Our experiment demonstrated that the quantity of seed loss from the buried seed bank was determined by both SDD and seed burial depth. Greater disturbance depth can turn over the buried seeds that would otherwise remain "safe" under lower disturbance depth. Although, wave disturbance might ease seed burial by promoting sediment mixing (Zhu et al., 2016a), the present study showed that amplified wave disturbance and sediment variability led to increased seed erosion. Deep burial improves seed persistence at tidal flats, yet it can lead to the failure of seed-seedling transition. Seedling emergence of cordgrass was found to decline with increasing seed burial depth (Bouma et al., 2016), as seeds germinated from deep depth are not able to reach the sediment surface (Greve et al., 2005). Hence, successful seed-seedling transition predominantly requires seeds to be positioned in moderate depths that benefit both seed persistence and seedling emergence.

The eroded seeds may be transported seaward to distant places or washed ashore (Huiskes et al., 1995). The landward transported seeds may either be trapped by the standing vegetation (Chang et al., 2008) or add into driftline materials deposited near/on the dike (Wolters and Bakker, 2002). Our results imply that, in coastal habitats with predicted intensifying storminess under global change, more frequent and stronger waves in winter and early spring might lower seed bank formation and persistence in more exposed areas, i.e., the pioneer zone and tidal flats. In contrast, seeds would tend to settle down in more sheltered areas (e.g., within vegetation), where seedling establishment is however less meaningful due to the lack of niches.

Sediment disturbance was primarily driven by hydrodynamics, but can also be shaped by benthos activities. Many benthic organisms (e.g., polychaetes and bivalves) are known to increase local sediment erodibility by bioturbating activities (Widdows and Brinsley, 2002; Meysman et al., 2006; Andersen et al., 2010), while some others (e.g., diatoms) can armor and stabilize the sediment (Stal, 2003). In our large-scale field experiments, the reduction of benthos resulted in overall higher sediment disturbance that caused lower seed persistence. This finding suggests that sediment erodiblity and seed bank mobility may be non-linearly enhanced by intensified wave disturbance, given that benthos abundance in intertidal flats tends to be lower under stronger physical forcing (e.g., Cozzoli et al., 2014).

Coastal vegetated systems like salt marshes are dynamic systems with long-term cyclic alternations between a retreating phase of cliff erosion and an establishment phase by seedling recruitment (van de Koppel et al., 2005; Bouma et al., 2016). Successful seedling establishment requires the presence of window of opportunity, i.e., disturbance free (or low) period (Balke et al., 2011, 2014; Hu et al., 2015). With amplified disturbance characteristics (frequency and magnitude) under climate change, seed colonization potential of coastal vegetated systems may decline due to worsened seed bank formation, and seed bank persistence. Such effect combined with reduced window of opportunity for seedling survival due to amplified physical disturbances can lead to a substantial reduction of regeneration capacity. Consequently, an impaired regeneration capacity might affect long-term vegetation persistence by disabling the shift of available niches from a bare state to a vegetated state, thus "locking" the system to the retreating phase. This will inevitably threaten long-term persistence of valuable coastal wetlands, thereby risking the loss of invaluable ecosystems services such as coastal defense values and carbon sequestration.

Biogeomorphic models are essential tools for predicting long-term evolution and persistence of coastal wetlands. However, in current biogeomorphic models that simulate lateral marsh dynamics, seeds are typically assumed to be present everywhere, with the seedling survival being related to bed-shear-stress (Temmerman et al., 2007; Fagherazzi et al., 2012). The current study clearly showed that seed persistence at tidal flats was dependent on both wave disturbance and sediment disturbance. To enable more accurate simulations of lateral marsh dynamics, the availability of seeds at tidal flats should be calculated as a function of bed shear stress induced by waves and the magnitude of sediment erosion. The quantitative relationship derived from our field measurements (**Figure 5**) could contribute to the parametrization of such a function.

CONCLUSION

The current study reveals that stronger wave disturbance and greater sediment disturbance erode more seeds from the seed bank at tidal flats, which advances the understanding of underlying mechanisms governing lateral dynamics of coastal wetlands. Given the critical role of seed colonization in lateral expansion of coastal vegetation and its sensitivity to environmental changes, the knowledge gained here enables more accurate predictions on how climatically driven environmental changes may alter the resilience and persistence of coastal foundation plants, with significant implications for nature-based solutions with coastal vegetation to mitigate climate change.

DATA AVAILABILITY STATEMENT

The raw data supporting the conclusions of this article will be made available by the authors, without undue reservation.

AUTHOR CONTRIBUTIONS

ZZ designed, carried out the experiment, analyzed the data, and wrote the initial version of the manuscript. All authors contributed to the improvement of the article and approved the submitted version.

FUNDING

ZZ, QZ, YC, and ZY were supported by the Program for Guangdong Introducing Innovative and Entrepreneurial Teams (2019ZT08L213) and the Key Special Project for Introduced Talents Team of Southern Marine Science and Engineering Guangdong Laboratory (Guangzhou) (GML2019ZD0403). TB was supported by the Perspectief Research Program "All-Risk" (project number P15-21B1), primarily financed by NWO Domain Applied and Engineering Sciences.

ACKNOWLEDGMENTS

We thank Lennart van IJzerloo, Jeroen van Dalen, Nanyang Chu, and Tao Hong for their assistances in the field.

SUPPLEMENTARY MATERIAL

The Supplementary Material for this article can be found online at: https://www.frontiersin.org/articles/10.3389/fmars.2021.728065/full#supplementary-material

REFERENCES

Andersen, T. J., Lanuru, M., van Bernem, C., Pejrup, M., and Riethmueller, R. (2010). Erodibility of a mixed mudflat dominated by microphytobenthos and Cerastoderma edule, East Frisian Wadden Sea, Germany. *Estuar. Coast. Shelf Sci.* 87, 197–206. doi: 10.1016/j.ecss.2009.10.014

Ayres, D. R., Zaremba, K., Sloop, C. M., and Strong, D. R. (2008). Sexual reproduction of cordgrass hybrids (Spartina foliosa x alterniflora) invading tidal marshes in San Francisco Bay. *Divers. Distrib.* 14, 187–195. doi: 10.1111/j.1472-4642.2007.00414.x

Baeyens, W., van Eck, B., Lambert, C., Wollast, R., and Goeyens, L. (1998). General description of the Scheldt estuary. *Hydrobiologia* 366, 1–14. doi: 10.1007/978-94-017-3573-5_1

Balke, T., Bouma, T. J., Horstman, E. M., Webb, E. L., Erftemeijer, P. L. A., and Herman, P. M. J. (2011). Windows of opportunity: thresholds to mangrove seedling establishment on tidal flats. *Mar. Ecol. Prog. Ser.* 440, 1–9. doi: 10.3354/meps09364

Balke, T., Herman, P. M., and Bouma, T. J. (2014). Critical transitions in disturbance-driven ecosystems: identifying Windows of Opportunity for recovery. *J. Ecol.* 102, 700–708. doi: 10.1111/1365-2745.12241

Balke, T., Webb, E. L., van den Elzen, E., Galli, D., Herman, P. M. J., and Bouma, T. J. (2013). Seedling establishment in a dynamic sedimentary environment: a conceptual framework using mangroves. *J. Appl. Ecol.* 50, 740–747. doi: 10.1111/1365-2664.12067

Beukema, J. J., Flach, E. C., Dekker, R., and Starink, M. (1999). A long-term study of the recovery of the macrozoobenthos on large defaunated plots on a tidal

flat in the Wadden Sea. *J. Sea Res.* 42, 235–254. doi: 10.1016/s1385-1101(99)00027-1

Blackburn, N. J., and Orth, R. J. (2013). Seed burial in eelgrass Zostera marina: the role of infauna. *Mar. Ecol. Prog. Ser.* 474, 135–145. doi: 10.3354/meps10103

Bortolus, A., Adam, P., Adams, J. B., Ainouche, M. L., Ayres, D., Bertness, M. D., et al. (2019). Supporting Spartina: interdisciplinary perspective shows Spartina as a distinct solid genus. *Ecology* 100:e02863.

Bouma, T. J., Friedrichs, M., Klaassen, P., van Wesenbeeck, B. K., Brun, F. G., Temmerman, S., et al. (2009). Effects of shoot stiffness, shoot size and current velocity on scouring sediment from around seedlings and propagules. *Mar. Ecol. Prog. Ser.* 388, 293–297. doi: 10.3354/meps08130

Bouma, T. J., van Belzen, J., Balke, T., van Dalen, J., Klaassen, P., Hartog, A. M., et al. (2016). Short-term mudflat dynamics drive long-term cyclic salt marsh dynamics. *Limnol. Oceanogr.* 61, 2261–2275. doi: 10.1002/lno.10374

Callaghan, D. P., Bouma, T. J., Klaassen, P., van der Wal, D., Stive, M. J. F., and Herman, P. M. J. (2010). Hydrodynamic forcing on salt-marsh development: distinguishing the relative importance of waves and tidal flows. *Estuar. Coast. Shelf Sci.* 89, 73–88. doi: 10.1016/j.ecss.2010.05.013

Chang, E. R., Veeneklaas, R. M., Buitenwerf, R., Bakker, J. P., and Bouma, T. J. (2008). To move or not to move: determinants of seed retention in a tidal marsh. *Funct. Ecol.* 22, 720–727. doi: 10.1111/j.1365-2435.2008.01434.x

Cheong, S.-M., Silliman, B., Wong, P. P., van Wesenbeeck, B., Kim, C.-K., and Guannel, G. (2013). Coastal adaptation with ecological engineering. *Nat. Clim. Chang.* 3, 787–791. doi: 10.1038/nclimate1854

Christianen, M. J. A., van Belzen, J., Herman, P. M. J., van Katwijk, M. M., Lamers, L. P. M., van Leent, P. J. M., et al. (2013). Low-Canopy Seagrass Beds Still Provide Important Coastal Protection Services. *PLoS One* 8:e62413. doi: 10.1371/journal.pone.0062413

Costanza, R., d'Arge, R., de Groot, R., Farberk, S., Grasso, M., Hannon, B., et al. (1997). The value of the world's ecosystem services and natural capital. *Nature* 387:253.

Cozzoli, F., Eelkema, M., Bouma, T. J., Ysebaert, T., Escaravage, V., and Herman, P. M. J. (2014). A mixed modeling approach to predict the effect of environmental modification on species distributions. *PLoS One* 9:e89131. doi: 10.1371/journal.pone.0089131

Delefosse, M., and Kristensen, E. (2012). Burial of *Zostera marina* seeds in sediment inhabited by three polychaetes: laboratory and field studies. *J. Sea Res.* 71, 41–49. doi: 10.1016/j.seares.2012.04.006

Donat, M., Renggli, D., Wild, S., Alexander, L., Leckebusch, G., and Ulbrich, U. (2011). Reanalysis suggests long-term upward trends in European storminess since 1871. *Geophys. Res. Lett.* 38:L14703.

Fagherazzi, S., Kirwan, M. L., Mudd, S. M., Guntenspergen, G. R., Temmerman, S., D'Alpaos, A., et al. (2012). Numerical models of salt marsh evolution: ecological, geomorphic, and climatic factors. *Rev. Geophys.* 50:RG1002.

Friess, D. A., Krauss, K. W., Horstman, E. M., Balke, T., Bouma, T. J., Galli, D., et al. (2012). Are all intertidal wetlands naturally created equal? Bottlenecks, thresholds and knowledge gaps to mangrove and saltmarsh ecosystems. *Biol. Rev.* 87, 346–366. doi: 10.1111/j.1469-185x.2011.00198.x

Gedan, K. B., Kirwan, M. L., Wolanski, E., Barbier, E. B., and Silliman, B. R. (2011). The present and future role of coastal wetland vegetation in protecting shorelines: answering recent challenges to the paradigm. *Clim. Change* 106, 7–29. doi: 10.1007/s10584-010-0003-7

Gray, A. J., Marshall, D. F., and Raybould, A. F. (1991). A century of evolution in *Spartina anglica*. *Adv. Ecol. Res.* 21, 1–62. doi: 10.1016/s0065-2504(08)60096-3

Greve, T. M., Krause-Jensen, D., Rasmussen, M. B., and Christensen, P. B. (2005). Means of rapid eelgrass (*Zostera marina* L.) recolonisation in former dieback areas. *Aquat. Bot.* 82, 143–156. doi: 10.1016/j.aquabot.2005.03.004

Groenendijk, A. M. (1986). Establishment of a *Spartina-anglica* population on a tidal mudflat - A field experiment. *J. Environ. Manage.* 22, 1–12.

Hu, Z., Belzen, J., Wal, D., Balke, T., Wang, Z. B., Stive, M., et al. (2015). Windows of opportunity for salt marsh vegetation establishment on bare tidal flats: the importance of temporal and spatial variability in hydrodynamic forcing. *J. Geophys. Res. Biogeosci.* 120, 1450–1469. doi: 10.1002/2014jg002870

Huiskes, A. H. L., Koutstaal, B. P., Herman, P. M. J., Beeftink, W. G., Markusse, M. M., and Munck, W. D. (1995). Seed dispersal of halophytes in tidal salt marshes. *J. Ecol.* 83, 559–567. doi: 10.2307/2261624

Kirwan, M., and Temmerman, S. (2009). Coastal marsh response to historical and future sea-level acceleration. *Quat. Sci. Rev.* 28, 1801–1808. doi: 10.1016/j.quascirev.2009.02.022

Kirwan, M. L., and Megonigal, J. P. (2013). Tidal wetland stability in the face of human impacts and sea-level rise. *Nature* 504, 53–60. doi: 10.1038/nature12856

Koch, E. W., Ailstock, M. S., Booth, D. M., Shafer, D. J., and Magoun, A. D. (2010). The role of currents and waves in the dispersal of submersed angiosperm seeds and seedlings. *Restor. Ecol.* 18, 584–595. doi: 10.1111/j.1526-100x.2010.00698.x

Liu, W., Strong, D. R., Pennings, S. C., and Zhang, Y. (2017). Provenance-by-environment interaction of reproductive traits in the invasion of Spartina alterniflora in China. *Ecology* 98, 1591–1599. doi: 10.1002/ecy.1815

Lovelock, C., Sorrell, B., Hancock, N., Hua, Q., and Swales, A. (2010). Mangrove Forest and Soil Development on a Rapidly Accreting Shore in New Zealand. *Ecosystems* 13, 437–451. doi: 10.1007/s10021-010-9329-2

Marani, M., D'Alpaos, A., Lanzoni, S., and Santalucia, M. (2011). Understanding and predicting wave erosion of marsh edges. *Geophys. Res. Lett.* 38:L21401.

Marion, S. R., and Orth, R. J. (2012). Seedling establishment in eelgrass: seed burial effects on winter losses of developing seedlings. *Mar. Ecol. Prog. Ser.* 448, 197–207. doi: 10.3354/meps09612

Meysman, F. J. R., Middelburg, J. J., and Heip, C. H. R. (2006). Bioturbation: a fresh look at Darwin's last idea. *Trends Ecol. Evol.* 21, 688–695. doi: 10.1016/j.tree.2006.08.002

Moller, I., Kudella, M., Rupprecht, F., Spencer, T., Paul, M., van Wesenbeeck, B. K., et al. (2014). Wave attenuation over coastal salt marshes under storm surge conditions. *Nat. Geosci.* 7, 727–731. doi: 10.1038/ngeo2251

Sistermans, P., and Nieuwenhuis, O. (2019). *Western scheldt estuary (the netherlands)*.

Sistermans, P., and O. Nieuwenhuis. (2019). *Western Scheldt Estuary (The Netherlands)*. EUROSION Case Study. Available online at: http://databases.eucc-d.de/plugins/projectsdb/project.php?show=380

Stal, L. J. (2003). Microphytobenthos, their extracellular polymeric substances, and the morphogenesis of intertidal sediments. *Geomicrobiol. J.* 20, 463–478. doi: 10.1080/713851126

Strong, D., and Ayres, D. (2009). *Spartina* introductions and consequences in salt marshes.) Human impacts on salt marshes: a global perspective. London: University of California Press Ltd.

Strong, D. R., and Ayres, D. R. (2013). Ecological and evolutionary misadventures of *Spartina*. *Annu. Rev. Ecol. Evol. Syst.* 44, 389–410. doi: 10.1146/annurev-ecolsys-110512-135803

Suykerbuyk, W., Bouma, T. J., Govers, L. L., Giesen, K., de Jong, D. J., Herman, P., et al. (2016). Surviving in changing seascapes: sediment dynamics as bottleneck for long-term seagrass presence. *Ecosystems* 19, 296–310. doi: 10.1007/s10021-015-9932-3

Temmerman, S., Bouma, T., Van de Koppel, J., Van der Wal, D., De Vries, M., and Herman, P. (2007). Vegetation causes channel erosion in a tidal landscape. *Geology* 35, 631–634. doi: 10.1130/g23502a.1

Temmerman, S., Meire, P., Bouma, T. J., Herman, P. M. J., Ysebaert, T., and De Vriend, H. J. (2013). Ecosystem-based coastal defence in the face of global change. *Nature* 504, 79–83. doi: 10.1038/nature12859

Tucker, M. J., and Pitt, E. G. (2001). *Waves In Ocean Engineering*. Amsterdam: Elsevier.

Van Colen, C., Montserrat, F., Vincx, M., Herman, P. M. J., Ysebaert, T., and Degraer, S. (2008). Macrobenthic recovery from hypoxia in an estuarine tidal mudflat. *Mar. Ecol. Prog. Ser.* 372, 31–42. doi: 10.3354/meps07640

van de Koppel, J., van der Wal, D., Bakker, J. P., and Herman, P. M. (2005). Self-organization and vegetation collapse in salt marsh ecosystems. *Am. Nat.* 165, E1–E12.

van der Wal, D., Wielemaker-Van den Dool, A., and Herman, P. M. J. (2008). Spatial patterns, rates and mechanisms of saltmarsh cycles (Westerschelde, The Netherlands). *Estuar. Coast. Shelf Sci.* 76, 357–368. doi: 10.1016/j.ecss.2007.07.017

Widdows, J., and Brinsley, M. (2002). Impact of biotic and abiotic processes on sediment dynamics and the consequences to the structure and functioning of the intertidal zone. *J. Sea Res.* 48, 143–156. doi: 10.1016/s1385-1101(02)00148-x

Wolters, M., and Bakker, J. P. (2002). Soil seed bank and driftline composition along a successional gradient on a temperate salt marsh. *Appl. Veg. Sci.* 5, 55–62. doi: 10.1111/j.1654-109x.2002.tb00535.x

Xiao, D., Zhang, L., and Zhu, Z. (2009). A study on seed characteristics and seed bank of *Spartina alterniflora* at saltmarshes in the Yangtze Estuary, China. *Estuar. Coast. Shelf Sci.* 83, 105–110. doi: 10.1016/j.ecss.2009.03.024

Young, I., Zieger, S., and Babanin, A. (2011). Global trends in wind speed and wave height. *Science* 332, 451–455. doi: 10.1126/science.1197219

Zhao, Z., Zhang, L., Li, X., Yuan, L., and Bouma, T. J. (2021). The onset of secondary seed dispersal is controlled by germination-features: a neglected process in sudden saltmarsh establishment. *Limnol. Oceanogr.* 66, 3070–3084. doi: 10.1002/lno.11860

Zhu, Q., Van Prooijen, B., Maan, D., Wang, Z., Yao, P., Daggers, T., et al. (2019). The heterogeneity of mudflat erodibility. *Geomorphology* 345:106834. doi: 10.1016/j.geomorph.2019.106834

Zhu, Z., Bouma, T. J., Ysebaert, T., Zhang, L., and Herman, P. M. J. (2014). Seed arrival and persistence at the tidal mudflat: identifying key processes for pioneer seedling establishment in salt marshes. *Mar. Ecol. Prog. Ser.* 513, 97–109. doi: 10.3354/meps10920

Zhu, Z., van Belzen, J., Hong, T., Kunihiro, T., Ysebaert, T., Herman, P. M. J., et al. (2016b). Sprouting as a gardening strategy to obtain superior supplementary food: evidence from a seed-caching marine worm. *Ecology* 97, 3278–3284. doi: 10.1002/ecy.1613

Zhu, Z., Cozzoli, F., Chu, N., Salvador, M., Ysebaert, T., Zhang, L., et al. (2016a). Interactive effects between physical forces and ecosystem engineers on seed burial: a case study using Spartina anglica. *Oikos* 125, 98–106. doi: 10.1111/oik.02340

Zhu, Z., Vuik, V., Visser, P. J., Soens, T., van Wesenbeeck, B., van de Koppel, J., et al. (2020b). Historic storms and the hidden value of coastal wetlands for nature-based flood defence. *Nat. Sustain.* 3, 853–862. doi: 10.1038/s41893-020-0556-z

Zhu, Z., van Belzen, J., Zhu, Q., van de Koppel, J., and Bouma, T. J. (2020a). Vegetation recovery on neighboring tidal flats forms an Achilles' heel of saltmarsh resilience to sea level rise. *Limnol. Oceanogr.* 65, 51–62. doi: 10.1002/lno.11249

Conflict of Interest: The authors declare that the research was conducted in the absence of any commercial or financial relationships that could be construed as a potential conflict of interest.

Publisher's Note: All claims expressed in this article are solely those of the authors and do not necessarily represent those of their affiliated organizations, or those of the publisher, the editors and the reviewers. Any product that may be evaluated in this article, or claim that may be made by its manufacturer, is not guaranteed or endorsed by the publisher.

Copyright © 2021 Zhu, Bouma, Zhu, Cai and Yang. This is an open-access article distributed under the terms of the Creative Commons Attribution License (CC BY). The use, distribution or reproduction in other forums is permitted, provided the original author(s) and the copyright owner(s) are credited and that the original publication in this journal is cited, in accordance with accepted academic practice. No use, distribution or reproduction is permitted which does not comply with these terms.

frontiers in Marine Science

ORIGINAL RESEARCH
published: 21 October 2021
doi: 10.3389/fmars.2021.742448

Salt Marsh and Tidal Flat Area Distributions Along Three Estuaries

Maarten G. Kleinhans[1], Harke Douma[1], Elisabeth A. Addink[1], Laura Coumou[1,2], Tessa Deggeller[1], Robert Jentink[3], Edwin Paree[3] and Jelmer Cleveringa[2]*

[1] *Faculty of Geosciences, Department of Physical Geography, Utrecht University, Utrecht, Netherlands,* [2] *Water & Environment Division, Arcadis, Zwolle, Netherlands,* [3] *Rijkswaterstaat CIV, Utrecht, Netherlands*

Estuarine landscapes form through interactions between fluvio-coastal processes and ecological processes within the boundaries imposed by hard substrate layers and man-made dikes and dams. As estuaries are ecologically valuable areas, monitoring and quantification of trends in habitats is needed for objective comparison and management. However, datasets of tidal flat and saltmarsh habitats along entire estuaries are scarce. The objective was to compare trends of biogeomorphological areas and habitat transitions along three estuaries in the Netherlands and assess whether these are generally comparable or mainly determined by system-specific histories. We present data for these estuaries obtained by automated classification of false-color aerial imagery. The automated method allows objective mapping of entire estuaries at unprecedented resolution. The estuaries are dominated by subtidal areas and tidal flats. The tidal flats have similar area along the estuaries while saltmarsh area decreases. Collective lengths of ecologically important transitions between saltmarsh, low-energy tidal flats and water differ more between the estuaries. These variations are due to presence of mid-channel bars and shore-connected embayments. Saltmarsh area is mainly determined by the different formation and embankment histories of the estuaries, embayments and side-branches. Much of the past saltmarsh flanking the estuaries was lost due to past land reclamation. In one system, ecologically important low-energy tidal flats are reduced by a sudden decrease of tidal amplitude, causing increase of subtidal area at the cost of intertidal area. Large areas of high-energy tidal flats in one estuary remain unexplained. The automated method can be applied in other estuaries, provided that high-quality areal imagery is available. Extensions of the data to other estuaries would allow for system-scale trend comparison between estuaries of ecologically relevant biogeomorphological characteristics.

Keywords: saltmarsh, tidal flats, estuary, object-based image analysis, habitat transitions, biogeomorphological classification

OPEN ACCESS

Edited by:
Iris Möller,
Trinity College Dublin, Ireland

Reviewed by:
Ian Townend,
University of Southampton, United Kingdom
Qinghua Ye,
Deltares, Netherlands

****Correspondence:***
Maarten G. Kleinhans
m.g.kleinhans@uu.nl

Specialty section:
This article was submitted to Coastal Ocean Processes, a section of the journal Frontiers in Marine Science

Received: *16 July 2021*
Accepted: *23 September 2021*
Published: *21 October 2021*

Citation:
Kleinhans MG, Douma H, Addink EA, Coumou L, Deggeller T, Jentink R, Paree E and Cleveringa J (2021) Salt Marsh and Tidal Flat Area Distributions Along Three Estuaries. Front. Mar. Sci. 8:742448. doi: 10.3389/fmars.2021.742448

1. INTRODUCTION

Estuarine landscapes form through interactions of tidal currents, wind-generated waves and river discharge and the balance of sediments transported by these processes, all of which may be modified by biological processes. At the same time, estuaries are topographically forced by antecedent morphology, especially by constraining, hard or unerodible substrates (Townend, 2012; de Haas et al., 2018; de Haas et al., 2019), henceforth referred to as initial conditions. In addition, estuaries

are also directly and indirectly, through reduction of tidal prism, constrained by the effects of land reclamation, embankments, barrages and storm-surge barriers. Constraints on width and on tidal amplitude immediately modify the hydromorphodynamics and gradually change the long-term, large-scale development of the entire system in multiple ways. The seaward boundary conditions of tidal hydrodynamics, wave climate and sediment fluxes are not only directly limited by constraints at the estuary mouth, but also by landward reduction of shallow areas, which reduces the flood storage. This, in turn, reduces the tidal prism in the entire system (Friedrichs and Aubrey, 1988) and may, on the longer term, lead to shrinking of the estuary (Braat et al., 2017, 2019; de Haas et al., 2018). This is also partly determined by river discharge and fluvial sediment supply (de Haas et al., 2018). There is evidence that the sedimentary filling of late-Holocene estuaries proceeds in a large-scale pattern: the main channel in shallow estuaries generally converges as a result of approximate balancing of tidal wave height and energy loss through friction (e.g., Savenije, 2015) and balancing ebb-directed and flood-directed sediment transport (e.g., Dronkers, 2017). Hereby the embayments and reaches that are wider than the converging shape are zones of bar formation, tidal flat sedimentation and, in the most sheltered areas, saltmarsh formation (Wang and Temmerman, 2013; Leuven et al., 2018a). This results in a diverse landscape with spatial variation in tidal flat area, substrate composition and biomorphodynamics, where tidal bars (or shoals) in the estuary are expected to be more dynamic than the partially sheltered, shore-connected flats and saltmarsh flanking the estuary.

1.1. Problem Definition

Due to the large spatiotemporal variability in conditions and substrates, shallow estuaries are known to be of special ecological significance. Estuaries have high primary production, spawning zones for fish, foraging areas for birds, gradual water-land transitions, and have a unique salinity gradient from a polyhaline to mesohaline to freshwater tidal environment on the fluvial-tidal transition, which, in turn, is important for certain fish species and leads to a rapid change in biodiversity of freshwater species and salinity-tolerant species (e.g., Whitfield et al., 2012; Greenberg, 2013; Telesh et al., 2013). Not surprisingly, estuaries show many interactions between hydromorphological processes and ecological processes that potentially change the landscape in morphology, sedimentology and spatial structure. Particularly eco-engineering species play a major role as they change the hydrodynamics, sedimentology and morphology in their own environment and facilitate other species (Jones et al., 1994). In particular, higher intertidal and supratidal zones are often pioneered and covered by saltmarsh species in temperate regions (e.g., Wang and Temmerman, 2013; Schwarz et al., 2018) and by mangroves in subtropical and tropical regions, while lower intertidal and subtidal zones are populated by a wealth of animal benthic species.

This leads to the question to what degree shallow estuaries share a general pattern of proportions of tidal flats and salt marsh habitats across and along the system, or whether all have unique, dominant patterns that are determined mainly by the constraints of geological setting and set by past and present human interferences. Spatial heterogeneity of, and gradients between, habitats is deemed important for many species and ecosystem quality in general (Wolter et al., 2016), but it is unknown whether the heterogeneity differs between estuaries because that requires a method for mapping and quantification that is presently lacking. Furthermore, it is at present unknown whether shore-connected tidal flats and saltmarshes and those on shoals differ in area and character, while it can be hypothesized that the shore-connected areas are less dynamic. Although methods have been developed to map benthic habitats (e.g., https://data.gov.uk/dataset/1707e638-6a2d-48f5-a534-1db0b240cc37/casi-and-lidar-habitat-map) and coastal land cover (e.g., Enwright et al., 2020), datasets are insufficiently available as is evident from the fact that review papers have had to focus on local case studies (e.g., de Jonge, 2000; Whitfield et al., 2012; Telesh et al., 2013; Dashtgard and Croix, 2015) and stress the need for combined terrestrial-aquatic ecosystem studies with remote sensing techniques (Soininen et al., 2015). We only found two studies for the Netherlands that extend to areas with multiple systems (Baptist et al., 2019) and cover complete systems (Ysebaert et al., 2003). The generic processes that form and populate estuaries could also be studied by numerical modeling, that increasingly incorporates interactions with eco-engineering species (e.g., Brückner et al., 2020, 2021) and by landscape experiments that may incorporate eco-engineering plant species (e.g., Kleinhans et al., 2015; Leuven et al., 2018b; Braat et al., 2019; Lokhorst et al., 2019). However, such modeling and experimentation also requires field data for validation. To compare systems and biogeomorphological models objectively and to monitor changes accurately through time, we urgently need detailed data and methods of biogeomorphological classification at the scale of entire estuarine systems.

The quantification of system-scale mapping of patterns by data is of immediate practical importance for protection of estuarine habitats worldwide. In the EU this is imposed by law, such as the European Natura2000 legislation, but also for coastal-protection managers from reliable and up-to-date estuarine maps are critical. Generic insights from similar systems would aid habitat protection and restoration, as would insights into what causes the differences in habitat area and heterogeneity between estuaries. Realistic goals for the areal extent and the distribution of estuarine habitats may be based on such trends, and are important to have in view of the competition between societal functions of flood safety, transport and access to ports and ecosystem health. Sustainable management of the estuaries, for instance by dredging and disposal schemes that incorporate ecological goals, requires data of the hydrogeomorphological processes and of habitats. Furthermore, policy documents frequently refer to the importance of gradual water-land transitions on the basis of ecological literature, but there is at present neither quantitative data of such transitions, nor an objective method to collect these.

1.2. Ecological Significance of Habitat Areas and Transitions Between Habitats

The highest macrobenthos diversity and biomass is found in intertidal areas (Ysebaert et al., 2003), making them important feeding areas for fish during high tide (Ysebaert et al., 2000).

Tidal marsh creeks are important nursery grounds for some fish and macrobenthic species (Ysebaert et al., 2016). During low tide the intertidal areas rich in macrobenthos are important feeding areas for birds, especially wader birds. Wader birds often forage along the waterlines of tidal flats and require a long feeding period during low water, and longer with lower body weight (Ysebaert et al., 2000). This means that the quantity of low-energy intertidal area is important, as well as the spread of its height distribution relative to the tidal levels. The saltmarsh provides breeding grounds for birds and may serve as resting ground during high water (Ysebaert et al., 2016), showing that animal species move across multiple habitat transitions.

Direct quantitative relations between species abundance and habitat area are simplistic, because species abundance depends on multiple variables such as tidal and seasonal dynamics (Cozzoli et al., 2013). Furthermore, ecological studies also demonstrated the importance of transitions between different habitats (or ecotopes) along the river-estuary transition for species occurrence and abundance. However, quantification of patch variation and gradients for entire landscapes remains a challenge, and many possible metrics with ecological connotations exist (Lausch et al., 2015). It is, regardless of interpretation, clear that species need such transitions in various life stages for feeding and reproduction cycles as discussed below, and that quantification of the transitions is useful.

Relations for individual species are likely to differ between areas, and the use of such species-specific relations for system management would require potentially controversial choices for targeted communities and indicator species by ecologists and policy makers. Instead, we limit ourselves to a minimal review of possible qualitative links between groups of species and the presence of biogeomorphological areas and transitions. The latter are empirically much more accessible and comparable between different systems. This points at the need for objective quantification of transitions between habitats. Habitat diversity and presence of transitions are important for the many species that rely on more than one habitat along estuaries during their life cycle. While most freshwater species do not enter saline waters, many marine species can extend into brackish waters and some fish species need the gradual transition for migration (Ysebaert et al., 2016). The tidal marsh creeks and the transition from the intertidal areas are important as nursery grounds for some fish species (Ysebaert et al., 2016), likely including the pioneer saltmarsh zones as transitions and partially sheltered zones. Possibly, the weakly brackish zone has a smaller number of animal species than the saline or freshwater zones (Whitfield et al., 2012), but the diversity of the primary producers may be larger than elsewhere (Telesh et al., 2013), which is important for macrobenthic and fish species (Herman et al., 1999). Together, this suggests that not only the area of low-energy intertidal flats but also the length of the transitions between intertidal habitats and deeper water are relevant measures for habitat availability.

1.3. Objective

The first objective of this paper is to compare trends of biogeomorphological areas along three estuaries and assess whether these are generally comparable or mainly determined by system-specific histories. The second objective is to quantify lengths of transitions between biogeomorphological classes and compare these between the estuaries. To this end, we present a novel image classification method that allows a detailed objective comparison of trends along three estuaries in a similar setting of tidal range and climate, similar shore-connected areas as well as mid-channel bars, but with different forcing histories. Three estuaries in the Netherlands have sufficient data of high quality for automatic image analysis at the required scale. While this low number limits the general applicability to estuaries worldwide, all three have similar boundary conditions, saltmarsh and benthic species and have contrasting historic developments and geologic constraints. For one of the estuaries, the new biomorphological map is compared with a manually created map as a moderate assessment of the accuracy.

2. METHODS

2.1. Approach

The analysis of habitat indicators along and across estuaries requires consistent data that cover entire systems and generalize the environmental conditions. Not surprisingly, there is very little data published in the scientific literature that cover entire systems. There are only few bathymetries (Leuven et al., 2018c), maps of mud presence (Braat et al., 2017), saltmarsh (Wang and Temmerman, 2013; van Belzen et al., 2017) and macrobenthic species (Cozzoli et al., 2013), mostly in north-western European estuaries.

Here, we take advantage of our newly developed method of automated object-based aerial image classification for biogeomorphological maps. We applied this to all relevant tidal systems in the Netherlands: the Wadden Sea (in progress) and three estuaries (**Table 1**), namely the Eems-Dollard, the Eastern Scheldt and the Western Scheldt (**Figure 1**, see **Table 1** for description of conditions and contrasting histories). For system-scale management purposes and monitoring for the Natura2000 legislation, Rijkswaterstaat has used ecotope maps (Bouma et al., 2005), where "ecotope" is defined as the physical environment for communities, which is akin to biotope and habitat (see Baptist et al., 2019, for discussion). The ecological significance of all ecotopes for the estuaries and the Wadden Sea in the Netherlands is reviewed on the basis of observations and discussed for target species in Bouma et al. (2005), who also acknowledge that boundaries on gradually varying surfaces are artifices on transitional surfaces but are needed for mapping, management and legal purposes (see discussion). Important classes of ecological indicators are saltmarsh and unvegetated tidal flats subdivided in low-dynamic and high-dynamic littoral zones (**Table 2**).

Ecotope maps can in part be generated from datasets of bathymetry, salinity, and hydrodynamics. Two methods have been applied to make ecotope maps: one based on numerical modeling of hydrodynamics, and one based on biogeomorphological characterization of the littoral zones from aerial photography. The first method relies mainly on numerical hydrodynamic modeling (Ysebaert et al., 2016; Cozzoli et al., 2017; Baptist et al., 2019) for quantification of conditions in

TABLE 1 | Key characteristics of the three estuaries: length of channel centerline (also shown in **Figure 4**, total mapped area (without the water class), spring-tidal range at the mouth, mean and maximum river discharge and general description (see text).

Estuary	Length km	Mouth km	Area km^2	Tidal range m	River m^3/s	Description
Western Scheldt	26.2	4.1	106	2.4	30–120	Fairway deepened 1 m, maintenance dredging with disposal on bar margins
Eems-Dollard	25.6	5.5	251	3	30–120	Upstream Ems river deepened and hyperturbid
Eastern Scheldt	22.0	7.5	108	2.5-3.5	0–0	Storm surge barrier reduced tidal range and sediment input

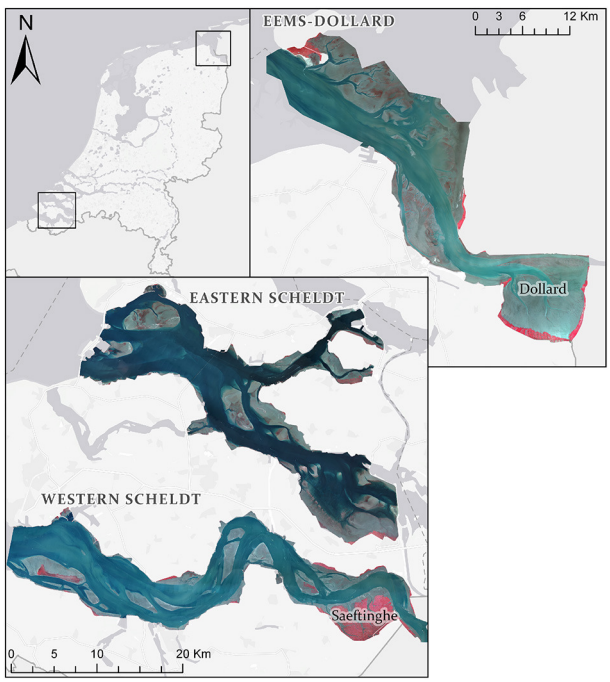


FIGURE 1 | Map of study areas with stretched false color aerial photographs. Within the estuaries, gray tones are bars, blue tones are water with lighter tones having more suspended sediment and red tones are vegetation or sometimes diatoms. Shading outside the estuaries: light gray is built area, white lines indicate roads and other infrastructure (including the storm surge barrier), dark gray is water of the sea and of embanked lakes. The landward boundary of the Western Scheldt is the Belgian-Dutch border and the eastern boundary of the Eems-Dollard is the German-Dutch border. The photographs were taken in 2016 in the Western Scheldt, 2016 in the Eastern Scheldt and 2014 in the Eems-Dollard.

the littoral zone. Such modeling is not only computationally expensive but is also inaccurate for the shallow areas of interest due to the large effects of wind and of chosen hydraulic resistance values, and the spatiotemporal propagation of errors in measured bathymetry and boundary conditions of tides and wind (Duran-Matute et al., 2014). Nevertheless, this is the most straightforward way to determine inundation duration, which is an important variable in habitat suitability and ecotope definition (Bouma et al., 2005; Cozzoli et al., 2013). Determining inundation time in estuaries with progressive tidal waves requires accurate bathymetry, which requires serious surveying time. It also requires many water level measurements and an accurate numerical model that is usually calibrated to measured water levels by adjusting hydraulic resistance spatially.

The second method to create ecotope maps is to produce biogeomorphological maps for the intertidal and supratidal areas on the basis of imagery. One difference between biogeomorphological mapping over image interpretation to infer habitat, or modeling of hydrodynamics over bathymetry, is that another kind of information is used about the physical processes that underlie the habitat definitions. Biogeomorphological maps have historically been drawn by hand from aerial photographs based on protocols and checked in the field with a frequency of about once per 2 years for the Western Scheldt, once per 6 years for the Eastern Scheldt, but not at all for the Wadden Sea and Eems-Dollard. The automated mapping method presented in this paper now allows for cost-effective production of biogeomorphological maps in all systems with high-quality imagery. Rijkswaterstaat has a workflow of combining hand-drawn biogeomorphological maps with calibrated water level modeling on measured bathymetry to produce ecotope maps for the Western Scheldt every 2 years and Eastern Scheldt every 6 years.

To work with consistent data for the three estuaries, here we used automatically generated biogeomorphological maps, i.e., not ecotope or habitat maps that can be derived from combination of hydrodynamic and biogeomorphological information, that were checked and corrected by experts for reasons of comparability of intertidal and supratidal habitat trends across and along the estuaries (explanation below). The manually produced maps of the Western Scheldt were used in the development stage as verification data for the automated method. We refer to the **Supplementary Material** for details of the method and a comparison with a manually created map of the Eastern Scheldt as validation.

2.2. Study Areas

All three estuaries are situated in the coastal plain of the Netherlands (**Figure 1** and **Table 1**) and formed only late in the Holocene by ingression due to the rising sea level, peat collapse and land subsidence due to dewatering for agriculture (see de Haas et al., 2018, for overview). The climate, the tidal boundary conditions and the river discharge are similar, except that the Eastern Scheldt is strictly no longer an estuary but a tidal basin, since it was disconnected from the Scheldt river. The Scheldt system in particular has been studied extensively and the brief descriptions below are limited to the main characteristics from selected publications.

TABLE 2 | Biogeomorphological classes and characteristics of intertidal and supratidal areas in the saline estuary.

Class name	Ecotope	Characteristics
Saltmarsh	S1a	Cover>50% for patch size>400 m^2
Open saltmarsh	S1c	10%<cover<50% for patch size<400 m^2
Pioneer vegetation	S2	Cover<10%
Saltmarsh creek	S3a	Elongated unvegetated objects surrounded by saltmarsh
Low-energy tidal flat	P1	Plane or slightly undulating bed, may be sandy or muddy, may have mussles
Mega-ripples	P2b	Mega-ripples with height>0.25 m, variation in brightness
High-energy tidal flat	P2c	Plane or slightly undulating bed, no variation in brightness
Bed invisible	P3	Tidal flat surface covered by shallow water
Hard substrate	H1	Natural hard substrates, e.g., early Holocene peat
Hard substrate	H2	Anthropogenic hard substrate
Other	O	Rest category

Relevant class abbreviations as also shown in the figures are taken from the original system by Bouma et al. (2005, Appendix 5) whereby ecological significance depends partly on mud content, salinity, pelagic primary production and spatiotemporal variations thereof (e.g., Herman et al., 1999; Ysebaert et al., 2003).

The Eems-Dollard estuary is situated in the Wadden Sea on the Dutch-German border. The lower estuary is not confined or embanked but connected during high water with surrounding tidal basins, and the mouth is confined between two barrier islands. Late-Holocene ingressions led to wide-spread land loss in the area, including a large embayment on the south-western bank of the estuary (Vos and van Kesteren, 2000; de Haas et al., 2018). Gradual embankment and stimulated saltmarsh accretion undid part of the land loss but a large embayment, the Dollard, still exists (**Figure 1**). The lower estuary has mutually-evasive ebb- or flood-dominated channels separated by tidal bars, where the tidal dominance is enforced by the bends in the system (van Veen, 1950). The mud concentrations in the estuary have increased over the past decades to levels that are considered harmful for primary production (de Jonge, 2000; Winterwerp et al., 2013; van Maren et al., 2015). Causes are not known with certainty but the deepening by several meters of the Ems river upstream of the Dutch-German border is likely to have played a role in the enhanced mud trapping, and both the deepening and the reduced roughness due to increased mud concentrations led to amplification of the tides landward of the Dollard (Winterwerp et al., 2013; van Maren et al., 2015). It is unknown whether this led to differences in ecotopes over time and in comparison to other estuaries in this region, because they were never mapped. The single-thread Ems river in Germany is excluded from our analysis.

The well-known storm-surge barrier of the Dutch Delta Works, built in the 1980's after the great flood of 1953, is located at the mouth of the Eastern Scheldt. Following late-Holocene ingressions, a large area was flooded with some remnant islands remaining. The silting up and damming of minor branches between these islands led to the present shape of the tidal basin with two minor branches to the north (van den Berg et al., 1996; Vos and van Kesteren, 2000; de Haas et al., 2018). These branches were disconnected from the northern basins as part of the Delta Works. Some large tidal bars exist in the estuary (Mulder and Louters, 1994; de Vet et al., 2017). The Eastern Scheldt was connected to the Scheldt river before the Western Scheldt formed in the early Middle Ages (van der Spek, 1997). The present-day lack of fluvial input means that this basin is entirely saline, estuarine circulation is absent and, while it receives only little mud from the seaward boundary, the water is generally clear (compare water color in **Figure 1**). Damming of the side-branches initially increased the tidal range, but installation of the storm-surge barrier has approximately halved the tidal range at the inlet and reduced the tidal prism and sand input from the North Sea littoral zone much more (Cozzoli et al., 2013). The fact that the tides and dynamic salinity gradient were not simply entirely removed by a dam, as in other systems in the Netherlands, was the result of a compromise between the aquaculture sector and the nature conservation organizations.

The Western Scheldt is situated in the south of the Dutch North Sea close to the Belgian border. As in the Eastern Scheldt case, the landscape in the Middle Ages was much more fragmented with large branches that originally provided nautical access to the late medieval ports of Middelburg, Gent, and Brugge but gradually silted up and were dammed (van den Berg et al., 1996; van der Spek, 1997). In 1570 a large embanked polder, Saeftinghe, was flooded as a defense in a war, and since then silted up to supratidal levels to form a large saltmarsh that was only partly reembanked (Wang and Temmerman, 2013; Jongepier et al., 2015). The mainport of Antwerp necessitates direct access to the North Sea, and a storm surge barrier was rejected after a very long societal and political debate. Tidal channels were deepened for ships that gradually increased in draft over the past decennia. A number of large tidal bars formed over time with a main, ebb-dominated channel and a number of flood-dominated channels (Wang et al., 2002; Hibma et al., 2003; Hiatt et al., 2020); a pattern enhanced by large-scale channel deepening (van Dijk et al., 2019). Meanwhile the tidal amplitude increased landward due to the channel fairway deepening (van der Spek, 1997; Wang et al., 2002). Small-scale channels cross-cut the bars as part of the general dynamics (van Veen, 1950; Swinkels et al., 2009), but historic analyses suggest that this reduced over the past half century (Cleveringa and Taal, 2015). The Scheldt river input causes a salinity gradient with the mesohaline zone around

the Dutch-Belgian border and the resulting estuarine turbidity maximum close to Antwerp (Winterwerp et al., 2013). In order to mitigate the increasing flood risk, controlled inundation is allowed in designated areas, again after considerable societal and international political debate. The single-thread Scheldt river in Flanders is excluded from our analysis.

The tidal bars with their intertidal flats showed opposite developments in the Western Scheldt and Eastern Scheldt over the past decades (de Vet et al., 2017). The bars in the Western Scheldt generally increased in height since fairway deepening was commenced, and as the system was confined in width, this caused general steepening of the bar margins (van Dijk et al., 2019). In contrast, the bars in the Eastern Scheldt lowered since the storm surge barrier was installed, mainly due to the relative increase in wave attack due to the tidal range reduction in combination with the excess accommodation space in the tidal channels, of which the dimensions were related to the much larger tidal prism preceding the Delta Works. As a result, the bar margins became less steep (de Vet et al., 2017).

All three systems are Natura2000 sites designated under the EU Birds Directive and the EU Habitats Directive, meaning that tidal flats and saltmarsh are important habitats to be monitored (e.g., Meire et al., 2005). The ecological consequences of human interference have largely been negative. The Delta Works have started a gradual decline of the surface area and height of the tidal flats and have limited rejuvenation the salt marshes in the Eastern Scheldt, with a low but steady reduction of bird habitat as a consequence. For the Western Scheldt and Eems-Dollard systems changes in tidal dynamics, salinity and mud concentration as a result of the ongoing morphological response to dredging of fairways in combination with past reductions of intertidal area by land reclamations have resulted in the loss of valuable habitats and a reduction of the quality of these habitats (de Jonge, 2000; Meire et al., 2005; Ysebaert et al., 2016).

2.3. Aerial Photographs and Image Classification

The biogeomorphological maps were based on high-quality digital aerial photographs with near-infrared, red and green bands and a ground resolution of 0.25 m. This resolution is much higher than obtained in satellite imagery, and is necessary because the morphological phenomena of interest on which the classification is based are then resolved, or nearly resolved. While Unmanned Airborne Vehicles would obtain an even higher resolution, the spatial extent possible with the aerial photographs is much larger, which is necessary given the focus on entire systems and fluvial-tidal river gradients. We found only the most recent sets to be of sufficient quality for digital classification, in part because of technological progress and in part because only these met the strict requirements of having been collected with a low tidal water level range, in the same season, and with uniform lighting and weather conditions to avoid large differences in reflection intensity and color, and avoiding direct reflection of the Sun.

After extensive testing an Object-Based Image Analysis ruleset was developed, of which a brief summary is provided here (see **Supplementary Material** for more information). Tiles of merged false-color aerial photographs were segmented multiple times, at different levels of scale, to yield a few tens of thousands of objects with a minimum degree of spectral heterogeneity. The smaller-scale objects were nested in the larger-scale objects. We developed the ruleset in eCognition to classify the objects into seven classes (**Table 2**). The classification was based on object shape and context (neighboring objects), relations between the nested objects, on average brightness and on a ratio between near-infrared and red reflection: the Normalized Difference Vegetation Index (NDVI). Distinguishing the mud content of the surface proved challenging for the entire system at this scale, despite earlier success with remote sensing imagery (van der Wal et al., 2010), and was not conducted. Hard stone surfaces, which in these systems all have an anthropogenic origin, were copied from digitized maps of Rijkwaterstaat of the Ministry of Public Works.

The ruleset is summarized as follows (see **Supplementary Material** for more information). Water was classified by a maximum NDVI. Saltmarsh was classified by a minimum NDVI. Saltmarsh objects smaller than 400 m^2 were dilated and eroded, which removes vegetation patches too small for the mapping scale. Merged saltmarsh objects larger than 400 m^2 were then classified as pioneer vegetation, which is less densely vegetated than open salt marsh. Saltmarsh creek objects were recognized from their unvegetated appearance, elongated shapes and vegetated neighbor objects. The remaining objects were unvegetated tidal flats, for which the two levels of segmentation were used. Mega-ripples were distinguished by variation of brightness and NDVI of sub-objects nested in the larger objects. The final discrimination between high-energetic and low-energetic tidal flat was made by combinations of non-overlapping thresholds of brightness and NDVI, where undecided objects between the thresholds were classified from the surrounding context.

The automated classification based on the ruleset produced a similar map as the visual method (example of the automated map of Eems-Dollard in **Figure 2**). The spatial detail at which surface areas were classified is illustrated for saltmarsh and tidal flats in **Figure 3**.

The automation reduced the map-production time considerably. For present conditions and an entire estuary, the total computation time is 24 h. In contrast, manual mapping cost several weeks, particularly because of the need to draw all map boundaries. An expert check of the digital map was fast because the boundaries were found to be accurately captured by the objects, even if objects were not correctly classified. The accuracy of the boundaries is partly determined by the scale number in the object-based image classification: earlier attempts with higher scale numbers occasionally resulted in clearly mislocated boundaries.

The automated classification and the expert-corrected maps of the Wadden Sea systems and the Eastern Scheldt have 90% or more correspondence and about 85% in the Western Scheldt. For saltmarsh areas, including partially covered areas, the agreement is about 95%, where differences arise due to objectified thresholds for partial cover and the detail in the boundaries in the automated

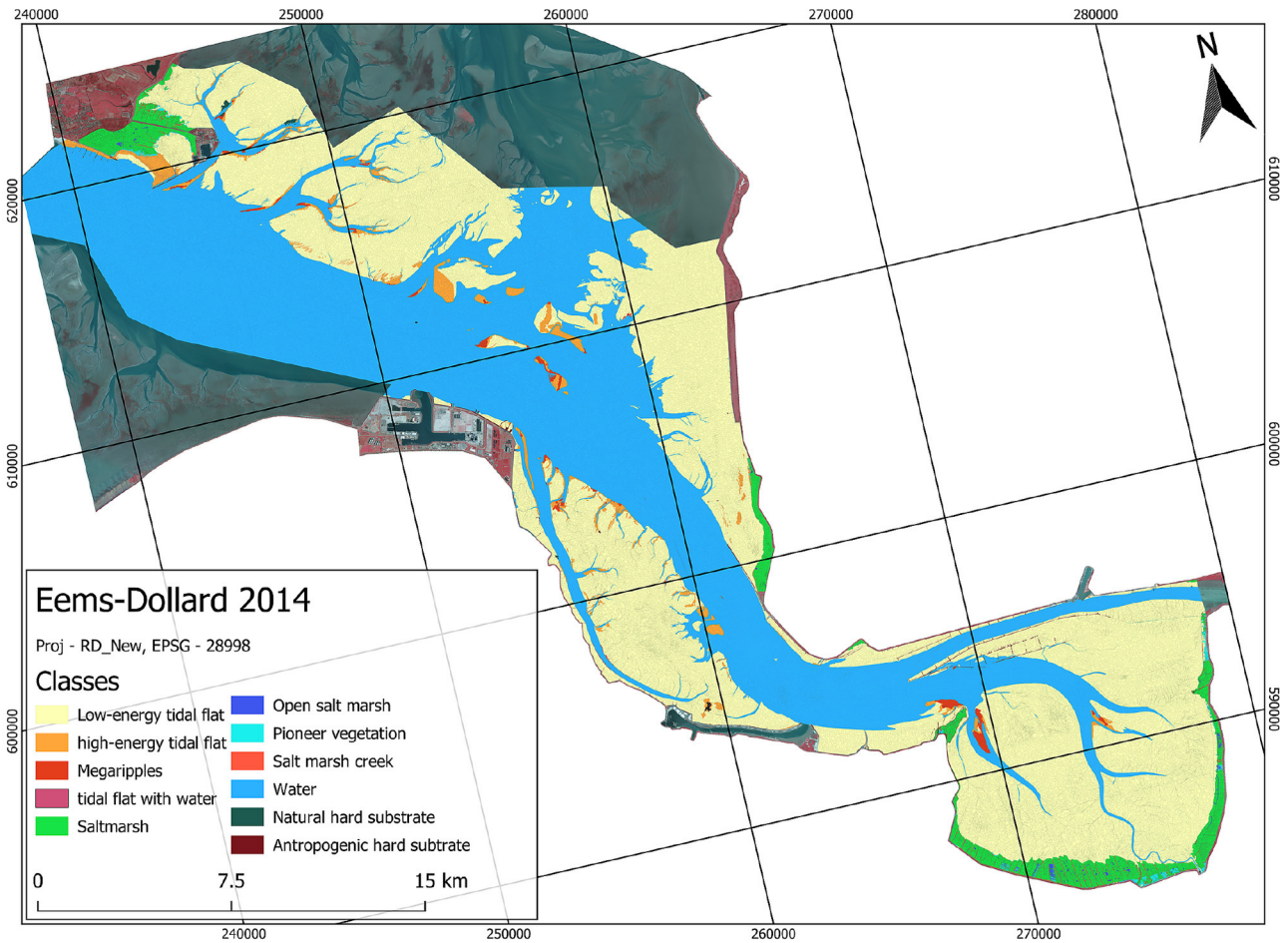


FIGURE 2 | Biogeomorphological map of the Eems-Dollard for 2014 showing boundaries of the objects used in the ruleset. See **Table 2** for explanation. Full image resolution maps for all three systems are provided in **Supplementary Material**.

method. Most of the disagreement between the maps occurs in the bare surface classes. We tested whether the use of bed slope and bed-slope variation calculated from bathymetry improved the classification of the bare surfaces. Although this increased the correspondence of mega-ripple area on both maps, it added low-energy and high-energy plane shoal areas to the mega-ripple areas that were in disagreement with the manually drawn map. Visual inspection shows that the boundaries between tidal flat and mega-ripples are sometimes poorly recognized in the automated method. The expert-corrected spatial data are made available online and in this paper we proceeded with the corrected data.

2.4. Map Analysis

The (corrected) classified objects were used in the following analyses, the information for which is included in the online data. To study spatial trends along estuaries we drew narrow segments across the estuaries and calculated the absolute fraction of the surface area covered by each legend class from the classified objects. These were plotted as absolute widths (surface area divided by the width of the segments) and as fractions of the surface area to visualize their absolute and relative importance along the estuary.

All three estuaries are characterized by the presence of large mid-channel bars. To test the hypothesis that such bars are more dynamic environments than the shore-connected tidal flats on the estuary margins that are partly protected from tides and waves, we also plot trends along the estuaries for the mid-channel intertidal areas and the shore-connected areas.

A measure for spatial habitat variability is the length of transitions between biogeomorphological classes. After merging objects of the same classes, the lengths of the borders between areas of different classes were calculated for the entire estuaries and for the mid-channel intertidal areas and the shore-connected areas. The resulting absolute lengths obviously depend on the scale of the Object-Based Image Analysis (OBIA), on the resolution of the images and on the actual spatial variation. The two method-related factors are the same for all three estuaries in this study. The pixel size of the images (0.25 m) used here is at a similar scale as the birds and fish, so that the analysis of

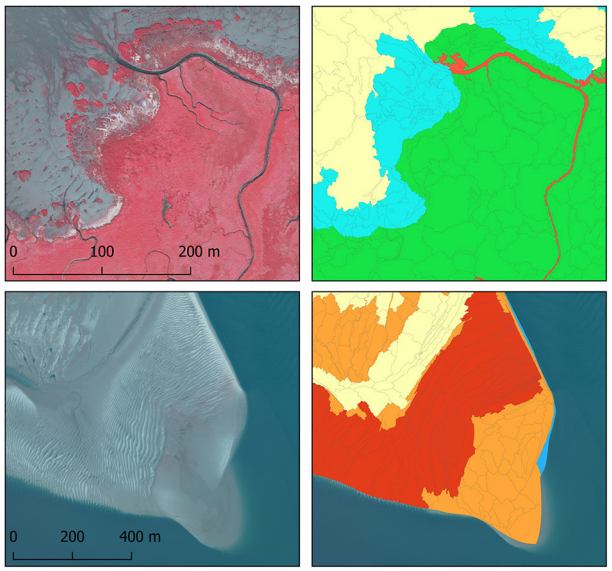


FIGURE 3 | Examples of the most common surfaces on the aerial photographs **(left)** and biogeomorphological maps **(right)** for vegetated classes **(top)** and intertidal flat classes **(bottom)**. For legend see **Figure 2**.

spatial heterogeneities and lengths of transitions is done on a similar scale as that of the locomotion paths of birds and fish. This suggests that the quantitative measures presented here are likely relevant for the organisms.

To contextualize the transition lengths, we normalized the more abundant, measured transition lengths by a length that is characteristic for the total length of the mapped area along each estuary. This characteristic length was calculated from the total mapped surface area of the estuary (without the water) divided by the mouth width (**Table 1**). We interpret the normalized transition length as the minimum distance that a transition between saltmarsh and tidal flats, and between tidal flats and water, would have in a highly idealized and regular estuary. The more irregular the mapped transitions between habitats are, the larger the normalized transition length. While the irregularity and length of transitions between tidal flat classes and between saltmarsh classes is at least partly determined by the definitions of the classes and the OBIA technique, the transition lengths between saltmarsh and tidal flat classes are quite likely robust due to the relatively straightforward recognition of vegetation on imagery with the near-infrared band. Furthermore, the image resolution and OBIA ruleset were identical in the three study areas.

3. RESULTS

3.1. Trends Along Estuaries

The relative area covered by the biogeomorphological classes show two trends that are similar between the three estuaries. First, there is much variation along the estuaries in the intertidal and supratidal width fraction (**Figure 4**) mainly related to the presence of large bar complexes (**Figure 1**). In all cases, the subtidal takes up the largest area, the tidal flats are second and the vegetated areas are smaller (**Figure 5**).

The second similarity is that the proportions of tidal flat and vegetated area reduce in seaward direction (**Figure 4**) but the absolute areas remain about the same (**Figure 5**). In the absolute sense, the most upstream reaches of the Western Scheldt and Eems-Dollard are in places wider than the estuary mouth, and in all three estuaries the landward ends have a disproportionally large area above the subtidal level.

There are three striking dissimilarities between the three estuaries. First, there is proportionally much more high-energetic tidal flat and megaripple fields in the Western Scheldt than in the other two estuaries (**Figure 4**). Second, the Eastern Scheldt and Western Scheldt contain a small but important fraction of hard substrates of natural origin, mainly compacted, early-Holocene peat layers (**Figure 4**).

The third dissimilarity is that much of the upstream area is vegetated in the Western Scheldt (Saeftinghe salt marsh), while in the other two estuaries low-energy tidal flat dominates the upstream area (**Figure 4**). In terms of absolute width, the vegetated area in the upstream reach of the Western Scheldt is almost as wide as the subtidal channel and the unvegetated flats together, as opposed to everywhere else in the estuary (**Figure 5**). Generally, the Western Scheldt has more vegetation than the other two estuaries. The Eastern Scheldt has two side branches that both have more vegetation than the main branch (**Figure 6**).

Two specific features in the Eems-Dollard are related to its position in the Wadden Sea and the somewhat arbitrary choice what to incorporate in the Eems-Dollard study area, because its boundaries within the Wadden Sea are hard to define and we used the administrative boundary of the area for simplicity. The large vegetated patch near the mouth of the Eems-Dollard is located on a barrier island in the Wadden Sea that is arguably not part of the estuary. The large widening of subtidal width in the Eems-Dollard between 5-10 km from the mouth is the historic connection to the eastern branch of the Eems estuary (**Figure 5**).

Unexpectedly, there is not proportionally more vegetation in the more sheltered shore-connected areas than on the tidal mid-channel bars, despite the fact that the latter are surrounded by channels and are less sheltered (**Figure 7**). The most obvious trend is a general reduction of shore-connected area and an increase of mid-channel bars associated to the seaward widening of all estuaries. However, there is more high-energetic and megaripple area on the mid-channel bars of all three estuaries in general and particularly in the Western Scheldt, except in the most upstream, single-thread reaches. Most of the hard substrates in the Eastern Scheldt are located on the shore-connected areas.

3.2. Transitions Between Biogeomorphological Classes

The sum of lengths of all the transitions is well above 2,000 km (**Figure 8**), which is, not surprisingly for a patchy landscape, about an order of magnitude larger than the circumference of each entire estuary. The analysis shows that a minority of all possible transitions dominates in all three systems: from saltmarsh (S1a) to pioneer vegetation (S2) and saltmarsh creek

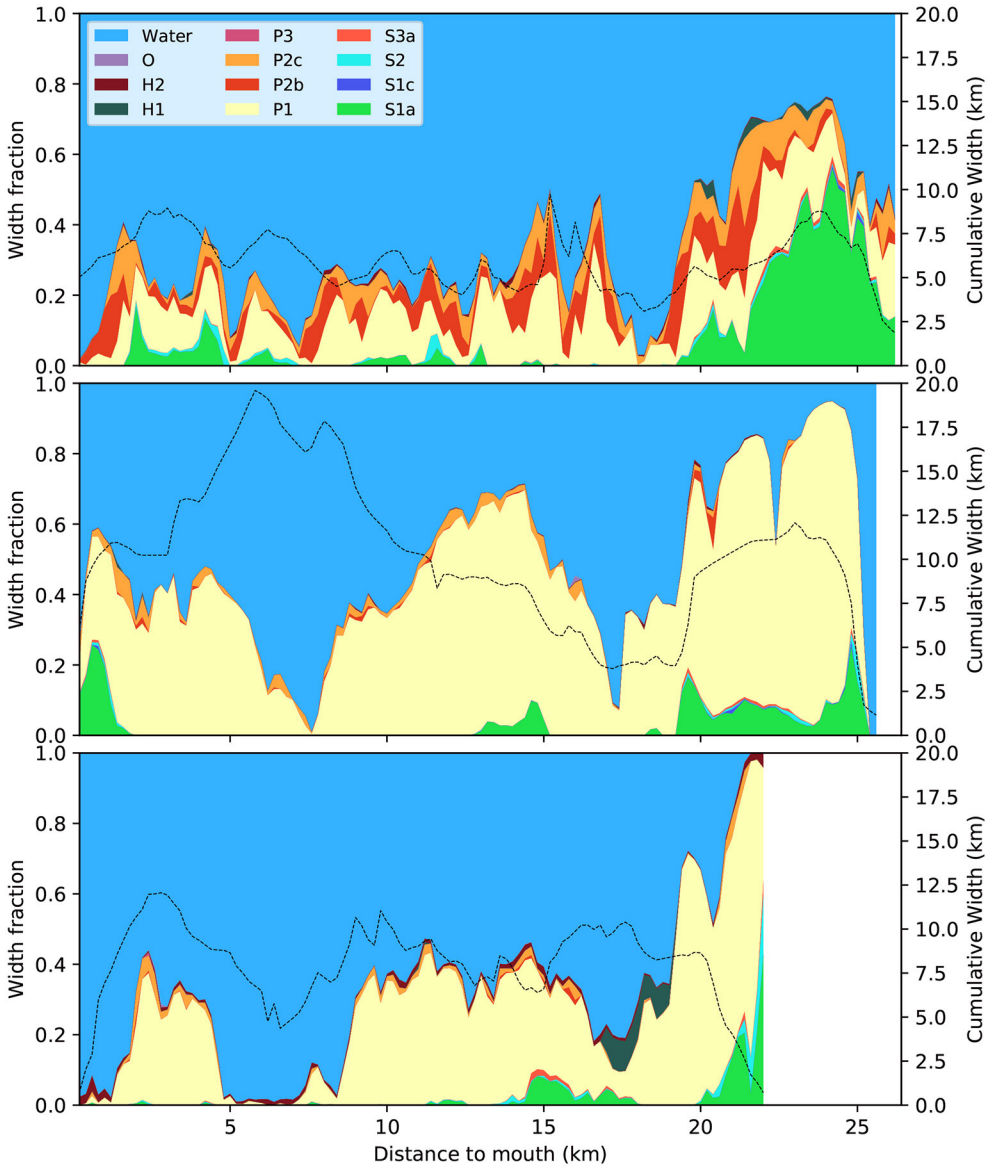


FIGURE 4 | Distribution of biogeomorphological classes as relative width along the Western Scheldt **(top)**, Eems-Dollard **(middle)**, and Eastern Scheldt **(bottom)**. Cumulative estuary width, the sum of all classes including water, is plotted as the dashed black line for the right vertical axis. Distance is measured along a smooth centerline between the banks from the narrowest cross-section in the seaward mouth. See **Table 2** for explanation of the legend. The data underlying these graphs are provided in **Supplementary Material**.

(S3a), from pioneer vegetation (S2) to low-energy tidal flat (P1) and from low-energy tidal flat (P1) to high-energy tidal flat (P2c), anthropogenic hard substrate (H2) and water. As expected, the saltmarsh classes occur frequently adjacently and saltmarsh also borders frequently on low-energy tidal flats. Furthermore, low-energy tidal flats border frequently on high-energy tidal flats, anthropogenic hard substrates such as bank protections and water.

On the other hand, some general differences between the estuaries emerge (also see **Figure 9**). The Western Scheldt has much more transition length between mega-ripples (P2b), high-energy tidal flat (P2c) and water than the other two, because the mega-ripples are more abundant in this system. These are also the classes for which the discrimination from low-energy tidal flats was more difficult than in the other two estuaries (see section 2). On the other hand, the Eastern Scheldt has much less transition length from saltmarsh (S1a) to low-energy tidal flat (P1) and from high-energy tidal flat (P2c) to water. In general, the Eems-Dollard can be said to take up an intermediate position between the Western Scheldt and Eastern Scheldt in absolute transition

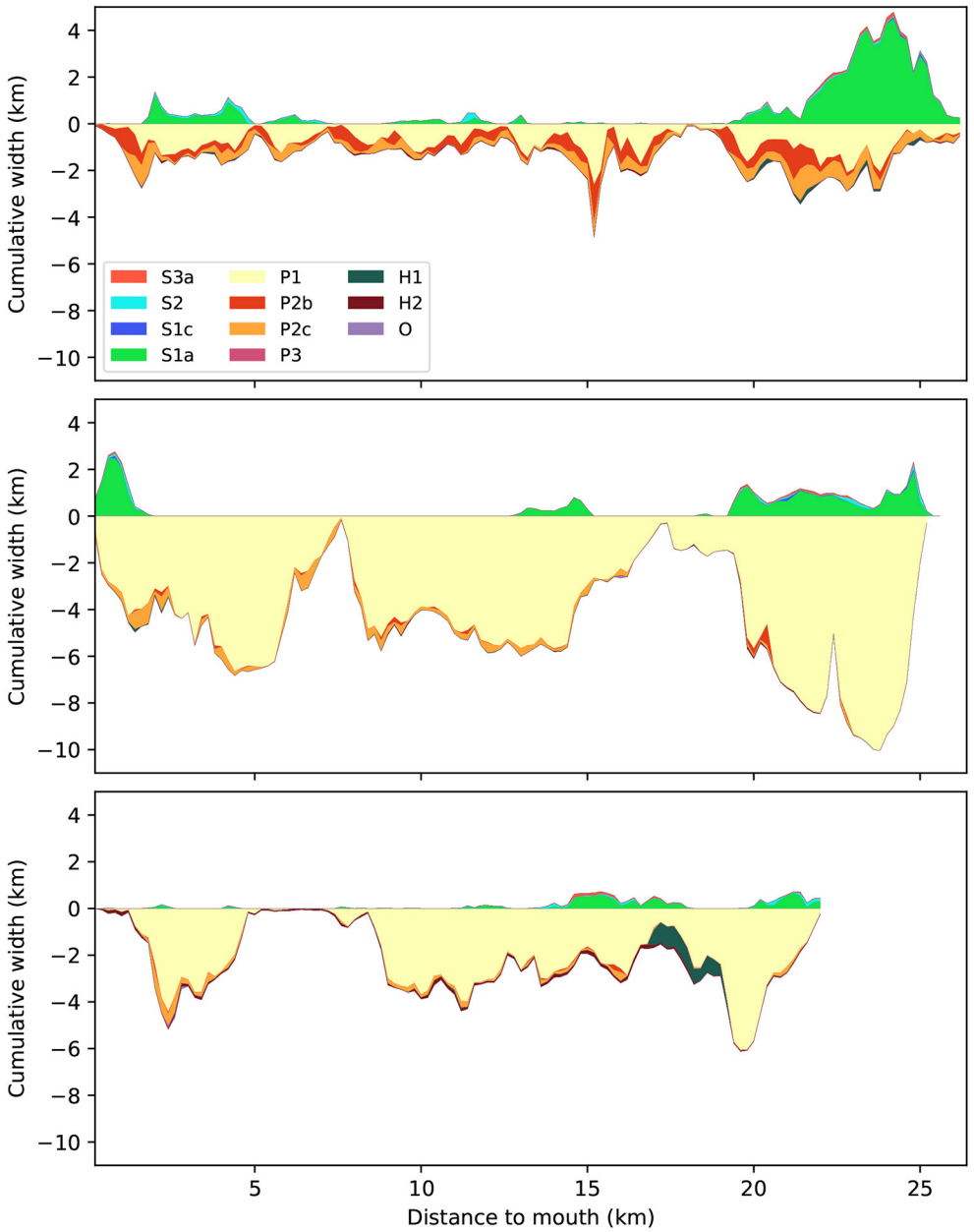


FIGURE 5 | Distribution of biogeomorphological classes divided by vegetated and unvegetated parts, plotted as absolute width along the Western Scheldt **(top)**, Eems-Dollard **(middle)**, and Eastern Scheldt **(bottom)**. Positive widths refer to subtidal bed surface and to all vegetated classes, negative widths refer to unvegetated intertidal flat classes and the sum of absolute widths is the cumulative estuary width excluding water. Distance is measured along a centerline from the narrowest cross-section in the seaward mouth. For explanation of legend see **Table 2**.

lengths between saltmarsh (S1a) and high-energy tidal flat (P2c), and between low-energy tidal flat (P1) and mega-ripples (P2b).

The lengths of transitions are different for shore-connected areas and mid-channel bars and shoals (**Figure 9**), which is obvious from the fact that the matrices are not perfectly mirrored on the diagonal. Main similarities between the three estuaries are that tidal flats (P1, P2b, P2c) border more frequently on water for the more exposed mid-channel bars than for the shore-connected areas, which supports the hypothesis that shore-connected areas are less dynamic than mid-channel areas. Furthermore, vegetated surfaces border on unvegetated surfaces about equally frequently on the bars and shore-connected areas. The more frequent occurrence on the shore-connected areas in all estuaries of low-energy tidal flats bordering on anthropogenic hard substrates

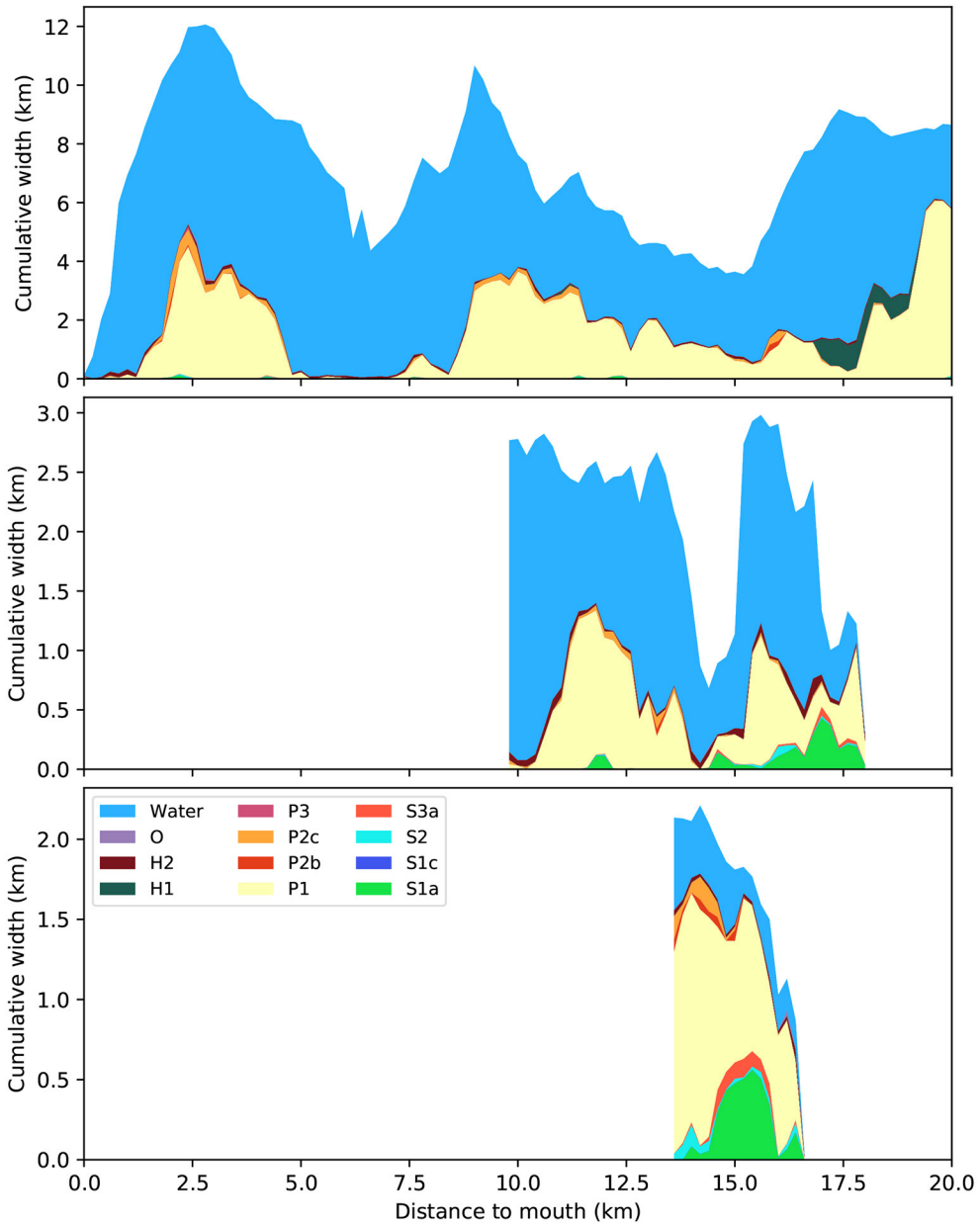


FIGURE 6 | Distribution of biogeomorphological classes separately plotted as cumulative width for the main branch **(top)** and two side branches of the Eastern Scheldt, one with a SW-NE orientation **(middle)**, and the small W-E channel (**bottom, middle** channel in **Figure 1**). The sum of the branches is plotted in **Figure 5 (middle)**. Distance is measured along a centerline from the narrowest cross-section in the seaward mouth. For explanation of legend see **Table 2**.

(H2), which includes bank protection works and infrastructure, is unsurprising.

The most abundant transition lengths were normalized by a characteristic length of each estuary for comparison between the three estuaries (**Table 3**). In all estuaries the transitions between saltmarsh classes and low-energy tidal flat are an order of magnitude longer than those with the high-energy tidal flats. The relative transition lengths between low-energy tidal flat and saltmarsh classes differ between the estuaries: the Western Scheldt has relatively more transition length to saltmarsh than to pioneer vegetation, while the Eastern Scheldt has relatively much more transition length to pioneer vegetation. The Eems-Dollard has the lowest relative transition lengths of all three estuaries.

There are striking differences between the estuaries that are consistent with the differences observed before. The Eastern Scheldt has no significant vegetated area on the bars, in contrast to the other two estuaries, and therefore has no

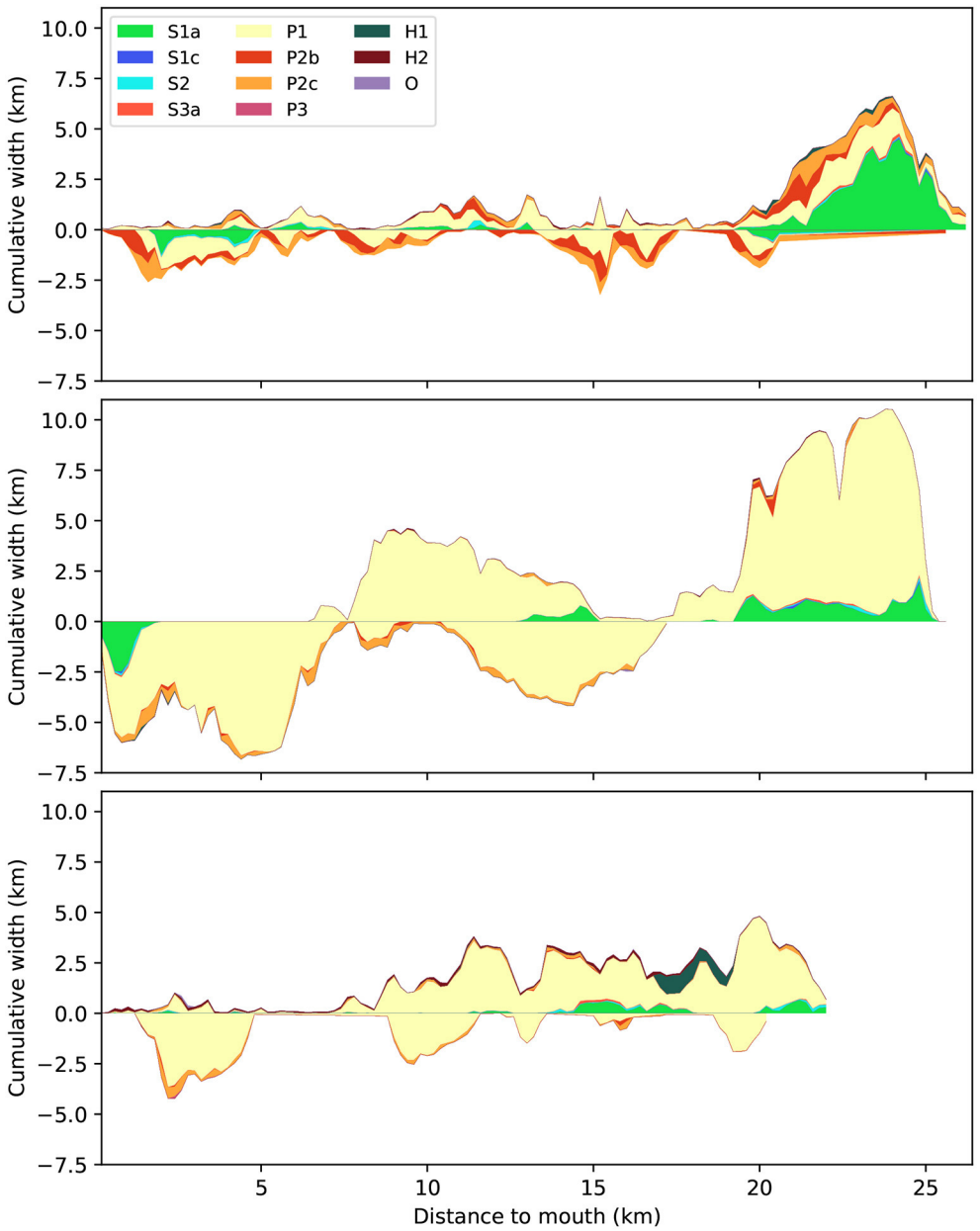


FIGURE 7 | Distribution of biogeomorphological classes separated for shore-connected and mid-channel areas as absolute width along the Western Scheldt **(top)**, Eems-Dollard **(middle)**, and Eastern Scheldt **(bottom)**. Positive widths refer to shore-connected tidal flats and saltmarsh and negative widths refer to the bars and shoals. Distance is measured along a centerline from the narrowest cross-section in the seaward mouth. For explanation of legend see **Table 2**.

significant transition length between vegetated and unvegetated habitats. The Western Scheldt has more shore-connected mega-ripples (P2b) and high-energy tidal flat (P2c) bordering on water, while the Eastern Scheldt has more low-energy tidal flat (P1) bordering on water and the Eems-Dollard takes an intermediate position. On the other hand, the Eastern Scheldt and Eems-Dollard have much more transitions from low-energy tidal flat (P1) to water on the bars than the Western Scheldt.

4. DISCUSSION

The main outcome is that the three estuaries have fairly similar biogeomorphological characteristics with predominantly subtidal areas, here unmapped, and a larger littoral zone of unvegetated tidal flats, than pioneer saltmarsh and supralittoral saltmarsh. The tidal flat width varies along the estuaries, which was already explained by formation of mid-channel bars and shore-connected embayments in zones wider than

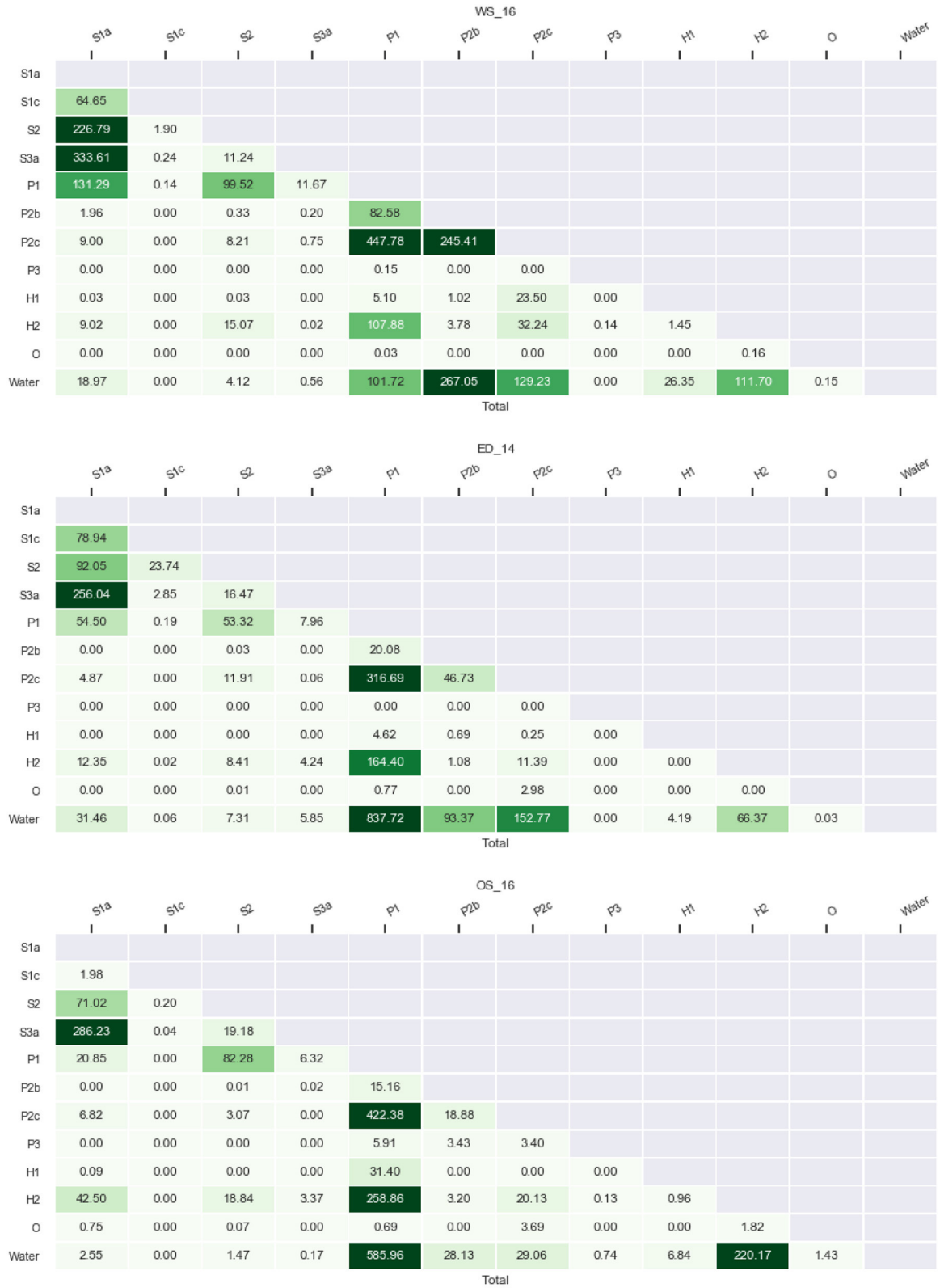


FIGURE 8 | Absolute lengths of transitions between biogeomorphological surface classes in km for the Western Scheldt **(top)**, Eems-Dollard **(middle)**, and Eastern Scheldt **(bottom)**. For explanation of classes see **Table 2**. The color is linearly scaled with the numbers.

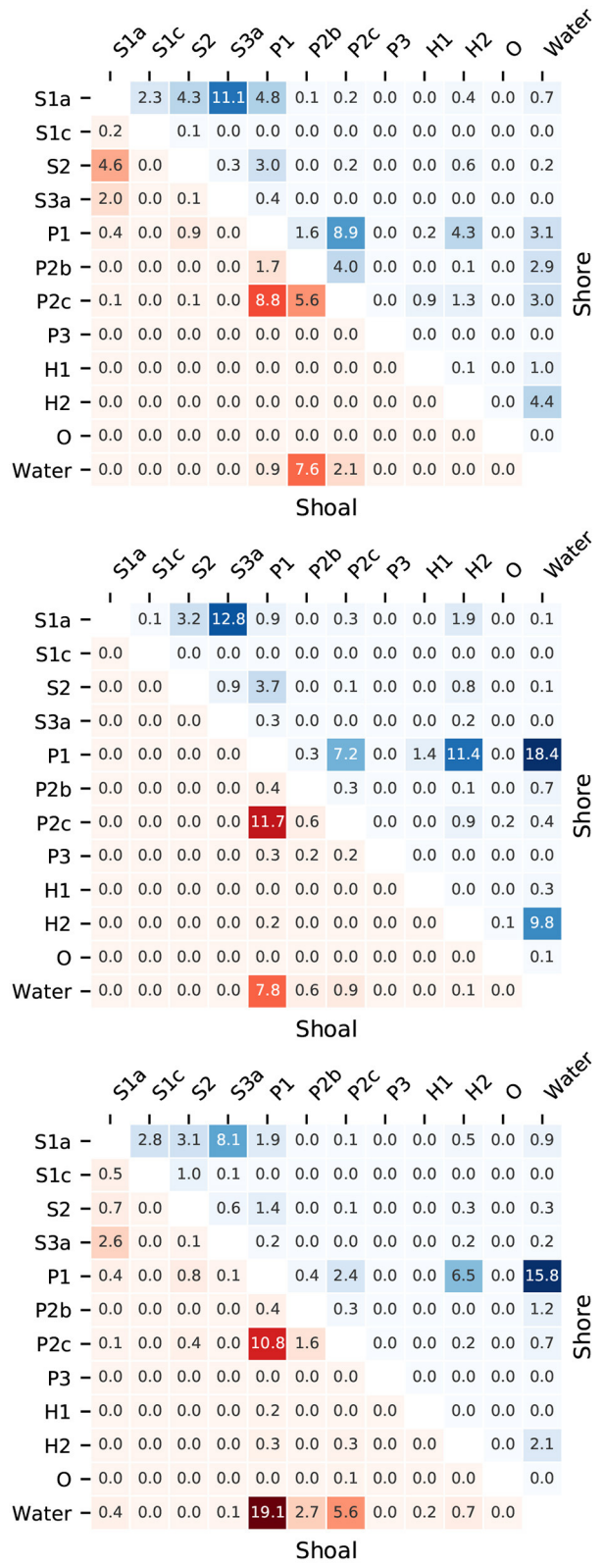


FIGURE 9 | Fraction of transition length between biogeomorphological surface classes for shore-connected areas (red) and islands and shoals (blue) *(Continued)*

FIGURE 9 | for the Western Scheldt **(top)**, Eems-Dollard **(middle)**, and Eastern Scheldt **(bottom)**. For explanation of classes see **Table 2**. The colors are linearly scaled with the numbers. The sum of each entire matrix is 100%.

a monotonically converging minimum estuary width (Leuven et al., 2018b,c). The quality of the classification is as good as expected from similar applications (e.g., Owers et al., 2016).

4.1. Interpretation in the Context of Contrasting Histories

The spatial variation of saltmarsh area is in all three cases most likely related to the processes of estuary formation by ingression on an inherited, embanked landscape, and by the land reclamation history. Historic and geologic reconstructions showed that parts of the presently embanked area were saltmarsh, and parts are former side-branches that silted up or were closed off (de Haas et al., 2018). The precise situations differ between estuaries: the Western and Eastern Scheldt had extensive side branches (Mulder and Louters, 1994; van der Spek, 1997). The majority of the upstream saltmarsh of the Western Scheldt developed over the past three centuries in Saeftinghe, a former polder flooded as a defense measure during a war. And the upstream saltmarsh in the Eems-Dollard formed in the Dollard, an inland bay that was a remnant of the ingression. Much of the original bay was reclaimed after saltmarsh formation intensified by human-built wave breakers with the intention to gain land, which was mainly successful in the predominantly downwind direction (Vos and van Kesteren, 2000; de Haas et al., 2018). It is not entirely clear, however, why Saeftinghe in the Western Scheldt silted up to high supratidal levels without human-built wave breakers, while the Dollard ceased to expand and fill. *Spartina anglica*, a highly effective species for human-aided salt marsh formation, was introduced and spread in the 1920s. There are also local dynamics in the saltmarsh on shorter timescales, such as quasiperiodic retreat and expansion (Wang and Temmerman, 2013; van Belzen et al., 2017), but these do not change the general trends. The patch of saltmarsh near the mouth of the Eems-Dollard is more associated to the barrier island than to the estuary. This leads to the interpretation that the large-scale pattern of landward increasing saltmarsh extent in all three estuaries is mainly caused by the initial landscape conditions prior to the ingressions and by the land reclamation history of the past centuries.

Human interference on the much shorter timescale of the past half century was also expected to have affected the littoral biogeomorphological patterns in all three estuaries. In the Eastern Scheldt, the installation of the storm surge barrier in the mouth instantaneously reduced the tides, which not only reduced the dynamics in the sea arm but also led to channel sedimentation, bar erosion and reduction of the littoral zone (Mulder and Louters, 1994). Indeed, dredged sand has now been dumped on the largest, western bar to attempt stalling of the loss of littoral habitat due to the reduced tidal energy in the adjacent channels. However, compared to the other two systems, the large-scale pattern is not yet very different. The Eastern Scheldt has

TABLE 3 | Normalized lengths of transitions between saltmarsh (rows) and tidal flat (columns) for the three systems.

Ecotope	Western Scheldt P1	Western Scheldt P2c	Eastern Scheldt P1	Eastern Scheldt P2c	Eems-Dollard P1	Eems-Dollard P2c
Saltmarsh (S1a)	5.09	0.35	1.45	0.47	1.20	0.11
Pioneer vegetation (S2)	3.86	0.32	5.71	0.21	1.17	0.26
Saltmarsh creek (S3a)	0.45	0.03	0.44	0	0.17	0

*Measured transition lengths were divided by a characteristic length calculated from the total mapped surface area of the estuary (without the water) divided by the mouth width (**Table 1**). See **Table 2** for explanation of ecotope labels.*

a much larger area of hard substrates than the other estuaries, which is likely partly due to the antecedent landscape conditions and partly due to loss of the sediment cover from these hard substrates to the subtidal zones. The intertidal areas of the Eems-Dollard are not notably different from those in the other systems, but note that our method cannot yet distinguish between sandy and muddy areas. Particularly the Dollard embayment has a very high mud content (van de Lageweg et al., 2018).

The two most striking differences between the systems are the presence of saltmarsh on the mid-channel tidal bars and the large high-energy area in the Western Scheldt. The formation of saltmarsh on the bars is likely an effect of dredging, fairway deepening and disposal of sediment on bar margins. The deepening enhanced the tidal amplitude throughout the estuary (van der Spek, 1997; Wang et al., 2002, 2015). While adaptation of the entire streamwise profile to the changed tidal properties and continuously disturbed sediment balance may take centuries (van der Wegen and Roelvink, 2012), the adaptation of the local "transverse" profiles and morphology were faster. The enhanced tidal currents scoured the channels further and transported sediment onto the bars, in addition to the disposal of dredged material on bar margins (van Dijk et al., 2021). Around the turn of the century the mid-channel bars became so high that the reduced inundation times allowed saltmarsh to settle and expand. Unlike the shore-connected intertidal flats and saltmarsh, this portion of the saltmarsh area is unrelated to the inherited landscape and land reclamation histories but is directly related to altered sediment dynamics. The reasons for the much larger high-energy area in the Western Scheldt are poorly understood, but the high proportion of mega-ripple fields predates the human interference (Cleveringa and Taal, 2015).

4.2. Significance for Potential Habitat Areas and Transitions

The review and the mapping exercise in Bouma et al. (2005) and in this paper emphasize the quantification of areas of different biogeomorphological units as well as their transitions. While no specific habitat is strongly preferable from an ecological perspective, a mosaic of habitats and transitions may be preferred over monotonous landscapes by animal species from several taxonomic groups. Ecological mapping has been argued to fall into either the category of patch delineation or the category of landscape gradient mapping (Lausch et al., 2015). The present mapping approach clearly falls into the category of quantification of habitat area by patch delineation, but the new measure for length of transition between habitat classes also honors the ecologically important idea of landscape gradients.

The low-energy intertidal area appears more important than the megarippled and high-energy tidal flat areas for abundance and biodiversity of macrobenthic species and their predators (Ysebaert et al., 2003, 2016). The sediment dynamics of the high-energy tidal flats restrict the number of benthic species that can successfully survive in and on these flats, and therefore also limits the foraging time for waders during the emergence period. Furthermore, it suggests that the large proportion of high-energy vs. low-energy intertidal area in the Western Scheldt is less desirable from the perspective of preservation in view of reducing habitat areas regionally and globally.

Regardless of the abundance of high-energy habitats in the Western Scheldt, the ecologically important habitats of saltmarshes, with relatively large lengths of transitions between low-energy tidal flats and saltmarsh creeks, occur more frequently than along the Eastern Scheldt and Eems-Dollard. The Eastern Scheldt has limited saltmarsh and reduced intertidal flat area due to the effects of the storm surge barrier (de Vet et al., 2017). The Eems-Dollard has limited saltmarsh with creeks because of human interference during saltmarsh accretion for embankment purposes. Furthermore, much of the lower estuary here is part of the Wadden Sea and therefore unconfined by shores where saltmarsh could have formed.

The presence of the large mid-channel bars, as opposed to single-channel estuaries, increases the intertidal area, the length of water-tidal flat transitions and the transitions from low-energy tidal flats to saltmarsh creeks in case saltmarsh develops on the bars. While the shore-connected tidal flats and saltmarshes along most of the systems may be more sheltered than their mid-channel counterparts, the total length of transitions on the sparse bars is as important numerically and, for the saltmarsh creeks, more important. More generally, this shows that multi-channel estuaries with bars have potentially much richer and more extensive habitats than estuaries that were confined to a single channel system for shipping and land-reclamation purposes. Additionally, access to mid-channel bars by land predators, including domesticated animals, is likely much lower than to the shore-connected areas.

The lengths of the most abundant mapped transitions between tidal flats and saltmarshes were compared after normalization (see **Table 3**). As expected, the normalized transition lengths are high for the transition between low-energy tidal flats and natural pioneer vegetation and saltmarsh creeks, but much less so in the Eems-Dollard than in the other two systems. This is consistent

with the higher human influence on saltmarsh formation in the Eems-Dollard, which renders the transitions between bare and vegetated surfaces much more regular and relatively shorter. On the other hand, the tidal flat transition to fully developed saltmarsh is especially long in the Western Scheldt, which fits with the large saltmarsh area in that system. The transition from high-energy tidal flats to pioneer vegetation is similar in the three estuaries after the normalization, despite the much higher abundance of high-energy tidal flats in the Western Scheldt. Overall, the relative length of transitions between low-energy tidal flat and the collective saltmarsh classes is about 4–5 times larger in the Western Scheldt and Eastern Scheldt than in the Eems-Dollard. In view of the policy that a range of habitats and spatial heterogeneity is required for ecologically meaningful transitions between the ecotope classes (Wolter et al., 2016; Ysebaert et al., 2016), this could suggest that the Eems-Dollard has fewer habitat transitions than possible, as observed in the other two estuaries.

4.3. Perspectives

The automated mapping of biogeomorphology from aerial photography is in principle repeatable for multiple years and for other areas, provided that aerial photographs of sufficient quality are available. The photos are ideally acquired on a single day or limited number of days, during low tide and with thin clouds higher in the atmosphere. We ordered orthomosaics with high geometric accuracy and processed them per acquisition day. The model starts with a calibration on Brightness and NDVI, which proved to be the main factors responsible for differences between the photos. The subsequent rules needed minor calibration. For the distinction between mud and sand, brightness appeared to have insufficient information: while mud often has a different moisture content and hence brightness than sand, more factors affect the brightness threshold than we have control over for the system-wide mapping, such as time since emergence and subtle lighting and bedform differences. Future extension of the method to distinguish between sediment types will likely require new techniques. Further extension to distinguish between vegetation types is also an interesting improvement to pursue (Owers et al., 2016). The present mapping will need to be complemented by further analyses and data to obtain habitat maps, or ecotope maps, that include hydrodynamics and salinity dynamics (e.g., Baptist et al., 2019). The natural biogeomorphodynamics of the systems are poorly quantified but significant within the seasons (e.g., Swinkels et al., 2009; van Dijk et al., 2019; Brückner et al., 2021), at least an annual repetition of the mapping is highly recommended. A comparison between sample data of surface and sediment properties and species with the biogeomorphological map could facilitate interpolation for mapping of the substrate and species data.

The high economic pressures in the three studied systems led to an accelerated deterioration of the ecological quality over the past decades, while the ecological importance for the rivers, the North Sea and the Eastern Atlantic Flyway of migratory birds is immeasurable. It is convenient for purposes of management and legislation to have a mapping method with objective and quantitative characteristics, because, alternatively, uncertainty about such numbers could lead to conflicts and legal disputes about conflicting economic and ecological interests (van Buuren et al., 2010). While the ecological significance of the biogeomorphological units, and the transitions between them (Soininen et al., 2015), need further quantification by comparison to ecological datasets and numerical, calibrated flow modeling (e.g., de Jonge, 2000; Ysebaert et al., 2003, 2016; Cozzoli et al., 2017; Brückner et al., 2020, 2021), qualitatively it is certain that they are important. The observed degradation of ecosystems leaves no doubt that effects of human interference urgently needs to be reduced and its effects reversed in order to stop the rapid decline of biodiversity (also see Crooks and Turner, 1999; Ysebaert et al., 2016). Habitat protection and expansion by "depoldering," or managed realignment, are essential to maintain and restore healthy ecosystems (e.g., Ysebaert et al., 2016). Quantification of areas of habitats, or ecotopes, has already been an efficient monitoring instrument in the Western Scheldt in this respect and the automated method employed here reduces the production time and costs considerably and potentially provides an important spatial dataset for analyses and, possibly, upscaling of ecological datasets.

5. CONCLUSIONS

A comparison of biogeomorphological maps of three estuaries with similar boundary conditions showed that saltmarsh decreases weakly in width proportion along the estuaries while tidal flats have similar area along the estuary. The subtidal areas have the largest surface area in all three systems, followed by tidal flats and salt marsh. The variations in their relative contribution along the estuaries are due to presence of mid-channel bars and shore-connected embayments.

However, the differences are more striking and are mainly due to the different histories of estuary formation and human interference. The estuary outlines are determined by their ingression and the subsequent land reclamations and embankments over the past centuries. Consequently, the heads of all three estuaries have disproportionately more area above subtidal, where one estuary has much more saltmarsh and the other has more low-dynamic tidal flat. Likewise, side-branches and embayments are remnants of past larger branches and their planforms are the result of the embankment history. The minor importance of saltmarsh flanking the estuaries is due to the land reclamation that turned most of the surrounding marshes into agricultural areas.

Human interference over the past decades strongly affected the areas of, and transitions between, biogeomorphological units as is illustrated by the contrasts between the three systems. The Western Scheldt has longer transitions between low-energy tidal flats and the saltmarsh creeks, that are nursery grounds, not only because of the saltmarsh developed on an abandoned polder, but also because the increasing tidal amplitude along the estuary that led to mid-channel bar accretion and tidal marsh settling. The Eastern Scheldt, on the other hand, had reduced tidal energy that leads to reduction of low-energy tidal flats. The Eems-Dollard, finally, has much less saltmarsh-creek area and proportionally smaller lengths of low-energy intertidal area to saltmarsh creek transitions due to the human-enhanced saltmarsh accretion for land reclamation purposes.

DATA AVAILABILITY STATEMENT

The spatial datasets generated for this study can be found in the UU YODA repository https://doi.org/10.24416/UU01-HTNVEV. The aerial photographs can be obtained from Rijkswaterstaat: https://www.rijkswaterstaat.nl/apps/geoservices/geodata/dmc/luchtfoto_geomorfologie/. The area distribution of biogeomorphological classes along the three estuaries are provided as **Supplementary Material**.

AUTHOR CONTRIBUTIONS

HD developed the OBIA ruleset and analysis codes and made the figures. MK wrote the manuscript. LC and TD did pilots as part of their BSc theses. RJ and EP validated the maps with expert knowledge. MK, JC, RJ, and EP interpreted the results. EA, RJ, and MK supervised the work. All authors contributed to the article and approved the submitted version.

FUNDING

HD was supported by grants from Rijkswaterstaat Noord Nederland and Centrale Informatie Voorziening. MK was supported by his ERC Consolidator project 647570.

ACKNOWLEDGMENTS

Reviewers are acknowledged for constructive and helpfull comments. Discussions with Charlotte Schmidt, Harm Jan Pierik, Martin Baptist, and Tom Ysebaert are gratefully acknowledged.

SUPPLEMENTARY MATERIAL

The Supplementary Material for this article can be found online at: https://www.frontiersin.org/articles/10.3389/fmars.2021.742448/full#supplementary-material

REFERENCES

Baptist, M., van der Wal, J., Folmer, E., Graewe, U., and Elschot, K. (2019). An ecotope map of the trilateral wadden sea. *J. Sea Res.* 152:101761. doi: 10.1016/j.seares.2019.05.003

Bouma, H., De Jong, D., Twisk, F., and Wolfstein, K. (2005). *A Dutch Ecotope System for Coastal Waters*. Technical report. Rijkswaterstaat, Middelburg.

Braat, L., Leuven, J., Lokhorst, I., and Kleinhans, M. (2019). Effects of estuarine mudflat formation on tidal prism and large-scale morphology in experiments. *Earth Surface Process. Landforms* 44, 417–432. doi: 10.1002/esp.4504

Braat, L., van Kessel, T., Leuven, J., and Kleinhans, M. (2017). Effects of mud supply on large-scale estuary morphology and development over centuries to millennia. *Earth Surf. Dynam.* 5, 617–652. doi: 10.5194/esurf-5-617-2017

Brückner, M., Braat, L., Schwarz, C., and Kleinhans, M. (2020). What came first, mud or biostabilizers? elucidating interacting effects in a coupled model of mud, saltmarsh, microphytobenthos and estuarine morphology. *Water Resour. Res.* 56, e2019WR026945. doi: 10.1029/2019WR026945

Brückner, M. Z., Schwarz, C., Coco, G., Baar, A., Boechat Albernaz, M., and Kleinhans, M. G. (2021). Benthic species as mud patrol - modelled effects of bioturbators and biofilms on large-scale estuarine mud and morphology. *Earth Surface Process. Landforms* 46, 1128–1144. doi: 10.1002/esp.5080

Cleveringa, J., and Taal, M. (2015). A smooth scheldt (36th IAHR World Congress, The Hague, the Netherlands)

Cozzoli, F., Bouma, T., Ysebaert, T., and Herman, P. (2013). Application of non-linear quantile regression to macrozoobenthic species distribution modelling: comparing two contrasting basins. *Mar. Ecol. Prog. Ser.* 475, 119–133. doi: 10.3354/meps10112

Cozzoli, F., Smolders, S., Eelkema, M, Ysebaert, T., Escaravage, V., et al. (2017). A modeling approach to assess coastal management effects on benthic habitat quality: A case study on coastal defense and navigability. *Est. Coast. Shelf Sci.* 184, 67–82

Crooks, S., and Turner, R. (1999). Integrated coastal management: Sustaining estuarine natural resources. *Adv. Ecol. Res.* 29, 241–289. doi: 10.1016/S0065-2504(08)60195-6

Dashtgard, S., and Croix, A. L. (2015). "Chapter 3: Sedimentological trends across the tidal-fluvial transition, Fraser River, Canada: a review and some broader implications," in *Fluvial-Tidal Sedimentology*, eds P. J. Ashworth, J. L. Best, and D. R. Parsons (Amsterdam: Elsevier), 111–126. doi: 10.1016/B978-0-444-63529-7.00005-5

de Haas, T., Pierik, H., van der Spek, A., Cohen, K., van Maanen, B., and Kleinhans, M. (2018). Long-term evolution of tidal systems: effects of rivers, coastal boundary conditions, eco-engineering species, inherited relief and human interference. *Earth Sci. Rev.* 177, 139–163. doi: 10.1016/j.earscirev.2017.10.006

de Haas, T., van der Valk, L., Cohen, K., Pierik, H., Weisscher, S., Hijma, M., et al. (2019). Long-term evolution of the old rhine estuary: unravelling effects of changing boundary conditions and inherited landscape. *Depositional Rec.* 5, 84–108. doi: 10.1002/dep2.56

de Jonge, V. N. (2000). Importance of temporal and spatial scales in applying biological and physical process knowledge in coastal management, an example for the ems estuary. *Continent. Shelf Res.* 20, 1655 – 1686. doi: 10.1016/S0278-4343(00)00042-X

de Vet, P., van Prooijen, B., and Wang, Z. (2017). The differences in morphological development between the intertidal flats of the eastern and western Scheldt. *Geomorphology* 281, 31–42. doi: 10.1016/j.geomorph.2016.12.031

Dronkers, J. (2017). Convergence of estuarine channels. *Cont. Shelf Res.* 144, 120–133. doi: 10.1016/j.csr.2017.06.012

Duran-Matute, M., Gerkema, T., de Boer, G. J., Nauw, J. J., and Gräwe, U. (2014). Residual circulation and freshwater transport in the Dutch Wadden sea: a numerical modelling study. *Ocean Sci.* 10, 611–632. doi: 10.5194/os-10-611-2014

Enwright, N., SooHoo, W., Dugas, J., Conzelmann, C., Laurenzano, C., Lee, D., et al. (2020). *Louisiana Barrier Island Comprehensive Monitoring Program–Mapping Habitats in Beach, Dune, and Intertidal Environments Along the Louisiana Gulf of Mexico Shoreline, 2008 and 2015–16*. Technical report. U.S. Geological Survey Open-File Report.

Friedrichs, C., and Aubrey, D. (1988). Non-linear tidal distortion in shallow well-mixed estuaries: a synthesis. *Estuar. Coast. Shelf Sci.* 27, 521–545.

Greenberg, R. (2013). "The ecology of estuarine wildlife," in *Estuarine Ecology, 2nd Edn*, eds J. W. Day, B. C. Crump, W. M. Kemp, and A. Yanez-Arancibia (Wiley), 357–380.

Herman, P., Middelburg, J., Koppel, J. V. D., and Heip, C. (1999). Ecology of estuarine macrobenthos. *Adv. Ecol. Res.* 29, 195–240. doi: 10.1016/S0065-2504(08)60194-4

Hiatt, M., Sonke, W., Addink, E., van Dijk, W., van Kreveld, M., Ophelders, T., et al. (2020). Geometry and topology of estuary and braided river channel networks automatically extracted from topographic data. *J. Geophys. Res. Earth Surface* 125:e2019JF005206. doi: 10.1029/2019JF005206

Hibma, A., Schuttelaars, H. M., and Wang, Z. B. (2003). Comparison of longitudinal equilibrium profiles of estuaries in idealized and process-based model. *Ocean Dyn.* 53, 252–269. doi: 10.1007/s10236-003-0046-7

Jones, C., Lawton, J., and Shachak, M. (1994). Organisms as ecosystem engineers. *Oikos* 69, 373–386. doi: 10.2307/3545850

Jongepier, I., Wang, C., Missiaen, T., Soens, T., and Temmerman, S. (2015). Intertidal landscape response time to dike breaching and stepwise re-embankment: a combined historical and geomorphological study. *Geomorphology* 236, 64–78. doi: 10.1016/j.geomorph.2015.02.012

Kleinhans, M. G., Braudrick, C., van Dijk, W., van de Lageweg, W., Teske, R., and van Oorschot, M. (2015). Swiftness of biomorphodynamics in Lilliput- to Giant-sized rivers and deltas. *Geomorphology* 244, 56–73. doi: 10.1016/j.geomorph.2015.04.022

Lausch, A., Blaschke, T., Haase, D., Herzog, F., Syrbe, R.-U., Tischendorf, L., et al. (2015). Understanding and quantifying landscape structure - a review on relevant process characteristics, data models and landscape metrics. *Ecol. Modell.* 295, 31–41. doi: 10.1016/j.ecolmodel.2014.08.018

Leuven, J., de Haas, T., Braat, L., and Kleinhans, M. G. (2018a). Topographic forcing of tidal sandbar patterns for irregular estuary planforms. *Earth Surf. Process. Landforms* 43, 172–186. doi: 10.1002/esp.4166

Leuven, J. R. F. W., Braat, L., van Dijk, W. M., de Haas, T., van Onselen, E. P., Ruessink, B. G., et al. (2018b). Growing forced bars determine nonideal estuary planform. *J. Geophys. Res. Earth Surface* 123, 2971–2992. doi: 10.1029/2018JF004718

Leuven, J. R. F. W., Selaković, S., and Kleinhans, M. G. (2018c). Morphology of bar-built estuaries: empirical relation between planform shape and depth distribution. *Earth Surface Dyn.* 6, 763–778. doi: 10.5194/esurf-6-763-2018

Lokhorst, I. R., de Lange, S. I., van Buiten, G., Selakovic, S., and Kleinhans, M. G. (2019). Species selection and assessment of eco-engineering effects of seedlings for biogeomorphological landscape experiments. *Earth Surface Process. Landforms*. 44, 2922–2935. doi: 10.1002/esp.4702

Meire, P., Ysebaert, T., Damme, S. V., Bergh, E. V. D., Maris, T., and Struyf, E. (2005). The scheldt estuary: a description of a changing ecosystem. *Hydrobiologia* 540, 1–11. doi: 10.1007/s10750-005-0896-8

Mulder, J. P. M., and Louters, T. (1994). *Changes in Basin Geomorphology After Implementation of the Oosterschelde Estuary Project.* Dordrecht: Springer.

Owers, C. J., Rogers, K., and Woodroffe, C. D. (2016). Identifying spatial variability and complexity in wetland vegetation using an object-based approach. *Int. J. Remote Sens.* 37, 4296–4316. doi: 10.1080/01431161.2016.1211349

Savenije, H. (2015). Prediction in ungauged estuaries: an integrated theory. *Water Resour. Res.* 51, 2464–2476. doi: 10.1002/2015WR016936

Schwarz, C., Gourgue, O., van Belzen, J., Zhu, Z., Bouma, T., van de Koppel, J., et al. (2018). Self-organization of a biogeomorphic landscape controlled by plant life-history traits. *Nat. Geosci.* 11, 672–677. doi: 10.1038/s41561-018-0180-y

Soininen, J., Bartels, P., Heino, J., Luoto, M., and Hillebrand, H. (2015). Toward more integrated ecosystem research in aquatic and terrestrial environments. *BioScience* 65, 174–182. doi: 10.1093/biosci/biu216

Swinkels, C., Jeuken, C., Wang, Z., and Nicholls, R. (2009). Presence of connecting channels in the Western Scheldt Estuary. *J. Coast. Res.* 25, 627–640. doi: 10.2112/06-0719.1

Telesh, I., Schubert, H., and Skarlato, S. (2013). Life in the salinity gradient: discovering mechanisms behind a new biodiversity pattern. *Estuar. Coast. Shelf Sci.* 135, 317–327. doi: 10.1016/j.ecss.2013.10.013

Townend, I. (2012). The estimation of estuary dimensions using a simplified form model and the exogenous controls. *Earth Surf. Process. Landforms* 37, 1573–1583. doi: 10.1002/esp.3256

van Belzen, J., van de Koppel, J., Kirwan, M., van der Wal, D., Herman, P., Dakosand, V., et al. (2017). Vegetation recovery in tidal marshes reveals critical slowing down under increased inundation. *Nat. Commun.* 8:15811. doi: 10.1038/ncomms15811

van Buuren, A., Gerrits, L., and Teisman, G. R. (2010). Understanding and managing the westerschelde - synchronizing the physical system and the management system of a complex estuary. *Hydrol. Earth Syst. Sci.* 14, 2243–2257. doi: 10.5194/hess-14-2243-2010

van de Lageweg, W., L. Braat, D. P., and Kleinhans, M. (2018). Controls on mud distribution and architecture along the fluvial-to-marine transition. *Geology* 46, 923–926. doi: 10.1130/G45504.1qsdc

van den Berg, J., Jeuken, M., and van der Spek, A. (1996). "Hydraulic processes affecting the morphology and evolution of the Westerschelde estuary," in *Estuarine Shores: Evolution, Environments and Human Alterations*, eds K. F. Nordstrom and C. J. Roman (Chicester: John Wiley), 157–184

van der Spek, A. (1997). Tidal asymmetry and long-term evolution of Holocene tidal basins in The Netherlands: simulation of palaeo-tides in the Schelde estuary. *Mar. Geol.* 141, 71–90.

van der Wal, D., van Kessel, T., Eleveld, M. A., and Vanlede, J. (2010). Spatial heterogeneity in estuarine mud dynamics. *Ocean Dyn.* 60, 519–533. doi: 10.1007/s10236-010-0271-9

van der Wegen, M., and Roelvink, J. (2012). Reproduction of estuarine bathymetry by means of a process-based model: Western scheldt case study, the Netherlands. *Geomorphology* 179, 152–167. doi: 10.1016/j.geomorph.2012.08.007

van Dijk, W., Hiatt, M., van der Werf, J., and Kleinhans, M. (2019). Effects of shoal margin collapses on the morphodynamics of a sandy estuary. *J. Geophys. Res. Earth Surface* 124, 195–215. doi: 10.1029/2018JF004763

van Dijk, W. M., Cox, J. R., Leuven, J. R., Cleveringa, J., Taal, M., Hiatt, M. R., et al. (2021). The vulnerability of tidal flats and multi-channel estuaries to dredging and disposal. *Anthropocene Coasts* 4, 36–60. doi: 10.1139/anc-2020-0006

van Maren, D. S., Winterwerp, J. C., and Vroom, J. (2015). Fine sediment transport into the hyper-turbid lower ems river: the role of channel deepening and sediment-induced drag reduction. *Ocean Dyn.* 65, 589–605. doi: 10.1007/s10236-015-0821-2

van Veen, J. (1950). EBB and flood channel systems in the Netherlands tidal waters. *J. R. Dutch Geograph. Soc.* 67, 303–325.

Vos, P., and van Kesteren, W. (2000). The long-term evolution of intertidal mudflats in the northern Netherlands during the Holocene; natural and anthropogenic processes. *Continent. Shelf Res.* 20, 1687–1710.

Wang, C., and Temmerman, S. (2013). Does biogeomorphic feedback lead to abrupt shifts between alternative landscape states?: An empirical study on intertidal flats and marshes. *J. Geophys. Res. Earth Surf.* 118, 229–240. doi: 10.1029/2012JF002474

Wang, Z., Jeuken, M., Gerritsen, H., de Vriend, H., and Kornman, B. (2002). Morphology and asymmetry of the vertical tide in the Westerschelde estuary. *Continent. Shelf Res.* 22, 2599–2609. doi: 10.1016/S0278-4343(02)00134-6

Wang, Z., van Maren, D., Ding, P., Yang, S., van Prooijen, B., de Vet, P., et al. (2015). Human impacts on morphodynamic thresholds in estuarine systems. *Continent. Shelf Res.* 111, 174–183. doi: 10.1016/j.csr.2015.08.009

Whitfield, A., Elliott, M., Basset, A., Blaber, S., and West, R. (2012). Paradigms in estuarine ecology - a review of the remane diagram with a suggested revised model for estuaries. *Estuar. Coast. Shelf Sci.* 97, 78–90. doi: 10.1016/j.ecss.2011.11.026

Winterwerp, J., Wang, Z., van Braeckel, A., van Holland, G., and Kosters, F. (2013). Man-induced regime shifts in small estuaries II: a comparison of rivers. *Ocean Dyn.* 63, 1293–1306. doi: 10.1007/s10236-013-0663-8

Wolter, C., Buijse, A. D., and Parasiewicz, P. (2016). Temporal and spatial patterns of fish response to hydromorphological processes. *River Res. Appl.* 32, 190–201. doi: 10.1002/rra.2980

Ysebaert, T., Herman, P., Meire, P., Craeymeersch, J., Verbeek, H., and Heip, C. (2003). Large-scale spatial patterns in estuaries: estuarine macrobenthic communities in the schelde estuary, NW Europe. *Estuar. Coast. Shelf Sci.* 57, 335–355. doi: 10.1016/S0272-7714(02)00359-1

Ysebaert, T., Meininger, P. L., Meire, P., Devos, K., Berrevoets, C. M., Strucker, R. C., et al. (2000). Waterbird communities along the estuarine salinity gradient of the schelde estuary, NW-Europe. *Biodivers. Conserv.* 9, 1275–1296. doi: 10.1023/A:1008976306651

Ysebaert, T., van der Hoek, D.-J., Wortelboer, R., Wijsman, J. W., Tangelder, M., and Nolte, A. (2016). Management options for restoring estuarine dynamics and implications for ecosystems: a quantitative approach for the southwest delta in the netherlands. *Ocean Coast. Manage.* 121, 33–48. doi: 10.1016/j.ocecoaman.2015.11.005

Conflict of Interest: The authors declare that the research was conducted in the absence of any commercial or financial relationships that could be construed as a potential conflict of interest.

Publisher's Note: All claims expressed in this article are solely those of the authors and do not necessarily represent those of their affiliated organizations, or those of the publisher, the editors and the reviewers. Any product that may be evaluated in this article, or claim that may be made by its manufacturer, is not guaranteed or endorsed by the publisher.

Copyright © 2021 Kleinhans, Douma, Addink, Coumou, Deggeller, Jentink, Paree and Cleveringa. This is an open-access article distributed under the terms of the Creative Commons Attribution License (CC BY). The use, distribution or reproduction in other forums is permitted, provided the original author(s) and the copyright owner(s) are credited and that the original publication in this journal is cited, in accordance with accepted academic practice. No use, distribution or reproduction is permitted which does not comply with these terms.

frontiers in Marine Science

ORIGINAL RESEARCH
published: 10 December 2021
doi: 10.3389/fmars.2021.782643

Experimental Tree Mortality Does Not Induce Marsh Transgression in a Chesapeake Bay Low-Lying Coastal Forest

David C. Walters[1], Joel A. Carr[1], Alyssa Hockaday[1], Joshua A. Jones[2], Eliza McFarland[1], Katya E. Kovalenko[3], Matthew L. Kirwan[4], Donald R. Cahoon[1] and Glenn R. Guntenspergen[1]*

[1] U.S. Geological Survey, Eastern Ecological Research Center, Laurel, MD, United States, [2] McDonogh School, Owings Mills, MD, United States, [3] Natural Resources Research Institute, University of Minnesota, Duluth, MN, United States, [4] Virginia Institute of Marine Science, William & Mary, Gloucester Point, VA, United States

OPEN ACCESS

Edited by:
Zhan Hu,
Sun Yat-sen University, China

Reviewed by:
Keryn Gedan,
George Washington University, United States
Luzhen Chen,
Xiamen University, China

***Correspondence:**
David C. Walters
davidwalters@usgs.gov

Specialty section:
This article was submitted to Coastal Ocean Processes, a section of the journal Frontiers in Marine Science

Received: *24 September 2021*
Accepted: *09 November 2021*
Published: *10 December 2021*

Citation:
Walters DC, Carr JA, Hockaday A, Jones JA, McFarland E, Kovalenko KE, Kirwan ML, Cahoon DR and Guntenspergen GR (2021) Experimental Tree Mortality Does Not Induce Marsh Transgression in a Chesapeake Bay Low-Lying Coastal Forest. Front. Mar. Sci. 8:782643. doi: 10.3389/fmars.2021.782643

Transgression into adjacent uplands is an important global response of coastal wetlands to accelerated rates of sea level rise. "Ghost forests" mark a signature characteristic of marsh transgression on the landscape, as changes in tidal inundation and salinity cause bordering upland tree mortality, increase light availability, and the emergence of tidal marsh species due to reduced competition. To investigate these mechanisms of the marsh migration process, we conducted a field experiment to simulate a natural disturbance event (e.g., storm-induced flooding) by inducing the death of established trees (coastal loblolly pine, *Pinus taeda*) at the marsh-upland forest ecotone. After this simulated disturbance in 2014, we monitored changes in vegetation along an elevation gradient in control and treatment areas to determine if disturbance can lead to an ecosystem shift from forested upland to wetland vegetation. Light availability initially increased in the disturbed area, leading to an increase in biodiversity of vegetation with early successional grass and shrub species. However, over the course of this 5-year experiment, there was no increase in inundation in the disturbed areas relative to the control and pine trees recolonized becoming the dominant plant cover in the disturbed study areas. Thus, in the 5 years since the disturbance, there has been no overall shift in species composition toward more hydrophytic vegetation that would be indicative of marsh transgression with the removal of trees. These findings suggest that disturbance is necessary but not sufficient alone for transgression to occur. Unless hydrological characteristics suppress tree re-growth within a period of several years following disturbance, the regenerating trees will shade and outcompete any migrating wetland vegetation species. Our results suggest that complex interactions between disturbance, biotic resistance, and slope help determine the potential for marsh transgression.

Keywords: transgression, sea level rise, marsh, forest, ecology

INTRODUCTION

Transgression into adjacent uplands is an important response of coastal wetlands that are threatened by accelerated rates of sea level rise (Raabe and Stumpf, 2016; Schieder and Kirwan, 2019). Where marshes are unable to migrate landward, it is likely that rising sea level and sediment budget deficiencies will lead to ecosystem loss in many regions around the globe (Schuerch et al., 2018). The formation of "ghost forests"—stands of dead trees in marshes—marks a signature characteristic of where transgression occurs on the landscape (Kirwan and Gedan, 2019; Schieder and Kirwan, 2019). The ability of marshes to transgress upslope as a means of responding to sea level rise varies and is dependent on upslope conditions and barriers to migration (Carr et al., 2020). Geological formations (Mitchell et al., 2017) and steep slopes (Kirwan et al., 2016) control the amount of land potentially available for transgression. Human interactions in the form of physical barriers such as roads, seawalls, levees, and other infrastructure prevent transgression in areas where it would otherwise occur (Enwright et al., 2016; Borchert et al., 2018). Humans also create socio-economic barriers to transgression such as private landowners mowing areas with potential wetland vegetation (Anisfeld et al., 2017) and agricultural practices of altering natural hydrology *via* digging ditches and building impoundments (Smith et al., 2017). Additionally, even in a natural setting with upslope areas within the range for potential transgression, ecological barriers are present in the form of competition with invasive species with low habitat value (i.e., *Phragmites australis*) (Smith, 2013) and the resiliency of pre-existing forest ecosystems where mature trees experience low mortality rates (Field et al., 2016).

Management plays a critical role in how transgression will occur, as adaptable strategies can facilitate marsh migration by removing upland barriers (Smith et al., 2017). "Managed retreat"—where human communities strategically relocate from low-lying coastal areas—can lead to a mutual benefit for increasing the opportunity for transgression of coastal ecosystems and human communities (Song et al., 2018). Another management strategy is to identify migration corridors where elevation is in the range for potential transgression and there are no physical barriers (Enwright et al., 2016) and to purchase easements from private landowners (Field et al., 2017b). Landowners with a vested interest in maintaining marsh habitat, that are poised along natural migration corridors (e.g., U.S. Fish and Wildlife Service National Wildlife Refuges) are uniquely positioned to take advantage of "planned retreat" strategies. However, more research is required to guide these agencies to make informed decisions about where and when marsh migration into adjacent uplands is likely to occur.

Recent remote sensing work illustrates that marsh migration into coastal forests is both rapid and geographically widespread (Smith, 2013; Enwright et al., 2016; Raabe and Stumpf, 2016; Borchert et al., 2018; Schieder et al., 2018; Ury et al., 2021). However, a better understanding of the mechanisms responsible for ecosystem transgression is needed to inform both models for projecting future transgression and management decisions. To do this, field studies that address the mechanisms of ecological change are critical. Abiotic factors such as inundation, soil salinity, and light availability are thought to be important drivers of marsh transgression (Poulter et al., 2009; Gedan and Fernández-Pascual, 2019; Taillie et al., 2019). However, there is a paucity of information on how changes in the forest canopy influence these abiotic factors as a forest transitions to marsh (Brinson et al., 1995; Fagherazzi et al., 2019). Light, inundation, and salinity potentially interact to create distinct ecotones across the marsh-upland forest boundary (Poulter et al., 2008, 2009; Taillie et al., 2019; Jobe and Gedan, 2021). Moreover, these abiotic factors can change slowly over time due to press changes such as sea level rise or can change rapidly due to pulse disturbances (Bender et al., 1984). Understanding these interacting factors is difficult with remote sensing and field-based monitoring in natural ecosystems.

It is also critical to monitor the successional shifts in vegetation, as the shift from upland to marsh is not immediate, and transitional communities are likely to have unique functional traits (Gedan and Fernández-Pascual, 2019). Forest species can also exhibit resistance to sea level rise which can inhibit marsh transgression in the short term (Field et al., 2016). This upland forest resistance could delay the transgression process until sea level crosses an elevation threshold, leading to direct conversion of forest to low marsh or ponds, "skipping" intermediate successional stages, and leading to loss of habitat function (Field et al., 2017a). Thus, experimental studies of the plant community at the marsh-upland forest boundary are needed to track the early stages and mechanisms of marsh plant species establishment and invasion across the marsh upland gradient.

We initiated a field experiment to better understand the role of disturbance in upland forests to potentially shift this system to one dominated by tidal wetland plant species. To better constrain the mechanisms of marsh transgression, we measured changes in vegetation after disturbance to a coastal marsh-adjacent forest along an elevation gradient to determine if tree mortality can lead to an ecosystem shift from forested upland to wetland vegetation.

MATERIALS AND METHODS

Study Site Description

The mid-Atlantic coast of North America is identified as a "hot spot" for eustatic sea level rise (Sallenger et al., 2012), with relative rates even higher in the Chesapeake Bay due to subsidence (Boon et al., 2010; Boesch et al., 2018). Additionally, the Chesapeake Bay is identified as a hot spot for both marsh loss and upland transgression in response to sea level rise (Stevenson et al., 1986; Mitchell et al., 2017; Schepers et al., 2017; Schieder et al., 2018). The setting for this study is at the U.S. Fish and Wildlife Service's Blackwater National Wildlife Refuge (USFWS BNWR), on the Eastern Shore of the Chesapeake Bay in Dorchester County, MD, United States (**Figure 1A**). Previous studies at the USFWS BNWR identified a history of transgression at sites with average upland slopes of less than 0.004, and in the past 150 years, marshes have migrated into the uplands at a rate of ∼2 m per year (Schieder and Kirwan, 2019). Since 1938, ∼2,000 hectares of marshland was

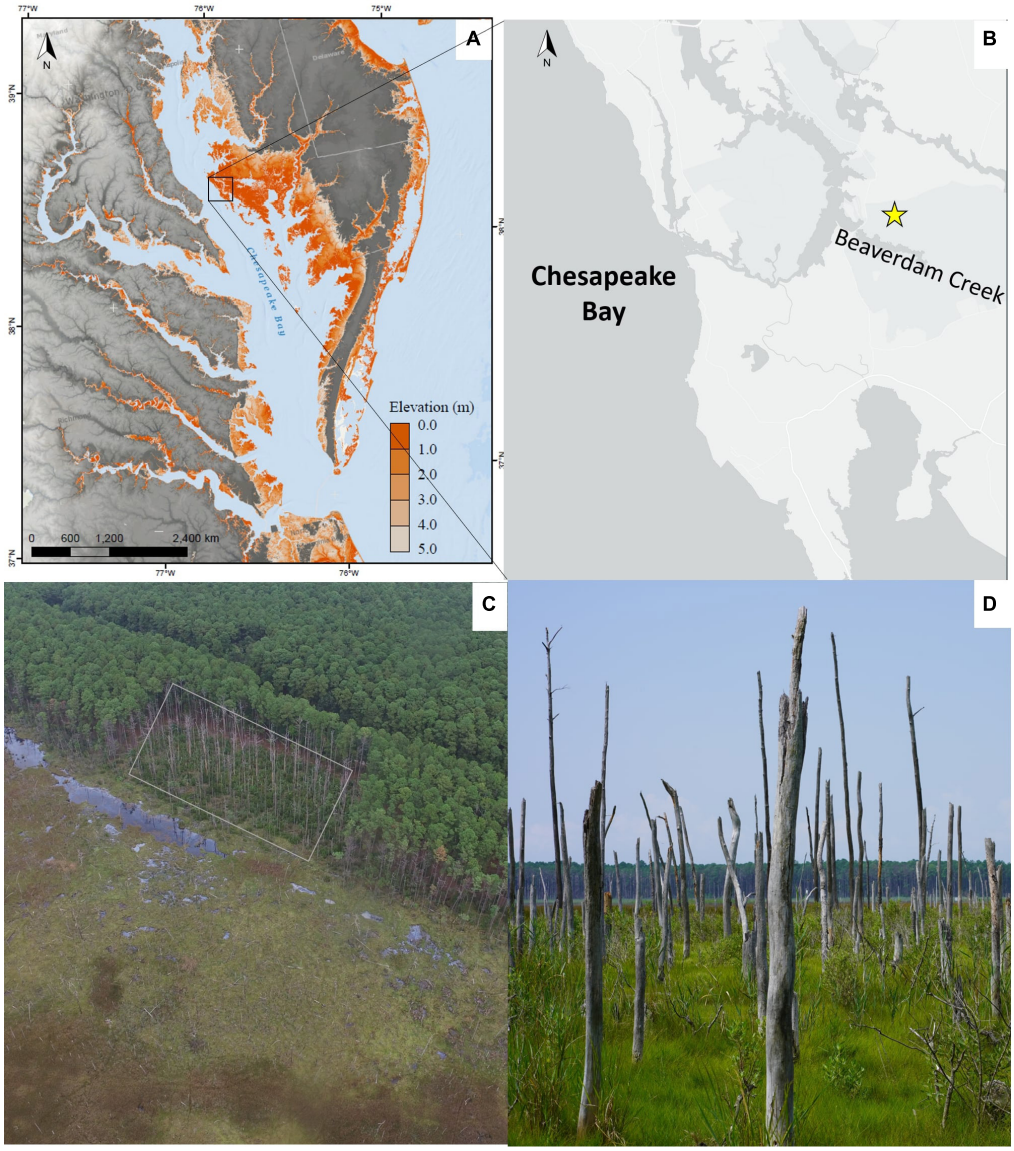


FIGURE 1 | (A) Map of Chesapeake Bay region with an overlaid topobathymetric digital elevation model that displays elevation of areas <5.0 m NAVD88, from the United States Geological Survey's Coastal National Elevation Database (Danielson and Tyler, 2016). Inset black box shows the position of the transgression experiment at the Blackwater National Wildlife Refuge on Maryland's Eastern Shore of the Chesapeake Bay. **(B)** Site map showing Moneystump Swamp (yellow star) at the Blackwater National Wildlife Refuge situated on Beaverdam Creek, a tributary of the Chesapeake Bay, where the transgression experiment took place. **(C)** Aerial image of the Moneystump transgression experiment taken in 2018. The Control area is on the right side of the image where there are live trees, showing the natural gradient of pine forest transitioning to emergent brackish marsh. The overlayed rectangle shows the area where trees were killed *via* girdling (Credit: Tyler Messerschmidt). **(D)** Picture taken from within the ghost forest in the high marsh at Moneystump, looking parallel to the marsh forest boundary with the live forest to the right and the marsh extending out to the left. These trees are a sign of natural transgression that has occurred at this site (Credit: David C. Walters).

lost within the refuge (∼50% of its original extent), but that loss was partially offset by a gain of ∼1,200 hectares (∼30%) from upland areas converting to marsh (Scott et al., 2009). BWNR is largely characterized by brackish marsh with dead and dying trees (ghost forests) embedded in the landscape, further signifying it as a hotspot of both marsh *loss* due to sea level rise and marsh *gain* due to transgression.

Moneystump Swamp, the USFWS BNWR property where this study takes place, is located on Beaverdam Creek which is a tributary of the Choptank River (**Figure 1B**). The average diurnal tide range at the site is 0.51 m, with a mean higher high water level of 0.34 m North American Vertical Datum 1988 (NAVD88), a mean water level of 0.12 m NAVD88, and an average salinity of 9.2 Practical Salinity Units (PSU) with a standard deviation of 3.3 PSU (Carr and Guntenspergen, 2020). The Moneystump property spans an elevation and ecological gradient that includes a large brackish marsh to the south and forested upland to the north. The vegetation transitions from low

marsh to the south adjacent to Beaverdam Creek—dominated by *Spartina alterniflora*, *Juncus roemerianus, and Schoenoplectus americanus*—to high marsh to the north adjacent to the upland forest—dominated by *Spartina patens* and *Distichlis spicata*. Near the marsh-upland forest boundary (picture in **Figure 1C**) there is a prominent ghost forest, with standing dead trees in the high marsh community (**Figure 1D**). Then at the transition from the high marsh to the forest, a narrow band of shrubby species such as *Morella cerifera* and *Iva frutescens* dominates. The upland forest canopy is a nearly monoculture stand of *Pinus taeda* (a facultative species—Lichvar et al., 2016) with little understory growth (**Figure 2**, control), and an average upland slope of ∼0.008. The U.S. Geological Survey (USGS) established long-term surface elevation tables (SETs) at this site in the year 2000 along an elevation gradient from the low marsh into the upland. Over the course of 15 years monitoring the site, tree mortality and subsequent transition to wetland vegetation were observed in the higher elevation plots, identifying this site as an area of active transgression that would be an ideal location for a transgression study.

Experimental Design

This experiment to understand the role of disturbance in marsh transgression was initiated in the summer of 2014 with the cutting and girdling of all live trees in designated areas at Moneystump Swamp by the USWS BWNR. The goal was to simulate a large-scale disturbance that could potentially induce changes in ecohydrological feedbacks such as changes in evapotranspiration rates that would influence salinity and inundation. To accomplish this, the size of the treatment areas had to be large beyond the scale of a mere mesocosm experiment. Therefore, with permission from the refuge, disturbance treatments were applied to whole sections of forest, killing off every tree within a large, forested area. In one 1.2-hectare portion of the forested study area, all trees were cut down by hand and harvested, in another 1.1-hectare portion, the trees were girdled at breast height by stripping the bark and cambium in a circle at the base of tree killing it slowly by terminating nutrient flow, and in another portion (1.1 hectares), the trees were left alive as a control area (**Figure 2A**). The scope of this large-scale environmental manipulation provides a unique opportunity

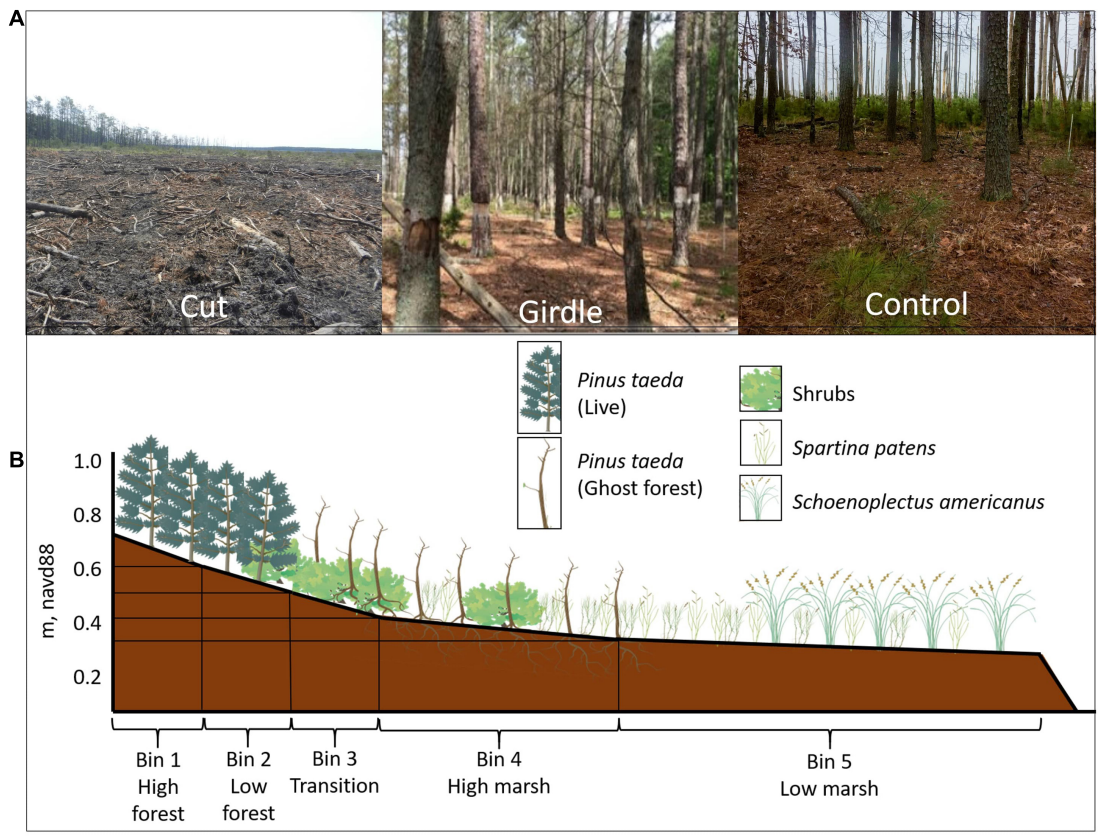


FIGURE 2 | (A) Pictures taken from Moneystump Swamp transgression experiment (Cambridge, MD, United States) in the highest elevation bin in the Cut treatment area immediately after the trees were cut down in 2014, the Girdled treatment area immediately after the bark was stripped from the trees to slowly kill them in 2014, and the Control area where the trees were left alive (Photo credit: Patrick Brennand). **(B)** Schematic showing typical vegetation zonation at Moneystump along elevation gradient spanning from the low marsh into the high forest, and how those ecotones align with the elevation bins chosen for the transgression study (graphics from Integration and Application Network, ian.umces.edu/media-library).

to test the application of ecological theories such as press-pulse disturbance in a coastal forest setting. The two different treatments (Cut and Girdled) simulate natural tree mortality events where the effect of a gradual (Girdled) and immediate (Cut) change in conditions can be observed over time and can test the impact of tree mortality on migration and establishment of wetland vegetation upslope. In the case of the Cut treatment area, the removal of the forest canopy produces an immediate change in the light environment, such as would happen from a strong windstorm. Whereas in the case of the Girdled treatment area, the light environment changes more gradually as the foliage, limbs, and eventually tree trunks fall over time, thus gradually opening the canopy, as would happen from a storm surge that resulted in inundation and/or salt spray killing the trees. The marsh adjacent to each forested area in the study was left unchanged, as there were no trees to girdle or cut.

Each treatment area in the study area was then sub-divided into five elevation bins, reflecting the natural elevation-ecotone gradient (**Figure 2B**). The topographic elevation ranges were identified *via* Real Time Kinematic (RTK) surveying in the open canopy portions of the site where there is available satellite coverage, and a DNA03 Digital Laser Level referenced to known elevation benchmarks for the forested portion. The identified elevation ranges for each ecotone were: bin 1—high forest (0.60–0.72 m NAVD88), bin 2—low forest (0.54–0.60 m NAVD88), bin 3—transition (0.44–0.51 m NAVD88), bin 4—high marsh (0.39–0.43 m NAVD88), and bin 5—low marsh (0.31–0.40 m NAVD88) (**Figure 2B** and **Supplementary Table 1**). The average change in surveyed elevation from the marsh-forest transition in bin 3 to the high forest in bin 1 is 0.008. Across each elevation bin, in each treatment area, vegetation, water level, and light level were monitored.

Environmental Variables

Change in light level was monitored over the course of the experiment with HOBO Pendant light loggers, deployed at each vegetation plot attached to polyvinyl chloride (PVC) poles at a height of 1 m above the ground. Inundation was measured with an array of continuously recording HOBO and Solinst water level loggers deployed in slotted PVC groundwater wells. One well was placed in each elevation bin in each treatment area to track the influence of elevation and changes in vegetation on inundation. Continuously recording Solinst salinity loggers were deployed in 2020 in upland forest bin 1 of each treatment area and in transition bin 3 and low marsh bin 5 of the Control to monitor how salinity varies with elevation. Monitoring groundwater salinity provides information to determine if reduced transpiration due to tree mortality leads to an increase in saltwater intrusion into the upland, in addition to natural processes influencing saltwater intrusion such as sea level rise, storm surge, and drought.

Vegetation Field Surveys

Within each of the five elevation bins in each of the treatments, there were initially five vegetation plots established. However, upon conducting a higher precision integrated total station-RTK survey to better constrain the narrow elevation ranges, the plots were re-assigned such that there were four to six long-term vegetation plots in each elevation bin, for a total of 76 plots. Each vegetation plot consisted of a 1 m × 2 m quadrat for monitoring herbaceous vegetation and an overlapping 2 m × 5 m quadrat for monitoring shrubs, with the long side of plots oriented parallel to the elevation contour. For this study, shrubs were defined as woody plants that have a maximum height of less than 4 m tall with a diameter at breast height (DBH) of less than 2.5 cm. Over the 5-year duration of the experiment, the herbaceous vegetation was sampled three times per year in the spring, summer, and fall, while the shrub plots were sampled once per year in the fall.

At each plot, the presence of each species was recorded along with an estimate of the percent basal cover, or the proportion of the ground obscured by a species' aboveground leaves and stems (Coulloudon et al., 1996). Percent cover was estimated following the cover class approach of the Daubenmire method (Daubenmire, 1959), with each species evaluated independently allowing for the possibility of the sum of cover classes in a plot exceeding 100% as plant covers from different species can overlap one another. The height of the tallest individual was also recorded for each species present. All the same measurements were recorded for the species that were identified in the shrub plot. For *P. taeda*, in addition to cover class and height, the total number of individuals rooted within the plot was counted for each survey, as it is the dominant tree species in this study and the density of individuals and rate of mortality is potentially an indicator of forest health and recovery.

Statistical Analyses

To compare the level of plant biodiversity across treatments, Shannon's diversity index *(H′)* was calculated for each plot, as a function of the number of species in the plot (*s*) and the plant cover proportion (*p*) of each individual species (*i*) (Begon et al., 2006):

$$H' = -\sum_{i=1}^{s} p_i \ln p_i$$

The presence and extent of wetland vegetation were analyzed through the use of the wetland prevalence index. Prevalence index (*PI*) is a metric of average species type which can be applied to wetland vegetation (Lichvar and Gillrich, 2014). *PI* is calculated by taking a weighted average of the cover class of all species (*S*) within a plot, weighted by wetland indicator status, from 1 for obligate wetland species *(obl)*, to 2 for facultative wetland *(facw),* 3 for facultative *(fac),* 4 for facultative upland *(facu),* and 5 for upland (*upl*) (Lichvar et al., 2016):

$$PI = \frac{\left(S_{obl} + 2S_{facw} + 3S_{fac} + 4S_{facu} + 5S_{upl}\right)}{\left(S_{obl} + S_{facw} + S_{fac} + S_{facu} + S_{upl}\right)}$$

Prevalence index values reflect the wetland indicator status of the vegetation community in the plot as a whole, from obligate wetland to upland vegetation. Values of less than 2.5 indicate a moderate probability that a vegetation community is wetland, and values less than 2 indicate a high probability that a vegetation community is wetland. H' and *PI* were calculated

for each vegetation survey that was done at each plot throughout the duration of the experiment. Analysis of variance was used to test for differences in *PI* and H' across treatment areas and elevation bins.

RESULTS

Light Environment

The measured light level was consistently low in the Control treatment with an intact overstory tree canopy. Only 21% of available light (determined by the maximum light levels recorded in un-shaded marsh plots) reached the 1 m level in high forest bin 1, the lowest light level recorded anywhere in the experiment. The next lowest light level was recorded in low forest bin 2 which is closer to the forest edge, and then in transition bin 3 where the canopy cover is thinnest (**Supplementary Figure 1**). No interannual trend in light environment was observed over the duration of the experiment in the Control. The Girdled forest initially had similar ranges of light levels as the Control (with light increasing from bin 1 to bin 3) then increased to maximum levels in 2018 as dead tree limbs fell and opened the canopy further, until it then began to decrease as new vegetation re-grew and shaded the sensors in 2019. The Cut forest by comparison experienced initially high light levels reaching close to the maximum light level in 2016 as the forest canopy was completely removed, then steadily decreased over time as vegetation continued to re-grow and shade the sensors. Overall, the trends show that the Cut forest resulted in an immediate increase in available light reaching the understory vegetation, while the Girdled forest resulted in a gradual increase in available light over several years.

Water Level and Salinity

Inundation measured from the groundwater wells was largely controlled by elevation (elevation effect $P < 0.017$) with average recorded inundation levels ranging from 50% in bin 5 to less than 1% in bins 1 and 2 (**Supplementary Figure 2**). There was no significant difference ($F = 0.002$, $P = 0.998$) between inundation levels in the different treatment areas in the upland elevation bins (bins 1, 2, and 3) with an average inundation of 1.2, 1.3, and 1.2% for the Control, Girdled, and Cut, respectively. Salinity values did not increase in the disturbed forest areas (bin 1) relative to the Control, with average values of 0.5 PSU, 0.8 PSU, and 1.2 PSU in the Cut, Girdled, and Control groundwater wells, respectively, and in fact Control salinity is greater than the salinity in the disturbed forest ($P < 0.01$). Groundwater salinity is greater in the marsh-upland forest transition (Control bin 3) at 9.3 PSU and greatest in the marsh (Control bin 5) at 11.2 PSU. Therefore, there was no treatment effect in the disturbed forest areas in flooding or salinity relative to the Control, but both salinity and inundation increase with decreasing elevation, regardless of treatment.

Forest Recovery

After the Cut and Girdled treatments were initiated in 2015, there were no live mature loblolly pines *(P. taeda)* remaining within the treatment areas (**Figure 3**, left). In the 5 years since, pine trees have largely recolonized the disturbed areas (**Figure 3**, right). Re-growing from seedlings, *P. taeda* has recovered to the point of once again being the dominant vegetation cover in the upland plots. *P. taeda* was never found above trace amounts in the low elevation plots (bins 4 and 5) where any seedling that did germinate died off shortly thereafter. Thus, the analysis of *P. taeda* growth and recovery focuses on the potential habitable range of the mid and high elevation plots (bins 1, 2, and 3).

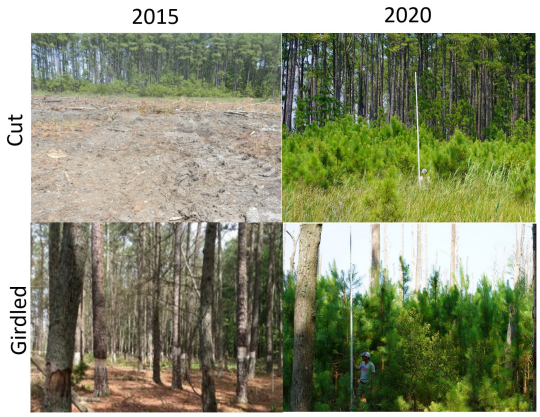


FIGURE 3 | Shows change at Moneystump Swamp transgression experiment (Cambridge, MD, United States) from clear-cut state immediately after tree cutting (top left, photo credit: Patrick Brennand) to tree regrowth after 5 years post-recovery (top right, photo credit: David C. Walters) and change from standing dead pines immediately after girdling (bottom left, photo credit: Patrick Brennand) to tree regrowth amongst standing dead trunks after 5 years post-recovery (bottom right, photo credit: David C. Walters). 2020 photos include a 5 m staff positioned at the first row of live pines for scale.

In both the high forest and low forest understory (bins 1 and 2), *P. taeda* has shown a positive rate of recovery in cover and height (**Figure 4**). Cover increased linearly for the first 3 years as the seedlings took advantage of the increased availability of light and grew into saplings, before plateauing at a maximum level in 2018 (**Figure 4**, top left and middle left). In the transition zone (bin 3), *P. taeda* did not show any recovery *via* increasing cover in the Cut treatment (**Figure 4**, bottom left). However, in the Girdled treatment, *P. taeda* did recover to an average cover of 48% of the plot area in 2019. Ground cover of pines in the Control did not change from near zero, which is representative of trace amounts of sporadic seedlings, over the course of the experiment. However, the mature forest canopy was unchanged in the Control treatment with a sustained population of fully mature live *P. taeda*. The increase in cover of the *P. taeda* seedlings and saplings in the Cut and Girdled treatments reflects the recovery and recolonization of a healthy pine forest.

The recovery of *P. taeda* can also be tracked through the increase in the height of the tallest individual of each plot (**Figure 4**, middle column). The increase in height is greatest in the Girdled and Cut treatments in upland bins 1 and 2 and the Girdled treatment transition bin 3, with an average height in 2019 of 2.0 m, and an average growth rate of 0.5 m/year. Control upland and transition (bins 1, 2, and 3) do not have discernible positive growth rates. This is because these plots contained

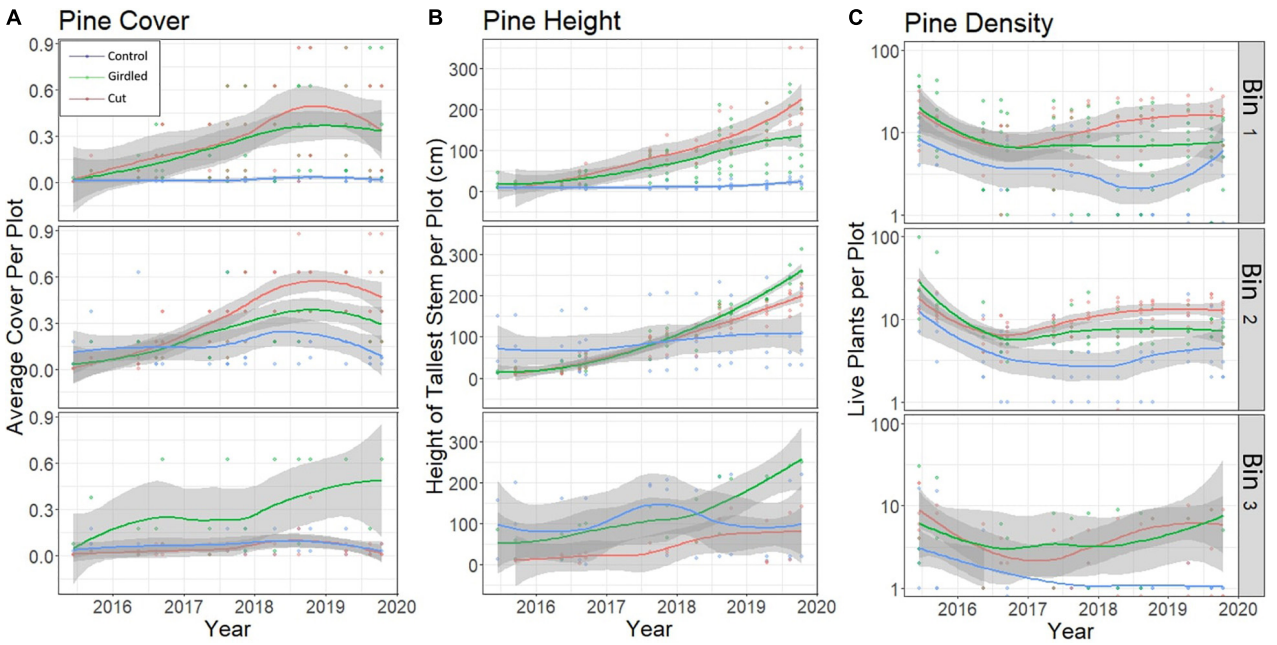


FIGURE 4 | Multiple metrics to represent forest recovery (e.g., pine tree regrowth) at the Moneystump Swamp transgression experiment (Cambridge, MD, United States) over time for the high forest (bin 1), low forest (bin 2), and marsh forest transition (bin 3). **(A)** Change in cover class over time for understory *P. taeda* seedlings and saplings. **(B)** Change in height for tallest understory *P. taeda* in each plot. **(C)** Count of individuals in the understory, or density of *P. taeda* per 2 m^2 plot. Each plot is color-coded for treatment, red is Cut, green is Girdled, and blue is Control. Trend lines depict Loess-smoothed local polynomial regression, with the shaded area around the trend lines showing the standard error.

understory *P. taeda* prior to the onset of the experiment that showed little to no signs of growth over the course of the experiment, as they are light limited due to forest canopy cover.

The count of individual *P. taeda* plants in the understory of each plot demonstrates the change in density over time as seedlings take root and die off. In the Cut and Girdled treatment, upland plots (bins 1 and 2), there were high recruitment rates at the beginning of the experiment (**Figure 4**, right column). After the first year, the density of seedlings in the Girdled upland plots decreased, as the increase in height and cover of the fastest growing individuals shades out the slower ones. Density of *P. taeda* is lower in the transition (bin 3) for each treatment area (**Figure 4**, bottom right) due to a high rate of mortality for seedlings, likely caused by increased inundation or salinity relative to the higher elevation bins. The light-limited Control plots also maintained consistently low density of *P. taeda* seedlings. Overall, these trends demonstrate that recruitment of *P. taeda* seedlings is sufficient for recruitment to outpace mortality in the upland (bins 1 and 2), leading to sapling growth on a trajectory toward full forest recovery.

Plant Community

The survey of the understory vegetation identified 70 distinct species and shows that the diversity is greatest in the upland and transition disturbed areas (i.e., the Cut and Girdled treatments) and marsh-upland forest transition across all treatment areas (one-way ANOVA $P = 0.0003$). Upland bins 1 and 2 in the Cut and Girdled, where forest disturbance allowed for more diverse herbaceous vegetation to colonize due to the opening of the canopy environment have an average Shannon's Index of 1 (**Supplementary Figure 3**). Herbaceous grasses such as *Panicum virgatum* and *Chasmanthium laxum* are the most prevalent of the early colonizers of the disturbed areas, before they are outcompeted by the recovering *P. taeda* (**Figure 5**). In the marsh forest transition (bin 3) of both the disturbed areas and the Control, shrubs *M. cerifera* and *I. frutescens* are prevalent, but the most common species are still grasses such as *P. virgatum* and common high marsh grasses such as *D. spicata* and *S. patens*. The marsh (bins 4 and 5) contains a less diverse plant community with an average Shannon Index of 0.8, where only salt and inundation tolerant species are found, mostly *S. patens* and *D. spicata* in bin 4, and *S. americanus* in bin 5 (**Figure 5**). However, the upland Control plots (bins 1 and 2) have the least diversity with a Shannon's Index of 0.4, and the vegetation community is dominated by mature loblolly pine *P. taeda* and the understory vegetation is made up of sporadic *C. laxum* and *P. taeda* seedlings. While the Cut and Girdled upland plots in bins 1 and 2 had greater diversity relative to the Control, wetland grasses were not among the species that colonized those areas.

Hydrophytic Vegetation

The most prominent species that occurs in the upland environment in this study area is *P. taeda*, which is classified with a wetland indicator status of facultative (Lichvar et al., 2016). According to the National Wetland Plant List (Lichvar et al., 2016), a facultative status indicates an equal likelihood of

occurring in either wetland or upland. The Prevalence Index (PI) provides a view of the gradient of hydrophytic vegetation that occurs within this site, since it subdivides hydrophytic vegetation along the gradient from facultative to obligate wetland species. According to the PI, wetland vegetation follows the expected elevation gradient across treatment areas and does not appear to have shifted over time (two-way ANOVA interaction effect $P = 0.90$, treatment effect $P = 0.10$, elevation effect $P = 0.006$, **Figure 6**). Bins 1 and 2 have the highest *PI* with no difference between treatments and an average of 2.6 ± 0.4, indicating a community with facultative species on average. The transition plots (bin 3) of the Girdled and Control treatments have the next highest PI's with an average of 2.3 ± 0.6, indicating a vegetative community tipping toward facultative wetland species.

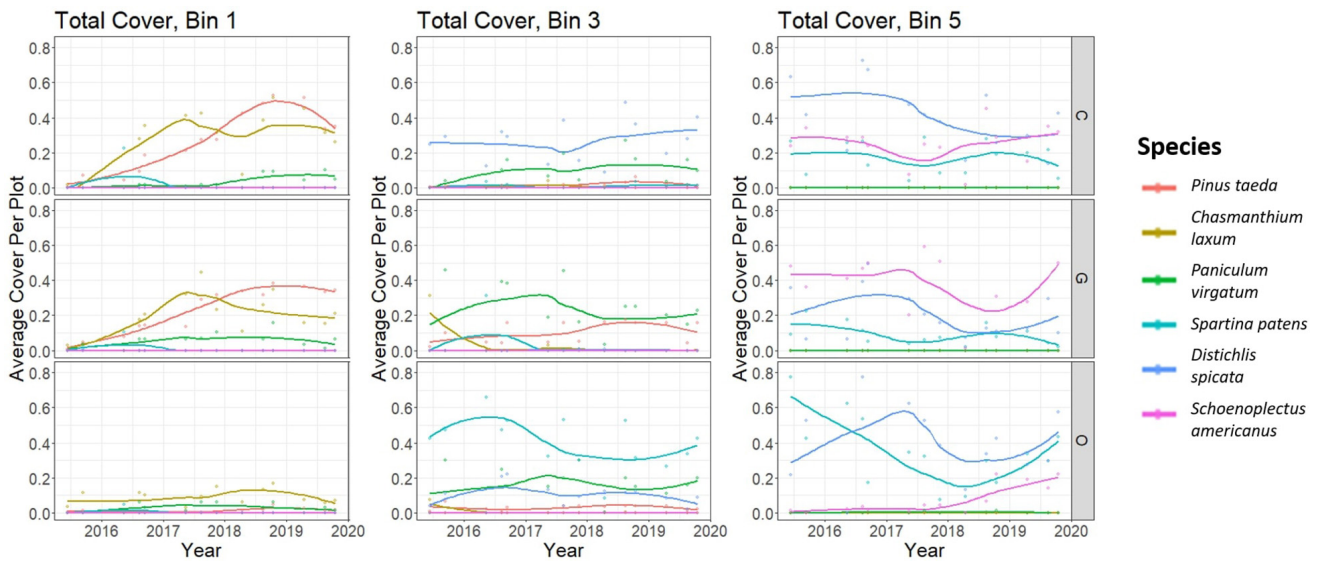


FIGURE 5 | Plant cover over time for the six species with the highest total cover in the study area at Moneystump Swamp transgression experiment (Cambridge, MD, United States) over the course of the experiment (see legend), broken down by elevation bin (bin 1 on the left, bin 3 in the middle, and bin 5 on the right, showing only the high forest, transition, and low marsh, respectively, for simplicity) and treatment (Cut on top, Girdled in middle, and Control on bottom). A value of 1 represents complete coverage of all vegetation plots, and a value of zero represents complete absence from all vegetation plots. Trend lines depict Loess-smoothed local polynomial regression.

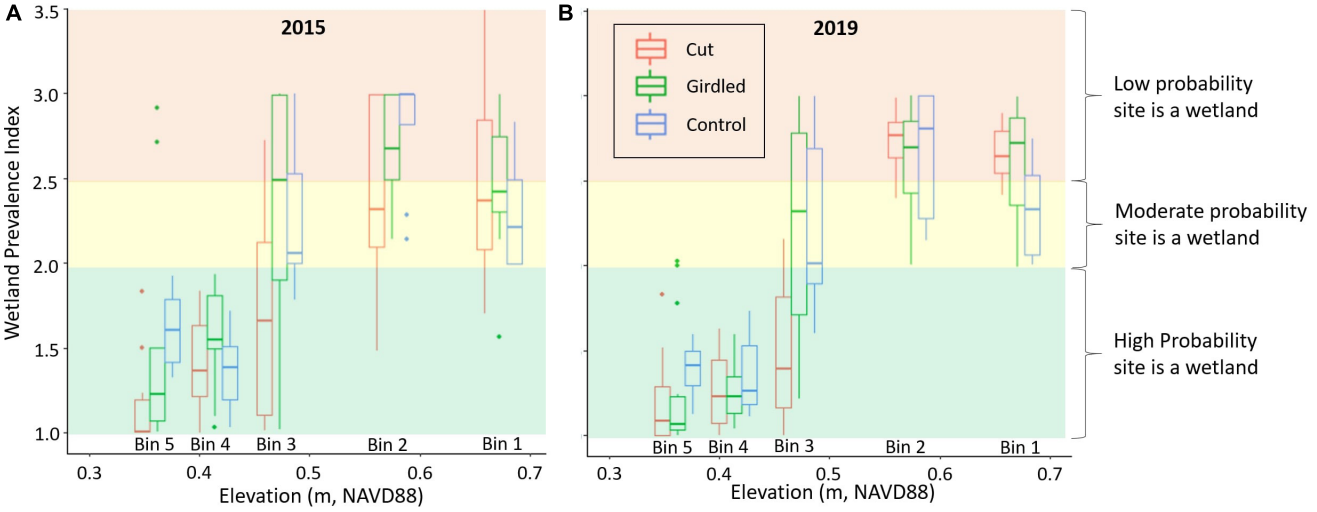


FIGURE 6 | Wetland vegetation dynamics as a function of elevation and forest disturbance with Prevalence Index (PI) for the occurrence of hydrophytic vegetation versus elevation, color-coded by treatment area for **(A)** the first year of the experiment (2015) and **(B)** the last year (2019). *PI* values greater than 2.5 indicate a low probability a site is a wetland, values between 2 and 2.5 indicate a good probability that a site is a wetland, and values less than 2 indicate a high probability that a site is a wetland. Boxplot centerline represents the median value of the data, the upper and lower box sides represent the 25th and 75th percentile datapoints, the whiskers extend to the largest and smallest values within the 1.5 interquartile range of the 25th and 75th percentile, and all remaining points are plotted as outliers.

The transition of the Cut treatment has the lowest *PI* of all the treatments outside of bins 4 and 5, with an average of 1.6 ± 0.5, which suggests a high probability that the site is a wetland. Of course, bins 4 and 5 have the lowest *PI* (1.3 ± 0.3), indicating mostly obligate wetland species. There was not a single vegetation survey over the 5 years of the experiment where the average *PI* of any of the Girdled, Cut, or Control upland bins (bins 1 and 2) was less than 2 (**Supplementary Figure 4**), indicating that wetland vegetation was not able to establish in the upland at any point.

The disturbed forest plots in Cut and Girdled upland elevation bins 1 and 2 showed no trend toward the occurrence of more wetland vegetation over time (**Figure 7**). Several individual plots in the Cut and Girdled upland bins recorded PI's in the range of wetland vegetation (1.5–2) within the first 2 years of the experiment, but on average the *PI*s were no different or greater than those in the Control plots. There was a greater range in *PI* of the experiment in the Cut and Girdled prior to 2017—there were plots with *PI* values greater than 3 and less than 2—as the diversity was higher before pine recovery had established as the dominant cover type (**Figure 5**). From 2017 onward, no individual plot in the upland elevation bins 1 and 2 recorded a *PI* of less than 2 (**Figure 7**), as the pine saplings shaded out any potential for wetland species colonization and the vegetation among the plots became more uniform.

DISCUSSION

Positive feedbacks between limiting resources and system state can lead to ecosystem dynamics that exhibit alternative stable states (Wilson and Agnew, 1992). Alternative stable state dynamics in an ecosystem are associated with the potential for strong non-linear behavior, whereby a small change in an environmental driver can lead to rapid shifts in ecosystem structure. Moreover, these systems are known to possess limited resilience in the sense that a disturbance or sequence of disturbances could shift the system past some critical threshold into an alternative state, whereby the original system state is unable to recover even if the disturbance is removed (Scheffer et al., 2001; van Nes and Scheffer, 2004). However, in this study, we observed a forest in a stable state which was able to recover following disturbance, suggesting that there are negative feedbacks increasing resiliency.

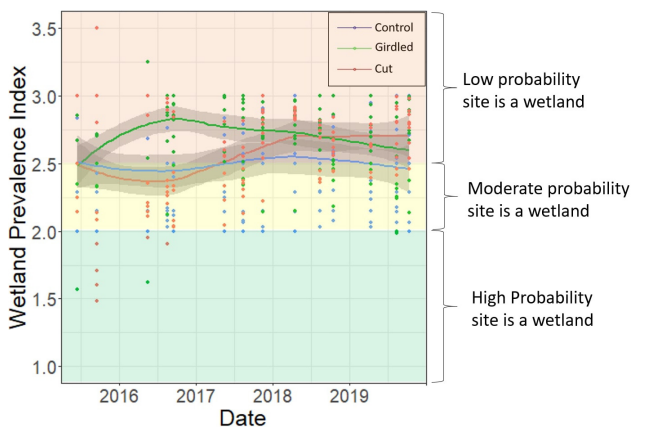


FIGURE 7 | Change in Wetland Prevalence Index (PI) over time in upland elevation bins 1 and 2, color-coded by treatment. *PI* values greater than 2.5 indicate a low probability a site is a wetland, values between 2 and 2.5 indicate a good probability that a site is a wetland, and values less than 2 indicate a high probability that a site is a wetland. Points represent the *PI* calculated from each vegetation survey conducted for each single vegetation plot in upland bins 1 and 2. Trend lines depict Loess-smoothed local polynomial regression, with the shaded area around the trend lines showing the standard error.

Across the marsh-upland forest, ecotones are gradients in light availability, inundation, and salinity which are affected by both the state of the system and environmental drivers. For example, near the edge of tidal inundation, overstory tree canopy loss could lead to increased salinity due to increased surface evaporation leading to potential further canopy loss or tree mortality as well as the inhibition of pine seedling establishment (Kurz and Wagner, 1957). Halophytic vegetation can contribute further to soil salinization (Sternberg et al., 2007; Wendelberger and Richards, 2017). Alternately, increased evapotranspiration due to the presence of herbaceous vegetation could lower the water table helping to facilitate seedling establishment (Poulter et al., 2009), which could be the cause of reduced groundwater salinity in the disturbed forest plots in our experiment. Our experiment uniquely tested the presence of alternative stable states by disturbing an established forest canopy (state 1) and measuring potential marsh establishment (state 2) at a scale large enough (>3 hectares of pre-treatment forested area) to potentially influence the light and water resources thought to govern the transition between states. However, we observed no difference in inundation between treatment areas, decreased groundwater salinity in the disturbed forest areas relative to the control, rapid pine re-growth (**Figure 4**) and little change in wetland prevalence across zones (**Figure 6**), indicating that dominant system states recovered quickly following disturbance, and that disturbance alone was not sufficient to induce an ecosystem state change.

The interplay of positive feedbacks, ecosystem state, and environmental drivers can lead to an "ecological ratchet" conceptual model of marsh transgression (Fagherazzi et al., 2019), whereby the coastal forest exists in zones determined by forest regeneration (i.e., the regenerative zone), or where seedling establishment ceases but mature trees are able to persist (i.e., the persistence zone). In this experiment, manipulated plots showed pine forest recovery in high elevation bins and the increase in height of the pine seedlings and subsequent saplings in the Girdled and Cut areas relative to the Control illustrates the trajectory of the plant community toward mature adult pines (**Figure 4**). This recovery suggests that these upper elevation bins exist within the regenerative zone where seedlings are able to establish and forest succession can occur (Kearney et al., 2019). This experiment is an ideal test for the concept of a persistence zone because the light restriction that might otherwise prevent regeneration has been removed. However,

across this low slope environment, the only location where the removal of mature trees did not result in complete regeneration was in the transition bin 3 (**Figure 6**), but this transition zone is located at the forest edge where removal of the remaining forest canopy had less of an impact on the light environment (**Supplementary Figure 1**). Moreover, the transition zone is a relatively narrow zone characterized by edge effects, and is not an extensive persistent zone where adult trees are underlain by marsh vegetation, suggesting that a prior transgressive event may have already pushed the trailing edge of the persistence zone up into the leading boundary of transgression, but further data are needed to test this hypothesis. As such, there is at most only a narrow band of elevation at this site where there is potential for wetland species to colonize and persist in the forested areas under current environmental conditions (Jackson et al., 2009). The lack of strong coastal marsh plant species response suggests that the shift in biotic and abiotic factors in the upper elevation bins of the experiment was not enough, and/or not fast enough, to induce a state change (Field et al., 2016).

This study site falls well within the range of low slope environments around the Chesapeake Bay where transgressions can occur rapidly (Schieder and Kirwan, 2019; Molino et al., 2021). However, it has been noted that even in low slope environments, transgression sometimes occurs slowly into forested upland areas (Schieder et al., 2018). This lack of transgression is likely not due to seedbank limitation as marsh species exist in the seedbank of the upland forest environment within this region and this study site (Kottler and Gedan, 2020), suggesting that competition between marsh and upland vegetation, rather than inadequate seed supply, may have limited the ability of marsh vegetation to become established in our experiment. While the opening of the canopy provided an opportunity for marsh species colonization, increases in the light environment and consequent environmental changes were not sufficient to push the system past a critical threshold where marsh species could establish and thrive as evidenced by the lack of marsh species across all upland manipulation and control plots (**Figure 7**). Even in elevation bin 3, where the transition between marsh vegetation and forest vegetation occurs and both upland and marsh species are found, removal of the canopy did not shift the vegetation composition (**Figure 5**). This study de-emphasizes the potential importance of episodic disturbance events that drive transgression on the century time-scale (Young, 1995), accompanied by changes in salinity and inundation.

Pulse disturbances, including storms (Gardner et al., 1992; Ross et al., 2009; Wang and Xu, 2009), drought (Desantis et al., 2007; NeSmith et al., 2018; Ury et al., 2021), wrack deposition (Tate and Battaglia, 2013), and changing hydroperiod (Antonellini and Mollema, 2010), are viewed as a first step in the conversion of coastal forests to salt marsh. However, press disturbances—such as gradual saltwater intrusion and changes in flooding—interact with pulse disturbances because they alter the recovery from the pulse disturbance by changing the environmental setting of the forested habitat so that tree regeneration fails and halophyte vegetation successfully colonizes a site (Fagherazzi et al., 2019). Despite the disturbance treatments, transgression was not facilitated in this experiment, likely due to a lack of enabling environmental stressors. Press stressors such as inundation level and soil salinization must cross a critical environmental threshold before wetland vegetation can outcompete tree seedling recovery. Wasson et al. (2013) observed a gradual movement of a total of 1 m of the marsh-upland forest transition ecotone over the course of a 10-year period in a California estuary, which was found to correlate with an increase in inundation from 2 to 4%. Despite very different slope conditions, this aligns well with the 3% inundation rate observed in the transition ecotone in our study, which also compares closely with the 3.6% inundation where Anisfeld et al. (2017) observed a transition from marsh to upland vegetation zones in a Long Island Sound salt marsh. This suggests that areas with inundations of less than 2% are unlikely to transition to marsh following a disturbance. However, elevation change and the water level inundation signal can feedback on one another, due to potential root zone collapse following forest disturbance (Cahoon et al., 2003). Alternatively, forest thinning has been shown to lead to elevation gain due to increased root production by colonizing understory vegetation (Chen et al., 2021). Also, certain seedlings of coastal tree species have been killed by high saline soils in north Florida, but then resprouted after salinity decreased when flushed with freshwater (Williams et al., 1998). This effect of saline soils suggests that the deposition of salt following storm surges is an important aspect of disturbance events, that leads to transgression, because even if salt deposition occurs in an area with low frequency of tidal inundation, it can create a delay in the recovery of tree seedlings that allows time for marsh plants to establish.

Loss of the forest canopy removes light limitation and results in the germination and establishment of a greater variety of plant species, suggesting that aboveground light competition outweighs belowground nutrient competition between species. However, if the overstory tree canopy recovers, the subsequent light limitation results in the establishment of a shade-tolerant plant community, regeneration of overstory tree species, and loss of marsh species which are shade intolerant. However, changes in salinity and flooding (press disturbances) can inhibit the regeneration of tree seedlings and allow marsh plants to become established. Over the duration of this experiment, loss of the tree canopy led to an initial increase of plant species diversity, but the absence of changes in soil salinity or site inundation (pressure disturbances) led to the germination and growth of the overstory tree species (*P. taeda*) and shading of the plant species that established initially (**Figure 6**).

A current paradigm in coastal ecology is that coastal forests follow a punctuated equilibrium response to sea level rise, where adult trees are generally resistant to gradual increases in inundation and salinity, and that rapid retreat follows episodic disturbance events (Williams et al., 1999; Fagherazzi et al., 2019; Kirwan and Gedan, 2019). For example, fast periods of forest retreat punctuated gradual forest retreat in portions of the Chesapeake Bay and Albemarle-Pamlico Sound estuaries following Hurricanes Katrina and Irene, respectively

(Schieder and Kirwan, 2019; Ury et al., 2021). However, recent numerical modeling suggests that the interplay between sea level rise and disturbance events depends on local conditions such as topographic slope and the rate of sea level rise, and emphasizes the potential for regeneration of forests after disturbance events (Carr et al., 2020). Our large-scale field experiment uniquely disturbed the forest canopy without directly altering environmental factors such as salinity that would accompany sea level rise in natural systems, and therefore isolates the effect of disturbance alone. Interestingly, we found increased light availability led primarily to a release of upland rather than wetland plant species, and that potential ecohydrological feedbacks associated with tree mortality were not sufficient to induce state changes. Thus, our work illustrated rapid recovery of a forested ecosystem, and suggests that disturbance alone is not sufficient for transgression to occur.

DATA AVAILABILITY STATEMENT

The datasets presented in this study can be found in the online repository USGS ScienceBase Catalog: https://www.sciencebase.gov/catalog/item/6196b7cad34eb622f691ac94 and doi: 10.5066/P9V4NJXW.

AUTHOR CONTRIBUTIONS

All authors contributed to writing the manuscript and provided valuable input to the project at various stages.

FUNDING

We acknowledge support from the USGS Climate Research and Development and Ecosystems Programs.

ACKNOWLEDGMENTS

We thank the staff at Blackwater National Wildlife Refuge for their support of this project. Any use of trade, firm, or product names is for descriptive purposes only and does not imply endorsement by the U.S. Government.

SUPPLEMENTARY MATERIAL

The Supplementary Material for this article can be found online at: https://www.frontiersin.org/articles/10.3389/fmars.2021.782643/full#supplementary-material

REFERENCES

Anisfeld, S. C., Cooper, K. R., and Kemp, A. C. (2017). Upslope development of a tidal marsh as a function of upland land use. *Glob. Chang. Biol.* 23, 755–766. doi: 10.1111/gcb.13398

Antonellini, M., and Mollema, P. N. (2010). Impact of groundwater salinity on vegetation species richness in the coastal pine forests and wetlands of Ravenna. Italy. *Ecol. Eng.* 36, 1201–1211. doi: 10.1016/j.ecoleng.2009.12.007

Begon, M., Townsend, C., and Harper, J. (2006). *Ecology: From Individuals to Ecosystems*. New York, NY: Wiley.

Bender, E. A., Case, T. J., and Gilpin, M. E. (1984). Perturbation experiments in community ecology: theory and practice. *Ecology* 65, 1–13. doi: 10.2307/1939452

Boesch, D. F., Galloway, G. E., Zoë, P., Johnson, P., Kopp, R. E., Li, M., et al. (2018). *Sea-level Rise: Projections for Maryland*. Cambridge, MD: University of Maryland Center for Environmental Science.

Boon, J. D., Brubaker, J. M., and Forrest, D. R. (2010). *Chesapeake Bay Land Subsidence and Sea Level Change: An Evaluation of Past and Present Trends and Future Outlook*. Washington, DC: U.S. Global Change Research Program.

Borchert, S. M., Osland, M. J., Enwright, N. M., and Griffith, K. T. (2018). Coastal wetland adaptation to sea level rise: quantifying potential for landward migration and coastal squeeze. *J. Appl. Ecol.* 55, 2876–2887. doi: 10.1111/1365-2664.13169

Brinson, M. M., Christian, R. R., and Blum, L. K. (1995). Multiple states in the sea-level induced transition from terrestrial forest to estuary. *Estuaries* 18, 648–659. doi: 10.2307/1352383

Cahoon, D. R., Hensel, P., Rybczyk, J., Kee, K. L. M., Proffitt, C. E., and Perez, B. C. (2003). Mass tree mortality leads to mangrove peat collapse at Bay Islands, Honduras after Hurricane Mitch. *J. Ecol.* 91, 1093–1105.

Carr, J., Guntenspergen, G., and Kirwan, M. (2020). Modeling marsh-forest boundary transgression in response to storms and sea-level rise. *Geophys. Res. Lett.* 47:e2020GL088998. doi: 10.1029/2020GL088998

Carr, J. A., and Guntenspergen, G. R. (2020). *Water Levels (November 11 2016 Through November 11 2017) for Four Wells: From Upland to Marsh, Moneystump Marsh, Blackwater National Wildlife Refuge*. Maryland: U.S. Geological Survey data release.

Chen, L., Lin, Q., Krauss, K. W., Zhang, Y., Cormier, N., and Yang, Q. (2021). Forest thinning in the seaward fringe speeds up surface elevation increment and carbon accumulation in managed mangrove forests. *J. Appl. Ecol.* 58, 1899–1909. doi: 10.1111/1365-2664.13939

Coulloudon, B., Eshelman, K., Gianola, J., Habich, N., Hughes, L., Johnson, C., et al. (1996). *Sampling Vegetation Attributes*. Scotts Valley, CA: CreateSpace Independent Publishing Platform.

Danielson, J., and Tyler, D. (2016). *Topobathymetric Model for Chesapeake Bay Region - District of Columbia, State of Delaware, Maryland, Pennsylvania, and Virginia, 1859 to 2015*. Available online at: https://topotools.cr.usgs.gov/topobathy_viewer/dwndata.htm (accessed on 29 January 2020).

Daubenmire, R. F. (1959). A canopy-cover method of vegetation analysis. *Northwest Sci.* 33, 43–46.

Desantis, L., Bhotika, S., Williams, K., and Putz, F. (2007). Sea - level rise and drought interactions accelerate forest decline on the Gulf Sea-level rise and drought interactions accelerate forest decline on the Gulf Coast of Florida, USA. *Glob. Chang. Biol.* 13, 2349–2360. doi: 10.1111/j.1365-2486.2007.01440.x

Enwright, N. M., Griffith, K. T., and Osland, M. J. (2016). Barriers to and opportunities for landward migration of coastal wetlands with sea-level rise. *Front. Ecol. Environ.* 14:307–316. doi: 10.1002/fee.1282

Fagherazzi, S., Anisfeld, S. C., Blum, L. K., Long, E. V., Feagin, R. A., Fernandes, A., et al. (2019). Sea level rise and the dynamics of the marsh-upland boundary. *Front. Environ. Sci.* 7:25. doi: 10.3389/fenvs.2019.00025

Field, C. R., Dayer, A. A., Elphick, C. S., and Kareiva, P. (2017b). Landowner behavior can determine the success of conservation strategies for ecosystem migration under sea-level rise. *PNAS* 114, 9134–9139. doi: 10.7910/DVN/NAKYZD

Field, C. R., Bayard, T. S., Gjerdrum, C., Hill, J. M., Meiman, S., and Elphick, C. S. (2017a). High-resolution tide projections reveal extinction threshold in response to sea-level rise. *Glob. Chang. Biol.* 23, 2058–2070. doi: 10.1111/gcb.13519

Field, C. R., Gjerdrum, C., and Elphick, C. S. (2016). Forest resistance to sea-level rise prevents landward migration of tidal marsh. *Biol. Conserv.* 201, 363–369. doi: 10.1016/j.biocon.2016.07.035

Gardner, L. R., Michener, W. K., Williams, T. M., Blood, E. R., Kjerfve, B., Smock, D. J., et al. (1992). Disturbance effects of Hurricane Hugo on a pristine coastal landscape: North Inlet, South Carolina, USA. *Netherlands J. Sea Res.* 30, 249–263.

Gedan, K. B., and Fernández-Pascual, E. (2019). Salt marsh migration into salinized agricultural fields: a novel assembly of

plant communities. *J. Veg. Sci.* 30, 1007–1016. doi: 10.1111/jvs.12774

Jackson, S. T., Betancourt, J. L., Booth, R. K., and Gray, S. T. (2009). Ecology and the ratchet of events: climate variability, niche dimensions, and species distributions. *Proc. Natl. Acad. Sci. U.S.A.* 106, 19685–19692. doi: 10.1073/pnas.0901644106

Jobe, J. G. D., and Gedan, K. (2021). Species-specific responses of a marsh-forest ecotone plant community responding to climate change. *Ecology* 102, 1–11. doi: 10.1002/ecy.3296

Kearney, W. S., Fernandes, A., and Fagherazzi, S. (2019). Sea-level rise and storm surges structure coastal forests into persistence and regeneration niches. *PLoS One* 14:e0215977. doi: 10.1371/journal.pone.0215977

Kirwan, M. L., and Gedan, K. B. (2019). Sea-level driven land conversion and the formation of ghost forests. *Nat. Clim. Change* 9, 450–457. doi: 10.1038/s41558-019-0488-7

Kirwan, M. L., Walters, D. C., Reay, W. G., and Carr, J. A. (2016). Sea level driven marsh expansion in a coupled model of marsh erosion and migration. *Geophys. Res. Lett.* 43, 4366–4373. doi: 10.1002/2016GL068507

Kottler, E. J., and Gedan, K. (2020). Seeds of change: characterizing the soil seed bank of a migrating salt marsh. *Ann. Bot.* 125, 335–344. doi: 10.1093/aob/mcz133

Kurz, H., and Wagner, K. (1957). *Tidal Marshes of the Gulf and Atlantic Coasts of Northern Florida and Charleston, South Carolina: Geology, Elevations, Soil Factors, Water Relations, Plant Zonation and Succession*. Tallahassee: Florida State University.

Lichvar, R. W., Banks, D. L., Kirchner, W. N., and Melvin, N. C. (2016). 2016 national wetland plant list. *Phytoneuron* 30, 1–17.

Lichvar, R. W., and Gillrich, J. J. (2014). *Examining Discrepancies Among Three Methods Used to Make Hydrophytic Vegetation Determinations for Wetland Delineation Purposes*. Hanover, NH: US Army Engine Research and Development Center.

Mitchell, M., Herman, J., Bilkovic, D. M., and Hershner, C. (2017). Marsh persistence under sea-level rise is controlled by multiple, geologically variable stressors. *Ecosyst. Heal. Sustain.* 3:1379888. doi: 10.1080/20964129.2017.1396009

Molino, G. D., Defne, Z., Aretxabaleta, A. L., Ganju, N. K., and Carr, J. A. (2021). Quantifying slopes as a driver of forest to marsh conversion using geospatial techniques: application to Chesapeake Bay Coastal-Plain, United States. *Front. Environ. Sci.* 9:1–13. doi: 10.3389/fenvs.2021.616319

NeSmith, J. E., Alba, C., and Flory, S. L. (2018). Experimental drought and plant invasion additively suppress primary pine species of southeastern US forests. *For. Ecol. Manag.* 411, 158–165. doi: 10.1016/j.foreco.2017.12.045

Poulter, B., Christensen, N. L., and Qian, S. S. (2008). Tolerance of Pinus taeda and Pinus serotina to low salinity and flooding: implications for equilibrium vegetation dynamics. *J. Veg. Sci.* 19, 15–22. doi: 10.3170/2007-8-18410

Poulter, B., Qian, S. S., and Christensen, N. L. (2009). Determinants of coastal treeline and the role of abiotic and biotic interactions. *Plant Ecol.* 202, 55–66. doi: 10.1007/s11258-008-9465-3

Raabe, E. A., and Stumpf, R. P. (2016). Expansion of tidal marsh in response to sea-level rise: Gulf Coast of Florida, USA. *Estuar. Coasts* 39, 145–157. doi: 10.1007/s12237-015-9974-y

Ross, M. S., O'Brien, J. J., Ford, R. G., Zhang, K., and Morkill, A. (2009). Disturbance and the rising tide: the challenge of biodiversity management on low-island ecosystems. *Front. Ecol. Environ.* 7:471–478. doi: 10.1890/070221

Sallenger, A. H., Doran, K. S., and Howd, P. A. (2012). Hotspot of accelerated sea-level rise on the Atlantic coast of North America. *Nat. Clim. Chang.* 2, 884–888. doi: 10.1038/nclimate1597

Scheffer, M., Carpenter, S., Foley, J. A., Folke, C., and Walker, B. (2001). Catastrophic shifts in ecosystems. *Nature* 413, 591–596. doi: 10.1038/35098000

Schepers, L., Kirwan, M., Guntenspergen, G., and Temmerman, S. (2017). Spatio-temporal development of vegetation die-off in a submerging coastal marsh. *Limnol. Oceanogr.* 62, 137–150. doi: 10.1002/lno.10381

Schieder, N. W., and Kirwan, M. L. (2019). Sea-level driven acceleration in coastal forest retreat. *Geology* 47, 1151–1155. doi: 10.1130/G46607.1

Schieder, N. W., Walters, D. C., and Kirwan, M. L. (2018). Massive upland to wetland conversion compensated for historical marsh loss in Chesapeake Bay, USA. *Estuar. Coasts* 41, 940–951. doi: 10.1007/s12237-017-0336-9

Schuerch, M., Spencer, T., Temmerman, S., Kirwan, M. L., Wolff, C., Lincke, D., et al. (2018). Future response of global coastal wetlands to sea-level rise. *Nature* 561, 231–234. doi: 10.1038/s41586-018-0476-5

Scott, M., McDermott, L., Silva, E., and Watson, E. (2009). *Project Report: Digital Spatial Data Capture of Marsh Extent in Blackwater National Wildlife Refuge, 1938 and 2006*. Salisbury, MD: Eastern Shore Regional GIS Cooperative.

Smith, J. A. M. (2013). The role of phragmites australis in mediating inland salt marsh migration in a mid-atlantic estuary. *PLoS One* 8:e0065091. doi: 10.1371/journal.pone.0065091

Smith, J. A. M., Hafner, S. F., and Niles, L. J. (2017). The impact of past management practices on tidal marsh resilience to sea level rise in the Delaware Estuary. *Ocean Coast. Manag.* 149, 33–41. doi: 10.1016/j.ocecoaman.2017.09.010

Song, J., Fu, X., Wang, R., Peng, Z. R., and Gu, Z. (2018). Does planned retreat matter? Investigating land use change under the impacts of flooding induced by sea level rise. *Mitig. Adapt. Strateg. Glob. Chang.* 23, 703–733. doi: 10.1007/s11027-017-9756-x

Sternberg, L. D. S. L., Teh, S. Y., Ewe, S. M. L., Miralles-Wilhelm, F., and DeAngelis, D. L. (2007). Competition between hardwood hammocks and mangroves. *Ecosystems* 10, 648–660. doi: 10.1007/s10021-007-9050-y

Stevenson, J. C., Ward, L. G., and Kearney, M. S. (1986). Vertical accretion in marshes with varying rates of sea level rise. *Estuar. Var.* 0, 241–259. doi: 10.1016/b978-0-12-761890-6.50020-4

Taillie, P. J., Moorman, C. E., Poulter, B., Ardón, M., and Emanuel, R. E. (2019). Decadal-scale vegetation change driven by salinity at leading edge of rising sea level. *Ecosystems* 22, 1918–1930. doi: 10.1007/s10021-019-00382-w

Tate, A. S., and Battaglia, L. L. (2013). Community disassembly and reassembly following experimental storm surge and wrack application. *J. Veg. Sci.* 24, 46–57. doi: 10.1111/j.1654-1103.2012.01447.x

Ury, E. A., Yang, X., Wright, J. P., and Bernhardt, E. S. (2021). Rapid deforestation of a coastal landscape driven by sea level rise and extreme events. *Ecol. Appl.* 0, 1–11. doi: 10.1002/eap.2339

van Nes, E. H., and Scheffer, M. (2004). Large species shifts triggered by small forces. *Am. Nat.* 164, 255–266. doi: 10.1086/422204

Wang, F., and Xu, Y. J. (2009). Hurricane Katrina-induced forest damage in relation to ecological factors at landscape scale. *Environ. Monit. Assess.* 156, 491–507. doi: 10.1007/s10661-008-0500-6

Wasson, K., Woolfolk, A., and Fresquez, C. (2013). Ecotones as indicators of changing environmental conditions: rapid migration of salt marsh-upland boundaries. *Estuar. Coasts* 36, 654–664. doi: 10.1007/s12237-013-9601-8

Wendelberger, K. S., and Richards, J. H. (2017). Halophytes can salinize soil when competing with glycophytes, intensifying effects of sea level rise in coastal communities. *Oecologia* 184, 729–737. doi: 10.1007/s00442-017-3896-2

Williams, K., Ewel, K. C., Stumpf, R. P., Putz, F. E., Workman, T. W., Williams, K., et al. (1999). Sea-level rise and coastal forest retreat on the West Coast of Florida, USA. *Ecology* 80, 2045–2063.

Williams, K., Meads, M. V., and Sauerbrey, D. A. (1998). The roles of seedling salt tolerance and resprouting in forest zonation on the west coast of Florida, USA. *Am. J. Bot.* 85, 1745–1752. doi: 10.2307/2446509

Wilson, J. B., and Agnew, A. D. (1992). Positive-feedback switches in plant communities. *Adv. Ecol. Res.* 23, 263–336. doi: 10.1016/S0065-2504(08)60149-X

Young, R. S. (1995). *Coastal Wetland Dynamics in Response to Sea-Level Rise: Transgression and Erosion*. Doctoral Dissertation.

Conflict of Interest: The authors declare that the research was conducted in the absence of any commercial or financial relationships that could be construed as a potential conflict of interest.

Publisher's Note: All claims expressed in this article are solely those of the authors and do not necessarily represent those of their affiliated organizations, or those of the publisher, the editors and the reviewers. Any product that may be evaluated in this article, or claim that may be made by its manufacturer, is not guaranteed or endorsed by the publisher.

Copyright © 2021 Walters, Carr, Hockaday, Jones, McFarland, Kovalenko, Kirwan, Cahoon and Guntenspergen. This is an open-access article distributed under the terms of the Creative Commons Attribution License (CC BY). The use, distribution or reproduction in other forums is permitted, provided the original author(s) and the copyright owner(s) are credited and that the original publication in this journal is cited, in accordance with accepted academic practice. No use, distribution or reproduction is permitted which does not comply with these terms.

frontiers in Marine Science

ORIGINAL RESEARCH
published: 07 February 2022
doi: 10.3389/fmars.2021.793235

Facilitating Salt Marsh Restoration: The Importance of Event-Based Bed Level Dynamics and Seasonal Trends in Bed Level Change

Pim W. J. M. Willemsen[1,2], Erik M. Horstman[1], Tjeerd J. Bouma[3], Martin J. Baptist[4,5], Marinka E. B. van Puijenbroek[4] and Bas W. Borsje[1]*

[1] Water Engineering and Management, University of Twente, Enschede, Netherlands, [2] Department of Ecosystems and Sediment Dynamics, Deltares, Delft, Netherlands, [3] Department of Estuarine and Delta Systems, NIOZ Royal Netherlands Institute for Sea Research, Utrecht University, Yerseke, Netherlands, [4] Wageningen Marine Research, Wageningen University & Research, Den Helder, Netherlands, [5] Aquatic Ecology and Water Quality Management Group, Wageningen University & Research, Wageningen, Netherlands

OPEN ACCESS

Edited by:
Simon Marius Mudd, University of Edinburgh, United Kingdom

Reviewed by:
Ya Ping Wang, Nanjing University, China
Mark Schuerch, University of Lincoln, United Kingdom

***Correspondence:**
Pim W. J. M. Willemsen
p.willemsen@utwente.nl

Specialty section:
This article was submitted to Coastal Ocean Processes, a section of the journal Frontiers in Marine Science

Received: *11 October 2021*
Accepted: *27 December 2021*
Published: *07 February 2022*

Citation:
Willemsen PWJM, Horstman EM, Bouma TJ, Baptist MJ, van Puijenbroek MEB and Borsje BW (2022) Facilitating Salt Marsh Restoration: The Importance of Event-Based Bed Level Dynamics and Seasonal Trends in Bed Level Change. Front. Mar. Sci. 8:793235. doi: 10.3389/fmars.2021.793235

Intertidal salt marshes provide a range of valuable ecosystem services which typically increase with marsh width. Understanding the drivers for salt marsh expansion versus retreat is thus key to managers. Previous research highlights the influence of short-term (daily/event) bed level dynamics on germination and establishment and subsequent vegetation presence. However, more recent literature suggests the importance of medium-term seasonal bed level dynamics on viable seed availability and subsequent vegetation presence. This study aims to assess event-based and seasonal bed level dynamics for vegetation presence in natural and semi-natural salt marshes and to provide generic thresholds for vegetation presence. To gain insight into bed level dynamics, data was used from autonomous Optical and Acoustic Surface Elevation Dynamics sensors (O-SED and A-SED) around the edge of natural and semi-natural salt marshes. Sensors were installed at vegetated and unvegetated measurement station Field observations from 22 O-SEDs deployed at 4 well-established natural salt marshes in the Western Scheldt estuary and 4 O-SEDs at a well-established semi-natural salt marsh in the Wadden Sea were reanalyzed. Six novel A-SEDs were deployed at a pioneer semi-natural salt marsh in the Ems-Dollard Estuary. The measurement duration at all salt marshes was at least 1 year. The A-SED sensor was successfully validated against manual measurements. Furthermore, vegetation data and water level data were obtained. No significant difference was observed between natural and semi-natural salt marshes. However, a significant difference between vegetated and unvegetated measurement stations for short-term bed level dynamics was observed. Vegetation was found to be present at locations restricted by short-term bed level variability smaller than or equal to 12 mm, emphasizing the presence of a short-term threshold. Although trends in the non-growing season were significantly different between vegetated and unvegetated stations, seasonal thresholds for vegetation presence were not found. The findings imply that knowledge of bed level-dynamics in well-established natural

marshes can be used to predict vegetation presence in constructed semi-natural marshes. The importance of local short-term dynamics for vegetation presence instead of longer-term dynamics highlights possibilities for developing favorable conditions for vegetation presence in marsh restoration projects and the construction of new salt marsh ecosystems.

Keywords: salt marsh dynamics, field monitoring, nature-based solutions, biogeomorphology, bed level dynamics, vegetation presence, thresholds

INTRODUCTION

Salt marshes have proven to deliver a range of valuable ecosystem services, like providing habitats to unique flora and fauna, carbon sequestration and coastal protection by wave attenuation (e.g., Duarte et al., 2013; Möller et al., 2014; Zhu et al., 2020). More recently, the long-term coastal protection services of salt marsh size has been quantified, by analyzing the relations between the width of the salt marsh and its wave attenuating capacity through time (Willemsen et al., 2018; Vuik et al., 2019). Such long-term analyses are needed for the successful implementation of salt marshes as nature-based solutions (NbS) in coastal management, as coastal defense schemes are built to last for decades (Borsje et al., 2011; Temmerman et al., 2013). Long-term (years to decades) lateral dynamics of the marsh edge that determine the width of a marsh via marsh expansion or retreat (Harmsworth and Long, 1986; Van der Wal et al., 2008) have been related to various factors. For example, at the large-scale marsh expansion and retreat has been related to changes in sea level (Allen, 2000), changes in wind and waves (Schwimmer, 2001; van der Wal and Pye, 2004), channel deepening and migration (Pringle, 1995; Pye, 1995; Cox et al., 2003), sediment supply (Ladd et al., 2019) and sedimentation and erosion processes (van der Wal et al., 2002). At a local scale the lateral dynamics of the marsh edge have been related to factors such as seed availability (Rand, 2000; van Regteren et al., 2017, 2020b) short-term sediment dynamics (Bouma et al., 2016; Willemsen et al., 2018) and soil properties (Wolters and Bakker, 2002).

Wave attenuation by marshes, as well as the buildup of the marsh soil, critically depends on the density of the vegetation (e.g., Barbier et al., 2008; Bouma et al., 2014). The establishment of pioneer plants is the first stage of making the environment more suitable for subsequent plant colonization and marsh development by locally decreasing hydrodynamic energy (van Regteren et al., 2020a). However, vegetation can only colonize locations where, amongst other factors, hydrodynamic forces and morphodynamic stresses remain below certain critical thresholds (Balke et al., 2016; Bouma et al., 2016). That is, given fulfillment of local biological conditions such as seed availability, an inundation-free period is required for initial establishment, followed by a calm period with rather low waves and limited bed level dynamics for subsequent growth (Hu et al., 2015b; Cao et al., 2018; Poppema et al., 2019), which is described as a Window of Opportunity (WoO; Balke et al., 2014). These WoOs capture the first weeks/months of vegetation establishment and growth (Cao et al., 2019; Poppema et al., 2019). The WoO theory is primarily focused on the growing season during which the seedlings establish (Balke et al., 2014). In addition to the growing season, year-round (including the non-growing season) bed level change has been observed to be an important factor in driving the lateral dynamics of the salt marsh edge (Willemsen et al., 2018; van Regteren et al., 2019). Extending on the WoO theory, these studies suggest that year-round disturbances are also important for the presence of vegetation.

Semi-natural salt marshes are marshes that are (partly) created by humans for their ecosystem services. They often consist of intertidal areas that are made suitable for vegetation establishment by engineering measures that reduce local disturbances. However, initial conditions differ, depending on the design and construction methods applied. For example, semi-natural marshes can be obtained by artificially elevating the intertidal area with dredged sediments (Ford et al., 1999; Schrift et al., 2008) and/or by reducing hydrodynamic and morphodynamic stresses by adding wave-attenuating structures (Baptist et al., 2021). Although the number of semi-natural (constructed) salt marshes is increasing (Maris et al., 2007; Mazik et al., 2007; Temmerman et al., 2013; Rahman et al., 2019), biophysical data on constructed salt marshes remain scarce. While daily to seasonal morphodynamics have been observed to drive the lateral location of the marsh edge in natural salt marshes (e.g., Bouma et al., 2016; Willemsen et al., 2018), observations of similar dynamics in constructed salt marshes are lacking. To be able to efficiently create constructed salt marshes for their ecosystem services, it is key to quantify morphodynamics and vegetation presence, and to compare those dynamics with those observed in natural salt marshes. We hypothesize that event-driven (short-term) and seasonal (medium-term) bed level dynamics do not differ between natural and semi-natural constructed salt marshes.

Continuous monitoring of bed level dynamics is required to enable the quantification of morphodynamics at a temporal resolution of hours, associated with the impacts of storm events. Simultaneously, these morphodynamics need to be monitored for a duration of multiple seasons to years to uncover seasonal bed level dynamics. Periodic bed level changes have been monitored extensively, by manual monitoring techniques using erosion pins (Stokes et al., 2010), steel reference plates (Andersen et al., 2006), sediment traps (Moskalski and Sommerfield, 2012), accretion poles (O'Brien et al., 2000) and sedimentation-erosion bars (Baptist et al., 2019). However, the use of autonomous systems (such as the Photo-Electronic Erosion Pin) to monitor bed level dynamics at a high temporal resolution (hours) over periods of seasons to years remains scarce due to instrument limitations and costs (Lawler, 2008; Hu et al., 2015a). More recently, the Optical

Surface Elevation Dynamics sensor (O-SED) was developed and applied for continuous monitoring of bed level dynamics in the intertidal area, when the sensor is not submerged, at a temporal resolution of hours and for a duration of multiple months (Hu et al., 2017, 2020; Willemsen et al., 2018). This instrument was further developed into an Acoustic Surface Elevation Dynamics (A-SED) sensor, now able to capture bed level change when submerged.

In this study, we used data of both O-SED (26) and novel A-SED (6) sensors around the edge of natural and semi-natural salt marshes in order (1) to assess the magnitude of event-based and seasonal bed level dynamics in natural and semi-natural (constructed) salt marshes and (2) to identify generic thresholds of event-based and seasonal bed level dynamics for vegetation presence, both in natural and semi-natural salt marshes. These thresholds quantify maximum accretion and/or erosion vegetation around the salt marsh edge can withstand. The structure of this paper is as follows. In section "Materials and Methods" the study sites are introduced, followed by a description of the state-of-the-art instruments deployed for year-round field data collection of high-resolution bed level dynamics. Section "Results" presents the results of data analyses based on the collected field data and quantifies the bed level change limits for vegetation growth across the study sites. In section "Discussion" the main findings of this paper are discussed, followed by the main conclusions in section "Conclusion."

MATERIALS AND METHODS

Study Sites

The study sites are located around the North Sea coast of the Netherlands at the Western Scheldt estuary, Wadden Sea and Ems-Dollard estuary (**Figure 1**). Field data were previously collected at four natural salt marshes in the Western Scheldt, that have been thriving for decades and at one artificial semi-natural salt marsh in the Wadden Sea with brushwood structures also existing for decades (Willemsen et al., 2018, 2020). This data was reanalyzed. State-of-the-art A-SED sensors were deployed at a second semi-natural salt marsh in the Ems-Dollard Estuary that has been constructed in 2018 by creating an elevated bed protected by brushwood structures.

Natural Salt Marshes

The four natural salt marsh sites are located in the Western Scheldt estuary, which is located in the southwestern delta of the Netherlands (51°20′N; 4°E; **Figure 1** and **Table 1**). Two sites, Zuidgors Hellegat and Zimmerman, are located at the northern shores of the Western Scheldt, approximately 20 and 50 km from the mouth of the estuary, respectively. The other two sites in the Western Scheldt, Paulina and Hellegat, are located at the southern shores, approximately 15 and 27 km from the mouth, respectively. The sites at the northern shore are exposed, whereas the sites at the southern shore are more sheltered from the prevailing south-westerly winds (Callaghan et al., 2010). The sites Zuidgors and Paulina, are saline at 20–25 psu, whereas the two study sites further inland, Hellegat and Zimmerman, are brackish at 15–20 psu (Damme et al., 2005). The mesotidal to macrotidal Western Scheldt estuary is tide dominated with a semi-diurnal tide (Baeyens et al., 1997). The spring tidal range at Paulina, the study site closest to the mouth of the Western Scheldt estuary, is approximately 4.4 m and increases to 5.5 m at Zimmerman, the study site closest to the landward boundary of the estuary (Van der Wal et al., 2008). The grain size of the top layer of the bed (D_{50}) varied between 18 and 132 μm (Willemsen et al., 2018; **Table 1**). In the more saline marshes in the west of the estuary, pioneer species such as perennial common cord grass (*Spartina anglica*) and the annual glasswort (*Salicornia spp.*) are occurring. Well-established vegetation, such as common saltmarsh grass (*Puccinellia maritima*), annual seablite (*Suaeda maritima*), and sea aster (*Aster tripolium*) are occurring higher in those marshes. At the most eastern, more brackish study sites, well-established seaside bulrush (*Bolboschoenus maritimus*) and common reed (*Phragmites australis*) are occurring as well as common cordgrass (*Spartina spp.*) (Van der Wal et al., 2008).

Semi-Natural Salt Marshes

The two semi natural salt marshes are located in the Wadden Sea and Ems-Dollard estuary. The semi-natural salt marsh site Uithuizen is located in the Wadden Sea area, close to the mouth of the Ems-Dollard estuary (53°27′N, 6°39′E; **Figure 1** and **Table 1**). The Wadden Sea is a mesotidal to macrotidal estuary (Dieckmann et al., 1987), with a tidal range of approximately 3.0 m at Uithuizen. The salinity near Uithuizen is approximately 30 psu (Zimmerman, 1976; Ysebaert et al., 2016). The D_{50} at the study site was approximately 87 μm (Folmer et al., 2017; **Table 1**). Salt marsh development in this particular marsh is supported by brushwood structures (van Loon-Steensma, 2015). At this site, common glasswort (*Salicornia europaea*), common salt marsh grass (*Puccinellia maritima*) and common cordgrass (*Spartina anglica*), are pioneer species occurring in the lower salt marsh. Vegetation species occupying the higher marsh are couch grass (*Elymus athericus*), sea aster (*Aster tripolium*), and seepweed (*Suaeda maritima*).

The semi-natural Marconi salt marsh (53°19′39.33″N, 6°56′40.75″E; **Figure 1** and **Table 1**) is located in the Ems-Dollard estuary, at Delfzijl. The mesotidal Ems-Dollard estuary is directly connected with the Wadden Sea estuary. The tidal range near Delfzijl is approximately 3.1 m, with a spring tidal range of 3.4 m (Dillingh, 2013). The salinity in the Ems-Dollard increases from southeast to northwest and is generally below 20 psu (Esselink et al., 1998), with approximately 23 psu locally near the Marconi salt marsh. The Marconi salt marsh was developed in 2018 at the seaward side of the jetty of the Port of Delfzijl. Mud (silt and clay) was mixed through the top layer of a sand fill on the foreshore of the jetty. The mud was collected during a local port extension project and temporarily stored in a land depot. The percentage of mud in the sand/mud mixture was varied intentionally between different sections of the salt marsh (ranging between 5 and 50%; **Figure 1**). The D_{50} at the top layer of the sections were measurement stations were located varied between 111 and 213 μm (De Vries et al., 2021; **Table 1**). To protect establishing vegetation from excessive hydrodynamic energy, permeable brushwood dams

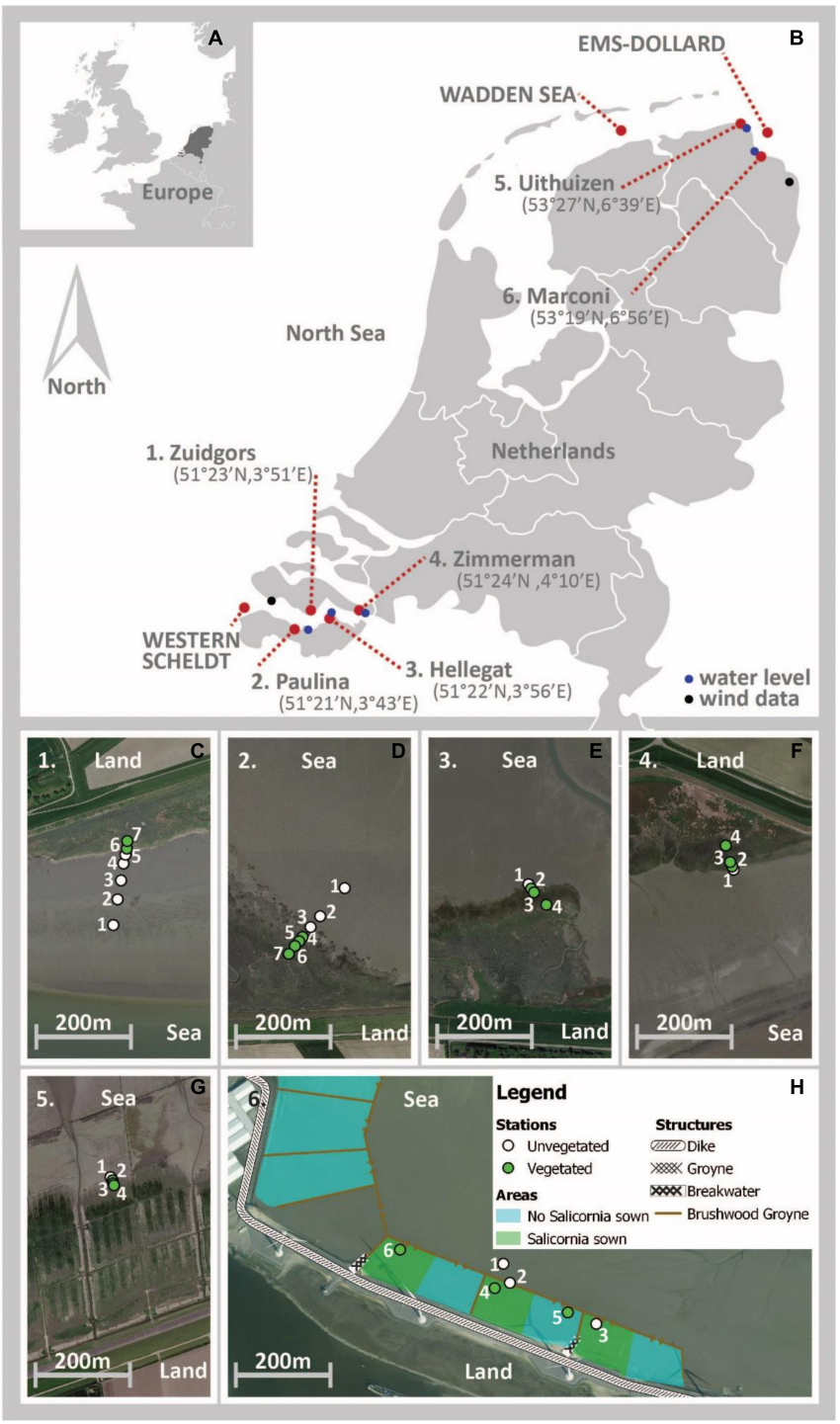


FIGURE 1 | Study sites around the North Sea area **(A)** indicated with a red dot **(B)**. Locations where water levels were continuously monitored are indicated with a blue dot and the location were wind data were collected is indicated with a black dot **(B)**. The measurement stations (numbered) for bed level dynamics are marked with green (vegetated) and white (unvegetated) dots for each of the study sites **(C–H)**. Source of background maps **(C–G)** is Google Maps, source of background map **(H)** is MapTiler and OpenStreetMap contributors.

were constructed surrounding the different salt marsh sections. Moreover, to enhance vegetation growth, *Salicornia procumbens* was sown in part of the salt marsh sections. After its first year, vegetation species established at the Marconi salt marsh were mainly the pioneer and lower marsh species glasswort (*Salicornia spp.*), seaside bulrush (*Bolboschoenus maritimus*), spear-leaved

TABLE 1 | Collection of bed level dynamics data using O-SED and A-SED sensors.

Study site	Estuary/coastal sea	Location	Start time series	End time series	Deployment duration	Number of instruments (instrument type)	D_{50} (min-max) μm
1. Zuidgors	Western Scheldt	51°23′21.95″N, 3°50′7.51″E	October 2015	October 2016	12 months	7 (O-SED)	39 (18–57)
2. Paulina	Western Scheldt	51°20′59.73″N, 3°43′3.37″E	February 2015	June 2016	16 months	7 (O-SED)	35 (21–58)
3. Hellegat	Western Scheldt	51°21′59.33″N, 3°56′44.67″E	December 2014	August 2016	20 months	4 (O-SED)	123 (113–132)
4. Zimmerman	Western Scheldt	51°24′8.05″N, 4°10′32.15″E	February 2015	June 2016	16 months	4 (O-SED)	85 (67–97)
5. Uithuizen	Wadden Sea	53°27′24.57″N, 6°39′32.07″E	March 2015	March 2016	12 months	4 (O-SED)	87
6. Marconi	Ems-Dollard	53°19′39.33″N, 6°56′40.75″E	September 2019	September 2020	12 months	6 (O-SED)	169 (111–213)

Data in the Western Scheldt and Wadden Sea is reanalyzed from Willemsen et al. (2018).

orache (*Atriplex prostrata*), seepweed (*Suaeda maritima*), salt sandspurry (*Spergularia sp.*) and common salt marsh grass (*Puccinellia distans*) (De Vries et al., 2021).

Field Data Collection

Vegetation Data

At the natural salt marshes in the Western Scheldt and semi natural salt marsh in the Wadden Sea, where vegetation has already been developing for decades, vegetation presence was determined for each of the measurement stations. Measurement stations where vegetation was absent during the measurement periods were defined as bare tidal flat, whereas stations where vegetation was present were defined as vegetated salt marsh. Vegetation cover at the salt marsh stations was characterized as pioneer, low marsh and high marsh, each with a vegetation cover of at least 5%.

A similar approach was applied at the constructed Marconi salt marsh. Vegetation was not present when the measurement stations were installed, due to recent construction of the semi-natural salt marsh. Measurement stations at Marconi were set-up around the local mean high water level (1.4 m +NAP). Vegetation cover was monitored at the end of the growing season (September) to be able to observe annual species as well, and vegetation density was estimated using a decimal scale (Londo, 1976) in permanent quadrats (PQ's) of 2 m × 2 m. At the end of the growing season, measurement stations were characterized either by vegetation presence or absence.

Water Level and Wind Data

Water level data were obtained from Rijkswaterstaat (Dutch waterways and public works Authority), for consistency across all study sites. Water level data were obtained at a 10 min interval at measurement stations near the study sites: Terneuzen, Bath, Hansweert, Uithuizen and Delfzijl (**Figure 1**). The surface elevation of the measurement stations, relative to NAP (Dutch Ordnance Datum), was initially measured with an RTK-DGPS for determining inundation periods of the individual measurement stations. The RTK-DGPS has a vertical accuracy of approximately 2 cm. Hourly wind data (wind speed and wind direction) were obtained from KNMI (The Royal Netherlands Meteorological Institute) measurement stations near the natural salt marsh Zuidgors and the constructed salt marsh Marconi, Vlissingen and Nieuw-Beerta, respectively.

Bed Level Dynamics

Bed level dynamics data were collected or reanalyzed at all study sites, both at locations with and without vegetation presence (**Figure 1**). All measurement stations were located close to the vegetation edge (or predicted vegetation edge at the end of the growing season), to assess the isolated influence of bed level dynamics on the occurrence of salt marsh vegetation, as well as the similarity of bed level dynamics at natural and semi-natural salt marshes. Field observations from a total of 32 measurement stations across the six study sites were analyzed, each for at least a 1 year duration (**Table 1**).

Bed level changes at the natural salt marshes in the Western Scheldt estuary were collected previously using the Optical Surface Elevation Dynamics (O-SED) sensor (Willemsen et al., 2018). This stand-alone sensor captures bed level change by using a measurement array of light sensitive cells (i.e., phototransistors) and has been successfully applied to quantify salt marsh dynamics in previous studies (Hu et al., 2015a, 2017). The sensors were installed firmly in the bed, with half of the measurement array of 400 mm below the surface and half of the array extending above the sediment surface. The instruments were serviced, cleaned and data were downloaded every 2–6 months The sensors were pushed in or pulled out of the bottom after excessive sedimentation and erosion. The observations were corrected for this action during post-processing. A single surface elevation measurement was collected every 30 min. Raw data were converted to bed level change data using an existing post-processing script (Willemsen et al., 2018). The post-processed data have previously been validated successfully against sedimentation-erosion bars (Hu et al., 2015a) and erosion pins (Willemsen et al., 2018), with an accuracy of the obtained bed level changes of approximately 5.0 mm (Hu et al., 2015a). Data was reanalyzed specifically for the current study.

Bed level changes at the semi-natural salt marsh Uithuizen at the Wadden Sea coast were also previously collected using the O-SED sensor (Willemsen et al., 2018). Data collection, post-processing and reanalysis, was equal to collection, post-processing and reanalysis for marshes in the Western Scheldt. At the semi-natural constructed Marconi salt marsh, bed level change data were collected using state-of-the-art Acoustic Surface Elevation Dynamics (A-SED) instruments (**Figure 2**). This recently developed instrument measures the distance between the bed and the instrument through the echo of an acoustic signal (**Appendix 1**). The sensor operates stand-alone without requiring external power and data-logging systems. Furthermore the instrument is relatively inexpensive (±1,000 euro) compared to other (acoustic) measurement instruments (see Hu et al., 2015a). The instrument is set-up to be able to collect measurements when the sensor of the instrument is fully inundated. A burst of eight samples (sampling frequency of 5 Hz) was stored at a measurement interval of 5–15 min. The instruments were installed downward looking, with the sensor head aimed vertically at the bottom (**Figure 2**). The instruments were serviced, cleaned and data were downloaded every 2–3 months. A post-processing script was developed in Python to convert the acoustic return signals to bed level change data (**Appendix 1**). The measurements were validated with manual readings of the height above bed (HAB) of the sensors every time the instruments were serviced.

Data Analysis

The distribution of the magnitude of bed level change per measurement (with a measurement every 5–30 min) was determined per study site both for the stations were vegetation was present and absent, by calculating the difference of subsequent measurements. The standard deviation of every full time series of bed level dynamics was calculated to capture short-term event-based dynamics, since larger bed level change was observed to coincide with larger waves and stronger winds (c.f. Hu et al., 2015a; Willemsen et al., 2018). Medium-term seasonal bed level change was captured by calculating the linear least-squares regression of the observed bed level dynamics per season, with the slope of the regression representing the linear rate of change of the bed level over a single season. For this analysis, the seasons were defined as the growing season (April–September) and non-growing season (October–March). If gaps in the SED data appeared for three or more consecutive months, either in the growing or in the non-growing season, the seasonal rate of change of the station was discarded. Additionally, local water level data were compared with RTK-DGPS-derived bed level data of the measurement stations, to compute the time each site was submerged/emerged.

Validation of the Accuracy of the Novel Sensors and the Processing Software

Bed level change measurements collected with the A-SED sensors at all measurement stations at Marconi and the post-processing script (**Appendix 1**) were validated with manual measurements, analog to what was done earlier for the O-SED (Hu et al., 2015a; Willemsen et al., 2018). An average height above bed (HAB) was calculated for each burst of eight individual A-SED measurements. The raw data each of those eight measurements were first converted to a height above bed (HAB), which were subsequently averaged. The HAB of the A-SED was also manually measured upon installation and retrieval of the sensors, every

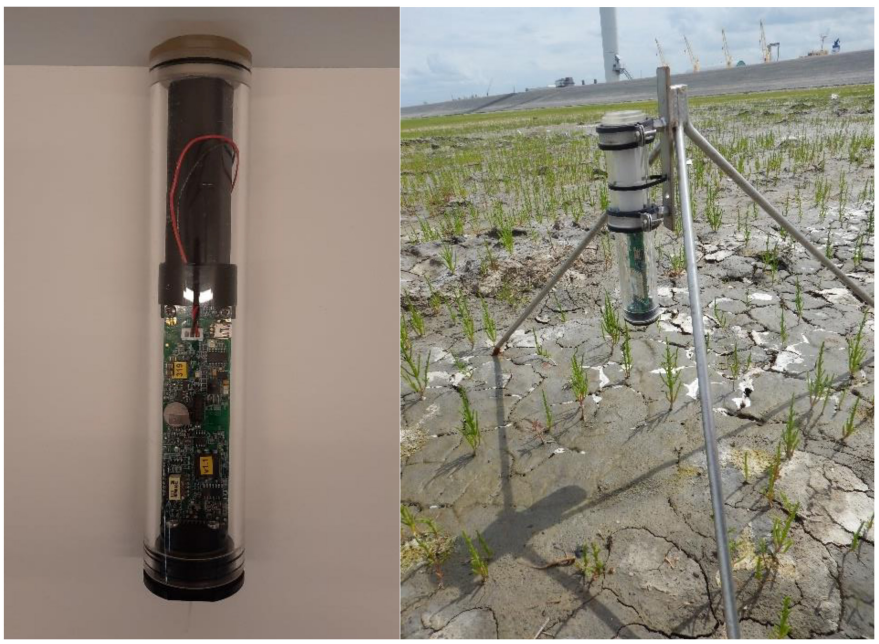


FIGURE 2 | The A-SED sensor **(left)** and the A-SED sensor deployed in the field **(right)**.

2–3 months. These manual measurements were compared with the first instrument measurement after installation and the last measurement before retrieval, respectively (**Figure 3**).

A direct comparison between the A-SED data and the manually obtained reference measurements provides a near-unity correlation: the least-squares regression line of the A-SED data and the manually obtained measurements has a slope of 1.0001 with an R^2 of 0.99 (**Figure 3**). The height measured by the A-SED sensors was systematically higher than the manual observations by 2.13 cm. This offset was subsequently applied as a fixed calibration constant in the post-processing of the A-SED data. For the current analysis, however, this constant offset is not affecting the results, since all A-SED observations are converted into bed level change relative to the initial measurement of the time series. The accuracy of the sensor is defined as the absolute error between the A-SED sensor measurement and the true value assumed to be measured manually (c.f. Hu et al., 2015a). Based on all manual measurements, the accuracy is 7.6 mm with a standard deviation of 6.1 mm. The accuracy of the O-SED sensor was observed to be 5.0 mm (Hu et al., 2015a), comparable to the A-SED sensor.

RESULTS

Vegetation Presence

Vegetation was present, for the full bed level dynamics measurement period, at 12 of the 22 measurement stations located at the natural salt marshes in the Western Scheldt (Zuidgors, Paulina, Hellegat, and Zimmerman). The vegetation cover at the vegetated stations was at least 5%. At the semi-natural salt marsh in the Wadden Sea vegetation was present at 3 of the 4 measurement stations (cover >5%) (**Figure 1**). Vegetation at the semi-natural salt marsh Marconi was still developing, due to its recent construction. Vegetation at the end of the growing season in September 2020 was present at 3 of the 6 measurement stations and consisted mainly of the annual *Salicornia spp*. The vegetation density at measurement stations 1, 2, 3, 4, 5, and 6 was 0, 0, 0, 10, 1, and 20%, respectively (**Figure 1**).

Inundation Time of the Measurement Stations

All well-established natural salt marshes in the Western Scheldt generally showed an inclining elevation from the most seaward measurement station toward the most landward measurement station. This is reflected in reducing inundation times at these measurement stations (**Figure 4**). The lowest elevation/inundation level where vegetation is present was strongly site-specific (**Figure 4**; dashed lines). In the Western Scheldt estuary, where four natural salt marshes were located, vegetation extended more seaward to lower elevations and was able to withstand shorter dry periods (i.e., longer inundation) at the southern shores (Paulina and Hellegat), compared to the northern shores (Zuidgors and Zimmerman). This might be explained by the prevailing wind conditions, adding local disturbances: Paulina and Hellegat are sheltered from the

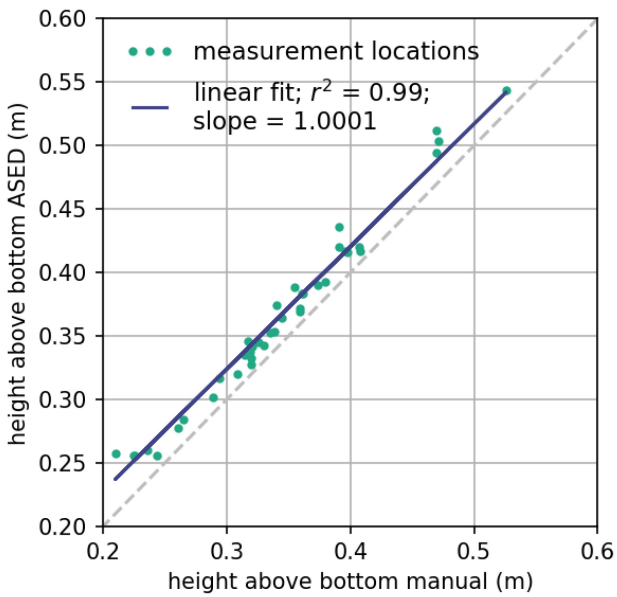


FIGURE 3 | Comparison of height above bed measured by the A-SED and manually measured height above bed of the A-SED, every time the A-SED is installed and retrieved from the field at all measurement stations at the Marconi salt marsh. Green dots show the data, the blue line represents a linear fit of the data (the gray dashed line represents a perfect 1:1 correlation).

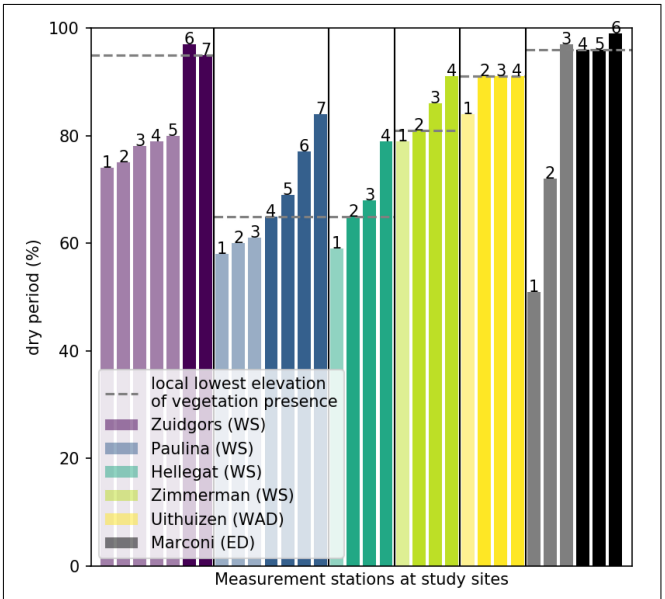


FIGURE 4 | The relative duration a measurement station is not inundated (i.e., dry period). The light colored bars indicate a location where vegetation is absent (bare tidal flat), whereas the dark colored bars indicate a location where vegetation is present (vegetated salt marsh). The dashed lines indicate the local lowest elevation where vegetation is present per study site. Numbers relate to the numbers of the measurement stations, introduced in **Figure 1**. WS indicates Western Scheldt, WAD indicates Wadden Sea and ED indicates Ems-Dollard.

prevailing wind conditions, whereas Zuidgors and Zimmerman are more exposed to the prevailing southwesterly winds.

At the semi-natural salt marsh Uithuizen in the Wadden Sea the inundation period increased from the seaward to landward measurement stations, similar to the observations in the Western Scheldt estuary. At the semi-natural (recently constructed) Marconi salt marsh in the Ems-Dollard estuary, the inundation duration is longer at the measurement stations in front of the brushwood dams (**Figure 4**; Marconi stations 1 and 2). In general, the dry period at the measurement stations sheltered by the brushwood dams is longer, enabling vegetation to establish (**Figure 4**; stations 3, 4, 5, and 6). Nevertheless, even though the elevation of the most eastward measurement station sheltered by the brushwood dams (station 3) exceeds the local lowest elevation for vegetation to grow, vegetation was still not able to grow there. This might be explained by both the location of the test section being near to the edge of the constructed salt marsh, thereby having slightly higher hydrodynamic energy and/or by the low clay content of this test section (5%), resulting in less favorable growing conditions.

Although similar patterns were observed at all study sites, the inundation threshold for vegetation to be present was different. So the results show that inundation time can explain the presence of vegetation locally, within each study site. However, this physical parameter, strongly related to elevation, does not provide a generic threshold to the presence of vegetation for all study sites around the North Sea.

Bed Level Change

Between the time series of bed level dynamics (time scale of minutes), both deposition (positive) and erosion (negative), at all study sites there was a significant difference [two-way ANOVA; $F(5,552643) = 7088$, $p < 0.001$], indicating unique dynamics for all individual sites. Between the vegetated and unvegetated measurement stations, over all study sites there was a significant difference in the full bed level dynamics time series [$F(1,552643) = 709$, $p < 0.001$], highlighting different dynamics at measurement stations with and without vegetation.

The frequency distribution of absolute bed level change measurements (magnitude; both accretion and erosion are positive), both for stations with and without vegetation, showed some similarities (**Figure 5**). Small bed level changes were observed most often at all sites. The frequency of bed level change declined with increasing magnitudes of bed level change, whereafter a trend break was observed (at bed level change between 5 and 10 mm) toward a steeper decline (**Figure 5**). The shape of the frequency distribution before the trend break varied largely between the different study sites as well as the vegetated and unvegetated stations. Largest differences between the vegetated and unvegetated distributions were observed at the natural salt marsh Zimmerman and semi-natural marshes Uithuizen and Marconi, although the frequency of larger bed level changes at unvegetated stations exceeded those at the vegetated stations at Zimmerman and Uithuizen contrary to Marconi.

The mean and 90th percentile of absolute bed level change (magnitude; both accretion and erosion are positive) at the stations without vegetation did not exceed values at the stations with vegetation at all sites, contrary to expectations. The mean and 90th percentile at the unvegetated stations at Paulina and Marconi did not exceed the values at the vegetated stations at these sites, whereas the opposite was observed at the other study sites. For example, the mean bed level change for Hellegat over the full time series was 0.9 mm at the unvegetated and 0.7 mm at the vegetated stations, whereas for Marconi the mean bed level change was 1.1 mm at the unvegetated and 1.6 mm at the vegetated stations. No generic mean or 90th percentile bed level change threshold was found that distinguished between vegetated and unvegetated for all study sites.

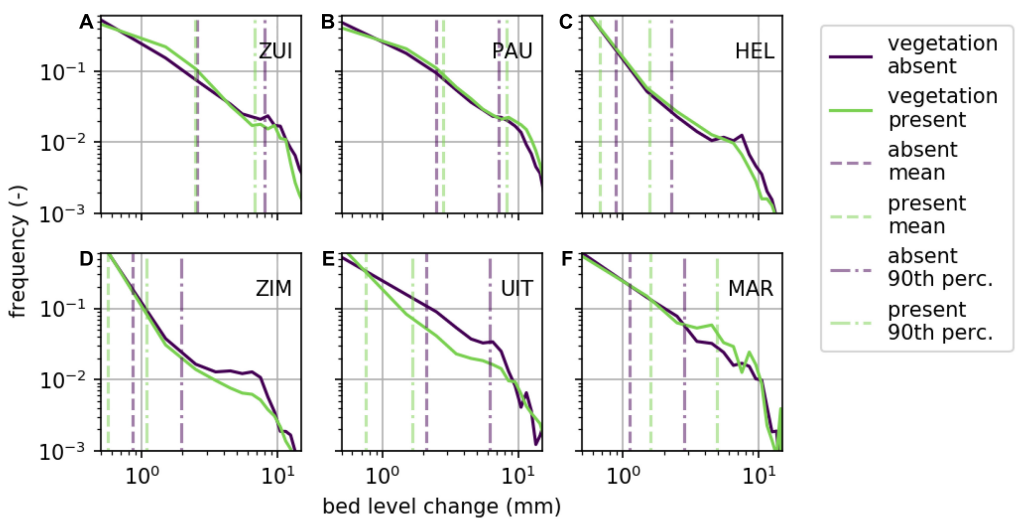


FIGURE 5 | Distribution of bed level change measurements at study sites Zuidgors **(A)**, Paulina **(B)**, Hellegat **(C)**, Zimmerman **(D)**, Uithuizen **(E)**, and Marconi **(F)**. Data are combined for stations where vegetation is present (green) and absent (purple).

Event-Based Bed Level Dynamics

Measured bed level change, both deposition (positive) and erosion (negative), was converted to a standard deviation to assess the magnitude of bed level change due to, e.g., wind-wave events. As an example bed level change data at the natural site Zuidgors were compared with locally occurring south and south-westerly wind conditions (associated with the longest fetch at this site), to highlight differences in bed level dynamics during storm and calm conditions that were captured with the (A-SED) sensors. The standard deviation of bed level change during a period with storm conditions (e.g. onshore wind speeds exceeding 75 km/h) generally was larger than the standard deviation during calm conditions, both at the unvegetated and vegetated measurement stations (**Figure 6**). Similar variability in the bed level dynamics due to storm conditions was observed at the semi-natural site Marconi. Storm conditions caused by locally occurring northerly onshore wind conditions (associated with the longest fetch for this site) were not present in the data. Nevertheless, bed level dynamics during onshore windy periods (periods with largest wind speeds, exceeding 40 km/h) were substantially larger than during calm periods (**Figure 7**), assuming no bed level change when stations were not inundated (**Figure 7**). At all study sites, unvegetated measurement stations showed substantially larger dynamics than measurement stations where vegetation was present (**Figures 6–8**). The standard deviation of bed level dynamics for the full measurement period generally showed larger values at the unvegetated stations than the vegetated stations across all measurement stations at the six study sites (**Figure 8**). A significant difference was observed between the measurement stations where vegetation was present and absent [two-way ANOVA; $F(1,29) = 45$, $p < 0.001$]. A significant difference for short-term event-based bed level change between measurement stations at natural and semi-natural salt marshes was not found.

The standard deviations of bed level dynamics for the full measurement period at all vegetated stations at the natural and semi-natural salt marshes were not exceeding 12 mm (**Figure 8**), indicating a threshold for vegetation presence. Event-based bed

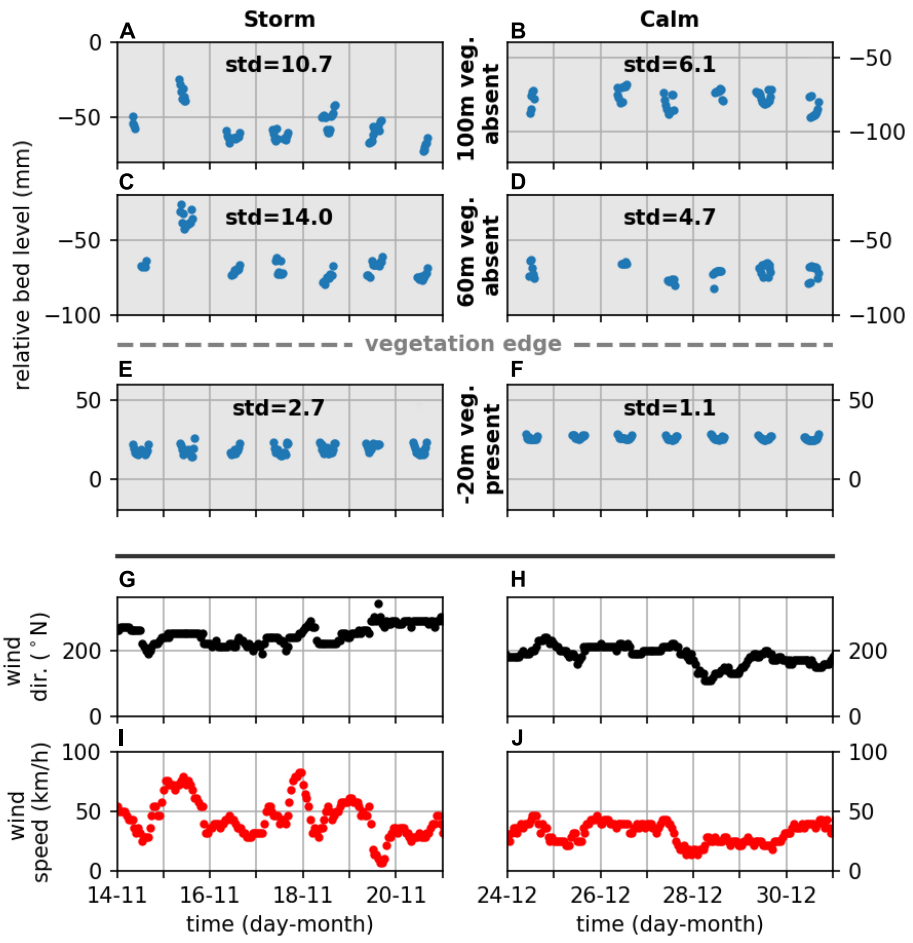


FIGURE 6 | Bed level change [**(A–F)**; blue dots], wind direction [**(G,H)**; black dots] and wind speed [**(I,J)**; red dots], during storm (left) and calm (right) wind conditions for three measurement stations at Zuidgors, two at unvegetated stations **(A–D)** and one at a vegetated station **(E,F)**. The standard deviation (mm) of the bed level for the represented time series is printed in the panel **(A–F)**.

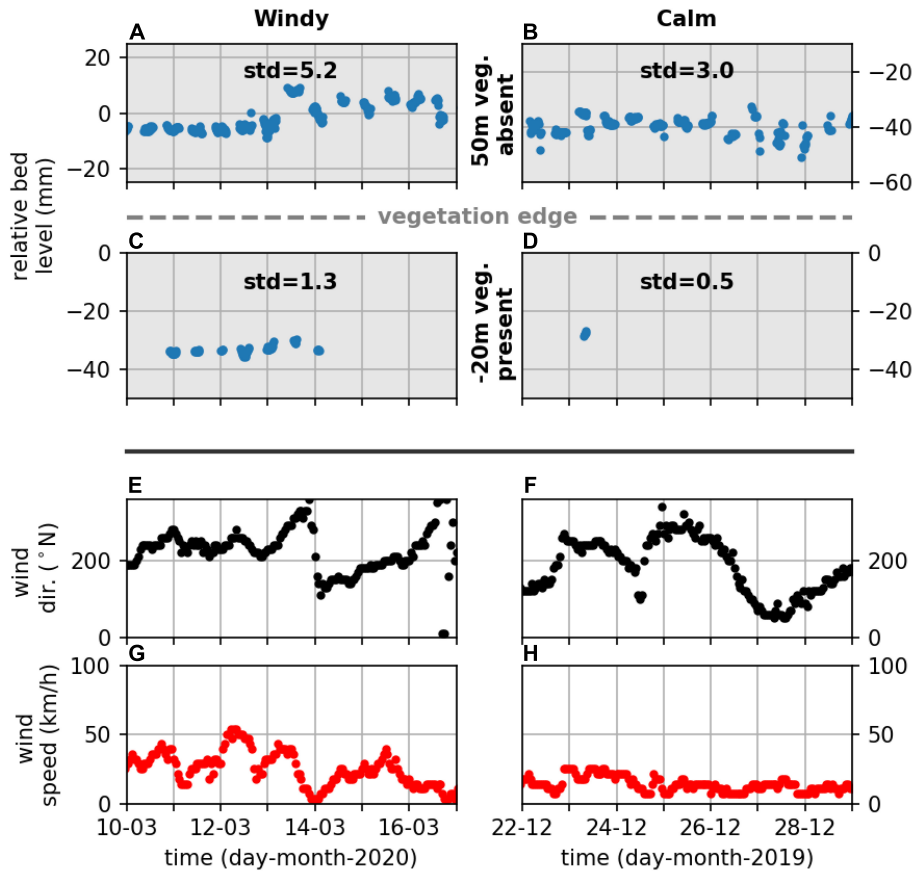


FIGURE 7 | Bed level change [**(A–D)**; blue dots], wind direction [**(E,F)**; black dots] and wind speed [**(G,H)**; red dots], during windy (left) and calm (right) wind conditions at two measurement stations at Marconi, one unvegetated and one vegetated. The standard deviation (mm) of the bed level for the represented time series is indicated **(A–D)**.

level change at unvegetated measurement stations was generally larger, except at one measurement station at Marconi (**Figure 8**). Supported by the significant difference between event-based bed level change at vegetated and unvegetated measurement stations: for vegetation to be present the maximum short-term bed level change should not exceed 12 mm.

Seasonal Trends in Bed Level Change

To extend from short-term, event-based bed level change toward medium-term seasonal trends in bed level change, seasonal rates of bed level change were computed (**Figures 9**, **10**). In general, vegetated areas were accreting (up to 111 mm/season) or slightly eroding (up to 30 mm/season) during the growing season. Surprisingly, rates of change at the unvegetated measurement stations were larger during the growing season, both for accretion (up to 155 mm/season) and erosion (up to 90 mm/season) (**Figure 10**). During the non-growing season, the rates of change at the vegetated stations were of similar size as during the growing season (up to 52 mm/season accretion and up to 33 mm/season erosion). Dynamics at the unvegetated measurement station were generally lower in the non-growing season compared to the growing season (up to 102 mm/season) (**Figure 10**). Although the rates of change at the vegetated stations seemed generally lower than at the unvegetated stations at each individual study site (**Figure 10**), a significant difference between all vegetated and all unvegetated measurement stations was only observed during the non-growing season [two-way ANOVA; $F(1,23) = 22$, $p < 0.001$]. No significant difference was observed between vegetated and unvegetated measurement stations during the growing season. Dynamics at vegetated and unvegetated stations both in the growing and non-growing season overlapped such that a general threshold for vegetation presence was not found.

Rates of change at the natural marshes ranged from 90 mm/season erosion to 155 mm/season accretion in the growing season and from 102 mm/season erosion to 25 mm/season accretion in the non-growing season. Observed differences at the semi-natural marshes ranged from 80 mm/season erosion to 70 mm/season accretion in the growing season and from −38 mm/year sedimentation to 52 mm/season accretion during the non-growing season, indicating a larger range over the growing season. No significant difference was observed between natural and semi-natural salt marshes both at the medium-term growing and non-growing season.

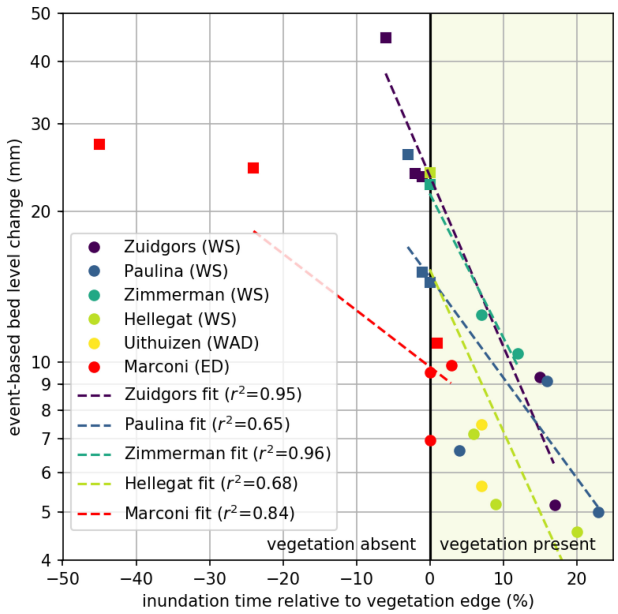


FIGURE 8 | Event-based bed level change related to the inundation time relative to the vegetation edge, with unvegetated (left part; square markers) and vegetated (right part; round markers) measurement stations. Data per study site is fitted with a logarithmic fit (dashed lines).

Combining Short-Term Event-Based Bed Level Dynamics and Medium-Term Seasonal Trends in Bed Level Change

When plotting event-based and seasonal bed level dynamics against each other, measurement stations where vegetation is present are all grouped in a parameter space delimited by relatively low event-based bed level change (i.e., standard deviation of bed level dynamics time series (**Figure 11**). We did not find specific seasonal limitations preventing vegetation presence. Vegetation was present at a short-term event-based bed level variability smaller than or equal to 12 mm, exceedance of this threshold was found to coincide with the absence of vegetation. This threshold was found to be valid both for natural and semi-natural salt marshes.

DISCUSSION

The current study highlights that (1) physical observations of bed level change at different timescales are similar at natural and semi-natural salt marshes including the recently constructed semi-natural Marconi salt marsh. Short-term event-based bed level change (2) was observed to be significantly different at vegetated and unvegetated measurement stations, and (3) limited the presence of vegetation. Although seasonal trends were significantly different between vegetated and unvegetated measurement stations during the non-growing season, seasonal thresholds for vegetation presence were not observed. Hence, the threshold for event-based bed level dynamics was sufficient for explaining vegetation presence.

Monitoring High-Resolution Bed Level Dynamics

A unique dataset of high-resolution bed level dynamics was compiled using state-of-the-art A-SED and O-SED measurement instruments. Bed level dynamics were analyzed at 32 measurement stations distributed across six study sites at the North Sea coast of the Netherlands. Previous studies have highlighted the importance of field observations of bed level dynamics with a high vertical spatial and temporal resolution, for example quantifying the influence of storms and vegetation establishment (Hu et al., 2015a,b, 2020; Willemsen et al., 2018). The current study extends on these previous observations by introducing and validating the A-SED sensor. Unlike manual observations and measurements with other sensors such as the O-SED (e.g., Lawler, 1991; O'Brien et al., 2000; Stokes et al., 2010; Baptist et al., 2019), the A-SED sensors allow for autonomous and continuous measurement of bed level changes when measurement stations are submerged. This allows the new A-SED sensors to monitor bed level change in real-time under hydrodynamic exposure, as opposed to these dynamics being derived from comparing pre- and post- hydrodynamic exposure measurements of the bed level during low-tide manually or with autonomous instruments such as the O-SED. The A-SED sensor is not restricted by light conditions, which is an advantage over previous optical sensors (Lawler, 1991; Hu et al., 2015a). Accuracy of the A-SED (7.6 mm) and O-SED (5.0 mm) was rather similar (Hu et al., 2015a). The A-SED measurements and manual measurements were not taken at exactly the same time, since the A-SED measures when submerged (requiring a water depth of approximately 0.3 m for the measurement head to be submerged) and the manual measurements were obtained when the stations were emerged, which might have caused the small difference between both measurements, thereby decreasing the accuracy. Nevertheless, the rather good agreement between both measurements suggest that the A-SED sensor, similar to the O-SED sensor, is a reliable instrument for continuous and autonomous measurements of bed level change.

Morphodynamic Disturbances for Vegetation Presence

In general, event-based bed level dynamics and seasonal rates of change were greater at the unvegetated locations at each site individually. The stabilizing effect of vegetation on bed level dynamics (Gacia and Duarte, 2001; Möller et al., 2014), was present in the well-established marshes in the Western Scheldt and Wadden Sea, since established annual and perennial vegetation species were present at the start of the measurements. However, vegetation was not yet present at the pioneer semi-natural Marconi salt marsh at the start of the measurements. So at this site, there was only an effect of the bed level dynamics on the presence of vegetation whereas there was no or negligible feedback of the vegetation on bed level dynamics. Despite the different feedback mechanisms in well-established versus

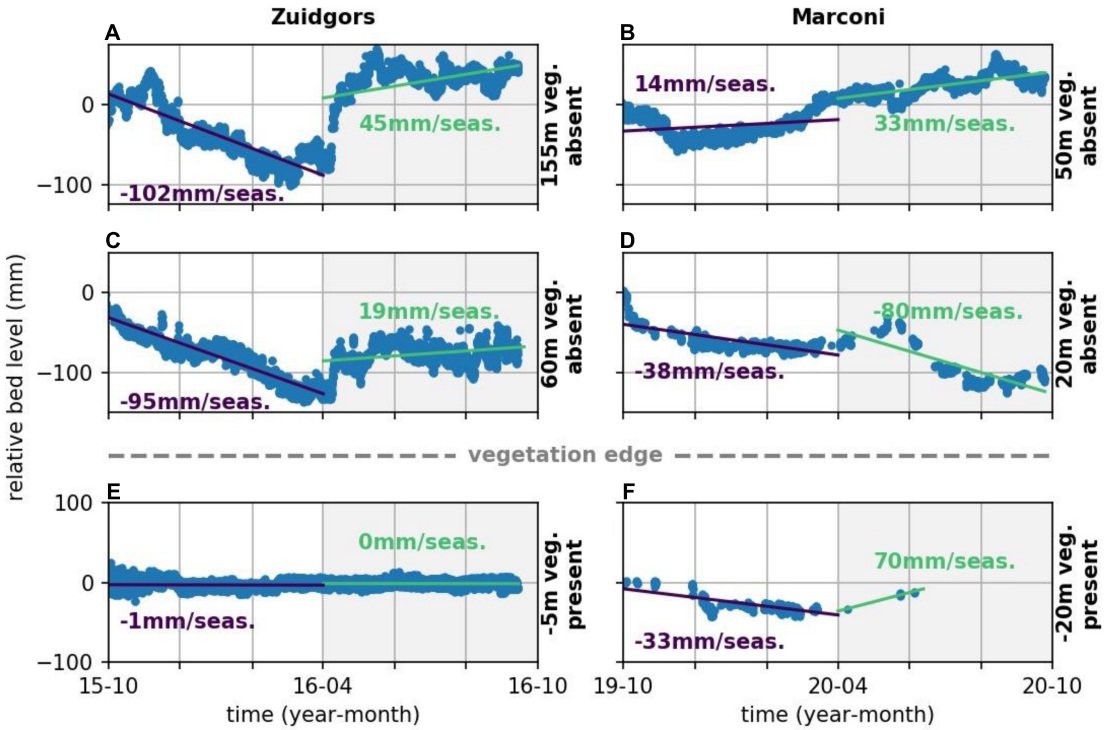


FIGURE 9 | Time series of bed level change (blue dots) at Zuidgors (left) and Marconi (right) at unvegetated stations **(A–D)** and vegetated stations **(E,F)**. The distance to the salt marsh edge (positive seaward and negative landward), is highlighted at the right-hand side of every subplot. The seasonal fit of the bed level change is indicated with a line and accompanied with a seasonal rate of change (purple for non-growing season and green for growing season).

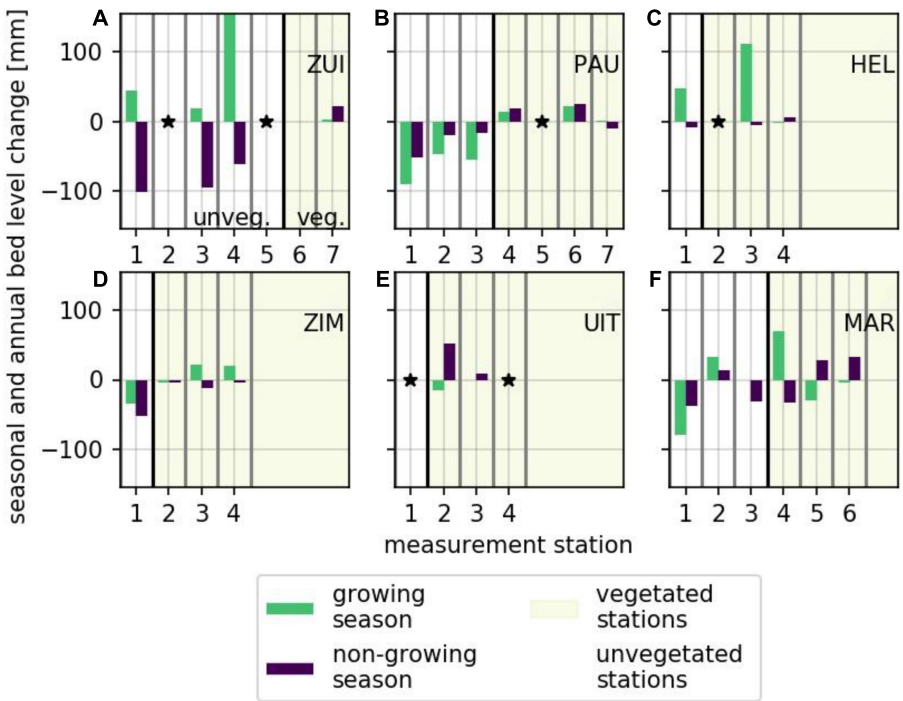


FIGURE 10 | Rates of bed level change during growing (green) and non-growing season (purple) at vegetated (no shading) and unvegetated (shading) measurement stations (separated by a thick black line). **(A)** Zuidgors. **(B)** Paulina. **(C)** Hellegat. **(D)** Zimmerman. **(E)** Uithuizen. **(F)** Marconi. Asterisks indicate insufficient data as explained in section "Data Analysis."

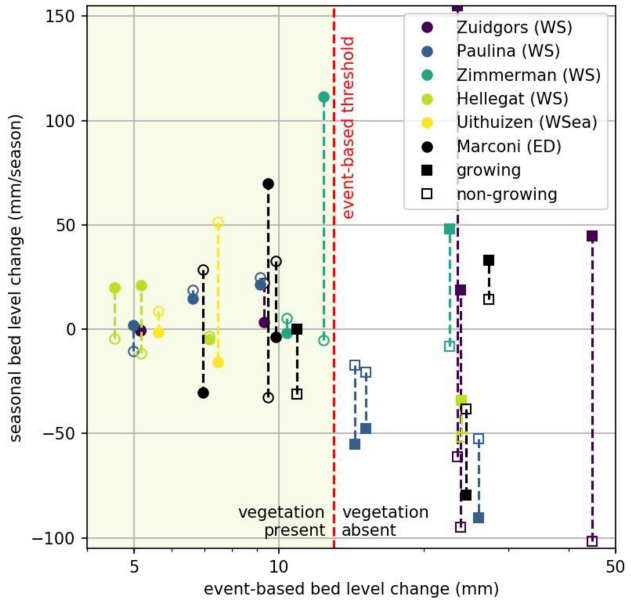


FIGURE 11 | Short-term event-based bed level change represented by the standard deviation (*x*-axis; log-scale) and medium-term seasonal rates of bed level change (*y*-axis) for all measurement stations. The maximum event-based threshold delimits the bed-level dynamics for which vegetation is present (left of graph). Circles: vegetated, squares: non-vegetated, filled: growing season, open: non-growing season.

pioneer marshes, both event-based and seasonal-based bed level dynamics were similar at all study sites. Moreover, vegetated and unvegetated stations at all salt marshes were characterized by a single event-based threshold for vegetation presence. At Marconi a single measurement station where vegetation presence could be expected by its short-term dynamics, was unvegetated (**Figure 11**). This might be explained by the fact that Marconi was a recently constructed marsh and the marsh profile still is developing toward a dynamic equilibrium, or if exposure is increasing, a persistent erosive trend will prevent for the presence of vegetation (**Figure 11**). This development and/or trend might be represented in the rate of change during the non-growing season. Still, bed level dynamics along the elevational gradient at the edge zone of well-established (natural) marshes does give insights in maximum dynamics for vegetation presence at semi-natural salt marsh construction and restoration sites.

Previous studies suggest that colonization of the bare tidal flat by pioneer vegetation depends on short-term morphodynamic dynamics (Balke et al., 2011; Hu et al., 2015b; Silinski et al., 2016; Poppema et al., 2019). Short-term bed level dynamics can prevent successful germination and dislodge young seedlings if roots are not anchored sufficiently (Hu et al., 2015b). The current study combines the studies on short-term bed level dynamics with studies suggesting medium-term seasonal and annual bed level change as explanation for vegetation presence (Bouma et al., 2016; van Regteren et al., 2019). For example erosion of the bed in the winter season might remove viable seeds of annual species, thereby limiting vegetation presence in the subsequent growing season (van Regteren et al., 2019). Interestingly, a prohibitive effect of accretion on the presence of vegetation was not observed at our study sites. Our findings show that vegetation presence is mainly driven by short-term event-based bed level dynamics. This might indicate that vegetation presence was not limited by viable seed availability at our study sites. Only a single unvegetated measurement station at the Marconi marsh might be hampered by a medium-term trend at the non-growing season.

Implications for Salt Marsh Construction and Restoration

While the salt marsh edge at natural salt marshes is relatively stable over the period of a year (Allen, 2000; Van der Wal et al., 2008; Singh Chauhan, 2009; Willemsen et al., 2020), the semi-natural constructed Marconi salt marsh was still developing, i.e., vegetation had first appeared only 1 year before starting the measurements. Similarities in variability of bed level dynamics around the marsh edge, both at the natural and semi-natural salt marshes, imply that bed level dynamics around natural salt marshes can be used as a proxy for the outline of salt marsh construction and restoration schemes. Locations where more hydrodynamic energy is present, leading to increasing bed level dynamics, require a higher elevation for vegetation to develop, or need additional protection (Cao et al., 2018, 2019; Willemsen et al., 2018). Similar bed level dynamics at the salt marsh edge suggest that disturbance-decreasing measures at the constructed Marconi salt marsh have been successful in creating sheltered areas to enhance vegetation presence (c.f. Fivash et al., 2021; Gijón Mancheño et al., 2021).

General parameterizations, such as the morphodynamic thresholds for vegetation presence presented in this study, can provide key insights for predictions of vegetation growth in intertidal areas. The current study highlights that local short-term bed level dynamics, that may be altered by local (temporary) management measures, control vegetation presence (c.f. Hu et al., 2021). Balke et al. (2016) introduced a generic hydrodynamic threshold for the presence of vegetation at the salt marsh edge, based on tidal inundation frequency. Combined, these thresholds can be used (1) to predict salt marsh development, and (2) to design nature-based solutions incorporating salt marshes including the requirement of sheltering structures to prevent structural medium-term erosion. Moreover, the use of thresholds instead of process-based modules for vegetation development in biogeomorphological models (Kirwan and Murray, 2007; Temmerman et al., 2007; Tonelli et al., 2010; Hu et al., 2015b; Best et al., 2018; Schwarz et al., 2018; Poppema et al., 2019; Willemsen et al., 2022), provides a simple rule-based approach for the simulation of vegetation development in numerical models (Huang et al., 2008), decreasing their complexity without assuming static vegetation (Horstman et al., 2015; Willemsen et al., 2016). Hence, existing numerical hydro-morphodynamic models for designing nature-based solutions (e.g., Siemes et al., 2020), can include the development of salt marsh vegetation by only assessing whether intertidal environments are suitable

for vegetation growth at different timescales, without increasing model complexity and computational cost. Obviously, a second step is to incorporate the feedbacks between the vegetation present and the hydro- and morphodynamics in its surroundings.

When aiming at salt marsh conservation, restoration or construction, e.g., for optimizing ecosystem services such as coastal protection (Möller et al., 2014) and carbon sequestration (Duarte et al., 2013), it is key to monitor the state of the ecosystem. In order to preserve the size of the ecosystem or to allow for its development, bed level dynamics induced by the combined action of tides and waves and modulated by the presence of vegetation should not exceed the event-based threshold that was identified to prevent vegetation from establishment and growth. The quantification of thresholds for bed level dynamics, combined with actively monitoring existing salt marshes and salt marsh restoration projects, provides critical insights on whether salt marsh systems are stable or will be accreting or eroding. Future research on longer-term periods than observed in the current study (years to decade) are essential for assessing the influence of climate change on long-term bed level change potentially hampering vegetation growth. Based on event-based and longer-term thresholds, adaptive management strategies can be developed. Once bed level dynamics come close to thresholds for vegetation presence, additional measures, such as construction of structures reducing physical stress and sediment nourishments, can be applied to protect the ecosystem and its services.

CONCLUSION

Present results suggest that event-based bed level dynamics can explain vegetation presence in salt marshes distributed across the Western Scheldt estuary, Wadden Sea and Ems-Dollard Estuary along the Dutch North Sea coast. Short-term bed level change is observed to provide a critical threshold for the presence of salt marsh vegetation. Vegetation at the well-established salt marsh was found to be present at event-based bed level variability smaller than or equal to 12 mm. The importance of local short-term dynamics for vegetation presence instead of longer-term dynamics highlights possibilities for developing preferential conditions for vegetation presence. So the limiting role of bed level dynamics on the presence of salt marsh vegetation is key to design and to predict the establishment of both restored and constructed salt marshes. Knowledge of these thresholds is critical for the development of adaptive management strategies for restoration and construction of salt marshes.

DATA AVAILABILITY STATEMENT

Data and scripts in support of this manuscript for the Western Scheldt and Wadden Sea study site and SED data conversion are available via DOI: 10.4121/uuid:c0be318c-9858-4a05-a546-782e29b4abef. Data and scripts for the Ems Dollard study site and ASED data conversion are available via DOI: 10.4121/16782613.

AUTHOR CONTRIBUTIONS

PW and MP conducted fieldwork for the study. MB was fieldwork leader of the constructed salt marsh. TB initiated the development of the optical-SED (O-SED) and acoustic-SED (A-SED) sensors used in this research. PW developed the post-processing script for the sensors and wrote the article with input from EH, TB, MB, MP, and BB. PW, EH, and BB designed the outline of the manuscript. All authors reviewed, revised, and approved the manuscript.

FUNDING

The Marconi field work was supported by the municipality of Delfzijl with funding from the Dutch Waddenfonds under grant number WF223001. Cash and in-kind co-funding was received from the consortium partners of EcoShape. Contributions by EH and PW were supported by the Mangrove-RESCUE project (Grant No. 15899), funded by the Dutch Research Council (NWO).

ACKNOWLEDGMENTS

We gratefully acknowledge A. de Vrieze and J. Veldman for their project guidance at the Marconi field site. We would like to thank Bente de Vries, Laura Coumou, Jelmer Cleveringa, Petra Dankers, and Kelly Elschot for collaboration during the EcoShape Marconi project. Furthermore, we would also like to thank A. Mus for extensively testing the A-SED sensors and J. van Dalen, L. van IJzerloo, and F. van Maarseveen for their technical assistance.

REFERENCES

Allen, J. R. L. (2000). Morphodynamics of Holocene salt marshes: a review sketch from the Atlantic and Southern North Sea coasts of Europe. *Quat. Sci. Rev.* 19, 1155–1231. doi: 10.1016/S0277-3791(99)00034-7

Andersen, T. J., Pejrup, M., and Nielsen, A. A. (2006). Long-term and high-resolution measurements of bed level changes in a temperate, microtidal coastal lagoon. *Mar. Geol.* 226, 115–125. doi: 10.1016/j.margeo.2005.09.016

Baeyens, W., van Eck, B., Lambert, C., Wollast, R., and Goeyens, L. (1997). General description of the Scheldt estuary. *Hydrobiologia* 366, 1–14. doi: 10.1023/a:1003164009031

Balke, T., Bouma, T. J., Horstman, E. M., Webb, E. L., Erftemeijer, P. L. A., and Herman, P. M. J. (2011). Windows of opportunity: thresholds to mangrove seedling establishment on tidal flats. *Mar. Ecol. Prog. Ser.* 440, 1–9. doi: 10.3354/meps09364

Balke, T., Herman, P. M. J., and Bouma, T. J. (2014). Critical transitions in disturbance-driven ecosystems: identifying windows of opportunity for recovery. *J. Ecol.* 102, 700–708.1.

Balke, T., Stock, M., Jensen, K., Bouma, T. J., and Kleyer, M. (2016). A global analysis of the seaward salt marsh extent: the importance of tidal range. *Water Resour. Res.* 52, 3775–3786. doi: 10.1002/2015WR018318

Baptist, M. J., Dankers, P., Cleveringa, J., Sittoni, L., Willemsen, P. W. J. M., Puijenbroek van, M. E. B., et al. (2021). Salt marsh construction as a Nature-based solution in an estuarine social-ecological system, the ems estuary. *Nat. Based Solut.* 1:100005. doi: 10.1016/j.nbsj.2021.100005

Baptist, M. J., Gerkema, T., van Prooijen, B. C., van Maren, D. S., van Regteren, M., Schulz, K., et al. (2019). Beneficial use of dredged sediment to enhance salt marsh development by applying a 'Mud Motor'. *Ecol. Eng.* 127, 312–323. doi: 10.1016/j.ecoleng.2018.11.019

Barbier, E. B., Koch, E. W., Silliman, B. R., Hacker, S. D., Wolanski, E., Primavera, J., et al. (2008). Coastal ecosystem-based management with nonlinear ecological functions and values. *Science* 319, 321–323. doi: 10.1126/science.1150349

Best, ÜS. N., Van der Wegen, M., Dijkstra, J., Willemsen, P. W. J. M., Borsje, B. W., and Roelvink, D. J. A. (2018). Do salt marshes survive sea level rise? Modelling wave action, morphodynamics and vegetation dynamics. *Environ. Modelling Softw.* 109, 152–166. doi: 10.1016/j.envsoft.2018.08.004

Borsje, B. W., van Wesenbeeck, B. K., Dekker, F., Paalvast, P., Bouma, T. J., van Katwijk, M. M., et al. (2011). How ecological engineering can serve in coastal protection. *Ecol. Eng.* 37, 113–122. doi: 10.1016/j.ecoleng.2010.11.027

Bouma, T. J., van Belzen, J., Balke, T., van Dalen, J., Klaassen, P., Hartog, A. M., et al. (2016). Short-term mudflat dynamics drive long-term cyclic salt marsh dynamics. *Limnol. Oceanogr.* 61, 2261–2275. doi: 10.1002/lno.10374

Bouma, T. J., van Belzen, J., Balke, T., Zhu, Z., Airoldi, L., Blight, A. J., et al. (2014). Identifying knowledge gaps hampering application of intertidal habitats in coastal protection: opportunities & steps to take. *Coast. Eng.* 87, 147–157. doi: 10.1016/j.coastaleng.2013.11.014

Callaghan, D. P., Bouma, T. J., Klaassen, P., van der Wal, D., Stive, M. J. F., and Herman, P. M. J. (2010). Hydrodynamic forcing on salt-marsh development: distinguishing the relative importance of waves and tidal flows. *Estuar. Coast. Shelf Sci.* 89, 73–88. doi: 10.1016/j.ecss.2010.05.013

Cao, H., Zhu, Z., Balke, T., Zhang, L., and Bouma, T. J. (2018). Effects of sediment disturbance regimes on Spartina seedling establishment: Implications for salt marsh creation and restoration. *Limnol. Oceanogr.* 63, 647–659. doi: 10.1002/lno.10657

Cao, H., Zhu, Z., James, R., Herman, P. M. J., Zhang, L., Yuan, L., et al. (2019). Wave effects on seedling establishment of three pioneer marsh species: survival, morphology and biomechanics. *Ann. Bot.* 125, 345–352. doi: 10.1093/aob/mcz136

Cox, R., Wadsworth, R. A., and Thomson, A. G. (2003). Long-term changes in salt marsh extent affected by channel deepening in a modified estuary. *Cont. Shelf Res.* 23, 1833–1846. doi: 10.1016/j.csr.2003.08.002

Damme, S. V., Struyf, E., Maris, T., Ysebaert, T., Dehairs, F., Tackx, M., et al. (2005). Spatial and temporal patterns of water quality along the estuarine salinity gradient of the Scheldt estuary (Belgium and The Netherlands): results of an integrated monitoring approach. *Hydrobiologia* 540, 29–45. doi: 10.1007/s10750-004-7102-2

De Vries, B., Willemsen, P., Van Puijenbroek, M., Coumou, L., Baptist, M., Cleveringa, J., et al. (2021). *Salt Marsh Pilot Marconi Monitoring Results (Report)*. Dordrecht: Ecoshape.

Dieckmann, R., Osterthun, M., and Partenscky, H. W. (1987). Influence of water-level elevation and tidal range on the sedimentation in a German tidal flat area. *Prog. Oceanogr.* 18, 151–166. doi: 10.1016/0079-6611(87)90031-0

Dillingh, D. (2013). *Kenmerkende Waarden Kustwateren En Grote Rivieren (Report)*. Delft: Deltares.

Duarte, C. M., Losada, I. J., Hendriks, I. E., Mazarrasa, I., and Marbà, N. (2013). The role of coastal plant communities for climate change mitigation and adaptation. *Nat. Clim. Change* 3:961. doi: 10.1038/nclimate1970

Esselink, P., Dijkema, K. S., Sabine, R., and Geert, H. (1998). Vertical accretion and profile changes in abandoned man-made tidal marshes in the dollard estuary, the Netherlands. *J. Coast. Res.* 14, 570–582.

Fivash, G. S., Temmink, R. J. M., D'Angelo, M., van Dalen, J., Lengkeek, W., Didderen, K., et al. (2021). Restoration of biogeomorphic systems by creating windows of opportunity to support natural establishment processes. *Ecol. Appl.* 31:e2333. doi: 10.1002/eap.2333

Folmer, E., Dekinga, A., Holthuijsen, S., Van der Meer, J., Mosk, D., Piersma, T., et al. (2017). *Species Distribution Models Intertidal Benthos: Tools For Assessing The Impact Of Physical And Morphological Drivers O Benthos And Birds In The Wadden Sea (Report)*.

Ford, M. A., Cahoon, D. R., and Lynch, J. C. (1999). Restoring marsh elevation in a rapidly subsiding salt marsh by thin-layer deposition of dredged material1Mention of trade names or commercial products does not constitute an endorsement or recommendation for use by the US Government.1. *Ecol. Eng.* 12, 189–205. doi: 10.1016/s0925-8574(98)00061-5

Gacia, E., and Duarte, C. M. (2001). Sediment retention by a mediterranean posidonia oceanica meadow: the balance between deposition and resuspension. *Estuar. Coast. Shelf Sci.* 52, 505–514. doi: 10.1006/ecss.2000.0753

Gijón Mancheño, A., Jansen, W., Uijttewaal, W. S. J., Reniers, A. J. H. M., van Rooijen, A. A., Suzuki, T., et al. (2021). Wave transmission and drag coefficients through dense cylinder arrays: implications for designing structures for mangrove restoration. *Ecol. Eng.* 165:106231. doi: 10.1016/j.ecoleng.2021.106231

Harmsworth, G. C., and Long, S. P. (1986). An assessment of saltmarsh erosion in Essex, England, with reference to the dengie peninsula. *Biol. Conserv.* 35, 377–387. doi: 10.1016/0006-3207(86)90095-9

Horstman, E. M., Dohmen-Janssen, C. M., Bouma, T. J., and Hulscher, S. J. M. H. (2015). Tidal-scale flow routing and sedimentation in mangrove forests: combining field data and numerical modelling. *Geomorphology* 228, 244–262. doi: 10.1016/j.geomorph.2014.08.011

Hu, Z., Borsje, B. W., van Belzen, J., Willemsen, P. W. J. M., Wang, H., Peng, Y., et al. (2021). Mechanistic modeling of marsh seedling establishment provides a positive outlook for coastal wetland restoration under global climate change. *Geophys. Res. Lett.* 48:e2021GL095596.

Hu, Z., van Belzen, J., van der Wal, D., Balke, T., Wang, Z. B., Stive, M., et al. (2015b). Windows of opportunity for salt marsh vegetation establishment on bare tidal flats: the importance of temporal and spatial variability in hydrodynamic forcing. *J. Geophys. Res.* 120, 1450–1469. doi: 10.1002/2014JG002870

Hu, Z., Lenting, W., van der Wal, D., and Bouma, T. J. (2015a). Continuous monitoring bed-level dynamics on an intertidal flat: introducing novel, stand-alone high-resolution SED-sensors. *Geomorphology* 245, 223–230. doi: 10.1016/j.geomorph.2015.05.027

Hu, Z., Willemsen, P. W. J. M., Borsje, B. W., Wang, C., Wang, H., van der Wal, D., et al. (2020). High resolution bed level change and synchronized biophysical data from 10 tidal flats in northwestern Europe. *Earth Syst. Sci. Data Discuss.* 2020, 1–19. doi: 10.5194/essd-2020-78

Hu, Z., Yao, P., van der Wal, D., and Bouma, T. J. (2017). Patterns and drivers of daily bed-level dynamics on two tidal flats with contrasting wave exposure. *Sci. Rep.* 7:7088. doi: 10.1038/s41598-017-07515-y

Huang, H.-M., Zhang, L.-Q., Guan, Y.-J., and Wang, D.-H. (2008). A cellular automata model for population expansion of Spartina alterniflora at Jiuduansha Shoals, Shanghai, China. *Estuar. Coast. Shelf Sci.* 77, 47–55. doi: 10.1016/j.ecss.2007.09.003

Kirwan, M. L., and Murray, A. B. (2007). A coupled geomorphic and ecological model of tidal marsh evolution. *Proc. Natl. Acad. Sci. U.S.A.* 104, 6118–6122. doi: 10.1073/pnas.0700958104

Ladd, C. J. T., Duggan-Edwards, M. F., Bouma, T. J., Pagès, J. F., and Skov, M. W. (2019). Sediment supply explains long-term and large-scale patterns in salt marsh lateral expansion and erosion. *Geophys. Res. Lett.* 46, 11178–11187. doi: 10.1029/2019gl083315

Lawler, D. M. (1991). A new technique for the automatic monitoring of erosion and deposition rates. *Water Resour. Res.* 27, 2125–2128. doi: 10.1029/91wr01191

Lawler, D. M. (2008). Advances in the continuous monitoring of erosion and deposition dynamics: developments and applications of the new PEEP-3T system. *Geomorphology* 93, 17–39. doi: 10.1016/j.geomorph.2006.12.016

Londo, G. (1976). The decimal scale for releves of permanent quadrats. *Vegetatio* 33, 61–64. doi: 10.1007/BF00055300

Maris, T., Cox, T., Temmerman, S., De Vleeschauwer, P., Van Damme, S., De Mulder, T., et al. (2007). Tuning the tide: creating ecological conditions for tidal marsh development in a flood control area. *Hydrobiologia* 588, 31–43. doi: 10.1007/s10750-007-0650-5

Mazik, K., Smith, J. E., Leighton, A., and Elliott, M. (2007). Physical and biological development of a newly breached managed realignment site, Humber estuary, UK. *Mar. Pollut. Bull.* 55, 564–578. doi: 10.1016/j.marpolbul.2007.09.017

Möller, I., Kudella, M., Rupprecht, F., Spencer, T., Paul, M., van Wesenbeeck, B. K., et al. (2014). Wave attenuation over coastal salt marshes under storm surge conditions. *Nat. Geosci.* 7, 727–731. doi: 10.1038/ngeo2251

Moskalski, S. M., and Sommerfield, C. K. (2012). Suspended sediment deposition and trapping efficiency in a Delaware salt marsh. *Geomorphology* 139-140, 195–204. doi: 10.1016/j.geomorph.2011.10.018

O'Brien, D. J., Whitehouse, R. J. S., and Cramp, A. (2000). The cyclic development of a macrotidal mudflat on varying timescales. *Cont. Shelf Res.* 20, 1593–1619. doi: 10.1016/S0278-4343(00)00039-X

Poppema, D. W., Willemsen, P. W. J. M., de Vries, M. B., Zhu, Z., Borsje, B. W., and Hulscher, S. J. M. H. (2019). Experiment-supported modelling of salt marsh establishment. *Ocean Coast. Manag.* 168, 238–250. doi: 10.1016/j.ocecoaman.2018.10.039

Pringle, A. W. (1995). Erosion of a cyclic saltmarsh in Morecambe Bay, North-West England. *Earth Surf. Process. Landf.* 20, 387–405. doi: 10.1002/esp.3290200502

Pye, K. (1995). Controls on long-term saltmarsh accretion and erosion in the wash, Eastern England. *J. Coast. Res.* 11, 337–356.

Rahman, H., Sherren, K., and van Proosdij, D. (2019). Institutional innovation for nature-based coastal adaptation: lessons from salt marsh restoration in nova scotia Canada. *Sustainability* 11:6735.

Rand, T. A. (2000). Seed dispersal, habitat suitability and the distribution of halophytes across a salt marsh tidal gradient. *J. Ecol.* 88, 608–621. doi: 10.1046/j.1365-2745.2000.00484.x

Schrift, A. M., Mendelssohn, I. A., and Materne, M. D. (2008). Salt marsh restoration with sediment-slurry amendments following a drought-induced large-scale disturbance. *Wetlands* 28, 1071–1085. doi: 10.1672/07-78.1

Schwarz, C., Gourgue, O., van Belzen, J., Zhu, Z., Bouma, T. J., van de Koppel, J., et al. (2018). Self-organization of a biogeomorphic landscape controlled by plant life-history traits. *Nat. Geosci.* 11, 672–677. doi: 10.1038/s41561-018-0180-y

Schwimmer, R. (2001). Rates and processes of marsh shoreline erosion in rehoboth bay, delaware, U.S.A. *J. Coast. Res.* 17, 672–683. doi: 10.2307/4300218

Siemes, R., Borsje, B. W., Daggenvoorde, R., and Hulscher, S. (2020). Artificial structures steer morphological development of salt marshes: a model study. *J. Mar. Sci. Eng.* 8:326. doi: 10.3390/jmse8050326

Silinski, A., van Belzen, J., Fransen, E., Bouma, T. J., Troch, P., Meire, P., et al. (2016). Quantifying critical conditions for seaward expansion of tidal marshes: a transplantation experiment. *Estuar. Coast. Shelf Sci.* 169, 227–237. doi: 10.1016/j.ecss.2015.12.012

Singh Chauhan, P. P. (2009). Autocyclic erosion in tidal marshes. *Geomorphology* 110, 45–57. doi: 10.1016/j.geomorph.2009.03.016

Stokes, D. J., Healy, T. R., and Cooke, P. J. (2010). Expansion dynamics of monospecific, temperate mangroves and sedimentation in two embayments of a barrier-enclosed lagoon, tauranga harbour, New Zealand. *J. Coast. Res.* 26, 113–122. doi: 10.2112/08-1043.1

Temmerman, S., Bouma, T. J., Van de Koppel, J., Van der Wal, D., De Vries, M. B., and Herman, P. M. J. (2007). Vegetation causes channel erosion in a tidal landscape. *Geology* 35, 631–634. doi: 10.1130/g23502a.1

Temmerman, S., Meire, P., Bouma, T. J., Herman, P. M. J., Ysebaert, T., and De Vriend, H. J. (2013). Ecosystem-based coastal defence in the face of global change. *Nature* 504, 79–83. doi: 10.1038/nature12859

Tonelli, M., Fagherazzi, S., and Petti, M. (2010). Modeling wave impact on salt marsh boundaries. *J. Geophys. Res.* 115:C09028.

van der Wal, D., and Pye, K. (2004). Patterns, rates and possible causes of saltmarsh erosion in the Greater Thames area (UK). *Geomorphology* 61, 373–391. doi: 10.1016/j.geomorph.2004.02.005

van der Wal, D., Pye, K., and Neal, A. (2002). Long-term morphological change in the Ribble Estuary, northwest England. *Mar. Geol.* 189, 249–266.

Van der Wal, D., Wielemaker-Van den Dool, A., and Herman, P. M. J. (2008). Spatial patterns, rates and mechanisms of saltmarsh cycles (Westerschelde, The Netherlands). *Estuar. Coast. Shelf Sci.* 76, 357–368. doi: 10.1016/j.ecss.2007.07.017

van Loon-Steensma, J. M. (2015). Salt marshes to adapt the flood defences along the Dutch Wadden Sea coast. *Mitig. Adapt. Strateg. Glob. Change* 20, 929–948. doi: 10.1007/s11027-015-9640-5

van Regteren, M., Colosimo, I., de Vries, P., van Puijenbroek, M. E. B., Freij, V. S., Baptist, M. J., et al. (2019). Limited seed retention during winter inhibits vegetation establishment in spring, affecting lateral marsh expansion capacity. *Ecol. Evol.* 9, 13294–13308. doi: 10.1002/ece3.5781

van Regteren, M., Meesters, E. H., Baptist, M. J., de Groot, A. V., Bouma, T. J., and Elschot, K. (2020b). Multiple environmental variables affect germination and mortality of an annual salt marsh pioneer: *Salicornia procumbens*. *Estuar. Coasts* 43, 1489–1501. doi: 10.1007/s12237-020-00735-y

van Regteren, M., Amptmeijer, D., de Groot, A. V., Baptist, M. J., and Elschot, K. (2020a). Where does the salt marsh start? Field-based evidence for the lack of a transitional area between a gradually sloping intertidal flat and salt marsh. *Estuar. Coast. Shelf Sci.* 243:106909.

van Regteren, M., ten Boer, R., Meesters, E. H., and de Groot, A. V. (2017). Biogeomorphic impact of oligochaetes (Annelida) on sediment properties and *Salicornia* spp. seedling establishment. *Ecosphere* 8:e01872.

Vuik, V., Borsje, B. W., Willemsen, P. W. J. M., and Jonkman, S. N. (2019). Salt marshes for flood risk reduction: quantifying long-term effectiveness and life-cycle costs. *Ocean Coast. Manag.* 171, 96–110. doi: 10.1016/j.ocecoaman.2019.01.010

Willemsen, P. W. J. M., Borsje, B. W., Hulscher, S. J. M. H., Van der Wal, D., Zhu, Z., Oteman, B., et al. (2018). Quantifying bed level change at the transition of tidal flat and salt marsh: can we understand the lateral location of the marsh edge? *J. Geophys. Res.* 123, 2509–2524. doi: 10.1029/2018JF004742

Willemsen, P. W. J. M., Borsje, B. W., Vuik, V., Bouma, T. J., and Hulscher, S. J. M. H. (2020). Field-based decadal wave attenuating capacity of combined tidal flats and salt marshes. *Coast. Eng.* 156:103628. doi: 10.1016/j.coastaleng.2019.103628

Willemsen, P. W. J. M., Horstman, E. M., Borsje, B. W., Friess, D. A., and Dohmen-Janssen, C. M. (2016). Sensitivity of the sediment trapping capacity of an estuarine mangrove forest. *Geomorphology* 273, 189–201.

Willemsen, P. W. J. M., Smits, B. P., Borsje, B. W., Herman, P. M. J., Dijkstra, J. T., Bouma, T. J., et al. (2022). Modelling decadal salt marsh development: variability of the salt marsh extent under influence of waves and sediment availability. *Water Resour. Res.* 58:e2020WR028962. doi: 10.1029/2020WR028962

Wolters, M., and Bakker, J. P. (2002). Soil seed bank and driftline composition along a successional gradient on a temperate salt marsh. *Appl. Veg. Sci.* 5, 55–62.

Ysebaert, T. J. W., Tjalling van der Wal, J., Tangelder, M., De Groot, A. V., and Baptist, M. J. (2016). *Ecotopenkaart Voor Het Eems-Dollard Estuarium (C095/15) (Report)*. IJmuiden: IMARES Wageningen UR.

Zhu, Z., Vuik, V., Visser, P. J., Soens, T., van Wesenbeeck, B., van de Koppel, J., et al. (2020). Historic storms and the hidden value of coastal wetlands for nature-based flood defence. *Nat. Sustain.* 3, 853–862. doi: 10.1038/s41893-020-0556-z

Zimmerman, J. T. F. (1976). Mixing and flushing of tidal embayments in the western Dutch Wadden Sea part I: distribution of salinity and calculation of mixing time scales. *Netherlands J. Sea Res.* 10, 149–191.

Conflict of Interest: The authors declare that the research was conducted in the absence of any commercial or financial relationships that could be construed as a potential conflict of interest.

Publisher's Note: All claims expressed in this article are solely those of the authors and do not necessarily represent those of their affiliated organizations, or those of the publisher, the editors and the reviewers. Any product that may be evaluated in this article, or claim that may be made by its manufacturer, is not guaranteed or endorsed by the publisher.

Copyright © 2022 Willemsen, Horstman, Bouma, Baptist, van Puijenbroek and Borsje. This is an open-access article distributed under the terms of the Creative Commons Attribution License (CC BY). The use, distribution or reproduction in other forums is permitted, provided the original author(s) and the copyright owner(s) are credited and that the original publication in this journal is cited, in accordance with accepted academic practice. No use, distribution or reproduction is permitted which does not comply with these terms.

APPENDIX 1

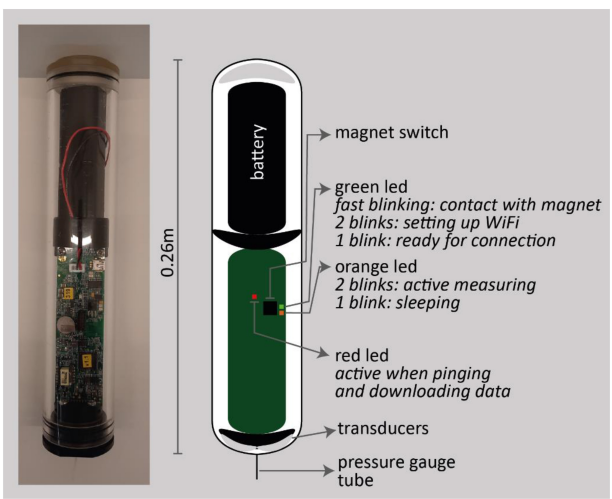
A-SED Data Conversion

The A-SED sensor is a stand-alone monitoring device for the measurement of bed level changes in submerged intertidal areas. The device consists of a vacuum housing containing a battery pack (eight alkaline AA batteries), circuit board and measurement head (**Appendix Figure A1**). The transparent housing is waterproof, with an airlock on top. Multiple LEDs are mounted on the circuit board, indicating the status of the device. Moreover, a magnet switch is installed on the circuit board to activate the instrument to establish a WiFi signal that is used to connect with a computer or mobile device. Once connected, A-SED settings and deployment settings can be adapted using a web browser. The measurement head at the bottom of the instrument consists of (1) two transducers for transmitting and receiving an acoustic signal for monitoring the distance between the instrument head and the bed, (2) a pressure gauge protected with a tube, and (3) a temperature sensor (**Appendix Figure A1**). The pressure is measured with increments of 0.1 mbar, both when the instrument is emergent and submerged. The temperature is monitored in degrees Celsius with a 2-decimal accuracy.

Bed level dynamics can be monitored with a number of samples at a fixed burst interval. In the current study a burst of 8 measurements (burst frequency is 5 Hz) was applied with an interval of 5–15 min. Since the A-SED instrument only collects data when inundated, the burst interval can be larger when the inundation period is relatively large at a measurement station and needs to be smaller when the inundation period is relatively shorter, in order to collect sufficient data during instrument submergence. Bed level dynamics are obtained with an acoustic signal of 300 kHz. The raw signal is transmitted by one transducer (emitter) and, after being reflected by the bed, received by the second transducer (receiver). The signal is received and stored every 250 ns over a domain of 4,000 timesteps (**Appendix Figure A2**). Due to initial contamination (initial noise) of the received signal due to the preceding signal emission (approximately first 500 timesteps in **Appendix Figure A2**), the optimal height above the bed of the instrument is 20–50 cm. After this initial noise dies out, a peak can be observed in the received signal which is induced by the reflection of the acoustic signal at the bed (**Appendix Figure A2**).

The raw data of the instrument is specified as intensity of the return signal. To obtain readable data, i.e., convert binary instrument output to real data values, the raw data are parsed. Subsequently, the readable data are post-processed to obtain the height above the bottom of the instrument. In the post-processing of the received signal, the first reflection of the bed is assumed to identify the distance to the bed, hence the minimum value of the reflected signal in front of the signal's peak, i.e., the moment were the first reflection of the bed is received by the transducer, determines the time it took the acoustic signal to travel to the bed and back. Post-processing consists of multiple steps (**Appendix Figure A2** and **Appendix Table TA1**):

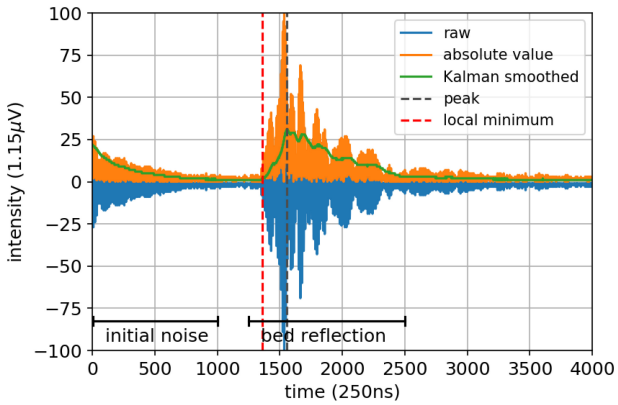
1. Absolute values of signal are calculated.
2. Check whether thresholds for initial noise in the first part of the return signal (window 1; to be manually specified) are exceeded.
3. Check whether thresholds for the peak value in the second part of the signal, where reflection of the bed can be expected (window 2; to be manually specified) are exceeded.
4. Absolute values of signal are smoothed using a Kalman filter.
5. Find location of peak value in window 1.



APPENDIX FIGURE A1 | Picture **(left)** and schematization **(right)** of A-SED instrument.

6. Find local minimum in the through in front of the peak.
7. Check whether a local minimum is obtained for all unique measurements in a single burst.
8. Calculate the distance to the bed for all unique measurements using a fixed speed of sound through (saline) water.
9. Apply a median filter per burst to calculate a burst averaged distance to the bed.
10. Calculate a standard deviation and remove burst averaged bed levels from data when a threshold is exceeded.
11. Convert the distance to the bed into a bed level with the (known) elevation of the instrument and apply calibration constant.

Parameters for calculating the HAB (**Appendix Table TA1**), can be adapted when the A-SED is deployed in a different environment. The Python script for parsing and post-processing data is available *via* DOI: 10.4121/16782613.



APPENDIX FIGURE A2 | Post-processing the raw signal to capture the HAB of the A-SED sensor.

APPENDIX TABLE TA1 | Parameter values for post-processing raw data.

Parameter	Value (unit)
Threshold for initial noise	40 (1.15 μV)
Threshold for peak value	50 (1.15 μV)
Kalman filter ratio	0.99 (–)
Speed of sound	1500 (m/s)
Threshold for standard deviation	0.002 (m)
Calibration factor	0.213

frontiers in Marine Science

ORIGINAL RESEARCH
published: 09 February 2022
doi: 10.3389/fmars.2021.814589

Green Nourishment: An Innovative Nature-Based Solution for Coastal Erosion

Wen L. Chen[1], Peter Muller[1†], Robert C. Grabowski[1] and Nicholas Dodd[2]*

[1] School of Water, Energy and Environment, Cranfield University, Cranfield, United Kingdom, [2] Faculty of Engineering, University of Nottingham, Nottingham, United Kingdom

Coastal erosion poses an urgent threat to life and property in low-lying regions. Sand nourishment is increasingly used as a nature-based solution but requires significant natural resources and replenishment over time. In this study, a novel form of nourishment is explored that combines shoreface nourishment and seagrass restoration to mitigate coastal erosion (i.e., green nourishment). Using the coastal morphodynamic model Xbeach, the impact of seagrass planting on wave energy dissipation, sediment erosion and transport, and morphological evolution of a cross-shore profile was studied for mild wave conditions and an intense storm. Model results indicate that a seagrass meadow enhances the wave energy dissipation provided by a shoreface nourishment, and suggests that it may be particularly effective in sediment transport mitigation when implemented in a sheltered nearshore area. The shoreface nourishment reduced the wave height on the seagrass meadow, and reduced the rate of seagrass destruction by deposition or erosion above the grass height after the storm event. Green nourishment also reduced beach foreshore erosion caused by a simulated storm event. An alternative, more cost-effective planting technique using seagrass seeds was explored, which showed similar coastal erosion protection benefits for seagrass transplants. This modeling study found that green nourishment is potentially an effective nature-based solution for coastal erosion and flooding on sandy coasts, and future studies are recommended to evaluate its morphological, ecological and flood risk reduction benefits in the field.

Keywords: shoreface nourishment, seagrass restoration, coastal retreat, storm resilience, coastal defense

OPEN ACCESS

Edited by:
Zhan Hu,
Sun Yat-sen University, China

Reviewed by:
A. Rita Carrasco,
University of Algarve, Portugal
Andrés Payo,
British Geological Survey, The Lyell Centre, United Kingdom

****Correspondence:***
Wen L. Chen
wenlong.chen@cranfield.ac.uk

†Present address:
Peter Muller,
Syndicat Mixte du Bassin de Thau (SMBT), Sète, France

Specialty section:
This article was submitted to Coastal Ocean Processes, a section of the journal Frontiers in Marine Science

Received: *13 November 2021*
Accepted: *20 December 2021*
Published: *09 February 2022*

Citation:
Chen WL, Muller P, Grabowski RC and Dodd N (2022) Green Nourishment: An Innovative Nature-Based Solution for Coastal Erosion. Front. Mar. Sci. 8:814589. doi: 10.3389/fmars.2021.814589

INTRODUCTION

Coastline retreat is a sign of the vulnerability of low-lying sandy coasts to erosion and sea level rise (Stronkhorst et al., 2018). This issue affects 70% of the world's sandy coasts and a large proportion of the United Kingdom's coastline experiences erosion rates higher than 0.1 m/year (30% in England) (Masselink and Russell, 2008; Williams et al., 2018). The severe threat induced by the gradual degradation of dunes, beaches and foreshores causes flood risks to people living nearby, and damage to buildings or infrastructure in coastal cities and villages (Stronkhorst et al., 2018). Existing literature and IPCC scenarios point to an increase in sea level rise (SLR) (Nicholls et al., 2007; Hinkel et al., 2013) and the frequency and intensity of extreme events associated with

waves (Menéndez and Woodworth, 2010; Izaguirre et al., 2011), resulting in a significant predicted increase in the number and severity of coastal flood events and erosion (Hinkel et al., 2013).

Measures for coastal protection often consist of engineering (i.e., hard) solutions such as breakwaters, dikes and groynes (Williams et al., 2018). However, hard sea defenses can exacerbate coastal erosion and cause adverse effects on the environment (Hamm et al., 2002). Therefore, there has been a shift away from hard coastal defenses to nature-based solutions. An alternative approach, commonly referred to as "Building with Nature," is to use natural materials such as sand, and to exploit the constructive forces of nature (i.e., currents and waves) to build and maintain natural flood defenses (Stronkhorst et al., 2018; Montgomery et al., 2019). In this vein, sand nourishments are increasingly used in the United Kingdom and Europe. Nourishments consist of collecting sand from offshore sandpits and placing the sand either directly on the beach or as a sand buffer on the eroding foreshore (van Duin et al., 2004), replenishing the beach and dissipating wave energy during storms (Stronkhorst et al., 2018). Over time, the deposited sand will be transported to and along the shore, providing an input to the coastal sediment budget. Such nature-based flood defenses provide several ecosystem services, including flood protection, recreation and nature conservation, in addition to long term intervention for SLR (Temmerman et al., 2013). They are considered to be unobtrusive coastal interventions with low costs and environmental impacts in comparison to traditional hard engineering (Bergillos et al., 2018). Shoreface nourishments are usually placed as relatively long (2–10 km) sand bodies, in depths ranging from Mean Sea Level (MSL) −10 to −4 m (Huisman et al., 2019), which reduce wave energy approaching the shore, thus providing protection. However, as these nourishments suffer from relatively quick sand loss, they need to be replenished periodically (typical 3–10 years interval), implying significant costs and the need for large sand resources that many maritime countries do not possess (de Schipper et al., 2016).

Seagrass provides a potential nature-based solution to reduce wave-generated erosion and extend the timespans for coastal benefits at nourishment sites. Seagrass has historically been found in temperate and subtropical oceans around the world, but its distribution has been significantly impacted by direct and indirect human activity (e.g., dredging, pollution). Seagrass beds are ecologically important marine habitats (Boudouresque et al., 2021; da Ros et al., 2021) that stabilize sandy substrates through the binding effects of their roots and rhizomes and, through the hydrodynamic buffering capabilities of their leaves, dissipate wave energy, tidal currents and storm surges (Fonseca, 1994; Reidenbach and Thomas, 2018; Montgomery et al., 2019). A dense seagrass meadow is able to reduce wave height by 40% during storm events (Ondiviela et al., 2014). Seagrass restoration projects are progressing worldwide and show promising survival rate of the seagrass planting (**Figure 1**; Marion and Orth, 2010; Tanner and Parham, 2010; van Katwijk et al., 2016; Unsworth et al., 2019; Boudouresque et al., 2021). Whilst sheltered hydrodynamic conditions are typically recommended, the use of large transplants (Paulo et al., 2019) and biodegradable materials to contain the seeds and stabilize the plant during the initial period of planting significantly increases the survival rate (Irving et al., 2014; Tan et al., 2020; Gagnon et al., 2021). Using hessian seed bags anchored along strings to seabed (**Figure 1C**), a *Zostera marina* restoration site in the sea at Cornwall and Swansea (under tide of 7.68 m range) had a 94% survival rate after 10 months of seagrass planting (Unsworth et al., 2019). Seagrass transplanting using containers made of corn anchored by steel rods in the Adriatic Sea reached a 30% survival rate in a stormy winter (da Ros et al., 2021; **Figure 1B**). Seagrass plantings have been successful even along coasts exposed to high wave energy, i.e., coasts in Portugal (Paulo et al., 2019), South Australia (Tanner and Parham, 2010; Wear et al., 2010) and Cornwall (Unsworth et al., 2019). Integrating vegetation, mangroves and salt marshes into coastal defense has the potential to significantly cut the cost of coastal protection (van Zelst et al., 2021). A recent successful field construction of salt marsh (Baptist et al., 2021) and an analysis on historic data (Zhu et al., 2020) revealed the high efficiency of coastal wet-land as a nature-based flood defense even with long-term sea level rise, which sheds light on the hidden role of seagrass restoration in coastal protection.

"Green nourishment," i.e., the combination of sand nourishment and seagrass meadow restoration, has the potential to provide a nature-based and effective method to mitigate coastal erosion and flooding. Whilst numerous studies have investigated the impacts of nourishment and, separately, the survival and growth of seagrass restoration, so far none has investigated the impacts of green nourishment on coastal geomorphic and flooding impacts. In particular, the influence of the seagrass meadow's location, size, and planting technique on its ability to reduce wave energy and sediment transport when combined with a nourishment must be investigated to provide an indication on how the seagrass meadow and nourishment could be combined in order to maximize coastal protection and reduce erosion. The aim of this study is to use a modeling approach to explore how green nourishment affects cross-shore sediment transport and geomorphic dynamics using the coastal morphodynamic model XBeach (Roelvink et al., 2009). Specific objectives are to determine the impacts of seagrass location, size and planting technique on the evolution of cross-shore morphology and wave height, and the resilience of a green nourishment to storm events.

MATERIALS AND METHODS

The simulations were carried out using XBeach, which is a widely used model to predict waves, currents, sediment transport, and morphology change under various wave conditions (Roelvink et al., 2009). It is an open-source code that has been validated in a large number of cases for hydrodynamics and morphological changes (McCall et al., 2010; Dissanayake et al., 2014; Lashley et al., 2018; Roelvink et al., 2018). In this study, the cross-shore time-dependent short wave action balance equation on the scale of wave groups was solved using the 1D instationary "surfbeat" mode of XBeach. The infragravity (IG) wave motions and mean flow were driven by the radiation stress gradient in the non-linear shallow water equations. The JONSWAP (Joint North Sea Wave

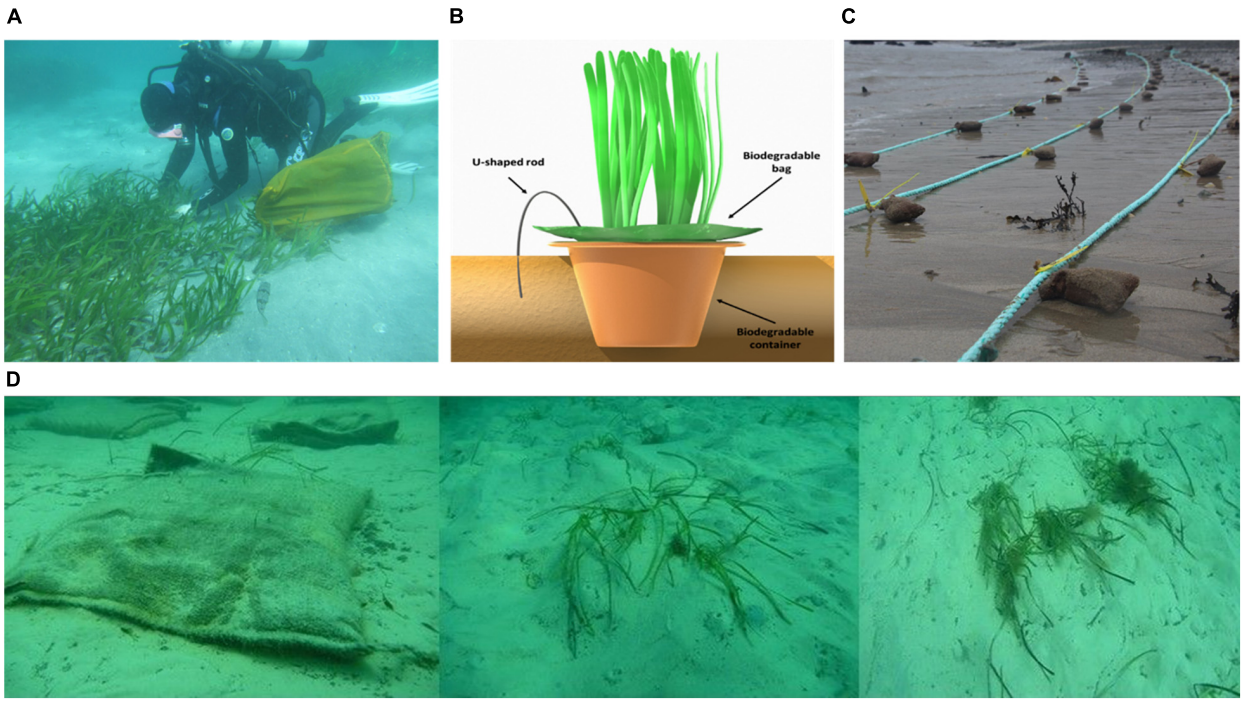


FIGURE 1 | (A) Seagrass transplant, ©Project SEAGRASS.LI (photos by Chris Pickerell, Cornell Cooperative extension of Suffolk County, NY); **(B)** seagrass transplant with biodegradable container (da Ros et al., 2021); **(C)** seagrass planting with hessian seed bags, ©Project Seagrass (photo taken in Porthdinllaen, Wales); **(D)** the germination and growth of hessian seed bag, ©SARDI (photos by Jason Tanner).

Project) spectral boundary conditions were applied along the offshore boundary. In approaching the coast, the wave energy was dissipated by wave breaking (Roelvink, 1993), bottom friction (van Dongeren et al., 2013; Quataert et al., 2015) and vegetation (Mendez and Losada, 2004). The short wave dissipation due to vegetation was calculated using the formulation of Mendez and Losada (2004), i.e., a function of the local wave height and several vegetation parameters at the designated seagrass location. The vegetation is notionally schematized as a rigid cylinder, with parameters including vegetation stem height (a_h), diameter (b_v), and density (N_v). Multiple layers of vegetation could be introduced to define for instance mangroves, which have dense roots and sparse stems. Here one vertically uniform vegetation layer was used to simulate seagrass. The seagrass was introduced through a characteristic file which defines the seagrass parameters and a vegetation location file. To account for the progressive growth of the seagrass, the vegetation module of XBeach was modified in this study to allow a time-dependent vegetation parameter. This modification adds a time parameter "$T_{v,m}$" to represent the mature period of the seagrass. In this study, growth rate was modeled as linear, but any growth rate curve can be implemented. The damping effect of vegetation not only affects the dissipation of wave energy, but also the infragravity waves and mean flow, and is modeled as a drag force added to the momentum equation (van Rooijen et al., 2016). The dissipation and drag effect of vegetation were present only where vegetation was defined in the location file. The XBeach with vegetation module (van Rooijen et al., 2016) has been successfully applied to evaluate the global role of vegetation in flood defense (van Zelst et al., 2021).

The sediment transport is simulated using a depth-averaged advection-diffusion equation where the van Thiel-van Rijn formulation is adopted for the calculation of sediment flux (van Rijn, 2007; van Thiel de Vries, 2009). One important mechanism for the onshore sediment flux is the wave non-linearity (Chen and Dodd, 2019), which is the change of wave shape due to wave shoaling and breaking. As a wave shoals, the wave shape changes from sinusoidal to an increasingly skewed shape, with a narrow-accentuated crest followed by a broad flat trough. Toward and after breaking, the wave shape progressively changes to a highly asymmetrical shape, i.e., a pitched-forward shape with a steep front face. As a result, the time histories of both near-bed flow velocity and acceleration also become asymmetric; i.e., the skewness (velocity skewness) and asymmetry (acceleration skewness) also increase. The increase of skewness and asymmetry of the wave as it propagates to the coast leads to increased onshore sediment flux. Here, the effect of change in wave shape on the sediment transport was approximated as an extra velocity term in the advection-diffusion equation, i.e.,

$$u_a = \gamma_{ua} (S_k - A_s) u_{rms}, \quad (1)$$

with S_k denoting the wave skewness, A_s the wave asymmetry, and u_{rms} the root mean square wave orbital velocity near bed. A higher value for u_a will simulate a stronger onshore sediment flux. Recent studies show that the parameter γ_{ua} should take a

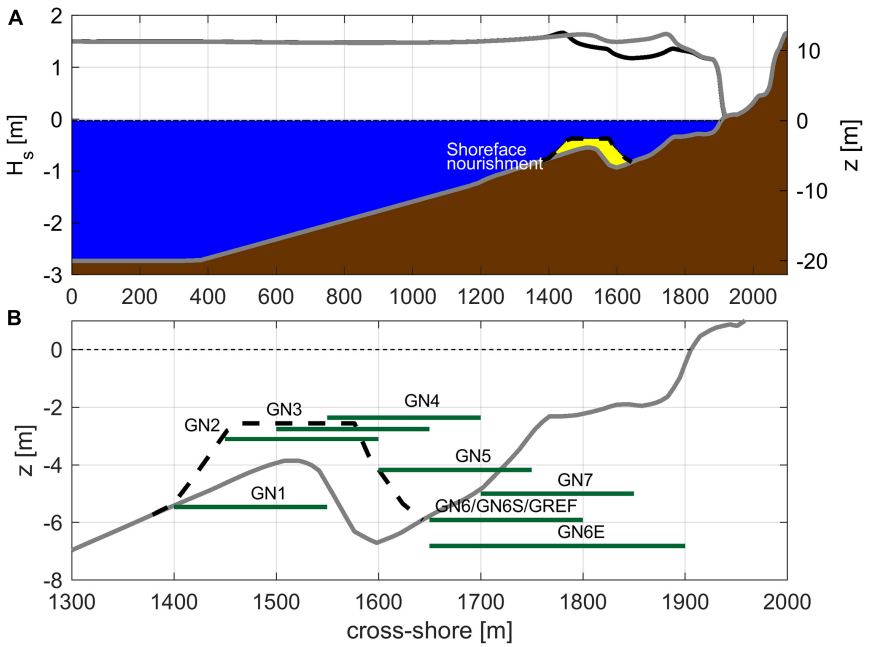


FIGURE 2 | Geometry showing: **(A)** nourishment on top of a nearshore sand bar and the significant wave height profile under mild wave condition (H_m = 1.5 m, T = 8 s), with gray line for wave height for the reference (REF) and black line for wave height for the nourishment reference (SN); **(B)** location and length of seagrass meadows.

higher value than the default ($\gamma_{ua} = 0.1$) to correctly simulate the beach erosion (Elsayed and Oumeraci, 2017). Here, a γ_{ua} value of 0.3 is taken (Jin et al., 2021). Seabed updating results from the Exner equation, i.e., convergence/divergence of sediment flux leads to deposition/erosion. The avalanching scheme is introduced to update the foreshore face of the dune to account for the slumping of sandy materials, where two separate critical slopes for dry and wet points are used. Sand is exchanged in between adjacent cells once this critical slope is exceeded. All parameters in XBeach take default value unless specified.

RESULTS

Geometry and Runs

The geometry consists of a beach connecting a region of constant depth 20 m, on which there is a longshore uniform sand bar (top of the bar at x = 1,520 m). At mean sea level, the shoreline is located at x = 1,905 m. A shoreface nourishment of 400 m^3/m sand was placed on top of the sand bar (**Figure 2**). Both the native sand and nourishment have median grain size of 0.3 mm and porosity of 0.4. The sediment characteristic and seabed profile represented typical Dutch coast (i.e., Kijkduin, Holland; Stronkhorst et al., 2018). The common eelgrass (*Zostera marina)* was chosen for the study because it is widely distributed. Its characteristics, such as height at maturity (a_h = 50 cm), drag coefficient, stem diameter (b_v = 1 cm), density (N_v = 1,000/m^2) and growth rate, were obtained from the literature (Fonseca, 1994; Tyler-Walters, 2008; Tanner and Parham, 2010; Folkard, 2011). In total 26 simulations were performed, including a reference (REF) case without nourishment or seagrass, a geomorphic reference (GREF) case without nourishment but with seagrass, and a shoreface nourishment (SN) case with the nourishment but without seagrass. The experimental simulations included seven green nourishment cases (GN1-7) with seagrass planting located at the nourishment or closer to the shore, a green nourishment with extended seagrass meadow (GN6E), and a green nourishment with seed planting technique (GN6S) (**Table 1**). Mature seagrass was assumed to be planted at the beginning of the simulation unless seed planting technique was applied in which a linear growth curve was adopted for seagrass parameters. The seagrass meadow covered 150 m in the cross-shore direction except for GN6E which covered 250 m. The sensitivity of green nourishment to wave conditions was tested (GN6W1-6) by varying wave height from H_m = 1.5 m to H_m = 4.5 m and wave period from T = 8 s to T = 11 s. The effect of seagrass parameters was studied (GN6a1-4 and GN6n1-4) by varying a_h from 10 to 90 cm and N_v from 200 to 1,800/m^2. All simulations lasted for 100 days, except in cases REF, GREF, SN, GN6, and GN6E, where a 1 week storm event (H_m = 5 m, T = 12 s) was performed following the 100 days simulation to investigate the resilience of green nourishment to storm attack. The wave climate implemented into the model is based on the typical United Kingdom and Dutch coasts' wave climates. It is characterized by average significant wave height oscillating between 1 and 2.5 m and a wave period ranging from 6 to 10 s, while the typical winter storms are characterized by wave heights of 4 to 5 m and a wave period ranging from 10 to 12 s (Wijnberg, 2002; Sembiring et al., 2015; Dhoop and Mason, 2018). A gradually refined grid toward the coast with maximum

TABLE 1 | Simulation runs tested the impacts of nourishment, the location of a seagrass meadow, the planting techniques, seagrass meadow length, and mild vs. storm waves.

Cases	Nourishment location	seagrass planting location	Seagrass parameters			Seagrass planting technique	Wave conditions			Storm event (H_m = 5 m, T = 12 s)
			a_h	b_v	N_v		H_m	T	duration	
REF	N/A	N/A	N/A	N/A	N/A	N/A	1.5 m	8 s	100 days	7 day
GREF		(1,650 m, 1,800 m)	50 cm	1 cm	1,000/m^2	Mature plant				
SN	(1,379 m, 1,673 m)	N/A	N/A	N/A	N/A	N/A				
GN1		(1,400 m, 1,550 m)	50 cm	1 cm	1,000/m^2	Mature plant				N/A
GN2		(1,450 m, 1,600 m)								
GN3		(1,500 m, 1,650 m)								
GN4		(1,550 m, 1,700 m)								
GN5		(1,600 m, 1,750 m)								
GN6		(1,650 m, 1,800 m)								7 day
GN7		(1,700 m, 1,850 m)								N/A
GN6E		(1,650 m, 1,900 m)								7 day
GN6S		(1,650 m, 1,800 m)				Seeds				N/A
GN6W1						Mature plant	2 m	8.5 s		
GN6W2							2.5 m	9s		
GN6W3							3 m	9.5 s		
GN6W4							3.5 m	10 s		
GN6W5							4 m	10.5 s		
GN6W6							4.5 m	11 s		
GN6a1			10 cm				1.5 m	8 s		
GN6a2			30 cm							
GN6a3			70 cm							
GN6a4			90 cm							
GN6n1			50 cm		200/m^2					
GN6n2					600/m^2					
GN6n3					1,400/m^2					
GN6n4					1,800/m^2					

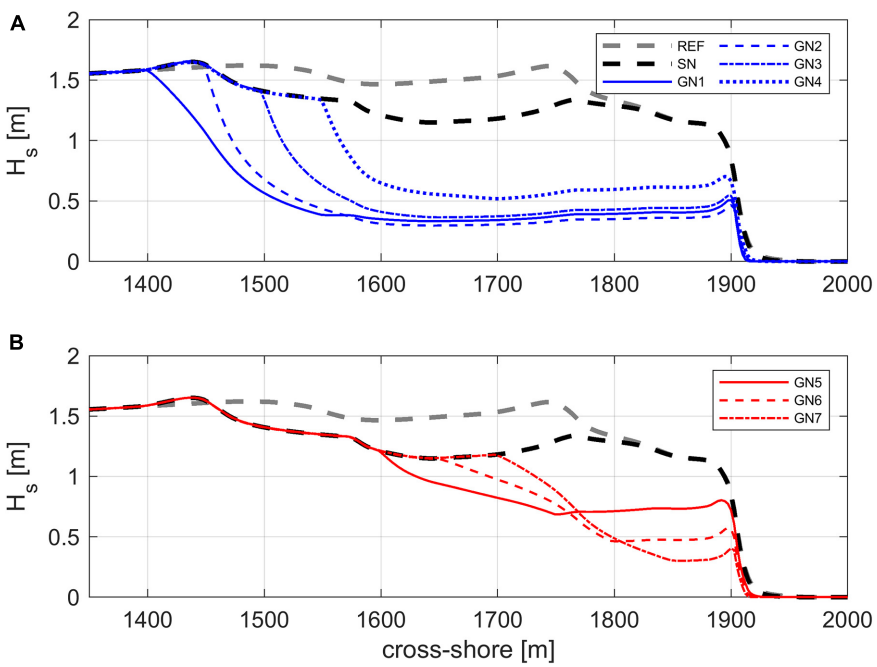


FIGURE 3 | Cross-shore wave height distribution under mild wave (i.e., H_m = 1.5 m, T = 8 s) for: **(A)** case REF, SN, GN1-4; and **(B)** case GN5-7.

cell size of 15 m at the offshore boundary and minimum cell size of 1 m in the nearshore region was selected considering a balance between accuracy and calculation burden. The maximum Courant number is given as 0.9 and a morphological acceleration factor of 10 is defined.

Under the mild wave condition (H_m = 1.5 m, T = 8 s), the gray profile for the REF case showed the incident waves beginning to break on the sandbar (x = 1,520 m), and then more pronounced breaking near shore (x = 1,745 m) (**Figure 2A**). The nourishment (SN) intensified the wave breaking on the bar and shifts seaward the breaking point to x = 1,440 m, which led to a reduced wave height shoreward, compared to the REF case, covering approximately 400 m in the cross-shore direction. A maximum drop of 22% of wave height was observed at shoreward side of the nourishment. Consequently, the shore breaking of SN case has a lower height than that of the REF case, i.e., 1.336 m compared with 1.615 m, and at a slightly shoreward location (x = 1,764 m).

The Evolution of Green Nourishment and Effect of Seagrass Meadow Location

The combination of shoreface nourishment and seagrass planting significantly reduced the wave height (**Figures 3**, **4**). This impact was particularly strong when the location of the seagrass meadow coincided with the wave breaking zone (i.e., at bar breaking region and shore breaking region for SN, **Figures 2**, **3**). For all GN cases, there was a rapid decrease in H_s at start of the seagrass bed (see **Figures 3**, **4**). This reduction was particularly rapid for GN1-4. In these cases, the plantings were entirely or partially on the nourishment and coincided to a greater or lesser extent with the bar breaker region. For GN1-3, H_s diminished to a similar, post-planting level ($H_s \approx 0.35$ m), which extended until the waves began to break again closer to the shore (at about x = 1,897 m). For GN4-5, H_s was also reduced by the planting, but because the local depth increased on the more shoreward section of the planting, H_s reached a larger post-planting constant value ($H_s \approx 0.55$ and 0.7 m), which extended until the shore break. In the final two cases, GN6 and GN7, the wave height decay showed a different cross-shore pattern. The plantings were located closer to shore, in the shallowest areas coinciding with the shore breaking region, and so, once again, there was a combined effect of breaking and the planting, which resulted in smaller post-planting H_s values.

The green nourishment provided the maximum dissipative effect when the vegetation region coincided with the bar breaker zone (GN1-3). For example, the seagrass meadow of GN2 was located on the nourishment in the area with the greatest wave height induced by the nourishment (SN, **Figure 2**) and led to a maximum reduction of 1.3 m in the wave height by the shoreward edge of the planting compared with the REF case, accounting for 80.3% of the REF wave height (**Figures 3A**, **4A**). The strong turbulence and high wave orbital velocities associated with the breaker zone could pose a high risk of erosion for seagrass. Thus, results from GN6 and GN7, which cover the shoaling and breaking zone of shore breaking of SN case, are particularly interesting, because they lead to a reduction of 0.9 m (73.8%, see **Figure 4B**) wave height at the shore breaking region, and, for GN7, a particularly small at the shore. At the shoreline, the wave reduction of green nourishment is up to 100%, which is because the seaward shift of the wave uprush at the coast induced by the wave attenuation.

Seagrass is able to effectively attenuate long period wave motion, i.e., the infragravity wave (**Figure 5**). Here the infragravity waves were generated by the variation in the water surface time series (Roelvink et al., 2009). Seagrass is responsible for the reduction of peak IG wave height. Among GN1-7, GN1 leads to the most prominent reduction, i.e., from 0.44 m in REF to 0.20 m in GN1. Under mild wave condition, the attenuation effect of seagrass on IG wave height is not as significant as on the incident wave height (**Figures 3**, **4**), with a maximum reduction of 54.5% on IG wave height compared with a 80.3% reduction on incident wave height. Variation in the attenuation effect on IG waves is big between GN1-4 but small in between GN4-7. Nourishment also leads to a minor reduction of peak IG wave height. A similar seaward shift is observed for the uprush of IG wave at the shoreline.

Onshore sediment flux was observed for SN and GN1-7 cases as waves shoal and break (**Figure 6A**). In contrast, for the REF case, there was relatively little onshore sediment movement within the offshore region. Furthermore, shoreward in the REF case, offshore sediment flux was observed shoreward, peaking at x = 1,750 m, probably induced by the return flow after breaking. Strong offshore sediment flux was observed at the coast for both REF and SN cases, which is induced by the combined effect of strong undertows during shore wave breaking and the backwash from the infragravity wave run-up (**Figure 6A**). Nourishment resulted in greater onshore sediment flux, especially on the nourishment itself, and also reduced the offshore sediment flux at the shore. For GN1-7 cases, the offshore sediment flux measured at the coast was almost one order of magnitude smaller than that of the REF and SN cases, as most of the incident wave energy was dissipated by the nourishment and the vegetation. The attenuation of the infragravity waves by the seagrass also contributes to the reduction of offshore sediment flux at the shore. At GN6 and GN7, the sediment fluxes at the seagrass meadow were significantly lower than that at GN2, suggesting less turbidity and better light condition in the water (**Figure 6B**). Compared with GN2, seagrass was located in a more sheltered environment in GN6 and GN7.

For green nourishment, the seabed stayed stable in the region immediately shoreward of the seagrass meadow and erosion at the shore is reduced compared to REF and SN in all cases (**Figure 7**). Bed change offshore was reduced most in case GN1, where the seagrass was located centrally on the nourishment, and at the shore in GN7, which had the most shoreward planting. Under mild wave conditions, onshore migration of the nearshore sand bar was observed as sand being eroded at the seaward side and deposited at shoreward side (i.e., in between x = 1,400 m and x = 1,650 m). Considerable erosion was observed at the foreshore of beach (i.e., for x > 1,905 m), which resulted from the strong offshore sediment flux induced by undertow as waves wash over the beach. For SN, the nourishment led to stronger onshore sand migration, which was due to the increased onshore sediment flux induced by amplified wave non-linearity on top

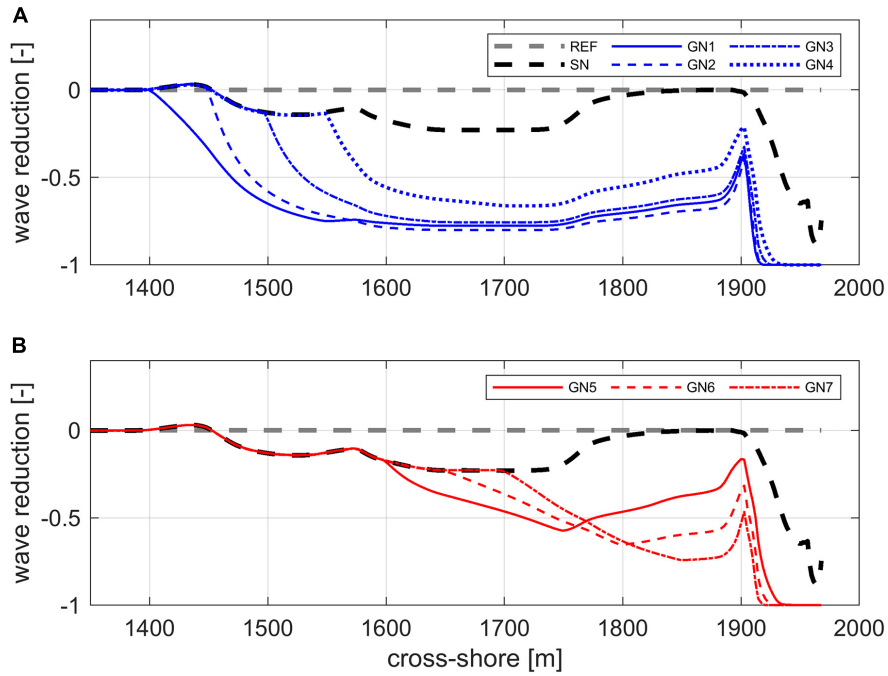


FIGURE 4 | Wave height reduction (i.e., wave height difference compared with the REF case) under mild wave for: **(A)** case SN, GN1-4; and **(B)** case GN5-7.

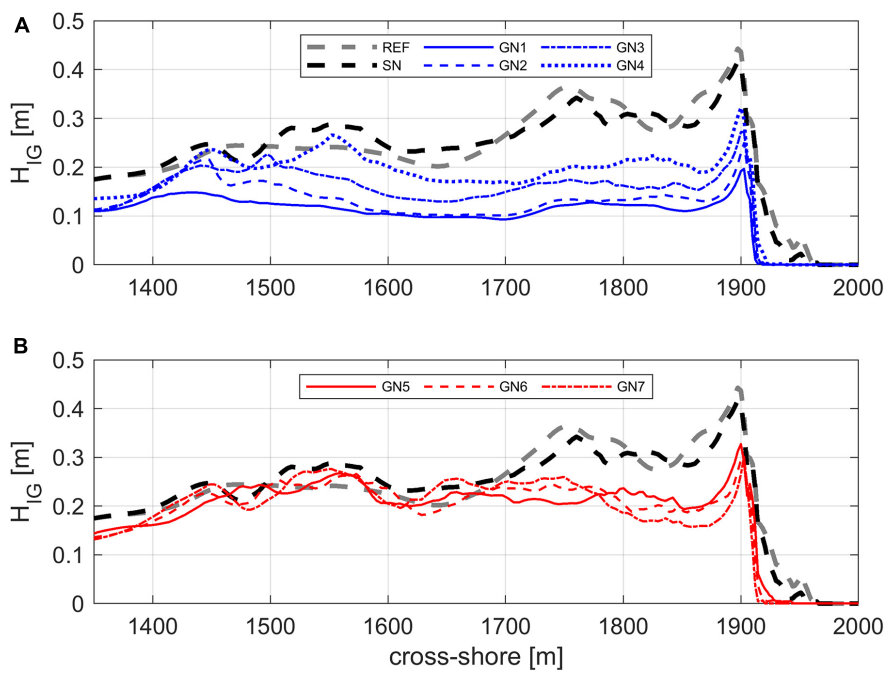


FIGURE 5 | Cross-shore infragravity wave height (H_{IG}) distribution under mild wave (i.e., H_m = 1.5 m, T = 8 s) for: **(A)** case REF, SN, GN1-4; and **(B)** case GN5-7.

of the nourishment (Chen and Dodd, 2019). For SN, a stable seabed was observed in between 1,650 and 1,750 m at the end of 100 days of simulation. As mentioned, little change was observed for GN1-7 immediately shoreward of the seagrass meadow, in contrast to the active bathymetry change over the whole shoaling and breaking zone of the REF case. GN1 seems to have the most stable seabed shoreward of seagrass meadow. However, more than half the seagrass meadow encounters disturbance of either erosion or deposition as revealed by the bury ratio analysis (i.e., $\Delta z_b/a_h$ the ratio of changed seabed divided by

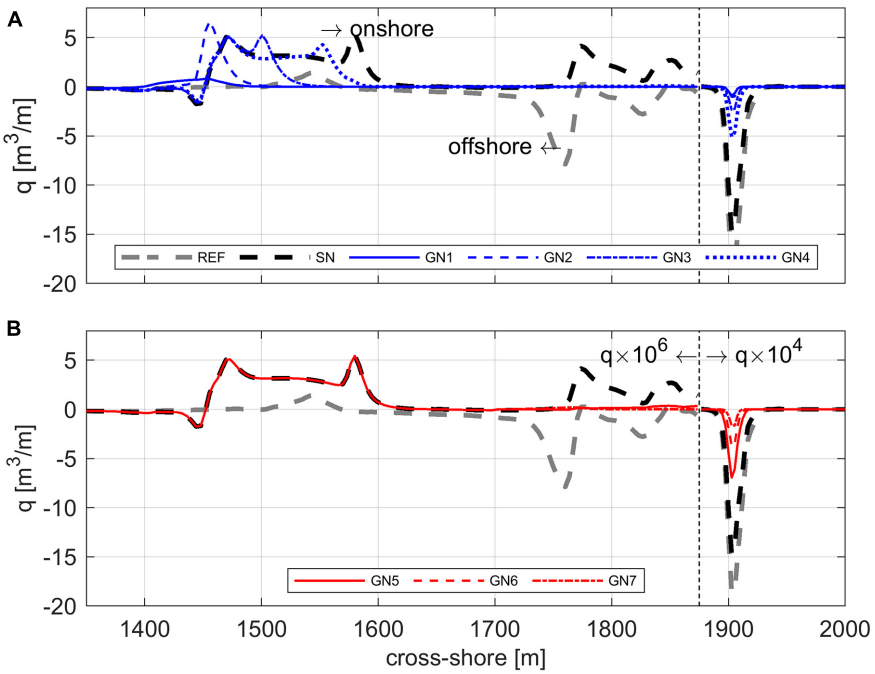


FIGURE 6 | Cross-shore sediment flux for: **(A)** case REF, SN, and GN1-4; and **(B)** case GN5-7. Note that the value was amplified for illustration purpose with a factor of 10^6 and 10^4 in seaward and shoreward of x = 1,875 m, respectively. Positive and negative value indicates onshore and offshore directed sediment flux.

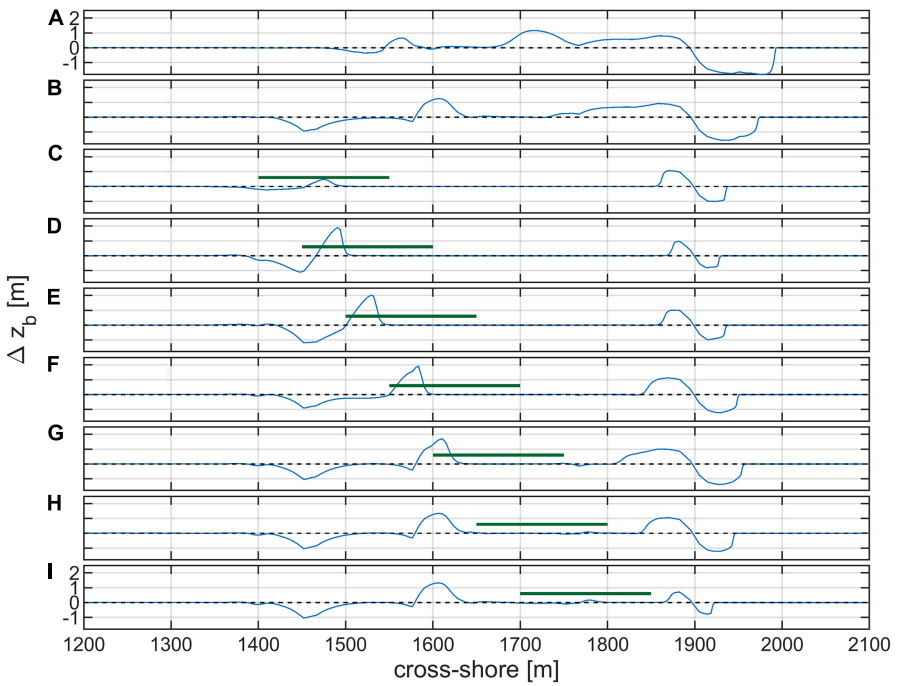


FIGURE 7 | Change of seabed under mild wave condition for 100 days, showing: **(A)** REF seabed; **(B)** SN bed; **(C–I)** GN1-7. Green horizontal line indicates the location of the seagrass meadow.

the seagrass shoot height, **Figure 8A**). The bury ratio of GN1 ranges from -0.75 to 1, suggesting either root removal or shoot burying. For a seagrass meadow located at more shoreward position, the percentage of burying seagrass meadow reduces. The maximum bury ratio of GN2, GN3, GN4, and GN5 is as high as 4. GN6 and GN7, on the other hand, have bury

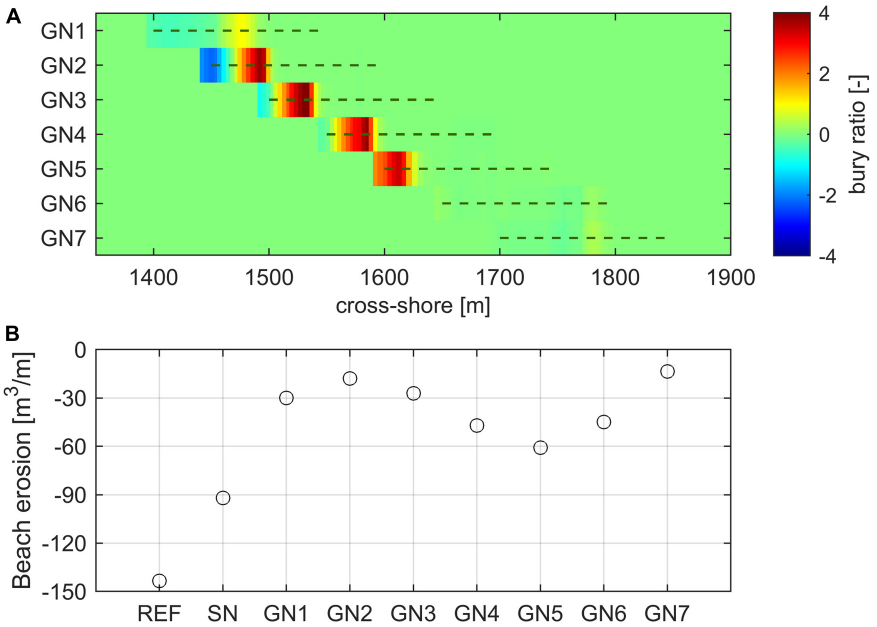


FIGURE 8 | The bury ratio of green nourishment **(A)** and beach erosion under 100 days mild wave condition for all cases **(B)**.

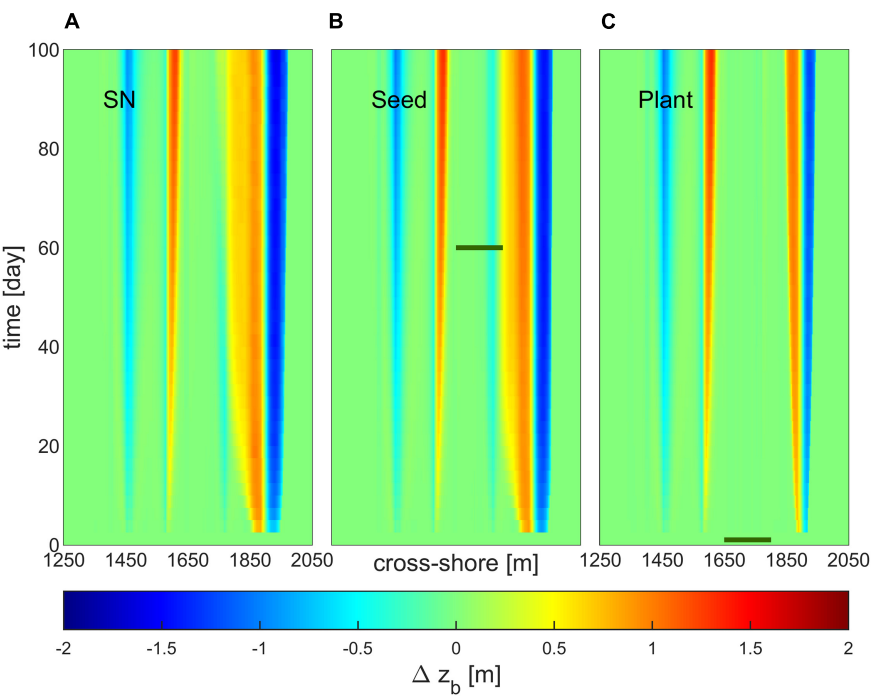


FIGURE 9 | Change of seabed over time for: **(A)** shoreface nourishment only; **(B)** seed planting assuming linear growing seagrass; **(C)** mature seagrass planting. Green lines indicate the range of the seagrass meadow and the mature timing of the plant.

ratio less than 0.2 all over the seagrass meadow and has the least disturbance percentage. For GN1-7, the beach erosion, i.e., defined as integrated sand erosion shoreward of the shoreline (i.e., $x > 1{,}905$ m), were significantly reduced compared with the REF case, i.e., from 150 m^3/m to less than 60 m^3/m (**Figure 8B**). Meanwhile, the landward limit of the beach erosion in GN1-7 has been limited to $x = 1{,}926$ m instead of $x = 1{,}971$ m in the REF case, which agrees with the seaward shift of both incoming wave and IG wave at the shoreline. Of the GN1-7 cases, GN7 had the least erosion whereas GN5 has the most erosion.

The severity of beach erosion highly correlated with the wave height and IG wave height at the coast (**Figures 3**, **5**).

Exploring the Seagrass Planting Technique: Seed Planting

Seed planting (GN6S) generated similar results to the deployment of pre-grown plants at the beginning of the simulation (GN6) (**Figure 9**). Most of the seeded region reached maturity at the end of 100 days simulation. The seed planting technique was implemented with an altered vegetation module, in which a slow linear growth rate was used for the first 10 days, i.e., 5 cm shoot height for the first 10 days, and a faster growth rate for another 50 days, i.e., 45 cm shoot growth for the following 50 days. The seagrass was supposed to reach a mature state on the 60th day after planting (i.e., $T_{v,m}$ = 60 days). Erosion at the shoreward end of the seagrass meadow is induced by the shoaling and breaking of wave at that region (i.e., shore breaking zone of SN in **Figure 3**) before the seagrass is mature enough to provide protection, which is the reason why not all seagrass reached maturity. In locations where the seagrass developed to maturity, wave energy was dissipated by vegetation and the seabed remained stable afterward.

Sensitivity of Green Nourishment to Wave Conditions and Seagrass Parameters

Seagrass meadow was sensitive to the offshore wave conditions and was vulnerable to more energetic wave of big height and long period (see **Figure 10**). Although wave reaching the seagrass meadow had been significantly damped, the morphodynamics was very dynamic. With increasing offshore wave height and period (i.e., GN6W2-6), both the seaward and shoreward edge of the meadow were buried at the end of 100 days simulation. For the most energetic wave (i.e., GN6W6), the entire seagrass meadow was buried. The meadow average bury ratio at the end of the simulation jumped to over 1.0 as wave height increased from 2.5 to 3 m along with wave period increased from 9.0 to 9.5 s, suggesting an appropriate wave condition to be under 3 m for the growth of seagrass. Taking average bury ratio of 1.0 as a survival criterion, seagrass meadow of GN6W3-6 can survive for 85, 60, 40, and 28 days after the planting.

Mature seagrass of high leaf and dense shoot provides strongest attenuation to wave height and best protection to the beach (see **Figures 11**, **12**). With higher a_h, the attenuation effect of seagrass meadow on the incoming wave and infragravity waves increases. H_s at the landward edge of the seagrass meadow reduces from 0.97 m of GN6a1 to 0.31 m of GN6a4, while H_{IG} reduces from 0.27 to 0.17 m. The effect of seagrass shoot density is similar to that of seagrass height, i.e., stronger attenuation and better protection with denser seagrass meadow. Under mild waves, all seagrass meadows examined seem to survive at the end of the 100 days simulation, except for seagrass with lowest leaf (GN6a1) and most sparse shoot (GN6n1) where erosion and deposition was observed at the shoreward edge of the meadow. The landward limit of beach erosion and the amount of beach erosion are highly related to the attenuation effect of the seagrass meadow. With better protection there is less beach erosion and limited eroded area. Although seagrass of lowest leaf (GN6a1) and most sparse shoot (GN6n1) provide the least protection to the coast, the beach erosion is still much less than the one without seagrass (SN), i.e., 72 m^3/m for the former two cases and 92 m^3/m for the latter case.

Resilience of Green Nourishment to Storm Event

The green nourishment provides protection to the coast against storm attack, by damping the wave and reducing beach erosion (**Figures 13**, **14**). The morphological response of the seabed to a 1-week storm event was examined for four cases (REF, SN, GN6, and GN6E). The final seabed of the 100 days simulation was taken as the pre-storm profile of the simulation. A maximum of 1.55 m reduction in the wave height (i.e., at x = 1,721 m) was observed for GN6 with respect to the REF case, which accounted for 58% of the wave height on REF bed. Seagrass also leads to significant reduction on IG wave height (**Figure 13B**). The IG wave height kept reducing over the seagrass meadow. Peak IG wave height reduced from 1.544 m for the REF case to 0.947 m for GN6. The shoreward limit of the erosion was shifted from x = 2,045 m (REF) to x = 2,000 m (GN6), preventing approximately a 45 m wide section of beach from eroding (**Figure 13D**). The total volume of beach erosion has also been reduced from 200 m^3/m (REF) to 53 m^3/m (GN6, **Figure 14B**). Extending the cross-shore coverage of seagrass meadow from 150 m (GN6) to 250 m (GN6E) intensified the protection of the green nourishment, i.e., 0.38 m lower wave height at x = 1,910 m, 0.36 m lower IG wave height and 17.5 m^3/m less beach erosion after the 1-week storm event. The seagrass at both the shoreward and seaward margins of the meadow was buried after the storm event. The seaward burial was caused by the shoaling and breaking of waves, and the shoreward burial results from the displacement of sand from the shoreline region. Seagrass in the interior of the meadow was not impacted by the waves or morphological change caused by the storm (Fonseca, 1994). In the GN6 case, 42% of the seagrass had a bury ratio above 1.0, suggesting a loss of nearly half of the seagrass in the designed storm event. With the enlarged seagrass meadow (GN6E), only 31% of the seagrass had a bury ratio above 1.0, suggesting a higher survival rate for seagrass meadow of greater cross-shore length.

Sheltering Effect of the Shoreface Nourishment

The shoreface nourishment increased the resilience of seagrass meadow through its impacts on wave attenuation and morphological change. A comparison between case GN6 and GREF, which had seagrass meadows in the same cross-shore location but only shoreface nourishment in GN6, shows the nourishment induced a reduction of 0.34 and 1 m in wave height at the seaward end of the seagrass bed for mild wave and stormy wave, respectively (**Figure 15**). The IG wave height distribution of GREF is similar to that of the GN6 (not shown). The nourishment created a more sheltered environment for the seagrass. Beach

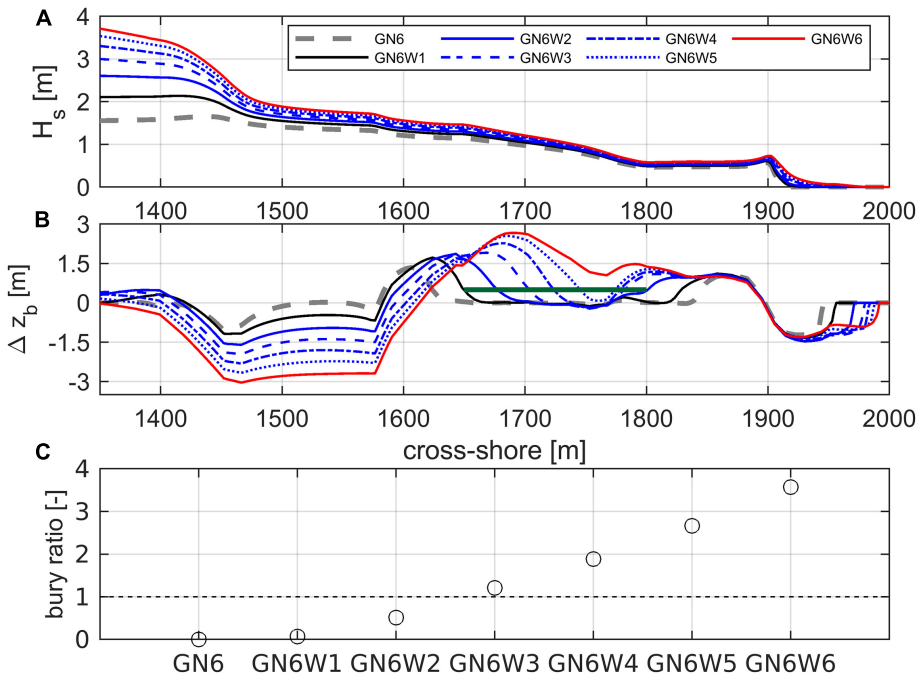


FIGURE 10 | Sensitivity of seagrass to offshore wave conditions, showing: **(A)** wave height distribution; **(B)** seabed change after 100 days simulation; and **(C)** meadow averaged bury ratio.

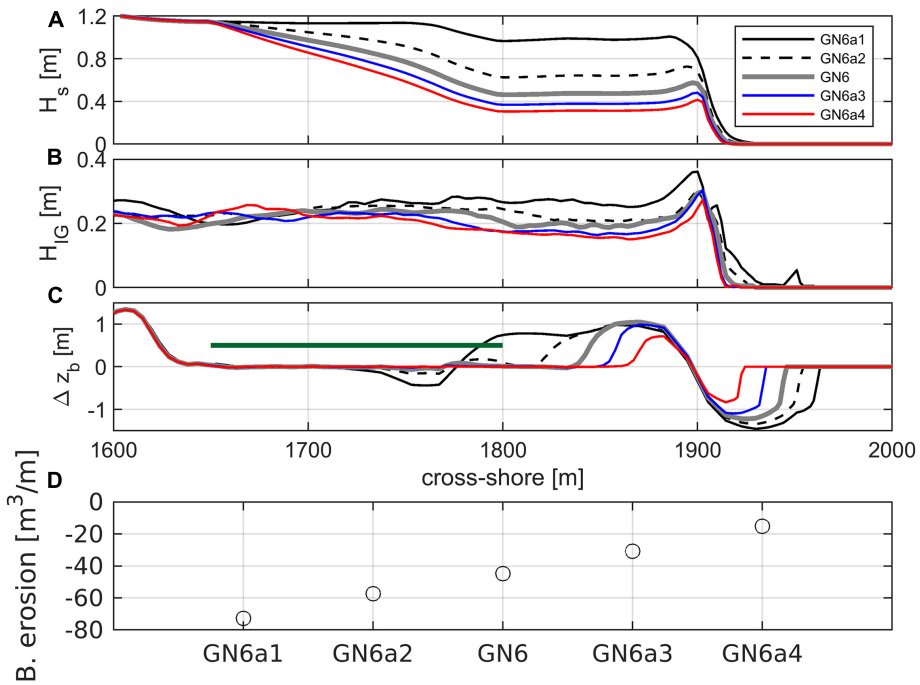


FIGURE 11 | Sensitivity to seagrass height ah, showing: **(A)** wave height distribution; **(B)** infragravity wave distribution; **(C)** seabed change after 100 days simulation; and **(D)** beach erosion.

erosion after 100 days of mild wave condition was lower in GN6 than GREF, i.e., 44.8 m^3/m compared with 71.4 m^3/m. Similarly, beach erosion after the storm event was about 91 m^3/m, which was substantially lower than the non-vegetated nourishment reference (REF). After 100 days mild wave condition, the burial analysis of GREF suggests a similar

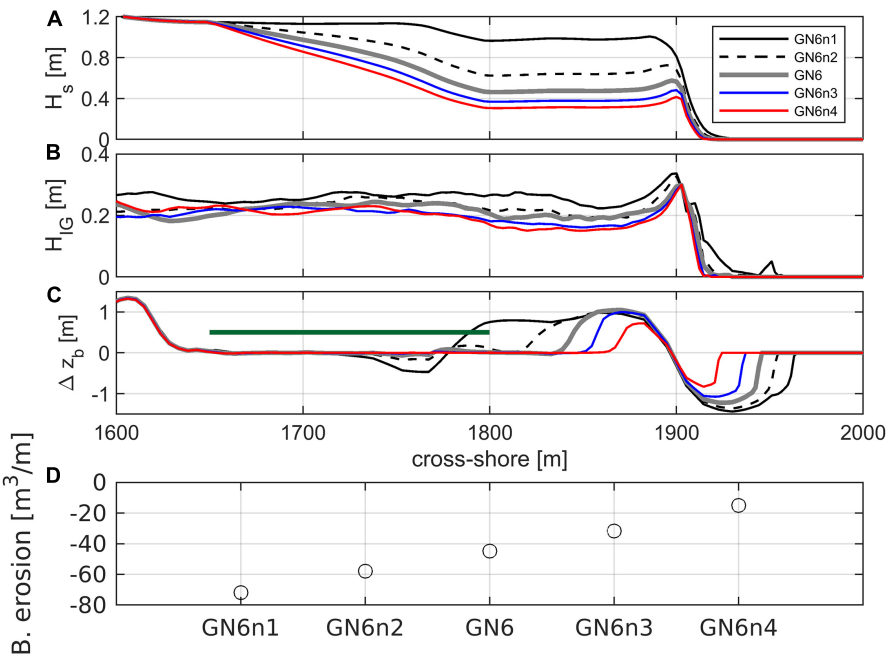


FIGURE 12 | Sensitivity to seagrass shoot density, showing: **(A)** wave height distribution; **(B)** infragravity wave distribution; **(C)** seabed change; and **(D)** beach erosion.

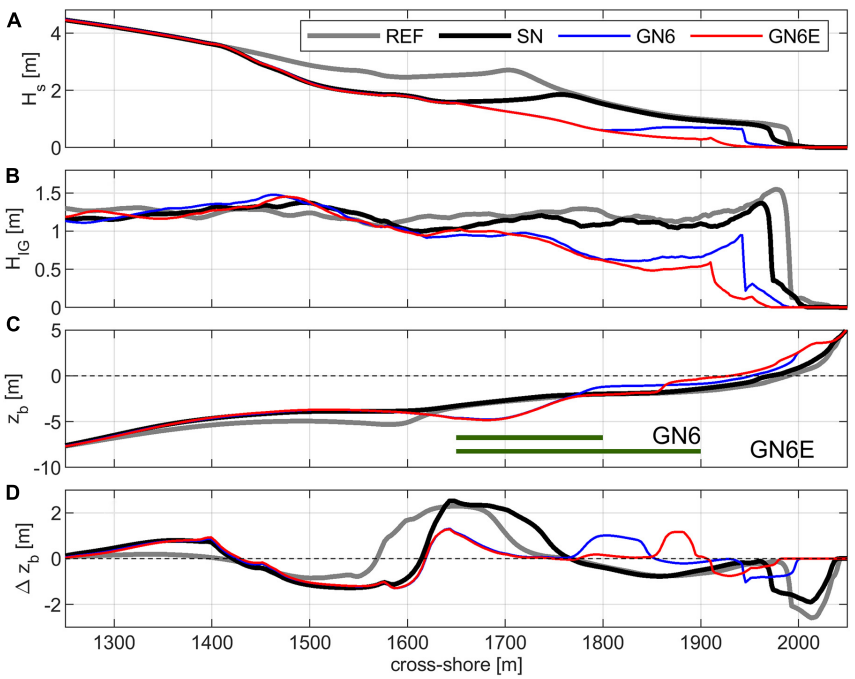


FIGURE 13 | Adaptation of green nourishment to a 1-week storm event (H_m = 5 m, T = 12 s), showing: **(A)** wave height simulated on pre-storm seabed profile; **(B)** infragravity (IG) wave height; **(C)** seabed after 1 week storm condition; **(D)** the change of seabed from initial profile (i.e., at the beginning of the 100 days simulation).

survival rate to the GN6 case. However, the storm event caused almost the entire seagrass meadow to be buried in the GREF case, except at the seaward edge where erosion was observed (**Figure 15E**). Whilst sediment deposition rates were high at the seaward and landward edges of the seagrass meadow in GN6, the interior of the meadow was barely affected, suggest that nourishment would benefit the resilience and survival of seagrass meadow restorations.

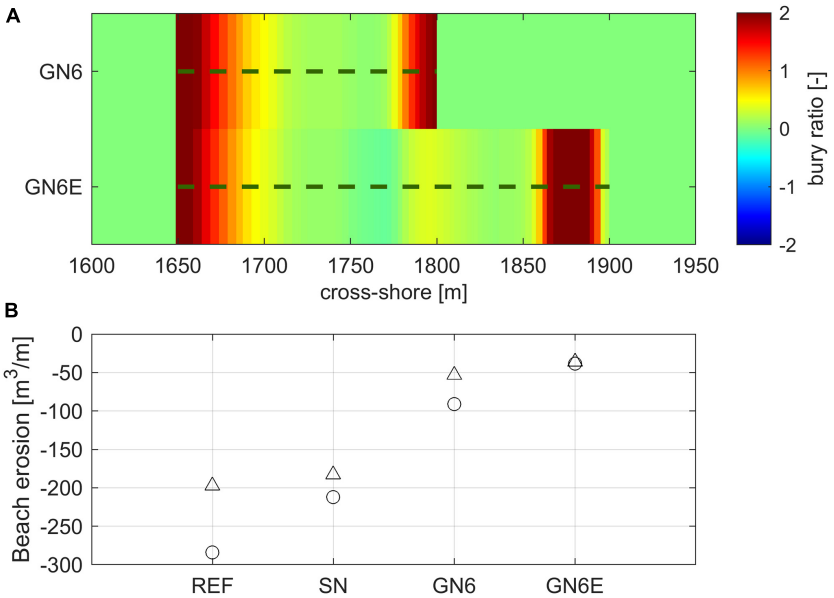


FIGURE 14 | The bury ratio of GN6 and GN6E after the storm are given in panel **(A)**. The beach erosion of REF, SN, GN6, and GN6E are given in panel **(B)** by integrating the difference of final seabed profile against pre-storm seabed (triangle) and initial seabed (circle).

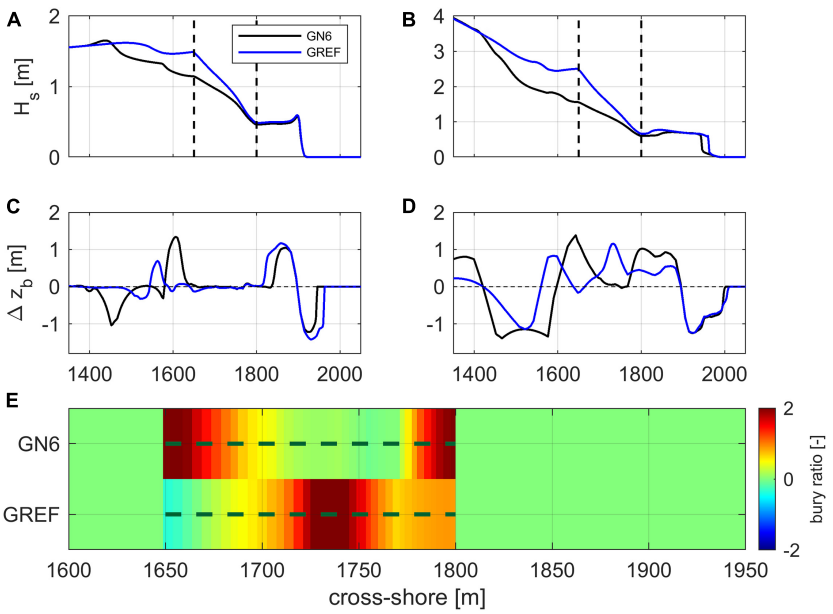


FIGURE 15 | Comparison of case GN6 and GREF, showing: **(A)** wave height profile under mild wave condition on initial bed profile; **(B)** wave height profile under storm wave condition on pre-storm profile; **(C)** seabed change at the end of 100 days simulation; **(D)** seabed change at the end of storm event; **(E)** bury analysis for seagrass meadow.

DISCUSSION

Most of the study runs simulated the impacts of planting of seagrass transplants, however the results of run GN6S suggest that planting seagrass seed is possible if relatively tranquil conditions persist for sufficient length of time for the seed to germinate and to grow to maturity. Seed planting technique has an advantage in greatly reducing the cost compared with mature seagrass transplanting technique (Marion and Orth, 2010; van Katwijk et al., 2016). However, were the seeds to have been sown further shoreward, it seems likely that their development may have been adversely affected by bed change prior to reaching a mature state. Therefore, practical work would be best timed for storm free seasons. The relatively short growth period, i.e.,

month to season, also benefits the recovery of seagrass meadows in between storm events. A hybrid planting with interior seed planting shielded by surrounding mature seagrass transplants would increase the chance of seed germination, as results show that the seagrass burial occurs at the margin of seagrass meadow (Fonseca, 1994). Sensitivity analysis shows that seagrass is able to survive for wave heights under 3 m for a considerable period. The protection of the coast by seagrass meadow is very sensitive to seagrass parameters. With mature seagrass of high leaf and dense shoots, the beach erosion significantly reduces. In this study, green nourishment with mature seagrass reduces erosion considerably at the shoreline in a severe storm. But to survive through a strong storm event, the size of the seagrass meadow should be sufficiently large (van Katwijk et al., 2016; Paulo et al., 2019).

Although this study shows that the hydrodynamic conditions could be favorable for the implementation of a green nourishment in the nearshore area, field experimentations for the implementation and development of a dense seagrass meadow on an open coast are required to validate the method. One concern is the light penetration in the area landward of the nourishment. For *Z. marina,* depth and light availability are critical determinants of seagrass restoration success (Xu et al., 2020). Insufficient light availability has been identified as one of the primary causes of transplantation failure (Moore et al., 2012; van Katwijk et al., 2016). The amount of suspended sediment in the water mobilized by wave breaking on the nourishment might cause high turbidity, which would limit light penetration to seagrass leaves and restrain its growth and development. However, this problem would become less important as the seagrass grows, and develops into a dense meadow. Several studies have shown that the direct effect of the seagrass meadows on currents, sediment trapping and decreasing resuspension creates a positive feedback circle for the seagrass. The sediment deposition indeed decreases the turbidity, which in turn increases light availability and allows for better growing conditions (de Boer, 2007; Luhar et al., 2010; Xu et al., 2020). As the seagrass meadow becomes more mature and denser, this circle is enhanced.

The characteristics of the substrate might affect seagrass growth. The nutrient content is very important. Research showed that seagrass planted on natural sediment grows better than on the construction sand, owing to higher nutrient content (Tanner and Parham, 2010), which supports the choice of planting seagrass on shoreward native seabed other than on top of the nourishment. Fine grain size might have negative impact on the density of seagrass (*z. noltti*) as low porosity of sediment affecting the pore-water exchange and leading to a hypoxic condition (Folmer et al., 2012). But this is not a universal law, as different seagrass has various suitabilities on different substrates, and seagrass has been documented on beds from mud to rock (Dahl et al., 2016). Furthermore, the seagrass meadow is found to be able to self-adjust to substrate material size through grain selection (Zhang et al., 2020).

Parameters used in this study were taken from existing XBeach studies including calibrations with both lab test and field observation (Roelvink et al., 2009; van Thiel de Vries, 2009; van Rooijen et al., 2016). Whilst uncertainty in the model results may arise from parameter choice such as wave energy dissipation and sediment formula (Berard et al., 2017), the protection mechanism of green nourishment through energy dissipation of nourishment and vegetation is likely to be a robust result, because the formulae are standard and in general use, and the trends in sensitivities will be reproducible. Seagrass meadow of various mature status at different cross-shore locations all provide considerable protection to the coast. The wave reduction by green nourishment is up to 80% under mild wave condition, which is higher than the effect of only seagrass meadow (i.e., 49% as in Reidenbach and Thomas, 2018). It must also be noted that that the study pertains in particular to North Sea conditions, as a JONSWAP spectrum was used.

As a first step, this study focused on the cross-shore dynamics of green nourishment and adopted a simplistic approach to model seagrass shoots. Future modeling studies should examine the longshore dynamics, i.e., particularly for a coast with strong longshore current induced by oblique wave or macro-tide. The effects of tides will also be significant, especially on coasts with large tidal ranges. Improvement of the representation of seagrass meadows and their effects on wave, current and sediment transport is also desirable (Nepf, 2011; Suzuki et al., 2019). Although the simplistic way of modeling seagrass shoots as rigid sticks in the vegetation module of XBeach is partially corrected by drag coefficients, the modeling of the effects of storms and high wave energy conditions on seagrass meadows (and vice versa) could be improved (van Rooijen et al., 2015, 2018). Furthermore, a failure scheme could be introduced for seagrass destroyed either by strong current or sediment burial in severe storms which could avoid the overestimation of seagrass attenuation under storm weather. Once being eroded or buried, the seagrass can no longer provide protection to the coast, which is not accounted for at the moment. The green nourishment proposed in this study could be combined with other nature-based solutions, such as beach nourishment, salt marsh construction (i.e., the Marconi project at Delfzijl Netherlands; Hu et al., 2015, 2021; Baptist et al., 2021) and mangrove development (Gijsman et al., 2021), to mitigate the coastal erosion.

CONCLUSION

The results of this study demonstrate that green nourishment has the potential to substantially reduce wave heights and erosion at the shore. The nourishment provides an input of sand into the system and, crucially, creates a morphological feature that generates a sheltered area landward that is conducive to seagrass establishment and growth. In turn, the seagrass stabilizes the sand substrate and reduces wave energy further. Thus, on high energy coastlines, the placement of the nourishment should be adjusted to maximize intense wave breaking to dissipate wave energy. The simulations suggest that the placement of the seagrass along the cross-shore profile affects substantially wave energy and morphological evolution. Whilst restoration on top of the nourishment (GN1) dissipated a large amount of wave energy,

a shoreward sheltered region may be more effective. The sharp shoreward decrease in the wave height and the sediment flux in GN1 leads to high rates of sand deposition that eventually bury the marginal seagrass. The turbulence and high current velocity at the breaking zone also jeopardize the growth of seagrass. In contrast, seagrass on a shoreward sheltered region experiences a quieter hydrodynamic environment and a more stable seabed, which allows a higher survival rate.

This study shows that green nourishment has potential as a nature-based solution to mitigate coastal erosion. Model results indicate that a seagrass meadow (i) enhances significantly the wave energy dissipation provided by a shoreface nourishment and (ii) can be effective in sediment transport mitigation when implemented in the sheltered nearshore area. Beach foreshore erosion after a storm event is reduced significantly with the protection of green nourishment. Using seed, rather than mature plants, to restore the seagrass meadow is found possible, which would significantly reduce the operation cost of a green nourishment project. This study also highlights the importance of a large seagrass meadow to cope with long-term exposure to mild wave conditions, as well as occasional storms. There are major challenges associated with implementing a green nourishment on an exposed open coast, but this study and the ongoing progress made in seagrass restoration techniques are promising. Future studies and field experiments are crucial to make green nourishment a sustainable, cost-effective and ecological solution to coastal erosion and flooding.

DATA AVAILABILITY STATEMENT

The datasets presented in this study can be found in online repositories. The names of the repository/repositories and accession number(s) can be found below: https://doi.org/10.17862/cranfield.rd.17005480.v1.

AUTHOR CONTRIBUTIONS

WC was responsible for the design, simulation, writing, and reviewing of the manuscript. PM was responsible for simulation and writing of the manuscript. RG was responsible for design, supervising, writing, and reviewing of the manuscript. ND was responsible for design, writing, and reviewing of the manuscript. All authors contributed to the article and approved the submitted version.

FUNDING

This work was supported primarily by the UK Engineering and Physical Science Research Council (EPSRC, Grant EP/T001100/1). Support is also acknowledged from the EPSRC under the MORPHINE project (Grant EP/N007379/1) and the UK Natural Environment Research Council (NERC, Grant NE/S01232X/1).

REFERENCES

Baptist, M. J., Dankers, P., Cleveringa, J., Sittoni, L., Willemsen, P. W. J. M., van Puijenbroek, M. E. B., et al. (2021). Salt marsh construction as a nature-based solution in an estuarine social-ecological system. *Nature-Based Solutions* 1:100005. doi: 10.1016/j.nbsj.2021.100005

Berard, N. A., Mulligan, R. P., da Silva, A. M. F., and Dibajnia, M. (2017). Evaluation of XBeach performance for the erosion of a laboratory sand dune. *Coastal Eng.* 125, 70–80. doi: 10.1016/j.coastaleng.2017.04.002

Bergillos, R. J., López-Ruiz, A., Principal-Gómez, D., and Ortega-Sánchez, M. (2018). An integrated methodology to forecast the efficiency of nourishment strategies in eroding deltas. *Sci. Total Environ.* 61, 1175–1184. doi: 10.1016/j.scitotenv.2017.09.197

Boudouresque, C.-F., Blanfuné, A., Pergent, G., and Thibaut, T. (2021). Restoration of seagrass meadows in the mediterranean sea: a critical review of effectiveness and ethical issues. *Water* 13:1034. doi: 10.3390/w13081034

Chen, W. L., and Dodd, N. (2019). An idealised study for the evolution of a shoreface nourishment. *Continental Shelf Res.* 178, 15–26. doi: 10.1016/j.csr.2019.03.010

da Ros, Z., Corinaldesi, C., Dell'Anno, A., Gambi, C., Torsani, F., and Danovaro, R. (2021). Restoration of *Cymodocea nodosa* seagrass meadows: efficiency and ecological implications. *Restoration Ecol.* 29:e13313. doi: 10.1111/rec.13313

Dahl, M., Deyanova, D., Gütschow, S., Asplund, M. E., Lyimo, L. D., Karamfilov, V., et al. (2016). Sediment properties as important predictors of carbon storage in *Zostera marina* meadows: a comparison of four european areas. *PLoS One* 11:e0167493. doi: 10.1371/journal.pone.0167493

de Boer, W. F. (2007). Seagrass–sediment interactions, positive feedbacks and critical thresholds for occurrence: a review. *Hydrobiologia* 591, 5–24. doi: 10.1007/s10750-007-0780-9

de Schipper, M. A., de Vries, S., Ruessink, G., de Zeeuw, R. C., Rutten, J., van Gelder-placeMaas, C., et al. (2016). Initial spreading of a mega feeder nourishment: observations of the Sand Engine pilot project. *Coastal Eng.* 111, 23–38. doi: 10.1016/j.coastaleng.2015.10.011

Dhoop, T., and Mason, T. (2018). Spatial characteristics and duration of extreme wave events around the English coastline. *J. Mar. Sci. Eng.* 6:14. doi: 10.3390/jmse6010014

Dissanayake, P., Brown, J., and Karunarathna, H. (2014). Modelling storm-induced beach/dune evolution: Sefton coast. CityplaceLiverpool Bay, country-regionUK. *Mar. Geol.* 357, 225–242. doi: 10.1016/j.margeo.2014.07.013

Elsayed, S. M., and Oumeraci, H. (2017). Effect of beach slope and grain-stabilization on coastal sediment transport: an attempt to overcome the erosion overestimation by XBeach. *Coastal Eng.* 121, 179–196. doi: 10.1016/j.coastaleng.2016.12.009

Folkard, A. M. (2011). Flow regimes in gaps within stands of flexible vegetation: laboratory flume simulations. *Environ. Fluid Mechan.* 11, 289–306. doi: 10.1007/s10652-010-9197-5

Folmer, E. O., van der Geest, M., Jansen, E., Olff, H., Michael Anderson, T., Piersma, T., et al. (2012). Seagrass–Sediment feedback: an exploration using a non-recursive structural equation model. *Ecosystems* 15, 1380–1393. doi: 10.1007/s10021-012-9591-6

Fonseca, M. S. (1994). *A Guide to Planting Seagrasses in the Gulf of Mexico. Texas A&M University Sea Grant College Program, TAMU-SG-94-601*. College Station, TX: Texas A&M University.

Gagnon, K., Christie, H., Didderen, K., Fagerli, C. W., Govers, L. L., Gräfnings, M. L. E., et al. (2021). Incorporating facilitative interactions into small-scale eelgrass restoration—challenges and opportunities. *Restoration Ecol.* 29:e13398. doi: 10.1111/rec.13398

Gijsman, R., Horstman, E. M., van der Wal, D., Friess, D. A., Swales, A., and Wijnberg, K. M. (2021). Nature-Based engineering: a review on reducing coastal flood risk with mangroves. *Front. Mar. Sci.* 8:702412. doi: 10.3389/fmars.2021.702412

Hamm, L., Capobianco, M., Dette, H. H., Lechuga, A., Spanhoff, R., and Stive, M. J. F. (2002). A summary of European experience with shore nourishment. *Coastal Eng.* 47, 237–264.

Hinkel, J., Nicholls, R. J., Tol, R. S. J., Wang, Z. B., Hamilton, J. M., Boot, G., et al. (2013). A global analysis of erosion of sandy beaches and sea-level rise: an application of DIVA. *Global Planetary Change* 111, 150–158. doi: 10.1016/j.gloplacha.2013.09.002

Hu, Z., Borsje, B. W., van Belzen, J., Willemsen, P. W. J. M., Wang, H., Peng, Y., et al. (2021). Mechanistic modelling of marsh seedling establishment provides a positive outlook for coastal wetland restoration under global climate change. *Geophys. Res. Lett.* 48:e2021GL095596. doi: 10.1029/2021GL095596

Hu, Z., van Belzen, J., van der Wal, D., Balke, T., Wang, Z. B., Stive, M., et al. (2015). Windows of opportunity for salt marsh vegetation establishment on bare tidal flats: the importance of temporal and spatial variability in hydrodynamic forcing. *J. Geophys. Res. Biogeosci.* 120, 1450–1469. doi: 10.1002/2014JG002870

Huisman, B. J. A., Walstra, D.-J. R., Radermacher, M., de Schipper, M. A., and Ruessink, B. G. (2019). Observations and modelling of shoreface nourishment behaviour. *J. Mar. Sci. Eng.* 7:59. doi: 10.3390/jmse7030059

Irving, A. D., Tanner, J. E., and Collings, G. J. (2014). Rehabilitating seagrass by facilitating recruitment: improving chances for success. *Restoration Ecol.* 22, 134–141. doi: 10.1111/rec.12036

Izaguirre, C., Méndez, F. J., Menéndez, M., and Losada, placeI. J. (2011). Global extreme wave height variability based on satellite data. *Geophys. Res. Lett.* 38:L10607. doi: 10.1029/2011GL047302

Jin, H., Do, K., Shin, S., and Cox, D. (2021). Process-Based model prediction of coastal dune erosion through parametric calibration. *J. Mar. Sci. Eng.* 9:635. doi: 10.3390/jmse9060635

Lashley, C. H., Roelvink, D., van Dongeren, A., Buckley, M. L., and Lowe, R. J. (2018). Nonhydrostatic and surfbeat model predictions of extreme wave run-up in fringing reef environments. *Coastal Eng.* 137, 11–27. doi: 10.1016/j.coastaleng.2018.03.007

Luhar, M., Coutu, S., Infantes, E., Fox, S., and Nepf, H. (2010). Wave-induced velocities inside a model seagrass bed. *J. Geophys. Res. Oceans* 115:C12. doi: 10.1029/2010JC006345

Marion, S. R., and Orth, R. J. (2010). Innovative techniques for large-scale seagrass restoration using *Zostera marina* (eelgrass) Seeds. *Restoration Ecol.* 18, 514–526. doi: 10.1111/j.1526-100X.2010.00692.x

Masselink, G., and Russell, P. (2008). *Coastal Erosion and Coastal Geomorphology. MCCIP (Marine Climate Group Impacts Partnership) Annual Report Card 2007–2008 Scientific Review*. Plymouth: University of Plymouth.

McCall, R. T., van Thiel, de Vries, J. S. M., Plant, N. G., van Dongeren, A. R., Roelvink, J. A., et al. (2010). Two-dimensional time dependent hurricane overwash and erosion modeling at placeSanta Rosa Island. *Coastal Eng.* 57, 668–683. doi: 10.1016/j.coastaleng.2010.02.006

Mendez, F. J., and Losada, placeI. J. (2004). An empirical model to estimate the propagation of random breaking and nonbreaking waves over vegetation fields. *Coastal Eng.* 51, 103–118. doi: 10.1016/j.coastaleng.2003.11.003

Menéndez, M., and Woodworth, P. L. (2010). Changes in extreme high water levels based on a quasi-global tide-gauge data set. *J. Geophys. Res. Oceans* 115:C10011. doi: 10.1029/2009JC005997

Montgomery, J. M., Bryan, K. R., Mullarney, J. C., and Horstman, E. M. (2019). Attenuation of storm surges by coastal mangroves. *Geophys. Res. Lett.* 46, 2680–2689. doi: 10.1029/2018GL081636

Moore, K. A., Shields, E. C., Parrish, D. B., and Orth, R. J. (2012). Eelgrass survival in two contrasting systems: role of turbidity and summer water temperatures. *Mar. Ecol. Prog. Series* 448, 247–258. doi: 10.3354/meps09578

Nepf, H. M. (2011). Flow and transport in regions with aquatic vegetation. *Ann. Rev. Fluid Mech.* 44, 123–142. doi: 10.1146/annurev-fluid-120710-101048

Nicholls, R. J., Wong, P. P., Burkett, V., Codignotto, J. O., Hay, J., McLean, R. F., et al. (2007). *Coastal Systems and Low-lying Areas*. Cambridge: Cambridge University Press.

Ondiviela, B., Losada, placeI. J., Lara, J. L., Maza, M., Galván, C., Bouma, T. J., et al. (2014). The role of seagrasses in coastal protection in a changing climate. *Coastal Eng.* 87, 158–168. doi: 10.1016/j.coastaleng.2013.11.005

Paulo, D., Cunha, A. H., Boavida, J., Serrão, E. A., Gonçalves, E. J., and Fonseca, M. (2019). PlaceNameOpen coast seagrass restoration. can we do it? large scale seagrass transplants. *Front. Mar. Sci.* 6:52. doi: 10.3389/fmars.2019.00052

Quataert, E., Storlazzi, C., van Rooijen, A., Cheriton, O., and van Dongeren, A. (2015). The influence of coral reefs and climate change on wave-driven flooding of tropical coastlines. *Geophys. Res. Lett.* 42, 6407–6415. doi: 10.1002/2015GL064861

Reidenbach, M. A., and Thomas, E. L. (2018). Influence of the Seagrass, *Zostera marina*, on wave attenuation and bed shear stress within a shallow coastal bay. *Front. Mar. Sci.* 5:397. doi: 10.3389/fmars.2018.00397

Roelvink, D., McCall, R., Mehvar, S., Nederhoff, K., and Dastgheib, A. (2018). Improving predictions of swash dynamics in XBeach: The role of groupiness and incident-band runup. *Coastal Eng.* 134, 103–123. doi: 10.1016/j.coastaleng.2017.07.004

Roelvink, D., Reniers, A., van Dongeren, A., van Thiel, de Vries, J., McCall, R., et al. (2009). Modelling storm impacts on beaches, dunes and barrier islands. *Coastal Eng.* 56, 1133–1152. doi: 10.1016/j.coastaleng.2009.08.006

Roelvink, J. A. (1993). Dissipation in random wave groups incident on a beach. *Coastal Eng.* 19, 127–150. doi: 10.1016/0378-3839(93)90021-y

Sembiring, L., van Ormondt, M., van Dongeren, A., and Roelvink, D. (2015). A validation of an operational wave and surge prediction system for the Dutch coast. *Nat. Hazards Earth Syst. Sci.* 15, 1231–1242. doi: 10.5194/nhess-15-1231-2015

Stronkhorst, J., Huisman, B., Giardino, A., Santinelli, G., and CityplaceSantos, F. D. (2018). Sand nourishment strategies to mitigate coastal erosion and sea level rise at the coasts of CityHolland (The Netherlands) and Aveiro (country-regionplacePortugal) in the 21st century. *Ocean Coastal Manag.* 156, 266–276. doi: 10.1016/j.ocecoaman.2017.11.017

Suzuki, T., Hu, Z., Kumada, K., Phan, L. K., and Zijlema, M. (2019). Non-hydrostatic modeling of drag, inertia and porous effects in wave propagation over dense vegetation fields. *Coastal Eng.* 149, 49–64. doi: 10.1016/j.coastaleng.2019.03.011

Tan, Y. M., Dalby, O., Kendrick, G. A., Statton, J., Sinclair, E. A., Fraser, M. W., et al. (2020). Seagrass restoration is possible: insights and lessons from Australia and New Zealand. *Front. Mar. Sci.* 7:617. doi: 10.3389/fmars.2020.00617

Tanner, C. E., and Parham, T. (2010). Growing *Zostera marina* (eelgrass) from seeds in land-based culture systems for use in restoration projects. *Restoration Ecol.* 18, 527–537. doi: 10.1111/j.1526-100X.2010.00693.x

Temmerman, S., Meire, P., Bouma, T. J., Herman, P. M. J., Ysebaert, T., and de Vriend, H. J. (2013). Ecosystem-based coastal defence in the face of global change. *Nature* 504, 79–83. doi: 10.1038/nature12859

Tyler-Walters, H. (2008). "*Zostera (Zostera)* marina Common eelgrass," in *Marine Life Information Network: Biology and Sensitivity Key Information Reviews, [On-line]*, eds H. Tyler-Walters and K. Hiscock (Plymouth: Marine Biological Association of the United Kingdom).

Unsworth, R. K. F., Bertelli, C. M., Cullen-Unsworth, L. C., Esteban, N., Jones, B. L., Lilley, R., et al. (2019). Sowing the seeds of seagrass recovery using hessian bags. *Front. Ecol. Evol.* 7:311. doi: 10.3389/fevo.2019.00311

van Dongeren, A., Lowe, R., Pomeroy, A., Trang, D. M., Roelvink, D., Symonds, G., et al. (2013). Numerical modeling of low-frequency wave dynamics over a fringing coral reef. *Coastal Eng.* 73, 178–190. doi: 10.1016/j.coastaleng.2012.11.004

van Duin, M. J. P., Wiersma, N. R., Walstra, D. J. R., van Rijn, L. C., and Stive, M. J. F. (2004). Nourishing the shoreface: observations and hindcasting of the Egmond case. The country-regionplaceNetherlands. *Coastal Eng.* 51, 813–837. doi: 10.1016/j.coastaleng.2004.07.011

van Katwijk, M. M., Thorhaug, A., Marbà, N., Orth, R. J., CityplaceDuarte, C. M., Kendrick, G. A., et al. (2016). Global analysis of seagrass restoration: the importance of large-scale planting. *J. Appl. Ecol.* 53, 567–578. doi: 10.1111/1365-2664.12562

van Rijn, L. C. (2007). Unified view of sediment transport by currents and waves. i: initiation of motion, bed roughness, and bed-load transport. *J. Hydraulic Eng.* 133, 649–667.

van Rooijen, A. A., McCall, R. T., van Thiel, de Vries, J. S. M., van Dongeren, A. R., Reniers, A. J. H. M., et al. (2016). Modeling the effect of wave-vegetation interaction on wave setup. *J. Geophys. Res. Oceans* 121, 4341–4359. doi: 10.1002/2015JC011392

Van Rooijen, A. A., Van Thiel de Vries, J. S. M., McCall, R. T., Van Dongeren, A. R., Roelvink, J. A., and Reniers, A. J. H. M. (2015). "Modeling of wave attenuation by vegetation with XBeach," in *E-Proceedings of the 36th IAHR World Congress, 2015*, Vol. 7, The Hague.

van Rooijen, A., Lowe, R., Ghisalberti, M., Conde-Frias, M., and Tan, L. (2018). Predicting current-induced drag in emergent and submerged aquatic vegetation canopies. *Front. Mar. Sci.* 5:449. doi: 10.3389/fmars.2018.00449

van Thiel de Vries, J. S. M. (2009). *Dune Erosion During Storm Surges*. Amsterdam: IOS Press.

van Zelst, V. T. M., Dijkstra, J. T., van Wesenbeeck, B. K., Eilander, D., Morris, E. P., Winsemius, H. C., et al. (2021). Cutting the costs of coastal protection by integrating vegetation in flood defences. *Nat. Commun.* 12:6533. doi: 10.1038/s41467-021-26887-4

Wear, R. J., Tanner, J. E., and Hoare, S. L. (2010). Facilitating recruitment of Amphibolis as a novel approach to seagrass rehabilitation in hydrodynamically active waters. *Mar. Freshwater Res.* 61, 1123–1133. doi: 10.1071/mf09314

Wijnberg, K. M. (2002). Environmental controls on decadal morphologic behaviour of the CityplaceHolland coast. *Mar. Geol.* 189, 227–247. doi: 10.1016/S0025-3227(02)00480-2

Williams, A. T., Rangel-Buitrago, N., Pranzini, E., and Anfuso, G. (2018). The management of coastal erosion. *Ocean Coastal Manag.* 156, 4–20. doi: 10.1016/j.ocecoaman.2017.03.022

Xu, S., Wang, P., Wang, F., Liu, P., Liu, B., Zhang, X., et al. (2020). In situ Responses of the Eelgrass *Zostera marina* L. to water depth and light availability in the context of increasing coastal water turbidity: implications for conservation and restoration. *Front. Plant Sci.* 11:582557. doi: 10.3389/fpls.2020.582557

Zhang, J., Lei, J., Huai, W., and Nepf, H. (2020). Turbulence and particle deposition under steady flow along a submerged seagrass meadow. *J. Geophys. Res. Oceans* 125:e2019JC015985. doi: 10.1029/2019JC015985

Zhu, Z., Vuik, V., Visser, P. J., Soens, T., van Wesenbeeck, B., van de Koppel, J., et al. (2020). Historic storms and the hidden value of coastal wetlands for nature-based flood defence. *Nat. Sustainabil.* 3, 853–862. doi: 10.1038/s41893-020-0556-z

Conflict of Interest: The authors declare that the research was conducted in the absence of any commercial or financial relationships that could be construed as a potential conflict of interest.

Publisher's Note: All claims expressed in this article are solely those of the authors and do not necessarily represent those of their affiliated organizations, or those of the publisher, the editors and the reviewers. Any product that may be evaluated in this article, or claim that may be made by its manufacturer, is not guaranteed or endorsed by the publisher.

Copyright © 2022 Chen, Muller, Grabowski and Dodd. This is an open-access article distributed under the terms of the Creative Commons Attribution License (CC BY). The use, distribution or reproduction in other forums is permitted, provided the original author(s) and the copyright owner(s) are credited and that the original publication in this journal is cited, in accordance with accepted academic practice. No use, distribution or reproduction is permitted which does not comply with these terms.

frontiers in Marine Science

ORIGINAL RESEARCH
published: 10 February 2022
doi: 10.3389/fmars.2022.787041

How Turbidity Mediates the Combined Effects of Nutrient Enrichment and Herbivory on Seagrass Ecosystems

*Xinyan Wang[1,2], Junhong Bai[1,2], Jiaguo Yan[1,2], Baoshan Cui[1,2] and Dongdong Shao[1,2,3]**

[1] State Key Laboratory of Water Environment Simulation and School of Environment, Beijing Normal University, Beijing, China, [2] Yellow River Estuary Wetland Ecosystem Observation and Research Station, Ministry of Education, Dongying, China, [3] Tang Scholar, Beijing Normal University, Beijing, China

While nutrient enrichment and herbivory have been well recognized as the main driving factors of seagrass meadow fragmentation and degradation, there is limited understanding of how their relative importance shifts across large spatial scales where environmental factors such as turbidity can vary. In this study, a field control experiment was conducted in two *Zostera japonica* meadows distributed on the two banks of the Yellow River Estuary with different turbidity, to investigate the combined effects of nutrient enrichment and herbivory on seagrass and macroalgae. Our results showed that turbidity had the mediating force of shifting the relative importance of nutrient enrichment and herbivory to seagrass and macroalgae. While herbivory played a vital role in maintaining the balance between the two primary producers in a turbid environment, nutrient enrichment tended to offset herbivory-induced biomass loss by promoting seagrass growth in a less turbid system. Additionally, two potential mechanisms that might regulate the responses of seagrasses and macroalgae to nutrient enrichment and herbivory under different turbidity are proposed. On the one hand, turbidity might mediate the feeding preference of herbivores. On the other hand, nutrient enrichment favors the growth of opportunistic macroalgae over seagrass in turbid systems. Our study emphasizes the mediating force of turbidity on seagrass ecosystems, and provides references for the protection and restoration of seagrass meadows under multiple environmental stressors, and prompts further studies on the feedback between sediment dynamics and seagrass meadows in the context of ecogeomorphology.

Keywords: seagrass meadow, turbidity, the Yellow River Estuary, nutrient enrichment, herbivory

OPEN ACCESS

Edited by:
Zeng Zhou,
Hohai University, China

Reviewed by:
Quan-Xing Liu,
East China Normal University, China
WenWen Liu,
Xiamen University, China

***Correspondence:**
Dongdong Shao
ddshao@bnu.edu.cn

Specialty section:
This article was submitted to Coastal Ocean Processes, a section of the journal Frontiers in Marine Science

Received: *30 September 2021*
Accepted: *24 January 2022*
Published: *10 February 2022*

Citation:
Wang X, Bai J, Yan J, Cui B and Shao D (2022) How Turbidity Mediates the Combined Effects of Nutrient Enrichment and Herbivory on Seagrass Ecosystems. Front. Mar. Sci. 9:787041. doi: 10.3389/fmars.2022.787041

INTRODUCTION

Seagrass meadows are among the most widely distributed coastal ecosystems in the world, and play a crucial role in the transitional zone between land and sea (Du et al., 2020; Orth et al., 2020). Seagrass ecosystems are recognized as the most productive ecosystems with an annual carbon sequestration potential as high as 43.9 ± 12.1 MtC yr^{-1} (Bertram et al., 2021), and provide US$100 million per year to the world's blue economy (Stockbridge et al., 2020). However, in recent years, the structure and function of seagrass ecosystems have been threatened by multiple global stressors caused by human activities and climate change, resulting in pervasive and continuous degradation of seagrass meadows across the world (Waycott et al., 2009). Environmental changes

such as warming (Repolho et al., 2017), eutrophication (Ontoria et al., 2019), sea-level rise (Albert et al., 2017) pose critical threats to the species composition, distribution, and productivity of seagrass ecosystems. Subject to the short or long-term effects of multiple environmental stressors, the response patterns of seagrass ecosystems need further studies.

Nutrient enrichment and herbivory have been recognized as the main global stressors that cause fragmentation and degradation of seagrass meadows (Leoni et al., 2008). It was found that eutrophication overrides warming as a dominant stressor for temperate seagrass meadows (Mvungi and Pillay, 2019). Many studies have explored the negative effects of nutrient enrichment on the structure and function of the seagrass ecosystem (Schmidt et al., 2012; Wang et al., 2020). For example, nutrient enrichment could cause epiphytic algae or macroalgae bloom (Leston et al., 2008; Archer et al., 2018), which leads to nutrient competition, algal shading, or direct toxicity of sulfide accumulation on seagrass (Darnell and Dunton, 2017; Viana et al., 2020). In parallel, it is also established that herbivory acts as a natural disturbance with a relatively high impact on seagrass. To some extent, herbivory significantly decreases seagrass biomass and structural complexity of canopy (Moran and Bjorndal, 2005; Fourqurean et al., 2010; Scott et al., 2021), and has long-term impacts on nitrogen and organic matter reserves of tissues (Moran and Bjorndal, 2007). Meanwhile, the selective grazing behavior of herbivores regulates the competition between seagrass and algae, and further affects the dynamics of the food web (Ebrahim et al., 2014; Fourqurean et al., 2019).

In addition to their separate effects, nutrient enrichment and herbivory interact in a variety of ways in seagrass communities (York et al., 2012; Whalen et al., 2013; Carr and Boyer, 2014). Numerous manipulative experiments have explored the combined effects of nutrient enrichment and herbivory as bottom-up and top-down controls on seagrass ecosystem. However, these experiments were mostly conducted in distinct natural habitats with wide-ranging varieties in latitude, trophic level, etc., occasionally leading to contrasting findings (Hughes et al., 2004; Duffy et al., 2015). For example, some studies showed that nutrient enrichment overrides top-down control on the shift of the dominant species from seagrass to algae (Hughes et al., 2004; Östman et al., 2016), while other studies revealed insignificant nutrient effects but strong top-down control on seagrass growth (Heck et al., 2000; Campbell et al., 2018). It is increasingly recognized that the separate or combined effects of top-down and bottom-up controls are context-dependent and vary across environmental gradients, thus emphasizing the mediating forces of other environmental factors of the habitat (Burkepile and Hay, 2006; Baden et al., 2010; Listiawati and Kurihara, 2021).

Regarding the environmental mediation of top-down and bottom-up controls on seagrass ecosystems, previous studies have revealed the importance of temperature as a mediating factor. For instance, Duffy et al. (2015) reported that similar to species richness, the effect of grazers controlling algae increased with temperature. Temperature-induced changes in the herbivore functional composition were further found to alter the relative importance of nutrients (Campbell et al., 2018). In addition to temperature, turbidity has been found to be one of the key factors driving the changes in the spatiotemporal distribution of seagrass (Garrido et al., 2013; Yamamoto et al., 2019). A short-term increase in turbidity would lead to long-term effects on the survival of seagrass (Li et al., 2021). Elevated turbidity is associated with a lower nutrient removal capacity of seagrass by reducing the intensity of light and photosynthesis (Bulmer et al., 2018). High turbidity is also related to high suspended sediment concentration which may carry extra nutrients available for algae growth in source-limited systems, and potentially enhance interspecific competition between primary producers (Schallenberg and Burns, 2004; Vieira et al., 2020). Furthermore, herbivory was found to be increased in turbid waters due to the reduced efficiency of predators (Savic et al., 2018). However, whether turbidity could play explicit mediating roles on bottom-up and top-down controls such as nutrient enrichment and herbivory needs to be examined.

Yellow River is one of the sandiest rivers in the world, with an annual sediment load of approximately 1.6 billion tons, creating a highly turbid Yellow River Estuary (YRE) (Wang et al., 2015; Yu et al., 2017). In this study, a field control experiment was conducted at the north and south banks of the YRE to investigate the combined effects of nutrient enrichment and herbivory on seagrass ecosystems under different turbidity. We hypothesized that turbidity had the mediating effect on shifting the relative importance of nutrient enrichment and herbivory on seagrass. In testing the hypothesis we aim to explore: (1) the effects of nutrient enrichment, herbivory and their interactions on the growth of two primary producers, i.e., seagrass and macroalgae; (2) the relative importance of nutrient enrichment and herbivory to the growth of seagrass under different turbidity; (3) potential mechanisms of turbidity that might regulate the responses of seagrasses and macroalgae to nutrient enrichment and herbivory. Our study emphasizes the mediating force of turbidity on seagrass ecosystems, and provides references for the protection and restoration of seagrass meadows under multiple environmental stressors, and prompts further studies on the feedback between sediment dynamics and seagrass meadows in the context of ecogeomorphology.

MATERIALS AND METHODS

Study Sites

The Yellow River Estuary is located on the southern bank of the Bohai Sea and the western part of the Laizhou Bay in Dongying City, Shandong Province, China (**Figure 1**). The tide is irregular semidiurnal, with spring and neap tidal ranges of 1.06–1.78 m and 0.46–0.78 m, respectively. Seagrass meadows in the YRE are dominated by the temperate seagrass *Zostera japonica*, which are distributed along the intertidal zones on the north and south banks of the estuary, and adjacent to the saltmarsh habitat of *Spartina alterniflora*. *Zostera japonica* and green macroalgae *Ulva intestinalis* (hereafter referred to as "seagrass" and "macroalgae," respectively) are the dominant primary producers of the seagrass meadows, which provide habitat for herbivores and predators. The dominant herbivores

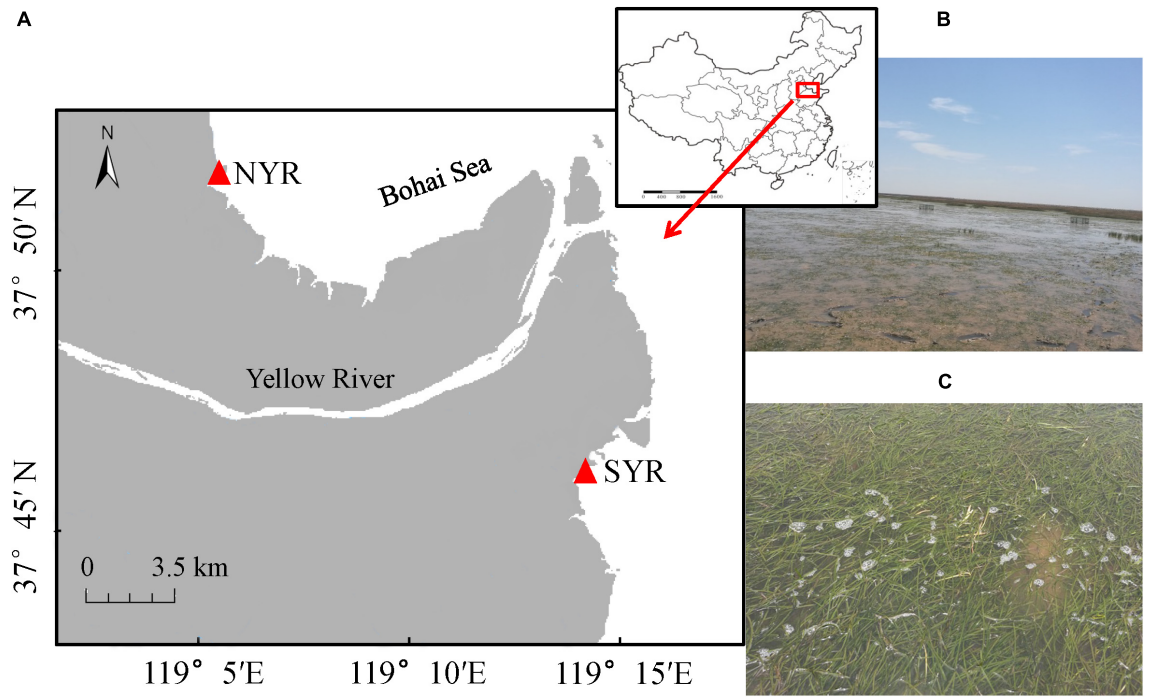


FIGURE 1 | Schematic diagram of the *Zostera japonica* meadows in the Yellow River Estuary: **(A)** location of the two study sites; **(B)** a illustrating photograph of the seagrass meadow in the north bank of the Yellow River Estuary (NYR); **(C)** a illustrating photograph of the seagrass meadow in the south bank of the Yellow River Estuary (SYR).

in the seagrass meadows are mainly intermediate consumers such as fishes and macrobenthic invertebrate, including small-sized herbivores such as small shrimps, Mollusca and Polychaetes (1∼3 cm in size), median-sized herbivores such as herbivorous crabs (3∼10 cm in size) and large-sized herbivores such as herbivorous fishes (> 10 cm).

Two study sites were selected on the north and south banks (NYR, SYR) of the river mouth which were both nutrient-limited systems with different water turbidity. Due to the prevailing estuarine circulation, a large amount of sediment is transported to the south bank of the estuary, especially during the Water-Sediment Regulation Scheme (WSRS) period, i.e., a 1-month period during the flood season every summer during which artificial flood pulses are created through dam regulation to mitigate the siltation both in the Xiaolangdi Reservoir and the lower reaches, and restore ecohydrological conditions downstream (Wang et al., 2017). As a result, significant differences in water turbidity are created between the two banks. Therefore, the seagrass meadows in the south bank are exposed to more turbidity than those in the north bank. Meanwhile, all meadows in the YRE are distributed in nutrient-limited areas with low nitrogen and phosphorus content in the water column, rendering them ideal for testing the interactive effects of nutrient enrichment and herbivory under different turbidity. NYR was located at 37°50′56.4″ N, 119°05′49.20″ E, where the water turbidity ranged from 11.7 to 25.4 NTU; SYR was located at 37°44′20.40″ N, 119°15′10.79″ E, where the water turbidity ranged from 50.80 to 90.36 NTU. The experiment was run for 120 days, from May to September in 2018, during which the salinity of the seawater ranged from 25.8 to 26.6 PPT, the temperature of the seawater ranged from 14.6 to 32.9°C, and the pH ranged from 8.04 to 8.25. Salinity was measured by a portable salinity meter (AZ8371, Shanghai Shuangxun Electronic, China), and temperature, pH and turbidity were measured by a multiparameter water quality probe (YSI Pro1020, RAE Systems, United States). No significant differences were found between the two sites during the experimental period except for the turbidity.

Experimental Design

Experiments of the same design were replicated in the two sites. We conducted a fully crossed 2 × 4 factorial design with two treatments of nutrients (nutrient enrichment or control) and four treatments of herbivory (seagrass only, crab inclusion, small and median-sized herbivores inclusion or all herbivores inclusion) to obtain different levels of herbivory intensity. The 8 treatments (n = 4 for each treatment) were randomly distributed across 32 plots at each site, totaling 64 experimental plots for the two sites. Experiment plots (1 m × 1 m × 1 m) were set up in areas without crab burrowing holes to eliminate the interference of crab, and were separated by a minimum distance of 10 m to prevent any nutrient transfer between each other (Campbell et al., 2018; Yan et al., 2020). Each plot was made of four metal reinforcing rods to fix the position.

Seagrass only plots (S) were set up by enclosing plots in cube-shaped cages made of plastic extruded nets (1 cm mesh size) to

prevent almost all the herbivory effects, and the nets were inserted 10 cm deep into the bottom sediment to prevent the entry of burrowing crabs. Crab inclusion plots (S + CR) were of similar construction to S plots, but the nets were parallel with the bottom sediment surface to allow the entry of burrowing crabs. Small and median-sized herbivore inclusion plots (S + MH) were enclosed in plastic extruded nets (3 cm mesh size), and the nets were raised 2 cm above the bottom surface to allow the entry of all the dominant small and median-sized herbivores, but prevent large herbivores. All herbivore inclusion plots (S + LH) were of similar construction, but had the two side panels parallel to the primary flow direction removed to allow the entry of all herbivores.

Nutrient enrichment plots received 500 g of slow-release Osmocote fertilizer (*N*:*P* = 14:14) enclosed in eight nylon mesh bags. Four of the bags were buried 5 cm under the four corners of the plot, and the other four bags were tethered in the middle of the metal rod of the plot to simulate changing nutrient enrichment under tidal fluctuations. Each bag was replaced every 4 weeks to ensure consistent nutrient delivery (Mutchler and Hoffman, 2017; Archer et al., 2018).

Plot Sampling

After 120 days, all the macroalgae and seagrasses of each plot were collected, washed on the spot, and brought back to the laboratory. We selected five seagrass shoots of each plot to assess seagrass morphological characteristics such as leaf length, leaf width, rhizome length, and number of leaves. Each seagrass shoot was subsequently divided into aboveground (leaf) and belowground (rhizome and root) samples. The seagrass and macroalgae samples were dried with an oven (60°C, 48 h), and weighed for dry mass per m^2. The total biomass of seagrass was the sum of the above- and below-ground biomass.

Herbivory Intensity

Seagrass only plots (S) were considered to have no herbivory, and the herbivory intensities of other treatments were calculated per plot by subtracting the seagrass biomass of each treatment (S + CR, S + MH, S + LH) from the biomass of seagrass only (S) treatment, all for nutrient control treatment (natural conditions). Herbivory intensities were divided into aboveground, belowground, and total herbivory intensities as the biomass.

Statistical Analyses

A Principal Component Analysis (PCA) was performed for each site to obtain a multi-metric index (MI) for seagrass growth among treatments (Garcia-Marin et al., 2013; Bourque and Fourqurean, 2014). The PCA was used to reduce data complexity and reveal variables that explained maximum variability in the seagrass growth characteristics. Six variables were included in the PCA analysis, i.e., aboveground biomass, belowground biomass, leaf length, leaf width, rhizome length and number of leaves.

Data were subject to normality (Shapiro-Wilk test) and homogeneity of variance checks (Levene's test) before analyses. Firstly, three-way ANOVA was used to examine the interactive effect of nutrient enrichment, herbivory and site (turbidity) on the biomass of macroalgae, above/belowground biomass and morphological characteristics of seagrass. Secondly, a two-way Analysis of Variance (ANOVA) followed by Tukey HSD *post-hoc* test was used to assess differences in the biomass of macroalgae, above/belowground biomass, morphological characteristics and multi-metric index of seagrass among nutrient enrichment and herbivory treatments in the two sites. One-way ANOVA was also used to compare the difference of herbivory intensity between the various herbivory treatments, in the above-, belowground and total parts, respectively. Data went through logarithm, square root or sine/cosine transformations when necessary to meet homogeneity of variance. The significance level was $P < 0.05$ (all variables were expressed as mean ± standard error). All statistical analyses were conducted using SPSS 20.0.

RESULTS

Herbivory Intensity

Herbivory intensity is defined as the seagrass biomass difference between the various herbivory treatments and the seagrass only treatment without nutrient enrichment. Our results showed that the belowground herbivory intensity was consistently higher than aboveground throughout all herbivory treatments in the NYR, whereas the opposite was found in the SYR, and the total herbivory intensity was consistently higher throughout all herbivory treatments in the NYR than SYR (**Figure 2**). Herbivory intensity of S + CR treatment was significantly lower in aboveground, belowground and total biomass than other treatments in the NYR, while S + MH (small- and median-sized herbivore inclusion) and S + LH treatments (additional large-sized herbivore) showed no significant differences ($P < 0.05$), which reflected the dominance of small- and median-sized herbivores. There was no significant difference in the herbivory intensity among the various herbivory treatments in the SYR, except for the total biomass of the S + CR treatment.

Seagrass Growth Index

In the NYR, PCA extracted two principal components that together described 60.24% of the variation in the original data, and PC1 explained 36.64% of the variation in the data set (**Supplementary Table 1**). In the SYR, two principal components together described 62.81% of the variation in the original data, and PC1 explained 36.81% of the variation in the dataset (**Supplementary Table 2**). MI of each plot was calculated by the equations shown in **Table 1**. Nutrient enrichment significantly affected MI ($P < 0.01$) in the NYR, while herbivory ($P < 0.05$) and nutrient enrichment × herbivory interactions ($P < 0.01$) had a significant effect on MI in the SYR (**Supplementary Tables 4, 5**).

Seagrass Response to Nutrient Enrichment and Herbivory

Nutrient enrichment × Site (Turbidity) interactions were detectable on seagrass biomass (above- and belowground) and morphological characteristics (leaf width and rhizome length), while Herbivory × Site (Turbidity) interactions were only observed on number of leaves ($P < 0.05$;

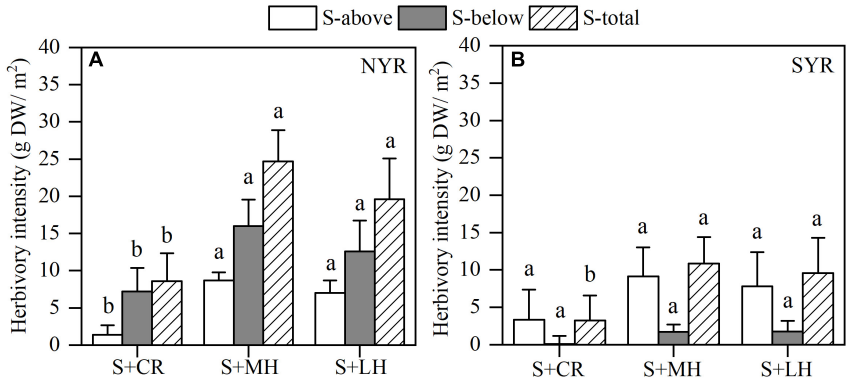


FIGURE 2 | Herbivory intensity of aboveground (S-above), belowground (S-below), and total parts (S-total) of seagrass among different herbivory treatments in the NYR **(A)** and SYR **(B)** (mean ± *SE*, *n* = 4). Within each parts of seagrass, bars sharing a letter are not significantly different from one another ($p > 0.05$).

TABLE 1 | Equations for the multi-metric index (MI) values of each site obtained from the eigenvectors of **Supplementary Tables 1, 2**.

	NYR	SYR
PC1	0.590 * AG + 0.550 * BG–0.230 * length–0.380 * width–0.340 * rhizome–0.190 * number	0.500 * AG + 0.520 * BG–0.170 * length + 0.220 * width + 0.390 * rhizome + 0.500 * number
PC2	0.070 * AG–0.01 * BG + 0.570 * length + 0.400 * width–0.420 * rhizome–0.570 * number	0.390 *AG + 0.340 * BG + 0.600 * length–0.540 * width–0.260 * rhizome–0.120 * number
MI	0.608 *PC1 + 0.392 * PC2	0.586 *PC1 + 0.414 * PC2

AG is the aboveground biomass; BG is the belowground biomass; length is the length of leaf; width is the width of leaf; rhizome is the length of rhizome; number is the number of leaves. All data has been standardized.

Supplementary Table 3), which suggested a rather strong interplay between turbidity and nutrient enrichment. Nutrient enrichment without herbivory decreased seagrass above- and belowground biomass in both sites (S plots; **Figures 3A,C**). When nutrient enrichment acted alongside herbivory treatment, however, the response of seagrass contrasted in the two sites. In the less turbid NYR, nutrient enrichment significantly increased seagrass belowground biomass ($P < 0.01$; **Figure 3C** and **Supplementary Table 4**). On the contrary, in the more turbid SYR, the above- and belowground biomass of seagrass did not show a significant response to nutrient enrichment ($P > 0.05$; **Figures 3B,D** and **Supplementary Table 5**), and the herbivory effect tended to dominate ($P < 0.01$; **Supplementary Table 5**). Positive nutrient enrichment effect on seagrass biomass manifested in the increase of rhizome length and number of leaves in the NYR ($P < 0.05$; **Figures 4B,C** and **Supplementary Table 4**), albeit a decline in leaf length ($P < 0.05$; **Figure 4A** and **Supplementary Table 4**). Similar to biomass, morphological characteristics in the SYR did not show a significant response to nutrient enrichment ($P > 0.05$; **Supplementary Table 5**), except for the reduction of rhizome length ($P < 0.05$; **Figure 4D** and **Supplementary Table 5**).

Generally, herbivory without nutrient enrichment decreased the above- and belowground biomass of seagrass with the maximum biomass attained in the seagrass only plots (S) in both sites (**Figure 3**). As herbivory intensity increased, seagrass biomass declined further. Herbivory combined with nutrient enrichment resulted in the maximum biomass attained in the plots with crab inclusion (S + CR), and the minimum in the seagrass only plots (S) where the competitor macroalgae appeared to be dominant as a result of the nutrient enrichment (**Figure 3**). This is especially prominent in the more turbid SYR site where the seagrass almost died off under nutrient enrichment without herbivory (**Figures 3B,D**). The negative effect of herbivory was detectable on the leaf length ($P < 0.05$) and number of leaves ($P < 0.01$) of seagrass in the NYR (**Figure 4**). Herbivorous crabs had a significant contribution to the decline of leaf length and leaf numbers as shown in the minimum leaf length and leaf numbers for the crab inclusion (S + CR) plots.

Macroalgae Response to Nutrient Enrichment and Herbivory

Nutrient enrichment without herbivory increased 161.42 and 207.83% of the macroalgae biomass in the NYR and SYR, respectively (S plots; **Figure 5**). Herbivory × Site (Turbidity) and Nutrient enrichment × Herbivory × Site (Turbidity) interactions were detectable on macroalgae biomass ($P < 0.001$; **Supplementary Table 3**), which indicated the regulation of turbidity on herbivory effect as well as Nutrient enrichment × Herbivory interaction. Herbivory had a significant negative effect on the biomass of macroalgae in both sites regardless of nutrient treatments ($P < 0.001$; **Supplementary Tables 4, 5**). However, the effect of inclusion of different body-sized herbivores was only detectable under nutrient enrichment in more turbid SYR, which was evidence for the mediating effect of turbidity on herbivory combined with nutrient enrichment.

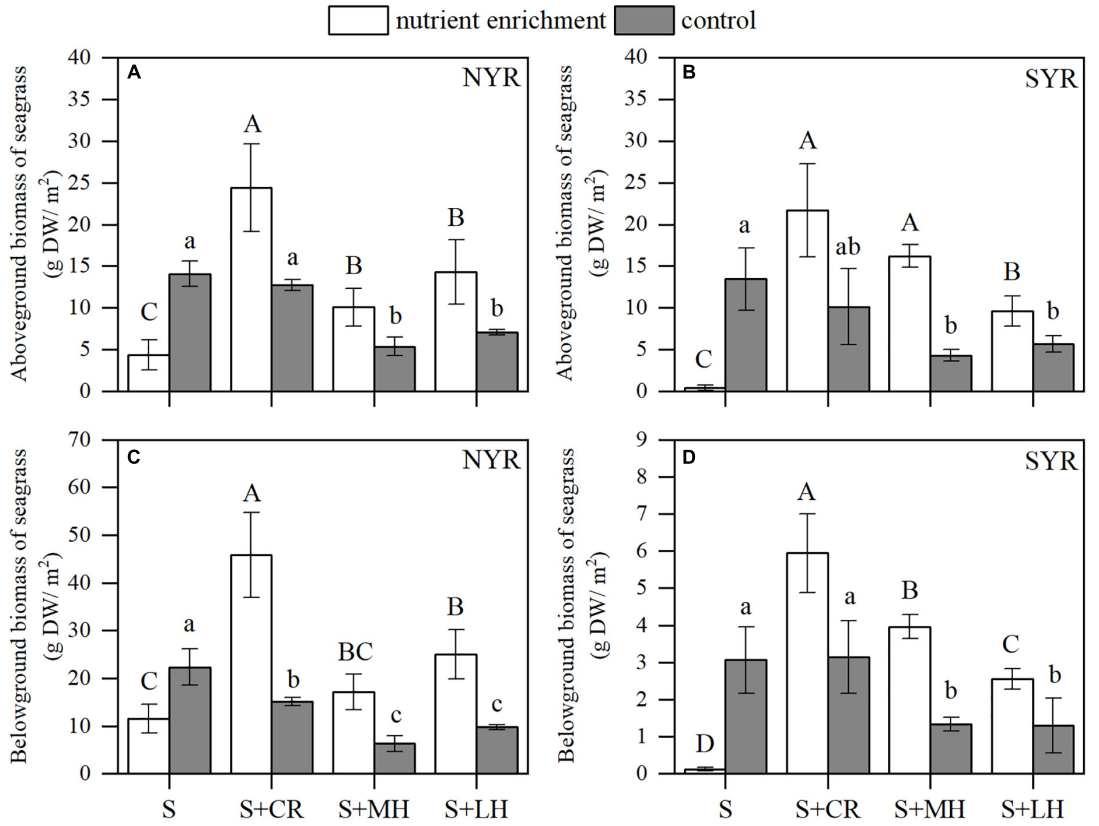


FIGURE 3 | Effects of nutrient enrichment and herbivory on seagrass biomass in the NYR and SYR (mean ± *SE*, *n* = 4). **(A)** Aboveground biomass of seagrass in the NYR; **(B)** aboveground biomass of seagrass in the SYR; **(C)** belowground biomass of seagrass in the NYR; **(D)** belowground biomass of seagrass in the SYR. Within nutrient treatments (enrichment or control), bars sharing a letter are not significantly different from one another ($p > 0.05$).

DISCUSSION

In coastal ecosystems, seagrass meadows are threatened by multiple short or long-term environmental stressors. While numerous studies have explored the effects of nutrient enrichment and herbivory on seagrass ecosystem structure and functioning, there is limited understanding of how their relative importance shifts across large spatial scales where environmental factors such as turbidity can vary significantly. Our study showed that turbidity mediated the nutrient enrichment effect on seagrass biomass and morphological characteristics, as well as the herbivory effect on macroalgae as the main competitive primary producer. In the less turbid site, nutrient enrichment alone suppressed seagrass biomass but promoted macroalgae growth. At the same time, herbivory without nutrient enrichment had a significant negative effect on the biomass of seagrass and macroalgae. When nutrient enrichment acted alongside herbivory, it significantly promoted seagrass above- and belowground biomass and resulted in the increase of rhizome length and number of leaves. Yet, the effect of inclusion of different body-sized herbivores on seagrass and macroalgae was not obvious. In the more turbid site, nutrient enrichment or herbivory alone induced similar effects as in the less turbid site. Notably, under nutrient enrichment alone, excessive macroalgae significantly suppressed seagrass growth and even led to seagrass mortality. When nutrient enrichment acted alongside herbivory, seagrass biomass as well as morphological characteristics (except for rhizome length) did not exhibit significant change. The herbivory effect tended to dominate where low intensity herbivory could suppress macroalgae proliferation due to the increased herbivory pressure and selective-grazing on macroalgae. And the effect of inclusion of different body-sized herbivores on seagrass and macroalgae was detectable.

Nutrient enrichment could facilitate the growth of seagrass as reported in many previous studies in the resource-limited system (Heck et al., 2000; Yan et al., 2020). In the less turbid NYR, nutrient enrichment increased rhizome length and thus significantly increased belowground biomass, while aboveground biomass did not increase as much as the belowground parts, e.g., leaf width showed no response and leaf length even decreased. This may be attributed to the fact that seagrass preferred to absorb nitrogen and phosphorus by belowground parts from sediment pore water (Archer et al., 2018; Ruocco et al., 2018). Another factor was the higher macroalgae cover on the aboveground parts which limited nutrient and other resource availability to seagrass, thereby reducing the seagrass aboveground biomass (Han and Liu, 2014; Han et al., 2016). The similar effect of macroalgae was also observed on seagrass

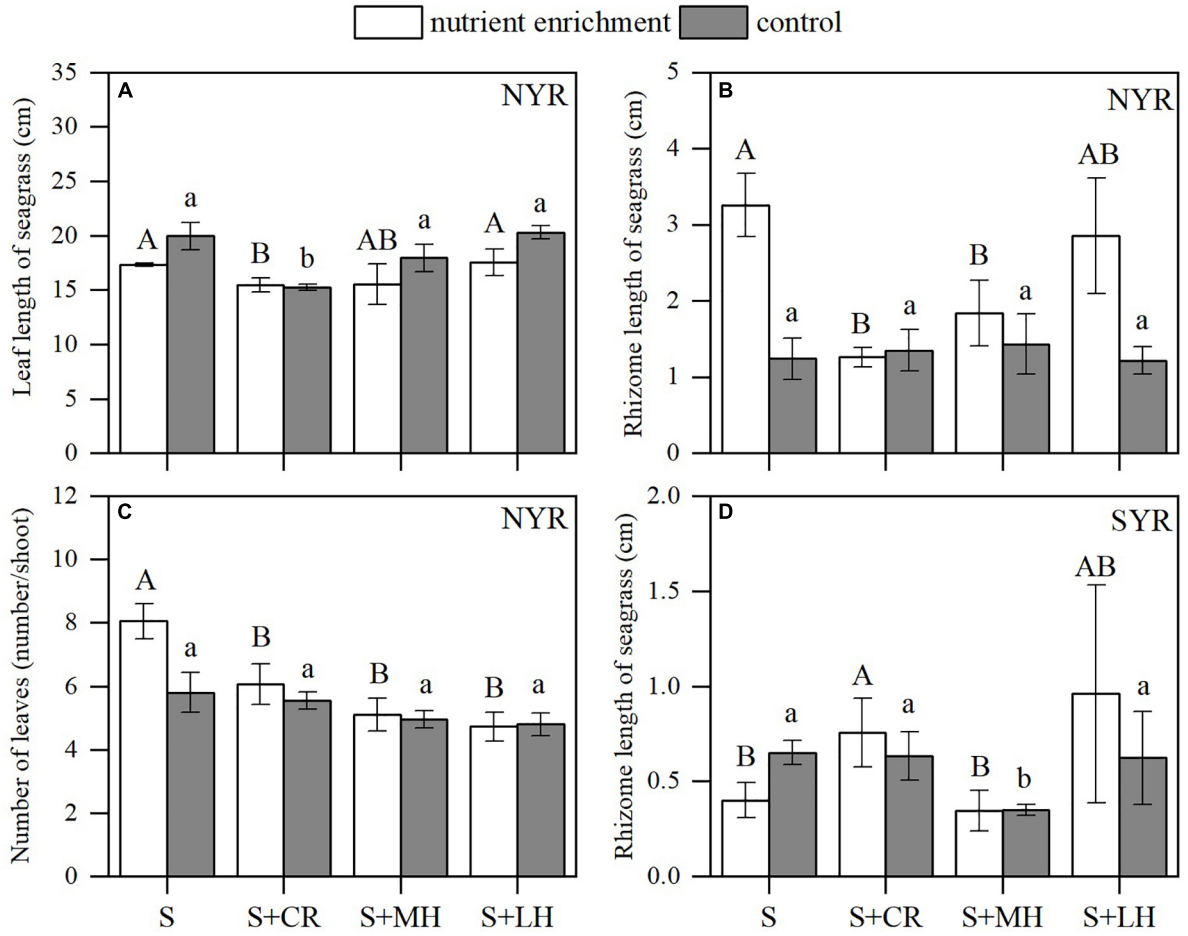


FIGURE 4 | Effects of nutrient enrichment and herbivory on the morphological characteristics of seagrass (mean ± *SE*, *n* = 4). **(A)** Leaf length in the NYR; **(B)** rhizome length in the NYR; **(C)** number of leaves in the NYR; **(D)** rhizome length in the SYR. Within nutrient treatments (enrichment or control), bars sharing a letter are not significantly different from one another ($p > 0.05$).

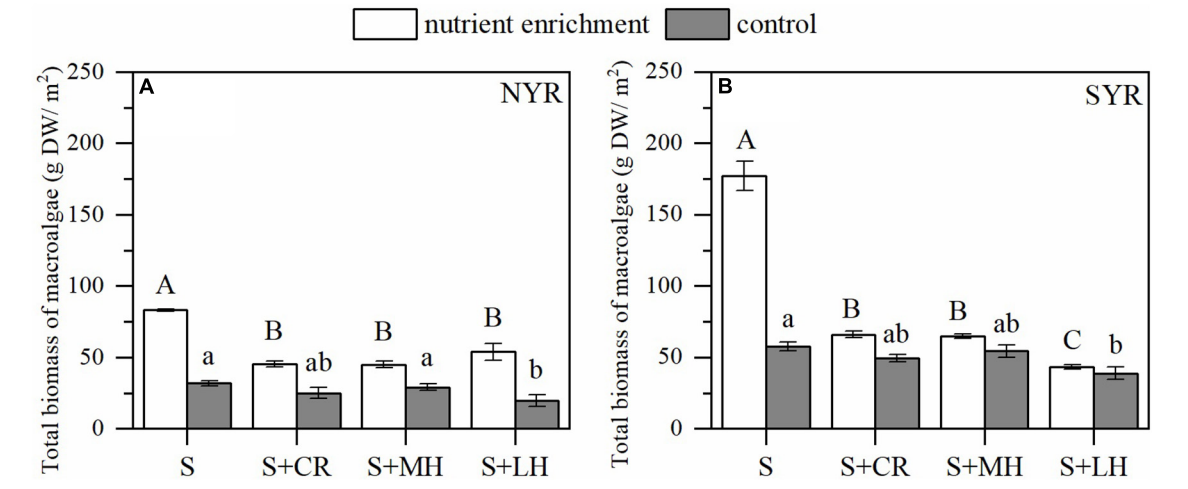


FIGURE 5 | Effects of nutrient enrichment and herbivory on the total biomass of macroalgae in the NYR **(A)** and SYR **(B)** (mean ± SE, *n* = 4). Within nutrient treatments (enrichment or control), bars sharing a letter are not significantly different from one another ($p > 0.05$).

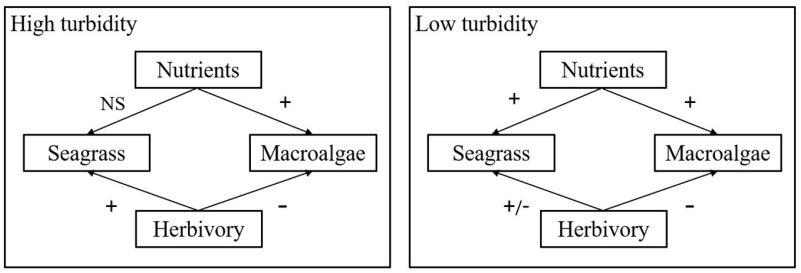


FIGURE 6 | A schematic diagram summarizing the combined effect of nutrient enrichment and herbivory on seagrass and macroalgae in high and low turbidity systems.

biomass in the SYR where both above- and belowground parts did not exhibit significant increase under nutrient enrichment. In the SYR, rhizome length also declined under nutrient enrichment, again presumably due to the nutrient-enhanced macroalgae competition (Wang et al., 2021). Previous studies have reported the fast-growing capacity of opportunistic macroalgae under nutrient enrichment (Glasby, 2012; Schmidt et al., 2012). Our study suggested nutrient enrichment promoted the proliferation of macroalgae to possess a competitive advantage against seagrass in a more turbid system. Previous studies also highlighted the negative effect of turbidity on seagrass nutrient uptake due to its high sensitivity to light reduction (Bulmer et al., 2018).

Herbivory plays a vital role in maintaining the balance between the two primary producers, especially in high turbidity systems. Nutrient enrichment without herbivory led to a dramatic decline or even death of seagrass, especially in the SYR with high turbidity where macroalgae exhibited fast-growing capacity. The presence of herbivores could counteract the negative effect of nutrient enrichment on the competition between seagrass and macroalgae. The herbivory effect on macroalgae between crab inclusion treatment and other treatments (additional small and median-sized herbivores or large-sized herbivores inclusion) did not differ significantly in the NYR, which showed that herbivorous crabs tended to be the dominant grazer of macroalgae (**Figure 5**). While in the SYR, other herbivores such as small-sized shrimps, Mollusca and Polychaetas as well as large herbivorous fishes were also found to preferentially feed on macroalgae under nutrient enrichment. It might be due to the long-term training for herbivores in high turbidity environments to form selective-grazing on nutrient-enriched food, which has also been recognized in other seagrass systems (Klumpp et al., 1993; Hays, 2005). Nutrient-induced herbivory of macroalgae was also evidenced by the overall reduced herbivory intensity on seagrass in the SYR than NYR (**Figure 1**).

Overall, the relative importance of nutrient enrichment and herbivory was shifted under the mediating effects of turbidity. Herbivory played a vital role in maintaining the balance between the two primary producers in high turbidity systems. While in a less turbid system, nutrient enrichment tended to offset the herbivory-induced biomass loss by promoting seagrass growth. The combined effect of nutrient enrichment and herbivory on seagrass and macroalgae in high and low turbidity systems are summarized in the schematic diagram shown in **Figure 6**. The responses of seagrasses and macroalgae to nutrient enrichment and herbivory varying under different turbidity suggested two potential mechanisms. Firstly, turbidity could mediate the grazing pressure and preference of herbivores. In a high turbidity environment, the majority of the different body-sized herbivores preferred to utilize the fast-growing and nutrient-enriched plant such as macroalgae, whereas herbivores tended to feed on seagrass in less turbid environments. Our results showed that herbivory had a significant effect on the multi-metric index of seagrass (**Supplementary Table 5**). And the significant effects of herbivory-site (turbidity) and herbivory-nutrient enrichment-site (turbidity) interactions on macroalgae biomass could also be evidence for this potential mechanism (**Supplementary Table 3**). The positive effect of turbidity to promote selective-grazing on macroalgae has been reported in previous studies conducted in seagrass meadow or other aquatic systems such as rivers (Ruiz and Romero, 2003; Savic et al., 2018). The positive effect of turbidity on herbivory could be attributed to the cascading effect of predators on herbivore, i.e., the reduced efficiency of predators caused by suspended sediment in turbid rivers (Savic et al., 2018). The selective-grazing of herbivores on algae in turbid waters could arise from the fast-growing ability as well as the distribution of algae covering the aboveground parts of seagrass (Ruiz and Romero, 2003; Savic et al., 2018). Therefore, the presence of herbivores is essential for the maintenance of ecosystem health in high turbidity sites.

The other potential mechanism was that nutrient enrichment favored the growth of opportunistic macroalgae over seagrass in a high turbidity system. Under nutrient enrichment alone, macroalgae suppressed seagrass and caused die off in the more turbid SYR, and yet the biomass of seagrass did not show a significant response to nutrient enrichment when combined with herbivory. On the contrary, in the less turbidity NYR, nutrients showed a significant effect on the biomass as well as the multi-metric index of seagrass (**Supplementary Table 4**). This potential mechanism was also evident in the effects of nutrient enrichment-site (turbidity) interactions on seagrass above- and belowground biomass (**Supplementary Table 3**).

Previous studies found that turbidity had significant negative effect on seagrass nutrient uptake due to its high sensitivity to light reduction (Bulmer et al., 2018). Meanwhile, the contribution of algae loads to light reduction on seagrass was also found to be critical in turbid waters (Ow et al., 2020). Thus, macroalgae has the superiority in competing for nutrients against seagrass in turbid system. It suggested that to some extent, nutrient enrichment had a positive effect on seagrass meadows under natural herbivory conditions in a less turbid environment, while in the more turbid system, it mainly caused negative effect and needs to be closely monitored.

This article provides field evidence for the mediating forces of turbidity on the combined effect of nutrient enrichment and herbivory. Herbivory played a vital role in maintaining the balance between seagrass and macroalgae in high turbidity systems. However, the importance of herbivores may have been underestimated in the context of coastal eutrophication management, especially in high turbidity systems where small increases in nutrients could have tremendous effects on the growth of seagrass. In a less turbid system, nutrient enrichment had a positive effect on seagrass meadows under natural herbivory conditions. Our study emphasizes the mediating force of turbidity on seagrass ecosystems, and provides references for the regulation of nutrient supply and herbivore exclusion in systems with varying turbidity. Many estuarine seagrass ecosystems face increasing hydrological alterations caused by human activities and climate change, which further alters sediment dynamics including sedimentation, resuspension, etc., and induces water turbidity and bed level changes (Palinkas and Koch, 2012; João et al., 2013). Feedback between seagrass meadows and sediment dynamics has been recognized as being vital to seagrass restoration (Suykerbuyk et al., 2016; Zhu et al., 2021), further studies are thus needed to investigate the influence of sediment dynamics on the distribution pattern and ecogeomorphological processes of seagrass meadows.

DATA AVAILABILITY STATEMENT

The raw data supporting the conclusions of this article will be made available by the authors, without undue reservation.

AUTHOR CONTRIBUTIONS

JB, JY, and XW: conceptualization. XW: data analysis and writing—original draft preparation. DS and BC: writing—review and editing. DS: supervision. All authors contributed to the article and approved the submitted version.

FUNDING

This research was funded by the National Key R&D Program of China (2019YFE0121500), the Key Project of National Natural Science Foundation of China (51639001 and U1901212), the Joint Funds of the National Natural Science Foundation of China (U2006215), and the National Natural Science Foundation of China (51909005).

ACKNOWLEDGMENTS

The staffs of the Yellow River Estuary Management Station, Yellow River Delta National Nature Reserve Administration Bureau, are also gratefully acknowledged for their assistance in this study.

SUPPLEMENTARY MATERIAL

The Supplementary Material for this article can be found online at: https://www.frontiersin.org/articles/10.3389/fmars.2022.787041/full#supplementary-material

REFERENCES

Albert, S., Saunders, M. I., Roelfsema, C. M., Leon, J. X., Johnstone, E., Mackenzie, J. R., et al. (2017). Winners and losers as mangrove, coral and seagrass ecosystems respond to sea-level rise in Solomon Islands. *Environ. Res. Lett.* 12:094009.

Archer, S. K., Hensel, E., and Layman, C. A. (2018). Ambient nutrient availability drives the outcome of an interaction between a sponge (Halichondria melanadocia) and seagrass (Thalassia testudinum). *J. Exp. Mar. Biol. Ecol.* 503, 86–91. doi: 10.1016/j.jembe.2018.02.005

Baden, S., Boström, C., Tobiasson, S., Arponen, H., and Moksnes, P.-O. (2010). Relative importance of trophic interactions and nutrient enrichment in seagrass ecosystems: a broad-scale field experiment in the Baltic-Skagerrak area. *Limnol. Oceanogr.* 55, 1435–1448. doi: 10.4319/lo.2010.55.3.1435

Bertram, C., Quaas, M., Reusch, T. B. H., Vafeidis, A. T., Wolff, C., and Rickels, W. (2021). The blue carbon wealth of nations. *Nat. Clim. Change* 11:886. doi: 10.1038/s41558-021-01089-4

Bourque, A. S., and Fourqurean, J. W. (2014). Effects of common seagrass restoration methods on ecosystem structure in subtropical seagrass meadows. *Mar. Environ. Res.* 97, 67–78. doi: 10.1016/j.marenvres.2014.03.001

Bulmer, R. H., Townsend, M., Drylie, T., and Lohrer, A. M. (2018). Elevated Turbidity and the Nutrient Removal Capacity of Seagrass. *Front. Mar. Sci.* 5:462. doi: 10.3389/fmars.2018.00462

Burkepile, D. E., and Hay, M. E. (2006). Herbivore VS Nutrient Control of Marine Primary Producers: context-Dependent Effects. *Ecology* 87, 3128–3139. doi: 10.1890/0012-9658(2006)87[3128:hvncom]2.0.co;2

Campbell, J. E., Altieri, A. H., Johnston, L. N., Kuempel, C. D., Paperno, R., Paul, V. J., et al. (2018). Herbivore community determines the magnitude and mechanism of nutrient effects on subtropical and tropical seagrasses. *J. Ecol.* 106, 401–412. doi: 10.1111/1365-2745.12862

Carr, L. A., and Boyer, K. E. (2014). Variation at multiple trophic levels mediates a novel seagrass-grazer interaction. *Mar. Ecol. Prog. Ser.* 508, 117–128. doi: 10.3354/meps10855

Darnell, K. M., and Dunton, K. H. (2017). Plasticity in turtle grass (Thalassia testudinum) flower production as a response to porewater nitrogen availability. *Aquat. Bot.* 138, 100–106. doi: 10.1016/j.aquabot.2017.01.007

Du, J., Hu, W., Nagelkerken, I., Sangsawang, L., Loh, K. H., Ooi, J. L.-S., et al. (2020). Seagrass meadows provide multiple benefits to adjacent coral reefs through various microhabitat functions. *Ecosyst. Health. Sustainabilit.* 6:1812433. doi: 10.1080/20964129.2020.1812433

Duffy, J. E., Reynolds, P. L., Boström, C., Coyer, J. A., Cusson, M., Donadi, S., et al. (2015). Biodiversity mediates top–down control in eelgrass ecosystems: a global comparative-experimental approach. *Ecol. Lett.* 18, 696–705. doi: 10.1111/ele.12448

Ebrahim, A., Olds, A. D., Maxwell, P. S., Pitt, K. A., Burfeind, D. D., and Connolly, R. M. (2014). Herbivory in a subtropical seagrass ecosystem: separating the functional role of different grazers. *Mar. Ecol. Prog. Ser.* 511, 83–91. doi: 10.3354/meps10901

Fourqurean, J. W., Manuel, S., Coates, K. A., Kenworthy, W. J., and Smith, S. R. (2010). Effects of excluding sea turtle herbivores from a seagrass bed: overgrazing may have led to loss of seagrass meadows in Bermuda. *Mar. Ecol. Prog. Ser.* 419, 223–232. doi: 10.3354/meps08853

Fourqurean, J. W., Manuel, S. A., Coates, K. A., Massey, S. C., and Kenworthy, W. J. (2019). Decadal Monitoring in Bermuda Shows a Widespread Loss of Seagrasses Attributable to Overgrazing by the Green Sea Turtle Chelonia mydas. *Estuar. Coast.* 42, 1524–1540. doi: 10.1007/s12237-019-00587-1

Garcia-Marin, P., Cabaco, S., Hernandez, I., Vergara, J. J., Silva, J., and Santos, R. (2013). Multi-metric index based on the seagrass Zostera noltii (ZoNI) for ecological quality assessment of coastal and estuarine systems in SW Iberian Peninsula. *Mar. Pollut. Bull.* 68, 46–54. doi: 10.1016/j.marpolbul.2012.12.025

Garrido, M., Lafabrie, C., Torre, F., Fernandez, C., and Pasqualini, V. (2013). Resilience and stability of Cymodocea nodosa seagrass meadows over the last four decades in a Mediterranean lagoon. *Estuar. Coast. Shelf Sci.* 130, 89–98. doi: 10.1016/j.ecss.2013.05.035

Glasby, T. M. (2012). *Caulerpa taxifolia* in seagrass meadows: killer or opportunistic weed? *Biol. Invasions.* 15, 1017–1035. doi: 10.1007/s10530-012-0347-1

Han, Q., and Liu, D. (2014). Macroalgae blooms and their effects on seagrass ecosystems. *J. Ocean. U. China.* 13, 791–798. doi: 10.1007/s11802-014-2471-2

Han, Q., Soissons, L. M., Bouma, T. J., van Katwijk, M. M., and Liu, D. (2016). Combined nutrient and macroalgae loads lead to response in seagrass indicator properties. *Mar. Pollut. Bull.* 106, 174–182. doi: 10.1016/j.marpolbul.2016.03.004

Hays, C. G. (2005). Effect of nutrient availability, grazer assemblage and seagrass source population on the interaction between Thalassia testudinum (turtle grass) and its algal epiphytes. *J. Exp. Mar. Biol. Ecol.* 314, 53–68. doi: 10.1016/j.jembe.2004.08.017

Heck, K. L. Jr., Pennock, J. R., Valentine, J. F., Coen, L. D., and Sklenar, S. A. (2000). Effects of nutrient enrichment and small predator density on seagrass ecosystems: an experimental assessment. *Limnol. Oceanogr.* 45, 1041–1057.

Hughes, A. R., Bando, K. J., Laura, F. R., and Susan, L. W. (2004). Relative effects of grazers and nutrients on seagrasses: a meta-analysis approach. *Mar. Ecol. Prog. Ser.* 282, 87–99.

João, D. L. E. S., Ana, A., Ana Isabel, L., and João Miguel, D. (2013). Turbidity under changing physical forcing over two contrasting locations of seagrass meadows. *J. Coastal Res.* 65, 2023–2028. doi: 10.2112/SI65-342.1

Klumpp, D. W., Salita-Espinosa, J. T., and Fortes, M. D. (1993). Feeding ecology and trophic role of sea urchins in a tropical seagrass community. *Aquat. Bot.* 45, 205–229. doi: 10.1016/0304-3770(93)90022-O

Leoni, V., Vela, A., Pasqualini, V., Pergent-Martini, C., and Pergent, G. (2008). Effects of experimental reduction of light and nutrient enrichments (N and P) on seagrasses: a review. *Aquat. Conserv. Mar. Freshwat. Ecosyst.* 18, 202–220. doi: 10.1002/aqc.842

Leston, S., Lillebø, A., and Pardal, M. (2008). The response of primary producer assemblages to mitigation measures to reduce eutrophication in a temperate estuary. *Estuar. Coast. Shelf. S.* 77, 688–696. doi: 10.1016/j.ecss.2007.11.002

Li, C., Zhang, Y.-H., Wu, X.-X., Jiang, Y.-S., Li, W.-T., and Zhang, P.-D. (2021). Changes in survival and growth in response to different combinations of turbidity and duration in eelgrass Zostera marina plants. *Estuar. Coast. Shelf. S.* 249, 107108. doi: 10.1016/j.ecss.2020.107108

Listiawati, V., and Kurihara, H. (2021). Ocean warming and acidification modify top-down and bottom-up control in a tropical seagrass ecosystem. *Sci. Rep.* 11:13605. doi: 10.1038/s41598-021-92989-0

Moran, K. L., and Bjorndal, K. A. (2005). Simulated green turtle grazing affects structure and productivity of seagrass pastures. *Mar. Ecol. Prog. Ser.* 305, 235–247. doi: 10.3354/meps305235

Moran, K. L., and Bjorndal, K. A. (2007). Simulated green turtle grazing affects nutrient composition of the seagrass Thalassia testudinum. *Mar. Biol.* 150, 1083–1092. doi: 10.1007/s00227-006-0427-9

Mutchler, T., and Hoffman, D. K. (2017). Response of seagrass (Thalassia testudinum) metrics to short-term nutrient enrichment and grazing manipulations. *J. Exp. Mar. Biol. Ecol.* 486, 105–113. doi: 10.1016/j.jembe.2016.09.015

Mvungi, E. F., and Pillay, D. (2019). Eutrophication overrides warming as a stressor for a temperate African seagrass (Zostera capensis). *PLoS One* 14:e0215129. doi: 10.1371/journal.pone.0215129

Ontoria, Y., Gonzalez-Guedes, E., Sanmartí, N., Bernardeau-Esteller, J., Ruiz, J. M., Romero, J., et al. (2019). Interactive effects of global warming and eutrophication on a fast-growing Mediterranean seagrass. *Mar. Environ. Res.* 145, 27–38. doi: 10.1016/j.marenvres.2019.02.002

Orth, R. J., Lefcheck, J. S., McGlathery, K. S., Aoki, L., Luckenbach, M. W., Moore, K. A., et al. (2020). Restoration of seagrass habitat leads to rapid recovery of coastal ecosystem services. *Sci. Adv.* 6:eabc6434. doi: 10.1126/sciadv.abc6434

Östman, Ö, Eklöf, J., Eriksson, B. K., Olsson, J., Moksnes, P. O., Bergström, U., et al. (2016). Top-down control as important as nutrient enrichment for eutrophication effects in North Atlantic coastal ecosystems. *J. Appl. Ecol.* 53, 1138–1147. doi: 10.1111/1365-2664.12654

Ow, Y. X., Ng, K. J., Lai, S., Yaakub, S. M., and Todd, P. (2020). Contribution of epiphyte load to light attenuation on seagrass leaves is small but critical in turbid waters. *Mar Freshwater Res.* 71, 929–934. doi: 10.1071/MF19178

Palinkas, C. M., and Koch, E. W. (2012). Sediment accumulation rates and submersed aquatic vegetation (SAV) distributions in the mesohaline Chesapeake Bay, USA. *Estuar Coast.* 35, 1416–1431. doi: 10.1007/s12237-012-9542-7

Repolho, T., Duarte, B., Dionísio, G., Paula, J. R., Lopes, A. R., Rosa, I. C., et al. (2017). Seagrass ecophysiological performance under ocean warming and acidification. *Sci. Rep.* 7:41443. doi: 10.1038/srep41443

Ruiz, J. M., and Romero, J. (2003). Effects of disturbances caused by coastal constructions on spatial structure, growth dynamics and photosynthesis of the seagrass Posidonia oceanica. *Mar. Pollut. Bull.* 46, 1523–1533. doi: 10.1016/j.marpolbul.2003.08.021

Ruocco, M., Marin-Guirao, L., Ravaglioli, C., Bulleri, F., and Procaccini, G. (2018). Molecular level responses to chronic versus pulse nutrient loading in the seagrass Posidonia oceanica undergoing herbivore pressure. *Oecologia* 188, 23–39. doi: 10.1007/s00442-018-4172-9

Savic, A., Pesic, V., Dordevic, M., Randelovic, V., Juskovic, M., and Andrzej, G. (2018). Effects of nutrients and turbidity on grazer-periphyton interactions: a case study from the Nisava River, Balkan Peninsula. *North-West. J. Zool.* 14, 226–231.

Schallenberg, M., and Burns, C. W. (2004). Effects of sediment resuspension on phytoplankton production: teasing apart the influences of light, nutrients and algal entrainment. *Freshw. Biol.* 49, 143–159. doi: 10.1046/j.1365-2426.2003.01172.x

Schmidt, A. L., Wysmyk, J. K., Craig, S. E., and Lotze, H. K. (2012). Regional-scale effects of eutrophication on ecosystem structure and services of seagrass beds. *Limnol. Oceanogr.* 57, 1389–1402. doi: 10.4319/lo.2012.57.5.1389

Scott, A. L., York, P. H., and Rasheed, M. A. (2021). Herbivory Has a Major Influence on Structure and Condition of a Great Barrier Reef Subtropical Seagrass Meadow. *Estuar. Coast.* 44, 506–521. doi: 10.1007/s12237-020-00868-0

Stockbridge, J., Jones, A. R., and Gillanders, B. M. (2020). A meta-analysis of multiple stressors on seagrasses in the context of marine spatial cumulative impacts assessment. *Sci. Rep.* 10, 1–11. doi: 10.1038/s41598-020-68801-w

Suykerbuyk, W., Bouma, T. J., Govers, L. L., Giesen, K., de Jong, D. J., Herman, P., et al. (2016). Surviving in changing seascapes: sediment dynamics as bottleneck for long-term seagrass presence. *Ecosystems* 19, 296–310.

Viana, I. G., Moreira-Saporiti, A., and Teichberg, M. (2020). Species-Specific Trait Responses of Three Tropical Seagrasses to Multiple Stressors: the Case of Increasing Temperature and Nutrient Enrichment. *Front. Plant Sci.* 11:571363. doi: 10.3389/fpls.2020.571363

Vieira, R., Martin, A., Engelen, A. H., Thomsen, M. S., and Arenas, F. (2020). Interactive effects of co-occurring anthropogenic stressors on the seagrass, Zostera noltei. *Ecol. Indic.* 109:105780. doi: 10.1016/j.ecolind.2019.105780

Wang, H., Wu, X., Bi, N., Li, S., Yuan, P., Wang, A., et al. (2017). Impacts of the dam-orientated water-sediment regulation scheme on the lower reaches and delta of the Yellow River (Huanghe): a review. *Global. Planet. Change* 157, 93–113. doi: 10.1016/j.gloplacha.2017.08.005

Wang, L., Tomas, F., and Mueller, R. S. (2020). Nutrient enrichment increases size of Zostera marina shoots and enriches for sulfur and nitrogen cycling bacteria in root-associated microbiomes. *FEMS. Microbiol. Ecol.* 96:fiaa129. doi: 10.1093/femsec/fiaa129

Wang, S., Fu, B., Piao, S., Lü, Y., Ciais, P., Feng, X., et al. (2015). Reduced sediment transport in the Yellow River due to anthropogenic changes. *Nat. Geosci.* 9, 38–41. doi: 10.1038/ngeo2602

Wang, X., Yan, J., Bai, J., Shao, D., and Cui, B. (2021). Effects of interactions between macroalgae and seagrass on the distribution of macrobenthic invertebrate communities at the Yellow River Estuary, China. *Mar. Pollut. Bull.* 164:112057. doi: 10.1016/j.marpolbul.2021.112057

Waycott, M., Duarte, C. M., Carruthers, T. J., Orth, R. J., Dennison, W. C., Olyarnik, S., et al. (2009). Accelerating loss of seagrasses across the globe threatens coastal ecosystems. *Proc. Natl. Acad. Sci.* 106, 12377–12381. doi: 10.1073/pnas.0905620106

Whalen, M. A., Duffy, J. E., and Grace, J. B. (2013). Temporal shifts in top-down vs. bottom-up control of epiphytic algae in a seagrass ecosystem. *Ecology* 94, 510–520. doi: 10.1890/12-0156.1

Yamamoto, T., Malingin, M. A. C. L., Marivic Pepino, M., Yoshikai, M., Campos, W., Miyajima, T., et al. (2019). Assessment of coastal turbidity improvement potential by terrigenous sediment load reduction and its implications on seagrass inhabitable area in Banate Bay, central Philippines. *Sci. Total. Environ.* 656, 1386–1400. doi: 10.1016/j.scitotenv.2018.11.243

Yan, J., Heide, T., Cui, B., Bai, J., Ysebaert, T., and Koppel, J. (2020). A healthy trophic structure underlies the resistance of pristine seagrass beds to nutrient enrichment. *Limnol. Oceanogr.* 65, 2748–2756. doi: 10.1002/lno.11545

York, P. H., Kelaher, B. P., Booth, D. J., and Bishop, M. J. (2012). Trophic responses to nutrient enrichment in a temperate seagrass food chain. *Mar. Ecol. Prog. Ser.* 449, 291–296. doi: 10.3354/meps09541

Yu, X., Xie, X., and Meng, S. (2017). Modeling the Responses of Water and Sediment Discharge to Climate Change in the Upper Yellow River Basin, China. *J. Hydrol. Eng.* 22:05017026. doi: 10.1061/(ASCE)HE.1943-5584.0001590

Zhu, Q., Wiberg, P. L., and Reidenbach, M. A. (2021). Quantifying Seasonal Seagrass Effects on Flow and Sediment Dynamics in a Back-Barrier Bay. *J. Geophys. Res. Oceans* 126:e2020JC016547. doi: 10.1029/2020JC016547

Conflict of Interest: The authors declare that the research was conducted in the absence of any commercial or financial relationships that could be construed as a potential conflict of interest.

Publisher's Note: All claims expressed in this article are solely those of the authors and do not necessarily represent those of their affiliated organizations, or those of the publisher, the editors and the reviewers. Any product that may be evaluated in this article, or claim that may be made by its manufacturer, is not guaranteed or endorsed by the publisher.

Copyright © 2022 Wang, Bai, Yan, Cui and Shao. This is an open-access article distributed under the terms of the Creative Commons Attribution License (CC BY). The use, distribution or reproduction in other forums is permitted, provided the original author(s) and the copyright owner(s) are credited and that the original publication in this journal is cited, in accordance with accepted academic practice. No use, distribution or reproduction is permitted which does not comply with these terms.

frontiers in Marine Science

ORIGINAL RESEARCH
published: 28 February 2022
doi: 10.3389/fmars.2022.832148

Short-Term Sedimentation Dynamics of Temperate Mangroves in Western Port Bay, Victoria

Sabrina Sayers and Ruth Reef*

School of Earth, Atmosphere and Environment, Monash University, Clayton, VIC, Australia

The promotion of sedimentation by mangrove ecosystems with adequate sediment supply has been well documented. However, predicting the amount of accretion or erosion at a specific point, is difficult due to the inherent stochasticity of sediment movement and deposition. Forcings which have been thought to influence short-term sedimentation rates, such as the amount of suspended matter in the incoming water, the wave regime at the site, elevation above sea level, distance from the low tide mark, and vegetation density, were investigated using large arrays of erosion pins at five sites around Western Port, Victoria over the course of one and a half years. We analyzed large scale/short-term and small-scale/longer-term vertical displacement within and between sites, and quantified small-scale intra-site variability. Results show, that while all study sites within Western Port were accreting sediment, they were not doing so at the same rate, and both intra-site and inter-site variability is high. Short-term large-scale or site wide analysis shows that total suspended matter and significant wave height (SWH) did not significantly affect vertical displacement rates. Surprisingly, neither distance from water nor vegetation density significantly affected vertical displacement or explain the spatial distribution of accretion and erosion within the sites. The coefficient of variation at each pin shows that there is high temporal variability in vertical displacement at each location, with individual pins alternating between erosion and accretion over time. Our study finds that while large scale (1 km^2) patterns of sedimentation are temporally consistent, small scale patterns ($< 100\ m^2$) are difficult to predict. This small-scale stochasticity therefore compounds management of mangrove ecosystems, especially as it relates to predicting the response to sea level rise. Thus, investment in small scale management of vegetation density, or microtopography, is perhaps not required for overall shoreline stability with sea level rise and blue carbon accumulation, making ecosystem restoration more feasible where resources are limited. However, at larger, forest-wide, spatial scales a higher level of predictability exists such as the overall response of the coastal tract to prevalent wave energy and sediment supply.

Keywords: temperate mangrove, sediment, ecosystem service, vegetation structure, biophysical interaction

OPEN ACCESS

Edited by:
Iris Möller,
Trinity College Dublin, Ireland

Reviewed by:
Andrew M. Fischer,
University of Tasmania, Australia
Qinghua Ye,
Deltares, Netherlands

****Correspondence:***
Sabrina Sayers
sabrina.sayers@monash.edu

Specialty section:
This article was submitted to Coastal Ocean Processes, a section of the journal Frontiers in Marine Science

Received: *09 December 2021*
Accepted: *07 February 2022*
Published: *28 February 2022*

Citation:
Sayers S and Reef R (2022) Short-Term Sedimentation Dynamics of Temperate Mangroves in Western Port Bay, Victoria. Front. Mar. Sci. 9:832148. doi: 10.3389/fmars.2022.832148

INTRODUCTION

Mangroves have developed morphological adaptations to the dynamic intertidal environments in which they exist. Specific adaptations such as extensive above ground root systems, vary among species and climate zones. These large root systems are known to affect the geomorphology of the coastlines along which they establish. For example, the root systems interact with incoming water by inducing drag forces and decreasing the velocity of the water that is in contact with vegetation, thus promoting the settling of allochthonous suspended sediment (Ellison, 2019).

The ability of coastal vegetation, including mangroves and salt marshes, to promote the settling of sediment through the reduction of flow velocities has been well studied (Furukawa and Wolanski, 1996; Reed et al., 1999; Moskalski and Sommerfield, 2012; Nolte et al., 2013; Sheehan and Ellison, 2015; Horstman et al., 2018). This bio-geomorphic function has become more important as of late because of the imminent threat to global coasts as a result of sea level rise due to climate change. This has led to an increase in research and government backed management schemes to employ nature-based solutions to coastal protection (Saleh and Weinstein, 2016). Some of these schemes fail because of improper planning and the deficit that exists in understanding the complexities of the biophysical interactions that determine sedimentation. The ability of mangroves to influence sedimentation depends on various parameters such as the availability of sediment, distance from sediment supply, prevailing hydrodynamics including wave climate, topography, and vegetation structure. These variables and their interactions affect the spatial and temporal distribution of sediment within vegetated coasts (Van Proosdij et al., 2006). The complexity of this physical environment operates at a range of spatial and temporal scales, thereby resulting in highly stochastic behavior.

Root system geometry of various species such as buttress roots, aerial roots, prop roots, and pneumatophores, each affect flow and sedimentation differently (Furukawa and Wolanski, 1996; Krauss et al., 2003; Krauss et al., 2014; Du et al., 2021). Other vegetation characteristics such as root and tree density affect vegetation induced drag. Pneumatophore density has been shown to be positively correlated to the dissipation of turbulent kinetic energy (Norris et al., 2017). The influence of vegetation elements on energy dissipation and therefore sediment transport, has been shown to occur in two modes. One showing that vegetation can increase drag to result in flow reduction thereby preventing sediment resuspension and promoting sedimentation (Horstman et al., 2018). In other areas of sparser pneumatophores, the generated turbulence can cause the resuspension of sediment within this zone (Mullarney et al., 2017; Horstman et al., 2018). Young and Harvey (1996) found that sediment accretion within *Avicennia marina* in New Zealand showed no statistical relationship to stem density and other measures of plant physiognomy, except for the density of pneumatophores. In a study to ascertain the sediment accretion abilities of two different species Du and Zhang (2020) found that vertical accretion had a greater relation to the total volume of aerial root structures. The distribution of pneumatophore density, length, and thickness within mangroves are variable as is the occurrence of biotic factors which alter vegetation roughness such as barnacles (Mullarney et al., 2017). Bed roughness, and therefore ease of resuspension is also affected by the presence of bioturbation, soil binding microorganisms (Stokes and Harris, 2015; Kakeh et al., 2016; Horstman et al., 2018), fine rootlets (Spenceley, 1977; Krauss et al., 2014), and detritus.

In addition to vegetation characteristics, incoming wave energy is an essential factor to be considered in sedimentation studies (Van Proosdij et al., 2006) as waves remobilize mudflat and offshore bed sediments (Fricke et al., 2017). Links between site hydrodynamics and vegetation characteristics alone are not sufficient to explain the dissimilarity seen within and between sites. This was also highlighted in salt marsh studies in Reef et al. (2018). Without a supply of sediment, accretion within these systems is not possible. The concentration of suspended particles in incoming water is therefore another relevant factor in determining sedimentation within a site (Moskalski and Sommerfield, 2012). Distance from this source water is also a parameter to be considered as suspended particle concentration decreases with distance from the source as settling occurs with movement through vegetation (Van Proosdij et al., 2006; Moskalski and Sommerfield, 2012). Site topography is another parameter for consideration in the spatial distribution of sedimentation (Van Proosdij et al., 2006) as elevation affects hydroperiod characteristics, thus both the settlement time for and the energy in tidal currents are impacted (Reed et al., 1999).

Numerous methods exist to spatially examine sedimentation within coastal environments. These include depositional methods such as filters and traps (Nolte et al., 2013) which are useful in shorter term studies that investigate spatial deposition patterns across single tide cycles (Reed et al., 1999; Van Proosdij et al., 2006). These shorter-term studies are useful in providing snapshots of the interaction of water depth, inundation time, and other tidal variables, with parameters such as suspended sediment concentration and elevation (Van Proosdij et al., 2006). Longer term methods such as SETs which also capture compaction do not allow for insight into spatial or temporal variation to be captured. Erosion pins offer an easy deployment of an array of pins across a site or numerous sites, allowing both short/medium term and spatial dynamics to be captured. They provide an advantage over other short term methods such as marker horizons and sedimentation plates, which are more prone to be affected by bioturbation (Nolte et al., 2013). Erosion pins have been shown to sometimes cause localized scour depending on their deployment (Spenceley, 1977; Nolte et al., 2013), however, in low energy environments, if pin distribution or density is not greater than that of pneumatophores, they should reflect the natural processes that occur, accurately. This is reflected in Spenceley (1977) where grids which had a greater density than that of the pneumatophores present displayed intense localized scour.

In this study, the influence of biotic and abiotic characteristics on the spatial and temporal patterns of sedimentation at five different sites around the Western Port embayment are investigated. These characteristics include wave climate,

suspended sediment concentration, distance from sediment source, microtopography, and vegetation density. These parameters have been highlighted as significant determinants in the distribution of sedimentation, however, the complex interactions between them are yet to be investigated. The use of five different sites allowed for the capture of the variation of vegetation characteristics of *Avicennia marina* var *australasica* as well as specific site wide characteristics of wave climate and sediment input. Spatial variation was analyzed by deploying an array of erosion pins based on the method used by Sheehan and Ellison (2015). Temporal variation was considered by conducting the study over a period of one and a half years with measurements planned during every season.

MATERIALS AND METHODS

Study Location

Western Port is an embayment located 80 km to the east of central Melbourne, Australia. The climate of the bay is temperate; Cerberus station recorded 29-year annual mean minimum, and maximum temperatures of 9.8 and 19.2°C. The bay has a semidiurnal tidal regime and experiences an average tidal range of approximately 2.2 m. The marine flora around the bay includes seagrass meadows, mangroves, and salt marsh. The only species of mangrove in Western Port Bay is *Avicennia marina* var *australasica*; the bay is close to the southern latitudinal limit of the A*vicennia marina* species.

The hydrodynamic complexity of the bay is influenced by the presence of French Island and Phillip Island. Sea water is primarily exchanged with the Bass Strait at the Western Segment entrance, where it is split into the North and East Arms by the presence of French Island (**Figure 1**).

Primary sources of fine sediment (<4 μm) into the north of the bay include the Bunyip river (27%) and Lang Lang river (20%) to the north, as well as the erosion of the Lang Lang cliffs (32%) (Wallbrink et al., 2003). Secondary sources of fine sediments are channel, and gully bank erosion (Wallbrink et al., 2003). The hydrodynamics within Western Port Bay impose clockwise sediment movement around French Island.

Sediment Data Collection

In order to investigate the sediment dynamics and the role of *Avicennia marina var australasica* in sedimentation within Western Port, five sites were chosen around the bay, as indicated in **Figure 1**. Mangrove vegetation structure varies around the bay therefore, sites were chosen to capture the breadth of structural variability.

A total of 50 cm long, 2 mm thick stainless-steel rods (erosion pins) were installed at each site in a grid based on Sheehan and Ellison (2015) in December 2019 at Stony Point, Hastings, Pioneer Bay, and Rhyll. Pins were installed at Tooradin in March 2020. A square grid of pins was deployed at each site, with shore-parallel rows of 10 erosion pins spaced 10 m apart. Row transects were laid at shore-perpendicular intervals from the low intertidal, every 10 m to the back of the mangrove vegetation, as seen in **Figure 2** at Pioneer Bay. Each pin was driven 30 cm deep into the sediment. Measurements of the height of each rod above the sediment were taken approximately every 3–6 months, until July 2021.

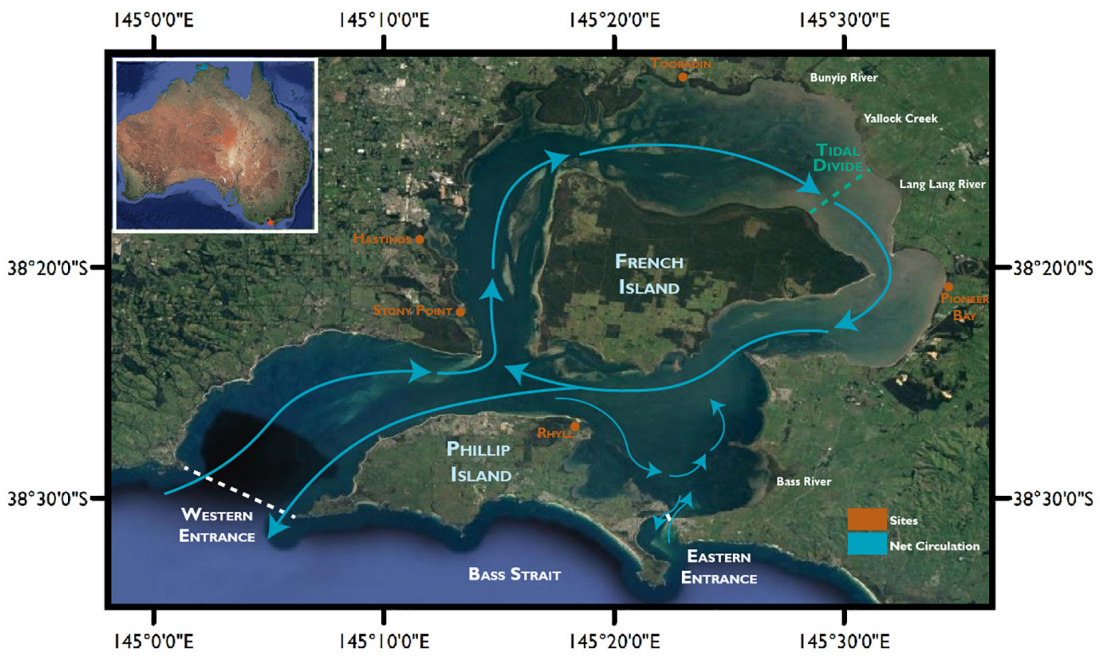


FIGURE 1 | Location of data collection sites, features and net water circulation around Western Port Bay. Net circulation patterns based on Harris et al. (1979). Map data: Google, Maxar Technologies.

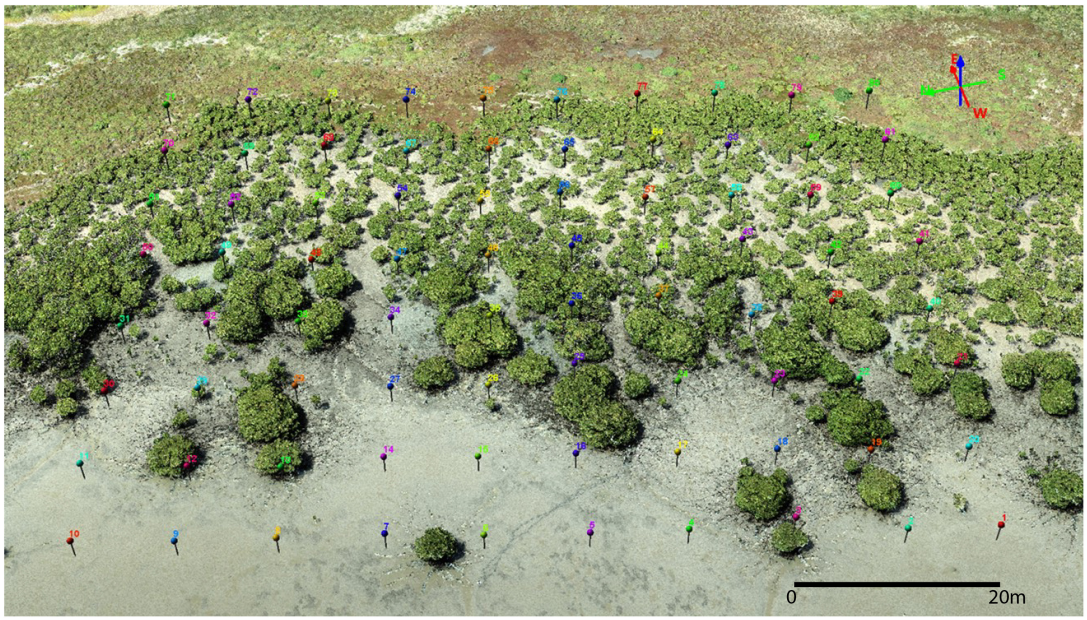


FIGURE 2 | Configuration of stainless-steel rods at Pioneer Bay, Western Port Bay. Site coordinates are 38°22′11.5″S 145°32′52.2″E.

Supplementary Data Collection

Elevation data was collected at each erosion pin using the Navcom sf-3040 D-GPS unit. The distance from the mean lower low water (MLLW), −0.6 m, as measured using the distance from point to line function in QGIS with MLLW calculated from Western Port bathymetry data. Total suspended matter (TSM) was captured from ESA Globcolour (Doerffer and Schiller, 2007) monthly mean of cloud free data, ACRI-ST company (Sophia Antipolis, France) with 4 km × 4 km spatial resolution. Site relevant monthly TSM measurements were extracted.

An RBR duet logger (RBR Ltd., Ottowa, CANADA) was placed at each site in May 2021 to July 2021 to analyze the differences in wave climate at each site including average incident significant wave height (SWH), wave energy, wave period, and depth. As waves within Western Port Bay are primarily wind driven, the data collected from the loggers was used to calibrate a wind/wave relationship at each site in order to simulate the wave climatology during the extent of the experiment.

Vegetation studies were conducted on site by measuring the percentage of bare sediment in 1 × 1 m quadrat around each pin. The percentage of bare sediment was calculated as 100 minus the total percentage of coverage of raft, pneumatophores, mangrove stems, cyanobacteria, algae, and salt marsh present.

Data Analysis

Differences in the height of the erosion pin above the sediment was calculated between measurements in 6-month intervals during the first year, and 3-month intervals thereafter, as well as the difference from the start of the experiment, T_0, when pin height was 20.0 cm. The average change at each site was then calculated. Analysis of results was broken down into three sections: Large-scale short-term site wide changes, small-scale long term within site changes, and finally intra-site variability. Both longer term changes, T_0-T_n and shorter-term changes $T_{(n-1)}$-T_n were averaged across site for comparison. A number of pins were trampled by kangaroos that frequent these sites. Pins that were lost or damaged during the experiment were not included in the long-term averages or analysis, but short-term changes were still tracked with replacement pins. No scouring was evident around the stainless-steel pins.

Large-scale short-term analysis sought to examine the inter-site variability throughout the length of the experiment by comparing the average pin change within sites during each measurement period. The relationship between the site average daily change per time period, total suspended matter (TSM), and wave energy was investigated using a multiple linear regression model in R.

Small-scale longer-term within site change analysis focused on the total daily change over the entirety of the experiment, at each pin at each site. Spatial analysis was conducted using Inverse Distance Weighted (IDW) interpolation in QGIS, and by calculating Moran's I in R. The dependence of these changes on the variables to MLLW, bare sediment, and elevation were then examined using a multiple non-linear regression model in R. Intra-site variability was scrutinized by calculating coefficient of variation (CV), which was then analyzed using IDW interpolation in QGIS.

RESULTS

Large-Scale Short-Term Analysis

SWH between the sites are mostly distinct (**Figure 3A**), with Pioneer Bay having consistently higher wave heights than all

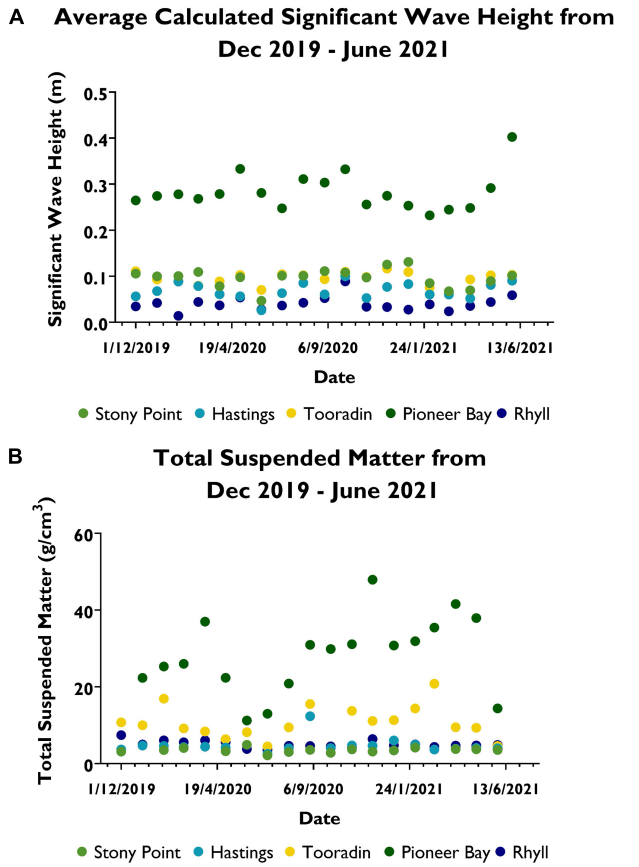


FIGURE 3 | (A) Average monthly calculated significant wave height during December 2019 to June 2021. **(B)** Total suspended matter (TSM) observed during December 2019 to June 2021.

other sites, with average monthly wave heights being above 0.2 m. Expected wave heights at Rhyll are constantly lower than that of other sites, with an average SWH of only 0.04 m. Hastings has the second lowest expected SWHs, averaging 0.07 m during this entire period. Wave heights at Tooradin and Stony Point are less distinct than that of other sites throughout the experiment. They are slightly higher on average, at Stony Point (0.096 m), than Tooradin (0.095 m).

Patterns of TSM (**Figure 3B**) during the experiment also follow a distinct pattern, despite monthly fluctuations at each site. Pioneer Bay has sustained significantly higher TSM values than other sites throughout the duration of the experiment, except in June and July, 2019. A substantial peak of 47.9 g/cm^3 was observed at this site in December 2020. The average value of TSM during the entire observation period is 28.3 g/cm^3 at Pioneer Bay, compared to 10.8 g/cm^3 at Tooradin. The maximum recorded value at Tooradin was 20.8 g/cm^3. TSM at Tooradin remained the second highest throughout the period, despite monthly fluctuations. This remained true, except in June 2021, when it was surpassed by Rhyll with an observed value of 4.87 g/cm^3. Average TSM at Rhyll was 5.03 g/cm^3 compared to 4.70 g/cm^3 at Hastings. Values at Hastings mostly remained slightly lower than that of Rhyll, except for a noticeable peak of 12.3 g/cm^3 in September, and smaller but notable increases in November 2020 and January 2021. TSM values at Stony Point remained lower than all other sites at an average of 3.48 g/cm^3, except in June 2020, when it peaked at 4.87 g/cm^3. This occurred during the same month that Pioneer Bay TSM values plummeted to its lowest of 11.2 g/cm^3. TSM at Tooradin 8.15 g/cm^3 was not significantly higher or lower than average, while Rhyll recorded its second lowest value of 3.80 g/cm^3 during this period. A value for Hastings was not recorded during this period. Missing values were only recorded in Dec 2019 for Pioneer Bay, October 2020 at Tooradin, June 2020 at Hastings, and in January 2020, April 2020, and March 2021 at Stony Point.

Average site change during measurement period (**Figure 4**) showed that sites have accreted during every period except during T_0-T_2, at both Hastings and Rhyll. During T_0-T_1 average change was 2.0 cm at both Rhyll and Hastings. Reported values at other sites were much lower, with a measured change of 0.9 and 0.7 cm, at Pioneer Bay and Stony Point, respectively. Change at Tooradin was 0.8 cm. However, it should be noted that T_0 for Tooradin, is March 2020. During T_0-T_2 average total change decreased to 1.8 and 1.5 cm, at Rhyll and Hastings, respectively. This shows that during T_1-T_2 more pins across the two sites recorded erosion, however, the total long-term change was still positive. Accretion was observed at Pioneer Bay with at increase to 1.3 cm, at Tooradin with a total change of 1.1 cm, and an increase to 1.2 cm at Stony Point. Changes during T_0-T_3 were much more conservative at Pioneer Bay, Tooradin, and Stony Point, with increases to 1.4, 1.2, and 1.3 cm, respectively; compared to a much more substantial jump to 2.1 cm at Rhyll and 1.8 cm Hastings. Between December 2019 and June 2021, Rhyll experienced the largest increase of 3.0 cm, followed by Pioneer Bay with 2.4 cm, Hastings with 2.2 cm, and Stony Point with 1.6 cm. For the period March 2020–June 2021, a change of 1.4 cm was noted at Tooradin.

The average daily change per site during each measurement period was plotted against TSM (**Figure 5A**) and average SWH (**Figure 5B**). No relationship was found between TSM or SWH with average daily change, as the calculated *p*-value was 0.5673 and 0.575, respectively. Therefore, neither TSM or SWH was statistically significant. An equation to predict short-term sedimentation based on these parameters could not be developed; R^2 was calculated as 0.02.

Rhyll had the highest average accretion of 3.0 cm over the course of the measurements, despite a period of erosion during the second measurement period, between July and November 2020. During this period of erosion, the average SWH was at its highest and average TSM was at the lowest recorded for the site. Rhyll experienced the highest average accretion during the final measurement period, between March and June 2021. Average calculated SWH during this time was only 0.01 m lower than that of the second measurement period. Average TSM was 0.363 g/cm^3 higher than that of the second measurement period (an increase of 10%). From December 2020 to February 2021, average net sedimentation at Pioneer Bay was 0 cm despite having the highest TSM on record. The lowest calculated wave heights, and average change during the next measurement period

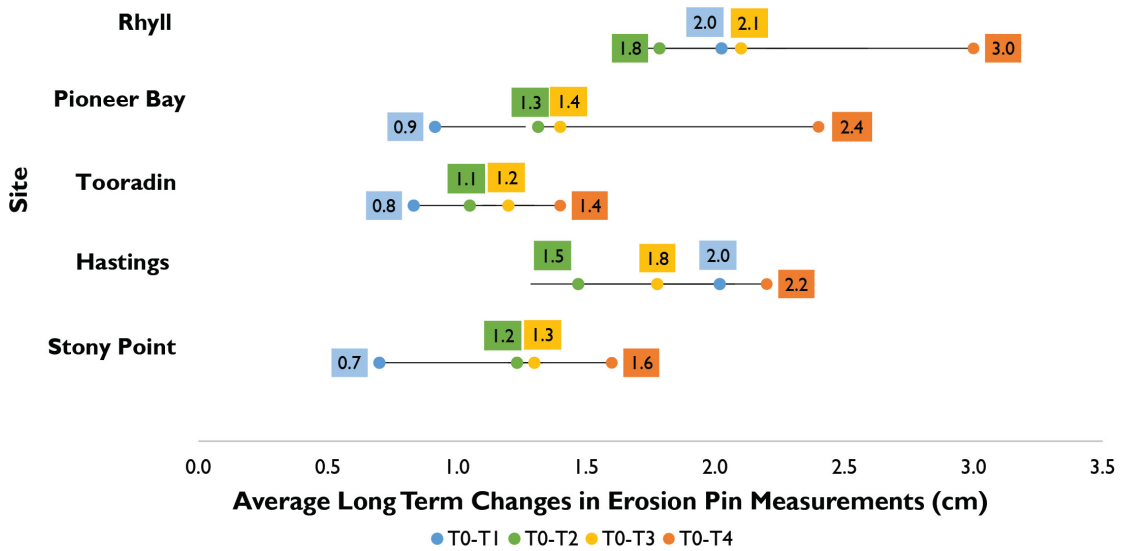


FIGURE 4 | Dumbbell plot showing long term average changes at each site.

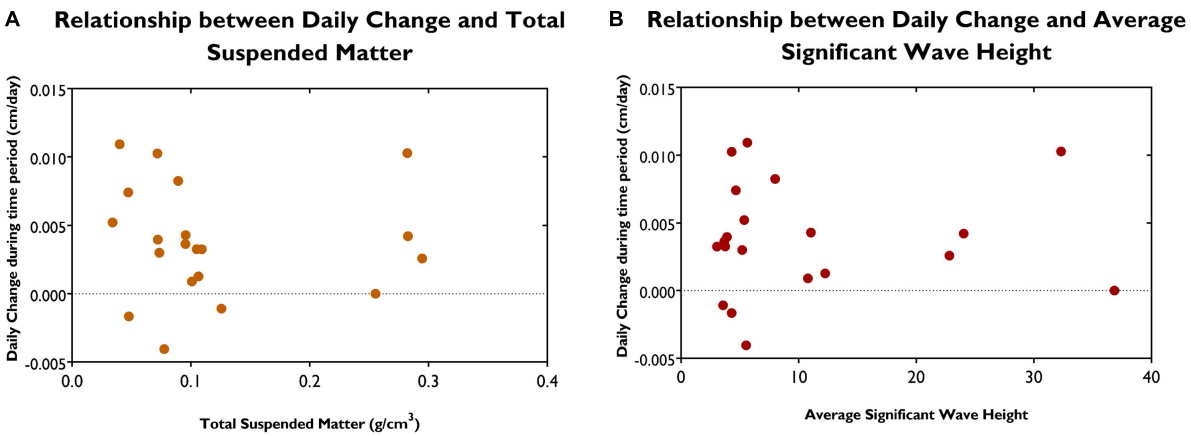


FIGURE 5 | (A) Relationship between daily change between measurement periods and total suspended matter at the various sites. **(B)** Relationship between daily change between measurement periods and average significant wave height at the various sites.

at Pioneer Bay was 1.1 cm. During this same period, SWH was the highest recorded, and TSM was lower than in the December to February period. Pioneer Bay had the second highest total accretion during the experiment of 2.4 cm over 18 months.

Small-Scale Longer-Term Analysis

TSM and SWH were treated as site wide parameters used in inter-site and temporal compositions. Smaller scale (intra-site) parameters included distance from MLLW, elevation, and vegetation characteristics (measured as a percentage of bare sediment) for each individual pin. Results of IDW interpolation at Stony Point in **Figure 6A**, show randomness in the distribution of areas of accretion and erosion across the site. The calculated *p*-value from Moran's I test was 0.058 indicating no significant spatial autocorrelation at this scale. At Hastings (**Figure 6B**), results show a pattern of erosion at the front of the mangrove, more accretion occurring in the middle of the site and erosion or less accretion occurring at the back of the site. There are still areas of erosion occurring within this area, and pins with higher rates of accretion are also randomly spread throughout. Moran's I test shows significant autocorrelation at Hastings ($p = 0.04$). At Tooradin (**Figure 6C**) spatial autocorrelation is present (Moran's I, $p < 0.0017$) but is opposite in pattern to that of Hastings, with more areas of higher accretion located at the seaward edge of the mangrove. Areas of accretion and erosion were randomly dispersed throughout the middle and back of the site. Pioneer Bay (**Figure 6D**) does not show any discernible large-scale pattern of accretion, but erosion and accretion patches occur, with a

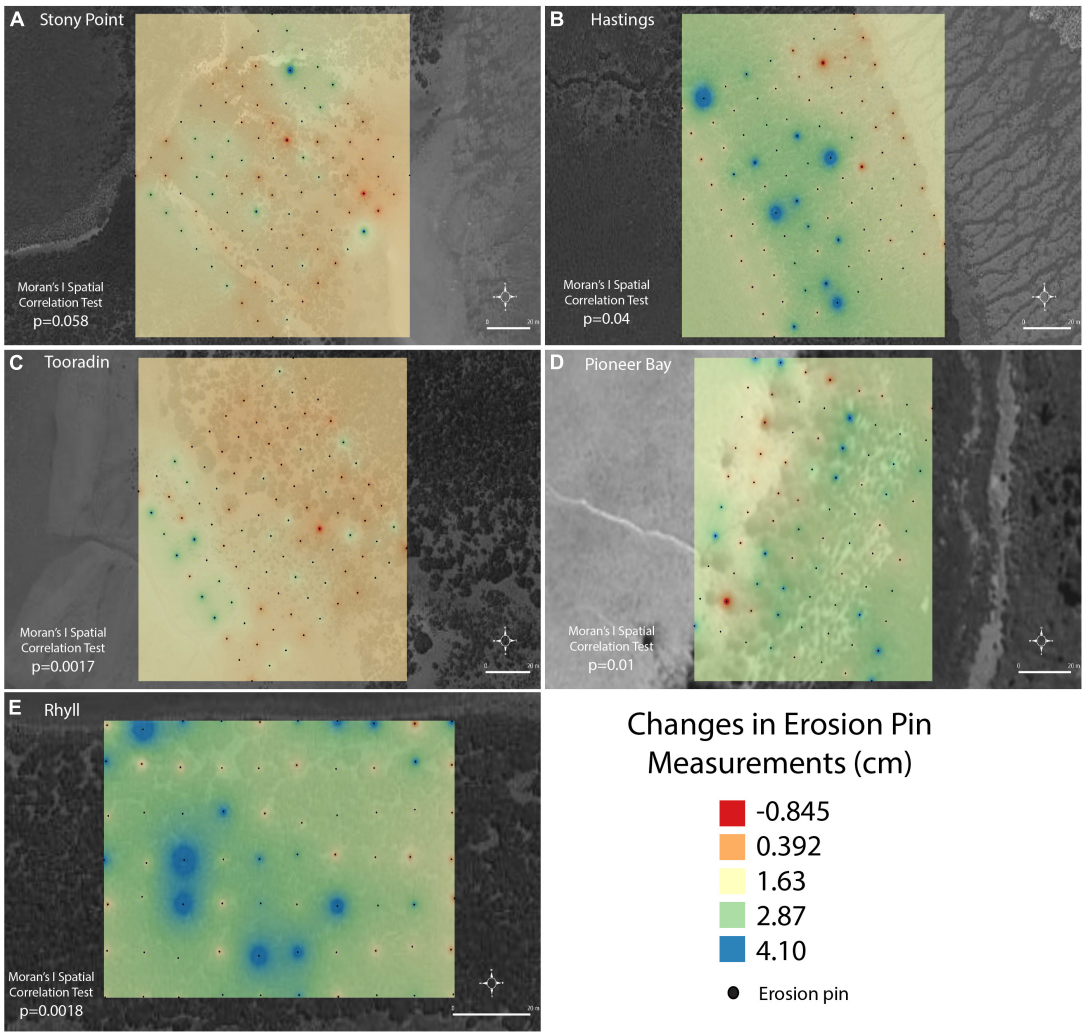


FIGURE 6 | Long term changes recorded at each erosion pin during experiment across the sites **(A)** Stony Point, **(B)** Hastings, **(C)**, Tooradin, **(D)** Pioneer Bay, **(E)** Rhyll.

significant spatial autocorrelation ($p = 0.01$). Most of the site was accreting. At Rhyll (**Figure 6E**), similar to Pioneer Bay, accretion and erosion do not follow a larger pattern but some clustering is present ($p = 0.00018$).

We found no significant relationship between average daily sedimentation and elevation above sea level (multiple non-linear regression, $p = 0.32$ and $p = 0.32$, respectively) or with the distance from MLLW (**Figures 7A,B**). The clustering of values at distances greater than 400 and 200 m from MLLW represent pins located at Pioneer Bay and Rhyll, respectively, where high wave energy restricts the mangrove to higher intertidal elevations. We found no relation between percentage of bare sediment in the immediate area around the pin and daily change (**Figure 7C**); pins surrounded by 100% bare sediment showed both erosion and accretion. While there is no significant increase in deposition with increased vegetation cover ($p = 0.065$), less erosion seems to be occurring at heavily vegetated pins. The synergistic relationships between bare sediment and distance or elevation, elevation and distance and finally bare sediment, distance and elevation were all found to be statistically insignificant with p-values of 0.663, 0.844, 0.557, and 0.433, respectively. An equation to predict long-term sedimentation or erosion could not be developed here; R^2 for the model was reported as 0.065.

Intra-Site Variability

The change in sedimentation at each pin over the measurement periods was assessed using the coefficient of variation (CV) of the long term mean (**Figure 8**). On average, CV at Rhyll (panel e) is lowest and spatially uniform, indicating the highest rate of stability in the sedimentation process. At other sites such as Stony Point and Hastings, higher CVs occur overall and the instability in sedimentation is distributed in a complex pattern that is not explained by the measured geographical parameters of distance from MLLW, vegetation density or elevation. At Pioneer Bay CV is low within the forest, but exceptionally high on the

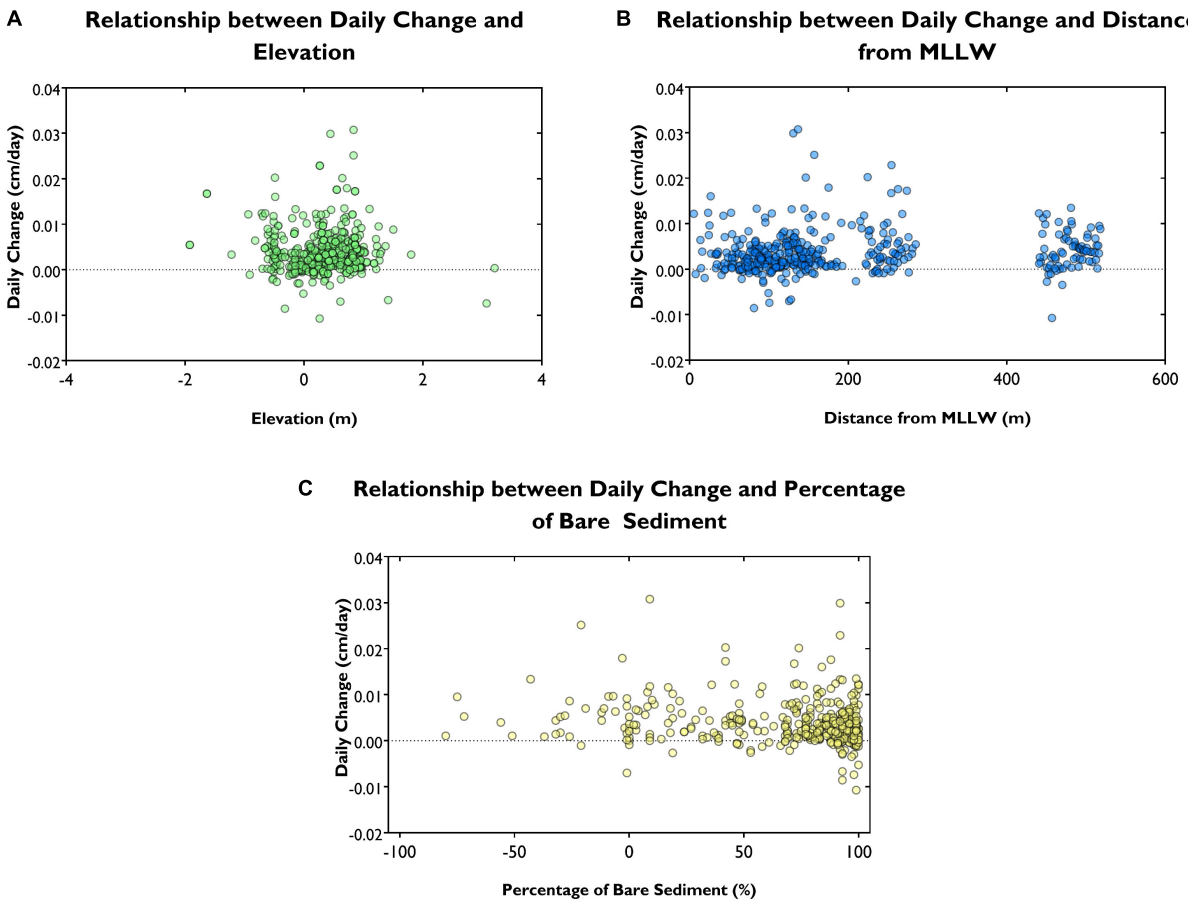


FIGURE 7 | The relationship between long term change and **(A)** elevation, **(B)** distance from MLLW and **(C)** percentage bare sediment.

mudflat. This pattern was not seen at other sites. On average, temporal variation between measurements is highest at Tooradin, particularly to the north of the site.

At Stony Point, the site showed an average of 1.6 cm accretion over the 18-month period. The pin which showed the largest erosion at this site (4 cm) is surrounded by both accreting and eroding pins. The 1 × 1 m quadrat around this pin had a high cover of mangrove vegetation and raft, including shells. Distance from MLLW was measured as 125.5 m and elevation was 0.612 m AHD. This pin is located firmly in the middle of the site. In comparison, the pin with the largest accretion of 11.5 cm was located at a similar elevation of 0.645 m and distance from MLLW of 146.3 m. It is surrounded by mostly accreting pins, however, none have accreted quite as much. Its distance from MLLW is greater, at 146.4 m, however, 74% of its surrounds was bare sediment. The difference between the elevations of these pins is not substantial either, with a difference of 0.033 m.

Measurements at Hastings range from −4.2 to 17.5 cm. The pin showing the most erosion at this site is located toward the front of the site, at a distance of 100.5 m from MLLW with 98% bare sediment. The pin with the largest increase is located toward the back of the site, at a distance of 136.6 m from MLLW, and was surrounded by 9% bare sediment. It is away from other highly accreting pins, and is surrounded by much slower accreting pins with measurements of 0.4, 0.5, and 1.2 cm.

Tooradin presents a unique situation. The pin with the highest accretion of 7.5 cm is located in the second row; erosion was only recorded at this pin during the final measurement period. The seaward rows at Tooradin were accreting. Points of higher erosion to the back of the site were randomly dispersed. The greatest sediment loss recorded at Tooradin was 4 cm; this pin showed periods of alternating erosion and accretion over the course of the experiment. Surrounding pins show a mix of erosion and accretion to varying amounts. Both of these pins are located within 100 m of the MLLW, and elevation was recorded as −0.322 and −0.486 m, respectively. Bare sediment around these pins were also recorded as 84 and 93%.

The pin with highest accretion, a measurement of 7.5 cm at Pioneer Bay was located in an area with 99% bare sediment. This is the same bare sediment percentage as the pin which recorded the most erosion at this site, and across all sites: −6.2 cm. As seen so far at other sites, this pin was not continually eroding over the course of the experiment, but instead gained sediment during the first and last measurement periods. This, in stark contrast with the highest accreting pin which continually gained sediment throughout the experiment.

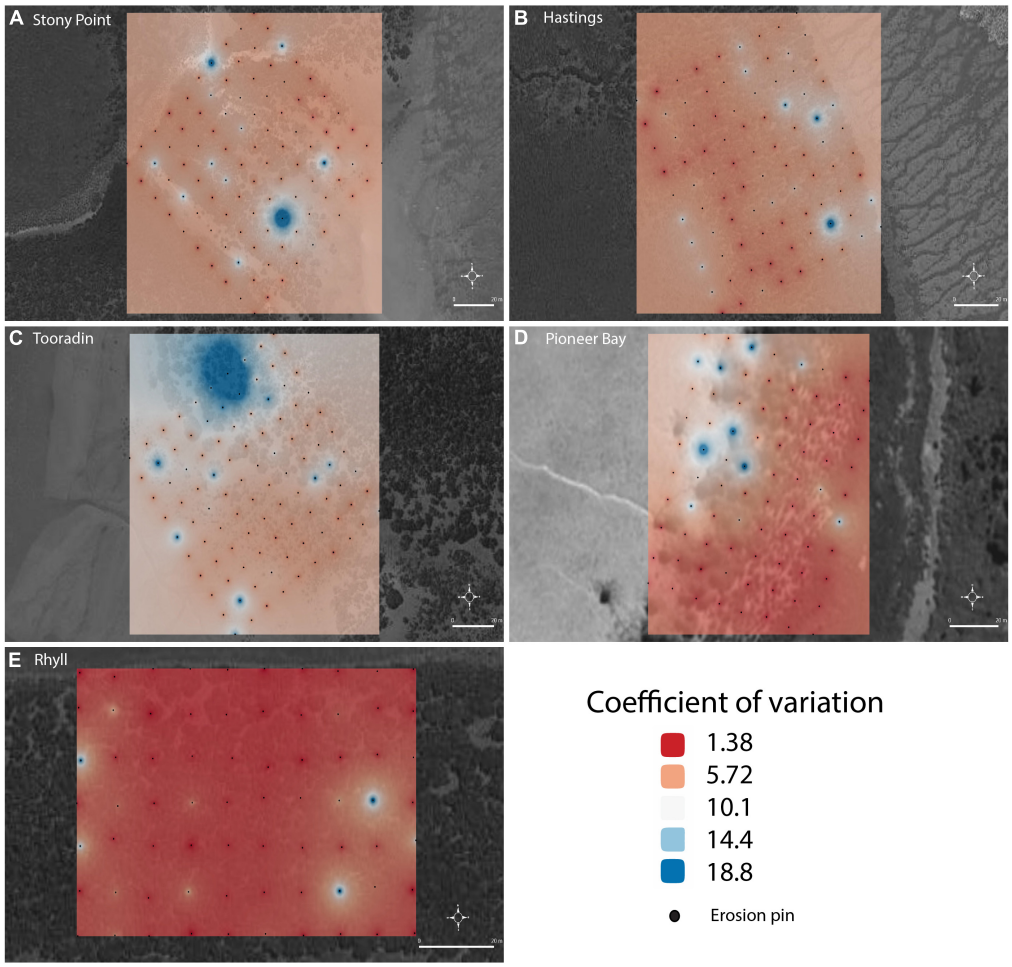


FIGURE 8 | Inter and intra-site measurement coefficient of variation at sites **(A)** Stony Point, **(B)** Hastings, **(C)**, Tooradin, **(D)** Pioneer Bay, **(E)** Rhyll.

At Rhyll, highly accreting pins of more than 4.1 cm seem to occur in pairs (the distance between pin pairs is 10 m), and accreting pins make up a larger proportion of the total of pins deployed than other sites, and accretion was more stable over time (as indicated by lower CVs). The pin that experienced the highest accretion, of 13 cm, was continuously accreting throughout the entirety of the experiment, and was located in the center of the site. Two other highly accreting pins are located near it, with a few surrounding pins showing erosion. 92% of the quadrat surrounding this pin was bare sediment in comparison to 19% around the pin with the lowest long-term erosion of 1.5 cm. The elevation at these pins were 0.263 and −0.459, respectively.

DISCUSSION

Large Scale Order

While intra-site variability was high, on average all sites exhibited net accretion over the 18-month period. The differences in environmental conditions, as defined by TSM and SWH in this study, did not significantly explain the overall erosion and accretion that occurred at these sites during these periods. Rhyll also experienced erosion between July and November 2020. In comparing these parameters at Hastings to that of Rhyll, average TSM was at its highest during this time of high erosion, and the average calculated SWH was at its second lowest value. The variation in sediment supply between measurements periods did not to significantly affect sedimentation, despite the importance placed on sediment supply by findings of Willemsen et al. (2016) in mangroves and Moskalski and Sommerfield (2012) in salt marshes. The overall net accretion over the measurement period could indicate that sediment supply is sufficient, which could be why sediment supply was not a governing factor of sedimentation within the mangrove. Variation in SWH was also insufficient to explain differences between measurement periods at all sites. These sites do show some important similarities. These sites receive the lowest wave energies of the five sites, and have similar TSM values. Vegetation within these sites is more, similar than other sites with trees being taller, stems being wider, and/or less multi-stemmed. Vegetation at the sites show differences at the vegetation edge and at the mangrove/salt marsh interface. At Rhyll, seaward vegetation is especially short with

single stemmed, more flexible vegetation, whereas at Hastings seaward vegetation is quite tall. At the saltmarsh/mangrove interface at Rhyll there is a sharp change from tall mangrove vegetation to saltmarsh, whereas at Hastings, there is a more gradual change with a decrease in the height of mangrove with an intermingling of saltmarsh and mangrove. The differences between the vegetation at these sites are apparent when looking at the spatial distribution of areas of erosion and accretion. The similarities of the parameters investigated between the two sites, and differences compared to the other three sites, are not sufficient to explain the erosion that occurred at these two sites between T_1 and T_2.

Pioneer Bay, the site which consistently received significantly higher SWH and TSM than all other sites the second highest sedimentation of all sites during the experiment. This high accretion in the presence of higher wave action was also noted by Fricke et al. (2017) in their study which found that the site with greater hydrodynamic energy showed more progradation due to the greater sediment input. The major fluvial sediment inputs in Western Port are highlighted in **Figure 1**. Erosion of the Lang Lang cliffs is also a known sediment input in the bay. Sediment transport within the bay and to the sites is then governed by the net clockwise circulation of water. Areas near Pioneer Bay and Rhyll sites are considered important depositional areas for mud (Harris et al., 1979). Differences in sedimentation between Rhyll and other sites could be partially linked to the difference in site hydrodynamics; where other sites are fringed by mangroves and sediment is delivered via wave action across the front margin of the mangrove. Sediment delivery and movement at Rhyll may be governed by tidal creek hydrodynamics as well as exchange along the sea margin given its location at the entrance of Rhyll Inlet. In considering the hydrodynamics at this site, the front or North of the site is located along the edge of the Rhyll Inlet. In a study of marsh surface deposition, Reed et al. (1999) showed that high tides which increase creek velocities may provide an increased supply of sediment to the vegetation edge through the amplified potential for sediment remobilization within the creek. Horstman et al. (2017) showed similar patterning at Whangapoua Harbour, New Zealand where greater deposition was recorded at the fringe. The site at Whangapoua Harbour is located behind a land spit, meaning, it is not exposed to direct wave action like most of the sites in this study (Horstman et al., 2017). The east of the site at Rhyll may then receive some more dampened wave energy from the sea/shore margin.

Small Scale Stochasticity

Despite the statistical insignificance of distance from MLLW, elevation, and vegetation characteristics, they can be useful in identifying and examining patterns within the sites as well as the similarity and dissimilarity of adjacent points.

Measurements at Stony Point fit the initial hypothesis of this site, showing lower accretion due to its location within Western Port Bay and the lower supply of sediment to this area. In a closer examination of the coefficient of variation of the pins which showed maximum erosion and accretion, neither of them were consistently eroding or accreting during the entire experiment with both experiencing one period of movement in the opposite direction. Larger scale patterns are not discernible at this site. There are some areas of clustering of accreting pins at the back edges of the site, with some occurring in the mid-back of the site. Both the foremost and hindmost rows show a mix of erosion and accretion. Stony Point also has some clear pathways for faster flow of water through the site. These are unlike smaller creeks or channels observed at other sites, which show erosion within the channel but accretion along the edges. Topography within Stony Point is more heterogenous than other sites. Within site topographic variation was shown to have an influence on sediment deposition through modeling by Horstman et al. (2015) that demonstrated that decreasing this characteristic lead to an increase in average deposition at a site. However, topography at the scale measured was not a significant forcing of sedimentation, suggesting a more complex incorporation of the planform is required. Bed roughness within Stony Point is extremely variable both within site and in comparison to other sites. The site is mostly sandy with muddier areas located in more vegetated areas. Shells are a frequent sight throughout; they were treated as raft in the calculation of bare sediment due to their influence on surface drag and due to covering the erodible material.

Patterns at Hastings were more apparent, with clearer erosion and lower rates of accretion at the foremost (seaward) and hindmost row (the transition zone between mangrove and salt marsh vegetation). Patterning at Hastings could be explained by the presence of runnels at the front of the site which have been shown to have the potential for erosion and resuspension of sediments (Fagherazzi and Mariotti, 2012). Hastings is an archetype for the expected sedimentation pattern where the sediment at the marsh/mudflat interface is remobilised and deposited further into the forest. Turbulence at the vegetation edge is particularly high because it introduces the first obstacles to flow of incoming water and waves (Horstman et al., 2018). Greater vegetation edge erosion than in site was also observed during field measurements by Le Nguyen and Vo Luong (2019) in an overall eroding site. Young and Harvey (1996) also found that sedimentation was lower toward the seaward edge of their study site in Hauraki Plains, New Zealand where the same species variety was present. Increasing pneumatophore density with distance from the sea was found to be the driver for this spatial pattern (Young and Harvey, 1996). Measurement at the highest accreting pin has not changed since the first measurement. There are large low-lying branches near this pin as well as a pathway for large marine debris. This measurement may reflect a combination of these factors. The pin showing the largest erosion exhibited erosion during periods one and two, but accretion during period three and four; a recurring pattern exhibited by the high CV of many of the pins (**Figure 8**). It should be noted that this pin is located near a crab hole so bioturbation could be a contribution this higher rate of erosion. Our visual inspection suggests that Hastings had a higher occurrence of crab holes throughout the site than the other sites measured, but bioturbation was not quantified in this study. Bioturbation affects bed roughness; the subsequent created drag could be double that of a smooth bed (Shull, 2019). Bioturbation can also result in biostablization of sediments (Horstman et al., 2014; Shull, 2019).

The biophysical characteristics of Tooradin are interesting, as vegetation here is markedly different from other sites with trees with anomalous roots and structure occurring at the front of the site. Tree geometry may play a role in the disparity observed at this site. Differences between the vegetation characteristics of *Avicennia marina* observed in tropical regions as opposed to temperate regions like these, can have an effect on the distribution of zones of accretion and erosion across a site (Horstman et al., 2018). Vegetation observed at Tooradin was the most heterogenous of all the sites with clustering of younger trees with anomalous roots in the south (front) and south east of the site. Despite this array of vegetation, clear patterns of increased or decreased sedimentation could not be observed between these areas. There is also a small channel that snakes parallel to a few of the pins located at the front of the mangrove. This could imply that hydrodynamics within this part of the site may be different from that of the back of the site. There is the added complication of the proximity of this site to a boat ramp, though wave logger readings did not reveal any significant occurrences of boat wake during the deployment period.

Like Hastings, the last row of erosion pins at Pioneer Bay is located at the transition zone between mangrove and salt marsh vegetation. However, unlike Hastings, there is no clear pattern in this zone with pins showing varying degrees of accretion, and a few of erosion. The differences at these vegetation transition zones can provide insight into the effects of mangroves on sediment supply and accumulation in salt marshes. Coleman et al. (2021) showed that fringing mangroves had no negative impact on sediment delivery or sedimentation in landward saltmarshes in New South Wales. However, results at Hastings show that further investigation could be needed. The vegetation edge at Pioneer Bay is also pointedly different from that of Hastings in terms of vegetation density. The mangrove edge at Hastings is denser and more clearly defined than that of Pioneer Bay, which has areas of large trees as well as areas of little or no vegetation in the first 20 m of the grid. The effect of epiphytic algae which is thought to increase friction (Adame et al., 2010; Le Minor et al., 2021) can also be investigated at Pioneer Bay. While all sites did display the typical landward gradient of a decrease in algal accumulation on pneumatophores, epiphytic algae were particularly prolific at Pioneer Bay. Some pneumatophore diameters were measured as 4 cm due to these algae. Wolanski (1995) mentions that particles sticking to algal mucus, amongst others, is an important process to trapping clay particles. However, sedimentation in these areas at Pioneer Bay were not markedly higher than other areas, in fact, some pins located in these sites showed erosion. A denser fringe can contribute to enhanced deposition within the forest as a result of increased flood dominance (Bryan et al., 2017). This denser fringe is also absent at Stony Point. It is important to note, however, that incident wave energy at Hastings is substantially lower than that of Pioneer Bay and even Stony Point. Sediment deposition may be encouraged in sites with low incoming wave energy where this coincides with higher inundation time (Van Proosdij et al., 2006), but differences in inundation dynamics were not considered in this study. At first glance, patterning at Pioneer Bay seems to be related to the presence or density of vegetation specifically in the North East of the site. Upon closer investigation, some pins located in areas of higher vegetation density are eroding. This is contradictory to findings by Horstman et al. (2015), where sediment deposition was controlled by microtopography (rather than vegetation density). In this study, neither of these factors are sufficient to explain the spatial variation observed.

Analyzing the distribution of sediment gain and loss throughout these sites show that small scale sedimentation is a stochastic process. Thresholds within the data could not be ascertained. This study further highlights the complex interplay of all the factors investigated here. Where previous mangrove and saltmarsh studies highlighted the importance of wave climate and sediment supply to sites (Moskalski and Sommerfield, 2012; Horstman et al., 2015; Willemsen et al., 2016), results from this study show that neither of those factors are statistically significant to explain the spatial variation observed between the study sites here. Young and Harvey (1996) showed that pneumatophore density was a significant factor in determining the distribution of sedimentation in their study while Horstman et al. (2015) stated that within site topography and relative elevation as opposed to vegetation density were determinant factors. This study found that neither of these characteristics were sufficient to explain the intra-site spatial variation exhibited. Findings of Reef et al. (2018) found that the interaction of vegetation characteristics and hydrodynamics are not sufficient to explain sediment deposition patterns was supported by the results found here. Clustering of similarly accreting or eroding pins was significant at all sites but Stony Point at the measured spatial scale (10 m), indicating that for some areas, erosion or deposition events occur at larger scales than the pin grid resolution. Where such clustering occurs, varied among sites and between time points. The clusters of eroding points were observed to be larger in size than clusters of accreting points, however, variation of cluster shape and size within and between sites is large making generalizations difficult (**Figure 5**). There is also heterogeneity associated with temporal patterns of sedimentation, with not all eroding pins continuously eroding or vice versa, even though some pins show less variation between consecutive measurements than others.

The parameters examined did not explain the temporal and spatial variability exhibited by these sites. In order to understand the spatial and temporal variation observed here and in other studies, more instrumentation and field studies would be needed (Le Minor et al., 2021). This could include short-term experiments which measure tidal characteristics such as inundation depth, time, and tidal pumping. Site specific measurements such as bed shear stress and erodibility would enable the exploration of the binding effects of the biological elements present such as fine rootlets and soil binding microorganisms. Particle size distribution can also provide useful insight into the dynamics on display here. It is important to note, however, that while this study only measured five parameters; TSM, SWH, elevation, distance to MLLW, and vegetation density, using a simple array of erosion pins, it did prove useful in allowing the replication of the study across multiple sites. A complex study which would encompass more variables and equipment would be expensive (Le Minor et al., 2021)

and would limit the simultaneous deployment at this many sites, at such a scale. The deployment of grids of erosion pins were also sufficient to provide the data gathered here. Issues with localized scour which was noted in Spenceley (1977) and Nolte et al. (2013) was not observed here. Data gathered here can therefore be used to define further experiments to continue to delve into sediment transport and retention within mangrove ecosystems. The study showed that all the sites are accreting, with the highest accretion occurring at Rhyll and Pioneer Bay. This is in keeping with previous studies which show that these areas are important depositional areas within Westernport Bay (Harris et al., 1979). These results are also in line with some horizontal measurements of growth of the shoreline within the bay with sites such as Tooradin and Hastings showing 0.5 and 0.3 m growth since 1988 (Bishop-Taylor et al., 2021a,b). These results also show that these sites are keeping up with predicted sea level rise in Southern Australia (IPCC, 2021).

DATA AVAILABILITY STATEMENT

The raw data supporting the conclusions of this article will be made available by the authors, without undue reservation.

AUTHOR CONTRIBUTIONS

SS conducted and led the field campaigns. SS and RR did the analysis of data and article composition. Both authors contributed to the article and approved the submitted version.

FUNDING

Funding for the fieldwork associated with this project was provided by the Department of Environment, Land, Water and Planning of the Victoria State Government as part of their project investigating changes within Western Port Bay and Australian Research Council Award DP180103444 to RR.

ACKNOWLEDGMENTS

We would like to acknowledge members of the School of Earth, Atmosphere and Environment at Monash University for technical support and help during the extensive field campaigns. GlobColour data (http://globcolour.info) used in this study has been developed, validated, and distributed by ACRI-ST, France.

REFERENCES

Adame, M. F., Neil, D., Wright, S. F., and Lovelock, C. E. (2010). Sedimentation within and among mangrove forests along a gradient of geomorphological settings. *Estuar. Coast. Shelf Sci.* 86, 21–30. doi: 10.1016/j.ecss.2009.10.013

Bishop-Taylor, R., Nanson, R., Sagar, S., and Lymburner, L. (2021a). *DEA Coastlines*. Australia: Commonwealth of Australia.

Bishop-Taylor, R., Nanson, R., Sagar, S., and Lymburner, L. (2021b). Mapping Australia's dynamic coastline at mean sea level using three decades of Landsat imagery. *Remote Sens. Env.* 267:112734. doi: 10.1016/j.rse.2021.112734

Bryan, K. R., Nardin, W., Mullarney, J. C., and Fagherazzi, S. (2017). The role of cross-shore tidal dynamics in controlling intertidal sediment exchange in mangroves in Cù Lao Dung. *Continent. Shelf Res.* 147, 128–143. doi: 10.1016/j.csr.2017.06.014

Coleman, D. J., Rogers, K., Corbett, D. R., Owers, C. J., and Kirwan, M. L. (2021). The geomorphic impact of mangrove encroachment in an Australian salt marsh. *Estuar. Coast. Shelf Sci.* 251:107238. doi: 10.1016/j.ecss.2021.107238

Doerffer, R., and Schiller, H. (2007). The MERIS Case 2 water algorithm. *Int. J. Remote Sens.* 28, 517–535. doi: 10.1080/01431160600821127

Du, Q., Qin, Z., Ming, S., and Zhang, C. (2021). Differences in the vertical accretion of sediment among mangrove species with different aerial root types. *Estuar. Coast. Shelf Sci.* 256:107375. doi: 10.1016/j.ecss.2021.107375

Du, Q., and Zhang, C. (2020). The vertical accretion of sediment under the alien mangrove species Sonneratia apetala and the indigenous species Aegiceras corniculatum. *Wetl. Ecol. Manage.* 28, 595–606. doi: 10.1007/s11273-020-09734-z

Ellison, J. C. (2019). "Biogeomorphology of mangroves," in *Coastal Wetlands: an Ecosystem Integrated Approach*, eds G. M. E. Perillo, E. Wolanski, and D. R. Cahoon, C.S. Hopkinson (Amsterdam: Elsevier Science), 687–715. doi: 10.1016/B978-0-444-63893-9.00020-4

Fagherazzi, S., and Mariotti, G. (2012). Mudflat runnels: evidence and importance of very shallow flows in intertidal morphodynamics. *Geophys. Res. Lett.* 39:14402. doi: 10.1029/2012GL052542

Fricke, A. T., Nittrouer, C. A., Ogston, A. S., and Vo-Luong, H. P. (2017). Asymmetric progradation of a coastal mangrove forest controlled by combined fluvial and marine influence, Cù Lao Dung, Vietnam. *Cont. Shelf Res.* 147, 78–90. doi: 10.1016/j.csr.2017.07.012

Furukawa, K., and Wolanski, E. (1996). Sedimentation in Mangrove Forests. *Mangroves Salt Marshes* 1, 3–10. doi: 10.1023/A:1025973426404

Harris, J. E., Hinwood, J. B., Marsden, M. A. H., and Sternberg, R. W. (1979). Water movements, sediment transport and deposition in Western Port. *Mar. Geol.* 30, 131–161. doi: 10.1016/0025-3227(79)90010-0

Horstman, E. M., Dohmen-Janssen, C. M., Bouma, T. J., and Hulscher, S. J. M. H. (2015). Tidal-scale flow routing and sedimentation in mangrove forests: combining field data and numerical modelling. *Geomorphology* 228, 244–262.

Horstman, E. M., Dohmen-Janssen, C. M., Narra, P. M. F., Van Den Berg, N. J. F., Siemerink, M., and Hulscher, S. J. M. H. (2014). Wave attenuation in mangroves: a quantitative approach to field observations. *Coast. Eng.* 94, 47–62. doi: 10.1016/j.coastaleng.2014.08.005

Horstman, E. M., Lundquist, C. J., Bryan, K. R., Bulmer, R. H., Mullarney, J. C., and Stokes, D. (2018). *The Dynamics of Expanding Mangroves in New Zealand. Threats To Mangrove Forests*. New York: Springer International Publishing AG.

Horstman, E. M., Mullarney, J. C., Bryan, K. R., and Sandwell, D. R. (2017). "Deposition gradients across mangrove fringes," in *Proceedings of Coastal Dynamics*, eds T. Aagaard, R. Deigaard, and D. Fuhrman (Denmark: Helsingør), 911–922.

IPCC (2021). *Climate Change 2021: The Physical Science Basis. Contribution of Working Group I to the Sixth Assessment Report of the Intergovernmental Panel on Climate Change*. Cambridge: Cambridge University Press.

Kakeh, N., Coco, G., and Marani, M. (2016). On the morphodynamic stability of intertidal environments and the role of vegetation. *Adv. Water Res.* 93, 303–314. doi: 10.1016/j.advwatres.2015.11.003

Krauss, K. W., Allen, J. A., and Cahoon, D. R. (2003). Differential rates of vertical accretion and elevation change among aerial root types in Micronesian mangrove forests. *Estuar. Coast. Shelf Sci.* 56, 251–259. doi: 10.1016/S0272-7714(02)00184-1

Krauss, K. W., Mckee, K. L., Lovelock, C. E., Cahoon, D. R., Saintilan, N., Reef, R., et al. (2014). How mangrove forests adjust to rising sea level. *New Phytol.* 202, 19–34. doi: 10.1111/nph.12605

Le Minor, M., Zimmer, M., Helfer, V., Gillis, L. G., and Huhn, K. (2021). "Flow and sediment dynamics around structures in mangrove ecosystems—a modeling perspective," in *Dynamic Sedimentary Environments of Mangrove Coasts*, eds F. Sidik and D. Friess (Netherlands: Elsevier, Amsterdam), 83–120. doi: 10.1016/B978-0-12-816437-2.00012-4

Le Nguyen, H. T., and Vo Luong, H. P. (2019). Erosion and deposition processes from field experiments of hydrodynamics in the coastal mangrove area of Can Gio. *Vietnam Oceanol.* 61, 252–264. doi: 10.1016/j.oceano.2018.11.004

Moskalski, S. M., and Sommerfield, C. K. (2012). Suspended sediment deposition and trapping efficiency in a Delaware salt marsh. *Geomorphology* 139-140, 195–204. doi: 10.1016/j.geomorph.2011.10.018

Mullarney, J. C., Henderson, S. M., Reyns, J. A. H., Norris, B. K., and Bryan, K. R. (2017). Spatially varying drag within a wave-exposed mangrove forest and on the adjacent tidal flat. *Cont. Shelf Res.* 147, 102–113. doi: 10.1016/j.csr.2017.06.019

Nolte, S., Koppenaal, E. C., Esselink, P., Dijkema, K. S., Schuerch, M., De Groot, A. V., et al. (2013). Measuring sedimentation in tidal marshes: a review on methods and their applicability in biogeomorphological studies. *J. Coast. Conserv.* 17, 301–325. doi: 10.1007/s11852-013-0238-3

Norris, B. K., Mullarney, J. C., Bryan, K. R., and Henderson, S. M. (2017). The effect of pneumatophore density on turbulence: a field study in a Sonneratia-dominated mangrove forest. *Vietnam Cont. Shelf Res.* 147, 114–127. doi: 10.1016/j.csr.2017.06.002

Reed, D. J., Spencer, T., Murray, A. L., French, J. R., and Leonard, L. (1999). Marsh surface sediment deposition and the role of tidal creeks: Implications for created and managed coastal marshes. *J. Coast. Conserv.* 5, 81–90. doi: 10.1007/bf02802742

Reef, R., Schuerch, M., Christie, E. K., Möller, I., and Spencer, T. (2018). The effect of vegetation height and biomass on the sediment budget of a European saltmarsh. *Estuar. Coast. Shelf Sci.* 202, 125–133. doi: 10.1016/j.ecss.2017.12.016

Saleh, F., and Weinstein, M. P. (2016). The role of nature-based infrastructure (NBI) in coastal resiliency planning: a literature review. *J. Environ. Manage* 183, 1088–1098. doi: 10.1016/j.jenvman.2016.09.077

Sheehan, M. R., and Ellison, J. C. (2015). Tidal marsh erosion and accretion trends following invasive species removal, Tamar Estuary, Tasmania. *Estuar. Coast. Shelf Sci.* 164, 46–55. doi: 10.1016/j.ecss.2015.06.013

Shull, D. H. (2019). Bioturbation. *Encyclopedia Ocean Sci.* 2, 671–676. doi: /10.1016/B978-0-12-409548-9.11493-9

Spenceley, A. P. (1977). The role of pneumatophores in sedimentary processes. *Mar. Geol.* 24, M31–M37. doi: 10.1016/0025-3227(77)90001-9

Stokes, D. J., and Harris, R. J. (2015). Sediment properties and surface erodibility following a large-scale mangrove (Avicennia marina) removal. *Cont. Shelf Res.* 107, 1–10.

Van Proosdij, D., Davidson-Arnott, R. G. D., and Ollerhead, J. (2006). Controls on spatial patterns of sediment deposition across a macro-tidal salt marsh surface over single tidal cycles. *Estuar. Coast. Shelf Sci.* 69, 64–86. doi: 10.1016/j.ecss.2006.04.022

Wallbrink, P. J., Hancock, G. J., Olley, J. M., Hughes, A. O., Prosser, I. P., Hunt, D., et al. (2003). *The Western Port Sediment Study*. Canberra, AU: CSIRO Land and Water.

Willemsen, P. W. J. M., Horstman, E. M., Borsje, B. W., Friess, D. A., and Dohmen-Janssen, C. M. (2016). Sensitivity of the sediment trapping capacity of an estuarine mangrove forest. *Geomorphology* 273, 189–201. doi: 10.1016/j.geomorph.2016.07.038

Wolanski, E. (1995). Transport of sediment in mangrove swamps. *Hydrobiologia* 295, 31–42. doi: 10.1007/978-94-011-0289-6_5

Young, B. M., and Harvey, L. E. (1996). A Spatial Analysis of the Relationship Between Mangrove (Avicennia marina var. australasica) Physiognomy and Sediment Accretion in the Hauraki Plains, New Zealand. *Estuar. Coast. Shelf Sci.* 42, 231–246. doi: 10.1006/ecss.1996.0017

Conflict of Interest: The authors declare that the research was conducted in the absence of any commercial or financial relationships that could be construed as a potential conflict of interest.

Publisher's Note: All claims expressed in this article are solely those of the authors and do not necessarily represent those of their affiliated organizations, or those of the publisher, the editors and the reviewers. Any product that may be evaluated in this article, or claim that may be made by its manufacturer, is not guaranteed or endorsed by the publisher.

Copyright © 2022 Sayers and Reef. This is an open-access article distributed under the terms of the Creative Commons Attribution License (CC BY). The use, distribution or reproduction in other forums is permitted, provided the original author(s) and the copyright owner(s) are credited and that the original publication in this journal is cited, in accordance with accepted academic practice. No use, distribution or reproduction is permitted which does not comply with these terms.

frontiers in Marine Science

ORIGINAL RESEARCH
published: 09 March 2022
doi: 10.3389/fmars.2022.808018

Oyster Reef Surfaces in the Central Wadden Sea: Intra-Reef Classification and Comprehensive Statistical Description

Jan Hitzegrad[1], Leon Brohmann[2], Kai Pfennings[3], Tom K. Hoffmann[4], Anne K. Eilrich[3,4], Maike Paul[5], Mario Welzel[1], Torsten Schlurmann[5,6], Jochen Aberle[1], Achim Wehrmann[3] and Nils Goseberg[1,6]*

[1] Leichtweiß-Institute for Hydraulic Engineering and Water Resources, Technische Universität Braunschweig, Braunschweig, Germany, [2] Institute of Structural Design, Technische Universität Braunschweig, Braunschweig, Germany, [3] Marine Research Department, Senckenberg am Meer, Wilhelmshaven, Germany, [4] Institute of Biology and Environmental Sciences, Carl von Ossietzky Universität Oldenburg, Oldenburg, Germany, [5] Ludwig Franzius Institute of Hydraulic, Estuarine and Coastal Engineering, Leibniz University Hannover, Hannover, Germany, [6] Coastal Research Center, Joint Research Facility of Leibniz University Hannover and Technische Universität Braunschweig, Hannover, Germany

OPEN ACCESS

Edited by:
Zeng Zhou,
Hohai University, China

Reviewed by:
Christian Buschbaum,
Alfred Wegener Institute, Helmholtz Centre for Polar and Marine Research (AWI), Germany
Andrew M. Fischer,
University of Tasmania, Australia

***Correspondence:**
Jan Hitzegrad
j.hitzegrad@tu-braunschweig.de

Specialty section:
This article was submitted to Coastal Ocean Processes, a section of the journal Frontiers in Marine Science

Received: *02 November 2021*
Accepted: *27 January 2022*
Published: *09 March 2022*

Citation:
Hitzegrad J, Brohmann L, Pfennings K, Hoffmann TK, Eilrich AK, Paul M, Welzel M, Schlurmann T, Aberle J, Wehrmann A and Goseberg N (2022) Oyster Reef Surfaces in the Central Wadden Sea: Intra-Reef Classification and Comprehensive Statistical Description. Front. Mar. Sci. 9:808018. doi: 10.3389/fmars.2022.808018

The Pacific oyster (*Magallana gigas*) is an invasive species in the Wadden Sea transforming parts of it permanently. *M. gigas*, as an ecosystem engineer, builds reef structures that are characterized by highly complex and variable surfaces consisting of densely packed, sharp-edged individuals connected with cement-like bonds. To investigate the interactions between reef structure, shape and formation and wave as well as tidal currents, an understanding of the surface roughness is essential. This work reports on observations of oyster reefs for which seven new structural classes (*Central Reef*, *Transitional Zone*, *Cluster I*, *Cluster II*, *Patch I*, *Patch II,* and *Garland*) are proposed. For each class, high resolution Digital Elevation Models (DEMs) have been elaborated based on Structure-from-Motion (SfM) photogrammetry and analyzed using spatial statistics. By determining probability density functions (PDFs), vertical porosity distributions, abundances, orientations and second-order structure functions (SSFs), topographical parameters that influence the hydraulic bed roughness have been determined. The results suggest, that by applying the structural classification and their distinct topographical roughness parameters, the oyster reef surfaces can be described appropriately accounting for their complexity. The roughness accounts to a total roughness height k_t = 103 ± 15 mm and root-mean-square roughness height k_{rms} = 23 ± 5 mm. These values were found similar across all structural classes, yet the shape of the PDFs reveal differences. With decreasing abundance, the distributions become more positively skewed and are characterized by more extreme outliers. This is reflected in the higher statistical moments, as the skewness ranges between *Sk* = 0.4–2.1 and the kurtosis between *Ku* = 2.2–11.5. The analysis of the orientations and the SSFs confirms anisotropic behavior across all structural classes. Further, the SSFs reveal the oyster shells as significant roughness elements with exception of *Cluster I* and *II*, where the clusters are identified as significant roughness elements. The provided set of topographical roughness parameters enhances the knowledge of oyster reef surfaces and gives insights into the interactions between biogenic structure and

surrounding hydrodynamics. The new intra-reef classification allows for more accurate determination of the overall roughness as well as the population dynamics of the habitat forming oyster. Combined with hydraulic measurements, the results can be used to estimate the hydraulic bed roughness induced by the oyster reef surfaces.

Keywords: oyster reef, *Magallana gigas*, bed roughness, invasive species, ecosystem engineer, field study, wave attenuation, current attenuation

INTRODUCTION

The non-indigenous Pacific oyster *Magallana gigas* (Thunberg, 1793 formerly referred to as *Crassostrea gigas*) has become an established species in European waters (Diederich, 2005; Reise et al., 2017; Ewers-Saucedo et al., 2020). Permanent establishment of oyster populations in the western and central Wadden Sea began in the late 1990s after unintended introduction with seed mussels from the Oosterschelde in the Dutch Wadden Sea and subsequent dispersal by larvae drift eastward (Wehrmann et al., 2000; Brandt et al., 2008). In the northern Wadden Sea, populations developed separately from a local aquaculture hotspot near the island of Sylt (Reise, 1998). Oyster larvae require hard substrates to settle, which they find in intertidal blue mussel beds (*Mytilus edulis*), shell layers or artificial structures (Reise, 1998; Wehrmann et al., 2000; Wrange et al., 2010). With sufficient hard substrate available, populations of the invasive Pacific oyster have spread exponentially which led to an irreversible system shift in the Wadden Sea ecology (Wehrmann, 2006; Nehls et al., 2011; Folmer et al., 2014, 2017; Reise et al., 2017). In its function as an ecosystem engineering species, the invasive Pacific oyster has replaced formerly native mussel beds as the pristine and predominant biogenic habitat by the formation of rigid oyster reefs (Brandt et al., 2008; Markert et al., 2013; Bungenstock et al., 2021). The oyster reefs, now permanently present in the Wadden Sea region, entail alterations in the biological composition as well as local hydro- and morphodynamics. The assessment of these effects and their relevance at larger scales requires a close examination of the ultra-rough surface formed by the reefs regarding its interaction with tides and waves, implications for the entire ecosystem central Wadden Sea, and the quantification of roughness effects and reef topographies (Markert et al., 2010; Borsje et al., 2011; van der Zee et al., 2012; Walles et al., 2015b; Folmer et al., 2017).

In contrast to *Mytilus*-beds, which form low-relief biogenic structures with an internal flexible meshwork, *M. gigas* form rigid reef-like structures (Smaal et al., 2005). While blue mussels are attached to each other by the flexible and degradable byssus threads, juvenile oysters are permanently cemented with their left valve to their substratum immediately after metamorphosis of the larvae (Burkett et al., 2010; Tibabuzo Perdomo et al., 2018). When individuals die, the shells remain connected and form a hard substrate for the next generation, as *M. gigas* larvae prefer to settle on conspecifics (Quayle, 1988; Arakawa, 1990; Diederich, 2005). The shells of mature *M. gigas* typically reach lengths of 80–200 mm and widths of about 50–100 mm (**Figure 1**). The shells are coarse concentric sculpted with about six bold raised ribs and a glossy crenulate, saw-toothed shell margin contributing to the reef topographies complex nature (García-March et al., 2007; Nehring, 2011; Gosling, 2015; Hayward and Ryland, 2017). Growth, shell shape and orientation are highly variable and dependent on, e.g., substrate and food availability, temperature as well as abundance (Miossec et al., 2009; Nehring, 2011; Gosling, 2015; Hayward and Ryland, 2017). Oyster reef surfaces are characterized by directional features that are governed by their specific shell shape, and sharp, edgy growth line that influence surrounding hydrodynamics (García-March et al., 2007) and vice versa (Nagle, 1967; Grinnell, 1974). Due to the rigid framework, oyster reefs are more resistant to mechanical stresses induced by waves, tidal currents or even partially ice drift compared to mussel beds (Taylor and Bushek, 2008; Bungenstock et al., 2021). Over several generations, solid structures amalgamate with the surrounding sediment and continue to grow vertically while also expanding horizontally (Folmer et al., 2017; Bungenstock et al., 2021). In the process, oyster reefs evolve through different growth stages (Markert, 2020). After initial settlement on a hard substrate, clumps of several oysters are formed that enlarge by repetitive settlement. Over time, clumps coalesce to cluster and finally large-scale connected surfaces. Hence, once established, oyster reefs are known to persist permanently (Harzhauser et al., 2015; Djuricic et al., 2016). The internal structure and topography of *M. gigas* reefs range from areas with high abundances and vertically grown, densely packed individuals over clustered settlements with lower abundances to areas of bare sediment and biodeposits (Nagle, 1967; Grinnell, 1974; Bungenstock et al., 2021). However, vertical growth is limited by the aerial exposure time at low tides as upper threshold. Rodriguez et al. (2014) and Ridge et al. (2017) found a threshold of a growth ceiling of 50–60% of the time during a tidal cycle. Several studies suggest classifications of oyster reefs in two or three reef types [e.g., high-relief or low-relief (Schulte et al., 2009; Lipcius et al., 2015); high reef density or low reef density (Mann et al., 2009; Wagner et al., 2012); high or low complexity (Grabowski, 2004; Grabowski and Powers, 2004; Markert, 2020)]. However, a closer examination of an intra-reef structure classification is currently unavailable despite its natural spatial heterogeneity, and this has thus largely motivated the present work.

Oysters are ecosystem engineers as they influence the intertidal flats beyond their biogenic habitat (Jones et al., 1994, 1997; Gutiérrez et al., 2003). It has been recognized that oyster reefs can serve as living breakwater as they attenuate wave energy effectively (Bouma et al., 2014; Manis et al., 2015; Chowdhury et al., 2019) and stabilize sediments through trapping and sheltering (Meyer et al., 1997; Piazza et al., 2005; Walles et al., 2015a) similar to wide-graded scour protection where sand deposition has been observed both in currents and waves

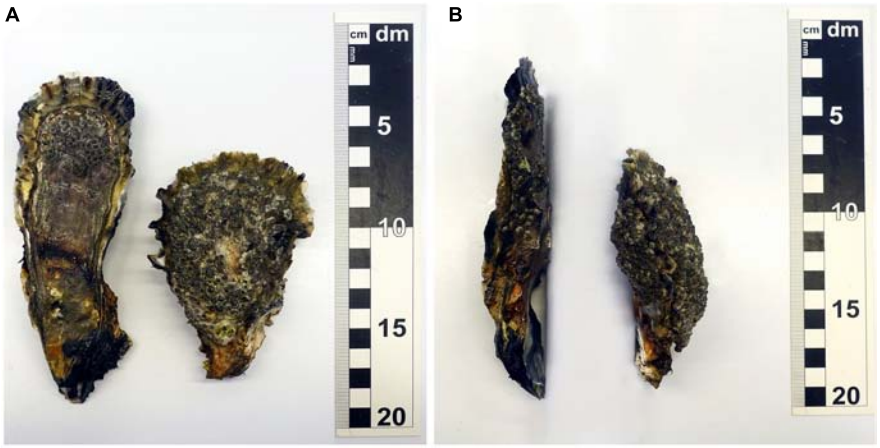


FIGURE 1 | Detailed view of two *Magallana gigas* individuals illustrating the variability of the oyster shell morphology of mature individuals. **(A)** View along the long axis of the oyster shells. **(B)** View along the short axis of the oyster shells.

(Schendel et al., 2016, 2018a,b). Oyster reefs even bear the potential to reduce vulnerability of coastal communities to natural hazards as flooding, eroding shorelines and sea-level rise (Piazza et al., 2005; Hossain et al., 2013; Walles et al., 2015b; Chowdhury et al., 2019).

While little research has focused on the bed roughness of *M. gigas* reefs in European waters, the hydrodynamic roughness of reefs formed by *Crassostrea virginica,* especially on the East Coast of the United States, have been subject to several studies. Whitman and Reidenbach (2012), Reidenbach et al. (2013), Styles (2015), and Kitsikoudis et al. (2020) measured flow dissipation over natural and restored *C. virginica* reefs. All studies derive site-specific hydrodynamic roughness parameters, namely the drag coefficient C_D or roughness length z_0 from flow measurements. However, these descriptors depend highly on site-specific characteristics of the oyster reefs and are thus difficult to apply to other locations or oyster species. Previous studies have used a mean number of roughness elements, their average height and width as site-specific topographic descriptors (Manis et al., 2015; Kitsikoudis et al., 2020) and illustrate a direct influence of the density and size of individual shells on wave attenuation. Morris et al. (2021) compared the effectiveness of several *C. virginica* reefs as breakwaters as part of a nature-based coastal protection strategy in a field study on the East Coast of the United States. While the authors conclude that the reef crest elevation is the most important parameter for wave attenuation, they also highlight the dependency of the reef crest to an optimal inundation duration, and thus, to the water level. Furthermore, they conclude that additional reef characteristics (e.g., width or oyster coverage) should be considered in future studies. The aforementioned studies illustrate the requirement of a detailed understanding of the surface topography to possibly transfer results to other locations and to better assess the effects of wave and current energy dissipation. However, detailed descriptions of the oyster reef topographies at the scale of individual oysters remain sparse. Besides the surface descriptions mentioned before, Margiotta et al. (2016) and Colden et al. (2017) report rugosities as measures of surfaces roughness. In their applied method, a fine link chain is laid over the surface conforming to the crevices. In a subsequent step, the length of the chain is divided by the linear length over the reef top, yielding a metric with which surface complexity can be estimated.

In the fields of hydraulic engineering and fluvial hydraulics, the analysis of bed topographies utilizing high-resolution digital elevation models (DEMs) and spatial statistics has become more and more popular in the past decades, as this approach offers an opportunity to link surface characteristics with hydraulic roughness (Powell, 2014). Apart from some exceptions (Krämer and Winter, 2016; Welzel et al., 2019, 2020) this approach has been used less in the field of coastal or ocean engineering. Conventionally, bed roughness due to small-scale roughness elements on plane beds, such as sand-grains or gravel, has been linked to a characteristic surface descriptor (e.g., grain size d_{50} or d_{84}) or to the equivalent sand roughness, i.e., the roughness used in the work of Nikuradse (1933). However, by utilizing a single descriptor many parameters such as particle size distribution, particle shape, orientations, arrangements and bed forms, etc., are neglected (Nikora et al., 1998). The emergence of high-resolution DEMs based on 3D laser scanning and structure-from-motion (SfM) photogrammetry nowadays allow for detailed analysis of complex bed topographies. This means that it is now feasible to switch from conventional singular parameters to information-richer parameter sets to describe key topographical properties (Musker, 1980; Clifford et al., 1992; Nikora et al., 1998; Smart et al., 2004; Aberle and Nikora, 2006; Flack and Schultz, 2010, 2014; Chung et al., 2021). DEMs can be evaluated using several statistical methods, e.g., probability density functions (Nikora et al., 1998; Smart et al., 2004; Aberle and Nikora, 2006; Coleman et al., 2011; Bertin and Friedrich, 2014), porosity distribution (Aberle, 2007; Navaratnam et al., 2018), or structure functions (Nikora and Walsh, 2004; Aberle and Nikora, 2006; Bertin and Friedrich, 2014; Qin et al., 2019). However, linking topographical properties to hydraulic roughness effects remains an ongoing topic of research (Chung et al., 2021). A comprehensive analysis

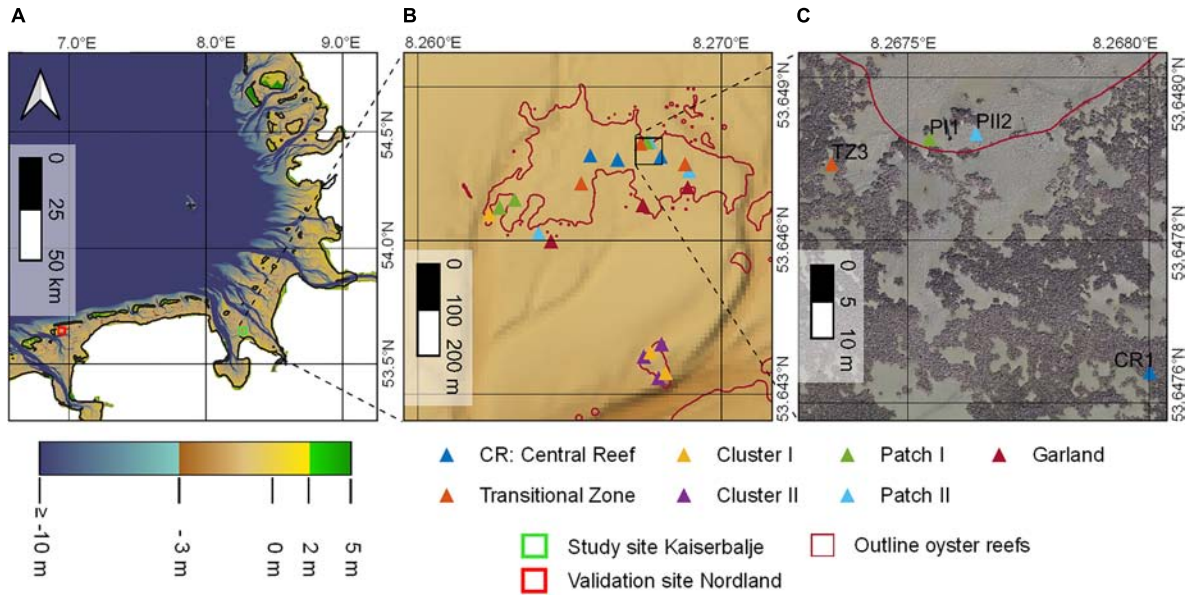


FIGURE 2 | (A) A map showing the bathymetry of the Wadden Sea in the German Bight (Sievers et al., 2020), the study site Kaiserbalje (green square) and the validation site (red square). **(B)** A map showing the study site oyster reef *Kaiserbalje*. The reef outlines are marked in magenta (Nationalparkverwaltung Niedersächsisches Wattenmeer, 2021). The triangles illustrate sampling locations with varying colors for each structural class, respectively. **(C)** An orthomosaic recorded in spring 2020 showing a section of the study site as an example for the complex surface structures.

of oyster-settled surfaces in the shallow marine environment using high-resolution DEMs has not yet been conducted to date. It is worth mentioning that DEMs of natural and constructed *C. virginica* reefs were analyzed by Rodriguez et al. (2014) and Ridge et al. (2015) to investigate vertical, areal, and hence volumetric reef growth, over time as well as impact factors such as aerial exposure time and sea-level rise. Parameters describing the roughness of the reef, e.g., topographical roughness lengths, have not been identified in these studies. It is hypothesized that, in case of oyster reefs, the shape, the orientation and protrusion of the individual oysters as well as abundance and formation of cluster are important topographical parameters that should be considered in a more accurate surface characteristics description.

Based on recent literature, several unresolved topics remain with respect to the characterization of roughness and topographies of oyster reefs. Only few studies address the description of oyster reef surfaces, but fall short to elaborate surface properties in detail. When topographic roughness parameters are reported, some factors that are assumed to affect the hydraulic roughness are not considered. Complex topographies and variability due to abundances, orientations or clustering have not been studied thoroughly. The complexity of oyster reefs caused by the variability of surface properties within reefs have not been addressed. No classification of internal structures of oyster reefs (*M. gigas*), neither worldwide nor for European waters exist. Based on the previously identified lack of knowledge, the specific objectives of this paper include the following:

- Gaining insights into the spatial topography of *M. gigas* reefs using high-resolution DEMs.
- To examine if and how SfM photogrammetry can be employed to derive detailed high-resolution topographical data under the adverse conditions during field studies in the eulittoral of the central Wadden Sea.
- To provide a detailed statistical surface description of *M. gigas* reef topographies at the scale of species-related oyster roughness.
- To propose a general intra-reef structural classification of oyster reefs, based on visual field observations and detailed statistical analyses of the bed topography.
- The introduction and application of a methodology which allows the transfer of hydrodynamic parameters across locations without considerable uncertainty, which can later be applied to other reef locations.

MATERIALS AND METHODS

Study Site

The present study focuses on the oyster reef *Kaiserbalje* (Mean Coordinates: 53.6470116°N, 008.2664760°E; **Figure 2**). It is located in the "Hohe Weg Watt" in the Lower Saxon Wadden Sea National Park north of the peninsula Butjadingen, Germany. The *Kaiserbalje* is situated on the intertidal flat at the vertex between the Jade and Weser estuaries. The reef is composed of a large continuous surface extending 600 m in WE and 300 m in NS direction with fringing boundaries as well as a second smaller surface at a distance of 500 m south of the main reef with extends of 50 by 50 m. The sediment cover within the central part of the reef is predominantly muddy,



FIGURE 3 | Examples of the proposed structural classes found during the initial observation phase at the study site: *Central Reef*, *Transitional Zone*, *Cluster I*, *Cluster II*, *Patch I*, *Patch II*, and *Garland*. The gray frame illustrates 1 m^2.

TABLE 1 | Descriptive parameters of the proposed structural classifications.

Structure class	Shape	Oyster coverage	Lateral shell orientation	Sediment gaps	Sediment coverage
Central Reef (CR)	Homogeneous coverage	High abundance	Vertical	Small gaps (up to 10 cm), mainly muddy	Isolated flats of mud and biodeposits (1–3 m)
Transitional Zone (TZ)	Homogeneous coverage	Moderate abundance	±Vertical, partly horizontal at edges	Moderate gaps (10–20 cm), mainly mud	Irregular flats of mud and biodeposits (1–3 m)
Cluster I (CI)	Homogeneous coverage, uniform accumulation of isolated clusters	Clusters with high abundances (cluster diameter 0.2–1 m)	Vertical and horizontal	–	Mainly sand
Cluster II (CII)	Homogeneous coverage, loose accumulation of isolated clusters	Clusters with moderate abundances (cluster diameter 0.2–0.3 m)	Irregular	–	Many (0.3–1 m), mainly sand
Patch I (PI)	Isolated, enclosed flats, round or elliptical shape (diameter of 1–3 m) with fuzzy edges	Dense to moderate abundance in patches	±Vertical	Up to 10 cm, mainly mud	Isolated patches are surrounded by mud or sand
Patch II (PII)	Isolated, enclosed flats, irregular form shape (diameter of 2–10 m), with many indentations and fuzzy edges	Dense to moderate abundance in patches	±Vertical, partly horizontal at edges	10–20 cm, mainly mud	Isolated patches are surrounded by mud or sand
Garland (G)	Isolated, enclosed flats with elongated shape (1 m wide, several meters long), perpendicular to flow direction	Low to moderate abundance in patches	±Vertical, partly horizontal at edges	Up to 10 cm, mud or sand	Isolated patches are surrounded by mud or sand

while the smaller part is predominantly sandy. The mean tidal range is 3.3 m (Bundesamt für Seeschifffahrt und Hydrographie [BSH], 2020) and the mean aerial exposure time is 3.5 h. At the time of the field study in October 2020, the oyster reef covered an area of 42,000 m^2 and was characterized by elevations ranging from −1.14 to −0.066 m above sea level (ASL). Markert (2020) categorizes the reef as a complex reef with a high oyster density. The biomass of the entire reef is estimated as total wet weight of *M. gigas* $TWW_{M.gigas}$ = 1,400 t and of *M. edulis* $TWW_{M.edulis}$ = 150 t (unpublished data).

The local transformation from a mussel bed to an oyster reef is well documented (Wehrmann, 2006; Markert, 2020). First Pacific oysters on the former mussel bed *Kaiserbalje* with shell length >25 mm were found in 2004 with mean abundances of less than 10 individuals per m^2 reef area (area covered by bivalves plus internal sediment areas) whereas no oysters have been found there in 2003. During the following years, the abundances first increased exponentially (2005: ∼120 inds./m^2; 2007: ∼215 inds./m^2; 2008: ∼240 inds./m^2; own data) before reaching a "plateau-like" status where values slightly fluctuate on a high level. This development in population dynamics was in general accordance with the overall development in the central Wadden Sea after the invasion passed through the region in an eastward direction. With the beginning of this study, mean abundances of oyster were ∼360 inds./m^2 representing a biomass of 21.7 kg/m^2 live wet weight (LWW) whereas the blue mussels, now part of the associated benthic fauna, show abundances of ∼620 inds./m^2 and 5.1 kg/m^2 LWW (recalculated for comparison to the reef area, i.e., area covered by oysters and internal sediment patches).

Proposed Structural Classification

This work proposes a structural classification within and in the surrounding of oyster reefs; the remainder of this work will test its applicability. Based on initial visual on-site observations, seven structural classes are proposed: *Central Reef*, *Transitional Zone*, *Cluster I*, *Cluster II*, *Patch I*, *Patch II,* and *Garland*. These classes are characterized by varying properties such as shape, oyster coverage and orientation as well as sediment gaps between individual oysters and sediment coverage (**Figure 3** and **Table 1**). Moreover, the structural classes can be subdivided into surfaces with homogenous oyster coverage (*Central Reef*, *Transitional Zone*), surfaces with dense agglomerations of oysters (*Cluster I* and *Cluster II*) as well as isolated and enclosed shapes (*Patch I*, *Patch II,* and *Garland*).

Data Collection and Processing

A total of 21 topographical samples were collected at distinct locations within the study site (**Figure 2**). For each proposed structural class, three samples were arbitrarily identified and visual determination on a map prior to the field campaigns ensured that the sample locations were evenly distributed over the entire reef. The samples are named after an abbreviation of their respective proposed structural class and a number (cf. **Table 1**).

Structure-from-motion photogrammetry, a non-destructive method, was used to generate DEMs as in numerous field studies before (Westoby et al., 2012; Leon et al., 2015; Micheletti et al., 2015; James et al., 2017; Morgan et al., 2017; Cullen et al., 2018; Verma and Bourke, 2019). The method allows for a rapid and accurate generation of DEMs of complex surfaces (see **Figure 4**). A rapid measurement was necessary for this study, as the areal exposure time of the oyster reef only allowed for a short timespan to collect the photographs and further data (3–4 h). Following the identification of a suitable sample, a surface of roughly 1.5 m^2 was photographed by a CANON EOS 750D camera using two lenses with focal lengths of 18 mm (Canon EF-S 18–135 mm f/3.5–5.6 IS STM) and 50 mm (Sigma Art 50 mm 1:1.4 DG HSM), respectively. The photographs were recorded as RAW-files with 24 megapixel (6000 × 4000 pixel). For each sample, approx. 200 photographs were taken of which approx. 100 were taken at a distance of around 1 m in a circular arrangement to assure high overlaps between the frames (>90%) and another 100 pictures were taken at a close-range (<0.5 m) to increase details of undercuts and tips of the shells (**Figure 4B**); similar to Cullen et al. (2018) and Verma and Bourke (2019). L- and I-shaped reference bars consisting of marine plywood boards with fixed distances in *x*, *y,* and *z* directions were equipped with visual targets (ground control points) and checkerboards to facilitate the image processing by the software Agisoft Metashape Professional (v. 1.7.3). Three reference bars were utilized suggested to impede systematic errors as, e.g., doming deformation (James and Robson, 2014). GPS measurements were taken at the reference points on the reference bars to relate the generated DEMs in a global coordinate system. A Stonex-9000-dGPS was used with a horizontal accuracy of 0.008 m and a vertical accuracy of 0.015 m.

The images were processed as follows: (1) Image quality was controlled to eliminate blurred and out-of-focus photographs. Colorcasts were removed using Adobe Camera RAW (v.13). (2) Meshes (DEMs) and orthomosaics were generated from the photographs using Agisoft Metashape Professional (v. 1.7.3) [see Leon et al. (2015) or James et al. (2017) for details]. Highest settings were applied during alignment of photos, building of dense clouds, meshing as well as export. The resulting dense point clouds had on average 100 million data points with an average total error of ±1.6 mm within the meshes. (3) A morphological filter was applied to isolate the species-related roughness from the superordinate morphology. Separation of surfaces in different orders of magnitude, also referred to as separation in waviness, roughness and micro-roughness profiles, is a common method in roughness determination (Raja et al., 2002; Le Goïc et al., 2015) and has been applied in geographical sciences (Liu et al., 2018). Hence, a morphological filter was developed in Rhinoceros 3D (v.6) and Grasshopper, a visual programming language environment within the CAD program Rhinoceros 3D. A non-uniform rational B-spline (NURBS) surface was formed after the topography of the DEM and approximated by a set of manually distributed (digital) reference points on the visible sediment surface. The number of reference points was dependent on the proportion of sediment-covered parts of the DEM. The NURBS surface was then subtracted from the mesh (**Figure 4D**). Differences in surfaces level elevation between Δz = 8–120 mm over the total area were eliminated. (4) Finally, rasterized point grids with point spacing of 2 mm and cropped to a surface area of 1 m^2 were exported for the analysis in MATLAB R2019a.

Figure 5 shows the DEMs of the 21 samples using their mean elevation as reference height z = 0 mm. The visualizations of the *Central Reef*, *Transitional Zone,* and *Patch II* samples show homogeneous distributions of surface level elevations for the entire section. For the *Cluster I* and *Cluster II* samples, concentrated agglomerations of the surface level elevations can be observed as expected (cf. **Table 1**). While the samples PI2, G1, and G3 show homogeneous distributions of the surface level

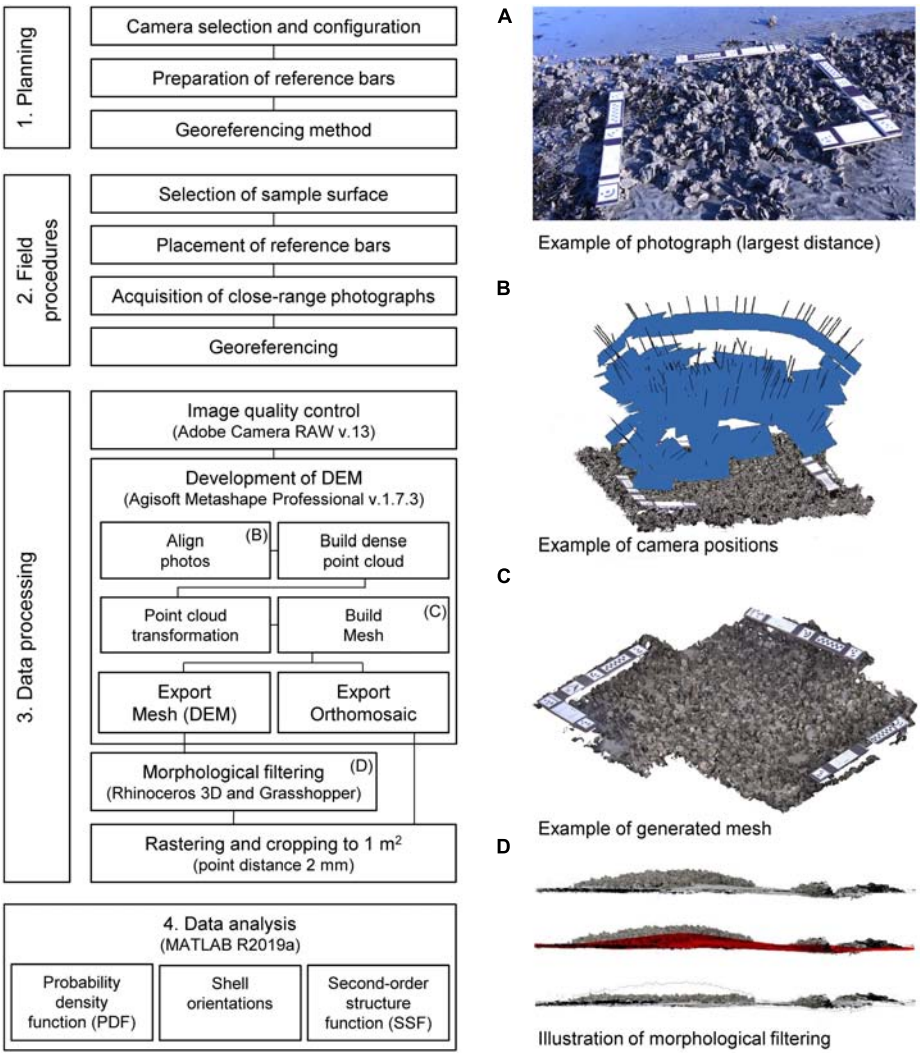


FIGURE 4 | A schematic diagram of the workflow for the development of digital elevation models (DEMs) and subsequent analysis. **(A)** Example of a photograph used for the SfM photogrammetry (largest distance). **(B)** Illustration of the camera positions in Agisoft Metashape. The blue patch and black lines illustrate the position of the camera and their orientations. **(C)** Example of a generated mesh including the reference bars before cropping. **(D)** Illustration of the morphological filtering. The NURBS surface is illustrated in red.

elevations, the samples PI1, PI3, and G2 show inhomogeneities. In these cases, the surface area of the isolated patches is smaller than 1 m^2. For the statistical analysis, a section of the surface with a homogeneous distribution of the surface level elevations is necessary. The analyzed surfaces are, hence, reduced until the edges of the patches and the surrounding bare sediment are eliminated and a homogenous surface remains (the eliminated area is illustrated in gray boxes in **Figure 5**).

Data Analysis

The data analysis used in this work aims to provide parameters describing the topography of oyster reef surfaces that pose significant influences on the hydraulic bed roughness. These parameters include the statistical moments derived from the probability density functions (PDFs) of the surface level elevations, the vertical porosity distribution as well as abundance, orientation and clustering.

Probability Density Functions

Probability density functions were determined from the DEMs of the sample surfaces similar to, e.g., Coleman et al. (2011) and Bertin and Friedrich (2014) (cf. **Figure 4**). Smoothed histograms using bins of 1 mm width were applied, which cover the vertical range of the surface level elevations. In addition, statistical parameters were determined that describe the geometrical bed roughness. The total roughness height k_t, describing the distance between the roughness peak to the trough, was defined as the 99%-percentile minus the 1%-percentile ($P_{99\%}$-$P_{1\%}$) to eliminate outliers, as suggested by Aberle et al. (2008). The root-mean-square roughness height, which is the standard deviation σ

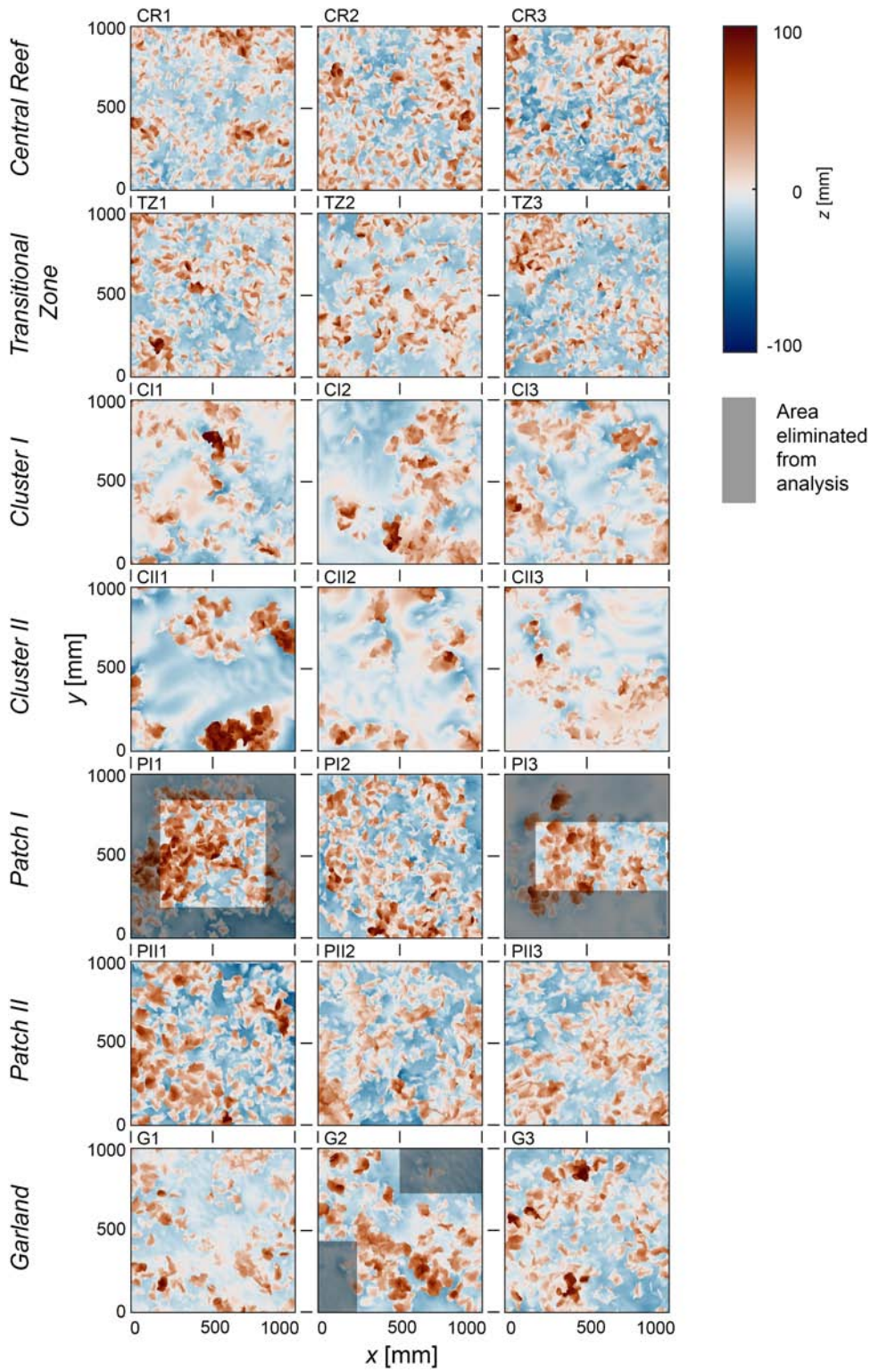


FIGURE 5 | Visualizations of the digital elevation models (DEMs) of the 21 samples in top view, sorted by proposed structural classes. The *x*-, *y*-, and *z*-axis are in mm. The color scale (Crameri, 2018) indicates surface level elevations in *z* centered around the zero mean. The point of origin (*x*, *y*) = (0 mm, 0 mm) has been defined as the southwest corner of the section. All samples are oriented with north on top. Area in gray boxes illustrate the areas that have been eliminated to assure homogeneous distribution of *z* in the analyzed section.

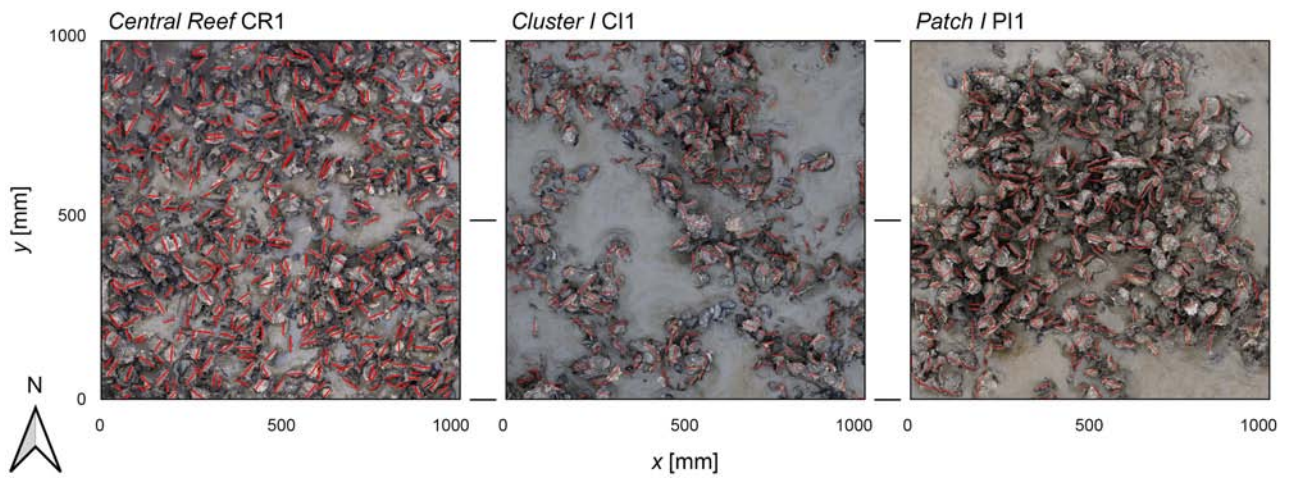


FIGURE 6 | Three examples of the orthomosaics used to derive the abundance and the dorso-ventral orientation. The *x*- and *y*-axis are in mm. Red lines mark the short axis of the identified individual oyster shells. The panels show the samples of *Central Reef* CR1, *Cluster I* CI1, and *Patch I* PI1. Each photo covers 1 m^2 with the upper side facing north.

around a zero mean, is a second measure of the geometrical roughness height (Chung et al., 2021). The third central moment, the skewness *Sk* is a measure for the asymmetry in the surface elevation distribution (Bendat and Piersol, 2010). Surfaces with protruding elements are positively skewed, also referred to as right-skewed, while pitted surfaces are negatively- or left-skewed (Jelly and Busse, 2018). The fourth central moment, the kurtosis *Ku*, describes the extremity of outliers in the tails of the distribution (Westfall, 2014). Further, integration of a PDF yields the cumulative distribution function (CDF) which reveals the vertical porosity distribution Φ (Aberle, 2007; Navaratnam et al., 2018). The bulk porosity Φ_{bulk} is the total fraction of voids over the total volume described by the lengths of the sections in *x* and *y* as well as the height between the lowest and highest surfaces elevation in *z*.

Abundance and Orientation

The abundance, as defined in this work, describes the number of oyster individuals per m^2 protruding from the sediment cover. It was determined visually by identifying the individual oyster shells from the orthomosaics (**Figure 6**). No differentiation was made between live and dead oysters, but only individuals with both valves present were counted. Further, widths *w* (the short axis of the individual shells) and dorso-ventral orientations ϕ of the individual oysters were recorded. The dorso-ventral orientation is the rotation around the long axis (length) of oyster shells (García-March et al., 2007).

Second-Order Structure Functions

Two dimensional second-order structure functions (2D-SSF) represent a tool to identify spatial correlation lengths and correlation patterns of surfaces (Nikora et al., 1998; Nikora and Walsh, 2004; Aberle and Nikora, 2006; Aberle et al., 2010; Bertin and Friedrich, 2014; Qin et al., 2019; Wang et al., 2020). In this work, 2D-SSFs were used to identify characteristic spatial scales related to roughness elements and their anisotropic behavior. A 2D-SSF is defined as:

$$D_{G2}\left(l_x, l_y\right) = \frac{1}{(N-n)(M-m)} \sum_{i=1}^{N-n} \sum_{j=1}^{M-m} \left(z\left(x_i + n\Delta x, y_j + m\Delta y\right) - z\left(x_i, y_j\right)\right)^2 \quad (1)$$

where $l_x = n\Delta x$ and $l_y = m\Delta y$ are the spatial lags; Δx and Δy are the sampling intervals; N and M are the number of observed elevation points; and z is the surface level elevations at the coordinate in x and y, respectively.

RESULTS

In the following, the analysis of the reef topographies shown in **Figure 5** is presented. First, topographical parameters derived from the statistical analysis are considered. Next, the results of the analysis on directionality and clustering are shown. In both steps, the proposed structural classification is tested against the suitability of the proposed classes. The proposed structural classification is then reassessed and its validity beyond the study site is verified.

Topographical Parameters

The topographical parameters, including the location within the oyster reef, the surface level elevations and their distributions, reveal differences between the respective structural classes.

The samples of *Central Reef* and *Transitional Zone* are located toward the center, while *Garland, Patches,* and *Cluster* are found at the margins of the reef (cf. **Figure 2** and **Table 2**). Further, the samples of *Central Reef* are located at highest elevations (−0.13 to −0.08 m ASL), followed by *Transitional Zone, Garland, Patches,* and *Cluster I* and *II* samples (−0.93 to −1.14 m ASL) as the lowest.

TABLE 2 | Summary of the results of the statistical analysis, where k_t is the total roughness height, k_{rms} is the root-mean-square roughness height, *Sk* is the skewness, *Ku* is the kurtosis, Φ_{bulk} is the bulk porosity, *A* is the abundance, w_{mean} is the mean width of the oyster shells, ϕ_{Shells} is the major direction of the oyster shells and ϕ_{2DSSF} is the orientation of the mean axis of the area of high correlation resulting from the second-order structure functions.

Structural class/Sample location		Position		Mean elevation	k_t	k_{rms}	*Sk*	*Ku*	Φ_{bulk}	*A*	w_{mean}	ϕ_{Shells}	ϕ_{2DSSF}	Roughness element
		[lat]	[lon]	[m ASL]	[mm]	[mm]	[–]	[–]	[–]	[inds./m^2]	[mm]	[deg]	[deg]	[–]
Central Reef	CR1	53.647637751N	008.268002139E	−0.13	96	21	0.9	3.6	0.68	448	36	35	5	Shells
	CR2	53.647585546N	008.266578077E	−0.08	100	22	0.9	3.6	0.66	351	40	85	80	Shells
	CR3	53.647662854N	008.265683268E	−0.07	117	27	0.6	3.0	0.65	380	42	45	36	Shells
Transitional Zone	TZ1	53.647495627N	008.268809303E	−0.12	97	22	1.1	4.1	0.72	530	32	105	120	Shells
	TZ2	53.647114528N	008.265381970E	−0.29	95	21	1.2	4.1	0.66	425	34	45	60	Shells
	TZ3	53.647893656N	008.267341925E	−0.20	105	25	0.8	3.1	0.65	443	35	5	50	Shells
Cluster I	CI1	53.646502663N	008.262351901E	−1.08	110	20	2.1	11.5	0.76	270	34	15	165	Shells
	CI2	53.643816898N	008.267665914E	−0.98	98	21	1.4	5.2	0.73	264	34	75	90	Shells
	CI3	53.643416323N	008.268143169E	−1.14	94	19	0.9	4.1	0.66	235	36	65	15	Cluster
Cluster II	CII1	53.643734006N	008.267414882E	−1.13	131	29	1.6	4.8	0.67	134	35	45	45	Cluster
	CII2	53.643971712N	008.268060367E	−0.93	96	18	1.7	6.7	0.70	134	35	45	45	Cluster
	CII3	53.643306529N	008.267914535E	−1.08	75	14	1.8	9.4	0.74	144	39	45	60	Cluster
Patch I	PI1	53.647924230N	008.267544924E	−0.30	118	31	0.4	2.2	0.63	475	42	15	–	Cluster
	PI2	53.646798178N	008.263195540E	−0.37	116	28	0.8	3.1	0.68	255	40	55	100	Shells
	PI3	53.646646494N	008.262696156E	−0.71	109	26	0.5	2.5	0.61	493	31	55/155	–	–
Patch II	PII1	53.646134588N	008.263978463E	−0.37	126	29	0.5	2.7	0.64	177	48	75	90	Shells
	PII2	53.647931467N	008.267641195E	−0.19	99	24	0.4	2.6	0.56	236	44	35/115	115	Shells
	PII3	53.647363701N	008.268910737E	−0.10	81	18	0.7	3.0	0.65	423	30	55	30	Shells
Garland	G1	53.646694945N	008.267417665E	−0.28	82	18	1.7	6.0	0.79	209	39	115	170	Shells
	G2	53.645990202N	008.264392112E	−0.41	107	27	1.0	3.1	0.69	383	37	5	–	–
	G3	53.647037563N	008.268918334E	−0.15	119	25	1.4	5.4	0.75	263	37	35	80	Shells
Nordland – CR		53.641551868N	006.941972378E	−0.15	98	23	0.4	2.7	0.64	340	35	15	105	Shells
Nordland – TZ		53.641419612N	006.942020178E	−0.02	88	18	1.2	4.9	0.72	150	37	35	65	Shells
Nordland – C		53.641092208N	006.942421384E	−0.51	62	13	2.0	7.0	0.83	50	34	45	50	Shells

All distributions are bell shaped but not normally distributed (tested by Kolmogorov–Smirnov-test; see **Figure 7**). The PDFs of the samples of each structural class exhibit small deviations between each other with the exception of *Garland*. Between the structural classes, clear differences can be observed apart from *Patch I* and *Patch II*, which show similar distributions. For the *Central Reef*, *Patch I,* and *Patch II* samples, the PDFs reach similar peak values at around 0.02. The peak values of the remaining structural classes increase from *Transitional Zone*, *Cluster I*, *Garland* to *Cluster II* samples up to 0.05. All distributions are right-skewed varying between *Sk* = 0.4–2.1 (**Table 2**) and reach their peak slightly below the zero mean as can be expected for surfaces with protruding roughness elements (Chung et al., 2021). The kurtosis-values scatter from around 3.0 (equal to normal distribution) to 11.5 reflecting strong variations in the shape of the tails of the distributions. The total roughness height k_t and the root-mean-square roughness height k_{rms} yield similar values across all samples and small deviations. The samples of *Garland* show largest deviations in the distribution, especially regarding the peak values. Comparing the DEMs of the *Garland* samples in **Figure 5** illustrates that the density of high surface level elevations of G1 is lower than that of the remaining samples, which explains the deviating form of the PDF.

Table 3 breaks the data down to average values per proposed structural class, further elucidating the class preposition set. Considering only the roughness height parameters k_t or k_{rms}, no clear trends can be observed for most structural classes. Only the higher variability of k_t for *Cluster II* stands out. The higher statistical moments as well as the bulk porosity, reveal differences across all structural classes. Both *Sk* and *Ku* values increase beginning from class *Patch I* and *Patch II*, with lowest values, over *Central Reef*, *Transitional Zone*, *Cluster I, Garland* to *Cluster II*, with highest values. The average statistical parameters of the samples of (1) *Central Reef* and *Transitional Zone,* (2) *Cluster I* and *Cluster II* as well as (3) *Patch I* and *Patch II* reveal strong similarities between the respective classes. The average values of *Transitional Zone* are slightly larger than those of *Central Reef*. Between *Cluster I* and *Cluster II* as well as *Patch I* and *Patch II* no clear differences can be determined. All other samples have larger *Ku* reflected in the increasing extremity of the positive tail of the distributions. For the *Cluster I* and *II* samples, with large *Sk* and *Ku* values, also the deviations within samples are significantly higher than for the remaining classes. The average values of the *Garland* samples lie between *Transitional Zone* and *Cluster I*. However, strong deviations between samples can be observed for the statistical moments.

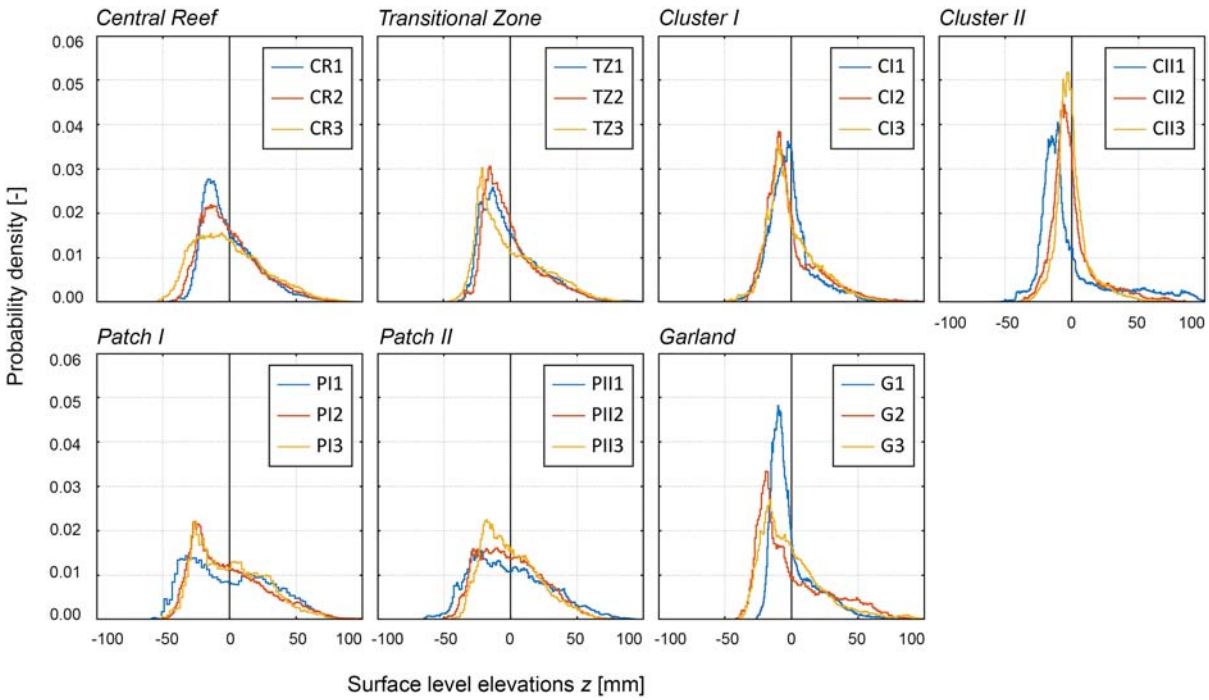


FIGURE 7 | Histograms based on surface level elevation z [mm] illustrating the probability density functions (PDFs) [-] of all samples distinguished by their structural classes. Top row: homogenous structural classes; Bottom row: enclosed structural classes. The PDFs are centered around the zero mean. The colors indicate the individual samples as presented in **Figure 5**, e.g., blue: CR1, orange: CR2, yellow: CR3, etc.

TABLE 3 | Average statistical parameters per proposed structural class, where k_t is the total roughness height, k_{rms} is the root-mean-square roughness height, Sk is the skewness, Ku is the kurtosis, Φ_{bulk} is the bulk porosity, A is the abundance, w_{mean} is the mean width of the oyster shells.

Structural class	Elevation	k_t	k_{rms}	Sk	Ku	Φ_{bulk}	A	w_{mean}	Roughness element
	[m ASL]	[mm]	[mm]	[–]	[–]	[–]	[inds./m^2]	[mm]	[–]
Central Reef	−0.09 ± 0.03	104 ± 11	23 ± 3	0.9 ± 0.2	3.5 ± 0.5	0.66 ± 0.02	393 ± 50	39 ± 3	Shells
Transitional Zone	−0.20 ± 0.09	99 ± 5	23 ± 2	1.0 ± 0.2	3.7 ± 0.6	0.68 ± 0.03	466 ± 56	34 ± 1	Shells
Cluster I	−1.07 ± 0.08	101 ± 8	20 ± 1	1.5 ± 0.6	7.0 ± 3.9	0.71 ± 0.05	256 ± 19	35 ± 1	Cluster
Cluster II	−1.05 ± 0.10	100 ± 28	20 ± 8	1.7 ± 0.1	7.0 ± 2.3	0.70 ± 0.04	137 ± 6	36 ± 2	Cluster
Patch I	−0.46 ± 0.22	114 ± 5	28 ± 3	0.5 ± 0.2	2.6 ± 0.5	0.64 ± 0.04	408 ± 133	38 ± 6	Shells
Patch II	−0.22 ± 0.14	105 ± 18	25 ± 4	0.5 ± 0.1	2.8 ± 0.2	0.62 ± 0.05	279 ± 128	41 ± 9	Shells
Garland	−0.28 ± 0.13	103 ± 19	23 ± 5	1.4 ± 0.3	4.9 ± 1.5	0.74 ± 0.05	285 ± 89	38 ± 1	Shells

The trends observed in **Table 3** reflect the shapes of the PDFs in **Figure 7**.

The differences in the shape of the PDFs and the corresponding statistical parameters can be explained by the compositions of the reef topographies. All surfaces are composed of two components, sediment and oyster shells. As the superordinate morphology has been eliminated in the pre-processing (cp. subsection "Data Collection and Processing"), the sediment components have low variations in elevation. The remaining height variations in the sediment surface are mainly due to small-scale current ripples, deposits or scours around individual shells. The oyster shells protrude from the sediment surface resulting in higher elevations and, hence, more pronounced positive tails of the PDFs (**Figure 7**). It is therefore possible to attribute the right-skewness of the distributions to the oyster shells. The oyster shells are more or less uniformly distributed in samples with high abundances such as *Patches I* and *II*, *Central Reef* and *Transitional Zone*, and individual shells tend not to peek out from the homogeneous topography. The resulting PDFs are therefore moderately right-skewed and exhibit little pronounced positive tails, hence, smaller *Sk* and *Ku* (**Figure 7** left side). With decreasing abundance for the samples of *Cluster I* and *II* as well as *Garland*, larger proportions of the surface are sediment-covered. The corresponding PDFs become more right-skewed and are characterized by more pronounced positive tails (**Figure 7** right side), hence, higher kurtosis, due to fewer oyster individuals. In addition, the oyster coverage becomes more instable as oysters lump together in clusters. This

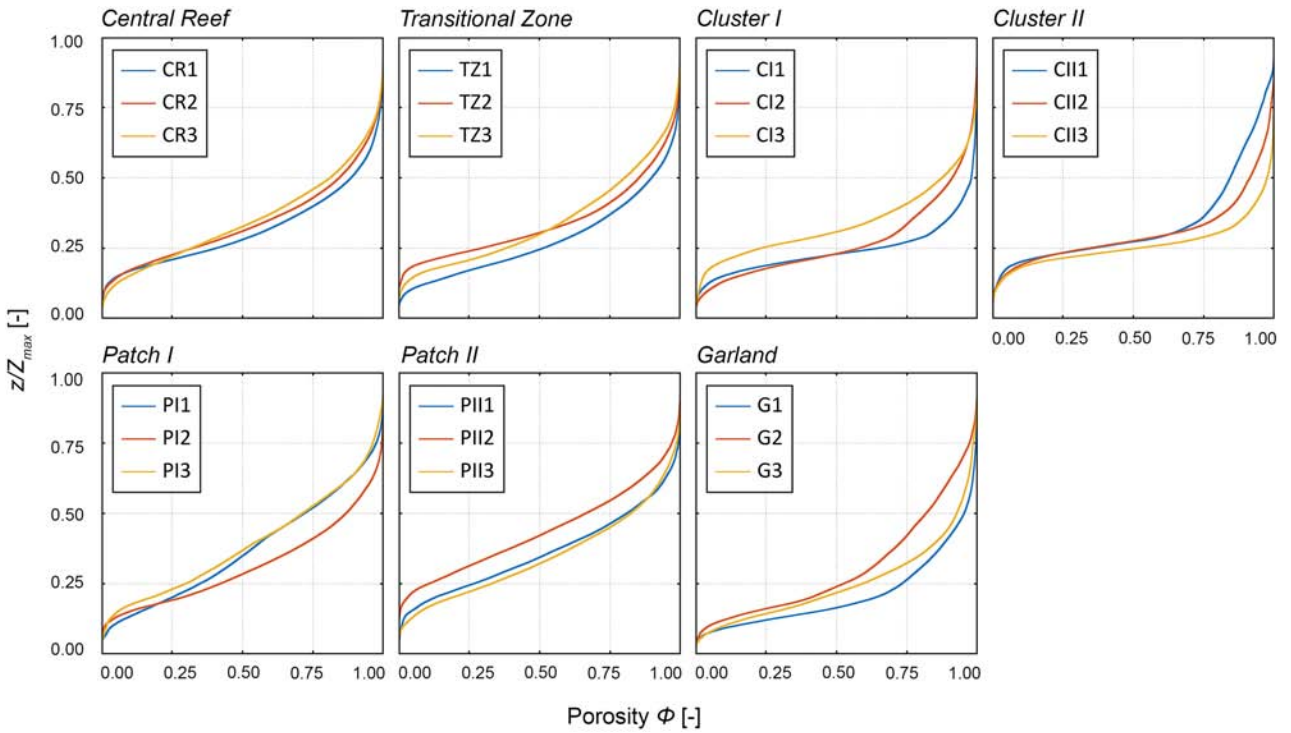


FIGURE 8 | Normalized vertical distribution of the porosity Φ [-] of all samples distinguished by their structural classes over the dimensionless height z/Z_{max} [-]. z is the surface level and Z_{max} is the total height of surface level elevations. Top row: homogenous structural classes; Bottom row: enclosed structural classes. The colors indicate the individual samples as presented in **Figure 5**, e.g., blue: CR1, orange: CR2, yellow: CR3, etc.

causes larger deviations within the three samples, and hence, larger scatter in the values of the statistical moments. Beginning from the samples TZ2 and TZ3 of *Transitional Zone*, the positive tail shows a sudden change in the gradient, hereafter referred to as dip, around the zero mean or at slightly positive values of z (z = 0–10 mm; compare **Figure 7**). This shape indicates the height at which the sediment coverage in the sample frame ends and the oyster shell coverage begins. For the samples of *Garland*, *Cluster I* and *Cluster II*, this dip becomes more and more pronounced simultaneous with a decreasing abundance. For the samples of *Patch I* and *II* and *Central Reef*, nearly the entire surface is covered with oyster shells and the proportion of sediment is too low for the dip to be recognizable.

The normalized vertical distributions of the porosity further illustrate differences between structural classes (**Figure 8**). For the structural classes with homogenous oyster coverage (**Figure 8**, top row), an increase in the gradient can be observed from *Central Reef* over *Transitional Zone, Cluster I* to *Cluster II*. The increasing gradient is in line with the increase in bulk porosities Φ_{bulk}, respectively (**Table 2**). For the *Cluster I* and *II* samples, a plateau around z/Z_{max} = 0.25 becomes visible for the porosity range Φ = ∼0.25–0.75. The *Patch I* and *II* samples exhibit similar moderate courses as *Central Reef*, while the *Garland* samples displays a plateau like the *Cluster I* and *II* samples around z/Z_{max} = 0.15 for the porosity range Φ = ∼0.05–0.50. The *Central Reef* samples nearly collapse on a single line, while all other samples exhibit deviations within the respective structural class. Largest deviations can be found for the *Garland* and *Cluster II* samples. It is striking that deviations within the *Patch I* and *Garland* samples are mostly noticeable at Φ > 0.5. At low porosity values, the samples show similar relationships between porosity and z/Z_{max}.

The plateau visible in the vertical porosity distribution illustrates the boundary between sediment coverage and oyster shell coverage similar to the dip in the PDFs. For all samples, variations in the sediment coverage occur in the bottom 15–25% of the surface level elevations. At higher z/Z_{max}, the porosity depends on the density of the oyster shells. For the structural classes with low abundance, as *Cluster I, Cluster II,* and *Garland*, porosity increases rapidly as few oyster shells protrude from the sediment. With increasing abundance, the slope of the porosity distribution becomes more moderate, as more oyster shells evenly distributed are present in the total volume. For the structural classes with low abundances, especially *Cluster I, Cluster II,* and *Garland*, deviations within samples increase at high porosities (Φ > 0.5), which is in line with the deviations of the statistical moments within the structural classes (**Table 3**).

Orientation and Clustering

The analysis of the dorso-ventral orientations of the individual oyster shells (**Figure 9**) reveals anisotropic behavior. Although all rose diagrams in **Figure 9** are characterized by scatter, a major direction ϕ_{Shells} can be determined. The latter is defined as the orientation of the bin (or two adjacent bins) with the

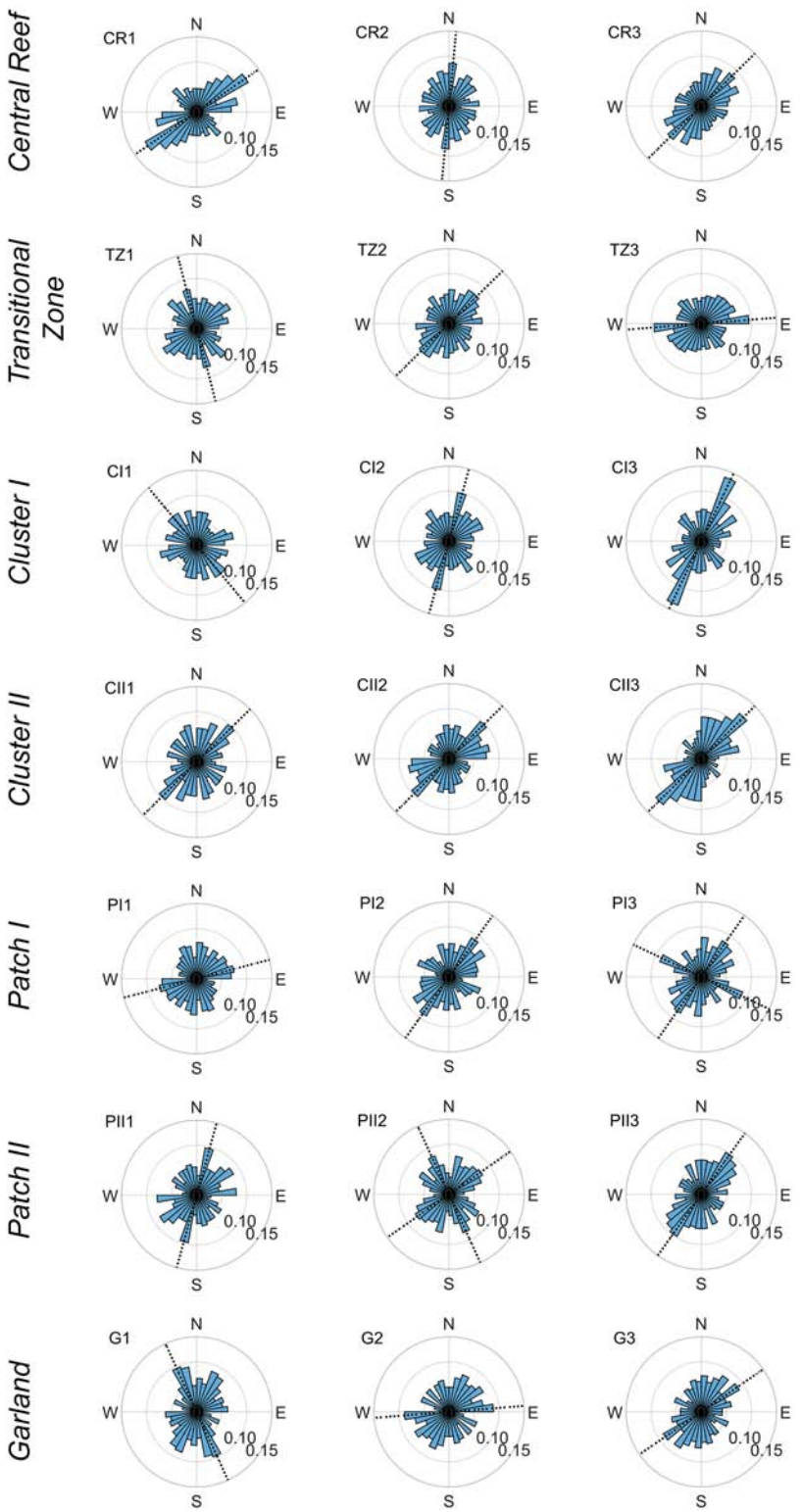


FIGURE 9 | Rose diagrams illustrating the dorso-ventral orientations of oyster shells and their respective frequency of the 21 samples sorted by proposed structural classes. The length of the bins represents the number of oysters oriented in that direction normalized by the total number of oyster shells in the sample. Each bin covers a range of 10°. The samples are mirrored along the north-south axis for illustration purposes. Dashed lines show the major orientation ϕ_{Shells} [°].

highest frequency of oyster shell orientations (dashed lines in **Figure 9** and **Table 2**). In two cases PI3 and PII2, two major orientations can be identified. The extent to which the bin of the major orientation is pronounced varies between samples. However, little differences can be identified between the structural classes. Still, a clear anisotropic characteristic of the dorso-ventral orientations across all structural classes can be confirmed. The major orientations of *Central Reef*, *Transitional Zone* as well as *Cluster I* and *Cluster II* samples are oriented from northeast to southwest with varying degrees, with exception of TZ1. For samples of *Garland*, *Patch I,* and *Patch II*, no common geographical orientation can be assigned.

The normalized 2D-SSFs (**Figure 10**) reveal both individual oyster shells and oyster clusters as significant roughness elements and emphasize the anisotropy of the sample surfaces. The shown 2D-SSFs were normalized by the respective variance $2\sigma_z{}^2$ and evaluated for maximum spatial lags l_x and l_y of $\pm$200 mm. High spatial correlations can be observed at small spatial lags characterizing individual oyster shells, while the spatial correlation decreases with increasing spatial lags. The samples CI1, CI3, and G2 were excluded from the analysis, as the reduced surface areas (cp. subsection "Data Collection and Processing") would only allow investigation for small spatial lags. Next, a threshold level was defined differentiating between high and low correlation to investigate roughness length scales based on the shown correlation functions (Aberle and Nikora, 2006; Aberle et al., 2010). For this purpose, possible characteristic roughness length scales were assumed that correspond either to the mean widths w_{mean} of the oyster shells or to the diameter of agglomerated clusters. In order to relate the 2D-SSFs to the width of the oysters, the blue circles plotted in **Figure 10** represent areas A_{shells} whose radii are equal to w_{mean}. As *Central Reef* is characterized by a homogeneous oyster distribution and both PDFs and porosity distributions reveal uniform trends, no clustering is expected. It is therefore supposed that the shells are the relevant roughness length scale in these samples. Hence, A_{shells} of the *Central Reef* samples are used to approximate a threshold level. $D_{G2}(l_x,l_y)/2\sigma_z{}^2 \leq 0.7$ proved to be in line with A_{shells} for all three samples (red lines in **Figure 10**), which is then applied to all samples.

The areas encircled by the threshold level have circular or elliptical shapes visualizing the area of significant correlation A_{corr}. The size and orientation of A_{corr} reveal roughness length scales and anisotropic behavior (compare **Table 2**). For the *Transitional Zone* samples, A_{corr} has similar extensions as A_{shells} indicating that the shells are the significant roughness length scale in accordance with *Central Reef*. Hence, oyster shells are confirmed as significant roughness elements. For the *Cluster I* and *II* samples, A_{corr} is two to four times larger as A_{shells}. Hence, the shells do not represent the significant length scale, but the individual cluster, as larger agglomerations, can be confirmed as roughness elements for the classes *Cluster I* and *II*. The sample CII3 is an exception as A_{corr} has similar extends as A_{shells} indicating that the oyster shells are the significant roughness elements. The size of A_{corr} within the samples of a structural class as well as the size of the individual cluster within every sample section are highly variable (compare **Figure 5**). Hence, no definite cluster size can be determined. For the *Patch I* and *II* as well as *Garland* samples, A_{corr} is slightly larger than A_{shells} but still in the same order of magnitude. The shells can be confirmed as significant roughness element for these structural classes. For all samples, A_{corr} has elliptical shapes with corresponding orientations ϕ_{2DSSF} of the mean axis. Comparing the orientations ϕ_{2DSSF} with the mean orientation of the oyster shells ϕ_{Shells} reveals deviations of $\pm$45°. However, similar geographical orientations are present further confirming the anisotropy of individuals' orientation across structural classes.

Structural Classification

In sub-section "Proposed Structural Classification," a proposed structural classification, using seven classes, was proposed, based on visual impressions and derived criteria during field visits. Through the statistical analysis of DEMs, differences between the structural classes have been elaborated. The higher statistical moments as well as the vertical porosity distribution reveal differences between them. The statistical parameters of the individual samples of *Central Reef* and *Transitional Zone* are overlapping. However, the averaged statistical parameters (**Table 3**) reveal distinctions between the two classes. Further, the higher frequency of sediment flats for *Transitional Zone* compared to *Central Reef* (cf. **Table 1**) justify to keep the distinct classes. Between *Cluster I* and *II*, no clear distinctions could be identified in the statistical analysis. However, the abundance as well as the vertical porosity distribution reveal differences. The statistical analysis of *Patch I* and *II* also reveals similar results. However, the differences in shape justifies keeping the respective structural classes even though the topographical roughness within the samples is the same. The *Garland* samples are distinctly different from the *Patch* classes despite the common enclosed shape. Further, within the samples strong deviations exist in the statistical analysis. The *Garland* partially resembles the *Transitional Zone* (G2) and partially *Cluster I* with clustering tendencies (G1 and G3). However, the enclosed shapes and its directionality define it as a structural class. The analysis of the 2D-SSFs demonstrates different roughness elements. While for the *Patch I*, *Patch II*, *Central Reef*, *Transitional Zone,* and *Garland* class the individual oyster shells are the most significant roughness element, for the *Cluster I* and *II* classes the clusters are the predominant roughness elements. Further, anisotropic directionality of all structure classes has been found; and it is hypothesized that this has important implications for associated hydraulic processes, sediment transport and distribution of larvae. Hence, the proposed structural classification is confirmed based on the statistical analysis in this work.

Validation

To ensure validity beyond the study site *Kaiserbalje*, three samples were recorded at the oyster reef *Nordland* (Mean Coordinates: 53.6424960° N, 008.9411970° E) located south of the island Juist, Germany. Three samples were collected, one each for *Central Reef*, *Transitional Zone,* and *Cluster II*. The PDFs (**Figure 11**) and the corresponding statistical parameters (**Table 2**) reveal high agreement with the respective structural class for the *Central Reef* and the *Transitional Zone* sample.

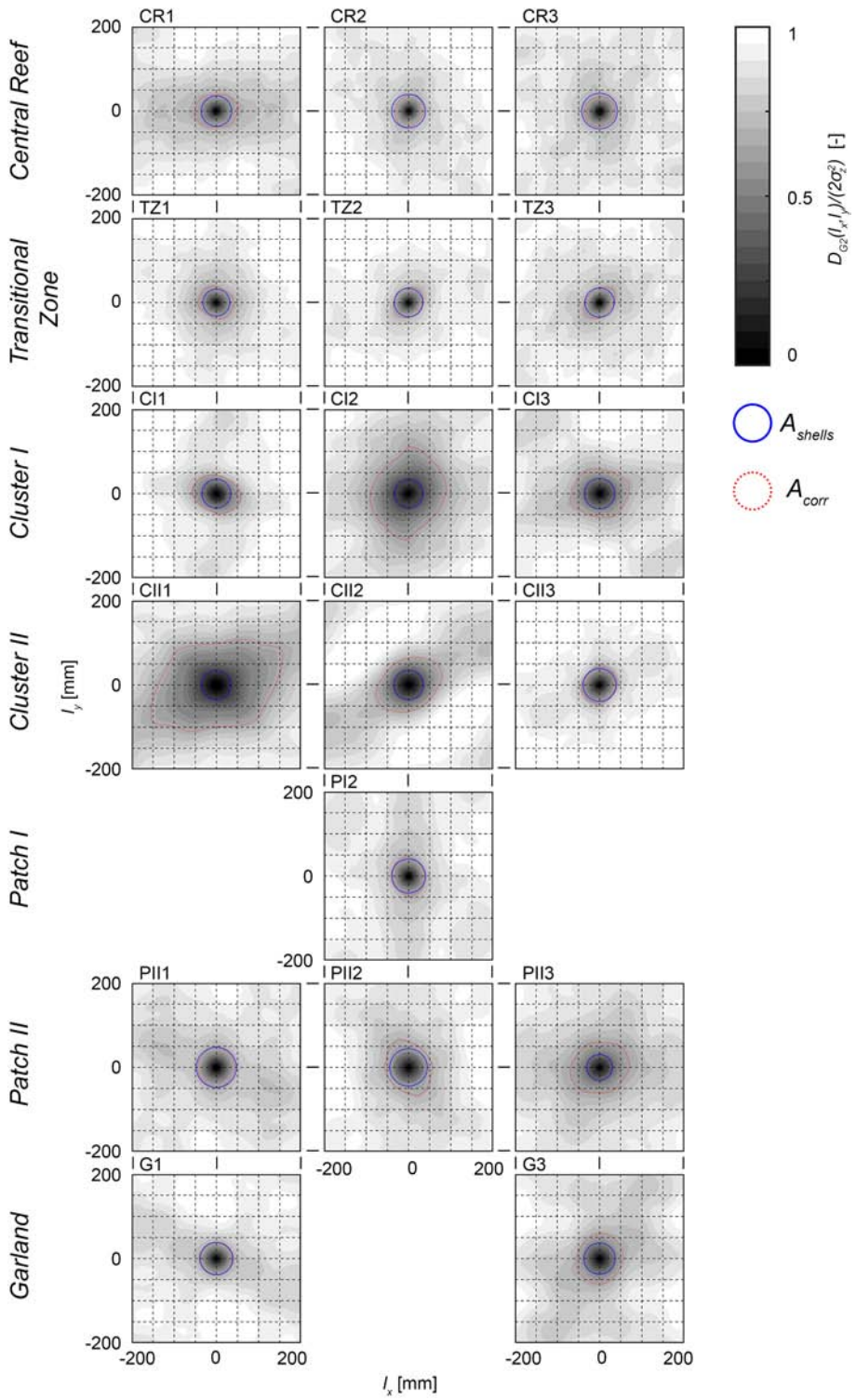


FIGURE 10 | Visualizations of the 2D second-order structure functions (2D-SSFs) for each sample surface normalized by the respective variances $D_{G2}(l_x,l_y)/2\sigma_z^2$. The *x*- and *y*-axis show the spatial lags l_x and l_y [mm]. The gray scale reflects the normalized 2D-SSF values [-], where dark areas indicate high levels of correlation approaching $D_{G2}(l_x,l_y)/2\sigma_z^2 = 0$. Blue circles represent the area A_{shells} whose radii are equal to the mean width w_{mean} of the oyster shells; Red dashed lines illustrate the area of significant correlations A_{corr} which is $D_{G2}(l_x,l_y)/2\sigma_z^2 \leq 0.7$. The sub-figures are sorted by proposed structural classes. PI1, PI3, and G2 are not evaluated.

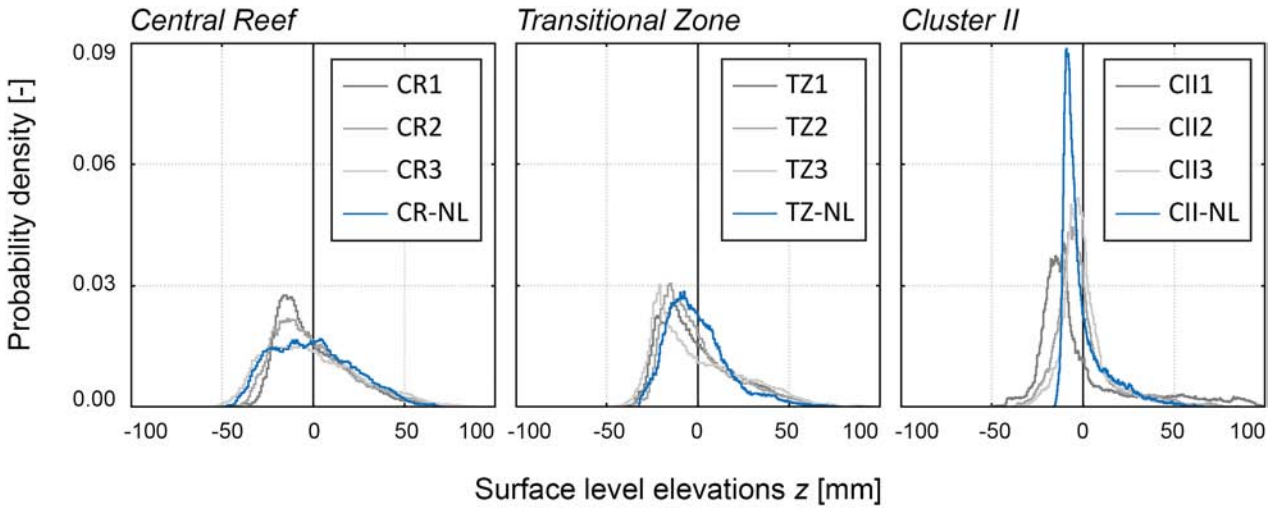


FIGURE 11 | Histograms based on surface level elevation *z* [mm] illustrating the PDFs [-] of the samples of *Central Reef, Transitional Zone*, and *Cluster II* including the validation samples recorded at the oyster *Nordland*. The PDFs are centered around the zero mean. The gray colors indicate the individual samples of *Kaiserbalje* as presented in **Figure 5** and the blue color indicates the sample of *Nordland*, e.g., dark gray: CR1, medium gray: CR2, light gray: CR3, blue: CR-NL, etc.

The *Cluster II* sample has a narrower shape and higher peak value of 0.09. Further, the total roughness height k_t, is smaller and the abundance of 50 inds./m^2 is approx. half of the *Cluster II* samples from *Kaiserbalje*. It is assumed that the structure is relatively young and oysters have not yet fully matured. This would explain why the total roughness k_t and the abundance are lower than of the *Cluster II* samples. However, the *Nordland Cluster II* sample does not reveal contrary trends to the proposed structural classification. Therefore, is it assumed that the structural classification is valid at least in a regional context of the central Wadden Sea, extending beyond the oyster reef *Kaiserbalje*. As nutrition availability and temperature ranges may affect oyster ecology, no conclusion as to a larger generality of the findings can be offered yet.

DISCUSSION

Separation of Oyster Roughness and Oyster as Habitat Defining Species

The aim of this work was to investigate the species-related geometrical roughness scale without considering the individual effects of the bed form caused by the overarching morphology. Hence, in the data processing, the species-related roughness scale was isolated, which allowed to statistically analyze the surfaces with the shown methods without influences of the superordinate morphology. However, when considering the entire reef, the morphology is characterized by strong three-dimensional reliefs (Folmer et al., 2017; Markert, 2020) that strongly influence the local hydrodynamic conditions (Frey et al., 1987; Moulin et al., 2007). Hence, bed roughness effects caused by the oysters are superimposed with the effect that bedform-induced roughness has on wave and current transformation processes. An isolated consideration and analysis of the effects enables a later superposition. Future studies will have to investigate the mutual effect of species- and bedform-induced roughness on the hydrodynamics.

Due to the resolution of the DEM with a grid size of 2 mm, micro-topographical changes were filtered from the analyzed data. Hence, one limitation of this study are the micro-morphological variations of the individual oysters especially of the saw-toothed shell margins sculpting the individuals (**Figure 1**). Influences of the micro-roughness scale on the hydraulic roughness development could be addressed in future research. Micro-computed tomography (Micro-CT) investigations of singular shells could be applied to resolve surfaces up to several µm (Chatzinikolaou et al., 2021; Keklikoglou et al., 2021). Despite this limitation, it is assumed that the provided topographical parameters represent the key factors that influence the hydraulic roughness.

The presence of *M. edulis* is not considered explicitly in the analysis despite high abundance and importance in studies focusing on population dynamics (Wehrmann, 2006; Markert et al., 2010; Reise et al., 2017; Markert, 2020). However, in regards to the bed roughness, *M. edulis* are only of subordinate importance due to the smaller size of mature individuals (∼40 mm) compared to *M. gigas* and the tendency of *M. edulis* to occupy the interspace between oyster shells (Buschbaum et al., 2016). Therefore, it is reasonable to focus on oyster individuals as predominant habitat-defining species in particular. However, as *M. edulis* and other species are also present in the sample surfaces, they are part of the analyzed surface elevation data and represented in the statistical parameters.

Structural Classification

In contrast to other classifications of oyster reefs that differentiate reef types, the presented work suggests an intra-reef classification. As a study site, the oyster reef *Kaiserbalje* was selected, which has

been categorized by Markert (2020) as a complex reef with a high oyster density. Due to the natural heterogeneity of oyster reefs, it is assumed that the complex reef covers all significant surface types possible. The structural classes are similar to the temporal growth stages in the creation of oyster reefs reported by this author. The differences in position and elevation further confirm the similarity between structural classes and growth stages. *Transitional Zone* and *Central Reef* are located toward the center of the reef with elevations corresponding to the aerial exposure times during a tidal cycle of 50–60%, which is the vertical growth threshold reported by Rodriguez et al. (2014) and Ridge et al. (2017). Further, *Cluster*, *Patches,* and *Garlands* are located at the margins of the reef at lower elevations, where the oyster coverage keeps expanding horizontally and vertically. Hence, the temporal sequence of growth stages reported by Markert (2020) also describes a spatial classification in the structural classes confirmed in this study.

Application of the structural classification and the respective parameters to drone or satellite images could considerably increase the accuracy in the description of oyster reefs. In previous investigations, oyster reefs have been viewed as surfaces with homogeneous distributions (Smaal et al., 2009) since no intra-reef classifications had been recorded. However, the results of this study illustrate that averaged parameters are insufficient to describe the highly complex and heterogenic surfaces of oyster reefs. By applying the intra-reef classification, areal proportions of the classes in the total reef surface and their impact on the overall roughness could be evaluated and monitored over several years. When linked to representative biological parameters such as abundance, total wet weight and length-frequencies distributions, the classification allows for a more accurate estimation of the population dynamics on the scale of oyster reefs or the whole Wadden Sea.

Roughness Parameters

The topographical parameters for oyster reef surfaces reported in this work, including statistical moments, porosity distributions, abundances and measures of directionality, provide a detailed description that did not exist before. Further, the reported parameters were chosen as they have been identified to exert an influence on the surrounding hydrodynamics in environmental hydraulics (Nikora et al., 1998; Aberle and Nikora, 2006; Coleman et al., 2011; Flack and Schultz, 2014; Navaratnam et al., 2018) and mechanical engineering (Flack and Schultz, 2010; Chung et al., 2021). Hence, a comprehensive set of topographical parameters has been provided adding to the call for understanding of roughness effects of this relatively new biogenic habitat on the intertidal flats of the central Wadden Sea (Markert et al., 2010; Borsje et al., 2011; Walles et al., 2015b; Folmer et al., 2017) and worldwide (Morris et al., 2021).

The topographical parameters can partially be linked to results of former studies on the roughness of oyster reefs. Manis et al. (2015) provide topographical information of oyster reefs in form of roughness elements that can be linked to the hydraulic roughness. The number of roughness elements (460 elements/m^2) for a *C. virginica* reef after 1 year of deployment compares to the abundance of *Central Reef* (393 $\pm$ 50 inds./m^2), *Transitional Zone* (466 $\pm$ 56 inds./m^2) or *Patch I* (408 $\pm$ 133 inds./m^2) on *Kaiserbalje*. The heights of the individual roughness elements of 150 $\pm$ 16 mm are larger than the total roughness heights k_t = 104 $\pm$ 11 mm of *Central Reef* by a factor of 1.5. However, k_t is not equal to the length of the shells but relates to the parts of the shells protruding from the sediment or reef structure, which could explain the differences. Further, the different oyster species *C. virginica* with other shell sizes could also contribute to the differences. Parameters describing the shape and extend of the surfaces as well as orientations or clustering of the individual oysters to assign a structural class are not provided by Manis et al. (2015). Despite these limitations, the described parameters are in the same order of magnitude compared to this study, which is why it is likely that similar wave attenuation effects can be expected for surfaces of the structural classes *Central Reef*, *Transitional Zone,* and *Patch I*. Kitsikoudis et al. (2020) similarly report numbers of roughness elements in *C. virginica* reefs with 121 $\pm$ 25 elements/m^2, which correspond to abundances of *Cluster II* (137 $\pm$ 5 inds./m^2). However, *Cluster II* is characterized by clusters as significant roughness elements with open sediment spaces in between, which is not reported for the *C. virginica* reef samples. As no clustering is reported by Kitsikoudis et al. (2020) it cannot be assumed that similar frictional resistance effects will occur. For the structural classes with homogeneous distribution of the oyster shells *Central Reef* and *Transitional Zone*, the abundance is three to four times higher. Hence, similarities regarding the impacts on the surrounding hydrodynamics with these structural classes are also not justifiable. Further, the reported average length of 82 $\pm$ 25 mm for the *C. virginica* reefs are smaller than the total roughness heights in this work. It is hence assumed that while similarities exist, additional structural classes for *C. virginica* reefs are possible. Margiotta et al. (2016) and Colden et al. (2017) used the rugosity to identify habitat composition and population trajectories for which a singular parameter serves the purpose. However, the one-dimensional, singular parameter neglects many three-dimensional effects that have been identified in this work to affect the hydraulic roughness. Further, the accuracy of the chain method is limited to the precision of the chain and cannot be recreated digitally. Hence, the results are not comparable to the topographical parameters reported in this study.

Knowledge of the topographical parameters alone does not allow for predictions of the impacts on the surrounding flow. Even though it is known that the aforementioned topographical parameters pose an influence, thus far no method to determine the hydraulic roughness directly from topographical parameters exists (Chung et al., 2021). To define the impacts of the surface on the hydrodynamics, systematic and comprehensive laboratory investigations are necessary. The reported topographical parameters can be used to develop simplified and scaled surrogate models that depict many important parameters influencing the hydraulic roughness. With these surrogate models, a wide range of hydrodynamic parameters can be evaluated in a controlled laboratory environment. Hence, results of field studies (Whitman and Reidenbach, 2012; Reidenbach et al., 2013; Styles, 2015;

Kitsikoudis et al., 2020), which are limited to the range of hydrodynamic conditions during the period of the field study, can be enhanced by a wider range of possible combinations. Like this, topographical parameters can be linked to the bed roughness to derive parameters such as the hydraulic roughness length z_0 (Lefebvre et al., 2010) or the wave friction factor f_w (Mirfenderesk and Young, 2003; Thompson et al., 2012; Yao et al., 2020).

Link to Population Dynamics

The statistical parameters reported in this study can partially be related to parameters of biological sampling used for population dynamics despite different methods of determination (Wehrmann, 2006; Brandt et al., 2008; Markert et al., 2010; Reise et al., 2017; Markert, 2020). The abundances in this study are lower than typical abundances of studies describing population dynamics, e.g., Reise et al. (2017) or Markert (2020) reaching up to 1500 inds./m^2 when live and dead individuals are considered (including all shells). This discrepancy is due to different methods of determination and different research objectives. While in the aforementioned studies all individuals up to a sediment depth of 10–15 cm are considered to identify changes in the population dynamics (e.g., biomass, length frequency distribution), in this study only individuals that protrude from the sediment cover are considered as they are relevant roughness elements. Further, small individuals (<25 mm) are not considered as their influence on the overall roughness is negligible. In addition to the visual determination from the orthomosaics (compare subsection "Abundance and Orientation"), abundances were determined by the same sampling method as in the aforementioned studies. A comparison of both methods reveals that the abundances from visual determination is lower by a factor of 2.8 $\pm$ 0.9, which can serve as a correction factor for study comparison. The total roughness height k_t and the form of the PDFs can be linked to shell length. However, as oyster individuals are typically partially embedded in the sediment, the distributions of surface level elevations do not represent shell length but the length of the protruding part of the oyster shells (compare subsection "Roughness Parameters"). Hence, k_t is smaller than maximum shell length.

Interactions Between Oyster Reef and Hydrodynamics

The analysis of the directionality reveals anisotropy of individuals' orientation for all structural classes. This observation is in line with previous investigations on shell alignment in oyster reefs (Grinnell, 1974; Frey et al., 1987; Harzhauser et al., 2015) and mussel beds (Nagle, 1967; Sanderson and Donovan, 1974; García-March et al., 2007), which further link orientations to tidal flows and wave action. Typically, the dorso-ventral axis' are oriented orthogonal to the mean flow direction or parallel to the wave crest orientation (Nagle, 1967; Grinnell, 1974). However, to correlate hydrodynamics and directionality of the oyster reef either *in situ* measurements or high-resolution numerical simulations of sea state conditions would be required that were not available at the time of this study. As hydrodynamics are strongly influenced by the reef morphology and less dependent on the large-scale hydrodynamic processes (Frey et al., 1987; Moulin et al., 2007), currently available numerical simulations [e.g., results documented through EasyGSH (Hagen et al., 2020) with grid size of 500 m] do not resolve the local morphology and response in hydrodynamics well enough. Still, the anisotropic orientations of oyster shells and cluster suggest impacts of the hydrodynamic forces on oyster directionality.

Several numerical studies of oyster reefs on macro- and meso-scale have focused mostly on larval dispersal patterns distribution (e.g., Kjelland et al., 2015; Arnold et al., 2017; Dye et al., 2021) while the influence of the rough surfaces on the surrounding hydrodynamics have not been subject of investigation. Here, the structural classification provided and the respective topographical roughness parameters can be used as input parameters for future investigations addressing the impact on the hydrodynamic and sediment transport similar to investigations by van Leeuwen et al. (2010) on mussel beds or by Ashall et al. (2016) on salt marshes.

The *Cluster I* and *II* samples are most exposed to hydrodynamic forces due to their positions at the margin of the reef and feature lower abundances than the other, more sheltered structural classes. This observation is in line with findings of a field study by Vozzo et al. (2021), who reported a negative correlation between abundances and surface area of oyster reefs with increasing wave exposure near Sydney, Australia. However, the creation process reported by Markert (2020) shows that the oyster clusters are able to form and coalesce into patches despite the hydrodynamic forces at the margins of the reef. A comparison of oyster reef outlines over several years with associated hydrodynamic parameters could lead to a threshold of bed shear stress that oyster reefs can withstand and expand upon.

CONCLUSION

The main objective of the present work was to record and document topographical roughness parameters of *Magallana gigas* oyster reef surfaces in the central Wadden Sea. A set of parameters that are known to influence the hydraulic bed roughness have been provided including roughness heights, statistical moments of the surface level elevations, abundance as well as measures of the directionality and clustering. Hereby, a proposed structural classification in seven classes has been tested and verified beyond the study site. It has been shown that the classes are characterized by distinct roughness properties and locations within the reef surface. Hence, by considering the classification, the complexity of the reef surface can be accounted for. The set of roughness parameters enhance the knowledge of oyster reef surfaces that influence the surrounding hydrodynamics and vice versa. Further, a methodology has been elaborated that utilizes structure-from-motion photogrammetry to derive detailed high-resolution digital elevation models under the adverse conditions in the central Wadden Sea. It can be applied to other reefs and allows comparison of hydrodynamic roughness effects across locations. The findings, hence, may pave the way for accurate determination of wave and tidal current

attenuation as well as population dynamics with implications for the sediment transport and effects on larvae distributions.

DATA AVAILABILITY STATEMENT

The raw data supporting the conclusions of this article will be made available by the authors, without undue reservation.

AUTHOR CONTRIBUTIONS

JH, LB, KP, TS, MP, AW, and NG contributed to the conceptualization. JH, LB, KP, JA, AW, and NG developed the methodology. JH, KP, TH, and AE carried out the investigation in the field studies. JH, LB, AE, and JA developed the software and conducted the formal analysis. JH and LB validated and curated the data. JH wrote the first draft of the manuscript and prepared visualizations. MW, AW, and NG provided supervision. NG, AW, TS, and MP organized funding acquisition. NG was responsible for the project administration. All authors contributed to manuscript revision, read and approved the submitted version.

FUNDING

This project "BIVA-WATT" on which this work is based was funded by the Federal Ministry of Education and Research of Germany (BMBF) under the funding code 03KIS127.

ACKNOWLEDGMENTS

We would like to thank the captain and the crew of the *FK Senckenberg* for providing the logistics needed during the field studies. Further, we want to thank Torsten Janßen (Senckenberg am Meer) for his organizational work in the background and assistance during field work. The Lower Saxon Wadden Sea National Park Authority (Wilhelmshaven) is thanked for permits and cooperation.

REFERENCES

Aberle, J. (2007). Measurements of armour layer roughness geometry function and porosity. *Acta Geophys.* 55, 23–32. doi: 10.247c:\yandy\yandytex\tex.bat+latexfevo-09-799637.tex8/s11600-006-0036-5

Aberle, J., and Nikora, V. (2006). Statistical properties of armored gravel bed surfaces. *Water Resour. Res.* 42:W11414. doi: 10.1029/2005WR004674

Aberle, J., Koll, K., and Dittrich, A. (2008). Form induced stresses over rough gravel-beds. *Acta Geophys.* 56, 584–600. doi: 10.2478/s11600-008-0018-x

Aberle, J., Nikora, V., Henning, M., Ettmer, B., and Hentschel, B. (2010). Statistical characterization of bed roughness due to bed forms: a field study in the Elbe River at Aken, Germany. *Water Resour. Res.* 46:W03521. doi: 10.1029/2008WR007406

Arakawa, K. Y. (1990). Natural spat collecting in the Pacific oyster *Crassostrea gigas* (Thunberg). *Mar. Behav. Physiol.* 17, 95–128. doi: 10.1080/10236249009378760

Arnold, W. S., Meyers, S. D., Geiger, S. P., Luther, M. E., Narváez, D., Frischer, M. E., et al. (2017). Applying a coupled biophysical model to predict larval dispersal and source/sink relationships in a depleted metapopulation of the eastern oyster *Crassostrea virginica*. *J. Shellfish Res.* 36, 101–118. doi: 10.2983/036.036.0112

Ashall, L. M., Mulligan, R. P., van Proosdij, D., and Poirier, E. (2016). Application and validation of a three-dimensional hydrodynamic model of a macrotidal salt marsh. *Coast. Eng.* 114, 35–46. doi: 10.1016/j.coastaleng.2016.04.005

Bendat, J. S., and Piersol, A. G. (2010). *Random Data: Analysis and Measurement Procedures*, Fourth Edn. Hoboken: Wiley.

Bertin, S., and Friedrich, H. (2014). Measurement of gravel-bed topography: evaluation study applying statistical roughness analysis. *J. Hydraul. Eng.* 140, 269–279. doi: 10.1061/(ASCE)HY.1943-7900.0000823

Borsje, B. W., van Wesenbeeck, B. K., Dekker, F., Paalvast, P., Bouma, T. J., van Katwijk, M. M., et al. (2011). How ecological engineering can serve in coastal protection. *Ecol. Eng.* 37, 113–122. doi: 10.1016/j.ecoleng.2010.11.027

Bouma, T. J., van Belzen, J., Balke, T., Zhu, Z., Airoldi, L., Blight, A. J., et al. (2014). Identifying knowledge gaps hampering application of intertidal habitats in coastal protection: opportunities & steps to take. *Coast. Eng.* 7, 147–157. doi: 10.1016/j.coastaleng.2013.11.014

Brandt, G., Wehrmann, A., and Wirtz, K. W. (2008). Rapid invasion of *Crassostrea gigas* into the German Wadden Sea dominated by larval supply. *J. Sea Res.* 59, 279–296. doi: 10.1016/j.seares.2008.03.004

Bundesamt für Seeschifffahrt und Hydrographie [BSH] (2020). *Gezeitenkalender – Hoch- und Niedrigwasserzeiten für die Deutsche Bucht und deren Flussgebiete*. Hamburg: Bundesamt für Seeschifffahrt und Hydrographie.

Bungenstock, F., Hertweck, G., Hochstein, M. L., and Wehrmann, A. (2021). Distribution pattern and controls of biosedimentary facies in backbarrier tidal flats of the central Wadden Sea (North Sea). *ZDGG J. Appl. Reg. Geol.* 172, 409–428. doi: 10.1127/zdgg/2021/0248

Burkett, J. R., Hight, L. M., Kenny, P., and Wilker, J. J. (2010). Oysters produce an organic-inorganic adhesive for intertidal reef construction. *J. Am. Chem. Soc.* 132, 12531–12533. doi: 10.1021/ja104996y

Buschbaum, C., Cornelius, A., and Goedknegt, M. A. (2016). Deeply hidden inside introduced biogenic structures – Pacific oyster reefs reduce detrimental barnacle overgrowth on native blue mussels. *J. Sea Res.* 117, 20–26. doi: 10.1016/j.seares.2016.09.002

Chatzinikolaou, E., Keklikoglou, K., and Grigoriou, P. (2021). Morphological properties of gastropod shells in a warmer and more acidic future ocean using 3D micro-computed tomography. *Front. Mar. Sci.* 8:645660. doi: 10.3389/fmars.2021.645660

Chowdhury, M. S. N., Walles, B., Sharifuzzaman, S. M., Shahadat Hossain, M., Ysebaert, T., and Smaal, A. C. (2019). Oyster breakwater reefs promote adjacent mudflat stability and salt marsh growth in a monsoon dominated subtropical coast. *Sci. Rep.* 9:8549. doi: 10.1038/s41598-019-44925-6

Chung, D., Hutchins, N., Schultz, M. P., and Flack, K. A. (2021). Predicting the drag of rough surfaces. *Annu. Rev. Fluid Mech.* 53, 439–471. doi: 10.1146/annurev-fluid-062520-115127

Clifford, N. J., Robert, A., and Richards, K. S. (1992). Estimation of flow resistance in gravel-bedded rivers: a physical explanation of the multiplier of roughness length. *Earth Surf. Process. Landforms* 17, 111–126. doi: 10.1002/esp.3290170202

Colden, A. M., Latour, R. J., and Lipcius, R. N. (2017). Reef height drives threshold dynamics of restored oyster reefs. *Mar. Ecol. Prog. Ser.* 582, 1–13. doi: 10.3354/meps12362

Coleman, S. E., Nikora, V. I., and Aberle, J. (2011). Interpretation of alluvial beds through bed-elevation distribution moments. *Water Resour. Res.* 47:W11505. doi: 10.1029/2011WR010672

Crameri, F. (2018). Geodynamic diagnostics, scientific visualisation and StagLab 3.0. *Geosci. Model Dev.* 11, 2541–2562. doi: 10.5194/gmd-11-2541-2018

Cullen, N. D., Verma, A. K., and Bourke, M. C. (2018). A comparison of structure from motion photogrammetry and the traversing micro-erosion meter for measuring erosion on shore platforms. *Earth Surf. Dynam.* 6, 1023–1039. doi: 10.5194/esurf-6-1023-2018

Diederich, S. (2005). *Invasion of Pacific oysters (Crassostrea gigas) in the Wadden Sea: Competitive Advantage Over Native Mussels*. Ph.D. Dissertation. Kiel: University Kiel.

Djuricic, A., Dorninger, P., Nothegger, C., Harzhauser, M., Székely, B., Rasztovits, S., et al. (2016). High-resolution 3D surface modeling of a fossil oyster reef. *Geosphere* 12, 1457–1477. doi: 10.1130/GES01282.1

Dye, B., Jose, F., Richard, J., Mortensen, J. B., and Milbrandt, E. C. (2021). An agent-based model accurately predicts larval dispersal and identifies restoration and monitoring priorities for eastern oyster (*Crassostrea virginica*) in a Southwest Florida estuary. *Restor. Ecol.* 30:e13487. doi: 10.1111/rec.13487

Ewers-Saucedo, C., Heuer, N., Moesges, Z., Ovenbeck, K., Schröter, N., and Brandis, D. (2020). First record of the Pacific oyster *Magallana gigas* (Thunberg, 1793) in the Baltic Sea proper. *Mar. Biodivers. Rec.* 13, 1–5. doi: 10.1186/s41200-020-00193-2

Flack, K. A., and Schultz, M. P. (2010). Review of hydraulic roughness scales in the fully rough regime. *J. Fluids Eng* 132:041203. doi: 10.1115/1.4001492

Flack, K. A., and Schultz, M. P. (2014). Roughness effects on wall-bounded turbulent flows. *Phys. Fluids* 26:101305. doi: 10.1063/1.4896280

Folmer, E. O., Drent, J., Troost, K., Büttger, H., Dankers, N., Jansen, J., et al. (2014). Large-scale spatial dynamics of intertidal mussel (*Mytilus edulis* L.) bed coverage in the German and Dutch Wadden Sea. *Ecosystems* 17, 550–566. doi: 10.1007/s10021-013-9742-4

Folmer, E., Büttger, H., Herlyn, M., Markert, A., Millat, G., Troost, K., et al. (2017). "Beds of blue mussels and Pacific oysters," in *Wadden Sea Quality Status Report 2017*, eds S. Kloepper, et al. (Wilhelmshaven: Common Wadden Sea Secretary).

Frey, R. W., Basan, P. B., and Smith, J. M. (1987). Rheotaxis and distribution of oysters and mussels, Georgia tidal creeks and salt marshes, U.S.A. *Palaeogeogr. Palaeoclimatol. Palaeoecol.* 61, 1–16. doi: 10.1016/0031-0182(87)90038-1

García-March, J. R., Pérez-Rojas, L., and García-Carrascosa, A. M. (2007). Influence of hydrodynamic forces on population structure of *Pinna nobilis* L., 1758 (Mollusca: Bivalvia): the critical combination of drag force, water depth, shell size and orientation. *J. Exp. Mar. Biol. Ecol.* 342, 202–212. doi: 10.1016/j.jembe.2006.09.007

Gosling, E. M. (2015). *Marine Bivalve Molluscs*, Second Edn. Chichester: Wiley-Blackwell.

Grabowski, J. H. (2004). Habitat complexity disrupts predator-prey interactions but not the trophic cascade on oyster reefs. *Ecology* 85, 995–1004. doi: 10.1890/03-0067

Grabowski, J. H., and Powers, S. P. (2004). Habitat complexity mitigates trophic transfer on oyster reefs. *Mar. Ecol. Prog. Ser.* 277, 291–295. doi: 10.3354/meps277291

Grinnell, R. S. (1974). Vertical orientation of shells on some florida oyster reefs. *J. Sediment. Res.* 44, 116–122. doi: 10.1306/74D72996-2B21-11D7-8648000102C1865D

Gutiérrez, J. L., Jones, C. G., Strayer, D. L., and Iribarne, O. O. (2003). Mollusks as ecosystem engineers: the role of shell production in aquatic habitats. *Oikos* 101, 79–90. doi: 10.1034/j.1600-0706.2003.12322.x

Hagen, R., Plüß, A., Freund, J., Ihde, R., Kösters, F., Schrage, N., et al. (2020). *Data From: EasyGSH-DB: Themengebiet - Hydrodynamik*. Karlsruhe: Bundesanstalt für Wasserbau. doi: 10.48437/02.2020.K2.7000.0003

Harzhauser, M., Djuricic, A., Mandic, O., Zuschin, M., Dorninger, P., Nothegger, C., et al. (2015). Disentangling the history of complex multi-phased shell beds based on the analysis of 3D point cloud data. *Palaeogeogr. Palaeoclimatol. Palaeoecol.* 437, 165–180. doi: 10.1016/j.palaeo.2015.07.038

Hayward, P. J., and Ryland, J S (eds.) (2017). *Handbook of the Marine Fauna of North-West Europe*, Second Edn. Oxford: Oxford University Press.

Hossain, M. S., Rothuis, A., Chowdhury, S. R., Smaal, A. C., Ysebaert, T., Sharifuzzaman, S. M., et al. (2013). Oyster aquaculture for coastal defense with food production in Bangladesh. *Aquacult. Asia* 18, 15–24.

James, M. R., and Robson, S. (2014). Mitigating systematic error in topographic models derived from UAV and ground-based image networks. *Earth Surf. Process. Landforms* 39, 1413–1420. doi: 10.1002/esp.3609

James, M. R., Robson, S., d'Oleire-Oltmanns, S., and Niethammer, U. (2017). Optimising UAV topographic surveys processed with structure-from-motion: ground control quality, quantity and bundle adjustment. *Geomorphology* 280, 51–66. doi: 10.1016/j.geomorph.2016.11.021

Jelly, T. O., and Busse, A. (2018). Reynolds and dispersive shear stress contributions above highly skewed roughness. *J. Fluid Mech.* 852, 710–724. doi: 10.1017/jfm.2018.541

Jones, C. G., Lawton, J. H., and Shachak, M. (1994). Organisms as ecosystem engineers. *Oikos* 69, 373–386. doi: 10.2307/3545850

Jones, C. G., Lawton, J. H., and Shachak, M. (1997). Positive and negative effects of organisms as physical ecosystem engineers. *Ecology* 78, 1946–1957. doi: 10.2307/2265935

Keklikoglou, K., Arvanitidis, C., Chatzigeorgiou, G., Chatzinikolaou, E., Karagiannidis, E., Koletsa, T., et al. (2021). Micro-CT for biological and biomedical studies: a comparison of imaging techniques. *J. Imaging* 7:172. doi: 10.3390/jimaging7090172

Kitsikoudis, V., Kibler, K. M., and Walters, L. J. (2020). In-situ measurements of turbulent flow over intertidal natural and degraded oyster reefs in an estuarine lagoon. *Ecol. Eng.* 143:105688. doi: 10.1016/j.ecoleng.2019.105688

Kjelland, M. E., Piercy, C. D., Lackey, T., and Swannack, T. M. (2015). An integrated modeling approach for elucidating the effects of different management strategies on Chesapeake Bay oyster metapopulation dynamics. *Ecol. Model.* 308, 45–62. doi: 10.1016/j.ecolmodel.2015.03.012

Krämer, K., and Winter, C. (2016). Predicted ripple dimensions in relation to the precision of in situ measurements in the southern North Sea. *Ocean Sci.* 12, 1221–1235. doi: 10.5194/os-12-1221-2016

Le Goïc, G., Bigerelle, M., Samper, S., Favrelière, H., and Pillet, M. (2015). Multiscale roughness analysis of engineering surfaces: a comparison of methods for the investigation of functional correlations. *Mech. Syst. Signal Process.* 66-67, 437–457. doi: 10.1016/j.ymssp.2015.05.029

Lefebvre, A., Thompson, C., and Amos, C. L. (2010). Influence of *Zostera marina* canopies on unidirectional flow, hydraulic roughness and sediment movement. *Cont. Shelf Res.* 30, 1783–1794. doi: 10.1016/j.csr.2010.08.006

Leon, J. X., Roelfsema, C. M., Saunders, M. I., and Phinn, S. R. (2015). Measuring coral reef terrain roughness using 'Structure-from-Motion' close-range photogrammetry. *Geomorphology* 242, 21–28. doi: 10.1016/j.geomorph.2015.01.030

Lipcius, R. N., Burke, R. P., McCulloch, D. N., Schreiber, S. J., Schulte, D. M., Seitz, R. D., et al. (2015). Overcoming restoration paradigms: value of the historical record and metapopulation dynamics in native oyster restoration. *Front. Mar. Sci.* 2:65. doi: 10.3389/fmars.2015.00065

Liu, G., Wang, J., Dong, P., Chen, Y., and Liu, Z. (2018). Estimating individual tree height and diameter at breast height (DBH) from terrestrial laser scanning (TLS) data at plot level. *Forests* 9:398. doi: 10.3390/f9070398

Manis, J. E., Garvis, S. K., Jachec, S. M., and Walters, L. J. (2015). Wave attenuation experiments over living shorelines over time: a wave tank study to assess recreational boating pressures. *J. Coast. Conserv.* 19, 1–11. doi: 10.1007/s11852-014-0349-5

Mann, R., Southworth, M., Harding, J. M., and Wesson, J. A. (2009). Population studies of the native Eastern oyster, *Crassostrea virginica*, (Gmelin, 1791) in the James River, Virginia, USA. *J. Shellfish Res.* 28, 193–220. doi: 10.2983/035.028.0203

Margiotta, A. M., Shervette, V. R., Hadley, N. H., Plante, C. J., and Wilber, D. H. (2016). Species-specific responses of resident crabs to vertical habitat complexity on intertidal oyster reefs. *J. Exp. Mar. Biol. Ecol.* 477, 7–13. doi: 10.1016/j.jembe.2016.01.007

Markert, A. (2020). How dense is dense? Toward a harmonized approach to characterizing reefs of non-native Pacific oysters – with consideration of native mussels. *NB* 57, 7–52. doi: 10.3897/neobiota.57.49196

Markert, A., Esser, W., Frank, D., Wehrmann, A., and Exo, K.-M. (2013). Habitat change by the formation of alien *Crassostrea*-reefs in the Wadden Sea and its role as feeding sites for waterbirds. *Estuar. Coast. Shelf Sci.* 131, 41–51. doi: 10.1016/j.ecss.2013.08.003

Markert, A., Wehrmann, A., and Kröncke, I. (2010). Recently established *Crassostrea*-reefs versus native *Mytilus*-beds: differences in ecosystem engineering affects the macrofaunal communities (Wadden Sea of Lower Saxony, southern German Bight). *Biol. Invasions* 12, 15–32. doi: 10.1007/s10530-009-9425-4

Meyer, D. L., Townsend, E. C., and Thayer, G. W. (1997). Stabilization and Erosion Control Value of Oyster Cultch for Intertidal Marsh. *Restor. Ecol.* 5, 93–99. doi: 10.1046/j.1526-100X.1997.09710.x

Micheletti, N., Chandler, J. H., and Lane, S. N. (2015). Investigating the geomorphological potential of freely available and accessible structure-from-motion photogrammetry using a smartphone. *Earth Surf. Process. Landforms* 40, 473–486. doi: 10.1002/esp.3648

Miossec, L., Le Dueff, R.-M., and Goulletquer, P. (2009). Alien species alert: *Crassostrea gigas* (Pacific oyster). *ICES Cooperative Res.* 299:42.

Mirfenderesk, H., and Young, I. R. (2003). Direct measurements of the bottom friction factor beneath surface gravity waves. *Appl. Ocean Res.* 25, 269–287. doi: 10.1016/j.apor.2004.02.002

Morgan, J. A., Brogan, D. J., and Nelson, P. A. (2017). Application of Structure-from-Motion photogrammetry in laboratory flumes. *Geomorphology* 276, 125–143. doi: 10.1016/j.geomorph.2016.10.021

Morris, R. L., La Peyre, M. K., Webb, B. M., Marshall, D. A., Bilkovic, D. M., Cebrian, J., et al. (2021). Large-scale variation in wave attenuation of oyster reef living shorelines and the influence of inundation duration. *Ecol. Appl.* 31:e02382. doi: 10.1002/eap.2382

Moulin, F. Y., Guizien, K., Thouzeau, G., Chapalain, G., Mülleners, K., and Bourg, C. (2007). Impact of an invasive species, *Crepidula fornicata*, on the hydrodynamics and transport properties of the benthic boundary layer. *Aquat. Living Resour.* 20, 15–31. doi: 10.1051/alr:2007012

Musker, A. J. (1980). Universal roughness functions for naturally-occurring surfaces. *Trans. Can. Soc. Mech. Eng.* 6, 1–6. doi: 10.1139/tcsme-1980-0001

Nagle, J. S. (1967). Wave and current orientation of shells. *J. Sediment. Res.* 37, 1124–1138. doi: 10.1306/74D71848-2B21-11D7-8648000102C1865D

Nationalparkverwaltung Niedersächsisches Wattenmeer. (2021). *Shape File of Mussel Beds 2020*. Wilhelmshaven: Nationalparkverwaltung Niedersächsisches Wattenmeer.

Navaratnam, C. U., Aberle, J., Qin, J., and Henry, P.-Y. (2018). Influence of gravel-bed porosity and grain orientation on bulk flow resistance. *Water* 10:561. doi: 10.3390/w10050561

Nehls, G., Büttger, H., and Ruth, M. (2011). *Miesmuschelmonitoring und Miesmuschelmanagement im Nationalpark Schleswig-Holsteinisches Wattenmeer*. Husum: BioConsult SH.

Nehring, S. (2011). *NOBANIS - Invasive Alien Species Fact Sheet - Crassostrea gigas. From: Online Database of the European Network on Invasive Alien Species - NOBANIS*. Bonn: NOBANIS.

Nikora, V. I., Goring, D. G., and Biggs, B. J. F. (1998). On gravel-bed roughness characterization. *Water Resour. Res.* 34, 517–527. doi: 10.1029/97WR02886

Nikora, V., and Walsh, J. (2004). Water-worked gravel surfaces: high-order structure functions at the particle scale. *Water Resour. Res.* 40:W12601. doi: 10.1029/2004WR003346

Nikuradse, J. (1933). *Strömungsgesetze in Rauhen Rohren*. Düsseldorf:VDI-Verlag.

Piazza, B. P., Banks, P. D., and La Peyre, M. K. (2005). The potential for created oyster shell reefs as a sustainable shoreline protection strategy in Louisiana. *Restor. Ecol.* 13, 499–506. doi: 10.1111/j.1526-100X.2005.00062.x

Powell, D. M. (2014). Flow resistance in gravel-bed rivers: progress in research. *Earth Sci. Rev.* 136, 301–338. doi: 10.1016/j.earscirev.2014.06.001

Qin, J., Aberle, J., Henry, P.-Y., Wu, T., and Zhong, D. (2019). Statistical significance of spatial correlation patterns in armoured gravel beds. *J. Hydraul. Res.* 57, 90–106. doi: 10.1080/00221686.2018.1459894

Quayle, D. B. (1988). Pacific oyster culture in British Columbia. *Can. Bull. Fish. Aqua. Sci.* 218:241.

Raja, J., Muralikrishnan, B., and Fu, S. (2002). Recent advances in separation of roughness, waviness and form. *Precision Eng.* 26, 222–235. doi: 10.1016/S0141-6359(02)00103-4

Reidenbach, M. A., Berg, P., Hume, A., Hansen, J. C. R., and Whitman, E. R. (2013). Hydrodynamics of intertidal oyster reefs: the influence of boundary layer flow processes on sediment and oxygen exchange. *Limnol. Oceanogr.* 3, 225–239. doi: 10.1215/21573689-2395266

Reise, K. (1998). Pacific Oysters Invade Mussel Beds in the European Wadden Sea. *Senckenberg. Marit.* 28, 167–175. doi: 10.1007/bf03043147

Reise, K., Buschbaum, C., Büttger, H., Rick, J., and Wegner, K. M. (2017). Invasion trajectory of Pacific oysters in the northern Wadden Sea. *Mar. Biol.* 164:68. doi: 10.1007/s00227-017-3104-2

Ridge, J. T., Rodriguez, A. B., and Fodrie, F. J. (2017). Evidence of exceptional oyster-reef resilience to fluctuations in sea level. *Ecol. Evol.* 7, 10409–10420. doi: 10.1002/ece3.3473

Ridge, J. T., Rodriguez, A. B., Joel Fodrie, F., Lindquist, N. L., Brodeur, M. C., Coleman, S. E., et al. (2015). Maximizing oyster-reef growth supports green infrastructure with accelerating sea-level rise. *Sci. Rep.* 5:14785. doi: 10.1038/srep14785

Rodriguez, A. B., Fodrie, F. J., Ridge, J. T., Lindquist, N. L., Theuerkauf, E. J., Coleman, S. E., et al. (2014). Oyster reefs can outpace sea-level rise. *Nat. Clim. Change* 4, 493–497. doi: 10.1038/NCLIMATE2216

Sanderson, D. J., and Donovan, R. N. (1974). The vertical packing of shells and stones on some recent beaches. *J. Sediment. Res.* 44, 680–688. doi: 10.1306/74D72ACC-2B21-11D7-8648000102C1865D

Schendel, A., Goseberg, N., and Schlurmann, T. (2016). Erosion Stability of Wide-Graded Quarry-stone material under unidirectional current. *J. Waterway Port Coast. Ocean Eng.* 142: 04015023. doi: 10.1061/(ASCE)WW.1943-5460.0000321

Schendel, A., Goseberg, N., and Schlurmann, T. (2018a). Influence of reversing currents on the erosion stability and bed degradation of widely graded grain material. *Int. J. Sediment. Res.* 33, 68–83. doi: 10.1016/j.ijsrc.2017.07.002

Schendel, A., Hildebrandt, A., Goseberg, N., and Schlurmann, T. (2018b). Processes and evolution of scour around a monopile induced by tidal currents. *Coast. Eng.* 139, 65–84. doi: 10.1016/j.coastaleng.2018.05.004

Schulte, D. M., Burke, R. P., and Lipcius, R. N. (2009). Unprecedented Restoration of a Native Oyster Metapopulation. *Science* 325, 1124–1128. doi: 10.1126/science.1176516

Sievers, J., Rubel, M., and Milbradt, P. (2020). *Data from: EasyGSH-DB: Themengebiet - Geomorphologie*. Karlsruhe: Bundesanstalt für Wasserbau. doi: 10.48437/02.2020.K2.7000.0001

Smaal, A. C., Kater, B. J., and Wijsman, J. (2009). Introduction, establishment and expansion of the Pacific oyster *Crassostrea gigas* in the Oosterschelde (SW Netherlands). *Helgol. Mar. Res.* 63, 75–83. doi: 10.1007/s10152-008-0138-3

Smaal, A. C., Stralen, M., and Craeymeersch, J. (2005). "Does the introduction of the Pacific oyster *Crassostrea gigas* lead to species shifts in the Wadden Sea?," in *The Comparative Roles of Suspension-Feeders in Ecosystems. NATO Science Series IV: Earth and Environmental Series*, Vol. 47, eds R. F. Dame and S. Olenin (Dordrecht: Springer), 277–289. doi: 10.1007/1-4020-3030-4_16

Smart, G., Aberle, J., Duncan, M., and Walsh, J. (2004). Measurement and analysis of alluvial bed roughness / Mesure et analyse de la rugosité de lit d'alluvion. *J. Hydraul. Res.* 42, 227–237. doi: 10.1080/00221686.2004.9641191

Styles, R. (2015). Flow and Turbulence over an Oyster Reef. *J. Coast. Res.* 31, 978–985. doi: 10.2112/JCOASTRES-D-14-00115.1

Taylor, J., and Bushek, D. (2008). Intertidal oyster reefs can persist and function in a temperate North American Atlantic estuary. *Mar. Ecol. Prog. Ser.* 361, 301–306. doi: 10.3354/meps07429

Thompson, C., Williams, J. J., Metje, N., Coates, L. E., and Pacheco, A. (2012). Turbulence based measurements of wave friction factors under irregular waves on a gravel bed. *Coast. Eng.* 63, 39–47. doi: 10.1016/j.coastaleng.2011.12.011

Tibabuzo Perdomo, A. M., Alberts, E. M., Taylor, S. D., Sherman, D. M., Huang, C.-P., and Wilker, J. J. (2018). Changes in cementation of reef building oysters transitioning from larvae to adults. *ACS Appl. Mater. Interf.* 10, 14248–14253. doi: 10.1021/acsami.8b01305

van der Zee, E. M., van der Heide, T., Donadi, S., Eklöf, J. S., Eriksson, B. K., Olff, H., et al. (2012). Spatially extended habitat modification by intertidal reef-building bivalves has implications for consumer-resource interactions. *Ecosystems* 15, 664–673. doi: 10.1007/s10021-012-9538-y

van Leeuwen, B., Augustijn, D., van Wesenbeeck, B. K., Hulscher, S., and de Vries, M. B. (2010). Modeling the influence of a young mussel bed on fine sediment dynamics on an intertidal flat in the Wadden Sea. *Ecol. Eng.* 36, 145–153. doi: 10.1016/j.ecoleng.2009.01.002

Verma, A. K., and Bourke, M. C. (2019). A method based on structure-from-motion photogrammetry to generate sub-millimetre-resolution digital elevation models for investigating rock breakdown features. *Earth Surf. Dynam.* 7, 45–66. doi: 10.5194/esurf-7-45-2019

Vozzo, M. L., Cumbo, V. R., Crosswell, J. R., and Bishop, M. J. (2021). Wave energy alters biodiversity by shaping intraspecific traits of a habitat-forming species. *Oikos* 130, 52–65. doi: 10.1111/oik.07590

Wagner, E., Dumbauld, B. R., Hacker, S. D., Trimble, A. C., Wisehart, L. M., and Ruesink, J. L. (2012). Density-dependent effects of an introduced oyster, *Crassostrea gigas*, on a native intertidal seagrass, *Zostera marina*. *Mar. Ecol. Prog. Ser.* 468, 149–160. doi: 10.3354/meps09952

Walles, B., Salvador de Paiva, J., van Prooijen, B. C., Ysebaert, T., and Smaal, A. C. (2015b). The ecosystem engineer *Crassostrea gigas* affects tidal flat morphology beyond the boundary of their reef structures. *Estuaries Coast.* 38, 941–950. doi: 10.1007/s12237-014-9860-z

Walles, B., Mann, R., Ysebaert, T., Troost, K., Herman, P. M., and Smaal, A. C. (2015a). Demography of the ecosystem engineer *Crassostrea gigas*, related to vertical reef accretion and reef persistence. *Estuar. Coast. Shelf Sci.* 154, 224–233. doi: 10.1016/j.ecss.2015.01.006

Wang, Q., Pan, Y., Yang, K., and Nie, R. (2020). Structural properties of the static armor during formation and reestablishment in gravel-bed rivers. *Water* 12:1845. doi: 10.3390/w12071845

Wehrmann, A. (2006). *Gefährdungspotenzial der eulitoralen Miesmuschelbänke im Niedersächsischen Wattenmeer durch die Bioinvasion der Pazifischen Auster Crassostrea gigas*. Wilhelmshaven: Forschungsinstitut Senckenberg.

Wehrmann, A., Herlyn, M., Bungenstock, F., Hertweck, G., and Millat, G. (2000). The distribution gap is closed — First record of naturally settled pacific oysters *Crassostrea gigas* in the East Frisian Wadden Sea, North Sea. *Senckenberg. Marit.* 30, 153–160. doi: 10.1007/bf03042964

Welzel, M., Schendel, A., Goseberg, N., Hildebrandt, A., and Schlurmann, T. (2020). Influence of structural elements on the spatial sediment displacement around a jacket-type offshore foundation. *Water* 12:1651. doi: 10.3390/w12061651

Welzel, M., Schendel, A., Schlurmann, T., and Hildebrandt, A. (2019). Volume-based assessment of erosion patterns around a hydrodynamic transparent offshore structure. *Energies* 12:3089. doi: 10.3390/en12163089

Westfall, P. H. (2014). Kurtosis as Peakedness, 1905 - 2014. R.I.P. *Am. Stat.* 68, 191–195. doi: 10.1080/00031305.2014.917055

Westoby, M. J., Brasington, J., Glasser, N. F., Hambrey, M. J., and Reynolds, J. M. (2012). 'Structure-from-Motion' photogrammetry: a low-cost, effective tool for geoscience applications. *Geomorphology* 179, 300–314. doi: 10.1016/j.geomorph.2012.08.021

Whitman, E. R., and Reidenbach, M. A. (2012). Benthic flow environments affect recruitment of *Crassostrea virginica* larvae to an intertidal oyster reef. *Mar. Ecol. Prog. Ser.* 463, 177–191. doi: 10.3354/meps09882

Wrange, A.-L., Valero, J., Harkestad, L. S., Strand, Ø, Lindegarth, S., Christensen, H. T., et al. (2010). Massive settlements of the Pacific oyster, *Crassostrea gigas*, in Scandinavia. *Biol. Invasions* 12, 1145–1152. doi: 10.1007/s10530-009-9535-z

Yao, Y., Yang, X., Liu, W., and He, T. (2020). The effect of reef roughness on monochromatic wave breaking and transmission over fringing reefs. *Mar. Georesources Geotechnol.* 29, 1–11. doi: 10.1080/1064119X.2019.1702746

Conflict of Interest: The authors declare that the research was conducted in the absence of any commercial or financial relationships that could be construed as a potential conflict of interest.

Publisher's Note: All claims expressed in this article are solely those of the authors and do not necessarily represent those of their affiliated organizations, or those of the publisher, the editors and the reviewers. Any product that may be evaluated in this article, or claim that may be made by its manufacturer, is not guaranteed or endorsed by the publisher.

Copyright © 2022 Hitzegrad, Brohmann, Pfennings, Hoffmann, Eilrich, Paul, Welzel, Schlurmann, Aberle, Wehrmann and Goseberg. This is an open-access article distributed under the terms of the Creative Commons Attribution License (CC BY). The use, distribution or reproduction in other forums is permitted, provided the original author(s) and the copyright owner(s) are credited and that the original publication in this journal is cited, in accordance with accepted academic practice. No use, distribution or reproduction is permitted which does not comply with these terms.

frontiers in Marine Science

ORIGINAL RESEARCH
published: 15 March 2022
doi: 10.3389/fmars.2022.807588

Coastal Wetland Surface Elevation Change Is Dynamically Related to Accommodation Space and Influenced by Sedimentation and Sea-Level Rise Over Decadal Timescales

Kerrylee Rogers[1], Atun Zawadzki[2], Laura A. Mogensen[1] and Neil Saintilan[3]*

[1] School of Earth, Atmospheric and Life Sciences, University of Wollongong, Wollongong, NSW, Australia, [2] Australian Nuclear Science and Technology Organisation, Lucas Heights, NSW, Australia, [3] School of Natural Sciences, Macquarie University, North Ryde, NSW, Australia

The fate of mangroves and saltmarshes under conditions of accelerating sea-level rise is dependent upon sedimentation and surface elevation gain that is sufficient to maintain substrate positions within a shifting tidal frame. This study focuses on coastal wetlands fringing Westernport Bay, a large tidal embayment of southeastern Australia where mangroves occupy lower tidal positions than saltmarshes. Estimates of vertical accretion, surface elevation change, and autocompaction derived from a 20-year record of observations were integrated with estimates of sedimentation at the decadal to century time-scale derived from ^{210}Pb chronology to model the relationship between surface elevation gain and accommodation space at timescales relevant to management and decision-making. This model was validated against records of shoreline changes extracted from time-series aerial photography. Sedimentation and surface elevation gain vary spatially on the basis of available accommodation space and sediment supply, which are influenced by hydrodynamic conditions within the bay. Since sea-level rise increases available accommodation space, these relationships provided the means to project the outcome of accelerating sea-level rise on equilibrium accommodation space of mangroves and saltmarshes. Sea-level rise will generally deepen substrate positions within the tidal frame, creating conditions favorable for mangrove forests. Where sediment supply is high, maintenance (and some progradation) of mangrove shorelines may occur under projected low rates of sea-level rise; these conditions are limited to shorelines near sedimentary basins and where there is considerable lateral accommodation space. The same fate is not likely under a high sea-level rise scenario where shoreline retreat is projected in all settings. Given the limited accommodation space within saltmarshes at Westernport Bay, sedimentation will not be sufficient to maintain tidal positions and landward retreat will be critical for maintenance of saltmarsh biodiversity. This will require planning decisions to facilitate tidal incursions and conserve retreat pathways.

Keywords: mangrove, saltmarsh, ^{210}Pb geochronology, sediment supply, autocompaction, equilibrium elevation

OPEN ACCESS

Edited by:
Zhan Hu,
Sun Yat-sen University, China

Reviewed by:
Ya Ping Wang,
Nanjing University, China
Barend van Maanen,
University of Exeter, United Kingdom

****Correspondence:***
Kerrylee Rogers
kerrylee@uow.edu.au

Specialty section:
This article was submitted to Coastal Ocean Processes, a section of the journal Frontiers in Marine Science

Received: *02 November 2021*
Accepted: *11 February 2022*
Published: *15 March 2022*

Citation:
Rogers K, Zawadzki A, Mogensen LA and Saintilan N (2022) Coastal Wetland Surface Elevation Change Is Dynamically Related to Accommodation Space and Influenced by Sedimentation and Sea-Level Rise Over Decadal Timescales. Front. Mar. Sci. 9:807588. doi: 10.3389/fmars.2022.807588

INTRODUCTION

Saline coastal wetlands dominated by mangrove and saltmarsh occupy the intertidal zone and their lateral distribution is generally delimited by the landward extent of tidal inundation. Accumulation of mineral and organic material within substrates is facilitated by the low energy conditions that promote sediment deposition and the growth of halophytic vegetation; this material provides an important vertical subsidy when coastlines are exposed to relative sea-level rise (RSLR) (Woodroffe et al., 2016). Observational data indicates that coastal wetlands may be able to increase surface elevations under low to moderate rates of RSLR (Kirwan et al., 2016). However, there remains ongoing debate about the ability of coastal wetlands to adjust to the high rates of RSLR that are anticipated as eustatic SLR accelerates toward the end of the 21st century (Oppenheimer et al., 2019). Large spatial-scale analyses of paleoecological data indicate that mangroves can adapt to rates of RSLR of less than 7 mm year^{-1} (Saintilan et al., 2020). Similarly, saltmarshes in the United Kingdom have been found to adapt when rates of RSLR does not exceed 7 mm year^{-1} (Horton et al., 2018). Process based modeling indicates higher tolerance thresholds for saltmarshes, sometimes in excess of 10 mm year^{-1} when suspended sediment concentrations are high (Kirwan et al., 2016). These analyses of tolerance thresholds typically rely upon meta-data analyses of reported rates of vertical adjustment to improve confidence in estimates and, in doing so, treat site-scale measurements as data points that contribute to understanding of coastal wetland resilience at larger spatial scales. Local-scale data remains crucial for improving confidence in global- and regional-scale analyses. However, global-scale models are insufficient at the landscape scale where management and decision making require both accuracy and precision. Local-scale information is therefore a crucial data need that will improve both large-scale analyses and models, and local-scale management and decision-making.

At the landscape scale, there is general consensus that sedimentation of tidally-borne material is related to tidal inundation frequency and duration, with positions lower in the tidal frame accumulating sediment at a higher rate than locations higher in the tidal frame (Allen, 2000; Woodroffe et al., 2016). This spatial variation in sedimentation has a significant control on the long-term evolution of coastal wetlands. Under stable sea-level conditions, sedimentation is delimited by maximum tidal extents and is proportional to the depth below maximum tide level whilst surface elevations asymptote toward the height of maximum tide level (Rogers, 2021). RSLR alters the elevation of tidal planes over time; however, as sedimentation is proportional to tidal inundation (Rogers et al., 2005a) and position in the tidal frame, an incremental increase in sea level may result in a proportional increase in elevation adjustment, providing mineral sediment supply is not limited and organic matter addition to substrates is sufficient. This negative feedback, first described by Pethick (1981), leads to self-organization of surface elevations with the outcome being the development of broad floodplains at elevations that asymptote toward a depth below maximum tide level where surface elevation gain matches the rate of RSLR.

Based on these negative feedbacks, mathematical simulations indicate that the depth of this asymptote below maximum tide level is dependent upon the proportion of substrate volume adjustment to the degree of RSLR (Fagherazzi et al., 2012). Where the proportion of elevation adjustment to RSLR is high, achieved through the accumulation of mineral and organic material within substrates, coastal wetland surfaces will asymptote at a higher elevation in the tidal frame. Where sediment supply and/or organic matter addition becomes increasingly limited, surface elevations asymptote at lower elevations in the tidal frame. When rates of mineral and organic matter addition to substrates are very low, substrates may asymptote at elevations too low to support vegetation, negative feedbacks breakdown, and the system can shift toward a chaotic state where erosional processes may dominate. Hence, rates of surface elevation adjustment with respect to RSLR is critical information needed to gauge whether wetland substrates will maintain their position within the tidal frame, shift toward a lower elevation in the tidal frame, or undergo existential breakdown.

The timescale over which data should be collected to establish relationships between sedimentation and RSLR has been debated. Breithaupt et al. (2018) propose that short-term measurements at inter-annual increments, particularly those derived from observations of surface elevation change using techniques such as surface elevation tables and marker horizons (SET-MH), may indicate rates of surface elevation change that are highly influenced by perturbations operating over the observational period. This has been confirmed with trajectories of surface elevation change being related to droughts (Rogers et al., 2005b, 2006), cyclones and hurricanes (Whelan et al., 2009; Osland et al., 2020; Yeates et al., 2020), groundwater availability (Rogers et al., 2005a; Whelan et al., 2005), and nutrient availability (Anisfeld and Hill, 2012; Reef et al., 2017). Irrespectively, analyses over shorter timescales provide useful information about processes influencing surface elevations, and, when collected over sufficient time, may provide reliable trajectories of surface elevation change and indicate processes influencing these trajectories (Rogers and Saintilan, 2021).

Radiometric techniques that focus on processes operating over longer interdecadal timescales tend to produce time averaged indications of sedimentation and the influence of short-term perturbations on trajectories is moderated (Nolte et al., 2013). A range of techniques can be used which are dependent upon the capacity to detect isotopes that undergo decay over time. Accordingly, different techniques can be selected to characterize sedimentation over a range of timescales. Measurements of unsupported ^{210}Pb, which has a half-life of 22.3 years, has been effectively used to ascribe chronology over the past 100–150 years for coastal wetland sediments (Swales et al., 2015; Ruiz-Fernández et al., 2016; Arias-Ortiz et al., 2018; Rogers et al., 2019; Marx et al., 2020; FitzGerald et al., 2021). This timescale is particularly useful for developing relationships between sedimentation and RSLR as it corresponds to (i) the most intensive period of industrialization when global sea levels have been increasing; and (ii) the timescale at which projections of the response of coastal wetlands are most relevant for planning and decision making (Woodroffe and Murray-Wallace, 2012).

Recent advances in models for ascribing a ^{210}Pb chronology now accommodate a range of ^{210}Pb supply conditions and composition of sediments (i.e., the degree of mineral and organic material) (FitzGerald et al., 2021; Iurian et al., 2021). As these factors vary over time, the length of time that sedimentation is averaged is diminished, and variation in sedimentation can be determined over shorter-time periods. This provides the opportunity to characterize changes in sedimentation under varying conditions of RSLR.

This study focuses on establishing relationships between rates of sedimentation, surface elevation gain and SLR relevant to decadal timescales, and specifically addresses two knowledge gaps. First, it provides comprehensive empirical data of coastal wetland sedimentation and elevation adjustment in the southern hemisphere, a region for which there is relatively little data at decadal timescales and represents a significant knowledge gap that limits the development of robust regional and global-scale models. Second, it addresses timescale bias by developing relationships between rates of sedimentation and SLR that are relevant at the annual to decadal scale useful for management and decision making. Relationships were validated against both short-term data derived from SET-MH techniques and against geomorphological information of shoreline change at the decadal timescale. Our specific hypothesis was that rates of sedimentation were related to the three-dimensional space available for mineral and organic matter accumulation. Commonly known as accommodation space (Jervey, 1988; Rogers et al., 2019; Rogers, 2021), this space is delimited by the existing surface elevation, the maximum tide level, and hydrodynamic conditions suitable for deposition, and is influenced by SLR. We expected the substrates lower in the tidal frame would have higher rates of sedimentation, the substrates higher in the tidal frame would have lower rates of sedimentation, and that rates of adjustment would change over time on the basis of tidal position. Additionally, we assessed the resilience of coastal wetlands by standardizing rates of sedimentation and surface elevation change relative to accommodation space and comparing surface elevation change to current and projected rates of RSLR. These analyses considered the elevation that substrates would asymptote toward under different SLR scenarios and projected sedimentation rates and surface elevation change at the upper and lower limits of mangrove and saltmarsh vegetation, and the approximate elevation of the transition between mangrove and saltmarsh vegetation. This study focuses on Westernport Bay, Australia; a large tidal embayment that supports mangroves at tidal positions approximately between mean tide level (MTL) and mean high water springs (MHWS), and saltmarsh at positions higher in the tidal frame. We integrate reliable estimates of vertical accretion, surface elevation change and autocompaction derived from a 20-year record of observations (Rogers and Saintilan, 2021), with estimates of sedimentation at the decadal to century scale derived from ^{210}Pb-dating techniques applied to cores extracted from mangrove and saltmarsh zones at each study site. To reconstruct surface elevation, rates of sedimentation were adjusted for autocompaction using a site-specific model developed by Rogers and Saintilan (2021). This manuscript compliments Rogers and Saintilan (2021), which assesses processes influencing surface elevation change over a 20-year timescale from a network of 24 SET-MH. It is anticipated that this study will provide knowledge relevant to management of coastal wetlands at Westernport Bay, and will inform global scale models of the behavior of coastal wetlands to SLR and their resilience.

MATERIALS AND METHODS

Study Site and Design

Westernport Bay (38°21′S, 145°13′E) is a large coastal embayment of ∼680 km^2 that drains a catchment area of 3,433 km^2 located east of Melbourne Victoria, Australia (**Figure 1**). The region is prone to drought associated with negative phases of the El Niño Southern Oscillation, and the influence of drought on rainfall has been associated with changes in surface elevations of coastal wetlands around Westernport Bay (Rogers et al., 2005b). The embayment has two entrances to Bass Strait; the constriction of the eastern entrance near San Remo (38°31′S, 145°22′E) causes tides to propagate relatively freely through the western entrance, clockwise around French Island until they converge with anticlockwise tidal movement (Harris et al., 1979). The tidal regime is semi diurnal with a tidal range of up to 3.1 m and significant tidal amplification along the upper Northern Arm of Westernport Bay, near the study sites at French Island and Koweerup (Water Technology, 2014b). Despite its size, the embayment is relatively shallow and tides are reported to comprise approximately 30% of the total volume at high tide (Lee, 2011). Westernport Bay includes extensive intertidal flats (∼270 km^2) that support mangrove and saltmarsh communities along its low energy intertidal shorelines, estimated to cover approximately 12.3 and 10.9 km^2, respectively (Boon, 2011). These wetlands comprise a lower elevation mangrove zone that supports the cold tolerant mangrove, *Avicennia marina*, which is near its most latitudinal limit at this location. The upper intertidal zone also supports dense thickets of saltmarsh shrubs of the genus *Tecticornia* and a landward zone of herbs, grasses and sedges that are regarded to be highly diverse (Boon, 2011).

This study focuses on four locations where surface elevation table (SET) monitoring stations were established in October 2000 to monitor mangrove and saltmarsh vegetation dynamics and rates of vertical accretion and surface elevation change. These study sites included the northern shoreline of French Island, near abandoned saltworks at Palmer Point (henceforth termed French Island), the northern shoreline of the bay near Tooradin airport which adjoins Kooweerup Swamp (henceforth termed Kooweerup), the eastern shoreline of Quail Island near Warneet (henceforth termed Quail Island), and the upper reaches of Rhyll Inlet on Philip Island (henceforth termed Rhyll).

The original study of Rogers et al. (2005b) commenced in 2000 and provided quantitative information on the dynamics of mangrove and saltmarsh vegetation and changes in rates of vertical accretion and surface elevation within mangrove and saltmarsh of Westernport Bay, with consideration given to varying degrees of catchment development. Rogers et al. (2005b) established a network of version IV SET-MH throughout Westernport Bay. The SET serves as a stable benchmark against

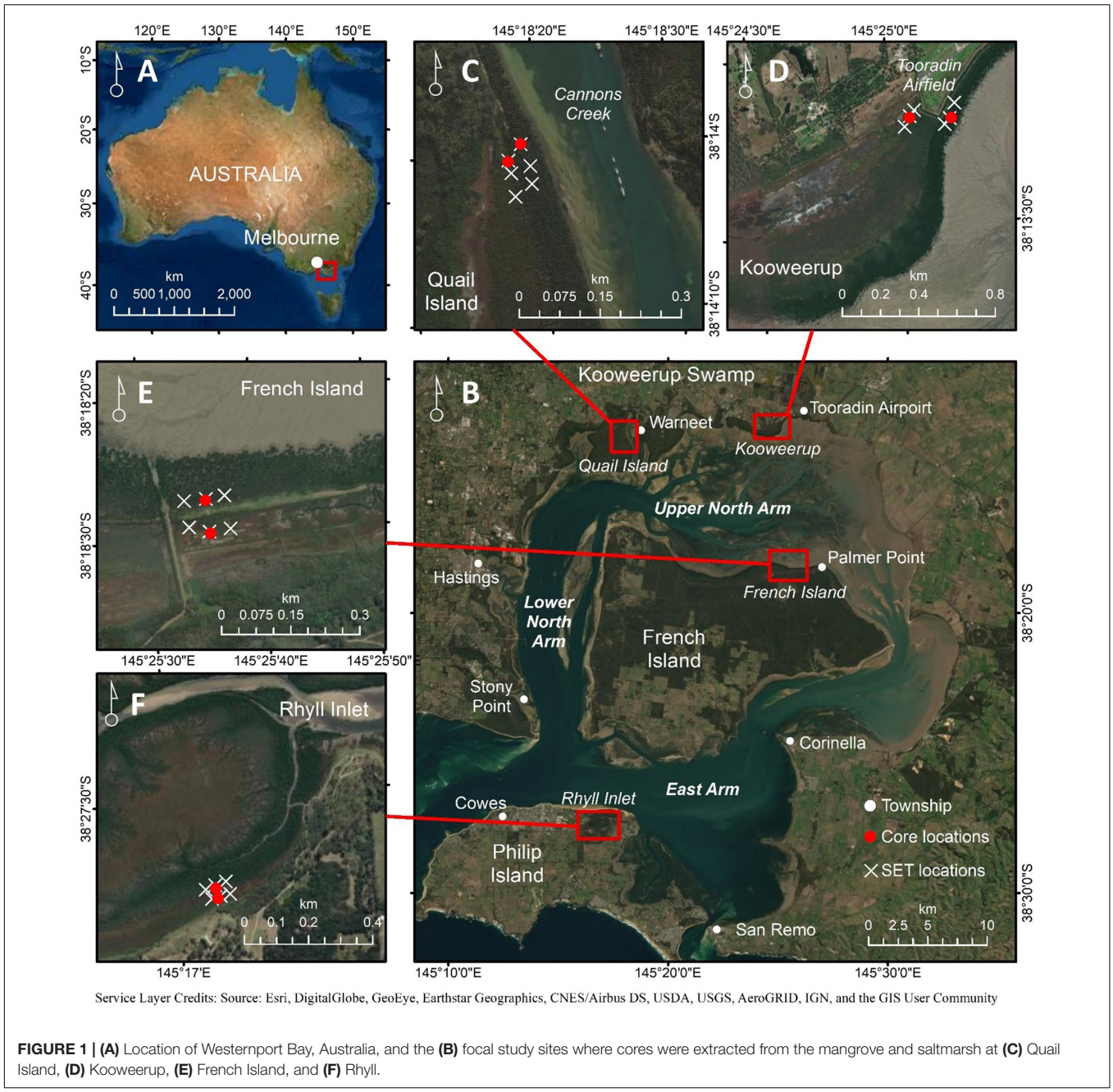


FIGURE 1 | (A) Location of Westernport Bay, Australia, and the **(B)** focal study sites where cores were extracted from the mangrove and saltmarsh at **(C)** Quail Island, **(D)** Kooweerup, **(E)** French Island, and **(F)** Rhyll.

which relative changes in surface elevation can be determined. Relative SET measurements can be converted to absolute measurements of surface elevation change by geolocating SET benchmarks using a real time kinematic global positioning system (RTK-GPS). The version IV SET has a reported 95% confidence limit of ±1.4 mm (Cahoon et al., 2002). Marker horizons of feldspar have been co-located with each SET and extraction of mini-cores from each MH at the time of SET measurements allows quantification of surface processes of vertical accretion. By deduction, the difference between the degree of surface elevation change and vertical accretion provides an indication of autocompaction processes operating in the substrate that alter the volume. This network comprised 24 SET-MH stations in a nested design whereby six SETs were co-located at French Island, Kooweerup, Quail Island, and Rhyll. At each location, SETs were positioned in groups of three within structurally similar vegetation: three located in the mangrove zone where the tidal position was lower; and three in the saltmarsh zone where the tidal position was higher. Rogers et al. (2005b) also determined sedimentation rates using ^{210}Pb-dating of sediments and undertook mapping from aerial photographs to determine changes in the distribution of mangrove and saltmarsh over the length of the aerial photographic records for each site. These study sites remain the focus of this research.

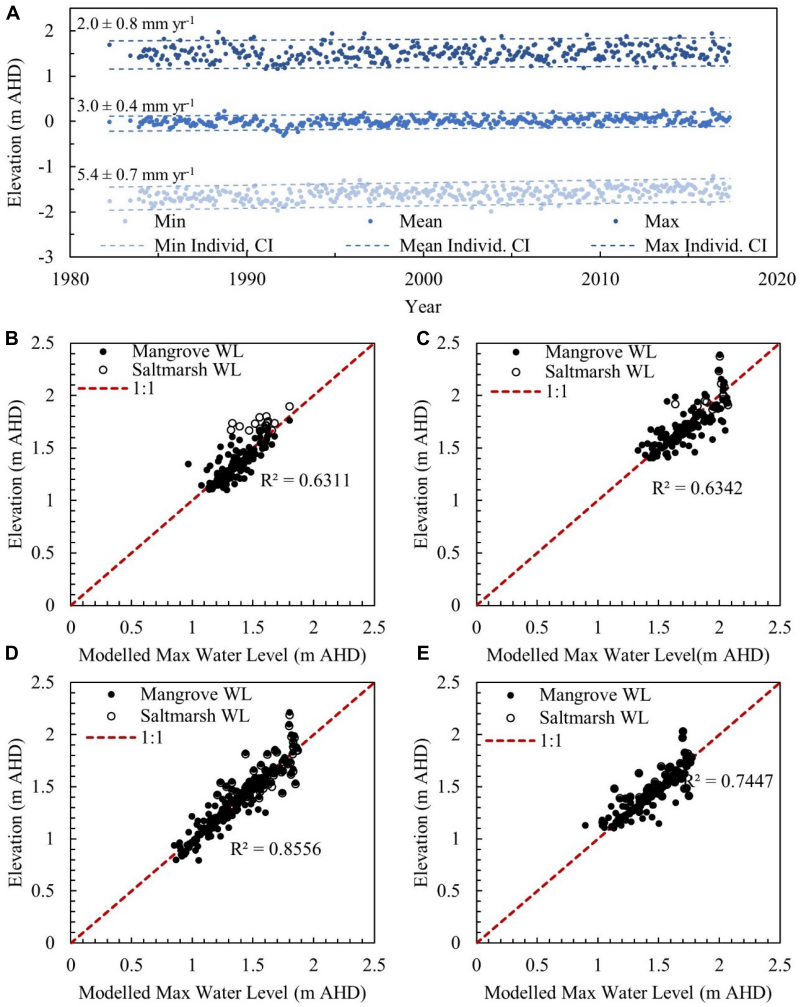


FIGURE 2 | (A) Minimum, mean, and maximum monthly water levels at the Stony Point tide gauge, with 5% and 95% confidence interval for each variable defined by the dashed lines. Relationship between observed daily maximum water levels in the mangrove and saltmarsh zones and modeled maximum water levels at **(B)** French Island, **(C)** Kooweerup, **(D)** Quail Island, and **(E)** Rhyll.

Since the commencement of the original study, access to spatial information, such as LiDAR point clouds and RTK-GPS technology, and access to low-cost sensors and data loggers has increased. Additional time-series mapping has been undertaken by Whitt et al. (2020) and an update of SET monitoring results is provided by Rogers and Saintilan (2021).

Tides and Accommodation Space

Water-level data from the tide gauge at Stony Point has been collected since 1981 and can be accessed as processed datasets indicating minimum, mean, and maximum monthly water levels (Bureau of Meteorology, 2021). This data was accessed for the full record length and analyzed to characterize RSLR over time. Water-level data underwent preliminary processing to remove any months where data gaps were greater than 10% of the gauging frequency each month. Linear regressions were used to identify the rate of change in minimum, mean, and maximum monthly water levels.

Water-level data from tide gauges can also be used to indicate the vertical position within the tidal frame that mangroves and saltmarshes occupy, and the space available for tidally-borne sedimentation, known as accommodation space. However, they may not be a precise indicator of tidal behavior at locations distal to tide gauges as tides can become amplified or attenuated as they propagate along estuaries and embayments (Kumbier et al., 2021). Tidal analyses have confirmed that tides do amplify along the northern arm of Westernport Bay (Water Technology, 2014a), due to the one quarter wavelength resonance of the lunar semidiurnal tide within Westernport Bay. Accordingly, the upper boundary of accommodation space at study sites along the Northern Arm, namely at French Island, Kooweerup and Quail Island, will likely be higher than indicated by tide gauge data alone.

To establish how much tidal amplification occurs at each study site, daily maximum water-level data from the Stony Point tide gauge was calibrated against water-level data collected

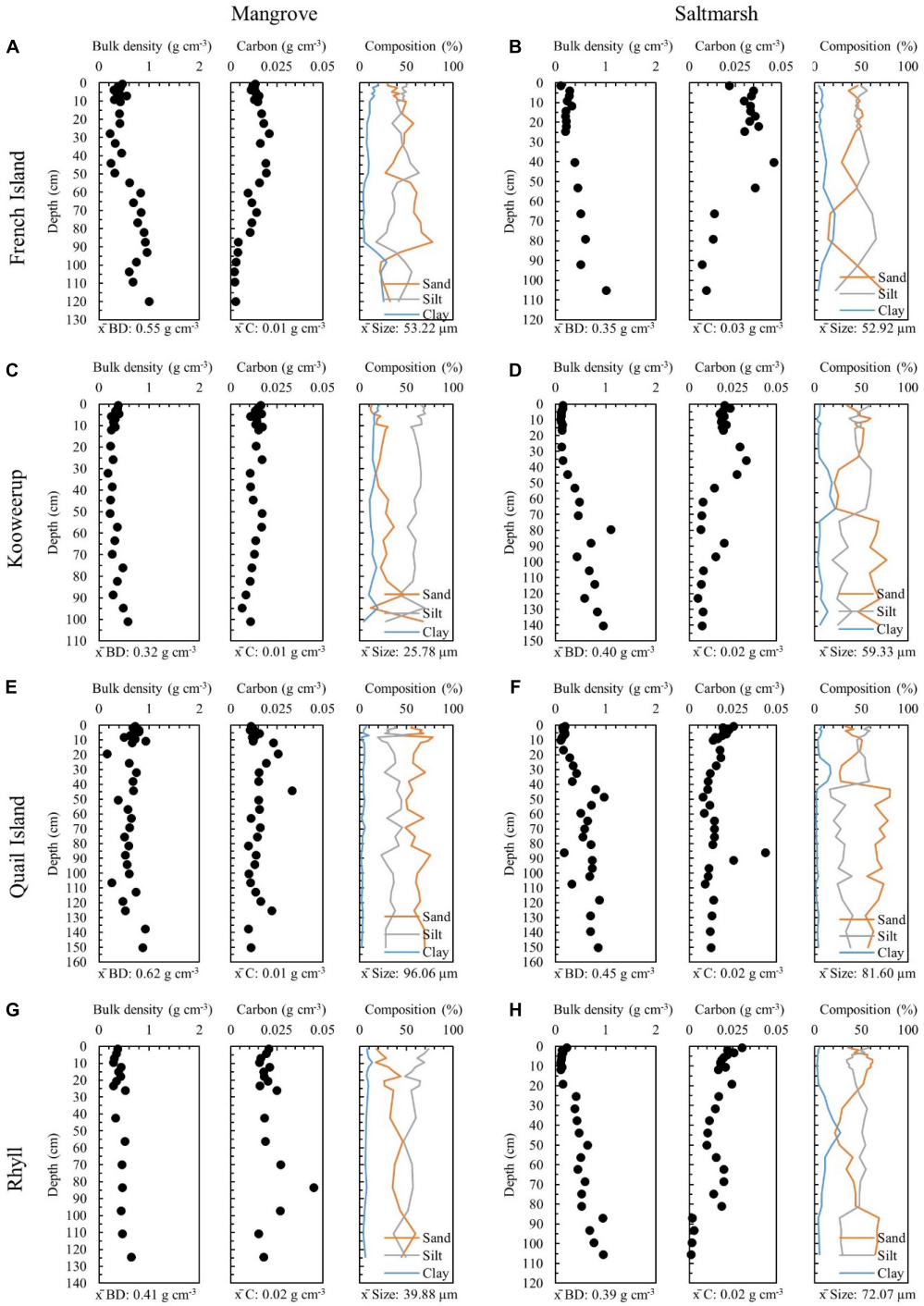


FIGURE 3 | Bulk density, carbon content, and grain size fraction down cores extracted from the mangrove and saltmarsh zones at **(A,B)** French Island, **(C,D)** Kooweerup, **(E,F)** Quail Island, and **(G,H)** Rhyll.

using Hobo water-level loggers that were placed within the mangrove and saltmarsh at each study site and co-located with SETs. The position of Hobo water-level loggers was determined using an RTK-GPS, and all values were calibrated against the Australian height datum (AHD). Hobo water-level loggers collected data at 15-min intervals from May 2015 to January 2016 at French Island, and April 2016 to November 2016 at Kooweerup, Quail Island, and Rhyll. These periods of data collection exceeded 6 months, included considerable variation in tidal height and included the high water spring

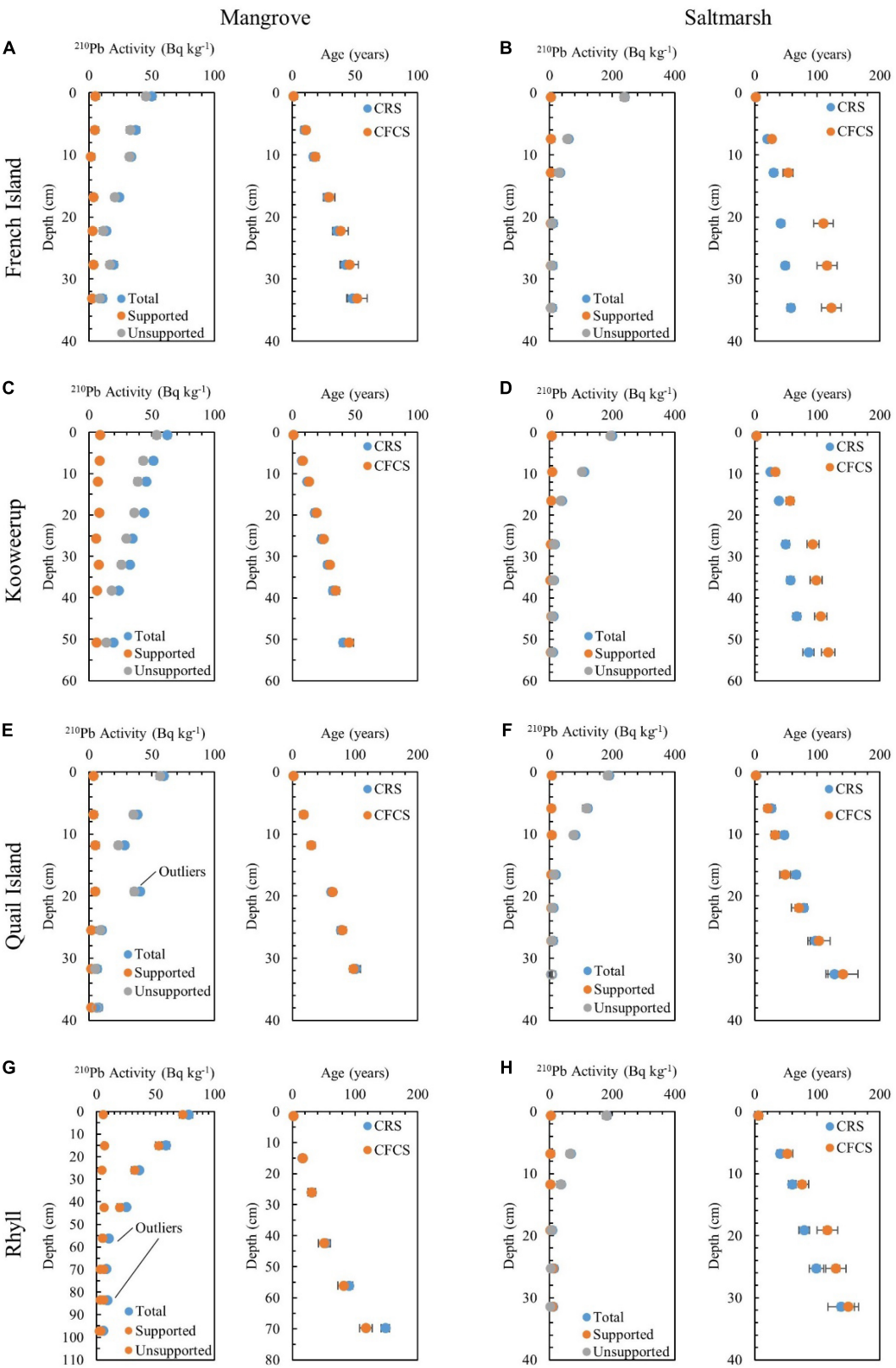


FIGURE 4 | ^{210}Pb activity and geochronological age of sediments at time of deposition down cores extracted from the mangrove and saltmarsh zones at **(A,B)** French Island, **(C,D)** Kooweerup, **(E,F)** Quail Island, and **(G,H)** Rhyll.

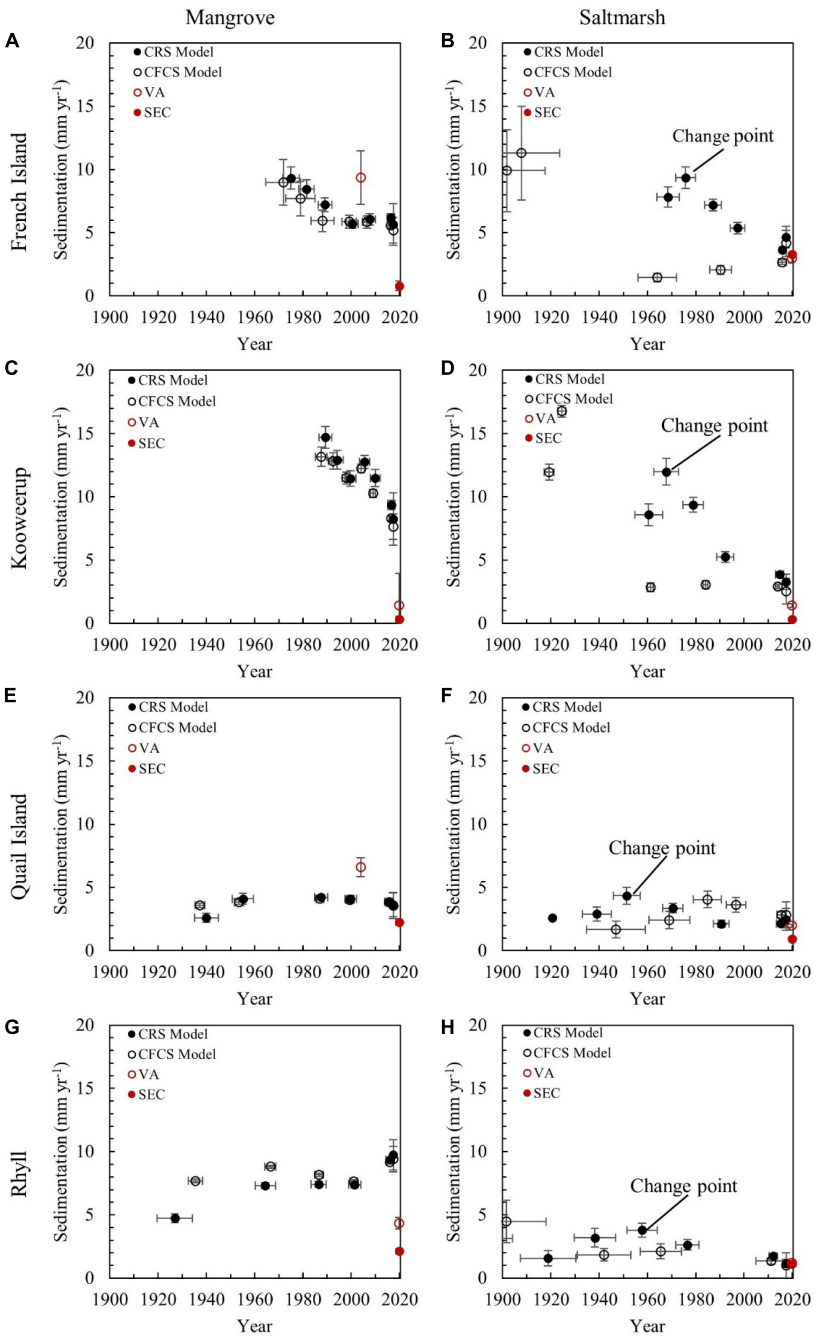


FIGURE 5 | Reconstructed sedimentation rates over time from the mangrove and saltmarsh zones at **(A,B)** French Island, **(C,D)** Kooweerup, **(E,F)** Quail Island, and **(G,H)** Rhyll. Sedimentation rates were validated against vertical accretion (VA) and surface elevation change (SEC) determined at the adjacent SET-MH monitoring station.

tides that occur approximately every 6 months. Modeled maximum daily tides at each study site were determined by calibrating daily maximum tides from the Stony Point tide gauge against observed water-level data collected using Hobo water level loggers by adding a tidal amplification factor to tide gauge data. The efficacy of calibration was determined using a matched pairs *t*-test and the deviation of observed values from the modeled values was determined using the coefficient of determination (r^2).

The upper boundary of accommodation space at each study site was subsequently modeled at any time step on the basis of the trend in the maximum monthly water-level data plus the tidal amplification factor determined for each study site. The lower boundary of the vegetated intertidal zone was presumed

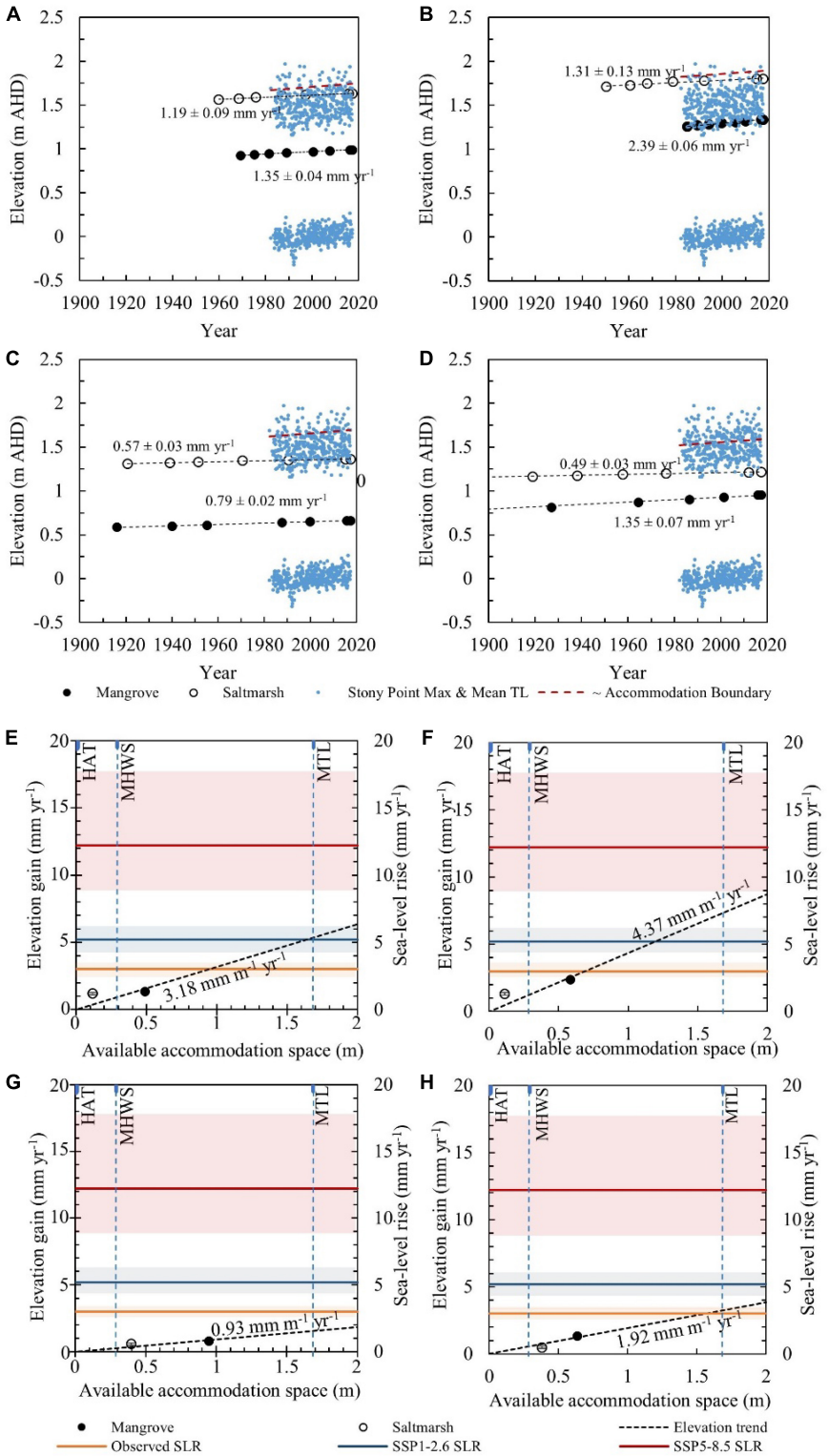


FIGURE 6 | Stony Point water levels, modeled upper boundary of accommodation space (based on amplification factor in **Supplementary Figure 2**) and reconstructed surface elevations (based on autocompaction relationship in **Supplementary Figure 1**) within the mangrove and saltmarsh zones at **(A)** French Island, **(B)** Kooweerup, **(C)** Quail Island, and **(D)** Rhyll; and relationship between surface elevation gain and available accommodation space at **(E)** French Island, **(F)** Kooweerup, **(G)** Quail Island, and **(H)** Rhyll. Observed rates and projected rates of SLR have been included for comparison of accommodation space dependent sedimentation rates in panels **(E–H)**.

TABLE 1 | Standardized rates of surface elevation gain (mm per meter of available accommodation space per year), derived from linear regression analyses in **Figure 6**; projected equilibrium available accommodation space where rates of surface elevation gain equal observed rates of sea-level rise (SLR) (3.0 mm year^{-1}), derived from intersection of linear regression and observed SLR in **Figure 6**; contemporary elevation and estimated available accommodation space at mean tide level (MTL) and mean high water springs (MHWS); projected rate of surface elevation gain, derived from intersection of linear regression and vertical dashed lines in **Figure 6** indicating MTL and MHWS; projected elevation deficit/surplus, derived from the difference between rates of surface elevation gain and observed rate of SLR; projected change in tidal position, based on evidence of a surface elevation deficit or surplus; and projected shoreline change at MTL and MHWS at each study site.

	French Island		**Kooweerup**		**Quail Island**		**Rhyll**	
Standardized surface elevation gain (mm m^{-1} year^{-1})	3.2		4.4		0.9		1.9	
Equilibrium accommodation space (m) at SLR 3 mm year^{-1}	0.9		0.7		3.2		1.6	
	MTL	**MHWS**	**MTL**	**MHWS**	**MTL**	**MHWS**	**MTL**	**MHWS**
Contemporary Elevation (m AHD)	0.1	1.5	0.1	1.6	0.1	1.4	0.1	1.3
Accommodation space (m)	1.7	0.3	1.8	0.3	1.6	0.3	1.5	0.3
Surface elevation gain (mm year^{-1})	5.4	0.9	8.0	1.3	1.5	0.3	3.0	0.6
Surface elevation deficit/surplus	2.4	−2.1	5.0	−1.7	−1.5	−2.7	0.0	−2.4
Tidal position change	↑	↓	↑	↓	↓	↓	Stable	↓
Projected shoreline change	– Progradation – Seaward mangrove expansion – Mangrove encroachment of saltmarsh		– Progradation – Seaward mangrove expansion – Mangrove encroachment of saltmarsh		– Shoreline retreat – Mangrove encroachment of saltmarsh		– No shoreline change – Mangrove encroachment of saltmarsh	

to be the elevation of mean sea level, as indicated on the Stony Point tide gauge.

Sediment Characterization

Sediment cores, eight in total, of approximately 1.5 m length were collected in 2017 adjacent to mangrove and saltmarsh SET monitoring stations at each study site. Cores were extracted in aluminium tubes of 75 mm diameter. The degree of sediment compaction that occurred during core collection was determined and cores were capped to ensure they remained continuous and intact for transport. Cores were placed in cold storage at 4°C until sample preparation was undertaken. The position of each core at the time of extraction was determined using an RTK-GPS with measurements made with respect to the AHD. Cores were split longitudinally and half of the core was subsampled at intervals of 2 cm in the upper strata of 10 cm, every 5 cm to depths of 1 m, and every 10 cm below 1 m for further analysis. These sample depths were adjusted for compaction and the remaining core was placed in storage. Samples were subsequently prepared for analysis of ^{210}Pb activity. Grain size of each sample was determined (μm) using a Malvern Mastersizer 2000 laser diffractometer and the proportion of each fraction determined. To determine dry bulk density (g cm^{-3}), samples were oven dried to constant weight at 60°C. Dry sample weight was determined and bulk density (BD) was estimated as the ratio of dry sample mass to wet sample volume. Dry bulk density was subsequently used to model sedimentation rates and quantify ^{210}Pb activity.

Lead-210 Activity and Chronology

Lead-210 is a naturally occurring radionuclide with a half-life of 22.3 years. Analysis of unsupported ^{210}Pb derived from the atmosphere facilitates the determination of sediment age at time of deposition. As sediments accumulate, ^{210}Pb decays according to its half-life, thus the rate of decline in unsupported ^{210}Pb with sediment depth allows the determination of sediment chronology and mass accumulation rates. Grain size can affect the adsorption of ^{210}Pb onto the sediment materials. Finer sediments with larger surface area adsorb ^{210}Pb more effectively than coarser grain size sediments with smaller surface area. To facilitate the detection of low level ^{210}Pb activities, samples from various core depths were sieved to concentrate the <63 μm fraction. Sieved samples were then provided to the Australian Nuclear Science and Technology Organisation (ANSTO) for ^{210}Pb dating by alpha particle spectrometry. Preliminary analysis was undertaken on five samples per core to determine whether unsupported ^{210}Pb activity decreased with core depth. Subsequent sample analyses were used to develop a more reliable chronology. Sample age was determined using both the constant rate of supply (CRS) (Appleby and Oldfield, 1978) and constant flux-constant rate of supply (CFCS) (Krishnaswamy et al., 1971) models. However, the CRS model has exhibited superior performance when dating sediment matrices comprised of significant organic matter in the sediment composite (Iurian et al., 2021). Accordingly, it was anticipated that the CRS model, which accounts for irregularities in unsupported ^{210}Pb activity would provide a more reliable chronology.

Independent validation of chronology is recommended to ensure high confidence in results (Smith, 2001). Measurements of ^{137}Cs peak activity is commonly used for validation; however, the relatively short-half-life of ^{137}Cs and lower activity within sediments of the southern hemisphere may limit validation using this approach (Arias-Ortiz et al., 2018). Analyses of ^{137}Cs activity did not yield results suitable for validation, hence an alternative

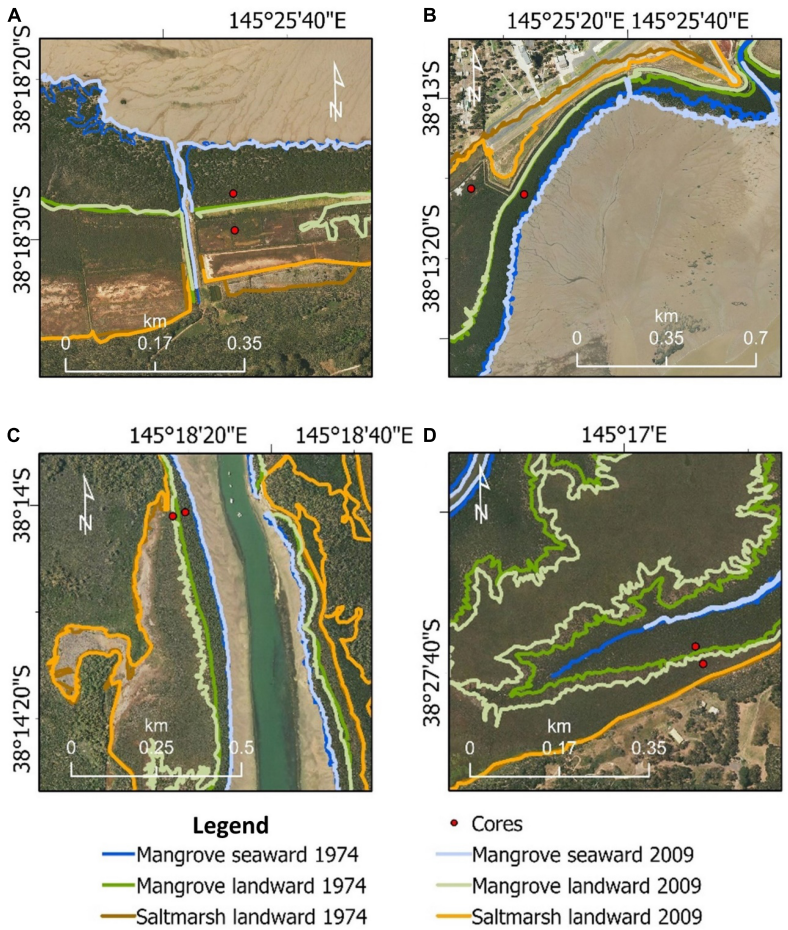


FIGURE 7 | Mangrove seaward and landward limits and saltmarsh landward limits digitized from 1973/74 and 2009 images at **(A)** French Island, **(B)** Kooweerup, **(C)** Quail Island, and **(D)** Rhyll. Notable shoreline progradation and mangrove expansion into saltmarsh is indicated. See **Supplementary Figures 3–6** for time-series maps.

TABLE 2 | Projected equilibrium accommodation space (or depth below the upper boundary of accommodation space) where rates of surface elevation gain equal projected sea-level rise (SLR) based on median values of a low and high SLR scenario, projected surface elevation deficit/surplus, and tidal position change at mean tide level (MTL) and mean high water springs (MHWS).

	French Island				Kooweerup				Quail Island				Rhyll			
SLR scenario	Low		High		Low		High		Low		High		Low		High	
Equilibrium accommodation space (m)	1.6		3.8		1.2		2.8		5.6		13.1		2.7		6.4	
	MTL	**MHWS**	**MTL**	**MHWS**	**MTL**	**MHWS**	**MTL**	**MHWS**	**MTL**	**MHWS**	**MTL**	**MHWS**	**MTL**	**MHWS**	**MTL**	**MHWS**
Surface elevation deficit/surplus (mm year^{-1})	0.2	−4.3	−6.8	−11.3	2.8	−3.9	−4.2	−10.9	−3.7	−4.9	−10.7	−11.9	−2.2	−4.6	−9.2	−11.6
Tidal position change	↑	↓	↓	↓	↑	↓	↓	↓	↓	↓	↓	↓	↓	↓	↓	↓

Median value of low SLR scenario from SSP1-2.6 at ~2,100, estimated at 5.2 mm year^{-1}. Median value of high SLR scenario from SSP5-8.5 at ~2,100, estimated at 12.2 mm year^{-1}.

approach was undertaken. Measurements of $^{239+240}$Pu activity, or bomb-pulse analyses, can also be undertaken, but can be costly and were not undertaken in this study as the results were validated using existing data from SET-MH analyses (Sanders et al., 2016; Marx et al., 2020). Initially, validation was undertaken by comparison with recent measurements of vertical accretion derived from SET-MH stations and reported in Rogers and Saintilan (2021). Validation of expected changes to shorelines

TABLE 3 | Sedimentation rates derived from ^{210}Pb geochronology for similar ecosystems in Australia and New Zealand, and reported global averages and common values.

Location	Dominant species/ community	Mean sedimentation rate (Range) (mm year^{-1})	Mean bulk density (Range) (g cm^{-3})	Sources
French Island, Westernport Bay	*A. marina*	6.9[a] (5.7–9.3)	0.38 (0.22–0.46)	This study
	Saltmarsh	6.3[a] (3.6–9.3)	0.30 (0.10–0.50)	
	Saltmarsh	1.4[b]		Rogers et al. (2005b)
Kooweerup, Westernport Bay	*A. marina*	11.6[a] (8.3–14.7)	0.26 (0.18–0.38)	This study
	Saltmarsh	7.1[a] (3.3–12.0)	0.18 (0.11–0.38)	
	Saltmarsh	1.63[b]		Rogers et al. (2005b)
Quail Island, Westernport Bay	*A. marina*	3.8[a] (2.6–4.2)	0.67 (0.0.60–0.72)	This study
	Saltmarsh	2.8[a] (2.1–4.3)	0.24 (0.11–0.42)	
	Saltmarsh	1.4[b]		Rogers et al. (2005b)
Rhyll, Westernport Bay	*A. marina*	7.7[a] (4.7–9.8)	0.42 (0.33–0.52)	This study
	Saltmarsh	2.3[a] (1.2–3.8)	0.23 (0.10–0.41)	
	Saltmarsh	2.5[b]		Rogers et al. (2005b)
Corinda Creek, Westernport Bay	Saltmarsh	(2.7–2.9)[a]		Lewis et al. (2019)
Terranora, Tweed River	*A. marina*	5.5[a] (2.1–8.3)		Marx et al. (2020)
Southern Moreton Bay, Brisbane	*A. marina*	4.2–6.7[a]	NA	Sanders et al. (2016)
Firth of Thames, New Zealand	*A. marina:*		NA	Swales et al. (2015)
	Upper	(7–12)[a]		
	Intermediate	(33–100)[a]		
	Basal	(10–22)[a]		
Global Mean	Mangrove[b]	2.8 mm/y	NA	Breithaupt et al. (2012)
Common Values	Mangrove[b]	7.7 (1.0–36)	0.45	Arias-Ortiz et al. (2018)
	Saltmarsh[b]	6.2 (0.7–42)	0.43	

[a]*Denotes values derived from constant rate of supply (CRS) model,* [b]*denotes values derived from constant initial concentration (CIC) model.*

was also undertaken using time-series aerial photograph analysis, as described below.

Sedimentation, Surface Elevation Gain, and Accommodation Space

As the CRS model accounts for variation in volume and mass of sediment accumulated over time, it provided the opportunity to assess changes in sedimentation rates over time on the basis of the age and depth of each sediment sample, as per Rogers et al. (2019). Change point detection was applied using JMP statistical software when a change in sedimentation trajectories was evident; peaks in sedimentation were interpreted in the context of available accommodation space.

Reconstructing surface elevations requires information about the elevation of the contemporary substrate surface, compaction associated with core extraction, and post-depositional autocompaction. The elevation of the contemporary substrate surface was determined at the time of core extraction using an RTK-GPS, and compaction associated was core extraction was quantified. To account for post-depositional autocompaction, we adapted the relationship established by Rogers and Saintilan (2021) between autocompaction and vertical accretion at Westernport Bay (see **Supplementary Data 1**, **Supplementary Figure 1**, and **Supplementary Table 2**). Autocompaction was modeled to be linearly related to sedimentation (r^2 = 0.82), with approximately 80% of deposited sediment within a year undergoing post-depositional autocompaction, resulting in 20% of annual sedimentation volume contributing to surface elevation gain. This relationship was applied to sedimentation rates at each time step to determine the rate of autocompaction. The rate of surface elevation change was established from the difference between the rates of sedimentation derived from ^{210}Pb analyses and autocompaction. The rate of surface elevation change was time-adjusted to determine the total surface elevation change between each time step, and absolute surface elevations were reconstructed using total surface elevation change between each time step. Mean rates of surface elevation change were determined by applying linear regression analysis to reconstructed surface elevations.

Standardized Rates of Surface Elevation Change

The upper boundary of accommodation space at the time of core extraction was determined by applying the tidal amplification factor to the modeled trend in maximum monthly water levels at each study site. Available accommodation space was defined as the vertical space between the upper boundary of accommodation space and the surface elevation at the time of core extraction. Mean rates of surface elevation gain within mangrove and saltmarsh cores at each study site were

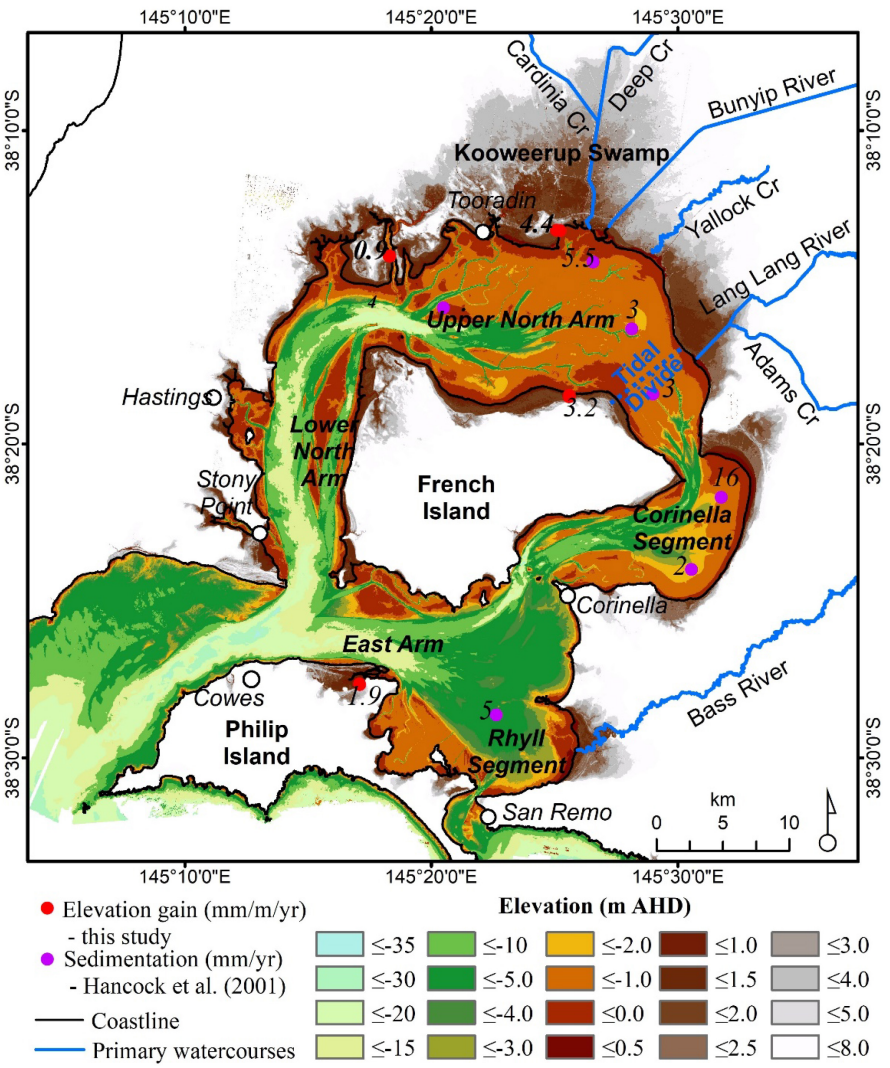


FIGURE 8 | Elevation and bathymetry of Westernport Bay, water circulation, and sedimentary basins in the Upper North Arm, Corinella Segment, and Rhyll Segment. Sedimentation rates detected in this study and within the sedimentary basins by Hancock et al. (2001) also indicated.

subsequently plotted against available accommodation space. As tidally-borne sedimentation is presumed to be negligible at the upper boundary of accommodation space, surface elevation change was also presumed to be negligible. Whether substrate elevations adjusted across the intertidal zone according to a linear or peak model relationship has received consideration globally and at this location (Kirwan and Megonigal, 2013; Mogensen and Rogers, 2018; Rogers and Saintilan, 2021). Quantifying sedimentation at multiple positions across the intertidal zone using lead-210 activity was not feasible due to the resources required to undertake this across the expanse of Westernport Bay. This limited the capacity to determine the behavior of substrate elevations at each study location and it was subsequently assumed that substrate elevations behaved linearly. On this assumption, linear regression analyses that passed through the origin were applied at each study site. A standardized rate of surface elevation gain per meter of available accommodation space was also determined at each study site. These standardized rates were used to determine whether a change in tidal position and shoreline change had occurred over the observational record when sea level was rising in the order of 3 mm year^{-1}. Under these conditions of SLR, it was expected that surface elevations would asymptote toward a depth below the upper boundary of accommodation space where rates of surface elevation gain correspond to rates of SLR, termed equilibrium accommodation space. At depths below the upper boundary of accommodation space where rates of surface elevation gain exceed rates of SLR, infilling will continue, tidal position should increase and shoreline progradation would occur over extended periods of time. Mangrove and saltmarsh distribution is expected to change accordingly, with seaward expansion of mangroves occurring where rates of surface elevation gain exceeds rates of SLR.

Where rates of surface elevation gain do not exceed rates of SLR at any tidal position, even when there is ample available accommodation space, tidal position will decrease and shoreline retreat will eventually occur. Mangrove expansion into the saltmarsh would also occur where surface elevation gain was less than SLR. Standardized rates of surface elevation gain were specifically used to estimate rates of surface elevation gain at MTL and MHWS. These elevations were selected as they approximate the lower boundary of mangrove vegetation and the lower boundary of saltmarsh vegetation. Changes in tidal position were subsequently projected as the difference between the observed rate of surface elevation gain and SLR: a deficit between surface elevation gain and SLR indicates retreat, whilst a surplus indicates progradation.

Time-Series Shoreline Analyses

Comparison of changes in shoreline position from aerial photography provides the capacity to confirm projections of changing tidal position and shoreline change. Observed patterns of vegetation change were delineated at each study site by mapping mangrove and saltmarsh distribution changes from historic and contemporary aerial photography that approximated the period of tide-gauge data collection (i.e., 1981–2017). The best available contemporary imagery was pre-processed orthophotography from 2009 provided by the Victorian Government. The best available historical color aerial photographs were captured at a resolution of 1:15,000 in 1973/4 near the commencement of tide-gauge data collection (**Supplementary Table 2**). These were scanned at 600 dpi and georectified against the contemporary orthophotography using a projective transformation. Each georectified image was merged into a single mosaic for each study site. This imagery was visually digitized to delineate the lower mangrove boundary (presumed to be near MTL), the boundary between mangrove and saltmarsh vegetation (presumed to be near MHWS), and the landward boundary of intertidal vegetation [presumed to be near highest astronomical tide (HAT)]. Lateral changes in the position of MTL and MHWS were subsequently measured within the vicinity of core extraction sites to establish the direction and extent of vegetation distribution changes. Changes in vegetation distribution that corresponded to projected vegetation changes served to validate standardized rates of surface elevation gain.

Implications of Projected Sea-Level Rise on Equilibrium Accommodation Space and Coastal Wetland Distribution

Following validation of standardized rates of surface elevation gain against observed changes in vegetation distribution, the resilience of each study site was projected under two different SLR scenarios that represent end-members of future scenarios: (i) the projected median rate of SLR for a low SLR scenario at ∼2100 (i.e., SSP1-2.6 = 5.2 mm year^{-1} (4.4–6.2 likely range); and (ii) the projected median rate of SLR for a high SLR scenario at ∼2100 (i.e., SSP5-8.5 = 12.2 mm year^{-1} (8.8–17.7 likely range) (Fox-Kemper et al., 2021). The equilibrium accommodation space was specifically quantified as the accommodation space where the rates of surface elevation gain and SLR corresponded under each SLR scenario. This was also assessed by estimating changes in tidal position on the basis of the difference between surface elevation gain at MTL and MHWS and projected rates of SLR; a deficit was presumed to indicate shoreline retreat, whilst a surplus was presumed to indicate progradation.

RESULTS

Tides and Accommodation Space

Minimum, mean, and maximum monthly tide levels increased at rates of 5.4 ± 0.7, 3.0 ± 0.4, and 2.0 ± 0.8 mm year^{-1}, respectively (**Figure 2A**) over the period 1981–2017. The observed rise in MTL was later used to consider the resilience of each study site to observed rates of SLR.

Observed daily maximum tide level within the mangrove and saltmarsh at each study site calibrated well against maximum water levels at Stony Point when amplification factors were applied (**Supplementary Figure 2**). Optimal amplification factors were estimated to be 0.2 m at French Island, 0.35 m at Kooweerup, 0.15 m at Quail Island, and 0.05 m at Rhyll. These amplification factors are reasonably consistent with hydrodynamic modeling of tidal amplification around Westernport Bay (Water Technology, 2014b). No significant difference between observed and modeled water levels (**Figures 2B–E**); however, greater deviation occurred at French Island (p = 0.7144, r^2 = 0.6311) and Kooweerup (p = 0.1408, r^2 = 0.6342) than Quail Island (p = 0.7796, r^2 = 0.8556) and Rhyll (p = 0.4278, r^2 = 0.7447). The deviation at French Island is most prominent in the saltmarsh and likely relates to pooling of tides within abandoned ponds previously used for salt production. The upper boundary of accommodation space was subsequently modeled at each study site based on the linear trajectory of daily maximum tide level plus the tidal amplification factor for the relevant site.

Sediment Characterization

Sediment analyses established that sediments comprised of both mineral and organic matter fractions, and confirmed that bulk density varied down core and was synchronous with variation in carbon content (**Figure 3**). Organic matter fractions were typically highest in the surface strata; however, peaks in carbon were also evident in other strata. Bulk density ranged between 0.32–0.62 g cm^{-3} with a mean of 0.44 ± 0.10 g cm^{-3}, whilst carbon ranged between 0.1–0.3 g cm^{-3} with a mean value of 0.02 ± 0.01 g cm^{-3}. Sediments were largely comprised of sand and silt fractions with mean grain sizes ranging between 26 and 96 μm. Mean grain size was higher in the saltmarsh than mangrove zones at Kooweerup and Rhyll, and was consistently high in both zones at Quail Island and French Island. The predominance of sand in some cores confirmed the need to concentrate the mineral fraction of sediments to <63 μm prior to undertaking ^{210}Pb analyses. In addition, sediment variably comprising of mineral and organic fractions supported assumptions that the CRS model, which determines

sedimentation rates on the basis of the sediment composite, would improve the accuracy of sedimentation rates.

Lead-210 Activity and Chronology

Lead-210 activity and modeled sediment ages using the CRS and CFCS models confirmed decay of unsupported ^{210}Pb activities against depth, as indicated in **Figure 4**. Outliers were excluded from age calculations and the three identified outliers were limited to mangrove sediments at Quail Island and Rhyll.

Sedimentation, Surface Elevation Gain, and Accommodation Space

For all cores, except the mangrove cores at Kooweerup and Rhyll, incremental rates of sedimentation derived from ^{210}Pb chronologies corresponded to rates of vertical accretion derived from nearby MH over the same time period (**Figure 5**). For mangrove cores at both Kooweerup and Rhyll, rates of sedimentation derived from ^{210}Pb chronologies were approximately twice the amount detected using the MH technique; these differences may arise from known limitations associated with determining accretion using MH, which are prone to bioturbation, erosion, and dispersal. General agreement between sedimentation rates derived from ^{210}Pb chronologies and MH data provided confidence in both estimates of vertical accretion derived from MH and sedimentation using ^{210}Pb chronologies.

Sedimentation rates ranged between a maximum of 15 ± 0.88 mm year^{-1} in the mangrove zone at Kooweerup to a minimum of 1.2 ± 0.34 mm year^{-1} in the saltmarsh zone at Rhyll. Sedimentation rates were typically higher in mangrove cores than saltmarsh cores at each study site but exhibited differences between sites. Deceleration of sedimentation was evident over the past 40–60 years in the mangrove and saltmarsh at French Island and Kooweerup, and the saltmarsh at Quail Island and Rhyll (**Figures 5A–D,F,H**). In all saltmarsh cores, deceleration followed an initial period of acceleration in sedimentation. Change point detection confirmed this same pattern in sedimentation occurring within all saltmarsh cores. The inflection between phases of acceleration and deceleration in saltmarsh cores occurred in the mid-20th century between 1951 (Quail Island) and 1975 (French Island). Contrasting other cores, acceleration in sedimentation was evident over the past 100 years in the mangrove at Rhyll (**Figure 5G**), and sedimentation rates remained relatively stable in the mangrove at Quail Island (**Figure 5E**). Given the considerable temporal variability in sedimentation, mean rates have not been reported as they provide little indication of realistic sedimentation over time.

Reconstruction of surface elevations with respect to accommodation space at each study site provides additional context to the conditions under which patterns of acceleration and deceleration occurred (**Figures 6A–D**). Deceleration was associated with surface elevations increasing and accommodation space becoming increasingly limited; that is surface elevations were higher in the tidal frame when sedimentation rates decelerated. Surface elevations, particularly in the mangrove and saltmarsh at French Island and Kooweerup (**Figures 6A,B**), were approaching the maximum elevation of inundation, and sedimentation was likely facilitated by high rates of sediment supply at these locations combined with lower hydrodynamic energy, as indicated in various models (Harris et al., 1979; Water Technology, 2014a). As accommodation space becomes increasingly limited in the saltmarsh, negative feedbacks between sedimentation and inundation, evident by consistent patterns of initial acceleration and subsequent deceleration, may indicate transition toward a dynamic equilibrium of surface elevations with respect to available accommodation space. In contrast, the mangrove at Rhyll has undergone relatively rapid accumulation of sediment as considerable accommodation space remains available and substrates continue to transition to higher intertidal positions (**Figure 6D**).

Standardized Rates of Surface Elevation Gain

Rates of surface elevation gain per unit of available accommodation space were highest at Kooweerup (4.37 mm m^{-1} year^{-1}), followed by French Island (3.18 mm m^{-1} year^{-1}), Rhyll (1.92 mm m^{-1} year^{-1}), and Quail Island (0.93 mm m^{-1} year^{-1}) (**Figures 6E–H**). These rates of surface elevation gain influenced the position at which elevation gain matched SLR; as such, this occurred at a higher position in the tidal frame where there was less available accommodation space at Kooweerup (**Figure 6F**), whilst there was no location within the vegetated intertidal zone at Quail Island (**Figure 6G**) where rates of surface elevation gain matched observed or projected SLR scenarios.

Based on current rates of SLR of 3.0 mm year^{-1}, it was estimated that equilibrium occurred where there was 0.7 m of available accommodation space at Kooweerup, 0.9 m at French Island and 1.6 m at Rhyll (**Table 1**). The depth below the upper boundary at which equilibrium occurred at Quail Island was 3.2 m. It is noted this is below MTL and not within the vegetated intertidal zone. The equilibrium available accommodation space, or depths below the upper boundary where the rate of surface elevation gain matched the rate of SLR, transitioned to lower elevations as the rate of SLR increased. Standardized rates of surface elevation gain were used to estimate rates of surface elevation gain at MTL and subsequently compared to observed rates of SLR to indicate whether shoreline building processes were significant; if so, it was expected that shoreline progradation would be evident within aerial photography.

Time-Series Shoreline Analyses

Changes to shoreline position, inferred from time-series analysis of vegetation distribution changes, validated projected changes to shoreline position. More specifically, at Kooweerup and French Island, as rates of surface elevation gain at MTL (**Table 1**) exceeded observed rates of SLR, shoreline progradation was projected, and this corresponded to observations of seaward mangrove expansion between 1973/74 and 2009. Progradation of the seaward mangrove boundary was in the order of ∼20 m quantified immediately seaward of the mangrove core at Kooweerup, and up to 80 m immediately east of the mangrove

core (**Figure 7B**). Similarly, at French Island shoreline retreat was not evident within the immediate proximity of cores and progradation of up to 20 m was evident by seaward expansion of the mangrove canopy (**Figure 7A**). Infilling of the tidal creek immediately adjacent to the mangrove core at Rhyll may indicate progressive infilling between 1973 and 2009 or may be related to increasing mangrove crown sizes. Infilling would be associated with higher rates of surface elevation gain than was projected using standardized rates of surface elevation gain. As the elevation of MTL coincides with the position of equilibrium accommodation space, stability was projected, and this corresponds to the stability of many of the shorelines at the margins of the inlet (**Figure 7D**).

The change in position of the seaward limit of mangrove vegetation at Quail Island, within the vicinity of the mangrove core, was less than 4 m (**Figure 7C**). This very modest increase likely relates to the increasing crown size as trees matured along the shoreline. Mature crown sizes along the shoreline were evident in 2009 imagery, and there was an absence of juvenile mangroves seaward of the mature trees. Low rates of sedimentation and surface elevation gain at Quail Island indicated that retreat may be expected, but it is probable that this could be delayed given the maturity and resilience of mangrove trees along this shoreline.

As the equilibrium elevation at all locations was projected to be below MHWS, landward encroachment of mangrove into saltmarsh was projected and this was confirmed at all study sites. Whilst the degree of lateral encroachment is dependent upon the slope of the saltmarsh, it remains informative that the degree of lateral encroachment is lower where standardized rates of surface elevation gain were higher (i.e., <5 m lateral encroachment at French Island, 5 m at Kooweerup) and more pronounced where rates were lower (i.e., 12 m at both Quail Island and Rhyll).

Implications of Projected Sea-Level Rise on Equilibrium Accommodation Space and Coastal Wetland Distribution

Under a low projected SLR scenario, shoreline progradation may continue at Kooweerup and French Island; however, despite high rates of sediment supply and deposition, shoreline resilience will not be maintained under a high SLR scenario (**Table 2**). At Rhyll and Quail Island, shoreline retreat is anticipated under all projected SLR scenarios. As the rate of surface elevation gain at MHWS is less than median projected rates of SLR at all study sites, mangrove encroachment of saltmarsh is likely, and saltmarsh will become increasingly restricted to elevations beyond their contemporary distribution.

DISCUSSION

Sedimentation, Surface Elevation Gain, and Accommodation Space

Sedimentation rates ranged from 1.2 to 15 mm $year^{-1}$ and at each study site sedimentation rates were typically higher where there was more accommodation space (i.e., in the mangrove zone) than where accommodation space was becoming exhausted (i.e., in the saltmarsh). Acceleration in sedimentation rates at each core location occurred when more vertical accommodation space was available whilst deceleration occurred when surface elevations were high in the tidal frame and accommodation space was becoming limited. High sedimentation rates and acceleration in sedimentation was dependent upon rates of sediment supply and favorable conditions for deposition, with mean deposition rates found to be highest at Kooweerup, followed by French Island, Rhyll, and Quail Island (**Table 3**). By accounting for autocompaction of sediments, standardized rates of surface elevation gain were established; critically, these rates were different between study sites, indicating significant variation in hydrodynamic energy, sediment supply, sedimentation, and surface elevation gain across Westernport Bay.

A range of factors may influence the spatial variation in the observed relationship with sedimentation. Sediment supplied to Westernport Bay largely arises from hillslope, gully, and riverbank erosion occurring in the sub-catchments located on the northeastern shorelines of Westernport Bay (Bunyip River, Cardinia Creek, Lang Lang River, Yallock Creek, and Bass River) and is reportedly in the order of 156 kt $year^{-1}$ (Hughes et al., 2003). Of this supply, approximately 96 kt $year^{-1}$ is estimated to be exported from catchments to Westernport Bay for deposition. Suspended sediment and bedload yields have been modeled using the Revised Universal Soil Loss Equation (RUSLE). Sediment yield was reported to be greatest from Lang Lang River (0.47 t ha^{-1} $year^{-1}$), Bass River (0.30 t ha^{-1} $year^{-1}$) and Bunyip River (0.25 t ha^{-1} $year^{-1}$), and least for Yallock Creek (0.21 t ha^{-1} $year^{-1}$) and Cardinia Creek (0.15 t ha^{-1} $year^{-1}$). Bedload export is reported to be greatest from Bunyip River (0.18 t ha^{-1} $year^{-1}$), Lang Lang River (0.14 t ha^{-1} $year^{-1}$) and Bass River (0.08 t ha^{-1} $year^{-1}$), and least for Yallock Creek (0.07 t ha^{-1} $year^{-1}$) and Cardinia Creek (0.05 t ha^{-1} $year^{-1}$) (Hughes et al., 2003). The Bunyip River, has the largest sub-catchment area (890 km^2) and contributed the greatest bedload yield; however, suspended sediment yield was greatest from the Lang Lang River which has a markedly smaller sub-catchment area (423 km^2). These differences may arise from the varying degrees of hillslope, bank, and gully erosion in each of the sub-catchments. Despite high bedload and suspended sediment supply from these tributaries, it is not sufficient to offset the prolonged erosion of peats and shoreline retreat occurring where these tributaries enter Westernport Bay. Fetch-based waves generated by prevailing westerly winds ensure that the northwestern shoreline remains a source of sediment and contributes to subaerial sedimentation. Accordingly, active cliff erosion occurs due to direct exposure to wave action during high tides and storms (Water Technology, 2014b).

Analyses of subaerial sediment redistribution within Westernport Bay confirm movement of sand and mud along the Upper North Arm toward depositional basins within the vicinity of the French Island and Kooweerup study sites (Harris et al., 1979), where deposition is reported to be approximately 55 mm $year^{-1}$ (Hancock et al., 2001). Sediment supply to Rhyll is limited by the prevailing transport of sediment away from Rhyll and along the Eastern Arm to the depositional

basin east of Rhyll Inlet, where deposition is reported to be 50 mm year^{-1}. Bathymetry along the Upper North Arm indicates that lateral accommodation space suitable for shoreline progradation is broad and low gradient mudflats dominate seaward of the latter sites (**Figure 8**). Indeed, recent imagery confirms active colonization of mudflats at Kooweerup and French Island and provides additional evidence of progradation (**Figure 7**). Sediment supply to the Quail Island study site is dependent upon the limited supply of sediment from catchments entering the western side of the bay or supply from Cannons Creek. Prior hydrodynamic modeling (Lee, 2011; Water Technology, 2014a,b) indicates conditions that promote sediment transport occur along Cannons Creek, the channel immediately adjacent to the Quail Island study site, whilst low energy hydrodynamic conditions prevail at Kooweerup and French Island. Given these restrictions on sediment supply to the eastern shoreline of Quail Island and high hydrodynamic energy, it is not surprising that observed sedimentation rates were low at this location. However, analyses of shoreline change at Quail Island indicate that progradation has been occurring in the reaches of the Upper Arm where lateral accommodation space remains available and sediment supply is not restricted by higher hydrodynamic energy. Conversely, high sedimentation rates at the remaining sites were facilitated by favorable hydrodynamic conditions and higher rates of sediment supply.

Rates of sedimentation reported in this study are reasonably high and, in most cases, well-beyond the average rates reported for mangroves (Breithaupt et al., 2012), but within the range observed elsewhere (Arias-Ortiz et al., 2018) (**Table 3**). The pattern of acceleration in sedimentation, followed by deceleration is consistent with analyses at Firth of Thames, New Zealand (Swales et al., 2015), where excess sediment facilitated rapid infilling of accommodation space and active mangrove colonization and progradation. Given the established relationship between accommodation space, sediment supply and sedimentation rates, we suggest that comparison of sedimentation rates from one site with another site is meaningless without also controlling for available accommodation space. Whilst comparisons within an ecosystem type (i.e., comparing saltmarsh rates from one location to another) partly recognizes the influence of accommodation space on sedimentation, it may not be sufficient when ecosystems occupy a large proportion of vertical accommodation space. In particular, mangrove forests dominated by *A. marina* occupy a larger vertical range of available accommodation space than saltmarsh and should exhibit greater variation in sedimentation rates. This was confirmed in this study by higher peaks in sedimentation within mangrove cores than saltmarsh cores.

Despite relatively high rates of sedimentation, particularly at Kooweerup and French Island, we demonstrate that this is likely to have translated to relatively modest rates of surface elevation gain. By converting sedimentation rates into rates of surface elevation gain by adjusting for autocompaction (following Rogers and Saintilan, 2021), we were able to reconstruct surface elevations through time. Comparisons with shoreline change in aerial photography provided some confidence that reconstructions of surface elevation were valid. Validation of ^{210}Pb chronology is typically undertaken against chronologies derived from alternative radiometric approach, such as using ^{137}Cs concentrations; however, given the relatively short half-life and decreasing availability of ^{137}Cs, particularly in the southern hemisphere where concentrations were initially low, efforts have now been directed toward validation using other approaches. ^{14}C bomb-pulse analyses have been successfully applied to validate ^{210}Pb chronology at other locations in southeastern Australia (Sanders et al., 2016; Marx et al., 2020). Given reductions in ^{137}Cs activity, the validation approach undertaken in this study using SET-MH data and shoreline analyses from aerial photography represent reliable alternative validation approaches. This validation provides sufficient confidence to consider the combined implications of SLR and sediment supply for shoreline resilience.

Implications for Resilience of Coastal Wetlands to Sea-Level Rise

The mid- to late-Holocene sea-level history for this region is one of considerable stability with evidence indicating sea level was near present levels or up to 2 m higher since about 7 ka (Sloss et al., 2007; Lewis et al., 2013; Dougherty et al., 2019). Under these conditions of relatively stable sea levels for a sustained period, surface elevations would increase toward maximum water levels, or may exceed maximum water levels if sea level fell over the previous millennia. Substrates beyond the vertical range of accommodation space would continue to increase elevation with terrigenous sediment being supplied overland and/or facilitated by organic production within substrates, as theorized by Allen (2000). Vertical accommodation space would become increasingly limited and sedimentation would occur laterally, resulting in shoreline progradation. The broad low-lying swamps and fringing marshes of Westernport Bay at elevations less than 8 m, particularly near Kooweerup Swamp, suggest this mode of shoreline evolution (**Figure 8**).

Recent observed SLR has created new vertical accommodation space, and this study has confirmed that sedimentation was related to accommodation space over the past century. At all locations, sedimentation rates in the saltmarsh, where accommodation space was limited, closely corresponded to observed rates of SLR at the nearest tide gauge for the period 1981–2017, indicating that substrates asymptote toward elevations below maximum tide level that support saltmarsh. Mangrove cores exhibited sedimentation rates, in some cases, well beyond observed rates of SLR, implying ongoing infill of accommodation space and progradation, although this is likely to be at a slower rate than occurred under stable sea-level conditions. Shoreline analyses of the lower and upper limits of intertidal vegetation and the mangrove-saltmarsh transition confirmed sediment supply and ensuing sedimentation were relatively high at Kooweerup, French Island, and Rhyll. However, this pattern of accommodation space infill only remains possible should anticipated rates of SLR by 2100 remain low.

Numerous studies indicate that substrate elevation changes peak at positions across the intertidal zone where both the

addition of organic material from vegetation and sediments are high (Morris et al., 2002; Temmerman et al., 2003; Kirwan and Megonigal, 2013); and there is evidence from Westernport Bay that peak models may provide an improved representation of the relationship between rates of surface elevation gain and accommodation space (Rogers and Saintilan, 2021). The ability to quantify the behavior of surface elevation gain across the intertidal zone at each study site was limited due to the resource intensive nature of determining sedimentation rates and rates of surface elevation gain using ^{210}Pb-dating and SET-MH techniques, and analyses were limited to measurements from a single tidal position in the mangrove and saltmarsh at each study site. Accordingly, simple linear regression analyses were applied in this study. The implications of applying a linear model, rather than a peak model is likely to be an over-estimation of the resilience of substrates at higher elevations, that is in the saltmarsh, and potentially an under-estimation of the resilience of lower elevations, that is in the mangrove zone. However, validation of the model against aerial photography provides some confidence that the difference between using linear or peak models may be marginal.

Established linear relationships between sedimentation, surface elevation gain, and accommodation space indicate only positions lower in the tidal frame that are dominated by mangroves (i.e., above MTL and below MHWS) can maintain rates of sedimentation that match or exceed anticipated rates of SLR under a low SLR scenario providing sedimentation remains proportional to accommodation space. Under a high SLR scenario, mangrove shorelines are projected to retreat at all study sites. The outcome of either SLR scenario will be increasing dominance of mangrove as they retreat across substrates that currently support saltmarsh, leading to declines in saltmarsh vegetation extent. The expansion of mangrove into saltmarsh has already been documented along tidal creeks of Westernport Bay (Rogers et al., 2005b; Whitt et al., 2020) and more broadly where mangrove and saltmarsh co-occur in southeastern Australia (Saintilan and Williams, 1999). Should this change in vegetation distribution continue, as our linear relationships between sedimentation, surface elevation gain, and accommodation space imply, the intertidal vegetated platform will develop at an asymptote elevation where rates of surface elevation gain match rates of increase in accommodation space created by SLR. This will result in surface elevations transitioning to elevations that are considerably deeper than current monthly maximum water levels, as proposed by other models (Fagherazzi et al., 2012). Transition of substrates to this asymptote elevation will create conditions suitable for mangrove dominance and considerable landward incursion of tides will eventuate. Decoupling of accretion from inundation has been simulated to occur as a result of mangrove vegetation modulating tidal currents (Xie et al., 2020), and an increase in the dominance of mangrove may hasten this process and further reduce the resilience of higher elevation saltmarshes. As sediment supply and hydrodynamic conditions are variable across Westernport Bay, it is expected that equilibrium elevations will vary with higher asymptote surface elevations developing where sediment budgets are high. Modifications within catchments that alter hydrodynamic conditions and sediment supply will modify relationships between surface elevation gain and accommodation space, and any reductions in sediment deposition will hasten a transition to lower equilibrium elevations.

CONCLUSION

Sedimentation rates reported in this study are beyond threshold rates derived from paleoecological studies of vertical mangrove growth (Saintilan et al., 2020) and vertical adjustment of United Kingdom saltmarshes (Horton et al., 2018); however, it is not anticipated that an equivalent degree of surface elevation gain will occur due to processes of autocompaction. It remains feasible that established mature mangroves can sustain vertical substrate growth providing mineral and organic matter addition is sufficient. Irrespective of the capacity for mangrove vertical growth at rates matching or exceeding SLR, saltmarsh substrates higher in the tidal frame will not be able to sustain the same rates of surface elevation gain due to lower rates of sedimentation. The resilience of saltmarsh will therefore be dependent upon landward space for saltmarsh retreat. There remains considerable low-elevation land at Kooweerup Swamp for saltmarsh retreat (**Figure 8**); though, decisions regarding the management of drains, floodgates, and bund walls are required to ensure tidal inundation occurs. Should engineering works (e.g., ring drains, bund walls, flood gates, buildings, elevated roadways, and culverts) and land-use decisions prevent landward tidal incursion, coastal squeeze of saltmarsh will occur (Rogers et al., 2016). In these circumstances, conservation reserves at French Island and Quail Island will become crucial sanctuaries for the highly diverse saltmarsh communities of Westernport Bay. Mangrove forests will have considerable space to encroach upon existing saltmarsh when SLR accelerates; however, planning decisions and management actions to establish setbacks and protect saltmarsh retreat pathways will be necessary to improve conservation outcomes for saltmarsh.

DATA AVAILABILITY STATEMENT

The raw data supporting the conclusions of this article will be made available by the authors, without undue reservation.

AUTHOR CONTRIBUTIONS

KR, AZ, and NS undertook data collection and analysis. LM led the timer-series mapping. KR led the writing. All authors contributed to the article and approved the submitted version.

FUNDING

The Victorian Government provided financial support to establish this research in 2000 and subsequent funding in 2017 to maintain research continuity and deliver knowledge that assist with management of coastal wetlands of Westernport

Bay. KR received an Australian Research Council Future Fellowship (FT130100532) that provided financial support for measurements and sediment analyses from 2014 to 2018.

ACKNOWLEDGMENTS

We acknowledge the custodians of the Western Port area, the Bunurong (Boonerwrung) people of the Kulin Nation. We recognize the contribution of field and laboratory assistants in undertaking this work; over 20 years of analysis there are too many to mention but we remember every field trip fondly. Special thanks is given to Lawrance Ferns who has supported this research and the Victorian Government who has provided financial support with the initial establishment and recent measurements.

SUPPLEMENTARY MATERIAL

The Supplementary Material for this article can be found online at: https://www.frontiersin.org/articles/10.3389/fmars.2022.807588/full#supplementary-material

REFERENCES

Allen, J. R. L. (2000). Morphodynamics of Holocene salt marshes: a review sketch from the Atlantic and Southern North Sea coasts of Europe. *Q. Sci. Rev.* 19, 1155–1231. doi: 10.1016/S0277-3791(99)00034-7

Anisfeld, S. C., and Hill, T. D. (2012). Fertilization effects on elevation change and belowground carbon balance in a Long Island Sound tidal marsh. *Estu. Coasts* 35, 201–211. doi: 10.1007/s12237-011-9440-4

Appleby, P., and Oldfield, F. (1978). The calculation of lead-210 dates assuming a constant rate of supply of unsupported 210Pb to the sediment. *Catena* 5, 1–8. doi: 10.1016/S0341-8162(78)80002-2

Arias-Ortiz, A., Masqué, P., Garcia-Orellana, J., Serrano, O., Mazarrasa, I., Marbà, N., et al. (2018). Reviews and syntheses: ^{210}Pb-derived sediment and carbon accumulation rates in vegetated coastal ecosystems–setting the record straight. *Biogeosciences* 15, 6791–6818. doi: 10.5194/bg-15-6791-2018

Boon, P. (2011). "Saltmarshes," in *Understanding the Western Port Environent: A summary of current knowledge and priorities for future research*, ed. S. G. O. Victoria (Melbourne: State Government of Victoria, Port Phillips and Westernport CMA, and Melbourne Water).

Breithaupt, J. L., Smoak, J. M., Byrne, R. H., Waters, M. N., Moyer, R. P., and Sanders, C. J. (2018). Avoiding timescale bias in assessments of coastal wetland vertical change. *Limnol. Oceanogr.* 63, S477–S495. doi: 10.1002/lno.10783

Breithaupt, J. L., Smoak, J. M., Smith, T. J. III, Sanders, C. J., and Hoare, A. (2012). Organic carbon burial rates in mangrove sediments: strengthening the global budget. *Glob. Cycles* 2012:26. doi: 10.1029/2012GB004375

Bureau of Meteorology. (2021). *Monthly sea levels for Stony Point* [Online]. Australian Government. Available: http://www.bom.gov.au/ntc/IDO71054/IDO71054SLD.shtml [Accessed 1 september 2021]

Cahoon, D. R., Lynch, J. C., Hensel, P., Boumans, R., Perez, B. C., Segura, B., et al. (2002). High-precision measurements of wetland sediment elevation: I. Recent improvements to the Sedimentation-Erosion Table. *J. Sediment. Res.* 72, 730–733. doi: 10.1306/020702720730

Dougherty, A. J., Thomas, Z. A., Fogwill, C., Hogg, A., Palmer, J., Rainsley, E., et al. (2019). Redating the earliest evidence of the mid-Holocene relative sea-level highstand in Australia and implications for global sea-level rise. *PLoS One* 14:e0218430. doi: 10.1371/journal.pone.0218430

Fagherazzi, S., Kirwan, M. L., Mudd, S. M., Guntenspergen, G. R., Temmerman, S., D'Alpaos, A., et al. (2012). Numerical models of salt marsh evolution: ecological, geomorphic, and climatic factors. *Rev. Geophys.* 50:RG1002. doi: 10.1029/2011RG000359

FitzGerald, D. M., Hein, C. J., Connell, J. E., Hughes, Z. J., Georgiou, I. Y., and Novak, A. B. (2021). Largest marsh in New England near a precipice. *Geomorphology* 379:107625. doi: 10.1016/j.geomorph.2021.107625

Fox-Kemper, B., Hewitt, H. T., Xiao, C., Aðalgeirsdóttir, G., Drijfhout, S. S., Edwards, T. L., et al. (2021). "Ocean, Cryosphere and Sea Level Change," in *Climate Change 2021: The Physical Science Basis. Contribution of Working Group I to the Sixth Assessment Report of the Intergovernmental Panel on Climate Change*, eds V. Masson-Delmotte, P. Zhai, A. Pirani, S. L. Connors, C. Péan, S. Berger, et al. (Cambridge, MA: Cambridge University Press).

Hancock, G. J., Olley, J. M., and Wallbrink, P. (2001). "Sediment transport and accumulation in Western Port: Report on Phase I of a study determining the sources of sediment to Western Port," in *Technical Report 47/01*, (Canberra: CSIRO).

Harris, J., Hinwood, J., Marsden, M., and Sternberg, R. (1979). Water movements, sediment transport and deposition, Western Port, Victoria. *Mar. Geol.* 30, 131–161. doi: 10.1016/0025-3227(79)90010-0

Horton, B. P., Shennan, I., Bradley, S. L., Cahill, N., Kirwan, M., Kopp, R. E., et al. (2018). Predicting marsh vulnerability to sea-level rise using Holocene relative sea-level data. *Na. Comm.* 9, 1–7. doi: 10.1038/s41467-018-05080-0

Hughes, A., Prosser, I., Wallbrink, P., and Stevenson, J. (2003). "Suspended sediment and bedload budgets for the Western Port Bay Basin," in *CSIRO Land Water Technical Report: Technical reprt 4/03*, (Canberra: CSIRO).

Iurian, A., Millward, G., Blake, W., and Hernández, J. A. (2021). Fine-tuning of ^{210}Pb-based methods for dating vegetated saltmarsh sediments. *Q. Geochronol.* 62:101153. doi: 10.1016/j.quageo.2021.101153

Jervey, M. (1988). Quantitative geological modeling of siliciclastic rock sequences and their seismic expression. *SEPM Special Publ.* 1988, 47–69. doi: 10.2110/pec.88.01.0047

Kirwan, M. L., and Megonigal, J. P. (2013). Tidal wetland stability in the face of human impacts and sea-level rise. *Nature* 504, 53–60. doi: 10.1038/nature12856

Kirwan, M. L., Temmerman, S., Skeehan, E. E., Guntenspergen, G. R., and Fagherazzi, S. (2016). Overestimation of marsh vulnerability to sea level rise. *Nature Climate Change* 6, 253–260. doi: 10.1038/nclimate2909

Krishnaswamy, S., Lal, D., Martin, J. M., and Meybeck, M. (1971). Geochronology of lake sediments. *Earth Planet. Sci. Lett.* 11, 407–414. doi: 10.1016/0012-821X(71)90202-0

Kumbier, K., Hughes, M. G., Rogers, K., and Woodroffe, C. D. (2021). Inundation characteristics of mangrove and saltmarsh in micro-tidal estuaries. *Est. Coast. Shelf Sci.* 261:107553. doi: 10.1016/j.ecss.2021.107553

Lee, R. (2011). "Physical and chemical setting," in *Understanding the Western Port Environent: A summary of current knowledge and priorities for future research*, ed. S. G. O. Victoria (Melbourne: State Government of Victoria, Port Phillips and Westernport CMA, and Melbourne Water).

Lewis, C. J. E., Baldock, J. A., Hawke, B., Gadd, P. S., Zawadzki, A., Heijnis, H., et al. (2019). Impacts of land reclamation on tidal marsh 'blue carbon'stocks. *Sci. Total Env.* 672, 427–437. doi: 10.1016/j.scitotenv.2019.03.345

Lewis, S. E., Sloss, C. R., Murray-Wallace, C. V., Woodroffe, C. D., and Smithers, S. G. (2013). Post-glacial sea-level changes around the Australian margin: a review. *Q. Sci. Rev.* 74, 115–138. doi: 10.1016/j.quascirev.2012.09.006

Marx, S. K., Knight, J. M., Dwyer, P. G., Child, D. P., Hotchkis, M. A., and Zawadzki, A. (2020). Examining the response of an eastern Australian mangrove forest to changes in hydro-period over the last century. *Est. Coast. Shelf Sci.* 241:106813. doi: 10.1016/j.ecss.2020.106813

Mogensen, L. A., and Rogers, K. (2018). Validation and Comparison of a Model of the Effect of Sea-Level Rise on Coastal Wetlands. *Sci. Rep.* 8:1369. doi: 10.1038/s41598-018-19695-2

Morris, J. T., Sundareshwar, P. V., Nietch, C. T., Kjerfve, B., and Cahoon, D. R. (2002). Responses of coastal wetlands to rising sea-levels. *Ecology* 83, 2869–2877. doi: 10.1890/0012-9658(2002)083[2869:ROCWTR]2.0.CO;2

Nolte, S., Koppenaal, E. C., Esselink, P., Dijkema, K. S., Schuerch, M., Groot, A. V., et al. (2013). Measuring sedimentation in tidal marshes: a review on methods and their applicability in biogeomorphological studies. *J. Coast. Conserv.* 17, 301–325. doi: 10.1007/s11852-013-0238-3

Oppenheimer, M., Glavovic, B., Hinkel, J., van de Wal, R., Magnan, A. K., Abd-Elgawad, A., et al. (2019). "Chapter 4: Sea level rise and implications for low lying islands, coasts and communities," in *IPCC special report on the ocean and cryosphere in a changing climate*, (Intergovenmental Panel on Climate Change).

Osland, M. J., Feher, L. C., Anderson, G. H., Vervaeke, W. C., Krauss, K. W., Whelan, K. R., et al. (2020). A tropical cyclone-induced ecological regime shift: Mangrove forest conversion to mudflat in Everglades National Park (Florida. USA). *Wetlands* 40, 1445–1458. doi: 10.1007/s13157-020-01291-8

Pethick, J. S. (1981). Long-term accretion rates on tidal salt marshes. *J. Sed. Res.* 51, 571–577. doi: 10.1306/212F7CDE-2B24-11D7-8648000102C1865D

Reef, R., Spencer, T., Moller, I., Lovelock, C. E., Christie, E. K., McIvor, A. L., et al. (2017). The effects of elevated CO_2 and eutrophication on surface elevation gain in a European salt marsh. *Glob. Chang. Biol.* 23, 881–890. doi: 10.1111/gcb.13396

Rogers, K. (2021). Accommodation space as a framework for assessing the response of mangroves to relative sea-level rise. *Sing. J. Tro. Geogr.* 42, 163–183. doi: 10.1111/sjtg.12357

Rogers, K., Boon, P. I., Branigan, S., Duke, N. C., Field, C. D., Fitzsimons, J. A., et al. (2016). The state of legislation and policy protecting Australia's mangrove and salt marsh and their ecosystem services. *Mar. Pol.* 72, 139–155. doi: 10.1016/j.marpol.2016.06.025

Rogers, K., Kelleway, J. J., Saintilan, N., Megonigal, J. P., Adams, J. B., Holmquist, J. R., et al. (2019). Wetland carbon storage controlled by millennialscale variation in relative sea-level rise. *Nature* 567, 91–95. doi: 10.1038/s41586-019-0951-7

Rogers, K., and Saintilan, N. (2021). Processes Influencing Autocompaction Modulate Coastal Wetland Surface Elevation Adjustment With Sea-Level Rise. *Front. Mar. Sci.* 8:879. doi: 10.3389/fmars.2021.694039

Rogers, K., Saintilan, N., and Cahoon, D. (2005a). Surface Elevation Dynamics in a Regenerating Mangrove Forest at Homebush Bay, Australia. *Wetl. Ecol. Manage.* 13, 587–598. doi: 10.1007/s11273-004-0003-3

Rogers, K., Saintilan, N., and Heijnis, H. (2005b). Mangrove encroachment of salt marsh in Western Port Bay, Victoria: the role of sedimentation, subsidence and sea level rise. *Estuaries* 28, 551–559. doi: 10.1007/BF02696066

Rogers, K., Wilton, K. M., and Saintilan, N. (2006). Vegetation change and surface elevation dynamics in estuarine wetlands of southeast Australia. *Est. Coast. Shelf Sci.* 66, 559–569. doi: 10.1016/j.ecss.2005.11.004

Ruiz-Fernández, A. C., Sanchez-Cabeza, J.-A., Serrato de la Pena, J. L., Perez-Bernal, L. H., Cearreta, A., Flores-Verdugo, F., et al. (2016). Accretion rates in coastal wetlands of the southeastern Gulf of California and their relationship with sea-level rise. *Holocene* 26, 1126–1137. doi: 10.1177/0959683616632882

Saintilan, N., Khan, N., Ashe, E., Kelleway, J., Rogers, K., Woodroffe, C. D., et al. (2020). Thresholds of mangrove survival under rapid sea level rise. *Science* 368, 1118–1121. doi: 10.1126/science.aba2656

Saintilan, N., and Williams, R. J. (1999). Mangrove Transgression into Saltmarsh Environments in South-East Australia. *Glob. Ecol. Biogeogr.* 8, 117–124. doi: 10.1046/j.1365-2699.1999.00133.x

Sanders, C. J., Santos, I. R., Maher, D. T., Breithaupt, J. L., Smoak, J. M., Ketterer, M., et al. (2016). Examining 239+ 240Pu, 210Pb and historical events to determine carbon, nitrogen and phosphorus burial in mangrove sediments of Moreton Bay, Australia. *J. Env. Radioact.* 151, 623–629. doi: 10.1016/j.jenvrad.2015.04.018

Sloss, C. R., Murray-Wallace, C. V., and Jones, B. G. (2007). Holocene sea-level change on the southeast coast of Australia: a review. *Holocene* 17, 999–1014. doi: 10.1177/0959683607082415

Smith, J. N. J. J. O. E. R. (2001). Why should we believe 210Pb sediment geochronologies? *J. Environ. Radioact.* 55, 121–123. doi: 10.1016/S0265-931X(00)00152-1

Swales, A., Bentley, S. J., and Lovelock, C. E. (2015). Mangrove-forest evolution in a sediment-rich estuarine system: opportunists or agents of geomorphic change? *Earth Surf. Proc. Landf.* 40, 1672–1687. doi: 10.1002/esp.3759

Temmerman, S., Govers, G., Wartel, S., and Meire, P. (2003). Spatial and temporal factors controlling short-term sedimentation in a salt and freshwater tidal marsh, Scheldt estuary, Belgium, SW Netherlands. *Earth Surf. Proc. Landf.* 28, 739–755. doi: 10.1002/esp.495

Water Technology (2014a). *Western Port Local Coastal Hazard Assessment: Report 04 (R04) – Inundation Hazards*. Melbourne: Melbourne Water.

Water Technology (2014b). *Western Port Local Coastal Hazard Assessment: Report 05 (R05) – Erosion Hazards*. Melbourne: Melbourne Water.

Whelan, K., Smith, T., Cahoon, D., Lynch, J., and Anderson, G. (2005). Groundwater control of mangrove surface elevation: Shrink and swell varies with soil depth. *Est. Coasts* 28, 833–843. doi: 10.1007/BF02696013

Whelan, K. R. T., Smith, T. J., Anderson, G. H., and Ouellette, M. L. (2009). Hurricane Wilma's Impact on Overall Soil Elevation and Zones Within the Soil Profile in a Mangrove Forest. *Wetlands* 29, 16–23. doi: 10.1672/08-125.1

Whitt, A. A., Coleman, R., Lovelock, C. E., Gillies, C., Ierodiaconou, D., Liyanapathirana, M., et al. (2020). March of the mangroves: drivers of encroachment into southern temperate saltmarsh. *Est. Coast. Shelf Sci.* 240:106776. doi: 10.1016/j.ecss.2020.106776

Woodroffe, C. D., and Murray-Wallace, C. V. (2012). Sea-level rise and coastal change: the past as a guide to the future. *Quat. Rev.* 54, 4–11. doi: 10.1016/j.quascirev.2012.05.009

Woodroffe, C. D., Rogers, K., McKee, K. L., Lovelock, C. E., Mendelssohn, I., and Saintilan, N. (2016). Mangrove sedimentation and response to relative sea-level rise. *Annu. Rev. Mar. Sci.* 8, 243–266. doi: 10.1146/annurev-marine-122414-034025

Xie, D., Schwarz, C., Brückner, M. Z., Kleinhans, M. G., Urrego, D. H., Zhou, Z., et al. (2020). Mangrove diversity loss under sea-level rise triggered by bio-morphodynamic feedbacks and anthropogenic pressures. *Env. Res. Lett.* 15:114033. doi: 10.1088/1748-9326/abc122

Yeates, A. G., Grace, J. B., Olker, J. H., Guntenspergen, G. R., Cahoon, D. R., Adamowicz, S., et al. (2020). Hurricane Sandy effects on coastal marsh elevation change. *Est. Coasts* 43, 1640–1657. doi: 10.1007/s12237-020-00758-5

Conflict of Interest: The authors declare that the research was conducted in the absence of any commercial or financial relationships that could be construed as a potential conflict of interest.

Publisher's Note: All claims expressed in this article are solely those of the authors and do not necessarily represent those of their affiliated organizations, or those of the publisher, the editors and the reviewers. Any product that may be evaluated in this article, or claim that may be made by its manufacturer, is not guaranteed or endorsed by the publisher.

Copyright © 2022 Rogers, Zawadzki, Mogensen and Saintilan. This is an open-access article distributed under the terms of the Creative Commons Attribution License (CC BY). The use, distribution or reproduction in other forums is permitted, provided the original author(s) and the copyright owner(s) are credited and that the original publication in this journal is cited, in accordance with accepted academic practice. No use, distribution or reproduction is permitted which does not comply with these terms.

frontiers in Marine Science

ORIGINAL RESEARCH
published: 16 March 2022
doi: 10.3389/fmars.2022.793818

Linkage Between Mangrove Seedling Colonization, Sediment Traits, and Nitrogen Input

*Ziying He[1,2,3], Lingwei Yen[1,2], Hongjie Huang[1,4], Zihao Wang[1,2], Lili Zhao[1,2], Zhonghan Chen[5], Shing Yip Lee[6] and Yisheng Peng[1,2]**

[1] School of Environmental Science and Engineering, Southern Marine Science and Engineering Guangdong Laboratory (Zhuhai), Sun Yat-sen University, Guangzhou, China, [2] Guangdong Provincial Key Laboratory of Environmental Pollution Control and Remediation Technology, Sun Yat-sen University, Guangzhou, China, [3] School of Marine Science, Guangdong Provincial Key Laboratory of Marine Resources and Coastal Engineering, Sun Yat-sen University, Guangzhou, China, [4] Institute of Urban Environment, Chinese Academy of Sciences, Xiamen, China, [5] South China Institute of Environmental Sciences, Ministry of Ecology and Environment, Guangzhou, China, [6] Simon F. S. Li Marine Science Laboratory, School of Life Sciences and Earth System Science Programme, The Chinese University of Hong Kong, Shatin, Hong Kong SAR, China

Mangroves around the world settle along coasts and estuaries, where they usually encounter aquaculture effluent that causes eutrophication and regulates the nitrogen cycle in their ecosystems. Moreover, the physical–chemical features of sediment in mangrove habitats might be altered by coastal wind, waves, and currents more frequently under the condition of increasing extreme climatic events. These events affect the process of colonization/regeneration of mangroves. To study how exogenous nitrogen input and sediment texture affect root system establishment of mangrove propagules and the early growth of seedlings, in turn, we set up a mesocosm experiment to explore the morphological and physiological responses of the root system of two mangroves, i.e., *Kandelia obovata* and *Sonneratia apetala*. We found that the root morphological features of mangrove seedlings mostly showed significant differences across the sediment texture treatment; *K. obovata* seedlings were more intensively influenced than *S. apetala* seedlings. It could be ascribed that the roots of *K. obovata* seedlings were more sensitive to sediment texture than *S. apetala* seedlings. Conversely, the treatment of exogenous nitrogen input showed a slighter even non-significant influence on the root features of mangrove seedlings. These results suggest that the seedlings of *S. apetala* and *K. obovata* performed similarly. In estuaries and coasts featuring eutrophication and various sediment textures, the conservation and restoration of mangroves should consider these conditions to ensure the sustainable development of mangroves.

Keywords: mangrove, nitrogen input, sediment type, seedling root establishment, colonization

OPEN ACCESS

Edited by:
Zeng Zhou,
Hohai University, China

Reviewed by:
Dongdong Shao,
Beijing Normal University, China
Guanglong Qiu,
Guangxi Mangrove Research Center, Guangxi Academy of Sciences, China

***Correspondence:**
Yisheng Peng
pyish@mail.sysu.edu.cn

Specialty section:
This article was submitted to Coastal Ocean Processes, a section of the journal Frontiers in Marine Science

Received: *12 October 2021*
Accepted: *17 February 2022*
Published: *16 March 2022*

Citation:
He Z, Yen L, Huang H, Wang Z, Zhao L, Chen Z, Lee SY and Peng Y (2022) Linkage Between Mangrove Seedling Colonization, Sediment Traits, and Nitrogen Input. Front. Mar. Sci. 9:793818. doi: 10.3389/fmars.2022.793818

INTRODUCTION

Mangroves mainly occur throughout tropical and sub-tropical coastal areas, usually in sheltered estuaries and bays with lower wind and waves energy (Romañach et al., 2018; Friess et al., 2019). These forests provide numerous ecosystem functions and benefits, such as carbon sequestration, storm and wave damping, and marine and coastal biodiversity conservation (Alongi, 2008;

Lee et al., 2014). Despite the ecological importance of mangrove forests, the global area of mangrove forests has presented a continuously decreasing trend. It has been estimated that an annual deforestation rate of 0.16–0.39% of mangrove forests has occurred since the 2000s (Valiela et al., 2001; He et al., 2018). Mangrove forests have undergone degradation and loss by 1646 km^2 globally from 2000 to 2012 (Hamilton and Casey, 2016). Despite continuous mangrove recession throughout the world, over the last two decades, China has observed a resilient trend in which the mangrove area had increased to 34472.14 ha in 2013, achieving a 56.69% increment from 2001 (Fan and Wang, 2017). In general, the worldwide loss of mangroves might be attributed to population growth and social development in the coastal zone (Thomas et al., 2017; Hargan et al., 2020). Recognized for their tremendous and irreplaceable ecological functionalities and services, the restoration of mangroves is currently an issue of considerable interest for ecology and conservation currently (Barbier, 2016).

For the natural reproduction process, mangroves are embellished by their unique viviparous and water-disposal features. Stranded propagules could anchor and grow rapidly under appropriate conditions after ripening and falling from the branches (Rabinowitz, 1978). Mangrove propagules can have a long-distance dispersal through the tide and current. Hence, the early seedling establishment and development of mangroves are regulated by many internal and external factors. The seedling may be affected by drag forces of fluid motion or buried or excavated when transported (Balke et al., 2011, 2014). Different mangrove species may exhibit distinct regenerating and colonizing strategies in accordance with their reproductive traits, which is closely related to their roles and niches in the successional stages of natural mangroves. The anchorage and establishment of seedlings are essentially vital to natural mangrove colonization or artificial restoration on the dynamic and unstable sediments. Mangroves are typical bio-geomorphic ecosystems in which their occurrence is strongly affected by coastal sedimentation dynamics (Kamal et al., 2017). Although mangrove forests usually occur in sheltered coastlines with more tranquil environments, physical conditions, such as sediment deposition, sediment erosion, and the physical components of sediment, can still affect the seedling establishment and even the floral composition of mangrove forests. The early establishment and development of seedling roots are sensitive to the physical composition of sediment in mangroves (Jiang et al., 2008).

In southern China, *Kandelia obovata* is one of the dominant native mangrove species (Sheue et al., 2003). The viviparous propagules of *K. obovata* grow rapidly once they drop into the soft and muddy substrate. Due to the great convenience of collecting and planting propagules directly on the mudflat, *K. obovata* has been highly preferred for many mangrove restoration programs in the past three decades. Another mangrove species usually recommended for restoration is *Sonneratia apetala* Buch.-Ham., which was introduced from Bangladesh to China in 1985 (Ren et al., 2009). Unlike the native and slow-growing *K. obovata*, *S. apetala* is non-viviparous and establishes seedlings on tidal flats *via* seeds released from the ripened fruit (Liao et al., 2004). As an introduced species with high adaptability and fast-growing characteristics, *S. apetala* had been widely planted in southern China for mangrove afforestation programs, and its plantation has expanded to 20.8 km^2 in the last two decades (Yang et al., 2018).

Many studies had previously shed light on the impacts of sediment dynamics, i.e., erosion or accretion of sediment, on the survival and growth of mangrove seedlings (Ellison, 1999; Balke et al., 2013). Therefore, sediment dynamics are crucial when considering the natural dispersal and colonization of mangrove seedlings (Balke et al., 2011). The allocation of root biomass was significantly different, exhibiting resistance to erosion between different sediment types in a mesocosm experiment with two saltmarsh species (Schwarz et al., 2015). The sediment texture may also cause root traits to respond to the inundation of trees (Wang et al., 2015). However, less is known about how sediment texture affects the development of mangrove root systems during the early growth stage.

Three major anthropogenic sources are responsible for the additional nutrient input to mangrove forests, including domestic sewage, agricultural drainage, and coastal aquaculture effluent. Lee (2016) estimated the scale of the C and N influx surrounding the South China Sea and compared it to the C and N input contributed by mangroves. Notably, the nutrients exported by artificial sources are more likely used by decomposers, e.g., microbes and algae, compared with those from mangrove forests, indicating that eutrophication will occur more frequently on the coast, especially where mangrove forests retreat (Lee, 2016). Sun et al. (2020) also verified that persistent aquaculture effluent input would substantially enhance eutrophication levels in mangrove forests. Most nutrients were eventually deposited and accumulated in the mangrove sediment, and the soil total organic carbon (TOC), total nitrogen (TN), and total phosphorus (TP) content increased in mangroves compared to those of unvegetated tidal flats (Sun et al., 2020). Continuous overloading of terrigenous nutrients may pose irreversible impacts on coastal ecosystems, such as temperate saltmarshes and tropical mangroves, resulting in the degradation and loss of existing wetland ecosystems (Ruiz et al., 2001; Lefcheck et al., 2018). Usually, mangrove propagules spread at the margin of the forest and along the tidal creek. The seedlings develop and colonize in the tidal creeks, which are frequently affected by the aquaculture effluent in southern China. The morphological and physiological features of seedling root systems may be sensitive to the additional nutrient input. However, the influence of persistent nutrient input on mangroves during their early growth stage remains vague and challenging. The influence of nutrient input on modifying the patterns of colonization and competition of native/exotic mangroves is still unclear.

In this study, we set up a mesocosm experiment to explore the growth and physiological responses of the propagule root system of two mangrove species, i.e., *K. obovata* and *S. apetala*, which are typically used in mangrove restoration and afforestation programs in southern China. Both the mangrove species had naturalized and dispersed extensively along the coasts. However, whether to plant the fast-growing exotic mangroves or slow-growing native ones, e.g., *S. apetala* vs. *K. obovata* in mangrove restoration programs is still controversial and inconclusive

(Ren et al., 2009). A comparison of their performance in various restoration sites featured by different sediment and nutrient input conditions may give valuable reference for the selection of mangrove species when conducting a restoration program in the future. The effects of sediment physical properties and additional N input on the growth and development of mangrove roots had been examined during their early growth period. It was hypothesized that the exotic *S. apetala* could be more adaptive to sediment texture and N input conditions than *K. obovata* and that the root system of different mangrove species may respond differently to sediment physical properties and N input in accordance with their morphological and physiological traits.

MATERIALS AND METHODS

Collection and Cultivation of Mangrove Propagules

In April 2020, the ripened propagules of *K. obovata* with similar individual lengths and weights were collected from the Pearl River Estuary, southern China. Later in July 2020, the fruits of *S. apetala* were collected in the same place, and seeds were removed from the ripened and softened fruits within 2 weeks. The propagules and seeds were cultivated for 15 days by placing them in nursing trays for acclimation before being planted for the mesocosm experiment. Simulated semidiurnal tides with a daily inundation period of 8 h were also applied to the seedlings according to the nursing process of mangroves described previously by Tam and Wong (1997).

Mesocosm Experiments of Seedling Cultivation

After propagules or seeds were acclimated for 15 days, the seedlings of *K. obovata* and *S. apetala* were then transplanted in three categories of sediment treatments of sand (SA), mud (MU), and a mixture of mud and sand by the volumetric ratio of 1:1 (MI) to test the influence of sediment texture on the growth and root development of mangrove seedlings. The bulk density and sediment mean value of grain size were measured as 1.104 ± 0.253 g·cm^{-3} and 131.73 ± 12.49 μm, 0.823 ± 0.374 g·cm^{-3} and 55.37 ± 8.68 μm, and 0.644 ± 0.208 g·cm^{-3} and 11.54 ± 2.86 μm for SA, MI, and MU, respectively, prior to the experiment. According to the «Report on the State of the Ecology and Environment in China» in the past 5 years,[1] one of the major pollutions in the nearshore sea areas, the major pollution indicator in key spawning grounds, feeding grounds, migration channels as well as in nature reserve areas for key fishery resources were inorganic nitrogen in China. Moreover, the main inorganic nitrogen pollutants in marine aquaculture wastewater was NH_4^+ (Yang et al., 2019; Ding et al., 2020; Liu et al., 2020). Therefore, to evaluate the impact of additional N input on the growth of mangrove seedlings, N as NH_4Cl was added to the seawater of the mesocosm at concentrations of 0 (CK), 10 (N10), and 50 (N50) mg N·L^{-1}. The set N content in seawater referred to the upper limit (10 mg N·L^{-1}, N10) and five times (50 mg N·L^{-1}, N50) the aquaculture effluent discharge in the coastal water of southern China (Li et al., 2013). Salinity in the mesocosm was set to 10 PSU according to the pore water salinity detected randomly *in situ* to meet the conditions of the mangrove in Pearl River Estuary, where the propagules were collected. There were nine tanks for each species in this experiment and divided into three groups for the 20th-, 40th-, and 60th-day cultivation experiment. Each group of tanks was for the three N input treatments, respectively. In each of the three tanks in one group contained seedlings planted in three different texture sediments. To avoid loss of seedlings' death during the experiment, five seedlings were planted in each sediment type. In total, 18 water tanks were used for mesocosm compartments, including two mangrove species, three categories of sediment treatment, and three concentrations of additional N input. Before the cultivation experiment, the seedlings were placed into a pot of 10 cm in height and 10 cm in diameter with different sediment treatments and then placed into the tank containing seawater with different concentrations of additional N input. The mean height of seedlings of *K. obovata* and *S. apetala* were 23.1 and 6.2 cm, respectively. The daily inundation period was unified to 8 h by pumping seawater between the mesocosm tanks and storage tanks with an automatic water pump.

Measurement of Morphological and Physiological Parameters of Mangrove Seedlings' Root

On the 20th, 40th, and 60th day of the cultivation experiment, the seedlings of both mangrove species were randomly chosen from each tank for the data collection process of morphological and physiological traits. Three replications were set up for the sediment and N input treatments. The measured and analyzed parameters of root samples were root respiratory rate, root length, root surface area, root volume, root branch number, root carbon content (TOC), root nitrogen content (TN), porosity (POR), nitrate reductase activity (NR), and moisture content. The specific methods of measurement and analysis were as follows:

Root Morphology Measurement

The WinRHIZO root analyzer equipped with an image capture system and a professional version of WinRHIZOpro 2005b analysis software (Fan Sheng Technology Co., Ltd., Shijiazhuang, China) was used to scan the root surface. When the scanning process was completed, the WinRHIZO root image analyzer was applied to obtain the morphological parameters of the fine roots scanned. The number, diameter, volume, and absorption surface area of fine roots at all levels were directly obtained through the image analysis process. After scanning, the weight of each level of the root system was measured.

Root Physiology Measurement

The *in vitro* root system method was used to measure the fine root respiratory rate. Since there are different levels of fine roots based on the root position in the branching hierarchy of the root system and may have different functions and compositions (Zhang et al., 2021). Therefore, root samples were selected from

[1] http://english.mee.gov.cn

the live fine roots at various levels as much as possible and were oven-dried to constant weight at 65°C. Root samples with a dry weight of 0.05–0.40 g were selected from the live fine roots at various levels and smeared on the fine root section with Vaseline to prevent traumatic breathing. Each fine root was wrapped with soaked filter paper, placed in an aluminum container, and connected to the AZG-300 portable soil/water greenhouse gas monitor (Ao Zuo Ecological Instrument Co., Ltd., Beijing, China) to measure the fine root respiratory rate. The aluminum container was immersed in dark and room temperature water to maintain a temperature similar to that of the soil (Lovelock et al., 2006b). Because the filter paper absorbs and removes CO_2 when measuring the fine root respiratory rate, the filter paper was measured separately as a blank and subtracted from the value of the fine root respiratory rate.

To determine the organic carbon and total nitrogen content of roots, the samples of roots were oven-dried and ground. Then, the organic carbon content and total nitrogen content of roots were measured by a Vario EL CHN autoanalyzer (Elementar Inc., Germany).

The porosity of the root was detected *via* the pycnometer method (Luxmoore et al., 1972; Mei et al., 2009), and the equation for calculation is as follows:

$$\mathrm{POR}(\%) = [(P_{\mathrm{vr}}) - P_{\mathrm{r}}]/[(p + r) - (P_{\mathrm{r}})] \times 100$$

where r refers to the weight of the fresh roots, p refers to the weight of the pycnometer filled with water, P_r refers to the total weight of the fresh roots in the pycnometer filled with water, and P_{vr} refers to the total weight of the fresh roots and the pycnometer filled with water after vacuuming.

To determine the root nitrate reductase activity, the collected root tissue was rinsed in cold tap water and cold deionized water and refrigerated for further use. The tissue was milled with 0.1 M tris buffer (pH 7.5) and 1 mM cysteine. A buffer-tissue ratio of 6:1 was applied. The filtrate was centrifuged at 20,000 g for 20 min, and the supernatant solution was mixed with 1.0 ml of 0.1 M potassium phosphate buffer, 0.2 ml of 0.1 M KNO_3, and 0.5 ml of 1.36×10^{-3} M DPNH. After incubation at 27°C for 20 min, the solutions were diluted with 4 ml of deionized water, and N-1-naphthyl-ethylene diamine hydrochloride reagent was added to the tubes and intensively mixed. Then, the optical density was measured at 540 nm with a spectrophotometer (UV-755B, Shanghai Precision Scientific Instrument Co., Ltd., Shanghai, China; Hageman and Flesher, 1960).

The root samples were oven-dried at 65°C to a constant weight. The ratio between the weight loss of water and the weight of the root sample was calculated as water content.

Statistical Analyses

The data obtained in the experiment were analyzed using IBM SPSS statistic 22.0 software (SPSS Inc., United States). All data were tested for normality and log-transformed if necessary. The differences in growth and physiological parameters of seedlings across different mangrove species, sediment texture, and N input treatments were explored with a three-way analysis of variance (ANOVA). Significant differences among multiple means were determined by the Student–Newman–Keuls (SNK) test at the $\alpha = 0.05$ level. The association of parameters was analyzed by the Pearson correlation test using R software (R Core Team, 2019). Origin (version 8.0) was applied to export graphs. Since the interval of seedlings' sampling was 20 days, the morphological and physiological features of mangrove seedlings did not change obviously between different sampling times in their early growth stage. Hence, the factor of "sampling time" was excluded in the statistical analysis followed.

RESULTS

Responses of Mangrove Seedling Roots to Sediment Texture and N Input

The root morphological features of mangrove seedlings exhibited distinct patterns across different sediment treatments in the mesocosm experiment (**Figure 1** and **Supplementary Table 1**). Seedlings of *K. obovata* and *S. apetala* cultivated in the SA had significantly lower root length, root surface area, root volume, and amounts of roots than those cultivated in MU and MI. Seedlings of *K. obovata* cultivated in SA (6.62%) had a significantly higher root porosity, indicating a more aerial condition in the sediment compared to those cultivated in MI (5.48%), while such pattern was not applied to those of *S. apetala*. The root growth of seedlings cultivated in MU and MI was not hindered compared to seedlings cultivated in SA. However, in terms of physiological features, no significant difference was detected among all sediment treatments except the seedlings of *S. apetala* cultivated in MU exhibited significantly lower root NR activity than those cultivated in SA and MI (**Figure 1 Supplementary Table 1**).

Apart from the patterns of different sediment treatments, the treatments of additional N input had no significant influence on either the morphological or physiological parameters of mangrove seedling roots for *S. apetala*. The same pattern of morphological parameters was also applied to the seedlings of *K. obovata*, while obviously higher root respiratory rate and root NR activity were detected from its seedlings in treatments of CK and N50, respectively (**Figure 2** and **Supplementary Table 1**).

With respect to the morphological and physiological response of two mangrove seedlings, *K. obovata* and *S. apetala*, significant differences were observed between the mangrove species and the interaction of sediment texture and mangrove species (**Supplementary Table 1**). The mangrove species differed significantly in all parameters. Therefore, we analyzed the responses of two mangrove species, *K. obovata* and *S. apetala*, in the treatment of sediment texture and nitrogen input for further results (**Supplementary Tables 2**, **3**). In terms of sediment texture, the morphological traits as root length, the amount of roots, root surface area, and root volume were lower in SA in both mangrove species (**Figure 1**). These parameters were higher in *K. obovata* than in *S. apetala*. The viviparous propagules of *K. obovata* were characterized by their larger size compared to those of *S. apetala*, which could have resulted in

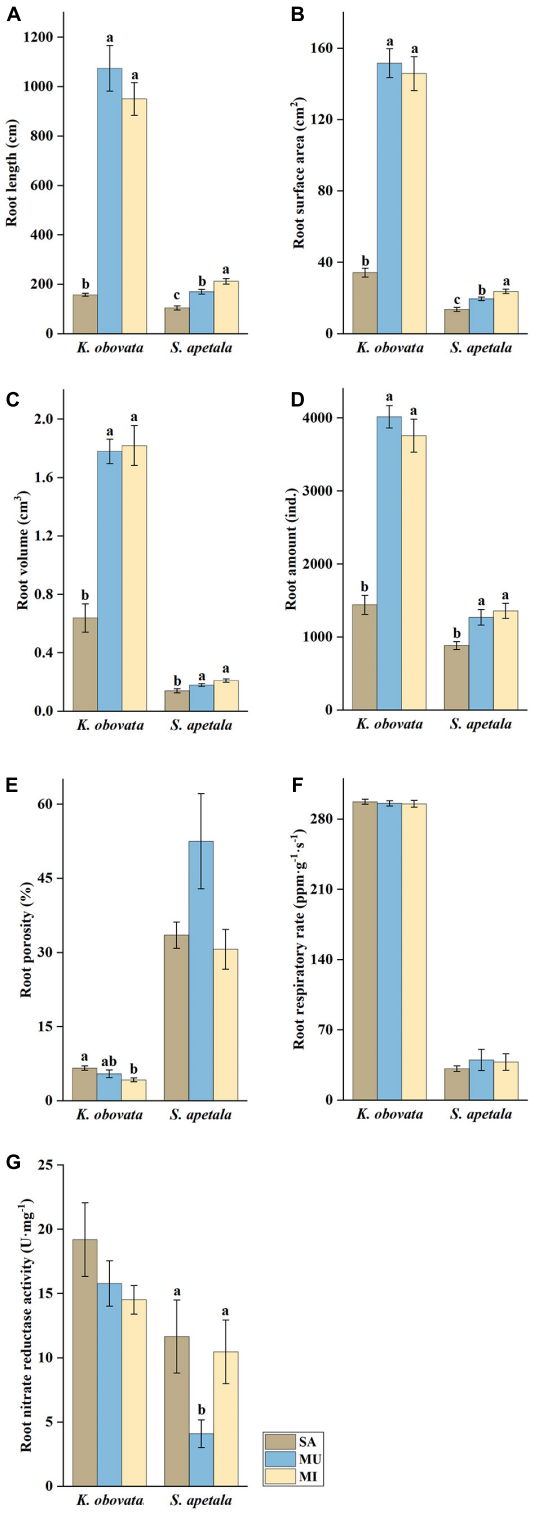


FIGURE 1 | Physiological and morphological root parameters **(A)** root length, **(B)** root surface area, **(C)** root volume, **(D)** amount of roots, **(E)** root porosity, **(F)** root respiratory rate, and **(G)** nitrate reductase activity of mangrove seedlings roots treated with different sediment texture for 60 days in a mesocosm experiment (means ± SE). Different letters indicate significant differences among different sediment textures in one species ($p < 0.05$).

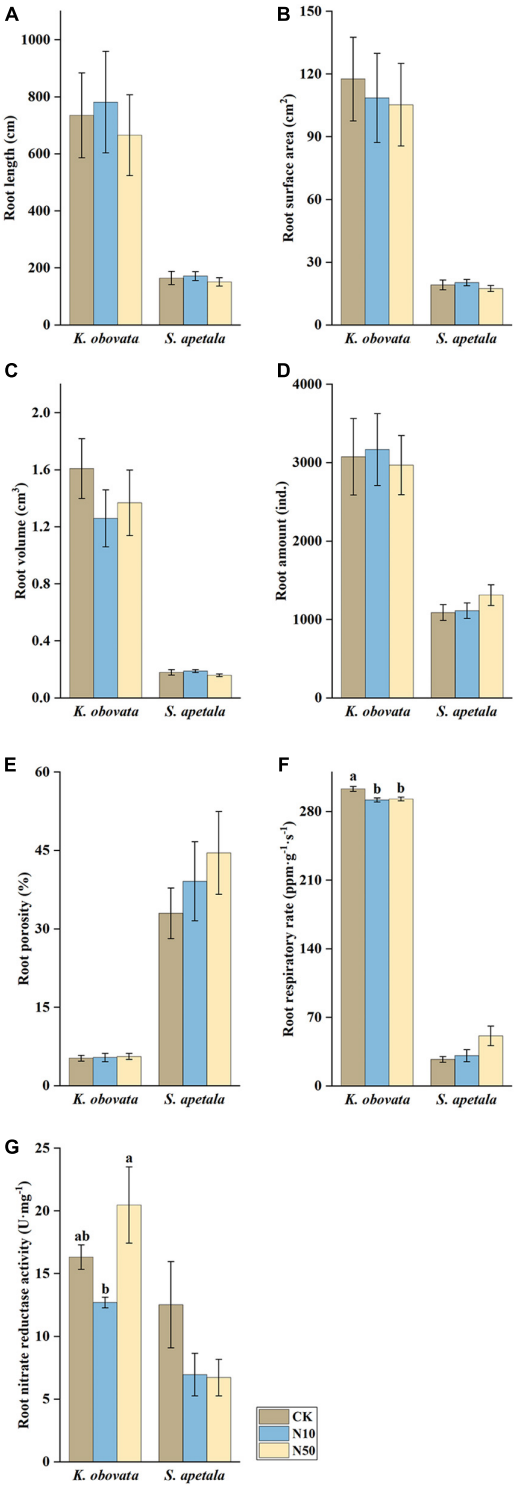


FIGURE 2 | Physiological and morphological root parameters **(A)** root length, **(B)** root surface area, **(C)** root volume, **(D)** amount of roots, **(E)** root porosity, **(F)** root respiratory rate, and **(G)** nitrate reductase activity of mangrove seedlings roots treated with different nitrogen concentrations for 60 days in a mesocosm experiment (means ± SE). Different letters indicate significant differences among different nitrogen concentration treatments in one species ($p < 0.05$).

their higher morphological parameters to meet the demands of early anchorage and colonization after falling onto the dynamic tidal flats. About the physiological features, the root porosity of *K. obovata* seedlings in SA was higher than those in MI, but for the root respiratory rate and root NR activity, they presented no significant difference among the sediment treatments. The root NR activity of *S. apetala* seedlings had the different profile for root porosity and root respiratory rate that root NR activity was higher in SA and MI than in MU. The root respiratory rate of *S. apetala* seedlings showed a similar pattern to *K. obovata* seedlings. In contrast to the root NR activity, the root porosity of *K. obovata* was far lower than that of *S. apetala*, especially in MU sediment, indicating that *S. apetala* seedlings had more physiological adaptability toward the MU treatment than *K. obovata* seedlings. For nitrogen input, except root porosity, both the morphological and physiological parameters of *K. obovata* were higher than those of *S. apetala*. However, the features of *S. apetala* presented no significant difference among nitrogen input treatments, while the root respiratory rate and root NR activity of *K. obovata* showed a significant difference among nitrogen input treatments. The highest root respiratory rate of *K. obovata* was found in the control (CK), which showed a significant difference with other treatments. The lowest NR of *K. obovata* was found in N50.

Regarding the interaction of nitrogen input and sediment texture, no significant interaction between the two treatments for *K. obovata* was detected in all parameters, while there was a significant interaction between the two treatments for root length in *S. apetala*. Although the root length of *S. apetala* did not show a significant difference in different nitrogen inputs, the interaction showed a significant difference, which means that the combination of the two treatments might influence the stability of *S. apetala* seedling roots. Sediment texture and species had a significant interaction on most of the parameters, except root respiratory rate and NR, which indicated different responses for these parameters between the two mangrove species. For root length, the interaction of nitrogen input and sediment texture was only detected in *S. apetala*. The root respiratory rate was affected by nitrogen input only in *K. obovata* (**Supplementary Tables 1–3**).

Correlation Across the Morphological and Physiological Traits of Mangrove Seedlings

A bivariate correlation analysis was applied to explore the common response of morphological and physiological traits to the sediment texture treatment. For *K. obovata*, the root respiratory rate had a significant negative correlation with root length and amount of roots and a significant positive correlation with NR in all sediment treatments. The root respiratory rate was significantly negatively correlated with root surface area in MI and MU but significantly positively correlated with root volume in SA. For the morphological traits of *K. obovata* seedlings, many features were interdependent among treatments. Root length had a significantly positive correlation with root surface area and amount of roots, while root surface area was significantly positively correlated with root volume in the three sediment treatments. However, root volume was negatively correlated with the amount of roots in SA and positively correlated with MU. A significant positive correlation of root surface area with the amount of roots was found in MU and MI but not SA. The root porosity rate had a significant negative correlation with root length and root surface area only in MU. In MU and MI, NR was negatively correlated with the amount of roots, and it was also significantly negatively correlated with root length and root surface area in MI. However, there was no significant correlation of NR with other traits in SA, except for root respiratory rate.

For *S. apetala*, root respiratory rate was not significantly correlated with other traits among sediment treatments. To morphological traits, root length was significantly positively correlated with root surface area, root volume, and amount of roots among sediment treatments. Root surface area had a significant positive correlation with root volume in the three sediment treatments. A significant positive correlation of root porosity with NR was observed in the SA and MI, while the amount of roots had a significant positive correlation with root surface area in SA and MU.

Compared with *K. obovata*, the traits of *S. apetala* seedlings had less significant correlations across all sediment treatments, and most of the correlations were observed for morphological rather than physiological traits. The only significant correlation involved in the physiological traits of *S. apetala* was that NR had a significant positive correlation with root porosity in MI and SA. However, such a correlation was not observed in *K. obovata*. For *K. obovata*, many morphological traits significantly interacted with physiological traits. The seedlings of *K. obovata* exhibited a more sensitive response toward sediment treatments than *S. apetala* (**Figure 3**).

DISCUSSION

Different Responses of Mangrove Seedling Roots to the Treatments of Sediment Texture and N Input Concentration

Root morphology is one of the fundamental indicators for describing the development and growth of plants (Lynch, 1995), and the sediment physical characteristics are key factors that affect root morphology. In this study, root length, root surface area, root volume, and the amount of roots were considered to briefly describe the mangrove seedlings' root morphology in treatments of sediment texture and nitrogen input. The results of root morphological features treated with different sediment textures showed a significant difference. The four morphological features had a less active response in SA treatment than in MU and MI treatments, except for root porosity. There were no significant differences between all sediment textures. Most of the morphological features in SA were less

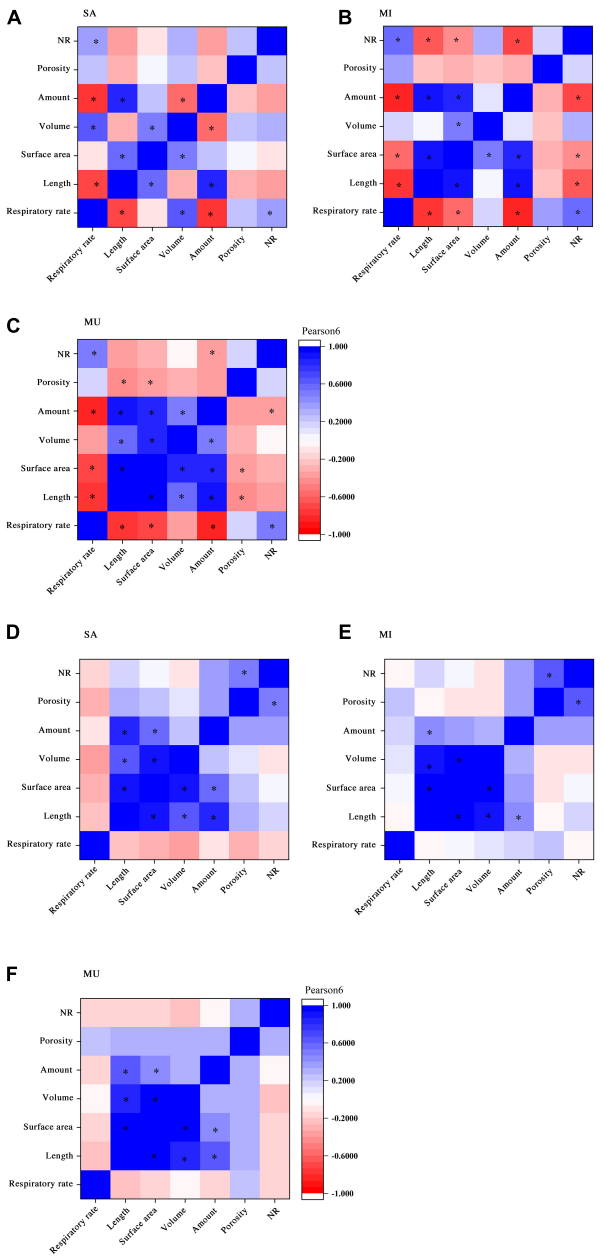


FIGURE 3 | Correlation between parameters of root morphology and physiology in sediment types [sand (SA), mud (MU), and mixture of mud and sand by volumetric ratio of 1:1 (MI)]. Graphs panels **(A–C)** represent the correlation of parameters in *K. obovata*, and graphs panels **(D–F)** represent the correlation of parameters in *S. apetala*. *Indicates a significant difference ($p < 0.05$) among the sediment treatments.

than half of those in MU and MI. The sediment physical characteristics may influence the morphological features of mangrove seedlings' roots, thus modifying the nutrient uptake of plants by affecting their root growth. For instance, the rooted submerged macrophyte *Vallisneria natans* develops thinner and longer roots to facilitate the absorption of nutrients in sediment with more sand (Xie et al., 2005), which is not consistent with our findings. Opposing patterns of root morphological features were observed in another submerged macrophyte, *Myriophyllum spicatum;* the root length decreased in sediment containing more sand (Wang et al., 2009; Bai et al., 2015). It can be inferred that the response of root morphological features to different sediment textures is species dependent. Furthermore, anoxia in sediment may play another key role in root growth and development. Increased sediment anoxic conditions might hamper the growth of roots and cause mortality of shoots in seagrass (Terrados et al., 1999). For mangroves extending along the coastline, mangrove plants are always flooded by the periodical tide, which results in the anoxia of sediment captured and settled by their massive aboveground root systems (Furukawa et al., 1997; Reef et al., 2010). Therefore, anoxic conditions played an important role in root morphology. Plants responded positively along the gradient in redox potential, showing that the emerged marsh plants had morphological responses that affected roots and biomass to meet their oxygen demand under anaerobic conditions (White and Ganf, 2001). For clay loam, similar to MU in our mesocosm experiment, more severe oxygen deficiency was observed compared to SA treatment. Thus, the morphological features of mangroves planted in MU were promoted more than those planted in SA.

In general, due to the high denitrification rate of vigorous microbial activities in anaerobic sediment (Flores-Mireles et al., 2007; Zhang et al., 2020), nitrogen limitation has been manifested to be ubiquitous in most mangroves (Lovelock et al., 2006a). Consequently, mangrove plants are susceptible to external nutrient input. The growth of the root system could be accelerated by moderate nutrient input (Wang et al., 2009; Chen et al., 2020). However, in our study, no significant difference in root features was detected among various levels of nitrogen input. The root development of both mangrove species was not affected by the simulated additional N input at the early growth stage after colonization along tidal creeks, which are frequently impacted by massive aquaculture effluent. Moreover, for the physiological features, including root respiratory rate and NR, there was no significant difference across the treatments of neither sediment texture nor nitrogen input concentration. The fine root respiratory rate obviously correlated to the nitrogen concentration that had been previously attested in terrestrial forests (Burton et al., 2002). Additional fertilization with nitrogen could not markedly enhance the fine root respiratory rate of mangroves. Such physiological responses in mangrove roots were attributed to the availability of physiologically active compounds of nitrogen and the phosphate limitation in soil, which may influence the root respiratory rate (Lovelock et al., 2006b). This interpretation was in line with our findings in the mesocosm experiment. Although mangrove root physiological activities were hindered in sediment with lesser aerated conditions (Lee et al., 1996; Ellison, 1999), the root respiratory rate did not vary across different sediment textures in our experiment. For aquatic macrophytes, root respiratory rates were closely correlated with root porosity, indicating that these plants can actively cope with the anaerobic stress (Lemoine et al., 2012). However, such variation was not

observed in seedlings of *K. obovata* and *S. apetala* during the early growth stage.

Adaptation to Sediment Texture of Different Mangrove Seedlings Was Linked to Their Biological Traits

Sediment texture constructs environmental conditions, such as nutrient availability and oxygen content, affecting the development of roots and colonization by seedlings (Lenssen et al., 1999; Krauss et al., 2014). In our experiment, all analyzed features showed a significant difference between mangrove species, and a species-specific adaptive mechanism of mangroves was at play. On this basis, how mangrove seedlings build up their early root structure in different sediment textures has been investigated. Notably, the sediment texture and mangrove species had a significant interaction with root length, root surface area, root volume, amount of roots, and root porosity.

For root morphological traits of two mangrove species, those of *K. obovata* were collectively higher than those of *S. apetala*. This is highly pertinent to the strategy of colonization presented by their propagules. As *K. obovata* is typically viviparous, characterized by its larger and longer propagules, namely the hypocotyl, a more extensive and robust root system is required in favor of its anchorage on the soft and dynamic tidal flats. In contrast, *S. apetala* is non-viviparous and reproduces numerous tiny and lightweight seeds with smaller and thinner roots. Despite the different root systems of the two mangrove species, they responded similarly to different sediment treatments. A more proliferating root system was found in the muddy sediment with a lower bulk density and finer particle size. The growth of littoral marsh plants might be hampered when cultivated with the soil of a higher bulk density. Plants have to deploy more biomass in proportion to the underground part to ensure the successful colonization of seedlings (Lenssen et al., 1999). Similarly, this finding also applies to the seedlings of mangrove plants in our study.

Compared to *S. apetala*, in *K. obovata,* the most porous roots occurred in the sediment composed of sand rather than mud, while the root porosity of *K. obovata* was lower than that of *S. apetala*. A higher root porosity rate may indicate higher adaptability to submerged or anoxic conditions by enhancing oxygen exchange (Justin and Armstrong, 1987). It can be inferred that *S. apetala* seedlings can acclimate more seaward in less elevated habitats than *K. obovata* does, which is coincident with their natural occurrence along the coastline of southern China (Ren et al., 2009). The strategy of plant roots coping with an anoxic environment may involve the balance between maintaining physiological function and decreasing tissue respiration (Purnobasuki and Suzuki, 2004).

For additional nitrogen input, no significant difference was found in *S. apetala,* but differences in NR and root respiration were detected in *K. obovata*. Although many studies reported that nitrogen enrichment could enhance the growth of many plants, no such trends existed were found in our experiment for either mangrove species. The simulated nitrogen input did not seem to significantly influence the early growth stage of mangroves newly colonized along tidal creeks. Notably, under more eutrophic conditions, *K. obovata* improved its efficiency for nitrogen use but lowered the root respiratory rate, which demonstrated the alteration of carbon allocation (Bae et al., 2015). Thus, the growth of saplings of *K. obovata* may be impacted in a nutrient-enriched habitat over a longer period.

The Effect of Sediment Texture and Nitrogen Input on Mangrove Conservation

Artificial fertilization has been shown to significantly modify the growth and ecological function of mangroves, especially at the sites of higher sedimentation (Lovelock et al., 2007). Therefore, the impacts of nutrient enrichment will be enlarged based on the sediment texture. The soil bulk density was vital to the establishment and development of the root system which was relevant to the biogeochemical process of mangrove ecosystems (Ola et al., 2019). It has been suggested that the sediment should also be considered when conducting mangrove restoration programs. The result of our study inferred that the seedling roots of *K. obovata* showed more sensitivity toward sediment texture and nutrient enrichment conditions, suggesting that *K. obovata* needed more suitable conditions for colonization than *S. apetala*. Currently, mangroves are widely suffering from terrigenous eutrophication on both regional and global scales (Friess et al., 2019). The nutrient-enriched environment will probably shift the existing status of mangrove populations in their assemblages (Luo et al., 2017; Yu et al., 2021).

In a heavily disturbed and eutrophicated estuary surrounded by megacities, such as the Pearl River Estuary, the natural regeneration and colonization of *K. obovata* and *S. apetala* is inclined to vary unintentionally. Both of these mangrove species are universally used in many mangrove restoration programs. Regarding the potential influence of sediment texture and nitrogen input on the early growth of seedlings, it is suggested that sediment and nutrient conditions be considered in conservation and restoration programs for mangroves in the future.

DATA AVAILABILITY STATEMENT

The original contributions presented in the study are included in the article/**Supplementary Material**, further inquiries can be directed to the corresponding author.

AUTHOR CONTRIBUTIONS

ZH and YP originally planned and designed the research. YP, LY, ZW, and ZH performed the field work and the mesocosm experiments. LY, HH, LZ, and ZW contributed to the laboratory analysis. YP and ZH wrote the first drafts of the manuscript and were further improved by ZH and SL. All authors commented and approved the manuscript.

FUNDING

This study was supported by Guangdong Basic and Applied Basic Research Foundation (2020A1515110657), National Nature Science Foundation Grant of China (41771095, 42106159, 91951207, and 42006138), project supported by the Southern Marine Science and Engineering Guangdong Laboratory (Zhuhai) (311021004 and SML2020SP004), and Guangdong Forestry Science and Technology Innovation Project (2021KJCX012 and 2022KJCX019).

ACKNOWLEDGMENTS

We sincerely thank Huaye Sun and Mengxing Wu for their help with fieldwork and laboratory analysis.

SUPPLEMENTARY MATERIAL

The Supplementary Material for this article can be found online at: https://www.frontiersin.org/articles/10.3389/fmars.2022.793818/full#supplementary-material

REFERENCES

Alongi, D. M. (2008). Mangrove forests: resilience, protection from tsunamis, and responses to global climate change. *Estuar. Coast. Shelf S.* 76, 1–13. doi: 10.1016/j.ecss.2007.08.024

Bae, K., Fahey, T. J., Yanai, R. D., and Fisk, M. (2015). Soil nitrogen availability affects belowground carbon allocation and soil respiration in northern hardwood forests of New Hampshire. *Ecosystems* 18, 1179–1191. doi: 10.1007/s10021-015-9892-7

Bai, X., Chen, K., Zhao, H., and Chen, X. (2015). Impact of water depth and sediment type on root morphology of the submerged plant Vallisneria natans. *J. Freshwater Ecol.* 30, 75–84. doi: 10.1080/02705060.2014.970672

Balke, T., Bouma, T., Herman, P., Horstman, E., Sudtongkong, C., and Webb, E. (2013). Cross-shore gradients of physical disturbance in mangroves: implications for seedling establishment. *Biogeosciences* 10, 5411–5419. doi: 10.5194/bg-10-5411-2013

Balke, T., Bouma, T. J., Horstman, E. M., Webb, E. L., Erftemeijer, P. L., and Herman, P. M. (2011). Windows of opportunity: thresholds to mangrove seedling establishment on tidal flats. *Mar. Ecol-prog. Ser.* 440, 1–9. doi: 10.3354/meps09364

Balke, T., Herman, P. M., and Bouma, T. J. (2014). Critical transitions in disturbance-driven ecosystems: identifying windows of opportunity for recovery. *J. Ecol.* 102, 700–708. doi: 10.1111/1365-2745.12241

Barbier, E. B. (2016). The protective service of mangrove ecosystems: a review of valuation methods. *Mar. Pollut. Bull.* 109, 676–681. doi: 10.1016/j.marpolbul.2016.01.033

Burton, A., Pregitzer, K., Ruess, R., Hendrick, R., and Allen, M. (2002). Root respiration in North American forests: effects of nitrogen concentration and temperature across biomes. *Oecologia* 131, 559–568. doi: 10.1007/s00442-002-0931-7

Chen, J., Liu, L., Wang, Z., Zhang, Y., Sun, H., Song, S., et al. (2020). Nitrogen fertilization increases root growth and coordinates the root-shoot relationship in cotton. *Front. Plant Sci.* 11:880. doi: 10.3389/fpls.2020.00880

Ding, Y., Guo, Z. S., Mei, J. X., Liang, Z. L., Li, Z. P., and Hpi, X. G. (2020). Investigation into the Novel Microalgae Membrane Bioreactor with Internal Circulating Fluidized Bed for Marine Aquaculture Wastewater Treatment. *Membranes-Basel.* 10:353. doi: 10.3390/membranes10110353

Ellison, J. C. (1999). Impacts of sediment burial on mangroves. *Mar. Pollut. Bull.* 37, 420–426. doi: 10.1016/S0025-326X(98)00122-2

Fan, H., and Wang, W. (2017). Some thematic issues for mangrove conservation in China (In Chinese). *J. Xiamen Univers. Nat. Sci.* 56, 323–330.

Flores-Mireles, A. L., Winans, S. C., and Holguin, G. (2007). Molecular characterization of diazotrophic and denitrifying bacteria associated with mangrove roots. *Appl. Environ. Microb.* 73, 7308–7321. doi: 10.1128/AEM.01892-06

Friess, D. A., Rogers, K., Lovelock, C. E., Krauss, K. W., Hamilton, S. E., Lee, S. Y., et al. (2019). The state of the world's mangrove forests: past, present, and future. *Annu. Rev. Env. Resour.* 44, 89–115. doi: 10.1146/annurev-environ-101718-033302

Furukawa, K., Wolanski, E., and Mueller, H. (1997). Currents and sediment transport in mangrove forests. *Estuar. Coast. Shelf S.* 44, 301–310. doi: 10.1006/ecss.1996.0120

Hageman, R., and Flesher, D. (1960). Nitrate reductase activity in corn seedlings as affected by light and nitrate content of nutrient media. *Plant Physio.* 35:700. doi: 10.1104/pp.35.5.700

Hamilton, S. E., and Casey, D. (2016). Creation of a high spatio-temporal resolution global database of continuous mangrove forest cover for the 21st century (CGMFC-21). *Global Ecol. Biogeogr.* 25, 729–738. doi: 10.1111/geb.12449

Hargan, K. E., Williams, B., Nuangsaeng, B., Siriwong, S., Tassawad, P., Chaiharn, C., et al. (2020). Understanding the fate of shrimp aquaculture effluent in a mangrove ecosystem: aiding management for coastal conservation. *J. Appl. Ecol.* 57, 754–765. doi: 10.1111/1365-2664.13579

He, Z., Peng, Y., Guan, D., Hu, Z., Chen, Y., and Lee, S. Y. (2018). Appearance can be deceptive: shrubby native mangrove species contributes more to soil carbon sequestration than fast-growing exotic species. *Plant Soil* 432, 425–436. doi: 10.1007/s11104-018-3821-4

Jiang, J., Zhou, C., An, S., Yang, H., Guan, B., and Cai, Y. (2008). Sediment type, population density and their combined effect greatly charge the short-time growth of two common submerged macrophytes. Ecol. Eng. 34, 79–90. doi: 10.1016/j.ecoleng.2008.07.003

Justin, S., and Armstrong, W. (1987). The anatomical characteristics of roots and plant response to soil flooding. *New Phytol.* 106, 465–495. doi: 10.1111/j.1469-8137.1987.tb00126.x

Kamal, S., Warnken, J., Bakhtiyari, M., and Lee, S. Y. (2017). Sediment distribution in shallow estuaries at fine scale: in situ evidence of the effects of three-dimensional structural complexity of mangrove pneumatophores. *Hydrobiologia* 803, 121–132. doi: 10.1007/s10750-017-3178-3

Krauss, K. W., McKee, K. L., Lovelock, C. E., Cahoon, D. R., Saintilan, N., Reef, R., et al. (2014). How mangrove forests adjust to rising sea level. *New Phytol.* 202, 19–34. doi: 10.1111/nph.12605

Lee, S. (2016). From blue to black: anthropogenic forcing of carbon and nitrogen influx to mangrove-lined estuaries in the South China Sea. *Mar. Pollut. Bull.* 109, 682–690. doi: 10.1016/j.marpolbul.2016.01.008

Lee, S., Tan, W., and Havanond, S. (1996). Regeneration and colonisation of mangrove on clay-filled reclaimed land in Singapore. *Hydrobiologia* 319, 23–35. doi: 10.1007/BF00020968

Lee, S. Y., Primavera, J. H., Dahdouh-Guebas, F., McKee, K., Bosire, J. O., Cannicci, S., et al. (2014). Ecological role and services of tropical mangrove ecosystems: a reassessment. *Global Ecol. Biogeogr.* 23, 726–743. doi: 10.1111/geb.12155

Lefcheck, J. S., Orth, R. J., Dennison, W. C., Wilcox, D. J., Murphy, R. R., Keisman, J., et al. (2018). Long-term nutrient reductions lead to the unprecedented recovery of a temperate coastal region. *Proc. Natl. Acad. Sci. USA.* 115, 3658–3662. doi: 10.1073/pnas.1715798115

Lemoine, D. G., Mermillod-Blondin, F., Barrat-Segretain, M. H., Massé, C., and Malet, E. (2012). The ability of aquatic macrophytes to increase root porosity and radial oxygen loss determines their resistance to sediment anoxia. *Aquat. Ecol.* 46, 191–200. doi: 10.1007/s10452-012-9391-2

Lenssen, J. P., Menting, F. B., van der Putten, W. H., and Blom, C. W. (1999). Effects of sediment type and water level on biomass production of wetland plant species. *Aquat. Bot.* 64, 151–165. doi: 10.1016/S0304-3770(99)00012-1

Li, Y. M., Liu, M., Wang, P., and Li, Y. J. (2013). Analysis of the water quality of aquaculture wastewater of Litopenaeus vannamei Boeen in tropics. *J. Aquacul.* 34, 42–45.

Liao, B. W., Zheng, S. F., Chen, Y. J., Li, M., and Li, Y. D. (2004). Biolofical characteristics and ecological adaptability for non-indigenous manfrove species *Sonneratia apetala* (In Chinese). *Chinese J. Ecol.* 23, 10–15.

Liu, X. G., Shao, Z. Y., Chen, G. F., Lu, S. M., Gu, Z. J., Zhu, H., et al. (2020). Ecological engineering in pond aquaculture: a review from the whole-process perspective in China. *Rev. Aquacult.* 13, 1060–1076. doi: 10.1111/raq.12512

Lovelock, C. E., Ruess, R. W., and Feller, I. C. (2006b). Fine root respiration in the mangrove *Rhizophora mangle* over variation in forest stature and nutrient availability. *Tree Physiol.* 26, 1601–1606. doi: 10.1093/treephys/26.12.1601

Lovelock, C. E., Feller, I. C., Ball, M. C., Engelbrecht, B. M., and Ewe, M. L. (2006a). Differences in plant function in phosphorus-and nitrogen-limited mangrove ecosystems. *New Phytol.* 172, 514–522. doi: 10.1111/j.1469-8137.2006.01851.x

Lovelock, C. E., Feller, I. C., Ellis, J., Schwarz, A. M., Hancock, N., Nichols, P., et al. (2007). Mangrove growth in New Zealand estuaries: the role of nutrient enrichment at sites with contrasting rates of sedimentation. *Oecologia* 153, 633–641. doi: 10.1007/s00442-007-0750-y

Luo, L., Meng, H., Wu, R. N., and Gu, J. D. (2017). Impact of nitrogen pollution/deposition on extracellular enzyme activity, microbial abundance and carbon storage in coastal mangrove sediment. *Chemosphere* 177, 275–283. doi: 10.1016/j.chemosphere.2017.03.027

Luxmoore, R., Sojka, R., and Stolzy, L. (1972). Root Porosity and Growth Responses of Wheat to Aeration and Light Intensity. *Soil Sci.* 113, 354–357. doi: 10.1097/00010694-197205000-00009

Lynch, J. (1995). Root architecture and plant productivity. *Plant Physiol.* 109:7–13. doi: 10.1104/pp.109.1.7

Mei, X., Ye, Z., and Wong, M. H. (2009). The relationship of root porosity and radial oxygen loss on arsenic tolerance and uptake in rice grains and straw. *Environ. Pollut.* 157, 2550–2557. doi: 10.1016/j.envpol.2009.02.037

Ola, A., Gauthier, A. R., Xiong, Y., and Lovelock, C. E. (2019). The roots of blue carbon: responses of mangrove stilt roots to variation in soil bulk density. *Biol. Lett.* 15:20180866. doi: 10.1098/rsbl.2018.0866

Purnobasuki, H., and Suzuki, M. (2004). Aerenchyma formation and porosity in root of a mangrove plant, *Sonneratia alba* (Lythraceae). *J. Plant Res.* 117, 465–472. doi: 10.1007/s10265-004-0181-3

R Core Team (2019). R: a language and environment for statistical computing. *Vienna: R foundation for statistical computing*. Available online at: https://www.r-project.org

Rabinowitz, D. (1978). Dispersal properties of mangrove propagules. *BIotropica* 10, 47–57. doi: 10.2307/2388105

Reef, R., Feller, I. C., and Lovelock, C. E. (2010). Nutrition of mangroves. *Tree Physiol.* 30, 1148–1160. doi: 10.1093/treephys/tpq048

Ren, H., Lu, H., Shen, W., Huang, C., Guo, Q., and Jian, S. (2009). *Sonneratia apetala* Buch. *Ham in the mangrove ecosystems of China: an invasive species or restoration species? Ecol. Eng.* 35, 1243–1248. doi: 10.1016/j.ecoleng.2009.05.008

Romañach, S. S., DeAngelis, D. L., Koh, H. L., Li, Y., Teh, S. Y., Barizan, R. S. R., et al. (2018). Conservation and restoration of mangroves: global status, perspectives, and prognosis. *Ocean Coast. Manage.* 154, 72–82. doi: 10.1016/j.ocecoaman.2018.01.009

Ruiz, J. M., Pérez, M., and Romero, J. (2001). Effects of fish farm loadings on seagrass (*Posidonia oceanica*) distribution, growth and photosynthesis. *Mar. Pollut. Bull.* 42, 749–760. doi: 10.1016/S0025-326X(00)00215-0

Schwarz, C., Bouma, T., Zhang, L., Temmerman, S., Ysebaert, T., and Herman, P. (2015). Interactions between plant traits and sediment characteristics influencing species establishment and scale-dependent feedbacks in salt marsh ecosystems. *Geomorphology* 250, 298–307. doi: 10.1016/j.geomorph.2015.09.013

Sheue, C. R., Liu, H. Y., and Yong, J. W. (2003). *Kandelia obovata* (Rhizophoraceae), a new mangrove species from Eastern Asia. *Taxon* 52, 287–294. doi: 10.2307/3647398

Sun, H., He, Z., Zhang, M., Yen, L., Cao, Y., Hu, Z., et al. (2020). Spatial variation of soil properties impacted by aquaculture effluent in a small-scale mangrove. *Mar. Pollut. Bull.* 160:111511. doi: 10.1016/j.marpolbul.2020.111511

Tam, N. F., and Wong, Y. S. (1997). Accumulation and distribution of heavy metals in a simulated mangrove system treated with sewage. *Asia-Pacific Confer. Sci Manage. Coast. Environ.* 123, 67–75. doi: 10.1007/978-94-011-5234-1_8

Terrados, J., Duarte, C., Kamp-Nielsen, L., Agawin, N., Gacia, E., Lacap, D., et al. (1999). Are seagrass growth and survival constrained by the reducing conditions of the sediment? *Aquat. Bot.* 65, 175–197. doi: 10.1016/S0304-3770(99)00039-X

Thomas, N., Lucas, R., Bunting, P., Hardy, A., Rosenqvist, A., and Simard, M. (2017). Distribution and drivers of global mangrove forest change, 1996–2010. *PLoS One* 12:e0179302. doi: 10.1371/journal.pone.0179302

Valiela, I., Bowen, J., and York, J. K. (2001). Mangrove forests: One of the world's threatened major tropical environments: at least 35% of the area of mangrove forests has been lost in the past two decades, losses that exceed those for tropical rain forests and coral reefs, two other well-known threatened environments. *Bioscience* 51, 807–815. doi: 10.1641/0006-3568(2001)051[0807:MFOOTW]2.0.CO;2

Wang, L., Zhao, C., Li, J., Liu, Z., and Wang, J. (2015). Root plasticity of Populus euphratica seedlings in response to different water table depths and contrasting sediment types. *PLoS One* 10:e0118691. doi: 10.1371/journal.pone.0118691

Wang, S., Jin, X., Jiao, L., and Wu, F. (2009). Response in root morphology and nutrient contents of *Myriophyllum spicatum* to sediment type. *Ecol. Eng.* 35, 1264–1270. doi: 10.1016/j.ecoleng.2009.05.012

White, S. D., and Ganf, G. G. (2001). The influence of convective flow and sediment type on root morphology in *Typha domingensis*. *Aquat. Bot.* 70, 151–161. doi: 10.1016/S0304-3770(00)00145-5

Xie, Y., An, S., Yao, X., Xiao, K., and Zhang, C. (2005). Short-time response in root morphology of *Vallisneria natans* to sediment type and water-column nutrient. *Aquat. Bot.* 81, 85–96. doi: 10.1016/j.aquabot.2004.12.001

Yang, J. Z., Hu, Y. H., Luo, Y., and Luo, C. Q. (2018). Study on the distribution status and dynamic changes of mangroves in Guangdong Province (In Chinese). *Forest. Environ. Sci.* 34, 28–31.

Yang, P., Yang, H., Lai, D. Y. F., Jin, B. S., and Tong, C. (2019). Production and uptake of dissolved carbon, nitrogen, and phosphorus in overlying water of aquaculture shrimp ponds in subtropical estuaries. *China. Environ. Sci. Pollut. R.* 26, 21565–21578. doi: 10.1007/s11356-019-05445-y

Yu, H., Liu, X. Y., Chao, Y., Peng, Y. S., Yu, X. L., Gu, H., et al. (2021). Co-symbiosis of arbuscular mycorrhizal fungi (AMF) and diazotrophs promote biological nitrogen fixation in mangrove ecosystems. *Soil Biol. Biochem.* 161:108382. doi: 10.1016/j.soilbio.2021.108382

Zhang, M., Dai, P., Lin, X., Hetharua, B., Zhang, Y., and Tian, Y. (2020). Nitrogen loss by anaerobic ammonium oxidation in a mangrove wetland of the Zhangjiang Estuary. *China. Sci. Total Environ.* 698:134291. doi: 10.1016/j.scitotenv.2019.134291

Zhang, Y. S., Xiao, L., Guan, D. S., Chen, Y. J., Motelica-Heino, M., Peng, Y. S., et al. (2021). The role of mangrove fine root production and decomposition on soil organic carbon component ratios. *Ecol. Indic* 125:107525. doi: 10.1016/j.ecolind.2021.107525

Conflict of Interest: The authors declare that the research was conducted in the absence of any commercial or financial relationships that could be construed as a potential conflict of interest.

Publisher's Note: All claims expressed in this article are solely those of the authors and do not necessarily represent those of their affiliated organizations, or those of the publisher, the editors and the reviewers. Any product that may be evaluated in this article, or claim that may be made by its manufacturer, is not guaranteed or endorsed by the publisher.

Copyright © 2022 He, Yen, Huang, Wang, Zhao, Chen, Lee and Peng. This is an open-access article distributed under the terms of the Creative Commons Attribution License (CC BY). The use, distribution or reproduction in other forums is permitted, provided the original author(s) and the copyright owner(s) are credited and that the original publication in this journal is cited, in accordance with accepted academic practice. No use, distribution or reproduction is permitted which does not comply with these terms.

frontiers | Frontiers in Marine Science

ORIGINAL RESEARCH
published: 05 April 2022
doi: 10.3389/fmars.2022.866570

A Minimalist Model of Salt-Marsh Vegetation Dynamics Driven by Species Competition and Dispersal

Alvise Finotello[1,2]*, *Andrea D'Alpaos*[2,3], *Marco Marani*[2,4] *and Enrico Bertuzzo*[1,2]*

[1] Department of Environmental Sciences, Informatics, and Statistics, Ca' Foscari University of Venice, Venice, Italy, [2] Center for Lagoon Hydrodynamics and Morphodynamics, University of Padova, Padova, Italy, [3] Department of Geosciences, University of Padova, Padova, Italy, [4] Department of Civil, Environmental, and Architectural Engineering, University of Padova, Padova, Italy

OPEN ACCESS

Edited by:
Zeng Zhou,
Hohai University, China

Reviewed by:
Ian Townend,
University of Southampton, United Kingdom
Dongdong Shao,
Beijing Normal University, China

***Correspondence:**
Alvise Finotello
alvise.finotello@unive.it
Enrico Bertuzzo
enrico.bertuzzo@unive.it

Specialty section:
This article was submitted to Coastal Ocean Processes, a section of the journal Frontiers in Marine Science

Received: *31 January 2022*
Accepted: *03 March 2022*
Published: *05 April 2022*

Citation:
Finotello A, D'Alpaos A, Marani M and Bertuzzo E (2022) A Minimalist Model of Salt-Marsh Vegetation Dynamics Driven by Species Competition and Dispersal. Front. Mar. Sci. 9:866570. doi: 10.3389/fmars.2022.866570

We present a new bidimensional, spatially-explicit ecological model describing the dynamics of halophytic vegetation in tidal saline wetlands. Existing vegetation models employ relatively simple deterministic or stochastic mechanisms, and are driven by local environmental conditions. In the proposed model, in contrast, vegetation dynamics depend not only on the marsh local habitat, but also on spatially-explicit mechanisms of dispersal and competition among multiple interacting species. The role of habitat quality, here determined by the local elevation relative to the mean sea level as a proxy for environmental conditions, is mathematically modeled by a logistic function that represents the fundamental (theoretical) niche of each halophytic species. Hence, the model does not artificially impose any constraints to the ability of a species to colonize elevated areas where it is usually not observed: such limitations naturally arise through competition with fitter species across marsh topographic gradients. We qualitatively test our model against field data based on a suitable assemblage of focus species, and perform a sensitivity analysis aimed at determining how dynamic equilibria in vegetation distributions are affected by changes in model input parameters. Results indicate that the model is robust and can predict realistic vegetation distributions and species-richness patterns. More importantly, the model is also able to effectively reproduce the outcomes of classical ecological experiments, wherein a species is transplanted to an area outside its realized niche. A direct comparison shows that previous models not accounting for dispersal and interspecific competitions are unable to reproduce such dynamics. Our model can be easily integrated into virtually any existing morphodynamic model, thereby strengthening our ability to simulate the coupled biotic and abiotic evolution of salt marshes under changing climate forcings.

Keywords: salt marshes, ecology, vegetation, competition, zonation, α-diversity, numerical modelling, ecomorphodynamics

1 INTRODUCTION

Salt marshes are widespread morphological features in coastal and estuarine tidal landscapes, and are ecologically and economically important as they significantly contribute to coastal primary production, support high biodiversity, and provide a broad range of valuable ecosystem services (Costanza et al., 1997; Barbier et al., 2011; D'Alpaos and D'Alpaos 2021). In particular, salt marshes are highly efficient in sequestering and storing large amounts of blue carbon (Chmura et al., 2003; Kirwan and Mudd, 2012; Yousefi Lalimi et al., 2018), filtering nutrients and pollutants (Nelson and Zavaleta, 2012; Ratliff et al., 2015), and dissipating wave energy thereby mitigating shoreline erosion and providing nature-based protection against storms (Temmerman et al., 2013; Möller et al., 2014). However, the sustainability of saltmarsh ecosystems is severely threatened by climate-change-induced sea-level rise and increasing anthropogenic pressures, such as land reclamation as well as both human-induced subsidence and sediment starvation (Kirwan and Megonigal, 2013; FitzGerald and Hughes, 2019). As a result, large areas of salt marshes are being lost around the world every year at increasingly alarming rates (Day et al., 2000; Valiela et al., 2009; Mcowen et al., 2017; Tommasini et al., 2019).

The ability of tidal marshes to counteract rising relative sea levels depends on complex, dynamic feedbacks between physical and biological processes acting at different spatial and temporal scales (Morris et al., 2002; Mudd et al., 2004; D'Alpaos et al., 2007; Marani et al., 2010). While salt-marsh evolution in the horizontal direction depends on the balance between wave-induced lateral erosion (Marani et al., 2011; Leonardi et al., 2016) and marsh progradation, for which the availability of external sediment supply is key (Goodwin and Mudd, 2020; Yang et al., 2020a; Roner et al., 2021; Willemsen et al., 2021), the equilibrium of tidal marshes in the vertical direction results from the interplay between organic and inorganic deposition, erosion, changes in relative sea level, and variations of atmospheric CO_2 concentration (Marani et al., 2007; D'Alpaos, 2011; Ratliff et al., 2015; Morris et al., 2016). Overall though, salt-marsh evolution, both in time and space, is intimately related to the dynamics of halophytic (i.e., salt-tolerant) plant communities colonizing the marsh platform.

The encroachment of pioneer halophytes capable of thriving in highly hypoxic and hypersaline soils facilitates sediment accumulation, ameliorate physical stresses, and promote further marsh growth thanks to the ability of these critical foundation species (*sensu* Dayton, 1975) to eco-engineer their habitats (Ranwell, 1972; Jones et al., 1994; Bruno, 2000; Bruno and Kennedy, 2000; Crain and Bertness, 2006; Morris, 2007; Vandenbruwaene et al., 2011; Da Lio et al., 2013; Marani et al., 2013; Lõhmus et al., 2020; van Regteren et al., 2020). Once foundation species are established, a network of emergent vegetation organized into recurrent zonation patterns develops along the gradients of elevation and salinity that characterize tidal wetlands (Pennings and Callaway, 1992; Belluco et al., 2006; Marani et al., 2006) (**Figures 1A, B**). Vegetation biomass actively contributes to marsh vertical accretion by reducing bottom shear stresses and the associated erosion processes (Ford et al., 2016), as well as by enhancing sediment deposition through both direct captures of suspended sediments and deposition of organic matter (Temmerman et al., 2005; Nyman et al., 2006; D'Alpaos et al., 2007). Moreover, vegetation allows tidal wetlands to sequester and store large amounts of organic carbon, sustaining the highest rate of carbon sequestration per unit area of all ecosystems, thanks to the fact that storage occurs predominantly in belowground biomass and soil is typically in anaerobic conditions (McLeod et al., 2011; Roner et al., 2016; Rogers et al., 2019; Wang et al., 2019; Ouyang and Lee, 2020). Finally, halophytes also exert critical control on soil aeration (Marani et al., 2006; Boaga et al., 2014), which in turn fuels vegetation zonation and the related biogeomorphic interactions typically observed in tidal marshes (Morris et al., 2002; Silvestri et al., 2005; Marani et al., 2006; Yang et al., 2020b).

Despite the importance of vegetation dynamics in controlling physical and biological processes that ultimately determine whether salt marshes will aggrade, persist, or drown in the face of climate changes, modeling these dynamics remains a major challenge both at the theoretical and practical level (e.g., Best et al., 2018; Brückner et al., 2019). This is mostly due to the fact that some key drivers of vegetation dynamics are not properly accounted for in common modeling practices.

Biotic interactions in numerical models are typically conceptualized based on the empirical observation that physical processes and stresses – such as salt-marsh vertical accretion rates, salinity, flooding frequency and duration (i.e., hydroperiod), and nutrient availability – exert a key role in regulating the realized distributions (i.e., observed niches) of marsh halophytes (Redfield, 1972; Snow and Vince, 1984; Kuhn and Zedler, 1997; Levine et al., 1998; Pennings and Bertness, 2001; Morris, 2007; Xin et al., 2013; Xin et al., 2017; Boyd et al., 2017; Schulte Ostermann et al., 2021). Realized niches typically display a maximum potential for presence and growth at an optimum intertidal elevation (Redfield, 1972; Silvestri et al., 2005), with different species confined to narrow elevation bands (Marani et al., 2004; Morris et al., 2005; Mudd et al., 2009) (**Figure 1D**). Consequently, local species diversity (i.e., α-diversity) also exhibits hump-shaped patterns, with intermediate elevations hosting the largest number of species (De Leeuw et al., 1992; Crain and Bertness, 2006) (**Figure 1E**). However, due to biotic interactions, the realized niche could be quite different from the theoretical one, the latter being the distribution a species would attain in the absence of interspecific competition. Indeed, field experiments involving transplantation of halophytes across marsh topographic gradients, outside their realized niches, indicate ever-increasing performances of each species as elevation increases from the lower to the upper marsh (Bertness and Ellison, 1987; Pennings and Bertness, 2001), in contrast with hump-shaped realized niches. Such a lack of correspondence between the physiological stress tolerance of marsh plants across topographic gradients and their realized distributions suggests that the latter may not necessarily resemble the fundamental (theoretical) niches, and urges a deeper understanding of ecological dynamics controlling species distribution. Indeed, this difference calls for factors other than environmental conditions to concur in creating the observed

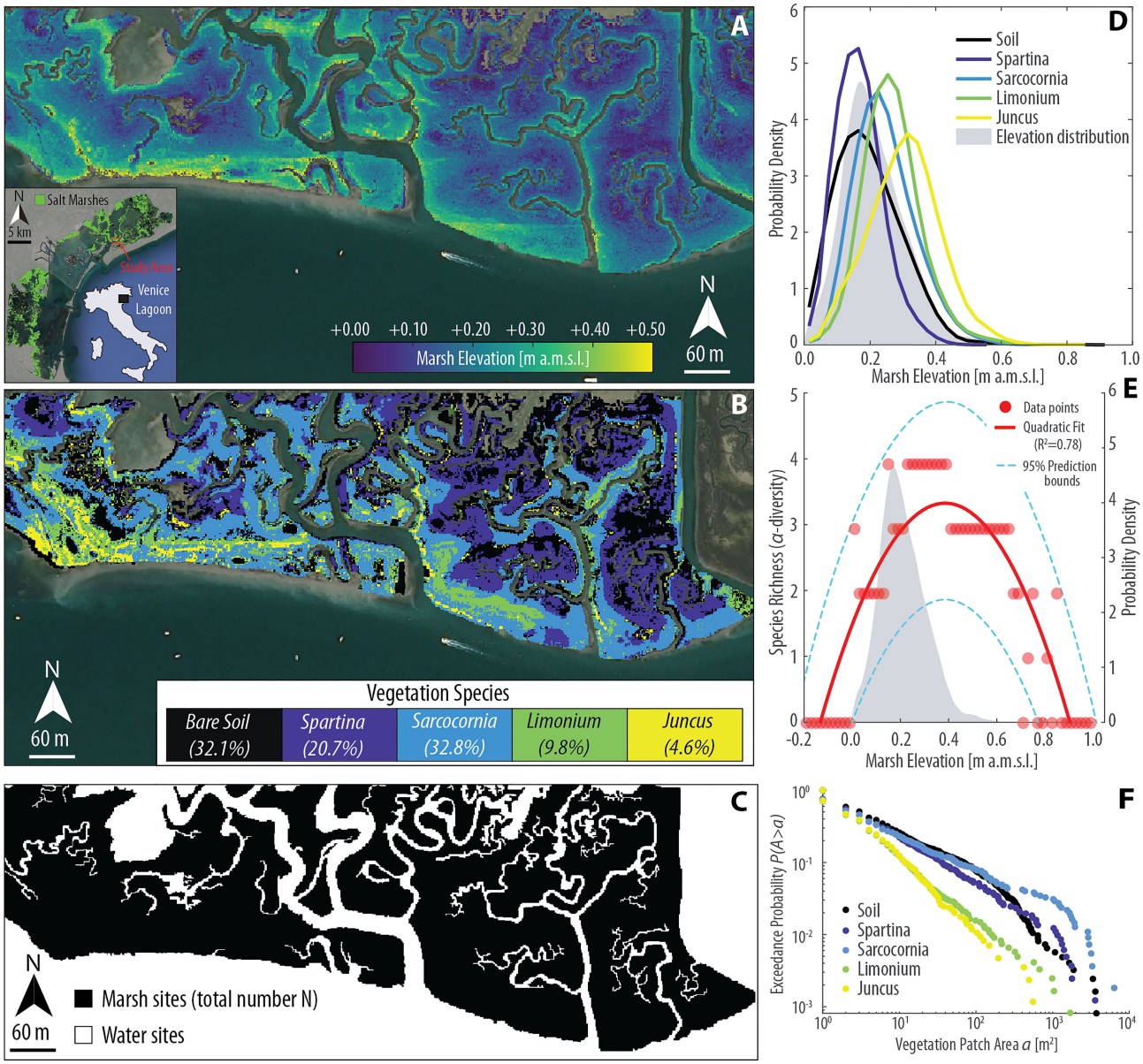


FIGURE 1 | Topographic gradients and vegetation zonation in the San Felice salt marsh (Venice Lagoon, Italy). **(A)** Lidar-derived digital elevation model (DEM, spatial resolution 1 m; mean elevation 0.21 ± 0.09 m above datum) superimposed to an aerial image of the study area (Aerial Imagery ©CNES/Airbus). Lidar data were collected on February 9, 2003. The reader is referred to Wang et al. (2009) for further details regarding data acquisition. **(B)** Classification map of vegetation species in the study area. The classification was carried out utilizing a Compact Airborne Spectral Imager (CASI) image, acquired on 29th September 2002 with a spatial resolution of 1.3 m from a flight altitude of 840 m (Belluco et al., 2006; Wang et al., 2007). Dominant vegetation species within each pixel were obtained based on relative fractional abundance estimated through the Random Forest soft classification method (see Yang et al., 2020b for further details), and upsampled using a bicubic interpolation method to meet the resolution of the Lidar data. The percent vegetation cover for each vegetation class is also reported in the legend. **(C)** Binary representation of the computational domain employed in the numerical simulations presented in this study. **(D)** Realized ecological niches observed in the study area based on DEM and vegetation data shown in panels **(A, B)**, respectively. Continuous lines represent the probability density estimates of each species (including bare soils) across marsh elevations, whereas the gray area denotes the probability density estimates of marsh elevation derived from DEM data. **(E)** Local species richness (i.e., α-diversity) as a function of marsh elevation. Red dots represent point data derived from the DEM and vegetation map shown in panels **(A, B)**, respectively. Red line denotes the best quadratic fit to point data, with dashed blue lines showing 95% prediction bounds. The gray area denotes the probability density estimates of marsh elevation derived from DEM data. **(F)** Empirical probability distributions of spatially-continuous vegetation patch areas, for different species including bare soil, are shown based on the exceedance probability for a given vegetation patch size. The analysis is based on vegetation data shown in panel **(B)**. Empirical probability distributions of patch area are derived by computing A for every vegetation patch and plotting the probability obtained by counting the relative proportion of patches of the same species whose total area exceeds a current value a, here expressed in square meters.

zonation patterns in salt marsh communities (Pennings and Bertness, 2001; Pennings and He, 2021).

Many experimental studies have demonstrated that there exists an inherent tradeoff between competitive ability and stress tolerance (*sensu* Grime, 1977), such that competitively superior plants occupy the more elevated, least stressful zones of the salt marsh and displace competitively inferior plants to the lower, more stressful portions of the intertidal frame (Snow and Vince, 1984; Bertness and Ellison, 1987; Bertness, 1991a; Bertness, 1991b; Pennings and Callaway, 1992; Levine et al., 1998; Ungar, 1998; Emery et al., 2001; Pennings et al., 2005; Morris, 2006). As a result, every halophytic species would be fully capable of persisting at elevations higher than where it normally occurs if competitors were absent, whereas species would die out if transplanted to elevations lower than the optimal realized niche. (Bertness and Ellison, 1987; Bertness, 1991a; Bertness, 1991b; Pennings and Bertness, 2001; Pennings et al., 2005). According to this paradigm, which is consistent with results from non-saline wetlands (Grace and Wetzel, 1981; Keddy, 1989), marsh halophytes could potentially colonize supratidal freshwater environments, where they are however outcompeted by glycophytes that are more fitted to hyposaline conditions. In view of the above, it is generally hypothesized that the lower limit of each species is determined by abiotic factors mostly related to marsh elevation and local climate (e.g., salinity, hydroperiod, redox potential, nutrient availability, soil moisture and chemistry, local microtopography, hydrodynamic stresses), while the upper limit is set by biotic factors (e.g., competition-facilitation and tradeoffs thereof, physiological adjustment, seedling recruitment, emergence and growth strategy, herbivory predation), among which interspecific competition is key (Lee and Kim, 2018; Sarika and Zikos, 2020; Pennings and He, 2021).

Despite competitive displacement and physiological tolerance to stressors having long been recognized as the most decisive factors in generating salt-marsh vegetation zonation (e.g., Pennings and Callaway, 1992), most of the existing ecomorphodynamic models of salt marshes employ oversimplifications that do not allow these processes to be effectively reproduced.

First, fundamental species niches are typically approximated by the realized ones. Therefore, although field studies suggest performances of individual species to increase steadily with elevation in the absence of competition, habitat quality and vegetation performances are typically assumed to peak at an optimum marsh elevation, and to decrease as elevation moves away from such optimum (Morris et al., 2002; Morris, 2006; Morris, 2007; D'Alpaos et al., 2007; Kirwan and Murray, 2007; Kirwan and Guntenspergen, 2010; Fagherazzi et al., 2012; Da Lio et al., 2013; Marani et al., 2013; Kirwan et al., 2016; Geng et al., 2021; Kalra et al., 2021; Sgarabotto et al., 2021).

Second, competition in numerical models of marsh vegetation dynamics, with few exceptions (e.g., Marani et al., 2006), does not occur by direct species interaction. Rather, the successful colonizer is chosen based on local habitat quality in a deterministic (i.e., "fittest-takes-it-all") or stochastic manner (i.e., proportionally to the local habitat quality of all species) (Morris et al., 2002; Morris, 2006; D'Alpaos et al., 2012; Da Lio et al., 2013; Marani et al., 2013). Therefore, competition occurs indirectly by virtue of changes in local marsh elevation, assuming specific competitive abilities to operate most efficiently within the optimal habitat quality range of each species.

Finally, it is often overlooked that biological dispersal and competition in tidal marshes are density-dependent processes, i.e., they are a function of local population size, as well as habitat quality and size (Bertness and Ellison, 1987; Ellison, 1987; Bouma et al., 2009; Balke et al., 2017; Lõhmus et al., 2020; Bertassello et al., 2021).

Altogether, these shortcomings are likely to limit the ability of current ecomorphodynamic models to predict the response of marsh ecosystems to changing externals forcings (e.g., Zhang et al., 2020). To bridge this gap, proper modelling treatments of biotic interactions are required, which assume fundamental niches consistent with field observations and account for spatially-explicit mechanisms of interspecific competition and dispersal. Improving our ability to model the drivers and outcomes of halophytic-species zonation is paramount to enhance projections of salt-marsh evolution (Kirwan and Temmerman, 2009; Kirwan et al., 2016; Schuerch et al., 2018), with direct practical implications for salt-marsh conservation and restoration worldwide (Broome et al., 1988; Day et al., 2007; Palaima, 2012). In particular, a model capable of reproducing vegetation dynamics observed in the field would allow for cost-effective community-level studies, helping us to clarify whether our understandings of marsh systems derived from small-scale experiments can be upscaled to explain marsh community dynamics at larger spatial scales.

Here we present a new bidimensional, spatially-explicit, species-interaction model aimed at simulating the dynamics of halophytic vegetation in tidal saline wetlands based on vegetation habitat quality, competition, and dispersal. We test the model's ability to reproduce patterns of vegetation zonation and species richness observed in nature. To demonstrate model robustness, we perform a sensitivity analysis and illustrate how changes in the key model parameters affect results. Moreover, we run exploratory numerical simulations aimed at assessing model performances in replicating results of ecological experiments involving the transplant of species outside their realized ecological niches. Even though the model can be easily extended to investigate morphological shifts from tidal flats to salt marshes driven by the colonization of pioneers species, here we do not focus on initial vegetation establishment (e.g., Balke et al., 2017; Brückner et al., 2019; Lõhmus et al., 2020) because our interest is in the medium to long-term outcomes of vegetation dynamics in mature marshes. Nonetheless, a discussion on how the initial vegetation distribution affects model results will be provided later in the text. Finally, we discuss the potential for integrating our model into a morphodynamic model to simulate the coupled evolution of vegetation and salt-marsh platforms under changing external forcings.

2 MATERIAL AND METHODS

2.1 Model

The model considers a system of I vegetation species, distributed in an equally-spaced 2D lattice with a uniform spatial resolution

dx, wherein each site (i.e., cell) j is characterized by a given elevation (z_j) relative to the mean sea level. The elevation z_j determines the habitat quality of species i at site j *via* a habitat quality function (*sensu* Rybicki and Hanski, 2013), which is here modeled through a logistic function (**Figure 2A**):

$$f_i(z_j) = \frac{1}{1 + e^{-k_i \cdot (z_j - z_{0_i})}} \quad (1)$$

where z_0 corresponds to the logistic sigmoid point, k is the logistic rate, and the maximum habitat quality is set equal to 1 for all species. Habitat quality determines the fitness (performance) of the species in the respective grid cell as described further below. The habitat quality function can be viewed as the dimension of a species' fundamental niche (*sensu* Hutchinson, 1957), that is, the space theoretically occupied by a species in the absence of competitors based on physical and biotic predictors alone. The realized niche is expected to be reduced in size as a result of interspecific competition (Bertness, 1991a; Ungar, 1998). The use of a monotonically increasing logistic function for habitat quality is justified by the empirical observation that halophytes are capable of living at elevations higher than where they are normally found if competitors are absent, whereas vegetation lower limit is set by plant tolerance to physical stresses (Pennings and He, 2021). Although these physical stresses are, in most cases, not fully identified, most of them (e.g., flooding frequency and duration, salinity, oxygen sufficiency, temperature) depend to some degree on the local hydroperiod, which is in turn primarily determined by the elevation of the marsh surface (Morris et al., 2002). Therefore, physical stresses in our habitat quality function are synthesized by means of the local marsh elevation (z_j), implicitly assuming that physical stresses decrease as marsh elevation increases, and that such gradient is consistent across the whole marsh. The latter condition does not necessarily hold in marshes that are not regularly flooded (Costa et al., 2003; Pennings et al., 2005) as we will discuss later in the text (see Section 4).

Each cell of the system can be occupied by a single individual of a generic species i. We explicitly model the process of death and colonization by offsprings of existing individuals *via* dispersal. Different species are characterized by different baseline competitive abilities δ_i (**Figure 2B**) that affect the probability of colonization when offsprings of different species are competing. As discussed in the introduction section, we introduce a tradeoff between competitive ability and stress tolerance so that species with lower stress tolerance (higher z_0) have an inherent higher competitive ability and vice versa (**Figures 2B, C**). Therefore, habitat quality modulates specific mortality and fertility rates, as well as their effective competitive ability.

Ecological interactions among species are simulated as follows. At each time step, the individual occupying a given site j dies according to the local mortality rate of the species i it belongs to. Such a mortality rate $\mu_i(z_j)$ is assumed to be inversely proportional to the specific habitat quality:

$$\mu_i(z_j) = \frac{\mu_{0_i}}{f_i(z_j)} \quad (2)$$

where μ_{0i} is the baseline mortality rate of species i. The mortality rate is minimum where the species have the maximum habitat quality and increases for lower habitat quality at lower elevations (**Figure 2A**). We model the occurrence of a death event as a Poisson process. Thus, the waiting time until the next death event occurs follows an exponential probability distribution characterized by a rate μ_i. Therefore, within a time step Δt, each individual dies with probability $1 - e^{-\mu_i \Delta t}$.

The cleared site can be recolonized by the offspring of any individual in the system. Colonization by an offspring of species i occurs at a rate C_{ij}. Such a rate is proportional to the fertility rate characterizing the i^{th} species, weighted through a dispersal kernel

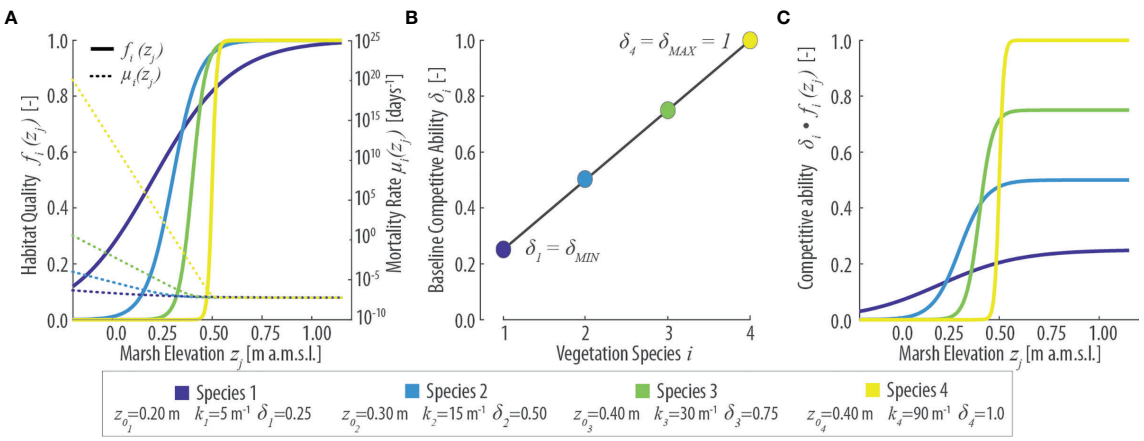


FIGURE 2 | Parametrization of vegetation features in the numerical model based on 4 virtual species. **(A)** Patterns of specific habitat quality function $f_i(z_j)$ (continuous lines, left y-axis) and mortality rate $\mu_i(z_j)$ (dotted lines, right y-axis) as a function of local marsh elevation (z_j). **(B)** Baseline specific competitive ability (δ_i) for different vegetation species i. **(C)** Specific competitive ability [$\delta_i f_i(z_j)$] as a function of local marsh elevation (z_j). Values of the parameters z_{0_i}, k_i, and δ_i for each species are reported in the lower inset.

function $K(d_{n,j})$ (Bullock et al., 2017) that depends on the euclidean distance d between the site j and any given site n colonized by the species i. Since K is typically inversely proportional to $d_{n,j}$, we will hereinafter assume K to be exponential:

$$K(d_{j,n}) = \frac{e^{-\frac{dj,n}{D_i}}}{2\pi D_i^2} \cdot dx^2 \quad (3)$$

where D_i denotes a characteristic dispersal length and dx is the domain spatial resolution. The choice of an exponential dispersal kernel to model vegetation colonization is justified by empirical observations suggesting that i) in mature marshes, marsh perennials colonize available bare spaces mostly vegetatively rather than by seedling; and, ii) species dispersal takes place at a relatively local scale (Bertness and Ellison, 1987; Ellison, 1987; Bullock et al., 2006; Chang et al., 2007; Lõhmus et al., 2020). The total colonization rate C_{ij} exerted by the species i on the site j can thus be expressed as follows:

$$C_{i,j} = \sum_{n=1}^{N} \delta_i \cdot f_i(z_j) \cdot \left[K(d_{j,n}) \cdot w_{i,n} \cdot f_i(z_n) \cdot \varphi_i\right] \quad (4)$$

where N is the total number of sites (i.e., cells) within the domain, $w_{i,n}$ is a binary occupation function that is equal to 1 when the site n is colonized by species i, and φ_i is the baseline fertility rate of species i corresponding to the maximum habitat quality f_i=1. Notably, C_{ij} depends on the habitat quality that the i^{th} potential colonizer has both on all the sites that it currently colonizes (as it affects the i^{th} species fertility: $f_i(z_n) \cdot \varphi_i$) and on the site j to be colonized (as it affects the i^{th} species competitive ability at site j: $\delta_i\ f_i(z_j)$, see **Figure 2C**). Colonization can also be allowed by offsprings of individuals not currently present within the system. This additional competitor is accounted for by adding a term $\delta_i \cdot f_i(z_j) \cdot \phi_{out}$ to C_{ij} at each time step, being ϕ_{out} the input of offsprings from outside the system, in this way potentially allowing for immigration of species not currently present in the system. To account also for this possible process, C_{ij} eventually reads:

$$C_{i,j} = \sum_{n=1}^{N} \delta_i \cdot f_i(z_j) \cdot \left[K(d_{j,n}) \cdot w_{i,n} \cdot f_i(z_n) \cdot \varphi_i + \phi_{out}\right] \quad (5)$$

The site j is colonized with a probability $1 - e^{-C_{tot_j} \cdot \Delta t}$, where C_{tot_j} is the total colonization rate at site j by any species i:

$$C_{tot_j} = \sum_{i=1}^{I} C_{i,j} \quad (6)$$

If the colonization event occurs, the colonizing species is randomly selected with a probability proportional to C_{ij}; otherwise, the site is left unvegetated.

The colonization rate C_{ij} can be seen as the bidimensional convolution between the field $w_{i,n} \cdot f_i(z_n)$ and the Kernel $K(d)$ (Rybicki and Hanski, 2013; see **Figures 3A–C**):

$$C_{i,j} = \delta_i \cdot f_i(z_j)\left[w_{i,n} \cdot f_i(z_n)\varphi_i \otimes K(d)\right] + \delta_i \cdot f_i(z_j) \cdot \phi_{out} \quad (7)$$

where $\otimes$ denotes the bidimensional convolution. Taking advantage of the properties of the Fourier bidimensional transforms, one can write (Rybicki and Hanski, 2013):

$$F(C_{i,j}) = \delta_i \cdot f_i(z_j)\left[F\left(w_{i,n} \cdot f_i(z_n)\varphi_i\right) \cdot F(K(d))\right] + \delta_i \cdot f_i(z_j) \cdot \phi_{out} \quad (8)$$

and eventually:

$$C_{i,j} = \delta_i \cdot f_i(z_j) \cdot F^{-1}\left[F\left(w_{i,n} \cdot f_i(z_n)\varphi_i\right) \cdot F(K(d))\right] + \delta_i \cdot f_i(z_j) \cdot \phi_{out} \quad (9)$$

being F and F^{-1}, respectively, the Fourier Transform and its inverse. **Figure 3C** illustrates the calculation of a bidimensional convolution between $w_{i,n}$ (**Figure 3A**) and $K(d_{n,j})$ (**Figure 3B**) on a synthetic square domain computed through the discrete Fast Fourier Transform (FFT) algorithm. **Figure 3D** shows the absolute difference between the explicit bidimensional convolution and the calculation carried out using the discrete FFT. The observed differences, which can be ascribed to approximation errors due to the use of the FFT algorithm, are in the order of 10^{-16} and can thus be neglected.

2.2 Numerical Simulations

We test our model against field data from the San Felice salt marsh (Venice Lagoon, Itay), for which combined elevation and vegetation data are available at a spatial resolution of 1 m (**Figures 1A, B**). Both the marsh domain and elevation were set equal to those observed in the field (**Figures 1A, C**), and elevation was held constant over the whole simulation duration. In this way, biotic interactions can emerge more clearly as no eco-morphodynamic feedbacks are allowed.

2.2.1 Sensitivity Analysis

To explore model performances and their sensitivity to input parameters, simulations of 50-year duration were carried out to allow time for convergence to a dynamic steady state in terms of vegetation distributions. In order to filter out oscillations due to demographic stochasticity, each simulation was repeated 20 times, and aggregated results of repeated simulations were finally analyzed. A constant timestep equal to 1 solar month was used in all simulations.

We considered a total of 4 virtual species (i.e., a suitable assemblage of focus species), equal in number to those observed in the field and characterized by different fundamental niches (e.g., **Figure 2A**). Besides being equal in number to the species observed in the San Felice salt marsh (**Figures 1B, D**), the virtual species we adopted are generally characterized by habitat quality functions aimed to mimic, at least qualitatively, features of vegetation species found in the field (**Figure 1D**). Specifically, progressively larger values of the sigmoid point (z_0) in the habitat quality function are generally adopted as the ordinal number of the virtual species increases, from i=1 to i=4. In this way, we implicitly assume higher ordinal species to be generally less adapted to lower marsh elevations (**Figure 2**). Therefore, a direct qualitative correspondence can be drawn between virtual and field species, with Species 1, 2, 3, and 4 ideally representing *Spartina*, *Sarcocornia*, *Limonium*, and *Juncus*, respectively (**Figures 1B, D**).

Though potentially feasible, we did not attempt to calibrate the parameters of the fundamental niches based on the realized

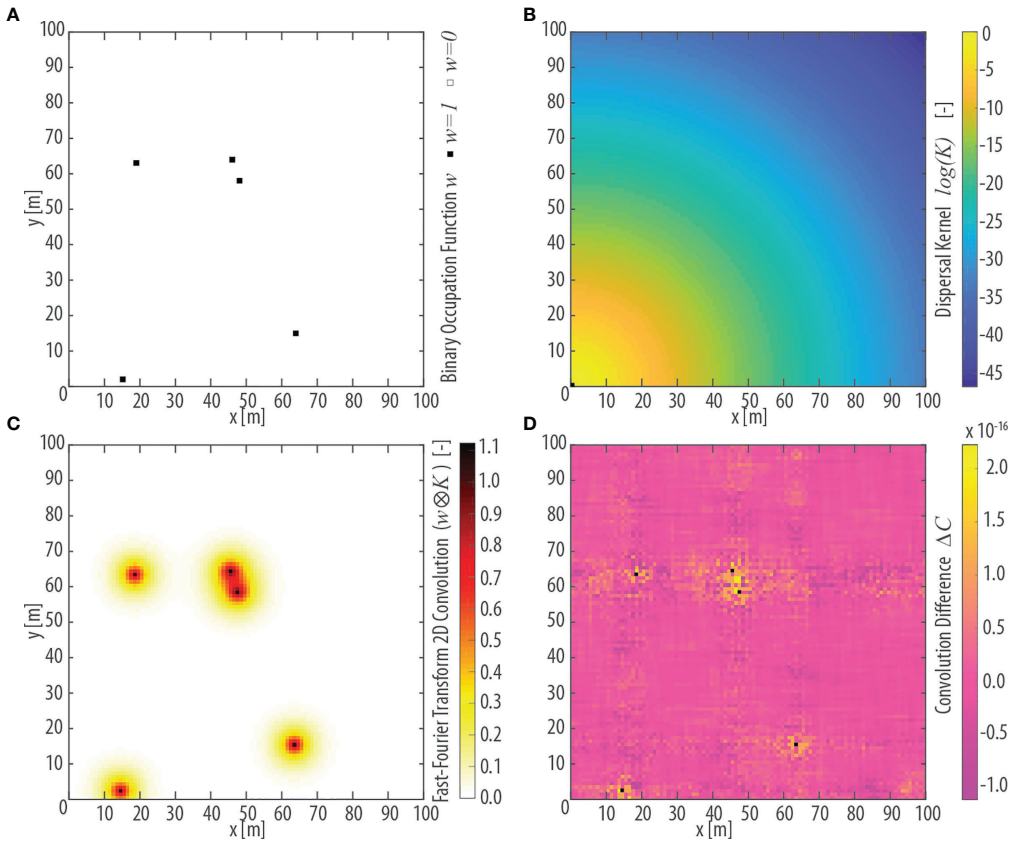


FIGURE 3 | Conceptualization of vegetation dispersal illustrated in a square, 100m-wide, idealized lattice domain. **(A)** The n=5 pixels colonized by a given focus species i are represented by a binary occupation function $w_{i,n}$.**(B)** Value of the dispersal kernel κ as a function of the euclidean distance d of each pixel from the pixel in the lower-left corner within the idealized lattice. The characteristic dispersal length for κ is assumed equal to D=3 m. **(C)** Results of the 2D convolution $w_{i,n} \otimes \kappa(d)$ between the occupancy field $w_{i,n}$ and the dispersal kernel $\kappa(d)$ shown in panel **(A, B)**, respectively, computed using the Fast-Fourier Transform (FFT) algorithm. **(D)** Absolute difference ΔC in the value of the 2D convolution $w_{i,n} \otimes \kappa(d)$ computed explicitly and using the FFT algorithm. Black dots denote pixels occupied by the focus species [see panel **(A)**] in which $\Delta C = 0$.

vegetation distributions. Rather, parameter values of fundamental niches were chosen to represent hypothetical species with plausible habitat-quality distributions that span topographic ranges along the intertidal gradient observed in the study case (D'Alpaos, 2011; Da Lio et al., 2013; Marani et al., 2013). This is because the present-day zonation of vegetation species in the salt marsh does not necessarily reflect ecological succession till now (Roozen and Westhoff, 1985), and the high frequency of environmental disturbances in tidal marshes often causes vegetation to be in a transient, non-equilibrium state (De Leeuw et al., 1992). Hence, realized distributions might not reflect dynamic-equilibrium conditions. Besides, although the general mechanisms driving vegetation zonation in tidal marshes may be universal, the importance of different physical factors is likely to vary geographically (Pennings et al., 2005). Therefore, realized niches for any given species can differ regionally as a function of local tidal range, salinity, and climate, as well as community assemblage (Silvestri et al., 2005). As such, the use of virtual species allows us to test our model and generalize our results beyond the study case analyzed here.

Our reference simulation (REF) employs an exponential dispersal kernel with a species-independent characteristic dispersal length D=1 m. At the beginning of the simulation, vegetation species and bare-soil patches are randomly distributed across the computational domain. The habitat quality function of all species is characterized by a constant rate k=90 m^{-1}, with logistic sigmoid points set equal to z_{0_i} ={0.05, 0.10, 0.15, 0.20} m for species i={1,2,3,4} respectively. We assume species-independent baseline mortality rate μ_0=5·10^{-3} [days^{-1}] and fertility rate φ=1/0.01 [days^{-1}], while the import fertility rate is defined as $\phi_{out} = \varphi/100$.

Finally, since different species are characterized by different interspecific competitive abilities, a baseline competitiveness coefficient δ_i is assigned to each species (**Figure 2B**). Though this coefficient can theoretically vary without limitations, in reality, we observe that more generalist and invasive species, typically restricted to lower marsh elevations, have comparably lower competitive ability than species occupying the higher portion of the intertidal range. Therefore, we hypothesized here that δ_i decreases linearly between δ=δ_{MAX}=1 and δ=δ_{MIN}≤δ_{MAX}, where

δ_{MAX} and δ_{MIN} represent the competitive ability of the species displaying the highest and lowest z_0 scores, respectively (**Figure 2B**). In our reference simulation, we set $\delta_{MIN}=\delta_{MAX}=1$, such that species have elevation-dependent habitat quality and otherwise neutral traits.

To demonstrate model robustness, we perform a sensitivity analysis and illustrate how changes in the key input parameters affect modelling results. Individual parameters are varied one at a time in order to study their effects on vegetation dynamics separately. In detail, we investigate the effects of different:

- w_cos_hair01_a.ddsinitial vegetation distribution (IVD series), assuming a marsh completely devoid of plant life (IDV_1) and a vegetation distribution equal to that observed in the field (IDV_2, see **Figure 1B**);
- habitat quality function (HQF series), considering four sets of values z_{0_i} equally spaced by 5 cm and spanning elevation ranges both lower (z_{0_i}={-5,0,5,10} cm for HQF_1; z_{0_i}={0,5,10,15} cm for HQF_2) and higher (z_{0_i}={10,15,20,25} cm for HQF_3; z_{0_i}={15,20,25,30} cm for HQF_4) than in the REF scenario. In addition, we also considered different sets of logistic rates k_i, the latter being assumed to either increase (k_i={5,30,60,90} m^{-1} for HQF_5; k_i={30,50,70,90} m^{-1} for HQF_6) or decrease (k_i={90,70,50,30} m^{-1} for HQF_5; k_i={90,60,30,5} m^{-1} for HQF_6) as z_{0_i} increases;
- interspecific competitive ability (ICA series), assuming progressively lower values of δ_{MIN}, corresponding to a progressively larger difference in interspecific competitive ability (δ_{MIN}=0.75 for ICA_1; δ_{MIN}=0.50 for ICA_2; δ_{MIN}=0.25 for ICA_3; δ_{MIN}=0.01 for ICA_4);
- base mortality rate (BMR series), considering values of μ_0 both larger ($\mu_0=5\cdot10^{-1}$ and $5\cdot10^{-2}$ $days^{-1}$ for BMR_1 and BMR_2, respectively) and lower ($\mu_0=5\cdot10^{-4}$ and $5\cdot10^{-5}$ $days^{-1}$ for BMR_3 and BMR_4, respectively) compared to the REF scenario, while maintaining the hypothesis of equal μ_0 for all the virtual species;
- fertility rate (VFR series), with φ values lower ($\varphi=10^0$ and 10^1 $days^{-1}$ for VFR_1 and VFR_2, respectively) and larger ($\varphi=10^3$ and 10^4 $days^{-1}$ for VFR_3 and VFR_4, respectively) than the REF scenario;
- dispersal kernel size (DKS series), considering different characteristic dispersal length D equal to 0.10 m (DKS_1), 0.50 m (DKS_2), 1.50 m (DKS_3), and 10 m (DKS_4), while maintaining the hypothesis of equal D for all the virtual species;

The parameter values for all the simulations are reported in **Table 1**. Results have been analyzed in terms of changes in the percent vegetation cover through time, as well as realized vegetation niches and probability distributions of continuous patch areas occupied by each species (see **Figure 1F**) at the end of the simulation. Moreover, we have also analyzed the patterns of species richness (i.e., α-diversity) as a function of marsh elevation by counting the number of species observed at given elevation intervals (see **Figure 1E**).

2.2.2 Transplant Experiment

To test the ability of our model to reproduce not only realistic patterns of vegetation zonation and species diversity at equilibrium but also dynamic evolution of marsh vegetation, we performed numerical simulations aimed to reproduce the outcomes of classical ecological experiments wherein a species is transplanted to an area outside its optimal (realized) niche.

After running the model for 50 years, in this way allowing for vegetation to reach a dynamic equilibrium condition, we simulated the transplant of marsh species outside their realized niches. To do so, we manually imposed species composition within a 20-by-20 m transplant plot. In the first series of simulations (TE_{COMP}), we did not remove established neighbor vegetation around the transplant plot, thereby allowing for interspecific competition. In contrast, in the second series of simulations (TE_{SOIL}), we created around the transplant plot a 5-meter-wide buffer layer of bare soil in which vegetation was systematically removed at each calculation timestep, in this way eradicating potential competitors. In simulations $TE1_{COMP}$ and $TE1_{SOIL}$, we transplanted Species 4, naturally occurring at high elevations, to a low-lying marsh area (average elevation of the transplant plot $\overline{z_{TP}}$ =14.19 ± 2.44 m), whereas in $TE2_{COMP}$ and $TE2_{SOIL}$ we moved Species 1, naturally occurring at low elevations, into a highly-elevated marsh plot ($\overline{z_{TP}}$=27.18 ± 5.19 cm). Simulation parameters for the transplant experiments were those of the ICA_1 series, in which the interspecific competitive ability increases linearly with z_{0_i} from δ_{MIN}=0.75 for Species 1 (z_{0_i}=0.05 m) to δ_{MAX}=1 for Species 4 (z_{0_i}=0.20 m). Individual simulations were repeated 20 times to filter out oscillations due to demographic stochasticity, and results were analyzed based on the evolution of percent vegetation cover through time within the transplant plot, monitoring monthly changes over a 10-year timespan.

In addition to this, we also compared results of the TE_{COMP} and TE_{SOIL} simulations with those obtained using a stochastic modelling approach that has been widely employed in previous studies (e.g., Morris et al., 2002; Morris, 2006; Da Lio et al., 2013; Marani et al., 2013; D'Alpaos and Marani, 2016). In such a stochastic model, vegetation habitat quality does not monotonically increase with marsh elevation, and mechanisms of dispersal and interspecific competitions are not explicitly accounted for. Specifically, habitat quality and interspecific competitive ability are jointly described by way of a simple analytical expression:

$$f_i(z_j) = 2 \cdot \left[exp\left(\lambda_i\left(z_j - \overline{z}_i\right)\right) + exp\left(-\lambda_i\left(z_j - \overline{z}_i\right)\right)\right] \qquad (10)$$

where $f_i(\overline{z_i})$=1 defines the elevation at which both habitat quality and competitive ability are highest, whereas λ_i is a specific scale parameter expressing the rate at which the habitat quality tends to zero as elevation departs from the optimal range, with larger (smaller) values of λ_i corresponding to more (less) "specialized" vegetation species. Similarly to our model, the mortality rate of species i at site j, characterized by an elevation z_j, is inversely proportional to local habitat quality $\mu_i(z_j) = \mu_{o_i} \cdot f_i^{-1}(z_j)$ [$days^{-1}$]. In contrast to our model, however, when vegetation dies at z_j, the successful colonizer is chosen stochastically, proportionally to the local habitat quality of all species at site j. Using this stochastic model, we replicated the TE_{COMP} and TE_{SOIL} simulations in terms of both transplant strategies and locations. A value of λ = 5 equal for all species was used in the

TABLE 1 | Simulation parameters for the different scenarios investigated in the sensitivity analysis.

Sim.	Param.of interest	Initial vegetation distribution	Habitat Quality		Comp. ability	Mortality rate	Fertility rate	Kernel size
			z_0 [cm]	k [m^{-1}]	δ_{MIN} [-]	μ_0 [$days^{-1}$]	φ [$days^{-1}$]	D [m]
REF	\	Random	{5,10,15,20}	{90,90,90,90}	1	$5{\cdot}10^{-3}$	10^2	1
IVD_1	\	Bare soil	{5,10,15,20}	{90,90,90,90}	1	$5{\cdot}10^{-3}$	10^2	1
IVD_2	\	**Figure 2C**	{5,10,15,20}	{90,90,90,90}	1	$5{\cdot}10^{-3}$	10^2	1
HQF_1	z_0	Random	{-5,0,5,10}	{90,90,90,90}	1	$5{\cdot}10^{-3}$	10^2	1
HQF_2	z_0	Random	{0,5,10,15}	{90,90,90,90}	1	$5{\cdot}10^{-3}$	10^2	1
HQF_3	z_0	Random	{10,15,20,25}	{90,90,90,90}	1	$5{\cdot}10^{-3}$	10^2	1
HQF_4	z_0	Random	{15,20,25,30}	{90,90,90,90}	1	$5{\cdot}10^{-3}$	10^2	1
HQF_5	k	Random	{5,10,15,20}	{5,30,60,90}	1	$5{\cdot}10^{-3}$	10^2	1
HQF_6	k	Random	{5,10,15,20}	{30,50,70,90}	1	$5{\cdot}10^{-3}$	10^2	1
HQF_7	k	Random	{5,10,15,20}	{90,70,50,30}	1	$5{\cdot}10^{-3}$	10^2	1
HQF_8	k	Random	{5,10,15,20}	{90,60,30,5}	1	$5{\cdot}10^{-3}$	10^2	1
ICA_1	δ_{MIN}	Random	{5,10,15,20}	{90,90,90,90}	0.75	$5{\cdot}10^{-3}$	10^2	1
ICA_2	δ_{MIN}	Random	{5,10,15,20}	{90,90,90,90}	0.5	$5{\cdot}10^{-3}$	10^2	1
ICA_3	δ_{MIN}	Random	{5,10,15,20}	{90,90,90,90}	0.25	$5{\cdot}10^{-3}$	10^2	1
ICA_4	δ_{MIN}	Random	{5,10,15,20}	{90,90,90,90}	0.01	$5{\cdot}10^{-3}$	10^2	1
BMR_1	μ_0	Random	{5,10,15,20}	{90,90,90,90}	1	$5{\cdot}10^{-1}$	10^2	1
BMR_2	μ_0	Random	{5,10,15,20}	{90,90,90,90}	1	$5{\cdot}10^{-2}$	10^2	1
BMR_3	μ_0	Random	{5,10,15,20}	{90,90,90,90}	1	$5{\cdot}10^{-4}$	10^2	1
BMR_4	μ_0	Random	{5,10,15,20}	{90,90,90,90}	1	$5{\cdot}10^{-5}$	10^2	1
VFR_1	ϕ	Random	{5,10,15,20}	{90,90,90,90}	1	$5{\cdot}10^{-3}$	10^0	1
VFR_2	ϕ	Random	{5,10,15,20}	{90,90,90,90}	1	$5{\cdot}10^{-3}$	10^1	1
VFR_3	ϕ	Random	{5,10,15,20}	{90,90,90,90}	1	$5{\cdot}10^{-3}$	10^3	1
VFR_4	ϕ	Random	{5,10,15,20}	{90,90,90,90}	1	$5{\cdot}10^{-3}$	10^4	1
DKS_1	D^{-1}	Random	{5,10,15,20}	{90,90,90,90}	1	$5{\cdot}10^{-3}$	10^2	0.1
DKS_2	D^{-1}	Random	{5,10,15,20}	{90,90,90,90}	1	$5{\cdot}10^{-3}$	10^2	0.5
DKS_3	D^{-1}	Random	{5,10,15,20}	{90,90,90,90}	1	$5{\cdot}10^{-3}$	10^2	1.5
DKS_4	D^{-1}	Random	{5,10,15,20}	{90,90,90,90}	1	$5{\cdot}10^{-3}$	10^2	10

Gray shading denotes the parameter of interest for each simulation.

simulations, whereas $\overline{z_i}$ was assumed equal to {0.15 0.23 0.25 0.30} m for species i={1,2,3,4}, respectively. These values of $\overline{z_i}$ approximately correspond to the elevations at which logistic habitat quality functions of individual species reach their maximum values in the ICA_1 scenario, which was considered in the transplant simulations carried out using our own model. Similarly to the other transplant experiments, in the $TE3_{COMP}$ and $TE3_{SOIL}$ simulations, we transplanted Species 4 ($\overline{z_4}$=0.30 m) to a low-lying marsh area, whereas in $TE4_{COMP}$ and $TE4_{SOIL}$ we moved Species 1 ($\overline{z_1}$=0.15 m) to upper marsh portions.

3 RESULTS AND DISCUSSION

3.1 Sensitivity Analysis

We qualitatively compared our modelling results with field data in terms of realized vegetation distributions (see **Figure 1D**) and α-diversity (see **Figure 1E**), as well as probability distributions of continuous patch areas occupied by each species (see **Figure 1F**) for different sets of model parameters. Moreover, we also monitored the evolution of percent vegetation cover over the whole simulation horizon.

Results obtained from the REF simulation show that dynamic equilibrium in vegetation spatial distribution is attained after a time τ_e equal to 20 to 30 years from the beginning of the simulation (see **Figure 4H**), suggesting the selected simulation duration to be adequate. Similarly to field data, plots of the modelled realized vegetation niches and α-diversity display hump-shaped patterns (**Figure 4M**), while empirical probability distributions of vegetation patch size, plotted as cumulative probability of exceedance to avoid binning issues, clearly show a power-law character, jointly with the finite-size scaling effect induced by the cutoff dictated by specific maximum patch area (e.g., Giometto et al., 2013; Rinaldo et al., 2014) (**Figure 4R**). This altogether indicates that a relatively simple model such as that employed in the REF scenario, where species have elevation-dependent habitat quality functions and otherwise neutral traits, suffice in reproducing realistic patterns of species niches, diversity, and zonation (see **Figures 1D–F** for comparison).

Initial vegetation distributions different from the REF scenario have limited effects on the model results at equilibrium. Specifically, results by all means similar to the REF simulation are obtained for the IDV_1 scenario (**Supplementary Figure 1**), whereas only slight differences are observed between the REF and IDV_2 scenarios, the latter being characterized by a longer τ_e (**Supplementary Figure 1**). Clearly, the similarity of results obtained for the IVD_1, IVD_2, and REF scenarios depends on the prescribed marsh elevations (**Figure 1A**), and above all on the fact that such elevations remain constant during the entire simulation. Since vegetation is not allowed to eco-engineer marsh topography through, e.g., organic matter deposition and sediment particle capture (D'Alpaos et al., 2007; Marani et al., 2013; Brückner et al., 2019), thereby ameliorating specific local habitat quality, the system is ineluctably destined to reach similar dynamic equilibrium

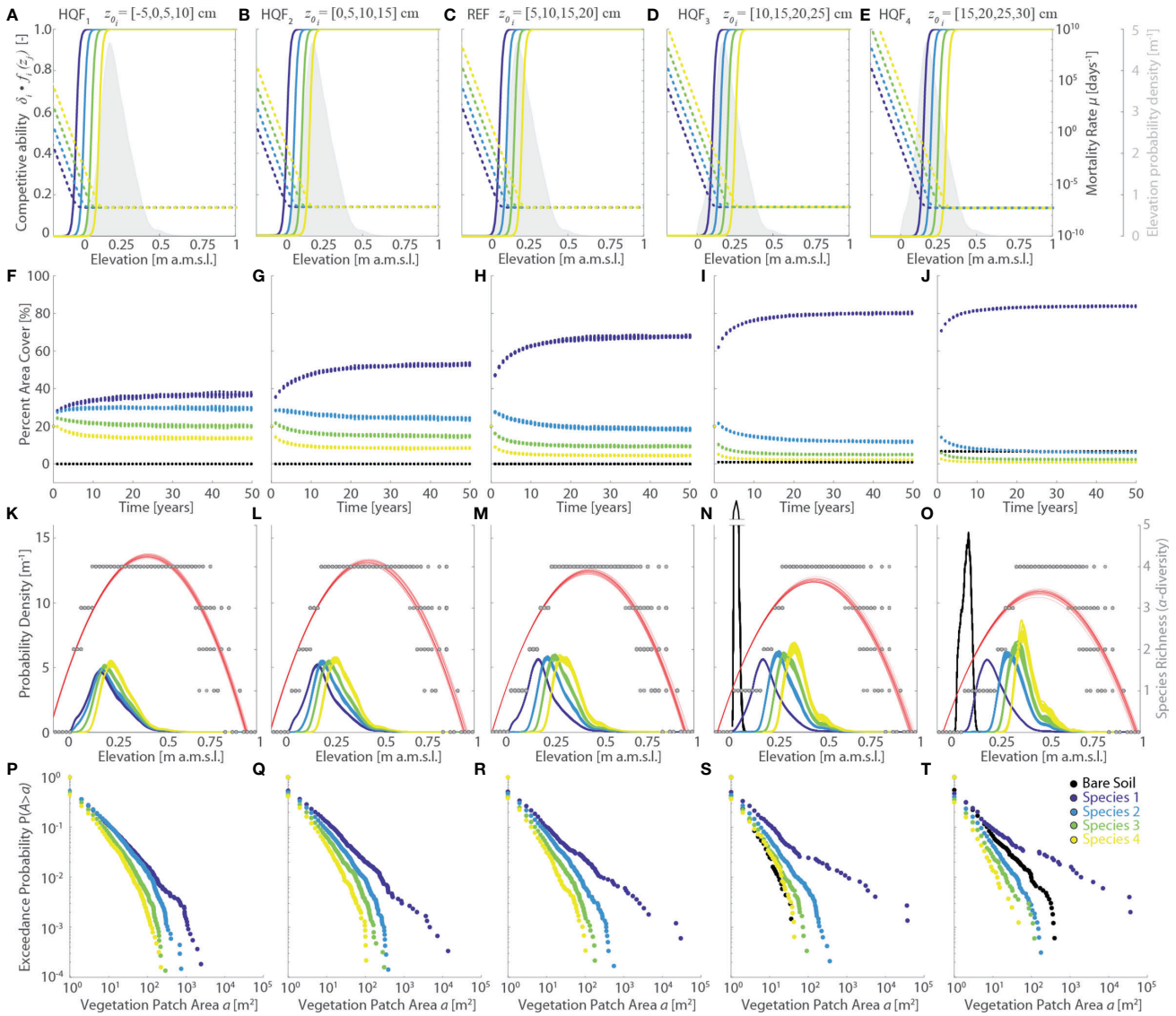


FIGURE 4 | Effects of changes in the vegetation habitat quality functions (HQF series, varying logistic sigmoid point z_0). Results of the reference simulation (REF, z_0={5,10,15,20} cm) are shown in the central column. The first and second columns report respectively the results of the HQF_1 (z_0={-5,0,5,10} cm) and HQF_2 (z_0={0,5,10,15} cm) simulations, whereas the fourth and fifth columns show the results of the HQF_4 (z_0={10,15,20,25} cm) and HQF_5 (z_0={15,20,25,30} cm) simulations, respectively. Each panel displays data derived from all the 20 numerical simulations performed for each scenario. Different colors denote different vegetation species, including bare soil, according to the legend shown in the lower-right panel. **(A–E)** Patterns of specific competitive ability $\delta_i f_i(z_j)$ (continuous lines, left y-axis) and mortality rate $\mu_i(z_j)$ (dotted lines, right y-axis) as a function of local marsh elevation (z_j). The gray area denotes the probability density estimates of marsh elevation within the computational domain. **(F–J)** Changes of percent vegetation cover over the whole simulation horizon. **(K–O)** Realized vegetation niches (left y-axis) and local species richness (i.e., α-diversity, right y-axis) as a function of marsh elevation at the end of the simulation horizon. Gray dots represent α-diversity point data with red lines showing the best quadratic fit to point data. **(P–T)** Empirical probability distributions of spatially-continuous vegetation patch areas are shown based on the exceedance probability for a given vegetation patch size.

conditions under fixed vegetation habitat quality functions, regardless of the prescribed initial vegetation distribution.

In contrast, changes in the parameters characterizing specific habitat quality functions have non-negligible effects. Progressively larger values of the logistic sigmoid point z_{0_i} (HQF_1 to HQF_4 simulations, **Figure 4**) enhance species mortality within the observed marsh elevation range, in this way shortening the time τ_e required to reach dynamic equilibrium conditions from about 35 years for HQF_1 to less than 20 years in the HQF_5 scenario (**Figures 4A–E**). Moreover, larger z_{0_i} promote the expansion of Species 1 - which occupies more than 80% of the marsh surface at the end of the HQF_5 run compared to 65% and 40% in the REF and HQF_1 scenarios, respectively – as well as of bare soil, which accounts for about 8%

of the marsh area in the HQF_5 simulation while being virtually absent in the HQF_1, HQF_2, and REF scenarios (**Figures 4F–I, L**). Not only do Species 1 and bare soil become more widespread for larger z_{0_i}, but also the average as well as the maximum size of the continuous patches they occupy increase, pointing to a more pronounced zonation for these two vegetation classes (**Figures 4P–T**). Expansion of Species 1 and bare soil occurs at the expenses of Species 2, 3, and 4, for which both the percent area cover (**Figures 4F–I, L**) and the average size of continuous patch areas (**Figures 4P–T**) decrease as z_{0_i} increases. Finally, increasing values of z_{0_i} produce a progressively more marked differentiation of the realized vegetation distributions, which nonetheless still display realistic hump-shaped patterns, much as the vegetation α-diversity (**Figures 4K–O**).

Variations in the logistic rate k_i (HQF_5 to HQF_8 simulations series, **Figure 5**) significantly affect habitat quality functions and, as a consequence, both specific competitive ability $\delta_i f_i(z_j)$ and mortality rates μ_i (**Figures 5A–E**). However, the most marked changes in $\delta_i f_i(z_j)$ occur at elevations z_j which are not commonly found within the studied marsh. Thus, the net effect of changing k_i on the simulation results is generally not significant, both in terms of final vegetation distributions (**Figures 5K–T**) and vegetation evolution through time (**Figures 5F–J**). The only exception is represented by the HQF_5 scenario, in which the low value of k_1 reduces the competitive ability of Species 1 at levels lower than any other species across most of the marsh elevation distribution (**Figure 5A**). This leads to a more widespread presence and a more marked zonation of both Species 2 and 3 (**Figures 5A, P**) relative to all the other scenarios, including the REF simulation. Although all other simulations seem to suggest otherwise, the HQF_5 run clearly demonstrates k_i to be a key parameters for the model results. Therefore, rather than pointing to a reduced sensitivity of the model to changes in the logistic rates k_i, our analyses suggest that simulation results depend not only on the specific parameters of habitat quality functions, and ratios thereof, but also on the elevation distributions of the computational domain.

The latter argument is further supported by the analyses of the ICA simulation series, in which we investigate the effect of changing interspecific competitive ability δ_i (**Figure 6**). By changing the baseline competitive ability of Species 1 (δ_1=δ_{MIN}) relative to Species 4 (δ_4= δ_{MAX}=1), and adjusting δ_i of all other species proportionally to the specific values of z_{0_i} based on δ_{MAX}-δ_{MIN}, we produced significant changes in the specific competitive abilities $\delta f_i(z_j)$ for z_j values that are widespread across our study site, without altering specific mortality (**Figures 6A–E**). These modifications have profound effects on the modelled vegetation distributions, as well as on the evolution of vegetation cover through time. In detail, progressively lower values of δ_{MIN}, corresponding to progressively larger differences in competitive ability relative to the REF scenario, lead to a progressive reduction in the area covered by Species 1 accompanied by an increase in the marsh areas occupied by all the other species (**Figures 6F–I, L**). Notably, Species 2 becomes dominant in the ICA_3 and ICA_4 scenarios despite ranking second-last in terms of maximum competitive ability. This is once again dictated by the distribution of topographic elevations characterizing our study marsh, which leads to Species 2 having the largest competitive ability for all elevations equal or lower than the average marsh elevation (**Figures 6D, E**). This favors the colonization of large portions of the marsh platform by a more generalist, less competitive species, which is in line with vegetation distributions typically observed in the field (Belluco et al., 2006; Wang et al., 2007; Bang et al., 2018; Yang et al., 2020b) (**Figure 1F**). Changes in the relative interspecific competitive ability also produce differences in the time τ_e required to reach dynamic equilibrium. Even though no clear trends emerge from our data, we highlight that τ_e is consistently shorter (<15 years) than in the REF simulation for all the analyzed ICA scenarios (**Figures 6F–I, L**). Analysis of patch size distribution suggests that vegetation zonation becomes more pronounced as the relative abundance of a given species increases, with the dominant species in terms of area cover typically displaying larger patches both in terms of average and maximum area size, in accordance with field data (see **Figure 1F**). Consistently with all the previous simulations, as well as with field data, realized vegetation niches and α-diversity plots exhibit hump-shaped patterns. Finally, we observe that larger differences in interspecific competitive abilities result in more differentiated vegetation realized niches, especially in terms of distribution peak magnitudes (**Figures 6K–O**).

Changes in vegetation base mortality rate μ_0 appear to mostly affect the time required to reach dynamic equilibrium (τ_e), with smaller μ_0 leading to longer τ_e (**Supplementary Figure 2**). However, if enough time is allowed for the system to reach equilibrium, no significant differences among distinct simulations are observed in terms of percent vegetation cover, realized vegetation distribution and α-diversity, and characteristic vegetation patch sizes (**Suppementary Figure 2**). Although our observations suggest μ_0 to have reduced effects on the final vegetation distributions, provided that times longer than τ_e are ensured, we should stress how vegetation mortality represents a key parameter to model the long-term marsh ecomorphodynamic evolution under changing climate forcings, since μ_0 dictates the characteristic timescale required by the marsh to respond to external perturbations (e.g., Brückner et al., 2019).

Changes in vegetation fertility rate φ have limited effects on the numerical simulation results (**Supplementary Figure 3**), the only appreciable difference being the appearance, for fertility rates one or two orders of magnitude lower than in the REF scenario, of patches of bare soil, which are however small in size and cover an extremely small portion of the computational domain (**Supplementary Figure 3**, VFR_1 and VFR_2 scenarios). Clearly, this is due to the fact that changes in fertility rate only affect the magnitude of specific colonization rate C_{ij} while leaving the relative (i.e, interspecific) ratios ($C_{i,j}/C_{i+1,j}$) of these rates unaltered. Such a reduced sensitivity of the model to changing φ points to a much stronger control of both marsh-elevation distribution and habitat quality functions in determining patterns of vegetation zonation in mature marshes. Notwithstanding the importance of fertility in determining the initial encroachment of pioneer species in emerging salt marshes,

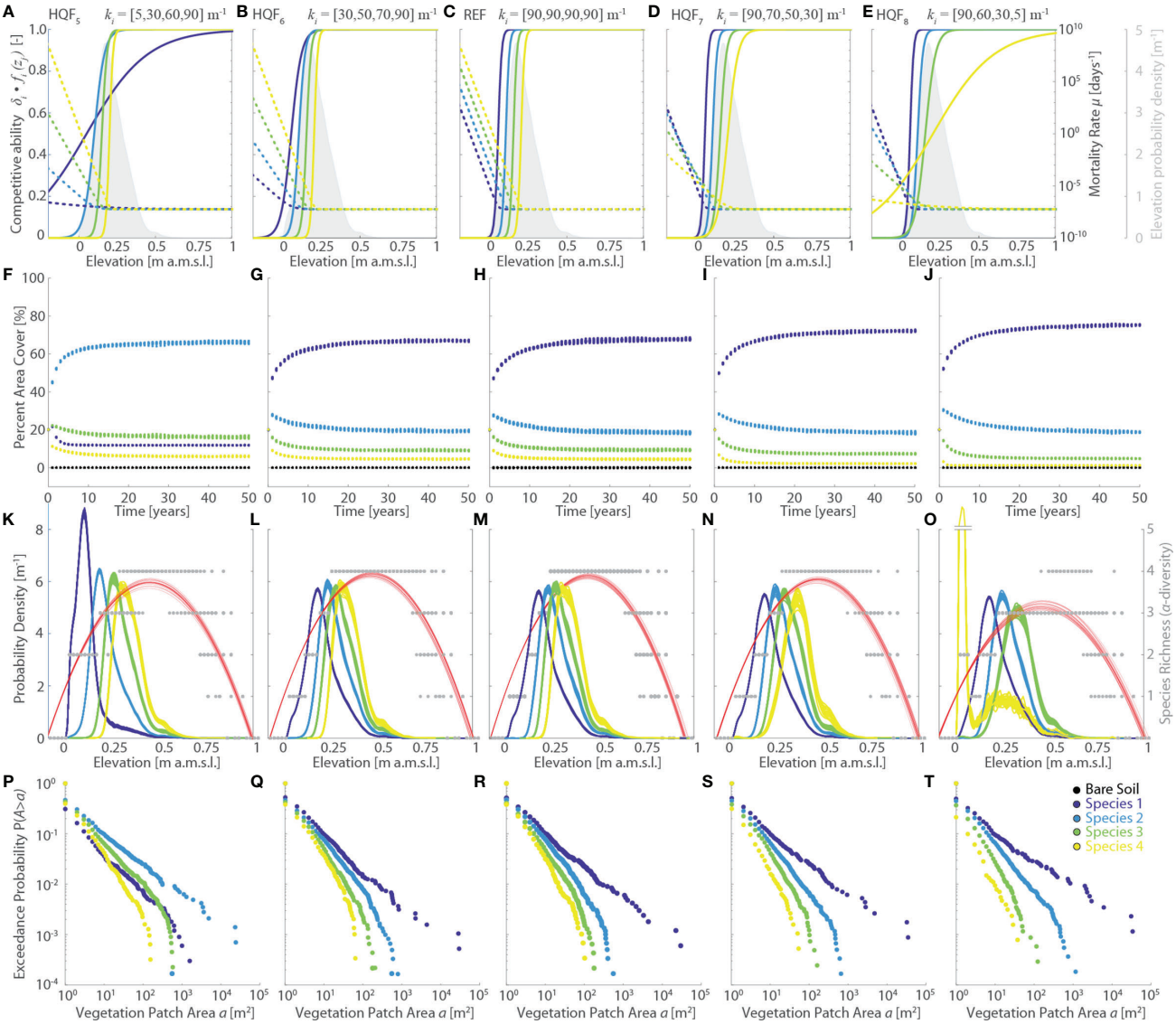


FIGURE 5 | Effects of changes in the vegetation habitat quality functions (HQF series, varying logistic rate k_i). Results of the reference simulation (REF, k_i= {90,90,90,90} m^{-1}) are shown in the central column. The first and second columns report respectively the results of the HQF_5 (k_i={5,30,60,90} m^{-1}) and HQF_6 (k_i={30,50,70,90} m^{-1}) simulations, whereas the fourth and fifth columns show the results of the HQF_7 (k_i = {90,70,50,30} m^{-1}) and HQF_8 (k_i= {90,60,30,5} m^{-1}) simulations, respectively. Each panel displays data derived from all the 20 numerical simulations performed for each scenario. Different colors denote different vegetation species, including bare soil, according to the legend shown in the lower-right panel. **(A–E)** Patterns of specific competitive ability $\delta_i f_i(z_j)$ (continuous lines, left y-axis) and mortality rate $\mu_i(z_j)$ (dotted lines, right y-axis) as a function of local marsh elevation (z_j). The gray area denotes the probability density estimates of marsh elevation within the computational domain. **(F–J)** Changes of percent vegetation cover over the whole simulation horizon. **(K–O)** Realized vegetation niches (left y-axis) and local species richness (i.e., α-diversity, right y-axis) as a function of marsh elevation at the end of the simulation horizon. Gray dots represent α-diversity point data with red lines showing the best quadratic fit to point data. **(P–T)** Empirical probability distributions of spatially-continuous vegetation patch areas are shown based on the exceedance probability for a given vegetation patch size.

field experiments indeed suggest that the availability of marsh area located at elevations potentially suitable for vegetation establishment and growth is a key driver for marsh ecological dynamics (e.g., Davy et al., 2011; Lõhmus et al., 2020; van Regteren et al., 2020).

Finally, changes in the size of the dispersal kernel, which were investigated by varying the characteristic dispersal length D (DKS series, **Figure 7**), generally have non-negligible effects on the observed vegetation distributions. Specifically, effects on realized vegetation distributions appear to be significant for values of D one order of magnitude different from the REF scenario (i.e., DKS_1 and DKS_4 simulations, **Figures 7K, O**). Increased dispersal abilities (i.e., larger values of D) result in progressively larger portions of the domain being colonized by Species 1, while the area occupied

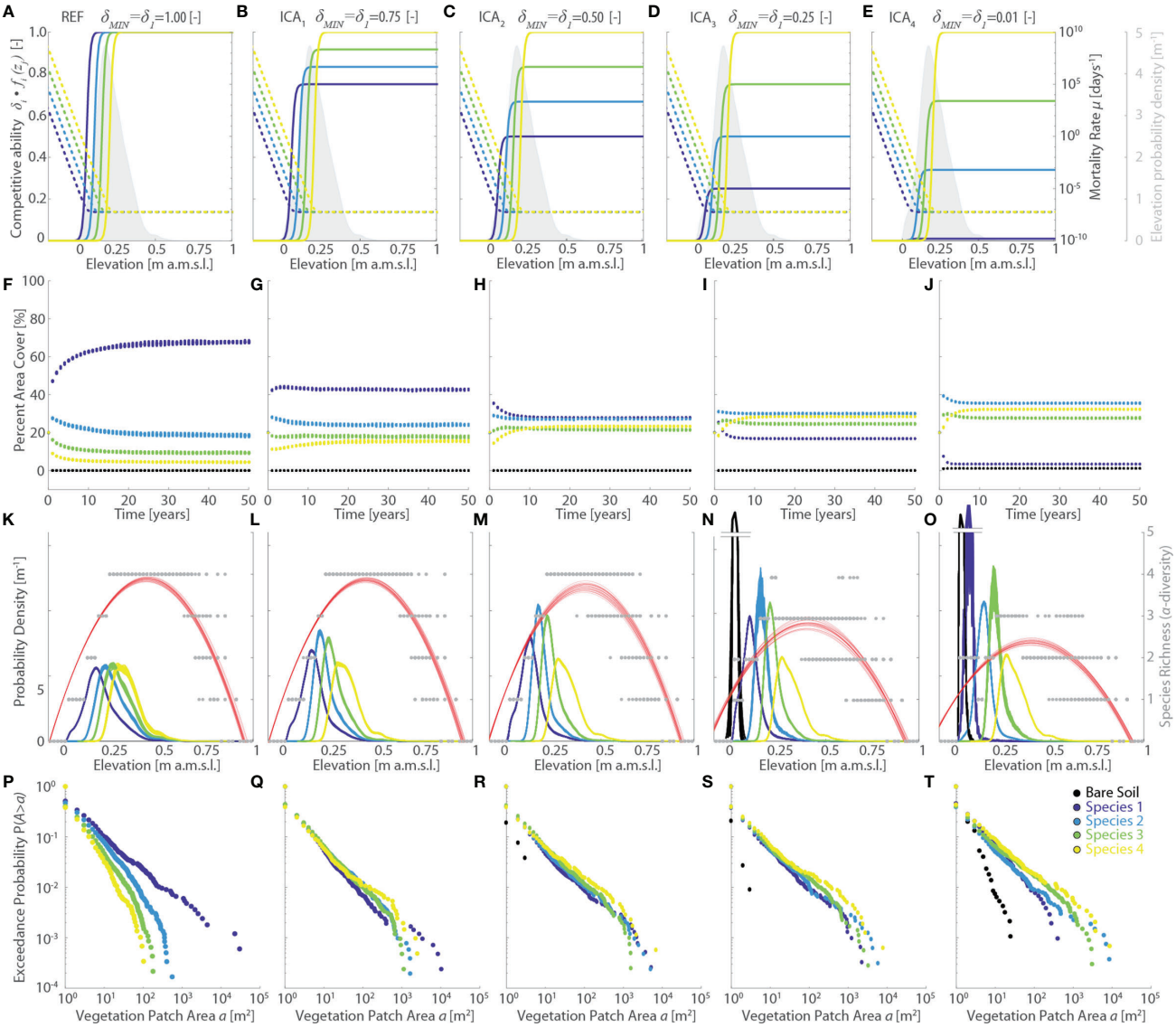


FIGURE 6 | Effects of changes in the vegetation interspecific competitive ability (ICA series, varying $\delta_1=\delta_{MIN}$). Results of the reference simulation (REF, δ_{MIN} = 1) are shown in the first column. Columns from second to fourth show results of the ICA$_1$ (δ_{MIN} = 0.75), ICA$_2$ (δ_{MIN}=0.50), ICA$_3$ (δ_{MIN}=0.25), and ICA$_4$ (δ_{MIN}=0.01) simulations, respectively. Each panel displays data derived from all the 20 numerical simulations performed for each scenario. Different colors denote different vegetation species, including bare soil, according to the legend shown in the lower-right panel. **(A–E)** Patterns of specific competitive ability $\delta_i f_i(z_j)$ (continuous lines, left y-axis) and mortality rate $\mu_i(z_j)$ (dotted lines, right y-axis) as a function of local marsh elevation (z_j).The gray area denotes the probability density estimates of marsh elevation within the computational domain. **(F–J)** Changes of percent vegetation cover over the whole simulation horizon. **(K–O)** Realized vegetation niches (left y-axis) and local species richness (i.e., α-diversity, right y-axis) as a function of marsh elevation at the end of the simulation horizon. Gray dots represent α-diversity point data with red lines showing the best quadratic fit to point data. **(P–T)** Empirical probability distributions of spatially-continuous vegetation patch areas are shown based on the exceedance probability for a given vegetation patch size.

by all the other species decreases (**Figures 7F–I, J**). Nonetheless, larger D tend to produce a more pronounced clusterization of vegetation within continuous patches (**Figures 7P–T**), even though both the maximum and average patch size are mediated by the proportion of marsh area occupied by each species. Thus, the characteristic patch size of Species 2,3, and 4 is reduced in the DKS$_4$ scenario as a result of the dominance of Species 1. The latter, which occupies more than 80% of the computational domain (**Figure 7J**), shows a significant increase in both maximum and average patch size relative to all other simulations (**Figure 7T**), thus supporting the hypothesis that enhanced dispersal abilities generally lead to more pronounced vegetation clustering.

It is difficult to relate our modelling results to field vegetation dynamics, since knowledge about dispersal abilities of salt-marsh species is limited and dispersal by water especially understudied (Bakker et al., 1985; Wolters et al., 2008; Bullock et al., 2017;

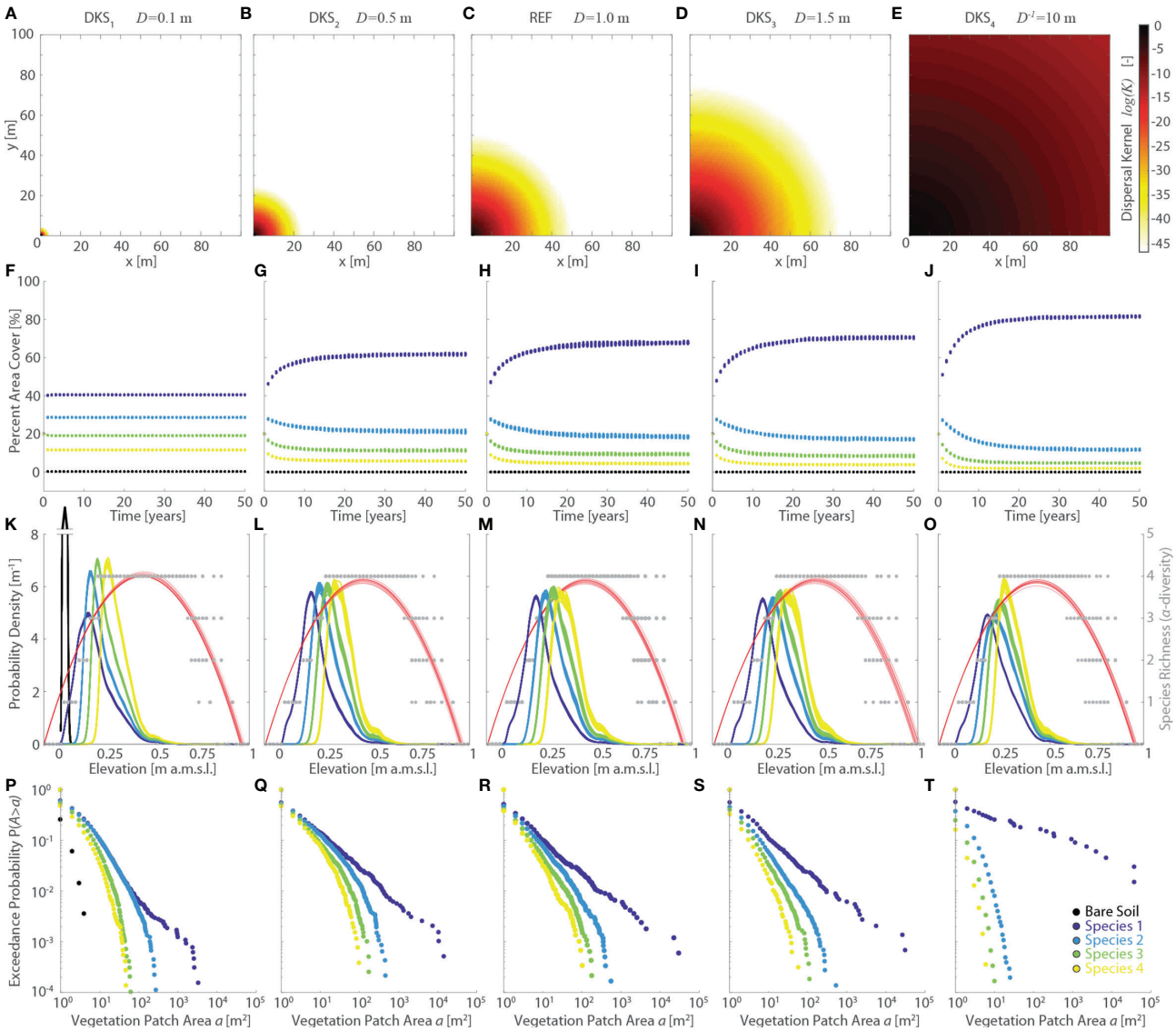


FIGURE 7 | Effects of changes in dispersal kernel size (DKS series, characteristic dispersal length D is assumed to be species-independent). Results of the reference simulation (REF, D = 1 m) are shown in the central column. The first and second columns report respectively the results of the DKS_1 (D=0.1 m) and DKS_2 (D = 0.5 m) simulations, whereas the fourth and fifth columns show the results of the DKS_3 (D = 1.5 m) and DKS_4 (D=10 m) simulations, respectively. Each panel displays data derived from all the 20 numerical simulations performed for each scenario. Different colors denote different vegetation species, including bare soil, according to the legend shown in the lower-right panel. **(A–E)** Representation of the dispersal kernel illustrated in a square, 100m wide, idealized lattice domain. Log-values of the dispersal kernel κ are shown as a function of the euclidean distance d of each pixel from the pixel in the lower-left corner within the idealized lattice. **(F–J, M)** Changes of percent vegetation cover over the whole simulation horizon. **(K–O)** Realized vegetation niches (left y-axis) and local species richness (i.e., α-diversity, right y-axis) as a function of marsh elevation at the end of the simulation horizon. Gray dots represent α-diversity point data with red lines showing the best quadratic fit to point data. **(P–T)** Empirical probability distributions of spatially-continuous vegetation patch areas are shown based on the exceedance probability for a given vegetation patch size.

Lõhmus et al., 2020). This is mostly because measurements of vegetation dispersal in the field, though much needed, are time-consuming and therefore scarce, despite significant recent advances derived from genetic approaches (see Shao et al., 2021, and references therein). In spite of this, however, care should be given in interpreting numerical results obtained by imposing values of D equal to, or lower than, the resolution of the computational domain. Indeed, numerical errors in the computation of the dispersal kernel become larger as D approaches the pixel size. Our analyses show that for a domain resolution equal to 1 m, numerical errors lower than 1% are obtained for D>1.5 m. Even though errors remain lower than 5% for D>0.9 m, they increase exponentially as D decreases further, reaching values as high as 27% for D =0.5 m (DKS_2 scenario).

Results of the sensitivity analysis are summarized in **Figure 8**, which shows, for each species and for all the investigated

scenarios, the average percent cover at the end of numerical simulations plotted against the power-law exponent *(β)* of the exceedance probability of vegetation patch. The exponent *β*, computed by performing linear regression on log-transformed data, is used here as a proxy for the characteristic size of continuous vegetation patch, with larger *β* values denoting more pronounced zonation of vegetation species (see **Figure 8**).

Overall, sensitivity analysis demonstrates that model outcomes vary smoothly as parameter values are changed, and that the model can reproduce realistic patterns of vegetation zonation across the marsh topographic gradients. Even a relatively simple model, in which species have elevation-dependent fitness and otherwise neutral traits, suffices in reproducing patterns of zonation qualitatively similar to those typically observed from field data. Since the model assumes theoretical niches described by habitat quality functions monotonically increasing with marsh elevation, our results provide proof of concepts that the upper limit of realized vegetation distributions in tidal marshes is set by spatially explicit mechanisms of interspecific competition and dispersal. Therefore, realized marsh vegetation distributions exhibiting enhanced productivity within a narrow elevation range (e.g., Silvestri and Marani, 2004; Morris et al., 2005) do not necessarily resemble the fundamental niches of individual marsh halophytes. This notion has important implications for the interpretation of observed vegetation patterns, as well as of vegetation-environmental stress relations.

Although realistic vegetation distributions are obtained for a wide range of model parameters, results are especially sensitive to changes in the parameters describing habitat quality and competitive abilities of individual species (HQF and ICA series, **Figure 8**), as well as the characteristic length of species dispersal (DKS series, **Figure 8**). In particular, larger differences in competitive abilities among species and larger dispersal lengths promote more pronounced vegetation zonation, with direct implications for relative species abundance. In contrast, changes in vegetation baseline mortality (BMR series) and fertility rate (VFR series) appear to only affect the speed at which vegetation reaches dynamic equilibrium conditions, with limited influence on the final vegetation distribution (**Figure 8**). These findings suggest that the proposed model can indeed be used to infer the underlying theoretical niches, based on the observed realized patterns.

3.2 Transplant Experiment

While sensitivity analysis demonstrates model ability to reproduce realistic vegetation distributions at equilibrium, results of transplant experiments clarify whether the model can predict vegetation dynamics in agreement with field observations.

Transplantation of Species 4 to lower marsh elevations proves unsuccessful regardless of whether interspecific competition is limited ($TE1_{SOIL}$) or not ($TE1_{COMP}$) (**Figures 9A, B**). The transplanted species dies almost instantaneously, and vegetation cover within the transplant plot returns to the pre-transplant condition, i.e. dominated by Species 1 and 2. Interestingly though, suppression of competition by manual removal of neighboring vegetation around the transplant plot ($TE1_{SOIL}$ scenario, **Figure 9B**) reduces the speed at which vegetation recovers to pre-transplant conditions compared to

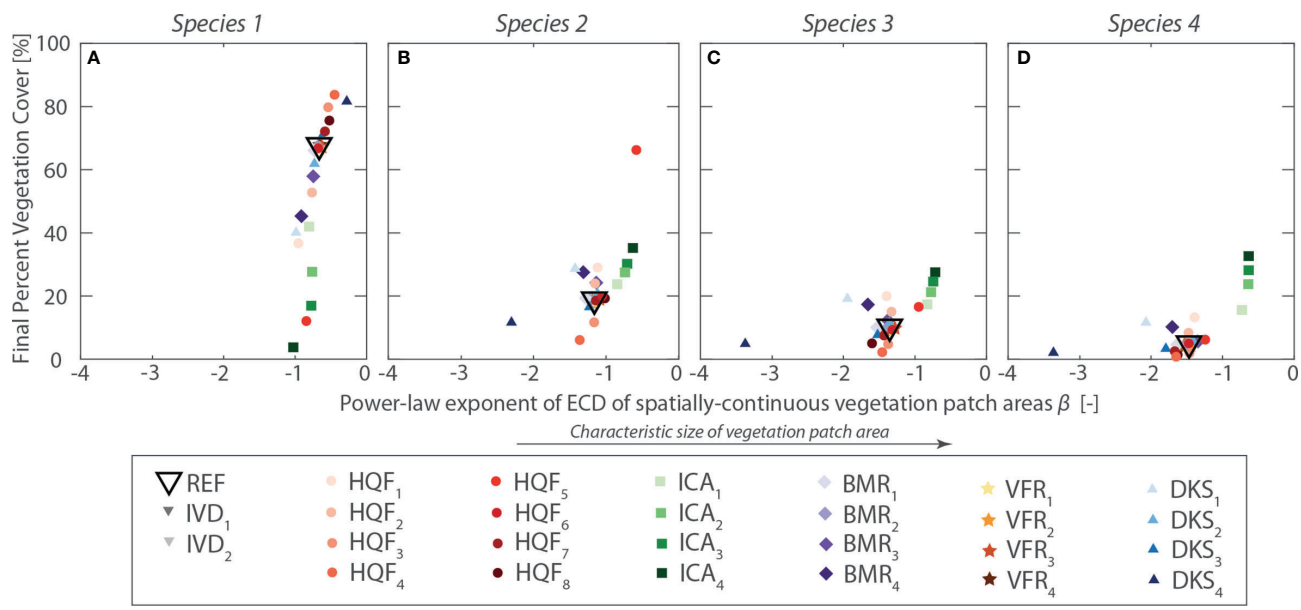


FIGURE 8 | Summary of sensitivity analysis. For each scenario explored in the sensitivity analysis, the average percent cover at the end of the numerical simulation is plotted against the power-law exponent *(β)* of the exceedance probability of vegetation patch. Panel **(A–D)** show the results for virtual Species 1 to 4, respectively. Different symbols denote different simulation series, whereas different colors are used to differentiate between different scenarios within each simulation series, as indicated in the lower inset.

the scenario in which competition is not limited ($TE1_{COMP}$, **Figure 9A**). This is dictated by the reduced colonization pressure exerted by neighbor vegetation when competition is limited, thus making vegetation dynamics within the transplant plot less dependent on vegetation distribution in neighboring sites. Our results agree qualitatively with the outcomes of field experiments, in which high-marsh species exhibit stunted growth and rapid mortality when transplanted to lower tidal elevations, irrespective of the fact that biotic competition is allowed or not (Bertness and Ellison, 1987; Bertness, 1991a; Bertness, 1991b). However, similar results can be obtained using the stochastic model ($TE3_{COMP}$ and $TE3_{SOIL}$ scenarios, **Figures 9E, F**), with the only difference that the results are not influenced in any way by limitations of competing neighbors. This is because interspecific competition is not treated in a spatially explicit way, as it only occurs as a function of the local marsh elevation. Therefore, in the stochastic model, vegetation distribution outside of the transplant plot does not influence the vegetation distribution inside of it.

If, on the one hand, these results suggest that our model does not necessarily perform better than previous, and perhaps less sophisticated, numerical frameworks in this case, on the other hand, the results obtained by transplanting Species 1 to upper marsh sites demonstrate otherwise. Being characterized by high habitat quality at high marsh elevations, Species 1 thrives on short timescales within the transplant plot, although in the long term the pre-transplant dynamic equilibrium is eventually reestablished over timescales that clearly depend on the level of interspecific competition, as well as on vegetation mortality and fertility. Specifically, when competition around the transplant plot is allowed, Species 1 is quickly outcompeted by Species 3 and 4, which are characterized by better competitive ability at higher

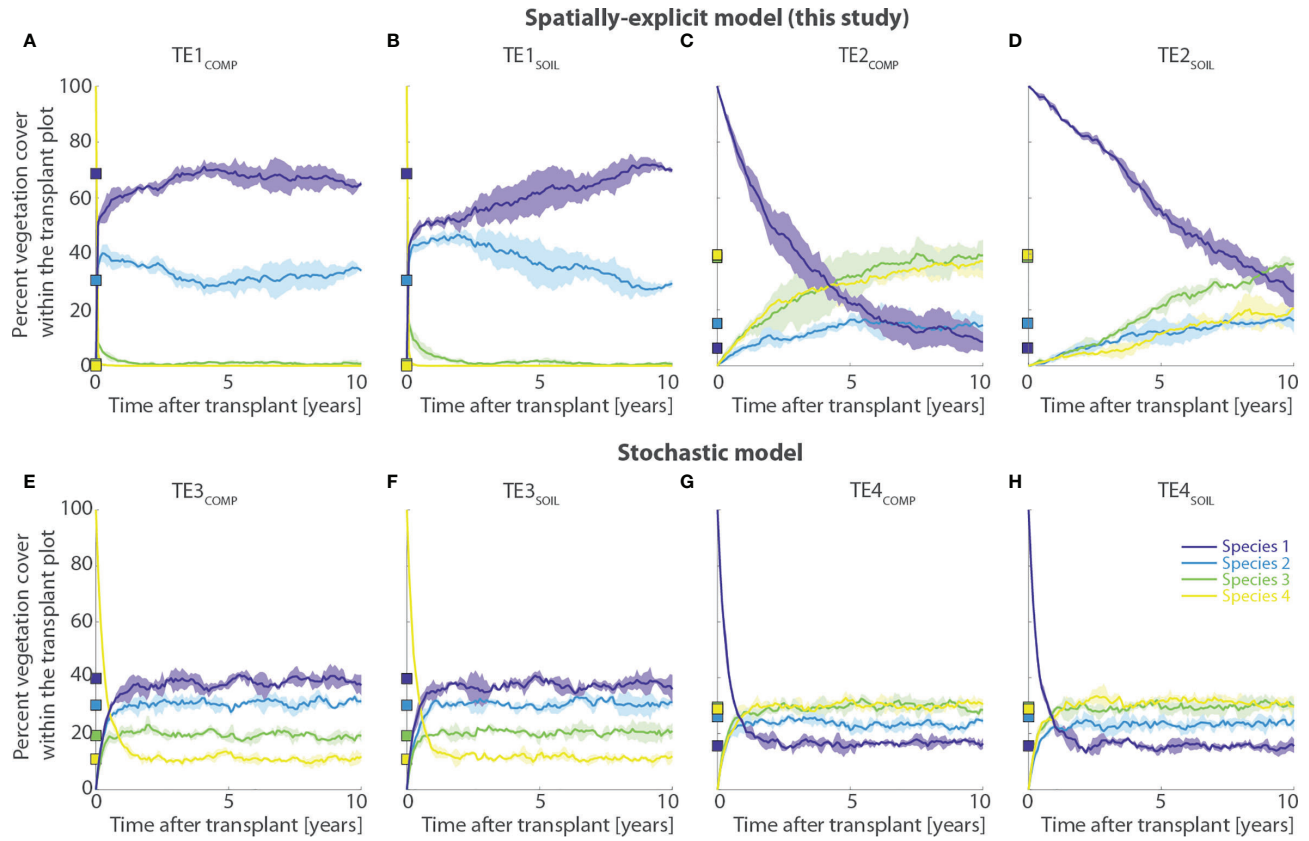


FIGURE 9 | Results of transplant experiments of marsh halophytes outside their realized ecological niches (TE simulation series). Each panel shows changes in percent vegetation cover through time within a 20-by-20 m transplant plot. The first row displays results obtained using the numerical model proposed in the present study, whereas the second row reports results derived from a stochastic model that does not account for spatially- and density-dependent mechanisms of species competition and dispersal (see Section 2.2.2). Names of numerical simulations are reported above each panel. The subscript "COMP" denote simulations in which biotic competition from neighbor sites was allowed within the transplant plot, whereas the subscript "SOIL" indicates simulations in which competition was artificially impeded by systematically removing vegetation within a 5-meter-wide buffer layer around the transplant plot. **(A, B)** Transplant of Species 4 from upper to lower marsh portions using the spatially-explicit model; **(C, D)** Transplant of Species 1 from lower to upper marsh portions using the spatially-explicit model; **(E, F)** Transplant of Species 4 from upper to lower marsh portions using the stochastic model; **(G, H)** Transplant of Species 1 from lower to upper marsh portions using the stochastic model. Each simulation was repeated 20 times to filter out oscillations due to demographic stochasticity. Continuous lines represent average values of aggregated simulation results, with shaded areas denoting standard deviations. Squares on the y-axis show the percent vegetation cover prior to the transplant. Different colors denote different vegetation species according to the legend shown in panel **(H)**. Percent cover of bare soil is deliberately not reported as it never accounted for more than 1% of the total transplant plot area.

marsh elevations ($TE2_{COMP}$, **Figure 9C**). Although it takes nearly 8 years to return to values of percent vegetation cover similar to the pre-experiment conditions, Species 1 undergoes a relatively fast decay, as it ceases to be the dominant species within the transplant plot in less than 4 years (**Figure 9C**). Conversely, if competition is artificially limited ($TE2_{SOIL}$, **Figure 9D**), performances decrease much more slowly, and Species 1 dominates the transplant plot 9 years after the transplant (**Figure 9D**). After that, Species 3 becomes dominant, but Species 1 still occupies about 25% of the plot area compared to less than 5% in the pre-transplant conditions. These results, which are in qualitative agreement with ecological manipulation field experiments, are not matched by the stochastic model (**Figures 9G, H**). In the latter, for the $TE4_{SOIL}$ and $TE4_{COMP}$ scenarios, the performances of Species 1 decrease rapidly and percent vegetation cover returns to the pre-transplant conditions in less than 2 years, regardless of whether competition from neighbor species is removed or not (**Figures 9G, H**).

One should appreciate that the observed slow, yet steady decline in Species 1 coverage in the $TE2_{SOIL}$ scenario does not contrast with experimental results suggesting that performances of low-marsh species do not decline significantly through time (e.g., Bertness and Ellison, 1987; Bertness, 1991a; Bertness, 1991b). Indeed, the duration of most field experiments does not exceed 2 years, and the rate of performance decay can vary according to both the elevation distribution within the transplant plot and, more importantly, the values of model parameters adopted in the simulations. The latter should be calibrated based on field data obtained for specific study cases of interest, which is beyond the scope of the present work.

Ultimately, replication of vegetation transplant experiments demonstrates that spatially explicit treatments of biotic interactions make our model comparatively better suited than traditional stochastic models to reproduce spatial dynamics of halophytes in tidal marshes.

4 MODEL LIMITATIONS AND FUTURE DEVELOPMENTS

Limitations in the proposed modelling framework need to be recalled.

First, most of the underlying assumptions are derived from the study of perennial halophytes in mature salt marshes. Hence, care should be given when utilizing this model for the study of initial plant establishment in juvenile marsh communities (Hu et al., 2015; Balke et al., 2017; Lõhmus et al., 2020). If, on the one hand, our model synthetizes mechanisms of species dispersal, which are recognized as the main drivers for vegetation evolution in well-developed marsh ecotones (Bertness and Ellison, 1987; Ellison, 1987; Chang et al., 2007; Lõhmus et al., 2020), on the other hand, it does not necessarily properly reproduce the initial establishment of pioneer annual halophytes. This is because the process of initial vegetation encroachment on a bare tidal flat depends on a number of factors, including specific seedling strategies, windows of opportunity for rooting, presence of microbenthic species that stabilize soil and facilitate vegetation establishment, and many physical environmental stresses such as waves, rainfalls, and tidal currents that critically mediate habitat quality, especially when vegetation is sparse (Craft, 2000; Temmerman et al., 2007; Friess et al., 2012; Hu et al., 2015; Brückner et al., 2019; van Regteren et al., 2020). Thus, the relative importance of dispersal vs. establishment mechanisms in emerging marshes needs additional effort to be properly described in the model. This shortcoming is also in part due to the lack of field data that would allow one to disentangle dispersal and establishment functions (e.g., Lõhmus et al., 2020). The collection of field data is however challenging due to the many factors involved. Besides, measuring dispersal is notoriously difficult and resource-consuming (Bullock et al., 2006).

Second, our model assumes physical stresses to be inversely proportional to the local marsh elevation. In marshes that are irregularly flooded, however, this paradigm may not apply because there may not be a consistent gradient in physical stresses across the marsh (Costa et al., 2003; Pennings et al., 2005). While the general mechanisms producing zonation patterns of vegetation in coastal salt marshes may be universal (Grime, 1977; Grace and Wetzel, 1981; Keddy, 1989; Pennings and Bertness, 2001), the importance of particular physical stresses is likely to vary geographically (Pennings et al., 2005). Particularly, salinity stress probably plays a much more important role in mediating plant zonation patterns at lower latitudes, as testified by the presence, in low-latitude marshes, of unvegetated salt pans that occur where soil salinities exceed levels that plants can tolerate (Pennings and Bertness, 1999; Pennings and Bertness, 2001; Pennings and He, 2021). In contrast, unvegetated areas in mid- and high-latitude marshes typically result from disturbance or waterlogging, rather than from high salinities (Pennings and Bertness, 2001; Mariotti et al., 2020). (Pennings and Bertness, 2001). Hence, ecological interactions are likely to vary with latitude due to different temperatures and evapotranspiration dynamics, and specific habitat quality functions need to be adapted accordingly. Therefore, fundamental vegetation niches are site-specific and need to be calibrated as such.

Third, in addition to salinity, many other abiotic and biotic factors can potentially modify habitat quality and should therefore be considered (Pennings and Bertness, 2001; Pennings and He, 2021). Biotic factors are mostly related to the feeding and grazing activities of domestic and wild fauna. Feeding on plant rhizomes by for example geese, sheep, nutria, and wild boar, as well as burrowing by crabs, can heavily disturb the upper layer of marsh soil, limit marsh vertical accretion, and reduce large areas of vegetation to bare mud (Wiegert and Freeman, 1990; Ungar, 1998; Perillo and Iribarne, 2003; Wolters et al., 2005; Xin et al., 2009). Abiotic factors include the burial of vegetation by rafts of floating wrack, fires, ice disturbance in high-latitude marshes, and hydrodynamic stresses due to tidal currents and wind waves. Waves in particular can actively modify sediment transport processes

and the morphodynamics of exposed marsh margins (Wang et al., 2017; Evans et al., 2019; Finotello et al., 2020; Tognin et al., 2021). This can create potential hotspots for biodiversity (Elsey-Quirk et al., 2019) and determine changes in vegetation distribution according to the ability of individual species to tolerate such stresses, which in turn depends on the specific vegetation traits (Leonard and Croft, 2006; Van Wesenbeeck et al., 2008; Schoutens et al., 2020; D'Alpaos et al., 2021; Schulte Ostermann et al., 2021). On the one hand, some of the abiotic factors, especially the hydrodynamic ones, could be included rather easily in the model, for example by weighting the habitat quality based on stresses calculated from hydrodynamic models or, alternatively, as a function of the distance of each site from marsh edges exposed to the action of waves and currents (see for example Gourgue et al., 2021a; Kalra et al., 2021). On the other hand, however, most of the biotic factors affecting vegetation dynamics are difficult to conceptualize, as they depend on the community ecology of marsh fauna (Gaskins et al., 2020; Burdick et al., 2021; Pennings and He, 2021).

Another important environmental factor we have not so far considered is the level of nutrients, which is also related to climate changes and anthropogenic pressures on salt marshes (Ratliff et al., 2015; Newton et al., 2020; Hughes et al., 2021). Since salt marshes are nitrogen-poor, yet very productive environments, they are potentially much sensitive to changes in nutrient availability (Valiela and Teal, 1974; Pennings et al., 2002; Muench and Elsey-Quirk, 2019; Carmona et al., 2021; Giblin et al., 2021) In fact, eutrophication may have marked effects on marsh plant community structure by shifting the competitive balance among plants and consequently altering the zonation and species composition of plant communities (Levine et al., 1998). Field experiments demonstrated that there exists a nutrient-dependent competitive hierarchy, with competitive outcomes being typically reversed when nutrients were abundant as better stress tolerators become dominant competitors (Emery et al., 2001). This is because competition for resources occurs primarily belowground under normal marsh conditions, but shifts to aboveground at enhanced high nutrient levels. Clearly, such dynamics cannot be currently predicted by our model of plant competition and dispersal, and should therefore be considered in the future.

Finally, our model does not explicitly account for facilitation mechanisms among plant species wherein neighbors can potentially buffer one another from physical stresses and mutually ameliorate their habitat quality (Bertness, 1991a; Bertness and Shumway, 1993; Castellanos et al., 1994; Bruno et al., 2017). The outcome of competition can be more complex than described in our model when facilitative mechanisms operate, potentially modifying the species' realized distributions dynamically (Bertness and Ewanchuk, 2002). Conceptualization of these mechanisms would require spatially explicit quantification of physical stresses, the latter being critical in mediating facilitative interactions. Nonetheless, many ecologists have suggested that while facilitation is common in secondary succession under harsh physical conditions, competition dominates vegetation dynamics under benign physical conditions, for which our model can therefore be considered reliable (see Pennings and He, 2021).

Despite the above-mentioned limitations, the model proposed in this study marks a significant step forward in the way salt-marsh ecological dynamics are modelled compared to earlier studies. In particular, spatially explicit treatments of vegetation dynamics can contribute to better understanding the effects of biotic processes that cannot be captured by 0D and 1D models, such as vegetation migration due to geomorphological displacement (Morris et al., 2002; Morris, 2006).

Our model can be coupled with virtually any hydro-morphodynamic model to simulate the intertwined evolution of marsh halophytes and topographic gradients under varying rates of relative sea-level rise and sediment supply. If the models employ different types of grids or spatial resolutions, the coupling can also be performed using subgrid schemes together with appropriate multiscale coupling techniques (e.g., Gourgue et al., 2021a; Gourgue et al., 2021b; Kalra et al., 2021). The evolution of marsh topography at each site will be obtained by a combined geomorphological balance between erosion and sedimentation, computed by the morphodynamic model, and organic production by halophytic vegetation, calculated by the vegetation model. The latter depends on biomass production, which can be expressed proportionally to habitat quality. Vegetation biomass can also influence abiotic morphodynamic processes by increasing the critical shear stress for erosion and promoting the capture of suspended sediments (D'Alpaos et al., 2007). Because biotic processes are typically slower than geomorphological ones, separate integration time scales can be adopted; for example, an hourly scale for geomorphological processes and a monthly or annual scale for ecological interaction processes. The model can be forced through a sequence of tides until it reaches a pseudo-stationary state where sedimentation and erosion and associated mean sea rise balance each other out.

Such an ecomorphodynamic model would improve our ability to model salt-marsh evolution numerically and allow for cost-effective ecological community-level studies, providing useful insights on the ecomorphodynamics of marsh landscapes that are of interest to the whole community of coastal scientists and managers.

5 CONCLUSIONS

We presented an innovative numerical model aimed to simulate the dynamics of salt-marsh vegetation. Different from previous models, we accounted for spatially explicit mechanisms of interspecific competition and dispersal and assumed species performances to monotonically increase with marsh elevation in accordance with field observations.

We demonstrated that the model is capable of reproducing patterns of vegetation zonation and ecological dynamics by all means similar to those observed from field data and experiments. Numerical simulations aimed to simulate the transplant of vegetation species outside their optimum (realized) niches

showed that our model can successfully reproduce the outcomes of classic field ecological experiments. Since a comparison proved that different models fail in reproducing such dynamics, this result has to be interpreted as a direct consequence of both the unique habitat quality functions and the novel spatial treatments of vegetation competition and dispersal we adopted. Besides, our numerical results support the idea that realized vegetation distributions in which a given species exhibits large productivity within a narrow elevation range do not reflect species fundamental niches. Rather, they arise directly from mechanisms of interspecific competition and dispersal.

Sensitivity analyses suggest that the model is especially sensitive to changes in specific habitat quality functions and competitive ability, even though the relative importance of each model parameter is critically mediated by the distribution of marsh topographic gradients relative to the competitive ability of the considered virtual species assemblage. Therefore, although both the conceptualization and results of our model are consistent with general paradigms about zonation and dynamics of marsh plants, we suggest that the nature of ecological interactions is likely to vary geographically because of variations in the physical environment, and these variations must be taken into account in order to successfully apply our model to study marsh evolution across different geographical scales and vegetation communities.

Our model can be easily coupled with any hydro-morphodynamic model to simulate the intertwined, dynamic evolution of salt marsh vegetation and topography under changing external forcings. Moreover, by using the model in an inverse fashion, one could also infer the underlying theoretical niches based on a comparison between the modelled and observed vegetation distributions.

DATA AVAILABILITY STATEMENT

The Matlab source code of the model presented in this study is freely available at https://doi.org/10.5281/zenodo.6285870, together with the elevation and vegetation data utilized in the simulations.

AUTHOR CONTRIBUTIONS

AF: designed research, developed model, performed and analyzed simulations, prepared figure, and wrote manuscript. EB: designed research, developed model, revised manuscript. AD'A: designed research, revised manuscript. MM: designed research, revised manuscript. All authors contributed to the article and approved the submitted version.

FUNDING

Scientific activity performed in the "Venezia2021" Research Programme, coordinated by CO.RI.LA, with the contribution of the Provveditorato for the Public Works of Veneto, Trentino Alto Adige and Friuli Venezia Giulia, Research Line 3.2 [AD'A (PI); EB (PI); and AF], that is gratefully acknowledged.

ACKNOWLEDGMENTS

The authors acknowledge constructive comments and suggestions by two reviewers and steering from the Guest Editor, which greatly helped to improve an early version of the manuscript. AF is grateful to Dr. Jim van Belzen for discussions regarding field experiments of marsh vegetation transplant and the related scientific literature, as well as to Dr. Zicheng Yang for providing the Lidar and vegetation data shown in **Figure 1**.

SUPPLEMENTARY MATERIAL

The Supplementary Material for this article can be found online at: https://www.frontiersin.org/articles/10.3389/fmars.2022.866570/full#supplementary-material

REFERENCES

Bakker, J. P., Dijkstra, M., and Russchen, P. T. (1985). Dispersal, Germination and Early Establishment of Halophytes and Glycophytes on a Grazed and Abandoned Salt-Marsh Gradient. *New Phytol.* 101, 291–308. doi: 10.1111/j.1469-8137.1985.tb02836.x

Balke, T., Lõhmus, K., Hillebrand, H., Zielinski, O., Haynert, K., Meier, D., et al. (2017). Experimental Salt Marsh Islands: A Model System for Novel Metacommunity Experiments. *Estuar. Coast. Shelf Sci.* 198, 288–298. doi: 10.1016/j.ecss.2017.09.021

Bang, J. H., Bae, M. J., and Lee, E. J. (2018). Plant Distribution Along an Elevational Gradient in a Macrotidal Salt Marsh on the West Coast of Korea. *Aquat. Bot.* 147, 52–60. doi: 10.1016/j.aquabot.2018.03.005

Barbier, E. B., Hacker, S. D., Kennedy, C., Koch, E. W., and Stier, A. C. (2011). And Silliman, B The Value of Estuarine and Coastal Ecosystem Services. *R. Ecol. Monogr.* 81, 169–93. doi: 10.1890/10-1510.1

Belluco, E., Camuffo, M., Ferrari, S., Modenese, L., Silvestri, S., Marani, A., et al. (2006). Mapping Salt-Marsh Vegetation by Multispectral and Hyperspectral Remote Sensing. *Remote Sens. Environ.* 105, 54–67. doi: 10.1016/j.rse.2006.06.006

Bertassello, L. E., Bertuzzo, E., Botter, G., Jawitz, J. W., Aubeneau, A. F., Hoverman, J. T., et al. (2021). Dynamic Spatio-Temporal Patterns of Metapopulation Occupancy in Patchy Habitats. *R. Soc Open Sci.* 8, 201309. doi: 10.1098/rsos.201309

Bertness, M. D. (1991a). Interspecific Interactions Among High Marsh Perennials in a New England Salt Marsh. *Ecology* 72, 125–137. doi: 10.2307/1938908

Bertness, M. D. (1991b). Zonation of Spartina Patens and Spartina Alterniflora in New England Salt Marsh Author (s): Mark D. Bertness Published by: Wiley on Behalf of the Ecological Society of America Stable URL: Https://Www.Jstor.Org/Stable/1938909 REFERENCES Linked Referen. *Ecol. Soc* 72, 138–148. doi: 10.2307/1938909

Bertness, M. D., and Ellison, A. M. (1987). Determinants of Pattern in a New England Salt Marsh Plant Community. *Ecol. Monogr.* 57, 129–147. doi: 10.2307/1942621

Bertness, M. D., and Ewanchuk, P. J. (2002). Latitudinal and Climate-Driven Variation in the Strength and Nature of Biological Interactions in New England Salt Marshes. *Oecologia* 132, 392–401. doi: 10.1007/s00442-002-0972-y

Bertness, M. D., and Shumway, S. W. (1993). Competition and Facilitation in Marsh Plants. *Am. Nat.* 142, 718–724. doi: 10.1086/285567

Best, Ü.S.N., Wegen, M., Van Der,, Dijkstra, J., Willemsen, P. W. J. M., and Borsje, B. W. (2018). Do Salt Marshes Survive Sea Level Rise? Modelling Wave Action, Morphodynamics and Vegetation Dynamics. *Environ. Model. Software* 109, 152–166. doi: 10.1016/j.envsoft.2018.08.004

Boaga, J., D'Alpaos, A., Cassiani, G., Marani, M., and Putti, M. (2014). Plant-Soil Interactions in Salt Marsh Environments: Experimental Evidence From Electrical Resistivity Tomography in the Venice Lagoon. *Geophys. Res. Lett.* 41, 6160–6166. doi: 10.1002/2014GL060983

Bouma, T. J., Friedrichs, M., Van Wesenbeeck, B. K., Temmerman, S., Graf, G., and Herman, P. M. J. (2009). Density-Dependent Linkage of Scale-Dependent Feedbacks: A Flume Study on the Intertidal Macrophyte Spartina Anglica. *Oikos* 118, 260–268. doi: 10.1111/j.1600-0706.2008.16892.x

Boyd, B. M., Sommerfield, C. K., and Elsey-Quirk, T. (2017). Hydrogeomorphic Influences on Salt Marsh Sediment Accumulation and Accretion in Two Estuaries of the U.S. Mid-Atlantic Coast. *Mar. Geol.* 383, 132–145. doi: 10.1016/j.margeo.2016.11.008

Broome, S. W., Seneca, E. D., and Woodhouse, W. W. (1988). Tidal Salt Marsh Restoration. *Aquat. Bot* 32, 1–22. doi: 10.1016/0304-3770(88)90085-X

Brückner, M. Z. M., Schwarz, C., van Dijk, W. M., van Oorschot, M., Douma, H., and Kleinhans, M. G. (2019). Salt Marsh Establishment and Eco-Engineering Effects in Dynamic Estuaries Determined by Species Growth and Mortality. *J. Geophys. Res. Earth Surf.* 124, 2962–2986. doi: 10.1029/2019JF005092

Bruno, J. F. (2000). Facilitation of Cobble Beach Plant Communities Through Habitat Modification By Spartina Alterniflora. *Ecology* 81, 1179–1192. doi: 10.1890/0012-9658(2000)081[1179:focbpc]2.0.co;2

Bruno, J. F., and Kennedy, C. W. (2000). Patch-Size Dependent Habitat Modification and Facilitation on New England Cobble Beaches by Spartina Alterniflora. *Oecologia* 122, 98–108. doi: 10.1007/PL00008841

Bruno, J. F., Rand, T. A., Emery, N. C., and Bertness, M. D. (2017). Facilitative and Competitive Interaction Components Among New England Salt Marsh Plants. *PeerJ* 2017, 1–15. doi: 10.7717/peerj.4049

Bullock, J. M., Mallada González, L., Tamme, R., Götzenberger, L., White, S. M., Pärtel, M., et al. (2017). A Synthesis of Empirical Plant Dispersal Kernels. *J. Ecol.* 105, 6–19. doi: 10.1111/1365-2745.12666

Bullock, J. M., Shea, K., and Skarpaas, O. (2006). Measuring Plant Dispersal: An Introduction to Field Methods and Experimental Design. *Plant Ecol.* 186, 217–234. doi: 10.1007/s11258-006-9124-5

Burdick, D. M., Moore, G. E., and Boyer, K. E. (2021). "Impacts of Exotic and Native Species Invading Tidal Marshes," in *Salt Marshes: Function, Dynamics, and Stresses*. Eds. D. M. FitzGerald and Z. J. Hughes (Cambridge: Cambridge University Press), 367–387. doi: 10.1017/9781316888933.017

Carmona, R., Muñoz, R., and Niell, F. X. (2021). Differential Nutrient Uptake by Saltmarsh Plants Is Modified by Increasing Salinity. *Front. Plant Sci.* 12. doi: 10.3389/fpls.2021.709453

Castellanos, E. M., Figueroa, M. E., and Davy, A. J. (1994). Nucleation and Facilitation in Saltmarsh Succession: Interactions Between Spartina Maritima and Arthrocnemum Perenne Author 82, 239–248. doi: 10.2307/2261292

Chang, A. E. R., Veeneklaas, R. M., and Bakker, J. P. (2007). Seed Dynamics Linked to Variability in Movement of Tidal Water Stable. *J. Veg. Sci.* 18, 253–262. doi: 10.1111/j.1654-1103.2007.tb02536.x

Chmura, G. L., Anisfeld, S. C., Cahoon, D. R., and Lynch, J. C. (2003). Global Carbon Sequestration in Tidal, Saline Wetland Soils. *Global Biogeochem. Cycles.* 17, 21–22. doi: 10.1029/2002gb001917

Costa, C. S. B., Marangoni, J. C., and Azevedo, A. M. G. (2003). Plant Zonation in Irregularly Flooded Salt Marshes: Relative Importance of Stress Tolerance and Biological Interactions. *J. Ecol.* 91, 951–965. doi: 10.1046/j.1365-2745.2003.00821.x

Costanza, R., d'Arge, R., de Groot, R., Farber, S. C., Grasso, M., Hannon, B., et al. (1997). The Value of the World's Ecosystem Services and Natural Capital. *Nature* 387, 253–260. doi: 10.1038/387253a0

Craft, C. (2000). Co-Development of Wetland Soils and Benthic Invertebrate Communities Following Salt Marsh Creation. *Wetl. Ecol. Manage.* 8, 197–207. doi: 10.1023/A:1008448620605

Crain, C. M., and Bertness, M. D. (2006). Ecosystem Engineering Across Environmental Gradients: Implications for Conservation and Management. *Bioscience* 56, 211–218. doi: 10.1641/0006-3568(2006)056[0211:EEAEGI]2.0.CO;2

Da Lio, C., D'Alpaos, A., and Marani, M. (2013). The Secret Gardener: Vegetation and the Emergence of Biogeomorphic Patterns in Tidal Environments. *Philos. Trans. A. Math. Phys. Eng. Sci.* 371, 20120367. doi: 10.1098/rsta.2012.0367

D'Alpaos, A. (2011). The Mutual Influence of Biotic and Abiotic Components on the Long-Term Ecomorphodynamic Evolution of Salt-Marsh Ecosystems. *Geomorphology* 126, 269–278. doi: 10.1016/j.geomorph.2010.04.027

D'Alpaos, A., Da Lio, C., and Marani, M. (2012). Biogeomorphology of Tidal Landforms: Physical and Biological Processes Shaping the Tidal Landscape. *Ecohydrology.* 5, 550–562. doi: 10.1002/eco.279

D'Alpaos, C., and D'Alpaos, A. (2021). The Valuation of Ecosystem Services in the Venice Lagoon: A Multicriteria Approach. *Sustainability* 13 (17), 9485. doi: 10.3390/su13179485

D'Alpaos, A., Finotello, A., Goodwin, G. C. H., and Mudd, S. M. (2021). "Salt Marsh Hydrodynamics," in *Salt Marshes: Function, Dynamics, and Stresses*. Eds. D. FitzGerald and Z. Hughes (Cambridge: Cambridge University Press), 53–81. doi: 10.1017/9781316888933.005

D'Alpaos, A., Lanzoni, S., Marani, M., and Rinaldo, A. (2007). Landscape Evolution in Tidal Embayments: Modeling the Interplay of Erosion, Sedimentation, and Vegetation Dynamics. *J. Geophys. Res. Earth Surf.* 112, 1–17. doi: 10.1029/2006JF000537

D'Alpaos, A., and Marani, M. (2016). Reading the Signatures of Biologic-Geomorphic Feedbacks in Salt-Marsh Landscapes. *Adv. Water Resour.* 93, 265–275. doi: 10.1016/j.advwatres.2015.09.004

Davy, A. J., Brown, M. J. H., Mossman, H. L., and Grant, A. (2011). Colonization of a Newly Developing Salt Marsh: Disentangling Independent Effects of Elevation and Redox Potential on Halophytes. *J. Ecol.* 99, 1350–1357. doi: 10.1111/j.1365-2745.2011.01870.x

Day, J. W., Boesch, D. F., Clairain, E. J., Kemp, G. P., Laska, S. D., Mitsch, W. J., et al. (2007). Restoration of the Mississippi Delta: Lessons From Hurricanes Katrina and Rita. *Science* 315, 1679–1684. doi: 10.1126/science.1137030

Day, J. W., Britsch, L. D., Hawes, S. R., Shaffer, G. P., Reed, D. J., and Cahoon, D. R. (2000). Pattern and Process of Land Loss in the Mississippi Delta: A Spatial and Temporal Analysis of Wetland Habitat Change. *Estuaries.* 23, 425–438. doi: 10.2307/1353136

Dayton, P. K. (1975). Experimental Evaluation of Ecological Dominance in a Rocky Intertidal Algal Community. *Ecol. Monogr.* 45, 137–159. doi: 10.2307/1942404

De Leeuw, J., Apon, L. P., Herman, P. M. J., de Munck, W., and Beeftink, W. G. (1992). Vegetation Response to Experimental and Natural Disturbance in Two Salt-Marsh Plant Communities in the Southwest Netherlands. *Netherlands J. Sea Res.* 30, 279–288. doi: 10.1016/0077-7579(92)90066-N

Ellison, A. M. (1987). Effects of Competition, Disturbance, and Herbivory on Salicornia Europaea. *Ecology* 68, 576–586. doi: 10.2307/1938463

Elsey-Quirk, T., Mariotti, G., Valentine, K., and Raper, K. (2019). Retreating Marsh Shoreline Creates Hotspots of High-Marsh Plant Diversity. *Sci. Rep.* 9, 1–9. doi: 10.1038/s41598-019-42119-8

Emery, N. C., Ewanchuk, P. J., and Bertness, M. D. (2001). Competition and Salt-Marsh Plant Zonation: Stress Tolerators may be Dominant Competitors. *Ecology* 82, 2471–2485. doi: 10.1890/0012-9658(2001)082[2471:CASMPZ]2.0.CO;2

Evans, B. R., Möller, I., Spencer, T., and Smith, G. (2019). Dynamics of Salt Marsh Margins are Related to Their Three-Dimensional Functional Form. *Earth Surf. Process. Landforms.* 44, 1816–1827. doi: 10.1002/esp.4614

Fagherazzi, S., Kirwan, M. L., Mudd, S. M., Guntenspergen, G. R., Temmerman, S., D'Alpaos, A., et al. (2012). Numerical Models of Salt Marsh Evolution: Ecological, Geomorphic, and Climatic Factors. *Rev. Geophys.* 50, 1–28. doi: 10.1029/2011RG000359

Finotello, A., Marani, M., Carniello, L., Pivato, M., Roner, M., Tommasini, L., et al. (2020). Control of Wind-Wave Power on Morphological Shape of Salt Marsh Margins. *Water Sci. Eng.* 13, 45–56. doi: 10.1016/j.wse.2020.03.006

FitzGerald, D. M., and Hughes, Z. (2019). Marsh Processes and Their Response to Climate Change and Sea-Level Rise. *Annu. Rev. Earth Planet. Sci.* 47, 481–517. doi: 10.1146/annurev-earth-082517-010255

Ford, H., Garbutt, A., Ladd, C., Malarkey, J., and Skov, M. W. (2016). Soil Stabilization Linked to Plant Diversity and Environmental Context in Coastal Wetlands. *J. Veg. Sci.* 27, 259–268. doi: 10.1111/jvs.12367

Friess, D. A., Krauss, K. W., Horstman, E. M., Balke, T., Bouma, T. J., Galli, D., et al. (2012). Are All Intertidal Wetlands Naturally Created Equal? Bottlenecks,

Thresholds and Knowledge Gaps to Mangrove and Saltmarsh Ecosystems. *Biol. Rev.* 87, 346–366. doi: 10.1111/j.1469-185X.2011.00198.x

Gaskins, L. C., Paxton, A. B., and Silliman, B. R. (2020). Megafauna in Salt Marshes. *Front. Mar. Sci.* 7. doi: 10.3389/fmars.2020.561476

Geng, L., D'Alpaos, A., Sgarabotto, A., Gong, Z., and Lanzoni, S. (2021). Intertwined Eco-Morphodynamic Evolution of Salt Marshes and Emerging Tidal Channel Networks. *Water Resour. Res.* 57, 1–25. doi: 10.1029/2021WR030840

Giblin, A. E., Fulweiler, R. W., and Hopkinson, C. S. (2021). "The Role of Marshes in Coastal Nutrient Dynamics and Loss," in *Salt Marshes: Function, Dynamics, and Stresses*. Eds. D. M. FitzGerald and Z. J. Hughes (Cambridge: Cambridge University Press), 113–154. doi: 10.1017/9781316888933.007

Giometto, A., Altermatt, F., Carrara, F., Maritan, A., and Rinaldo, A. (2013). Scaling Body Size Fluctuations. *Proc. Natl. Acad. Sci. U. S. A.* 110, 4646–4650. doi: 10.1073/pnas.1301552110

Goodwin, G. C. H., and Mudd, S. M. (2020). Detecting the Morphology of Prograding and Retreating Marsh Margins-Example of a Mega-Tidal Bay. *Remote Sens.* 12, 13. doi: 10.3390/RS12010013

Gourgue, O., van Belzen, J., Schwarz, C., Bouma, T. J., van de Koppel, J., and Temmerman, S. (2021a). A Convolution Method to Assess Subgrid-Scale Interactions Between Flow and Patchy Vegetation in Biogeomorphic Models. *J. Adv. Model. Earth Syst.* 13, 1–25. doi: 10.1029/2020MS002116

Gourgue, O., van Belzen, J., Schwarz, C., Vandenbruwaene, W., Vanlede, J., Belliard, J.-P., et al. (2021b). Biogeomorphic Modeling to Assess Resilience of Tidal Marsh Restoration to Sea Level Rise and Sediment Supply. *Earth Surf. Dyn. Discuss.*, 1–38. doi: 10.5194/esurf-2021-66

Grace, J. B., and Wetzel, R. G. (1981). Habitat Partitioning and Competitive Displacement in Cattails (Typha): Experimental Field Studies. *Am. Nat.* 118, 463–474. doi: 10.1086/283841

Grime, J. P. (1977). Evidence for the Existence of Three Primary Strategies in Plants and Its Relevance to Ecological and Evolutionary Theory. *Am. Nat.* 111, 1169–1194. doi: 10.1086/283244

Hughes, Z. J., FitzGerald, D. M., and Wilson, C. A. (2021). "Impacts of Climate Change and Sea Level Rise," in *Salt Marshes: Function, Dynamics, and Stresses*. Eds. D. M. FitzGerald and Z. J. Hughes (Cambridge: Cambridge University Press), 476–481. doi: 10.1017/9781316888933.021

Hutchinson, E. G. (1957). Concluding Remarks. *Cold Spring Harb. Symp. Quant. Biol.* 22, 415–442. doi: 10.1201/9781315366746

Hu, Z., van Belzen, J., van der Wal, D., Balke, T., Wang, Z. B., Stive, M., et al. (2015). Windows of Opportunity for Salt Marsh Vegetation Establishment on Bare Tidal Flats: {The} Importance of Temporal and Spatial Variability in Hydrodynamic Forcing. *J. Geophys. Res. Biogeosci.* 120, 1450–1469. doi: 10.1002/2014JG002870

Jones, C. G., Lawton, J. H., and Shachak, M. (1994). Organisms as Ecosystem Engineers. *Oikos* 69, 373–386. doi: 10.2307/3545850

Kalra, T. S., Ganju, N. K., Aretxabaleta, A. L., Carr, J. A., Defne, Z., and Moriarty, J. M. (2021). Modeling Marsh Dynamics Using a 3-D Coupled Wave-Flow-Sediment Model. *Front. Mar. Sci.* 8. doi: 10.3389/fmars.2021.740921

Keddy, P. A. (1989). Effects of Competition From Shrubs on Herbaceous Wetland Plants: A 4-Year Field Experiment. *Can. J. Bot.* 67, 708–716. doi: 10.1139/b89-094

Kirwan, M. L., and Guntenspergen, G. R. (2010). Influence of Tidal Range on the Stability of Coastal Marshland. *J. Geophys. Res.* 115, 1–11. doi: 10.1029/2009JF001400

Kirwan, M. L., and Megonigal, J. P. (2013). Tidal Wetland Stability in the Face of Human Impacts and Sea-Level Rise. *Nature* 504, 53–60. doi: 10.1038/nature12856

Kirwan, M. L., and Mudd, S. M. (2012). Response of Salt-Marsh Carbon Accumulation to Climate Change. *Nat. Publishing Group* 489, 550–553. doi: 10.1038/nature11440

Kirwan, M. L., and Murray, A. B. (2007). A Coupled Geomorphic and Ecological Model of Tidal Marsh Evolution. *Proc. Natl. Acad. Sci. U. S. A.* 104, 6118–6122. doi: 10.1073/pnas.0700958104

Kirwan, M. L., and Temmerman, S. (2009). Coastal Marsh Response to Historical and Future Sea-Level Acceleration. *Quat. Sci. Rev.* 28, 1801–1808. doi: 10.1016/j.quascirev.2009.02.022

Kirwan, M. L., Temmerman, S., Skeehan, E. E., Guntenspergen, G. R., and Fagherazzi, S. (2016). Overestimation of Marsh Vulnerability to Sea Level Rise. *Nat. Clim. Change* 6, 253–260. doi: 10.1038/nclimate2909

Kuhn, N. L., and Zedler, J. B. (1997). Differential Effects of Salinity and Soil Saturation on Native and Exotic Plants of a Coastal Salt Marsh. *Estuaries* 20, 391–403. doi: 10.2307/1352352

Lee, J. S., and Kim, J. W. (2018). Dynamics of Zonal Halophyte Communities in Salt Marshes in the World. *J. Mar. Isl. Cult.* 7, 84–106. doi: 10.21463/jmic.2018.07.1.06

Leonard, L. A., and Croft, A. L. (2006). The Effect of Standing Biomass on Flow Velocity and Turbulence in Spartina Alterniflora Canopies. *Estuar. Coast. Shelf Sci.* 69, 325–336. doi: 10.1016/j.ecss.2006.05.004

Leonardi, N., Ganju, N. K., and Fagherazzi, S. (2016). A Linear Relationship Between Wave Power and Erosion Determines Salt-Marsh Resilience to Violent Storms and Hurricanes. *Proc. Natl. Acad. Sci.* 113, 64–68. doi: 10.1073/pnas.1510095112

Levine, J. M., Brewer, J. S., and Bertness, M. D. (1998). Nutrients, Competition and Plant Zonation in a New England Salt Marsh. *J. Ecol.* 86, 285–292. doi: 10.1046/j.1365-2745.1998.00253.x

Lõhmus, K., Balke, T., and Kleyer, M. (2020). Spatial and Temporal Patterns of Initial Plant Establishment in Salt Marsh Communities. *J. Veg. Sci.* 31, 1124–1134. doi: 10.1111/jvs.12915

Marani, M., Da Lio, C., D'Alpaos, A., and D'Alpaos, A. (2013). Vegetation Engineers Marsh Morphology Through Multiple Competing Stable States. *Proc. Natl. Acad. Sci.* 110, 3259–3263. doi: 10.1073/pnas.1218327110

Marani, M., D'Alpaos, A., Lanzoni, S., Carniello, L., and Rinaldo, A. (2007). Biologically-Controlled Multiple Equilibria of Tidal Landforms and the Fate of the Venice Lagoon. *Geophys. Res. Lett.* 34, 1–5. doi: 10.1029/2007GL030178

Marani, M., D'Alpaos, A., Lanzoni, S., Carniello, L., and Rinaldo, A. (2010). The Importance of Being Coupled: Stable States and Catastrophic Shifts in Tidal Biomorphodynamics. *J. Geophys. Res. Earth Surf.* 115, F04004. doi: 10.1029/2009JF001600

Marani, M., D'Alpaos, A., Lanzoni, S., and Santalucia, M. (2011). Understanding and Predicting Wave Erosion of Marsh Edges. *Geophys. Res. Lett.* 38, 1–5. doi: 10.1029/2011GL048995

Marani, M., Lanzoni, S., Silvestri, S., and Rinaldo, A. (2004). Tidal Landforms, Patterns of Halophytic Vegetation and the Fate of the Lagoon of Venice. *J. Mar. Syst.* 51, 191–210. doi: 10.1016/j.jmarsys.2004.05.012

Marani, M., Silvestri, S., Belluco, E., Ursino, N., Comerlati, A., Tosatto, O., et al. (2006). Spatial Organization and Ecohydrological Interactions in Oxygen-Limited Vegetation Ecosystems. *Water Resour. Res* 42, W06D06. doi: 10.1029/2005WR004582

Mariotti, G., Spivak, A. C., Luk, S. Y., Ceccherini, G., Tyrrell, M., and Gonneea, M. E. (2020). Modeling the Spatial Dynamics of Marsh Ponds in New England Salt Marshes. *Geomorphology* 365, 107262. doi: 10.1016/j.geomorph.2020.107262

McLeod, E., Chmura, G. L., Bouillon, S., Salm, R., Björk, M., Duarte, C. M., et al. (2011). A Blueprint for Blue Carbon: Toward an Improved Understanding of the Role of Vegetated Coastal Habitats in Sequestering CO2. *Front. Ecol. Environ.* 9, 552–560. doi: 10.1890/110004

Mcowen, C. J., Weatherdon, L. V., Van Bochove, J. W., Sullivan, E., Blyth, S., Zockler, C., et al. (2017). A Global Map of Saltmarshes. *Biodivers. Data J.* 5, e11764. doi: 10.3897/BDJ.5.e11764

Möller, I., Kudella, M., Rupprecht, F., Spencer, T., Paul, M., Van Wesenbeeck, B. K., et al. (2014). Wave Attenuation Over Coastal Salt Marshes Under Storm Surge Conditions. *Nat. Geosci.* 7, 727–731. doi: 10.1038/NGEO2251

Morris, J. T. (2006). Competition Among Marsh Macrophytes by Means of Geomorphological Displacement in the Intertidal Zone. *Estuar. Coast. Shelf Sci.* 69, 395–402. doi: 10.1016/j.ecss.2006.05.025

Morris, J. T. (2007). Ecological Engineering in Intertidial Saltmarshes. *Hydrobiologia* 577, 161–168. doi: 10.1007/s10750-006-0425-4

Morris, J. T., Barber, D. C., Callaway, J. C., Chambers, R., Hagen, S. C., Hopkinson, C. S., et al. (2016). Contributions of Organic and Inorganic Matter to Sediment Volume and Accretion in Tidal Wetlands at Steady State. *Earth's Futur.* 4, 110–121. doi: 10.1002/2015EF000334

Morris, J. T., Porter, D., Neet, M., Noble, P. A., Schmidt, L., Lapine, L. A., et al. (2005). Integrating LIDAR Elevation Data, Multi-Spectral Imagery and Neural Network Modelling for Marsh Characterization. *Int. J. Remote Sens.* 26, 5221–5234. doi: 10.1080/01431160500219018

Morris, J. T., Sundareshwar, P. V. V. V., Nietch, C. T., Kjerfve, B. B., and Cahoon, D. R. (2002). Responses of Coastal Wetlands to Rising Sea Leve. *Ecology* 83, 2869–2877. doi: 10.1890/0012-9658(2002)083[2869:ROCWTR]2.0.CO;2

Mudd, S. M., Fagherazzi, S., Morris, J. T., and Furbish, D. J. (2004). "Flow, Sedimentation, and Biomass Production on a Vegetated Salt Marsh in South Carolina: Toward a Predictive Model of Marsh Morphologic and Ecologic Evolution," in *The Ecogeomorphology of Tidal Marshes, Coastal and Estuarine Studies N.59*. Eds. S. Fagherazzi, M. Marani and L. K. Blum (Washington, D.C: American Geophysical Union), 165–188. doi: 10.1029/CE059p0165

Mudd, S. M., Howell, S. M., and Morris, J. T. (2009). Impact of Dynamic Feedbacks Between Sedimentation, Sea-Level Rise, and Biomass Production on Near-Surface Marsh Stratigraphy and Carbon Accumulation. *Estuar. Coast. Shelf Sci.* 82, 377–389. doi: 10.1016/j.ecss.2009.01.028

Muench, A., and Elsey-Quirk, T. (2019). Competitive Reversal Between Plant Species is Driven by Species-Specific Tolerance to Flooding Stress and Nutrient Acquisition During Early Marsh Succession. *J. Appl. Ecol.* 56, 2236–2247. doi: 10.1111/1365-2664.13458

Nelson, J. L., and Zavaleta, E. S. (2012). Salt Marsh as a Coastal Filter for the Oceans: Changes in Function With Experimental Increases in Nitrogen Loading and Sea-Level Rise. *PloS One* 7(8), e38558. doi: 10.1371/journal.pone.0038558

Newton, A., Icely, J., Cristina, S., Perillo, G. M. E., Turner, R. E., Ashan, D., et al. (2020). Anthropogenic, Direct Pressures on Coastal Wetlands. *Front. Ecol. Evol.* 8. doi: 10.3389/fevo.2020.00144

Nyman, J. A., Walters, R. J., Delaune, R. D., and Patrick, W. H. (2006). Marsh Vertical Accretion *via* Vegetative Growth. *Estuar. Coast. Shelf Sci* 69, 370–380. doi: 10.1016/j.ecss.2006.05.041

Ouyang, X., and Lee, S. Y. (2020). Improved Estimates on Global Carbon Stock and Carbon Pools in Tidal Wetlands. *Nat. Commun.* 11, 1–7. doi: 10.1038/s41467-019-14120-2

Palaima, A. (2012). *Ecology, Conservation, and Restoration of Tidal Marshes: The San Francisco Estuary. 1st ed.* Ed. A. Palaima (Berkeley, CA (US):University of California Press). Available at: http://www.jstor.org/stable/10.1525/j.ctt1ppw94.

Pennings, S. C., and Bertness, M. D. (1999). Using Latitudinal Variation to Examine Effects of Climate on Coastal Salt Marsh Pattern and Process. *Curr. Top. Wetl. Biogeochem* 3, 100–111.

Pennings, S. C., and Bertness, M. D. (2001). "Salt Marsh Communities," in *Marine Community Ecology*. Eds. M. D. Bertness, S. D. Gaines and M. Hay (Sunderland, Massachusetts: Sinauer Associates), 289–316.

Pennings, S. C., and Callaway, R. M. (1992). Salt Marsh Plant Zonation: The Relative Importance of Competition and Physical Factors. *Ecology* 73, 681–690. doi: 10.2307/1940774

Pennings, S. C., Grant, M. B., and Bertness, M. D. (2005). Plant Zonation in Low-Latitude Salt Marshes: Disentangling the Roles of Flooding, Salinity and Competition. *J. Ecol.* 93, 159–167. doi: 10.1111/j.1365-2745.2004.00959.x

Pennings, S. C., and He, Q. (2021). "Community Ecology of Salt Marshes," in *Salt Marshes: Function, Dynamics, and Stresses*. Eds. D. M. FitzGerald and Z. J. Hughes (Cambridge: Cambridge University Press), 82–112. doi: 10.1017/9781316888933.006

Pennings, S. C., Stanton, L. E., and Brewer, J. S. (2002). Nutrient Effects on the Composition of Salt Marsh Plant Communities Along the Southern Atlantic and Gulf Coasts of the United States. *Estuaries* 25, 1164–1173. doi: 10.1007/BF02692213

Perillo, G. M. E. E., and Iribarne, O. O. (2003). New Mechanisms Studied for Creek Formation in Tidal Flats: From Crabs to Tidal Channels. *Eos (Washington. DC).* 84, 1–3. doi: 10.1029/2003EO010001

Ranwell, D. S. (1972). *Ecology of Salt Marshes and Sand Dunes* (London:Chapman and Hall).

Ratliff, K. M., Braswell, A. E., and Marani, M. (2015). Spatial Response of Coastal Marshes to Increased Atmospheric CO 2. *Proc. Natl. Acad. Sci.* 112, 201516286. doi: 10.1073/pnas.1516286112

Redfield, A. C. (1972). Development of a New England Salt Marsh. *Ecol. Monogr.* 42, 201–237. doi: 10.2307/1942263

Rinaldo, A., Rigon, R., Banavar, J. R., Maritan, A., and Rodriguez-Iturbe, I. (2014). Evolution and Selection of River Networks: Statics, Dynamics, and Complexity. *Proc. Natl. Acad. Sci. U. S. A.* 111, 2417–2424. doi: 10.1073/pnas.1322700111

Rogers, K., Kelleway, J. J., Saintilan, N., Megonigal, J. P., Adams, J. B., Holmquist, J. R., et al. (2019). Wetland Carbon Storage Controlled by Millennial-Scale Variation in Relative Sea-Level Rise. *Nature* 567, 91–95. doi: 10.1038/s41586-019-0951-7

Roner, M., D'Alpaos, A., Ghinassi, M., Marani, M., Silvestri, S., Franceschinis, E., et al. (2016). Spatial Variation of Salt-Marsh Organic and Inorganic Deposition and Organic Carbon Accumulation: Inferences From the Venice Lagoon, Italy. *Adv. Water Resour.* 93-B, 276–287. doi: 10.1016/j.advwatres.2015.11.011

Roner, M., Ghinassi, M., Finotello, A., Bertini, A., Combourieu-nebout, N., Donnici, S., et al. (2021). Detecting the Delayed Signatures of Changing Sediment Supply in Salt-Marsh Landscapes: The Case of the Venice Lagoon (Italy). *Front. Mar. Sci.* 8. doi: 10.3389/fmars.2021.742603

Roozen, A. J. M., and Westhoff, V. (1985). A Study on Long-Term Salt-Marsh Succession Using Permanent Plots. *Vegetatio* 61, 23–32. doi: 10.1007/BF00039807

Rybicki, J., and Hanski, I. (2013). Species-Area Relationships and Extinctions Caused by Habitat Loss and Fragmentation. *Ecol. Lett.* 16, 27–38. doi: 10.1111/ele.12065

Sarika, M., and Zikos, A. (2020). "Coastal Salt Marshes," in *Handbook of Halophytes: From Molecules to Ecosystems Towards Biosaline Agriculture*. Ed. M.-N. Grigore (Cham: Springer International Publishing), 1–39. doi: 10.1007/978-3-030-17854-3_7-1

Schoutens, K., Heuner, M., Fuchs, E., Minden, V., Schulte-ostermann, T., Belliard, J., et al. (2020). Nature-Based Shoreline Protection by Tidal Marsh Plants Depends on Trade-Offs Between Avoidance and Attenuation of Hydrodynamic Forces. *Estuar. Coast. Shelf Sci.* 236, 106645. doi: 10.1016/j.ecss.2020.106645

Schuerch, M., Spencer, T., Temmerman, S., Kirwan, M. L., Wolff, C., Lincke, D., et al. (2018). Future Response of Global Coastal Wetlands to Sea-Level Rise. *Nature* 561, 231–234. doi: 10.1038/s41586-018-0476-5

Schulte Ostermann, T., Heuner, M., Fuchs, E., Temmerman, S., Schoutens, K., Bouma, T. J., et al. (2021). Unraveling Plant Strategies in Tidal Marshes by Investigating Plant Traits and Environmental Conditions. *J. Veg. Sci.* 32, e13038. doi: 10.1111/jvs.13038

Sgarabotto, A., D'Alpaos, A., and Lanzoni, S. (2021). Effects of Vegetation, Sediment Supply and Sea Level Rise on the Morphodynamic Evolution of Tidal Channels. *Water Resour. Res.* 57, e2020WR028577. doi: 10.1029/2020WR028577

Shao, D., Liu, K., Mossman, H. L., Adams, M. P., Wang, H., Li, D., et al. (2021). A Prioritization Metric and Modelling Framework for Fragmented Saltmarsh Patches Restoration. *Ecol. Indic.* 128, 107833. doi: 10.1016/j.ecolind.2021.107833

Silvestri, S., Defina, A., and Marani, M. (2005). Tidal Regime, Salinity and Salt Marsh Plant Zonation. *Estuar. Coast. Shelf Sci.* 62, 119–130. doi: 10.1016/j.ecss.2004.08.010

Silvestri, S., and Marani, M. (2005). (2004). Salt-Marsh Vegetation and Morphology: Basic Physiology, Modelling and Remote Sensing Observations. In The Ecogeomorphology of Tidal Marshes (eds S. Fagherazzi, M. Marani and L. K. Blum), chapter 2. American Geophysical Union, special series on "Coastal and Estuarine Studies" n.59, Washington, DC. p. 5-25 doi: 10.1029/CE059p0005

Snow, A. A., and Vince, S. W. (1984). Plant Zonation in an Alaskan Salt Marsh: II. An Experimental Study of the Role of Edaphic Conditions. *J. Ecol.* 72, 669. doi: 10.2307/2260075

Temmerman, S., Bouma, T. J., Govers, G., Wang, Z. B., De Vries, M. B., Herman, P. M. J., et al. (2005). Impact of Vegetation on Flow Routing and Sedimentation Patterns: Three-Dimensional Modeling for a Tidal Marsh. *J. Geophys. Res. Earth Surf.* 110, 1–18. doi: 10.1029/2005JF000301

Temmerman, S., Bouma, T. J., Van de Koppel, J., van der Wal, D., De Vries, M. B., and Herman, P. M. J. (2007). Vegetation Causes Channel Erosion in a Tidal Landscape. *Geology* 35, 631–634. doi: 10.1130/G23502A.1

Temmerman, S., Meire, P., Bouma, T. J., Herman, P. M. J., Ysebaert, T., and de Vriend, H. J. (2013). Ecosystem-Based Coastal Defence in the Face of Global Change. *Nature* 504, 79–83. doi: 10.1038/nature12859

Tognin, D., D'Alpaos, A., Marani, M., and Carniello, L. (2021). Marsh Resilience to Sea-Level Rise Reduced by Storm-Surge Barriers in the Venice Lagoon. *Nat. Geosci* 14, 906–911. doi: 10.1038/s41561-021-00853-7

Tommasini, L., Carniello, L., Ghinassi, M., Roner, M., and D'Alpaos, A. (2019). Changes in the Wind-Wave Field and Related Salt-Marsh Lateral Erosion: Inferences From the Evolution of the Venice Lagoon in the Last Four Centuries. *Earth Surf. Process. Landforms* 44, 1633–1646. doi: 10.1002/esp.4599

Ungar, I. A. (1998). Are Biotic Factors Significant in Influencing the Distribution of Halophytes in Saline Habitats? *Bot. Rev.* 64, 176–199. doi: 10.1007/BF02856582

Valiela, I., Kinney, E., Culberston, J., Peacock, E., and Smith, S. (2009). "Global Losses of Mangroves and Salt Marshes," in *Global Loss of Coastal Habitats: Rates, Causes and Consequences*, vol. 184. Ed. C. M. Duarte (Bilbao:Fondacion BBVA).

Valiela, I., and Teal, J. M. (1974). Nutrient Limitation in Salt Marsh Vegetation," *in Ecology of halophytes*, eds. R. J. Reimold and W. H. Queen (New York, NY: Academic Press), 547–563.

Vandenbruwaene, W., Temmerman, S., Bouma, T. J., Klaassen, P. C., De Vries, M. B., Callaghan, D. P., et al. (2011). Flow Interaction With Dynamic Vegetation Patches: Implications for Biogeomorphic Evolution of a Tidal Landscape. *J. Geophys. Res. Earth Surf.* 116, 1–13. doi: 10.1029/2010JF001788

van Regteren, M., Amptmeijer, D., de Groot, A. V., Baptist, M. J., and Elschot, K. (2020). Where Does the Salt Marsh Start? Field-Based Evidence for the Lack of a Transitional Area Between a Gradually Sloping Intertidal Flat and Salt Marsh. *Estuar. Coast. Shelf Sci.* 243, 106909. doi: 10.1016/j.ecss.2020.106909

Van Wesenbeeck, B. K., Van De Koppel, J., Herman, P. M. J. J., and Bouma, T. J. (2008). Does Scale-Dependent Feedback Explain Spatial Complexity in Salt-Marsh Ecosystems? *Oikos* 117, 152–159. doi: 10.1111/j.2007.0030-1299.16245.x

Wang, F., Lu, X., Sanders, C. J., and Tang, J. (2019). Tidal Wetland Resilience to Sea Level Rise Increases Their Carbon Sequestration Capacity in United States. *Nat. Commun.* 10, 1–11. doi: 10.1038/s41467-019-13294-z

Wang, C., Menenti, M., Stoll, M. P., Belluco, E., and Marani, M. (2007). Mapping Mixed Vegetation Communities in Salt Marshes Using Airborne Spectral Data. *Remote Sens. Environ.* 107, 559–570. doi: 10.1016/j.rse.2006.10.007

Wang, C., Menenti, M., Stoll, M., Feola, A., Belluco, E., and Marani, M. (2009). Separation of Ground and Low Vegetation Signatures in LiDAR Measurements of Salt-Marsh Environments. *IEEE Trans. Geosci. Remote Sens.* 47, 2014–2023. doi: 10.1109/TGRS.2008.2010490

Wang, H., van der Wal, D., Li, X., van Belzen, J., Herman, P. M. J., Hu, Z., et al. (2017). Zooming in and Out: Scale Dependence of Extrinsic and Intrinsic Factors Affecting Salt Marsh Erosion. *J. Geophys. Res. Earth Surf.* 122, 1455–1470. doi: 10.1002/2016JF004193

Wiegert, R. G., and Freeman, B. J. (1990). Tidal Salt Marshes of the Southeast Atlantic Coast: A Community Profile. *Biol. Rep. - US Fish Wildl. Serv.* doi: 10.2172/5032823

Willemsen, P. W. J. M., Smits, B. P., Borsje, B. W., Herman, P. M. J., Dijkstra, J. T., Bouma, T. J., et al. (2021). Modelling Decadal Salt Marsh Development: Variability of the Salt Marsh Edge Under Influence of Waves and Sediment Availability. *Water Resour. Res.* 58, e2020WR028962. doi: 10.1029/2020WR028962

Wolters, M., Garbutt, A., and Bakker, J. P. (2005). Salt-Marsh Restoration: Evaluating the Success of De-Embankments in North-West Europe. *Biol. Conserv.* 123, 249–268. doi: 10.1016/j.biocon.2004.11.013

Wolters, M., Garbutt, A., Bekker, R. M., Bakker, J. P., and Carey, P. D. (2008). Restoration of Salt-Marsh Vegetation in Relation to Site Suitability, Species Pool and Dispersal Traits. *J. Appl. Ecol.* 45, 904–912. doi: 10.1111/j.1365-2664.2008.01453.x

Xin, P., Jin, G., Li, L., and Barry, D. A. (2009). Effects of Crab Burrows on Pore Water Flows in Salt Marshes. *Adv. Water Resour.* 32, 439–449. doi: 10.1016/j.advwatres.2008.12.008

Xin, P., Li, L., and Barry, D. A. (2013). Tidal Influence on Soil Conditions in an Intertidal Creek-Marsh System. *Water Resour. Res.* 49, 137–150. doi: 10.1029/2012WR012290

Xin, P., Zhou, T., Lu, C., Shen, C., Zhang, C., D'Alpaos, A., et al. (2017). Combined Effects of Tides, Evaporation and Rainfall on the Soil Conditions in an Intertidal Creek-Marsh System. *Adv. Water Resour.* 103, 1–15. doi: 10.1016/j.advwatres.2017.02.014

Yang, Z., D'Alpaos, A., Marani, M., and Silvestri, S. (2020b). Assessing the Fractional Abundance of Highly Mixed Salt-Marsh Vegetation Using Random Forest Soft Classification. *Remote Sens.* 12, 3224. doi: 10.3390/rs12193224

Yang, S. L., Luo, X., Temmerman, S., Kirwan, M. L., Bouma, T., Xu, K., et al. (2020a). Role of Delta-Front Erosion in Sustaining Salt Marshes Under Sea-Level Rise and Fluvial Sediment Decline. *Limnol. Oceanogr.* 65, 1990–2009. doi: 10.1002/lno.11432

Yousefi Lalimi, F., Silvestri, S., D'Alpaos, A., Roner, M., and Marani, M. (2018). The Spatial Variability of Organic Matter and Decomposition Processes at the Marsh Scale. *J. Geophys. Res. Biogeosci.* 123, 3713–3727. doi: 10.1029/2017JG004211

Zhang, Y., Rowland, J. C., Xu, C., Wolfram, P. J., Svyatsky, D., Moulton, J. D., et al. (2020). Understanding the Eco-Geomorphologic Feedback of Coastal Marsh Under Sea Level Rise: Vegetation Dynamic Representations, Processes Interaction, and Parametric Sensitivity. *J. Geophys. Res. Earth Surf.* 125, e2020JF005729. doi: 10.1029/2020JF005729

Conflict of Interest: The authors declare that the research was conducted in the absence of any commercial or financial relationships that could be construed as a potential conflict of interest.

Publisher's Note: All claims expressed in this article are solely those of the authors and do not necessarily represent those of their affiliated organizations, or those of the publisher, the editors and the reviewers. Any product that may be evaluated in this article, or claim that may be made by its manufacturer, is not guaranteed or endorsed by the publisher.

Copyright © 2022 Finotello, D'Alpaos, Marani and Bertuzzo. This is an open-access article distributed under the terms of the Creative Commons Attribution License (CC BY). The use, distribution or reproduction in other forums is permitted, provided the original author(s) and the copyright owner(s) are credited and that the original publication in this journal is cited, in accordance with accepted academic practice. No use, distribution or reproduction is permitted which does not comply with these terms.

frontiers | Frontiers in Marine Science

ORIGINAL RESEARCH
published: 06 May 2022
doi: 10.3389/fmars.2022.860910

An Eco-Morphodynamic Modelling Approach to Estuarine Hydrodynamics & Wetlands in Response to Sea-Level Rise

Kristian Kumbier[1]*, *Kerrylee Rogers*[1], *Michael G. Hughes*[2], *Kirti K. Lal*[2], *Laura A. Mogensen*[1] and *Colin D. Woodroffe*[1]

[1] School of Earth Atmospheric and Life Sciences, University of Wollongong, Wollongong, NSW, Australia, [2] Science, Economics and Insights Division, NSW Department of Planning, Industry and Environment, Sydney, NSW, Australia

OPEN ACCESS

Edited by:
Zeng Zhou,
Hohai University, China

Reviewed by:
Mark Schuerch,
University of Lincoln, United Kingdom
A. Rita Carrasco,
University of Algarve, Portugal
Jean-Philippe Belliard,
University of Antwerp, Belgium

***Correspondence:**
Kristian Kumbier
kak609@uowmail.edu.au

Specialty section:
This article was submitted to Coastal Ocean Processes, a section of the journal Frontiers in Marine Science

Received: 24 January 2022
Accepted: 01 April 2022
Published: 06 May 2022

Citation:
Kumbier K, Rogers K, Hughes MG, Lal KK, Mogensen LA and Woodroffe CD (2022) An Eco-Morphodynamic Modelling Approach to Estuarine Hydrodynamics & Wetlands in Response to Sea-Level Rise. Front. Mar. Sci. 9:860910. doi: 10.3389/fmars.2022.860910

Tidal inundation is the primary driver of intertidal wetland functioning and will be affected by sea- level rise (SLR). The morphology of estuaries and friction across intertidal surfaces influences tidal propagation; accordingly, sea-level rise not only increases inundation frequency, but will also alter other tidal parameters, such as tidal range. To investigate responses of estuarine intertidal vegetation, primarily mangrove and saltmarsh, to SLR an eco-morphodynamic modelling approach was developed that accounted for some of the feedbacks between tidal inundation and changes to wetland substrate elevations. This model partially accounts for adjustment in estuarine hydrodynamics, and was used to examine the potential effect of SLR on mangrove and saltmarsh distribution in a micro-tidal channelised infilled barrier estuary in southeast Australia. The modelling approach combines a depth-averaged hydrodynamic model (Telemac2D) and an empirical wetland elevation model (WEM) that were coupled dynamically to allow for eco-geomorphological feedbacks. The integrated model was parameterised to consider two SLR scenarios, and two accretion scenarios within the WEM. Time series of observed water levels, tidal inundation and flow velocity were used to validate the hydrodynamic model for present-day sea level, whereas wetland mapping was used to verify predictions of mangrove and saltmarsh distribution. Tidal range varied along the estuary, increasing in response to low and high SLR scenarios (by up to 8%), and responded non-linearly under high SLR. Simulations of low and high SLR scenarios indicated that wetlands mostly withstand modest SLR rates (+ 5mm yr^{-1}) through sedimentation, but submerge and convert to subtidal areas under fast SLR rates (> 10mm yr^{-1}). Projected changes in tidal range are linked to eco-geomorphological feedbacks caused by changing wetland extents and adjustments of intertidal wetland geomorphology through sedimentation. Potential changes arising from morphological change at the entrance and in the tidal channels is not obtained from the model. The results of this study demonstrate

interconnections between hydrodynamics and intertidal wetlands, which need to be accounted for when estimating wetland response to SLR in channelised estuaries. Integrated models of estuarine-wetland systems are more precise as they account for the dynamic feedbacks between hydrodynamics and wetlands. For example, they also consider alterations to tidal range resulting from SLR and the effects of these on wetland inundation and sedimentation.

Keywords: hydrodynamic modelling, Telemac2D, mangrove, saltmarsh, hydroperiod, Australia

1 INTRODUCTION

Intertidal wetlands, comprising mangroves and/or saltmarsh, are among the most productive ecosystems in the world, providing ecosystem services to coastal communities, such as coastal protection, erosion control, maintenance of fisheries, and opportunities to mitigate climate change through carbon sequestration (Barbier et al., 2011; Gedan et al., 2011; Rogers et al., 2019a). Low-energy coastal environments within deltas and estuaries that are regularly inundated by tidal water provide the shelter intertidal wetlands require to develop (Woodroffe et al., 2016). Many studies suggest that tidal dynamics control halophytic species distribution through variation in characteristics of wetland inundation regime, such as inundation duration or frequency (Watson, 1928; Baltzer, 1969; Spier et al., 2016; Kumbier et al., 2021). Sea-level rise (SLR), as projected by the Intergovernmental Panel on Climate Change (IPCC) and others (Church et al., 2013; Dangendorf et al., 2017), will change the tidal regime and alter relationships between sedimentation and wetland elevation (Allen, 2000; McKee et al., 2012). This may cause wetlands to respond through a combination of landward migration and vertical adjustment, which both depend on the rate of SLR (Woodroffe, 2018). Eco-geomorphological feedbacks serve to maintain coastal wetland substrates *in situ* by facilitating vertical growth when the sea is rising (Kirwan et al., 2010; McKee et al., 2012).

Many empirical and physical studies involving hydrodynamic modelling have investigated the response of tidal wetlands to SLR (e.g. Morris et al., 2002; Craft et al., 2009; Alizad et al., 2016a). Numerical models of physical processes resolve water and sediment flows across the wetland based on simplified hydrodynamic schemes, whilst empirical models use statistical relationships derived from observations of spatial sedimentation patterns, below-ground processes, and tidal inundation (Fagherazzi et al., 2012).

The geomorphological evolution of intertidal wetlands involves feedbacks between wetland inundation regime and sedimentation, which manifests in a development from low to high elevated wetlands. This evolution is driven by initially prolonged tidal inundation and high sedimentation that gradually decrease in time with increasing surface elevation (e.g. potentially leading to mangroves being replaced by saltmarsh). However, these natural dynamics are modified by SLR. Wetland vegetation zonation arises in response to inundation regimes, and a change to these inundation regimes (e.g. by SLR) will result in changes to the vertical distribution of wetlands, which is reflected in recent observations of mangrove encroachment into saltmarsh in southeast Australian estuaries (e.g. Saintilan et al., 2014). Within estuaries, changes in wetland inundation regime are not only driven by SLR itself (e.g. an increase in mean water level) but also by alteration of the overall hydrodynamics of the estuarine system, such as increasing tidal range in response to SLR (Lee et al., 2017; Du et al., 2018; Kumbier et al., 2018a). However, changes in estuarine hydrodynamics are rarely considered in assessments of wetland response to SLR, despite research indicating interconnections between the two and suggestions that wetland modelling in estuaries may have to account for tidal modifications (Mogensen and Rogers, 2018). This most likely relates to the challenges of coupling computationally demanding hydrodynamic models with empirical models of wetland evolution, but may cause imprecise estimates of wetland response to SLR in complex estuarine environments where tidal dynamics change under SLR.

Empirical models of wetland change with SLR aim to account for and quantify biophysical processes involved in the evolution of wetlands, such as trapping of mineral sediment, organic sedimentation through vegetation growth, or soil compaction (Cahoon et al., 2006; Cahoon et al., 2011; Krauss et al., 2014). Model inputs commonly include field measurements of surface elevation change using techniques such as the surface elevation table (SET) approach (Morris et al., 2002; Oliver et al., 2012; Rogers et al., 2012), suspended sediment concentrations (Temmerman et al., 2003a; Temmerman et al., 2003b) and dating of sediment cores for accretion rates (Mudd et al., 2009; Thorne et al., 2018). Such empirical data on sedimentation has been combined with tidal measurements (e.g. depth below high tide) to estimate the evolution of wetlands, with studies suggesting either linear or exponential relationships between inundation (or elevation used as a proxy for inundation) and mineral sedimentation (Krone, 1987; Cahoon and Reed, 1995; Temmerman et al., 2003b). However, relationships between tidal inundation and sedimentation may differ between sites due to the complex multidimensional interconnection of geomorphology, hydrodynamics, and ecology in tidal wetlands. In consequence, empirical models of wetland evolution developed for one study site may have limited applicability to other sites (Mogensen and Rogers, 2018; Wiberg et al., 2020; Rogers and Saintilan, 2021), which is particularly true for highly parameterised, site-specific models. Overall, empirical modelling studies as outlined above

contribute to process understanding of wetland evolution, and can be used to estimate wetland responses to SLR (e.g. Morris et al., 2002; Craft et al., 2009); however, the complex field data collection associated with the development and parameterisation of such models has restricted most studies to individual wetland sites rather than entire estuarine systems. A limitation of locally focused studies is the representation of tidal hydrodynamics and wetland inundation regimes, which are generally inferred from a few tide gauges in the vicinity of the study site, with tidal range assumed to remain unaffected by SLR (Morris et al., 2002; Rogers et al., 2012; Thorne et al., 2018). Furthermore, inferring wetland inundation regimes from a calculation of tide gauge data and surface elevation neglects the drag wetland vegetation can exert on tidal flow (Temmerman et al., 2005). In addition, tidal regimes inside estuaries have been shown to alter under SLR (Lee et al., 2017; Du et al., 2018; Kumbier et al., 2018a), which may affect wetland sedimentation as, for example, inundation durations can increase and so may mineral sediment supplied to a wetland (Temmerman et al., 2003a).

Numerical modelling studies of physical processes driving wetland response to SLR involving hydrodynamic modelling can resolve limitations regarding alteration of hydrodynamics (e.g. tidal regime) and representation of wetland inundation regimes if applied at the scale of an entire estuary; however, most studies combining hydrodynamic and wetland evolution models have been restricted to small study sites (e.g. D'Alpaos et al., 2007; Temmerman et al., 2007; Rodríguez et al., 2017), and thus, responses in estuarine hydrodynamics could not be represented properly. This limitation is likely related to research objectives focusing on processes operating over small scales, and the high computational demands of modelling at the scale of an estuary. Only a few numerical modelling studies estimated wetland response to SLR at the scale of an estuary whilst accounting for hydrodynamic system responses (Hagen et al., 2013; Alizad et al., 2016a; Alizad et al., 2016b; Alizad et al., 2018). For example, a two-dimensional hydrodynamic model has been coupled with a zero-dimensional marsh model to assess the response of saltmarsh to SLR in the lower St. Johns River in northern Florida, USA. Utilising a hydrodynamic model (ADCIRC), Hagen et al. (2013) extended the Morris et al. (2002) zero-dimensional empirical wetland model for saltmarsh productivity and surface elevation change, to develop a coupled two-dimensional model that accounts for alteration of hydrodynamics. The hydrodynamic modelling component thereby provided generalised tidal levels (e.g. Mean High Water [MHW]), which were then included as inputs into the Morris et al. (2002) wetland model to calculate biomass productivity, vertical accretion rates and surface elevation change under different SLR scenarios. This eco-hydraulic model has been further refined for the same study site to include bio-physical feedback through a time-stepping framework which facilitates stepwise increases in wetland surface elevation and adjustment of bottom friction coefficients at defined intervals (Alizad et al., 2016a), as well as consideration of river discharge for fluvial estuarine systems (Alizad et al., 2016b).

Coupled eco-hydraulic models as outlined above allow for an assessment of wetland response to SLR whilst accounting for system responses in hydrodynamics; however, the applicability of this particular model (Alizad et al., 2016a; Alizad et al., 2016b; Alizad et al., 2018) may be limited only to *Spartina* saltmarsh sites through North and South America (and similar settings) due to the coupling with Morris et al.'s (2002) model, which was specifically developed for low elevated saltmarshes in the US which are characterised by low biodiversity (e.g. *Spartina* only) and decomposition rates that are well balanced against additions. However, many wetlands are more complex, with more zonation and vegetation diversity, which may limit the model's application in complex wetlands comprising co-existing mangrove and high saltmarsh, such as found in southeast Australia where decomposition and autocompaction has been shown to be particularly important (Rogers and Saintilan, 2021). Furthermore, coupled hydrodynamic-wetland models may be improved through spatially explicit consideration of wetland inundation regimes rather than generalised tidal levels (e.g. MHW), as the latter have been shown to represent wetland zonation patterns only at the broadest level (Kumbier et al., 2021). Such modelling of spatially explicit wetland inundation regimes (e.g. inundation duration) would also allow for consideration of floodplain flow attenuation (Temmerman et al., 2005).

This study presents a coupled eco-morphodynamic modelling approach utilising a depth-averaged hydrodynamic model (Telemac2D) and an empirical wetland elevation model developed for this study (WEM). The two-way coupled model accounts for responses in estuarine hydrodynamics caused by SLR, as well as alteration in hydrodynamics due to eco-geomorphological feedbacks on the wetland only (e.g. surface elevation changes). Thereby, the distribution of mangrove and saltmarsh in response to SLR is estimated through a spatially explicit calculation of wetland inundation regime (e.g. average inundation duration). Changes in wetland surface elevation are implemented using two empirical relationships (slow and moderate growth) between simulated wetland inundation regime and observations of changes in wetland surface elevation derived from a 20-year observational record. Low and high SLR scenarios have been simulated to investigate responses of mangrove and saltmarsh to increased inundation in a micro-tidal infilled barrier estuary in southeast Australia. Whereas components of the coupled eco-morhodynamic model were specifically developed and parameterised for the study site (e.g. WEMs), it was an overall aim to present a transferable modelling framework with respect to the technical aspects of coupling estuarine hydrodynamics and intertidal wetlands.

The objectives of this study were to:

1. develop a transferable eco-morphodynamic modelling framework by coupling a hydrodynamic model and an empirical wetland elevation model; and
2. estimate changes in mangrove/saltmarsh distribution in response to SLR at the scale of an entire estuary, as well as changes in system hydrodynamics relevant for wetland modelling.

Improved understanding of interconnections between hydrodynamics and wetlands under SLR can support planning and decision making for estuarine-wetland systems, which are at present typically studied in separation.

2 MATERIALS AND METHODS

2.1 Study Site

Minnamurra River estuary is located on the wave-dominated southeastern coast of NSW, Australia. The estuarine system is classified as a wave-dominated barrier estuary (Roy et al., 2001), and tides are the dominant source of hydrodynamic energy within the estuary. Hydrodynamics inside the estuary are only affected by river discharge during and following large rainfall events (Ryan, 1992), with tides being semi-diurnal and displaying a significant diurnal inequality. The open ocean tide range reaches a maximum of approximately 2 m during spring tides, but is attenuated at the estuary's entrance during spring tide conditions by approximately 20%, and is comparatively constant throughout the lower 7 km of the estuary, except for minor tidal amplification of a few centimetres occurring where the main channel narrows (Kumbier et al., in review). The estuary has a catchment of approximately 142 km^2, with Rocklow Creek being the largest tributary (24 km^2). A well-defined main channel, which is partly surrounded by low-lying intertidal areas where mangrove and saltmarsh occur (**Figure 1**), evolved as a result of sedimentary infilling in the past 8000 years (Panayotou et al., 2007; Haslett et al., 2010). Elevations in **Figure 1** are given in metres relative to Australian Height Datum (AHD), with mean sea level inside the estuary now positioned at approximately 0.1 m AHD due to rising sea-level since the datum's establishment in 1968, and the temporary increases in mean water level during spring tides when tidal pumping elevates mean water level.

Intertidal wetlands of mangrove and saltmarsh occur in the upper half of the tidal frame, and have been mapped broadly by Chafer (1998) and in more detail by Owers et al. (2016). A detailed analysis of wetland inundation regimes for these mangrove and saltmarsh communities has been presented by Kumbier et al. (2021). Accordingly, *Avicennia marina* occupy intertidal areas with a total inundation duration of approximately 30-75% of the time, at a frequency of 1.5-2 inundations per day, and for an average duration of 2.7-5 hours per event. An ecotone with a combination of *Avicennia marina* mangroves and dense shrubby *Aegiceras corniculatum* mangroves occurs where the total inundation duration is approximately 15-30%, the daily inundation frequency between 0.9-1.5, and the average inundation duration 2-2.7 hours per event. Higher in the tidal frame (approximately from an elevation of 0.55 m AHD), saltmarsh species such as *Sporobolus virginicus*, *Sarcocornia quinqueflora* and *Juncus krausii* occupy elevations being subject to total inundation duration of <15%, inundation frequencies below 0.9 tides per day, and average inundation duration of 0.85-2 hours per event. *Casuarina glauca* forest border saltmarsh in supratidal positions on the floodplain. Mangroves, saltmarsh and *Casuarina* follow a distinct zonation across the floodplain, but the encroachment of mangroves into saltmarsh, as well as saltmarsh beneath *Casuarina*, associated with contemporary SLR in recent

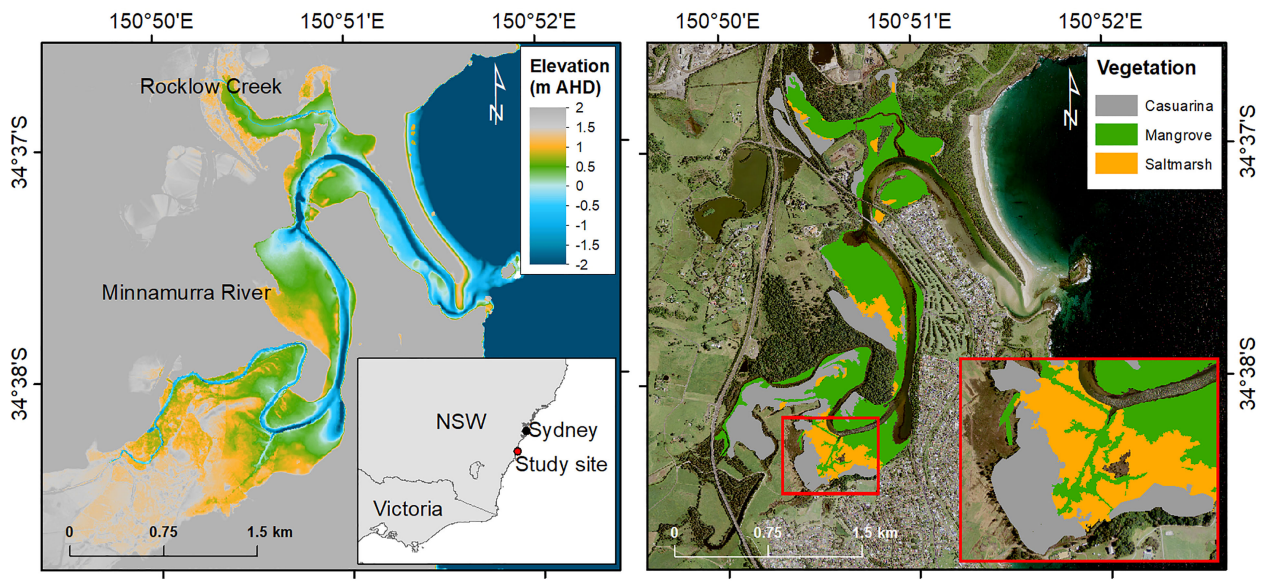


FIGURE 1 | Bathymetry and topography of Minnamurra River estuary (left), and intertidal wetland vegetation communities (right). Lidar-derived topography and sonar-derived bathymetry sourced from Geoscience Australia (2018; 2011), Department of Planning Industry and Environment (2017) and University of New South Wales (2017). Wetland mapping adjusted from Owers et al. (2016) and Chafer (1998).

decades may at times obscure these patterns (Chafer, 1998; Saintilan et al., 2018).

2.2 Methods

2.2.1 Overall Model Description

The coupled eco-morphodynamic model consists of two main components, a hydrodynamic model and an empirical wetland elevation model (WEM) (**Figure 2**). Tidal conditions under SLR at Minnamurra River estuary were simulated utilising the hydrodynamic model Telemac2D (more details in section 2.2.2). Mean sea level was increased incrementally at 10-year intervals and model outputs of each tidal simulation (length of 28 days) were processed into maps of average inundation duration. These maps were imported into ArcGIS to project intertidal wetland vegetation zonation (mangrove and saltmarsh). Changes in wetland surface elevation were determined using two linear relationships (slow and moderate vertical growth) between modelled average inundation duration and observations of surface elevation changes in mangrove and saltmarsh from the past 20 years (2001 – 2021). Updates of wetland topography and bottom friction in response to SLR were implemented utilising the pre-/post-processing software BlueKenue®, and subsequently used in the hydrodynamic model for the next iteration. The coupling time step between the hydrodynamic and wetland model was set to 10 years, and thus allows for eco-geomorphological feedback exchange between estuarine hydrodynamics and intertidal wetlands every 10 years.

2.2.2 Hydrodynamic Model

The hydrodynamic model Telemac2D solves the depth-averaged Saint-Venant shallow water equations in two dimensions and thus accounts for processes such as continuity and momentum transfer (Hervouet, 2000). The model has been demonstrated to be suitable for simulating estuarine hydrodynamics (Seenath et al., 2016; Stark et al., 2017; Iglesias et al., 2019). In this study the model was set up using a finite element method solver for numerical discretization of the shallow water equations on an unstructured triangular mesh grid, which provided the flexibility required for modelling hydrodynamics in complex environments with varying channel width, as occurs at Minnamurra River estuary (**Figure 3**). For a full description of the equations solved by Telemac2D, refer to Hervouet (2007) and the software user manual (Telemac2D, 2014).

The graphical user interface BlueKenue® was used to create a triangular mesh grid with varying mesh sizes in order to resolve the hydrodynamics observed in the field. Larger mesh elements of 15-65 m size were created offshore, whereas the narrow entrance channel was refined to a mesh element size of 5 m length. A mesh size of 5 m was also chosen along the thalweg of the river, which was refined to 3 m in the most upstream locations due to the narrowing of the main channel. Intertidal areas were represented with mesh elements of 10 m length, which resulted in an overall triangular mesh grid with 86563 nodes and 170094 elements (**Figure 3**). Parallel computation was used to overcome the computational demands caused by a large and detailed modelling domain. An open boundary for tidal forcing was defined along the eastern margin of the model domain that was driven by a time-series of water level data collected at the Jervis Bay tide gauge located approximately 50 km south of the study site. It was assumed that the Jervis Bay tidal data was representative of open coast tidal conditions offshore of Minnamurra River estuary. The model did not consider short-period waves as these have been shown to only affect water levels in the entrance channel (Kumbier et al., 2022).

Particular care was taken to ensure the correct representation of topography and bathymetry in the study area. Accordingly, a seamless topo-bathymetric digital elevation model (DEM) was developed, which included a combination of three LiDAR data sets (Geoscience Australia, 2011; University of New South Wales, 2017; Geoscience Australia, 2018), as well as single beam

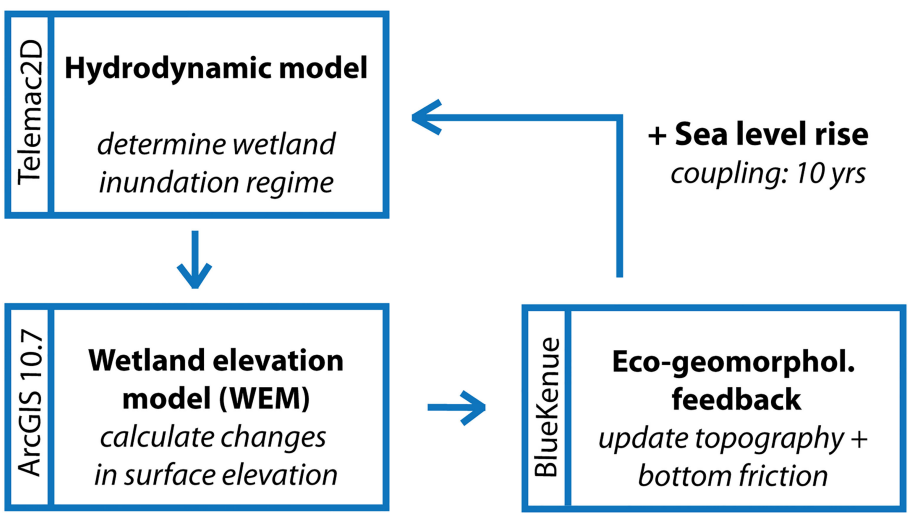


FIGURE 2 | Schematic illustration of the coupled hydrodynamic-wetland modelling framework.

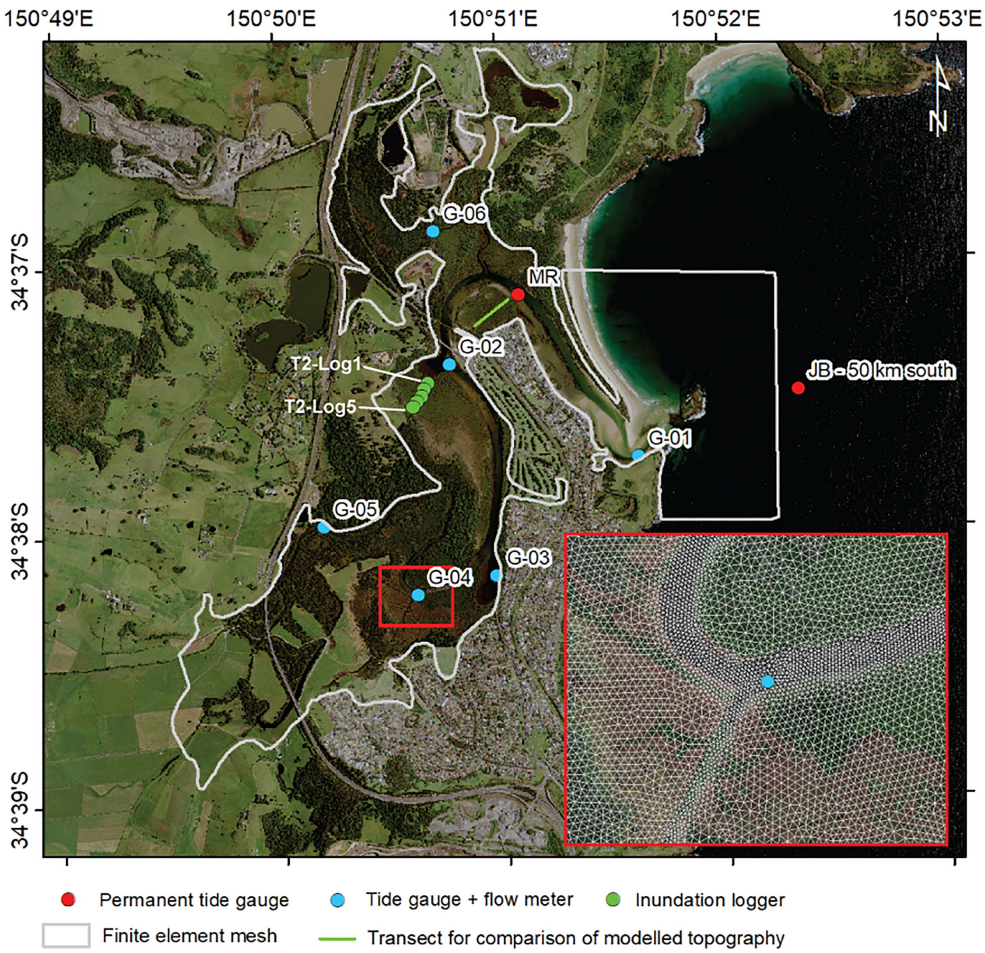


FIGURE 3 | Telemac2D finite element mesh model and location of tidal observations used for calibration and validation procedures. The grey polygon shows the extent of the Telemac2D model whereas the red box presents an example of the mesh-grid layout. The green transect indicates where modelled changes in wetland topography have been compared.

bathymetry data (OEH, 2017). As intertidal areas surrounding Rocklow Creek were found to be poorly represented, 350 real time kinematics-global positioning system (RTK-GPS) elevation measurements were collected (vertical accuracy of 1.5 cm), to correct the DEM. Since inundation modelling and assessing wetland response to SLR is particularly sensitive to topographic inputs (Mogensen and Rogers, 2018; Alizad et al., 2020), the quality of the seamless topo-bathymetric DEM was investigated by comparison with 1128 RTK-GPS elevation measurements taken in mangrove and saltmarsh areas across the estuary. These RTK-GPS points were not used in the creation of the seamless DEM and were only used to verify the quality of the seamless DEM; a high coefficient of determination of 0.89 and RMSE of 0.07 m with no spatially distributed biases provided support that the seamless DEM was a reasonable representation of intertidal wetland topography (**Supplementary S1**).

Spatially varying bottom roughness with regard to land-use types and wetland vegetation communities was defined using Manning's friction coefficients taken from the literature (Chow, 1959; Arcement and Schneider, 1989; Kaiser et al., 2011). Accordingly, open water and channels were represented with a value of 0.02, mangroves with a value of 0.035, saltmarsh with a value of 0.05 and *Casuarina* forest with a friction coefficient of 0.1.

The hydrodynamic model was calibrated and validated following commonly applied procedures of using separate time periods for model calibration and validation (Williams and Esteves, 2017). The model calibration was undertaken by comparison of modelled and observed water levels and wetland inundation depths from 23 November 2019 to 26 November 2019. This relatively short time-period allowed for repeated model runs to iteratively calibrate the model by varying mesh element sizes in critical locations (e.g. refinement in narrow channel sections to prevent tidal energy dissipation) and testing different bottom friction coefficients in the main channel and intertidal areas. A spin-up period of 1 day was found to be reasonable to dissipate the effects of initial conditions inside the model domain.

Validation of the model was based on comparison of observed and modelled water levels, flow velocities and inundation depths for an extended time period covering spring and neap tide conditions between 27 November and 10 December 2019. This validation was undertaken for various locations along the estuary (see **Figure 3**) and considered tidal gauge data from one permanent tide gauge (MR) and water-level time-series data from pressure transducers (G-01 to G-06), tidal velocity measurements using an acoustic Doppler current profiler (ADCP) near the permanent tide gauge (MR), tidal velocity measurement using drag-tilt flow meters (JCU Geophysics Laboratory, 2020), as well as wetland inundation logger data. The quality of water-level outputs of the hydrodynamic model was calculated using correlation coefficients and RMSE following Kumbier et al. (2018b).

SLR scenarios of 0.4 m (RCP2.6) and 0.9 m (RCP8.5) by 2100 (relative to 1986-2005) were selected to represent the lower and upper boundary of the IPCC's AR5 SLR projections and estimates for the Australian coastline (Church et al., 2013; McInnes et al., 2015; Zhang et al., 2017). These two scenarios were selected to investigate the response of wetlands to slow and fast rates of SLR. Mean sea level was increased from 2020 incrementally every 10 years in a linear manner for the lower RCP2.6 (+ 5 mm yr^{-1}) and an exponential manner for the higher RCP8.5 (+ 7-14 mm yr^{-1}) SLR scenario (**Supplementary S2**) as reported by Church et al. (2013). These increases in mean sea level were added to time-series of water level from the open ocean tide gauge in Jervis Bay, and the model was run for one lunar tidal cycle (28 days) to account for water-level variations during the spring-neap cycle. River discharge was not included in the model because spatial distribution of wetland vegetation in this estuary is largely a function of tidal inundation regime (Kumbier et al., 2021), only negligible discharge was recorded during the calibration data collection due to low flow conditions, and field observations indicated that the estuary's hydrodynamics are primarily driven by tides and only affected by discharge during larger rainfall events (Ryan, 1992).

Water-level outputs from tidal simulations were further investigated for changes in spring tidal range at monitoring locations shown in **Figure 3**. Peaks and troughs were extracted to determine differences between consecutive high and low waters, and to ultimately determine the maximum modelled tidal range under SLR at a particular location.

2.2.3 Empirical Wetland Elevation Model

2.2.3.1 Wetland Inundation Regime

Outputs of intertidal water depths from the hydrodynamic model were converted at each 10-year coupling time step to raster data of average inundation duration per inundation event. Therefore, Benson's (2020) Matlab code for processing of Telemac2D files was extended to iterate through all output time steps (every 5 min * 28 days = 40320 time steps) and mesh elements (170094), to determine average inundation durations per event at each mesh element. In particular, the average inundation duration was determined by identification of all high water inundation peaks and their respective duration exceeding a threshold of 0.01 m water depth, and averaging these durations for all inundation peaks. These spatially explicit estimates of average inundation duration per event were then used to determine the distribution of mangrove and saltmarsh based on site-specific empirical inundation observation reported in Kumbier et al. (2021). Accordingly, areas with an average inundation duration greater than 5 hours per inundation event were assumed to be low-elevation tidal flats or river channel, areas with a duration between 2-5 hours were assumed to be mangroves, whereas areas with a duration of between 0.85-2 hours were assumed to be saltmarsh. No separation between *Avicennia marina* and *Aegiceras corniculatum* mangroves was made because of overlap in their distribution and limited knowledge on sedimentation and inundation dynamics of *Aegiceras corniculatum* (Kumbier et al., 2021). Supratidal *Casuarina* wetlands were not included in the model because too little is known on their preferred tidal inundation regime.

2.2.3.2 Wetland Model Parameterisation

Empirical data on wetland surface elevation change was extracted from a 20-year data series of surface elevation change observed using a network of three SETs in the mangrove zone and three SETs in the saltmarsh zone between 2001 and 2021 (**Supplementary S3**). SETs serve as a benchmark against which changes in wetland surface elevation can be determined over time and the technique has been described by Cahoon et al. (2002) and previously reported for this site (Oliver et al., 2012; Rogers et al., 2012; Lal, 2019).

The WEM developed for this study considered vertical changes in surface elevation beneath mangrove and saltmarsh through a linear relationship between the average rates of elevation gain of mangrove/saltmarsh over the 20 year monitoring period and simulated average inundation duration. Most studies relate wetland surface elevation change and tidal inundation using either a linear or exponential model structure (Cahoon and Reed, 1995; Morris et al., 2002; Temmerman et al., 2003b). Given there is not enough evidence to differentiate whether the relationship at the study site is exponential or linear (Mogensen and Rogers, 2018), and the increase in computational demands when using a complex model structure, a decision was made to apply two simple linear relationships between modelled average inundation duration (hours per inundation event) and wetland surface elevation changes (**Figure 4**). This decision was further supported by previous ^{210}Pb analyses of lower intertidal mudflat, mangrove, and saltmarsh sediments, which showed that long-term accretion on the mudflat was higher than in saltmarsh and mangrove zones, and supported assumptions of a linear relationship (Lal, 2019).

A total of 14 visits per SET site over 20 years have been taken into account when determining the approximate surface elevation change at each SET (yellow and green symbols) shown on the y axis in **Figure 4**. These SET records have been used to construct two linear relationships that differ with respect to underlying assumptions and maximum changes in surface elevation. Linear model 1 (moderate wetland growth) presumes

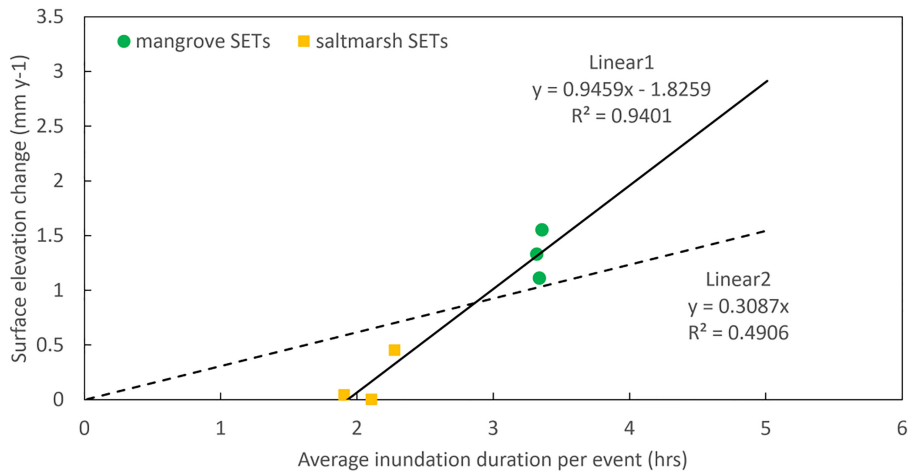


FIGURE 4 | Linear relationship between modelled average inundation duration per inundation event (hours) and wetland surface elevation change (mm yr^{-1}). Green and orange symbols are based on the six SETs with the orange squares being saltmarsh sites and the green circles representing the mangrove sites.

that sedimentation is negligible where inundation is negligible and allows for maximum elevation gains of 2.8 mm yr^{-1}, whilst linear model 2 (slow wetland growth) allows for sedimentation throughout the tidal frame and maximum increases in surface elevation of 1.5 mm yr^{-1}. Using a continuous linear relationship between inundation and sedimentation rather than separate relationships for mangrove and saltmarsh respectively, allowed for a representation of mangrove encroachment into saltmarsh as experienced at Minnamurra River and many other estuaries in southeast Australia (Chafer, 1998; Saintilan et al., 2018). The use of surface elevation change observations in WEM allows for an indirect consideration of above- and below-ground processes influencing wetland surface elevations that moderate the response of wetlands to SLR, whereas tidal simulation outputs in combination with empirical inundation tolerances adequately resembles wetland vegetation distribution. However, it is acknowledged that lower in the tidal frame where *Avicennia* and *Aegiceras* mangroves co-exist, as well as at higher elevations where saltmarsh and *Casuarina* establish, salinity may be an equally important factor for wetland species distribution (Silvestri et al., 2005). Changes in wetland distribution and surface elevation change were calculated in ArcGIS 10.7 at each coupling time step. The wetland component of the coupled modelling was verified by a combination of statistical measures (Matthew's correlation) and visual comparison of modelled wetland inundation regime at present day sea level, and the best available wetland vegetation mapping as presented in **Figure 1** (Chafer, 1998; Owers et al., 2016).

Simulated changes in intertidal wetland topography triggered by the combination of the above SLR and WEM scenarios were investigated for a selected transect approximately 1 km upstream from the entrance of the estuary (see **Figure 3**). This was undertaken by extracting surface elevations and modelled inundation regime along the same transect after topography updates at each coupling time step in ArcGIS 10.7.

3 RESULTS

3.1 Eco-Morphodynamic Model Validation

The hydrodynamic modelling setup was validated for the simulation of tidal conditions using observational field data such as water levels (**Figure 5A**), intertidal inundation depth measurements (**Figure 5B**) and flow velocities (**Table 1**). High correlation coefficients of mostly 0.99 and reasonably low RMSE in water level below 0.05 m at locations MR and further upstream confirm that the calibrated model effectively replicates tidal dynamics within the estuary (**Table 1**). However, at the entrance (G-01), modelled and observed water levels did not match as well, and this may be related to water-level fluctuations caused by ocean swell in the entrance area affecting the measurements. Modelled and observed inundation depths at locations T2Log1 – T2Log5 (**Figure 3**) correlating between 0.98 and 0.99 (RMSE's of below 0.03 m), indicate that inundation dynamics within intertidal areas are resolved adequately (**Figure 5B**). A good model performance is further shown by only small underestimations in spring tide peak flood velocities of between 0 and 0.1 m s^{-1} in upstream locations (**Table 1**).

Downstream at the entrance (G-01), peak velocity was overestimated by 1.3 m s^{-1}; however, flow velocities experienced during equipment deployment at the dynamic entrance area were considerably higher than those recorded by the bottom mounted flow meter, and thus deviations between the modelled and observed flow velocity were not surprising. The best match between modelled and observed peak velocities was achieved at location MR, which likely relates to the fact that modelling of depth averaged flow velocity is compared to observations of depth averaged rather than near-bed flow velocities due to an ADCP being used for data collection. The slight increasing trend in velocity underestimation upstream may be explained by the model domain not extending to the tidal limit of the estuary, which is due to the unavailability of

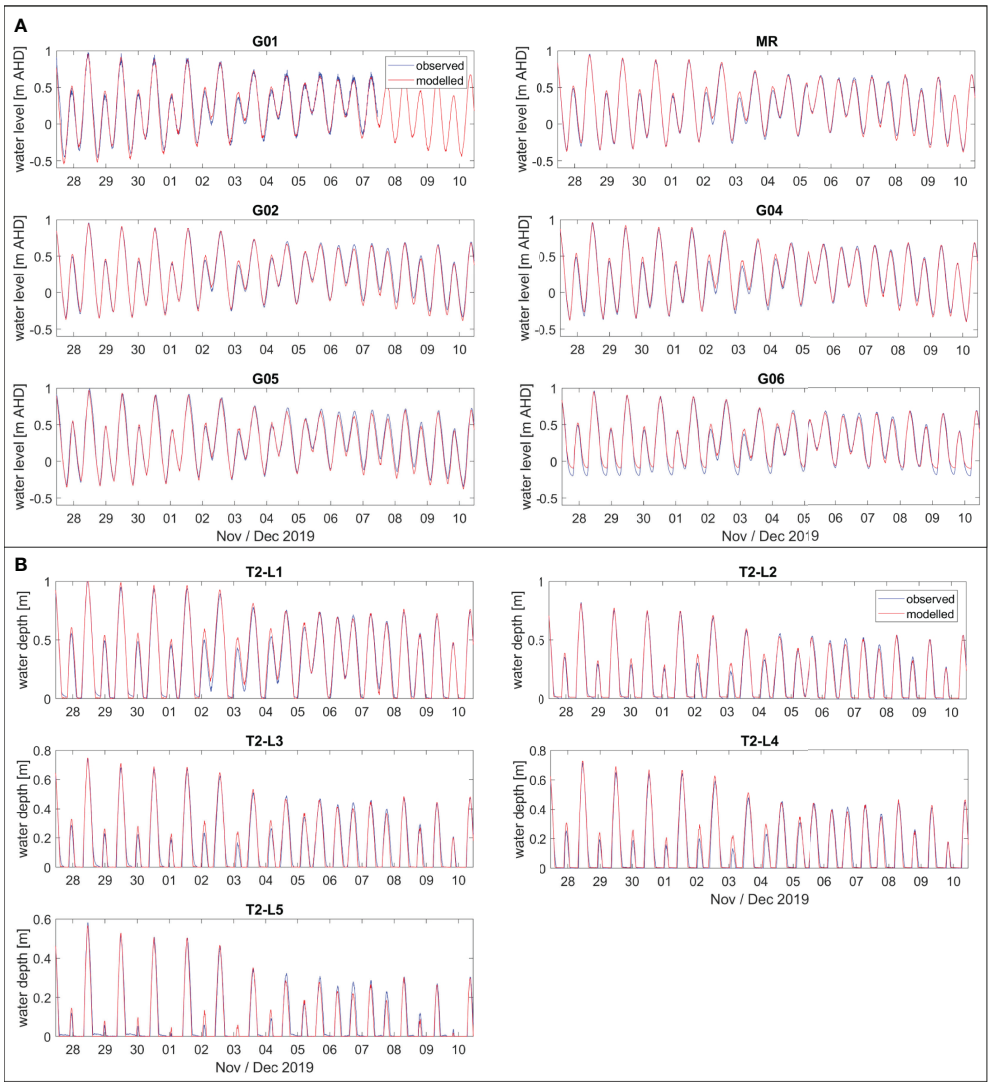


FIGURE 5 | Observed and modelled tidal water levels **(A)** and water depths **(B)** between 27 November and 10 December 2019 for monitoring locations at the Minnamurra River estuary.

TABLE 1 | Statistical measures calculated from comparison of modelled and observed flow velocities at Minnamurra River estuary. Peak velocity deviations refer to maximum over (+) and under (-) estimations by the hydrodynamic model for spring tide flood flows on 28 November 2019.

Monitoring site	r^2	RMSE (m)	Peak velocity (m s^{-1})
G-01	0.856	0.17	+1.30
MR	0.993	0.04	0.00
G-02	0.992	0.04	-0.05
G-04	0.991	0.04	-0.05
G-05	0.990	0.05	-0.10
G-06	0.988	0.05	–

This comparison was made between bottom-mounted velocity measurements and depth averaged velocity predictions except at site MR where depth-averaged ADCP measurements were obtained.

bathymetry data beyond the presented model domain. In consequence, tidal dynamics modelled upstream may have not been as variable as occurs in reality.

The predictive capability of the eco-morphodynamic model with respect to distribution patterns of mangrove and saltmarsh has been assessed by visual comparison of the best available wetland mapping (**Figure 6A**) with model predictions of mangrove and saltmarsh distribution based on simulated hydrodynamics (28 days) at contemporary sea level (**Figure 6B**).

Model predictions of mangrove distribution visually correlate well with the observed distribution patterns for floodplains surrounding Rocklow Creek in the north, the central floodplain and most of the southern floodplain. Small deviations in mangrove

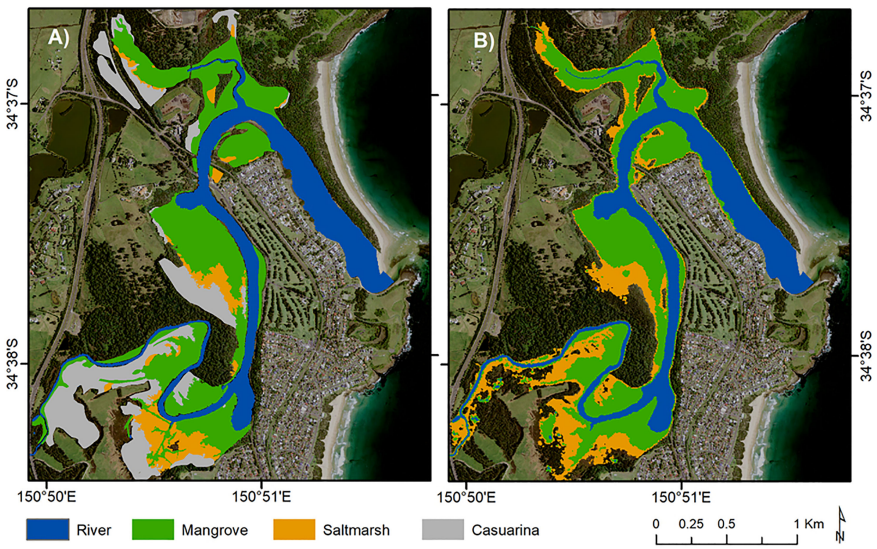


FIGURE 6 | Comparison of wetland vegetation mapping based on Owers et al. (2016) **(A)** and eco-morphodynamic model predictions of mangrove and saltmarsh distribution **(B)** based on average inundation durations per event from a 28-day tide simulation for November/December 2019. Note that *Casuarina* are not included in the model.

distribution were observed at the southern floodplain where tidal creeks with a width of less than 5 m and mostly unknown bathymetry intersect the floodplain, which were not properly resolved by the mesh grid and resulted in an over-representation of mangroves in these areas. Model predictions of saltmarsh distribution with the wetland mapping correlate well at the boundary to the mangrove zone, but saltmarsh distribution appears more extensive in the landward direction where the wetland mapping mostly suggests *Casuarina* forest. A field survey in these areas revealed that most of the *Casuarinas* that are predicted to be saltmarsh by the model, have saltmarsh beneath the *Casuarina* canopy (also reported by Oliver et al., 2012), and consequently the model predictions can be interpreted as reasonable. RTK-GPS measurements showed that these sites share surface elevations similar to those occupied by saltmarsh in nearby locations. Above outlined issues regarding the mapping of saltmarsh also impacted the calculation of Matthew's correlation coefficient (0.52); however, predictions of contemporary mangrove and saltmarsh areas were overall good (accuracy of 84%).

3.2 Eco-Morphodynamic Modelling Results

3.2.1 Intertidal Wetland Topography Response to SLR

Vertical changes in intertidal wetland topography were greatest for low SLR simulations coupled with WEM Linear 1, and at elevations low in the tidal frame (**Figure 7A**). To assist with interpretation of changes in wetland topography, **Figure 7** also includes simulated average inundation durations (per event) and corresponding wetland vegetation configurations under SLR.

At a distance along the transect of 100 m, large increases in surface elevation of up to 0.18 m by 2100 were modelled for the lower SLR simulation (RCP2.6) and WEM Linear 1, which is presently at an elevation below 0.2 m AHD (**Figure 7A**). By contrast, predictions of surface elevation from the higher SLR scenario (RCP8.5) for the same location were 0.08 m, suggesting slower vertical changes under the higher SLR scenario. Higher in the tidal frame (above 0.4 m AHD present elevation), gains in wetland surface elevation were quite similar for both SLR scenarios (approximately 0.1 m); however, from an elevation of 0.5 m AHD (present day), surface elevation increased at a higher rate considering the higher SLR scenario.

Predictions of topographic change for SLR simulations coupled with WEM Linear 2 showed similar spatial patterns with respect to differences between the lower and higher SLR scenario (**Figure 7B**). Overall vertical changes were approximately half of those described above, except for slightly greater elevation gains (up to 0.04 m) high in the tidal frame (above 0.5 m AHD present level) for simulations of the low SLR scenario. Analyses of changes in intertidal wetland topography from another profile located in the vicinity of tide gauge G-03 (see **Figure 3** for location) reinforces above described trends in adjustments of intertidal wetland topography in response to SLR (**Supplementary Figure 5**).

3.2.2 Tidal Range Response to SLR

Tidal dynamics in the main channel of the estuary were affected by SLR and differed spatially (lower and upper estuary), but also between simulations of the low and high SLR scenarios (**Figure 8**). For the simulation of low SLR and WEM Linear 1, tidal range increased linearly with SLR by approximately 0.01 m every 10 years, with total increases of + 0.08 m at the downstream location MR and + 0.09 m at the upstream location G04. For the high SLR simulation, tidal range was shown to

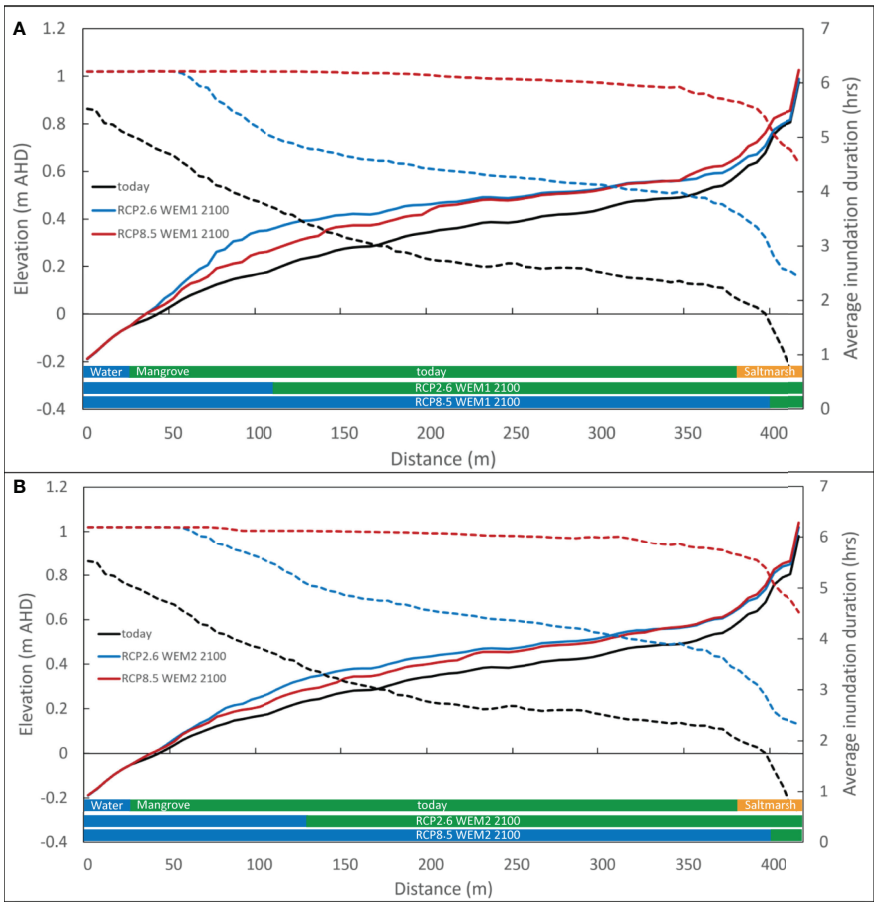


FIGURE 7 | Topographic changes in response to SLR for a selected intertidal wetland transect (see **Figure 3** for location) as of today (black), for the simulation of the low SLR (blue) and high SLR (red), as well as WEM Linear 1 (panel **A**) and Linear 2 (panel **B**). Blue, green and orange bars at the bottom of each panel indicate wetland vegetation configurations resulting from changing wetland inundation regimes under the different scenarios. Dashed lines represent the simulated average inundation duration (per event) corresponding to each scenario.

initially increase linearly (+ 0.11 m and + 0.09 m up- and downstream by 2080, respectively), but remain unchanged or decrease after sea level exceeded an increase of 0.6 m. Absolute increases in tidal range by 2100 are projected to translate into relative increases of approximately 6-7% for the lower SLR scenario and 7-8% for the higher SLR scenario compared to 2020 levels. Projections of tidal range under SLR coupled with WEM Linear 2 were almost identical (+/- 1-2 mm) to the patterns described above (**Figure 8B**).

3.2.3 Mangrove and Saltmarsh Response to SLR

The choice of SLR and wetland elevation adjustment scenario influenced the model outputs. The differences in distributional patterns of mangrove and saltmarsh for each scenario are described below (**Figure 9**). For WEM Linear 1 under a low SLR scenario (RCP2.6) mangroves adjusted to rising sea level for most of the century and expanded landward into saltmarsh when mean sea level exceeded an increase of 0.2 m (which corresponds to a surface elevation of 0.3 m AHD) (**Figure 9**). After this, mangrove at elevations <0.2 m AHD converted to open water due to the increasing inundation, which was particularly observed where the intertidal topography is gently sloped (e.g. shallow bays at the north of the central floodplain (**Figure 10**) and east of the southern floodplain). Saltmarsh expanded landward for WEM Linear 1 under simulation of low SLR; however, net changes in total saltmarsh extent were minimal due to the expansion of mangroves into lower elevation saltmarsh.

Changes in the ratio of mangrove, saltmarsh and open water (**Figure 11** – solid lines) indicate that overall the extent of mangroves and open water increased gradually over the century (+ 43% and + 31% respectively), whereas saltmarsh extent increased marginally (+ 6%). However, the model did not include the full intertidal extent under the highest SLR scenarios at 2100 due to an absence of suitable bathymetry data in the most upstream areas which are currently not tidally influenced.

For WEM Linear 1 under high SLR (RCP8.5) mangroves expanded in a landward direction into saltmarsh throughout the simulation period, which resulted in an overall increase of 70% in mangrove coverage. Most of this increase in mangrove area

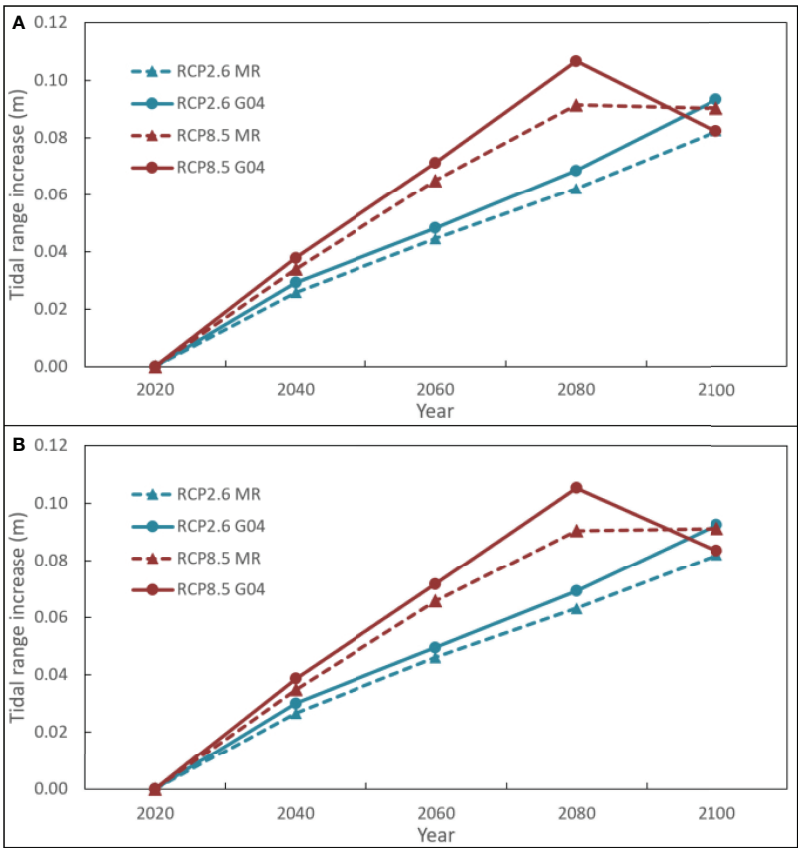


FIGURE 8 | Increases in spring tidal range under low (blue) and high SLR (red) for an upstream (G04 –solid lines) and downstream location (MR – dashed lines), as well as WEM Linear 1 (panel **A**) and Linear 2 (panel **B**). See **Figure 3** for the exact location of both monitoring sites. Values are with respect to maximum spring tidal range modelled for 2020.

occurred in the upper estuary surrounding the southern floodplain and further upstream (**Figure 9**). Mangroves further downstream appeared to be subject to coastal squeeze and were not projected to expand to higher elevations because the topography of the central and northern floodplain inhibited their establishment (**Figure 10**).

Under high SLR and WEM Linear 1, saltmarsh expanded landward but its total extent increased marginally (+ 4%). A large increase in open water extent was observed once mean sea level exceeded 0.5 m (corresponding to a surface elevation of 0.6 m AHD), which totalled to an increase in these areas of + 169% by 2100. This large increase in open water areas resulted in a shift in the proportion of mangrove, saltmarsh and open water areas, with a domination of open water areas from approximately 2070 under high SLR (**Figure 11A** – dashed lines).

Projections of wetland distribution for SLR simulations and WEM Linear 2 were very similar to those of WEM Linear 1 (**Figure 9** and **Figure 11B**). Under a low SLR scenario, open water areas were marginally larger by the end of the century (+ 5.6%), mangrove areas slightly smaller (- 3.6%), whereas saltmarsh extents were slightly larger mid-century (+ 4.3-7.3%) and largely unchanged by 2100 (- 0.2%). Similar trends were observed using a high SLR scenario and WEM Linear 2, except for slightly larger saltmarsh extents by 2100 (+ 4.7%).

4 DISCUSSION

4.1 Wetland and Tidal Regime Responses to SLR at Minnamurra

This analysis demonstrated that the rate of SLR affects wetland elevation adjustment, wetland inundation regimes, and the lateral distribution of wetland vegetation. At the same time, changes in wetland distribution also alter tidal hydrodynamics. These projections were only achieved by coupling tidal hydrodynamics to a model of wetland elevation adjustment developed for this study (i.e. WEM). High correlation coefficients and low RMSEs between observed and modelled water levels and wetland inundation, and reasonable correlation and accuracy between detailed wetland mapping and model projections of mangrove and saltmarsh at contemporary sea level, provided considerable confidence that the model setup was appropriate.

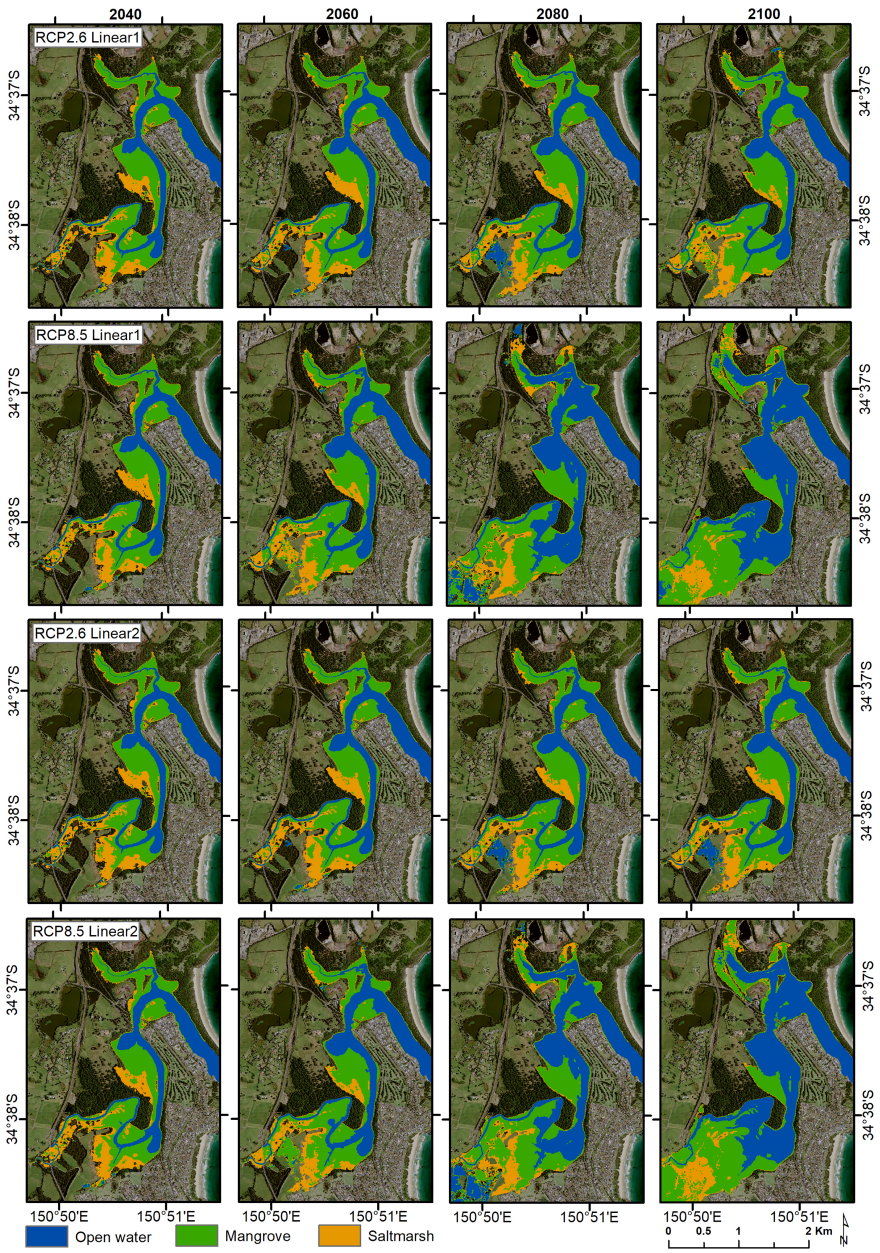


FIGURE 9 | Projections of intertidal wetland vegetation communities (mangrove and saltmarsh) for low and high SLR scenarios, as well as WEM scenarios Linear 1 and Linear 2.

Modelling of four simulations including low (RCP2.6) and high (RCP8.5) SLR scenarios, as well as two wetland adjustment scenarios (Linear 1 and Linear 2), showed consistent patterns of mangroves expanding into saltmarsh, saltmarsh transitioning to higher elevations (currently occupied by *Casuarina* forest), and substantially larger open water areas at relatively high rates of SLR.

Simulations using the lower SLR scenario indicate that tidal wetlands adjust to rising sea levels by increasing substrate elevation (up to 0.18 m) and by vegetation transitions to higher elevations, leading to an increase in extent, particularly for mangroves (+ 43%). Only mangroves positioned lower in the tidal frame converted to open water areas, whereas higher in the tidal frame mangroves replaced saltmarsh due to increasing tidal inundation. This modelled encroachment of mangroves into saltmarsh has been observed in the field in recent decades and attributed to SLR (Chafer, 1998; Saintilan and Rogers, 2013; Saintilan et al., 2018). The ability of mangroves to withstand comparatively lower rates of SLR, as shown here (modelling of SLR + 5mm yr^{-1}), aligns well with previous suggestions that

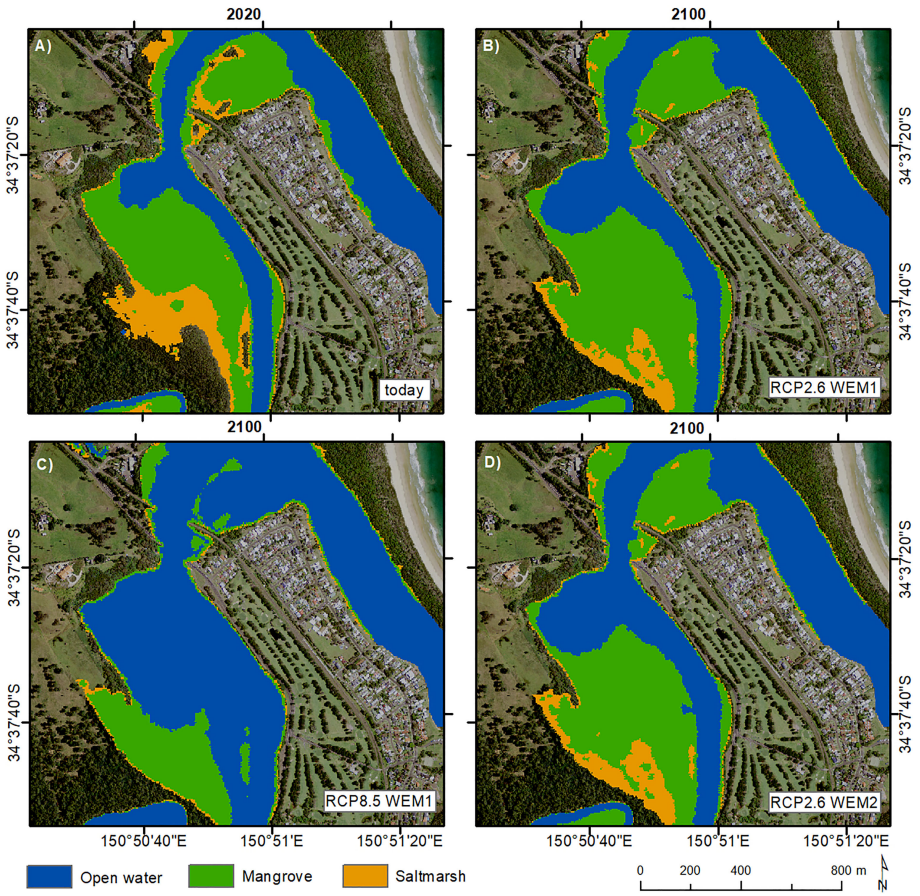


FIGURE 10 | Projections of intertidal wetland vegetation communities (mangrove and saltmarsh) for today **(A)**, WEM1 and low SLR **(B)**, WEM1 and high SLR **(C)**, and WEM2 and low SLR **(D)**.

mangroves may tolerate increases in the rate of mean sea level rise of up to 7 mm yr^{-1} (Saintilan et al., 2020). Saltmarsh expanded to higher elevations where tidal inundation was sufficient (+ 6% in coverage by 2100), which appears to be only on the southern floodplain. Saltmarsh, being preferentially located in the upper intertidal, was more sensitive to coastal squeeze than mangroves.

Simulations using the higher SLR scenario indicated that the ability of mangroves to adjust to SLR decreases when the rate of sea-level rise accelerates (> 10 mm yr^{-1} and up to 14 mm yr^{-1} at the end of the century), which was particularly shown during the last quarter of the century when low elevated mangroves mainly converted to open water areas (**Figures 9**, **10** and **11**). Nevertheless, mangrove areas overall substantially expanded (+ 70%), whereas landward expansion of saltmarsh resulted in only a minor increase in coverage (+ 4%). Differences in wetland resilience between low and high SLR simulations presented here show parallels to SLAMM modelling for lagoon marshes in Portugal by Carracso et al. (2021) who demonstrated a non-linearity in wetland response to SLR and critical thresholds when wetland systems are no longer in pace with SLR.

The selection of wetland adjustment scenarios (Linear 1 and Linear 2) marginally affected projections of mangrove, saltmarsh and open water area extents under SLR (+/- 5%); however, comparison between scenarios showed how assumptions regarding sedimentation influence model outcomes, with WEM Linear 1 simulations (moderate wetland growth) showing greater mangrove resilience and less open water conversion. Simulations of WEM Linear 2 (slow wetland growth) projected mangroves to be more vulnerable to SLR and saltmarsh to be more resilient to SLR. These differences relate to differences in WEM Linear 1 and WEM Linear 2 for low inundation durations. WEM Linear 1 did not allow for sedimentation for low inundation durations characteristic of much of the saltmarsh extent (**Figure 4**).

Wetland dynamics under SLR as projected by the eco-morphodynamic model show some parallels but also differences with earlier modelling for selected sites at Minnamurra River estuary (Oliver et al., 2012; Mogensen and Rogers, 2018). For example, spatial modelling by Oliver et al. (2012) has indicated that mangrove and saltmarsh on the central floodplain may be able to withstand a lower rate of SLR, but conversion of low elevation mangroves to open water areas and

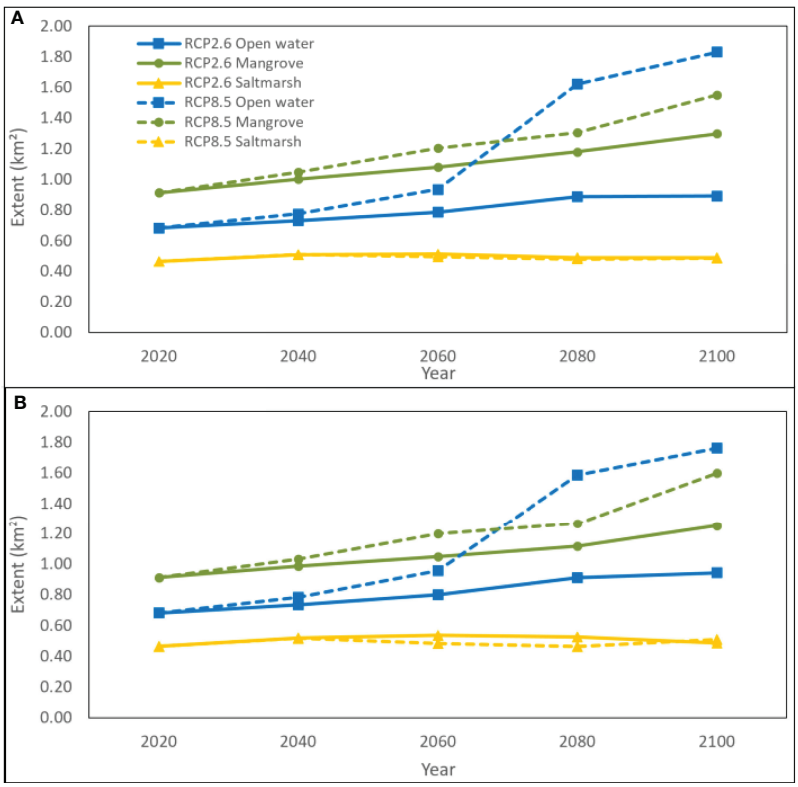


FIGURE 11 | Projections of river (blue squares), mangrove (green circles) and saltmarsh (orange triangles) extents in response to the lower RCP2.6 SLR scenario (solid) and the higher RCP8.5 SLR scenario (dashed) for WEM scenarios Linear 1 (panel **A**) and Linear 2 (panel **B**).

replacement of lower elevation saltmarsh by mangroves expanding landward under a higher rate of SLR. Similar wetland responses to high rates of SLR for the central floodplain were indicated by Mogensen and Rogers (2018) using SLAMM and two empirically-based spatial models following methods presented by Oliver et al. (2012) and Temmerman et al. (2003b). However, exponential modelling by Mogensen and Rogers's (2018) that projects mangroves largely adjusting to SLR on the southern floodplain differs substantially from results here, indicating a conversion of low elevation mangroves to open water areas. A potential explanation for this stronger mangrove resilience suggested by Mogensen and Rogers (2018) could be the exponential relationship for vertical accretion underlying one of their empirical spatial models (after Temmerman et al., 2003), which facilitates much higher sedimentation and surface elevation gains than the linear relationship between wetland inundation regime and surface elevation change applied here. There is increasing evidence that organic matter additions at lower elevation occupied by mangroves may provide substantial sedimentation contributions justifying an exponential model structure (Morris et al., 2002; Kirwan and Murray, 2007; Rogers and Saintilan, 2021), however given the lack of field data supporting such relationships at Minnamurra, the Linear WEMs presented here appear to be the best approximations. We acknowledge that this linear model structure influences the model outcomes and conclusions of this study, and that using an exponential model structure would likely increase the resilience of mangroves low in the tidal frame; however, previous ^{210}Pb analysis of low elevated mangroves has not suggested high accretion rates supporting the use of an exponential model structure (Lal, 2019).

Projections of intertidal wetland topography illustrate how the rate of SLR and assumptions regarding wetland elevation change (WEM Linear 1 and Linear 2) influence wetland geomorphology in response to SLR (**Figure 7** and **Supplementary Figure 5**). When the rate of SLR is low and wetland elevation change was assumed to be moderate (Linear 1), mangroves positioned low in the tidal frame adjusted to rising sea level by increasing in surface elevation (by up to 0.18 m), and in consequence the intertidal geomorphology became increasingly horizontal and developed towards a platform with a flat profile. This can be explained by mangroves lower in the tidal frame increasing surface elevation throughout the simulation period under the low SLR scenario (80 years), whereas under high SLR scenario, positions in the tidal frame suitable for mangroves shifted upwards and thus gains in surface elevation eventually stopped when mangroves converted to open water areas. It is acknowledged that treating tidal flats as static substrates does not represent reality as sediment supply may allow tidal flats to increase elevation at a rate similar to SLR; however, the WEM was not parameterised to model main-channel

morphodynamics or tidal flat vertical adjustments. Model simulations assuming low rates of wetland elevation adjustment (Linear 2) projected approximately 50% smaller gains in wetland surface elevation, but slightly higher saltmarsh resilience under low SLR due to the construction of the linear relationship.

Simulations for both SLR scenarios indicated that hydrodynamics of the estuary change in response to rising sea level, with tidal range shown to increase by up to 8% (**Figure 8**). Under both SLR scenarios, tidal range appeared to increase linearly with SLR; however, simulations using the higher SLR scenario indicated downstream stabilisation and upstream decline in tidal range when SLR exceeded 0.6 m, which coincides with the conversion of large mangrove areas low in the tidal frame to open water areas (**Figure 11**). This non-linear behaviour of tidal range under high SLR may be explained by substantial widening of the main channel along with increased intertidal storage areas, which have been associated with tidal energy dissipation and potential reduction in tidal range under SLR (Du et al., 2018; Kumbier et al., 2018a). This is an important finding given the significant role of tidal range as a parameter of wetland functioning and since many wetland modelling studies assume a constant tidal range when estimating wetland response to SLR. Even though absolute changes in tidal range were comparatively small (+ 0.1 m), due to the micro-tidal regime of Minnamurra River, such alterations in tidal range can increase the vertical space available for wetland establishment, lengthen the duration of inundation, and thus impact modelling outcomes. Therefore, it is proposed that wetland modelling in estuaries similar to the one presented here should account for alteration in tidal regime, which may be particularly important for meso- and macro-tidal systems as absolute changes in tidal range will likely be of greater magnitude than results presented here and justify the extra complexity added by considering wetland sedimentation.

4.2 Modelling Implications

In this study, such consideration of alteration in tidal dynamics was achieved by coupling a depth averaged hydrodynamic model with an empirical wetland elevation model. This approach allowed for inclusion of interrelations between hydrodynamics, wetland extent and intertidal geomorphology, which have been shown to be responsible for alteration and non-linear responses in tidal range observed here. Integrating modelling approaches can account for these eco-geomorphological feedbacks between estuarine hydrodynamics and intertidal wetlands, which should be considered when modelling wetland response to SLR at the scale of an estuary. This is particularly important for infilled channelised estuaries, like Minnamurra River, where main channel hydrodynamics and intertidal wetlands have been shown to be interconnected (Kumbier et al., 2022). In these estuaries, tides may be amplified before dissipating along the estuary, which occurs as an outcome of main channel hydrodynamics and propagation of tides across intertidal wetlands.

The eco-morphodynamic model presented here differs from previous coupled hydrodynamic-wetland models in the way it accounts for tidal modifications. Whereas previous studies utilised hydrodynamic modelling to produce generalised tidal water levels (e.g. MHW) to delineate wetland zonation (Alizad et al., 2016a; Rodríguez et al., 2017), the framework presented in this study calculates spatially explicit estimates of wetland inundation regime that are explicitly linked to vegetation occurrence. This procedure is an advancement given the spatial variability of tides along an estuary, and the influence of vegetation on tidal flow in wetlands (Mazda et al., 1995; Temmerman et al., 2005). However, it is acknowledged that the representation of bottom roughness could be improved by incorporation of depth-dependent coefficients considering the effects of vegetation structure (Mazda et al., 1997), such as used in more detailed small scale studies (Horstmann et al., 2015; Horstmann et al., 2021). This simplification of bottom roughness in the present study could have affected projections of tidal dynamics in response to SLR, also because a replacement of mangrove areas with open water would most likely imply a transitional time where woody mangrove biomass slowly decomposes and continues to interact with tidal flow. Consideration of site-specific changes in wetland surface elevation from 20 years of observation utilising SETs provides a robust foundation to extrapolate trends in surface elevation change using hydrodynamic modelling. The comparatively simple wetland adjustment model used here (i.e. WEM) allows for indirect consideration of mineral and organic matter accumulation, as well as below-ground processes, such as auto-compaction. Whereas the presented model structure assumes that sedimentation on estuarine wetlands is fully independent of temporal and spatial sediment availability, more realistic future projections could be achieved by considering changes in sediment transport and availability in response to SLR to account for processes, such as sediment dispersion resuspension, within the estuary and wetlands (e.g. using a 3D hydrodynamic-sediment transport model); however, such considerations add considerable complexity and computational demands due to the 3D model structure.

Trade-offs between model complexity and over-parameterisation are a known challenge of coupled hydrodynamic-ecological estuarine models (Ganju et al., 2016), and model design should be driven by the purpose of the modelling framework. This study aimed to develop a reduced complexity wetland model framework with improved representation of estuarine hydrodynamics, which is transferable to other locations provided sufficient data is available to empirically define a wetland elevation model. This transferability is achieved by determining wetland response to SLR based on modelling of inundation regimes, which allows for consideration of any wetland vegetation as long as inundation preferences are known. The procedures of the eco-morphodynamic model presented in this study can be adopted for wetland vulnerability assessments in other estuarine environments providing reliable wetland surface elevation trajectories are available (e.g. from SETs or sediment dating); however, model results for estuarine wetlands where vertical accretion is dominated by tidal supply of mineral sediments may be limited, as the model does not specifically account for mineral sediment transport within the estuary and wetlands.

In this study supratidal wetlands of *Casuarina* forest were not considered despite evidence of saltmarsh beneath forest canopies, modelled evidence of saltmarsh encroachment upon supratidal forests elsewhere, and that *Casuarina* may have capacity to adjust to rising sea level (Rogers et al., 2019b). However, too little is

known about their response to SLR to adequately parameterise the WEM, and further research of the vertical adjustment of these forests is required to understand their behaviour under SLR and to consider them in future modelling studies of wetland response to SLR. Additionally, the interconnections between estuarine hydrodynamics and intertidal wetlands demonstrated here, suggest that studies into tidal hydrodynamics in estuaries (e.g. flow velocities, asymmetry) can be affected by intertidal geomorphology. Whilst it has been known and researched for some time (Aubrey and Speer, 1985; Friedrichs and Aubrey, 1988; Friedrichs et al., 1990), widespread adoption of modelling approaches that recognise the interconnection between tidal hydrodynamics and geomorphology has not occurred. Modelling results here align with similar modelling of estuarine marshes in the US (Donatelli et al., 2018), and show how intertidal geomorphology may change in response to SLR, which demonstrably affected tidal range. It is anticipated that the response of entrance morphology and sub-tidal channel morphology to SLR, not simulated here, will also cause morphodynamic feedbacks that affect tidal range. Similarly, other tidal properties, such as velocity or asymmetry, may be affected by changing intertidal wetland geomorphology under SLR; however, these effects are yet to be sufficiently quantified and previous SLR modelling studies have predominantly focussed on hydrodynamics only. Effective planning and decision making for SLR in estuaries would benefit from simultaneous investigation of estuarine and intertidal wetland processes.

5 CONCLUSIONS

Eco-morphodynamic modelling at Minnamurra River estuary has demonstrated that the fate of intertidal wetlands depends on the rate of SLR, with projections based on slow SLR (+ 5mm yr^{-1}) indicating mangroves may adjust to SLR, but when exposed to a higher rate of SLR (> 10mm yr^{-1}) conversion of low elevated mangroves to open water areas were projected. Within model scenarios, tidal range inside the estuary was shown to increase overall under low and high SLR (by up to + 8%), and to respond non-linearly to high SLR. This non-linear response may be related to eco-geomorphological feedbacks caused by changing wetland extents and intertidal geomorphology. As low elevated mangrove areas convert to open water, tidal energy dissipates in intertidal storage areas and reduces tidal range. Model projections of mangrove and saltmarsh distribution and their associated rates of wetland elevation adjustment are a function of SLR, with feedbacks demonstrated between the ecology, morphology and hydrodynamics. Comparisons of model simulations based on two SLR scenarios and two wetland elevation adjustment scenarios indicate that macrophyte distribution at Minnamurra River is highly dependent upon the rate of SLR and its influence on wetland elevation adjustment.

Whereas many wetland modelling studies of responses to SLR assume tidal range to remain unchanged, modelling in this study indicates that hydrodynamics in estuaries, such as tidal range, can alter in response to SLR, if entrance and channel morphology do not change elevation significantly in response to SLR. Integrated modelling approaches, such as the coupled eco-morphodynamic model presented here, are required to account for the dynamic eco-geomorphological feedbacks resulting from the interaction of estuarine hydrodynamics and intertidal wetlands under SLR. More generally, incorporating hydrodynamic modelling into wetland research as applied here allows for a spatially explicit calculation of wetland inundation regimes, which improves the representation of tidal inundation in wetland modelling. Altogether these improvements in intertidal flow representation and consideration of tidal responses to SLR advance modelling of wetland response to SLR in estuaries, and may contribute to better understanding and management of estuarine-wetland systems.

DATA AVAILABILITY STATEMENT

The modelling output data supporting the conclusions of this article will be made available by the authors upon request.

AUTHOR CONTRIBUTIONS

KK, KR, MH and CW conceived and designed the study. KK, MH, KL, LM and KR collected and analysed the field data. KK set-up the modelling and ran the simulations. KK, KR, MH and CW analysed and interpreted the modelling results. KK wrote the paper with substantial input from KR, MH and CW. All authors contributed to the article and approved the submitted version.

FUNDING

The University of Wollongong and the NSW Department of Planning, Industry and Environment provided financial support for this research.

ACKNOWLEDGMENTS

KK expresses gratitude to the University of Wollongong and the NSW Department of Planning, Industry and Environment for supporting his PhD research with a scholarship. The authors thank everyone who contributed to the SET data collection and analysis in the past 20 years, and the School of Aviation at the University of New South Wales for the provision of LiDAR data. The authors acknowledge the Dharawal people who are the traditional custodians of the Minnamurra River catchment area.

SUPPLEMENTARY MATERIAL

The Supplementary Material for this article can be found online at: https://www.frontiersin.org/articles/10.3389/fmars.2022.860910/full#supplementary-material

REFERENCES

Alizad, K., Hagen, S. C., Medeiros, S. C., Bilskie, M. V., Morris, J. T., Balthis, L., et al. (2018). Dynamic Responses and Implications to Coastal Wetlands and the Surrounding Regions Under Sea Level Rise. *PloS One* 13, 1–27. doi: 10.1371/journal.pone.0205176

Alizad, K., Hagen, S. C., Morris, J. T., Bacopoulos, P., Bilskie, M. V., Weishampel, J. F., et al. (2016a). A Coupled, Two-Dimensional Hydrodynamic-Marsh Model With Biological Feedback. *Ecol. Modell.* 327, 29–43. doi: 10.1016/J.ECOLMODEL.2016.01.013

Alizad, K., Hagen, S. C., Morris, J. T., Medeiros, S. C., Bilskie, M. V., and Weishampel, J. F. (2016b). Coastal Wetland Response to Sea-Level Rise in a Fluvial Estuarine System. *Earth's Futur.* 4, 483–497. doi: 10.1002/2016EF000385

Alizad, K., Medeiros, S. C., Foster-Martinez, M. R., and Hagen, S. C. (2020). Model Sensitivity to Topographic Uncertainty in Meso- And Microtidal Marshes. *IEEE J. Sel. Top. Appl. Earth Obs. Remote Sens.* 13, 807–814. doi: 10.1109/JSTARS.2020.2973490

Allen, J. R. L. (2000). Morphodynamics of Holocene Salt Marshes: A Review Sketch From the Atlantic and Southern North Sea Coasts of Europe. *Quat. Sci. Rev.* 19, 1155–1231. doi: 10.1016/S0277-3791(99)00034-7

Arcement, G. J., and Schneider, V. R. (1989). *Guide for Selecting Manning's Roughness Coefficients for Natural Channels and Flood Plains, US Geological Survey Water-Supply Paper 2339*. Available at: https://doi.org/10.3133/wsp2339.

Aubrey, D. G., and Speer, P. E. (1985). A Study of non-Linear Tidal Propagation in Shallow Inlet/Estuarine Systems Part I: Observations. *Estuar. Coast. Shelf Sci.* 21, 185–205. doi: 10.1016/0272-7714(85)90096-4

Baltzer, F. (1969). Les Formations Végétales Associés Au Delta De La Dumbea (Nouvelles Calédonies) Et Leurs Indications Écologiques, Géomorphologiques Et Sédimentologiques Mises En Évidence Par La Cartographie. *Ser. Géol.* 1, 59–84.

Barbier, E. B., Sally, D. H., Chris, K., Evamaria, W. K., Adrian, C. S., and Brian, R. S. (2011). The Value of Estuarine and Coastal Ecosystem Services. *Ecol. Monogr.* 81, 169–193. doi: 10.1890/10-1510.1

Benson, T. (2020). *Telemac Tools* (MATLAB Central File Exchange). Available at: https://www.mathworks.com/matlabcentral/fileexchange/25021-telemac-tools (Accessed 12.16.20).

Cahoon, D. R., Hensel, P. F., Spencer, T., Reed, D. J., McKee, K. L., and Saintilan, N. (2006). "Coastal Wetland Vulnerability to Relative Sea-Level Rise: Wetland Elevation Trends and Process Controls," in *Wetlands and Natural Resource Management*. Eds. J. T. A. Verhoeven, B. Beltmn, R. Bobbink and D. F. Whigham (Berlin, Germany: Springer Heidelberg), 271–292. doi: 10.1007/978-3-540-33187-2_12

Cahoon, D. R., Lynch, J. C., Hensel, P., Boumans, R., Perez, B. C., Segura, B., et al. (2002). High-Precision Measurements of Wetland Sediment Elevation: I. Recent Improvements to the Sedimentation-Erosion Table. *J. Sediment. Res.* 72, 730–733. doi: 10.1306/020702720730

Cahoon, D. R., Perez, B. C., Segura, B. D., and Lynch, J. C. (2011). Elevation Trends and Shrink-Swell Response of Wetland Soils to Flooding and Drying. *Estuar. Coast. Shelf Sci.* 91, 463–474. doi: 10.1016/j.ecss.2010.03.022

Cahoon, D. R., and Reed, D. J. (1995). Relationships Among Marsh Surface Topography, Hydroperiod, and Soil Accretion in a Deteriorating Louisiana Salt Marsh. *J. Coast. Res.* 11, 357–369. doi: 10.2307/4298345

Carrasco, A. R., Kombiadou, K., Amado, M., and Matias, A. (2021). Past and Future Marsh Adaptation: Lessons Learned From the Ria Formosa Lagoon. *Sci. Total Environ.* 790, 148082. doi: 10.1016/j.scitotenv.2021.148082

Chafer, C. J. (1998). A Spatio-Temporal Analysis of Estuarine Vegetation Change in the Minnamurra River 1938 - 1997. *Rep. Minnamurra Estuary Manage. Committee.* 47pp.

Chow, V. T. (1959). *Open-Channel Hydraulics, Science*. (Europe, New York, USA: McGraw-Hill Education).

Church, J. A., Clark, P. U., Cazenave, A., Gregory, J. M., Jevrejeva, S., Levermann, A., et al. (2013). Chapter 13: Sea Level Change, IPCC. *Am. Assoc. Adv Sci.* 1535pp. doi: 10.1126/science.342.6165.1445-a

Craft, C., Clough, J., Ehman, J., Joye, S., Park, R., Pennings, S., et al. (2009). Forecasting the Effects of Accelerated Sea-Level Rise on Tidal Marsh Ecosystem Services. *Front. Ecol. Environ.* 7, 73–78. doi: 10.1890/070219

D'Alpaos, A., Lanzoni, S., Marani, M., and Rinaldo, A. (2007). Landscape Evolution in Tidal Embayments: Modeling the Interplay of Erosion, Sedimentation, and Vegetation Dynamics. *J. Geophys. Res.* 112, F01008. doi: 10.1029/2006JF000537

Dangendorf, S., Marcos, M., Wöppelmann, G., Conrad, C. P., Frederikse, T., and Riva, R. (2017). Reassessment of 20th Century Global Mean Sea Level Rise. *Proc. Natl. Acad. Sci. U. S. A.* 114, 1–6. doi: 10.1073/pnas.1616007114

Department of Planning Industry and Environment (2017). *Single Beam Bathymetry Data. Provided on Request* (Sydney, Australia).

Donatelli, C., Ganju, N. K., Zhang, X., Fagherazzi, S., and Leonardi, N. (2018). Salt Marsh Loss Affects Tides and the Sediment Budget in Shallow Bays. *J. Geophys. Res. Earth Surf.* 123, 2647–2662. doi: 10.1029/2018JF004617

Du, J., Shen, J., Zhang, Y. J., Ye, F., Liu, Z., Wang, Z., et al. (2018). Tidal Response to Sea-Level Rise in Different Types of Estuaries: The Importance of Length, Bathymetry, and Geometry. *Geophys. Res. Lett.* 45, 227–235. doi: 10.1002/2017GL075963

Fagherazzi, S., Kirwan, M. L., Mudd, S. M., Guntenspergen, G. R., Temmerman, S., D'Alpaos, A., et al. (2012). Numerical Models of Salt Marsh Evolution: Ecological, Geomorphic, and Climatic Factors. *Rev. Geophys.* 50, RG1002. doi: 10.1029/2011RG000359

Friedrichs, C. T., and Aubrey, D. G. (1988). Non-Linear Tidal Distortion in Shallow Well-Mixed Estuaries: A Synthesis. *Estuar. Coast. Shelf Sci.* 27, 521–545. doi: 10.1016/0272-7714(88)90082-0

Friedrichs, C. T., Aubrey, D. G., and Speer, P. E. (1990). Impacts of Relative Sea-Level Rise on Evolution of Shallow Estuaries. *Residual Curr. Long-term Transp.* 38, 105–122. doi: 10.1007/978-1-4613-9061-9_9

Ganju, N. K., Brush, M. J., Rashleigh, B., Aretxabaleta, A. L., del Barrio, P., Grear, J. S., et al. (2016). Progress and Challenges in Coupled Hydrodynamic-Ecological Estuarine Modeling. *Estuaries Coasts* 39, 311–332. doi: 10.1007/s12237-015-0011-y

Gedan, K. B., Kirwan, M. L., Wolanski, E., Barbier, E. B., and Silliman, B. R. (2011). The Present and Future Role of Coastal Wetland Vegetation in Protecting Shorelines: Answering Recent Challenges to the Paradigm. *Clim. Change* 106, (1), 7–29 doi: 10.1007/s10584-010-0003-7

Geoscience Australia. (2011). *LiDAR Elevation Data*. Available at: https://elevation.fsdf.org.au/ (Accessed 2.10.20).

Geoscience Australia. (2018). *LiDAR Elevation Data*. Available at: https://elevation.fsdf.org.au/ (Accessed 8.15.20).

Hagen, S. C., Morris, J. T., Bacopoulos, P., and Weishampel, J. F. (2013). Sea-Level Rise Impact on a Salt Marsh System of the Lower St. *Johns River. J. Waterw. Port Coastal Ocean Eng.* 139, 118–125. doi: 10.1061/(asce)ww.1943-5460.0000177

Haslett, S. K., Davies-Burrows, R., Panayotou, K., Jones, B. G., and Woodroff, C. D. (2010). Holocene Evolution of the Minnamurra River Estuary, Southeast Australia: Foraminiferal Evidence. *Z. Für Geomorphol.* 45, (3), 79–98. doi: 10.1127/0372-8854/2010/0054S3-0020

Hervouet, J.-M. (2000). TELEMAC Modelling System: An Overview. *Hydrol. Process* 14, 2209–2210. doi: 10.1002/1099-1085(200009)14:13<2209::AID-HYP23>3.0.CO;2-6

Hervouet, J.-M. (2007). *Hydrodynamics of Free Surface Flows: Modelling With the Finite Element Method, Hydrodynamics of Free Surface Flows: Modelling With the Finite Element Method* (Chichester, UK: John Wiley & Sons, Ltd). Available at: https://doi.org/10.1002/9780470319628.

Horstman, E. M., Bryan, K. R., and Mullarney, J. C. (2021). Drag Variations, Tidal Asymmetry and Tidal Range Changes in a Mangrove Creek System. *Earth Surf. Process. Landforms* 46 (9), esp.5124. doi: 10.1002/esp.5124

Horstman, E. M., Dohmen-Janssen, C. M., Bouma, T. J., and Hulscher, S. J. M. H. (2015). Tidal-Scale Flow Routing and Sedimentation in Mangrove Forests: Combining Field Data and Numerical Modelling. *Geomorph* 228, 244–262. doi: 10.1016/j.geomorph.2014.08.011

Iglesias, I., Avilez-Valente, P., Bio, A., and Bastos, L. (2019). Modelling the Main Hydrodynamic Patterns in Shallow Water Estuaries: The Minho Case Study. *Water* 11, 1–23. doi: 10.3390/w11051040

JCU Geophysics Laboratory. (2020). *Marotte HS-I User Guide*. Available at: https://www.marinegeophysics.com.au/current-meter/users-guide/.

Kaiser, G., Scheele, L., Kortenhaus, A., Løvholt, F., Römer, H., and Leschka, S. (2011). The Influence of Land Cover Roughness on the Results of High Resolution Tsunami Inundation Modeling. *Nat. Hazards Earth Syst. Sci.* 11, 2521–2540. doi: 10.5194/nhess-11-2521-2011

Kirwan, M. L., Guntenspergen, G. R., D'Alpaos, A., Morris, J. T., Mudd, S. M., and Temmerman, S. (2010). *Limits on the Adaptability of Coastal Marshes to Rising Sea Level* (n/a-n/a: Geophys. Res. Lett. 37). doi: 10.1029/2010GL045489

Kirwan, M. L., and Murray, A. B. (2007). A Coupled Geomorphic and Ecologic Model of Tidal Marsh Evolution. *Proc. Natl. Acad. Sci. U. S. A.* 104, (15), 6118–6122. doi: 10.1073/pnas.0700958104

Krauss, K. W., Mckee, K. L., Lovelock, C. E., Cahoon, D. R., Saintilan, N., Reef, R., et al. (2014). How Mangrove Forests Adjust to Rising Sea Level. *New Phytol.* 202, 19–34. doi: 10.1111/nph.12605

Krone, R. B. (1987). "A Method for Simulating Historic Marsh Elevations," in *Specialty Conference on Advances in Understanding of Coastal Sediment Processes*. Ed. N. C. Kraus (New Orleans: American Society of Civil Engineers), 316–322.

Kumbier, K., Carvalho, R. C., Vafeidis, A. T., and Woodroffe, C. D. (2018b). Investigating Compound Flooding in an Estuary Using Hydrodynamic Modelling: A Case Study From the Shoalhaven River, Australia. *Nat. Hazards Earth Syst. Sci.* 18, 463–477. doi: 10.5194/nhess-18-463-2018

Kumbier, K., Carvalho, R., and Woodroffe, C. (2018a). Modelling Hydrodynamic Impacts of Sea-Level Rise on Wave-Dominated Australian Estuaries With Differing Geomorphology. *J. Mar. Sci. Eng.* 6, 66. doi: 10.3390/jmse6020066

Kumbier, K., Hughes, M. G., Carvalho, R. C., and Woodroffe, C. D. (2022). Intertidal Wetland Geomorphology Influences Main Channel Hydrodynamics in a Mature Barrier Estuary. *Estuar. Coast. Shelf Sci.* 267, 107783. doi: 10.1016/j.ecss.2022.107783

Kumbier, K., Hughes, M. G., Rogers, K., and Woodroffe, C. D. (2021). Inundation Characteristics of Mangrove and Saltmarsh in Micro-Tidal Estuaries. *Estuar. Coast. Shelf Sci.* 261, 107553. doi: 10.1016/j.ecss.2021.107553

Lal, K. (2019). *Surface Elevation Dynamics Across a Range of Timescales in Coastal Wetlands of South-Eastern Australia. PhD Thesis* (Wollongong: University of Wollongong).

Lee, S. B., Li, M., and Zhang, F. (2017). Impact of Sea Level Rise on Tidal Range in Chesapeake and Delaware Bays. *J. Geophys. Res. Ocean.* 122, 3917–3938. doi: 10.1002/2016JC012597

Mazda, Y., Kanazawa, N., and Wolanski, E. (1995). Tidal Asymmetry in Mangrove Creeks. *Hydrobiologia* 295, 51–58. doi: 10.1007/BF00029110

Mazda, Y., Wolanski, E., King, B., Sase, A., Ohtsuka, D., and Magi, M. (1997). Drag Force Due to Vegetation in Mangrove Swamps. *Mangroves Saltmarshes* 1, 193–199. doi: 10.1023/A:1009949411068

McInnes, K., Church, J., Monselesan, D., Hunter, J., O'Grady, J., Haigh, I., et al. (2015). Information for Australian Impact and Adaptation Planning in Response to Sea-Level Rise. *Aust. Meteorol. Oceanogr. J.* 65, 127–149. doi: 10.22499/2.6501.009

McKee, K., Rogers, K., and Saintilan, N. (2012). Response of Salt Marsh and Mangrove Wetlands to Changes in Atmospheric CO2, Climate, and Sea Level, in: Global Change and the Function and Distribution of Wetlands. *Springer Netherlands Dordrecht* pp, 63–96. doi: 10.1007/978-94-007-4494-3_2

Mogensen, L. A., and Rogers, K. (2018). Validation and Comparison of a Model of the Effect of Sea-Level Rise on Coastal Wetlands. *Sci. Rep.* 8, 1–14. doi: 10.1038/s41598-018-19695-2

Morris, J. T., Sundareshwar, P. V., Nietch, C. T., Kjerfve, B., and Cahoon, D. R. (2002). Responses of Coastal Wetlands to Rising Sea Level. *Ecology* 83, 2869–2877. doi: 10.1890/0012-9658(2002)083[2869:ROCWTR]2.0.CO;2

Mudd, S. M., Howell, S. M., and Morris, J. T. (2009). Impact of Dynamic Feedbacks Between Sedimentation, Sea-Level Rise, and Biomass Production on Near-Surface Marsh Stratigraphy and Carbon Accumulation. *Estuar. Coast. Shelf Sci.* 82, 377–389. doi: 10.1016/j.ecss.2009.01.028

OEH. (2017). *Single Beam Bathymetry Data. Provided on Request* (Sydney, Australia).

Oliver, T. S. N., Rogers, K., Chafer, C. J., and Woodroffe, C. D. (2012). Measuring, Mapping and Modelling: An Integrated Approach to the Management of Mangrove and Saltmarsh in the Minnamurra River Estuary, Southeast Australia. *Wetl. Ecol. Manage.* 20, 353–371. doi: 10.1007/s11273-012-9258-2

Owers, C. J., Rogers, K., and Woodroffe, C. D. (2016). Identifying Spatial Variability and Complexity in Wetland Vegetation Using an Object-Based Approach. *Int. J. Remote Sens.* 37, 4296–4316. doi: 10.1080/01431161.2016.1211349

Panayotou, K., Woodroffe, C. D., Jones, B. G., Chenhall, B., McLean, E., and Heijnis, H. (2007). Patterns and Rates of Sedimentary Infill in the Minnamurra River Estuary, South-Eastern Australia. *J. Coast. Res.* (50), 688–692. doi: 10.2307/26481674

Rodríguez, J. F., Saco, P. M., Sandi, S., Saintilan, N., and Riccardi, G. (2017). Potential Increase in Coastal Wetland Vulnerability to Sea-Level Rise Suggested by Considering Hydrodynamic Attenuation Effects. *Nat. Commun.* 8, 1–12. doi: 10.1038/ncomms16094

Rogers, K., Kelleway, J. J., Saintilan, N., Megonigal, J. P., Adams, J. B., Holmquist, J. R., et al. (2019a). Wetland Carbon Storage Controlled by Millennial-Scale Variation in Relative Sea-Level Rise. *Nature* 567, 91–95. doi: 10.1038/s41586-019-0951-7

Rogers, K., Mogensen, L. A., Davies, P., Kelleway, J., Saintilan, N., and Withycombe, G. (2019b). Impacts and Adaptation Options for Estuarine Vegetation in a Large City. *Landsc. Urban Plan.* 182, 1–11. doi: 10.1016/j.landurbplan.2018.09.022

Rogers, K., and Saintilan, N. (2021). Processes Influencing Autocompaction Modulate Coastal Wetland Surface Elevation Adjustment With Sea-Level Rise. *Front. Mar. Sci.* 8, 694039. doi: 10.3389/fmars.2021.694039

Rogers, K., Saintilan, N., and Copeland, C. (2012). Modelling Wetland Surface Elevation Dynamics and its Application to Forecasting the Effects of Sea-Level Rise on Estuarine Wetlands. *Ecol. Modell.* 244, 148–157. doi: 10.1016/J.ECOLMODEL.2012.06.014

Roy, P. S., Williams, R. J., Jones, A. R., Yassini, I., Gibbs, P. J., Coates, B., et al. (2001). Structure and Function of South-East Australian Estuaries. *Estuar. Coast. Shelf Sci.* 53, 351–384. doi: 10.1006/ecss.2001.0796

Ryan, T. J. (1992). The Contemporary Hydrodynamics and Evolutionary Development of the Minnamurra Estuary, New South Wales. Honors Thesis (University of Wollongong), 1–93.

Saintilan, N., Khan, N. S., Ashe, E., Kelleway, J. J., Rogers, K., Woodroffe, C. D., et al. (2020). Thresholds of Mangrove Survival Under Rapid Sea Level Rise. *Science (80-.)* 368, 1118–1121. doi: 10.1126/science.aba2656

Saintilan, N., and Rogers, K. (2013). The Significance and Vulnerability of Australian Saltmarshes: Implications for Management in a Changing Climate. *Mar. Freshw. Res.* 64, (1), 66–79. doi: 10.1071/MF12212

Saintilan, N., Rogers, K., Kelleway, J. J., and Sloane, D. R. (2018). Climate Change Impacts on the Coastal Wetlands of Australia. *Wetlands* 39, 1–10. doi: 10.1007/s13157-018-1016-7

Saintilan, N., Wilson, N. C., Rogers, K., and Rajkaran, A. (2014). Mangrove Expansion and Salt Marsh Decline at Mangrove Poleward Limits. *Glob. Change Biol.* 20, 147–157. doi: 10.1111/gcb.12341

Seenath, A., Wilson, M., and Miller, K. (2016). Hydrodynamic Versus GIS Modelling for Coastal Flood Vulnerability Assessment: Which is Better for Guiding Coastal Management? *Ocean Coast. Manage.* 120, 99–109. doi: 10.1016/j.ocecoaman.2015.11.019

Silvestri, S., Defina, A., and Marani, M. (2005). Tidal Regime, Salinity and Salt Marsh Plant Zonation. *Estuar. Coast. Shelf Sci.* 62, 119–130. doi: 10.1016/j.ecss.2004.08.010

Spier, D., Gerum, H. L. N., Noernberg, M. A., and Lana, P. C. (2016). Flood Regime as a Driver of the Distribution of Mangrove and Salt Marsh Species in a Subtropical Estuary. *J. Mar. Syst.* 161, 11–25. doi: 10.1016/j.jmarsys.2016.05.004

Stark, J., Smolders, S., Meire, P., and Temmerman, S. (2017). Impact of Intertidal Area Characteristics on Estuarine Tidal Hydrodynamics: A Modelling Study for the Scheldt Estuary. *Estuar. Coast. Shelf Sci.* 198, 138–155. doi: 10.1016/J.ECSS.2017.09.004

Telemac2D. (2014). *Telemac2D User Manual V7p0*. Available at: http://www.opentelemac.org/index.php/manuals/viewcategory/13-telemac-2d (Accessed 5.11.21).

Temmerman, S., Bouma, T. J., Govers, G., Wang, Z. B., De Vries, M. B., and Herman, P. M. J. (2005). Impact of Vegetation on Flow Routing and Sedimentation Patterns: Three-Dimensional Modeling for a Tidal Marsh. *J. Geophys. Res. Earth Surf.* 110, 1–18. doi: 10.1029/2005JF000301

Temmerman, S., Bouma, T. J., Van de Koppel, J., van der Wal, D., De Vries, M. B., and Herman, P. M. J. (2007). Vegetation Causes Channel Erosion in a Tidal Landscape. *Geology* 35, 631. doi: 10.1130/G23502A.1

Temmerman, S., Govers, G., Meire, P., and Wartel, S. (2003a). Modelling Long-Term Tidal Marsh Growth Under Changing Tidal Conditions and Suspended Sediment Concentrations, Scheldt Estuary, Belgium. *Mar. Geol.* 193, 151–169. doi: 10.1016/S0025-3227(02)00642-4

Temmerman, S., Govers, G., Wartel, S., and Meire, P. (2003b). Spatial and Temporal Factors Controlling Short-Term Sedimentation in a Salt and

Freshwater Tidal Marsh, Scheldt Estuary, Belgium, SW Netherlands. *Earth Surf. Process. Landforms* 28, 739–755. doi: 10.1002/esp.495

Thorne, K., MacDonald, G., Guntenspergen, G., Ambrose, R., Buffington, K., Dugger, B., et al. (2018). U.S. Pacific Coastal Wetland Resilience and Vulnerability to Sea-Level Rise. *Sci. Adv.* 4, 1–10. doi: 10.1126/sciadv.aao3270

University of New South Wales. (2017). *LiDAR Elevation Data. Provided on Request* (Sydney, Australia).

Watson, J. G. (1928). Mangrove Forests of the Malay Peninsula. *Malayan For. Rec.* 6, 1–275.

Wiberg, P. L., Fagherazzi, S., and Kirwan, M. L. (2020). Improving Predictions of Salt Marsh Evolution Through Better Integration of Data and Models. *Ann. Rev. Mar. Sci.* 12, 389–413. doi: 10.1146/annurev-marine-010419-010610

Williams, J. J., and Esteves, L. S. (2017). Guidance on Setup, Calibration, and Validation of Hydrodynamic, Wave, and Sediment Models for Shelf Seas and Estuaries. *Adv. Civ. Eng.* 2017, 1–26. doi: 10.1155/2017/5251902

Woodroffe, C. D. (2018). Mangrove Response to Sea Level Rise: Palaeoecological Insights From Macrotidal Systems in Northern Australia. *Mar. Freshw. Res.* 69, 917–932. doi: 10.1071/MF17252

Woodroffe, C. D., Rogers, K., McKee, K. L., Lovelock, C. E., Mendelssohn, I. A., and Saintilan, N. (2016). Mangrove Sedimentation and Response to Relative Sea-Level Rise. *Ann. Rev. Mar. Sci.* 8, 243–266. doi: 10.1002/andp.18341081502

Zhang, X., Church, J. A., Monselesan, D., and McInnes, K. L. (2017). Sea Level Projections for the Australian Region in the 21st Century. *Geophys. Res. Lett.* 44, 8481–8491. doi: 10.1002/2017GL074176

Conflict of Interest: The authors declare that the research was conducted in the absence of any commercial or financial relationships that could be construed as a potential conflict of interest.

Publisher's Note: All claims expressed in this article are solely those of the authors and do not necessarily represent those of their affiliated organizations, or those of the publisher, the editors and the reviewers. Any product that may be evaluated in this article, or claim that may be made by its manufacturer, is not guaranteed or endorsed by the publisher.

Copyright © 2022 Kumbier, Rogers, Hughes, Lal, Mogensen and Woodroffe. This is an open-access article distributed under the terms of the Creative Commons Attribution License (CC BY). The use, distribution or reproduction in other forums is permitted, provided the original author(s) and the copyright owner(s) are credited and that the original publication in this journal is cited, in accordance with accepted academic practice. No use, distribution or reproduction is permitted which does not comply with these terms.

frontiers | Frontiers in Marine Science

ORIGINAL RESEARCH
published: 30 May 2022
doi: 10.3389/fmars.2022.874818

Wave Attenuation Over Mangroves in the Nanliu Delta, China

Xiaoyan Zhou[1], *Zhijun Dai*[1,2*], *Wenhong Pang*[1], *Jie Wang*[1] *and Chuqi Long*[1]

[1] *State Key Laboratory of Estuarine and Coastal Research, East China Normal University, Shanghai, China,* [2] *Laboratory for Marine Geology, Qingdao National Laboratory for Marine Science and Technology, Qingdao, China*

Mangrove forests grow on tropical and subtropical coastlines and play a significant role in reducing hydrodynamic energy. However, little information is known about the mechanism of wave attenuation caused by mangroves of different ages, even though the effects of mangroves on wave damping have received widespread concern. Here, a series of systemic biohydrological data were collected along a cross-shore transect through mangroves with different ages of native *Aegiceras corniculatum* (*AC*) distribution in the Nanliu Delta of China and were analyzed to investigate wave attenuation over mangroves during different tidal conditions. The results showed that the wave height decreased nearly 58.33%, with a transport distance of 275 m in the *AC* seedling-sapling region, and approximately 80%, with a transport distance of 1,000 m in the sapling-adult region, on average. The largest wave height attenuation rate of 3×10^{-3} was found in the measured time period and occurred in the seedling-sapling section during the neap tide, while the sapling-adult region had a basically constant reduction rate of 0.8×10^{-3} under changing tidal conditions. Moreover, the drag coefficient calculation indicated that an *AC* seedling with a height of nearly 0.55 m was more effective in attenuating wave energy than the stem part of a grown tree with a height of nearly 1.2 m. *AC* seedlings and saplings have significant impacts on wave damping, even though the stem part of an adult *AC* could produce a decline in wave energy. Moreover, differences in the drag coefficient caused by stems and canopies were responsible for wave attenuation, and the degree of *AC* inundation volume induced by water level fluctuation might affect the wave damping effect. Our results documented distinct differences in the wave attenuation process by mangroves of different ages, which can inform superior designs of mangroves along coasts against a background of sea-level rise and the occurrence of frequent typhoons.

Keywords: mangroves, tidal flat, wave attenuation, drag coefficient, Nanliu Delta

OPEN ACCESS

Edited by:
Zheng Gong,
Hohai University, China

Reviewed by:
Yining Chen,
Ministry of Natural Resources, China
Zhiyuan Wu,
Changsha University of Science and Technology, China

***Correspondence:**
Zhijun Dai
zjdai@sklec.ecnu.edu.cn

Specialty section:
This article was submitted to Coastal Ocean Processes, a section of the journal Frontiers in Marine Science

Received: *13 February 2022*
Accepted: *27 April 2022*
Published: *30 May 2022*

Citation:
Zhou X, Dai Z, Pang W, Wang J and Long C (2022) Wave Attenuation Over Mangroves in the Nanliu Delta, China. Front. Mar. Sci. 9:874818. doi: 10.3389/fmars.2022.874818

1 INTRODUCTION

As one of the most productive halophytic populations situated in the intertidal areas of tropical and subtropical coastlines (Tomlinson, 2016; Van der Stocken et al., 2019), mangrove forests have extraordinary buffering and carbon stock functions (Horstman et al., 2014; Atwood et al., 2017). A 100-m-wide belt of mangroves with 30 trees per 100 m^2 has the capacity of 90% to reduce flow pressure by 90% during a catastrophic tsunami (Danielsen, 2005). Several examples have indicated

that mangrove forests prevent urban areas and villages from being destroyed by large waves, storm surges, and tsunami disasters (Danielsen, 2005, Mazda et al., 1997a, McIvor et al., 2015). Hurricane Wilma, which attacked the gulf coast of south Florida in America on 24 October 2005, was attenuated by a 6–30-km-wide mangrove band and prevented an area of 1,800 km^2 from becoming inundated by decreasing the wave amplitudes (Zhang et al., 2012). Hepu County in Guangxi Province in China, as the starting point of the Maritime Silk Road in the Han Dynasty (Han and Yang, 2004), suffered the destructive Typhoon Sarah (No. 8609) with a wave height of greater than 3 m on 21 and 22 July 1986, resulting in a large financial loss of 172 million CNY and affecting more than 418 thousand people. Ninety percent of the sea walls were damaged, yet those that were protected by stretched mangroves were slightly broken or even intact (Chen et al., 2013). (Wu et al., 2021) adopted an applicable numerical model and indicated that the average typhoon wave height in the South China Sea was within 3.0–9.2 m. Therefore, while potential climate change has induced an increase in the occurrence of extreme events (Easterling, 2000), there is an urgent need to comprehend the living and coping mechanisms of these crucial forests in increasingly harsh circumstances.

Mangrove forests survive in a relatively quiescent zone of estuaries and bays; nevertheless, they experience moderate waves in normal weather or attenuate large waves from tsunamis and typhoons (Alongi, 2008; Alongi, 2009). Studies on the function of the wave attenuation of mangroves have received attention and have employed field and laboratory experiments or numerical models since the late nineties (Quartel et al., 2007; Alongi, 2009; Bao, 2011; Willemsen et al., 2016; Montgomery et al., 2019). For instance, Vo-Luong and Massel (2008) observed a significant wave reduction in a mixed mangrove forest of *Avicennia* sp. and *Rhizophora* sp. in Vietnam. Through laboratory experiments, Tuyen and Hung (2009) indicated that shallower water obtained a larger wave energy reduction rate. Parvathy and Bhaskaran (2017) revealed that a mild slope along mangrove tidal flats can reduce 93–98% of wave energy by Simulating Waves Nearshore (SWAN) modeling. Popular field observations in recent decades have mainly focused on mangrove trees grown over a single age period, and normal laboratory experiments have adopted artificial structures to simulate the dissipation process (Bao, 2011; McIvor et al., 2012; Abdullah et al., 2019). Moreover, most of the numerical models concentrate on biomechanical or hydrodynamic conditions of specific vegetation (Peralta et al., 2008; Vo-Luong and Massel, 2008; Thuy et al., 2017). Nonetheless, the wave attenuation process during half a lunar cycle for different ages of mangroves has been poorly captured by field observations.

Furthermore, both laboratory studies and field observations demonstrate that a proportional relationship between the submerged conditions of mangroves and attenuation effects can be found in dense mangroves in Vietnam and China (Quartel et al., 2007; Augustin et al., 2009; Chen et al., 2016). However, Mazda (2006) found that the wave reduction rate was proportional to the water level when the water rose above the canopy of *Sonneratia* sp. in northern Vietnam. Kinver (2016) indicated that the wave damping rate was determined by the distance of wave propagation along a mangrove band. Moreover, drag forces controlled by the inundation volume of young *Rhizophora* specimens generated the highest wave damping efficiency (Maza et al., 2021). Thereafter, various factors resulted in the distinct effects of wave dissipation based on the measured cases from Japan, China, and Australia (Brinkman, 2006; Cao et al., 2016). The conundrum about the leading mechanism of wave reduction among mangroves of different ages needs to be resolved.

Approximately 8,374.9 hm^2 of mangroves extend along the coastline of the Beibu Gulf, located in the subtropical and tropical zones, where approximately 30% of the total area is occupied by mangroves in China. Moreover, more than 45% of the mangrove forests around the Beibu Gulf are predominantly distributed in the Nanliu Delta (**Figure 1A**). The Nanliu Delta, as the largest delta of the Beibu Gulf in Southwest China, is fed with 51.3×10^8 m^3 of water discharge and 1.18×10^6 t of sediment discharge from the Nanliu basin yearly (Li et al., 2017) (**Figures 1A, B**). Mangroves are distributed widely along deltaic tidal flats, which can be highly efficient in protecting coastal zones over 500 km from the typhoon-induced wave attraction, especially as in the case of the unprecedented storms in 1986 (Chen et al., 2013). Therefore, the seaward mangrove tidal flat of Qixing Island, located in the central Nanliu Delta, provides a typical case for determining the coupling effects between mangroves and hydrodynamic behavior, especially the attenuation process across the entire tidal flat from low to high areas, with distributions of aboriginal *Aegiceras corniculatum* (*AC*) of different ages. The aims of this study are to reveal the wave damping process during half a lunar cycle among *AC* of different ages and to discern the respective wave attenuation abilities induced by the stem and canopy parts of *AC* under different tidal conditions. The results derived from this study are beneficial references for constructing a "green embankment" as a defense against storm hazards in the context of global warming.

2 METHODS

2.1 Data Collection

The Nanliu Delta is dominated by irregular diurnal tides with an average and maximum tidal range of 2.46 and 5.36 m, respectively. The nearshore wave climate in this region varies seasonally with a maximum average wave height of 1.36 m (State Oceanic Administration, 1998), yet the maximum current speeds are 0.26–0.36 m/s (Huang et al., 2022). *AC* is dominantly distributed over Qixing Island, which is located at the delta center with scattered *Cyperus malaccensis* patches. The mean grain size of sediments over the *AC* tidal flat ranges from 0.2 mm in the seedling-sapling region to 0.04 mm in the sapling-adult region. A transverse transect through an *AC* tidal flat composed of 3 hydrological tripods was set up on the south side of Qixing Island (**Figure 1C**). Three tripods were positioned along a transect with a length of 1.275 km. The Tripod SC (109°2'12.69"E, 21° 36'9.73"N), with a location height of 2.63 m above mean sea level in Beihai, was set at the upper part of the *AC* tidal flat, with mixed adults and saplings (**Figures 2C**, **F**). The Tripod SB (109°2'2.04"E, 21°35'39.03"N) with a relative location height of 1.17 m, was set at

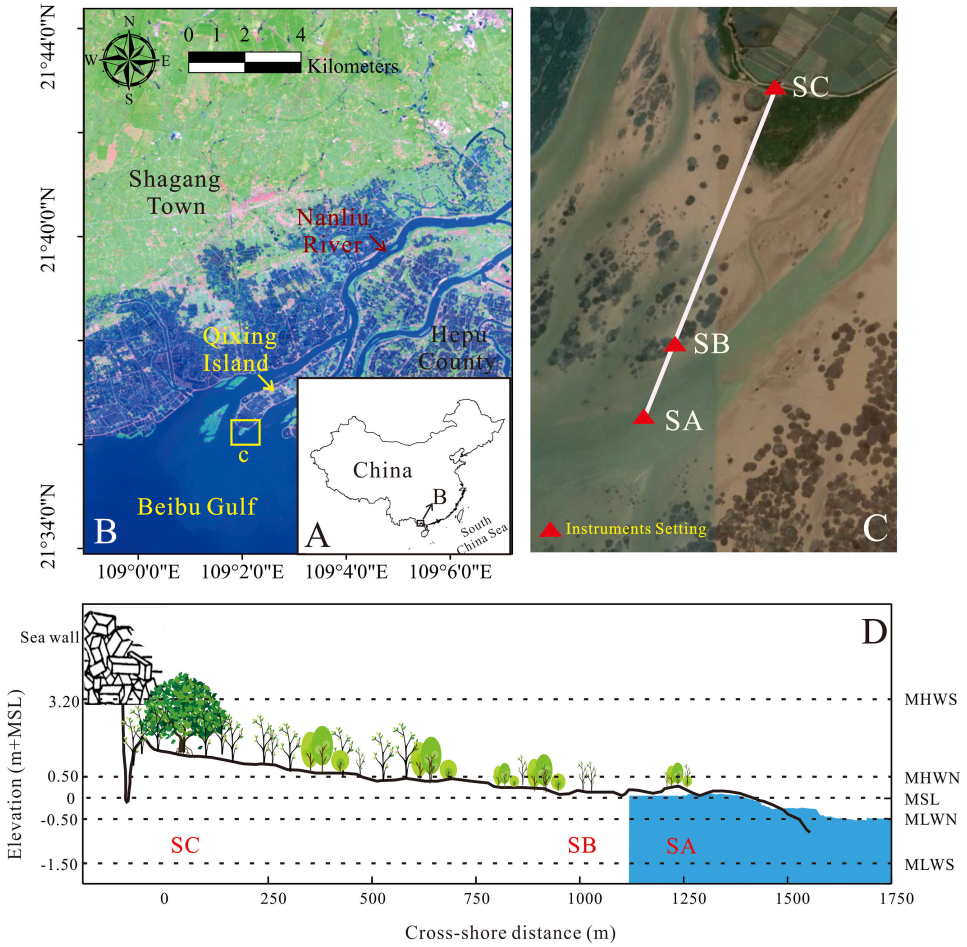


FIGURE 1 | **(A)** Map of the Beibu Gulf with its location in relation to China; **(B)** study area in relation to Hepu County, Beibu Gulf, and Nanliu River; **(C)** tripod setting location on the *Aegiceras corniculatum* tidal flat; **(D)** elevation with respect to the mean sea level (MSL) of the cross-shore transects with relative distance from the inshore tripod, with instrument tripods and mixed age *A. corniculatum*. Tidal water levels are indicated on the right axis (MHWS, mean high water level at spring tide; MLWS, mean low water level at spring tide; MHWN, mean high water level at neap tide; MLWN, mean low water level at neap tide).

the transition region between the adult *AC* tree region and the seedling region. Additionally, tripod SA (109°1'58.48"E, 21°35'30.47"N), with a relative location height of 0.25 m, was set offshore in an area with mixed saplings and small seedlings. The distance from tripod SA to tripod SB was 0.275 km, and that from SB to SC was 1 km (**Figure 1D**).

Furthermore, wave recorders (RBR-2050 and RBR-solo3) were placed in line at these three tripods along the *AC* transect to obtain the wave and tide information from the 16th to the 29th of August 2019. These recorders are robust and have internal memory and battery housing so that they can collect the data autonomously. The sampling start time can be set at every deployment. Based on previous work conducted in mangrove tidal flats (Quartel et al., 2007; Horstman et al., 2014), the instruments logged data at 4 Hz over a consecutive 512 s (~8 min) period every 20 min (2,048 samples per burst), and they were fixed 10 cm above the ground, which can indicate the wave variation during an entire tidal period. The wave recorder used in this observation had an effective measuring range for wave heights of 0.005–10 m. The measured water depth was converted to the water level based on mean sea level.

2.2 Data Processing

2.2.1 Mangrove Volumetric Cover Calculation

Three investigation zones were selected along the tripod transect to quantify vegetation parameters, and two plots were randomly distributed per zone to acquire general information about the area. Each plot was 5 × 5 m^2 and was close to the hydrodynamic (**Figures 2A–C**) tripod, where *AC*, including adults, saplings, and seedlings, were present (**Figures 2D–F**). The height (H), length (L), and width (W) of the *AC* canopy in these three plots were measured (**Figure 3**). Stem diameters were obtained at 0.1, 0.3, 0.5, and 0.8 H above the bed. Each stem diameter and the number of stems at each height was also collected during the measurement (**Figure 3**, **Table 1**). Then, detailed information was transformed into volumetric cover (%) at different heights *via* Formula (1)

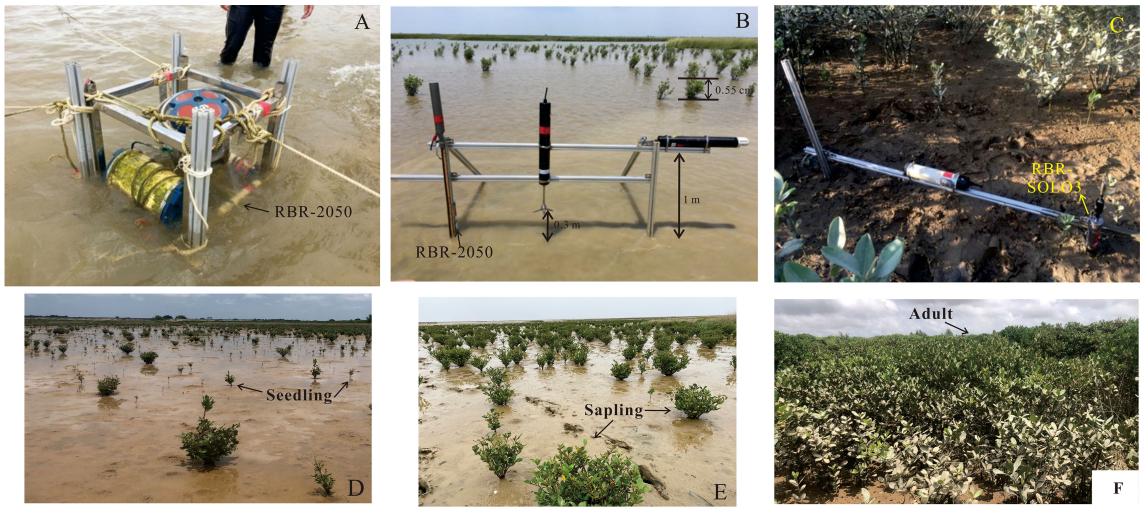


FIGURE 2 | **(A–C)** show the deployment of each tripod and instrument placement method, which includes SA) RBR-2050; SB) RBR-2050; and SC) RBR-SOLO^3. **(D–F)** show the distribution of mangroves of different ages. .

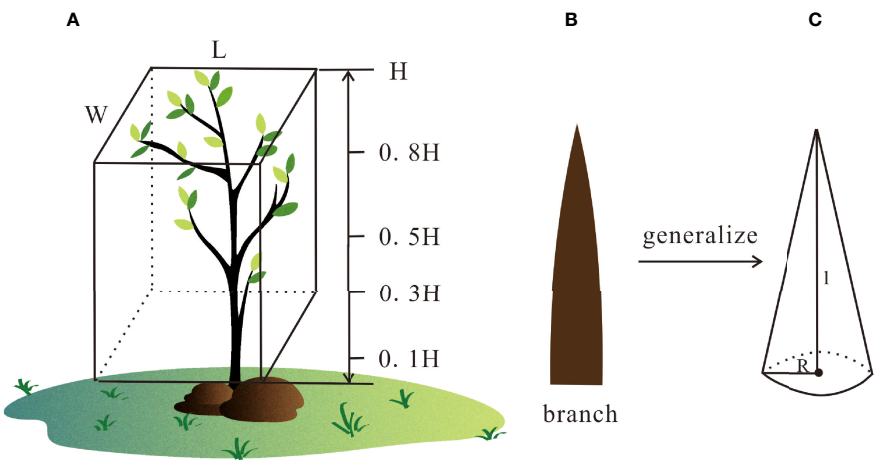


FIGURE 3 | Calculation method of the volumetric cover. **(A)** W, L, and H refer to the width, length, and height of the plant canopy; **(B)** a single branch extracted from *Aegiceras corniculatum*, which is generalized in **(C)** l and R refer to the length and radius of a single branch, respectively.

deployed by Mazda et al. (1997b), which can quantify the occupation of the different parts of mangroves and the effect caused by this part.

To calculate the volumetric cover at different heights, every branch was simplified to a circular cone (**Figure 3**), and its radius and length were obtained. The volumetric cover of a single tree was acquired by Formula (1):

$$\text{Volumetric cover} = \frac{\frac{1}{3}\pi \times \left(\sum_{i\ =\ 0.1H,\ 0.3H,\ 0.5H,\ 0.8H\ \ and\ \ H} R_i^2 \times l_i \times n_i\right)}{W \times L \times H} \quad (1)$$

where R, l, and n are the mean radius, length, and number of branches at different heights, respectively. For small seedlings or samplings that were not high enough, only 0.1 to 0.5 H were measured. W, L, and H are the width, length, and height of the canopy, respectively. Since seedlings and saplings were not high enough to reach 0.5 H, measurements were limited to 0–0.5 H for these plants.

2.2.2 Wave Attenuation Calculation

Based on the wave data collected from 16 to 29 of August 2019, the average wave heights, periods, and wave energies every 20 min at the three stations were acquired directly from the wave

TABLE 1 | Station information with *in situ* typical *ACs*' features.

	Elevation (m)	Age	Density (per m^2)	Position at *AC*	R (m)	n	L (m)	Volumetric Cover (%)
SA	0.25	Se	0.12	/	0.0015	72	0.15	16.53
		Sa		0.1 H	0.005	14	0.38	4.22
			0.2	0.3 H	0.0045	27	0.09	1.56
				0.5 H	/	/	0.3	54.55
SB	1.17	Se	0.32	/	0.0025	15	0.15	5.25
		Sa		0.1 H	0.008	20	0.4	2.12
			1.04	0.3 H	0.004	87	0.12	0.69
				0.5 H	/	/	0.4	60.61
SC	2.63	Sa	2.8	0.1 H	0.045	5	0.7	28.27
				0.3 H	0.005	13	0.3	0.39
				0.5–0.8 H	/	/	0.6	40
		Ad	1.6	0.1 H	0.09	10	0.75	14.68
				0.3 H	0.065	32	0.5	16.33
				0.5–1 H	/	/	0.7	46.67

Se, seedling; Sa, sapling; Ad, adult.

recorders at each spring, middle, and neap tide. Water surface fluctuation data were processed by fast Fourier transforms (FFT) at bursts of 90–94, 236–241, and 570–576 to observed density spectrum changes with different frequencies at flood tide during spring, middle and neap tides, respectively. Bursts 95–98, 242–244, and 577–578 were observed at the ebb tide during the spring, middle, and neap tides, respectively. The wave components were also detected *via* this method. Moreover, the wave energy density for each burst was also calculated based on (Hegge and Masselink, 1996) Fourier analysis scheme.

Moreover, according to the definition proposed by (Mazda et al., 2006), the wave height reduction rate per unit length is:

$$r = \frac{\Delta H}{H}\frac{1}{\Delta x} \tag{2}$$

where r is the wave attenuation rate and Δx is the distance between two observation stations. H is the wave height offshore, and ΔH is the wave height difference observed by the two stations. Here, the wave height reduction rate was calculated by adopting this formula to infer the attenuation ability of mangroves.

Regarding wave propagation in the shoaling zone, Mazda et al., (1997b) proposed the following:

$$\frac{H_1}{H_2} = \frac{1}{1 + \frac{C_D \pi H_1 \Delta x}{32\sqrt{2}h^2}} \tag{3}$$

where H_1 and H_2 are offshore and onshore wave heights, respectively. Δx is the distance between two observation stations. h is the average water depth of the two stations. Thus, the drag coefficient C_D can be inferred as:

$$C_D = \frac{32\sqrt{2}}{\pi} \cdot \frac{h^2}{H_1 \Delta x}\left(\frac{H_1}{H_2} - 1\right) \tag{4}$$

The coefficient is affected by vegetation density. Since each region had a unique density, C_D was calculated for each region to manifest the resistance effect generated by *AC*.

3 RESULTS

3.1 Distributions of *AC*

AC along the selected transect from SA to SB covered seedlings of 1 year of age and sparse saplings of 2–3 years of age. Seedlings in this region were approximately 0.19 m high, with canopy sizes of 0.09 m in width and 0.09 m in length. Saplings in this region were 0.55 m high with a canopy size of 0.2 m in width and 0.3 m in length (**Table 1**). Adults were distributed at a relative elevation of 2.63 m, which was above the mean high water level during spring tide (MHWS), with heights, widths, and lengths of 1.5, 1.7, and 1.7 m, respectively (**Figure 4**).

Moreover, canopy locations of adult *AC* were slightly higher than the MHWS water level (**Figures 1D**, **4A, B**), and canopies of saplings or seedlings still emerged when tides arrived at the mean high water level during neap tide (MHWN).

Furthermore, the mean water levels during the spring tide were 2.38, 1.46, and 0.73 m at the locations of tripods SA to SC (**Figure 4B**), respectively, indicating that the canopies of mangroves at SA and SB were submerged most of the time due to tidal level fluctuations. *AC* at the SC site could be inundated only to the branch position with the canopy part exposed to the air. The same situation also occurred at middle tide, with water levels of 1.99, 1.34, and 0.62 m (**Figure 4B**), respectively, from offshore to the inshore station. Moreover, during the neap tide, *AC* at the SA station was wholly submerged, as the depth was 1.17 m. The water level was 0.49 m at tripod SB, where branches of mangroves can be submerged. At tripod SA, a fully adult mangrove was almost exposed to the air since the water level was less than 0.07 m (**Figure 4D**).

3.2 Characteristics of the Wave Density Spectrum at Different Mangrove Locations

The energy density varied distinctly with the *AC* of different ages at each station (**Figures 5A, B**). Specifically, the wave spectra remained unimodal during spring and neap tides (**Figures 5A, C**) and bimodal (**Figure 5B**) during midtide. The wave energy densities increased with rising water levels (**Figure 5**, blue lines in boxes **A**, **C**) and decreased with falling water levels during

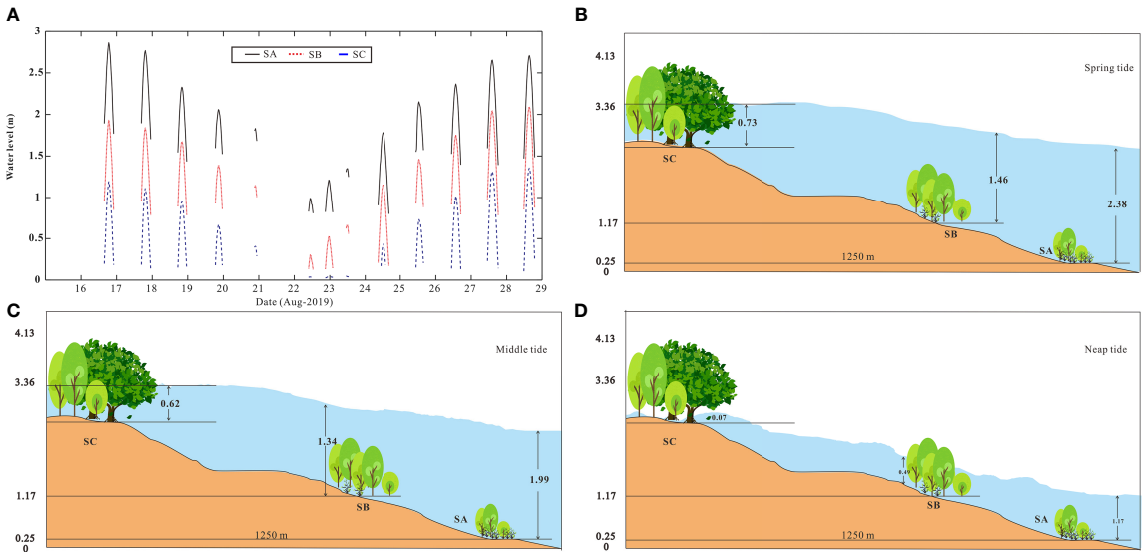


FIGURE 4 | **(A)** Hydrodynamic information obtained by the three tripods from the 16th to the 29th of August 2019. Black lines refer to the data captured by tripod SA. Red dotted lines refer to the data captured by tripod SB, and blue lines refer to the data captured by tripod SC; **(B–D)** show the inundation states of mangroves in the spring, middle, and neap tides, respectively.

spring and neap tides (**Figure 5**, red lines in boxes **A** and **C**). The energy density in the seedling-sapling region during the spring tide accepted the most powerful energy. The values varied from 0.03 to 0.055×10^{-3} m^2s and decreased to 0.009×10^{-3} m^2s from bursts of 90–94 (**Figure 5A**, 1–5) to 95–98 (**Figure 5A**, 6–9), respectively. For SB (**Figure 5A**, 10–14), the value first increased from 0.005 to 0.013 and finally decreased to nearly zero (**Figure 5A**, 15–18). Although the wave energy at SC was weak at every burst, its trend was the same as that of the other two tripods that were proportional to the water level (**Figure 5A**, 19–23). Similar to the spring tide, the energy density changed from 0.21 to 1.18×10^{-6} m^2s during rising water and declined to 0.18×10^{-6} m^2s in SA.

The energy spectrum shape at the middle tide appeared bimodal, with the related high-frequency crest tending to occur during the falling water period (**Figure 5B**, 7–9) in the seedling-sapling region, and the higher-frequency crest occurred first. The energy of the former crest decreased, while that of the latter increased. The interaction between waves and seedlings-saplings was drastic during the middle tide with a relatively constant water

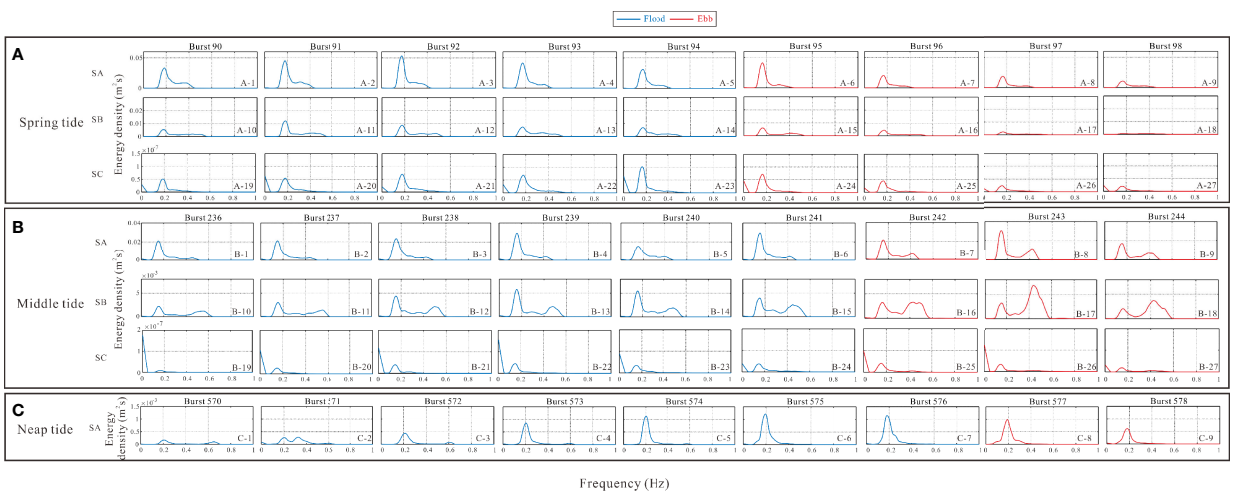


FIGURE 5 | Energy density of the three observation tripods depicted from spring (box **A**), middle (box **B**) and neap (box **C**) tides.

level (**Figure 4C**), resulting in a transition of wave composition from unimodal to bimodal, with the latter crest occurring at 0.4–0.6 hz (**Figure 5B**, 10–18).

3.3 Variations in Wave Conditions Along the *AC* Tidal Flat

The wave environment during the observation period was dominated by a southwest (SW) wind with speeds of 0.15–0.32 m/s, indicating normal weather (**Figure 6A**). Significant wave heights showed distinct attenuation along the transect during different periods (**Figure 6B**). The average significant wave height was attenuated when it passed through every region during the spring tide. Specifically, from SA to SC, the wave height values were 0.1, 0.05, and 0.01 m, respectively. A similar declining trend was observed in every tidal period. At middle tide, the mean wave height along the transect decreased from 0.08 and 0.04 m to 0.008 m from SA to SC. Only wave data at tripod C were valid during neap tide, where the significant wave height was 0.02 m (**Figure 6A**). Limited by the low water level, no valid data were captured by the instruments at SB and SC in the neap tide. In summary, the wave height decreased by 58.33% in the SA–SB region and 80% in the SB–SC region on average during different tidal conditions.

However, wave periods did not exhibit the same trend from the SA to SC station as wave height did. During spring tide, the average wave periods from SA to SC were 5.07, 4.52, and 5.34 s, respectively. Periods shortened at the middle of the tide, when the values were 4.20, 2.31, and 4.04 s, respectively. Only the SA station had a 2.31 s wave period during the neap tide. The average wave periods of the SB station were the shortest of all tide periods. However, from spring to middle to neap tide, the wave periods all shortened at these observation stations (**Figure 6B**).

Moreover, the average wave energy dissipated along this transect under different tidal conditions (**Figure 6C**). During spring tide, the wave energy decreased from 7.44 J/m^2 at tripod SA to 5.65 J/m^2 at tripod SB and finally remained at 0.12 J/m^2 when the wave arrived at tripod SC, reducing nearly 98.39% of the incident wave energy. During the middle tide, the wave energy declined from 6.86 and 4.18 to 0.08 J/m^2 from SA to SC, reducing the incident wave energy by nearly 98.83%. During the neap tide, only tripod SA detected a faint energy of 0.48 J/m^2. Both the significant wave height and energy experienced an obvious decline when the waves spread from offshore to the *AC* tidal flat.

3.4 Variation in the Wave Reduction Rate With Wave Propagation Distance

The wave height reduction rate along the *AC* transect was measured to evaluate the wave damping ability at these three tripods (**Figure 7**). The rate of the incident wave height reduction experienced a declining process with a longer propagation distance under different tidal conditions. Specifically, during spring tide, the rate varied from 1.8×10^{-3} to 0.79×10^{-3} from the areas of SA–SB to SB–SC. The variation ranges were 2.3 to 0.8×10^{-3} in the middle tide from the SA–SB region to the SB–SC region. The rate was 3.0×10^{-3}m^{-3}/m from region SA to SB during the neap tide. The wave height reduction rate was negatively related to the water level during the whole tidal period along the observation transect (**Figure 7**), indicating that deeper water may cause a weaker reduction rate. However, the region from SB to SC experienced an extremely low water level during the neap tide, and an emerged state of the *AC* (**Figure 3D**) was induced when no wave attenuation occurred.

Moreover, the trend of the wave height reduction rate showed a large difference during the different tidal periods. Sparse *AC* seedlings and a few saplings were observed in the SA–SB region (**Table 1**), and the reduction rate increased nearly 27.78% from spring to middle tide and 30.43% from middle to neap tide. In contrast, in the SB–SC region, where dense adult trees of *AC* were vegetated (**Table 1**), this rate increased by less than 5% during the entire tidal period. Obviously, the variation degree of the wave attenuation rate was impacted by the water level fluctuation, which caused the variational drag effect and indirectly dominated the intensity of the wave height reduction rate.

4 DISCUSSION

4.1 Impacts From *AC*

Coastal vegetation obstructs wave propagation *via* the drag effect caused by dense root or canopy systems (Augustin et al., 2009; Hu et al., 2014; Foster-Martinez et al., 2018; Devi et al., 2021). Moreover, the spatial distribution of vegetation densities may also play a crucial role in wave attenuation (Massel et al., 1999; Hashim et al., 2013). (Vo-Luong and Massel, 2008) indicated that wave breaking occurring in a sparse forest induced an obvious attenuation effect instead of the wave–trunk interactions that occur in a denser forest. Here, our results showed distinct differences in the wave attenuation process among the three tripods. During the entire tidal period, the wave height attenuated to an average of 2.37×10^{-3} m in the area of SA–SB and 0.82×10^{-3} m in the area of SB–SC per meter. The bed material from SA to SC was mainly composed of fine and very fine sand, indicating that the attenuation difference was caused by the plant drag effect rather than bottom friction.

However, the reduction rate from SB to SC was 50% less than the value from SA to SB during the entire tidal period. Furthermore, the rate from the SB to SC region rarely varied along with the SA to SB region, and the rate increased nearly 67% from the spring to neap tide (**Figure 7**), illustrating the difference in the volumetric cover of *AC* to induce the change in the drag effect and higher wave energy attenuation. Specifically, the seedling and sapling volumetric cover below 0.5 H was 16.53 and 60.33% at the SA station, respectively. At the SB station, this value was 5.25 and 63.42%, respectively. Although adult trees at the SC station had a larger canopy, their volumetric cover of the stem part (below 0.3 H) was only 31% (**Figures 8A–C**). At a low water level, dense vegetation structures occupied more space in the SA and SB regions at a low water level, which generated a larger drag effect compared to the relatively sparse parts in the SC region. Therefore, there is an obvious attenuation phenomenon at a low water level that occurs in the seedling and sapling areas rather than in the adult area. According to **Figures 9D, E**, when the water level

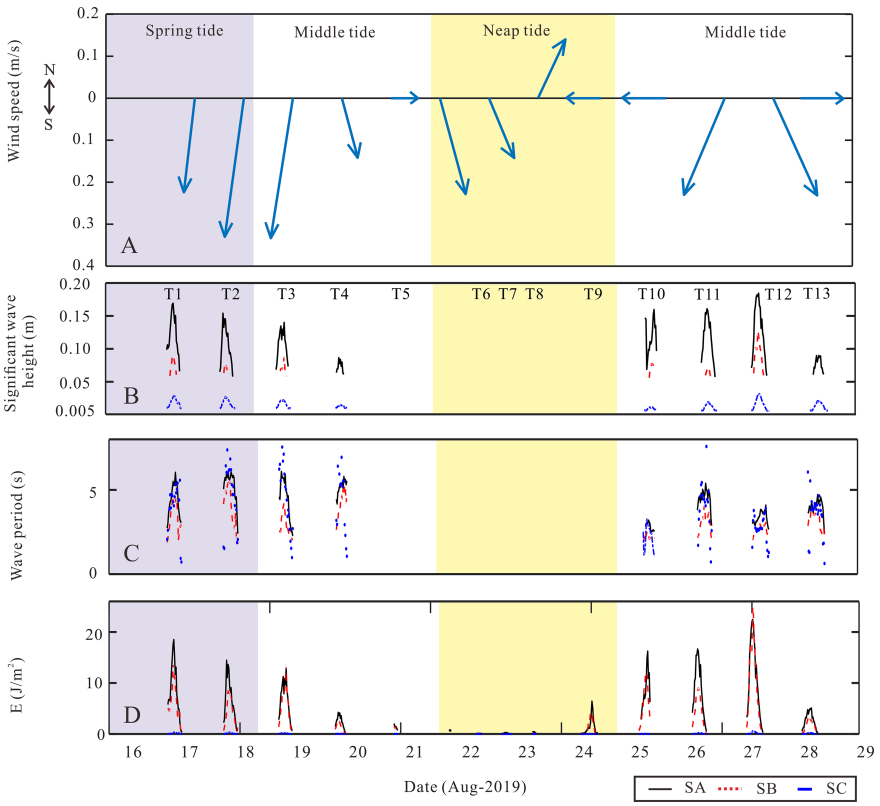


FIGURE 6 | Purple, white, and yellow shadows representing the periods during spring, middle, and neap tides, respectively. The figure describes **(A)** wind information during the observation period; **(B)** significant wave height; **(C)** wave period; and **(D)** wave energy. Data from the SA station are shown as black lines. Data from the SB station are shown as red dotted lines and data in the SC station are shown as blue lines. .

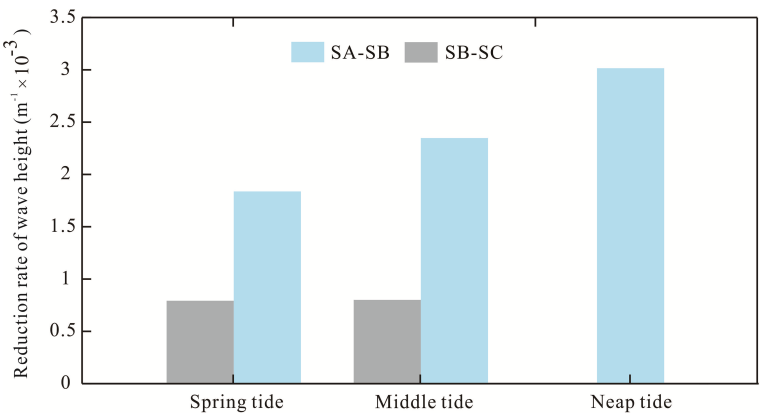


FIGURE 7 | Wave height reduction rate from spring to the neap tide. Blue bars are the rate along the transect from tripod SA to SB, and gray bars are the rate along the transect from tripod SB to SC.

was shallower than 1.5 m, the mean drag coefficient generated by mangroves in the SA–SB region was 3.74, but the value in the SB–SC region was 1.48, indicating that seedlings and saplings contributed to the attenuation process; however, only the stem part of an adult contributed to this process. Additionally, the SC station was at the high tidal flat (**Figure 1D**), with adult mangroves emerging at most times during the observation period, when the canopy part did not submerge due to the water level; this induced

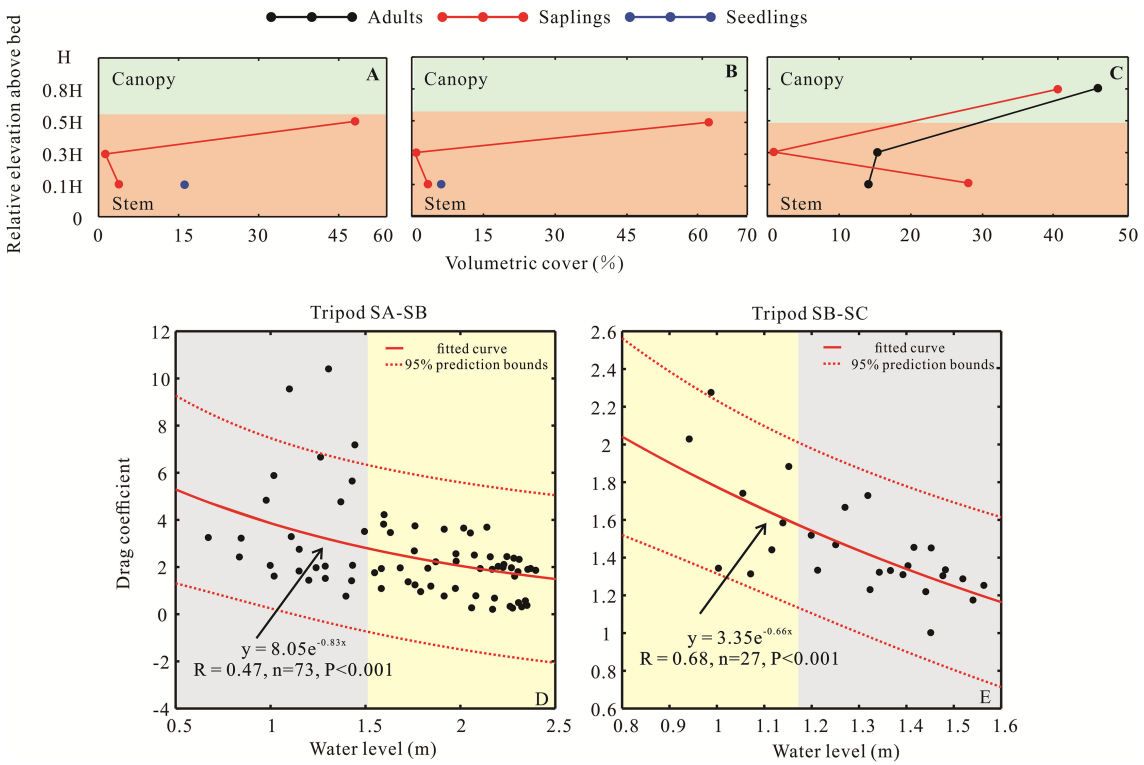


FIGURE 8 | Volumetric cover in three measurement plots **(A–C)**, corresponding to the three hydrodynamic tripods. The relationship between the volumetric cover and relative elevation above the bed is described as follows: a) black and red dots and lines refer to the adults and saplings at the SA station; b) red dots and lines and blue dots refer to the saplings and seedlings at the SB station; and c) red dots and lines and blue dots refer to the saplings and seedlings at the SC station. The relationship between the water level and drag coefficient is shown for **(D)** tripods SA-SB and **(E)** tripods SB-SC. The gray shadow is the period of the high drag effect, and the yellow shadow is the period of the low drag effect.

no drag effect, which explains why smaller mangroves had more power for attenuating wave energy than larger mangroves because the parts of the adult trees that are most effective at attenuation did not participate in this process (**Figures 4D, 8E**).

4.2 Coupled Impacts Between Water Level Fluctuations and the Inundation state of *AC*

The drag effect difference generated by vegetation mostly depends on the inundation state (**Figure 8**). An abrupt change in the reduction rate occurred in the spring tide when the water rose up from the stem to the canopy (**Figures 9A, D**). In other words, the attenuation effect was distinctly different when the *AC* was in a shifted inundation state with different water levels. Particularly, if a typhoon event happens at a low water level when saplings and seedlings have submerged but the canopy parts of adults are emerged, the former can attenuate waves effectively, since adults always locate at the high part of a tidal flat.

For the seedling-sapling region, seedling mangroves were approximately 55 cm (**Figures 3B–D**), which often flooded due to the mean water level of 117 cm at this location. Moreover, the *Cd* reduction rate decreased rapidly below the 150 cm water level, and then the decreasing rate slowed down when the water level was above 150 cm ($k1 = -1.30 \times 10^{-3}$ for L1 and $k2 = -6.79 \times 10^{-4}$ for L2 in **Figure 8D**), inferring that seedlings have an effective wave attenuation ability below the 150 cm water depth. However, from SB to SC, with the height of standing adult *AC* greater than 150 cm, which is seldom flooded due to the average water level of approximately 73 cm in this area during the spring tide (**Figure 4B**), only the branches were submerged, and the canopies could not be reached. Taken together, the change in the drag force followed the inundated volume variation in *AC* and controlled the wave attenuation rate.

4.3 Relationship Between the Wave Height Reduction Rate and *Cd*

The wave height reduction rate was negatively correlated with the water fluctuations (**Figure 9**) and water-level variations for different drag coefficients induced by mangroves with different inundation states (**Figures 8D, E**). Furthermore, the similar structure and distribution of mangrove forests produce similar drag effect values, in which water fluctuation works as a medium. Therefore, a similar vegetation distribution may generate a similar drag coefficient (Hu et al., 2014; Foster-Martinez et al., 2018), even though the water level fluctuates during one tidal cycle. Thereafter, a direct relationship between the wave height reduction rate and *Cd* can explicitly express the impacts of mangrove vegetation on

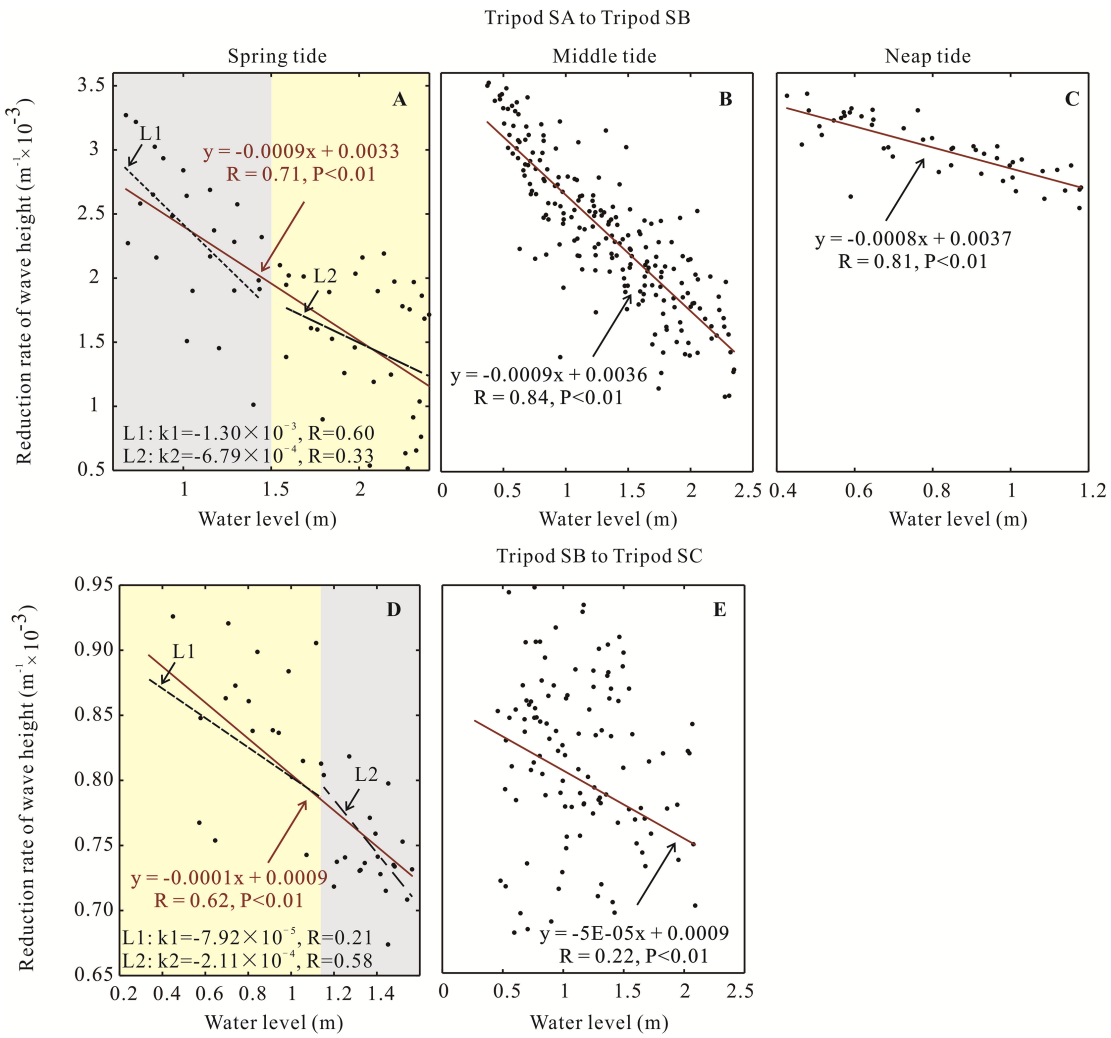


FIGURE 9 | Relationship between the water level and wave height reduction rate shown along the transect from tripod SA to SB **(A–C)** and tripod SB to SC **(D, E)** during spring to neap tides. Black dots are the measured data, and red lines are the linear fitted relationship. Gray and yellow shadows in **(A, D)** represent the periods of high and low attenuation reduction rates, respectively.

wave height, while wave data from most field observations are extremely difficult to obtain because of the inaccessibility of dense mangroves.

As the seedling-sapling region had a more powerful ability to attenuate waves than the sapling-adult region (**Figure 7**), the wave height reduction rate and *Cd* along this area during the spring tide were selected. An exponential relationship between these two parameters was deduced, which was $R = -0.0023 \times e^{-0.64Cd} + 0.0025$. While the water level rose and the seedlings were not entirely submerged, an obvious increase in the drag effect accelerated the wave attenuation process (blue box in **Figure 10**). Although the drag effect increased weakly when the water level was higher than the height of a plant, the wave could still be disturbed and attenuated within a certain water level range, and the reduction rate rose slowly beyond the canopy height of plants. The mechanism for the wave attenuation effect of seedlings and saplings of the *AC* illustrated that water depths shallower than 0.7 m were the most effective range of damping wave energy (**Figure 10**). Predictably, when a typhoon event happens during the spring tide, meeting the high fluvial discharge, such as in the case of Hepu County in 1986, the high tidal flat is submerged, and the canopy part of the *AC* plays a crucial role in this attenuation process.

Furthermore, (Massel et al., 1999) inferred that the wave attenuation mechanism was the same both with and without a typhoon event, demonstrating that both mangroves and bottom friction played important roles in the attenuation process regardless of whether short waves propagated in cyclonic weather or long waves propagated in normal weather. Similarly, the exponential relationship between *Cd* and the reduction rate for seedlings and saplings can also be adopted during the typhoon period. Since the location of SC is in the upper mudflat, no quantitative relationship

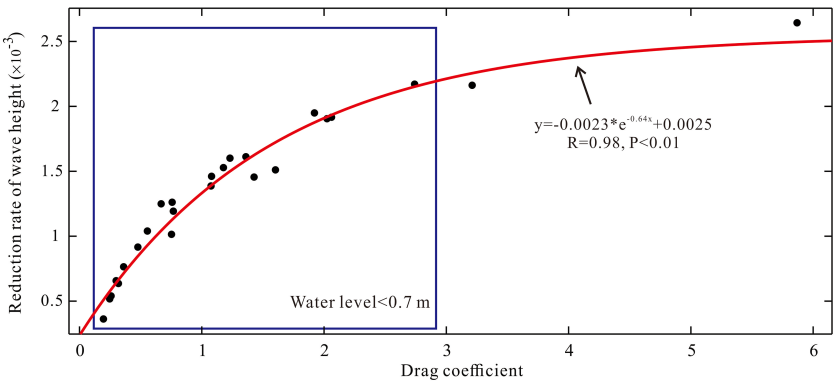


FIGURE 10 | Descriptions of the drag coefficient. A fitting relationship is shown between the drag coefficient and wave height reduction rate. The fitting formula is shown in the figure. The relationship when the water level is shallower than 0.7 m is shown in the blue box.

for adult *AC* between *Cd* and the water level can be constructed. However, according to the dense canopy of an adult tree (**Figure 8C**), it can be speculated that the canopy part of an adult mangrove is of great significance in the wave attenuation process during an extreme event. Therefore, the "green-embankment" definition has been proposed (Temmerman et al., 2013) recently to defend against extreme events, replacing "hard engineering." Our in-field observational data elucidated that the *AC* at different ages has distinct volumetric cover from the bottom to the canopy part, which can attenuate wave heights in stages *via* water-level variations. During normal or slight typhoon weather conditions, the number of seedlings can effectively attenuate the wave energy with lower economic costs and higher plant survival rates. When the weather conditions become more severe with greater wave energy, adult mangroves can participate in this attenuation process. Obviously, the distribution of mangroves for constructing a "green embankment" should consider the age of mangroves to cope with different attenuation effects with changing water levels from offshore to inshore to obtain a longer defense period with lower economic costs.

5 CONCLUSIONS

Mangrove forests have received worldwide attention because they provide significant habitats for organisms and play a crucial role in dissipating hydrodynamic energy. Therefore, in this study, the wave attenuation process over an *AC* tidal flat of Qixing Island in the Nanliu Delta in China was analyzed to highlight the importance of mangroves with different ages for wave damping. We found that between the spring and neap tides, the wave height decreased by 58.33% in the seedling-sapling region and 80% in the sapling-adult region. The lowest water level in the neap tide leads to the largest wave height reduction rate over half a lunar cycle. Meanwhile, the wave attenuation ability of the seedlings had a larger drag impact on the incident wave than the half-submerged grown trees due to larger drag forces, indicating that the seedlings had a remarkable attenuation ability. Furthermore, we proposed a relationship of $R = -0.0023 \times e^{-0.64Cd} + 0.0025$ between the wave attenuation rate and the drag coefficient, which demonstrates that wave attenuation is induced by vegetation obstruction.

Given that coastal urbanization, economic activities, and climate change have induced the dramatic deforestation of mangroves, leading to the potential failure of "hard-engineering," our work provides new insight into the ecological embankment construction by an optimized combination of mangroves of different ages.

DATA AVAILABILITY STATEMENT

The raw data supporting the conclusions of this article will be made available by the authors, without undue reservation.

AUTHOR CONTRIBUTIONS

XZ analyzed the data and wrote the original paper. ZD conceived the idea for the study and participated in its writing. WP analyzed part of the data. JW and CL participated in the discussion. All authors listed have made a substantial, direct, and intellectual contribution to the work and approved it for publication.

FUNDING

This study was supported by the National Natural Science Key Foundation of China (NSFC) (41930537), the Key Projects of Science and Technology of Guangxi Province (AB21076016), the ECNU Academic Innovation Promotion Program for Excellent Doctoral Students (YBNLTS2021-031), and the Fundamental Research Funds for the Central Universities.

ACKNOWLEDGMENTS

The author thank Bingbin Feng, Riming Wang, Binbin Ma and Gaojian Hu for their help in the field observations. The authors also acknowledge the editor and the two anonymous reviewers for their valuable comments on this study.

REFERENCES

Abdullah, F. A. R., Husrin, S., and Bachtiar, H. (2019). Experimental Data Analysis of Wave Attenuation in Mangroves. *J. Phys. Conf. Ser.* 1245, 012095. doi: 10.1088/1742-6596/1245/1/012095

Alongi, D. M. (2008). Mangrove Forests: Resilience, Protection From Tsunamis, and Responses to Global Climate Change. *Estuar. Coast. Shelf. Sci.* 76, 1–13. doi: 10.1016/j.ecss.2007.08.024

Alongi, D. M. (2009). *The Energetics of Mangrove Forests* (Netherlands: Springer).

Atwood, T. B., Connolly, R. M., Almahasheer, H., Carnell, P. E., Duarte, C. M., Ewers Lewis, C. J., et al. (2017). Global Patterns in Mangrove Soil Carbon Stocks and Losses. *Nat. Clim. Change.* 7 (7), 523–528. doi: 10.1038/nclimate3326

Augustin, L. N., Irish, J. L., and Lynett, P. (2009). Laboratory and Numerical Studies of Wave Damping by Emergent and Near-Emergent Wetland Vegetation. *Coast. Eng.* 56 (3), 332–340. doi: 10.1016/j.coastaleng.2008.09.004

Bao, T. Q. (2011). Effect of Mangrove Forest Structures on Wave Attenuation in Coastal Vietnam. *Oceanologia.* 53 (3), 807–818. doi: 10.5697/oc.53-3.807

Brinkman, R. (2006). *Wave Attenuation in Mangrove Forests: An Investigation Through Field and Theoretical Studies* (Australia: James Cook University).

Cao, H., Chen, Y., Tian, Y., and Feng, W. (2016). Field Investigation Into Wave Attenuation in the Mangrove Environment of the South China Sea Coast. *J. Coast. Res.* 32 (6), 1417–1427. doi: 10.2112/JCOASTRES-D-15-00124.1

Chen, Y., Li, Y., Cai, T., Thompson, C., and Li, Y. (2016). A Comparison of Biohydrodynamic Interaction Within Mangrove and Saltmarsh Boundaries. *Earth Surf. Proc. Land.* 41 (13), 1967–79. doi: 10.1002/esp.3964

Chen, X., Liu, H., Dong, D., Qiu, S., and Chen, B. (2013). Analysis of Guangxi Marine Disaster Risk. *Guangxi. Sci.* 20 (3), 248–253.

Danielsen, F. (2005). The Asian Tsunami: A Protective Role for Coastal Vegetation. *Science* 310 (5748), 643–643.

Devi, C., Jairaj, P. G., and Balan, K. (2021). Laboratory Investigations on Wave Attenuation Characteristics of Rhizophora Mucronata Poir Using Physical Models With Bottom Friction. *Environ. Fluid. Mech.* 21 (2), 361–81. doi: 10.1007/s10652-020-09777-z

Easterling, D. R. (2000). Climate Extremes: Observations, Modeling, and Impacts. *Science.* 289 (5487), 2068–2074. doi: 10.1126/science.289.5487.2068

Foster-Martinez, M. R., Lacy, J. R., Ferner, M. C., and Variano, E. A. (2018). Wave Attenuation Across a Tidal Marsh in San Francisco Bay. *Coast. Eng.* 136, 26–40. doi: 10.1016/j.coastaleng.2018.02.001

Han, H. C, and Yang, S. H. (2004). A Review on Researches in Earliest Departure Harbor of Silk Road on Sea in Ancient China. *Scient. Geograph. Sinica.* 24 (6), 738–745. doi: 10.3969/j.issn.1000-0690.2004.06.017

Hashim, A. M., Catherine, S., and Takaijudin, H. (2013). Effectiveness of Mangrove Forests in Surface Wave Attenuation: A Review. *Res. J. Appl. Sci. Eng. Technol.* 5 (18), 4483–4488. doi: 10.19026/rjaset.5.4361

Hegge, B. J., and Masselink, G. (1996). Spectral Analysis of Geomorphic Time Series: Auto–Spectrum. *Earth Surf. Process. Landf.* 21, 1021–1040. doi: 10.1002/(SICI)1096-9837(199611)21:11<1021::AID-ESP703>3.0.CO;2-D

Horstman, E. M., Dohmen-Janssen, C. M., Narra, P. M. F., van denBerg, N. J. F., Siemerink, M., Hulscher, S. J. M. H., et al. (2014). Wave Attenuation in Mangroves: A Quantitative Approach to Field Observation. *Coast. Eng.* 94, 47–62. doi: 10.1016/j.coastaleng.2014.08.005

Huang, Z. M., Zhou, X. Y., Dai, Z. J, Che, Z. W, et al. (2022). Analysis of Suspended Sediment Concentration Variations Invertical Profile Near-Bed of Aegiceras Corniculatum Tidal Flat. *J. Trop. Oceanogr*. doi: 10.11978/2021167

Hu, Z., Suzuki, T., Zitman, T., Uittewaal, W., and Stive, M. (2014). Laboratory Study on Wave Dissipation by Vegetation in Combined Current–Wave Flow. *Coast. Eng.* 88, 131–142. doi: 10.1016/j.coastaleng.2014.02.009

Kinver, M. (2016). *Let Mangroves Recover to Protect Coasts* (London, British: BBC News). Available at: http://www.bbc.com/news/science-environment-37386267.

Li, S., Dai, Z., Mei, X., Huang, H., Wei, W., Gao, J., et al. (2017). Dramatic Variations in Water Discharge and Sediment Load From Nanliu River (China) to the Beibu Gulf During 1960s–2013. *Quater. Int.* 440, 12–23. doi: 10.1016/j.quaint.2016.02.065

Massel, S. R., Furukawa, K., and Brinkman, R. M. (1999). Surface Wave Propagation in Mangrove Forests. *Fluid. Dyn. Res.* 24 (4), 219–249. doi: 10.1016/S0169-5983(98)00024-0

Maza, M., Lara, J. L., and Losada, I. J. (2021). Predicting the Evolution of Coastal Protection Service With Mangrove Forest Age. *Coast. Eng.* 168, 103922. doi: 10.1016/j.coastaleng.2021.103922

Mazda, Y., Wolanski, E., King, B., Sase, A., Ohtsuka, D., and Magi, M. (1997b). Drag Force Due to Vegetation Inmangrove Swamps. *Mangr. Salt. Marshes.* 1, 193–199. doi: 10.1023/A:1009949411068

Mazda, Y., Magi, M., Ikeda, Y., Kurokawa, T., and Asano, T. (2006). Wave Reduction in a Mangrove Forest Dominated by Sonneratia Sp. *Wetl. Ecol. Manage.* 14 (4), 365–378. doi: 10.1007/s11273-005-5388-0

Mazda, Y., Magi, M., Kogo, M., and Nguyen, H. P. (1997a). Mangroves as a Coastal Protection From Waves in the Tong King Delta, Vietnam. *Mangr. Salt. Marshes.* 1 (2), 127–135. doi: 10.1023/A:1009928003700

McIvor, A. L., Möller, I., Spencer, T., and Spalding, M. (2012). Reduction of Wind and Swell Waves by Mangroves. *Natural Coastal Protection Series.*

McIvor, A., Spencer, T., Spalding, M., Lacambra, C., and Möller, I. (2015). "Chapter 14 - Mangroves, Tropical Cyclones, and Coastal Hazard Risk Reduction A2 - Shroder, John F," in *Coastal and Marine Hazards, Risks, and Disasters*. Eds. J. T. Ellis and D. J. Sherman (Boston: Elsevier), 403–429.

Montgomery, J. M., Bryan, K. R., Mullarney, J. C., and Horstman, E. M. (2019). Attenuation of Storm Surges by Coastal Mangroves. *Geophys. Res. Lett.* 46 (5), 2680–2689. doi: 10.1029/2018GL081636

Parvathy, K. G., and Bhaskaran, P. K. (2017). Wave Attenuation in Presence of Mangroves: A Sensitivity Study for Varying Bottom Slopes. *Int. J. Ocean. Climate Syst.* 8 (3), 126–134. doi: 10.1177/1759313117702919

Peralta, G., van Duren, L., Morris, E., and Bouma, T. (2008). Consequences of Shoot Density and Stiffness for Ecosystem Engineering by Benthic Macrophytes in Flow Dominated Areas: A Hydrodynamic Flume Study. *Mar. Ecol. Prog. Ser.* 368, 103–115. doi: 10.3354/meps07574

Quartel, S., Kroon, A., Augustinus, P. G. E. F., Van Santen, P., and Tri, N. H. (2007). Wave Attenuation in Coastal Mangroves in the Red River Delta, Vietnam. *J. Asian Earth Sci.* 29 (4), 576–584. doi: 10.1016/j.jseaes.2006.05.008

State Oceanic Administration (1998). *China's Coastal Embayment (Volume 14: Important Estuaries)* (Beijing, China: China Ocean Press), 754–781.

Temmerman, S., Meire, P., Bouma, T. J., Herman, P. M. J., Ysebaert, T., De Vriend, H. J., et al. (2013). Ecosystem-Based Coastal Defence in the Face of Global Change. *Nature* 504 (7478), 79–83. doi: 10.1038/nature12859

Thuy, N. B., Nandasena, N. A. K., Dang, V. H., Kim, S., Hien, N. X., Hole, L. R., Thai, T. H., et al. (2017). Effect of River Vegetation With Timber Piling on Ship Wave Attenuation: Investigation by Field Survey and Numerical Modeling. *Ocean. Eng.* 129, 37–45. doi: 10.1016/j.oceaneng.2016.11.004

Tomlinson, P. B. (2016). *The Botany of Mangroves. 2nd Ed* (Cambridge. UK: Cambridge Univ Press).

Tuyen, N. B., and Hung, H. V. (2009). "An Experimental Study on Wave Reduction Efficiency of Mangrove Forests," in *Proceeding of the 5th International Conference on Asian Pacific Coasts (APAC2009).* (Singapore: Nanyang Technological University (NTU). Vol. 4, 336–43

Van der Stocken, T., Dustin, C., Dimitris, M., Carroll, D., Menemenlis, D., Simard, M., et al. (2019). Global-Scale Dispersal and Connectivity in Mangroves. *P. Natl. Acad. Sci. U S A* 116 (3), 915–922. doi: 10.1073/pnas.1812470116

Vo-Luong, P., and Massel, S. (2008). Energy Dissipation in non-Uniform Mangrove Forests of Arbitrary Depth. *J. Mar. Syst.* 74 (1-2), 603–622. doi: 10.1016/j.jmarsys.2008.05.004

Willemsen, P. W. J. M., Horstman, E. M., Borsje, B. W., Friess, D. A., Dohmen-Janssen, C. M., et al. (2016). Sensitivity of the Sediment Trapping Capacity of an Estuarine Mangrove Forest. *Geomorphology.* 273 (15), 189–201. doi: 10.1016/j.geomorph.2016.07.038

Wu, Z., Chen, J., Jiang, C., and Deng, B. (2021). Simulation of Extreme Waves Using Coupled Atmosphere-Wave Modeling System Over the South China Sea. *Ocean. Eng.* 221, 108531. doi: 10.1016/j.oceaneng.2020.108531

Zhang, K., Liu, H., Li, Y., Xu, H., Shen, J., Rhome, J., et al. (2012). The Role of Mangroves in Attenuating Storm Surges. *Estuar. Coast. Shelf. S.* 102-103, 11–23. doi: 10.1016/j.ecss.2012.02.021

Conflict of Interest: The authors declare that the research was conducted in the absence of any commercial or financial relationships that could be construed as a potential conflict of interest.

Publisher's Note: All claims expressed in this article are solely those of the authors and do not necessarily represent those of their affiliated organizations, or those of the publisher, the editors and the reviewers. Any product that may be evaluated in

this article, or claim that may be made by its manufacturer, is not guaranteed or endorsed by the publisher.

Copyright © 2022 Zhou, Dai, Pang, Wang and Long. This is an open-access article distributed under the terms of the Creative Commons Attribution License (CC BY). The use, distribution or reproduction in other forums is permitted, provided the original author(s) and the copyright owner(s) are credited and that the original publication in this journal is cited, in accordance with accepted academic practice. No use, distribution or reproduction is permitted which does not comply with these terms.

Advantages of publishing in Frontiers

OPEN ACCESS
Articles are free to read for greatest visibility and readership

FAST PUBLICATION
Around 90 days from submission to decision

HIGH QUALITY PEER-REVIEW
Rigorous, collaborative, and constructive peer-review

TRANSPARENT PEER-REVIEW
Editors and reviewers acknowledged by name on published articles

Frontiers
Avenue du Tribunal-Fédéral 34
1005 Lausanne | Switzerland

Visit us: www.frontiersin.org
Contact us: frontiersin.org/about/contact

REPRODUCIBILITY OF RESEARCH
Support open data and methods to enhance research reproducibility

DIGITAL PUBLISHING
Articles designed for optimal readership across devices

FOLLOW US
@frontiersin

IMPACT METRICS
Advanced article metrics track visibility across digital media

EXTENSIVE PROMOTION
Marketing and promotion of impactful research

LOOP RESEARCH NETWORK
Our network increases your article's readership